AD A056 800

HANDBOOK OF GEOPHYSICS AND SPACE ENVIRONMENTS

Scientific Editor
Shea L. Valley
Air Force Cambridge Research Laboratories

Apr 65
612 p.
Tech rept.
AFCRL-65-1(1)-1

U.S. AIR FORCE, CAMBRIDGE RESEARCH LABORATORIES
OFFICE OF AEROSPACE RESEARCH
UNITED STATES AIR FORCE
1965

011800

HANDBOOK OF GEOPHYSICS AND SPACE ENVIRONMENTS

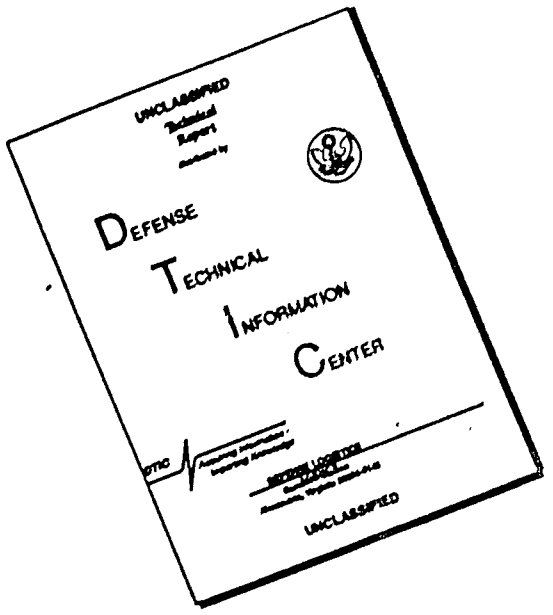
Scientific Editor
Shea L. Valley
Air Force Cambridge Research Laboratories

Apr 65
692 p.
Interim rept.
AFCRL-65-1922

U.S. AIR FORCE CAMBRIDGE RESEARCH LABORATORIES
OFFICE OF AEROSPACE RESEARCH
UNITED STATES AIR FORCE
1965

011800

DISCLAIMER NOTICE



THIS DOCUMENT IS BEST QUALITY AVAILABLE. THE COPY FURNISHED TO DTIC CONTAINED A SIGNIFICANT NUMBER OF PAGES WHICH DO NOT REPRODUCE LEGIBLY.

SECURITY CLASSIFICATION OF THIS PAGE *(When Data Entered)*

REPORT DOCUMENTATION PAGE

READ INSTRUCTIONS BEFORE COMPLETING FORM

1. REPORT NUMBER: AFCRL-65-0922	2. GOVT ACCESSION NO.
3. RECIPIENT'S CATALOG NUMBER	
4. TITLE *(and Subtitle)*: Handbook of Geophysics and Space Environments	5. TYPE OF REPORT & PERIOD COVERED: Scientific Interim
	6. PERFORMING ORG. REPORT NUMBER: AFCRL-65-0922
7. AUTHOR(s): Shea L. Valley, Editor	8. CONTRACT OR GRANT NUMBER(s): N/A
9. PERFORMING ORGANIZATION NAME AND ADDRESS: Air Force Geophysics Laboratory, Hanscom AFB, Massachusetts, 01731	10. PROGRAM ELEMENT, PROJECT, TASK AREA & WORK UNIT NUMBERS: N/A
11. CONTROLLING OFFICE NAME AND ADDRESS: Air Force Geophysics Laboratory (XOP), Hanscom AFB, Massachusetts, 01731	12. REPORT DATE: April, 1965
	13. NUMBER OF PAGES: 682
14. MONITORING AGENCY NAME & ADDRESS *(if different from Controlling Office)*	15. SECURITY CLASS. *(of this report)*: Unclassified
	15a. DECLASSIFICATION/DOWNGRADING SCHEDULE

16. DISTRIBUTION STATEMENT *(of this Report)*

Approved for Public Release. Distribution Unlimited

17. DISTRIBUTION STATEMENT *(of the abstract entered in Block 20, if different from Report)*

18. SUPPLEMENTARY NOTES

As of July, 1978, the following chapters of the Handbook have been revised and are available from DDC or NTIS: Chapter 5 (AD 703288); Chapter 9 (AD 703310); Chapter 11 (AD 759837); Chapter 17 (AD 686749); and Chapter 22 (AD 663717). No additional revisions are anticipated.

19. KEY WORDS *(Continue on reverse side if necessary and identify by block number)*

Geophysics, Space Physics, Geodesy, Gravity, Atmosphere, Ionosphere, Meteoroids, Solar Physics, Geomagnetism, Electromagnetic Radiation, Infrared Radiation, Planetary Environments, Radio Astronomy, Astrophysics, Astronomy, Lunar Environment.

20. ABSTRACT *(Continue on reverse side if necessary and identify by block number)*

This handbook is a comprehensive collection of data, formulas, definitions, and theories concerning the natural environment. It was written by scientists of the Air Force Cambridge Research Laboratories (AFCRL) which, in 1976, became the Air Force Geophysics Laboratory (AFGL). It was designed to serve a broad spectrum of users: the planner, designer, developer, and operator of aerospace systems; the scientist who will find the tables and figures a convenient reference in his own field; the specialist who needs environmental data in another discipline; and science minded people who seek a summary of space-age environmental CONT →

DD FORM 1 JAN 73 1473 EDITION OF 1 NOV 65 IS OBSOLETE

78 07 24 038

Unclassified

SECURITY CLASSIFICATION OF THIS PAGE *(When Data Entered)*

20. Abstract (continued)

research.

Revisions of individual chapters and sections of this handbook will be published as additional environmental research efforts pay off in new knowledge. ~~(See Block 18, Supplementary Notes, of this form).~~

EDITORIAL STAFF

William P. Kist

Editor

Associate Editors

M. Hale	H. Mack	D. Mellott
K. Levy	P. Maletich	R. Tonner

CONTRIBUTING AUTHORS

	Chapter
Aarons, J.	16
Atlas, D.	5, 9
Basu, S.	16
Carrigan, A. L.	13
Castelli, J. P.	16, 22
Champion, K. S. W.	3
Chernosky, E. J.	11
Cole, A. E.	2, 3, 5
Cormier, R. J.	12
Court, A.	2
Cunningham, R. M.	9
Dieter, N. H.	22
Donaldson, R. J., Jr.	5
Dubs, C.	17
Eckhard, D. H.	19
Elterman, L.	7
Evans, J. W.	15
Filz, R.	17
Fitzgerald, D. R.	8
Fougere, P. F.	11
Garing, J. S.	10
Gast, P. R.	16
Gringorten, I. I.	3, 4
Gutnick, M.	3
Hering, W. S.	6
Hernandez, G. J.	13
Howard, J. N.	10
Huffman, R. E.	6
Hunt, M. S.	19
Hunt, W. W., Jr.	6
Hutchinson, R. O.	11
Jursa, A. S.	16
Kantor, A. J.	2, 3, 5
Kantor, [illegible]	9
Katz, L.	17
Keneshea, T. J.	12
Klobuchar, J. A.	12
Lenhard, R. W., Jr.	4
Manson, J. E.	5
Markham, [illegible]	13
Newman, P.	9
Paulson, J. R.	6
Pfister, W.	12
Sagalyn, R. C.	8
Salisbury, J. W.	19, 20
Salmela, H. A.	4
Silverman, S. M.	13
Sissenwine, N.	4
Smart, D.	17
Soberman, R. K.	5, 14
Stergis, C. G.	3, 6
Szabó, Bela	1
Toolin, R. B.	7
Ulwick, J. C.	12
Ushakoff, D. W.	22
Valley, S. L.	21
Van Tassel, R. A.	20
Walker, R. G.	10
Weinberg, A.	17
White, M. L.	18
Yates, K.	17

RECD 12 OCT 1965 AFCRL RESEARCH LIBRARY
Accountability
Cancelled

DDC -
Do not copy this page.

FOREWORD

The *Handbook of Geophysics and Space Environments* is a comprehensive collection of data, formulas, definitions, and theories about the earth's environment. This information was obtained by many experts: Air Force scientists, scientists of other government organizations, industrial and university contractors, and private individuals.

The Handbook was written by scientists of the Air Force Cambridge Research Laboratories (AFCRL) to serve a broad spectrum of users: the planner, designer, developer, and operator of aerospace systems; the scientist who will find the tables and figures a convenient reference in his own field; the specialist who needs reliable environmental data in another discipline; and science-minded people who seek a summary of space-age environmental research. Thus, I consider this work a highly effective transfer mechanism for relating recent results of OAR's environmental research program to Air Force needs.

Certainly this document does not represent a final effort. As continued environmental research efforts pay off in new knowledge, AFCRL will provide the reader with the latest available information by issuing revisions of individual chapters and sections of the Handbook in the form of *Air Force Surveys in Geophysics*.

As a final note, I would like to stress that AFCRL provides scientific advice and consultation in response to requests for technical information on subjects covered in this Handbook. Specific and definable problems in these areas should be directed by government agencies and their contractors to the Evaluations Division, Deputy for Technical Plans and Operations, AFCRL, L. G. Hanscom Field, Bedford, Massachusetts 01371.

Don R. Ostrander

DON R. OSTRANDER
Major General, USAF
Commander
Office of Aerospace Research

ACCESSION for
NTIS White Section
DDC Buff Section
UNANNOUNCED
JUSTIFICATION
BY
DISTRIBUTION/AVAILABILITY CODES
Dist. SPECIAL
A

PRECEDING PAGE BLANK-NOT FILMED

INTRODUCTION

Use of the word geophysics in the title of this Handbook requires some justification. Inspection of the Table of Contents will reveal that many topics in geophysics, for example geology, oceanography, and seismology, are missing. The topics included are those which currently concern the scientists and engineers who are engaged in research, planning, design, development, and operation of aerospace systems. Even with this restriction, some aspects had to be neglected, and others given scant treatment, in order to limit this Handbook to one volume of manageable size. As scientific editor, I am responsible for the selection of the material included or omitted; the authors are not accountable for the resulting emphasis. My decisions were based on several years experience with requests to the Air Force Cambridge Research Laboratories for technical information and assistance from Air Force agencies and their contractors. A different editor undoubtedly would have made a somewhat different selection.

The time lag between the writing and final publication of a handbook is such that there is always the risk that information in the book has become obsolete. In the case of this Handbook, the first manuscript was submitted in July 1962 and the last in October 1964. It was impractical to attempt rewriting all submissions to include information available subsequent to their preparation, but in the process of revision and review it was often possible to substitute more recent results in place of the data originally submitted.

The efforts of many individuals in addition to the authors were essential in preparing this Handbook. I cannot attempt to acknowledge each person's contribution. I must, however, thank at least three individuals by name. To M. B. Gilbert, Helen Mack, and William Kist, I owe more than acknowledgment and gratitude; without their encouragement, assistance, and guidance this Handbook would not have been published.

April, 1965

SHEA L. VALLEY

PRECEDING PAGE BLANK-NOT FILMED

TABLE OF CONTENTS

CHAPTER 1. GEODESY AND GRAVITY

1.1	FIGURE OF THE EARTH AND REFERENCE SURFACES	1-1
1.1.1	The Geoid	1-1
1.1.2	The Reference Ellipsoid	1-2
1.2	HORIZONTAL GEODETIC SURVEYING	1-2
1.2.1	Reduction to the Geoid	1-2
1.2.2	Deflections of the Vertical	1-2
1.2.3	Projection to the Ellipsoid	1-3
	1.2.3.1 The Development Method	1-3
	1.2.3.2 The Translative Method	1-3
	1.2.3.3 Pizzetti's Projection	1-3
	1.2.3.4 Projective Method of Astronomical Geodesy	1-4
1.2.4	Earth Ellipsoids	1-4
	1.2.4.1 Reference Ellipsoids	1-4
	1.2.4.2 Best-Fitting Ellipsoids	1-4
	1.2.4.3 Arc-Measuring Method	1-4
	1.2.4.4 Area Method	1-5
	1.2.4.5 Partial Systems Method	1-5
	1.2.4.6 Mean Earth Ellipsoid	1-5
1.3	VERTICAL GEODETIC SURVEYING	1-6
1.4	GRAVITY	1-6
1.4.1	The Spheroidal Earth and Normal Gravity	1-6
1.4.2	International Gravity Formula	1-7
1.4.3	Disturbing Potential and Gravity Anomaly	1-7
1.4.4	Gravimetrical Geoid and Deflections of the Vertical	1-8
1.4.5	Application of Gravity Anomalies for Geodesy	1-10
	1.4.5.1 Existing Gravity Material	1-10
	1.4.5.2 Existing Geoids	1-10
	1.4.5.3 World Geodetic System	1-10
1.4.6	Gravity Measurements	1-13
	1.4.6.1 Absolute Measurements	1-13
	1.4.6.2 Relative Measurements	1-14
1.4.7	Reduction of Gravity Measurements	1-14
1.4.8	Isostatic Equilibrium and Reduction	1-14
	1.4.8.1 Reduction Tables	1-16
	1.4.8.2 Reduction Maps	1-16
1.4.9	New Reduction Methods	1-16
1.5	GRAVITY FIELD EXTENDED TO HIGH ALTITUDES	1-16
1.5.1	Normal Gravity or Gravitation	1-16
1.5.2	Continuation of Gravity Anomalies and Disturbance	1-17
1.6	ELECTRONIC DISTANCE MEASUREMENTS	1-17
1.7	LUNAR OBSERVATIONS	1-18
1.7.1	Solar Eclipses	1-18
1.7.2	Occultations	1-18
1.7.3	Lunar Camera	1-18
1.8	ROCKET-FLASH TRIANGULATION	1-18
1.9	SATELLITE GEODESY	1-19
1.9.1	Orbits	1-20
	1.9.1.1 Geocentric Coordinate System	1-20
	1.9.1.2 Computation of Orbital Elements	1-21
	1.9.1.3 Kepler's Equation	1-21
1.9.2	Orbit Perturbations	1-21
1.9.3	Position Determination	1-22
1.9.4	Analysis of Satellite Motions to Determine Gravitational Potential	1-23
1.10	REFERENCES	1-27

PRECEDING PAGE BLANK-NOT FILMED

CHAPTER 2. MODEL ATMOSPHERES

2.1	ATMOSPHERIC STRUCTURE AND DEFINITIONS	2-1
2.2	U.S. STANDARD ATMOSPHERE, 1962	2-2
2.3	SUPPLEMENTAL ATMOSPHERES	2-2
2.4	EXTREME ATMOSPHERES	2-6
2.5	REFERENCES	2-6

CHAPTER 3. ATMOSPHERIC TEMPERATURE, DENSITY, PRESSURE, AND MOISTURE

3.1	THERMAL PRCPERTIES UP TO 90 KM	3-1
3.1.1	Energy Supply and Transformation	3-1
3.1.2	Station Temperatures	3-2
	3.1.2.1 Probability Distributions	3-7
	3.1.2.2 Highest and Lowest Temperatures	3-8
3.1.3	Upper Air Temperatures	3-11
	3.1.3.1 Variability Below 30 Km	3-12
	3.1.3.2 Variability Above 30 Km	3-12
3.1.4	Speed of Sound vs Temperature	3-14
3.1.5	The Lower Level Air Temperatures	3-14
3.1.6	Earth/Air Interface Temperatures	3.19
3.1.7	Subsoil Temperatures	3-20
3.1.8	Miscellaneous	3-23
3.2	ATMOSPHERIC DENSITY UP TO 90 KM	3-23
3.2.1	Distribution Below 30 Km	3-23
	3.2.1.1 Statistical Applications to Reentry Problems	3-23
	3.2.1.2 Latitudinal Variations	3-23
	3.2.1.3 Seasonal Variations	3-25
	3.2.1.4 Interdiurnal and Diurnal Variations	3-25
	3.2.1.5 Interlevel Correlations	3-26
	3.2.1.6 Density-Wind Correlations	3-27
3.2.2	Distribution Between 30 and 90 Km	3-27
	3.2.2.1 Latitudinal and Seasonal Variability	3-28
	3.2.2.2 Interdiurnal and Diurnal Changes	3-28
3.3	ATMOSPHERIC PRESSURE UP TO 90 KM	3-29
3.3.1	Sea-Level Pressure	3-29
3.3.2	Variations in Height of Constant Pressure Surfaces	3-30
	3.3.2.1 Seasonal and Daily Variations	3-30
	3.3.2.2 Diurnal and Semidiurnal Variations	3-31
3.4	ATMOSPHERIC WATER VAPOR	3-31
3.4.1	Polar Model	3-34
3.4.2	Midlatitude Model	3-34
3.4.3	Tropical Observations	3-34
3.5	TEMPERATURE, DENSITY, AND PRESSURE (90 TO 300 KM)	3-34
3.6	VARIATIONS ABOVE 200 KM	3-38
3.6.1	Diurnal Density Variations	3-39
3.6.2	Density as a Function of Solar Flux	3-39
3.6.3	Annual and Semiannual Density Variations	3-40
3.6.4	Effects of Magnetic Storms on Density	3-40
3.6.5	Latitude Effects	3-41
3.6.6	Diurnal Temperature Variations	3-41
3.6.7	Temperature as a Function of Solar Flux	3-43
3.6.8	Effects of Magnetic Storms on Temperature	3-43
3.7	REFERENCES	3-43

CHAPTER 4. WINDS

4.1	MEAN WIND AS A FUNCTION OF HEIGHT	4-1
4.1.1	Variation of Mean Wind Speed (Lowest 300 Ft)	4-1

4.1.2	Wind Direction Shifts (Lower 10,000 Ft)	4-2
4.1.3	Diurnal Variation and Low-Level Jet Streams (Lower 6000 Ft)	4-4
4.2	LARGE-SCALE WIND STRUCTURE	4-6
4.2.1	Time Variability up to 30 Km	4-6
4.2.2	Spatial Variability up to 30 Km	4-8
4.2.3	Variability Above 30 Km	4-8
	4.2.3.1 Seasonal Variation	4-15
	4.2.3.2 Diurnal Variation	4-17
4.3	WIND SHEAR	4-17
4.4	TROPOSPHERIC WIND PROFILES FOR VEHICLE DESIGN	4-20
4.4.1	Synthetic or Discrete Wind Profiles for Preliminary Design	4-21
4.4.2	Other Methods of Predicting Winds for Design Purposes	4-27
4.4.3	Final Design Calculations	4-27
4.4.4	Ballistic Profiles	4-28
4.5	DESIGN DATA ON WINDS	4-29
4.5.1	Hourly Surface Wind Speeds	4-33
4.5.2	Extreme Surface Wind Speeds	4-33
4.5.3	Wind Direction, Speed, and Variability Below 100,000 Ft	4-38
4.5.4	Structure of Jet Streams	4-44
4.5.5	Observed Winds Above 100,000 Ft	4-45
4.6	REFERENCES	4-45

CHAPTER 5. PRECIPITATION, CLOUDS, AND AEROSOLS

5.1	PRECIPITATION	5-1
5.1.1	Surface Rates of Precipitation	5-1
	5.1.1.1 Clock Hourly Rates	5-1
	5.1.1.2 Instantaneous Rates of Precipitation	5-2
	5.1.1.3 Separation of Rainfall and Snowfall	5-4
	5.1.1.4 Extreme Rates of Rainfall	5-4
5.1.2	Hail	5-5
	5.1.2.1 Horizontal Extent	5-5
	5.1.2.2 Vertical Extent	5-6
	5.1.2.3 Size of Hail	5-6
5.2	MODEL ATMOSPHERES FOR PRECIPITATION	5-6
5.2.1	Widespread Precipitation	5-6
	5.2.1.1 Water Content of Clouds	5-9
	5.2.1.2 Particle Size Distribution	5-10
	5.2.1.3 Integrals of Diameter over the Size Distribution	5-10
5.2.2	Thunderstorm Rainfall	5-10
5.2.3	Real Precipitation Distributions	5-11
5.3	CLOUDS	5-11
5.3.1	Data Available from Surface Observations	5-11
	5.3.1.1 Summaries of Surface Observations	5-12
	5.3.1.2 Limitations in the Use of Summaries for a Particular Station	5-12
5.3.2	Data Available from Aircraft and Radar	5-14
5.3.3	Vertical Extent of Cirrus Clouds	5-14
5.3.4	Frequency of Occurrence of Cloud Formations Above 20,000 Ft.	5-14
5.3.5	Horizontal Extent of Cirrus Clouds	5-15
5.3.6	Maximum Water Content of Clouds	5-15
5.4	NOCTILUCENT CLOUDS	5-20
5.5	AEROSOLS	5-22
5.5.1	Size Range and Field of Importance	5-22
5.5.2	Size Distribution	5-23
5.5.3	Characteristics of Aerosols at Various Altitudes	5-24
5.5.4	Interaction with Radioactive Material	5-25
5.5.5	Impaction of Aerosol Particles on Aircraft	5-25
5.6	REFERENCES	5-25

CHAPTER 6. ATMOSPHERIC COMPOSITION

6.1	PRINCIPAL CONSTITUENTS	6-1
6.2	OZONE	6-2
6.2.1	Regions of Ozone Formation	6-3
6.2.2	Distribution of Total Ozone	6-3
6.2.3	Vertical Ozone Distribution	6-3
6.3	ABSORPTION AND IONIZATION IN THE UPPER ATMOSPHERE	6-7
6.3.1	Molecular Nitrogen	6-9
6.3.2	Molecular Oxygen	6-12
6.3.3	Nitric Oxide	6-13
6.3.4	Atomic Oxygen and Nitrogen	6-13
6.3.5	Minor Constituents	6-14
6.3.6	Absorption Cross Sections, 100 to 1 Å	6-14
6.3.7	Average Absorption Coefficients	6-15
6.4	RECOMBINATION	6-15
6.4.1	Radiative Recombination	6-15
6.4.2	Dissociative Recombination	6-16
6.4.3	Three-Body Recombination	6-17
6.4.4	Ion-Ion Recombination	6-17
6.5	ELECTRON ATTACHMENT	6-18
6.6	ELECTRON DETACHMENT FROM NEGATIVE IONS	6-18
6.6.1	Photodetachment	6-19
6.6.2	Collisional Detachment	6-19
6.7	NON-DETACHMENT REACTIONS OF NEGATIVE IONS WITH NEUTRALS	6-20
6.8	REACTIONS OF POSITIVE IONS WITH NEUTRALS	6-20
6.9	REFERENCES	6-23

CHAPTER 7. ATMOSPHERIC OPTICS

7.1	ATMOSPHERIC ATTENUATION MODEL	7-1
7.1.1	Parameters of Atmospheric Attenuation	7-1
7.1.2	Applications	7-2
	7.1.2.1 Turbid Atmosphere	7-2
	7.1.2.2 Rayleigh Atmosphere	7-2
7.2	REFLECTANCE	7-3
7.2.1	Ground Reflectance	7-3
	7.2.1.1 Water Surfaces	7-3
	7.2.1.2 Snow, Bare Areas, and Soils	7-4
	7.2.1.3 Vegetative Formations	7-4
7.2.2	Polarization	7-4
7.2.3	Observations at High Altitudes	7-4
7.2.4	Cloud Reflectance	7-5
7.3	FLUX EMERGING FROM THE ATMOSPHERE	7-6
7.4	OPTICAL RADIATION IN THE ATMOSPHERE	7-6
7.4.1	Rayleigh Scattering (Molecular) and Polarization	7-7
7.4.2	Aerosol (Mie) Scattering	7-8
7.4.3	Atmospheric Scattering	7-8
7.4.4	Absorption Coefficients for Ozone	7-9
7.5	MEASUREMENTS OF SKYLIGHT	7-9
7.6	REFERENCES	7-36

CHAPTER 8. ATMOSPHERIC ELECTRICITY

8.1	FAIR WEATHER ELECTRICITY	8-1
8.1.1	Electrical Conductivity	8-1
8.1.2	Electric Field	8-1
8.1.3	Currents and Space Charge	8-2
8.1.4	Atmospheric Ions	8-2

8.1.5 Equilibrium Conditions 8-4
8.1.6 Variations in the Exchange Layer 8-5
8.1.7 Variations in the Free Atmosphere 8-5
8.1.8 Worldwide Current System and Maintenance of Earth's Charge 8-6
8.2 THUNDERSTORM ELECTRICITY 8-6
8.2.1 Electrostatic Field Patterns 8-7
8.2.2 Precipitation Static 8-8
8.2.3 Power Line and Building Strikes 8-8
8.2.4 Possible Strike Patterns 8-10
8.2.5 Charge and Field Variations 8-10
8.2.6 Frequency Characteristics of Radiation 8-11
8.3 REFERENCES 8-23

CHAPTER 9. SOME ASPECTS OF ELECTROMAGNETIC WAVE PROPAGATION

9.1 REFRACTIVE MODULUS IN THE TROPOSPHERE 9-1
9.1.1 Optical Wavelengths 9-1
9.1.2 Radio Wavelengths 9-1
9.1.3 Standard Profiles of Refractive Modulus 9-2
9.1.4 Variations of Refractive Moduli 9-2
9.2 ATTENUATION AND BACKSCATTERING IN THE TROPOSPHERE 9-2
9.2.1 Dielectric Properties 9-3
9.2.2 Backscattering and Attenuation Cross Sections 9-3
9.2.3 Total Reflectivity 9-9
9.2.4 Total Attenuation 9-14
9.3 IONOSPHERIC INTERACTIONS 9-14
9.3.1 Some Magneto-Ionic Formulas 9-16
9.3.2 Ionsondes and Ionograms 9-17
9.4 RADIO REFLECTIONS FROM METEOR TRAILS 9-17
9.4.1 Characteristics of a Meteor Trail 9-17
9.4.1.1 The Underdense Trail 9-19
9.4.1.2 The Overdense Trail 9-19
9.5 WHISTLERS, IONOSPHERICS, AND HYDROMAGNETIC WAVES 9-19
9.5.1 Definitions 9-20
9.5.2 Theory of Whistlers and Ionospherics 9-22
9.5.2.1 Phase Refractive Index, Neglecting Collision Effects 9-22
9.5.2.2 Eckersley Dispersion Law 9-22
9.5.2.3 Nose Frequency 9-22
9.5.2.4 Effect of Ions, Neglecting Collisions 9-22
9.5.3 Theory of Hydromagnetic Waves 9-23
9.5.4 Whistlers, Observations 9-23
9.5.5 Occurrence Statistics of Ionospherics 9-24
9.6 REFERENCES 9-26

CHAPTER 10. TRANSMISSION AND DETECTION OF *INFRARED RADIATION*

10.1 SOURCES AND DETECTORS 10-1
10.1.1 Infrared Radiation Sources 10-1
10.1.2 Infrared Detectors 10-1
10.1.3 Infrared Window Materials 10-2
10.2 ATMOSPHERIC ABSORPTION 10-2
10.3 ATMOSPHERIC EMISSION 10-6
10.3.1 Measurements from the Ground 10-7
10.3.2 Balloon Measurements 10-15
10.3.3 Clouds 10-15
10.3.4 Horizon Gradient (Limb Darkening) 10-17
10.3.5 Satellite Measurements 10-17
10.4 INFRARED CELESTIAL BACKGROUNDS 10-20

10.4.1 Stellar Backgrounds 10-25
10.4.2 IR Backgrounds Originating in the Solar System 10-28
10.5 REFERENCES 10-36

CHAPTER 11. THE GEOMAGNETIC FIELD

11.1 UNITS, DEFINITIONS, AND MEASUREMENTS 11-1
11.1.1 Elements of the Geomagnetic Field 11-1
11.1.2 Magnetic Coordinates 11-2
11.1.3 Geomagnetic Measurements 11-2
11.2 THE MAIN FIELD OF THE EARTH 11-7
11.2.1 Magnetic Charts 11-7
11.2.2 Analysis of the Main Field 11-7
11.2.2.1 Spherical Harmonic Analysis and Magnetic Dipoles 11-17
11.2.2.2 Taylor Series Analysis 11-18
11.3 THE MAIN FIELD AT HIGH ALTITUDES 11-18
11.3.1 Spherical Harmonic Extrapolation 11-19
11.3.2 Taylor Series Extrapolation 11-19
11.3.3 Comparison of Predicted and Observed Values 11-19
11.4 TIME VARIATIONS OF THE GEOMAGNETIC FIELD 11-28
11.4.1 Diurnal Variations and Direct Solar Flare Effect 11-28
11.4.2 Magnetic Disturbances and Storms 11-28
11.4.3 Magnetic Activity Indices 11-30
11.4.3.1 Indices K, a, and A 11-32
11.4.3.2 Polar Range Index Q 11-37
11.4.3.3 Variability Indices C, C_i, and C_p 11-37
11.4.3.4 Difference Indices U, u, u_i and Δ 11-39
11.4.3.5 Examples of the Activity Indices 11-39
11.4.4 Rapid Geomagnetic Variations 11-39
11.5 THE DISTANT GEOMAGNETIC FIELD 11-41
11.6 REFERENCES 11-61

CHAPTER 12. IONOSPHERIC PHYSICS

12.1 IONOSPHERIC REGIONS AND DISTURBANCES 12-1
12.1.1 Sudden Ionospheric Disturbance 12-1
12.1.2 High Latitude Absorption Events 12-2
12.1.3 F-Region Effects 12-2
12.2 ELECTRON AND ION DENSITY AND TEMPERATURE 12-2
12.2.1 Densities 12-2
12.2.2 Electron and Ion Temperatures 12-6
12.3 TOTAL ELECTRON CONTENT 12-6
12.3.1 Lunar Reflections, Cross Section, and Libration 12-6
12.3.2 Faraday Rotation of Plane of Polarization 12-15
12.3.3 Variations in Electron Content 12-15
12.4 NON-DEVIATIVE ABSORPTION 12-15
12.4.1 Absorption in an Isotropic Medium 12-17
12.4.2 Effect of the Geomagnetic Field 12-21
12.4.3 Effect of Electron Collisions With Ions 12-25
12.4.4 Absorption Due to Collisions of Ions With Neutral Particles 12-25
12.5 IONOSPHERIC WINDS 12-28
12.5.1 Drift Directions 12-28
12.5.2 Drift Velocities 12-34
12.5.3 Characteristic Velocity 12-35
12.5.4 Orientation of the Correlation Ellipse 12-35
12.5.5 Axial Ratio of Correlation Ellipses 12-35
12.5.6 Area of the 0.5-Correlation Ellipse 12-36
12.6 SPORADIC E 12-36
12.6.1 Worldwide Occurrence of E_s 12-37
12.6.2 Results of Analysis of Radio Amateur Data 12-37
12.7 REFERENCES 12-53

CHAPTER 13. AIRGLOW AND AURORAE

13.1	AIRGLOW	13-1
13.1.1	Spectrum	13-1
13.1.2	Intensity	13-1
13.1.3	Altitudes	13-1
13.1.4	Latitude Variation	13-1
13.1.5	Diurnal, Annual, and Secular Variations	13-2
	13.1.5.1 Diurnal Variation	13-3
	13.1.5.2 Annual Variation	13-3
	13.1.5.3 Secular Variation	13-4
13.2	AURORAE	13-4
13.2.1	Forms, Brightness, and Color	13-4
	13.2.1.1 Form, Condition, and Structure	13-5
	13.2.1.2 Brightness Index	13-5
	13.2.1.3 Color Class	13-6
13.2.2	Spectrum	13-6
13.2.3	Altitudes	13-6
13.2.4	Occurrences and Variations	13-6
13.3	REFERENCES	13-29

CHAPTER 14. METEORITIC PHENOMENA

14.1	DEFINITIONS	14-1
14.2	METEOROID COMPOSITION AND DENSITY	14-1
14.3	METEOROID MAGNITUDE	14-1
14.4	INTERACTION WITH ATMOSPHERE	14-2
14.5	SPEED	14-4
14.6	METEOROID MASS AND FLUX	14-5
14.7	TEMPORAL VARIATIONS AND SHOWERS	14-7
14.8	METEOROID DAMAGE	14-8
14.9	REFERENCES	14-8

CHAPTER 15. THE SUN

15.1	BASIC CHARACTERISTICS OF THE SUN	15-1
15.2	STEADY-STATE FEATURES OF THE SOLAR ATMOSPHERE	15-1
15.2.1	The Photosphere and the Line Absorbing Layer	15-1
15.2.2	The Chromosphere	15-3
15.2.3	The Corona	15-5
15.3	ENERGY OF THE SUN	15-6
15.4	TRANSIENT SOLAR PHENOMENA	15-7
15.4.1	Prominences	15-7
15.4.2	Active Centers	15-10
15.4.3	Flares	15-11
15.5	PROTON SHOWERS IN SPACE NEAR EARTH	15-12
15.6	TERRESTRIAL EFFECTS OF SOLAR EMISSIONS	15-12
15.7	SOLAR TRANSIENTS AND WEATHER	15-13

CHAPTER 16. SOLAR ELECTROMAGNETIC RADIATION

16.1	SOLAR IRRADIANCE	16-1
16.1.1	Irradiance Outside the Earth's Atmosphere	16-1
16.1.2	Irradiance Within the Earth's Atmosphere	16-7
16.2	SOLAR ULTRAVIOLET AND X RAYS	16-10
16.2.1	Solar Spectrum, 3000 to 1800 Å	16-10
16.2.2	Solar Emission Lines, 1900 to 60 Å	16-10
16.2.3	Solar X-Ray Emission	16-12
16.2.4	Intensity of Radiation Below 3000 Å	16-12
16.3	SOLAR RADIO EMISSION	16-18
16.3.1	Quiet Sun Temperature and Flux	16-18

16.3.2 Calculation of Solar Temperature and Flux from Antenna Temperature ... 16-21
16.3.3 Flux of the Slowly Varying Component ... 16-23
16.3.4 Description of the Rapidly Varying Component ... 16-24
16.3.4.1 Meter-Wave Range (25 to 580 Mcps) ... 16-24
16.3.4.2 Decimeter-Wave Range (500 to 950 Mcps) ... 16-25
16.3.4.3 Centimeter-Wave Range (3000 to 30,000 Mcps) ... 16-25
16.3.5 The Disturbed Sun as a Radio Source ... 16-26
16.4 REFERENCES ... 16-38

CHAPTER 17. CORPUSCULAR RADIATION

17.1 BASIC RELATIONS ... 17-1
17.1.1 Nomenclature and Definitions ... 17-1
17.1.2 Trapped Particle Motion in a Magnetic Field ... 17-2
17.2 TRAPPED RADIATION ... 17-3
17.2.1 Spatial Parameters of Trapped Particles ... 17-3
17.2.2 Injection and Loss of Particles ... 17-6
17.2.3 Measurements of Naturally Occurring Trapped Radiation ... 17-7
17.2.4 Protons ... 17-7
17.2.5 Electrons ... 17-10
17.2.6 Man-Made Trapped Radiation ... 17-10
17.3 COSMIC RADIATION ... 17-11
17.3.1 Composition and Energy ... 17-12
17.3.2 Charged Particle Flux Within the Atmosphere ... 17-14
17.3.2.1 Latitude and Longitude Dependence ... 17-14
17.3.2.2 Minimum Momentum ... 17-14
17.3.3 Flux Modulations ... 17-14
17.4 HIGH ENERGY PARTICLES FROM SOLAR FLARES ... 17-19
17.4.1 Composition, Rigidity, and Flux of Solar Cosmic Rays ... 17-19
17.4.2 Variations in Time and Direction of Solar Cosmic Rays ... 17-21
17.5 REFERENCES ... 17-31

CHAPTER 18. INTERPLANETARY SPACE AND THE SOLAR ATMOSPHERE

18.1 OBSERVATIONAL DATA FOR INTERPLANETARY SPACE ... 18-1
18.1.1 Electron Densities ... 18-1
18.1.2 Interplanetary Magnetic Fields ... 18-2
18.1.3 Solar Wind ... 18-2
18.2 MODELS OF THE CORONAL ATMOSPHERE ... 18-2
18.2.1 Inverse Square and Semi-Empirical Models ... 18-2
18.2.2 Chapman's Model ... 18-3
18.2.3 Chamberlain's Models ... 18-4
18.2.4 Sen's Electric Field Models ... 18-5
18.2.5 Parker's Models ... 18-5
18.2.6 Alternate Interpretations of Parker's Equations ... 18-5
18.2.7 Scale Heights for the Solar Atmosphere ... 18-7
18.3 SOLAR AND INTERPLANETARY MAGNETIC FIELDS ... 18-7
18.3.1 Solar Magnetic Cycle and Sunspots ... 18-8
18.3.2 Interplanetary Magnetic Field and Distortion of Solar Dipole Field 18-9
18.3.3 Effects of Rotation on Magnetic Lines of Force ... 18-11
18.4 SOLAR METEOROLOGY AND ENERGY TRANSPORT ... 18-11
18.4.1 Solar Rotation ... 18-11
18.4.2 Reynolds and Prandtl Numbers ... 18-13
18.4.3 Transport Coefficients from Gas Kinetics ... 18-13
18.4.4 Solar-Wide Atmospheric Motions ... 18-14
18.4.5 Energy Transport Processes ... 18-16
18.5 TENTATIVE MORPHOLOGY OF THE SOLAR CYCLE ... 18-17
18.6 REFERENCES ... 18-19

CHAPTER 19. THE LUNAR ENVIRONMENT

19.1	ATMOSPHERE	19-1
19.2	THERMAL ENVIRONMENT	19-1
19.3	MAGNETIC FIELD	19-1
19.4	COMPOSITION	19-6
19.5	SURFACE AND SUBSURFACE STRUCTURE	19-6
19.5.1	Lunar Surface Roughness	19-9
19.6	LUNAR RESOURCES	19-13
19.7	LUNAR MOTION	19-13
19.7.1	Rotation and Librations	19-13
19.7.2	Librations and the Lunar Mechanical Figure	19-14
19.8	LUNAR GRAVITY FIELD	19-14
19.9	SUGGESTED VALUES OF LUNAR CONSTANTS	19-15
19.10	REFERENCES	19-16

CHAPTER 20. PLANETARY ENVIRONMENTS

20.1	MERCURY	20-1
20.1.1	General	20-1
20.1.2	Tabular Data for Mercury	20-1
20.2	VENUS	20-1
20.2.1	Atmosphere	20-1
	20.2.1.1 Clouds	20-2
	20.2.1.2 Pressure and Temperature	20-2
	20.2.1.3 Circulation	20-2
20.2.2	Thermal Environment	20-3
20.2.3	Magnetic Field	20-3
20.2.4	Surface Features	20-3
20.2.5	Satellites	20-3
20.2.6	Tabular Data for Venus	20-5
20.3	MARS	20-5
20.3.1	Atmospheric Composition	20-5
20.3.2	Atmospheric Structure	20-5
20.3.3	Atmospheric Circulation	20-7
20.3.4	Yellow and White Clouds	20-10
20.3.5	Blue Haze	20-10
20.3.6	Magnetic Field	20-11
20.3.7	Surface Temperatures and Features	20-11
20.3.8	Satellites	20-13
20.3.9	Tabular Data for Mars	20-13
20.4	JUPITER	20-13
20.4.1	Satellites	20-15
20.4.2	Tabular Data for Jupiter	20-15
20.5	SATURN	20-15
20.5.1	Satellites	20-15
20.5.2	Tabular Data for Saturn	20-16
20.6	URANUS	20-16
20.6.1	Satellites	20-16
20.6.2	Tabular Data for Uranus	20-16
20.7	NEPTUNE	20-16
20.7.1	Satellites	20-16
20.7.2	Tabular Data for Neptune	20-16
20.8	PLUTO	20-17
20.8.1	General	20-17
20.8.2	Tabular Data for Pluto	20-17
20.9	REFERENCES	20-19

CHAPTER 21. ASTROPHYSICS AND ASTRONOMY

21.1	GENERAL SURVEY	21-1
21.2	DEFINITIONS, UNITS, AND BASIC RELATIONS	21-1
21.2.1	Time, Distance and Motion; Solar Values as Units	21-1
21.2.2	Celestial Coordinate Systems	21-4
	21.2.2.1 Horizon System (Azimuth and Altitude)	21-4
	21.2.2.2 Equatorial Systems	21-4
	21.2.2.3 Conversion Between Horizon and Equatorial Systems	21-7
	21.2.2.4 Ecliptic System	21-7
	21.2.2.5 Galactic Systems	21-7
21.2.3	Names and Categories of Stars	21-7
	21.2.3.1 Supergiants, Giants, Dwarfs, and White Dwarfs	21-7
	21.2.3.2 Binary and Multiple Stars	21-7
21.2.4	Stellar Magnitudes	21-9
21.2.5	Color Index and Photometric Color Systems	21-10
21.2.6	Spectroscopic Terminology	21-10
21.2.7	Curve of Growth	21-10
21.2.8	Spectral Type and Temperature	21-11
21.2.9	Saha Theory of Ionization	21-12
21.2.10	Luminosity, Temperature, and H-R Diagrams	21-12
21.3	STELLAR MASSES AND LUMINOSITIES	21-14
21.3.1	Direct Measurement of Mass	21-14
21.4	CLASSIFICATION OF STARS	21-14
21.4.1	Luminosity Criteria	21-14
	21.4.1.1 MK (Luminosity Class) System	21-14
	21.4.1.2 Two-Color Diagram (U — B vs B — V)	21-15
21.4.2	Quantitative Methods of Spectral Classification	21-17
	21.4.2.1 Barbier-Chalonge Classification	21-17
	21.4.2.2 Strömgren's Narrow-Band Photometry	21-18
21.5	INTERSTELLAR GAS AND DUST	21-18
21.5.1	Interstellar Absorption Lines	21-18
21.5.2	Interstellar Gas Clouds	21-19
21.5.3	Interstellar Reddening and Color Excess	21-19
	21.5.3.1 Interstellar Dust and Polarization	21-19
	21.5.3.2 Statistically Corrected Distance of a Star	21-19
21.5.4	Relation of Dust Clouds to Gas Clouds	21-19
21.6	STELLAR EVOLUTION	21-20
21.6.1	Nuclear Reactions, Stellar Interiors, and H-R Diagrams	21-20
21.6.2	Loss of Mass During Evolution	21-21
21.6.3	Populations I and II	21-21
21.6.4	Clusters and Associations	21-21
	21.6.4.1 O and T Associations	21-21
	21.6.4.2 Galactic (Open) Clusters	21-22
	21.6.4.3 Globular Clusters	21-22
21.6.5	H-R Diagrams of Clusters	21-22
21.7	INTRINSICALLY VARIABLE STARS	21-23
21.7.1	Dwarf Irregular Variable Stars	21-23
	21.7.1.1 T Tauri Stars	21-23
	21.7.1.2 Flare or UV Ceti Stars	21-23
	21.7.1.3 U Geminorum (SS Cygni) Stars	21-24
21.7.2	Pulsating Stars	21-24
	21.7.2.1 RR Lyrae Stars	21-26
	21.7.2.2 Cepheids	21-26
21.7.3	Novae and Supernovae	21-27
21.8	DETERMINATION OF STELLAR DISTANCES	21-27
21.8.1	Parallax and Proper Motion	21-27
21.8.2	Spectroscopic Methods	21-28
21.8.3	The Period-Luminosity Relation	21-28
21.8.4	The Distance Scale	21-28
21.9	GALAXIES	21-28
21.10	REFERENCES	21-29

CHAPTER 22. RADIO ASTRONOMY

22.1	FUNDAMENTAL CONCEPTS AND DEFINITIONS	22-1
22.2	EFFECTS OF THE EARTH'S ATMOSPHERE	22-2
22.2.1	Refraction	22-2
22.2.2	Scintillation	22-3
22.2.3	Absorption	22-3
22.3	RADIO EMISSION FROM THE MOON AND PLANETS	22-3
22.3.1	The Moon	22-3
22.3.2	The Planets	22-5
	22.3.2.1 Mercury	22-5
	22.3.2.2 Venus	22-5
	22.3.2.3 Mars	22-5
	22.3.2.4 Jupiter	22-5
	22.3.2.5 Saturn	22-5
22.4	SOURCES OF RADIO EMISSIONS	22-5
22.4.1	Maps of Background Radiation	22-5
22.4.2	Discrete Sources	22-7
22.5	HYDROGEN 21-CM LINE	22-7
22.6	OH LINE AT 18 CM	22-9
22.7	REFERENCES	22-15

APPENDIX A — UNITS, CONSTANTS, AND CONVERSION FACTORS

APPENDIX B — BLACKBODY RADIATION

INDEX

Chapter 1

GEODESY AND GRAVITY

Bela Szabó*

The objectives of geodesy are to determine the size and shape of the earth and to establish a uniform and precise system of specifying positions on the surface (latitude, longitude, and elevation). Classical geodesy is geometrical; triangulation, geodetic astronomy and astronomical, spirit, and trigonometric levelings are used to determine positions. Triangulation and astronomical observations are limited to accessible land areas, and astrogeodetic systems extended homogeneously over a continent are relative systems, incomparable with each other. Physical geodesy uses gravity anomalies (differences between theoretical and observed values) and considers effects of topography and the internal structure of the crust. In principle, the methods of physical geodesy can reduce the relative astrogeodetic systems to a single absolute system without direct survey connections across the oceans; however, there is not enough gravimetric information to employ this method universally. The gravimetric method cannot furnish accurate long distance information necessary for the establishment of the scale of a universal geodetic system.

New geodetic methods have been developed as a result of the advances in electronics, astronomical and photographic techniques, time-communication systems, high-altitude rockets and artificial satellites. These new methods connect isolated areas and continents. Some of the new methods are not yet developed to their full capacity; however, in the long range they promise great accuracy. Most of the modern methods are three dimensional, and some of them provide absolute positions.

1.1 FIGURE OF THE EARTH AND REFERENCE SURFACES

In geodesy, three different earth surfaces are used: the earth's surface on which all geodetic observations and measurements are made; the geoid, to which the astronomical and geodetic observations are referred and to which the measurements carried out on the actual surface are reduced; and the reference ellipsoid along which the mathematical computations are made and the mathematical images (projections) of the points on the earth's surface are established. Figure 1-1 illustrates the relation between the geoid and a reference ellipsoid.

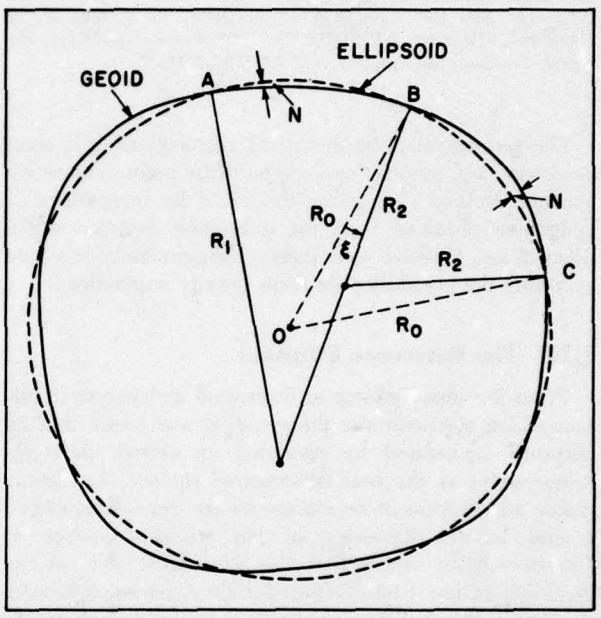


Fig. 1-1. Comparison of the geoid with a reference ellipsoid, showing the undulations (N), the meridian component of the deflection of the vertical (ξ), and the radii of various arcs; arc AB of the geoid gives too large a radius, whereas arc BC gives one too small. (From W. A. Heiskanen, Contract AF19(604)-287, *Air Force Cambridge Research Laboratories Rpt. No. AFCRC TN-56-475.*)

1.1.1 The Geoid

The geoid is defined as the equipotential surface of the gravity potential at mean sea level; thus the force of gravity is everywhere perpendicular to this surface. The undisturbed surfaces of the oceans are approximately equipotential surfaces. The surface of the earth is two-thirds water, and the continental masses are relatively small with respect to the mass of the whole earth. As a result, the geoid can be described as the mean sea level surface extended across the continents. Figure 1-2 indicates how the geoid rises in mountainous areas due to the attraction of the mass of the mountains, and is depressed in areas of mass deficiencies. The geoid, therefore, is an irregular wrapped surface, fluctuating according to the irregular distribution of masses near the earth's surfaces.

* The author acknowledges the contribution of Armando Mancini, who wrote the original rough draft of Section 1.9, Satellite Geodesy.

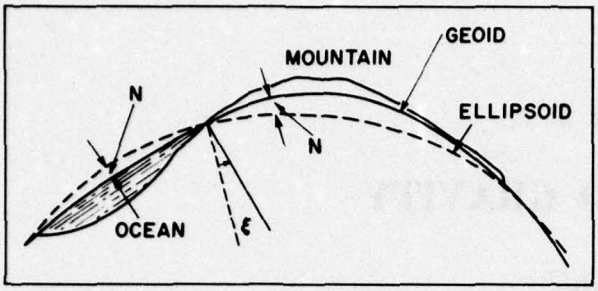


Fig. 1-2. Mass surplus of mountains and deficiencies of oceans that cause deflections of the vertical (the meridian component, ξ, is shown) and the undulation of the geoid, N. (From W. A. Heiskanen, Contract AF19(604)-287, *Air Force Cambridge Research Laboratories Rpt. No. AFCRC TN-56-475.*)

The geoid cannot be described geometrically; it must be determined by observations, point by point. The astrogeodetic method determines the geoid by integration of deflections obtained from the differences between astronomical and geodetic coordinates; the gravimetric method computes the geoid directly from gravity anomalies.

1.1.2 The Reference Ellipsoid

From the many efforts to determine an analytical surface which approximates the geoid, it was found that an ellipsoid (generated by revolving an ellipse about its minor axis) is the best geometrical surface. Geodesists define an ellipsoid of revolution by the *equatorial radius* a and by the flattening of the *meridian ellipse* f; $f = (a - b)/a$, where b is the semi-minor axis of the meridian ellipse. Many values for these parameters were derived in the past two hundred years; most of them are only of historical value because none of the purely geometrical solutions represent the best mathematical figure of the earth. Some of these ellipsoids, however, are still in use as the reference surfaces of existing geodetic control systems (land surveys).

1.2 HORIZONTAL GEODETIC SURVEYING

The horizontal survey determines the positions on the geoid of the natural projections of points lying on the earth's surface. The *natural projection* of a point is the image of the point on the geoid, projected from the earth surface along its local vertical (plumb line). The classical method of geodesy for determination of a set of horizontal positions relative to each other is the triangulation. Triangulation is the measurement of the internal angles of a chain (network) of consecutive triangles and the length of one triangle side. If the position of one point in the network and the direction of one triangle side (azimuth) are observed astronomically, or if they are known from another survey, then the coordinates of the other points in the net are computed with respect to the origin or fundamental station. To perform these computations, the observed horizontal angles and the length of the measured triangle side must be referred to a regular surface along which geometrical computations are possible; the length of the measured triangle side (base line) provides the scale, and the observed angles determine the shape of the triangulation. Theoretically, only one base line is needed; however, new base lines are measured at intervals of 200 to 300 km in order to localize the accumulation of observation errors. Redundant observations, and special observational methods to insure the elimination of the systematic effects of the instrument errors, are necessary.

1.2.1 Reduction to the Geoid

Several factors must be taken into account in reducing measurements made on the actual earth surface to the geoid. The acceleration of gravity, g, increases with the geographic latitude, so the potential $g\Delta h$ is constant only if Δh (the altitude increment) decreases with increasing g. Therefore, equipotential (level) surfaces at different heights are not parallel with one another, and they are not parallel with the basic level surface, the geoid.

The convergence of the level surfaces toward the poles creates a problem; the local plumb lines used to project points from the earth surface to the geoid are curved. This physical peculiarity requires that, in the reduction to the geoid of geodetic and astronomical observations made on the earth's surface, the plumb line's curvature must be considered. This is possible only by gravimetric means, because the horizontal gradient of g in the vertical of the station is required for the reduction. The magnitude of the effect of the plumb line curvature depends on the elevation of the station. In high mountains, it is close to the observational accuracy required for high precision work (0.1 second of arc); therefore, the reduction cannot be neglected for first order work in such areas. Horizontal angles observed at lower altitudes are reduced to the geoid without any correction, because the reduction is less than the accuracy of the observation. Base lines of triangulations are reduced to the geoid by utilizing ellipsoidal normals for the projection from the earth's surface to the geoid.

Geodetic measurements are projected to the regular surface of a selected ellipsoid of rotation. The relative position of the ellipsoid with respect to the geoid may be arbitrary within certain limits; however, the semi-minor axis of the ellipsoid must be parallel with the earth's rotation axis. This can be achieved by good astronomical observations, and it must be satisfied, because the deflections of the vertical used for the computation of the distances between geoid and ellipsoid, are defined with respect to such relative position between the two surfaces.

1.2.2 Deflections of the Vertical

The astronomical position of a station on the earth's surface, given by the *astronomical latitude* (ϕ') and *longitude* (λ'), represents the physical plumb line at that station. This plumb line is perpendicular to the level surface of the point (or to the geoid, if reduction for the vertical curvature was applied). The geodetic coordinates

of the image of this point on the reference ellipsoid, the *geodetic latitude* (ϕ) and longitude (λ), represent the geometrical normal to the ellipsoid at the image. The difference in the direction or the angle between these two directions is the deflection of the vertical; the *meridian component* of this angle is ξ and the *prime vertical component* is η. The components can be computed by the following equations:

$$\begin{aligned} \xi &= \phi' - \phi, \\ \eta &= (\lambda' - \lambda) \cos \phi, \\ \eta &= (\alpha' - \alpha) \cot \phi. \end{aligned} \tag{1-1}$$

The relation between astronomical azimuth α', and the geodetic azimuth α, is the classical Laplace equation;

$$\alpha' - \alpha = (\lambda' - \lambda) \sin \phi. \tag{1-2}$$

(Triangulation stations where astronomical longtitude and azimuth were observed are called Laplace stations.) Equation (1-2) should be satisfied in the case of errorless observations in the triangulation. The magnitude of the residual (w) is a measure of the accuracy of the observations;

$$w = (\alpha' - \alpha) - (\lambda' - \lambda) \sin \phi. \tag{1-3}$$

The deflections of the vertical computed from Eq. (1-1) are relative values. They depend on the parameters of the reference ellipsoid, on the arbitrary position of the reference ellipsoid to the geoid, and on the method of projection used between the geoid and the reference ellipsoid. Any change in these quantities or conditions will change the deflections of the vertical in the network.

1.2.3 Projection to the Ellipsoid

There are several methods of projecting the observation data from the earth's surface or from the geoid to the surface of the ellipsoid.

1.2.3.1 *The Development Method.* The triangulation net is adjusted to satisfy the geometrical conditions, then starting from the known fundamental station as origin and from an observed or adopted azimuth, the triangulation net is developed on the ellipsoid surface. The scale is determined by the measured base line, which is reduced to the geoid, but is not projected to the ellipsoid. The position of the selected reference ellipsoid relative to the geoid is determined usually by coinciding the ellipsoidal normal at the origin with the plumb line. The observed astronomical coordinates of the origin are adopted as geodetic coordinates on the ellipsoid. The geoid and ellipsoid axes must be parallel and the two normals coincident, hence the deflection of the vertical is zero at the origin. No other astronomical positions or deflections of the vertical are used in the adjustment, and usually no Laplace equations exist to control the spread of the errors in longitude and azimuth. Generally the origin and the base line are chosen approximately at the center of the surveyed area, where the reference ellipsoid is fitted close to the geoid, by shifting it in height, along the common normal at the origin. This reduces both the scale error (due to omission of base line projection from geoid to the ellipsoid) and the effect of the curvature differences between the two surfaces, provided the area of the survey is not too large and a reasonable reference ellipsoid is chosen. The resulting geodetic positions are the functions of the coordinates ϕ_o, λ_o, and α_o of the origin, and of a and f for the particular reference ellipsoid. The five parameters determine the *datum* of a geodetic system. (Geodetic positions referred to different datums are not comparable with each other in any geodetic computation; it is necessary to distinguish one geodetic control system from another by specifying their datums.) The development method has serious limitations in application; for example, if astronomical position determinations are made at geodetic positions computed by this method, the deflections of the vertical and the gap between geoid and ellipsoid systematically increase toward the edges of the survey.

1.2.3.2 *The Translative Method (Helmert's projection).* In this method, points are projected from the earth's surface directly onto the ellipsoid, using the ellipsoid normals. The relative deflections of the vertical, as direction differences between the astronomically observed physical verticals at the earth's surface and the projecting ellipsoid normals, are used and the astrogeodetic deflections are adjusted. First, the triangulation net is geometrically adjusted, then the preliminary geodetic coordinates are computed on the ellipsoid with respect to an origin where the relative deflection of the vertical is zero. Finally, the net is shifted on the surface of the reference ellipsoid under the condition that the lengths of the *geodesics* (shortest distance between two points along the surface of the ellipsoid) remain unchanged. (The net may be considered as replaced by a system of geodesics connecting each point individually with the origin.) The translative equations of Helmert [1884] give the shift at any point ($d\phi$, $d\lambda$, $d\alpha$) as a function of the shift applied at the origin ($d\phi_o$, $d\lambda_o$, $d\alpha_o$). By taking $d\phi_o$, and $d\alpha_o$ as unknowns, in terms of a minimum condition for the remaining deflections of the vertical, the solution yields the shift at the origin and the minimum position of the net. If Laplace equations were used in the net, $d\lambda_o$ and $d\alpha_o$ cannot change independently, and the minimum condition for the Laplace stations changes to $\Sigma(2\xi^2 + \eta^2\lambda + \eta^2\alpha)$ is minimum. This method eliminates the reduction of the observations for the curvature of the plumb line, which is an advantage since the information required to do this is seldom available. The disadvantage is that the deflections of the vertical are treated by the minimum least squares-solution as random errors instead of as physical quantities.

1.2.3.3 *Pizzetti's Projection.* Points from the earth's surface are projected first by the curved verticals to the geoid, then the images are projected from the geoid to the ellipsoid by the ellipsoid normals. The reduction of all geodetic and astronomic observations for the curvature of the plumb line insures that the deflections of the vertical,

the horizontal angles and lengths, are referred to the same height. The projection to the ellipsoid is achieved by an astrogeodetic adjustment similar to Helmert's projection. The system of geodetic positions computed also depends on the parameters ϕ_o, λ_o, α_o, a and f; the network and the deflections of vertical are relative.

1.2.3.4 *Projective Method of Astronomical Geodesy.* Instead of shifting the triangulation net on the ellipsoid, a parallel shift is applied to the ellipsoid with respect to the geoid. This shift changes the deflections of the vertical and the distances (geoid heights) between the ellipsoid and geoid. The second projection on the shifted ellipsoid is obtained by the projective equations [Vening-Meinesz, 1958a] without a new adjustment. These equations provide, at any station of the net, the changes in the deflection components and geoid heights caused by a change in these quantities at the origin. Similar projective equations yield the changes in the deflection of the vertical and geoid height due to the change of the equatorial radius and flattening of the ellipsoid of reference [Vening-Meinesz, 1958b].

1.2.4 Earth Ellipsoids

Table 1-1 gives the authors and the parameters of several ellipsoids, which either are used as reference surfaces for various geodetic systems or were used for significant scientific studies. With the exception of the Hayford, Krassowskij [1942], and Kaula ellipsoids, the listed values were determined as best-fitting ellipsoids to a particular section of the geoid. The Everest, Airy, Bessel, Clarke [1886, 1880], Hayford, and the Krassowoskij [1938] ellipsoids are the reference surface of major geodetic systems. Hayford's isostatically compensated solution was adopted as the International Ellipsoid recommended for general use by the General Assembly of the International Union of Geodesy and Geophysics (IUGG) in Madrid in 1924.

1.2.4.1 *Reference Ellipsoids.* These are used as a computation surface for a triangulation or for a geodetic system of an area. Usually an ellipsoid derived from previous arc measurements is chosen for this purpose. Equatorial radius and flattening are assumed to be free of errors and held fixed during the computation and adjustment of the coordinates of the points. Due to the limited extent of the survey and the special relative positioning of the selected ellipsoid with respect to the geoid of the surveyed area, the results are satisfactory for the purpose. Table 1-2 gives the reference ellipsoids and parameters of the major geodetic systems.

1.2.4.2 *Best-Fitting Ellipsoids.* These ellipsoids depend on the astrogeodetic deflection material used for the computations. The determined parameters will change with the addition of astrogeodetic information (either by densification of the stations or by the expansion of the surveyed area). They do not represent the best-fitting mathematical figure of the earth as a whole; they are only the best-fitting analytical surfaces to various limited portions of the geoid. A best-fitting ellipsoid to the geoid section of the surveyed area can be derived by either translative or projective methods. Application of the projective method is desirable from the theoretical point of view. If ellipsoidal parameter changes (radius and flattening) are also included in the solution of minimizing the deflection components, the minimum position of the system on the best-fitting ellipsoid is achieved. The projective method minimizing the remaining geoid heights has not yet been applied due to the lack of necessary data. The translative determination of a best-fitting ellipsoid may be obtained by the arc-measuring method, the area method, or the method of partial systems.

Table 1-1. Dimensions of various ellipsoids; a is equatorial radius and f is flattening of the meridian.

Identification	Year	a (meter)	1/f
Walbeck	1819	6376896	302.6
Everest	1830	6377276	300.8
Airy	1830	6377491	299.3
Bessel	1841	6377397	299.15
Pratt	1863	6378245	295.3
Clarke	1866	6378206	295.0
Clarke	1880	6378249	293.5
Helmert	1907	6378200	298.3
Hayford (International)	1910	6378388	297.0
Heiskanen	1926	6378397	(297.0) *
Krassowoskij	1938	6378245	298.3
Krassowoskij	1942	6378295	298.4
Jeffreys	1948	6378099	297.1
Ledersteger	1951	6378298	(297.0) *
U.S. Army Map Service (Hough)	1956	6378260	(297.0) *
Kaula	1961	6378163	298.24

* adopted value

1.2.4.3 *Arc-Measuring Method.* The arc measured by triangulation is divided in parts by astronomical observations at points selected along the arc between the terminals. The lengths of the parts of the arc are considered errorless; however, the central angles are corrected in the adjustment. These corrections contain the differences in the meridian component of the deflections of the verticals. The position of the arcs on the selected preliminary reference ellipsoid and the parameters of this surface are then changed to minimize the differences between geodetic and astronomic latitudes, without changing the lengths of the arcs. Each separate arc yields a separate solution. Several arc measurements can be combined and a common ellipsoid derived. Because the individual arcs will have

Table 1-2. Major geodetic systems and their parameters.

Identification and Name of Origin	Reference Ellipsoid	Geographic Coordinates of Origin		Deflections of Vertical at Origin		N* at Origin
		Latitude	Longitude	ξ_o	η_o	
European Datum 1950, (ED 50) "Helmert Tower" Potsdam	International a = 6378388 m f = 1/297	52° 22′ 51.″4469N	13° 03′ 58.″7406E	3.″363	1.″784	2.0(m)
North American Datum—1927 (NAD 27) "Meades Ranch"	Clarke 1866 a = 6378206 m f = 1/295	39° 13′ 26.″686N	98° 32′ 30.″506W	−1.″32	1.″94	6.0(m)
Tokyo Datum** (TD) Tokyo Observatory	Bessel a = 6377397.155 m f = 1/299.2	35° 39′ 17.″5148N	139° 44′ 40.″5020E	0	0	0
Indian Datum** (ID—Everest) Kalimpur	Everest a = 6377276 m f = 1/300.8	24° 07′ 11.″26N	77° 39′ 17.″57E	−0.″29	0	0
Indian Datum (ID—Intern.) Kalimpur	International a = 6378388 m f = 1/297	24° 07′ 08.″55N	77° 39′ 14.″10E	2.″42	3.″17	9.4(m)
Russian Datum** "Pulkovo 1932" Pulkovo Obs.	Bessel a = 6377397.155 m f = 1/299.2	59° 46′ 18.″710N	30° 19′ 38.″550E	0	0	0
Russian Datum "Pulkovo 1942" Pulkovo Obs.	Krassowski a = 6378245 m f = 1/298.3	59° 46′ 18.″55N	30° 19′ 42.″09E	0.″16	−1.″78	0

* See Figure 1-3.

** Initial azimuths of systems for which deflections and geoid height are not specified are:
Tokyo Datum, 156°25′ 30.″156 Tokyo Observatory to Kano Zan;
Indian Datum (Everest) 190°27′ 05.″10 (corrected by 2.″89) Kalimpur to Surantol;
Russian Datum 1932, 317°02′ 50.″62 Sablino to Bugru.

individual shifts to achieve the minimum position, the relationship between ellipsoid and geoid remains undetermined and the ellipsoid can be used only as a reference surface.

1.2.4.4 *Area Method.* The same translative adjustment of deflections of the vertical are applied to a homogenous area triangulation or to a closed frame of arcs. The basic difference between this and the arc measuring method is that this method yields the relationship between the ellipsoid and the geoid of the survey area.

1.2.4.5 *Partial Systems Method.* An extensive astrogeodetic network of a continent is divided into parts according to the geographic graticule of any other subdivision. Each part is first individually adjusted to a minimum position on the given reference surface; then, each part is substituted by the representative deflection components at the gravity center of the area. The coordinates of these gravity centers do not change with the change of the ellipsoid, provided the deflection system was previously adjusted into a minimum position. Gaps and overlaps appear at the margins of the blocks; these are eliminated as far as possible by the change of the given ellipsoid parameters. This method was used for several best-fitting ellipsoids for Europe and Russia derived by Ledersteger.

1.2.4.6 *Mean Earth Ellipsoid.* This is defined geometrically as the best-fitting ellipsoid to the whole geoid. Geodesists once believed that the translative minimum solution would yield not only the mean earth ellipsoid, but also its absolute position relative to the geoid. According to the potential theory, however, the geoid is systematically higher below the continents and its radius of curvature is shorter under the continents than above the seas. The ellipsoid which fits best the geoid below the continents thus has a systematically short equatorial radius respective to the whole earth. Because the astrogeodetic or relative deflections contain a systematic component due to the arbitrary reference ellipsoid and its arbitrary position relative to the true geoid and this systematic component cannot be separated from another

systematic part (physical) by the minimum condition of the adjustment, the absolute position of the best-fitting ellipsoid cannot be achieved by application of the translative minimum principle. There are two methods for the derivation of the mean earth ellipsoid; in both, astronomical and geometrical observations and the structure of the earth's interior are considered. One method, based on the physical character of the earth, is the adjustment of topographic-isostatic deflections of the vertical. Hayford used this method for the derivation of the International Ellipsoid. After deriving a best-fitting ellipsoid (from astrogeodetic deflection material of the U.S.A. by the area method), he computed topographic corrections to the observed deflections of the vertical and finally reduced the material according to the theory of isostatic equilibrium. Various depths were tried, from which Hayford concluded that 122.2 km is the most probable value. (From the same observational material the geometrically best-fitting solution gave a $= 6378062$ m, $1/f = 298.2$, in comparison to the values given in Table 1-1.) The other method, astrogravimetric adjustment, substitutes the relative astrogeodetic deflections with the gravimetrically computed absolute values. The results of the adjustment will be the absolute geodetic positions on the mean earth ellipsoid. Krassowoskij's ellipsoid of 1942 is an example of this method. He applied the area method for the large material of the USSR, Europe, and U.S.A.; the deflections of the vertical were in part isostatically reduced and in part gravimetrically computed.

1.3 VERTICAL GEODETIC SURVEYING

The reference (zero level) surface of the vertical geodetic surveys is the geoid. In geometrical or spirit leveling the direction of the vertical axis of the instruments coincides with the local vertical, and the tangential plane to the center of the level bubble represents a short section of the level surface at the height of the instrument. The relative differences observed by leveling are the distances between successive level surfaces measured along the local verticals. The convergence of the level surfaces affects the leveling; the technique of spirit leveling assumes that the level surfaces are parallel. A systematic effect, greater than the allowable observational errors, accumulates. Corrections, therefore, are applied for these errors.

The vertical surveys result in a system of correlated vertical control, referred to an initial quantity or datum. If the mean sea level surface is the starting point for a level line, the elevations obtained are absolute (i.e., referred to the geoid). Precise leveling lines connecting the various mean sea levels established by tidal gauges indicate that the absolute vertical datums established at different coasts are in good agreement. The largest discrepancy found, between Kornstadt USSR and the Pacific Ocean, was 1.89 m. Mean sea level, however, is not constant. Geological effects raise or lower the continents and ocean beds so that changes in the relative heights between different mean sea levels may occur.

Elevation of points are also determined by trigonometrical or physical methods. From the observed elevation angle and horizontal distance between two points, the elevation difference is computed. This method, which is less accurate than the geometrical leveling, is used in geodesy for the measurement of elevation differences between triangulation sites. The change of air pressure with the altitude provides relative and approximate values of elevation within a limited area.

1.4 GRAVITY

The gravitational acceleration can be easily computed at any point for a Newtonian field of force from the law of universal gravitation; $F = G\, m_1\, m_2/r_2$, where m_1 and m_2 are the masses of the two spherical and homogenous bodies. The earth, however, has an irregular shape, and its mass distribution is neither homogenous nor concentric; therefore, the earth's gravitational attraction on or close to the actual surface cannot be expressed accurately by this simple law. Also, because of the diurnal rotation, the earth is an accelerating frame of reference, and the force field has an additional component, the centrifugal force. At the equator this is approximately 1/3% of the gravitational attraction. The combined effect of the attraction and centrifugal forces is *gravity*, as distinguished from gravitation. Objects participating in the earth's rotation are subject to the effect of gravity; the moon, artificial satellites, and high-altitude missiles are subject to gravitation only.

The *gravitational potential* at a point is defined as the work done by gravitation when a unit mass is brought from infinity to the point. The *potential of the centrifugal force*, however, is defined as the work done by this force in moving a unit mass from a point on the earth's rotation axis to infinity. The gravitational potential combined with the potential of the centrifugal force is the potential of gravity, or *geopotential*, W. This is related to the acceleration of gravity, g, by

$$g = -\frac{\partial W}{\partial n}, \tag{1-4}$$

where n is the external normal. Gravity or gravitation is everywhere perpendicular to the respective equipotential surface, which is called a niveau surface or a level surface. The equipotential surface of gravity at mean sea level is the geoid, which is defmed by the potential equation, $W_0 =$ constant.

The part of the earth's field that can be represented by a regular mathematical model is called *normal gravity;* this is the field of an idealized earth. The irregular part of the field is the *anomalous* or *disturbing field;* it results from irregularities in mass density and distribution (deviation from the idealized earth).

1.4.1 The Spheroidal Earth and Normal Gravity

Whereas geometrical geodesy refers the geoid to a reference ellipsoid which best fits the geoid geometrically, in the potential theory the geoid is referred to a regular level surface with the same potential as the geoid ($U = W_0$). This surface, called normal spheroid, is a spheroid of revolution of regular shape, having the same mass,

volume, and flattening as the geoid; its center of gravity and rotation axis coincide with those of the earth. According to the mathematical form of its potential, the surface has a more or less complicated shape, but it is always simplier than the geoid. Spheroids which could be managed mathematically coincide within several meters with ellipsoids of rotation having axes of the same lengths; therefore, the normal spheroid can be substituted by a mean earth ellipsoid with coinciding gravity centers and rotation axis.

The normal gravity field of an ellipsoid of rotation is a mathematical convenience only. It is based on the assumptions that the normal figure of the earth is an ellipsoid of rotation, and that the mass of the earth is distributed inside this ellipsoid in such a way that the ellipsoid is an equipotential surface of the normal gravity. Thus, the ellipsoid of rotation can be used as a common reference surface for both geometrical and physical quantities, and these quantities can be computed with high precision by simple formulas.

The *potential of normal gravity* is the *spheropotential*, U. This is expressed in closed forms in terms of elliptic coordinates by Hirvonen [1960] as

$$U = \frac{GM}{c}\,\alpha + \frac{\omega^2 a^2}{2q_o}\,q\left(\sin^2\beta - \frac{1}{3}\right) + \frac{\omega^2 c^2}{2}\,\frac{\cos^2\beta}{\sin^2\alpha}\,\ldots, \qquad (1\text{-}5)$$

where G is the universal gravitational constant, M is mass of the ellipsoid, ω is the angular (rotational) velocity, c is focal radius of the ellipsoid, a is equatorial radius of the ellipsoid, α is angular eccentricity of the co-focal ellipsoid through the masspoint, and β is reduced latitude of the masspoint. $q = \frac{1}{2}[\alpha - 3\ \text{cotan}\ \alpha(1 - \alpha\ \text{cotan}\ \alpha)]$, and $q_o = \frac{1}{2}[\alpha_o - 3\ \text{cotan}\ \alpha_o(1 - \alpha_o\ \text{cotan}\ \alpha_o)]$, where α_o is angular eccentricity of the ellipsoid. At the surface of the ellipsoid U is constant and Eq. (1-5) becomes

$$U_o = \frac{GM}{c}\,\alpha_o + \frac{1}{3}\,\omega^2 a^2 . \qquad (1\text{-}6)$$

The last term of Eq. (1-5) represents the potential of the centrifugal force; without this term the formula gives the *potential of the normal gravitation*, V.

The negative gradient of the potential U is the *normal gravity*, γ,

$$\gamma = -\frac{\partial U}{\partial n} . \qquad (1\text{-}7)$$

Similarly, the *acceleration of the normal gravitation*, Γ, is the negative gradient of the potential V,

$$\Gamma = -\frac{\partial V}{\partial n} . \qquad (1\text{-}8)$$

The variation of normal gravity as a function of geographic latitude ϕ is given by empirical gravity formulas computed by the extended theorem of Clairaut; the most familiar form is

$$\gamma = \gamma_e(1 + \beta\sin^2\phi - \epsilon\sin^2 2\phi) , \qquad (1\text{-}9)$$

where γ_e is the normal gravity at the equator, $\beta = \frac{5\omega^2 a}{2\gamma_e} - f - \frac{17\,\omega^2 a}{14\,\gamma_e} f$, and $\epsilon = \frac{5}{8}\,\frac{\omega^2 a}{\gamma_e} f - \frac{1}{8} f^2$. β, the coefficient of the main latitude term, and γ_e are computed from gravity measurements; ϵ can be derived theoretically.

The original Clairaut theorem,

$$f + \frac{\gamma_{pole} - \gamma_e}{\gamma_e} = \frac{5}{2}\,\frac{\omega^2 a}{\gamma_e}, \qquad (1\text{-}10)$$

gives the simple relationship between the flattening of the ellipsoid, the angular velocity of rotation, and acceleration of normal gravity at the equator. Equation (1-10) is used for determining the earth's flattening from gravity observations, if the equatorial radius is known from other measurements. For the computation of the normal gravity for different latitudes on the surface of a given reference ellipsoid, gravity formulas [Heiskanen and Vening-Meinesz, 1958] have been derived from gravity observations in various parts of the world and from the parameters of the chosen ellipsoid. The general formula is Eq. (1-9).

1.4.2 International Gravity Formula

The General Assembly of the IUGG (Stockholm, 1930) adopted a gravity formula corresponding to the parameters of the International Ellipsoid. This formula is

$$\gamma = 978\,0490\,(1 + 0.0052884\ \sin^2\phi - 0.0000059\ \sin^2 2\phi)\quad [\text{cm sec}^{-2}]. \qquad (1\text{-}11)$$

Table 1-3 lists the constants used in connection with the International Ellipsoid and Gravity Formula. (Note that these values are not identical with those in Table 1-7, which are used in satellite geodesy.) Equation (1-11) is based on the world gravity base station at Potsdam, Germany. Any change in the gravity system (Sec. 1.4.6.1) by changing the reference value will require a corresponding change in the gravity formula.

1.4.3 Disturbing Potential and Gravity Anomaly

The actual potential of the earth's gravity field at a point P is defined as

$$W_P = U_P + T_P , \qquad (1\text{-}12)$$

where U_P is the normal potential, and T_P is the disturbing potential caused by irregularities in mass density and distribution or the deviation of actual mass density and distribution from the assumptions used in the derivation of U_P. If the normal gravity computed for P is γ_P and the actual gravity for the same point is g_P, the difference, $g_P - \gamma_P$, is the *gravity disturbance*, δg.

Gravity and astronomical observations together determine the magnitude and direction of g at any point on the surface of the earth. It is not possible, however, to compute the vector of the normal gravity for the same point, because the coordinates of point P, relative to the mass center of the earth are generally unknown. In prac-

Table 1-3. Constants used in connection with International Ellipsoid and Gravity Formula.

Semi-major axis (equatorial radius)	$a = 6{,}378{,}388.000$ meter
Semi-minor axis	$b = 6{,}356{,}911.946$ meter
Flattening, $(a - b)/a$	$f = 0.003367003367$
	$1/f = 297$
Eccentricity, $\sqrt{f(2-f)}$	$e = 0.08199188998$
	$e^2 = 0.006722670022$
Angular velocity (earth's rotation)	$\omega = 0.7292115146 \times 10^{-4}$ rad sec^{-1}
	$\omega^2 = 0.53174943305 \times 10^{-8}$ rad^2 sec^{-2}
Centrifugal acceleration at equator	$\omega^2 a = 3.391704203$ cm sec^{-2}
Normal gravity at equator	$\gamma_e = 978.049000$ cm sec^{-2}
Gravitational constant	$G = 6.673 \times 10^{-8}$ cm^3 g^{-1} sec^{-2}
Mass of earth	$M = 5.973 \times 10^{27}$ g
Product GM	$\mu = 3.986329045 \times 10^{20}$ cm^3 sec^{-2}
Gravity reference (Potsdam)	$g_i = 981.274 \pm 0.0003$ cm sec^{-2}
Gravity reference correction (provisional)	-0.0128 cm sec^{-2}

tice, γ is computed for another point Q, which is located along the vertical of P, and its normal potential (U) has the same value as the actual potential (W) obtained at P; $U_Q = W_P$. The two equipotential surfaces, geopotential for the observed and spheropotential for the theoretical values, having the same values do not coincide. Their separation, N, can be computed from observations. (In the special case of the geoid and ellipsoid, N is the geoid height or geoid undulation.)

If g_P was observed at a point P and the normal gravity computed at point Q on the corresponding spheropotential surface, the difference,

$$\Delta g = g_P - \gamma_Q, \tag{1-13}$$

is the *gravity anomaly* at P. In terms of the disturbing potential, T,

$$\Delta g = -\frac{\partial T}{\partial r} - \frac{2T}{r}, \tag{1-14}$$

where the first term is the gravity disturbance (δg) and the second term is called the term of Bruns. Equation (1-14) is the differential equation of physical geodesy. In a simplified practical form, it is

$$\Delta g = \delta g - \frac{2\gamma}{R} N, \tag{1-15}$$

where R is the mean radius of the earth. Figure 1-3 illustrates the physical relations between Δg, ξ, N, and a surplus or deficiency in mass.

If the geocentric rectangular coordinates (x, y, z) of P are given (as in the case of missile trajectories and satellite orbits), gravity disturbances are used. If the elevation of the point above the geoid is known (as in the case of points on the earth's surface, or in airborne gravimetry), gravity anomalies are used. In the latter case, the observed gravity at P on the surface of the earth is reduced to the geoid (sea level) to obtain g_o, and the normal gravity is computed for the corresponding point Q on the ellipsoid (γ_o). The difference,

$$\Delta g_P = g_o - \gamma_o, \tag{1-16}$$

is the *observed gravity anomaly* at P.

Centrifugal force is the same in both the normal and observed quantities so that the gravity anomaly is equal to the gravitational anomaly.

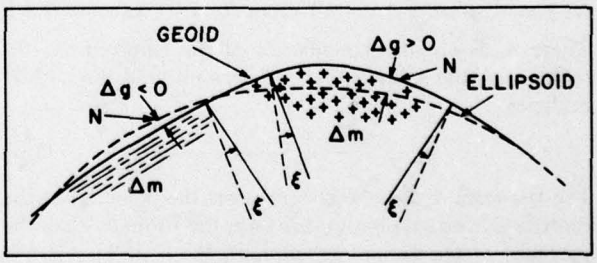


Fig. 1-3. Mass anomalies (Δm), gravity anomalies (Δg), the meridian component of the deflection from the vertical (ξ), and the undulation of the geoid (N). (From W. A. Heiskanen, Contract AF19(064-287, *Air Force Cambridge Research Laboratories Rpt. No. AFCRC TN-56-475.*)

1.4.4 Gravimetrical Geoid and Deflections of the Vertical

Equations (1-14) and (1-15) interrelate gravity anomaly, normal gravity, and the disturbing potential. If a solution for T is found, then the geoid undulation can be computed by

$$N = T/\gamma. \tag{1-17}$$

T is a harmonic function and can be solved by successive approximations using developments in series, or by a solution such as a boundary value problem without series. A closed integral expression (Stokes') for N is

$$N = \frac{R}{4\pi\gamma_m} \int_{\Psi=0}^{\pi} \int_{\alpha=0}^{2\pi} \Delta g(\Psi, \alpha) S(\Psi) \sin \Psi \, d\Psi \, d\alpha, \tag{1-18}$$

where γ_m is the mean value of normal gravity, Ψ is spherical distance from the point of computation, and α is azimuth in the coordinate system with origin at the computation point. $S(\Psi)$, Stokes' function, is

$$S(\Psi) = \operatorname{cosec} \frac{\Psi}{2} + 1 - 6 \sin \frac{\Psi}{2} - 5 \cos \Psi - 3 \cos \Psi \ln \left(\sin \frac{\Psi}{2} + \sin^2 \frac{\Psi}{2} \right). \tag{1-19}$$

Because the function $S(\Psi)$ will be too large, the effect of the area close to the point should be computed by

$$N = \frac{R}{\gamma_m} \int_{\Psi=0}^{\pi} \Delta g_m (\Psi) F(\Psi) \, d\Psi, \tag{1-20}$$

where

$$F(\Psi) = \tfrac{1}{2} \sin \Psi \cdot S(\Psi)$$

and $\Delta g_m (\Psi)$ is the mean anomaly of the circular ring.

The Stokes' formula provides the *geoid undulation*, or the distance between the geoid and ellipsoid, with respect to an ellipsoid which has the same volume as the geoid and is geocentric in location; the undulations are absolute and the formula determines only the shape, not the scale, of the geoid. There are certain conditions which restrict the validity and applicability of the theorem. The integral must be extended over the whole earth, and gravity anomalies are not available over the greater part of it. Practically, however, if the anomalies are well known for a few hundred kilometers around the point and the rest of the field can be estimated, the effect of distant anomalies are slight on the computed value of N. The formula is not valid if there are masses above the geoid; therefore, Helmert's reduction, assuming condensation of the continental masses below the geoid, must be applied. Assumptions concerning densities and the reduction of gravity observations from the surface to the geoid are also required.

The deflection of the vertical is the angle between the normals at a point to the ellipsoid and to the geoid. If the geoid is determined from gravity anomalies with respect to a reference ellipsoid the center of which coincides with the gravity center of the earth, the deflection of the vertical between the two corresponding normals will be absolute. The relationships between geoid undulations and the meridian and prime vertical components of the deflection are

$$\xi = -\frac{\partial N}{\partial x} \quad \text{and} \quad \eta = -\frac{\partial N}{\partial y}, \tag{1-21}$$

where x and y are the directions of the north-south and east-west axes respectively. Because ξ and η are small, the total deflection, ϵ, can be written in the form,

$$\epsilon = \sqrt{\xi^2 + \eta^2}. \tag{1-22}$$

For practical computation, Eq. (1-18) is written as a finite sum:

$$N = \frac{R}{4\pi\gamma_m} \Sigma \Delta g_q \int_q S(\Psi) \, dq \tag{1-23}$$

where q is a fixed surface element in the unit sphere (e.g., $1^\circ \times 1^\circ$), and Δg_q is the mean anomaly of the surface element.

For numerical computations, Eq. (1-23) is separated as follows:

$$N = \Sigma c_q \Delta g_q, \tag{1-24}$$

$$c_q = \frac{R}{4\pi\gamma_m} \int_q S(\Psi) \, dq. \tag{1-25}$$

Δg_q is taken from gravity anomaly maps; c_q is computed. The summation over the whole earth gives the geoid undulation; for the computation of c_q, the preparation of the anomalies for the selected surface elements, and a method for the use of high-speed computers, see Uotila [1960].

The formulas for the computation of the deflection of the vertical components from gravity anomalies derived by Vening-Meinesz are:

$$\xi = \frac{1}{4\pi\gamma_m} \int_{\Psi=0}^{\pi} \int_{\alpha=0}^{2\pi} \Delta g (\Psi, \alpha) \frac{dS(\Psi)}{d\Psi} \sin \Psi \cos \alpha \, d\Psi \, d\alpha, \tag{1-26}$$

$$\eta = \frac{1}{4\pi\gamma_m} \int_{\Psi=0}^{\pi} \int_{\alpha=0}^{2\pi} \Delta g (\Psi, \alpha) \frac{dS(\Psi)}{d\Psi} \sin \Psi \sin \alpha \, d\Psi \, d\alpha$$

where

$$\frac{dS(\Psi)}{d\Psi} \sin \Psi = -\left(\sin \frac{\Psi}{2} \right)^{-1} - 3 - 8 \sin \frac{\Psi}{2} + 32 \sin^2 \frac{\Psi}{2} + 12 \sin^3 \frac{\Psi}{2} - 32 \sin^4 \frac{\Psi}{2} + 3 \sin^2 \Psi \ln \left(\sin^2 \frac{\Psi}{2} + \sin \frac{\Psi}{2} \right). \tag{1-27}$$

The values of the functions

$$\frac{1}{2}\frac{dS(\Psi)}{d\Psi}\cdot\sin\Psi \text{ and } \frac{1}{2}\int_{\Psi=10\text{ m}}^{r}\frac{dS(\Psi)}{d\Psi}\sin\Psi d\Psi$$

are tabulated by Sollins [1947]. Equations (1-26) cannot be used close to the computation point because [illegible] $\left(\sin\frac{\Psi}{2}\right)^{-1}$ approaches infinity. For the computation of the effect of the inside circle, with a radius r_o of a few kilometers, the formulas are:

$$\Delta\xi = \frac{1}{2\gamma_m}\frac{\Delta g}{\Delta x}r_o, \qquad \Delta\eta = \frac{1}{2\gamma_m}\frac{\Delta g}{\Delta y}r_o, \tag{1-28}$$

where $\Delta g/\Delta x$ and $\Delta g/\Delta y$ are the gradients of gravity inside the circle r_o in the direction of the meridian and the prime vertical respectively. The horizontal gravity gradients can be computed by using point values at 45° azimuth intervals along a circular ring, a method introduced by Rice [1952].

The total deflection components are computed in parts according to the angular distance of the considered area from the computation point. The required accuracy and quantity of the gravity material decrease with the distance. Uotila divides the computations into four parts: (1) effect of the inner circle, the radius r_o (usually between 1 and 5 km) depending on the gravity field; (2) effect of the area where a detailed gravity map and the circular ring method should be used, which is up to 3° distance from the point; (3) effect of the area where 1° × 1° mean anomalies can be used, which is usually the area between 3° and 20° distance from the point; and (4) effect of the area where 5° × 5° mean anomalies can be used, which is the area between 20° and 180° from the point. The arrangement of the computations, preparation of the required maps and templates, high-speed computation of the coefficients, and summation of the products are given in detail by Uotila [1960].

1.4.5 Application of Gravity Anomalies for Geodesy

The irregularities of the geoid are caused mostly by the disturbing mass of the topography and by invisible mass anomalies inside of the earth's crust, see Fig. 1-2 and 1-3. If sufficient quantity of observed values of Δg are available, then the geoid can be determined with respect to the ellipsoid (model of the theoretical field) by computing N, ξ, and η. If the gravimetrically computed absolute geoid undulations and deflections of the vertical were utilized with triangulation and other measurements, the ellipsoid obtained would be the mean earth ellipsoid fitting best the whole geoid, rather than only a section. The geodetic control stations would then have absolute geodetic coordinates on the mean earth ellipsoid. This cannot be accomplished today with the desired accuracy because of insufficient gravity coverage.

1.4.5.1 *Existing Gravity Material.* In 1950 Ohio State University, supported by the USAF Cambridge Research Laboratories, initiated a program for the collection, analysis, cataloging and unification of available world-wide gravity material. This library now has about 300,000 stations on IBM punch cards. From the collected and analyzed material free air and isostatic mean anomalies were computed for blocks of 5° × 5°, 1° × 1°, and smaller. Certain areas are well covered but the large gaps in observational material for both land and ocean areas, especially in the southern hemisphere, represent serious deficiencies.

1.4.5.2 *Existing Geoids.* The Columbus geoid is a gravimetric geoid for the northern hemisphere [Heiskanen, 1957]. From existing free-air anomalies, 1° × 1° and 5° × 5° mean values were computed with elevation corrections. Values of N were computed at corners of 5° × 5° squares, and 5-m contour curves were drafted. Figure 1-4 shows the detailed Columbus geoid of Europe; for this the N values are computed at the corners of 1° × 1° squares and the contour interval is 2 m. Kaula [1961] published a geoid based on a combination of gravimetric, astrogeodetic, and satellite data. Geoid heights were estimated for 10° × 10° squares with standard deviation from ±10 to ±22 m. The free-air geoid is referred to an ellipsoid with flattening 1/298.24. Uotila, using in part coefficients of zonal harmonics obtained from satellite data, computed in part coefficients for spherical harmonics from direct gravity observations (free air). From these coefficients undulation values were computed in an ellipsoid with flattening 1/298.24. Figure 1-5 shows this geoid. Relative geoids were obtained from astrogeodetic deflection material for the restricted areas of each major geodetic system; examples are the geoid of the United States on Northern American Datum 1927 (published by the Army Map Service) and the geoid of Europe on European Datum 1950 [Bomford, 1962].

1.4.5.3 *World Geodetic System.* Present geodetic systems determined by the adjustment of astrogeodetic deflections of the vertical are relative systems and depend on their own initial parameters or datums. The unification of these systems without survey connections across the oceans into an earth centered world geodetic system can be accomplished by the gravimetric method, but many prerequisites must be satisfied for a theoretically correct and accurate solution. The most important of these are: (1) enough uniformly distributed gravity material for the computation of the gravimetric geoid and flattening; (2) detailed gravity surveys in specific areas to compute accurate deflection components and geoid heights at selected astronomical stations; (3) very accurate astronomical observations and the necessary gravity material to reduce these to the geoid; and (4) a correct equatorial radius of the ellipsoid. Several attempts have been made to use the existing gravity material in combination with other geodetic information to unify widely separated geodetic sys-

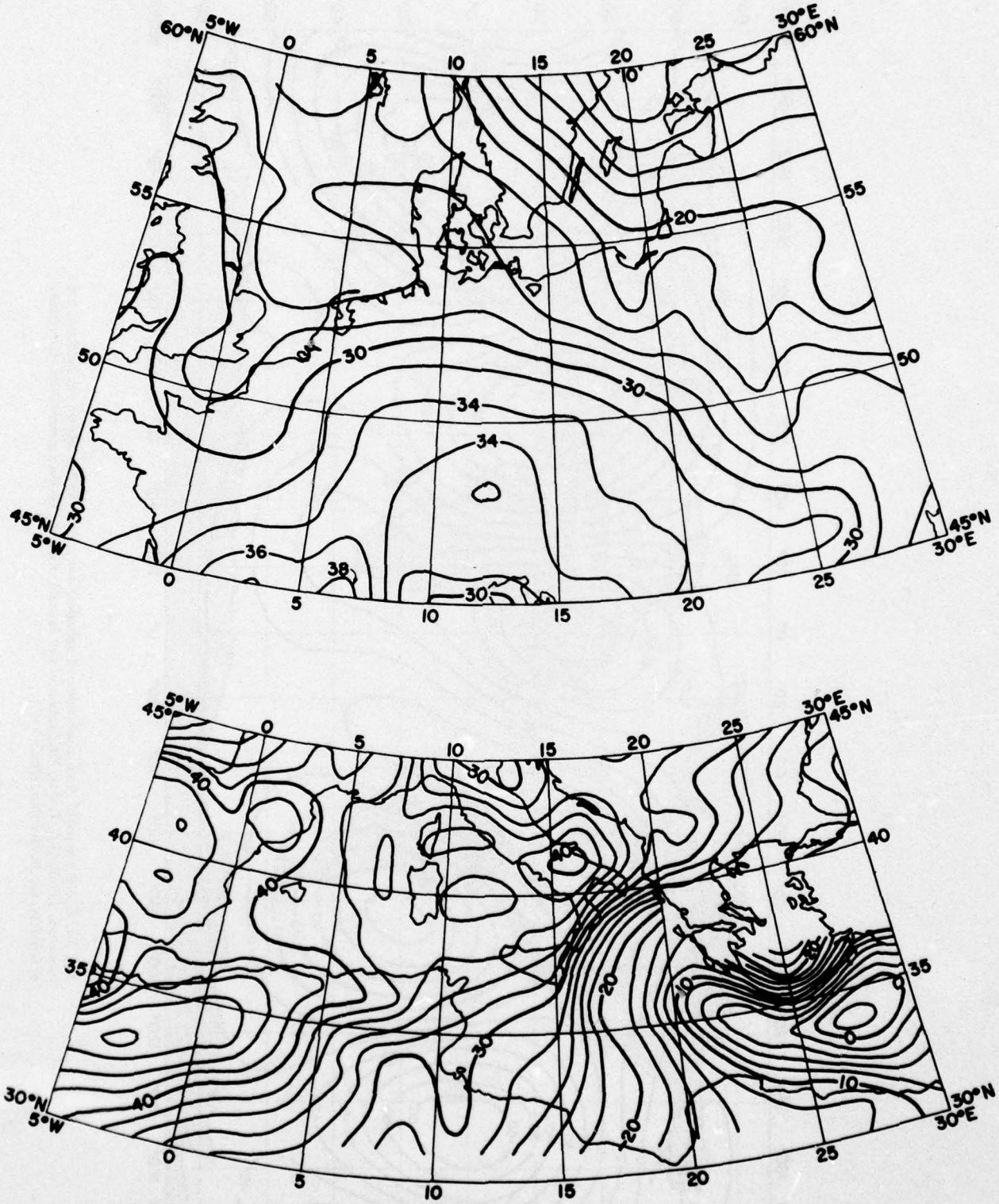


Fig. 1-4. Gravimetrically computed geoid for Europe. Values shown on contours are in meters. (From W. A. Heiskanen [1957].)

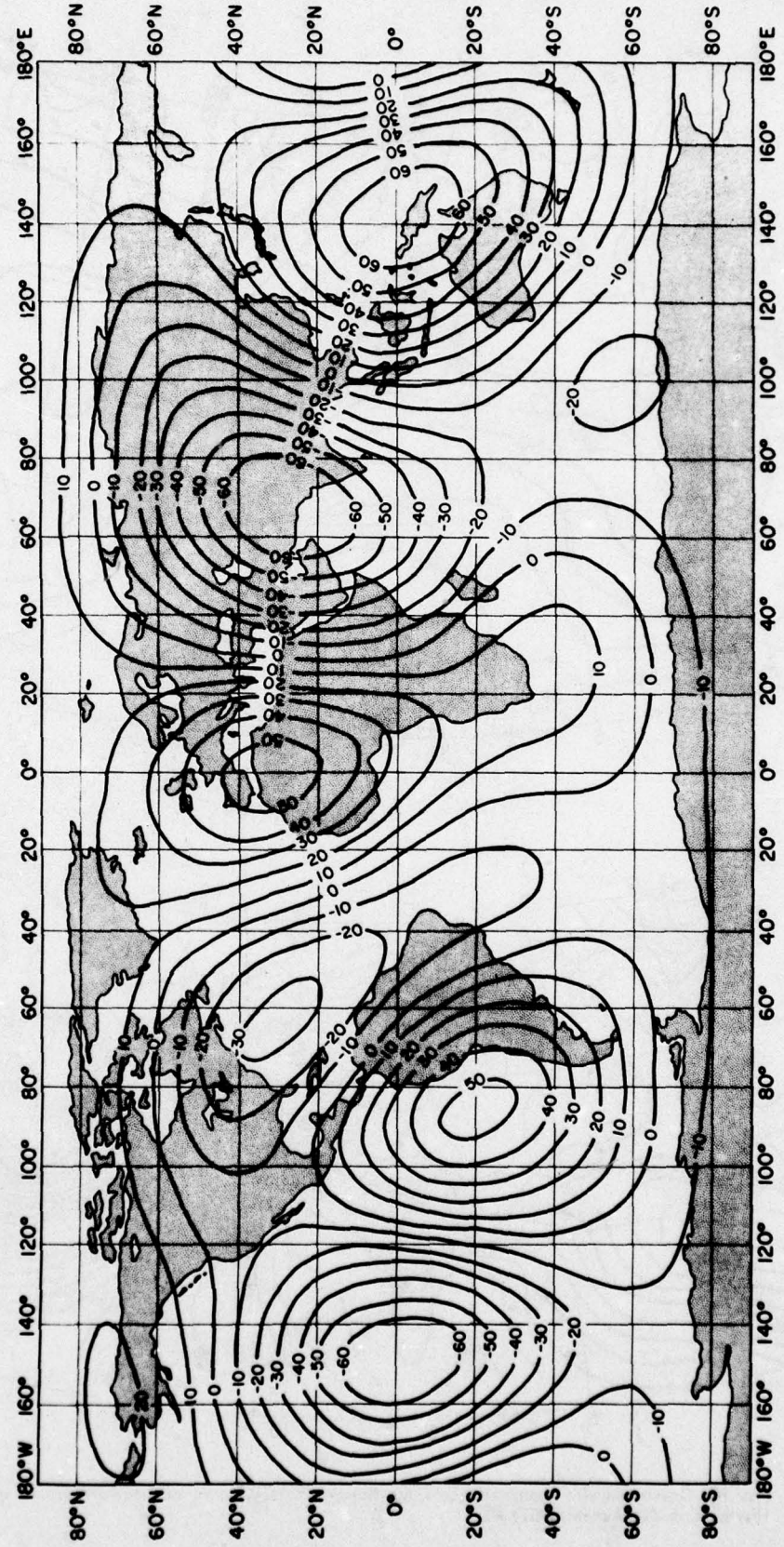


Fig. 1-5. Geoid computed from coefficients of spherical harmonics. Values shown on contours are in meters. (From U.A. Uotila, *Publication of the Isostatic Institute of the International Association of Geodesy*, no. 39, Helsinki, 1962.)

tems. The procedures and results can be found in Heiskanen [1950], Fischer [1960], Kaula [1961] and Szabo [1962].

1.4.6 Gravity Measurements

Gravity measurements are absolute if g is determined independently at the site. Measurements are relative when the difference in g between two or more sites is determined; one of the sites (reference or base station) may be known from previous observations or it may have an assumed value only.

1.4.6.1 *Absolute Measurements.* The determination of the absolute gravity acceleration requires a dynamic experiment where the motion of a mass under the effect of gravity is observed in terms of time and length. For example, the period T of a free-swinging pendulum of length l is

$$T = 2\pi\,(l/g)^{1/2}, \qquad (1\text{-}29)$$

and g can be computed from measurements of T and l. Other experiments consist of timing of free-falling objects or of the upward and downward flight of a projected body. In such experiments, time and length must be determined with high precision, and systematic effects must be eliminated. Modern determinations are internally accurate within ± 0.4 to ± 1 mgal (1 mgal is 10^{-3} cm sec^{-2}); however, comparisons between various experiments reveal much higher discrepancies. At the present time, gravity measurements are referred to the absolute value determined at a station in the Pendelsaal of the Geodetic Institute in Potsdam, Germany. This station is accepted by the International Gravity Commission as the International Reference Station. The datum value, $g = 981.274 \pm 0.003$ cm sec^{-2}, is referred by convention to the height of 87 m above mean sea level. Table 1-4 lists existing absolute determinations and discrepancies, with respect to Potsdam, based on relative connections between the sites. Uncertainties in the absolute measurements and in the relative connections between the absolute sites (especially between Europe and America) are such that there is not yet enough information to justify a final correction to the Potsdam value. The recommended preliminary correction is -12.8 mgal.

Table 1-4. Existing absolute determinations of gravity.

Station	Author	Year	Method*	Observed (mgal)	Discrepancy** (mgal)
Potsdam	Kuhnen & Furtwangler	1898 to 1906	R.P.	981,274.0 ± 3.0***	
	Heyl	1935	R.P.	981,260.0	
Potsdam Revisions	Dryden	1942	R.P.	981,262.3	
	Jeffreys	1948	R.P.	981,263.3 ± 2.2	
	Berroth	1949	R.P.	981,262.3	
	Average of Revisions			981,262.0	−12.0
Nat. Bureau of Standards Washington, D. C.	Heyl & Cook	1936	R.P.	980,080.4 ± 3.0	
	Jeffreys	1948	R.P.	980,081.6 ± 1.2	−17.9
Nat. Physical Laboratory Teddington, England	Clark	1939	R.P.	981,181.7 ± 1.6	
	Jeffreys	1948	R.P.	981,183.2 ± 0.6	−13.2
Leningrad, USSR	Agaletzi & Jegorov	1956 to 1958	R.P.	981,918.8 ± 0.4	−12.5
	Agaletzi	1956	F.F.	981,921.5 ± 1.6	−9.8
	Martsiniak	1956 to 1959	F.C.F.	981,922.9 ± 1.3	−8.4
Sèvres, I.B.W.M.	Thulin	1958-60	F.F.	980,928.0 ± 1.0	−12.9
Ottawa, N. R. C.	Preston-Thomas	1960	F.F.	980,613.2 ± 1.5	−13.8
Princeton Univ.	Faller	1963	F.F.	980,160.4 ± 0.7	−14.5

* R.P. is reversible pendulum; F.F. is free fall; F.C.F. is free and constrained fall.

** Observed minus data (Potsdam).

*** Datum adopted by International Gravity Commission in 1924.

1.4.6.2 *Relative Measurements.* All gravity observations should be referred to the same gravity system or datum. In the past, local gravity surveys utilized different and sometimes arbitrary reference stations and values. Local surveys gradually developed into larger national or regional systems, usually referred to a national base station that in turn was directly or indirectly connected to the international absolute base station in Potsdam. This system does not satisfy present-day needs for homogeneity and accuracy. An international effort (directed by Special Study Group 5 of the International Association of Geodesy and coordinated with the International Gravity Commission) to establish a uniform world gravity reference system began in 1963. Figure 1-6 is an outline of the program; for details see Morelli [1963].

1.4.7 Reduction of Gravity Measurements

Measurements are made on the earth's surface at various elevations above sea level, in the air at different altitudes, and on or below the surface of the sea. Because of these elevation differences, measurements obtained at different points are not comparable unless the observations are reduced to the same level. The classical method uses the geoid for the reduction. Because there are various hypotheses regarding the effect and the treatment of the masses outside of the geoid, different reductions are applied. The most frequently used are the free-air reduction, Bouguer reduction with terrain correction, and isostatic reduction. (Sec. 1.4.8).

According to the reductions applied to the observed gravity, different types of anomalies result. In physical geodesy, free-air and isostatic anomalies are used. The Bouguer reduction causes significant changes in the geoid, so that Bouguer anomalies are not directly applied in geodetic work. In most cases, however, it must be computed to supplement the isostatic reduction.

Free-air reduction, g_f, involves only the elevation of the station and neglects the mass between the station and sea level. The correction is positive on the continents, except in areas below sea level, such as the Caspian Sea, Dead Sea, and Death Valley regions, where h is negative. If g is the observed gravity value at altitude h, and g_o is the value of gravity at sea level, the free-air reduction is $g_o - g$. Since

$$g_o = G\,M/R^2$$

and

$$g = \frac{G\,M}{(R+h)^2} = g_o\left(1 - \frac{2h}{R} + \frac{3h^2}{R^2} \cdots\right),$$

where R is the radius of the earth, neglecting second and higher order terms,

$$g_f \cong 2\,g_o\,h/R. \qquad (1\text{-}30)$$

Equation (1-30) can be used for the free-air reduction except in mountains higher than 2,000 m; numerically $g_f \cong 0.3086$ h mgal (h in meters).

In addition to the attraction of the earth mass below the geoid surface (which can be thought of as concentrated at the earth's center), the mass between the geoid and the observation point exerts an influence on the observed gravity. The attraction of this additional mass should be subtracted from the observed gravity values. The vertical component of gravitational attraction of an infinite horizontal layer of thickness h and density ρ beneath the observation station is

$$g_l = \frac{3}{2}\frac{\rho}{<\rho>}\frac{h}{R}\,g_o, \qquad (1\text{-}31)$$

where $<\rho>$ is the mean density of the earth. Combining Eq. (1-30) and (1-31), the proper *Bouguer reduction,* g_B, is

$$g_B = \frac{2\,g_o\,h}{R}\left(1 - \frac{3}{4}\frac{\rho}{<\rho>}\right). \qquad (1\text{-}32)$$

The numerical values for this reduction depend on the values used for ρ and $<\rho>$. Typical values and the resulting g_B (h in meters) are:

ρ (g cm^{-3})	$<\rho>$ (g cm^{-3})	g_B (mgal)
2.67	5.576	0.2009 h
2.80	5.52	0.1918 h
2.67	5.53	0.1968 h

(The effect of Bouguer's plate diminishes the free-air reduction by about one-third.)

Equation (1-32) is reliable for locations where the terrain is level. However, a *terrain correction* term is required in mountainous areas and on oceanic islands. This correction term is always positive. On a mountain top, because the surrounding terrain does not reach the height of the observing station, too much was subtracted by assuming a horizontal layer of uniform thickness, so a terrain correction must be added. At valley stations, because the masses above the station reduce the gravity observed, a terrain correction must also be added. The correction is obtained by dividing the terrain surrounding the observation station into ring-shaped sections, estimating the height of the terrain in each ring, and calculating the attraction of each ring. The terrain corrections are usually carried out to the Hayford zone 0 (166.7 km from the station). A fourth correction term, that removes the effect of that part of the horizontal layer lying outside Hayford zone 0 and adds the correction due to the earth's curvature, may be used.

Although the Bouguer reduction accounts for the station elevation and the attraction of the visible masses, the Bouguer gravity anomalies are close to zero only at lowland stations. In general, these anomalies are strongly negative in the mountains and strongly positive on the oceans. This strange result occurs because the attraction of the isostatically compensating masses are not considered.

1.4.8 Isostatic Equilibrium and Reduction

If hydrostatic equilibrium prevails in the earth's interior, at a certain depth (the depth of compensation)

the pressure on a unit area is constant regardless of whether the area is under mountain or ocean. The concepts of isostasy is that mountains are compensated by masses of smaller density under the mountains and oceans are compensated by masses of higher density under the oceans. There are several isostatic systems based on different assumptions regarding this compensation. The most important from the geodetic point of view are the Pratt-Hayford and the Airy-Heiskanen systems.

According to the Pratt-Hayford hypothesis, the mountains rose from the underlayer in such a way that the higher the mountain, the smaller the crustal density; the deeper the ocean, the larger the density of the crust. The relationship between the density of compensation (ρ_c), topographic elevation (h), density of the compensated topography (ρ_c), and the depth of compensation (D) is

$$\rho_c = -h\,\rho_c/D. \qquad (1\text{-}33)$$

The depth of compensation, according to Helmert, to Hayford, and to Bowie, is 122, 113, and 96 km, respectively.

According to Airy's hypothesis, the crust is floating in the underlayer which is much denser than the crust. The higher the mountains, the deeper they penetrate into the underlayer, so that the crust is thicker under mountains than under lowlands; the bases of the less dense material submerged deep in the underlayer are called *roots*. The mass deficiencies of the oceans are compensated by the *antiroots* of the heavy underlayer; here the crust is thinnest. Heiskanen obtained a value of 30 km for the average thickness of the normal crust (corresponding to zero elevation of the topography).

Isostatic studies indicate that 85 to 90% of the large mass surplus of mountains and deficiency of the oceans are isostatically compensated. (Small mountains or islands, in fact, cannot be in isostatic equilibrium.) Undulations of the gravimetrically computed Columbus geoid seldom exceed 50 m on a worldwide basis; this would not be possible without isostatic compensation. Both the Pratt-Hayford and Airy-Heiskanen systems assume that the compensation is complete and local; i.e., the compensating layers are directly under the topographic masses. Studies of the extension of topographic features which are large enough to be compensated completely show that a complete equilibrium is unlikely because of the strength of the crust. This led Vening-Meinesz [1931] to modify the Airy floating theory, replacing the local with a regional compensation concept.

1.4.8.1 *Reduction Tables.* The U.S. Coast and Geodetic Survey developed reduction formulas and computed the required reduction tables for the Pratt-Hayford system [Hayford and Bowie, 1912; Bowie, 1917]. For the computation of the effect of the topography and of the corresponding compensation to the gravity station, the circular-zone method of Hayford is used. The mean elevations or depths of the consecutive zones around the station to the antipode are estimated from maps and the effect of each zone computed using the reduction tables. Heiskanen computed reduction tables, also based on the Hayford zones, for the Airy-Heiskanen system for thicknesses of 40, 60, 80, and 100 km, and for 20, 30, and 40 km [Heiskanen and Nuotio, 1938].

1.4.8.2 *Reduction Maps.* The estimation of the mean elevations of the many circular zones has to be made separately for almost every station. This station-by-station method for isostatic reduction of gravity observations is uneconomical. The Isostatic Institute has published many detailed isostatic reduction maps for different zone groups and areas. Topographic-isostatic reduction maps in the Hayford zones 19-1 for the Airy-Heiskanen systems were published for Europe in 1959 and for the world in 1961.

1.4.9 New Reduction Methods

There are many objections to the classical reduction methods. One is that transfer of masses from outside the geoid to its interior creates an artificial co-geoid, and the masses outside of this must be considered in the reduction (indirect effect). Another objection is that the free-air anomalies are not sufficiently representative in areas with rough topography. Because of such difficulties, the geoid cannot be computed with the required accuracy. New methods compare the actual and the theoretical values of gravity at the earth's surface and compute the differences between geopotential and spheropotential surfaces at the physical earth surface (rather than at sea level). Different new surfaces resulting from such studies are: the model earth of de Graaf-Hunter [1960]; the quasi-geoid of Molodenski [1945]; the hypothesis free reference surface of Ledersteger [1958]; and the telluroid of Hirvonen [1960].

1.5 GRAVITY FIELD EXTENDED TO HIGH ALTITUDES

Various methods of computation for the external field of a mathematical model (ellipsoid) and for the continuation of surface gravity anomalies and disturbances have been investigated. The external gravitational field is also determined indirectly from observations of the perturbations of artificial satellites. As in the treatment of the problem on the earth surface, the external field is studied in two parts: the external normal field, and the continuation of the disturbances or anomalous gravity to high altitudes.

1.5.1 Normal Gravity or Gravitation

Methods for the computation of the normal field at high altitudes solve the problem either by exact or closed formulas or by series. The assumptions regarding the ellipsoid of rotation are that it has the same mass as the actual earth and the mass distribution inside of the rotating ellipsoid is such that the combined potential of the attraction and centrifugal force is constant at the surface and is very close to the actual potential of gravity at the mean sea level.

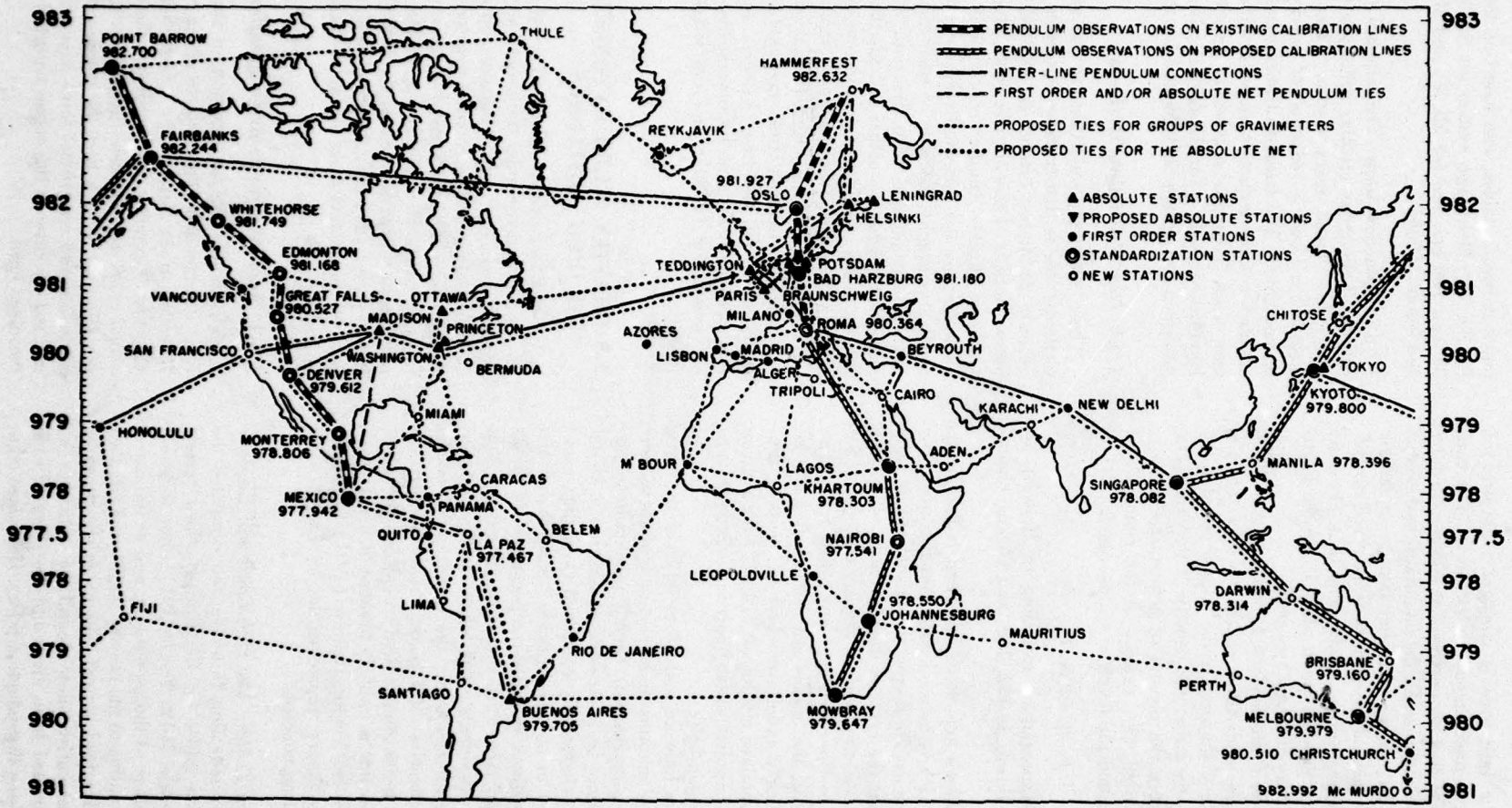


Fig. 1-6. Uniform world gravity reference system. (From B. Szabó, "World Calibration Standard, first order gravity map and absolute gravity system," *Bollettino di Geofisica ed Applicata*, v. 5, no. 19, 1963.)

Hirvonen and Moritz [1963] developed a method for the computation of the normal gravity or gravitational vector at high altitudes that is suitable for a great number of points (e.g., for trajectories and satellite orbits). The components of the gravity vector are computed in a local and then transformed into an earth-centered, coordinate system. Formulas adapted for high-speed computers are furnished. Daugherty and Define [1963] performed a numerical evaluation of several computational methods; computing up to 1850 km altitude, they are in agreement within half a milligal.

1.5.2 Continuation of Gravity Anomalies and Disturbance

To obtain the actual gravity outside the earth surface, the normal value computed from the field of the ellipsoid should be corrected by the effect of the mass disturbances of the actual earth. Two kinds of corrections are used: anomalies for points with altitude referred to the sea level and disturbances, if the position of the point relative to the mass center of the earth is known (x, y, z coordinates of a point on a trajectory or orbit).

Basically, the upward continuation of gravity anomalies is a boundary value problem of potential theory. Theoretically only two different types of solutions exist, the integration method and the development in Taylor series.

The integration method can be simplified and modified by: (1) developing the functions Δg and Δg_H in a series of orthogonal functions (the coefficients of these developments are connected by simple linear transformations, therefore the integral transformations are replaced by linear transformations); or (2) replacing the anomaly function at the earth's surface by an analytically defined statistical model so that integration can be performed by closed formulas (the statistical method). For accurate computations, the integration method is recommended; the integration should be extended over a circular area with radius 10 times the elevation. In smooth areas for elevations less than 5 km, the statistical method can be used.

For the integration method, considering the earth as a sphere, the formula is:

$$\Delta g_H = \frac{\tau^2(1-\tau^2)}{4\pi} \iint_{\sigma=0}^{\sigma=\pi} \frac{\Delta g}{u^3}\, d\sigma, \qquad (1\text{-}34)$$

where $d\sigma$ is the element of solid angle σ, $\tau = R/(R+H)$, $u = (1 - 2\tau \cos \Psi + \tau^2)^{1/2}$ and Ψ is the angular distance of $d\sigma$ from the computation point. In most cases, the plane approximation, called the *upward continuation integral*, is sufficient. This is

$$\Delta g_H = \frac{H}{2\pi} \int_{-\infty}^{\infty} \int \frac{\Delta g}{D^3}\, dxdy, \qquad (1\text{-}35)$$

where $D = (x^2 + y^2 + H^2)^{1/2}$, and x and y are the plane rectangular coordinates which represent the earth's surface. (Equation [1-35] can be used for the upward continuation not only of Δg but of any harmonic quantity given on the xy-plane; e.g., the disturbing potential, the separation between geopotential and spheropotential surfaces, the deflections of the vertical, etc.) The integral can be evaluated through summations. Templates for *manual evaluations* have been designed by Henderson [1960] and by Hirvonen [1962]. The difference between Henderson's and Hirvonen's template is small and both are equally well suited for practical computations (Hirvonen's is preferable for theoretical reasons). Mean $5' \times 5'$ anomalies are suitable for high-speed computation of Δg_H.

For the computation of the gravity disturbances at high altitudes, there are several different methods according to the material available. If Δg, N, ξ, and η are available, the upward continuation of the surface disturbance can be used; the requirement for the deflection components makes this, however, impractical. If Δg and N are given, then the coating method for the horizontal components and the upward continuation for the vertical component can be used [Hirvonen and Moritz, 1963].

1.6 ELECTRONIC DISTANCE MEASUREMENTS

The base lines of classical triangulations were measured with great care and remarkable accuracy, but they had two deficiencies. The calibration of the measuring devices was not highly accurate, and by using variable standards the scale of networks was not uniform. In addition, directly measured lengths were relatively short and the networks, developing the measured base lines into a length of an average triangle side, considerably downgraded the accuracy. The light interference comparator solved the problem of calibration. Standard base lines 860 m and 500 m long were measured with relative accuracies of 1:17,000,000 and 1:9,000,000 [Heiskanen, 1950]. The International Association of Geodesy in 1954 adopted and recommended the use of the Väisälä light interference comparator for uniform calibration of base line measuring instruments.

Two instruments in general use today are the geodimeter and the tellurometer. These instruments calibrated on accurate standard base lines can achieve accuracies of 1:800,000 and 1:200,000 respectively. Their use, however, is limited to accessible land areas. The geodetic applications consist of base line measurements, geodetic traverse and trilateration.

Hiran (high-precision Shoran) is a high-frequency time measuring pulse system that utilizes two ground stations and one airborne station to measure the round-trip time of a radio pulse from the airborne transmitter to the ground stations. Hiran measurements, however, are applicable only to line of sight conditions. Where ground stations can be established within approximately 400 to 500 miles, the sides of long triangles can be measured (trilateration), making possible the connection of widely separated geodetic systems or measurement of long arcs. The accuracy of the measured lines varies greatly and

depends on many factors. Generally, short lines are less accurate than long ones. Compared with ground survey data, the accuracy of the lines of the tie between the United States and South America ranges from 1:25,000 to 1:100,000, and in the North Atlantic tie, from 1:25,000 to 1:250,000.

The accuracy of geodetic positions computed from Hiran surveys depends not only on the accuracy of the measured lines but also on the strength of the network and azimuth control. Hiran surveys are either extensions of or connections between existing triangulations. The azimuths used for computation of positions are usually azimuths of one or more common lines between triangulation and Hiran survey. The lack of observed azimuths along the trilateration downgrades the accuracy of the computed positions, especially along long and narrow chains. This problem can be solved by photographing against the fixed field of stars light flashes made by the Hiran aircraft during line crossings, with cameras from both ground stations of the line. Experiments show that accuracies of one second of arc can be attained. This technique will increase substantially the reliability of the Hiran networks.

1.7 LUNAR OBSERVATIONS

Theoretically, the fixed station methods and general occultations could determine the geocentric coordinates of the station and, from a large amount of data, the shape and size of the geoid. Eclipses and special occultations cannot furnish geocentric rectangular coordinates because only one observation is made at one site. The relationship between different geodetic systems of the world, however, can be obtained in terms of distances and azimuths.

1.7.1 Solar Eclipses

On the basis of the ellipsoidal parameters (a, f), preliminary coordinates (ϕ', λ'), and the computed geocentric radius vector (r), the local circumstances (time of contacts, mid-totality, etc.) of the eclipse are predicted in terms of universal time. The times of contacts observed at the sites will be different from the predicted times. These differences can be used to correct the relative distance and azimuth between the two stations; it is necessary to know only the relative angular motions of the sun and moon with high precision. In this case the differences in mid-totality between predicted and observed values at each site multiplied by the known shadow velocity gives the distance correction and, similarly, the azimuth corrections [O'Keefe and Anderson, 1953].

There are three observational methods. The Bonsdorff method utilizes high-speed motion picture photography to photograph the diminishing crescent of the sun immediately before second contact, and the increasing crescent immediately following third contact. First and fourth contacts may be similarly photographed. Direct measurements of the film containing both crescent images and time signals furnish the required data. The Sibland method utilizes motion picture photography of the flash spectrum and superimposed time signals. The instants of totality are found from these measurements. The photoelectric method utilizes photoelectric cells to measure the amount of light reaching the cell from the sun. The diminishing light before and the increasing light after totality are recorded on the same tape as time signals. The light curves give the instant of minimum light assumed to be the instant of mid-totality.

1.7.2 Occultations

The time at which a star disappears behind and emerges from the limb of the moon can be recorded visually or, more accurately, by photoelectric methods. If two observers are located at stations where the occultation of the same star can be recorded, corrections to the observer's positions may be found. The geometrical considerations are similar to those of the eclipse method. This method has been used to determine the distance to the moon and to measure arcs [O'Keefe and Anderson, 1953].

1.7.3 Lunar Camera

The lunar camera is a dual-rate moon position camera which simultaneously photographs the moon and surrounding stars. By holding the moon fixed relative to the stars during the time of exposure, high accuracy is achieved. The reduction of the plate gives the position of the center of the moon relative to known fixed star positions. If the geocentric coordinates of the moon at the time of the observation are known relative to the earth's center of mass, a line of position between the observer and moon is determined. Theoretically, another observation of the moon from the same site, when the moon is in another position, would determine the observer's geocentric coordinates by the intersection of the two lines of position. If, from a sufficient number of stations, many observations at various altitudes and azimuths are made, the geocentric coordinates and the radius vectors of the stations can be derived [Markowitz, 1958].

During the International Geophysical Year (1957-1958) the Markowitz moon cameras were used at 20 observatories. The large number of plates (about 600 at each site) are close to the final reduction. The results should provide geocentric coordinates and radius vector for each site, the general shape of the earth, size of the lunar orbit, and corrections to orbital elements of the moon and Ephemeris time.

1.8 ROCKET-FLASH TRIANGULATION

Figure 1-7 illustrates the principle of photographing flares on rockets or satellites against a stellar background for the purpose of developing a network of spatial triangulation. A minimum of two stations are required to fix the position of the source in space. If two stations are fixed with respect to a geodetic datum, the third station can be treated as an unknown, and its coordinates established relative to the known sites. As new stations are derived by this process, the triangulation network can be extended laterally into a continental survey; if the target is sufficiently high, it can bridge across the ocean to connect with other major datums.

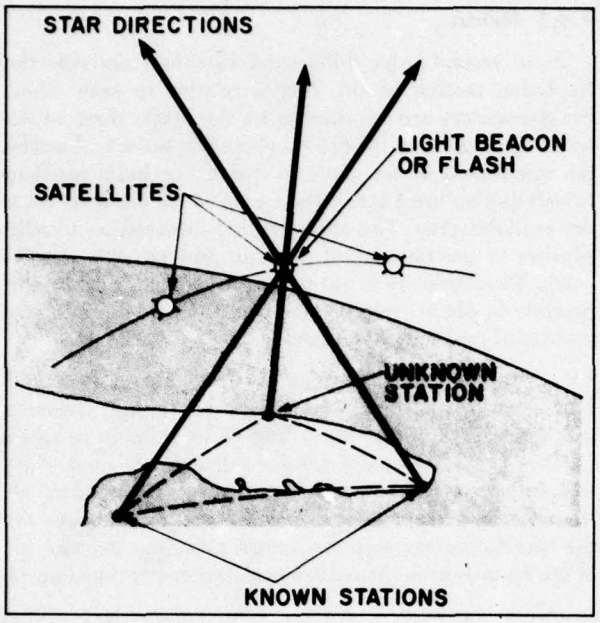


Fig. 1-7. Three-station flash triangulation geometry. Geodetic stellar cameras at station record a series of flashes from a rocket or satellite; the star background and time record supply data to compute positions of light source needed for special triangulation.

The types of cameras used and the method of photographing the optical target can vary considerably depending on the mission requirements [Williams, 1961]. In general, however, a geodetic camera should have a focal length ranging from 500 to 1000 mm to permit final measuring precision on the order of one second of arc. Accuracy in measuring camera plates is currently around 3 microns, which represents the combined effects of setting error and emulsion instability. Based on star calibration reductions, ANNA operations, and missile calibration programs, the accuracy of the PC-1000 mm f/5 and the Ballistic Camera BC-4 averages 1.0 second of arc and 2.0 seconds of arc, respectively. The accuracy of the Baker-Nunn system is the order of 2.0 seconds of arc.

The central problem of photogrammetry is the reconstruction of configurations in the object space by means of image space data. Figure 1-8 illustrates the relationship between object and image spaces. A spatial point Q with coordinates X, Y, Z in an arbitrary Cartesian system is photographed by a camera with center of projection at C (X^c, Y^c, Z^c). The image of Q is at I (X^I, Y^I, Z^I) in the image plane which, for convenience, is presented as a diapositive (i.e., the image plane is regarded as lying between the center of projection and the object space). The coordinates of I, referred to an arbitrary Cartesian system in the image plane, are $\bar{x}$, $\bar{y}$ ($\bar{x}$, $\bar{y}$ coordinates are commonly referred to as plate coordinates or image coordinates). The specific relationship sought is that existing between the space coordinates X, Y, X and the image coordinates $\bar{x}$, $\bar{y}$. To facilitate the derivation, an auxiliary coordinate system x, y, z is constructed with origin at C and the x, y axes parallel respectively to $\bar{x}$, $\bar{y}$. The z axis, which is normal to the image plane, is usually referred to as the principal axis or the camera axis. The intersection of z with the image plane defines the principal point P which is assumed to have plate coordinates $\bar{x}_p$, $\bar{y}_p$. The distance CP from the center of projection to the principal point is the principal distance, denoted here by c. Note that the principal distance is not necessarily the same as the focal length, although ideally the two would be identical.

From the construction of the x, y, z system,

$$\begin{bmatrix} x \\ y \\ z \end{bmatrix} = \begin{bmatrix} \bar{x} - \bar{x}_p \\ \bar{y} - \bar{y}_p \\ c \end{bmatrix}, \qquad (1\text{-}36)$$

and, from similar triangles,

$$\begin{bmatrix} X^1 - X^c \\ Y^1 - Y^c \\ Z^1 - Z^c \end{bmatrix} = K' \begin{bmatrix} X - X^c \\ Y - Y^c \\ Z - Z^c \end{bmatrix}, \qquad (1\text{-}37)$$

where K′ is introduced as a constant of proportionality. If the direction cosines of x relative to X, Y, Z, respectively, are denoted by A, B, C; those of y by A′, B′. C′; and those of z by D, E, F, then it follows from analytic geometry that,

$$\begin{bmatrix} x \\ y \\ z \end{bmatrix} = \begin{bmatrix} A\,B\,C \\ A'B'C' \\ D\,E\,F \end{bmatrix} \begin{bmatrix} X^1 - X^c \\ Y^1 - Y^c \\ Z^1 - Z^c \end{bmatrix}. \qquad (1\text{-}38)$$

Substitution of Eq. (1-36) and (1-37) into Eq. (1-38) yields

$$\begin{bmatrix} \bar{x} - \bar{x}_p \\ \bar{y} - \bar{y}_p \\ c \end{bmatrix} = K' \begin{bmatrix} A\,B\,C \\ A'B'C' \\ D\,E\,F \end{bmatrix} \begin{bmatrix} X - X^c \\ Y - Y^c \\ Z - Z^c \end{bmatrix}, \qquad (1\text{-}39)$$

which upon the elimination of K′ leads to the following condition equation

$$\frac{\bar{x} - \bar{x}_p}{c} = \frac{A\,(X - X^c) + B\,(Y - Y^c) + C\,(Z - Z^c)}{D\,(X - X^c) + E\,(Y - Y^c) + F\,(Z - Z^c)}$$

$$\frac{\bar{y} - \bar{y}_p}{c} = \frac{A'(X - X^c) + B'(Y - Y^c) + C'(Z - Z^c)}{D\,(X - X^c) + E\,(Y - Y^c) + F\,(Z - Z^c)}. \qquad (1\text{-}40)$$

Equation (1-40) relates the X, Y, Z space coordinates of an object point to the $\bar{x}$, $\bar{y}$ plate coordinates of its image. Thus, if the camera parameters and the station position are known, two observations from two stations will provide four equations and three unknowns. Similarly, if two space positions are known, the X, Y, Z coordinates of the unknown station can be derived.

1.9 SATELLITE GEODESY

The accuracy of the results derived from observations of satellites depends on the validity of the adopted potential function; the accuracy, frequency, and distribution of the observations; the accuracy of the starting coordinates of the tracking sites; and the statistical treatment of the data in order to separate gravitational effects, mechanical

effects (drag), and the geodetic positional errors. The satellite may be used purely as an elevated target as in flash triangulation (Sec. 1.8); this technique is essentially an outgrowth of classical triangulation involving longer ground distances and, as such, provides only relative geodetic positions. Another approach explores the motion of the satellite about the earth's center of mass and from orbit analysis derives geodetic quantities that are referred to a geocentric coordinate system.

The motion of a satellite is governed primarily by the gravitational forces due to the earth, sun, and moon. The nongravitational forces result from atmospheric drag, radiation pressure, and magnetic fields. By proper selection of the orbit parameters and the vehicle configuration, the effects of these nongravitational forces can, for practical purposes, be eliminated. Under gravitational forces only, an earth satellite traces out an orbit that approximates an ellipse. Only elliptical orbits are of interest to geodesy, since a truly circular orbit is exactly limiting, hence unstable. In many cases, however, it is convenient to assume near circularity for computational purposes.

1.9.1 Orbits

Three second-order differential equations describe the Keplerian motion of two bodies relative to each other. Six parameters are required to fix the orbit; three to describe the motion in the orbital plane and three to describe the orientation of the plane in space. The basic problem in defining an orbit is to obtain a set of six elements from the available data. The observational information usually consists of position, or of position and velocity components. When velocity is not directly available, it is usually possible to obtain velocity components by differentiating a series of position coordinates.

1.9.1.1 *Geocentric Coordinate System.* Figures 1-9 and 1-10 show a convenient coordinate system, and elements that describe the orbit (a, e) and its orientation in space (i, Ω, ω). (Other sets of similar elements are used when this set is not convenient.) In this coordinate system all the observational data must be reduced to components; the transformation equations must take into account all of the variations in the earth's orientation as a function of

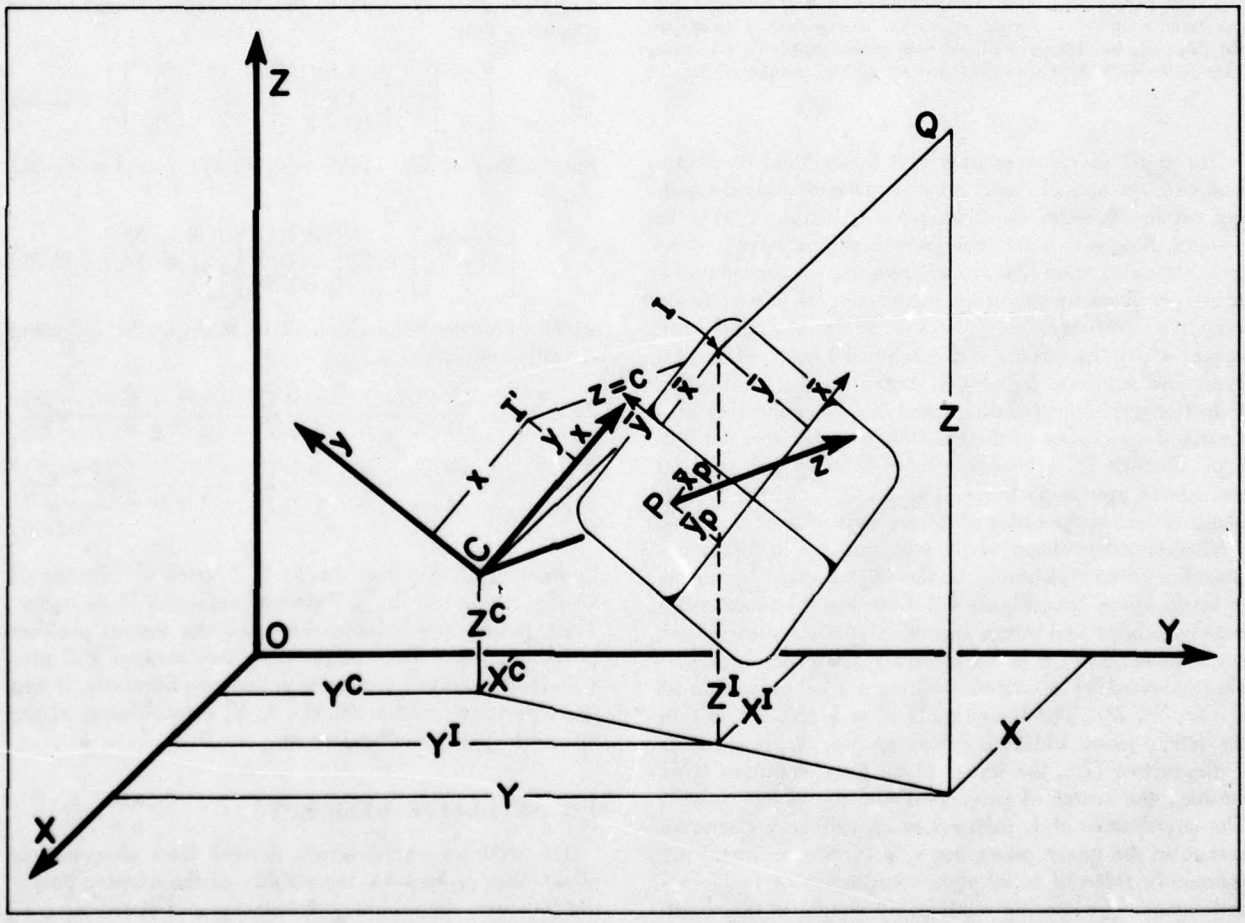


Fig. 1-8. Object and image space coordinates for determining positions in flash-triangulation. (After D. Brown, *RCA Technical Report No. 39*, 1957.)

time, and the time variation in the position of the vernal equinox. Considerable observation data are usually available, so statistical techniques are employed in the data reduction and orbital computation.

1.9.1.2 *Computation of Orbital Elements.* Given the position (x, y, z) and velocity ($\dot{x}$, $\dot{y}$, $\dot{z}$) components, the elements are computed using the following definitions:

$$r = i\,x + j\,y + k\,z \qquad \alpha = i \cdot (r \times v)$$

$$v = i\,\dot{x} + j\,\dot{y} + k\,\dot{z} \qquad \beta = j \cdot (r \times v)$$

$$r = |r| \qquad \gamma = k \cdot (r \times v)$$

$$v = |v| \qquad \delta = k \cdot r/r = z/r$$

$$r = r \cdot v/r \qquad \epsilon = i \cdot r/r = x/r$$

$$H = [(r \times v) \cdot (r \times v)]^{1/2}$$

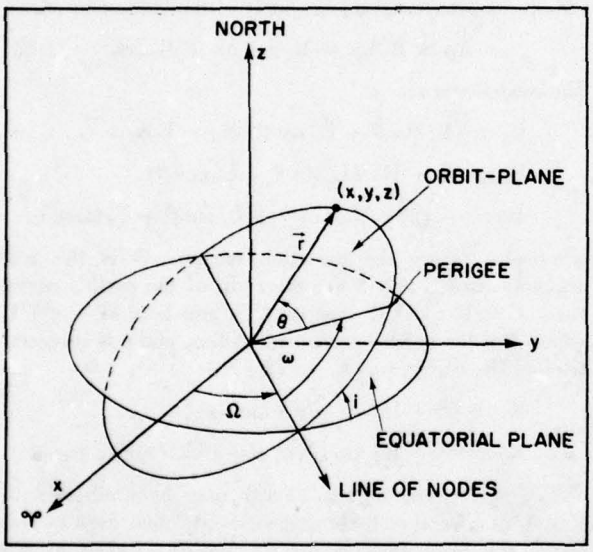


Fig. 1-9. Geocentric coordinate system and orbital elements. The x axis lies in the equatorial plane and is directed toward the vernal equinox (Sec. 21.2.2). The z axis lies along the earth's rotational axes. The y axis lies in the equatorial plane and is perpendicular to the x axis. i is the inclination, Ω is right ascension (Sec. 21.2.2.2) of the ascending node, and ω is the argument of perigee.

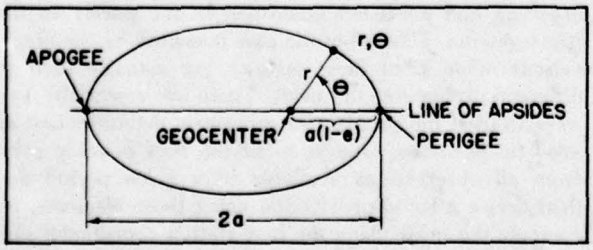


Fig. 1-10. Elements in the orbital plane of an elliptical orbit in polar coordinates (r, θ), a is the semi-major axis and e is the numerical eccentricity; the angle θ is the true anomaly.

The elements are:

Semi-Major Axis, $a = r(2 - v^2 r/\mu)$,

where μ is GM (the product of the universal gravitational constant and the mass of the Earth);

Numerical Eccentricity, $e = [1 - H^2/a\mu]^{1/2}$;

Inclination Angle, $i = \cos^{-1}(\gamma/H)$, where $0 \leq i \leq \pi$;

Right Ascension of the Ascending Node,

$$\Omega = \sin^{-1}(\alpha/H \sin i),$$

$$\Omega = \cos^{-1}(-\beta/H \sin i),$$

where $0 \leq \Omega \leq 2\pi$;

Argument of Perigee $\omega = \sin^{-1}(\delta/\sin i) - \theta$

$$\omega = \cos^{-1}(\epsilon \sec \Omega + \delta \tan \Omega \cot i) - \theta$$

where θ is the true anomaly, and

$$\cos \theta = [a(1 - e^2) - r]/er;$$

Mean Anomaly, $\bar{M}$.

1.9.1.3 *Kepler's Equation.* The *mean anomaly* is obtained from Kepler's equation,

$$\bar{M} = E - e \sin E = \bar{n}\,(t - T). \qquad (1\text{-}41)$$

E is the *eccentric anomaly,* which is defined by the relation $\cos E = (a - r)/ae$, and T is the time of perihelion passage. The mean angular velocity, $\bar{n}$, is called the *mean motion;* $\bar{n} = 2\pi/P$, where P is the period of revolution. From Kepler's third law,

$$P^2/a^3 = 4\pi^2/G(m + M), \qquad (1\text{-}42)$$

and because the mass of an artificial satellite is negligible compared to the earth's mass,

$$\bar{n} = (\mu/a^3)^{1/2}. \qquad (1\text{-}43)$$

1.9.2 Orbital Perturbations

The inhomogeneities in the earth's density and its nonsphericity result in a gravitational field that is not spherically symmetric. This causes the orbital elements of a satellite to change with time both harmonically and secularly. The potential function can be written as

$$U = \frac{\mu}{r} + B, \qquad (1\text{-}44)$$

where μ/r is the potential due to the theoretically spherical earth and B is the *disturbing potential* due to nonsphericity effects and to lunar and solar perturbations. Although atmospheric resistance is not a potential function, it can be included by suitable adjustment of the equations.

In the presence of perturbations, the orbital elements change according to the following *Lagrangian planetary equations:*

$$\frac{da}{dt} = \frac{2}{\bar{n}a}\frac{\partial B}{\partial M}$$

$$\frac{de}{dt} = \frac{1-e^2}{\bar{n}a^2e}\frac{\partial B}{\partial M} - \frac{(1-e^2)^{1/2}}{\bar{n}a^2e}\frac{\partial B}{\partial \omega}$$

$$\frac{d\omega}{dt} = -\frac{1}{\bar{n}a^2(1-e^2)^{1/2}\sin i}\cos i\frac{\partial B}{\partial i} + \frac{(1-e^2)^{1/2}}{\bar{n}a^2e}\frac{\partial B}{\partial e}$$

$$\frac{di}{dt} = \frac{1}{\bar{n}a^2(1-e^2)^{1/2}\sin i}\left\{(\cos i)\frac{\partial B}{\partial \omega} - \frac{\partial B}{\partial \Omega}\right\} \qquad (1\text{-}45)$$

$$\frac{d\Omega}{dt} = \frac{1}{\bar{n}a^2(1-e^2)^{1/2}\sin i}\frac{\partial B}{\partial i}$$

$$\frac{d\bar{M}}{dt} = \bar{n} - \frac{1-e^2}{\bar{n}a^2e}\frac{\partial B}{\partial e} - \frac{2}{\bar{n}a}\frac{\partial B}{\partial a}.$$

These equations can be integrated numerically and, with certain restrictions, analytically.

The basic problem in celestial geodesy is to determine the exact form of the disturbing potential B that produces perturbations of the orbit. It is, therefore, necessary to adopt some form for the perturbing potential B and then seek those values of the coefficients in this potential that satisfy the observations.

1.9.3 Position Determination

Assuming the orbit of an earth satellite has been determined, any observation (O_i) of the satellite can be expressed in terms of the time and three coordinates describing the location of the observer. The first-order differential expressions follow from the leading term of the Taylor expansion; i.e.,

$$\Delta O_i = \sum_j \frac{\partial O_i}{\partial X_j}\Delta X_j,$$

where X_j are the three-station coordinates. When there are m observational equations available, a set of m differential expressions can be written

$$(\Delta O_i) = (C_{ij})\ (\Delta X_j),$$

where (C_{ij}) is an $m \times 3$ matrix. The elements of this matrix are the partial derivatives of the observed quantities with respect to the station coordinates. The solution takes the form

$$(\Delta X_j) = [(C_{ij})^T (C_{ij})]^{-1} (C_{ij})^T (\Delta O_i), \quad (1\text{-}46)$$

where the superscripts -1 and T denote inverse matrix and transpose matrix respectively. The bracketed quantity is the least squares matrix, N.

When weighting is required in the determination to account for different types of tracking data or different tracking instruments, the least squares matrix can be constructed according to

$$N = (C_{ij})^T (P_{ip})\ (C_{ij}),$$

where P_{ip} is the diagonal weight matrix, defined as $P_{ip} = \omega_{oi}$ for $i = p$, and $P_{ip} = 0$ for $i \neq p$; ω_{oi} is the weighting factor of the observation O_i. The solution takes the form

$$(\Delta X_j) = N^{-1} (C_{ij})^T (P_{ip})\ (O_i). \qquad (1\text{-}47)$$

In order to illustrate the reductions, assume that O_i is a range measurement from the observation site made at time t_i with X_1, Y_1, and Z_1 defining the station-location vector. The components of the topocentric range vector (station to satellite) are

$$\rho_x = x - X_1,$$
$$\rho_y = y - Y_1,$$
$$\rho_z = z - Z_1,$$

where x, y, and z are the geocentric components of the satellite vector computed from the orbital elements.

The range residual, $\Delta\rho$, is related to the errors in latitude ϕ, longitude λ, and height H of the station by

$$\Delta\rho = R_1\Delta\phi + R_2\cos\Delta\lambda + R_3\Delta H. \qquad (1\text{-}48)$$

The coefficients are

$$R_1 = (L_x\cos\theta + L_y\sin\theta)\ K_2 - L_zK_4,$$

$$R_2 = (C + H)\ (L_x\sin\theta - L_y\cos\theta),$$

$$R_3 = -\cos\phi\ (L_x\cos\theta + L_y\sin\theta + L_z\tan\phi),$$

where $L_{x,y,z}$ are the direction cosines, Θ is the true anomaly, and C and S are the radii of the earth's curvature; $C = R\ (1 - e^2\sin^2\phi)^{-1/2}$, and $S = (1 - e^2)\ C$, where R is the earth's equatorial radius, and e is its eccentricity. The coefficients K_2 and K_4 are:

$$K_2 = (S + H) + e^2SC^2\sin^2\phi$$

$$K_4 = (S + H)\sin\phi\cot\phi + e^2SC^2\sin^2\phi\cos\phi.$$

The coefficients in Eq. (1-48) may be multiplied by a weighting factor; these quantities are then used to construct the least squares matrix and the equations are solved to obtain $\Delta\phi$, $\Delta\lambda$, and ΔH for the tracking station. A series of such determinations from a global network of stations will ultimately provide the geodetic shift of each datum to orient that datum with respect to the center of mass; Kaula [1963] gives results derived from Baker-Nunn optical network observations of five satellites.

It was assumed, in the above treatment, that the orbit is known precisely and that the difference between the observed and predicted quantities is due purely to the station errors. This is not the case inasmuch as the observations made from these stations are actually used to differentially correct the orbit. There are essentially two ways to treat the problem of geocentric determination of geodetic positions. One is to fit the best possible orbit from all observations available in a given period and then derive a station correction using those elements, recompute the orbit using the new station coordinates and obtain a new station correction, etc. This process will ultimately converge to a stable determination if realistic limits are placed on the amount of station displacement.

The other is to treat the orbit and station corrections in a simultaneous solution and obtain the most likely change for the orbital elements and station coordinates. This type of solution can also be extended to include correction to the gravitational coefficients, drag, and other factors. In principle, both approaches should ultimately provide the same results; however, the second method is more general and will probably require less computer time.

1.9.4 Analysis of Satellite Motions to Determine Gravitational Potential

Satellite observations are used to determine the coefficients in the earth's potential field by correlating theory with observation. For a specified disturbing function and specified observational error, tracking data is differentially corrected to minimize errors in satellite and tracking station positions while determining the orbit ephemeris. Once the ephemeris is compatible with the observation, the elements and their rates of change with time are computed. These elements are used in conjunction with the Lagrangian planetary equations and the disturbing function to estimate the various coefficients in this function.

One technique employs an expansion of spherical harmonic terms for the disturbing potential;

$$B = \sum_{n=2}^{\infty} \sum_{m=0}^{n} U_{nm}, \tag{1-49}$$

where

$$U_{nm} = \frac{\mu}{r}\left(\frac{R}{r}\right)^{n} P_{nm}(\sin\phi)\ (C_{nm}\cos m\lambda + S_{nm}\sin m\lambda), \tag{1-50}$$

R is the equatorial radius of Earth, λ is east longitude, and ϕ is latitude. $P_{nm}(\sin\phi)$ are the associated Legendre functions, and C_{nm} and S_{nm} are the harmonic coefficients; terms with $m = 0$ (latitude dependent) are called the zonal harmonics, terms $(nm) \neq 0$ (latitude and longitude dependent) are called the tesseral harmonics. Table 1-5 lists various determinations of C_{nm} and S_{nm}. This form of the potential does not include lunar and solar perturbation effects.

Transformed from a function of ϕ and λ to a function of the satellite's orbital elements,

$$U_{nm} = \frac{\mu R^n}{a^{n+1}} \sum_{p=0}^{n} F_{nmp}(i) \sum_{q=-\infty}^{\infty} G_{npq}(e)\ S_{nmpq}(\omega, \bar{M}, \Omega - \theta). \tag{1-51}$$

In this equation, θ is the Greenwich sidereal time expressed in radians. The various terms in this expression for U_{nm} are as follows:

$$F_{nmp}(i) = \sum_{t=0}^{T} \frac{(2n-2t)!\ \sin^{n-m-2t} i}{t!\,(n-t)!\,2^{2n-2t}} \sum_{s=0}^{m} \binom{m}{s} \cos^{s} i \sum_{c=\alpha}^{\delta} \frac{\binom{n-m-2t+s}{c}\binom{m-s}{p-t-c}}{(n-m-2t)!} (-1)^{\gamma}, \tag{1-52}$$

where

$$T = \begin{cases} p \text{ if } p \leq \dfrac{n-m}{2}, \\ \dfrac{n-m}{2} \text{ if } p \geq \dfrac{n-m}{2} \text{ and } n-m \text{ is even}, \\ \dfrac{n-m-1}{2} \text{ if } p \geq \dfrac{n-m}{2} \text{ and } n-m \text{ is odd}. \end{cases}$$

$$\alpha = \begin{cases} 0 \text{ if } m+t \geq p+s, \\ p-t-m+s, \text{ if } m+t \leq p+s. \end{cases}$$

$$\delta = \begin{cases} n-m-2t+s, \text{ if } n+p+t \geq n+s, \\ p-t, \text{ if } m+p+t \leq n+s. \end{cases}$$

$$\lambda = \begin{cases} c - \tfrac{1}{2}(n-m), \text{ if } n-m \text{ is even}, \\ c - \tfrac{1}{2}(n-m-1), \text{ if } n-m \text{ is odd}. \end{cases}$$

If $n - 2p + q \neq 0$,

$$G_{npq}(e) = (-1)^{q}(1+\beta^2)^{n}\beta^{q} \sum_{k=0}^{\infty} P_{npqk}\, Q_{npqk}\, \beta^{2k} \tag{1-53a}$$

where

$$\beta = \frac{e}{1+\sqrt{1-e^2}},$$

$$P_{npqk} = \sum_{r=0}^{h} \binom{2p'-2n}{h-r} \frac{(-1)^r}{r!} \left(\frac{(n-2p'+q')\,e}{2\beta}\right)^{r},$$

$$Q_{npqk} = \sum_{r=0}^{u} \binom{n-2p'}{u-r} \frac{1}{r!} \left(\frac{(n-2p'+q')\,e}{2\beta}\right)^{r}.$$

$$p' = \begin{cases} p & \\ n-p & \end{cases} \qquad q' = \begin{cases} q & \text{if } p \leq \dfrac{n}{2} \\ -q & \text{if } p > \dfrac{n}{2} \end{cases}$$

$$h = \begin{cases} k+q' & \\ k & \end{cases} \qquad u = \begin{cases} k & \text{if } q' > 0 \\ k-q' & \text{if } q' < 0 \end{cases}$$

If $n - 2p + q = 0$,

$$G_{npq} = \frac{1}{(1-e^2)^{n-1/2}} \sum_{d=0}^{p'-1} \binom{n-1}{2d-n-2p'} \binom{2d+n-2p'}{d} \left(\frac{e}{2}\right)^{2d+n-2p'} \tag{1-53b}$$

and,

$$S_{nmp} = A \cos [(n-2p)\omega + (n-2p+q)\bar{M} + m(\Omega-\theta)] + B \sin [(n-2p)\omega + (n-2p+q)\bar{M} + m(\Omega-\theta)], \quad (1\text{-}54)$$

where $A = \begin{cases} C_{n,m} \\ -S_{n,m} \end{cases}$ $B = \begin{cases} S_{n,m} & \text{if } n-m \text{ is even,} \\ C_{n,m} & \text{if } n-m \text{ is odd,} \end{cases}$

and $C_{n,m}$ and $S_{n,m}$ are the harmonic coefficients in U.

Denoting the derivative of the functions with respect to their arguments by primes and their integrals with respect to time by an integral sign, the operations on S are $\int S = -S'/\dot{\zeta}$ and $\int S' = S/\dot{\zeta}$, where $\zeta = (n-2p)\omega + (n-2p+q)\bar{M} + m(\Omega-\theta)$. If $q = m = 0$ and n is even, $S' = \int S' = 0$ and $\int S = C_{n,0}(t-t_0)$. These operations assume that the elements in S change secularly with time.

If the disturbing potential given in Eq. (1-49) and (1-51), with subscripts of F, G, S omitted for simplicity, is inserted into Eq. (1-45), the *perturbations to the orbital elements* become

$$\dot{a}_{nmpq} = \bar{n}\left(\frac{R}{a}\right)^n 2\,FGS' - (n-2p+q),$$

$$\dot{e}_{nmpq} = \bar{n}\left(\frac{R}{a}\right)^n \cdot \frac{FGS'\epsilon}{e}[\epsilon(n-2p+q) - (n-2p)],$$

$$\dot{i}_{nmpq} = \bar{n}\left(\frac{R}{a}\right)^n \cdot \frac{FGS'}{\epsilon \sin i}[(n-2p)\cos i - m],$$

$$\dot{M}^{\bullet}_{nmpq} = \bar{n}\left(\frac{R}{a}\right)^n \cdot FS\left[-\frac{\epsilon^2}{e}G' + 2(n+1)G\right],$$

$$\dot{\omega}_{nmpq} = \bar{n}\left(\frac{R}{a}\right)^n \cdot S\left[\frac{\epsilon}{e}FG' - \frac{\cot i}{\epsilon}F'G\right],$$

$$\dot{\Omega}_{nmpq} = \bar{n}\left(\frac{R}{a}\right)^n \frac{F'GS}{\epsilon \sin i},$$

Table 1-5. Gravitational coefficients determined by various methods; all values listed must be multiplied by 10^{-6}.

Coefficient	Zhongolovitch 1952	Kaula 1959	Kozai 1961	Kaula 1963
C_2	−1095.0 ± 4.3	−1087	−1082.19 ± 0.02	−1082.3
C_{22}	5.74	0.46	0.60 ± .29	5.13
S_{22}	−1.58	−0.41	−2.24 ± .29	−4.78
C_3	4.3	0.2 ± 1.3	2.29 ± .02	2.56
C_{31}	1.99	0.56	2.99 ± .36	1.64
S_{31}	−0.96	0.81	1.18 ± .31	−0.054
C_{32}	0.36	0.10	0.20 ± .20	0.478
S_{32}	−0.50	0.05	0.36 ± .20	1.435
C_{33}	0.42	0.14	−1.71 ± .29	0.84
S_{33}	0.34	0.13	0.84 ± .27	1.215
C_4	3.0	3.0 ± 0.9	2.13 ± .04	2.04
C_{41}	−0.67	−0.31	−0.25 ± .04	−.313
S_{41}	−0.40	−0.34	0.08 ± .03	.427
C_{42}	0	−0.01	−0.05 ± .06	.00224
S_{42}	0.08	0.08	0.16 ± .06	.121
C_{43}	0.03	0	0.04 ± .03	.0161
S_{43}	−0.01	−0.01	−0.03 ± .04	.0101
C_{44}	0.01	0	−0.05 ± .03	−.00021
S_{44}	0.02	0.02	−0.02 ± .03	.0038
C_5	0.7	−1.7 ± .6	0.23 ± .02	.0664

where

$$M^* = \int_0^t \bar{n}\,(\gamma)\,d\gamma - \bar{n}\,(t) + \bar{M}_0,$$

$$\bar{n} = (\mu/a^3)^{1/2},$$

and $\bar{M}_0$ is the mean anomaly of the reference orbit. From these equations, it is apparent that there are *no* secular first-order changes in a, e, and i, and no long-period variations in a. For long-period variations, the factor $(n - 2p + q)$ in Eq. (1-54) must be zero since $\bar{M}$ is the only orbital element that has a short period. In G, the quantity e^q appears; hence, for small eccentricity only values of q near zero are of interest.

Equations (1-55) integrate to

$$\Delta a_{nmpq} = \bar{n}\left(\frac{a_e}{a}\right)^n 2\,FG\,\frac{S}{\dot{\zeta}}\,(n - 2p + q)$$

or

$$\Delta a_{nmpq} = \dot{a}_{nmpq}\,\frac{S}{S'\dot{\zeta}},$$

$$\Delta e_{nmpq} = \frac{\dot{e}\,S}{S'\dot{\zeta}},$$

$$\Delta \dot{i} = \frac{\dot{i}\,S}{S'\dot{\zeta}},$$

$$\Delta M^*_{nmpq} = -\frac{S'}{\dot{\zeta}S}\,\dot{M}^*_{nmpq},$$

$$\Delta \omega_{nmpq} = -\frac{S'}{\dot{\zeta}S}\,\dot{\omega}_{nmpq},$$

$$\Delta \Omega_{nmpq} = -\frac{S'}{\dot{\zeta}S}\,\dot{\Omega}_{nmpq}.$$

The first-order long-period effects of any of the potential terms are readily determined by solving the equations using the associated subscripts and the nominal value of the harmonic coefficient. The converse, deriving the harmonic coefficients from changes in the orbital elements, is not quite so simple since the effects of many harmonic coefficients are of the same frequency. Statistical techniques for spectrum analysis must be introduced and several satellites in different orbits and altitudes must be analyzed in order to firmly determine many terms of the gravitational potential U.

The definition of the harmonic coefficients C_{nm}, S_{nm} of U from satellite observations provides additional data to calculate geodetic parameters such as the flattening and the major axis of the spheroid and plot the shape of the geoid. The even-order harmonics, C_0, C_2, C_4, C_6, where C_0 is the μ term, are related to the flattening and the equatorial radius (after the rotation of the earth is considered) by the expression:

$$C_0 = \mu = a_e^2\,g_e\left[1 + \frac{3}{2}\,\xi - f - \frac{15}{4}\,\xi f - \frac{1}{294}\,\xi f^2 - O(f^4)\right],$$

$$-C_2 = \frac{2}{3}\,f\left(1 - \frac{1}{2}\,f\right) - \frac{1}{3}\,\xi\left[1 - \frac{3}{2}\,\xi - \frac{2}{7}\,f + \frac{9}{4}\,\xi^2 + \frac{11}{49}\,f^2 + O(f^3)\right],$$

$$-C_4 = -\frac{4}{35}\,f\,(7f - 5\xi) + O(f^3),$$

$$-C_6 = O(f^3),$$

where a_e is the semi-major axis of the ellipsoid, f is the flattening, and ξ is the ratio of centrifugal acceleration to g_e, the acceleration of gravity at the equator. Table 1-6 gives the best values of zonal harmonic coefficients available from orbital analysis.

The geoid representation relative to an accepted ellipsoid of semi-major axis a can be derived from Eq. (1-50). The geoid height, Δh, is

$$\Delta h = a_e\left[\Delta C_2 P_2 + (C_{22}\cos 2\lambda + S_{22}\sin 2\lambda)\,P_{22}\sin\phi + \sum_{n=3}^{\infty}\sum_{m=0}^{n}(C_{nm}\cos m\lambda + S_{nm}\sin m\lambda)\,P_{nm}\sin\phi\right],$$

where ΔC_2 is the difference between the accepted flattening of the particular ellipsoid and the flattening represented by the value C_2 obtained from satellite analysis; r^n was taken equal to a^n, which is valid for practical purposes when one considers the equipotential function of the geoid. A series of such points for latitude and longitude will define the geoid. Figure 1-11 shows a geoid obtained from optical observations of the Echo rocket.

Table 1-7 gives values of geometrical and gravitational parameters that are used extensively in satellite orbit computations; these are the values recommended to the International Astronomical Union for adoption. There are no recommended or standardized values for the tesseral harmonics; the most recent published values are those of Izsak [1964].

Table 1-6. Best available values for zonal harmonic coefficients. (From Y. Kozai, "Numerical Results from Orbits" Smithsonian Inst., *Astrophys. Observatory Report No. 101*, July 31, 1962.)

Term	(Multiply value by 10^{-6})
$C_2 = -J_2$	-1082.48 ± 0.06
$C_4 = -J_4$	$+1.84 \pm 0.08$
$C_6 = -J_6$	$-0.39 + 0.12$
$C_8 = -J_8$	$+0.02 \pm 0.02$
$C_3 = -J_3$	$+2.562 \pm 0.012$
$C_5 = -J_5$	$+0.064 \pm 0.019$
$C_7 = -J_7$	$+0.470 \pm 0.021$
$C_9 = -J_9$	-0.117 ± 0.025

Table 1-7. Geometrical and gravitational parameters used for satellite orbit computations. (From W. M. Kaula, *NASA Technical Note D-1847*, 1963.)

	Parameter
a	6,378,165.0 ± 25 meter
f	1/298.30
γ_e	978.0300 ± 0.012 cm sec^{-2}
ω	$0.729211585 \times 10^{-4}$ rad sec^{-1}
μ	$3.986032 \pm 0.000030 \times 10^{20}$ cm^3 sec^{-2}
C_2	-1082.30×10^{-6}
C_3	$+2.3 \times 10^{-6}$
C_4	$+1.8 \times 10^{-6}$

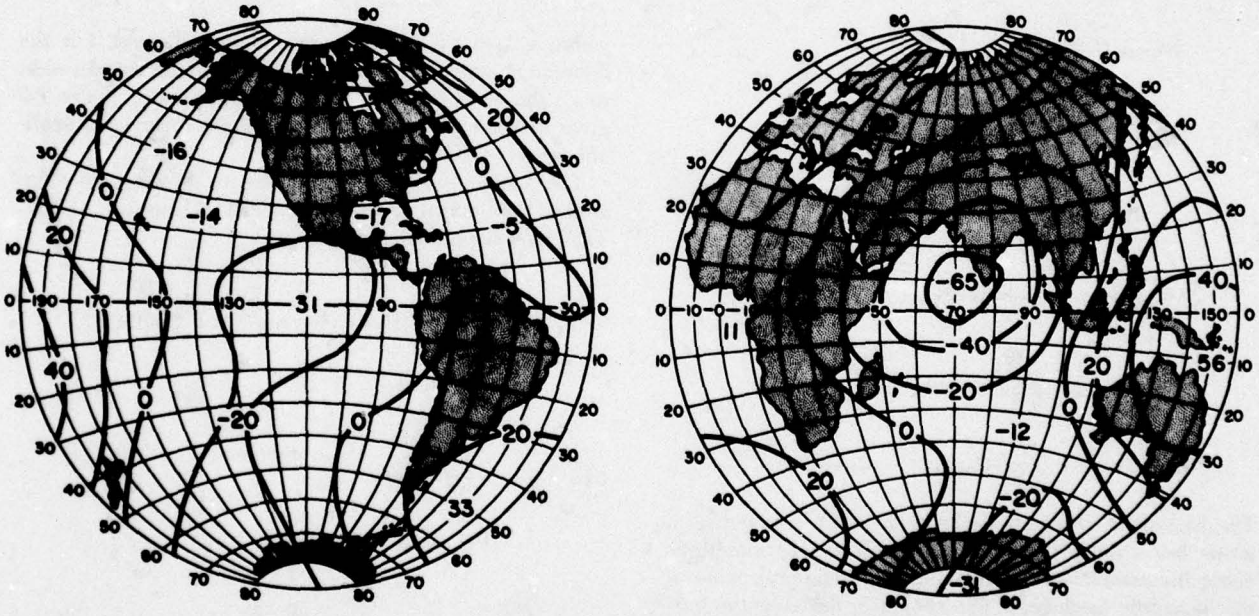


Fig. 1-11. Echo rocket geoid; heights in meters, referred to an ellipsoid of flattening 1/298.24, determined from observations of satellite 1960 *i*2, (From Kaula, [1963]).

1.10 REFERENCES

Bomford, G., 1962, "Geodesy," 2nd ed., Oxford University Press, London.

Bowie, W., 1917, "Investigations of Gravity and Isostasy," *U.S. Coast and Geodetic Survey, Special Publication*, no. 40.

Daugherty, K. I., and Define, J. D., 1963, "Comparison of Methods for Determining the Earth's Normal External Gravitational Field," XIII General Assembly of IUGG, Berkeley, Calif., Aug. '63.

deGraff-Hunter, J., 1960, "The Shape of the Earth's Surface Expressed in Terms of Gravity at Ground Level," *Bull. Geod.*, v. 56, p. 191.

Fischer, I., 1960, "An Astrogeodetic World Datum from Geoidal Heights Based on the Flattening $f = 1/298.3$," *J. Geophys. Res.*, v. 65, p. 2067.

Hayford, J. F., and W. Bowie, 1912, "The Effect of Topography and Isostatic Compensation upon the Intensity of Gravity," *U.S. Coast and Geodetic Survey, Special Publication*, no. 10.

Heiskanen, W. A., and U. Nuotio, 1938, "Topographic-Isostatic World Maps of the Effect of the Hayford Zones 10, 9, 8, and 7 to 1," *Publ. Isost. Inst. Int. Assoc. Geod.*, no. 3, Helsinki.

Heiskanen, W. A., 1950, "On the World Geodetic System," *Publ. of the Finnish Geodetic Institute*, no. 39.

Heiskanen, W. A., 1957, "The Columbus Geoid," *Trans. Am. Geophys. Union*, v. 38, p. 841.

Heiskanen, W. A., and F. A. Vening-Meinesz, 1958, "The Earth and Its Gravity Field," McGraw-Hill, New York.

Helmert, F. R., 1884, "Die Mathematischen und Physicalischen Theorien der Höheren Geodesie," Leipzig. Reprint: 1962 Minerva G.M.B.H., Frankfurt/Main.

Henderson, R. G., 1960, "A Comprehensive System of Automatic Computation in Magnetic and Gravity Interpretation," *Geophysics*, v. 25, p. 569.

Hirvonen, R. A., 1960, "New Theory of the Gravimetric Geodesy," *Publ. Isost. Inst.*, no. 32.

Hirvonen, R. A., 1962, "Statistical Analysis of Gravity Anomalies," *Publications of the Isostatic Institute of the International Association of Geodesy*, no. 37.

Hirvonen, R. A., and H. Moritz, 1963, "Practical Computation of Gravity at High Altitudes," *Publications of the Institute of Geodesy, Photogrammetry and Cartography*, no. 27, Ohio State University.

Izsak, I. G., 1964, "Tesseral harmonics of the geopotential and corrections to station coordinates," *J. Geophys. Res.*, v. 69, p. 2621.

Kaula, W. M., 1961, "A Geoid and World Geodetic System Based on a Combination of Gravimetric, Astrogeodetic, and Satellite Data," *J. Geophys. Res.*, v. 66, p. 1799.

Kaula, W. M., 1963, "Improved Geodetic Results from Camera Observations of Satellites," *J. Geophys. Res.*, v. 68, no. 18, p. 5183.

Ledersteger, K., 1958, "Gedanken zu Einer Hypothesenfreien Ableitung des Mittleren Erdellipsoides und der Undulationen des Geoides," *Bull. Geod.*, no. 50.

Markovitz, W., 1958, "Use in Geodesy of the Results of Lunar Observations and Eventual Observations of Artificial Satellites," *Bull. Geod.*, no. 49.

Molodenski, M. S., 1945, "Grundbegriffe der Geodätischen Gravimetrie" (in Russian), *Publ. Inst. Geod. Aerophot. Cartogr.*, Moscow, 1945. German Translation: VEB Verlag Technik, Berlin, 1958.

Morelli, C., 1963, "Report of the Special Study Group 5 on the Absolute and First Order World Net," *Bur. Gravimetrique Internat. Assoc., Internat. Geod., Bull. Inform.*, v. 4.

O'Keefe, J. A., and I. P. Anderson, 1953, "The Earth's Equatorial Radius and the Distance of the Moon," *Bull. Geod.*, no. 29.

Rice, D. A., 1952, "Deflections of the Vertical from Gravity Anomalies," *Bull. Geod.*, no. 25.

Sollins, A. D., 1947, "Tables for the Computation of Deflections of the Vertical from Gravity Anomalies," *Bull. Geod.*, no. 6.

Szabó, B., 1962, "Application of the Gravimetric Method for a World Geodetic System," *Bull. Geod.*, no. 65.

Uotila, U. A., 1960, "Investigation on the Gravity Field and Shape of the Earth," *Publ. Inst. Geodesy, Photogrammetry, and Cartography*, no. 10, Ohio State University.

Vening-Meinesz, F. A., 1931, "Une Nouvelle Methode pour la Reduction Isostatique Regionale de l'Intensité de la Pensanteur," *Bull. Geod.*, no. 29.

Vening-Meinesz, F. A., 1958: a, "New Formula for System of Deflection of the Plumb Line and Laplace's Theorem," and b, "Change of the Deflection of the Vertical Brought About by a Change of the Reference Ellipsoid," *Bull. Geod.*, no. 15.

Williams, O. W., 1961, "The Impact of Rocket-Flash Triangulation Upon Geodesy," *Annales Academiae Scientiarum Fennicae*, Series A, III.

Chapter 2

MODEL ATMOSPHERES

A. E. Cole
A. Court
A. J. Kantor

Because atmospheric properties vary with height in a generally regular manner, several layers or shells are recognized. This chapter describes the various layers according to their thermal structure. The *U.S. Standard Atmosphere, 1962,* which supersedes the ARDC Model Atmosphere, 1959, and the U.S. Extension to the ICAO Standard Atmosphere, 1956, provides specific description of the model atmosphere. Supplemental atmospheres describe properties for 15°N, 30°N, 45°N and 60°N up to 90 km, and at 75°N up to 30 km.

2.1 ATMOSPHERIC STRUCTURE AND DEFINITIONS

Two basic equations are used in establishing the relations among temperature, pressure, and density. The *hydrostatic* (or barometric) *equation* is

$$dP = -\rho g\, dz = -\rho g_o\, dh, \qquad (2\text{-}1)$$

where P is pressure, ρ is density, z the geometrical height, g the acceleration of gravity at height z, g_o standard acceleration of gravity at sea level, and dh is the geopotential height, a parameter defined by the relation

$$dh = \frac{g}{g_o}\, dz.$$

The *equation of state for air* (ideal gas law) is

$$P = \rho R T_m/M_o = \rho R_a T, \qquad (2\text{-}2)$$

where R is the universal gas constant, R_a is the gas *constant for air,* T is the kinetic (actual) temperature in degrees Kelvin, and M_o is the average molecular weight of air at sea level. The *molecular scale temperature,* T_m, is defined by the relation

$$T_m = TM_o/M, \qquad (2\text{-}3)$$

where M is the molecular weight of air at a specific altitude. Thus, R_a equals R/M and is a constant up to about 90 km, where the molecular weight of air begins to vary.

Atmospheric composition is essentially constant up to 90 km, above which molecular dissociation increases with altitude (see Chapter 6). Pressure and density decrease approximately exponentially with height. Water vapor decreases irregularly with height except for a slight increase between 15 and 35 km (see Chapter 3).

Temperature variation with height is the most pronounced feature of the earth's atmosphere, and layers and shells can be described most easily by temperature. Usually, temperature decreases with increasing height in the lowermost several kilometers; any increase of temperature with height in this region is called an *inversion.* The *lapse rate* is defined as $-dq/dz$, the rate of decrease with height of any atmospheric variable, q. Temperature *gradient,* however, is the rate of increase of temperature with height, dT/dz.

Except for the first two kilometers above the earth's surface, the normal lapse rate is about 6.5°C km^{-1} in the *troposphere,* which extends from the surface to the tropopause. The *tropopause* is the atmospheric surface at which the temperature decrease either stops abruptly or the lapse rate becomes less than some arbitrary low value. The height of the tropopause varies with latitude, season, and weather situation; in general, it is lowest (8 to 10 km) in arctic regions in winter, and highest (16 to 18 km) in the tropical and equatorial regions.

Temperatures averaged by months or seasons suggest isothermal conditions for several kilometers above the tropopause—a "tropopause layer"—but on individual days true isothermal layers of any appreciable thickness are rare. Above the tropopause temperatures usually increase with height, slowly at first, then more rapidly up to about 50 km, where the average temperature is within a few degrees of the freezing point. The surface of maximum temperature is now designated as the *stratopause,* and the entire layer below it down to the tropopause is the *stratosphere.*

Formerly, the stratosphere was considered to be a region of constant or only slightly increasing temperature (up to 20 or 25 km), and the term "mesopeak" was applied by some authors to the maximum temperature layer. Recent action by the World Meteorological Organization and other groups has now extended the region of the stratosphere by definition up to the "warm" isothermal layer near 50 km, and restricted the term *mesosphere* to the region of decreasing temperature above the stratopause.

CHAPTER 2

The mesosphere ends at the *mesopause*, at 80 to 90 km, where the lowest temperatures of the atmosphere are found (about −90°C). Above the mesopause lies the *thermosphere*, whose upper limit is undefined. In it, temperature increases rapidly with height up to about 200 km, then, more slowly or not at all. Above 200 km, temperature varies widely according to the degree of solar activity; it is about 600°C when the sun is quiet and possibly 2000°C during sunspot maxima. The *exosphere* (roughly 550 km) is the region where the mean free path is so great that particles escape from the atmosphere. In this region, temperature can no longer be defined in the usual way.

2.2 U. S. STANDARD ATMOSPHERE, 1962

Generalized description of the vertical structure of the earth's atmosphere has been provided during the past half century by a succession of "Standard Atmospheres." The first were developed in the 1920's primarily for the standardization of aircraft instruments and for performance standards. The model presented here was adopted March 1962, and supersedes the ARDC Model Atmosphere, 1959.

The lowermost 20 km of this 1962 Standard are essentially unchanged from previous ARDC model atmospheres. The major difference is a decrease of 0.01 of a degree throughout, resulting from adoption of the latest international value of 273.15°K for the ice point. The corresponding change of one or two units in the fifth place of other atmospheric properties (pressure, density, speed of sound, etc.) is inconsequential for most engineering applications.

Figure 2-1 shows that from 20 to 28 km, the 1962 Standard is warmer than the 1956 and 1959 Models; above 28 km, it is colder. The stratopause is at about the same height as, but 12° colder than, the earlier models. The height of the mesopause is about the same as that previously used. The earlier models are compared with the standard in Table 2-1. As shown in Fig. 2-2 in the thermosphere and above, the 1962 Standard is warmer at some heights and colder at others than the previous models.

Table 2-5, at the end of this chapter, is an abridged version of detailed tables of the *U.S. Standard Atmosphere, 1962*. The original publication should be consulted for additional information at these levels and others not tabulated.

The entire 1962 Standard is defined by linear temperature gradients which are changed at specified heights above the surface. Up to 80 km, these heights are in geopotential units, above 80 km in geometric units; the 80-km level was chosen for the transition because 79.006 geopotential km is 80.000 geometric km above sea level. (Conversion of geopotential to geometric units usually results in awkward numbers; e.g., the 50-km geopotential surface is at 50.396 km geometric height.)

Because atmospheric composition and, hence, molecular weight of air changes above the mesopause, the atmosphere in and above the thermosphere is defined by molecular-scale temperature, T_m. Above 90 km the molecular weight of air is not known exactly and air temperatures, T, are not directly measurable. T can be derived only if the molecular weight is known; however, T_m can be found by the substitution of measured pressures or densities into Eq. (2-2) and (2-3). Thus the introduction of the parameter T_m increases the validity of tabulated properties. Figure 2-2 shows molecular-scale temperatures. Elsewhere in this chapter the actual or kinetic temperatures based on estimated molecular weights above 90 km are used. Figure 2-3 shows other properties of the 1962 Standard.

Also used in the construction of the 1962 Standard, but not discussed in this chapter, is the concept of "scale height." This is the reciprocal of the rate of change with height of the natural logarithm of the parameter in question, usually pressure or density (see Chapter 3).

The 1962 Standard, like its predecessors, represents average conditions in mid-latitudes around 45°N. The following sea-level values of temperature, pressure, and density have been standard for decades:

288°K temperature is ~~273.15°K~~, 15°C, or 59°F;
pressure is 1013.25 mb, 760 mm of Hg, or 29.92 in. of Hg;
density is 1225.00 g m^{-3}, or 0.076474 lb ft^{-3}.

Table 2-1. Changes in stratopause and mesopause.

Atmospheric Layer	ARDC Models		U.S. Standard
	1956	1959	1962
Stratopause			
altitude range (km)	47.35 to 53.45	47.4 to 53.0	47.35 to 52.43
temperature (°K)	282.66	282.66	270.65
Mesopause			
altitude range (km)	75.80 to 91.29	80.0 to 91.0	79.99 to 90.00
temperature (°K)	196.86	165.7	180.65

2.3 SUPPLEMENTAL ATMOSPHERES

Actual conditions may differ from those depicted by the 1962 Standard. Chapter 3 discusses differences caused by day-to-day weather changes and by changes throughout the 11-yr solar cycle. Latitudinal differences and those caused by seasonal changes are depicted by a family of supplemental atmospheres. These supplemental atmospheres, like the 1962 Standard, are hydrostatically consistent, and represent conditions that can occur on any one day.

These atmospheres are constructed to 90 km for 15°, 30°, 45°, and 60°N latitude and to 30 km for 75°N. At 15°N, where seasonal variation appears to be less than at higher latitudes, one atmosphere for all seasons is presented. At other latitudes, both January and July atmospheres are given. Three atmospheres are needed to de-

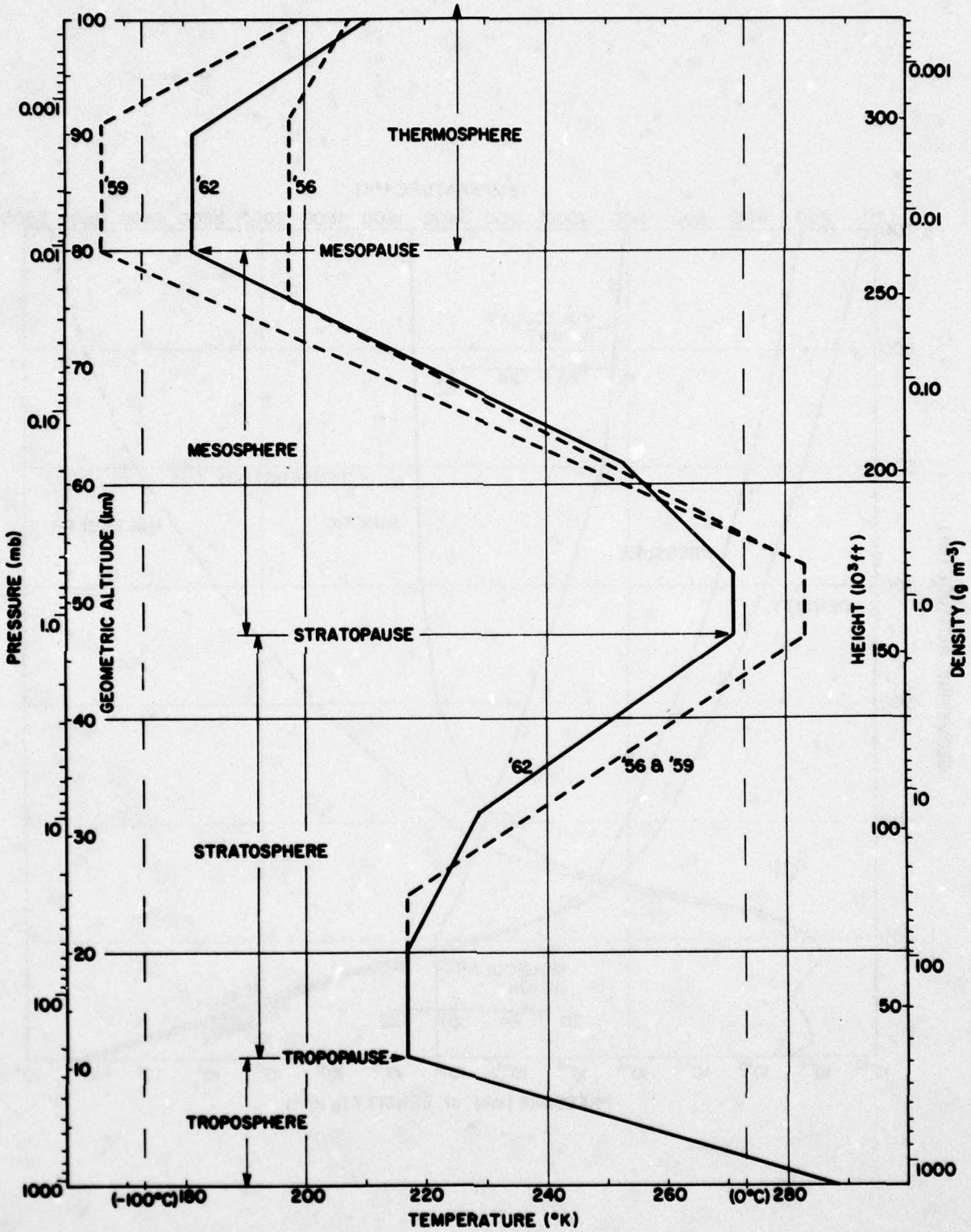


Fig. 2-1. Temperature-height profiles to 100 km of *U. S. Standard Atmosphere, 1962*, compared to those of ARDC Model Atmospheres, 1956 and 1959. (The 1956 Model agrees with the 1954 "U. S. Extension to the ICAO Standard Atmosphere.") The names shown for atmospheric shells and boundaries are those adopted by the World Meteorological Organization.

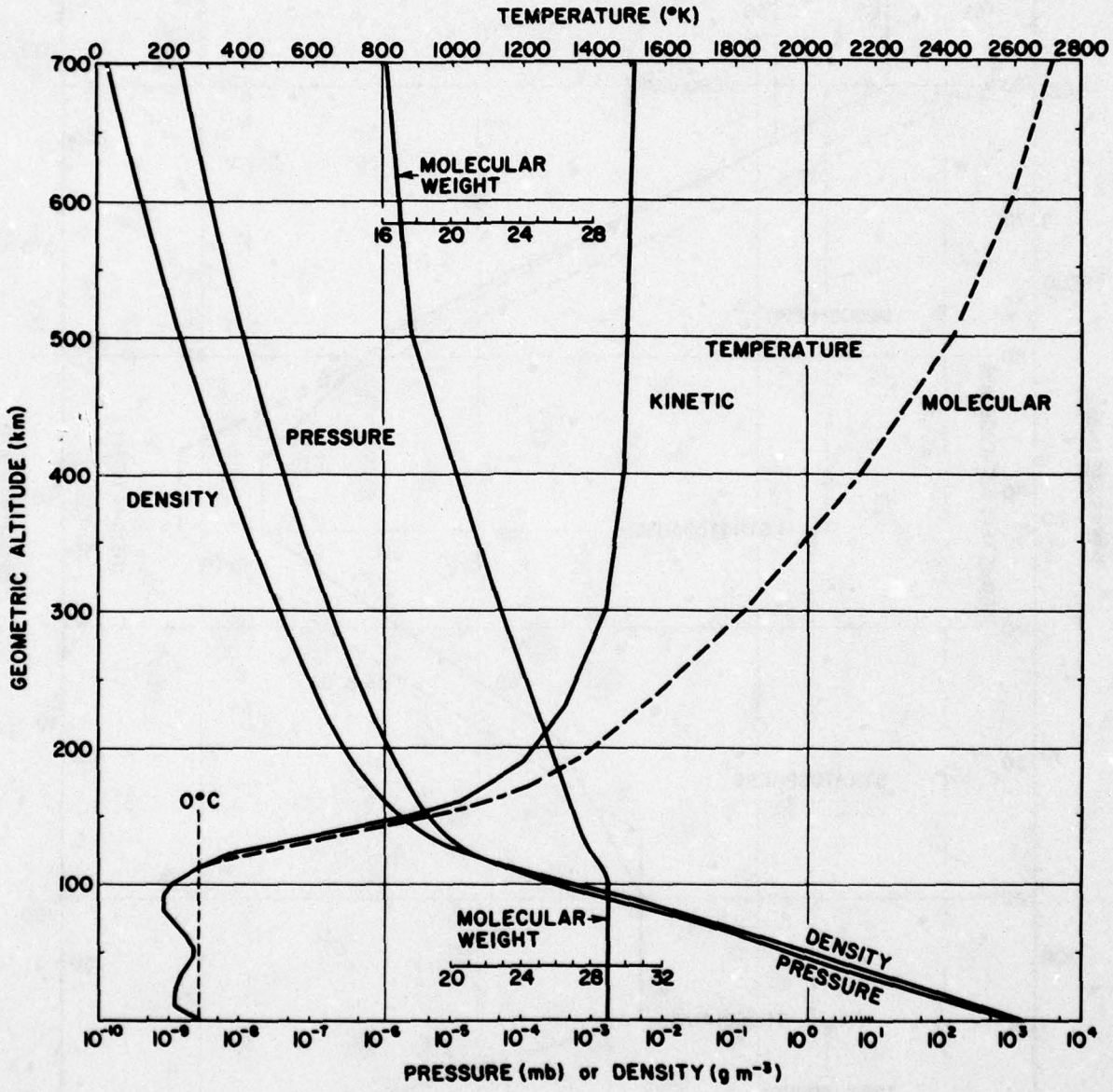


Fig. 2-2. Profiles to 700 km of temperature, pressure, density, and molecular weight, according to *U. S. Standard Atmosphere, 1962*. Scales for temperature (°K) and molecular weight are linear; for pressure (mb) and density (g m^{-3}), logarithmic.

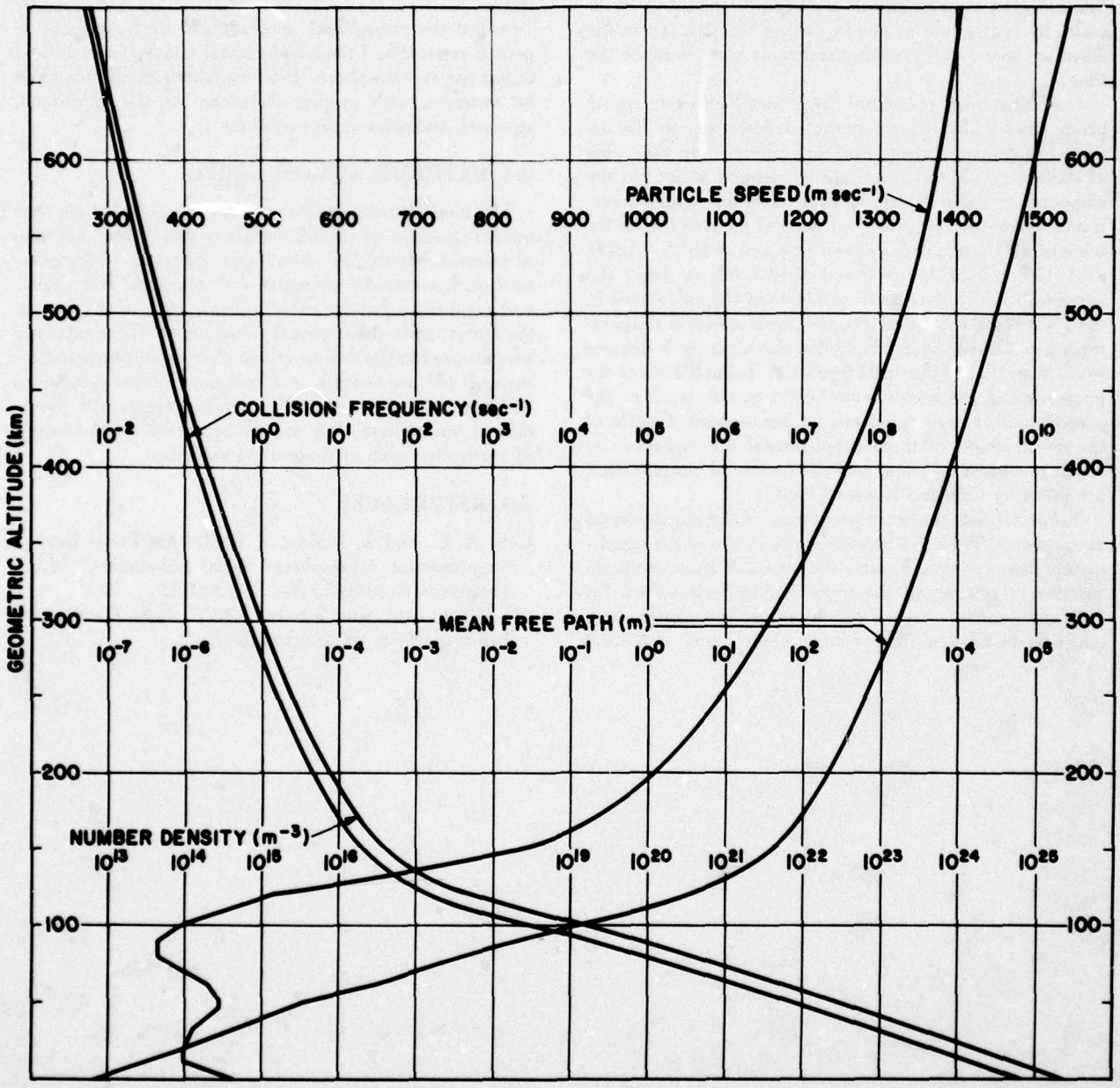


Fig. 2-3. Profiles to 700 km of number density, collision frequency, mean free path, and particle speed, according to *U. S. Standard Atmosphere, 1962*. Scales for mean free path (m) and particle speed (m sec^{-1}) are linear; for number density (m^{-3}) and collision frequency (sec^{-1}), logarithmic.

scribe adequately the structure of the winter atmosphere at 60°N and 75°N. Warm and cold atmospheres that reflect the bimodal distribution of winter stratospheric temperatures noted at these latitudes, as well as mean hemispheric January atmospheres, are presented. Stratospheric studies of subpolar temperatures indicate that the frequency of occurrence of warm and cold stratospheric conditions varies with longitude. Cold conditions prevail over warm by nearly four to one in eastern Canada, but in the Aleutian Islands area warm conditions exist most of the time.

In these atmospheres humidity is specified where appropriate, and densities are computed according to the assumed moisture content. For each atmosphere the value of surface gravity applicable to its latitude is used in the computation of geometric altitudes and the assumed sea-level conditions are the best estimate of the true means for the latitude. Hence, the sea-level pressure at 45°N is taken as 1018.0 mb in January and 1013.5 mb in July; the average, 1015.75, is 2.5 mb higher than the value used in the 1962 Standard. Similarly, the mean sea-level temperatures are 272.15° and 294.15°K; the mean is 5 degrees lower than that of the 1962 Standard. Table 2-2 gives the properties of the temperature-height profile used in the preparation of each supplemental atmosphere. Details of the construction of these supplemental atmospheres, including sources of data and discussion of peculiarities, are given by Cole and Kantor [1963].

Table 2-3 lists moisture properties of the supplemental atmospheres. Table 2-4 lists other properties of the supplemental atmospheres. Figures 2-4 and 2-5 show temperature-height profiles of the mean hemispheric values for July and January. Figure 2-6 shows profiles of the warm and cold 60°N and 75°N winter atmospheres. Table 2-3 gives details of the moisture profile of these atmospheres up to 10 km.

Linear interpolation between July and January values cannot be used to obtain values for the fall and spring months, because the extreme mean monthly values of temperature, pressure, and density do not occur at all levels in these months, and the change with season is not linear.

Above the mesopause, observations are insufficient to permit extension of the supplemental atmospheres. In and above the thermosphere, 1962 Standard conditions must be assumed, with proper allowance for the latitudinal, seasonal, and solar-cycle variations.

2.4 EXTREME ATMOSPHERES

The most extreme conditions that can occur at any one level, regardless of conditions above and below, are also of interest. Figure 2-7 shows such extremes of temperature, with associated pressures and densities. They represent conditions that are exceeded only 10% of the time in the hottest and coldest geographical areas. These extremes may be used in the design of vehicles passing horizontally through the atmosphere, but because extreme conditions will not occur simultaneously over any appreciable thickness of atmosphere, they are not applicable to the design of vertically rising or descending vehicles.

2.5 REFERENCES

Cole, A. E., and A. J. Kantor, 1963, "Air Force Interim Supplemental Atmospheres to 90 Kilometers," *A. F. Surveys in Geophysics No. 153*, AFCRL.

"U.S. Standard Atmosphere, 1962," U.S. Government Printing Office, Washington, D. C.

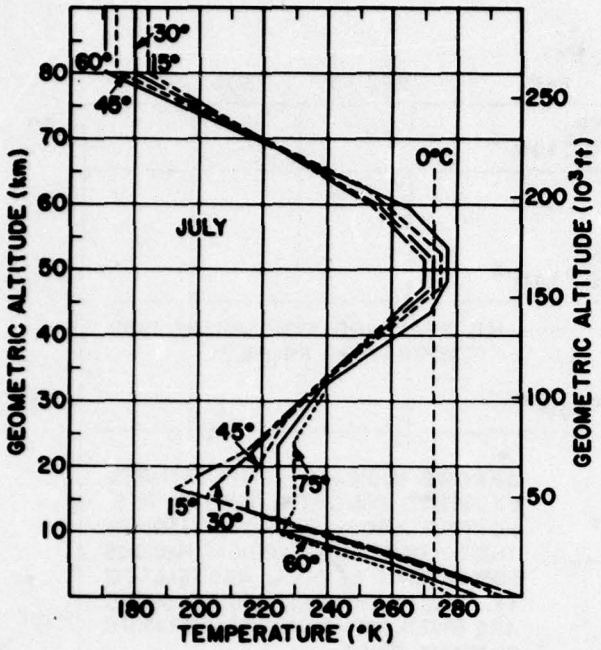


Fig. 2-4. Temperature profiles to 90 km of the "July Supplemental Atmosphere" for 15°, 30°, 45°, 60° and 70° N latitude.

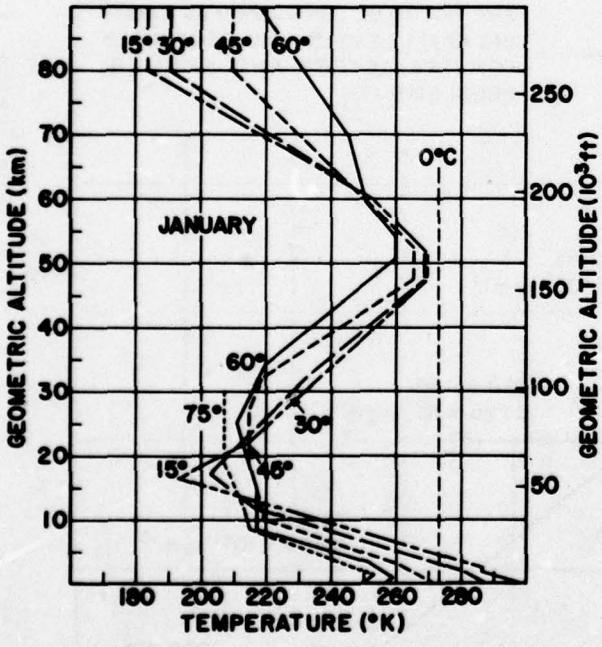
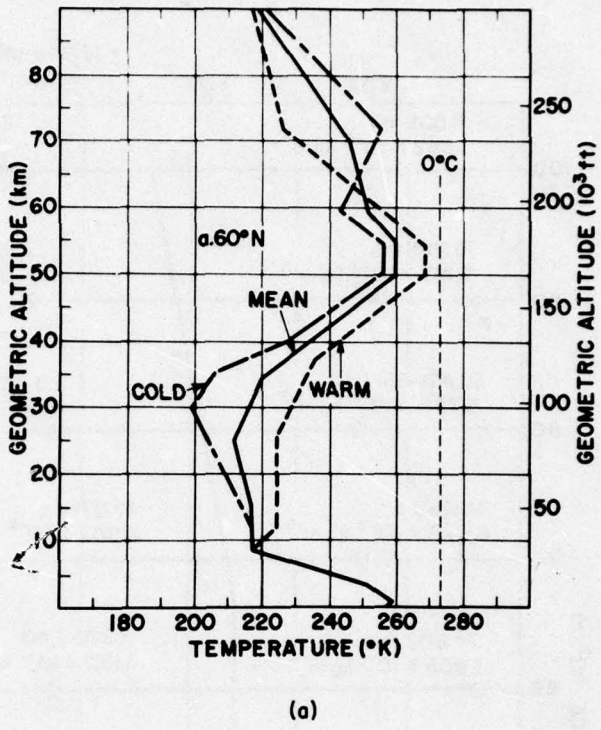


Fig. 2-5. Temperature profiles to 90 km of the "January Supplemental Atmosphere" for 15°, 30°, 45°, 60° and 75° N latitude.



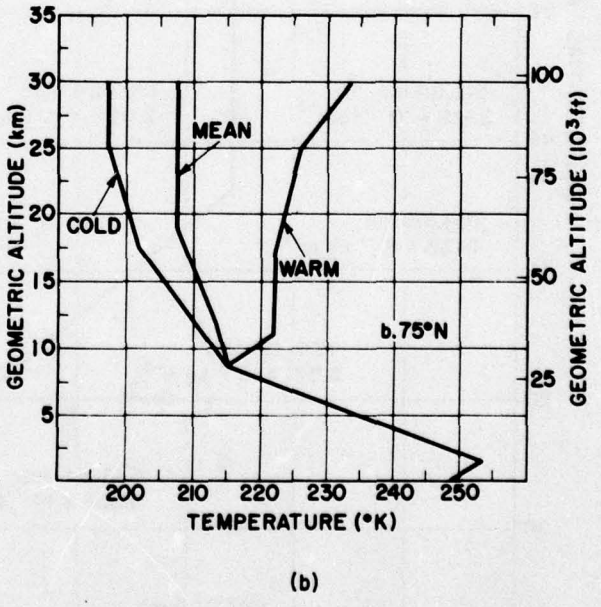


Fig. 2-6. Temperature profiles of the "Warm and Cold Winter Atmosphere" for (a) 60° and (b) 75° N latitude and the hemispheric winter means at these latitudes.

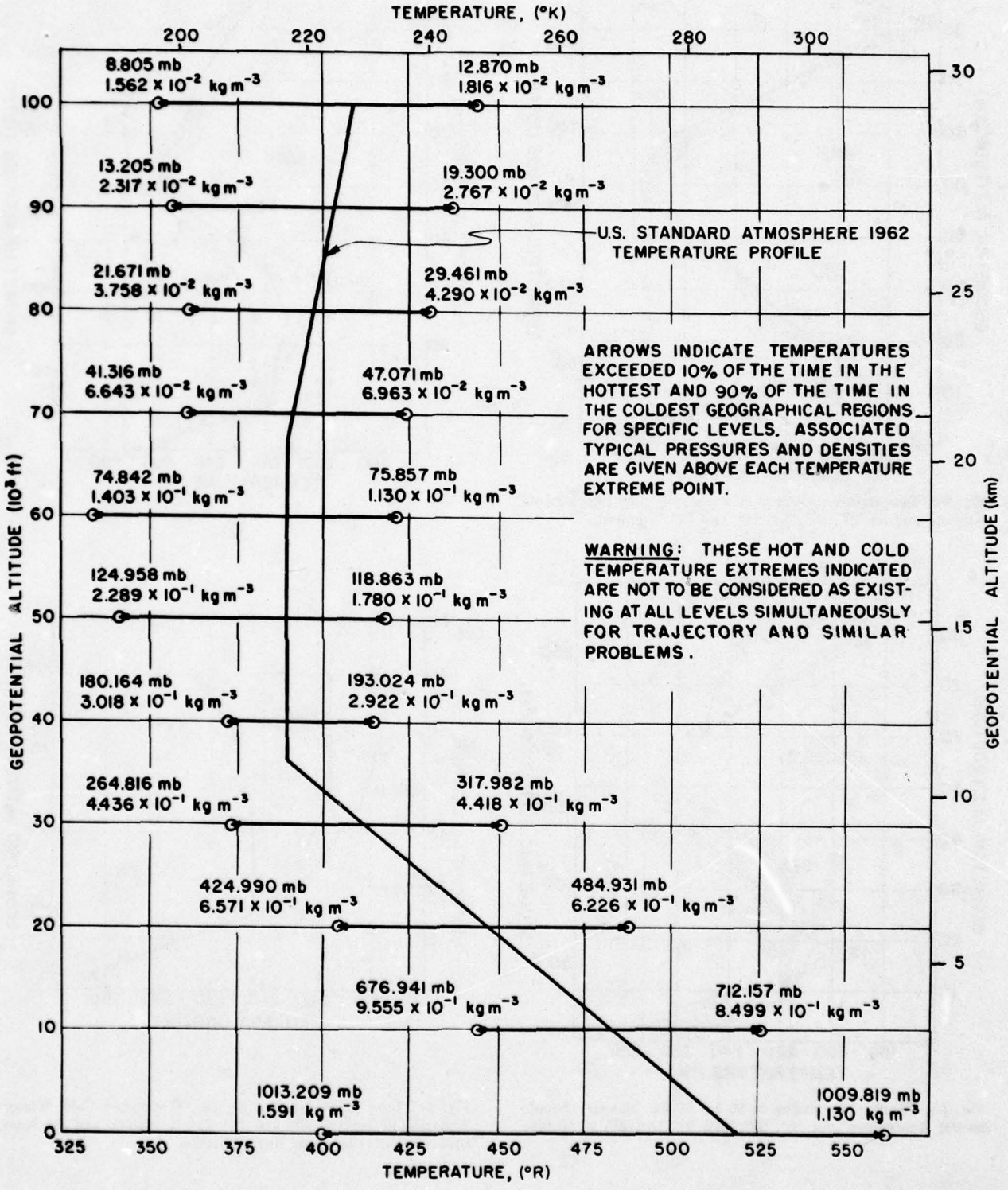


Fig. 2-7. Hot and cold temperature extremes and the *U. S. Standard Atmosphere, 1962*, temperature-height profile to 100,000 ft.

Table 2-2. Heights and temperatures at points of change in vertical temperature gradient.

U.S. Standard, 1962

Altitude (km) Geom	Altitude (km) Geop	Annual °C
0.000	0.000	+15.0
11.019	11.000	−56.5
20.063	20.000	−56.5
32.162	32.000	−44.5
47.350	47.000	−2.5
52.429	52.000	−2.5
61.591	61.000	−20.5
79.994	79.000	−92.5
90.000	88.743	−92.5

Tropical (15°N)

0.000	0.000	+26.5
2.256	2.250	+13.0
2.507	2.500	+13.8
16.582	16.500	−80.0
22.128	22.000	−58.0
47.463	47.000	−3.0
51.535	51.000	−3.0
59.695	59.000	−19.0
80.186	79.000	−89.0
90.000	88.533	−89.0

Subtropical (30°N)

		Jul °C	Jan °C
0.000	0.000	+28.0	+14.0
1.002	1.000	+20.5	—
2.003	2.000	—	+8.0
6.014	6.000	−7.0	—
12.039	12.000	—	−57.0
15.056	15.000	−70.0	—
16.062	16.000	−70.0	—
17.069	17.000	—	−70.0
18.076	18.000	—	−70.0
21.099	21.000	−59.0	—
22.107	22.000	—	−60.0
32.206	32.000	−37.0	−40.0
47.416	47.000	−1.0	−4.0
51.484	51.000	−1.0	−4.0
59.636	59.000	−17.0	−20.0
80.107	79.000	−93.0	−82.0
90.000	88.620	−93.0	−82.0

Midlatitude (45°N)

0.000	0.000	+21.0	−1.0
2.001	2.000	+12.0	—
3.001	3.000	—	−11.5
6.006	6.000	−12.0	—
10.016	10.000	—	−53.5
13.027	13.000	−57.5	—
17.046	17.000	−57.5	—
19.057	19.000	—	−58.0
27.115	27.000	−45.5	−58.0
32.162	32.000	−35.0	−54.0
47.350	47.000	+2.5	−7.5
52.429	52.000	+2.5	−7.5
62.611	62.000	−22.5	—
64.651	64.000	—	−31.5
79.994	79.000	−99.0	−63.0
90.000	88.743	−99.0	−63.0

U.S. Standard, 1962 (Continued)

Altitude (km) Geom	Altitude (km) Geop	Jul °C	Jan °C
Subarctic (60°N)			
0.000	0.000	+14.0	−16.0
0.999	1.000	—	−14.0
3.497	3.500	—	−22.0
4.998	5.000	−13.0	—
8.501	8.500	—	−56.0
10.003	10.000	−48.0	—
15.003	15.000	—	−56.0
23.054	23.000	−48.0	—
25.067	25.000	—	−62.0
32.121	32.000	−34.5	—
34.139	34.000	—	−53.0
43.237	43.000	−1.5	—
48.303	48.000	+4.0	—
50.331	50.000	—	−13.0
53.376	53.000	+4.0	—
54.392	54.000	—	−13.0
59.476	59.000	−8.0	−22.0
69.666	69.000	—	−27.0
79.890	79.000	−102.0	—
90.000	88.858	−102.0	−54.8012

		Winter Warm	Winter Cold
12.007	12.000	−49.0	−56.0
25.570	25.500	−49.0	—
30.104	30.000	—	−74.0
35.149	35.000	—	−67.0
37.169	37.000	−37.5	—
40.201	40.000	—	−45.0
50.331	50.000	−5.0	−17.0
54.392	54.000	−5.0	−17.0
59.476	59.000	—	−30.0
71.709	71.000	−47.5	−18.0
90.000	88.858	−56.429	−53.716

Arctic (75°N)

		Jul °C	Jan °C
0.000	0.000	+5.0	−24.0
1.497	1.500	—	−19.5
2.495	2.500	−1.5	—
8.492	8.500	—	−58.0
9.493	9.500	−47.0	—
11.495	11.500	—	−59.5
13.498	13.500	−43.0	—
19.014	19.000	—	−65.5
23.534	23.500	−43.0	—
30.074	30.000	—	−65.5
31.082	31.000	−34.0	

		Winter Warm	Winter Cold
10.994	11.000	−51.0	—
17.007	17.000	−51.0	—
17.509	17.500	—	−71.5
25.042	25.000	−47.0	−76.0
30.074	30.000	−39.5	−76.0

Table 2-3. Moisture properties of the supplemental atmospheres.

Altitude (km) Geom	Geop	Temperature (°K)		Virtual Temp (°K)		Relative Humidity, %	
Tropical (15°N)							
0.000	0.000	299.65		302.588		75	
1.002	1.000	293.65		295.893		75	
2.005	2.000	287.65		289.336		75	
2.256	2.250	286.15		287.717		75	
2.507	2.500	286.95		287.743		35	
4.012	4.000	276.90		277.363		35	
6.020	6.000	263.50		263.709		35	
8.029	8.000	250.10		250.172		30	
10.039	10.000	236.70		236.717		20	
		Temp (°K) Jan	July	Virtual Temp (°K) Jan	July	Rel Hum (%) Jan	July
Subtropical (30°N)							
0.000	0.000	287.15	301.15	288.519	304.583	80	80
1.002	1.000	284.15	293.65	285.244	295.580	70	65
2.003	2.000	281.15	288.15	281.862	289.536	50	60
3.006	3.000	274.65	282.65	275.098	283.716	45	60
4.008	4.000	268.15	277.15	268.389	277.823	35	50
6.014	6.000	255.15	266.15	255.239	266.445	30	40
8.021	8.000	242.15	252.15	242.185	252.266	30	40
10.030	10.000	229.15	238.15	229.162	238.179	30	30
Midlatitude (45°N)							
0.000	0.000	272.15	294.15	272.594	296.216	77	75
1.000	1.000	268.65	289.65	268.998	291.142	70	65
2.001	2.000	265.15	285.15	265.427	286.192	65	55
3.001	3.000	261.65	279.15	261.850	279.777	55	45
4.003	4.000	255.65	273.15	255.774	273.552	50	40
6.005	6.000	243.65	261.15	243.698	261.299	45	30
8.010	8.000	231.65	248.15	231.664	248.211	35	30
10.016	10.000	219.65	235.15	219.654	235.172	30	30
Subarctic (60°N)							
0.000	0.000	257.15	287.15	257.285	288.449	80	75
0.999	1.000	259.15	281.75	259.311	282.685	70	70
1.998	2.000	255.95	276.35	256.089	277.062	70	70
2.998	3.000	252.75	270.95	252.861	271.447	65	65
3.497	3.500	251.15	268.25	251.245	#	60	—
3.997	4.000	247.75	265.55	247.824	265.889	60	60
4.998	5.000	240.95	260.15	#	260.376	—	55
5.998	6.000	234.15	253.15	234.170	253.277	50	50
8.000	8.000	220.55	239.15	220.550	239.185	40	40
10.003	10.000	—	225.15	—	225.155	—	30
Arctic (75°N)							
0.000	0.000	249.15	278.15	249.216	278.924	80	85
0.998	1.000	252.15	275.55	252.231	276.187	65	75
1.497	1.500	253.65	274.25	253.741	#	60	—
1.996	2.000	250.90	272.95	250.976	273.463	60	65
2.495	2.500	248.15	271.65	#	272.144	—	65
2.995	3.000	245.40	268.40	245.448	#	55	—
3.994	4.000	239.90	261.90	239.929	262.131	50	55
5.992	6.000	228.90	248.90	228.911	248.978	45	45
7.992	8.000	217.90	235.90	217.90	235.922	40	35
9.493	9.500	—	226.15	—	226.158	—	30
9.993	10.000	—	226.65	—	226.656	—	20

Not a virtual temperature breakpoint.

Table 2-4. Temperature, pressure, and density of Supplemental Atmosphere; for pressure and density values +04 equals $\times 10^4$.

Geom Alt (km)	Temp (°K)	Press (mb)		Density (g m^{-3})	
		Tropical (15°N)			
0	299.650	0.101325	+04	0.116655	+04
1	293.662	0.904134	+03	0.106443	04
2	287.680	0.804790	03	0.968878	+03
3	283.654	0.714754	03	0.875708	03
4	276.980	0.633206	03	0.795068	03
5	270.307	0.559266	03	0.719873	03
6	263.634	0.492402	03	0.650142	03
7	256.961	0.432099	03	0.585483	03
8	250.294	0.377918	03	0.525844	03
9	243.628	0.329330	03	0.470827	03
10	236.961	0.285890	03	0.420269	03
11	230.302	0.247214	03	0.373951	03
12	223.642	0.212859	03	0.331571	03
13	216.982	0.182451	03	0.292928	03
14	210.322	0.155637	03	0.257790	03
15	203.669	0.132109	03	0.225967	03
16	197.023	0.111548	03	0.197234	03
17	194.810	0.937040	+02	0.167566	03
18	198.778	0.788798	02	0.138241	03
19	202.746	0.666272	02	0.114482	03
20	206.714	0.564623	02	0.951540	+02
21	210.678	0.480069	02	0.793821	02
22	214.642	0.409413	02	0.664484	02
23	217.049	0.350059	02	0.561852	02
24	219.229	0.299734	02	0.476296	02
25	221.407	0.257079	02	0.404495	02
26	223.583	0.220859	02	0.344124	02
27	225.761	0.189993	02	0.293175	02
28	227.936	0.163701	02	0.250193	02
29	230.112	0.141247	02	0.213835	02
30	232.286	0.122061	02	0.183059	02
31	234.459	0.105624	02	0.156940	02
32	236.633	0.915227	+01	0.134739	02
33	238.807	0.794080	01	0.115839	02
34	240.978	0.689953	01	0.997425	+01
35	243.149	0.600237	01	0.859978	01
36	245.319	0.522906	01	0.742560	01
37	247.490	0.456029	01	0.641909	01
38	249.659	0.398236	01	0.555687	01
39	251.826	0.348221	01	0.481718	01
40	253.993	0.304839	01	0.418106	01
41	256.162	0.267127	01	0.363279	01
42	258.327	0.234404	01	0.316106	01
43	260.494	0.205886	01	0.275339	01
44	262.659	0.181056	01	0.240137	01
45	264.824	0.159389	01	0.209671	01
46	266.986	0.140478	01	0.183298	01
47	269.149	0.123937	01	0.160416	01
48	270.150	0.109438	01	0.141124	01
49	270.150	0.966452	00	0.124627	01
50	270.150	0.853587	00	0.110073	01
51	270.150	0.753903	00	0.972185	00
52	269.236	0.665795	00	0.861481	00
53	267.274	0.587601	00	0.765886	00
54	265.312	0.518113	00	0.680308	00
55	263.350	0.456416	00	0.603762	00
56	261.390	0.401737	00	0.535416	00
57	259.430	0.353269	00	0.474377	00
58	257.470	0.310346	00	0.419912	00
59	255.510	0.272369	00	0.371353	00
60	253.104	0.238822	00	0.328711	00
61	249.677	0.209071	00	0.291711	00
62	246.254	0.182715	00	0.258481	00
63	242.828	0.159358	00	0.228621	00
64	239.405	0.138737	00	0.201883	00
65	235.985	0.120561	00	0.177976	00
66	232.562	0.104537	00	0.156592	00
67	229.142	0.904640	−01	0.137534	00
68	225.726	0.781276	−01	0.120576	00
69	222.307	0.673125	−01	0.105483	00
70	218.891	0.578697	−01	0.921004	−01
71	215.475	0.496334	−01	0.802445	−01
72	212.062	0.424719	−01	0.697712	−01
73	208.646	0.362460	−01	0.605184	−01
74	205.234	0.308570	−01	0.523773	−01
75	201.825	0.262029	−01	0.452286	−01
76	198.416	0.221889	−01	0.389581	−01
77	195.007	0.187357	−01	0.334702	−01
78	191.528	0.157167	−01	0.285869	−01
79	188.189	0.132375	−01	0.245048	−01
80	184.783	0.110762	−01	0.208818	−01
81	184.150	0.924748	−02	0.174940	−01
82	184.150	0.772164	−02	0.146075	−01
83	184.150	0.644757	−02	0.121973	−01
84	184.150	0.538372	−02	0.101847	−01
85	184.150	0.449540	−02	0.850423	−02
86	184.150	0.375436	−02	0.710235	−02
87	184.150	0.313547	−02	0.593156	−02
88	184.150	0.261860	−02	0.495377	−02
89	184.150	0.218734	−02	0.413793	−02
90	184.150	0.182711	−02	0.345646	−02
		Subtropical (30°N) Jul			
0	301.150	0.101350	+04	0.115919	+04
1	293.665	0.904644	+03	0.106614	04
2	288.166	0.805035	03	0.968553	+03
3	282.683	0.714840	03	0.877627	03
4	277.194	0.633106	03	0.793730	03
5	271.710	0.559359	03	0.715890	03
6	266.227	0.492915	03	0.644277	03
7	259.269	0.433038	03	0.581389	03
8	252.297	0.379127	03	0.523249	03
9	245.325	0.330683	03	0.469437	03
10	238.353	0.287287	03	0.419834	03
11	231.388	0.248576	03	0.374246	03
12	224.423	0.214135	03	0.332398	03
13	217.458	0.183593	03	0.294116	03
14	210.500	0.156649	03	0.259247	03
15	203.542	0.132948	03	0.227545	03
16	203.150	0.112484	03	0.192891	03
17	205.198	0.952596	+02	0.161724	03
18	207.383	0.808145	02	0.135755	03
19	209.568	0.686781	02	0.114165	03
20	211.752	0.584629	02	0.961813	+02
21	213.935	0.498574	02	0.811870	02
22	215.938	0.425848	02	0.687010	02
23	217.922	0.364256	02	0.582295	02
24	219.904	0.312062	02	0.494362	02
25	221.886	0.267718	02	0.420325	02
26	223.866	0.230024	02	0.357950	02
27	225.848	0.197871	02	0.305214	02
28	227.828	0.170462	02	0.260651	02
29	229.806	0.147062	02	0.222934	02

(Continued)

Table 2-4. Temperature, pressure, and density of Supplemental Atmosphere; for pressure and density value of +04 equals $\times 10^4$. (Continued)

Geom Alt (km)	Temp (°K)	Press (mb)		Density (g m^{-3})	
30	231.786	0.127015	02	0.190901	02
31	233.764	0.109855	02	0.163711	02
32	235.742	0.951285	+01	0.140576	02
33	238.032	0.824936	01	0.120732	02
34	240.403	0.716377	01	0.103810	02
35	242.774	0.622966	01	0.893922	+01
36	245.145	0.542471	01	0.770887	01
37	247.514	0.473072	01	0.665833	01
38	249.883	0.413089	01	0.575898	01
39	252.252	0.361174	01	0.498793	01
40	254.618	0.316222	01	0.432655	01
41	256.985	0.277206	01	0.375780	01
42	259.351	0.243297	01	0.326804	01
43	261.715	0.213817	01	0.284611	01
44	264.079	0.188127	01	0.248174	01
45	266.443	0.165713	01	0.216666	01
46	268.805	0.146152	01	0.189412	01
47	271.169	0.129025	01	0.165758	01
48	272.150	0.114036	01	0.145973	01
49	272.150	0.100786	01	0.129012	01
50	272.150	0.890858	00	0.114035	01
51	272.150	0.787441	00	0.100797	01
52	271.136	0.695946	00	0.894183	00
53	269.172	0.614673	00	0.795522	00
54	267.208	0.542397	00	0.707140	00
55	265.244	0.478178	00	0.628032	00
56	263.282	0.421222	00	0.557350	00
57	261.320	0.370699	00	0.494182	00
58	259.358	0.325922	00	0.437776	00
59	257.398	0.286311	00	0.387500	00
60	254.794	0.251217	00	0.343478	00
61	251.073	0.220100	00	0.305392	00
62	247.349	0.192431	00	0.271021	00
63	243.629	0.167821	00	0.240112	00
64	239.909	0.146226	00	0.212332	00
65	236.189	0.127059	00	0.187406	00
66	232.472	0.110174	00	0.165100	00
67	228.756	0.953143	−01	0.145152	00
68	225.040	0.822631	−01	0.127346	00
69	221.327	0.708360	−01	0.111496	00
70	217.611	0.608326	−01	0.973856	−01
71	213.902	0.521216	−01	0.848872	−01
72	210.189	0.445303	−01	0.738046	−01
73	206.480	0.379443	−01	0.640185	−01
74	202.772	0.322387	−01	0.553871	−01
75	199.067	0.273134	−01	0.477987	−01
76	195.358	0.230646	−01	0.411296	−01
77	191.653	0.194172	−01	0.352947	−01
78	187.948	0.162917	−01	0.301973	−01
79	184.247	0.136242	−01	0.257603	−01
80	180.545	0.113522	−01	0.219044	−01
81	180.150	0.943781	−02	0.182505	−01
82	180.150	0.784759	−02	0.151754	−01
83	180.150	0.652532	−02	0.126184	−01
84	180.150	0.542584	−02	0.104923	−01
85	180.150	0.451162	−02	0.872441	−02
86	180.150	0.375215	−02	0.725577	−02
87	180.150	0.312052	−02	0.603436	−02
88	180.150	0.259522	−02	0.501855	−02
89	180.150	0.215876	−02	0.417454	−02
90	180.150	0.179570	−02	0.347247	−02

Geom Alt (km)	Temp (°K)	Press (mb)		Density (g m^{-3})	
		Subtropical (30°N) Jan			
0	287.150	0.102100	+04	0.123279	+04
1	284.156	0.906591	+03	0.110719	04
2	281.159	0.803784	03	0.993403	+03
3	274.689	0.711253	03	0.900557	03
4	268.202	0.627395	03	0.814194	03
5	261.722	0.551763	03	0.733970	03
6	255.241	0.483671	03	0.659910	03
7	248.760	0.422537	03	0.591578	03
8	242.286	0.367862	03	0.528848	03
9	235.812	0.319059	03	0.471301	03
10	229.338	0.275634	03	0.418699	03
11	222.871	0.237159	03	0.370701	03
12	216.403	0.203149	03	0.327032	03
13	213.664	0.173438	03	0.282780	03
14	211.080	0.147808	03	0.243944	03
15	208.496	0.125718	03	0.210058	03
16	205.911	0.106714	03	0.180543	03
17	203.329	0.904107	+02	0.154902	03
18	203.150	0.765066	02	0.131196	03
19	205.443	0.647964	02	0.109875	03
20	207.925	0.549879	02	0.921295	+02
21	210.405	0.467627	02	0.774251	02
22	212.885	0.398435	02	0.652004	02
23	214.922	0.340061	02	0.551206	02
24	216.904	0.290708	02	0.466905	02
25	218.886	0.248873	02	0.396094	02
26	220.866	0.213390	02	0.336576	02
27	222.848	0.183189	02	0.286371	02
28	224.828	0.157499	02	0.244043	02
29	226.806	0.135612	02	0.208296	02
30	228.786	0.116900	02	0.178002	02
31	230.764	0.100915	02	0.152344	02
32	232.742	0.872243	+01	0.130557	02
33	235.032	0.755011	01	0.111909	02
34	237.403	0.654480	01	0.960392	+01
35	239.774	0.568141	01	0.825452	01
36	242.145	0.493878	01	0.710530	01
37	244.514	0.429970	01	0.612593	01
38	246.883	0.374831	01	0.528912	01
39	249.252	0.327192	01	0.457302	01
40	251.618	0.286014	01	0.395989	01
41	253.984	0.250333	01	0.343360	01
42	256.351	0.219375	01	0.298119	01
43	258.715	0.192503	01	0.259212	01
44	261.079	0.169125	01	0.225670	01
45	263.443	0.148759	01	0.196713	01
46	265.804	0.131012	01	0.171707	01
47	268.168	0.115497	01	0.150039	01
48	269.150	0.101940	01	0.131943	01
49	269.150	0.899705	00	0.116451	01
50	269.150	0.794168	00	0.102791	01
51	269.150	0.701011	00	0.907336	00
52	268.136	0.618705	00	0.803835	00
53	266.172	0.545690	00	0.714203	00
54	264.208	0.480845	00	0.634011	00
55	262.244	0.423305	00	0.562323	00
56	260.282	0.372343	00	0.498353	00
57	258.320	0.327198	00	0.441257	00
58	256.358	0.287244	00	0.390340	00
59	254.398	0.251950	00	0.345016	00

(Continued)

Table 2-4. Temperature, pressure, and density of Supplemental Atmosphere; for pressure and density value of +04 equals $\times 10^4$. (Continued)

Geom Alt (km)	Temp (°K)	Press (mb)		Density (g m^{-3})	
60	252.043	0.220731	00	0.305089	00
61	249.008	0.193145	00	0.270214	00
62	245.970	0.168707	00	0.238939	00
63	242.936	0.147134	00	0.210989	00
64	239.901	0.128099	00	0.186016	00
65	236.866	0.111330	00	0.163737	00
66	233.834	0.965951	−01	0.143908	00
67	230.802	0.836556	−01	0.126268	00
68	227.770	0.723117	−01	0.110599	00
69	224.742	0.623936	−01	0.967152	−01
70	221.710	0.537200	−01	0.844090	−01
71	218.684	0.461712	−01	0.735516	−01
72	215.656	0.395934	−01	0.639588	−01
73	212.630	0.338844	−01	0.555154	−01
74	209.604	0.289339	−01	0.480889	−01
75	206.582	0.246541	−01	0.415753	−01
76	203.556	0.209543	−01	0.358614	−01
77	200.534	0.177695	−01	0.308692	−01
78	197.511	0.150310	−01	0.265115	−01
79	194.492	0.126840	−01	0.227192	−01
80	191.472	0.106751	−01	0.194224	−01
81	191.150	0.896969	−02	0.163471	−01
82	191.150	0.753796	−02	0.137378	−01
83	191.150	0.633477	−02	0.115450	−01
84	191.150	0.532362	−02	0.970222	−02
85	191.150	0.447388	−02	0.815357	−02
86	191.150	0.376044	−02	0.685334	−02
87	191.150	0.316077	−02	0.576045	−02
88	191.150	0.265673	−02	0.484184	−02
89	191.150	0.223346	−02	0.407045	−02
90	191.150	0.187763	−02	0.342196	−02
Midlatitude (45°N) Jul					
0	294.150	0.101350	+04	0.119194	+04
1	289.650	0.902198	+03	0.107953	04
2	285.154	0.801594	03	0.975726	+03
3	279.156	0.710433	03	0.884585	03
4	273.168	0.628063	03	0.799782	03
5	267.174	0.553615	03	0.721113	03
6	261.186	0.486632	03	0.648694	03
7	254.702	0.426404	03	0.582972	03
8	248.215	0.372351	03	0.522462	03
9	241.734	0.324024	03	0.466877	03
10	235.254	0.280904	03	0.415928	03
11	228.773	0.242550	03	0.369346	03
12	222.299	0.208581	03	0.326869	03
13	215.825	0.178571	03	0.288235	03
14	215.650	0.152506	03	0.246363	03
15	215.650	0.130245	03	0.210402	03
16	215.650	0.111251	03	0.179719	03
17	215.650	0.950271	+02	0.153510	03
18	216.789	0.812140	02	0.130507	03
19	217.982	0.694686	02	0.111022	03
20	219.174	0.594726	02	0.945290	+02
21	220.367	0.509578	02	0.805568	02
22	221.559	0.437053	02	0.687200	02
23	222.750	0.375159	02	0.586725	02
24	223.942	0.322292	02	0.501363	02
25	225.132	0.277141	02	0.428845	02
26	226.323	0.238504	02	0.367119	02
27	227.513	0.205416	02	0.314533	02
28	229.492	0.177123	02	0.268872	02
29	231.573	0.152931	02	0.230062	02
30	233.654	0.132216	02	0.197129	02
31	235.735	0.114455	02	0.169141	02
32	237.814	0.992199	+01	0.145345	02
33	240.225	0.861267	01	0.124899	02
34	242.697	0.748802	01	0.107483	02
35	245.170	0.651947	01	0.926367	+01
36	247.642	0.568409	01	0.799602	01
37	250.115	0.496251	01	0.691194	01
38	252.585	0.433891	01	0.598427	01
39	255.055	0.379863	01	0.518837	01
40	257.525	0.332989	01	0.450452	01
41	259.992	0.292305	01	0.391664	01
42	262.460	0.256908	01	0.340998	01
43	264.927	0.226070	01	0.297272	01
44	267.395	0.199169	01	0.259482	01
45	269.860	0.175697	01	0.226811	01
46	272.325	0.155167	01	0.198495	01
47	274.787	0.137207	01	0.173947	01
48	275.650	0.121431	01	0.153465	01
49	275.650	0.107476	01	0.135829	01
50	275.650	0.951246	00	0.120219	01
51	275.650	0.842033	00	0.106417	01
52	275.650	0.745358	00	0.941988	00
53	274.245	0.659666	00	0.837960	00
54	271.787	0.583315	00	0.747673	00
55	269.330	0.515225	00	0.666424	00
56	266.872	0.454565	00	0.593377	00
57	264.417	0.400635	00	0.527834	00
58	261.960	0.352641	00	0.468961	00
59	259.507	0.310106	00	0.416292	00
60	257.052	0.272332	00	0.369075	00
61	254.600	0.238893	00	0.326876	00
62	252.147	0.209295	00	0.289163	00
63	248.931	0.183112	00	0.256257	00
64	244.521	0.159876	00	0.227775	00
65	240.111	0.139244	00	0.202024	00
66	235.701	0.120964	00	0.178786	00
67	231.295	0.104821	00	0.157877	00
68	226.890	0.905822	−01	0.139080	00
69	222.484	0.780538	−01	0.122217	00
70	218.079	0.670582	−01	0.107121	00
71	213.678	0.574425	−01	0.936510	−01
72	209.277	0.490475	−01	0.816457	−01
73	204.880	0.417458	−01	0.709824	−01
74	200.484	0.354072	−01	0.615248	−01
75	196.087	0.299215	−01	0.531584	−01
76	191.691	0.251894	−01	0.457778	−01
77	187.299	0.211250	−01	0.392916	−01
78	182.907	0.176426	−01	0.336024	−01
79	178.515	0.146698	−01	0.286279	−01
80	174.150	0.121421	−01	0.242889	−01
81	174.150	0.100283	−01	0.200605	−01
82	174.150	0.828248	−02	0.165682	−01
83	174.150	0.684195	−02	0.136866	−01
84	174.150	0.565195	−02	0.113061	−01
85	174.150	0.466893	−02	0.933969	−02
86	174.150	0.385689	−02	0.771528	−02
87	174.150	0.318670	−02	0.637464	−02
88	174.150	0.263297	−02	0.526696	−02
89	174.150	0.217545	−02	0.435175	−02
90	174.150	0.179779	−02	0.359628	−02

(*Continued*)

Table 2-4. Temperature, pressure, and density of Supplemental Atmosphere; for pressure and density value of +04 equals $\times 10^4$. (Continued)

Geom Alt (km)	Temp (°K)	Press (mb)		Density (g m^{-3})	
		Midlatitude (45°N) Jan			
0	272.150	0.101800	+04	0.130098	+04
1	268.650	0.897340	+03	0.116211	04
2	265.154	0.789746	03	0.103651	04
3	261.654	0.693761	03	0.922974	+03
4	255.668	0.608132	03	0.828225	03
5	249.674	0.531322	03	0.741093	03
6	243.686	0.462749	03	0.661404	03
7	237.698	0.401636	03	0.588557	03
8	231.710	0.347333	03	0.522172	03
9	225.728	0.299275	03	0.461856	03
10	219.746	0.256837	03	0.407161	03
11	219.159	0.219907	03	0.349556	03
12	218.661	0.188249	03	0.299915	03
13	218.163	0.161092	03	0.257234	03
14	217.665	0.137803	03	0.220550	03
15	217.167	0.117839	03	0.189031	03
16	216.670	0.100747	03	0.161984	03
17	216.172	0.861032	+02	0.138758	03
18	215.675	0.735727	02	0.118838	03
19	215.178	0.628431	02	0.101741	03
20	215.150	0.536674	02	0.868975	+02
21	215.150	0.458314	02	0.742096	02
22	215.150	0.391458	02	0.633844	02
23	215.150	0.334355	02	0.541483	02
24	215.150	0.285581	02	0.462409	02
25	215.150	0.243961	02	0.395018	02
26	215.150	0.208407	02	0.337449	02
27	215.150	0.178034	02	0.288270	02
28	215.852	0.152146	02	0.245552	02
29	216.644	0.130097	02	0.209198	02
30	217.437	0.111307	02	0.178331	02
31	218.230	0.952848	+01	0.152106	02
32	219.022	0.816277	01	0.129834	02
33	221.723	0.700062	01	0.109993	02
34	224.789	0.601741	01	0.932552	+01
35	227.855	0.518290	01	0.792416	01
36	230.921	0.447305	01	0.674806	01
37	233.987	0.386792	01	0.575870	01
38	237.049	0.335147	01	0.492532	01
39	240.112	0.290933	01	0.422101	01
40	243.175	0.253005	01	0.362450	01
41	246.235	0.220437	01	0.311870	01
42	249.294	0.192389	01	0.268847	01
43	252.354	0.168188	01	0.232179	01
44	255.414	0.147270	01	0.200867	01
45	258.470	0.129175	01	0.174103	01
46	261.527	0.113478	01	0.151159	01
47	264.580	0.998513	00	0.131472	01
48	265.650	0.879632	00	0.115353	01
49	265.650	0.774975	00	0.101629	01
50	265.650	0.682770	00	0.895370	00
51	265.650	0.601612	00	0.788942	00
52	265.650	0.530101	00	0.695164	00
53	264.526	0.467019	00	0.615041	00
54	262.560	0.411144	00	0.545511	00
55	260.594	0.361607	00	0.483404	00
56	258.628	0.317729	00	0.427977	00
57	256.664	0.278938	00	0.378600	00
58	254.698	0.244604	00	0.334562	00
59	252.736	0.214337	00	0.295439	00
60	250.772	0.187596	00	0.260605	00
61	248.810	0.164042	00	0.229681	00
62	246.848	0.143293	00	0.202224	00
63	244.886	0.125033	00	0.177869	00
64	242.926	0.108996	00	0.156306	00
65	240.932	0.949100	−01	0.137232	00
66	238.874	0.825474	−01	0.120385	00
67	236.818	0.717187	−01	0.105501	00
68	234.762	0.622342	−01	0.923507	−01
69	232.706	0.539367	−01	0.807449	−01
70	230.650	0.466861	−01	0.705135	−01
71	228.596	0.403641	−01	0.615126	−01
72	226.543	0.348523	−01	0.535945	−01
73	224.491	0.300576	−01	0.466437	−01
74	222.439	0.258872	−01	0.405427	−01
75	220.387	0.222647	−01	0.351939	−01
76	218.336	0.191221	−01	0.305104	−01
77	216.286	0.164020	−01	0.264185	−01
78	214.236	0.140484	−01	0.228440	−01
79	212.187	0.120146	−01	0.197255	−01
80	210.150	0.102596	−01	0.170075	−01
81	210.150	0.875578	−02	0.145146	−01
82	210.150	0.747237	−02	0.123870	−01
83	210.150	0.637812	−02	0.105731	−01
84	210.150	0.544411	−02	0.902476	−02
85	210.150	0.464687	−02	0.770318	−02
86	210.150	0.396639	−02	0.657513	−02
87	210.150	0.338610	−02	0.561318	−02
88	210.150	0.289071	−02	0.479197	−02
89	210.150	0.246780	−02	0.409090	−02
90	210.150	0.210710	−02	0.349296	−02
		Subarctic (60°N) Jul			
0	287.150	0.101000	+04	0.121981	+04
1	281.745	0.896006	+03	0.110422	04
2	276.339	0.792943	03	0.997059	+03
3	270.939	0.700066	03	0.898483	03
4	265.539	0.616426	03	0.807675	03
5	260.136	0.541403	03	0.724405	03
6	253.136	0.473962	03	0.651944	03
7	246.143	0.413419	03	0.584923	03
8	239.150	0.359183	03	0.523143	03
9	232.157	0.310757	03	0.466273	03
10	225.171	0.267710	03	0.414172	03
11	225.150	0.230030	03	0.355919	03
12	225.150	0.197706	03	0.305904	03
13	225.150	0.169949	03	0.262957	03
14	225.150	0.146090	03	0.226040	03
15	225.150	0.125580	03	0.194306	03
16	225.150	0.107965	03	0.167052	03
17	225.150	0.928219	+02	0.143621	03
18	225.150	0.798025	02	0.123476	03
19	225.150	0.686092	02	0.106157	03
20	225.150	0.589948	02	0.912809	+02
21	225.150	0.507277	02	0.784895	02
22	225.150	0.436258	02	0.675009	02
23	225.150	0.375181	02	0.580506	02
24	226.560	0.322798	02	0.496348	02
25	228.051	0.278003	02	0.424674	02
26	229.540	0.239693	02	0.363776	02
27	231.030	0.206861	02	0.311923	02
28	232.519	0.178695	02	0.267726	02
29	234.007	0.154530	02	0.230050	02

(Continued)

Table 2-4. Temperature, pressure, and density of Supplemental Atmosphere; for pressure and density value of +04 equals $\times 10^4$. (Continued)

Geom Alt (km)	Temp (°K)	Press (mb)		Density (g m^{-3})	
30	235.495	0.133757	02	0.197867	02
31	236.983	0.115882	02	0.170347	02
32	238.470	0.100500	02	0.146815	02
33	241.266	0.872537	+01	0.125987	02
34	244.236	0.759057	01	0.108269	02
35	247.209	0.661358	01	0.931988	+01
36	250.179	0.577262	01	0.803823	01
37	253.149	0.504669	01	0.694495	01
38	256.116	0.441956	01	0.601147	01
39	259.086	0.387577	01	0.521138	01
40	262.053	0.340442	01	0.452577	01
41	265.017	0.299515	01	0.393717	01
42	267.984	0.263851	01	0.342995	01
43	270.948	0.232787	01	0.299302	01
44	272.479	0.205609	01	0.262873	01
45	273.565	0.181721	01	0.231410	01
46	274.651	0.160687	01	0.203816	01
47	275.736	0.142156	01	0.179602	01
48	276.821	0.125839	01	0.158363	01
49	277.150	0.111421	01	0.140053	01
50	277.150	0.986818	00	0.124040	01
51	277.150	0.873882	00	0.109844	01
52	277.150	0.773966	00	0.972849	00
53	277.150	0.685475	00	0.861618	00
54	275.922	0.606998	00	0.766372	00
55	273.954	0.537138	00	0.683041	00
56	271.986	0.474900	00	0.608266	00
57	270.018	0.419497	00	0.541221	00
58	268.052	0.370269	00	0.481213	00
59	266.086	0.326518	00	0.427488	00
60	262.729	0.287618	00	0.381369	00
61	258.109	0.252819	00	0.341228	00
62	253.494	0.221743	00	0.304734	00
63	248.879	0.194019	00	0.271579	00
64	244.263	0.169338	00	0.241509	00
65	239.652	0.147434	00	0.214315	00
66	235.042	0.128018	00	0.189742	00
67	230.436	0.110865	00	0.167604	00
68	225.825	0.957176	−01	0.147658	00
69	221.219	0.824023	−01	0.129764	00
70	216.613	0.707160	−01	0.113729	00
71	212.012	0.604977	−01	0.994071	−01
72	207.410	0.515790	−01	0.866324	−01
73	202.809	0.438180	−01	0.752668	−01
74	198.208	0.370858	−01	0.651815	−01
75	193.611	0.312706	−01	0.562658	−01
76	189.015	0.262595	−01	0.483982	−01
77	184.418	0.219568	−01	0.414766	−01
78	179.826	0.182798	−01	0.354125	−01
79	175.234	0.151466	−01	0.301116	−01
80	171.150	0.124883	−01	0.254194	−01
81	171.150	0.102777	−01	0.209198	−01
82	171.150	0.845836	−02	0.172166	−01
83	171.150	0.696109	−02	0.141690	−01
84	171.150	0.572886	−02	0.116608	−01
85	171.150	0.471570	−02	0.959860	−02
86	171.150	0.388172	−02	0.790106	−02
87	171.150	0.319587	−02	0.650504	−02
88	171.150	0.263067	−02	0.535461	−02
89	171.150	0.216586	−02	0.440852	−02
90	171.150	0.178354	−02	0.363031	−02

Geom Alt (km)	Temp (°K)	Press (mb)		Density (g m^{-3})	
		Subarctic (60°N) Jan			
0	257.150	0.101350	+04	0.137230	+04
1	259.147	0.887820	+03	0.119275	04
2	255.940	0.777484	03	0.105767	04
3	252.740	0.679806	03	0.936597	+03
4	247.736	0.593227	03	0.833949	03
5	240.936	0.515833	03	0.745693	03
6	234.136	0.446737	03	0.664636	03
7	227.343	0.385313	03	0.590407	03
8	220.550	0.330845	03	0.522584	03
9	217.150	0.282900	03	0.453848	03
10	217.150	0.241793	03	0.387902	03
11	217.150	0.206659	03	0.331538	03
12	217.150	0.176630	03	0.283364	03
13	217.150	0.150989	03	0.242228	03
14	217.150	0.129070	03	0.207063	03
15	217.150	0.110333	03	0.177004	03
16	216.562	0.943106	+02	0.151711	03
17	215.964	0.805803	02	0.129983	03
18	215.367	0.688189	02	0.111318	03
19	214.769	0.587484	02	0.952934	+02
20	214.172	0.501375	02	0.815527	02
21	213.575	0.427698	02	0.697629	02
22	212.979	0.364744	02	0.596609	02
23	212.382	0.310917	02	0.509993	02
24	211.786	0.264915	02	0.435760	02
25	211.190	0.225617	02	0.372167	02
26	212.077	0.192194	02	0.315706	02
27	213.070	0.163844	02	0.267884	02
28	214.063	0.139780	02	0.227479	02
29	215.055	0.119357	02	0.193346	02
30	216.047	0.101992	02	0.164458	02
31	217.039	0.872158	+01	0.139990	02
32	218.030	0.746455	01	0.119269	02
33	219.022	0.639222	01	0.101672	02
34	220.012	0.547947	01	0.867621	+01
35	222.282	0.470136	01	0.736812	01
36	224.757	0.404118	01	0.626373	01
37	227.232	0.347947	01	0.533434	01
38	229.705	0.300114	01	0.455149	01
39	232.180	0.259229	01	0.388952	01
40	234.652	0.224294	01	0.332990	01
41	237.122	0.194390	01	0.285587	01
42	239.595	0.168699	01	0.245286	01
43	242.065	0.146637	01	0.211033	01
44	244.535	0.127642	01	0.181840	01
45	247.002	0.111278	01	0.156944	01
46	249.470	0.971437	00	0.135655	01
47	251.937	0.849186	00	0.117422	01
48	254.402	0.743392	00	0.101797	01
49	256.870	0.651528	00	0.883605	00
50	259.332	0.571887	00	0.768231	00
51	260.150	0.502397	00	0.672762	00
52	260.150	0.441439	00	0.591133	00
53	260.150	0.387877	00	0.519408	00
54	260.150	0.340814	00	0.456386	00
55	259.074	0.299452	00	0.402664	00
56	257.302	0.262894	00	0.355939	00
57	255.531	0.230592	00	0.314368	00
58	253.762	0.202101	00	0.277448	00

(Continued)

Table 2-4. Temperature, pressure, and density of Supplemental Atmosphere; for pressure and density value of +04 equals $\times 10^4$. (Continued)

Geom Alt (km)	Temp (°K)	Press (mb)		Density (g m^{-3})	
59	251.992	0.176968	00	0.244650	00
60	250.892	0.154829	00	0.214983	00
61	250.401	0.135414	00	0.188394	00
62	249.910	0.118419	00	0.165072	00
63	249.419	0.103529	00	0.144601	00
64	248.928	0.904874	−01	0.126635	00
65	248.437	0.790786	−01	0.110887	00
66	247.947	0.690899	−01	0.970720	−01
67	247.457	0.603550	−01	0.849674	−01
68	246.966	0.527031	−01	0.743424	−01
69	246.476	0.460153	−01	0.650376	−01
70	245.692	0.401641	−01	0.569489	−01
71	244.322	0.350391	−01	0.499608	−01
72	242.951	0.305445	−01	0.437979	−01
73	241.580	0.266058	−01	0.383666	−01
74	240.210	0.231569	−01	0.335836	−01
75	238.841	0.201418	−01	0.293785	−01
76	237.471	0.175053	−01	0.256801	−01
77	236.102	0.152016	−01	0.224299	−01
78	234.734	0.131921	−01	0.195784	−01
79	233.367	0.114388	−01	0.170758	−01
80	231.999	0.991021	−02	0.148811	−01
81	230.632	0.857987	−02	0.129598	−01
82	229.266	0.742175	−02	0.112773	−01
83	227.900	0.641440	−02	0.980507	−02
84	226.533	0.553891	−02	0.851787	−02
85	225.168	0.477939	−02	0.739442	−02
86	223.803	0.412033	−02	0.641364	−02
87	222.440	0.354947	−02	0.555892	−02
88	221.075	0.305443	−02	0.481315	−02
89	219.711	0.262639	−02	0.416434	−02
90	218.349	0.225657	−02	0.360029	−02
Subarctic (60°N) Winter Warm					
0	257.150	0.101350	+04	0.137230	+04
1	259.147	0.887820	+03	0.119275	04
2	255.940	0.777484	03	0.105767	04
3	252.740	0.679806	03	0.936597	+03
4	247.736	0.593227	03	0.833949	03
5	240.936	0.515833	03	0.745693	03
6	234.136	0.446737	03	0.664636	03
7	227.343	0.385313	03	0.590407	03
8	220.550	0.330845	03	0.522584	03
9	218.148	0.282950	03	0.451853	03
10	220.144	0.242182	03	0.383242	03
11	222.140	0.207579	03	0.325533	03
12	224.136	0.178166	03	0.276918	03
13	224.150	0.153049	03	0.237865	03
14	224.150	0.131473	03	0.204332	03
15	224.150	0.112939	03	0.175527	03
16	224.150	0.970325	+02	0.150805	03
17	224.150	0.833663	02	0.129566	03
18	224.150	0.716248	02	0.111317	03
19	224.150	0.615370	02	0.956392	+02
20	224.150	0.528780	02	0.821817	02
21	224.150	0.454375	02	0.706178	02
22	224.150	0.390499	02	0.606903	02
23	224.150	0.335603	02	0.521585	02
24	224.150	0.288423	02	0.448260	02
25	224.150	0.247877	02	0.385244	02
26	224.577	0.213076	02	0.330527	02
27	225.570	0.183263	02	0.283030	02
28	226.563	0.157726	02	0.242523	02
29	227.555	0.135857	02	0.207986	02
30	228.547	0.117096	02	0.178587	02
31	229.539	0.100991	02	0.153273	02
32	230.530	0.871695	+01	0.131727	02
33	231.522	0.752760	01	0.113267	02
34	232.512	0.650651	01	0.974857	+01
35	233.503	0.562659	01	0.839443	01
36	234.493	0.486937	01	0.723405	01
37	235.483	0.421663	01	0.623798	01
38	237.705	0.365524	01	0.535693	01
39	240.180	0.317280	01	0.460197	01
40	242.652	0.275842	01	0.396017	01
41	245.122	0.240190	01	0.341358	01
42	247.595	0.209407	01	0.294638	01
43	250.065	0.182844	01	0.254722	01
44	252.535	0.159863	01	0.220528	01
45	255.002	0.139972	01	0.191221	01
46	257.470	0.122713	01	0.166036	01
47	259.937	0.107717	01	0.144362	01
48	262.402	0.946826	00	0.125702	01
49	264.870	0.833150	00	0.109579	01
50	267.332	0.734181	00	0.956730	00
51	268.150	0.647469	00	0.841162	00
52	268.150	0.571108	00	0.741958	00
53	268.150	0.503753	00	0.654453	00
54	268.150	0.444342	00	0.577269	00
55	266.655	0.391904	00	0.511998	00
56	264.195	0.345283	00	0.455290	00
57	261.735	0.303847	00	0.404419	00
58	259.277	0.267097	00	0.358875	00
59	256.820	0.234504	00	0.318097	00
60	254.362	0.205630	00	0.281626	00
61	251.905	0.180082	00	0.249041	00
62	249.450	0.157524	00	0.219990	00
63	246.995	0.137610	00	0.194089	00
64	244.540	0.120051	00	0.171023	00
65	242.087	0.104604	00	0.150526	00
66	239.635	0.910159	−01	0.132314	00
67	237.185	0.790912	−01	0.116166	00
68	234.732	0.686188	−01	0.101838	00
69	232.282	0.594531	−01	0.891654	−01
70	229.832	0.514334	−01	0.779600	−01
71	227.385	0.444331	−01	0.680743	−01
72	225.507	0.383269	−01	0.592081	−01
73	225.018	0.330386	−01	0.511497	−01
74	224.528	0.284708	−01	0.411739	−01
75	224.039	0.245302	−01	0.381430	−01
76	223.550	0.211282	−01	0.329250	−01
77	223.061	0.181920	−01	0.284116	−01
78	222.573	0.156612	−01	0.245127	−01
79	222.084	0.134780	−01	0.211419	−01
80	221.596	0.115953	−01	0.182288	−01
81	221.108	0.997380	−02	0.157143	−01
82	220.620	0.857621	−02	0.135422	−01
83	220.132	0.737201	−02	0.116665	−01
84	219.644	0.633475	−02	0.100473	−01
85	219.156	0.544245	−02	0.865125	−02
86	218.669	0.467427	−02	0.744671	−02
87	218.182	0.401377	−02	0.640874	−02
88	217.694	0.344490	−02	0.551273	−02
89	217.207	0.295610	−02	0.474114	−02
90	216.721	0.253618	−02	0.407679	−02

(Continued)

Table 2-4. Temperature, pressure, and density of Supplemental Atmosphere; for pressure and density value of +04 equals $\times 10^4$. (Continued)

Geom Alt (km)	Temp (°K)	Press (mb)		Density (g m^{-3})	
Subarctic (60°N) Winter Cold					
0	257.150	0.101350	+04	0.137230	+04
1	259.147	0.887820	+03	0.119275	04
2	255.940	0.777484	03	0.105767	04
3	252.740	0.679806	03	0.936597	+03
4	247.736	0.593227	03	0.833949	03
5	240.936	0.515833	03	0.745693	03
6	234.136	0.446737	03	0.664636	03
7	227.343	0.385313	03	0.590407	03
8	220.550	0.330845	03	0.522584	03
9	217.150	0.282900	03	0.453848	03
10	217.150	0.241793	03	0.387902	03
11	217.150	0.206659	03	0.331538	03
12	217.150	0.176630	03	0.283364	03
13	216.160	0.150935	03	0.243250	03
14	215.163	0.128884	03	0.208675	03
15	214.166	0.109974	03	0.178886	03
16	213.170	0.937839	+02	0.153264	03
17	212.174	0.799177	02	0.131217	03
18	211.178	0.680504	02	0.112259	03
19	210.182	0.579013	02	0.959690	+02
20	209.187	0.492361	02	0.819950	02
21	208.192	0.418353	02	0.700031	02
22	207.198	0.355251	02	0.597294	02
23	206.204	0.301430	02	0.509246	02
24	205.210	0.255560	02	0.433843	02
25	204.216	0.216496	02	0.369317	02
26	203.223	0.183286	02	0.314192	02
27	202.230	0.155044	02	0.267084	02
28	201.237	0.131046	02	0.226857	02
29	200.245	0.110689	02	0.192566	02
30	199.253	0.934156	+01	0.163325	02
31	200.395	0.788356	01	0.137049	02
32	201.782	0.666197	01	0.115016	02
33	203.171	0.563523	01	0.966248	+01
34	204.557	0.477376	01	0.812989	01
35	205.944	0.404785	01	0.684720	01
36	209.859	0.343959	01	0.570974	01
37	214.215	0.293245	01	0.476890	01
38	218.567	0.250852	01	0.399826	01
39	222.923	0.215216	01	0.336324	01
40	227.274	0.185219	01	0.283905	01
41	230.359	0.159829	01	0.241706	01
42	233.128	0.138145	01	0.206433	01
43	235.895	0.119627	01	0.176664	01
44	238.661	0.103764	01	0.151462	01
45	241.425	0.901656	00	0.130106	01
46	244.188	0.784746	00	0.111955	01
47	246.952	0.684062	00	0.964987	00
48	249.713	0.597290	00	0.833265	00
49	252.476	0.522233	00	0.720579	00
50	255.234	0.457398	00	0.624300	00
51	256.150	0.401004	00	0.545371	00
52	256.150	0.351637	00	0.478232	00
53	256.150	0.308348	00	0.419358	00
54	256.150	0.270388	00	0.367731	00
55	254.595	0.237075	00	0.324394	00
56	252.037	0.207611	00	0.286963	00
57	249.478	0.181564	00	0.253533	00
58	246.923	0.158587	00	0.223740	00
59	244.367	0.138323	00	0.197192	00
60	243.665	0.120508	00	0.172290	00
61	244.648	0.105022	00	0.149547	00
62	245.630	0.915893	−01	0.129898	00
63	246.612	0.799184	−01	0.112894	00
64	247.594	0.697724	−01	0.981708	−01
65	248.575	0.609557	−01	0.854270	−01
66	249.556	0.532814	−01	0.743782	−01
67	250.536	0.466042	−01	0.648027	−01
68	251.517	0.407796	−01	0.564825	−01
69	252.497	0.357063	−01	0.492637	−01
70	253.477	0.312803	−01	0.429903	−01
71	254.456	0.274206	−01	0.375407	−01
72	254.580	0.240477	−01	0.329070	−01
73	252.622	0.210765	−01	0.290646	−01
74	250.664	0.184534	−01	0.256461	−01
75	248.708	0.161421	−01	0.226104	−01
76	246.752	0.141054	−01	0.199142	−01
77	244.796	0.123125	−01	0.175218	−01
78	242.842	0.107372	−01	0.154031	−01
79	240.888	0.935319	−02	0.135264	−01
80	238.934	0.813839	−02	0.118659	−01
81	236.982	0.707430	−02	0.103994	−01
82	235.030	0.614222	−02	0.910418	−02
83	233.078	0.532667	−02	0.796146	−02
84	231.126	0.461387	−02	0.695433	−02
85	229.176	0.399219	−02	0.606848	−02
86	227.226	0.345000	−02	0.528932	−02
87	225.278	0.297815	−02	0.460539	−02
88	223.328	0.256717	−02	0.400451	−02
89	221.380	0.221035	−02	0.347826	−02
90	219.434	0.190092	−02	0.301785	−02
Arctic (75°N) Jul					
0	278.150	0.101250	+04	0.126458	+04
1	275.545	0.895017	+03	0.112895	04
2	272.940	0.790196	03	0.100668	04
3	268.368	0.696714	03	0.903040	+03
4	261.861	0.612489	03	0.814111	03
5	255.354	0.536671	03	0.731714	03
6	248.848	0.468619	03	0.655826	03
7	242.348	0.407775	03	0.586045	03
8	235.848	0.353487	03	0.522082	03
9	229.354	0.305246	03	0.463615	03
10	226.657	0.262609	03	0.403616	03
11	227.656	0.225975	03	0.345796	03
12	228.654	0.194608	03	0.296497	03
13	229.652	0.167704	03	0.254396	03
15 14	230.150	0.124690	03	0.188739	03
16 15	230.150	0.107522	03	0.162751	03
17 16	230.150	0.927306	+02	0.140362	03
18 17	230.150	0.799862	02	0.121072	03
19 18	230.150	0.689830	02	0.104417	03
20 19	230.150	0.595023	02	0.900661	+02
21 20	230.150	0.513246	02	0.776878	02
22 21	230.150	0.442774	02	0.670207	02
23 22	230.150	0.381921	02	0.578097	02
24 25	230.707	0.329508	02	0.497558	02
25 24	231.900	0.284515	02	0.427409	02
26 28	233.092	0.245851	02	0.367437	02
27 26	234.285	0.212600	02	0.316123	02
28 27	235.478	0.183982	02	0.272184	02
29 28	236.670	0.159355	02	0.234564	02
30 29	237.861	0.138124	02	0.202295	02
31 30	239.053	0.119808	02	0.174594	02
14	230.150	0.144000	03	0.218880	03

(Continued)

Table 2-4. Temperature, pressure, and density of Supplemental Atmosphere; for pressure and density value of +04 equals $\times 10^4$. (Continued)

Geom Alt (km)	Temp (°K)	Press (mb)		Density (g m^{-3})	
		Arctic (75°N) Jan			
0	249.150	0.101350	+04	0.141673	+04
1	252.156	0.884156	+03	0.122112	04
2	250.878	0.772129	03	0.107185	04
3	245.372	0.672739	03	0.954935	+03
4	239.867	0.584305	03	0.848506	03
5	234.362	0.505834	03	0.751836	03
6	228.856	0.436400	03	0.664263	03
7	223.356	0.375202	03	0.585187	03
8	217.856	0.321371	03	0.513897	03
9	214.896	0.274351	03	0.444749	03
10	214.396	0.233982	03	0.380193	03
11	213.897	0.199511	03	0.324939	03
12	213.247	0.170078	03	0.277845	03
13	212.448	0.144904	03	0.237610	03
14	211.650	0.123382	03	0.203082	03
15	210.852	0.104992	03	0.173468	03
16	210.053	0.892889	+02	0.148083	03
17	209.256	0.758998	02	0.126358	03
18	208.459	0.644891	02	0.107772	03
19	207.661	0.547506	02	0.918485	+02
20	207.650	0.464754	02	0.779703	02
21	207.650	0.394509	02	0.661856	02
22	207.650	0.334937	02	0.561913	02
23	207.650	0.284313	02	0.476984	02
24	207.650	0.241381	02	0.404958	02
25	207.650	0.204965	02	0.343864	02
26	207.650	0.174043	02	0.291987	02
27	207.650	0.147787	02	0.247937	02
28	207.650	0.125491	02	0.210532	02
29	207.650	0.106576	02	0.178800	02
30	207.650	0.905127	+01	0.151850	02
		Arctic (75°N) Winter Warm			
0	249.150	0.101350	+04	0.141673	+04
1	252.156	0.884156	+03	0.122112	04
2	250.878	0.772129	03	0.107185	04
3	245.372	0.672739	03	0.954935	+03
4	239.867	0.584305	03	0.848506	03
5	234.362	0.505834	03	0.751836	03
6	228.856	0.436400	03	0.664263	03
7	223.356	0.375202	03	0.585187	03
8	217.856	0.321371	03	0.513897	03
9	216.570	0.274436	03	0.441451	03
10	219.370	0.234624	03	0.372592	03
11	222.150	0.201017	03	0.315228	03
12	222.150	0.172416	03	0.270377	03
13	222.150	0.147885	03	0.231908	03
14	222.150	0.126844	03	0.198913	03
15	222.150	0.108797	03	0.170611	03
16	222.150	0.937488	+02	0.147014	03
17	222.150	0.800524	02	0.125536	03
18	222.644	0.686952	02	0.107486	03
19	223.143	0.589605	02	0.920484	+02
20	223.641	0.506302	02	0.788672	02
21	224.139	0.434916	02	0.675968	02
22	224.636	0.373778	02	0.579658	02
23	225.134	0.321294	02	0.497162	02
24	225.632	0.276313	02	0.426618	02
25	226.129	0.237744	02	0.366262	02
26	227.578	0.204688	02	0.313329	02
27	229.069	0.176400	02	0.268270	02
28	230.560	0.152169	02	0.229922	02
29	232.049	0.131411	02	0.197282	02
30	233.539	0.113591	02	0.169442	02
		Arctic (75°N) Winter Cold			
0	249.150	0.101350	+04	0.141673	+04
1	252.156	0.884156	+03	0.122112	04
2	250.878	0.772129	03	0.107185	04
3	245.372	0.672739	03	0.954935	+03
4	239.867	0.584305	03	0.848506	03
5	234.362	0.505834	03	0.751836	03
6	228.856	0.436400	03	0.664263	03
7	223.356	0.375202	03	0.585187	03
8	217.856	0.321371	03	0.513897	03
9	214.389	0.274325	03	0.445758	03
10	212.889	0.233785	03	0.382561	03
11	211.391	0.199043	03	0.328019	03
12	209.894	0.169298	03	0.280989	03
13	208.397	0.143831	03	0.240435	03
14	206.900	0.122051	03	0.205504	03
15	205.403	0.103446	03	0.175447	03
16	203.951	0.880126	+02	0.150334	03
17	202.410	0.740543	02	0.127455	03
18	201.357	0.625619	02	0.108239	03
19	200.758	0.528125	02	0.916435	+02
20	200.161	0.445675	02	0.775671	02
21	199.563	0.375906	02	0.656201	02
22	198.966	0.316952	02	0.554948	02
23	198.369	0.267061	02	0.469002	02
24	197.772	0.224945	02	0.396233	02
25	197.175	0.189406	02	0.334641	02
26	197.150	0.159436	02	0.281727	02
27	197.150	0.134209	02	0.237150	02
28	197.150	0.112973	02	0.199626	02
29	197.150	0.951144	+01	0.168069	02
30	197.150	0.800786	01	0.141500	02

Table 2-5. Properties of the *U. S. Standard Atmosphere, 1962*, condensed from the complete tabulations. Numbers following the plus or minus sign are the power of ten by which that entry and each following entry should be multiplied.

Geom Alt (m)	Temperature (°K)	Temperature (°C)	Pressure (mb)	Density (Kg m^{-3})	Density (no. m^{-3})	Particle Speed (m sec^{-1})	Collision Frequency (sec^{-1})	Mean Free Path (m)	Molecular Weight	Sound Speed (m sec^{-1})	Coefficient of Viscosity (Kg m^{-1} sec^{-1})	Kinematic Viscosity (m^2 sec^{-1})	Thermal Conductivity (K-cal m^{-1} sec^{-1} [°K]$^{-1}$)
−5000	320.676	47.526	1.77762 +3	1.9311 +0	4.0154 +25	484.15	1.1507 +10	4.2075 −8	28.964	358.986	1.9422 −5	1.0058 −5	6.6545 −6
−4000	314.166	41.016	1.59598	1.7697	3.6798	479.22	1.0438	4.5912	28.964	355.324	1.9123	1.0806	6.5356
−3000	307.659	34.509	1.42973	1.6189	3.3662	474.23	9.4488 +9	5.0189	28.964	351.625	1.8820	1.1625	6.4161
−2000	301.154	28.004	1.27783	1.4782	3.0735	469.19	8.5356	5.4968	28.964	347.888	1.8515	1.2525	6.2958
−1000	294.651	21.501	1.13931	1.3470	2.8009	464.09	7.6939	6.0320	28.964	344.111	1.8206	1.3516	6.1748
0	288.150	15.000	1.01325 +3	1.2250 +0	2.5471 +25	458.94	6.9193 +9	6.6328 −8	28.964	340.294	1.7894 −5	1.4607 −5	6.0530 −6
1000	281.651	8.501	8.98762 +2	1.1117 +0	2.3115 +25	453.74	6.2079 +9	7.3090 −8	28.964	336.435	1.7579 −5	1.5813 −5	5.9305 −6
2000	275.154	2.004	7.95014	1.0066	2.0929	448.48	5.5558	8.0723	28.964	332.532	1.7260	1.7147	5.8073
3000	268.659	−4.491	7.01211	9.0925 −1	1.8906	443.15	4.9591	8.9361	28.964	328.583	1.6938	1.8628	5.6833
4000	262.166	−10.984	6.16604	8.1935	1.7037	437.76	4.4144	9.9166	28.964	324.589	1.6612	2.0275	5.5586
5000	255.676	−17.474	5.40482	7.3643	1.5313	432.31	3.9183	1.1033 −7	28.964	320.545	1.6282	2.2110	5.4331
6000	249.187	−23.963	4.72176 +2	6.6011 −1	1.3726 +25	426.79	3.4674 +9	1.2309 −7	28.964	316.452	1.5949 −5	2.4162 −5	5.3068 −6
7000	242.700	−30.450	4.11052	5.9002	1.2268	421.20	3.0586	1.3771	28.964	312.306	1.5612	2.6461	5.1798
8000	236.215	−36.935	3.56516	5.2579	1.0933	415.53	2.6889	1.5453	28.964	308.105	1.5271	2.9044	5.0520
9000	229.733	−43.417	3.08007	4.6706	9.7116 +24	409.79	2.3556	1.7396 −7	28.964	303.848	1.4926	3.1957	4.9235
10000	223.252	−49.898	2.64999	4.1351	8.5981	403.97	2.0559	1.9649	28.964	299.532	1.4577	3.5251	4.7942
11000	216.774	−56.376	2.26999 +2	3.6480 −1	7.5853 +24	398.07	1.7872 +9	2.2273 −7	28.964	295.154	1.4223 −5	3.8988 −5	4.6642 −6
12000	216.650	−56.500	1.93994	3.1194	6.4861	397.95	1.5278	2.6047	28.964	295.069	1.4216	4.5574	4.6617
13000	216.650	−56.500	1.65796	2.6660	5.5433	397.95	1.3057	3.0477	28.964	295.069	1.4216	5.3325	4.6617
14000	216.650	−56.500	1.41704	2.2786	4.7378	397.95	1.1160	3.5659	28.964	295.069	1.4216	6.2391	4.6617
15000	216.650	−56.500	1.21118	1.9475	4.0495	397.95	9.5386 +8	4.1720	28.964	295.069	1.4216	7.2995	4.6617
16000	216.650	−56.500	1.03528 +2	1.6647 −1	3.4614 +24	397.95	8.1533 +8	4.8808 −7	28.964	295.069	1.4216 −5	8.5397 −5	4.6617 −6
17000	216.650	−56.500	8.84971 +1	1.4230	2.9589	397.95	6.9696	5.7098	28.964	295.069	1.4216	9.9902	4.6617
18000	216.650	−56.500	7.56522	1.2165	2.5294	397.95	5.9580	6.6793	28.964	295.069	1.4216	1.1686 −4	4.6617
19000	216.650	−56.500	6.46748	1.0400	2.1624	397.95	5.0935	7.8130	28.964	295.069	1.4216	1.3670	4.6617
20000	216.650	−56.500	5.52930	8.8910 −2	1.8487	397.95	4.3546	9.1387	28.964	295.069	1.4216	1.5989	4.6617
21000	217.581	−55.569	4.72893 +1	7.5715 −2	1.5743 +24	398.81	3.7163 +8	1.0731 −6	28.964	295.703	1.4267 −5	1.8843 −4	4.6804 −6
22000	218.574	−54.576	4.04749	6.4510	1.3414	399.71	3.1735	1.2595	28.964	296.377	1.4322	2.2201	4.7004
23000	219.567	−53.583	3.46686	5.5006	1.1437	400.63	2.7121	1.4772	28.964	297.049	1.4376	2.6135	4.7204
24000	220.560	−52.590	2.97174	4.6938	9.7598 +23	401.53	2.3196	1.7310	28.964	297.720	1.4430	3.0743	4.7403
25000	221.552	−51.598	2.54922	4.0084	8.3346	402.43	1.9853	2.0270	28.964	298.389	1.4484	3.6135	4.7602
26000	222.544	−50.606	2.18837 +1	3.4257 −2	7.1230 +23	403.33	1.7005 +8	2.3719 −6	28.964	299.056	1.4538 −5	4.2439 −4	4.7800 −6
28000	224.527	−48.623	1.61619	2.5076	5.2141	405.12	1.2503	3.2402	28.964	300.386	1.4646	5.8405	4.8197
30000	226.509	−46.641	1.19703	1.8410	3.8280	406.91	9.2197 +7	4.4134	28.964	301.709	1.4753	8.0134	4.8593
32000	228.490	−44.660	8.89063 +0	1.3555	2.8185	408.68	6.8180	5.9942	28.964	303.025	1.4859	1.0962 −3	4.8988
34000	233.743	−39.407	6.63412	9.8874 −3	2.0559	413.35	5.0300	8.2177	28.964	306.489	1.5140	1.5312	5.0031

(*Continued*)

Table 2-5. Properties of the *U. S. Standard Atmosphere, 1962,* condensed from the complete tabulations. Numbers following the plus or minus sign are the power of ten by which that entry and each following entry should be multiplied. (Continued)

Geom Alt (m)	Temperature (°K)	Temperature (°C)	Pressure (mb)	Density (Kg m^{-3})	Density (no. m^{-3})	Particle Speed (m sec^{-1})	Collision Frequency (sec^{-1})	Mean Free Path (m)	Molecular Weight	Sound Speed (m sec^{-1})	Coefficient of Viscosity (Kg m^{-1} sec^{-1})	Kinematic Viscosity (m^2 sec^{-1})	Thermal Conductivity (K-cal m^{-1} sec^{-1} [°K]$^{-1}$)
36000	239.282	−33.868	4.98522 +0	7.2579 −3	1.5091 +23	418.22	3.7358 +7	1.1195 −5	28.964	310.099	1.5433 −5	2.1264 −3	5.1125 −6
38000	244.818	−28.332	3.77138	5.3666	1.1159	423.03	2.7941	1.5140	28.964	313.665	1.5723	2.9298	5.2213
40000	250.350	−22.800	2.87143	3.9957	8.3082 +22	427.78	2.1037	2.0335	28.964	317.189	1.6009	4.0067	5.3295
42000	255.878	−17.272	2.19967	2.9948	6.2270	432.48	1.5940	2.7131	28.964	320.672	1.6293	5.4404	5.4370
44000	261.403	−11.747	1.69496	2.2589	4.6968	437.13	1.2152	3.5970	28.964	324.116	1.6573	7.3371	5.5438
46000	266.925	−6.225	1.31340 +0	1.7141 −3	3.5642 +22	441.72	9.3188 +6	4.7401 −5	28.964	327.521	1.6851 −5	9.8305 −3	5.6501 −6
48000	270.650	−2.500	1.02296	1.3167	2.7378	444.79	7.2079	6.1709	28.964	329.799	1.7037	1.2939 −2	5.7214
50000	270.650	−2.500	7.97790 −1	1.0269	2.1352	444.79	5.6214	7.9125	28.964	329.799	1.7037	1.6591	5.7214
52000	270.650	−2.500	6.22283	8.0097 −4	1.6655	444.79	4.3847	1.0144 −4	28.964	329.799	1.7037	2.1270	5.7214
54000	267.560	−5.590	4.84917	6.3137	1.3128	442.24	3.4365	1.2869	28.964	327.911	1.6883	2.6740	5.6622
56000	263.628	−9.522	3.76572 −1	4.9762 −4	1.0347 +22	438.98	2.6885 +6	1.6328 −4	28.964	325.492	1.6686 −5	3.3531 −2	5.5867 −6
58000	259.699	−13.451	2.91373	3.9086	8.1271 +21	435.70	2.0959	2.0788	28.964	323.058	1.6487	4.2182	5.5109
60000	255.772	−17.378	2.24606	3.0592	6.3610	432.39	1.6280	2.6560	28.964	320.606	1.6287	5.3241	5.4349
62000	251.046	−22.104	1.72457	2.3931	4.9760	428.38	1.2617	3.3952	28.964	317.630	1.6045	6.7047	5.3431
64000	243.202	−29.948	1.31504	1.8837	3.9168	421.63	9.7749 +5	4.3134	28.964	312.628	1.5638	8.3020	5.1896
66000	235.363	−37.787	9.94067 −2	1.4713 −4	3.0594 +21	414.78	7.5111 +5	5.5223 −4	28.964	307.549	1.5226 −5	1.0348 −1	5.0352 −6
68000	227.529	−45.621	7.44483	1.1399	2.3701	407.82	5.7213	7.1218	28.964	302.387	1.4808	1.2991	4.8796
70000	219.700	−53.450	5.52047	8.7535 −5	1.8201	400.74	4.3174	9.2821	28.964	297.139	1.4383	1.6431	4.7230
72000	211.876	−61.274	4.05013	6.6593	1.3847	393.54	3.2254	1.2201 −3	28.964	291.800	1.3953	2.0952	4.5654
74000	204.057	−69.093	2.93758	5.0151	1.0428	386.21	2.3838	1.6202	28.964	286.365	1.3515	2.6949	4.4067
76000	196.24	−76.91	2.1045 −2	3.736 −5	7.768 +20	378.7	1.741 +5	2.175 −3	28.964	280.83	1.307 −5	3.499 −1	4.247 −6
78000	188.43	−84.72	1.4877	2.750	5.719	371.1	1.256	2.954	28.964	275.18	1.262	4.588	4.086
80000	180.65	−92.50	1.0366	1.999	4.157	363.4	8.940 +4	4.065	28.964	269.44	1.216	6.085	3.925
85000	180.65	−92.50	4.1250 −3	7.955 −6	1.654 +20	363.4	3.558 +4	1.021 −2	28.964	269.44	1.216 −5	1.529 +0	3.925 −6
90000	180.65	−92.50	1.6438	3.170	6.591 +19	363.4	1.418	2.563	28.96	269.44	1.216	3.837	3.925
95000	195.51	−77.64	6.8012 −4	1.211	2.520	378.2	5.640 +3	6.705	28.94				
100000	210.02	−63.13	3.0075	4.974 −7	1.037	392.4	2.409	1.629 −1	28.88				
105000	233.90	−39.25	1.4318	2.117	4.434 +18	415.0	1.089	3.810	28.75				
110000	257.00	−16.15	7.3544 −5	9.829 −8	2.073 +18	436.5	5.356 +2	8.150 −1	28.56				
115000	303.78	30.63	4.1224	4.623	9.830 +17	476.5	2.773	1.719 +0	28.32				
120000	349.49	76.34	2.5217	2.436	5.226	513.4	1.588	3.233	28.07				
125000	442.35	169.20	1.6863	1.275	2.761	580.3	9.484 +1	6.118	27.81				
130000	533.80	260.65	1.2214	7.589 −9	1.657	640.2	6.280	1.019 +1	27.58				
135000	624.30	351.15	9.3330 −6	4.921 −9	1.083 +17	694.9	4.454 +1	1.560 +1	27.37				
140000	714.22	441.07	7.4104	3.394	7.516 +16	745.7	3.317	2.248	27.20				
145000	803.74	530.59	6.0560	2.451	5.458	793.2	2.562	3.095	27.05				
150000	892.79	619.64	5.0617	1.836	4.107	838.0	2.037	4.114	26.92				
155000	957.94	684.79	4.2992	1.446	3.251	870.1	1.674	5.197	26.79				

(Continued)

Table 2-5. Properties of the *U. S. Standard Atmosphere, 1962*, condensed from the complete tabulations. Numbers following the plus or minus sign are the power of ten by which that entry and each following entry should be multiplied. (Continued)

Geom Alt (m)	Temperature (°K)	Temperature (°C)	Pressure (mb)	Density (Kg m^{-3})	Density (no. m^{-3})	Particle Speed (m sec^{-1})	Collision Frequency (sec^{-1})	Mean Free Path (m)	Molecular Weight	Sound Speed (m sec^{-1})	Coefficient of Viscosity (Kg m^{-1} sec^{-1})	Kinematic Viscosity (m^2 sec^{-1})	Thermal Conductivity (K-cal m^{-1} sec^{-1} [°K]$^{-1}$)
160000	1022.23	749.08	3.6943 −6	1.159 −9	2.618 +16	901.0	1.396 +1	6.454 +1	26.66				
165000	1062.74	789.59	3.2019	9.611 −10	2.182	921.1	1.190	7.741	26.52				
170000	1105.51	832.36	2.7926	8.036	1.830	940.7	1.019	9.233	26.45				
175000	1130.97	857.82	2.4477	6.845	1.568	954.2	8.854 +0	1.078 +2	26.30				
180000	1156.12	882.97	2.1536	5.858	1.349	967.5	7.727	1.252	26.15				
185000	1180.97	907.82	1.9018 −6	5.036 −10	1.166 +16	980.7	6.771 +0	1.448 +2	26.00				
190000	1205.50	932.35	1.6852	4.347	1.013	993.6	5.955	1.668	25.85				
195000	1220.84	947.69	1.4976	3.792	8.886 +15	1002.8	5.274	1.901	25.70				
200000	1235.95	962.80	1.3339	3.318	7.818	1011.8	4.682	2.161	25.56				
210000	1265.49	992.34	1.0652 −6	2.558 −10	6.097 +15	1029.8	3.716 +0	2.771 +2	25.27				
220000	1294.09					1047.3	2.976	3.519	24.98				
230000	1321.70	1048.55	6.9604	1.564	3.815	1064.7	2.404	4.429	24.69				
240000	1339.90	1066.75	5.6857	1.245	3.074	1078.3	1.962	5.496	24.40				
250000	1357.28	1084.13	4.6706	9.978 −11	2.493	1091.8	1.611	6.778	24.11				
260000	1373.84	1100.69	3.8573 −7	8.043 −11	2.034 +15	1105.1	1.330 +0	8.307 +2	23.82				
270000	1389.59	1116.44	3.2019	6.521	1.669	1118.2	1.105	1.012 +3	23.53				
280000	1404.54	1131.39	2.6708	5.315	1.377	1131.2	9.223 −1	1.227	23.24				
290000	1418.70	1145.55	2.2381	4.354	1.143	1144.1	7.738	1.478	22.95				
300000	1432.11	1158.96	1.8838	3.585	9.528 +14	1156.8	6.524	1.773	22.66				
310000	1439.40	1166.25	1.5919 −7	2.976 −11	8.011 +14	1167.2	5.534 −1	2.109 +3	22.37				
320000	1446.15	1173.00	1.3498	2.479	6.761	1177.5	4.712	2.499	22.08				
330000	1452.41	1179.26	1.1484	2.073	5.727	1187.7	4.026	2.950	21.80				
340000	1458.23	1185.08	9.8014 −8	1.740	4.869	1197.8	3.452	3.470	21.52				
350000	1463.67	1190.52	8.3915	1.465	4.153	1207.8	2.969	4.068	21.24				
360000	1468.79	1195.64	7.2061 −8	1.237 −11	3.554 +14	1217.7	2.562 −1	4.754 +3	20.97				
370000	1473.66	1200.51	6.2061	1.049	3.051	1227.6	2.217	5.538	20.70				
380000	1478.33	1205.18	5.3599	8.914 −12	2.626	1237.4	1.924	6.433	20.44				
390000	1482.88	1209.73	4.6417	7.600	2.267	1247.1	1.674	7.451	20.19				
400000	1487.38	1214.23	4.0304	6.498	1.963	1256.7	1.460	8.607	19.94				
410000	1487.12	1213.97	3.5077 −8	5.588 −12	1.709 +14	1264.3	1.279 −1	9.888 +3	19.70				
420000	1487.05	1213.90	3.0591	4.816	1.490	1271.8	1.122	1.134 +4	19.47				
430000	1487.22	1214.07	2.6731	4.160	1.302	1279.2	9.858 −2	1.298	19.24				
440000	1487.70	1214.55	2.3405	3.600	1.140	1286.6	8.678	1.483	19.03				
450000	1488.52	1215.37	2.0531	3.122	9.991 +13	1294.0	7.652	1.691	18.82				
460000	1489.73	1216.58	1.8043 −8	2.713 −12	8.773 +13	1301.3	6.758 −2	1.926 +4	18.63				
470000	1491.38	1218.23	1.5886	2.362	7.716	1308.6	5.976	2.190	18.44				
480000	1493.49	1220.34	1.4012	2.061	6.796	1315.8	5.293	2.486	18.26				
490000	1496.10	1222.95	1.2380	1.801	5.994	1323.0	4.694	2.819	18.10				
500000	1499.22	1226.07	1.0957	1.577	5.294	1330.2	4.168	3.191	17.94				

(Continued)

Table 2-5. Properties of the *U. S. Standard Atmosphere, 1962*, condensed from the complete tabulations. Numbers following the plus or minus sign are the power of ten by which that entry and each following entry should be multiplied. (Continued)

Geom Alt (m)	Temperature (°K)	Temperature (°C)	Pressure (mb)	Density (Kg m^{-3})	Density (no. m^{-3})	Particle Speed (m sec^{-1})	Collision Frequency (sec^{-1})	Mean Free Path (m)	Molecular Weight	Sound Speed (m sec^{-1})	Coefficient of Viscosity (Kg m^{-1} sec^{-1})	Kinematic Viscosity (m^2 sec^{-1})	Thermal Conductivity (K-cal m^{-1} sec^{-1} [°K]$^{-1}$)
510000	1497.35	1224.20	9.7111 −9	1.388 −12	4.698 +13	1334.9	3.712 −2	3.596 +4	17.79				
520000	1496.10	1222.95	8.6173	1.223	4.172	1339.5	3.308	4.049	17.65				
530000	1495.47	1222.32	7.6556	1.079	3.708	1334.1	2.950	4.556	17.52				
540000	1495.44	1222.29	6.8091	9.532 −13	3.298	1348.8	2.633	5.122	17.40				
550000	1495.99	1222.84	6.0630	8.430	2.936	1353.4	2.352	5.755	17.29				
560000	1497.09	1223.94	5.4048 −9	7.464 −13	2.615 +13	1357.9	2.102 −2	6.460 +4	17.19				
570000	1498.69	1225.54	4.8233	6.616	2.331	1362.5	1.880	7.247	17.09				
580000	1500.77	1227.62	4.3091	5.872	2.080	1367.1	1.683	8.123	17.00				
590000	1503.27	1230.12	3.8538	5.216	1.857	1371.6	1.508	9.098	16.92				
600000	1506.13	1232.98	3.4502	4.640	1.659	1376.1	1.352	1.018	16.84				
610000	1505.83	1232.68	3.0917 −9	4.140 −13	1.487 +13	1379.0	1.214 −2	1.136 +5	16.76				
620000	1505.81	1232.66	2.7727	3.697	1.334	1381.9	1.091	1.267	16.69				
630000	1506.00	1232.85	2.4884	3.304	1.197	1384.9	9.811 −3	1.412	16.63				
640000	1506.33	1233.18	2.2350	2.955	1.075	1387.8	8.828	1.572	16.56				
650000	1506.73	1233.58	2.0090	2.645	9.658 +12	1390.6	7.950	1.749	16.50				
660000	1507.14	1233.99	1.8071 −9	2.370 −13	8.685 +12	1393.5	7.164 −3	1.945 +5	16.43				
670000	1507.50	1234.35	1.6267	2.124	7.816	1396.4	6.461	2.161	16.37				
680000	1507.73	1234.58	1.4654	1.906	7.040	1399.3	5.831	2.400	16.30				
690000	1507.78	1234.63	1.3210	1.711	6.347	1402.2	5.267	2.662	16.24				
700000	1507.61	1234.46	1.1918	1.537	5.726	1405.0	4.762	2.950	16.17				

Chapter 3

ATMOSPHERIC TEMPERATURE, DENSITY, PRESSURE, AND MOISTURE

Section 3.1 I. I. Gringorten, A. J. Kantor
Section 3.2 A. E. Cole, A. J. Kantor
Section 3.3 A. J. Kantor, A. E. Cole
Section 3.4 Murray Gutnick
Section 3.5 K. S. W. Champion
Section 3.6 C. G. Stergis

Physical properties of the earth's atmosphere are discussed in this chapter. Atmospheric properties are mutually related by the ideal gas law, $P = \rho TR$, see Eq. (2-2). The pressure scale height, H_P, and the density scale height, H_ρ, are useful parameters. They are defined by

$$H_P = \frac{R}{M_o} \frac{T_m}{g}, \tag{3-1}$$

and

$$H_\rho = \frac{H_P}{1 + \frac{R}{M_o g} \frac{dT_m}{dz}}, \tag{3-2}$$

where R is the universal gas constant, T_m is the molecular scale temperature, M_o is the sea-level value of the molecular weight of air, g is the acceleration due to gravity, and z is geometric altitude.

Except for the 1/10,000th of a percent of the atmosphere lying above 90 km (300,000 ft), various dry gases form the atmosphere in essentially constant proportions. Water vapor is the most variable of the constituents of the atmosphere. The density depends, in part, on the composition and, hence, is most affected by variations in water vapor. Despite the mutual dependence of the basic physical properties of the atmosphere, they are discussed separately in this chapter for the region below 90 km. Sections 3.5 and 3.6 cover the variations of all properties from 90 to 200 km and above 200 km, respectively.

3.1 THERMAL PROPERTIES UP TO 90 KM

Until recently, in the United States all meteorological parameters were measured in degrees Fahrenheit and in English units of length. It was not practical to attempt accurate conversion of all these data. Also, conversion to the metric system would convey a false impression of the precision of the measurements. As a result, the mixture of metric and English units in this section is unavoidable. Wherever practical, both temperature scales are given on figures, and preference is given to the metric system in the text.

3.1.1 Energy Supply and Transformation*

The prime source of energy that produces and maintains the atmospheric motions and the spatial and temporal variations of meteorological elements is the solar radiation intercepted by the earth. In comparison with the sun's radiation, other energy sources, such as heat from the interior of the earth, radiation from celestial bodies, or mechanical pull of tidal forces from moon and sun, are practically negligible.

The rate at which solar energy is received on a plane surface perpendicular to the incident radiation, outside of the atmosphere at the earth's mean distance from the sun, is the *solar constant* (Sec. 16.1.1); the value used here is 2.0 cal cm^{-2} min^{-1}, 2.0 Langley min^{-1}, or 1400 W m^{-2}. The rate at which direct solar radiation is received on a unit horizontal surface at, or in the atmosphere above, the earth's surface is called the *insolation*. The planetary albedo, which is the reflected radiation divided by the total incident solar radiation (energy reflected/total incident energy), varies primarily with angle of incidence of the radiation, the type of surface, and the amount of cloudiness. On the average, roughly 30% to 40% of the incident energy is reflected back to space by the cloud surfaces, the clear atmosphere, the earth/air interface, and particles such as dust and ice crystals suspended in the atmosphere (see Chapter 5). The balance is available energy.

When the earth with its enveloping atmosphere is considered as a complete thermodynamic system, there appears within recent climatological history to be no major net change of energy in the system. There is no obvious

* This is based on the section by H. H. Lettau and D. A. Haugen in the *Handbook of Geophysics for Air Force Designers*, 1957.

systematic trend in (1) heating of the earth's surface or the atmosphere, (2) long-term weakening or intensifying of the atmospheric circulation, or (3) the balance between evaporation and precipitation. The processes affecting the internal and latent heat and the mechanical energy within the earth-atmospheric system appear perfectly balanced. Figure 3-1, in which are summarized the main features of the global energy transformations, may be used to determine the relative importance of the major energy cycles within the thermodynamic system of the earth-atmosphere. The numerical data presented in this figure are useful for various quantitative estimates. For example, if all energy inputs for the system ceased and rates of energy expenditure were maintained, the reservoir of mechanical energy (momentum) would be depleted in about 3 days; the reservoir of latent heat (precipitable water) in about 12 days; and the reservoir of internal energy (thermal) in about 100 days.

Although an absolutely dry and motionless atmosphere is conceivable, it is difficult to imagine an atmosphere at zero degrees Kelvin. It is perhaps more appropriate to interpret the time intervals of Fig. 3-1 as fictitious cycles of turnover of the atmospheric properties. The relative magnitudes of these life cycles show that, in comparison with rainfall and winds, temperature is the most conservative, and will exhibit the smallest, and thus most regular, temporal and spatial large-scale variation.

The solar energy input into the atmosphere at any one point varies with the earth's rotation about its axis and revolution about the sun. A consistent feature of this driving force on a global scale is that produced by differential latitudinal solar heating of the earth's surface. The reaction of the atmosphere to the solar driving force on an hourly, a daily, or an annual basis is observed most easily in the temperature field at low levels. Consequently, a classification of climatic zones by daily and annual mean temperatures is roughly identical with a classification by latitude circles (Sec. 3.1.2).

The solar energy input also varies according to season, latitude, orientation of terrain to the incident energy, soil structure, and the surface differential between the solar and sky radiation (*short wave*) and the atmospheric-terrestrial radiation (*long wave*). The difference between short-wave and long-wave radiation is the *net radiation*. Locally, net radiation is decreased primarily by atmospheric moisture (vapor and clouds). Evaporation of soil moisture diminishes, by the latent heat required, the portion of net radiation available for heating air and soil at the ground. The importance of moisture in establishing general climatic zones is shown by comparing desert climates with adjacent climates at roughly the same latitude. Table 3-1 gives the effect of soil moisture on the heat budget of the earth/air interface.

Slopes facing south receive maximum solar energy. Slopes facing west are usually warmer and drier than those facing east, because the time of maximum insolation on a west slope is shifted to the afternoon when the general level of air temperature is higher than in the forenoon.

The energy balance of the earth/air interface requires that net radiation equals the sum of heat fluxes into the air and soil plus the heat equivalent of evaporation. In general, the maximum of heat flux into the soil precedes the maximum of heat flux into the air. The temperature maximum at standard instrument height (about 6 ft) follows the maximum of heat flux into the air by roughly one to two hours.

3.1.2 Station Temperatures

The station temperature of synoptic meteorology is called the "surface air temperature" and "standard shelter

Table 3-1. Short-wave radiation on horizontal plane, net radiation, and estimated constituents of heat budget at the earth/air interface, showing effect of difference in soil moisture, caused by rains before 9 August and a dry spell before 7 September 1953 [Davidson and Lettau, 1957].

	Radiation ($W\ m^{-2}$)								
Mean Local Time	04 h	06 h	08 h	10 h	12 h	14 h	16 h	18 h	20 h
9 August 1953*									
Short-wave	0	141	544	733	796	823	537	144	—
Net	−59	47	364	497	540	525	273	−13	—
Flux into soil	−40	29	186	63	74	73	28	−65	—
Flux into air	−11	—	81	158	176	190	64	−17	—
Heat of evap.	− 8	—	97	276	290	262	181	69	—
7 September 1953**									
Short-wave	0	54	441	765	870	735	407	44	0
Net	−54	−32	181	403	488	398	154	−69	−77
Flux into soil	−44	−25	36	84	95	66	13	−29	−28
Flux into air	− 6	− 6	98	230	303	299	114	−30	−39
Heat of evap.	− 4	− 1	47	89	90	33	27	−10	−10

* Mean soil moisture in 0 to 4 in. layer, about 10% wet weight basis.
** Mean soil moisture in 0 to 4 in. layer, about 4% wet weight basis.

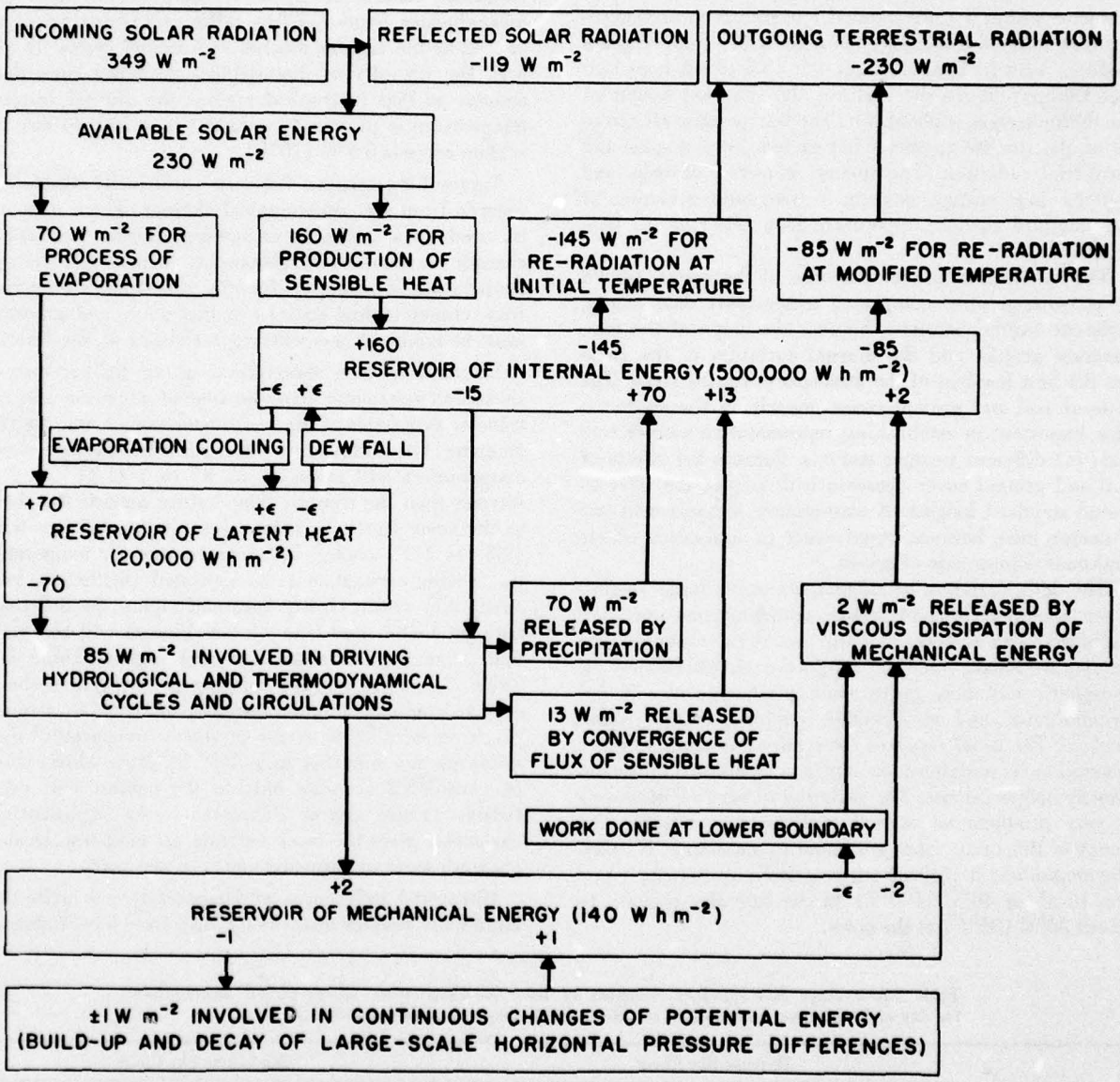


Fig. 3-1. The global mean energy cycles of the atmosphere. A solar constant of 1395 W m^{-2} and a global albedo value of 0.34 are assumed. The average total incoming radiation to the globe is ¼ of the solar constant. ϵ denotes an average rate of less than 0.5 W m^{-2}. The estimated reliability of the solar constant is 3%; of the derived energy rates, this totals approximately 10% [Lettau, 1954a].

temperature." In the United States the standard maximum station temperature for a given day is measured with a mercury-in-glass thermometer; the minimum, with an alcohol-in-glass thermometer; and the hourly values, with a mercury-in-glass thermometer. The thermometer readings are usually supplemented by recordings of a bimetallic thermograph. Sometimes the thermograph is the only instrument used for measuring temperature.

The standard method of observing is to enclose a thermometer within a white-painted louvered box, or Stevenson screen, mounted in an open field (close-cropped grass surface) with its base at about 4 ft (5.5 to 6.5 ft in central Europe) above the surface; the standard height of the thermometers is about 6 ft. The box permits air circulation past the thermometer but excludes direct solar and terrestrial radiation. The shelter, however, absorbs and radiates heat energy, causing a systematic deviation of the standard shelter temperature from the true air temperature.

The standard height of the base of the screen should be considered when comparing temperature data among different weather stations, because the slope of the temperature profile, and the diurnal variation of the slope for the first few feet of the atmosphere can be steep. The type of soil and ground cover underlying the shelter is also important in establishing representative temperature data for different weather stations. Because the effects of soil and ground cover decrease with height, the international standard heights of temperature measurement are a compromise between suppressing ground-cover effects and maintaining ease of access.

The daily variation of air temperature is fairly regular when variations due to fronts, thunderstorms, etc., are excluded. The factors affecting the daily variation are short-wave solar radiation, long-wave terrestrial and atmospheric radiation, mean wind speed, type of soil and ground cover, and aerodynamic roughness of the ground surface. The usual result of these effects is a temperature maximum in midafternoon and a temperature minimum shortly before sunrise. The variation of net radiation over a year produces an annual cycle of temperature. The range of this cycle, from minimum to maximum, is called the *amplitude;* it varies from practically zero at the equator, to about 40°C (100°F) in the subpolar regions, to about 30°C (80°F) at the poles.

In the polar regions, where periods of darkness or light extend for several months of the year, the diurnal variation of temperature is controlled primarily by the prevailing cloudiness and surface wind speed. In the summer, nearly all the solar energy is expended melting the ice, and the maximum temperature seldom exceeds 0°C (32°F).

In extra-tropical zones, the daily and annual pattern frequently reflects the effects of weather disturbances (airmass changes, wind-direction shifts, and frontal passages) as well as the regular diurnal and annual cycles. In general, the intensity of disturbances decreases toward the equator so that in tropical regions the diurnal range of temperature is practically constant from day to day and seldom exceeds 5.5°C (10°F).

Figure 3-2 presents a full year (arbitrarily selected) of records from six climatological stations. These data may be used as a guide in estimating diurnal and annual climatic extremes and day-to-day variability. Detailed temperature information for any zone must be obtained from climatological stations in that zone, and allowance must be made for temperature variations at low levels.

Standard surface observations of air temperature are subject to systematic error because of radiation and heat transfer properties of the instrument shelter and the thermometer. On calm, sunny days, recorded daytime shelter temperatures will normally be ½° to 1°C (1° to 2°F) warmer than the true air temperature outside the shelter at the same level; on calm, clear nights, 0.2° to 0.5°C (0.5° to 1°F) cooler. To measure true air temperature, the sensing element must be aspirated (artificially ventilated). On windy, cloudy days and nights, the differences between shelter and true air temperature will be smaller than during calm, clear days and nights (Table 3-2). Table 3-3 gives average differences between a shelter-enclosed mercury-in-glass thermometer and an aspirated psychrometer. These errors in shelter temperature measurements are inherent in published data, which should be considered accurate only to the nearest half degree Celsius (whole degree Fahrenheit). An aspirated psychrometer gives the most accurate air temperature at the place where exact measurements are necessary.

Horizontal differences of temperature can arise from large-scale weather disturbances and from local influences.

Table 3-2. Average and standard deviation of true air temperature minus shelter temperature for day and nighttime conditions of sky cover and hourly mean wind speed at 21 ft.

Wind Speed Range (knots)	Daytime Sky Cover				Nighttime Sky Cover			
	Clear & Scattered		Broken & Overcast		Clear & Scattered		Broken & Overcast	
	(°F)	(No.*)	(°F)	(No.*)	(°F)	(No.*)	(°F)	(No.*)
0.0 to 2.7	−1.2 ± 2.6	18	−0.1 ± 1.4	18	0.8 ± 1.4	76	0.5 ± 1.5	47
2.8 to 5.4	−1.3 ± 2.2	64	−0.3 ± 2.0	69	0.2 ± 1.6	53	0.2 ± 1.3	68
> 5.5	−1.1 ± 2.2	62	−0.5 ± 1.7	126	0.0 ± 1.4	17	0.2 ± 1.0	96

* Number of observations.

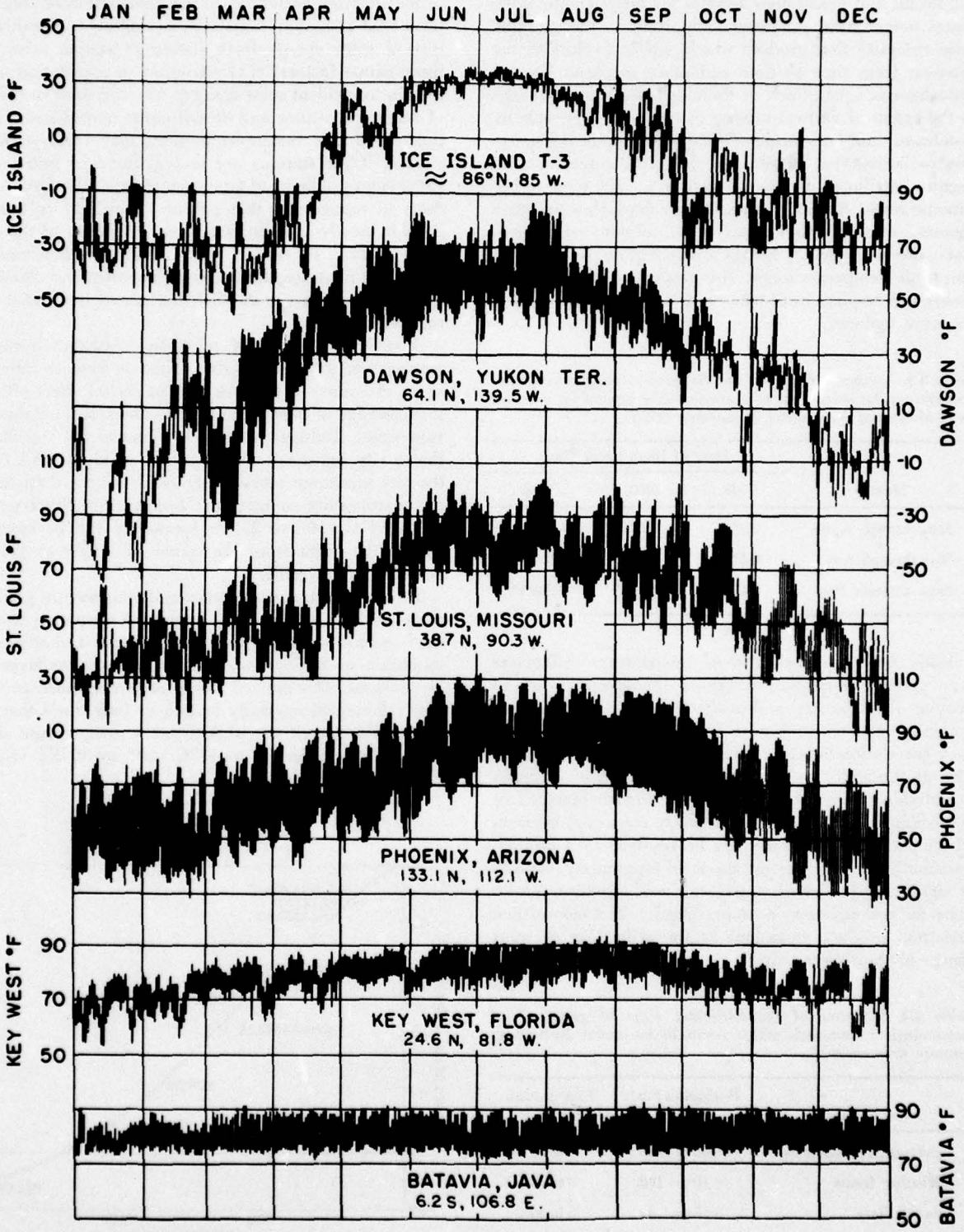


Fig. 3-2. Climatic extremes of daily diurnal range of standard surface temperature at various stations for 1943 (Batavia); 1953 (Key West, Phoenix, St. Louis, Ice Island T-3); and November-December 1952, January-October 1953 (Dawson, Canada).

CHAPTER 3

Weather disturbances such as cold and warm fronts, thunderstorms, and squall lines account for unsystematic horizontal temperature gradients (important to the synoptic meteorologist) that produce widely varying values of the gradient from time to time and place to place. Frontal disturbances, squall lines, or thunderstorms cause changes in the extent of vertical mixing of the lower troposphere, cloudiness, and large-scale vertical air motions. Temperature variations that accompany air-mass changes are frequently attributed to the advection of air from other climatic zones. Arrival of an arctic air mass (low-moisture content) or a subtropical air mass (high-moisture content), however, usually brings a new regime of net radiation to the temperate zones. This results in different daily means and amplitudes of temperature even if the low-level air is not replaced.

Table 3-3. Average difference, true air temperature minus shelter temperature, for sunny days over grass-covered ground for different times of day and year. (After Grundmann [1935].)

Month	Hour of Mean Local Time		
	0700	1400	2100
Jan. through April	0.2°F	−0.5°F	−0.2°F
May through Aug.	0.1°F	−0.6°F	−0.3°F
Sept. through Dec.	0.1°F	−1.1°F	0.0°F

Table 3-4 gives estimates of temperature differences over varying horizontal distances for several types of weather disturbances and meteorological conditions of synoptic importance. Figure 3-3 illustrates the average cross-correlation between simultaneous temperature anomalies at climatological stations as a function of distance. In individual cases of large-scale uniform air masses free of weather disturbances, the relatively consistent horizontal temperature differences can be resolved to a fair approximation by considering the local topography, vicinity of significant bodies of water, and soil structure. Variations in soil-moisture content, usually a nonconsistent variation, produce variations in the utilization of solar energy for heating the air.

Table 3-4. Estimates of the horizontal scale of certain local meteorological conditions which result in horizontal shelter-temperature differences.

Local Condition	Horizontal Scale (miles)	Temperature Difference (°F)
Difference in air mass	100 to 1000	5 to 40
Weather fronts	10 to 100	5 to 40
Squall lines	5 to 50	5 to 30
Thunderstorms	5 to 15	5 to 30
Sea breezes	5 to 10	2 to 20
Land breezes	2 to 5	2 to 10

Systematic horizontal gradients of temperature arise primarily from variations in the distribution of solar and terrestrial radiation. Consistent variations in the distribution of solar energy from station to station arise from three prime factors: (1) variation in orientation of the terrain to incident solar energy; (2) variation in the type of surface structure and of soil cover underlying the stations; and (3) variations in solar time from station to station, if the stations are several hundred miles apart. Horizontal gradients of temperature arise also from variations in topography that permit "pools" of cold air to develop locally at night, and from the length of the night from station to station. Also, normally nonconsistent variations in atmospheric moisture content and cloudiness produce variations in the distributions of reradiated longwave energy.

A striking example of relatively consistent horizontal temperature gradients is that found in heavily congested areas. A variety of features such as shelter effect of buildings, storage of heat in buildings, smog, fuel combustion, rain water drainage, and snow removal act together so that a city represents a heat source at night; this causes the city minimum temperature to be higher than that of the surrounding countryside. Temperature differences of 5° to 14°C (10° to 25°F) frequently can be measured during the night from the center of a city to the surrounding countryside.

The most pronounced horizontal temperature gradients are probably found in early summer at temperate latitudes near coast lines on days with sea breezes, and at night in mountainous regions, where the valleys act as large cold air pockets. The diurnal range of temperature over the valley floor will normally be two or four times that over the peaks, permitting peak-to-valley temperature differences of the order 5° to 17°C (10° to 30°F) [Geiger, 1957].

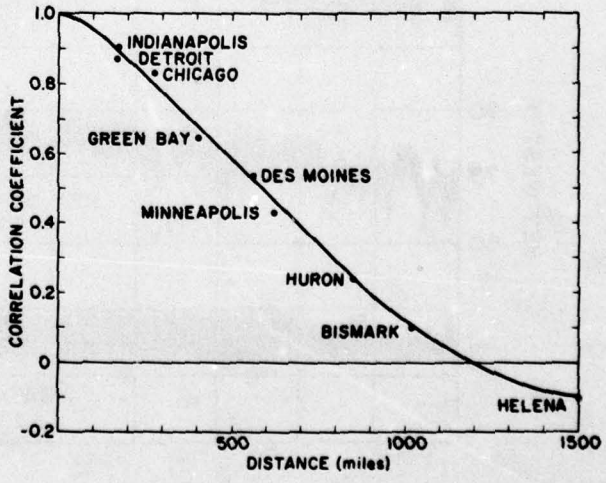


Fig. 3-3. The correlation of daily mean temperature anomaly at Columbus, Ohio, with daily mean temperature anomaly at nine other U.S. stations at indicated distances from Columbus.

In general, daily mean shelter temperatures as recorded by climatological stations will be representative within about 1°C (2°F) for a few hundred miles over uniform terrain, as will shelter temperatures under comparative conditions observed during the middle of the day and night. Temperature differences of about 5°C (10°F) are normally encountered near sunrise and sunset when local temperatures are changing most rapidly.

Daily mean temperatures that are reported by a climatological station will be generally representative, over uniform terrain, within 1°C (2°F) for an area of a few hundred miles radius. During the middle of the day or the night, the shelter temperature also is representative of the temperature over a large area. At times near sunrise and sunset, however, when local temperatures are changing most rapidly, shelter temperature differences of about 5°C (10°F) are normally encountered.

In the United States, the separation between weather stations is about 160 km (100 miles), with the exception of the eastern states, where the separation is between 30 to 80 km. For practical application, statistical analysis of the temperature differences among stations of interest will account for the systematic differences due to local climatic variations. Differences due to synoptic scale variations and nonsystematic climatic variations will, in general, be reflected in deviations from the systematic temperature differences.

Because the length of the landing strip required for aircraft takeoff is directly related to the air temperature, any discrepancy between free air temperatures over runways and shelter temperatures is important in establishing safe aircraft payloads and runway lengths. It has been sometimes believed that on days with strong insolation the mean free air temperature over airfield landing strips is significantly higher than standard shelter temperatures over the grassy area surrounding airstrips. Results of observations over four airstrips (Easterwood Airport, Hearne Air Force Satellite Field, and Bryan Air Force Base in Texas, and an auxiliary naval airstrip near Houma, Louisiana), however, show that the air between 1 and 20 ft over a landing strip is normally about 1°F cooler than indicated by the shelter temperature over adjacent grassy areas. The relative smoothness of runway surfaces is the physical factor causing daytime temperature reductions when air flows from grass to runway. During the transition from flow over a rough surface to a smooth surface, the wind speeds up and air descends from higher (cooler) levels onto the runway. After the transition is completed, a daytime equilibrium state of a smooth-surface temperature profile is established with a relatively strong concentration of high lapse rates close to the ground. This conclusion applies to both concrete and blacktop airstrips and is qualified only slightly by the type of vegetation surrounding the airstrip.

When short-time mean air temperatures over the runway and over grass are measured, a whole spectrum of differences is found. Although averages and median values are on the "safe" side, in the exceptional cases the free air temperature over the runways exceeded the shelter temperature, but by no more than 1°F (10-min mean temperatures) to 2°F (1-min mean temperatures) for a dry soil environment, and 0.5°F (5-min mean temperatures) for a swamp environment. The runway temperatures used for Table 3-5 are interpolated for the 5-ft level from temperature profiles measured with shielded, aspirated thermistors at 0.5, 2.5, 10, and 20 ft. The shelter temperatures are standard observations made by CAA personnel at Easterwood Airport. An unpublished, independent study by the 4th Weather Group, Eglin Air Force Base, obtained substantially the same results by comparing temperatures measured with mercury-in-glass thermometers in shelters placed on the airstrips and on surrounding grass.

Standard daytime shelter temperatures are normally 1° to 2°F warmer than true free air temperatures at the same height and location (Tables 3-2 and 3-3). This error, coupled with the above results, demonstrates that the standard method of temperature measurement in a properly exposed shelter over grass will provide a sufficient safety factor in the computation of runway lengths and aircraft payloads.

3.1.2.1 *Probability Distributions.* The basic statistical population of hourly values are used in routine day-to-day operations to obtain probabilities or likelihoods of high or low temperatures at specific times. The duration or persistence of high or low temperatures becomes important in timing events such as the takeoff of jet aircraft and the determination of the heat load and cold stress to which equipment will be subjected.

Neglecting the diurnal variations, the hourly observations of air temperature at a single station make up a population that is, more or less, symmetrically distributed about the mean monthly, seasonal, or annual temperature. Because there are significant departures from this general rule, an investigator should use an original historical record of at least five years of hourly observations to obtain firsthand estimates of lower or upper quantile values of temperature. In the absence of a large climatological record for the point of interest, or throughout the country as a whole, it becomes necessary to make reasonable estimates of temperature of specific calculated risks.

Table 3-5. A representative frequency distribution (based on 40 observations) of daytime difference between 1-min mean temperatures over concrete airfield landing strips and shelter temperatures over grass, Easterwood Airport, Texas.

Temperature Differences, (°F)	Frequency of Occurrence (%)
4.6 to 6.5	10
2.9 to 4.5	18
1.0 to 2.8	27
−0.9 to 0.9	40
−2.0 to −1.0	5

3.1.2.2 *Highest and Lowest Temperatures.* Figure 3-4 provides a means of estimating the lower 20% to 1% quantiles of hourly temperatures in January; Fig. 3-5, the upper 20% to 1% quantiles of hourly temperatures in July. These figures were prepared from data on the distributions of hourly temperatures at more than 130 North American stations, for as much as 10 years of record [Rayner, 1960]. The distribution of January, or July, temperatures for each station was plotted on Normal Gaussian Probability paper and a straight line was drawn, by eye, to fit as closely as possible to the lower, or upper, 20% to 1% of the data. The line was extended upward, or downward, to provide a graphical approximation to the mean and standard deviation of the sample. These approximations, plotted on a map of North America, were used for drawing the smoothed isotherms shown in the figures.

To estimate the temperature $\hat{T}$ that is attained or exceeded with a frequency p, find from the appropriate figure, by interpolation as needed, the mean temperature $\bar{T}$, and standard deviation, s_T, and substitute these in the equation

$$\hat{T} = \bar{T} + s_T \cdot y_s \quad [°F].$$

Values of y_s for various calculated risks are:

p	y_s
.20	± 0.84
.10	± 1.28
.05	± 1.65
.025	± 1.96
.01	± 2.33

In estimating low temperatures, y_s is negative. For example, at 45°N, 100°W, there is a 1% calculated risk that the temperature will be −26°F or lower; $\hat{T} = 9 + 15\ (-2.33) = -26°F$. For high temperatures at the same location, the 1% calculated risk is $\hat{T} = 75 + 10\ (2.33) = 98°F$.

Figures 3-4 and 3-5 should be considered only as first approximations to the probabilities of hourly temperatures for design purposes, because January is not always the coldest month of the year, nor is July always the hottest. Moreover, the isotherms are drawn without regard for differences between cities and suburbs, the topographic effects of valleys or hills, vegetation, local nocturnal radiation, and so on. For other maps of percent frequencies, or design temperatures, see Rayner [1961]; Van Valkenburg et al [1959]; Lackey [1958]; Hague [1956].

For operations of a continuous nature, such as air conditioning, a different statistic applies. The extreme annual temperatures should be studied as individual populations. Meteorologists often fit extreme values by the double exponential distribution [Gumbel, 1958], which is the limiting form of distributions of exponential type. But distributions of annual low and high extremes of temperature might fall well short of the limiting form [Gringorten, 1962].

"Pools" of cold air apparently are associated with extreme cold temperatures reported in various parts of the world. Most low-temperature extremes for various states and countries are confined to single stations, and the temperatures at stations near the one where the record is set are not especially low. Figure 3-6 shows some temperature extremes. Maps of extremes of high and low temperatures have been published by the U.S. Army Research Laboratories and are periodically revised.

U.S. military equipment has been designed to operate within a broad range of environmental conditions, set forth in detail in MIL-STD-210A [Dept. of Defense, 1957]. The climatic extremes specified do not necessarily represent the absolute extremes observed; rather they are the values determined by scientific judgment not to be surpassed on more than 10% (three days) of the most extreme month.

Although temperature extremes under which equipment must operate depend on intended region of operation, all items must be able to withstand, while in transit or storage, temperatures of −80°F for 24 h, −40°F indefinitely, and a diurnal cycle ranging from 10 h at 90°F to 4 h at 160°F. Meteorological thermometers must cover from −140° to +160°F [Court and Salmela, 1962].

The durations of hot and cold weather have not yet been studied in detail. Table 3-6 presents data for two locations known for their high temperatures (Death Valley, California and Andimishk, Iran). The values apply when the maximum temperature is 110°F or higher.

Table 3-6. Average durations of very hot temperatures within given amounts below the maximum temperature (110°F or higher).

Degrees F Below Maximum	Average No. of Hours
0	2
1	3
2	4
3	5
4	6
5	7
6	7.5
7	8
8	9
9	9.5
10	10
11	10.5
12	11
13	12
14	12.5
15	13
16	13.5
17	14
18	14.5

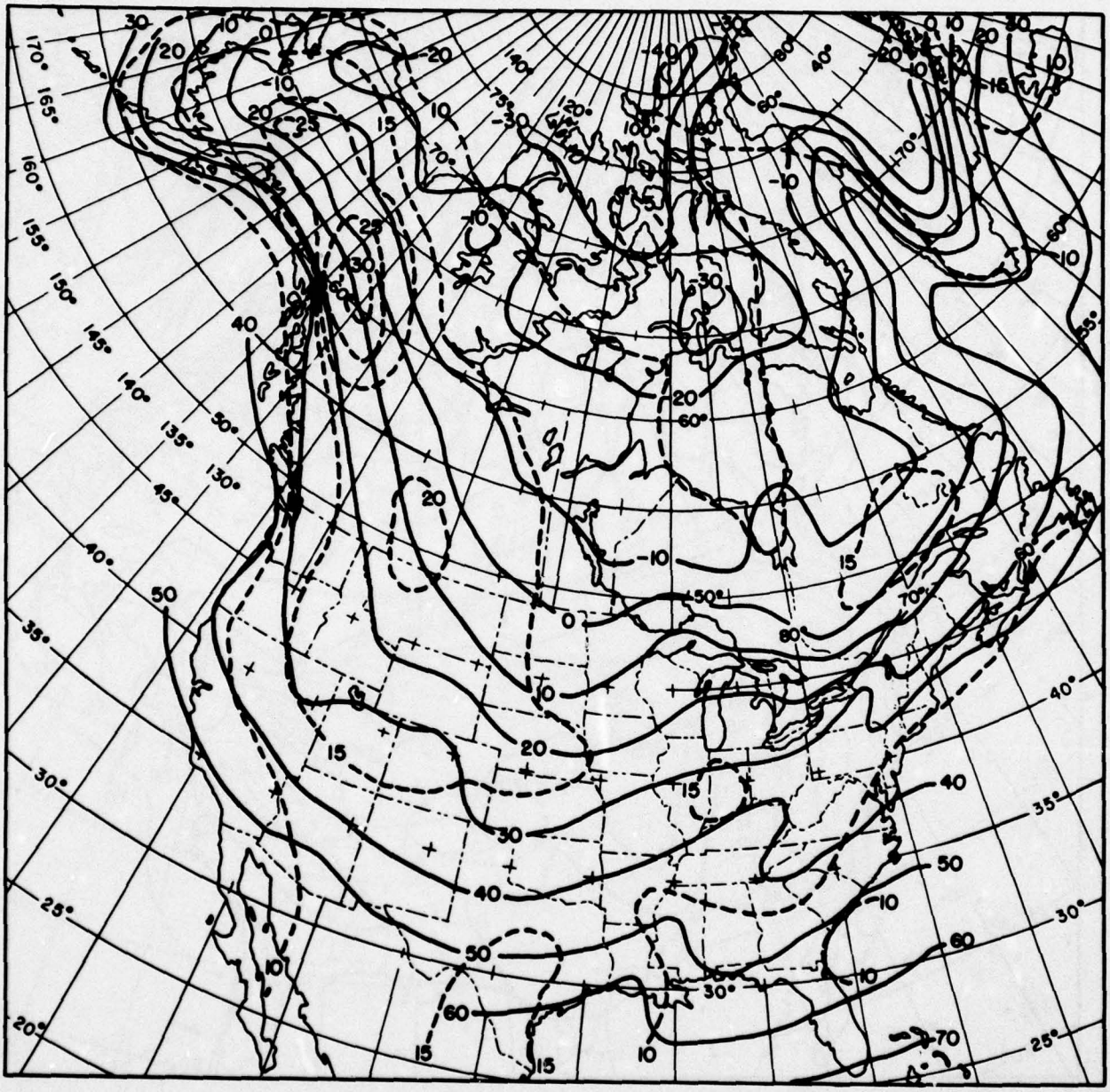


Fig. 3-4. Isotherms of January hourly surface temperatures. Approximate mean values are shown by solid lines, standard deviations by broken lines. The approximations were made to give best estimates of lower 1 to 20 percentile values of temperature by normal distribution (see Sec. 3.1.2.2.).

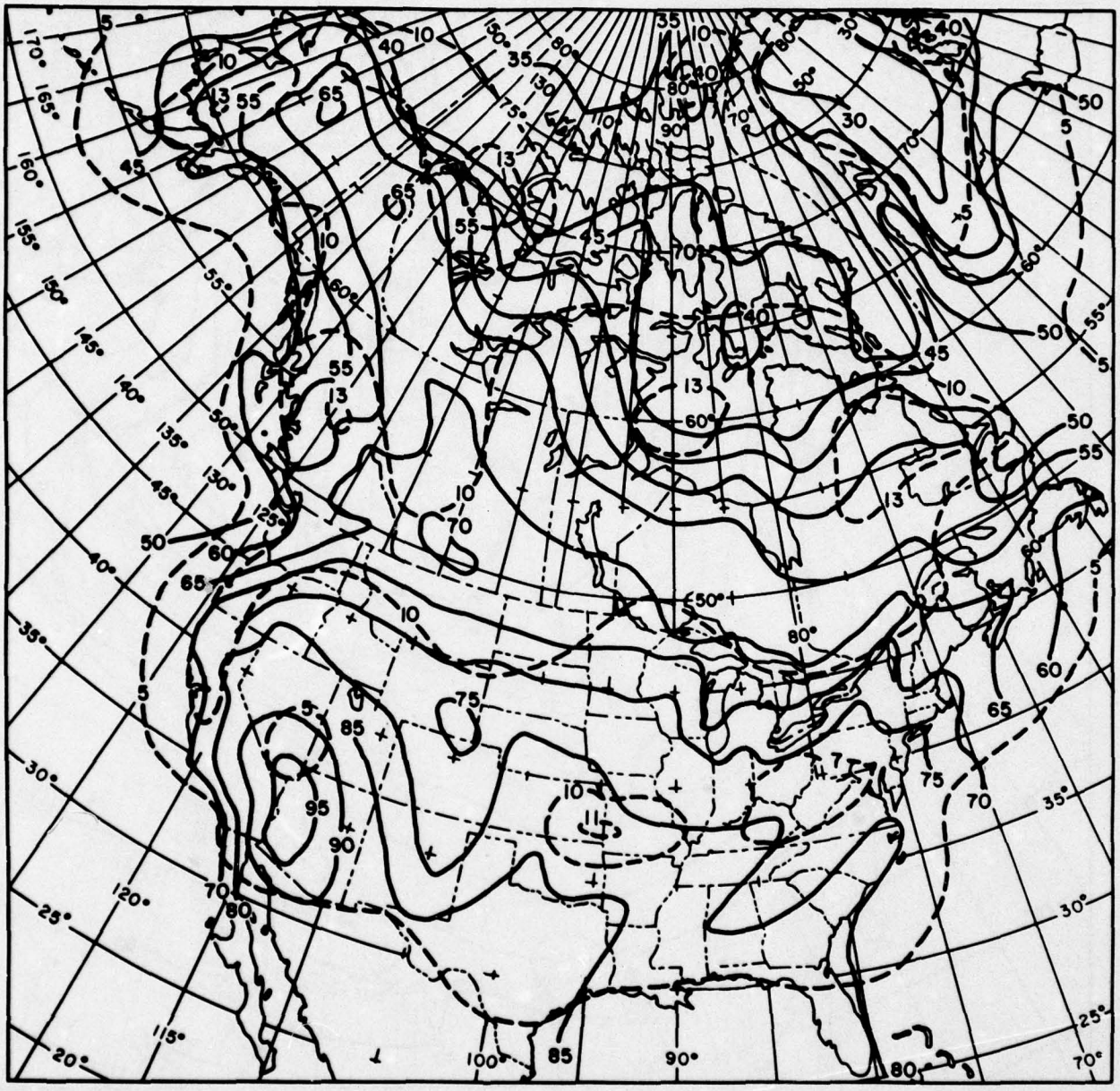


Fig. 3-5. Isotherms of July hourly surface temperatures. Approximate mean values are shown by solid lines, standard deviations by broken lines. The approximations were made to yield the best estimates of upper 20 to 1 percentile values by normal distribution (see Sec. 3.1.2.2).

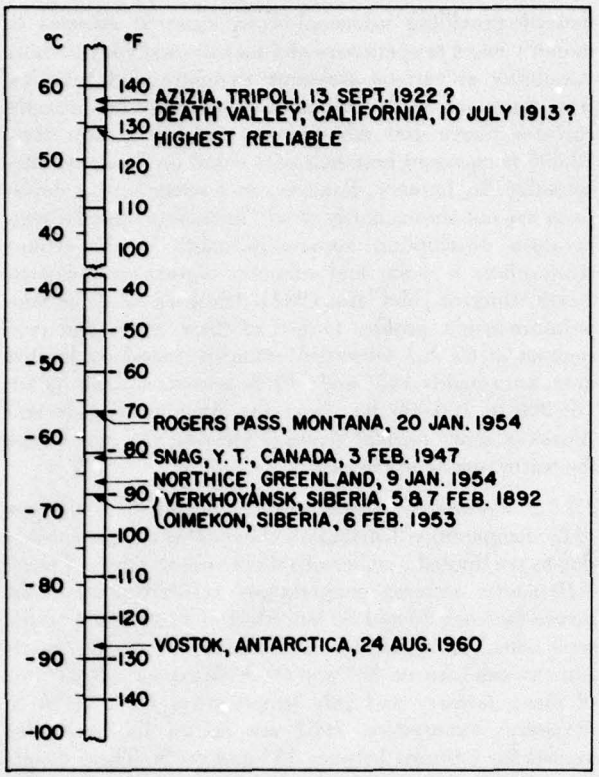


Fig. 3-6. Record temperatures around the world.

Tables 3-7 and 3-8 show, for very cold periods and for specified latitudinal ranges and minimum temperature, the diurnal variation of temperature and durations of low temperatures. These tables are useful as first approximations of design criteria for equipment to be operated in cold areas. Recently, the U.S. Army has revived the study of duration [Westbrook, 1962].

A pilot study was made of the hourly temperatures at Minneapolis, Minnesota, in the coldest month (January) and the hottest month (July), 1943 to 1952. Figure 3-7 shows that for the month of January the hourly values of temperature (24 per day) have a 1% likelihood of being equal to or less than −19°F; three hourly averages (8 per day) have a 1% likelihood of being equal to or less than −19°F, a 5% likelihood of being equal to or less than −12°F, and so on. Similarly, for the month of July, the hourly values have a 1% likelihood of being equal to or greater than 94°F; three hourly averages have a 1% likelihood of being equal to or greater than 93°F and a 5% likelihood of being equal to or greater than 88°F, etc. The graph gives the distribution of the n-hourly averages, up to $n = 24$, or of m-day averages, up to $m = 32$ (from 1 January through 1 February, and 1 July through 1 August, inclusive). The long duration of the low values of temperature is unexpected.

Figure 3-8 shows the distribution of the lowest n-hourly average of each day, for n equals 1 to 24; even this statistic shows an unexpected persistence.

3.1.3 Upper Air Temperatures

The general thermal structure of the atmosphere is described (Sec. 2.2) by the *vertical temperature gradient*, dT/dZ (Z is geopotential altitude) or its negative, the *lapse rate.*

As dry air rises through the atmosphere adiabatically (with no external source or sink of heat), it cools at the *dry-adiabatic lapse rate* of 10°K per km (5.5°F per 1000 ft). As it sinks it warms at the same rate. Rising moist air, however, cools at the dry-adiabatic rate only until it reaches its dewpoint (or frostpoint), after which liberation of the latent heat of condensation keeps the *saturation adiabatic lapse rate* smaller than the dry rate. At high dewpoints the saturation rate is only one-third the dry rate, whereas at very low dewpoints, when little water vapor is present, the two rates are almost equal.

Figure 3-9 shows the average vertical distribution of temperature for January and July from the equator to 75°N, based on the various supplemental atmospheres

Table 3-7. Average temperature differences (°F) from minimum temperatures, by hourly increments from time of minimum temperature.

	Hours Before Time of Minimum Temp.											
	−12	−11	−10	−9	−8	−7	−6	−5	−4	−3	−2	−1
	Latitude 40° to 52.5°N											
Temp. difference	17	16	14	13	11	9	7	6	4	4	3	2
	Latitude 52.5° to 65°N											
Temp. difference	13	11	9	9	8	7	6	5	4	3	2	1
	Latitude 65° to 90°N											
Temp. difference	7	6	6	5	5	4	4	3	3	2	2	1

	Hours After Time of Minimum Temp.											
	+1	+2	+3	+4	+5	+6	+7	+8	+9	+10	+11	+12
	Min. Temp. −30°F or below											
Temp. difference	4	8	13	17	20	23	26	27	27	26	25	24
	Min. Temp. −45°F or below											
Temp. difference	2	5	6	8	10	11	12	13	13	13	13	12
	Min. Temp. −55°F or below											
Temp. difference	2	2	3	4	5	5	6	7	7	8	8	9

Table 3-8. Average hourly duration of low temperatures.

Latitude	Degrees F Above Minimum						
	2°	4°	6°	8°	10°	15°	20°
40° to 52.5°N	3	6	8	9	12	15	20
52.5° to 65°N	6	10	16	18	20	28	
65° to 90°N	11	20	24	31	37	52	

(Sec. 2.3). This temperature-height cross section differs from most other such representations in that it has been adjusted to agree with the best available averages of temperature and of wind. Given the surface-pressure field, the wind at a higher level is governed by the vertical and horizontal temperature distributions up to that level. Any representation, therefore, of the temperature field must be consistent with the observed wind field. Also, the temperature field at any level must be consistent with the observed pressure and density at that level. Some reported values of temperature in the 40 to 60 km range, however, imply either winds much stronger than observed or densities not in agreement with other evidence; these have been adjusted for this model.

The largest seasonal variation in temperature occurs between 70 and 80 km at 60°N, where the temperature fluctuates from near 230°K in January to about 170°K in July. At 80 km the temperature increases toward the pole in winter and toward the equator in July, whereas at 50 km the latitudinal gradient is reversed, and temperature decreases toward the pole in January and toward the equator in July. Between 15 and 20 km (the first cold layer) temperature decreases toward the equator and increases toward the pole during both seasons.

3.1.3.1 *Variability Below 30 Km (100,000 Ft).* Tables 3-9 and 3-10, based on standard radiosonde data, give mean January and July temperatures over North America for standard pressure levels up to 10 mb, and for 10,000 ft height increments to 100,000 ft. Standard deviations of the daily values around these means are also shown, thereby providing information on seasonal changes in monthly mean temperatures and interdiurnal (day-to-day) variability at various pressures (heights) and latitudes. Root mean square deviations of temperature for pressure surfaces above 100 mb and for heights greater than 50,000 ft represent best estimates based on data currently available. In January, however, root mean square deviations are not shown north of 50° because a bimodal temperature distribution apparently exists in the winter stratosphere in polar and subpolar regions over eastern North America [McClain, 1962]. (Section 2.3 gives temperature-height profiles typical of these warm and cold regimes at 60°N.) Observed extremes, based on limited data, are roughly 190° and 240°K between 20 and 30 km (65,000 to 100,000 ft). Near the Aleutian Islands and Alaska a more normal stratosphere prevails, not unlike the warm regime to the east.

3.1.3.2 *Variability Above 30 Km.* A statistical analysis of the temperature distribution above 30 km is not feasible due to the limited number of reliable observations. Figure 3-10 shows extreme temperatures (circled points) observed between 30 and 80 km. Most of these observations were taken during daylight hours at several North American stations between 30° and 60°N. Maximum departures of mean January and July temperatures from the *U.S. Standard Atmosphere, 1962* are shown by horizontal arrows for latitudes between 15° and 60°N. These departures do not represent an absolute range of mean monthly temperatures because maximum and minimum values do not occur in January and July at all heights between 30 and 80 km. Estimates of seasonal fluctuations are least

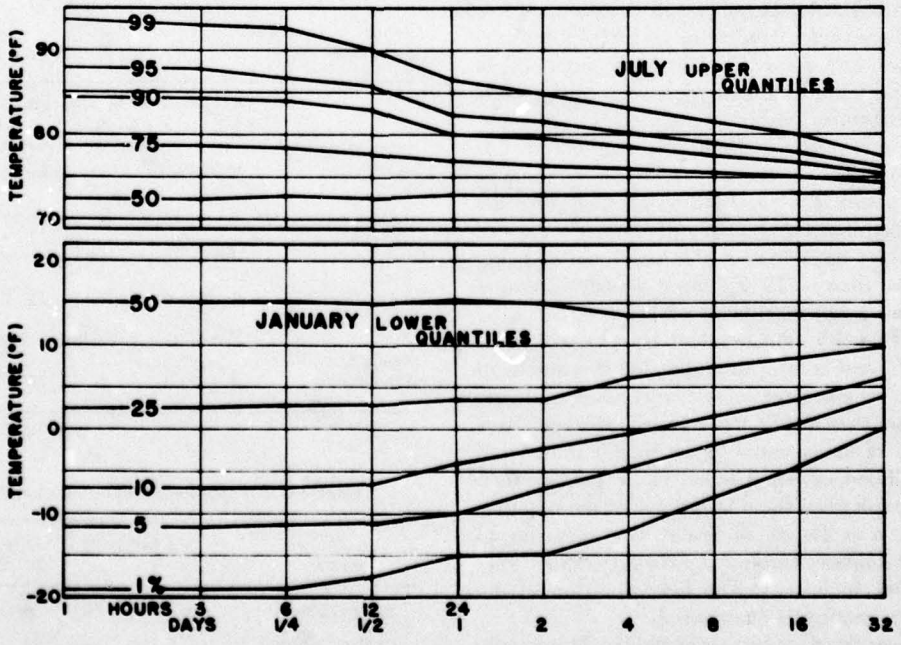


Fig. 3-7. The distribution of the averages of consecutive hours of temperature at Minneapolis, Minnesota. Lower half of distribution from 1 January to 1 February inclusive, and upper half of distribution from 1 July to 1 August, inclusive.

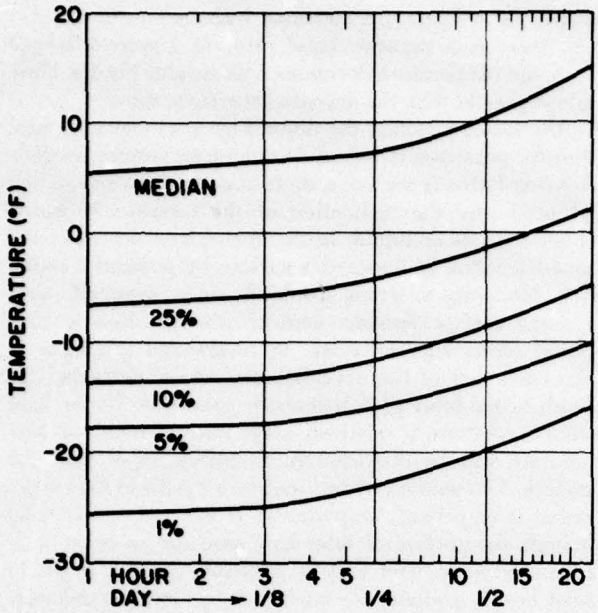


Fig. 3-8. The distribution of the lowest n-hourly average of each day.

accurate above 65 km where temperature measurements apparently are subject to the largest errors. Temperatures given for these levels are based primarily on rocket-grenade observations, and temperatures so derived depend upon the assumed value of wind velocity. Because both grenade and chemical release experiments thus far indicated strong wind shear and turbulence between 80 and 120 km, temperatures given for this region are not considered as reliable as at other altitudes. Below 65 km, extremes are obtained more reliably from rocket observations of the Meteorological Rocket Network, as well as from grenades and other experimental devices. At 60°N and above 60 km, warm January temperatures show large positive departures from the 1962 Standard profile. January and July temperature profiles at all latitudes approach or cross the 1962 Standard near the 60-km level. Above this, January temperatures are greater and July temperatures generally less than the 1962 Standard. More specific information such as mean seasonal variability at various latitudes and/or altitudes can be determined from Fig. 3-9 and from the appropriate supplemental atmosphere tables of Sec. 2.3.

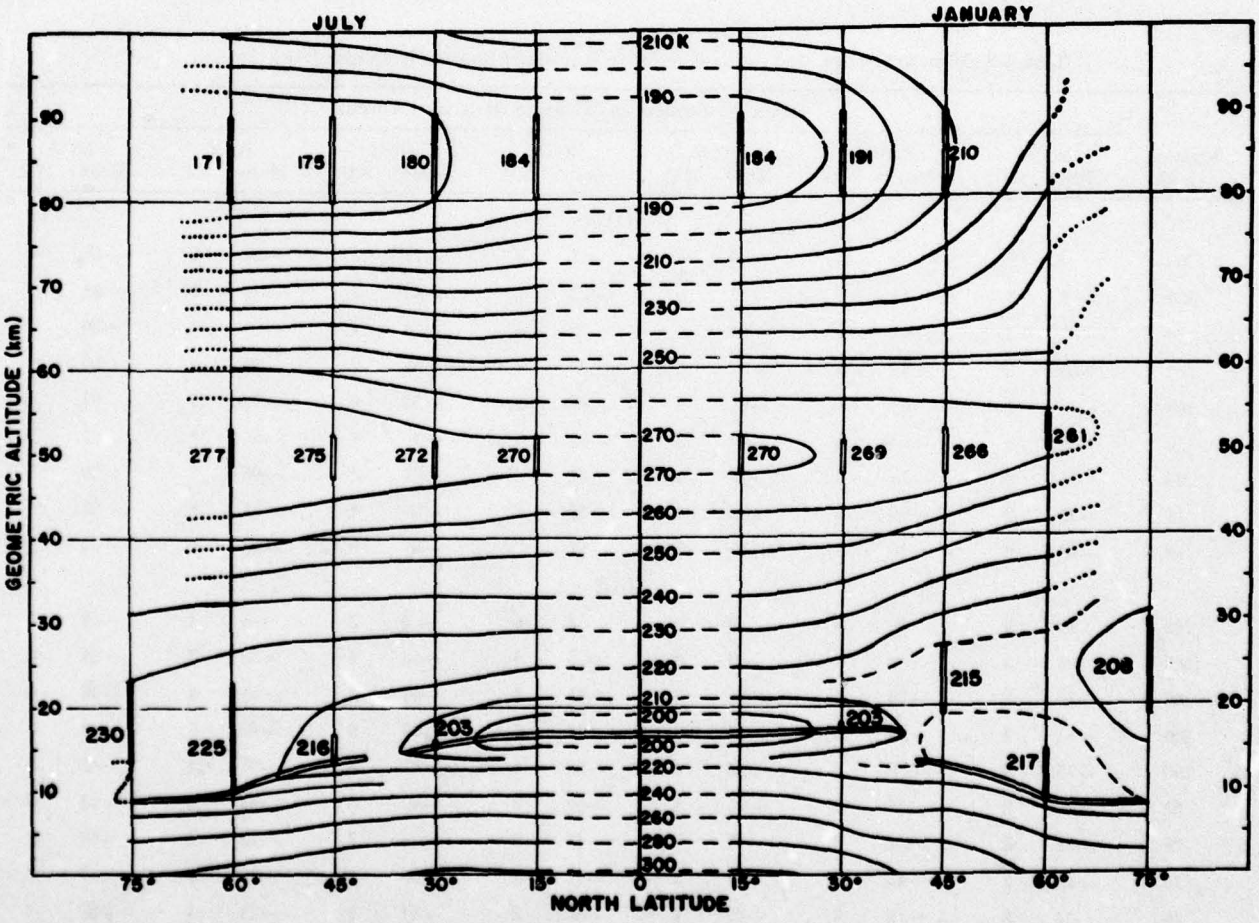


Fig. 3-9. Latitudinal temperature-height cross section. Vertical bars depict isothermal regions; temperature in °K is given beside the bar. Double horizontal lines show the tropopause.

3.1.4 Speed of Sound vs Temperature

For many design problems it is necessary to know the speed of sound. Because this parameter is a function of temperature, Figure 3-11 can be used with the various temperature presentations given in this section to derive the probable speed of sound for various altitudes and geographical areas.

3.1.5 The Lower Level Air Temperatures

An atmosphere cleaned of all impurities is transparent, except in the wavelength regions of carbon dioxide, water vapor, and ozone absorption bands, to solar and terrestrial radiation. The major portion of solar energy entering the atmosphere penetrates to the ground, and heat is transferred to the air via conduction and convection. The result is that temperature gradients are normally modified from the earth's surface upward. The vertical extent of the modification is primarily controlled by the degree of turbulence in the wind. Without the operation of convective heat transfer processes, the depth of an inversional layer or of a superadiabatic layer would be restricted to a few inches. (An *inversional layer* is one in which the temperature increases with increasing height; i.e., there is a negative lapse rate; in a *superadiabatic layer* the temperature decreases with height, but the lapse rate is greater than the dry-adiabatic lapse rate.)

Any factor affecting the diurnal cycle of radiative heat transfer processes is reflected in the temperature profiles. A prime factor is the sun's angle at noon (i.e., season and latitude) and the inclination of the terrain. Moisture, either gaseous or liquid, in the atmosphere decreases the rate of cooling of the earth's surface by terrestrial radiation. Moderate to strong low-level winds, especially over a rough surface, enhance vertical mixing, which in turn causes either superadiabatic or inversional gradients to approach that of the dry-adiabatic, while increasing the depth of the layer of nonadiabatic gradients. Under light wind conditions, a relatively large diurnal range of temperature will be restricted to a shallow layer near the surface. The amount of soil moisture available for evaporation is of primary importance. If the moisture content is high, the portion of solar heat used for evaporation is relatively great, and only a relatively small portion of solar heat is available for modifying low-level temperature gradients (Sec. 3.1.6).

Table 3-9. Mean temperature and standard deviation at standard pressure levels over North America.

Pressure (mb)	Mean Temperature and Standard Deviation (°Celsius)													
	20°N		30°N		40°N		50°N		60°N		70°N		80°N	
	Mean	S.D.	Mean	S.D.	Mean	S.D.	Mean	S.D.	Mean	S.D.	Mean	S.D.	Mean	S.D.
							JANUARY							
700	7	2	2	5	−6	6	−17	8	−22	8	−26	7	−28	6
500	−9	3	−14	4	−21	6	−31	7	−35	7	−39	5	−41	5
300	−37	3	−41	3	−46	4	−52	4	−53	4	−56	4	−59	5
200	−56	3	−57	5	−57	6	−54	7	−54	7	−57	6	−60	6
100	−75	3	−69	4	−61	4	−56	5	−54	6	−57	7	−63	6
50	−65	3	−64	3	−60	3	−58	4	−57	*	−60	*	−67	*
25	−55	2	−55	3	−57	4	−61	5	−61	*	−65	*	−70	*
15	−48	2	−50	3	−52	4	−55	6	−58	*	−62	*	−66	*
10	−43	2	−46	3	−49	4	−52	6	−56	*	−60	*	−64	*
							JULY							
700	10	2	10	2	9	3	2	4	−3	3	−5	4	−8	4
500	−6	2	−6	2	−9	3	−15	4	−18	4	−20	4	−24	4
300	−33	2	−33	2	−36	3	−41	4	−44	4	−45	4	−46	4
200	−55	2	−55	2	−54	3	−52	5	−49	5	−47	5	−43	4
100	−73	3	−70	3	−63	3	−53	4	−47	3	−45	2	−42	2
50	−60	2	−58	2	−55	3	−52	3	−47	3	−45	3	−43	3
25	−51	2	−51	2	−48	2	−46	2	−44	2	−41	2	−40	2
15	−45	2	−45	2	−44	2	−41	2	−38	3	−37	3	−37	3
10	−41	2	−40	2	−39	2	−36	2	−34	3	−33	3	−32	3

* Not normally distributed.

Near noontime in clear summer weather a considerable portion (normally 60 to 70%) of the direct solar radiation penetrates to the lower boundary of the atmosphere. Modification of air temperature starts essentially at the ground level, controlled by the structure of the earth/air interface. Any variability of surface features causes a considerable variability of thermal response to the net radiation. With increasing height, the horizontal temperature distribution becomes more uniform because of the mixing action of wind and turbulence. The local vertical temperature gradient normally changes with height so as to align itself with the conditions in the free atmosphere.

Mean temperature lapse rates in the first inch of the atmosphere over bare, black surfaces such as black soil and asphalt roads have been measured in excess of 200,000 times the dry-adiabatic lapse rate of 0.55°F/100 ft [Ramdas, 1948]. The darker the surface, the greater the temperature lapse in the air lying above the surface. When the surface is covered with dense vegetation, the plants act as radiating surfaces. Air temperature maxima and minima are more likely to be found near the top of the vegetation than at the earth/air interface. Nighttime temperature minima can also occur 5 to 10 in. above bare surfaces [Fleagle, 1956].

The predominant feature of low-level vertical profiles of mean temperature is their diurnal range between superadiabatic and inversional (see Table 3-11). When the sun is more than 10 to 15° above the horizon, the incoming solar radiation usually exceeds the outgoing terrestrial radiation, the earth's surface is warmed, and the low-level lapse rate becomes superadiabatic. At night, terrestrial radiation cools the earth's surface and the low-level gradient becomes inversional. Roughly 1 to 2 h after sunrise and 1 h before sunset the temperature gradient passes through the isothermal phase.

Under temperature lapse conditions, at some critical wind speed the temperature gradients between 1 in. and 6 ft are maximum. Under temperature inversional conditions, a light, relatively steady wind is necessary to propagate upward the cooling of the earth's surface. Above some nighttime critical wind speed, measured wind speeds have little effect on low-level temperature gradients [Sutton, 1953].

Table 3-10. Mean temperature and standard deviation at given heights over North America.

Altitude (10^3 ft)	Mean Temperature and Standard Deviation (°Celsius)													
	20°N		30°N		40°N		50°N		60°N		70°N		80°N	
	Mean	S.D.	Mean	S.D.	Mean	S.D.	Mean	S.D.	Mean	S.D.	Mean	S.D.	Mean	S.D.
JANUARY														
10	8	2	2	5	−6	6	−18	8	−23	8	−28	7	−30	6
20	−11	3	−17	4	−25	6	−36	7	−40	7	−44	5	−46	5
30	−34	3	−39	4	−46	4	−52	5	−53	5	−56	5	−59	5
40	−55	3	−58	5	−57	6	−54	7	−54	7	−57	6	−60	6
50	−70	3	−66	4	−60	4	−56	5	−54	6	−58	7	−62	6
60	−70	3	−66	3	−61	3	−57	4	−56	*	−59	*	−66	*
70	−63	3	−61	3	−59	3	−59	4	−58	*	−62	*	−68	*
80	−56	2	−56	3	−57	4	−60	5	−61	*	−65	*	−69	*
90	−49	2	−51	3	−53	4	−56	6	−58	*	−62	*	−65	*
100	−43	2	−46	3	−49	4	−52	6	−56	*	−59	*	−63	*
JULY														
10	11	2	11	3	10	3	2	4	−3	3	−5	4	−9	4
20	−7	2	−7	2	−10	3	−18	4	−22	4	−24	4	−27	4
30	−29	2	−29	2	−33	3	−39	4	−43	4	−45	4	−46	4
40	−53	2	−53	2	−53	3	−52	5	−49	5	−47	5	−43	4
50	−67	3	−65	3	−60	3	−53	4	−47	4	−45	3	−42	3
60	−68	2	−65	3	−60	3	−53	4	−47	3	−45	3	−42	3
70	−60	2	−57	2	−54	2	−52	3	−46	3	−45	3	−43	3
80	−53	2	−52	2	−50	2	−48	2	−45	3	−42	3	−41	3
90	−47	2	−47	2	−46	2	−43	2	−41	3	−39	3	−39	3
100	−42	2	−41	2	−40	2	−38	2	−36	3	−35	3	−35	3

* Not normally distributed.

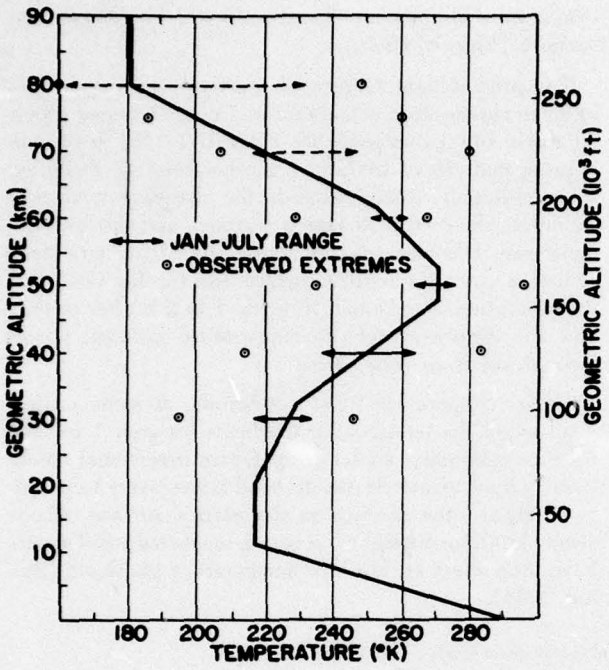


Fig. 3-10. Northern Hemisphere seasonal variability of temperature about the *U. S. Standard Atmosphere, 1962*. Horizontal arrows show range of mean January and mean July temperature. Points are observed extremes.

Figure 3-12 gives examples of extreme lapse rates that can occur in the first few feet of the atmosphere. Observations are at various hours in Death Valley, California, where average monthly temperatures in July and August are as high as any in the world. Temperature-height profiles from 14 in. below to 50 ft above a barren surface of compressed gravel and sand are shown.

The difference between maximum and minimum temperature during a 24-h cycle, sometimes referred to as the "diurnal amplitude of temperature," decreases with height. The time lag between occurrence of temperature maxima and noontime also varies with height. Diurnal cycles of temperature can be observed fairly regularly to about 3000 ft. In the first few inches of the atmosphere, temperature gradients can exhibit a daily range from roughly —1000 to +500 times the dry-adiabatic; in the layer above this to about 500 ft, from —10 to +5 times; and in the layer from 500 to 3000 ft, from —1.5 to +0.5 times. Table 3-12 gives values of amplitude and time lag for various heights above a smooth, grass-covered terrain.

Short-time temperature variability at any one point in the air usually is discussed in terms of fluctuations caused by a turbulent wind field moving air parcels of varying temperature past the point, or by "blobs" or "boils" of air that maintain a relative consistency of identity while being moved by the wind field. The latter concept is generally associated with mean lapse conditions; the former with mean inversion conditions when the usual effect of the wind field is to bring the mean temperature gradient within the inversional layer nearer the adiabatic while increasing the depth of the inversional layer.

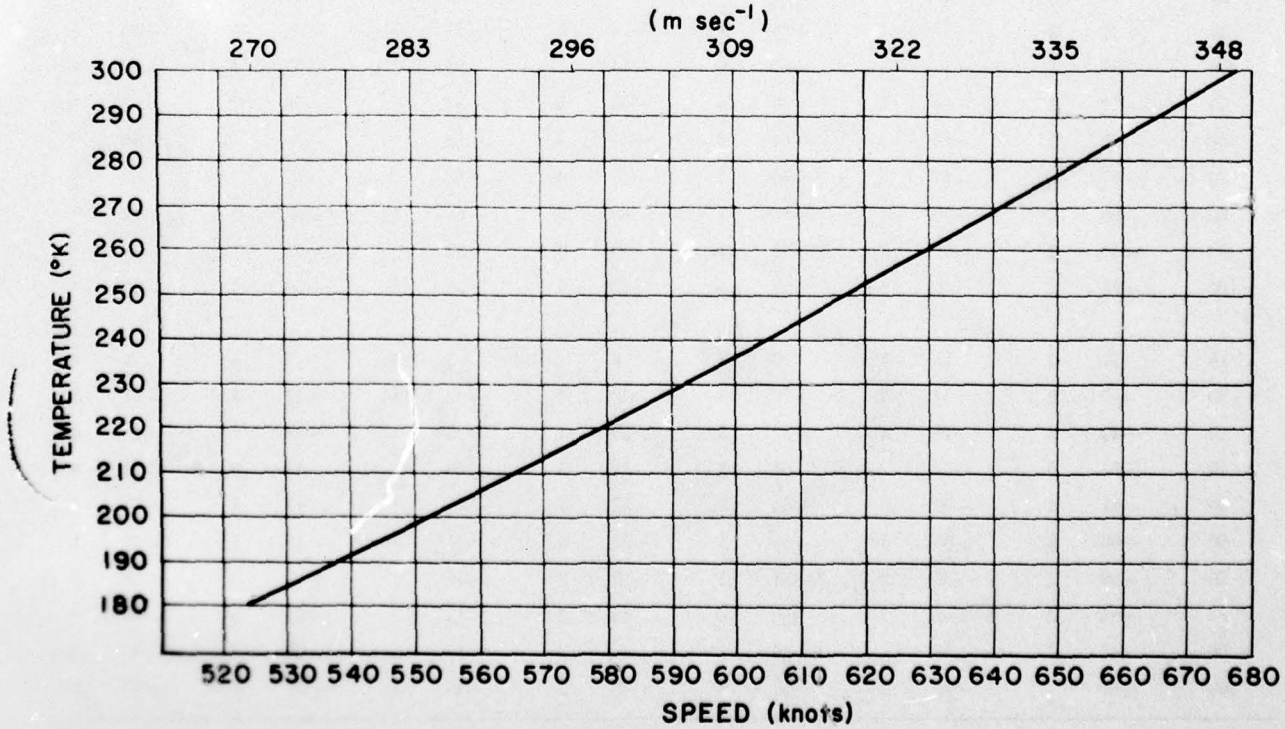


Fig. 3-11. Speed of sound vs absolute temperature.

Another type of temperature fluctuation is produced by short-time variations in the net radiation, such as that produced by the shadows of drifting cumulus clouds. According to wind speed and cloud cover, the periods of such net radiation variations vary from a few seconds to several minutes. The theory of two-medium heat transfer of the earth/atmosphere system shows that such short-period net radiation fluctuations are nearly completely absorbed in the soil heat flux, whereas the eddy heat transfer into the atmosphere responds only sluggishly to a short-period reduction of the radiation. As a result, the effect of drifting cloud shadows on air temperature at standard height is surprisingly small, compared with the decrease in the net radiation that is caused by the cloud shadows.

A special case is the low-level temperature decrease that accompanies a solar eclipse. Even under most favorable conditions; that is, near noontime with clear skies in the arid zone, the resulting temperature decrease at 5 ft above the surface is usually less than 3°F, although the soil surface temperature may fall by 10 to 15°F depending upon the thermal admittance of the soil.

Temperature fluctuations near the ground tend to be skewed toward positive fluctuations. During a single 24-h period the vertical temperature gradient in the low altitudes can fluctuate considerably. Under superadiabatic conditions these fluctuations will be large and irregular because of convective turbulence as well as the turbulence caused by rough terrain. Under isothermal conditions these fluctuations almost disappear. With inversional conditions a thin turbulent layer under the inversion may be set up, in which case there will be relatively small regular fluctuations. Horizontal dimensions of thermal eddies are greater with inversional temperature gradients than with temperature lapse conditions; the size generally increases with height above the surface.

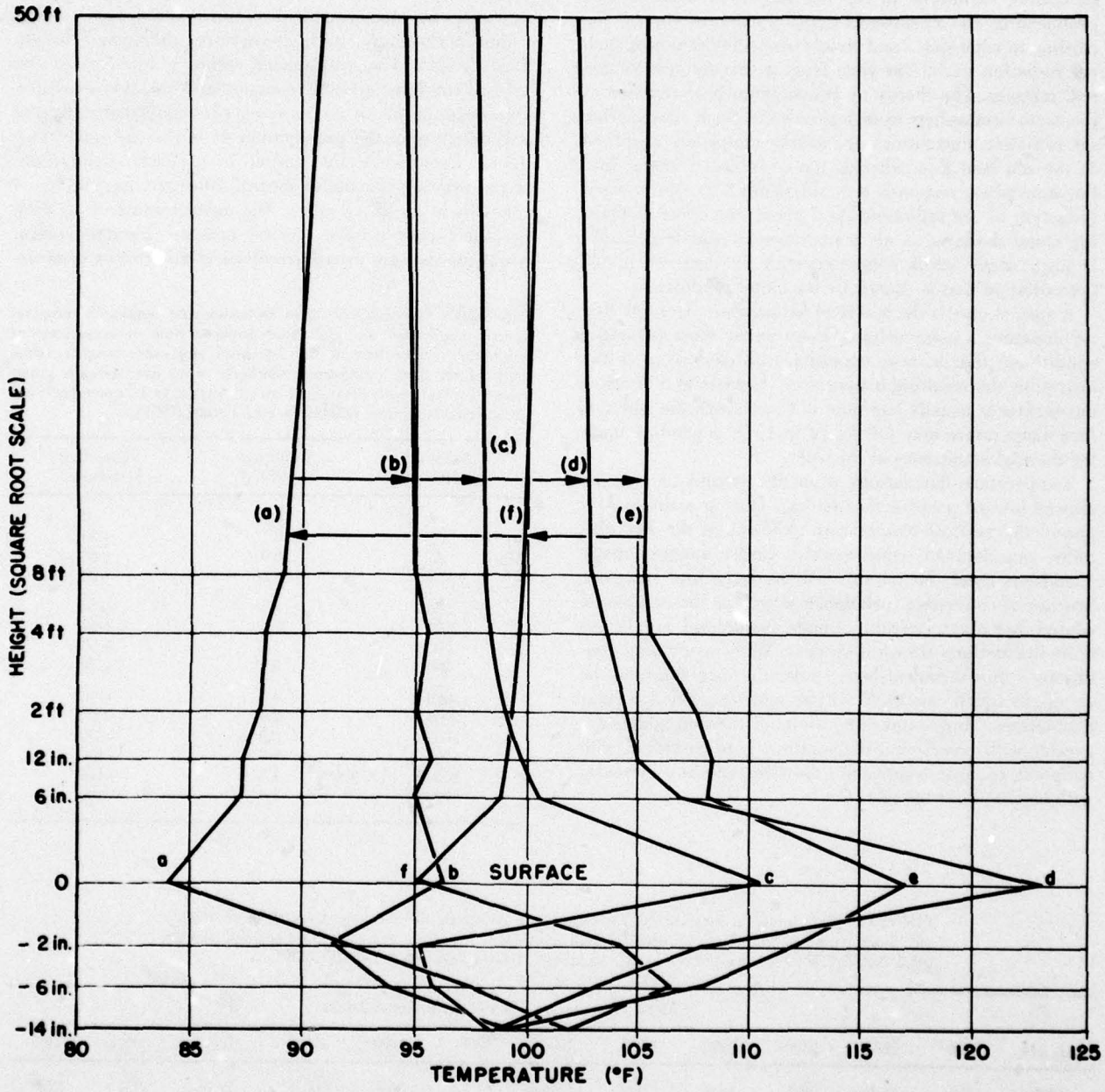
Temperature fluctuations, although relatively small in comparison with wind fluctuations, are of practical significance in meteorological optics (atmospheric boil), radio meteorology, and atmospheric diffusion [Sutton, 1951, 1953]. The atmosphere within a few feet of the ground can have a highly complex and variable structure. One example of an engineering problem created by the variability is in the propagation of ultrasonic waves outdoors. Even when the output is perfectly steady, the signal intensity fluctuates several times per second, sometimes by ±15 dB or more. The measurement of air temperatures close to the ground presents instrumentation problems that are usually resolved in an attempt to meas-

Table 3-12. Difference between minimum and maximum temperatures (amplitude) and difference between time of occurrence of minimum temperature at the 5-ft level and other heights (time lag) of the 24-h oscillation. Southerly wind over smooth grass-covered terrain with clear skies on 31 August to 1 September 1953 at O'Neill, Nebraska [Davidson and Lettau, 1957].

Height (ft)	Amplitude (°F)	Time Lag (minutes)
5	10.5	0
10	10.1	+15
25	8.9	+30
50	8.8	+30
100	8.6	+30
200	8.3	+40
300	7.5	+50
500	6.7	+70
1000	4.7	+10
2000	2.0	+20
3000	0.9	−250
4000	1.2	−480
5000	1.8	−440
6000	2.0	−330

Table 3-11. Mean temperature vs height for clear skies. Averages of 6 daytime cases (0600 to 1600h) and 5 nighttime cases (1800 to 0400h) with southerly flow over smooth, grass-covered terrain (42.5°N; 98.6°W; 1978 ft mean sea level) Aug.-Sept., 1953 [Davidson & Lettau, 1957].

	Mean Temperature (°F) at Mean Local Time											
Height	0000	0200	0400	0600	0800	1000	1200	1400	1600	1800	2000	2200
6000	57.7	58.1	58.4	58.6	60.6	61.4	61.1	60.6	60.2	57.7	57.0	57.4
5000	61.2	61.8	62.6	62.7	63.9	64.2	63.3	63.8	63.4	60.3	60.0	60.6
4000	64.8	65.2	66.4	66.5	66.9	66.7	66.1	67.1	67.4	62.8	63.1	63.9
3000	67.4	67.4	69.2	69.1	70.2	69.4	69.4	71.2	72.3	66.6	66.2	67.1
2500	68.0	68.0	69.4	70.0	71.2	70.5	71.0	74.0	75.0	68.7	68.1	68.4
2000	68.9	68.7	69.4	69.9	72.2	71.8	73.0	76.5	77.5	71.1	69.7	69.1
1500	70.1	69.8	69.0	69.4	71.2	72.3	75.5	79.0	80.2	73.2	71.2	70.7
1000	70.5	69.7	68.4	68.7	70.4	74.7	78.6	82.0	82.7	75.7	73.0	72.0
500	69.7	68.4	66.6	66.9	71.1	77.5	81.3	84.7	85.4	77.8	72.9	71.6
300	68.6	67.4	65.1	65.8	72.0	78.8	82.4	85.8	86.7	78.6	72.0	70.7



CURVE LABEL	a	b	c	d	e	f
HOUR OF OBSERVATION (PACIFIC STANDARD TIME)	0425 TO 0540	0755 TO 0813	0930 TO 1000	1155 TO 1305	1327 TO 1550	1430 TO 2047
INSOLATION (LANGLEY min-1)	0.006	0.76	1.18	1.38	1.02	0.00
BLACKBODY SKY TEMP. (°F)	66	54	52	62	61	–
WIND SPEED AT 12 FT (mph)	5.0	3.6	3.0	4.1	4.0	14.2
NUMBER OF OBSERVATIONS	5	11	8	9	8	5

Fig. 3-12. Average vertical temperature gradient above and below surface in Death Valley, California, 31 July to 13 August 1950.

ure true air temperature rather than the temperature of objects experiencing the temperature variations.

Although control of the macroclimate now appears beyond the reach of human engineering possibilities, the microclimate of certain localities has been successfully altered and controlled. Examples are frost protection work in plantations, irrigation, and wind sheltering [Geiger, 1957].

3.1.6 Earth/Air Interface Temperatures

The earth/air interface is either a land, snow, or water surface. At many locations, the physical structure of the interface is overwhelmingly complex. The land surface can be covered with seasonally varying vegetation of great diversity, and even without plant cover there is normally a considerable variability produced by small-scale terrain features, differences in soil moisture, cultivation, etc. A snow surface is markedly affected by aging. The physical conditions of water in a shallow puddle are quite different from the open ocean. All these conditions reflect themselves in the microclimatological aspects of natural surfaces.

In the measurement of surface temperature the use of ordinary thermometers will result in meaningful values only in the rare cases of a flat, uniform, and homogeneous surface. In general, area averages of temperature obtained by a temperature integrating method over certain defined sections will be more representative than any of a multitude of widely varying point values. Bolometric temperature measurements from an airplane cruising at low altitude provide a more reasonable approach to the problem of surface temperature determination than a series of thermometric point measurements.

Table 3-13 lists some results of bolometric measurements from an airplane. The data illustrate the great horizontal variability of surface temperature even when effects on the scale of less than 20-ft linear dimension are averaged out.

The processes that determine the temperature of the earth/air interface and the surface characteristics that influence these processes may be separated into four classes:

(1) radiative energy transformation (or net radiation intensity), which depends upon the albedo and selective absorption and emission (color);
(2) convective heat transfer into the air (mechanical turbulence and structure of low-level wind profiles), for which surface roughness is the important factor;
(3) conduction of heat into the ground, which depends upon the thermal admittance of the soil; and
(4) transformation of radiant energy into latent heat, which depends upon the dampness of the surface or available soil moisture at the ground level.

The aerodynamic roughness of a natural surface determines the momentum exchange between ground and air flowing past it. The momentum exchange establishes the curvature of the low-level profile of mean wind speed. The mechanical turbulence produced by surface roughness also determines to a certain degree the relative amount of heat transported into or from the air at mean ground level.

Other conditions being equal, an increase in roughness will cause lowering of maximum surface temperature during daytime and raising of minimum surface temperature during nighttime. Under average conditions of overall air flow and net radiation on summer days in temperate

Table 3-13. Bolometric records of area (approximately 400 ft^2) surface temperature from airplane cruising at approximately 1200 ft along a constant flight path, April 1944. (Condensed from Albrecht [1952].)

Day	Hour	Sun's Elevation (degree)	Sky Cover	Standard Shelter Temp. at Airport (°F)	Surface Temperature (°F)—Bolometric Data					
					Baltic Sea	Sand Beach	Down Land	City	Woods	Opening in Woods
9	13 to 14	40.4	10/10	49	36	54	57	46	45	47
11	19 to 20	−1.6	1/10	50	36	45	36	37	38	41
16	19 to 20	−1.8	9/10	58	40	46	45	44	39	36
20	05 to 06	0.5	1/10	35	41	28	21	31	26	20
29	14 to 15	42.1	4/10	44	44	115	108	63	60	73
				Wind Speed (knots)	Woods	Clear Cutting in Woods	Dry Peat	Swamp	Pond	
7	19	—	4/10	1	35	28	21	32	34	
20	20	—	2/10	3	32	30	25	32	32	
26	20	—	3/10	5	36	27	30	31	34	
Albedo values as determined by Albrecht:					5%	8%	8%	7%	5%	

zones, for ordinary sandy soil, the diurnal range of surface temperature is about 30°F if the roughness coefficient is 0.0025 in. or 25°F if it is 0.25 in. (roughness coefficient, "length," is $\epsilon/30$, where ϵ is the average height of surface irregularities in inches).

A special and rather extreme case of surface roughness is represented by forests. The trees intercept solar radiation, and the heat absorbed is given off into the air that is trapped between the stems. Although deep snow may lie on the ground, daytime temperature in wooded areas in spring can reach 60°F.

The thermal admittance (Sec. 3.1.7) of most soils depends on porosity and moisture content. Because both thermal conductivity and heat capacity increase with soil moisture, the thermal admittance may be significantly affected by humidity variations during rainy or wet weather periods, whereas the normal diffusivity may remain unaltered. These effects are difficult to assess, however, because the dampness of the surface is also a major factor in the utilization of solar energy for evaporation. If soil moisture is readily available at the earth's surface, the part of the net radiation, which would have been used for heating air and ground, is used for latent heat of evaporation. Table 3-1 shows the effect of difference in average soil moisture on utilization of net radiation energy. Table 3-14 lists observed temperatures in the air and soil at levels close to the earth/air interface.

Engineers must consider the effect of albedo and color on net radiation in artificially changing surface or ground temperature. In India, a very thin layer of white powdered lime dusted over a test surface made ground temperatures up to 27°F cooler; the effect was felt at a depth of at least 8 in.

Another effective control method is shading. Thin roofs (metal, canvas), however, may attain a temperature so high that the under surface acts as an intense radiator of long-wavelength radiation. In hot climates, multilayer shades with natural or forced ventilation in the intermediate space, or active cooling of the outer surface by water sprinkling, can be used with some success. Table 3-15 lists surface temperature measurements of various materials.

3.1.7 Subsoil Temperatures

The thermal reaction of the soil to the pulses (due to the earth's rotation and its revolution about the sun) of net radiation is governed by the *molecular thermal conductivity* of the soil, k, and by its *volumetric heat capacity*, $C = \rho c$ (where ρ is the density, and c is the heat capacity per unit mass). For a cyclic forcing function of frequency n, the quotient $(nk/C)^{1/2}$ (which has the physical units of velocity) determines the downward propagation, or *amplitude decrement with depth*, of the soil-temperature response. The product $(nkC)^{-1/2}$, which has the physical units of degrees divided by Langleys per unit time (one Langley per second equals 4.186×10^4 Wm^{-2}), governs the amplitude of the temperature wave at the soil surface. The ratio k/C is the *thermal diffusivity* (physical units of length squared per unit time). The expression $(kC)^{1/2}$ defines the *thermal admittance* of the soil.

The continuous flow of heat from the earth's interior to the surface is the order of 10^{-5} Langley min^{-1}. This is very small compared with a solar constant of 2 Langleys min^{-1}, average net-radiation rates of 0.2 Langley min^{-1}, and induced soil-heat fluxes in the uppermost few feet of the earth's crust of 0.1 Langley min^{-1}. Only for depth intervals in excess of about 100 ft must the heat flow from the earth's interior be considered, inasmuch as it results in vertical temperature gradients of the order of 7° to 70°F per mile.

Table 3-16 gives experimental data on thermal admittance and theoretical values of the half-amplitude depth interval based on experimental thermal diffusivity data for diverse ground types. The smaller the thermal admittance, the larger the surface-temperature amplitude for a given forcing function. An inverse proportionality would be valid only when convective heat transfer into the atmosphere is negligible.

In a simple theoretical model of thermal diffusion, an *effective atmospheric thermal conductivity*, K, is introduced. For air, K is many times larger than the molecular thermal conductivity of the air. For the same forcing function, the surface-temperature amplitudes at two different kinds of ground (1 and 2) follow the ratio

$$\left[(\mathrm{TAR})_2 + (\mathrm{K/k})_{\mathrm{air}}^{1/2}\right]\left[(\mathrm{TAR})_1 + (\mathrm{K/k})_{\mathrm{air}}^{1/2}\right]^{-1},$$

where TAR represents the ratio of the thermal admittance of the ground to that of air. For diurnal cycles of net radiation, the ratio $(K/k)_{air}$ is the order of 10^4.

The most extreme surface temperature oscillation occurs over feathery snow where the amplitude may reach approximately four times that over still water or sandy soil, and is at least 100 times as large as that over the turbulent ocean. An amplitude ratio of about 3.5 can be expected for surface temperature over dry vs moist sand surfaces. Theoretically, the penetration of thermal pulses into the soil is inversely proportional to the frequency of the pulse [Lettau, 1954b]. The best insulator is still air or any porous material with air-filled pores, such as feathery snow; materials such as leaf litter have similar insulating properties [Geiger, 1957].

Much information is available on soil-temperature variations in various climatic zones [Crawford, 1951]. Table 3-17 gives annual and daily cycles in different soil types. In addition to the type of ground, certain meteorological factors such as rainfall and melting of snow have marked effects on the soil temperature. Snow cover is a leading factor in protecting the soil from severe frost. On one extreme occasion with an air temperature of −1°F, the temperature was +30°F under a 5-in. snow cover, whereas on bare soil it was −7°F.

The soil temperature variations illustrated in Fig. 3-13 were obtained at a station cleared of pine trees but in generally wooded country. Topsoil and brown sandy loam (0 to 2 ft) changes to brown sand and gravel that varies from medium (2 to 6 ft), to coarse (6 to 14 ft), and again to medium (14 to 60 ft). The water level was at 49 ft. The figure illustrates the amplitude decrease and phase

Table 3-14. Temperature of the air 4.0 in. above, and of the soil 0.2 in. below, the earth/air interface measured by thermocouples [Davidson and Lettau, 1957].

Condition	Air Temperature (°F) at Mean Local Time								
	0400	0600	0800	1000	1200	1400	1600	1800	2000
*Air	58.5	62.2	73.4	81.9	87.3	89.0	89.6	84.0	76.1
*Soil	63.6	64.2	73.4	88.0	96.0	97.2	92.9	84.7	77.9
**Air	46.6	49.1	65.8	76.8	83.7	86.0	82.6	73.6	66.8
**Soil	53.3	52.9	65.1	86.2	100.0	99.1	88.4	76.7	69.4

* Mean soil moisture in 0 to 4 in. layer about 10% wet weight basis.
** Mean soil moisture in 0 to 4 in. layer about 4% wet weight basis.

Table 3-15. Comparison of air and soil temperature with surface temperatures of materials exposed on a tropical island with normal trade winds. Air and surface temperatures at 4 ft above, soil temperature at 1 in. below, the earth/air interface. Exposed surface area about 1 ft² [Draeger and Lee, 1953].

Material	Temperature (°F)		
	Highest Recorded	Average	
		Max.	Min.
Air (4 ft)	84	82	78
Soil (1 in.)	94	93	79
Wood	106	98	77
Aluminum	104	97	77
Galvanized Iron	113	101	77
Black Iron	123	108	77
Concrete Slab	98	94	77

Table 3-17. Annual and daily temperature cycles. Annual values are averages for the years 1939 through 1940 at Giessen, Germany [Kreutz, 1943]. Daily values are averages of clear weather, 10 through 12 August 1893, Finland, after Homén [Geiger, 1957].

	Temperature (°F)					
	Annual Means			Daily Means		
	Loam	Sand	Humus	Swamp Land	Sandy Heath	Granite Rock
Surface	48.4°	48.7°	50.2°	61.9°	77.0°	76.3°
3.3 ft above	51.3°	52.3°	52.3°	—	—	—
2.0 ft above	—	—	—	52.7°	57.2°	68.7°
Surface Amplitude	18.9°	19.2°	20.6°	18.7°	30.6°	18.3°
	Half-Amplitude Depth Interval (ft)					
Depth	5.8	5.3	4.7	0.16	0.26	0.49

Table 3-16. Physical parameters of diverse ground types.

Ground Type	Thermal Admittance Ratio (TAR), Ground to Air	Half-Amplitude Depth Interval (theoretical)	
		Annual Cycle (ft)	Diurnal Cycle (ft)
SOILS			
Quartz sand,			
medium-fine dry	110	3.2	0.17
8% moisture	230	5.1	0.27
22% moisture	360	4.9	0.26
Sandy clay, 15% moisture	280	4.4	0.23
Swamp land, 90% moisture	340	3.4	0.18
ROCKS			
Basalt	350	5.9	0.31
Sandstone	380	7.2	0.38
Granite	440	8.1	0.42
Concrete	440	7.4	0.39
SNOW, ICE, AND WATER			
Feathery snow	10	2.2	0.12
Packed snow	100	4.6	0.24
Still water	280	2.7	0.14
Ice	320	4.5	0.24
Turbulent ocean	10^3 to 10^5	200 to 2000	10 to 100

retardation of the annual cycle with depth. Amplitudes of weather disturbances with periods of several days, as illustrated by the temperature curve of the 2.5-ft level, decrease with depth more rapidly than the annual amplitudes. Qualitatively, this agrees with the theoretical prediction of an amplitude decrement proportional to the square root of the length of the period of the oscillation. The actual half-amplitude depth interval of the annual cycle can be estimated from Fig. 3-13 as nearly 9 ft, which is much larger than follows from experimental values of thermal diffusivity. The discrepancy may be caused by seepage or downward migration of rain water and the accompanying advection or transfer of heat. This process could increase the apparent or effective thermal diffusivity for annual soil-temperature variations by factors of 4 to 8 times the experimental values obtained in soil of constant moisture. The data in Table 3-17 are more in line with experimental findings than the curves in Fig. 3-13. The limitation of Table 3-17 is that the data are for clearly defined and near-to-ideal soil types that are seldom matched by actual ground conditions.

Factors that must be investigated and assessed for any one set of soil temperature observations are: (1) type and state of compaction of the soil; (2) moisture content of the soil during the test; (3) position of water table during the test; (4) type and color of surface cover; (5) amount and nature of traffic over site; and (6) local climatic conditions.

Subsoil temperature information is useful in computing thermal stresses and loads. Examples are the determination of the economic depth to which a structure should be buried when approach to natural isothermal conditions is desired to conserve on the air-conditioning load, or to dissipate heat generated by power cables. The determination of frost penetration depths is usually of main importance. For engineering purposes, the effect of snow cover in protecting against severe frost is not very important because, excepting arctic climates, no amount of snow can be depended upon for any particular winter. Also, it is often necessary to remove the snow from the area that requires protection.

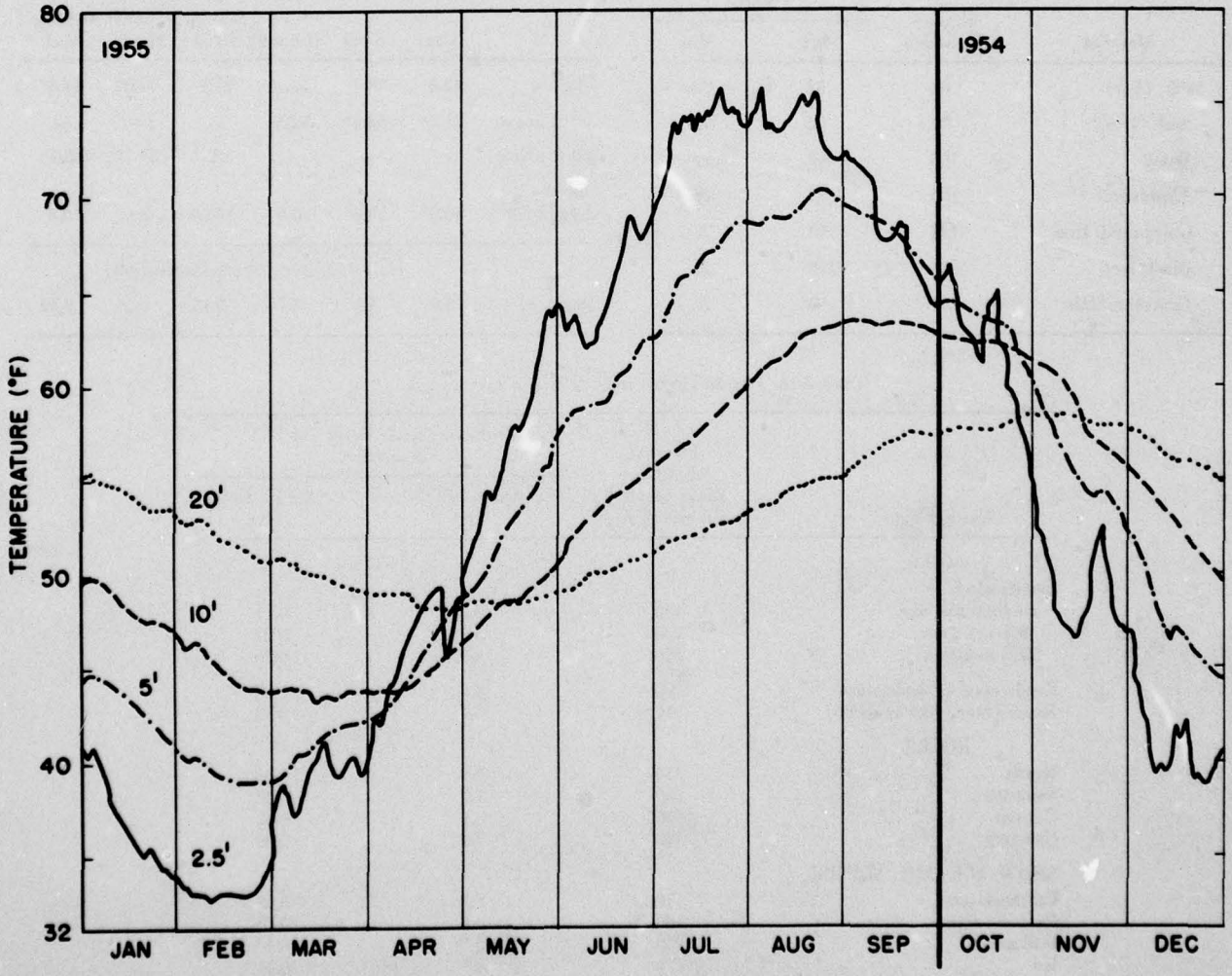


Fig. 3-13. Variations of soil temperature at indicated depths (ft); North Station, Brookhaven, Long Island, October 1954 through September 1955, after Singer and Brown [1956].

3.1.8 Miscellaneous

The heating degree day is defined as the departure toward lower temperatures of the main daily temperature from the standard temperature of 65°F. The U.S. Weather Bureau studies and publishes figures and charts of heating degree days.

Wind chill is a measure of the quantity of heat that the atmosphere is capable of absorbing within an hour from an exposed surface. The U.S. Army has studied wind chill on a hemispheric basis [Westbrook, 1961] because, frequently, the limitations of a particular weapons system result from such human limitations as the inability to operate during extreme weather conditions in arctic and subarctic regions where the wind strength complicates the problem.

In thermal equilibrium design problems it is frequently important to know the maximum steady wind speeds likely to be encountered at various temperatures. Figure 3-14, which was prepared from 4 years of 6-hourly and 1 year of hourly data for 22 stations in the United States, gives maximum steady (five-min) wind speed that occurred with temperatures in the range from −35° to +115°F during this period. The stations used in this study were selected as representative of climatic areas in the United States. Mountainous stations were not selected because extreme wind and temperature conditions in such locations are not representative of general operational areas. Also, high wind speeds found in hurricanes and tornadoes, although important in structural design problems, are not included.

The wind speeds shown on Fig. 3-14 occurred at station anemometer heights, usually 40 to 100 ft above the surface. The wind speeds at 10 ft above the surface are approximately 80% of the values given, falling to approximately 50% for the extreme cold temperatures (about −5°F) where the winds are light.

The values recommended for United States thermal equilibrium design criteria (the probability of being exceeded is very low) are a wind speed of 5 mile h^{-1} at −35°F, which increases linearly to 65 mile h^{-1} at 17°F, remains constant at 65 mile h^{-1} to 80°F, then decreases linearly to 14 mile h^{-1} at 112°F. This recommendation is not valid in mountainous areas or in Death Valley. Design criteria for the extreme hot conditions in Death Valley are the same as for the world-wide criteria shown in Fig. 3-14.

3.2 ATMOSPHERIC DENSITY UP TO 90 KM

The data discussed in this section are from direct and indirect observations obtained from balloon-borne instrumentation for altitudes up to 30 km, and measurements from rockets and instruments released from rockets for heights between 30 and 90 km.

3.2.1 Distributions Below 30 Km

The large number of available radiosonde observations permit a detailed analysis of the characteristics of atmospheric density profiles below 30 km. Statistical arrays of monthly means and standard deviations of daily values of density about these means for 2-km intervals of altitude, and coefficients of correlation between levels are available for locations representative of subtropical, temperate, subarctic and arctic climatic regimes [Sissenwine et al, 1958; and Cole and Court, 1962]. Table 3-28 at the end of this chapter gives arrays for the months of January and July at Tampa, Florida, at Omaha, Nebraska, and at St. Paul, Alaska.

3.2.1.1 *Statistical Applications to Reentry Problems.* Variations in range or deceleration of free-falling objects or of ballistic missiles that arise from day-to-day changes in atmospheric density can be estimated from statistical arrays of density. The mean effect, E, of atmospheric density on the range of a missile can be determined for a specific location by computer "flights" through mean monthly or seasonal density profiles. The mean effect, E, is

$$E = \sum C_i \bar{\rho}_i , \qquad (3\text{-}3)$$

where C_i is the proper influence coefficient for the missile at the ith level and $\bar{\rho}_i$ is the mean monthly density at the same level. The influence coefficients depend upon aerodynamic characteristics, reentry angle, and speed of the vehicle. The integrated standard deviation in range, or deceleration, σ, due to day-to-day variations from the mean seasonal or the monthly density profile, can be obtained from

$$\sigma^2 = \sum_{i=0,\ j=1}^{i,\ j} C_i C_j r_{ij} \sigma_i \sigma_j , \qquad (3\text{-}4)$$

where C_i and C_j are influence coefficients at the ith and j^{th} levels, σ_i and σ_j are the standard deviations of the density at the two levels, and r_{ij} is the correlation coefficient between densities at the two levels. If, in the computation, the density is assumed to have a Gaussian distribution at all levels, the variation in range of a free-falling object that is exceeded 50% of the time will cause an error of less than 15%, generally less than 10%.

3.2.1.2 *Latitudinal Variations.* Figure 3-15 shows variations in mean monthly density profiles with geographical location as percentage of the departure from the *U.S. Standard Atmosphere, 1962.* Profiles given are based on three years of radiosonde observations for January, April, July, and October, 1958 through 1960.

The altitude of minimum geographical variability near 8 km is the *isopycnic level.* At this level, densities usually do not depart by more than 1 or 2% from the standard, regardless of season or location. A second level of minimum geographical variability occurs near 24 km, but unlike the isopycnic level, this second level tends to change position with the seasons. Departures of the mean point of converging profiles from standard are roughly −2% in January, nearly zero in April, +7% in July, and +2% in October. The density profiles for Tampa and St. Paul Island (the southernmost and northernmost stations) form an envelope for the other four profiles during all seasons. At the altitude of maximum variability (12 to 14

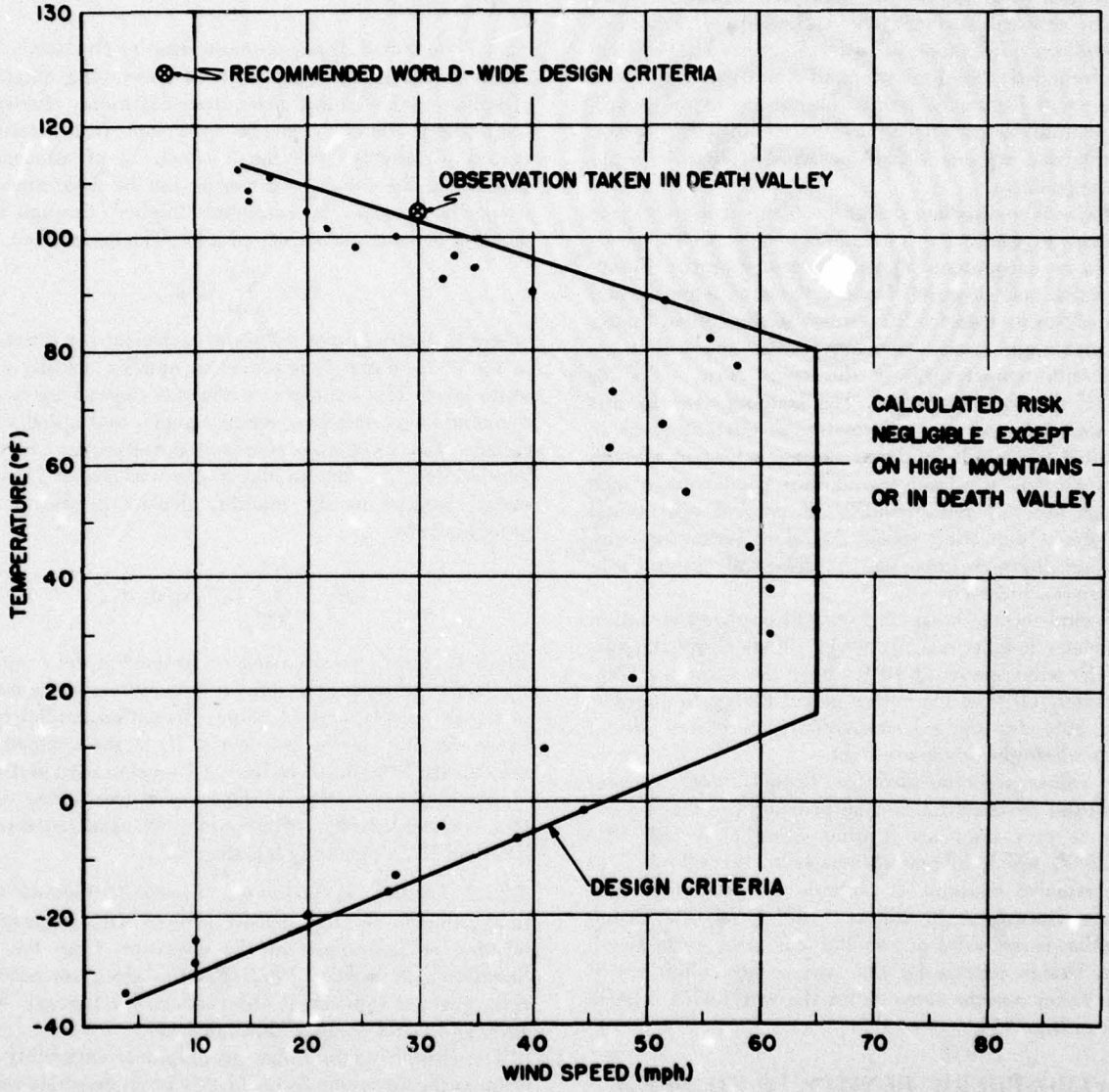


Fig. 3-14. Strongest wind (five-min average) for temperature range observed during a five-yr period. Wind speeds are, in general, for 40 to 100 ft above the surface. Speeds at 10 ft are approximately 80% of the values given, except for the coldest temperatures, where winds are 50% of the indicated values. Stations used for this study are:

Caribou, Me.
Burlington, Vt.
Boston, Mass.
New York, N. Y.
Washington, D. C.
Hatteras, N. C.
Jacksonville, Fla.
Miami, Fla.
Galveston, Tex.
Oklahoma City, Okla.
Phoenix, Ariz.
Los Angeles, Calif.
San Francisco, Calif.
Tatoosh I., Wash.
Great Falls, Mont.
Salt Lake City, Utah
Wichita, Kansas
Minneapolis, Minn.
Chicago, Ill.
Buffalo, N. Y.
Pittsburgh, Pa.
Columbus, Ohio

km) the profiles for all six stations remain in the same relative positions to each other during the four seasons, indicating a strong latitudinal relationship.

3.2.1.3 *Seasonal Variations.* Figure 3-16 shows variations in mean monthly profiles with season for four locations. The largest seasonal variations occur at midlatitude stations (Washington and Omaha), where the entire shapes of the profiles change. There is little seasonal difference in the shape of the Tampa profiles and only the July profile at St. Paul Island differs from the others. The largest seasonal variations occur between 12 and 14 km, and range from approximately 5% at Tampa to 13% at Washington. Seasonal variability is least near the isopycnic level.

3.2.1.4 *Interdiurnal and Diurnal Variations.* The *coefficient of variation* is the ratio (expressed as a percentage) of the standard deviation to the monthly mean. Figure 3-17 gives coefficients of the day-to-day variations around the mean values for January and for July for six locations. The largest day-to-day variations occur at approximately the height of the tropopause, which is 16 km at Tampa, and 12 km in winter and 14 km in summer at Washington and Great Falls. Variability is greatest in winter, ranging from 3% at Tampa to nearly 6% at Bitburg, Germany. The least variability occurs at the isopycnic level near 8 km. The root mean square errors of individual density observations are estimated to be less than 0.5 and 0.9% below the 12 and 26 km levels, respectively. Such errors

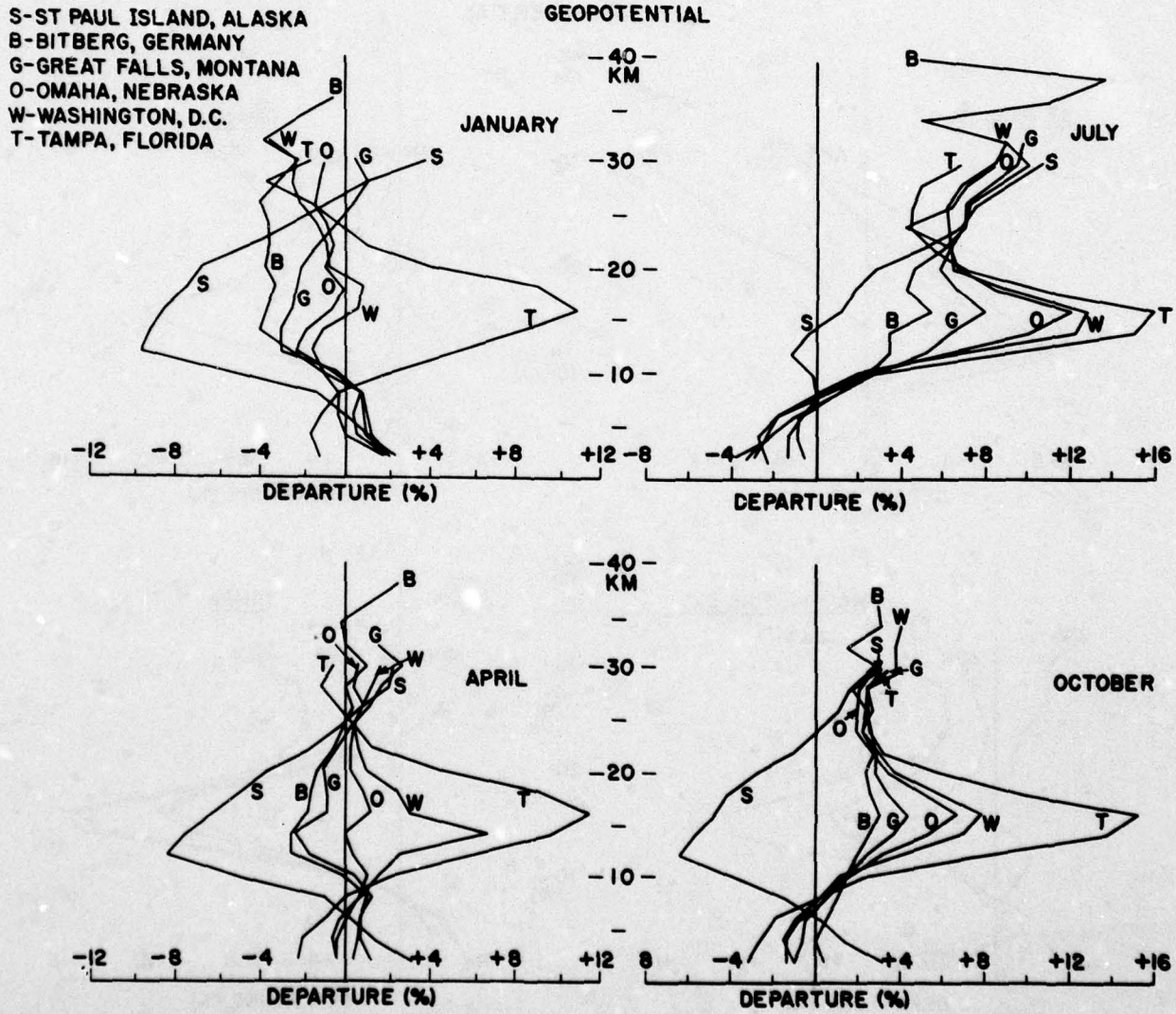


Fig. 3-15. Latitudinal variation of mean monthly density profiles as percentage of departure from *U. S. Standard Atmosphere, 1962.*

have little effect on the mean monthly values but tend to increase the coefficients of variation.

Studies of the diurnal pressure and temperature variability [Harris et al, 1962, and Chiu, 1959] indicate that the diurnal variability of density is less than $\pm 2\%$ of the daily mean between 1 and 30 km. Below 1 km, variations may be slightly larger.

3.2.1.5 *Interlevel Correlations.* The interlevel density correlations (see Table 3-28 at end of chapter) show a negative relationship between densities at levels above and below the 8-km isopycnic level. When density near the surface is greater than normal, pressure decreases more rapidly than usual with altitude, with the result that pressures and densities are less than normal above 8 km. This compensating effect allows surface pressure to remain relatively constant even though large variations in density occur at individual levels. Correlations of density at or near the isopycnic level with densities at levels above or below are much smaller than between levels not involving isopycnic altitudes.

The correlation between the density at two levels decreases, "decays," with increasing separation between the levels. Similar correlation decay is found for most climatic elements—wind speed, temperature, precipitation, pressure—as the horizontal or vertical distance between the points of observation, or the time between observations, increases. There is no fully satisfactory description of the rate of decay based on fundamental properties or assumptions. Consequently, many empirical formulas, valid for specific elements over restricted ranges, have been proposed.

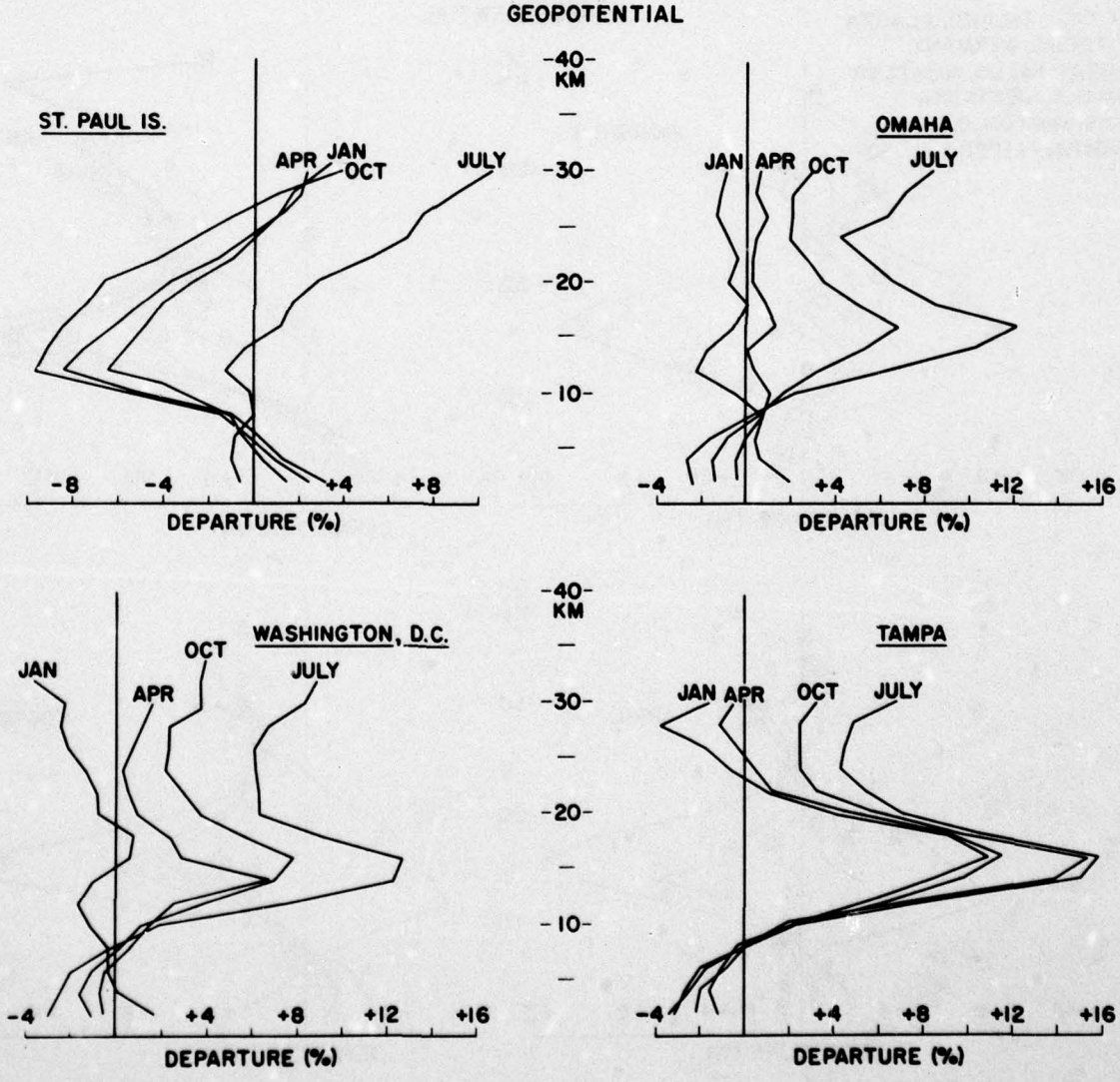


Fig. 3-16. Seasonal variation of mean monthly density profiles as percent departure from *U. S. Standard Atmosphere, 1962.*

The correlation, r_h, between the density at 12 km and that at 14, 16, 18, 20, 22, and 24 km can be approximated by the relation

$$r_h = c^h, \tag{3-5}$$

where h is the separation in kilometers and c is a constant somewhat less than unity [Sissenwine et al, 1958]. Equation (3-5) is a special case of the general exponential decay,

$$r_h = \exp(-\alpha h). \tag{3-6}$$

Above 12 km, correlation decay with layer separation is generally slower in winter than in summer, and slower at northern stations than at southern ones. In January, the decay in correlation at both St. Paul and Bitburg is approximated reasonably well between 12 and 24 km by Eq. (3-6) with α equal to 0.05. With the exception of Tampa, the decay in correlation at the other stations follows this equation for the first 6 km but deviates widely from it at separations greater than 6 km. In July, the decay in correlation at Bitburg and St. Paul is reasonably well represented by Eq. (3-6) with α equal to 0.08. The decay at other stations, however, is not exponential.

3.2.1.6 *Density-Wind Correlations.* Table 3-18 shows the correlation of atmospheric density with strength of zonal and meridional components of the wind at various altitudes for six locations. The correlation coefficients are not very high at any level. The relationship is strongest and most consistent below 2 km and at inland stations. Although the low correlations at other levels are significant statistically and of theoretical importance, they are probably of little practical importance in the design of aerospace vehicles. Equations for determining the density-wind relationship with the standard error of estimate are given by Cole and Court [1962] for nine locations. Such data can be used to investigate the importance of the density-wind correlations at various altitudes on a reentry vehicle.

3.2.2 Distribution Between 30 and 90 Km

Data available for determining the density distribution between 30 and 90 km consist of measurements from searchlight observations in New Mexico and observations from rockets and instruments released from rockets. The rockets were fired at ranges in California, New Mexico,

Table 3-18. Correlation of atmospheric density with strength of zonal and meridional components of wind at various levels, 1948-1957, by seasons; values in each column must be multiplied by 10^{-2}. Columns labeled u are correlations of density with zonal wind (positive toward east); those labeled v are correlations with meridional wind (positive toward north).

Alti-	Shemya, Aleutian Islands								Thule, Greenland								Wiesbaden, Germany							
tude	Winter		Spring		Summer		Autumn		Winter		Spring		Summer		Autumn		Winter		Spring		Summer		Autumn	
(km)	u	v	u	v	u	v	u	v	u	v	u	v	u	v	u	v	u	v	u	v	u	v	u	v
24	−42	+11	−33	+19	+18	−15	−36	−35	+22	−22	−28	−11	−19	−08	−46	−01	−39	−07	−58	−01	+04	+00	−59	+12
22	−44	−12	−27	+03	+00	−23	−30	−27	+34	−27	−27	−07	−18	−03	−38	+04	−40	−04	−51	−09	−04	−08	−56	+12
20	−39	−14	−15	−15	−02	−10	−22	−35	+34	−29	−21	−11	−13	+01	−23	+04	−36	−07	−45	−10	−09	−11	−45	+10
18	−37	−08	−04	−11	+12	−07	−17	−41	+31	−26	−15	−16	−10	−02	−05	+08	−22	−12	−32	−17	−11	−24	−29	+03
16	−30	+01	−07	+03	+25	−04	−07	−31	+22	−20	−08	−15	−06	−05	+11	+05	−11	−08	−22	+08	+05	−22	−17	−04
14	−20	−04	−02	+10	+24	−02	+05	−33	+22	−03	+03	−15	−00	−14	+20	+01	+01	−15	−13	−10	+06	−23	−09	−08
12	−05	+14	+15	−10	+22	−01	+18	−23	+31	+04	+15	−15	+08	−21	+30	+05	+03	−17	−05	−08	−01	−18	−05	−07
10	+02	+06	+05	−09	+06	−14	+04	−21	+28	+10	+17	−08	+07	−10	+25	+04	−02	−09	−15	−04	−21	−08	−09	+03
8	+05	−02	−05	−19	−06	−24	+05	−28	+22	+06	+07	−05	+03	−09	+08	−05	−27	+06	−37	−11	−35	−14	−33	+02
6	+19	−06	+03	−17	−15	−16	+16	−18	+21	−09	+07	−19	−05	−00	−01	−16	−39	−04	−27	−21	−18	−09	−26	−12
4	+38	−12	+15	−08	−14	−18	+21	−15	+16	−07	+07	−08	−07	+13	+05	−04	−33	−27	−20	−30	−07	−17	−15	−22
2	+32	−17	+17	−18	−15	−27	+19	−19	+07	+10	+05	+08	−07	+21	+10	+03	−41	−35	−15	−44	+11	−34	−10	−40
0.5	+10	−05	+02	−07	−19	−16	+04	−12	+14	−01	+07	+01	+10	+05	+20	−16	−56	−39	−06	−29	+18	−24	−12	−19
	Cape Kennedy, Florida								Great Falls, Montana								Washington, D. C.							
24	−25	−04	−26	−07	−21	−07	−57	−06	+00	−24	−31	+04	−06	−08	−34	+17	−39	−10	−56	−12	−33	−09	−61	−10
22	−32	+00	−30	−08	−22	−09	−60	+01	−19	−19	−39	+20	−11	+08	−37	+02	−26	−23	−47	−16	−31	−03	−54	−16
20	−29	−01	−17	−11	−10	−10	−50	−17	−17	−20	−39	+12	−06	−09	−34	−18	−14	−14	−38	−24	−31	−09	−58	−25
18	−24	+01	−19	−04	−15	−09	−40	−16	−16	−15	−40	+01	+11	−01	−18	−23	+10	−14	−32	−27	−29	−15	−44	−27
16	−35	−06	−28	−05	−26	+03	−57	−11	−18	−27	−25	−03	+23	−05	−08	−19	+24	−12	−25	−24	−27	−09	−31	−32
14	−29	−17	−24	−07	−22	−06	−47	−03	−03	−32	−19	−05	+32	−07	+02	−18	+32	−15	−17	−23	−25	−08	−18	−25
12	−34	−23	−39	−05	−30	−06	−45	−15	+09	−32	−03	−07	+24	−12	+01	−14	+26	−10	−15	−19	−31	−10	−19	−30
10	−58	−31	−46	−16	−23	−04	−16	−35	+05	−22	−14	−04	−07	−18	−15	−06	+08	−11	−20	−20	−36	−21	−32	−39
8	−53	−25	−29	−18	−13	−00	+09	−31	−27	−07	−12	−10	−16	−14	−31	−03	−28	−28	−32	−34	−22	−19	−29	−38
6	−30	−26	−15	−15	−10	+06	+09	−23	−28	00	+15	−23	−06	−13	−15	−13	−24	−29	−08	−27	−14	−13	−05	−17
4	−15	−23	−08	−17	−07	+12	+02	−18	−35	−19	+13	−38	+04	−36	−10	−32	−12	−31	+01	−27	−12	−10	+09	−07
2	−21	+28	+10	−31	−19	+08	+06	−31	−55	−35	−03	−29	+09	−26	−10	−30	−13	−45	+02	−37	−26	−18	+09	−23
0.5	+00	−67	−08	43	−21	+05	+14	−39	—	—	—	—	—	—	—	—	−24	−40	−07	−33	−41	−15	+00	−30

Florida, Virginia, Guam, and Australia (all south of 38°N), at Churchill, Canada (60°N), and on shipboard. Densities obtained directly or indirectly from these experimental observations (grenades, falling spheres, pressure gauges, etc.) are estimated to have a mean error of roughly 2 to 5% between 30 and 60 km, and 8 to 10% from 60 to 90 km.

Sufficient observations are not available above 30 km for the preparation of statistical matrices of seasonal means, standard deviation, and correlation coefficients between levels. It is possible, however, to make rough estimates of the seasonal, latitudinal, interdiurnal and diurnal variations.

3.2.2.1 *Latitudinal and Seasonal Variability.* Winter and summer densities, from the supplemental atmospheres described in Chapter 2, for 15°, 30°, 45° and 60°N, are shown in Fig. 3-18 as percentage of departures from standard. Seasonal variability is greatest at 70 km, ranging from roughly 15% at 30°N to 50% at 60°N. Above this level, the variability decreases, reaching a second minimum near 85 to 90 km. Seasonal profiles tend to converge toward or cross the standard in this region. It has been suggested that this may be a second isopycnic level; indications are that it is a region of high wind shear and turbulence. Pressure distributions in the seasonal atmospheres also indicate a wind reversal in this region.

3.2.2.2 *Interdiurnal and Diurnal Changes.* The density at a specific height may differ from the seasonal mean because of diurnal and interdiurnal changes. Estimates of the interdiurnal variations around the mean seasonal densities, which are exceeded less than 5% of the time, are shown by horizontal arrows in Fig. 3-18. Above 30 km the variations are estimates based on rocket observations. Variations are largest near 70 km where they range from ±26% in winter at 60°N to ±14% at 15°N. Variability is least at 85 to 90 km. The 95% values shown in Fig. 3-18 would not be encountered at all altitudes at a given location and time.

Diurnal variations of density are caused by the thermal expansion and contraction of the atmosphere due to changes in solar heating and gravitational tides resulting from lunar and solar attraction. Only rough estimates of the magnitude of these variations are possible from the limited number of observations between 30 and 90 km. Variations due to lunar tides can magnify or decrease changes caused by solar heating depending on the part of the lunar month being considered. Much of the varia-

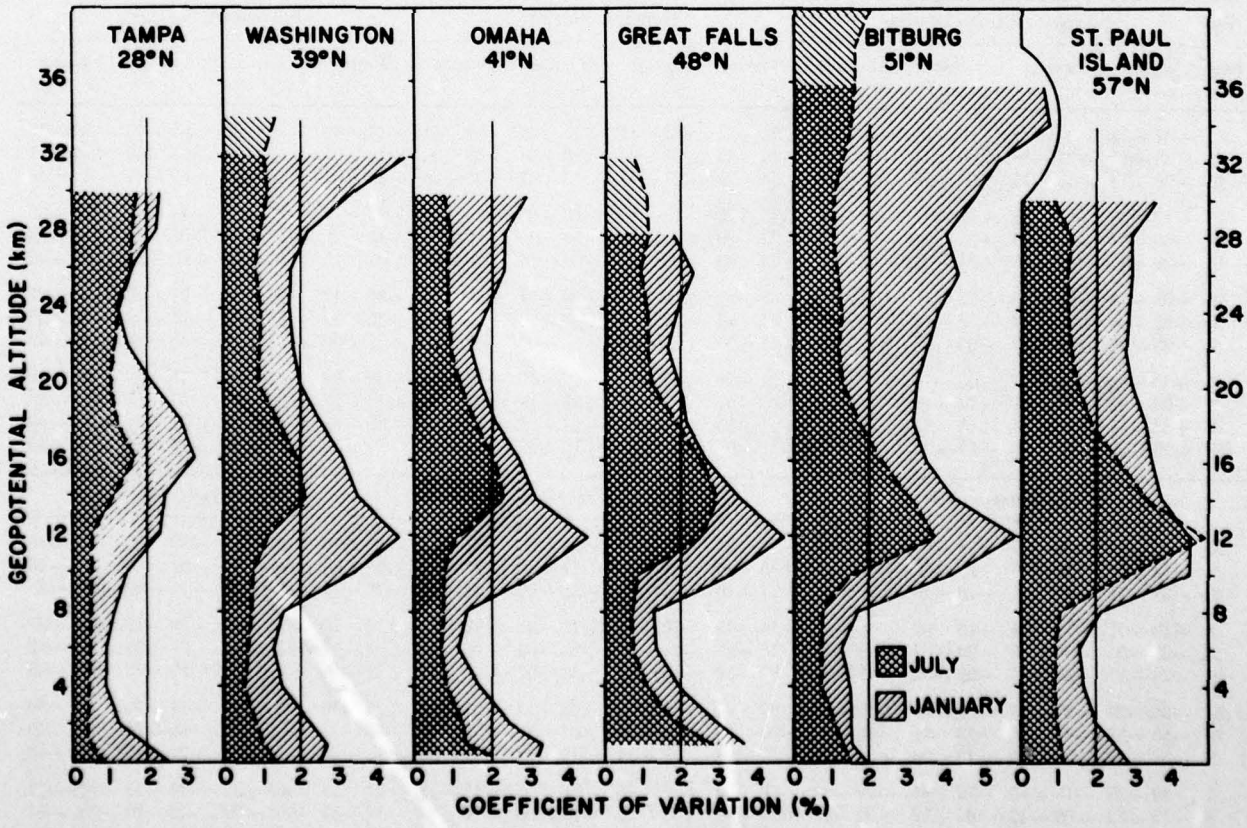


Fig. 3-17. Coefficient of variation (standard deviation/monthly mean × 100) around mean values for January and July.

bility caused by lunar tides is probably contained in the interdiurnal variations shown in Fig. 3-18, which are based on individual observations taken at random times with respect to the lunar cycle. Several series of density and wind observations taken in a 24-h period during the spring and autumn months at Eglin AFB suggest that the sum of the systematic diurnal and semidiurnal density variability caused by solar heating or attraction is approximately ±2% of the daily mean between 30 and 45 km, and ±6% to 7% between 50 and 65 km. Rocket grenade observations at Churchill, Canada, indicate the diurnal variations of density at 80 to 90 km may amount to 10% of the daily mean. Radar measurements of the diffusion rate of ionization trails produced by meteors above Jodrell Bank (50°14′N) indicate much larger diurnal variations at 92 km. The sum of the observed diurnal and semidiurnal density oscillations shows an amplitude $\left(A = \frac{\Delta\rho}{\bar{\rho}}\right)$ of 25% in July and August and 16% in May and June. If these are real, fluctuations over southerly latitudes may be slightly larger because the sun will be more nearly overhead, particularly during summer. Additional and more accurate observations are required before refined estimates can be made; the probable error in the available observations is nearly the same magnitude as the estimated diurnal fluctuations.

3.3 ATMOSPHERIC PRESSURE UP TO 90 KM

Mean seasonal profiles of pressure vs height to altitudes of 90 km can be obtained for various latitudes from the supplemental atmospheres (Sec. 2.3). The data provided in this section are based on routine radiosonde observations that extend to approximately 100,000 ft. These data are intended for use in design problems involving variations in the height of constant pressure surfaces or the day-to-day changes in pressure at specific altitudes. For example, in the design of vehicle guidance systems that use barometric altimeters for altitude control, it is often important to know the variations in altitude (geographical, seasonal, and daily) that can be expected over specific regions when a constant pressure setting is used. Thus, standard deviations of heights of various constant pressure surfaces around their mean altitudes over North America are provided.

More detailed information than that presented in this section is available. Consequently, special studies should be requested for specific design problems if, based on the information given below, conditions appear critical.

3.3.1 Sea-level Pressure

The variation of sea-level pressure normally has little effect on the operation of surface equipment. In the design of certain items, however, such as sealed units that

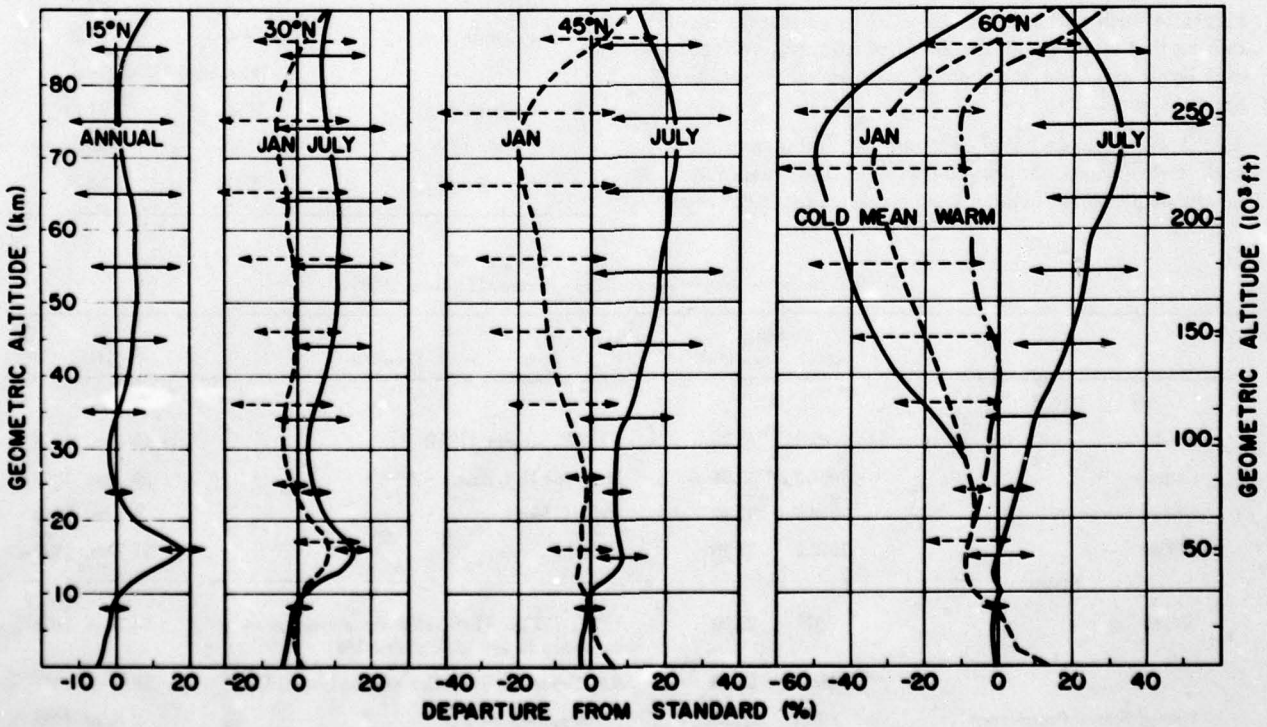


Fig. 3-18. Percentage departure of mean seasonal density profiles at various latitudes from *U. S. Standard Atmosphere, 1962*. (Arrows indicate range of day-to-day variations on 95% of the days around seasonal means.)

might explode or collapse with pressure changes, the range of surface pressure likely to be encountered must be considered. Standard atmospheric pressure at sea level is 1013.25 mb (29.92 in. of mercury). There are relatively large variations from this standard in both time and place.

Table 3-19 indicates the extreme sea-level pressures that may be encountered in the Northern Hemisphere. During the month of January, pressures given are exceeded 99% of the time in areas under the influence of semipermanent cyclones, and 1% of the time in areas under the influence of anticyclones. Extreme values (if tropical cyclones and tornadoes are not considered) are most likely to occur in these areas and during the month of January in the Northern Hemisphere. Table 3-20 lists, for comparison, some actual worldwide pressure extremes, including those resulting from storms of tropical origin. Table 3-21 provides estimated mean sea-level pressures for the midmonth of each season and the standard deviations of daily values around these means for specific locations.

3.3.2 Variations in Height of Constant Pressure Surfaces

Changing synoptic situations, movements of high and low pressure centers and their associated ridges and troughs, and variations in the energy absorbed directly by the atmosphere cause day-to-day changes in the height of constant pressure surfaces. Information on the magnitude of monthly, day-to-day, and diurnal variations in the height of such surfaces can be used by engineers in obtaining first approximations. Detailed information for specific levels and locations should be requested if conditions appear critical.

3.3.2.1 *Seasonal and Daily Variations.* By assuming normal distributions, approximations of the variation in height of pressure surfaces near sea level for 68% of the time can be obtained. Multiplying the standard deviation of the mean sea-level pressure in millibars by 28 gives the height in feet. (Near sea level, 1 mb is equivalent to a change of approximately 28 ft altitude.) For example, to obtain the standard deviation of the height of the 1000-mb surface around the seasonal mean height for 30°N and 65°W in January, multiply 5 (the value given in Table 3-21 for the standard deviation of the sea-level pressure) by 28; the height of the 1000-mb surface at this location during January will be within 140 ft of the mean height 68% of the time. The mean height of the 1000-mb surface can be obtained by multiplying the difference in pressure between the mean sea-level pressure and 1000 mb by 28. In this case, the mean height would be 616 ft (22×28) above mean sea level.

Table 3-22 lists mean heights in January and July of pressure surfaces and their standard deviations for mid-North America. These data indicate the variation in the mean height of constant pressure surfaces between 700 and 10 mb with latitude and season, and the estimated distributions of day-to-day variability around the monthly

Table 3-19. Sea-level pressures exceeded 99% and 1% of the time in January.

Location	Pressure (mb)	Pressure (in. Hg)
	Exceeded 99% of time	
Aleutian low	973	28.73
Icelandic low	955	28.20
	Exceeded 1% of time	
Siberian high	1055	31.15
Pacific high	1037	30.62
Canadian high	1041	30.74

Table 3-20. Some worldwide pressure extremes [Ludlam, 1962].

	Pressure (mb)	Pressure (in. Hg)	Location	Date
HIGH				
World	1075.2	31.75	Irkutsk, Siberia, USSR	14 Jan. 1893
Canada	1067.3	31.51	Medicine Hat, Alta.	24 Jan. 1897
United States	1063.3	31.40	Helena, Mont.	9 Jan. 1962
Alaska	1062.2	31.36	Bethel	21 Dec. 1937
LOW				
World	877	25.90	19°N, 135°E. (Estimated by aerial reconnaissance in eye of Typhoon Ida)	24 Sept. 1958
	886.6	26.18	*S.S. Sapoerea*, 460 miles east of Luzon, P.I.	18 Aug. 1927
United States (hurricane)	892.3	26.35	Matecumbe Key, Fla.	2 Sept. 1935
United States (extra-tropical)	954.9	28.20	Canton, N. Y. Block Island, R. I.	3 Jan. 1913 7 Mar. 1932

means. (Standard deviations at 50, 25, 15, and 10 mb are based on radiosonde data at or near peak heights and should be treated only as rough estimates of latitudinal, seasonal, and day-to-day variability at these levels.) Table 3-23 gives average January and July pressures for specific heights between 10,000 and 100,000 ft over mid-North America.

3.3.2.2 *Diurnal and Semidiurnal Variations.* Mean hourly sea-level pressures follow a systematic (diurnal and semidiurnal) daily succession somewhat variable in amplitude and time of occurrence according to location and season, but generally characterized by minima near 0400 and 1600 h and maxima near 1000 and 2200 h local time. The amplitude approaches 1 mb, which is small relative to daily synoptic changes in midlatitudes. In the tropics (latitudes 20°N and below), however, only minor changes occur synoptically from day to day; as a result, interdiurnal pressure changes are small compared to the systematic daily variations in these latitudes. Upper-air pressures appear to follow a systematic daily pattern similar to that at sea level; however, extremes occur at somewhat different hours. Table 3-24 lists amplitudes and times of occurrence of diurnal and semidiurnal maxima to 10 mb (near 100,000 ft) over Terceira, Azores, thereby providing an estimate of mean annual systematic pressure variations at a maritime location near 40°N. The semidiurnal variations at climatically and geographically different locations such as Washington, D. C. and Terceira, Azores, appear to be similar. The diurnal maxima and minima, however, that result from solar insolation and terrestrial radiation, may differ considerably in time of occurrence and amplitude at various locations, particularly at or near surface levels.

3.4 ATMOSPHERIC WATER VAPOR

The maximum amount of water vapor the atmosphere can contain is regulated by the temperature. For example, at the highest recorded station temperature of about 55°C, the air could hold about 100 g m^{-3}. The amount actually present in the atmosphere is a complex function of various weather parameters. The highest water-vapor content recorded is about 30 g m^{-3}, corresponding to a dewpoint of approximately 30°C. As the temperature decreases, the amount of water vapor the air contains decreases rapidly, approaching a negligible amount (for most engineering purposes) at temperatures below —40 to —50°C. At these low temperatures, the amount of water vapor the air can contain at the surface is 10^{-1} and 4×10^{-2} g m^{-3}, respectively. Although the water-vapor content at temperatures below —40°C is extremely small, even this amount is important in the transmission of infrared radiation over long path lengths.

The *mixing ratio*, w, is defined as the ratio of the mass of water vapor present to the mass of dry air present in a unit volume. *Precipitable water*, W, is strictly defined as the amount of water contained in a vertical air column

Table 3-21. Mean monthly sea-level pressures and standard deviations of daily values.

Location		January		April		July		October	
Latitude	Longitude	Mean (mb)	S.D. (mb)	Mean (mb)	S.D. (mb)	Mean (mb)	S.D. (mb)	Mean (mb)	S.D. (mb)
10°N	70°W	1013	2	1012	1	1013	1	1011	1
20°N	70°W	1018	2	1017	2	1018	2	1014	2
30°N	65°W	1022	5	1020	5	1021	3	1018	4
40°N	65°W	1018	11	1016	8	1016	5	1017	8
50°N	65°W	1015	13	1013	11	1011	7	1013	11
60°N	65°W	1008	11	1012	10	1008	6	1007	10
70°N	70°W	1007	11	1015	10	1010	6	1008	10
80°N	70°W	1014	11	1022	*	1016	*	1015	*
10°N	20°E	1011	4	1008	3	1009	2	1009	1
20°N	20°E	1017	4	1011	3	1007	2	1011	2
30°N	15°E	1020	5	1014	4	1012	3	1015	3
40°N	15°E	1017	9	1013	6	1014	3	1016	5
50°N	15°E	1018	12	1012	7	1013	5	1016	8
60°N	15°E	1012	16	1011	10	1011	7	1010	11
70°N	20°E	1003	15	1010	9	1013	7	1007	11
80°N	20°E	1008	15	1016	10	1014	7	1011	9

* No data available.

of unit cross section extending between two specified levels of pressure, P_1 and P_2, according to the relation

$$W = \frac{1}{g}\int_{P_1}^{P_2} w\, dP, \qquad (3\text{-}7)$$

where g is the acceleration of gravity. The physical units of W are mass per unit area. Precipitable water, however, is commonly reported as the height at which the liquid would stand if it were completely condensed in a vessel of the same unit cross section as the air column. A height of 1 cm corresponds to 1 g cm^{-2} of precipitable water.

Although climatic humidity data are relatively plentiful for the lowest 7 km of the troposphere, there are no maps (except for the surface layer) that present, for an adequate period of record, even average distributions in time and space of basic humidity parameters such as dewpoint or mixing ratio. (Maps are available for local areas but not on a hemispheric basis.) World maps [Bannon and Steele, 1960] of the mean precipitable water above the surface and above the 850, 700, and 500 mb levels (in

Table 3-22. Average height and standard deviation at standard pressure levels over North America, 90 to 100°W longitude. [Heastie and Stephenson, 1960; Muench, 1962; Ratner, 1957].

	Average Height and Standard Deviation													
Pressure (mb)	20°N		30°N		40°N		50°N		60°N		70°N		80°N	
	Mean (km)	S.D. (m)	Mean (km)	S.D. (m)	Mean (km)	S.D. (m)	Mean (km)	S.D. (m)	Mean (km)	S.D. (m)	Mean (km)	S.D. (m)	Mean (km)	S.D. (m)
							JANUARY							
700	3.165	30	3.115	55	3.015	85	2.865	100	2.770	100	2.710	90	2.690	75
500	5.845	40	5.745	85	5.565	125	5.340	145	5.180	150	5.075	140	5.055	125
300	9.595	55	9.425	125	9.150	175	8.825	195	8.585	230	8.425	210	8.380	180
200	12.280	70	12.090	130	11.765	165	11.430	175	11.180	190	10.995	200	10.920	195
100	16.455	55	16.325	95	16.110	110	15.890	145	15.655	175	15.400	195	15.195	190
50	20.540	130	20.500	200	20.415	215	20.280	215	20.075	200	19.775	180	19.440	180
25	24.900	210	24.865	245	24.790	335	24.555	275	24.380	245	23.905	245	23.425	230
15	28.100	245	28.050	335	28.000	365	27.750	365	27.650	350	27.000	335	26.350	305
10	30.600	250	30.550	380	30.500	440	30.250	380	30.150	380	29.500	320	28.750	260
							JULY							
700	3.185	15	3.190	20	3.170	35	3.080	55	3.005	60	2.975	65	2.930	65
500	5.890	20	5.910	25	5.875	50	5.720	85	5.600	90	5.540	90	5.465	95
300	9.675	30	9.705	35	9.630	80	9.405	130	9.215	125	9.125	125	9.010	130
200	12.395	40	12.430	50	12.345	100	12.080	135	11.870	135	11.790	135	11.710	135
100	16.570	45	16.625	50	16.605	65	16.515	80	16.455	85	16.420	80	16.390	75
50	20.765	75	20.865	90	20.940	105	20.975	105	21.005	105	21.045	90	21.050	75
25	25.180	150	25.330	150	25.440	175	25.530	175	25.625	165	25.715	150	25.765	150
15	28.300	170	28.450	170	28.650	175	28.800	175	28.900	175	29.100	170	29.200	165
10	30.800	190	30.950	190	31.200	190	31.400	190	31.550	190	31.750	185	31.950	180
	(10^3 ft)	(ft)	(10^3 ft)	(ft)	(10^3 ft)	(ft)	(10^3 ft)	(ft)	(10^3 ft)	(ft)	(10^3 ft)	(ft)	(10^3 ft)	(ft)
							JANUARY							
700	10.38	100	10.22	180	9.89	280	9.34	330	9.09	330	8.89	295	8.83	245
500	19.18	130	18.85	280	18.26	410	17.52	475	16.99	490	16.65	460	16.58	410
300	31.46	180	30.92	410	30.02	575	28.95	640	28.17	750	27.64	690	27.49	590
200	40.29	230	39.67	425	38.60	540	37.50	575	36.68	625	36.07	655	35.83	640
100	53.99	180	53.56	310	52.85	360	52.13	475	51.36	575	50.52	640	49.85	625
50	67.39	420	67.26	650	66.98	700	66.54	700	65.86	650	64.88	600	63.78	600
25	81.69	700	81.58	800	81.33	1100	80.56	900	79.99	800	78.43	800	76.85	750
15	92.19	800	92.03	1100	91.86	1200	91.04	1200	90.72	1150	88.58	1100	86.45	1000
10	100.39	830	100.23	1250	100.07	1450	99.25	1250	98.92	1250	96.78	1050	94.32	850
							JULY							
700	10.45	50	10.47	65	10.40	115	10.10	180	9.86	195	9.76	215	9.61	215
500	19.32	65	19.39	80	19.27	165	18.77	280	18.37	295	18.18	295	17.93	310
300	31.74	100	31.84	115	31.59	260	30.86	425	30.23	410	29.94	410	29.56	425
200	40.67	130	40.78	165	40.50	330	39.63	445	38.94	445	38.68	445	38.42	445
100	54.36	150	54.54	165	54.48	215	54.18	260	53.99	280	53.87	260	53.77	245
50	68.13	250	68.45	290	68.70	340	68.82	340	68.91	340	69.05	290	69.06	250
25	82.61	500	83.10	500	83.46	580	83.76	580	84.07	550	84.37	500	85.43	500
15	92.85	560	93.34	560	94.00	580	94.49	580	94.82	580	95.47	560	95.80	550
10	101.05	620	101.54	620	102.36	620	103.02	620	103.51	620	104.17	610	104.82	600

practice, "above" is from the level to a pressure altitude of 300 mb) for each of the midseason months are available. Unfortunately, neither the mixing ratios nor the dewpoints used to construct the precipitable water maps can be rederived.

Moisture data at levels above 7 km are scarce; at higher altitudes, most information was obtained from experimental ascents using special humidity-measuring equipment. With two exceptions, stratospheric moisture measurements have been sporadic, and to date few ascents have reached or exceeded 31 km. The British and the Japanese Meteorological Agency made probes of the moisture in the stratosphere. Using aircraft platforms and manually operated frostpoint hygrometers, the British flew at maximum altitudes of 14 to 15 km; most of the ascents were made over southern England [Tucker, 1957] but some were made as far north as Norway and as far south as Kenya. Almost all these observations in the lower stratosphere indicate a dry stratosphere, with mixing ratios above about 150 mb of 2 mg kg^{-1} and frostpoints between —80 and —85°C. Frostpoint is the highest temperature at which atmospheric moisture will sublime in the form of hoar frost on a cooled, polished surface; it is analogous to dewpoint, applying when moisture will not condense. The observations between 14 and 15 km are remarkably constant regardless of time of year or geographical location. In contrast, Japanese and American measurements with balloon-borne automatic hygrometer probes indicate that stratospheric moisture is highly variable and, in general, much greater than the British data at comparable stratospheric altitudes. The reasons for these contradictory data are not known [Gutnick, 1961 and Dobson et al, 1962].

Table 3-23. Average pressure at various altitudes over North America, 90 to 100°W longitude.

Altitude (10^3 ft)	Pressure (mb) 20°N	30°N	40°N	50°N	60°N	70°N	80°N
				JANUARY			
10	709	706	694	683	671	666	663
20	484	477	464	448	434	428	426
30	317	310	304	283	274	268	264
40	201	196	187	178	171	166	161
50	122	119	114	111	107	103	99
60	73	72	70	68	66	63	60
70	44	44	43	42	41	38	36
80	27	27	27	26	25	23	21
90	17	17	17	17	16	14	13
100	10	10	10	10	10	9	8
				JULY			
10	712	714	710	703	695	692	689
20	488	489	486	475	467	462	457
30	320	321	318	308	301	296	294
40	205	206	204	196	191	188	187
50	125	127	125	122	120	119	119
60	75	76	76	76	75	75	75
70	46	47	47	47	48	48	48
80	28	29	29	30	30	31	32
90	17	18	18	19	19	19	20
100	11	11	11	12	12	12	12

One feature of the vertical distribution of moisture that is gaining acceptance is the structure of the mixing ratio profile. Recent humidity measurements show a decrease with altitude from the surface to a minimum value at several kilometers above the tropopause. Above this point the mixing ratio increases up to at least 32 km. This increase of mixing ratio with increasing altitude beyond the minimum is a feature of two atmospheric moisture models. Because of the paucity and questionable reliability of much of the data on stratospheric moisture, both models are of necessity largely subjective.

Table 3-24. Amplitudes of systematic pressure variations and time of maximum at Terceira, Azores [Harris et al, 1962].

Pressure Level (mb)	(ft) *	Diurnal Ampl. (mb)	Diurnal Time (h)	Semidiurnal Ampl. (mb)	Semidiurnal Time (h)
Sfc	0	0.10	2100	0.50	0948
1000	400	0.10	1904	0.53	0950
950	1870	0.12	1824	0.46	0956
900	3390	0.16	1612	0.49	1002
850	4770	0.18	1604	0.47	1002
800	6650	0.20	1612	0.44	1002
750	8430	0.20	1616	0.38	1010
700	10,260	0.25	1548	0.37	1002
650	12,240	0.18	1608	0.40	1030
600	14,320	0.25	1608	0.33	1020
550	16,570	0.27	1508	0.33	1034
500	18,970	0.28	1516	0.29	1032
450	21,610	0.27	1424	0.24	1036
400	24,440	0.31	1504	0.24	1046
350	27,590	0.31	1504	0.20	1046
300	31,110	0.32	1444	0.18	1108
250	35,130	0.33	1420	0.16	1102
200	39,860	0.32	1408	0.14	1110
175	42,620	0.32	1352	0.13	1120
150	45,760	0.30	1348	0.11	1100
125	49,430	0.28	1328	0.11	1124
100	53,880	0.26	1304	0.09	1128
80	58,320	0.24	1300	0.09	1120
60	64,130	0.23	1256	0.07	1124
50	67,810	0.21	1256	0.07	1114
40	72,430	0.20	1244	0.06	1116
30	78,780	0.18	1256	0.05	1110
20	87,510	0.16	1256	0.04	1128
15	91,880	0.15	1252	0.03	1136
10	100,090	0.12	1304	0.01	1204

* Estimated mean annual height.

3.4.1 Polar Model

Figure 3-19 shows the profile of the mean annual polar model of stratospheric mixing ratios. To derive the mixing ratios, climatological data from a network of stations ranging in latitude from 58° to 73°N were used to ascertain a mean tropopause pressure and temperature. A relative humidity of 50% was assumed at the tropopause and a mixing ratio at the tropopause of 24 mg kg^{-1} was computed from these values. Three additional assumptions made were:

(1) from the polar tropopause to 12.2 km, an exponential decrease in the mixing ratio by a factor of 10;
(2) between 12.2 and 16.8 km, a constant mixing ratio;
(3) between 16.8 and 30.5 km, an exponential increase in the mixing ratio by a factor of 30.

Although this mean polar atmosphere is drier than most data indicate, the authors consider the dryness as conservative.

3.4.2 Midlatitude Model

Figure 3-20 gives mean annual vertical profiles of mixing ratios and dewpoint-frostpoint. These profiles are for middle latitudes up to 31 km and were obtained as independent means from the same basic measurements of stratospheric moisture and routine tropospheric radiosonde observations. Neither profile can be obtained from the other, because the relation between mixing ratio and condensation temperature (dewpoint-frostpoint) is nonlinear. A direct approach using conventional radiosonde humidity measurements was used to derive the basic profiles up to 7.2 km (400 mb). Above 400 mb, the profiles are based upon selected experimental data, subjectively chosen and weighted [Gutnick, 1962].

Table 3-25 lists various values for the moisture content of the atmosphere. For air saturated at ambient temperature and pressure of the *U.S. Standard Atmosphere, 1962*, the pressure of water vapor (e_s), the absolute humidity (ρ_s), and mixing ratio (w_s) were derived. From these and from $\bar{w}$, the estimated mean midlatitude mixing ratio, values for the pressure of water vapor (e_v), absolute humidity (ρ_v), relative humidity (U), and precipitable water (W) were determined from the following relations:

$$e_v = \bar{w}P/0.622, \tag{3-8}$$

where P is the standard pressures in millibars;

$$\rho_v = \rho\bar{w}, \tag{3-9}$$

where ρ is the standard air density;

$$U = e_v/e_s, \tag{3-10}$$

$$W = (P_2 - P_1)\,\bar{w}/g, \tag{3-11}$$

where g is the acceleration of gravity, and w is the mean mixing ratio between the pressures P_1 and P_2. The dewpoints-frostpoints, T_f, are taken from the Smithsonian Meteorological Tables 94 and 96 for the given values of e_v.

Values of typical moisture content (primed quantities) were also determined from $\bar{T}_f$, the estimated mean midlatitude frostpoints or dewpoints. The pressure of water vapor (e'_v) and absolute humidity (ρ'_v) are from the Smithsonian Meteorological Tables for the estimated value of $\bar{T}_f$. Relative humidities at 6 km and below are the weighted average of observed relative humidities above 6 km; values were calculated from $U' = e'_v/e_s$. The mixing ratio, w′, and precipitable water, W′, were calculated from the relations

$$w' = \rho'_v/\rho \text{ and } W' = \bar{\rho}'_v h, \tag{3-12}$$

where h is the layer thickness and ρ_v is the mean vapor density of the layer.

Almost all the individual mixing ratio measurements, of which averages are shown in Fig. 3-20, lie within plus or minus an order of magnitude of the mean curve. Until more observations of known reliability are available, this interval may be considered as covering the range of usual variation of the mixing ratio—including perhaps 90% of all stratospheric values in middle latitudes. The tropospheric range is not known.

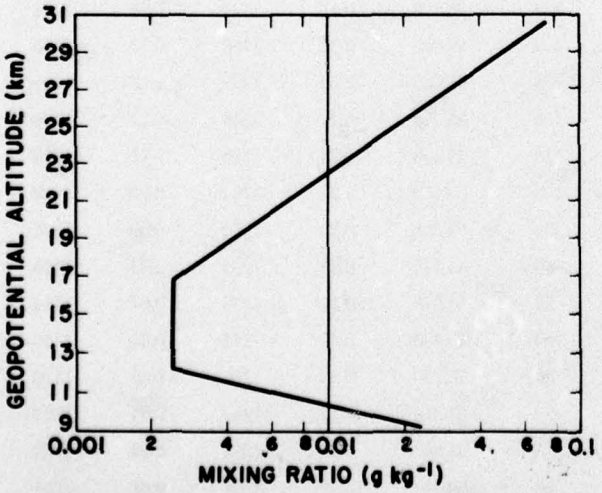


Fig. 3-19. Profile of mean annual polar stratospheric mixing ratio, after unpublished work of E. M. Hansen and W. G. Tank.

3.4.3 Tropical Observations

Three ascents to measure frostpoint were made at Hyderabad, India (latitude 17°N) [Mastenbrook, 1961]. A composite profile of mixing ratio and of frostpoint from these observations is presented in Table 3-26. The increase of mixing ratio with height above the tropopause is apparent also in these data.

3.5 TEMPERATURE, DENSITY, AND PRESSURE (90 TO 300 KM)

Data obtained by different methods of measurement may have a maximum spread in the measured values that is not at all representative of the actual variability of the parameter. This must be kept in mind when comparing observed values of atmospheric properties above 90 km.

Figure 3-21 shows molecular-scale temperature vs height for the *U. S. Standard Atmosphere, 1962*, other models, and some of the observed values above 120 km. Experimental data were obtained primarily at White Sands Proving Ground, at Fort Churchill, Canada, and at Russian rocket sites. All the data in the 90- to 200-km range (including data not shown) lie within 100°K of the 1962 Standard except for three sets of measurements. Two of these, for which the temperatures are substantially higher, were made at Churchill (high geomagnetic latitude) during the IGY near the peak of solar activity when the solar power flux density at 10.7-cm wavelength was about 350×10^{-22} W m^{-2} cps^{-1}, for which a daytime temperature of 2000° to 2200°K at 200 km would be predicted at low latitudes. Also, solar flares were frequent, and the solar corpuscular radiation would be expected to be particularly intense. For these reasons, the measured temperatures are probably reasonably accurate but apply under unusual conditions. The third set of measurements gives temperatures as much as 300°K below the standard. The measurements were made in terms of the Doppler broadening of the D lines of sodium released in the atmosphere. Why these measurements give lower temperatures is not known; temperatures at higher altitudes measured by this technique are in good agreement with other data. Various models of atmospheric density and some of the density measurements are compared with the *U.S. Standard Atmosphere, 1962* in Fig. 3-22. At 90 km, measured values lie within a factor of less than two on either side of the 1962 Standard. Actual atmospheric densities probably lie within a factor of two on either side of the 1962 Standard up to 200 km, although the range of variability is slowly increasing at the higher altitudes.

In Fig. 3-23 pressure data are compared with the *U.S. Standard Atmosphere, 1962*. These data are derived from density measurements by means of the gas laws. Because

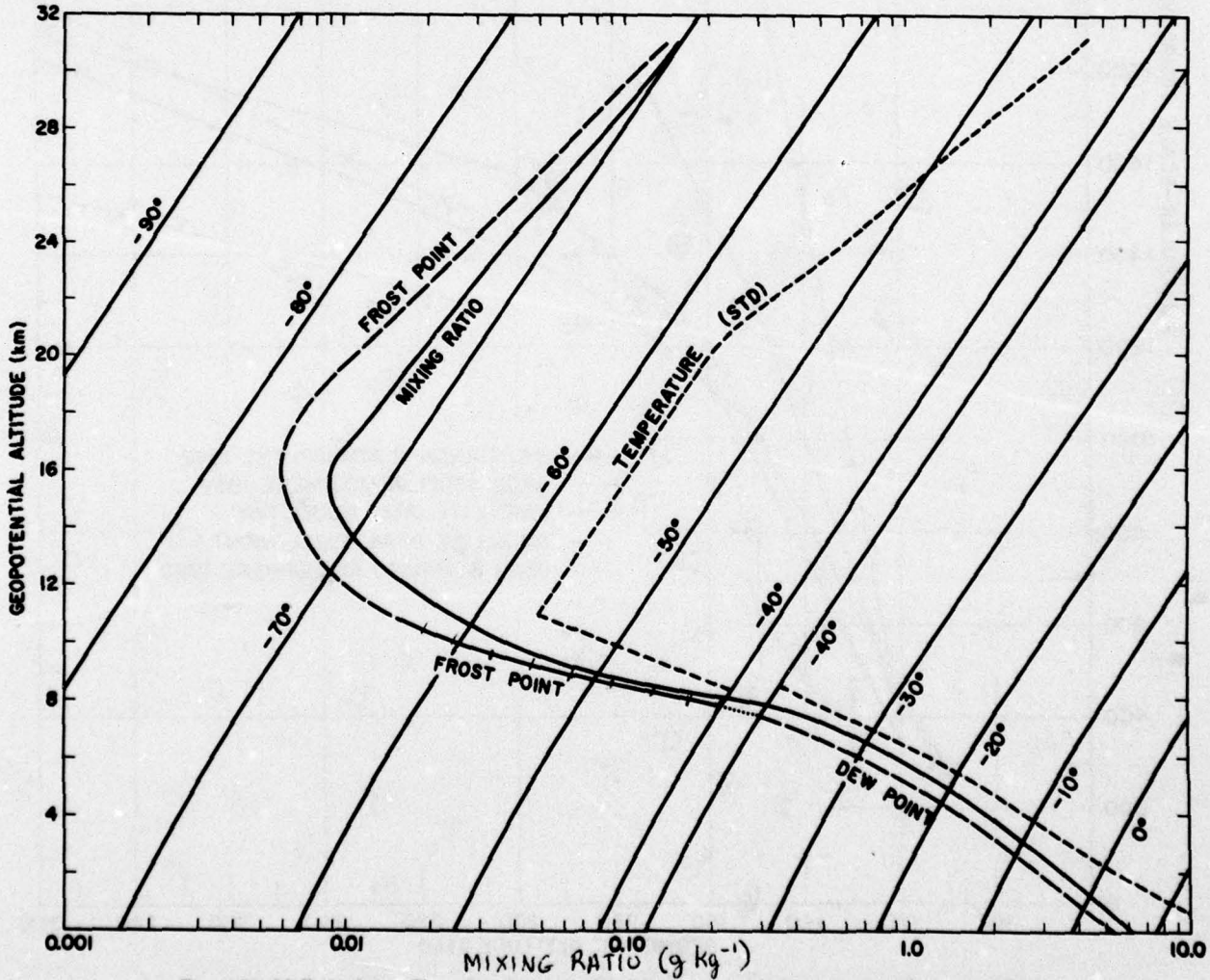


Fig. 3-20. Midlatitude profiles of mean annual mixing ratio and frostpoint or dewpoint. The diagonal solid curves are temperatures in degrees Celsius. The broken curve gives frostpoints (≤ -40°C) and dewpoints (≥ -40°C). The dotted curve is the *U. S. Standard Atmosphere, 1962*.

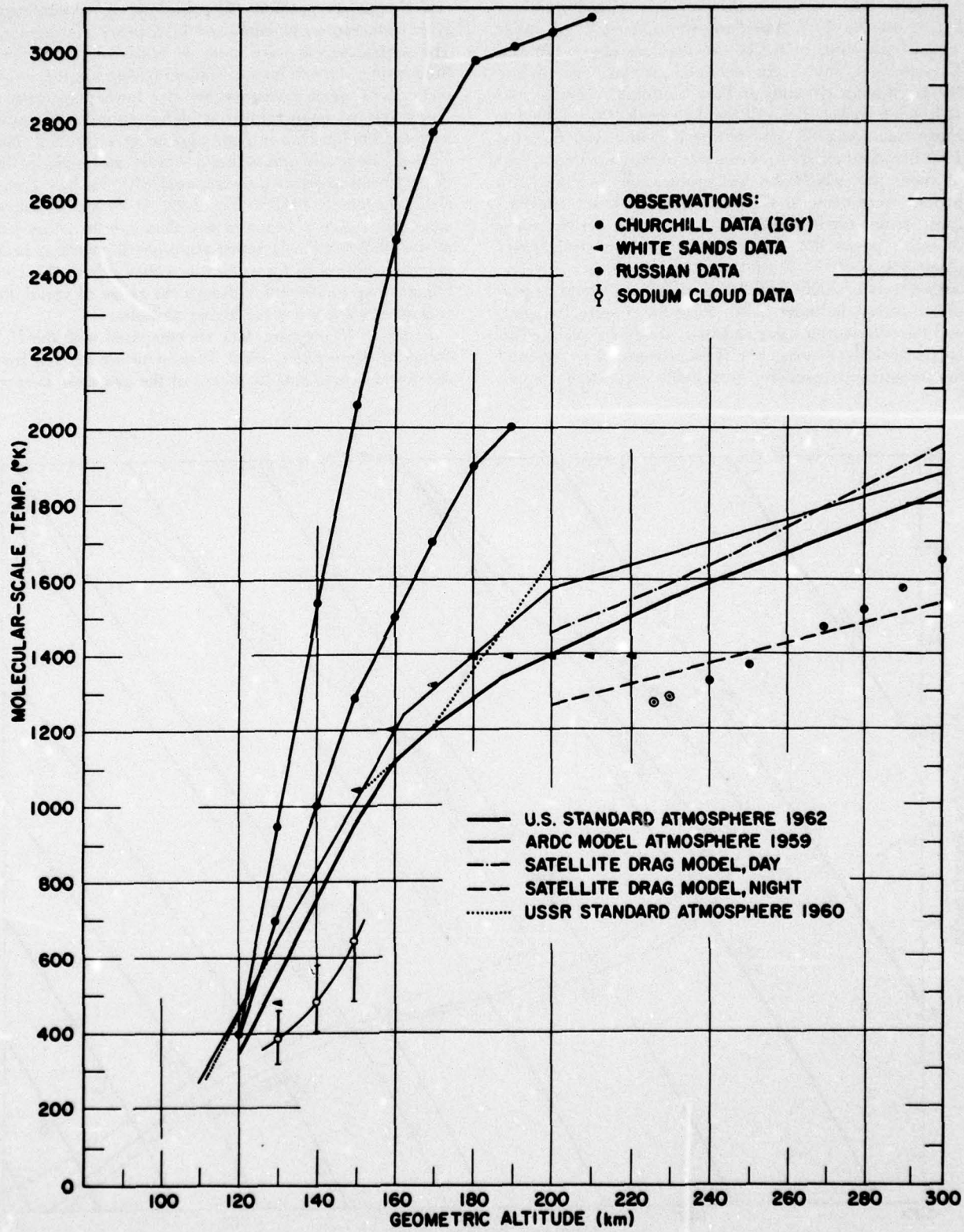


Fig. 3-21. Molecular-scale temperature vs geometric altitude for various standard and model atmospheres and some of the observed values. All observations below 200 km lie within 100°K of the *U. S. Standard Atmosphere, 1962* with the exception of the Churchill and sodium-cloud data.

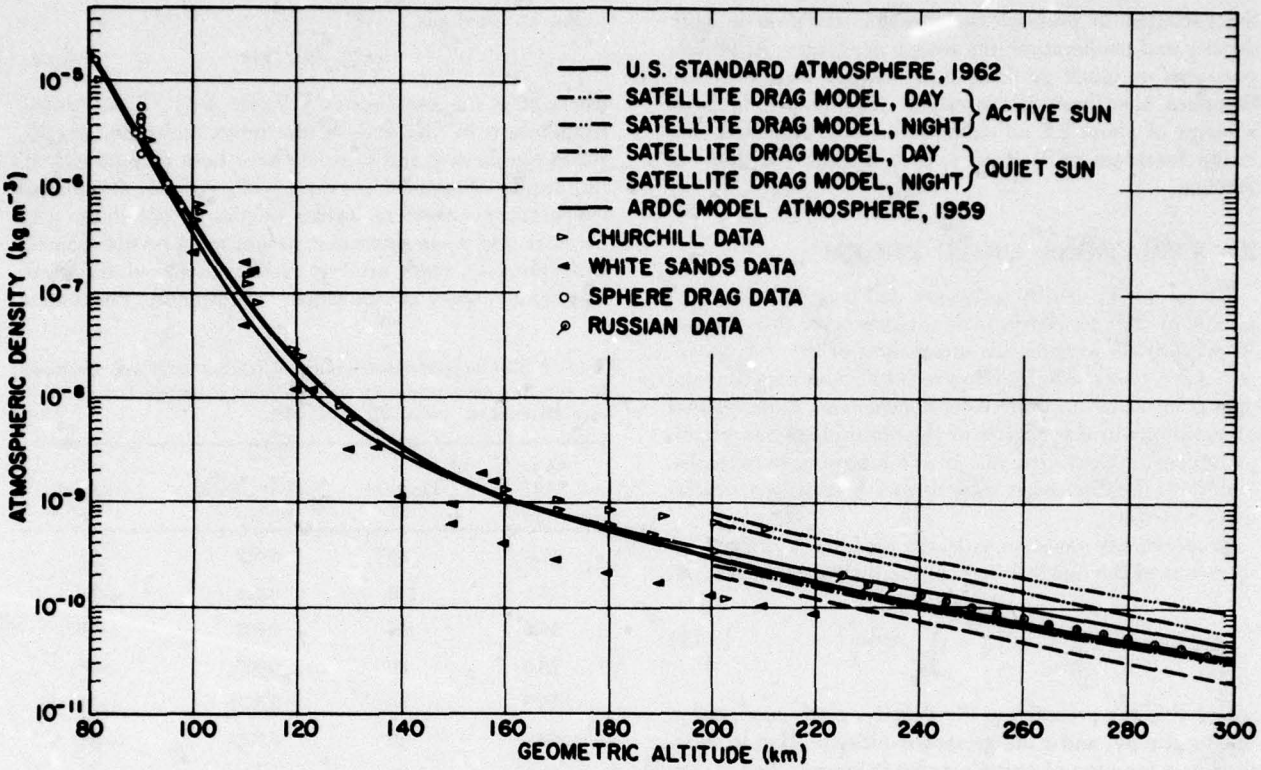


Fig. 3-22. Atmospheric density vs geometric altitude for *U. S. Standard Atmosphere, 1962*, compared with other models and some of the observed values.

Table 3-25. Mean annual mixing ratios and related quantities in middle latitudes for geopotential altitudes up to 31 km, computed for conditions of *U. S. Standard Atmosphere, 1962*. Values in columns marked * are recommended for general use.

	U. S. Standard 1962			Saturated (Derived)			Typical Moisture Content from:											
							Mean Mixing Ratio						Mean Frostpoint					
Geop. Alt (km)	Temp (°C)	Pres (mb)	Dens (g/m³)	e_s (μb)	ρ_s (mg/m³)	w_s (ppm)	* $\bar{w}$ (ppm)	e_v (μb)	ρ_v (mg/m³)	U (%)	T_f (°C)	* W (μ)	* $\bar{T}_f$ (°C)	* e_v' (μb)	* ρ_v' (mg/m³)	* U' (%)	w' (ppm)	W' (μ)
0	+15.0	1013	1225	17044	12830	10473	6300	10260	7718	60	+7	11224	+5	8719	6797	75	5549	9743
2	+2.0	795	1006	7055	5559	5526	3800	4857	3823	69	−3	5206	−7	3618	2946	62	2928	4210
4	−11.0	616	819	2644	2186	2669	1900	1882	1556	71	−15	2057	−18	1488	1264	49	1543	1717
6	−24.0	472	660	883	768	1163	900	683	594	77	−28	710	−30	509	453	43	686	54.8
8	−37.0	356	525	257	236	449	270	154	142	60	−42	150	−46	99.6	95	39	181	106
10	−50.0	264	413	39.35	38.21	92	37	15.70	15.3	40	−57	22	−60	10.8	11	28	26	14
12	−56.5	193	311	17.22	17.25	55	17	5.27	5.3	31	−65	8	−69	3.03	3.22	18	10	6
14	−56.5	141	227	17.22	17.25	76	10	2.27	2.3	13	−71	4	−74	1.42	1.55	8	7	2
16	−56.5	103	165	17.22	17.25	104	9	1.49	1.5	9	−74	3	−77	.89	.98	5	6	2
18	−56.5	75.0	121	17.22	17.25	142	13	1.57	1.8	9	−73	3	−78	.76	.84	4	7	2
20	−56.5	54.7	88.0	17.22	17.25	196	18	1.58	1.6	9	−73	4	−77	.89	.98	5	11	2
22	−54.5	40.0	63.7	22.32	22.16	348	27	1.74	1.7	8	−73	4	−76	1.04	1.14	5	18	2
24	−52.5	29.3	46.3	28.80	28.32	616	38	1.79	1.8	6	−73	4	−75	1.22	1.33	4	29	3
26	−50.5	21.5	33.7	36.99	36.06	1070	58	2.01	2.0	5	−72	4	−74	1.43	1.55	4	46	3
28	−48.5	15.9	24.6	47.30	45.62	1854	86	2.19	2.1	5	−71	5	−73	1.66	1.80	4	73	4
30	−46.5	11.7	18.0	60.22	57.57	3198	128	2.41	2.3	4	−71	2	−72	1.94	2.08	3	116	4
31	−45.5	10.1	15.4	67.84	64.57	4193	150	2.43	2.3	4	−70	-	−71	2.09	2.25	3	146	-

Key: e_s, e_v, e_v' pressure of water vapor in microbars; ρ_s, ρ_v, ρ_v' absolute humidity in ~~micrograms~~ milligrams per cubic meter: w_s, $\bar{w}$, w' mixing ratio in parts per million; U, U' relative humidity; T_f, $\bar{T}_f$, dewpoint-frostpoint; W, W' precipitable water (in microns) in the 2-km layer above the given geopotential altitude.

the variation in pressure includes the variation in both density and temperature, the ranges are larger. At 90 km, pressures as much as three times higher than the 1962 Standard have been measured. At 120 km, the range is a factor of about 2.5 on either side of the standard. The range increases until it is almost a factor of four at 200 km.

3.6 VARIATIONS ABOVE 200 KM

Variations in density, pressure, and temperature in the region of 200 to 700 km are discussed in this section. Above 700 km which is the upper limit of the *U.S. Standard Atmosphere, 1962*, there are insufficient experimental data from which to draw valid conclusions. Experimental observations in this region of the atmosphere are principally density measurements. In the following paragraphs, therefore, the discussion concentrates primarily on variations in density.

From density measurements, the pressure is determined by means of the integral form of the hydrostatic equation,

$$P = P_o - \int_{z_o}^{z} \rho g dz, \qquad (3\text{-}13)$$

where P is the pressure, ρ the density, g the acceleration due to gravity, and z the geometric altitude. If ρ is measured as a function of altitude and g is known, then P may be determined by assuming a value of P_o at z equals z_o. Equation (3-13) shows that pressure variations closely resemble density variations.

For an ideal gas,

$$P = \rho RT/M, \qquad (3\text{-}14)$$

where R is the gas constant (Table A-3), T the kinetic temperature in °K, and M, the mean molecular weight. When the density and pressure have been determined, all that can be obtained from Eq. (3-14) is T/M, the ratio of temperature to mean molecular weight. To obtain the temperature, the mean molecular weight must be determined. Unfortunately, there are few measurements of the mean molecular weight of the upper atmosphere. Theoretical

Table 3-26. Composite distribution of mixing ratio and frostpoint for the indicated pressures and altitudes based on three ascents over Hyderabad, India, in April 1961.

Geop Alt* (km)	Pressure (mb)	Mixing Ratio (g kg^{-1})	Frostpoint (°C)
12.4	200	0.022	—62
14.1	150	0.005	—75
16.6	100	0.003	—81
18.0	80	0.003	—83
19.7	60	0.0036	—83
22.2	40	0.0056	—83
26.3	20	0.019	—79

* Estimated geopotential altitude based on tropical atmosphere (Sec. 2.3).

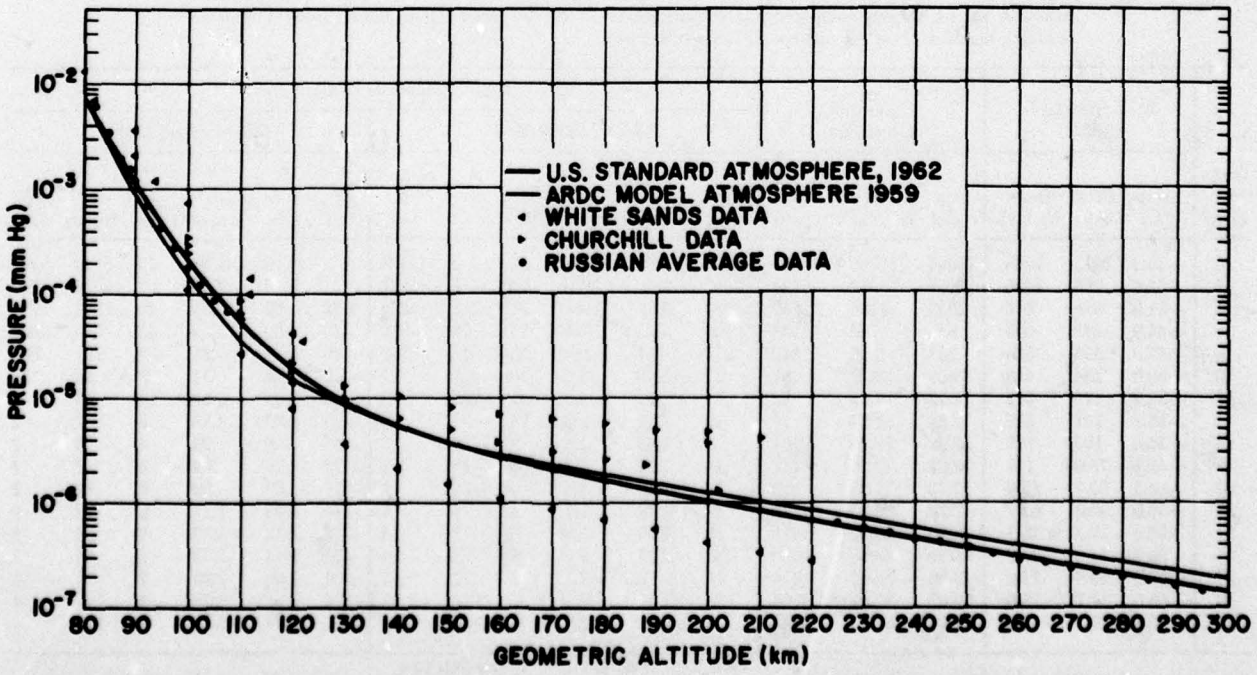


Fig. 3-23. Pressure vs geometric altitude for *U. S. Standard Atmosphere, 1962*, compared with U. S. detailed data, USSR average data, and the ARDC Model Atmosphere, 1959.

values are derived by considering the absorption of solar energy and heat conduction by the upper atmosphere, and by assuming diffusive equilibrium above a selected altitude. The concentrations of all the constituents must be assumed at the level above which diffusive equilibrium is assumed. These concentrations are not known sufficiently well, and the principal reason why theoretical models differ is that different boundary conditions are assumed. The temperatures calculated may differ by several hundred degrees, depending on the boundary conditions chosen. This fact should be taken into account in what follows.

3.6.1 Diurnal Density Variations

One of the first effects discovered from observations of satellite orbits was that the daytime density of the upper atmosphere is markedly different from the nighttime density. Figure 3-24 shows the density throughout a 24-h period calculated from satellite behavior at an altitude of 660 km. The peak of the curve occurs at about 1400 h and the minimum at about 0400 h local time. This variation is caused by heating of the upper atmosphere by solar radiations. A lag of the peak from solar maximum by several hours is to be expected as the atmosphere cannot respond instantaneously.

The solar radiations that have the most effect on the upper atmosphere are the extreme ultraviolet and corpuscular radiations. Extreme ultraviolet radiations are absorbed by constituents of the upper atmosphere (Sec. 16.2). The density of the upper atmosphere changes markedly during a magnetic storm [Groves, 1961], a period during which corpuscular radiations play a major role. Heating by hydromagnetic waves is also a possible means of corpuscular radiation affecting the upper atmosphere.

It would be desirable to monitor routinely all solar radiations that affect the upper atmosphere. Until this is accomplished, it appears that the 10- and 20-cm radio emissions, which are routinely monitored (Sec. 16.3), are fairly good indicators of solar activities that affect the upper atmosphere. Figure 3-25 shows monthly averages of solar power flux densities at 10.7 cm (2800 Mcps); there are large variations in the solar flux during the 11-yr solar cycle. In addition, variations due to the 27-day solar rotation period may amount up to 50% of the monthly means shown on Fig. 3-25. Knowledge of the magnitude of the true solar flux and spectral distribution at a given time is essential before any sense can be made out of density variations in the upper atmosphere.

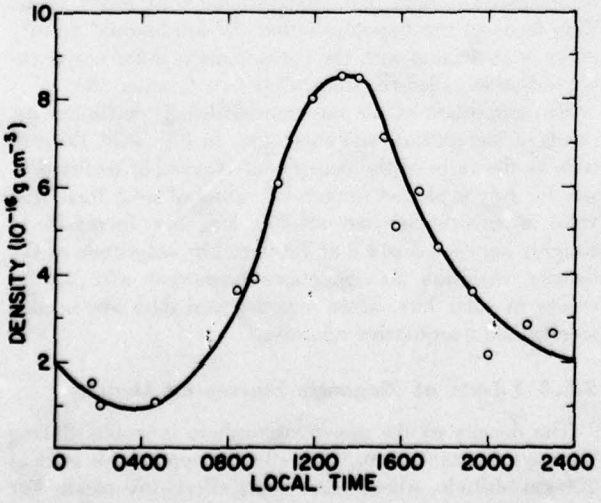


Fig. 3-24. Diurnal density variation at 660 km, derived from observations by Priester et al [1960] of 1958 β 2.

Figure 3-26 shows the ratio of ρ_{14}, the density at 1400 h, to ρ_4, the density at 0400 h, as a function of altitude and the 10.7-cm solar power flux density. These curves are based on an empirical model derived by Paetzold [1962] from observations of seven satellites. Figure 3-27 shows the same functions, but the curves are based on the theoretical model of Harris and Priester [1962]. This model is obtained by considering absorption of solar energy and heat conduction by the upper atmosphere, the barometric law, and assuming certain arbitrary boundary conditions at an altitude of 120 km.

Examination of Fig. 3-26 and 3-27 shows there is qualitative agreement between theory and experiment, but quantitative agreement is lacking. The day-to-night density ratio increases rapidly with altitude, because of the expansion of the atmosphere upwards that results from heating of the lower levels of the atmosphere by solar radiation. This expansion is the diurnal bulge. At the higher levels the concentration of particles is always low, so that any addition to this concentration is manifested as a large relative increase. Below 200 km, the day-to-night density ratio is about 0.95. This is to be expected from the conservation of mass. The atmosphere as a whole does not increase in density so that in some region there must be a compensatory decrease; this decrease occurs between approximately 100 to 200 km.

In general, as the solar flux diminishes, the day-to-night density ratio at a given height increases. This is to be expected because when less solar energy is received, the heating of the upper atmosphere is less. Thus the density at a given altitude in the upper atmosphere will be relatively low, and solar radiations have greater effect on low density than on high density regions. For low solar power flux density of 10^{-20} W m^{-2} cps^{-1} at 10.7 cm, the curve based on the theoretical model shows the day-to-night ratio first increasing rapidly with altitude and then decreasing. Although the curve based on the empirical model does not reverse, a definite decrease in slope shows that a much slower rate of increase in the density ratio occurs at higher altitudes. This effect, if real, should become even more pronounced during the minimum of the solar cycle. Until sufficient density measurements are made during periods of low solar flux, the day-to-night density ratio for these low values remains uncertain.

3.6.2 Density as a Function of Solar Flux

The variation in solar flux with the 11-yr solar cycle (at 10.7 cm the power flux density varies from around 250×10^{-22} W m^{-2} cps^{-1} at solar maximum to around 65×10^{-22} W m^{-2} cps^{-1} at minimum) causes a similar

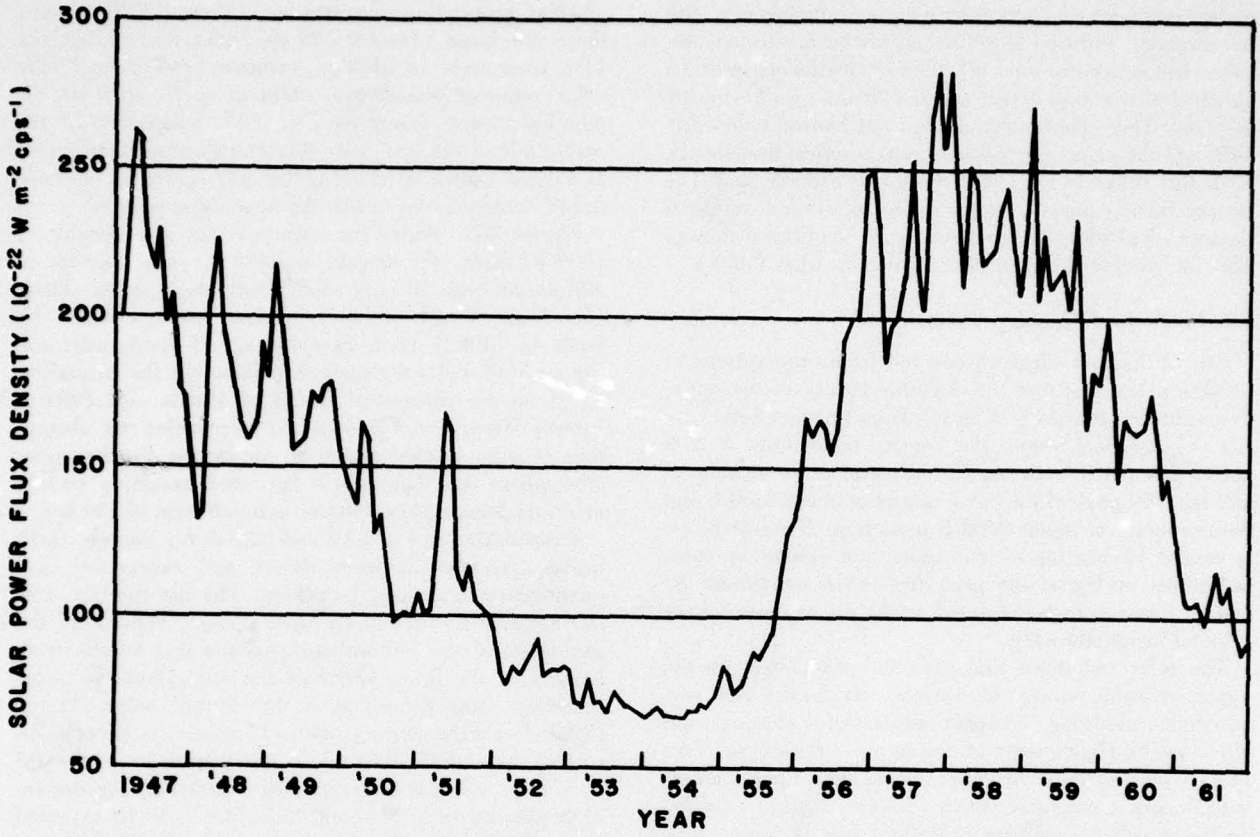


Fig. 3-25. Monthly averages of the 10.7-cm solar power flux density; measurements of the National Research Council of Canada.

cyclic variation in density. From the power law, the density at a given high altitude will be much greater at the maximum of the solar cycle. Superimposed on this long-term variation in density there is a 27-day variation; this variation is also much greater at periods of solar maximum than at minimum.

Table 3-27 gives upper-atmosphere density for various stages of solar activity. These densities increase during intense magnetic storms. The relationship for the increase is given approximately by

$$\rho = \rho_o (1 + \beta A_p), \qquad (3\text{-}15)$$

where ρ is the density during the storm, ρ_o is the density before the storm, β is the coefficient which varies with altitude from about 3×10^{-3} at 200 km to 1.5×10^{-2} at 700 km, and A_p is the planetary magnetic index.

3.6.3 Annual and Semiannual Density Variations

After normalizing the density values to a solar power flux density of 2.2×10^{-20} W m^{-2} cps^{-1} at 10.7 cm and to 1400 h local time, there still remains a density variation with annual and semiannual components. This residual effect is evident in the curves of Fig. 3-28. There are two maxima, one during the February-April period and one during the October-November period. Minima occur during the December-January and the June-July periods, the June-July minimum being more pronounced. The curves closely parallel those of semiannual oscillations in geomagnetic indices that are averaged over many years. This leads to the hypothesis that the semiannual density effect is associated with the component of solar corpuscular radiation called the solar wind (see Chapter 18).

The amplitude of the semiannual density variation depends on the altitude and solar flux. In Fig. 3-29, the altitude vs the ratio of the density for November to the density for July is plotted for several values of solar flux. This ratio is practically one at 200 km, but increases to roughly between 2 and 3 at 700 km. The amplitude of the density variation also increases somewhat with an increase in solar flux. More experimental data are needed to establish quantitative relations.

3.6.4 Effects of Magnetic Storms on Density

The density of the upper atmosphere increases during intense magnetic storms. This effect is appreciable even at 200-km altitude, where other solar effects are small. For example, the density at 200 km increased by a factor of two during the magnetic storm of 13 November 1960.

Analysis [McDermott and Groves, 1962] shows a correlation with the A_p magnetic index. Equation (3-15) holds from values of A_p as low as 20 to as high as 300. Their value of β in the region of 200 km is 3×10^{-3}, with an error the order of 30%.

Jacchia and Slowey [1962] found a close correlation between the A_p magnetic index and density at altitudes of 660 and 740 km. They do not give a value for β, but examination of eleven major peaks in their density values indicates that β is approximately 1.5×10^{-2} with an error the order of 30%, which is 5 times the value at 200 km. Thus the coefficient β increases approximately by a factor of 5 between 200 and 700 km; more exact values must await further experimental results.

3.6.5 Latitude Effects

No systematic variation of density with latitude has been found in the region of 200 to 700 km. Because of the high conductivity of the upper atmosphere, large latitude effects are not expected.

3.6.6 Diurnal Temperature Variations

The attempt to deduce temperature variations from the measured density variations is difficult because of lack of knowledge of the mean molecular weight of the upper atmosphere. The temperature above 300 km is essentially independent of height, and this exospheric temperature may be calculated using Nicolet's [1961b] theoretical model.

From analysis of observations of four satellites, it appears that the maximum daytime exospheric temperature is approximately 35% greater than the minimum nighttime temperature. Figure 3-30 shows this variation. Not all the daytime points are 35% greater than the nighttime, but considering the assumptions that must be made to obtain any values, only approximate relations can be derived at this time.

An approximation for the temperature at various positions from the peak of the density curve is

$$T = T_N \left[1 + 0.35 \left(\cos \frac{\psi}{2} \right)^n \right], \qquad (3\text{-}16)$$

where T represents the temperature at an angular distance ψ from the center of the diurnal bulge and T_N the minimum nighttime temperature; the exponent, n, is between 4 and 6.

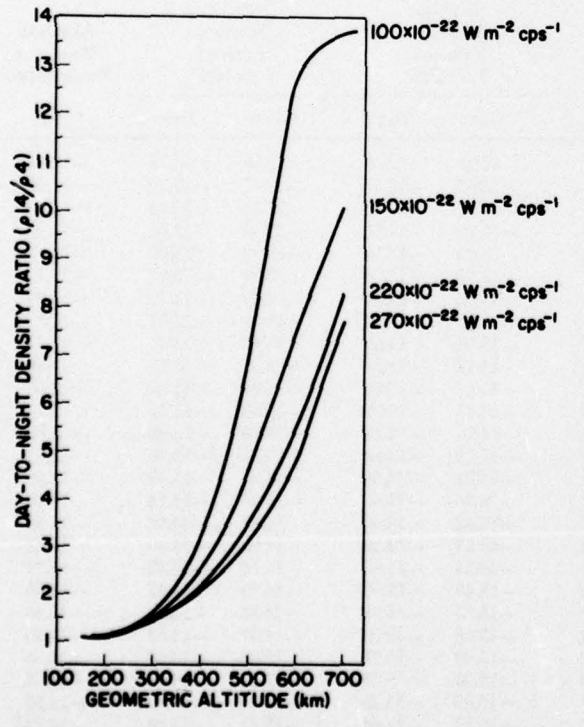


Fig. 3-26. Day-to-night density ratio as a function of altitude and solar power flux density at 10.7-cm wavelength. Empirical model after Paetzold [1962].

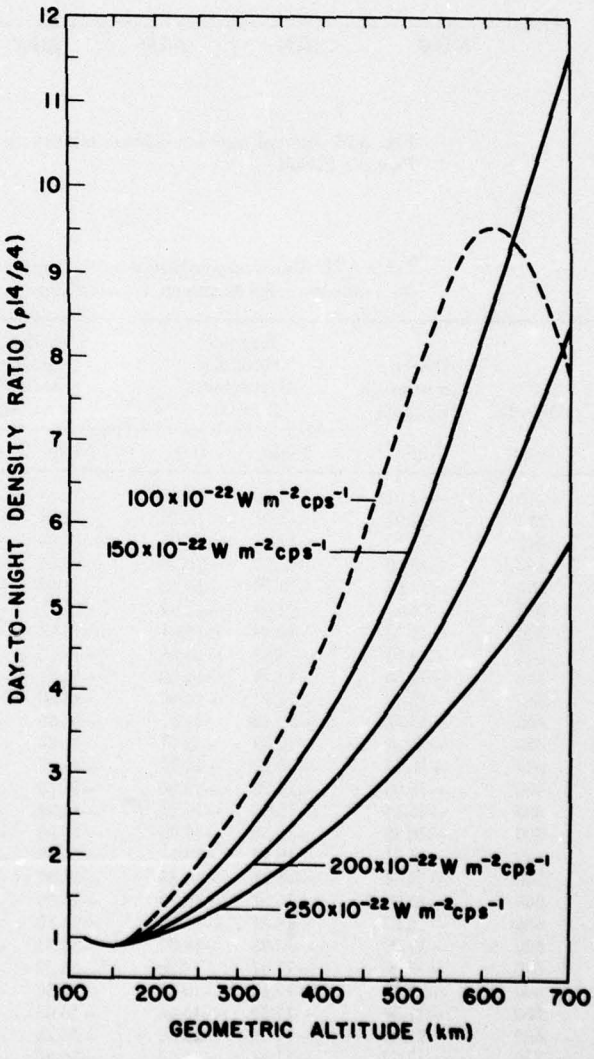


Fig. 3-27. Day-to-night density ratio as a function of altitude and solar power flux density at 10.7-cm wavelength. Theoretical model after Harris & Priester [1962].

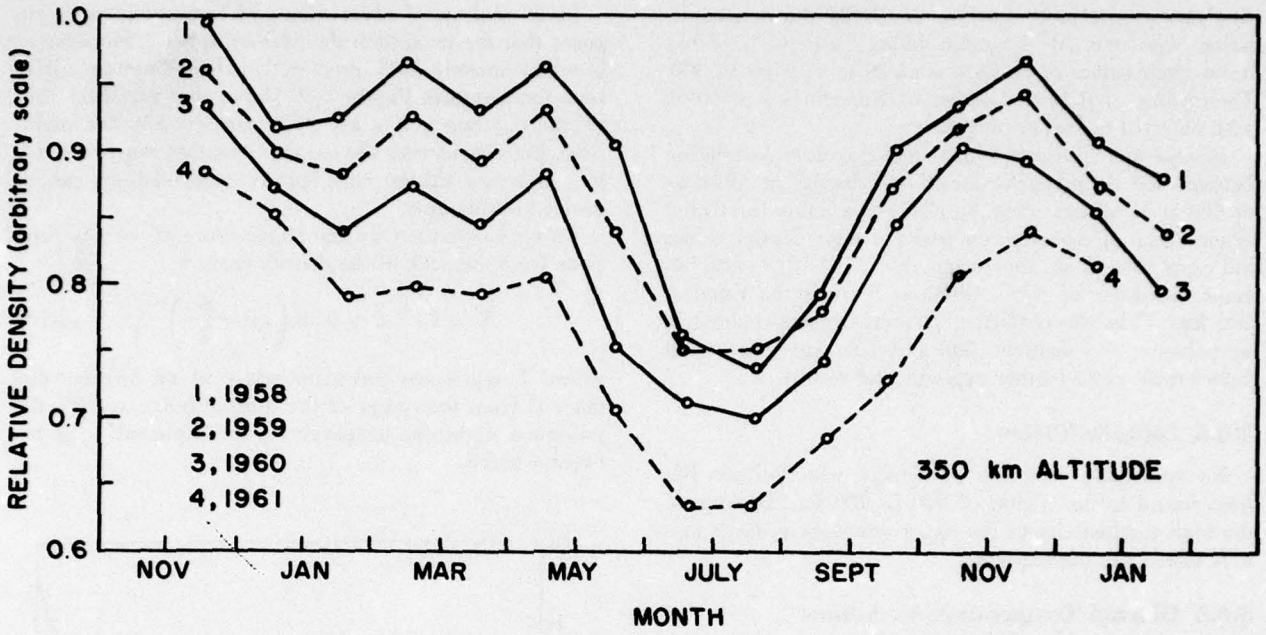


Fig. 3-28. Annual and semiannual relative density variations derived from satellite 1958 α after Paetzold [1962].

Table 3-27. Upper-atmosphere density (log of ρ in g/cm^3) at various stages of solar activity, and for minimum and maximum temperatures.

Altitude	Absolute Temperature Minimum	Sunspot Minimum (Quiet Sun) F = 70*		Average Sunspot Activity F = 140*		Average at Sunspot Maximum F = 200*		Very High Sunspot Activity F = 300*		Absolute Maximum Temperature
(km)	Night	Night	Day	Night	Day	Night	Day	Night	Day	Day
200	−12.61	−12.58	−12.43	−12.45	−12.38	−12.38	−12.36	−12.36	−12.38	−12.42
220	−12.97	−12.91	−12.70	−12.74	−12.61	−12.63	−12.57	−12.57	−12.57	−12.60
240	−13.29	−13.22	−12.96	−13.00	−12.83	−12.85	−12.77	−12.76	−12.73	−12.76
260	−13.60	−13.52	−13.20	−13.25	−13.04	−13.06	−12.94	−12.92	−12.87	−12.90
280	−13.88	−13.79	−13.42	−13.49	−13.23	−13.26	−13.10	−13.08	−13.00	−13.02
300	−14.15	−14.05	−13.64	−13.71	−13.41	−13.45	−13.26	−13.23	−13.13	−13.14
320	−14.40	−14.30	−13.84	−13.92	−13.58	−13.62	−13.40	−13.37	−13.26	−13.26
340	−14.64	−14.53	−14.04	−14.12	−13.75	−13.80	−13.54	−13.50	−13.37	−13.37
360	−14.88	−14.75	−14.22	−14.31	−13.91	−13.96	−13.68	−13.63	−13.48	−13.47
380	−15.10	−14.97	−14.40	−14.50	−14.06	−14.12	−13.81	−13.75	−13.58	−13.56
400	−15.32	−15.18	−14.57	−14.68	−14.21	−14.27	−13.93	−13.87	−13.68	−13.65
420	−15.54	−15.39	−14.74	−14.85	−14.35	−14.41	−14.05	−13.99	−13.77	−13.74
440	−15.75	−15.59	−14.90	−15.02	−14.49	−14.56	−14.17	−14.10	−13.86	−13.82
460	−15.95	−15.78	−15.06	−15.18	−14.62	−14.69	−14.28	−14.21	−13.96	−13.91
480	−16.14	−15.98	−15.21	−15.34	−14.75	−14.83	−14.39	−14.31	−14.05	−13.99
500	−16.33	−16.16	−15.36	−15.50	−14.88	−14.96	−14.50	−14.41	−14.14	−14.07
520	−16.51	−16.34	−15.51	−15.65	−15.00	−15.08	−14.60	−14.51	−14.22	−14.15
540	−16.68	−16.51	−15.65	−15.80	−15.12	−15.21	−14.70	−14.61	−14.30	−14.22
560	−16.83	−16.67	−15.79	−15.95	−15.24	−15.33	−14.80	−14.70	−14.38	−14.29
580	−16.97	−16.81	−15.93	−16.10	−15.36	−15.45	−14.90	−14.79	−14.46	−14.36
600	−17.09	−16.95	−16.07	−16.24	−15.47	−15.57	−14.99	−14.88	−14.54	−14.43
620	−17.20	−17.07	−16.20	−16.37	−15.58	−15.68	−15.08	−14.97	−14.62	−14.50
640	−17.30	−17.18	−16.33	−16.50	−15.69	−15.80	−15.18	−15.06	−14.69	−14.56
660	−17.38	−17.28	−16.46	−16.63	−15.80	−15.91	−15.26	−15.14	−14.76	−14.62
680	−17.45	−17.36	−16.58	−16.75	−15.91	−16.02	−15.35	−15.22	−14.82	−14.68
700	−17.52	−17.44	−16.69	−16.86	−16.01	−16.13	−15.44	−15.31	−14.88	−14.73

* F, the solar flux density at 10.7-cm wavelength, in units of 10^{-22} W m^{-2} cps^{-1}.

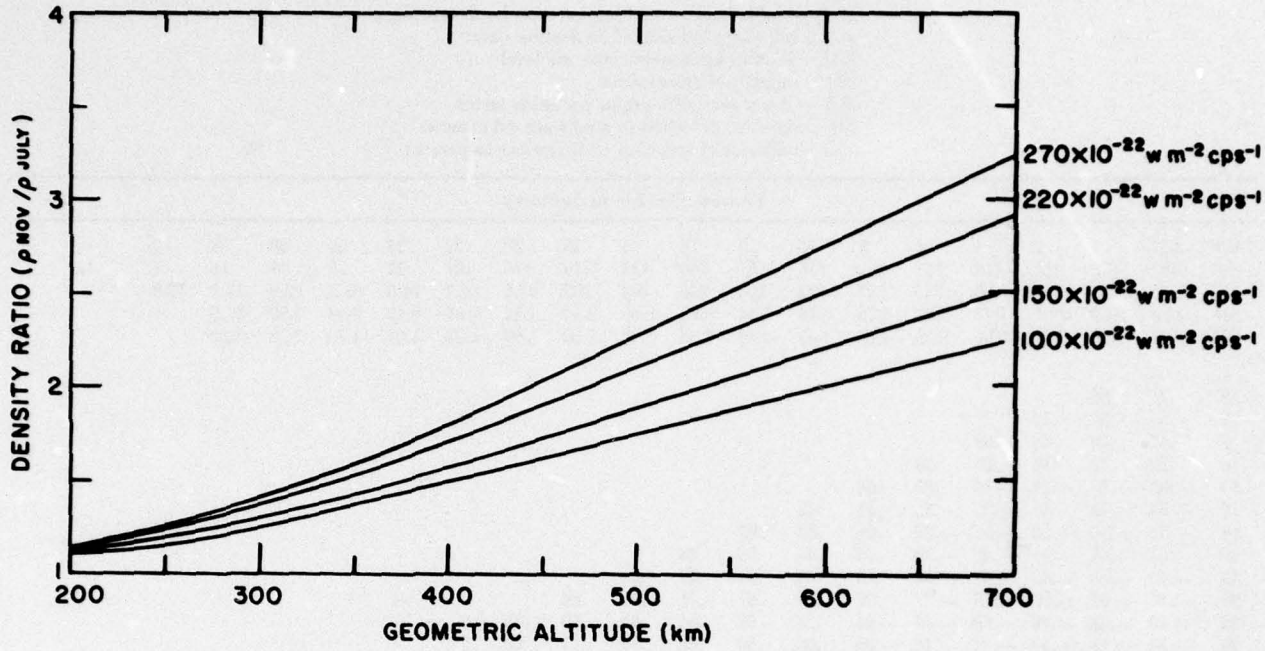


Fig. 3-29. Amplitude of semiannual density variation as a function of altitude and solar power flux density at 10.7-cm wavelength. Empirical model after Paetzold [1962].

3.6.7 Temperature as a Function of Solar Flux

Changes in exospheric temperature, presumably due to heating of the atmosphere by solar extreme ultraviolet radiations, can be related to the solar power flux density, F, at 21 cm. The relation is

$$\Delta_1 T \cong 2.5° \Delta F, \tag{3-17}$$

where T is in degrees Kelvin.

Concerning heating of the atmosphere by corpuscular radiations, Jacchia [1962] reports that the monthly means of the 10.7-cm solar flux are good indicators. The expression for this effect is

$$\Delta_2 T \cong 2° \Delta \bar{F}, \tag{3-18}$$

where $\bar{F}$ represents the monthly mean of the solar power flux density at 21 cm. These approximate expressions are obtained from the data shown in Fig. 3-30.

Semiannual temperature variations corresponding to the semiannual density variations are given by the following approximate expression,

$$\Delta_3 T \cong 0.5° \bar{F} \cos (4\pi \Delta t/365), \tag{3-19}$$

in which, for lack of better information, a sinusoidal relation has been assumed with the maximum around April 7, so Δt is time interval in days after April 7.

Combining the various temperature effects, the relation for exospheric temperature changes as a function of solar flux becomes

$$\Delta T \cong 2.5° \Delta F + 2° \Delta \bar{F} + 0.5° \bar{F} \cos (4\pi \Delta t/365). \tag{3-20}$$

3.6.8 Effects of Magnetic Storms on Temperature

During magnetic storms, changes in exospheric temperature, according to Jacchia [1962], are approximately linear with the geomagnetic index A_p. The approximate relation for this is

$$\Delta T \cong 1.5° A_p. \tag{3-21}$$

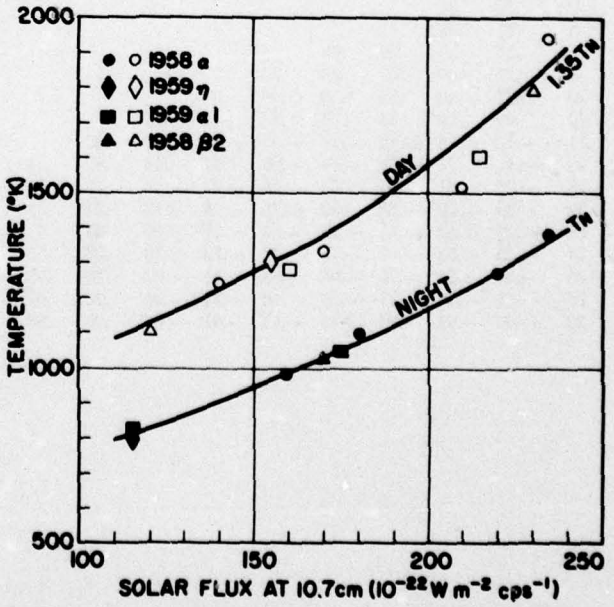


Fig. 3-30. Exospheric temperature as a function of solar power flux density at 10.7-cm wavelength as derived from Jacchia [1962].

Table 3-28. Correlation of atmospheric density at pairs of levels, 1958 to 1960.

Body of table lists correlations between levels indicated at top and along left side. First five lines are:
KM — level in kilometers above sea level
NO — number of observations
MN — mean density in grams per cubic meter
SD — standard deviation in grams per cubic meter
CV—coefficient of variation (S.D./mean) in percent

Tampa, Florida in January

KM	.011	1	2	4	6	8	10	12	14	16	18	20	22	24	26	28	30	32
NO	187	168	166	162	161	160	156	151	140	134	119	116	101	91	78	49	14	1
MN	1236	1109	995	806	653	527	422	328	246	183	132	91.6	64.4	46.0	33.1	23.9	17.7	12.8
SD	31.8	21.7	13.3	7.77	5.77	5.74	5.94	7.54	5.86	5.85	3.70	1.82	0.89	0.49	0.48	0.52	0.39	
CV	2.57	1.96	1.34	0.96	0.88	1.09	1.41	2.30	2.38	3.20	2.80	1.99	1.38	1.07	1.45	2.18	2.20	
1	.84																	
2	.71	.86																
4	.53	.59	.72															
6	.42	.40	.48	.63														
8	.20	.12	.16	.20	.58													
10	—.08	—.24	—.24	—.14	.05	.67												
12	—.33	—.49	—.55	—.50	—.35	.11	.62											
14	—.51	—.68	—.68	—.57	—.39	.06	.52	.81										
16	—.45	—.65	—.61	—.46	—.30	.07	.44	.59	.83									
18	—.49	—.66	—.62	—.47	—.32	.09	.53	.64	.80	.90								
20	—.46	—.59	—.56	—.52	—.37	.07	.45	.61	.71	.79	.86							
22	—.40	—.48	—.48	—.60	—.44	—.06	.24	.52	.56	.54	.60	.79						
24	—.19	—.25	—.29	—.21	—.12	—.03	.08	.30	.25	.10	.15	.23	.53					
26	.03	.04	.05	.08	—.01	—.07	.00	.05	—.02	—.10	—.14	—.24	.03	.67				
28	.03	.13	.10	.04	—.16	—.09	—.01	—.01	—.10	—.18	—.20	—.38	—.10	.46	.86			
30	—.18	—.07	—.10	—.06	—.10	—.31	—.12	.15	.14	.09	.04	—.15	.09	.67	.82	.90		

Tampa, Florida in July

KM	.011	1	2	4	6	8	10	12	14	16	18	20	22	24	26	28	30
NO	186	166	165	160	154	153	152	151	147	138	131	127	121	110	70	35	4
MN	1170	1068	972	798	648	525	423	337	261	191	134	94.2	67.2	48.3	35.1	25.8	19.2
SD	10.9	5.33	4.11	3.53	2.91	2.71	2.32	1.70	2.65	3.07	1.54	0.93	0.73	0.58	0.51	0.40	0.31
CV	0.93	0.50	0.42	0.44	0.45	0.52	0.55	0.50	1.02	1.61	1.15	0.99	1.09	1.20	1.45	1.55	1.61
1	.57																
2	.33	.84															
4	.21	.55	.71														
6	.31	.55	.66	.80													
8	.27	.49	.61	.63	.77												
10	.27	.46	.55	.59	.69	.87											
12	.09	.09	.14	.14	.23	.41	.58										
14	—.16	—.36	—.42	—.47	—.45	—.38	—.28	.45									
16	—.41	—.70	—.69	—.64	—.60	—.47	—.46	—.02	.54								
18	—.20	—.51	—.55	—.49	—.46	—.22	—.21	.10	.38	.66							
20	—.25	—.48	—.38	—.29	—.26	—.14	—.13	.21	.35	.51	.50						
22	—.29	—.62	—.52	—.40	—.33	—.11	—.16	.20	.45	.54	.57	.62					
24	—.28	—.63	—.67	—.55	—.43	—.22	—.20	.23	.53	.64	.61	.56	.72				
26	—.26	—.74	—.75	—.66	—.58	—.41	—.27	.16	.61	.78	.73	.65	.70	.78			
28	—.11	—.70	—.77	—.59	—.48	—.31	—.10	.26	.62	.77	.70	.76	.73	.77	.89		
30	—.93	—.95	—.93	—.18	—.17	—.41	—.04	.90	.93	.75	.94	.97	.89	.90	.88	.95	

(Continued)

Table 3-28. Correlation of atmospheric density at pairs of levels, 1958 to 1960. (Continued)

Body of table lists correlations between levels indicated at top and along left side. First five lines are:
KM — level in kilometers above sea level
NO — number of observations
MN — mean density in grams per cubic meter
SD — standard deviation in grams per cubic meter
CV—coefficient of variation (S.D./mean) in percent

St. Paul Island, Alaska in January

KM	.007	1	2	4	6	8	10	12	14	16	18	20	22	24	26	28	30	32	34
NO	186	186	186	186	186	186	183	182	176	170	161	156	140	123	86	59	28	3	1
MN	1289	1155	1031	826	659	517	390	281	206	151	112	82.5	60.9	45.1	33.4	24.9	18.7	14.0	10.4
SD	36.7	28.6	20.6	13.5	9.77	10.4	17.2	12.8	7.59	5.18	3.48	2.41	1.65	1.27	0.97	0.71	0.67		
CV	2.85	2.48	2.00	1.63	1.48	2.01	4.41	4.56	3.68	3.43	3.11	2.92	2.71	2.82	2.90	2.85	3.58		
1	.89																		
2	.73	.90																	
4	.47	.59	.78																
6	.39	.44	.59	.84															
8	.42	.27	.19	.16	.41														
10	.27	.12	−.02	−.13	.05	.80													
12	.23	.09	.01	−.02	.11	.69	.90												
14	.22	.09	.04	.02	.13	.64	.82	.95											
16	.20	.05	.02	.02	.15	.63	.76	.89	.97										
18	.23	.07	.04	.05	.17	.60	.70	.83	.93	.98									
20	.29	.13	.09	.05	.16	.58	.65	.78	.90	.94	.98								
22	.35	.18	.12	.02	.12	.55	.62	.72	.84	.89	.94	.97							
24	.49	.28	.18	.06	.15	.56	.55	.62	.74	.78	.84	.88	.95						
26	.46	.29	.23	.05	.10	.43	.40	.52	.68	.68	.76	.81	.86	.95					
28	.56	.45	.40	.26	.26	.33	.24	.35	.53	.53	.62	.68	.68	.75	.91				
30	.76	.56	.52	.37	.35	.38	.31	.37	.52	.47	.52	.61	.62	.73	.88	.98			

St. Paul Island, Alaska in April

KM	.007	1	2	4	6	8	10	12	14	16	18	20	22	24	26	28	30	32
NO	180	180	180	180	179	178	176	175	173	167	164	160	143	123	96	64	22	2
MN	1297	1165	1039	830	661	519	391	285	210	155	115	84.7	62.5	46.1	34.1	25.1	18.4	13.4
SD	27.7	22.5	17.1	11.9	8.74	10.3	16.8	12.3	7.04	4.85	2.93	1.88	1.11	0.66	0.48	0.44	0.32	
CV	2.14	1.93	1.65	1.43	1.32	1.98	4.30	4.32	3.35	3.13	2.55	2.22	1.78	1.43	1.41	1.75	1.74	
1	.88																	
2	.69	.88																
4	.48	.63	.81															
6	.31	.39	.50	.72														
8	.14	.01	−.06	−.10	.37													
10	−.04	−.19	−.33	−.47	−.14	.73												
12	−.06	−.21	−.35	−.45	−.16	.60	.92											
14	−.06	−.21	−.34	−.42	−.13	.59	.86	.95										
16	−.11	−.26	−.38	−.41	−.16	.49	.75	.87	.96									
18	−.15	−.29	−.41	−.43	−.18	.44	.68	.80	.92	.97								
20	−.12	−.23	−.35	−.35	−.11	.42	.58	.71	.85	.92	.97							
22	.00	−.13	−.26	−.28	−.09	.34	.49	.63	.78	.88	.92	.97						
24	.07	−.01	−.16	−.20	−.07	.18	.30	.45	.64	.76	.82	.89	.95					
26	.26	.21	.05	−.06	−.06	.02	.09	.24	.43	.54	.61	.70	.81	.91				
28	.35	.28	.05	−.05	−.09	−.03	.07	.25	.41	.48	.53	.60	.67	.79	.95			
30	.56	.60	.45	.40	.04	.32	−.12	.27	.50	.56	.58	.61	.66	.80	.94	.98		

(Continued)

Table 3-28. Correlation of atmospheric density at pairs of levels, 1958 to 1960. (Continued)

Body of table lists correlations between levels indicated at top and along left side. First five lines are:
KM — level in kilometers above sea level
NO — number of observations
MN — mean density in grams per cubic meter
SD — standard deviation in grams per cubic meter
CV—coefficient of variation (S.D./mean) in percent

Omaha, Nebraska in January

KM	.406	1	2	4	6	8	10	12	14	16	18	20	22	24	26	28	30	32
NO	186	185	185	185	185	184	183	181	179	178	175	174	147	125	84	29	12	1
MN	1269	1161	1026	823	662	529	411	304	223	164	121	87.2	63.4	45.9	33.2	24.3	17.8	13.4
SD	40.4	37.8	26.3	13.5	7.48	6.97	12.9	13.6	7.03	4.40	2.45	1.44	0.89	0.83	0.77	0.55	0.50	
CV	3.18	3.26	2.56	1.64	1.13	1.32	3.14	4.47	3.15	2.68	2.02	1.65	1.40	1.81	2.32	2.26	2.81	
1	.82																	
2	.75	.88																
4	.70	.75	.87															
6	.50	.47	.56	.73														
8	—.10	—.26	—.25	—.10	.37													
10	—.34	—.59	—.62	—.54	—.23	.61												
12	—.37	—.62	—.70	—.62	—.39	.35	.83											
14	—.41	—.62	—.73	—.65	—.45	.29	.74	.94										
16	—.48	—.65	—.74	—.67	—.46	.27	.68	.85	.93									
18	—.48	—.58	—.68	—.63	—.47	.17	.54	.68	.78	.90								
20	—.55	—.57	—.63	—.61	—.45	.14	.39	.51	.61	.77	.89							
22	—.42	—.40	—.42	—.43	—.26	.11	.19	.23	.30	.50	.65	.82						
24	—.32	—.27	—.21	—.20	—.08	.08	—.02	—.07	—.01	.19	.36	.59	.80					
26	—.09	—.07	.07	.07	.12	.03	—.12	—.19	—.13	.04	.16	.28	.49	.86				
28	—.09	.14	.29	.07	.02	—.16	—.41	—.36	—.24	.02	.21	.40	.37	.68	.94			
30	.04	.09	.23	—.01	—.56	—.50	—.26	—.24	—.12	.18	.20	—.06	—.23	.25	.80	.93		

Omaha, Nebraska in July

KM	.406	1	2	4	6	8	10	12	14	16	18	20	22	24	26	28	30	32	34	36
NO	198	194	193	192	191	191	188	187	182	172	163	157	150	132	97	67	16	3	2	1
MN	1133	1068	972	797	649	526	422	331	250	185	131	93.7	67.7	49.2	35.8	26.3	19.5	14.2	10.6	7.90
SD	22.5	14.3	12.1	6.57	4.29	3.92	3.07	3.34	5.71	3.76	2.01	1.02	0.61	0.42	0.28	0.22	0.13			
CV	1.99	1.34	1.24	0.82	0.66	0.75	0.73	1.01	2.28	2.03	1.53	1.09	0.90	0.85	0.78	0.84	0.67			
1	.77																			
2	.58	.83																		
4	.41	.48	.69																	
6	.13	.16	.33	.67																
8	.02	.09	.34	.51	.76															
10	.01	.04	.25	.42	.62	.77														
12	—.15	—.26	—.29	—.30	—.26	—.24	.07													
14	—.19	—.29	—.46	—.60	—.52	—.59	—.49	.49												
16	—.29	—.39	—.53	—.65	—.45	—.51	—.42	.40	.88											
18	—.32	—.39	—.45	—.44	—.22	—.19	—.16	.31	.57	.71										
20	—.29	—.32	—.33	—.29	—.12	—.09	—.03	.31	.41	.53	.74									
22	—.43	—.37	—.32	—.27	—.06	—.07	.03	.27	.38	.49	.62	.76								
24	—.39	—.35	—.24	—.24	—.06	.01	.11	.32	.28	.36	.50	.66	.82							
26	—.26	—.34	—.23	—.27	—.01	.06	.19	.36	.20	.32	.41	.53	.63	.79						
28	—.17	—.33	—.32	—.31	—.14	—.08	.04	.42	.27	.38	.41	.53	.58	.61	.82					
30	.10	.03	—.16	—.44	—.30	—.17	—.25	.23	.20	.14	.05	.05	.16	.23	.25	.87				

3.7 REFERENCES

Albrecht, F., 1952, "Mikrometeorolgische Temperaturmessungen vom Flugzeug aus," *Ber. Deutsch. Wetterd. Bad Kissingen*, v. 38, p. 332.

Bannon, B. A., and J. P. Steele, 1960, "Average Water Vapor Content of the Air," *Geophys. Memoirs No. 102*, Meteorological Office, Air Ministry, London.

Chiu, Wan-Cheng, 1959, "The Diurnal Temperature Variation of the Stratosphere Due to Radiative Processes," *J. Meteorol.*, v. 16, p. 354.

Cole, A. E., and A. Court, 1962, "Density Distribution, Inter-level Correlations and Variation with Wind," *Air Force Surveys in Geophysics No. 151*, AFCRL.

Court, A., and H. A. Salmela, 1962, "Measurement Range Required of Meteorological Equipment," *Instrumentation for Geophysics and Astrophysics, No. 22*, AFCRL.

Crawford, C. B., 1951, "Soil Temperatures, a Review of Published Records," *Res. Paper No. 6, NRC No. 2785*, National Research Council, Div. of Building Research, Ottawa, Canada.

Davidson, B., and H. Lettau, ed., 1957, "Great Plains Turbulence Field Program," Pergamon Press, New York.

Department of Defense, 1957, "MIL-STD-210A, Climatic Extremes for Military Equipment," Washington, D.C.

Dobson, G. M. B., A. W. Brewer, and J. T. Houghton, 1962, "The Humidity of the Stratosphere," *J. Geophys. Res.*, v. 67, no. 2, p. 902.

Draeger, R. H., and R. H. Lee, 1953, "Meteorological Data Eniwetok Atoll," *Naval Medical Res. Inst. Memo Rept. 53-8*, Bethesda, Md.

Fleagle, R. G., 1956, "The Temperature Distribution Near a Cold Surface," *J. Meteorol.*, v. 13, p. 160.

Geiger, R., 1957, "The Climate Near the Ground," Harvard University Press (translated by M. N. Stewart et al).

Gringorten, I. I., 1962, "Fitting Meteorological Extremes by Various Distributions," *Quart. J. Royal Meteorol. Soc.*, v. 88, no. 326, p. 170.

Groves, G. V., 1961, "Correlation of Upper Atmosphere Air Density with Geomagnetic Activity, November, 1960," *Space Research II*, Proc. Second Intern. Space Sci. Symp., H. C. van de Hulst, C. de Jager, and A. F. Moore, ed., North Holland Pub. Co., Amsterdam.

Grundmann, W., 1935, Temperature Mess Geraete, "Handbuch der Meteorologie Instrumente," Berlin.

Gumbel, E. J., 1958, "Statistics of Extremes," Columbia University Press, New York.

Gutnick, M., 1962, "Mean Mid-Latitude Moisture Profiles to 31 Km," *Air Force Surveys in Geophysics No. 147*, AFCRL.

Gutnick, M., 1961, "How Dry Is the Sky," *J. Geophys. Res.*, v. 66, no. 9, p. 2867.

Hague, D. W., 1956, "Temperatures of Northern North America," *Res. Study Rept. RER-9*, U.S. Army Quartermaster R & E Command, Environmental Protection Research Div., Fort Lee, Va.

Harris, I., and W. Priester, 1962, "Time-Dependent Structure of the Upper Atmosphere," *Space Research III*, Proc. Third Intern. Space Sci. Symp., W. Priester, ed., North Holland Pub. Co., Amsterdam.

Harris, M. F., F. G. Finger, and S. Teweles, 1962, "Diurnal Variation of Wind, Pressure and Temperature in the Troposphere and Stratosphere over the Azores," *J. Atmos. Sci.*, v. 19, p. 136.

Heastie, H., and P. M. Stephenson, 1960, "Upper Winds over the World," *Geophys. Memoirs No. 103*, Meteorological Office, Air Ministry, London.

Jacchia, L. G., 1962, "Electromagnetic and Corpuscular Heating of the Upper Atmosphere," *Space Research III*, Proc. Third Intern. Space Sci. Symp., W. Priester, ed., North Holland Pub. Co., Amsterdam.

Jacchia, L. G., and J. Slowey, 1962, "Preliminary Analysis of the Atmospheric Drag of the Twelve-foot Balloon Satellite (1961 δ_1)," *Smithsonian Astrophys. Rept. No. 84*.

Lackey, E. E., 1958, "A Method for Assessing and Mapping the January Minimum Temperatures of Northern North America," *Tech. Rept. EP-88*, U.S. Army Quartermaster R & E Command, Environmental Protection Research Div., Fort Lee, Va.

Lettau, H., 1954a, "A Study of the Mass, Momentum and Energy Budget of the Atmosphere," *Archiv für Meteorologie, Geophysik and Bioklimatologie, Serie A*, v. 7, p. 133.

Lettau, H., 1954b, "Improved Models of Thermal Diffusion in the Soil," *Trans. Am. Geophys. Union*, v. 35, p. 121.

Ludlam, D. L., 1962, "Extremes of Atmospheric Pressure in the United States," *Weatherwise*, v. 15.

McClain, E. P., 1962, "A Contribution to the Climatology of the Arctic Stratosphere," *J. Appl. Meteorol.*, v. 1, no. 1, p. 107.

McDermott, D. P., and G. V. Groves, 1962, "Solar Effects on Air Density at 200 and 230 Km," *Space Research III*, Proc. Third Intern. Space Sci. Symp., W. Priester, ed., North Holland Pub. Co., Amsterdam.

Muench, S. W., 1962, "Atlas of Monthly Mean Stratospheric Charts, 1955-1959," *Air Force Surveys in Geophysics No. 141*, AFCRL.

Nicolet, M., 1961a, "The Properties and Constitution of the Upper Atmosphere," *Space Research II*, Proc. Second Intern. Space Sci. Symp., H. C. van de Hulst, C. de Jager, and A. F. Moore, ed., North Holland Pub. Co., Amsterdam.

Nicolet, M., 1961b, "Density of the Heterosphere Related to Temperature," *Smithsonian Astrophys. Rept. No. 75.*

Nicolet, M., 1960, The Properties and Constitution of the Upper Atmosphere, "Physics of the Upper Atmosphere," J. A. Radcliffe, ed., Academic Press.

Paetzold, H. K., 1962, "Satellite Observations," *Space Research III*, Proc. Third Intern. Space Sci. Symp., W. Priester, ed., North Holland Pub. Co., Amsterdam.

Priester, W., H. A. Martin, and K. Kramp, 1960, "Diurnal and Seasonal Density Variations in the Upper Atmosphere," *Nature*, v. 188, p. 202.

Ramdas, L. A., 1948, "The Physics of the Bottom Layers of the Atmosphere," *Proc. 35th Ind. Sc. Cong., Part II: Presidential Addresses.*

Ratner, B., 1957, "Upper-Air Climatology of the United States," *Tech. Paper No. 22,* U.S. Weather Bureau, Dept. of Commerce, Washington 25, D. C.

Rayner, J. N., 1961, "Atlas of Surface Temperature Frequencies for North America and Greenland," *Arctic Meteorol. Res. Group Publ. Meteorol.,* no. 33, McGill University, Montreal.

Rayner, J. N., ed., 1960, "Temperature and Wind Frequency Tables for North America and Greenland," *Arctic Meteorol. Res. Group Publ. Meteorol.,* v. 1, no. 24, and v. 2, no. 25, McGill University, Montreal.

Singer, I. A., and R. M. Brown, 1956, "Annual Variation of Sub-Soil Temperatures About a 600-Foot Diameter Circle," *Trans. Am. Geophys. Union,* v. 37, p. 743.

Sissenwine, N., W. S. Ripley, and A. E. Cole, 1958, "Behavior of Atmospheric Density Profiles," *Air Force Surveys in Geophysics, No. 109,* AFCRL.

Sutton, O. G., 1953, "Micrometeorology," McGraw-Hill Book Co., New York.

Sutton, O. G., 1951, Atmospheric Turbulence and Diffusion, "Compendium of Meteorology," American Meteorological Society.

Tucker, G. B., 1957, "An Analysis of Humidity in the Upper Troposphere and Lower Stratosphere over Southern England," *Meteorol. Res. Paper No. 1052,* Meteorological Office, Air Ministry, London.

Van Valkenburg, S., H. J. Warman, and W. C. Robison, 1959, "Atlas of Mean Daily Minimum Temperatures," *Tech. Rept. EP-110,* U.S. Army Quartermaster R & E Command, Fort Lee, Va.

Westbrook, J. H., 1961, "A Method of Predicting the Frequency Distribution of Wind Chill," *Environmental Tech. Rept. EP-143,* U.S. Army Quartermaster R & E Command, Fort Lee, Va.

Westbrook, J. H., 1962, "A Method for Predicting the Probable Hourly Duration of High Temperatures," U.S. Army Natick Research Labs.

Chapter 4

WINDS

Irving I. Gringorten
Robert W. Lenhard, Jr.
Henry A. Salmela
Norman Sissenwine

The classification of empirical wind structure models is primarily a result of the difficulties in studying the features of atmospheric wind variations of a given scale in time and space. The atmosphere, of course, does not recognize such a classification; it exhibits all the variations continuously in time and space. Application of a particular feature of the atmospheric wind structure to a given engineering problem must be dictated by the physical dimensions of the particular problem.

It should be emphasized that extrapolation of the data beyond the indicated limitations is risky. Local conditions may give extreme wind variations in excess of those presented, even when the local wind structure is free from perturbations such as fronts, thunderstorms, squalls, etc. This being the case, the practicing engineer should avail himself of applicable local meteorological records whenever possible. Information other than that given below is available, and special studies should be made to provide precise answers for specific design problems. A comprehensive source of micrometeorological data on winds and turbulence and of methods of measurement is the Great Plains Turbulence Field Program conducted at O'Neill, Nebraska [Lettau and Davidson, 1957].

4.1 MEAN WIND AS A FUNCTION OF HEIGHT*

4.1.1 Variation of Mean Wind Speed (Lowest 300 Ft)

The vertical change of wind direction within the lowest 300 ft at a given time is usually negligible, particularly if the speed of the overall airflow is strong, and the site is free of major obstruction. The mean wind speed, V, at height z, can be approximated by the following expressions:

Simple power: $$V \propto z^a, \qquad (4\text{-}1)$$

Generalized power: $$V \propto [(z + z_o)^{1-b} - z_o^{1-b}]/(1 - b), \qquad (4\text{-}2)$$

Logarithmic: $$V \propto \ln [(z + z_o)/z_o], \qquad (4\text{-}3)$$

Extended logarithmic: $$V \propto \ln [(z + z_o)/z_o] + f(z, V_1, dT_1/dz_1). \qquad (4\text{-}4)$$

The *roughness parameter*, z_o, is a length determined by the characteristic ground surface. V_1 is the mean wind speed at a reference height z_1 (anemometer level), and dT_1/dz_1 is the mean vertical temperature gradient at z_1. The boundary condition is $V = 0$ at $z = 0$.

The exponent a depends on the height, terrain, thermal stratification, and speed of the overall airflow; it is larger for rough ground, for altitudes below z_1, for relatively small V_1, or for $dT_1/dz_1 < 0$. Values of a vary within limits approximately 0.05 to 0.5. The use of Eq. (4-1) to compute wind profiles is permissible only for crude estimates; a may be taken as 1/7 to 1/5 for $z > z_1$ and as 1/6 to 1/4 for $z < z_1$, exclusive of situations of intense heating or cooling and of weak overall airflow. Table 4-1 lists mean values of a, determined for several locations and two types of terrain.

Equations (4-2), (4-3), and (4-4) have the advantage that the effect of terrain is included explicitly. Typical

Table 4-1. Mean values for the height range from 30 to 300 ft, for $a = (\log V/V_{30})/\log(z/30)$.

Location and Terrain	a
FAIRLY LEVEL OPEN COUNTRY	
Ann Arbor, Michigan	0.14
Sale, Victoria, Australia	0.16
Cardington, Bedfordshire, Eng.	0.17
Leafield, Oxfordshire, Eng.	0.17
FAIRLY LEVEL WOODED COUNTRY	
Quickborn, Germany	0.23
Upton, Long Island, New York	0.26
Akron, Ohio	0.22

* Based on original article by H. H. Lettau and D. A. Haugen *Handbook of Geophysics for Air Force Designers*, 1957.

values for z_o are given in Table 4-2. The exponent b depends primarily upon thermal stratification. For $dT/dz = 0$ (neutral condition), b is unity. Equation (4-3) is the asymptomatic form of Eq. (4-2) as b approaches unity. Table 4-3 lists mean values of the exponents a and b that were determined for typical daytime ($dT/dz < 0$) and nighttime ($dT/dz > 0$) conditions in the lowest 30 ft over open prairie country (Great Plains Turbulence Field Program). The behavior of b at levels above 30 ft is not very well known. The same is true for the function in Eq. (4-4). Lake [1952] shows that b can be computed on the basis of Eq. (4-4). For relatively strong overall airflow, even intense surface heating or cooling causes only a small deviation of thermal stratification from the neutral. In such cases, Eq. (4-3) represents the true conditions with relatively high accuracy. Table 4-4 lists $V_z/V_1 = [\log(1 + z/z_o)] / [\log(1 + z_1/z_o)]$ for a variety of roughness parameters.

Table 4-5 shows the ratio of wind speed at various heights to that at 300 ft; values are based on actual wind measurements taken during the Great Plains Turbulence Field Program.

The wind profile formulas may be used for reducing or standardizing wind data reported by individual stations with different anemometer levels. The result of a wind extrapolation, however, is decisively dependent on the representativeness of the wind measurement at the reference level. If the anemometer mast is in a poorly defined terrain, the validity of the wind profile formulas is questionable. Uniformity of the terrain is a factor which improves the result. Winds observed with a land-situated anemometer cannot be used to estimate the wind speed over an adjacent water surface. In certain cases, the wind speed over uniform terrain may attain a maximum value at a level significantly below 300 ft. Such cases usually occur in cold air flow; for example, nocturnal slope winds or sea breezes.

Table 4-2. Typical values of the roughness parameter, z_o.

Type of Surface	z_o (ft)
Smooth (mud flats, ice)	0.00003
Lawn, grass up to 0.4 in.	0.003
Downland, thin grass up to 4 in.	0.02
Thick grass, up to 4 in.	0.075
Thin grass, up to 20 in.	0.16
Thick grass, up to 20 in.	0.30

Table 4-3. Mean values for the lowest 30 ft of exponents in Eq. (4-1) and (4-2), determined from wind profile measurements.

z (ft)	exponent a			exponent b	
	day	night	neutral	day	night
30	0.11	0.38	0.14	1.25	0.45
15	0.13	0.31	0.16	1.15	0.50
3	0.18	0.23	0.21	1.05	0.75

Table 4-4. Ratios of wind at height z at two reference levels (z_1) for various roughness parameters (z_o), calculated by Eq. (4-3).

z (ft)	$z_o = 1$ ft	$z_o = 0.1$ ft	$z_o = 0.01$ ft
	V_z/V_1 FOR $z_1 = 20$ FT		
300	1.87	1.51	1.36
200	1.74	1.43	1.30
100	1.52	1.30	1.21
50	1.28	1.17	1.12
20	1.00	1.00	1.00
10	0.79	0.87	0.91
5	0.59	0.74	0.82
2	0.36	0.57	0.70
	V_z/V_1 FOR $Z_1 = 10$ FT		
300	2.38	1.73	1.49
200	2.21	1.65	1.43
100	1.92	1.50	1.33
50	1.64	1.35	1.23
20	1.27	1.15	1.10
10	1.00	1.00	1.00
5	0.75	0.85	0.90
2	0.46	0.66	0.80

Table 4-5. Ratio of wind speed at height z to speed at 300 ft over open prairie (Great Plains Turbulence Field Program).

z (ft)	V_z/V_{300}		
	Day	Night	Neutral
300	1.000	1.000	1.000
100	0.965	0.689	0.872
70	0.944	0.608	0.829
50	0.915	0.538	0.792
30	0.866	0.452	0.733
20	0.825	0.403	0.686
10	0.749	0.339	0.604
5	0.662	0.275	0.518
2	0.556	0.236	0.424
1	0.470	0.200	0.336
0.5	0.383	0.166	0.300

4.1.2 Wind Direction Shifts (Lower 10,000 Ft)

Normally, the wind direction shifts with height. Shifts with increasing height are termed *veering* if the wind turns clockwise, and *backing* if the wind turns counterclockwise. Veering is usually expressed as the rate of turning in degrees per height interval (negative for backing).

Wind direction shifts with height are caused by surface frictional effects, and by height changes of the horizontal pressure patterns controlling the mean airflow. The following discussion excludes such phenomena as slope winds, land and sea breezes, nocturnal low-level airflow conditions in the equatorial zone, and rapid, small-scale wind fluctuations.

In the free atmosphere, the mean horizontal airflow blows approximately parallel to the isobars, the lower pressure being to the left. The *gradient wind* is defined as a horizontal wind velocity, tangent to the contour line of a constant pressure surface or to the isobar of a geopotential surface. Surface friction reduces the speed, causing a component of the surface wind to blow across the isobars toward lower pressure. Thus, the wind direction changes with height to align itself with the gradient wind in the free atmosphere. A height change of the horizontal pressure pattern is caused by horizontal temperature gradient effects such that the advection of relatively cold air is associated with weakening, and the advection of relatively warm air with strengthening, of the frictional wind direction shift with height.

To a first approximation, it can be said that under strong mean wind conditions on the Northern Hemisphere, the winds will veer with height in the lower 3000 ft, the magnitude of the veering being determined by the intensity of advection processes. Warm air advection increases and cold air advection decreases the magnitude of frictional veering or causes backing of the winds. The conditions for veering and backing are reversed for the Southern Hemisphere. North of approximately 20°N latitude, winds in the lowest 3000 ft of the atmosphere will usually display varying degrees of veering with relatively few cases of backing. Southerly surface winds will veer more with height than northerly surface winds. Above approximately 3000 ft, southerly winds will continue to veer with height, while northerly winds will begin to show backing with height.

Tables 4-6, 4-7, and 4-8 indicate the order of magnitude of veering with associated general meteorological condi-

Table 4-6. Typical frictional veering of wind over plain land with moderately strong gradient winds (34 knots) and no advection; 51.3°N, 12.5°E, 20 October, 1931. (After H. Lettau, *Tellus*, v. 2, p. 125, 1950.)

Height (1000 ft)	Average Speed (knots)	Angle* (deg)	Veering (deg/100 ft)
2.0 to 3.0	34	7	0.7
1.0 to 2.0	32	15	0.8
0.5 to 1.0	26	21	0.8
0.0 to 0.5	18	25	0.7

* Angle between wind and the gradient wind.

Table 4-7. Average angle formed by the wind and the gradient wind, and average veering for weather stations in Germany, grouped according to topography. (After H. Lettau, *Atmospharische Turbulenz*, Akademische Verlagsgesellschaft M. B. H., Leipzig, 1939.)

Height (1000 ft)	Coastal Plains	Rolling Country	Hilly Land
	ANGLE (deg)		
3.0 to 5.0	0	2	3
2.0 to 3.0	2	5	10
1.0 to 2.0	10	17	25
0.5 to 1.0	22	30	36
0.0 to 0.5	29	36	43
	VEERING (deg/100 ft)		
3.0 to 5.0	0.1	0.2	0.3
2.0 to 3.0	0.2	0.6	1.2
1.0 to 2.0	1.3	1.8	1.6
0.5 to 1.0	1.5	1.4	1.3
0.0 to 0.5	1.5	0.9	1.3

Table 4-8. Average veering (deg/100 ft) for various ranges of height; means (1918 to 1920) for three stations in U.S.A. in the latitude zone 31° to 36° (average 33°N), and three in latitude zone 40° to 45° (average 43°N). (Condensed from W. R. Gregg, *Monthly Weather Review*, Suppl. No. 20, 1922.)

	Southerly Surface Winds				Northerly Surface Winds			
	Summer		Winter		Summer		Winter	
Height (1000 ft)	33°N	43°N	33°N	43°N	33°N	43°N	33°N	43°N
9.0 to 12.0		0.7	1.0	0.7		−1.0	−0.9	−0.7
5.0 to 9.0	0.3	1.0	0.7	1.0	−0.3	−1.0	−0.3	−0.7
2.0 to 5.5	0.3	0.7	0.7	0.9	−0.5	−0.4	−0.3	−0.7
1.2 to 2.0	0.9	0.7	1.0	1.0	−0.3	−0.3	0.9	0.9
0.5 to 1.2	0.7	0.7	0.9	1.3	0.7	0.7	0.9	1.3
0.0 to 0.5	0.7	0.7	1.1	1.3	0.5	0.7	1.1	1.3

tions. Because no advection is permitted for the situation described in Table 4-6, the veering is almost constant and represents the gradual decrease of the surface frictional effect with height. Once the gradient level of the free atmosphere is reached, frictional effects and, hence, veering become negligible in the case of no advection. Strong surface winds generally make an angle with the gradient wind of 10° to 30°; this is the overall veering found in the frictional layer of the atmosphere when little or no advection exists. The direction of the surface wind is insignificant. Total veering over the entire layer of frictional influence depends primarily on the roughness characteristics of the earth surface: the average for oceans is 5° to 15°; for continents, 25° to 45°. The average veering is usually greater in winter than in summer, and greater at northern stations than at southern stations. The averaging process masks the variability of veering that would be encountered with isolated observations in time and space. In the first 3000 ft of the atmosphere, however, the importance of the general direction of the surface wind in obtaining reasonable estimates of veering appears doubtful. Above this layer, southerly winds veer with height, northerly winds back with height. Maximum values of veering in the frictional layer are near 3°/100 ft; isolated cases of backing of the same order of magnitude are observed. The average total veering (or backing) in the lower 3000 ft is 20° to 40°, with isolated cases of 70° to 90°. To a first approximation, it may be assumed that this veering (or backing) is evenly distributed throughout the layer. Above this layer, primarily dependent on horizontal advection conditions, winds will show veering or backing with approximately the same average order of magnitude as in the frictional layer.

4.1.3 Diurnal Variation and Low-Level Jet Streams (Lower 6000 Ft)

The mean diurnal variation of wind speed at various heights above any given site is caused by diurnal variations of the force due to the horizontal pressure gradient and the frictional force. The regular variations of the former are controlled by solar and lunar tidal effects, which produce predominantly a 12-hourly wave, and by differential solar heating of the air over different locations and consequent horizontal density gradients. In the troposphere the tidal motions of the atmosphere are small (range less than 1 knot). The barometric effects of differential solar heating produce marked diurnal wind variations only in special locations; for example, along coast lines and the rims of extended high plateaus. Over most parts of the continents the diurnal variation is controlled by the horizontally uniform effects of the cycle of solar heating and nocturnal cooling of the earth's surface. Consequent changes in the vertical thermal stratification of the atmosphere at 3000 to 6000 ft significantly influence the effective frictional force in large-scale airflow. The vertical extent of the atmosphere that has diurnal variations of mean wind speed varies roughly as the height of convective activity (normally, about 6000 ft).

Over relatively smooth land the daytime thermal stratification intensifies, whereas nocturnal thermal stratification weakens, the vertical mixing. This causes a wind speed maximum near the ground at about midafternoon, and a minimum in the early morning hours. Figure 4-1 shows that the phase of diurnal wind variation reverses in the atmosphere above the layer close to the ground. The boundary between the atmospheric layers of opposite phase varies with climatic zone, season, and surface roughness; average height is 300 to 600 ft. The amplitude of the diurnal variation of wind speed normally has two maxima, approximately 20 and 2000 ft.

Over the midwestern United States, the nocturnal maximum of wind speed (above approximately 300 ft) frequently leads to a sharp peak of the velocity profile at heights of 1000 to 3000 ft. The peak, usually at the top of the nocturnal inversion, is significantly stronger (supergeostrophic) than predicted from a balance between the horizontal pressure gradient and the Coriolis forces; it is often associated with extremely large values of wind shear. These peak winds are called low-level jet streams. The supergeostrophic wind speeds (peak speeds up to 50 knots in a pressure field resulting in 20 to 30 knots of geostrophic speed) suggest that an inertial oscillation of the air masses is induced when the constraint imposed by the daytime mixing is released by the initiation of an inversional thermal stratification at about the time of sunset. Average wind profiles showing the development of a low-level nocturnal jet stream over O'Neill, Nebraska, are

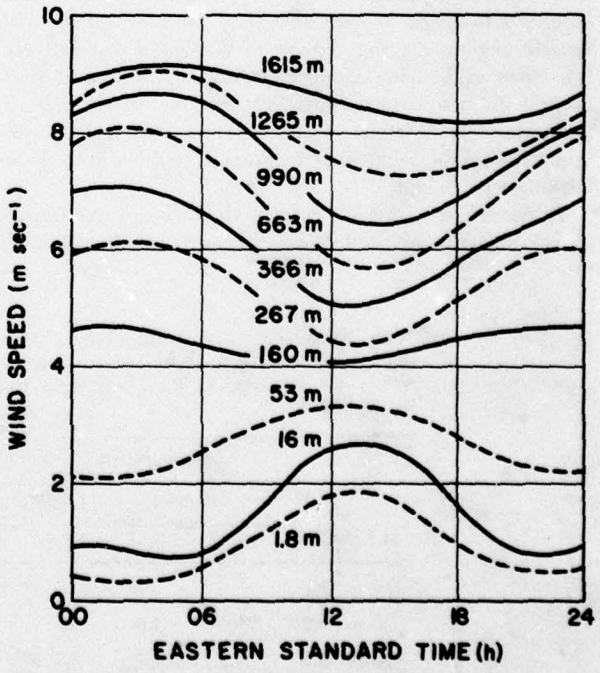


Fig. 4-1. Diurnal curves (slightly smoothed) of annual mean wind speed at Oak Ridge, Tennessee, average for 1948 to 1952. The wind speed data at heights of 1.8 and 16 m are from anemometer recordings; for other heights, data were obtained from pilot-balloon soundings at 4-h intervals. (Dashes are for clarity of illustration.)

given in Table 4-9. The largest value of wind speed variation, with height recorded during the development of a low-level jet stream, was obtained by kite observation at Drexel, Nebraska, on the night of 18 March 1918. The surface wind speed was 5 knots, but at an elevation of 780 ft, the reported wind speed was 70 knots. Wind records from the 1428-ft Cedar Hill television transmitter tower near Dallas, Texas, show that in the early morning hours (23 February 1961), after development of a low-level jet, a wind speed maximum of 63.7 mile h^{-1} occurred at 1200 ft, while at 30 ft the speed was 14.9 mile h^{-1}.

Over the ocean the diurnal variation of wind speed is negligible because diurnal variations in thermal stratification are extremely small. In coastal regions where land and sea breezes are experienced, the amplitude and phase of the diurnal variation of wind speed are comparable with those over land. A reversal of phase with height is questionable, however. The vertical extent of sea breezes is normally about 3000 ft, the land breeze about 1500 ft, the overall land-sea breeze system about 10,000 ft.

In mountainous regions, the daytime, up-slope valley winds (2 to 6 knots) are normally stronger than the nighttime down-slope mountain winds (1 to 4 knots). The mean amplitude of the variation decreases very slightly with height. A reversal of phase with height is occasionally found. The vertical extent of the valley breeze is about that of the height of the surrounding ridges; the moun-

Table 4-9. Average wind profiles (speed and direction at various heights) showing development of nocturnal low-level jet stream. (Average of five nights of observations, Great Plains Turbulence Field Program, O'Neill, Nebraska.)

	Mean Local Time							
	1800		2000		2200		2400	
Height (1000 ft)	Speed (knots)	Dir. (deg)	Speed (knots)	Dir. (deg)	Speed (knots)	Dir. (deg)	Speed (knots)	Dir. (deg)
6.5	11.8	223	8.3	225	6.8	223	6.0	231
6.0	14.0	219	9.8	226	7.8	227	6.6	233
5.0	18.3	213	16.1	225	10.8	229	9.7	232
4.0	21.2	207	23.8	217	21.0	225	17.2	223
3.0	22.6	194	28.6	202	27.0	211	25.4	219
2.5	22.8	190	30.2	193	30.8	204	31.5	213
2.0	22.6	182	30.6	190	33.4	196	38.0	203
1.5	22.3	180	30.4	185	34.8	190	39.0	196
1.0	21.0	177	28.5	178	35.0	183	36.7	189
0.5	18.9	174	26.4	171	29.0	175	29.4	183
0.3	17.9	173	23.7	167	24.9	170	25.0	179 ← 179
	0200		0400		0600		0800	
	Speed (knots)	Dir. (deg)	Speed (knots)	Dir. (deg)	Speed (knots)	Dir. (deg)	Speed (knots)	Dir. (deg)
6.5	7.8	227	7.1	214	6.4	208	8.8	208
6.0	8.1	226	7.5	220	7.1	212	9.5	208
5.0	10.4	226	8.8	227	9.3	213	12.0	204
4.0	16.5	227	15.5	228	13.0	218	16.2	203
3.0	26.2	224	23.6	228	20.3	220	21.8	213
2.5	32.0	219	28.2	225	24.7	220	24.1	215
2.0	36.7	211	34.0	217	30.4	217	27.0	215
1.5	38.6	203	36.8	209	33.4	213	29.0	213
1.0	37.0	196	36.3	199	33.6	204	27.2	204
0.5	33.2	189	31.4	191	28.2	195	24.5	195
0.3	26.0	187	27.0	189	24.6	191	23.0	191

tain breeze, a few hundred feet; the whole system, about 1000 ft above the height of the ridges.

The various features of local wind variation discussed here occur frequently. In general, they are easily observable during conditions of clear skies and light to moderate intensity of the large-scale airflow. It should be remembered, however, that when the diurnal variations are not readily observable, they might be superimposed on the large-scale airflow. Empirical wind structure models not accounting for possible diurnal variations would then be in error.

4.2 LARGE-SCALE WIND STRUCTURE

The change and movement of pressure patterns in the atmosphere cause standard wind observations (e.g., the mean wind over 1 min) to vary from time to time at a given place, and from place to place at a given time. In general, as shown in Fig. 4-2, the amount of change in wind between two observations increases with the time interval between them and with the distance between observing points. The rate of increase in wind change with increasing time or space interval between observations is, in turn, a variable depending upon season, geographic location, average wind speed, nature of the sample, and, to some extent, height above the ground.

Most of the wind variability data pertaining to the free atmosphere are derived from standard pilot balloon or rawinsonde observations. Lower limits of resolution of these observations are such that minimum intervals for wind variability are about 15 min or 4 miles. The small-scale fluctuations appear to be fairly random, and their combined effect on ballistic or synoptic-scale forecasting problems normally cancel out and, thus, are neglected.

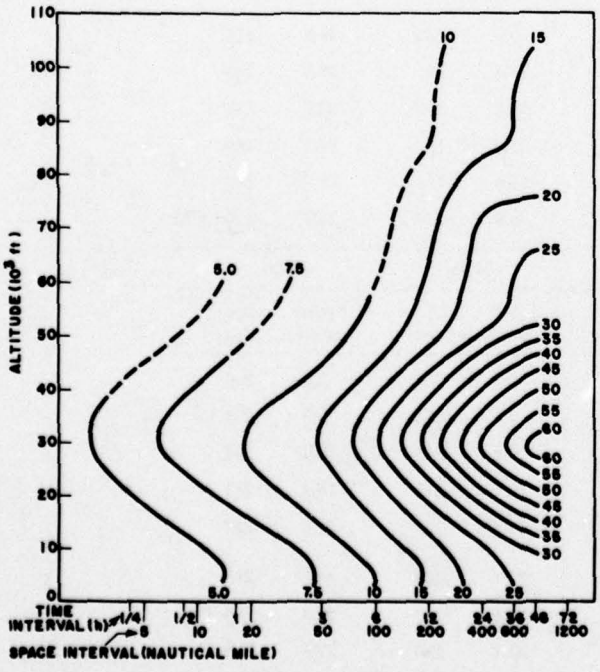


Fig. 4-2. Isopleths of time and space variabilitities of changes in the mean vector wind with altitude; the rms (63rd percentile) values, in knots, of observed changes for various time lags between observations, and of derived changes for various distances are given on each curve. (From Ellsaesser [1960].)

Several measures of wind variability are possible. The most useful measure is the root-mean-square of the vector change in wind; others commonly used are the mean and the median absolute vector differences. All of these are scalar measures computed from the magnitudes of the difference vectors. They are related in a circular normal distribution which is usually a good approximation to the frequency distribution of wind changes. The rms value is 1.13 times the absolute mean and 1.205 times the median.

4.2.1 Time Variability up to 30 Km

The time rate of change of wind in the frictional layer is affected by the topography and the thermal structure. The results in Table 4-10 are for steady southerly flow conditions from seven observational periods, all but one of which extended over 24 h (pilot balloon, rawinsonde, and smoke-puff observations are combined). The effect of thermal stratification is indicated by comparison of the day and night values for time differences up to 8 h.

The change in wind variability above the frictional layer with increasing time between observations and with altitude is illustrated in Fig. 4-2. Figure 4-3 shows the effect of latitude and season for a 24 h lag between wind observations.

For relatively short periods during which the pattern of the winds is fairly stable, the variability of the wind is given directly by

$$S_t = Kt^p, \tag{4-5}$$

where S_t is the rms change in wind during the time interval t, and K is a constant. The exponent p depends on r_t, the correlation coefficient between winds separated by the time interval t. At short lags where r_t is 1, p is 1; at greater lags where r_t is 0, p is 0.5. For t in hours and S_t in miles per hour,

$$S_t = 4\,t^{0.5} \tag{4-6}$$

is a suitable generalization for middle latitudes and for lag intervals of 30 min to about 12 h. Although this empirical relation is an acceptable average, K actually depends on the mean wind speed. The mean wind varies with season, altitude, and geographic location (see Table 4-21 at end of chapter), hence values of K other than 4 will, on some occasions, be more applicable to engineering problems. Values of K from 3.4 to 14.2 are tabulated by Arnold and Bellucci [1957]. An analysis of the relationship of K to the mean wind in a stable flow pattern shows that K increases from about 1 at speeds of 5 mile h^{-1} to perhaps 5 or 6 at speeds of 35 mile h^{-1} and higher.

An indirect model relates the variability in time to r_t and to the climatological dispersion of the winds. This relationship is given by

$$S_t = \sigma_t \sqrt{2\,(1 - r_t)}, \tag{4-7}$$

Table 4-10. Mean and standard deviation of absolute value of vector velocity differences at various time intervals, Δt, in the lower 6000 ft over smooth open terrain (Great Plains Turbulence Field Program).

Height (1000 ft)	Velocity Differences (knots)					
	Δt = 2 hours		Δt = 4 hours		Δt = 8 hours	
	Day	Night	Day	Night	Day	Night
6.0	5.8 ± 3.3	6.4 ± 4.7	9.7 ± 5.0	8.7 ± 6.2	14.4 ± 4.7	7.8 ± 5.6
4.5	5.0 ± 2.9	5.4 ± 3.7	8.2 ± 4.9	8.2 ± 5.0	10.5 ± 5.4	9.9 ± 6.4
3.0	5.0 ± 3.3	7.6 ± 4.9	8.0 ± 4.3	10.9 ± 5.0	10.5 ± 3.7	14.6 ± 6.0
1.8	6.0 ± 4.3	7.8 ± 5.4	9.3 ± 6.0	12.6 ± 6.8	13.2 ± 5.4	18.7 ± 6.0
1.2	5.8 ± 3.7	7.8 ± 5.8	9.3 ± 6.4	13.4 ± 8.7	13.8 ± 6.8	12.0 ± 6.8
0.6	5.0 ± 4.7	6.6 ± 6.0	8.3 ± 5.6	11.7 ± 10.5	12.1 ± 6.0	17.3 ± 9.5

	Δt = 12 hours	Δt = 16 hours	Δt = 20 hours	Δt = 24 hours
6.0	11.1 ± 5.6	12.4 ± 6.0	14.6 ± 6.8	12.6 ± 6.4
4.5	12.2 ± 6.0	12.8 ± 5.8	11.5 ± 4.1	9.3 ± 5.0
3.0	15.2 ± 5.8	15.0 ± 6.8	11.5 ± 5.4	8.5 ± 5.0
1.8	19.8 ± 7.6	17.1 ± 8.0	13.4 ± 7.8	9.5 ± 6.4
1.2	20.2 ± 8.0	17.1 ± 7.0	13.8 ± 9.5	8.9 ± 5.6
0.6	16.1 ± 7.2	14.0 ± 7.4	11.7 ± 9.5	8.3 ± 7.6

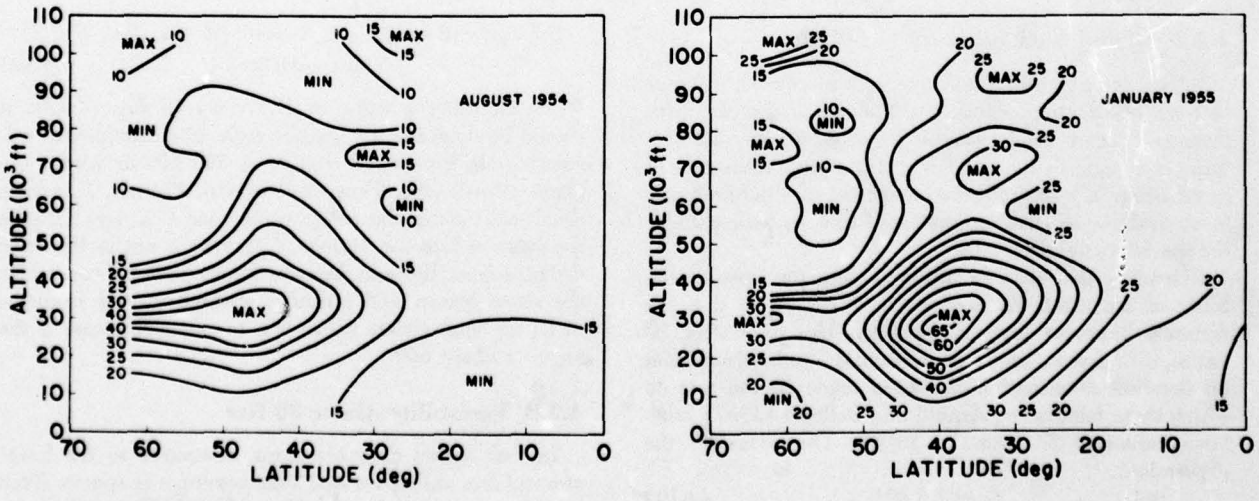


Fig. 4-3. Distribution in latitude and altitude of the vector wind variability (S_t) for a 24-h time lag between observations along the meridian 75°W in summer and winter (August 1954 data are for East Africa); rms values in knots are shown on curves. (From Ellsaesser [1960].)

where σ_t is the standard vector deviation of the winds (rms deviation from the vector resultant wind). The vector stretch correlation coefficient between the initial wind having components u and v, and the wind after a time interval t, having components x and y, is given by

$$r_t = \frac{\Sigma(ux + vy)}{\sqrt{\Sigma(u^2 + v^2)\ \Sigma(x^2 + y^2)}} \ . \qquad (4\text{-}8)$$

This parameter undergoes an exponential decay, with increasing lag for intervals up to 24 h or more, and then appears to oscillate about zero. The relation,

$$r_t = \exp\ (-0.0248t), \qquad (4\text{-}9)$$

with t in hours, is widely used. This equation, in conjunction with Eq. (4-7) and values of σ_t given in Table 4-21, allows an estimate of the wind variability for a desired lag interval that pertains specifically to the place, season, and altitude of interest. This model has two serious limitations; it will not permit r_t to become negative, nor does the constant coefficient of t allow for variations in the rate of decay of the correlation. At sufficiently large time intervals, r_t does become negative, and r_t is so close to zero for lags in excess of 72 h that the model becomes unreliable. In some cases r_t becomes negative at shorter lags, and the lag at which this occurs varies from place to place. Investigations of the rate of decay of correlation show that it varies geographically, seasonally, and probably with altitude. The variation has been mapped only for the United States at 18,000 ft [Ellsaesser, 1960].

Attempts to develop a more precise model of the variability of winds with time have resulted either in only moderate improvement or extremely complex models. Thus Eq. (4-9) is considered the most useful approximation. When precision in estimating the wind variability with time is required, a special climatological study must be made.

4.2.2 Spatial Variability up to 30 Km

In general, varability increases with increasing distance between observation points, and the rate of increase with distance depends on geographic location, season, and altitude. A change in the wind with time can be thought of as resulting in part from the movement of wind-field patterns over the observing point, and thus as analogous to the spacial variability.

Extending this analogy to the models, the space variability of the wind, S_d, is given by $K'd^p$, where d is the distance between observing points. The parameter K′ varies with season, geographic location, and altitude, but no detailed examination has been made of the way in which these factors act. Arnold and Bellucci [1957] tabulated values of K′ from 1.1 to 6.1. They consider the expression,

$$S_d = 1.5\ d^{0.5}, \qquad (4\text{-}10)$$

where S_d is in mile h^{-1} and d in miles, as representative for middle latitudes.

The indirect model provides several empirical curves [Durst, 1954] for the decay of the correlation coefficient of winds with increasing separation between observing points. These curves indicate differing rates of decay depending upon latitude and upon the orientation of the line connecting the observing points. The analogy between time and space variability of the winds extends to these curves. Figure 4-2 indicates that, for temperate latitudes, a general approximation to the space variability of winds can be obtained by taking 3 h as equivalent to 50 nautical miles. The space variability is then estimated in a manner similar to time variability from $\sigma_d \sqrt{2(1 - r_d)}$; r_d is the correlation coefficient between winds separated by the distance interval d.

In a more sophisticated model that permits negative correlations, the winds are resolved into components along and across the line connecting the two observation points. The behavior of the correlation of these components is independent of the orientation of this line, but differs between components. The component correlation coefficients are expressed by empirical equations:

$$r_{ux} = k \exp\ (-d^2/2L^2),$$
and
$$r_{vy} = k\ (1 - d^2/L^2)\ \exp\ (-d^2/2L^2). \qquad (4\text{-}11)$$

The winds at two points, separated by the distance d, are resolved into longitudinal components u and x parallel to the line connecting the observing points and transverse components v and y. The parameter k is related to errors of observation and to the magnitude of small-scale eddies; it usually falls in the range $0.7 < k < 1.0$. The parameter L is related to the size of the large-scale wind systems; it varies appreciably with the season and to some degree with altitude and geographic location. Figures 4-4 through 4-9 are charts of this variation. The rms vector change of wind with distance may be estimated for a specific place and season by use of these charts and Eq. (4-11), and by assuming a circular normal distribution of the winds, so that

$$S_d^2 = \sigma^2\ (2 - r_{ux} - r_{vy}) = \sigma^2\ [2 - k\ (2 - d^2/L^2)\ \exp\ (-d^2/2L^2)]. \qquad (4\text{-}12)$$

When selecting a value of L for use in Eq. (4-12), it should be done for the specific path. For example, in calculating the rms wind change at 500 mb in winter between Brownsville, Texas and Miami, Florida, L is very nearly 725 along the entire route (see Fig. 4-4); this is the value of L to use. Omaha, Nebraska is nearly the same distance from Brownsville as is Miami, but the route (for the same season and altitude) crosses several isopleths of L; the appropriate value of L to use in this case is the mean of about 650.

4.2.3 Variability Above 30 Km

In this region data are scant, compared to the lower atmosphere, and space and time coverage is sparse. Even the Meteorological Rocket Network (MRN) wind observations are from a limited network of stations and for selected dates. Because both turbulence and organized wave motions exist in the mesosphere and upper stratosphere, it is inferred that time variability of winds should

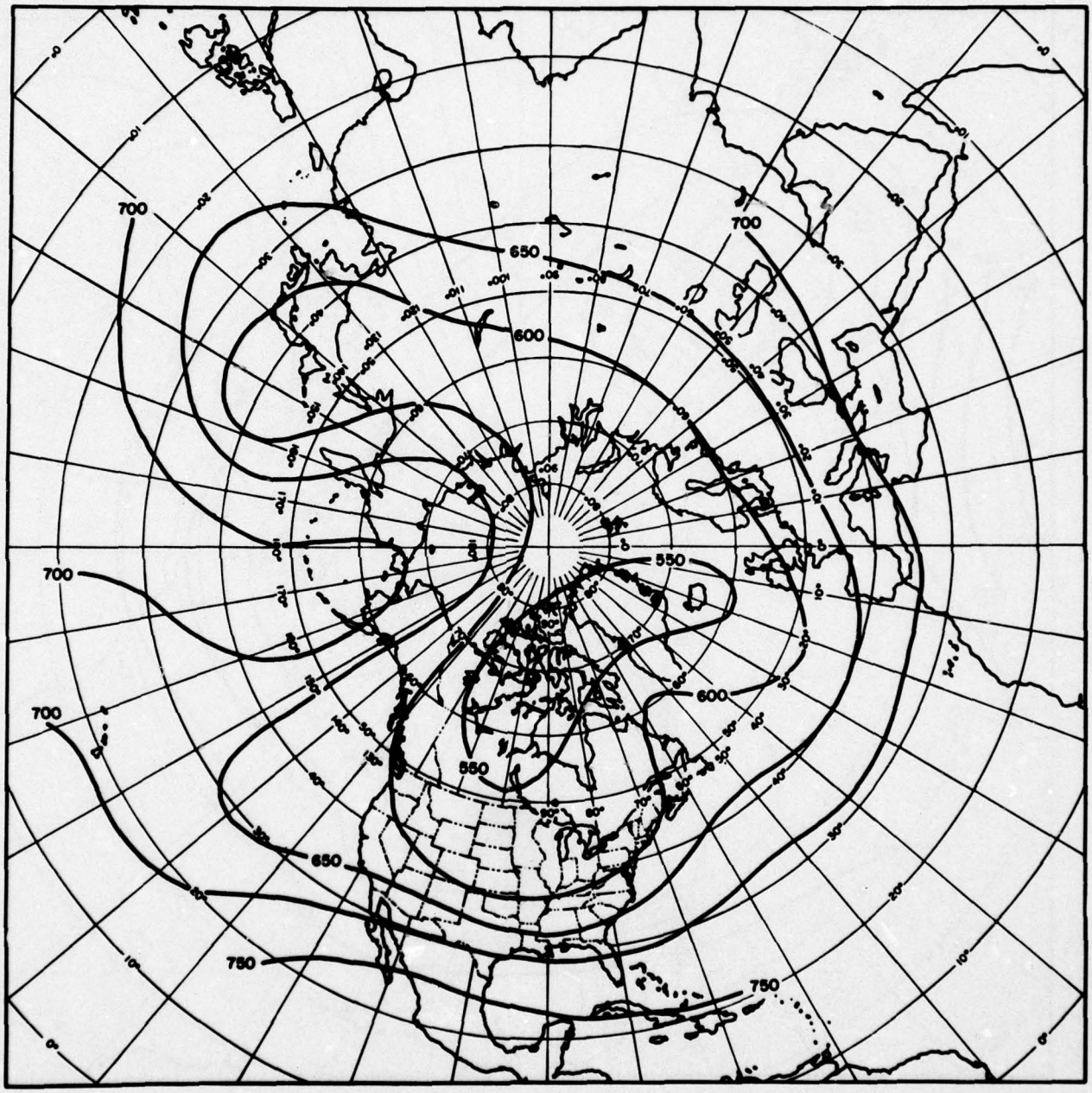


Fig. 4-4. Isopleths of the size parameter, L, at 500 mb (see Eq. 4-15 and 4-16) pressure level in Winter; numbers on curves are values of L in nautical miles. (From C. E. Buell, Final Report Contract AF19(604)-7282, July 1962.)

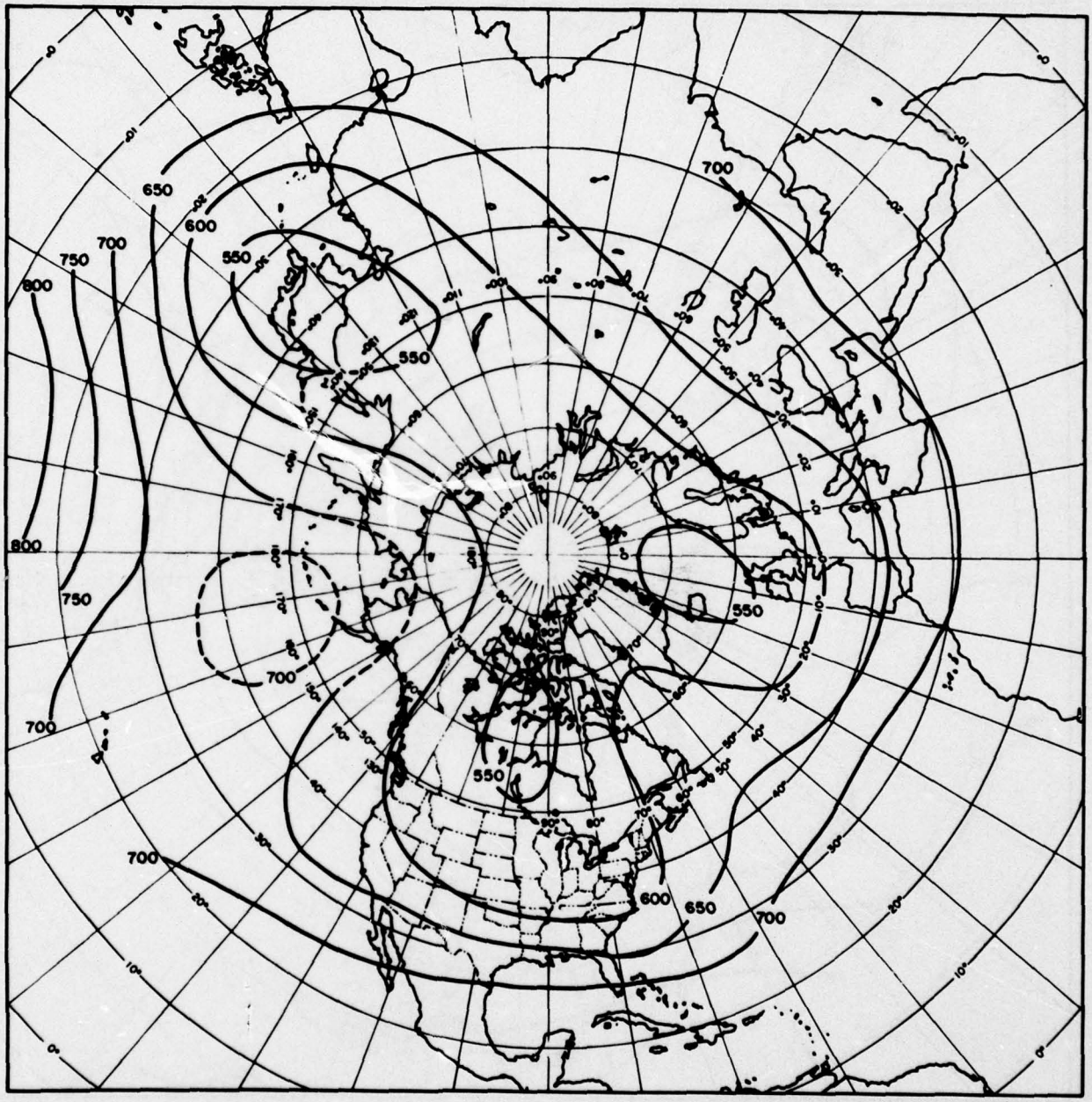


Fig. 4-5. Isopleths of the size parameter, L, at 300 mb (see Eq. 4-15 and 4-16) pressure level in Winter; numbers on curves are values of L in nautical miles. (From C. E. Buell, Final Report Contract AF19(604)-7282, July 1962.)

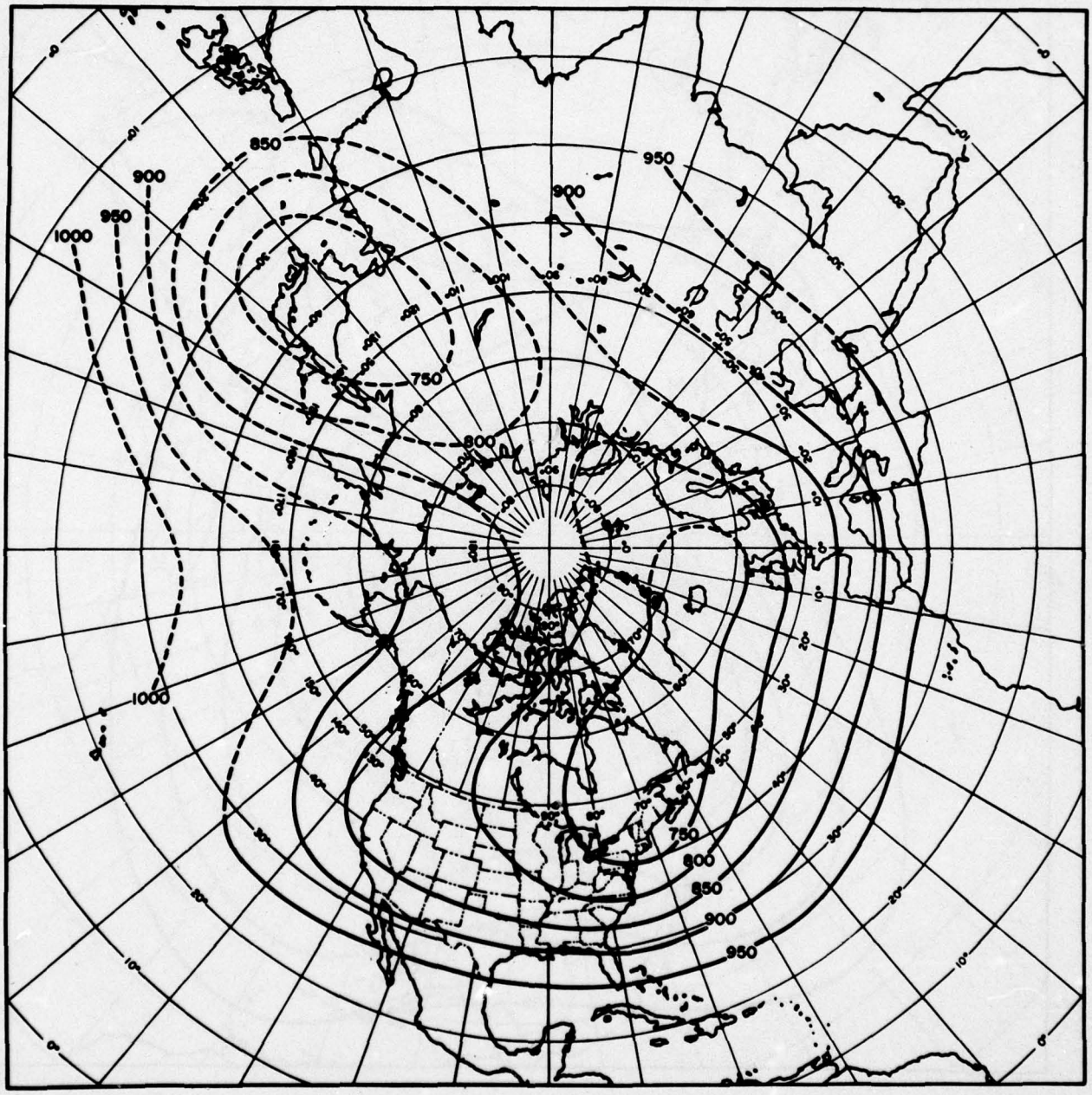


Fig. 4-6. Isopleths of the size parameter, L, at 100 mb (see Eq. 4-15 and 4-16) pressure level in Winter; numbers on curves are values of L in nautical miles. (From C. E. Buell, Final Report Contract AF19(604)-7282, July 1962.)

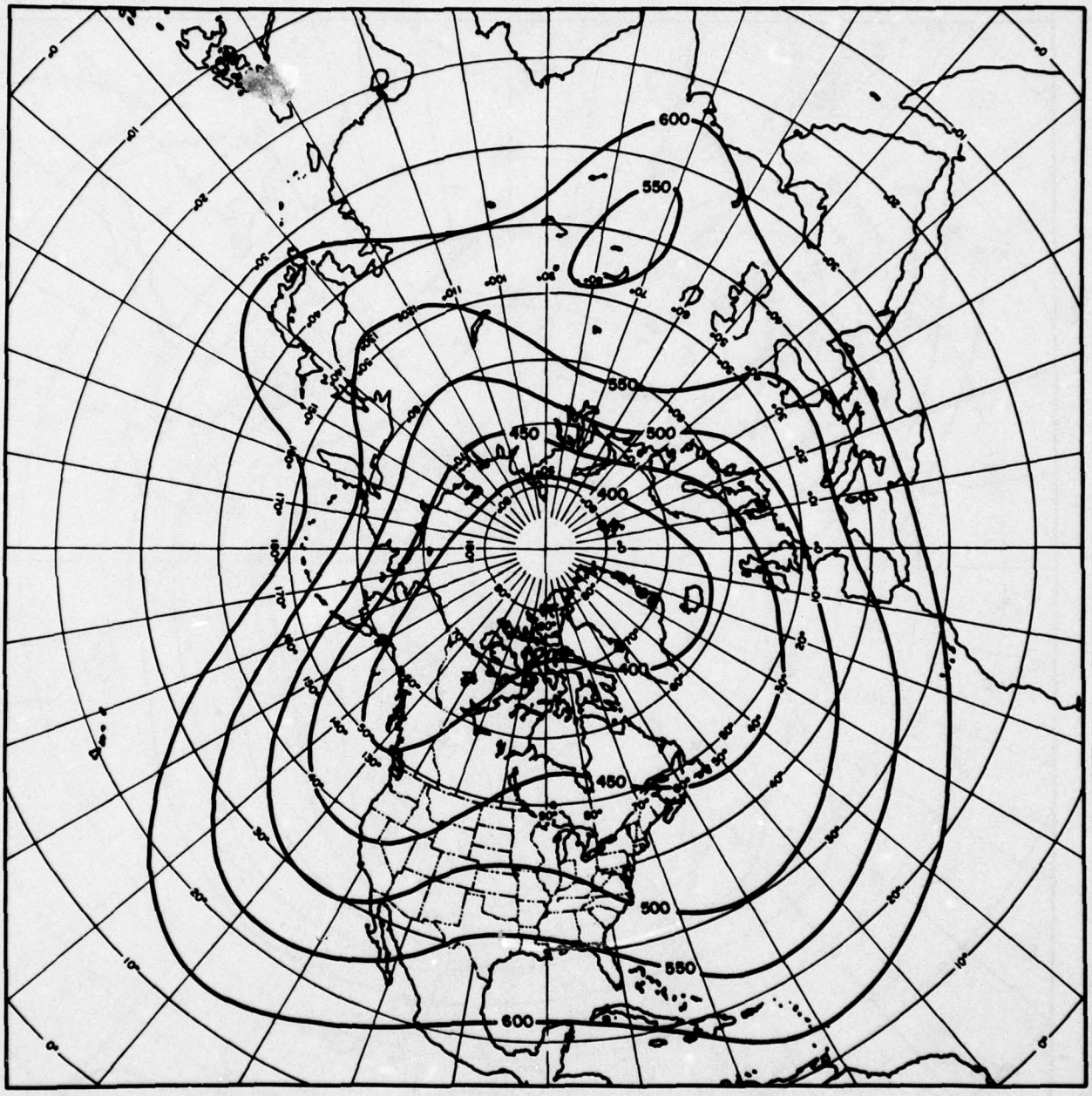


Fig. 4-7. Isopleths of the size parameter, L, at 500 mb (see Eq. 4-15 and 4-16) pressure level in Summer; numbers on curves are values of L in nautical miles. (From C. E. Buell, Final Report Contract AF19(604)-7282, July 1962.)

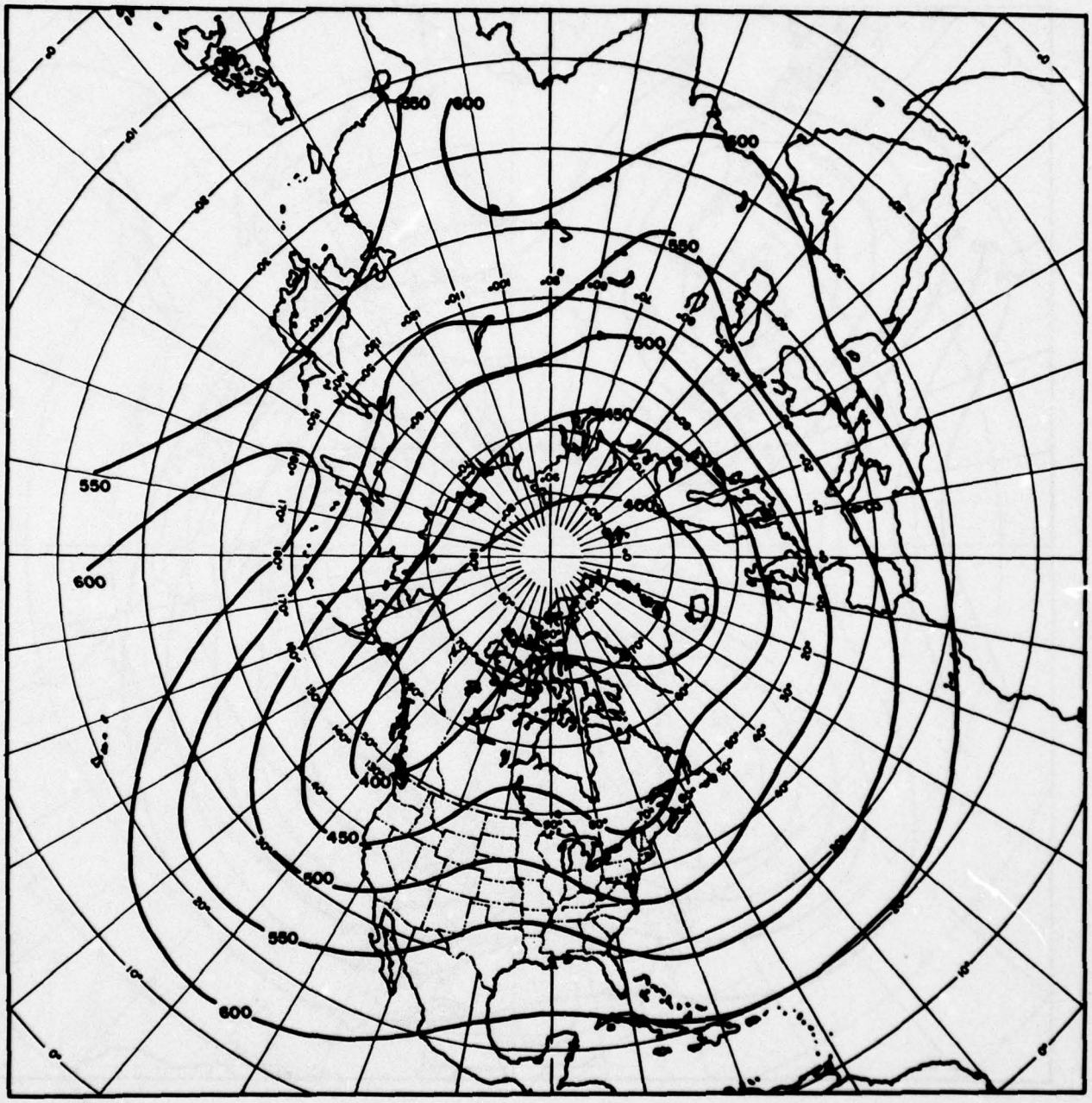


Fig. 4-8. Isopleths of the size parameter, L, at 300 mb (see Eq. 4-15 and 4-16) pressure level in Summer; numbers on curves are values of L in nautical miles. (From C. E. Buell, Final Report Contract AF19(604)-7282, July 1962.)

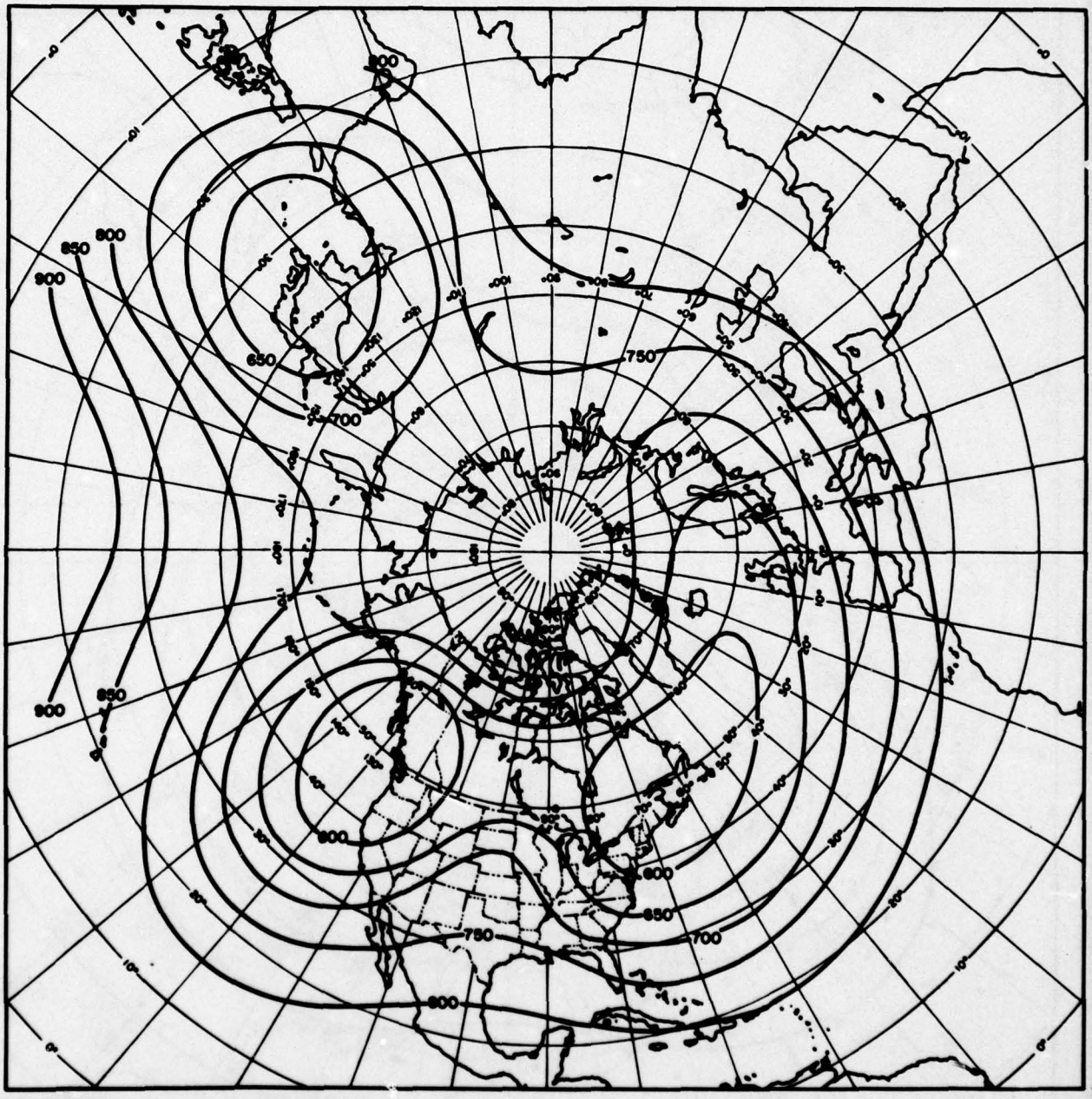


Fig. 4-9. Isopleths of the size parameter, L, at 100 mb (see Eq. 4-15 and 4-16) pressure level in Summer; numbers on curves are values of L in nautical miles. (From C. E. Buell, Final Report Contract AF19(604)-7282, July 1962.)

be similar to the tropospheric pattern. When allowance is made for observing error, the computed mean wind change at 45 km for lags of 24, 48, and 72 h (based on MRN data) appears to increase according to the relation

$$S_t = 6\,t^{0.5},$$

where S_t is mile h^{-1} and t is hours.

The spatial variability of winds is related to time variability through the size of the typical wind systems and their average rate of movement past a fixed point. The data can be manipulated to yield an estimate of space variability expressed by

$$S_d = 0.9\,d^{0.5},$$

where S_d is mile h^{-1} and d is miles.

Both relations are derived from observations that are nominally 24 h apart. Interpolation for intervals of less than one day, or less than one day's motion of the typical wind system, is not valid; a marked diurnal variation of winds occurs at these altitudes. As Fig. 4-10 shows, the variability of winds can be as great after 8- to 12-h lag as after a 48-h lag. A model of the variability of wind with time or with distance that would be universally applicable in the upper stratosphere and mesosphere would have to superimpose a sinusoidal oscillation on the exponential model applicable to the troposphere.

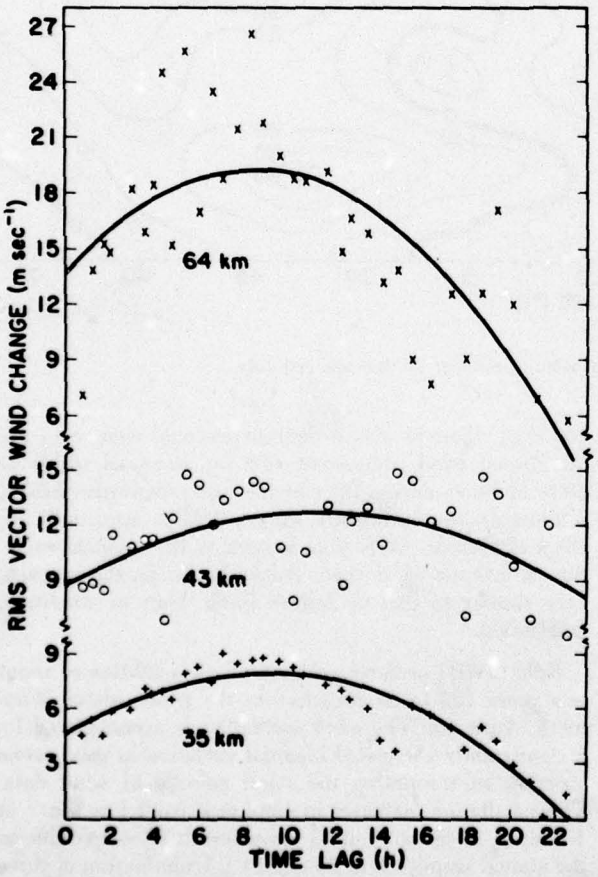


Fig. 4-10. Lag variability of wind over Eglin AFB, Florida, 9-10 May, 1961. (After R. W. Lenhard, *J. Geophys. Research*, v. 68, p. 227, 1963.)

At higher levels, between 85 and 100 km, meteor trail observations give evidence [Greenhow and Neufeld, 1961] of large day-to-day variations, of tidal variations within the period of a day, of eddies 150 km in size and with 100-min life span, and of small-scale turbulence down to 20 km in size and with 10- to 30-sec life span. It would seem that wind variability would be similar to that in the mesosphere. Because it has not been specifically investigated, however, it is not known at what rates variability increases, either from day to day or within the span of a day.

4.2.3.1 *Seasonal Variation.* The broad features of the seasonal change in winds between 30 and 90 km are reasonably well established [Kantor, 1962]. Figure 4-11 shows a meridional cross section of the mean monthly zonal wind components for January and July, from the surface to 100 km. Wind components given at the various levels between the surface and 80 km agree very well with both rocket observations and the latitudinal pressure gradients depicted by the supplemental atmospheres described in Chapter 2. Values above 80 km are based on winds obtained by tracking meteor trails and chemically formed clouds. These observations indicate that extremely strong wind shears and turbulence occur in the region between 80 and 100 km over midlatitude locations.

This seasonal change in the stratospheric and mesospheric wind field differs from tropospheric seasons in timing and in length of the seasons. Long periods of easterly and westerly flow are separated by shorter periods of transition. As shown in Fig. 4-12, the changeover begins near the top of the mesosphere and proceeds downward. The spring transition is estimated as being from 15 March through 31 May, and the fall season from 15 August to 30 September. Similar computations for latitude 30°N, made from data used in compiling Table 4-22 at the end of the chapter, indicate that the changeover proceeds downward at a rate of about 1 km per day. These data indicate that the transition seasons may be somewhat shorter than estimated by Appleman (Fig. 4-12). The spring season averages about 45 days and begins about 15 March at 65 km; the fall season is about 30 days long and begins about 15 August at 65 km. The sample of data that is available is still too small to expect any great precision in estimates. Division of the year into seasons for compiling Table 4-22 was for estimated average conditions. There does not appear to be any systematic seasonal variation in the meridional wind component.

Above the mesosphere, the seasonal wind regime undergoes another change. Figure 4-12 includes a curve for 92 km which shows that through the mesopause winds are predominantly westerly except for weak easterly flow during spring. Seasons correspond to those in the troposphere. Extremely high winds do not seem to occur. The strongest westerly flow averages between 10 and 20 knots and occurs both in winter (December to February) and in summer (June to August). In this altitude zone (80 to

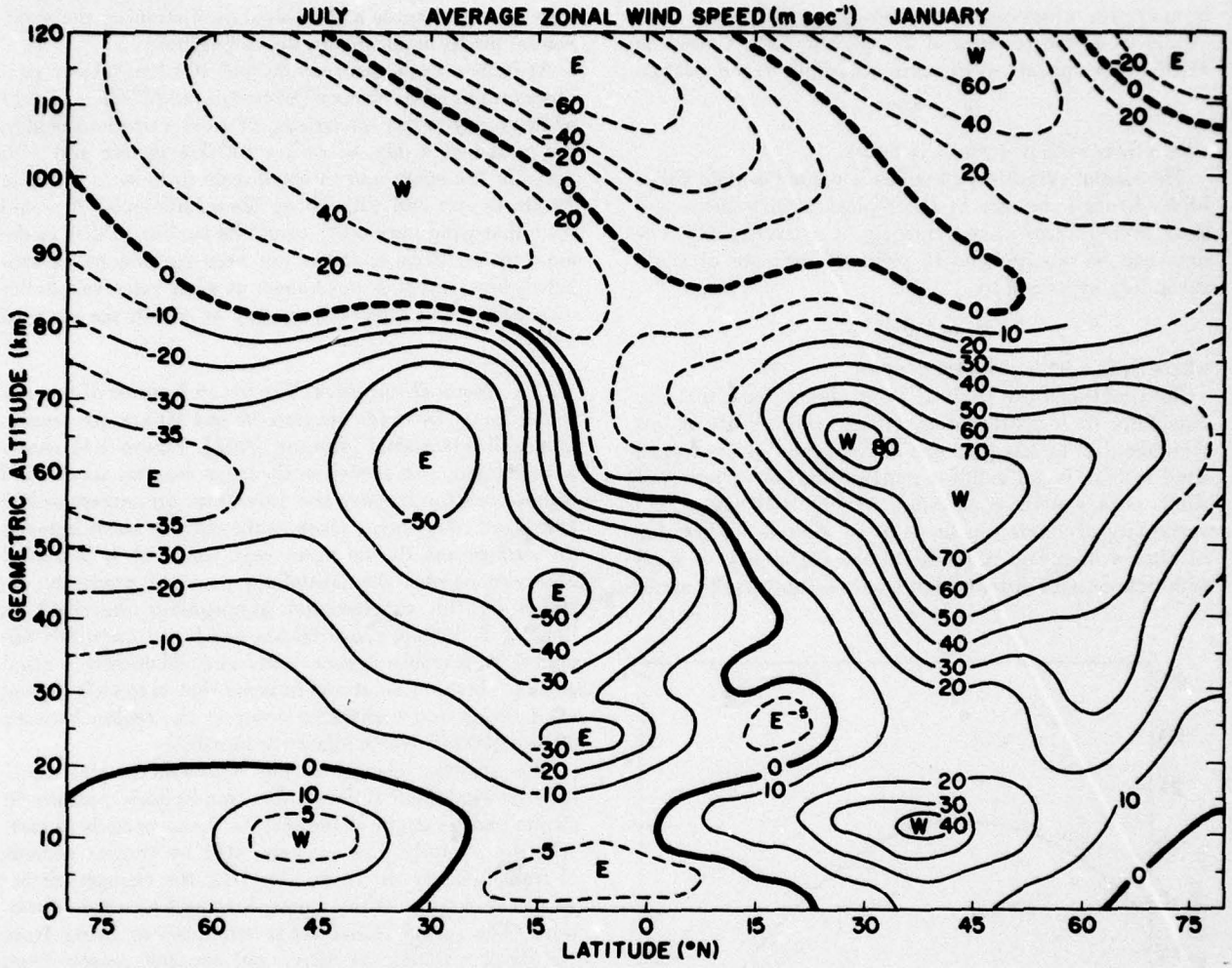


Fig. 4-11. Meridional cross section of the zonal wind component for January and July.

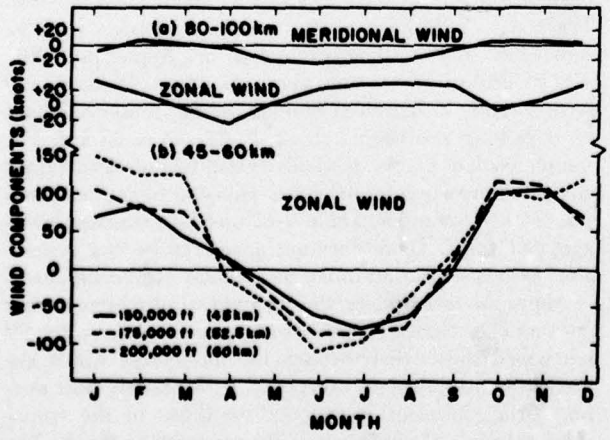


Fig. 4-12. Annual variation of the wind: (a) zonal and meridional components at 53°N [Greenhow and Neufeld, 1961], (b) zonal component about 35°N (H. S. Appleman, *Technical Rept. No. 166*, Air Weather Service, 1963.)

100 km), there is also a definite seasonal change in the meridional wind component with equatorward winds of 10 to 20 knots during the summer and poleward winds of 5 knots or less during the winter. This is apparently an effect of altitude rather than latitude as the seasonal variation at latitude 35°S (over Adelaide) is, on the average, very similar to that at Jodrell Bank, both in amplitude and timing.

Rofe [1963] presents evidence of an oscillation of about two years (22 to 24 months) in the winds above Woomera, Australia. The wind oscillation is accompanied by a significantly correlated biennial variation in total ozone amount, substantiating the small amount of wind data. This oscillation increases in amplitude from 1 m sec^{-1} at 18 km to 18 m sec^{-1} at 37 km where it is comparable to the annual amplitude of 25 m sec^{-1}. Examination of three years of MRN data for Cape Kennedy, White Sands, and Point Mugu revealed an annual cycle with amplitudes comparable to those found by Rofe. The biennial cycle in

the MRN data was statistically significant at 24 km and equal to that at Woomera in amplitude. The amplitudes of the biennial cycles at 30 and 37 km in the MRN data were less than at Woomera for the same altitudes, and less than the amplitude at 24 km in the United States. These amplitudes were also too small to be statistically significant. The period of record is too short to detect a 24-month cycle with any certainty. The evidence can be taken only as an indication that a 2-yr cycle in the winds has a sufficiently high probability of existence to warrant further attention.

4.2.3.2 *Diurnal Variation.* Observations show that pronounced diurnal and semidiurnal oscillations exist in winds above 30 km, but the data accumulated are not yet sufficient to permit development of a generally satisfactory model. The figures presented in this section are probably representative of a season of less than average diurnal variability of the winds above 30 km.

Physical explanations for various aspects of the observed behavior of these oscillations are available; for example, Hines [1963]. Basically, the oscillations seem to be thermally excited tidal motions, with the ozone layer playing an important role in the process. The motions can be described by

$$V = \bar{V} + A_1 \sin(15t + \theta_1) + A_2 \sin(30t + \theta_2), \quad (4\text{-}13)$$

where V is the speed of a wind component, $\bar{V}$ is the mean component speed, t is the time of day in hours beginning with midnight local standard time, A_1 and A_2 are the amplitudes of the diurnal and semidiurnal oscillations, and θ_1 and θ_2 are their phase angles. Figure 4-13 illustrates amplitudes and phases that may occur in the upper atmosphere for May.

Because the solar tide is dominant in the atmosphere, thermal excitation is implied; but the amplitude of the diurnal wave does not exceed that of the semidiurnal as expected. For a long time, the existence of a natural period of 12 h in the atmosphere that would provide resonant amplification of the semidiurnal tide was postulated. The mechanism involves reflection of tidal energy rising from the troposphere with a suitable phasing of the reflected wave, and a tendency of the tidal amplitude to increase with increasing height. This upward increase would be reversed at the reflecting layer where the amplitude of the oscillation would become zero and the phase would shift 180°. Some fraction of the tidal energy would penetrate the layer, however, and above it the amplitude would again increase with height. Resonance theory requires the reflecting layer to be at about 30 km. Figure 4-13 shows continuing increase in amplitude but no abrupt phase change through this layer.

Acquisition of observational data led to reexamination of this resonance theory and recognition that the physical processes involved are much more complex. The increase of amplitude with height is now recognized to be characteristic of internal atmospheric waves in general and not a peculiar feature of a resonance enhancement. Figure 4-13 shows that reflection may be occurring at about 80 km. Amplitudes increase rather regularly for such a heterogeneous sample up to 80 km. Above that level, amplitudes are smaller than immediately below and show some tendency to increase with further increase in altitude.

It appears that ozone heating is capable of producing both the observed amplitude and phase of the semidiurnal tide. Maximum heating of the ozone layer occurs near 50 km. Figure 4-13 shows a general tendency of the semidiurnal phase angles to decrease away from the 50-km level, indicating energy propagation in these directions, downward below 50 km and upward above.

Not all of the features of Fig. 4-13 can be explained by tidal theory. The amplitude of the semidiurnal tide should not vary as much as it does with latitude, according to tidal theory. Discrepancies such as this cannot be assigned definite physical causes with the scant observational data available.

The amplitudes of these oscillations vary seasonally. At 80 to 100 km, the amplitude of the diurnal oscillation is largest in the summer and smallest in the winter. The semidiurnal amplitude is largest in winter and smallest in spring or summer when it is less than half as large as the winter values. The seasonal variation in amplitude at lower levels has not been determined. The only records available show irregular changes from month to month which may reflect errors in the determination of the harmonic coefficients due to the quality of the data.

4.3 WIND SHEAR

Wind shear is the derivative of the wind vector with respect to distance and is itself a vector. The shear of the horizontal wind is of primary interest and is the one discussed in this section. The terms vertical wind shear and horizontal wind shear are commonly used to refer to the *shear of the horizontal wind* in the vertical and horizontal directions respectively. The *horizontal wind shear* is the derivative of the horizontal wind with respect to an axis parallel to the earth's surface. Its applications are restricted largely to meteorological analysis. The *vertical wind shear* is $\Delta W/\Delta y$, where ΔW is the change in the horizontal wind in the altitude interval Δy; the unit of shear is sec^{-1}. Although direction is also necessary to specify the shear vector, it is usually ignored. In applications, shear is usually applied in the most adverse possible direction (Sec. 4.4).

The climatology of vertical wind shear is applicable to problems dealing with designing and launching vertically rising vehicles and jet aircraft, radioactive fallout investigations, and many phases of high altitude research. Area climatology, which is very scarce, is needed for these purposes. Most investigations of shear climatology are for specific locations, having been made to satisfy design and operational requirements of missiles at actual or planned launching sites. The U.S. Weather Bureau Technical Paper No. 32, 1959 gives charts for the United States of the seasonal mean vertical wind shears and their standard deviations for eight layers between standard pressure levels from the 700- to 500-mb layer to the 80- to 50-mb layer.

CHAPTER 4

Measurements of vertical wind shear indicate that shear behaves inversely with layer thickness, the *scale-of-distance*. This is illustrated in Fig. 4-14 which is based on a relatively large number of observations during the windiest months over Cape Kennedy, Florida. Figure 4-15, based on the same data, shows the variation of shear with altitude and with layer thickness; the vertical wind shear spectrum with a 1% probability of occurrence is given. Figures 4-16 through 4-20 show 1% probability shear profiles computed for the four windiest months through 1000-ft layers for a representative set of Northern Hemisphere stations. These profiles should be used with caution; studies have shown that shears for 1000-ft layers, based on the standard meteorological sounding system GMD-1 rawinsonde data as these are, may be too strong at jet stream levels by 0.01 to 0.02 sec^{-1} and have an rms uncertainty of approximately 0.025 sec^{-1}. With the exception of Keflavik, Iceland, and Bitburg, Germany, the stations are located in regions of strong tropospheric winds. Strong shears can also arise when light or nearly calm wind layers are overlain by relatively strong winds, a type of synoptic situation that occurs occasionally over southern California.

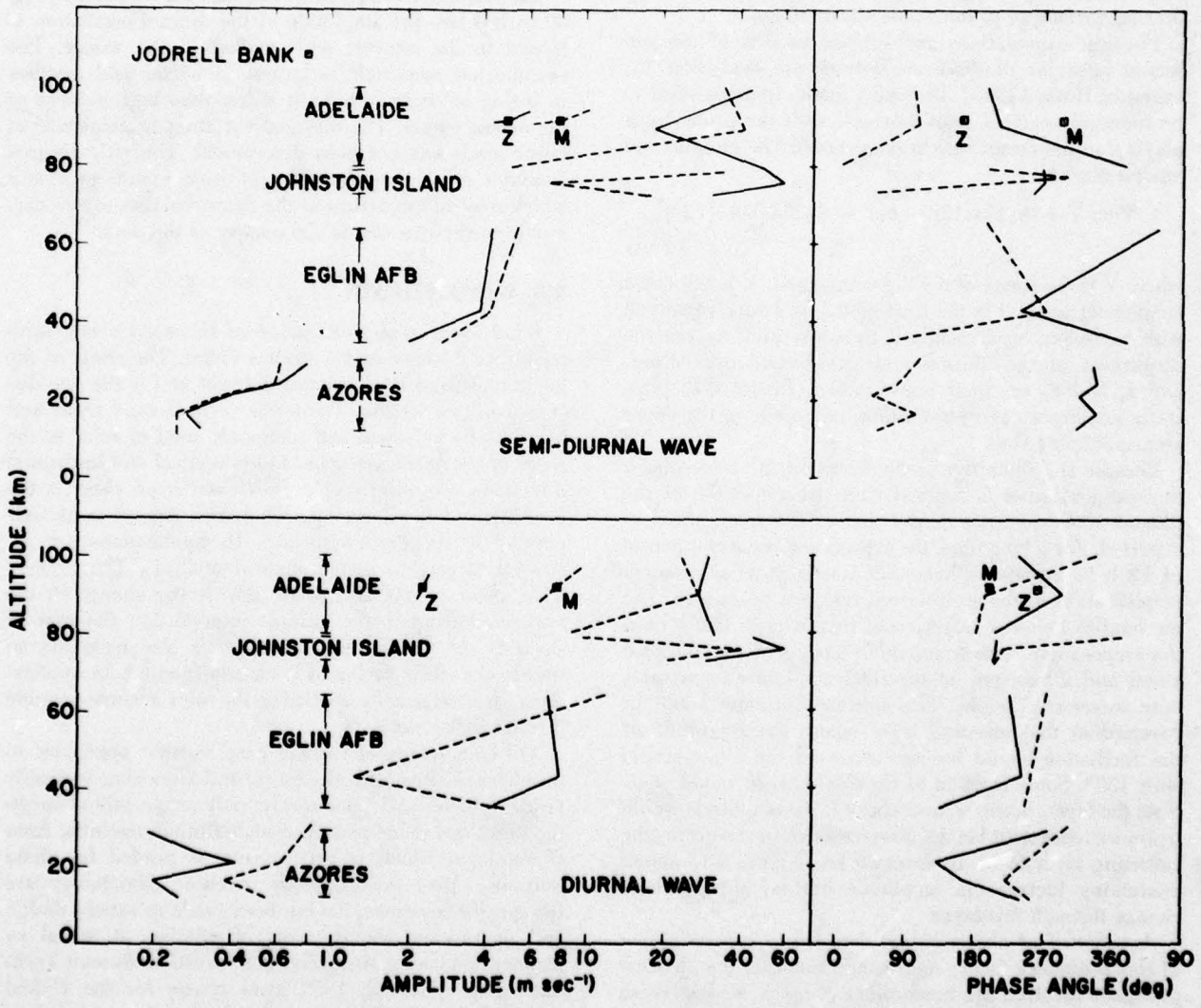


Fig. 4-13. Variation with height of the amplitude of diurnal and semidiurnal oscillations in the zonal, Z (solid line), and meridional, M (dashed line), wind components. (After Greenhow and Neufeld [1961], Harris et al [1962], Smith [1960], and Elford [1959].)

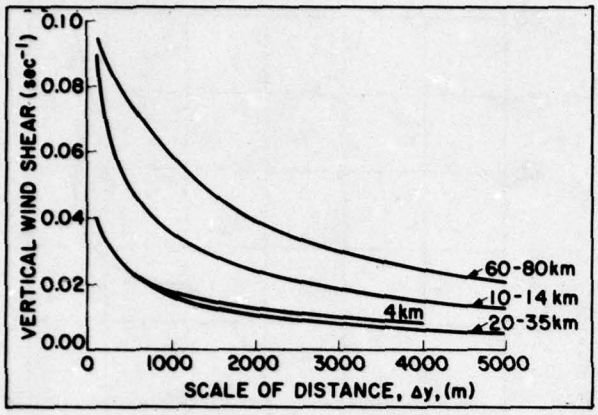


Fig. 4-14. Selected vertical wind shear spectrums (4, 10 to 14, 20 to 35, and 60 to 80 km altitude) for use with 5% and 1% probability level wind profile envelope, Cape Kennedy, Florida. (From Scoggins and Vaughan [1962].

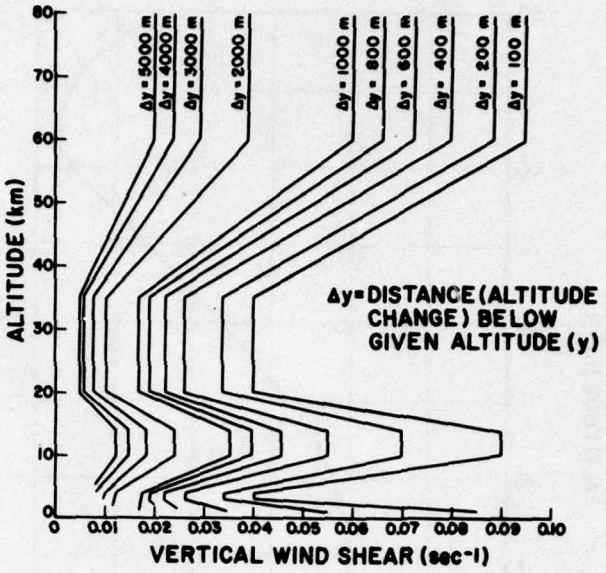


Fig. 4-15. One percent probability-of-occurrence vertical wind shear spectrum as function of altitude and scale-of-distance for association with the 5% and 1% wind speed profile envelope for Cape Kennedy, Florida. (From Scoggins and Vaughan [1962].)

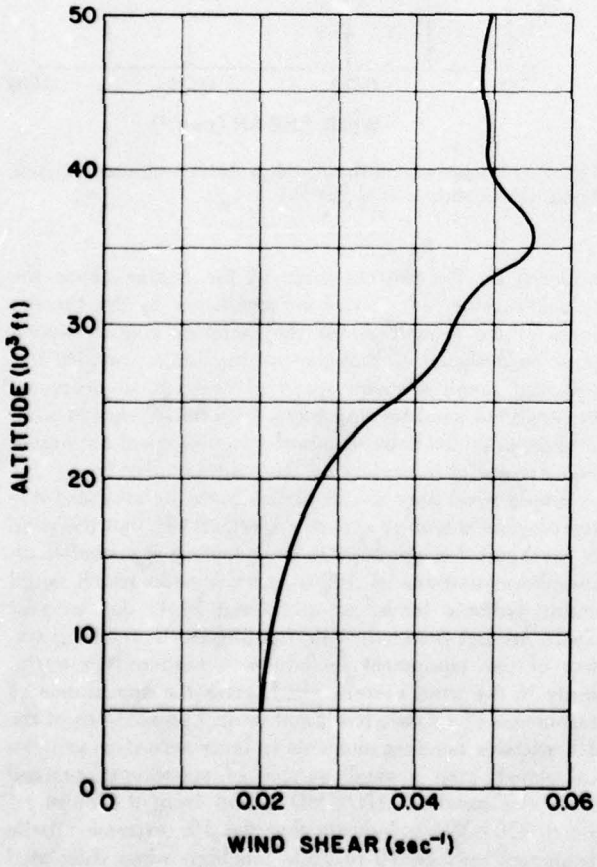


Fig. 4-16. Resultant wind shear; 1% probable occurrence, Caribou, Maine. (From Mazzola et al [1963].)

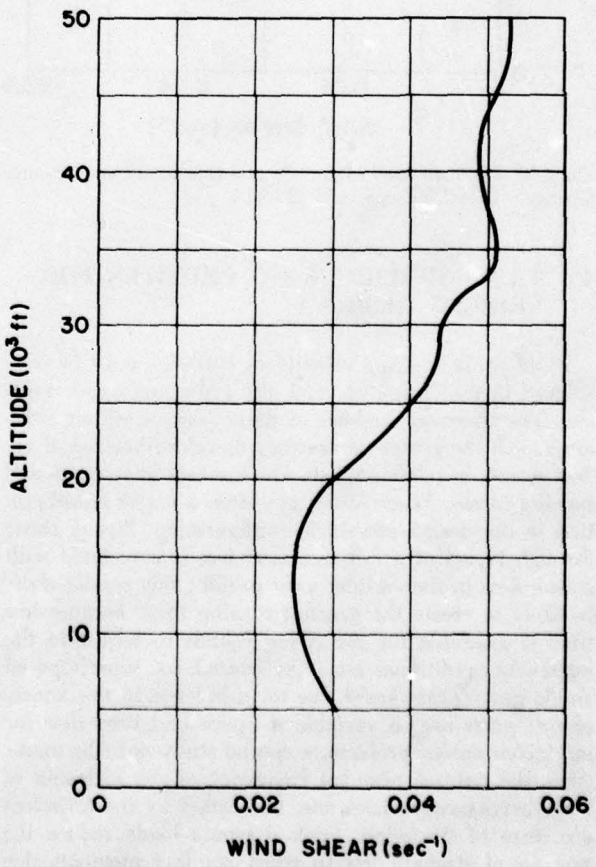


Fig. 4-17. Resultant wind shear; 1% probable occurrence, Keflavik, Iceland. (From Mazzola et al [1963].)

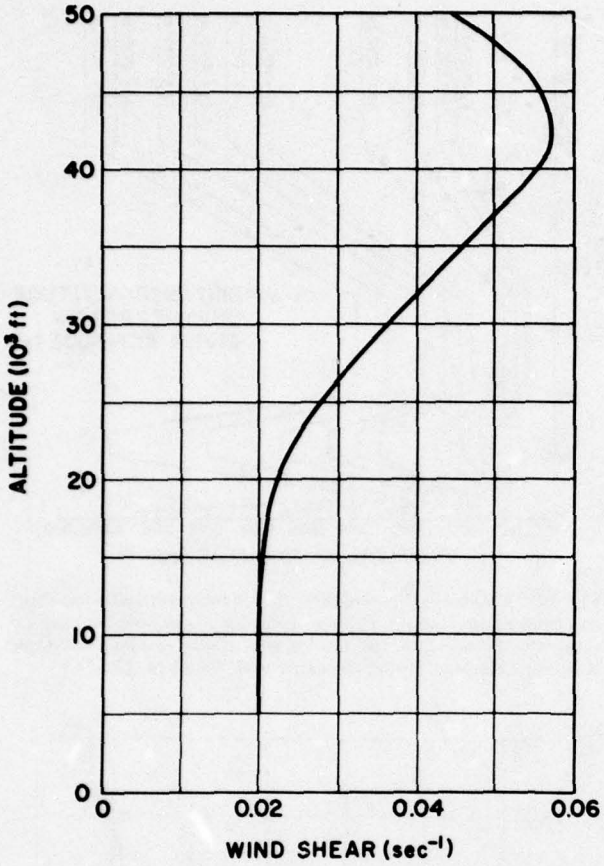


Fig. 4-18. Resultant wind shear; 1% probable occurrence, Bitburg, Germany. (From Mazzola et al [1963].)

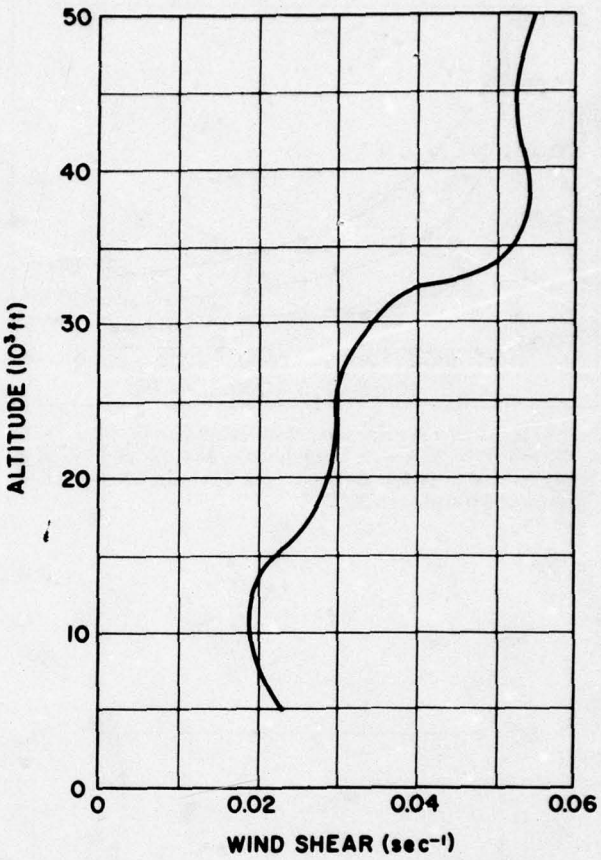


Fig. 4-19. Resultant wind shear; 1% probable occurrence, Tripoli, Libya. (From Mazzola et al [1963].)

4.4 TROPOSPHERIC WIND PROFILES FOR VEHICLE DESIGN

Wind profiles (wind velocity vs altitude) must be considered in the design of vertically rising aerospace vehicles. The center of pressure of these vehicles seldom coincides with the center of gravity; therefore horizontal air flow results in relative winds which create unprogrammed turning forces. These forces are often a major consideration in the design of vehicle configuration. Strong shear through layers of a few thousand feet is associated with strong flow in the vertical wind profile; this *profile shear* is likely to create the greatest turning force because less time is available for the rising vehicle to adjust to the wind. An additional stress is caused by superimposed single gust *(gust shear)* due to turbulence in the atmosphere; gusts are so variable in space and time that for any given design problem, a special study must be made. Also, the natural resonant frequency of the airframe of large aerospace vehicles may be excited by the turbulent structure of the wind. Such dynamic loads reduce the margin of strength left to resist bending moments due to the profile shear. The vehicle structure must be built to withstand the strongest bending moment likely to be imposed by the turning force of the engine about the vehicle's center of gravity in opposition to the turning force of the relative wind; the guidance control system must be designed so that the turning force provided has sufficient amplitude and speed of reaction to overcome the expected wind turning force. Generalized design wind profiles provided from standard meteorological air soundings are useful in evaluating these design criteria.

Ample wind data are available from the *standard meteorological sounding system* (AN/GMD-1), but the wind is averaged through 2000-ft thick layers; the smaller atmospheric motions of 100-ft vertical scale which could cause dynamic loads, or additional loads due to gust shear, are not detected. Also, hunting in the tracking system of this equipment introduces a random-type variability in the wind vectors which gives the appearance of turbulence of a somewhat larger scale. Comparisons of the 1% extreme bending moments in large aerospace vehicles calculated from a small sample of soundings obtained from the standard AN/GMD-1, and from the more refined AN/GMD-2, indicate that the 1% extreme missile responses may be 10 to 15% too high when calculated from AN/GMD-1 soundings. (The probability that a factor will equal or exceed a given value is indicated cus-

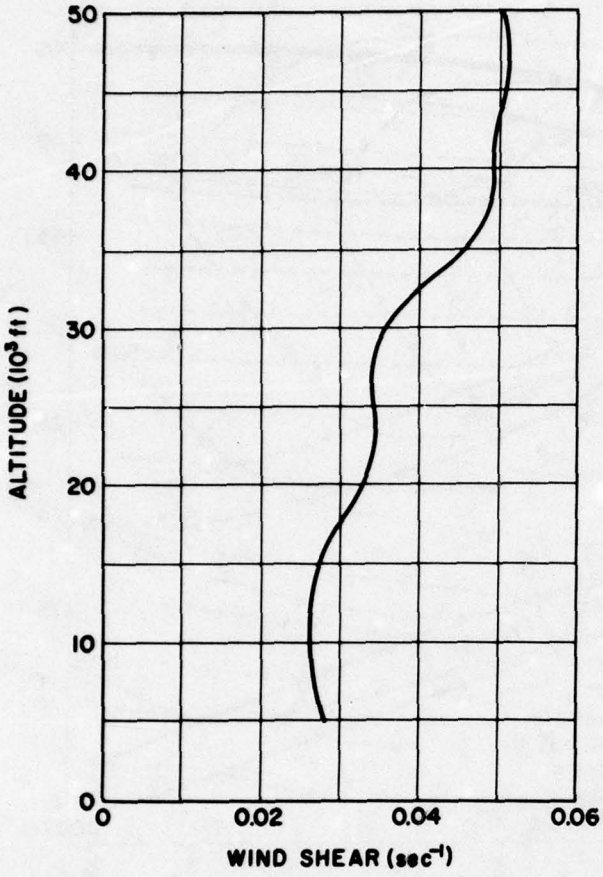


Fig. 4-20. Resultant wind shear; 1% probable occurrence, Kadena, Okinawa. (From Mazzola et al [1963].)

tomarily by the phrase "percent probable" or "percent extreme"; e.g., 5% probable wind speed or 1% extreme response.)

Bending moment and guidance-control problems are in general most critical at the altitude region where the dynamic pressure is greatest (usually found between 9 and 14 km). By coincidence, winds and shears at mid-latitudes are also strongest at 9 to 14 km during seasons of well-developed upper air flow. These strong winds, which approach speeds of 100 m sec^{-1} (200 knots), are called jet streams, see Fig. 4-21. Clear air turbulence is known to be closely associated with the strong shears found in jet streams; this increases the probability of an additional momentary turning force due to the shear in a single turbulence-created gust, and the probability of dynamic loads due to excitation of the air frame by a series of these gusts during vehicle passage through a critical part of the wind profile.

The design problem is additionally complicated because the relative wind on an aerospace vehicle at any one altitude depends upon the wind profile encountered at lower altitudes. The differences between aerospace vehicles of different aerodynamics, guidance, and trajectory control are so great that the response of any one vehicle to a given wind profile can serve only as a preliminary estimate in determining the response of a different vehicle. A wind profile that for a given location is not the most severe for one vehicle may be the most severe for another.

Experience indicates that it is not generally feasible to design for the most severe wind profiles that are estimated to be possible. Military vehicles are designed with a calculated risk such that if launched in representative directions during the worst season of the year, and from locations where the wind profiles are the severest, there would be a low probability (usually 1%) of failure. (For some locations, it is not clear that a worst season of the year can be isolated.) Noncombat aerospace vehicles are subject to the same type of calculated risk in their design, although a higher probability of inoperativeness is frequently acceptable for noncombat missions; if a critical wind profile is predicted for the launching, the flight can be postponed.

4.4.1 Synthetic or Discrete Wind Profiles for Preliminary Design

The problem of what wind profile information to use as a design criteria (the *design wind profile*) led to an estimated *synthetic profile* (also called a *discrete profile*) which presented the 1% probable wind speed and associated shear at the most critical altitude, and speeds at other altitudes typical for such wind fields. Subsequent investigations revealed that if accuracy in the calculated risk is desired, it is hazardous to use synthetic wind profiles. However, logically developed synthetic profiles are useful in preliminary design, especially when trade offs are being examined and extensive use of high-speed computers is not warranted. Figure 4-22 is a synthetic wind profile that was developed in 1954 to determine vehicle responses which would be exceeded only 1% of the windiest season of the year in that area of the U.S. where tropospheric wind stresses were subjectively considered the strongest. It is applicable to vehicles having a sharp maximum wind-influence near 35,000 ft (107 km). It is reasonable to shift the curve upward or downward by as much as 5000 ft (1.5 km) to make the peak wind speed coincide with the altitude of maximum wind-influence. Computer studies of statistical distributions of maximum bending moments for many samples of AN/GMD-1 wind soundings revealed that maximum bending moments were 9, 7, and 14% higher on three different vehicles than the 1% extreme values for the windiest regime in the U.S. (over Montgomery, Alabama). Recent studies of five vehicles show that conditions over Caribou, Maine, which is slightly less windy, are 21, 39, 23, 7, and 0.6% more severe than at Montgomery, probably because of lower altitude for the peak velocity and stronger shears below the peak winds. In utilizing this synthetic wind profile (or others in which direction is not included), flight azimuth of the vehicle is arbitrarily chosen as that in which wind stresses are greatest; this leads to overdesign. A more realistic approach, but somewhat more difficult to employ, is to use a true 1% profile, a nebulous concept,

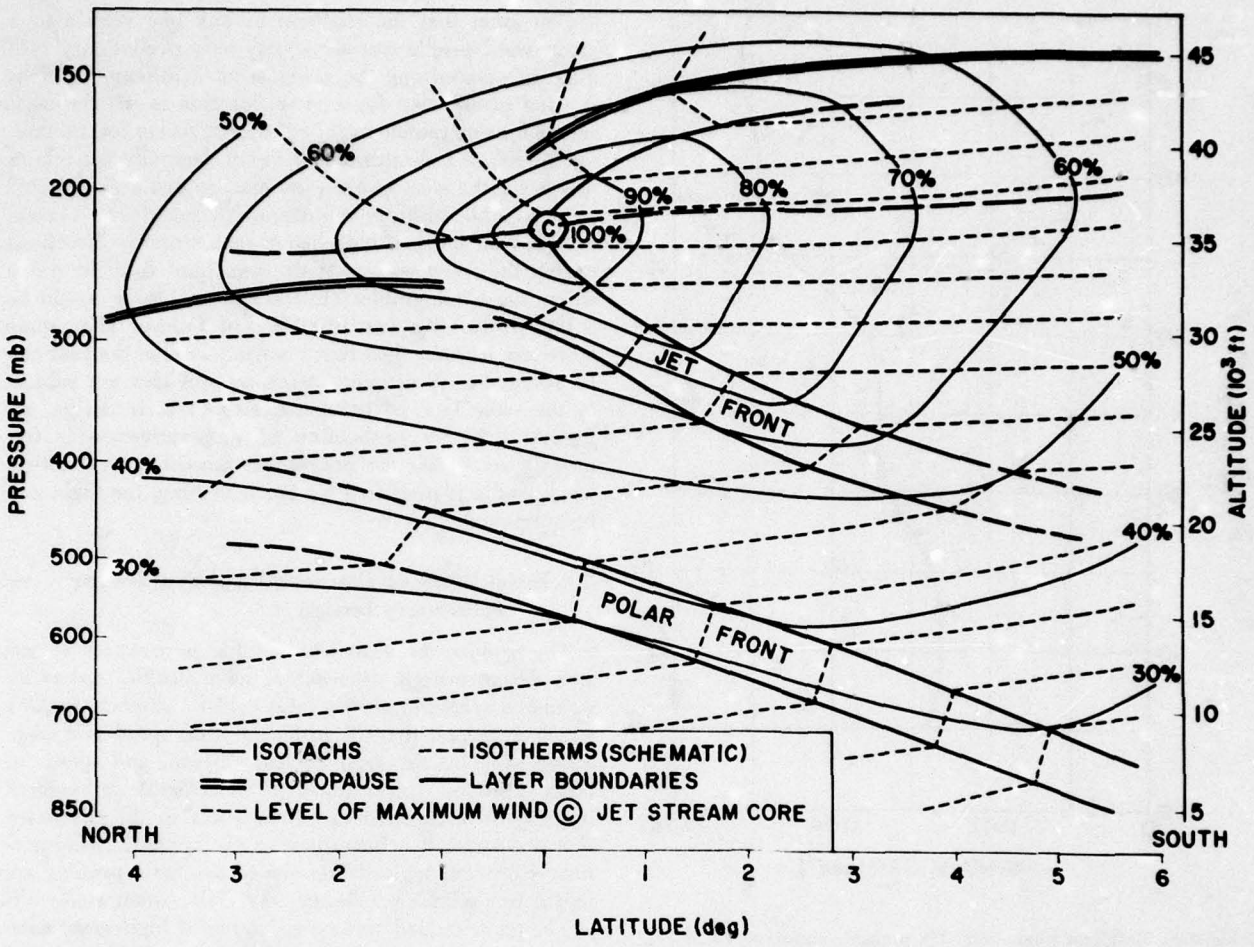


Fig. 4-21. Idealized model of the jet stream, average structure in a cross section perpendicular to the flow. Percent of the core speed is given for each isotach; wind direction is into the page.

with a properly weighted set of boost directions. Figure 4-23 is an actual wind profile selected from a study of about 50 AN/GMD-2 soundings obtained near Boston during the early part of 1957. It is recommended as a useful preliminary design tool which permits investigation of the effect of realistic boost directions and turning of the wind. This profile will probably require vehicle response fairly close to the 1% extreme for the windiest season, windiest regime of the U.S.

Other studies indicate that, if the lower atmosphere is very calm, extremely strong missile response can be required in the locations where winds at the altitude of maximum dynamic pressure are somewhat less than those encountered in geographical locations of strong winds. Figure 4-24 presents an actual wind profile from Vandenberg Air Force Base which required missile responses of a magnitude about the same, for some types of vehicles, as that exceeded only 1% of the time during the winter in the windier, eastern part of the U.S. This profile is also recommended as a supplemental wind profile for preliminary design.

Upper air flow over the Japanese islands is recognized as the strongest in the world. Preliminary studies of three designs show that this wind regime will require far greater response than that for Montgomery, Alabama. It is highly probable that Japan will present the severest wind problem for aerospace vehicle design, although this does not necessarily follow, because below the level of maximum winds, turning of the wind and low winds have frequently been primary factors in the creation of strong missile responses. For preliminary design of a vehicle to be flown on a worldwide basis, however, consideration must be given to the wind profiles likely to be encountered over Japan. Figure 4-25 gives synthetic profiles for wind speed exceeded 1% and 5% of the winter at an altitude of 9 km and results of soundings that show strong wind shear at 9 km. Figure 4-26 presents analogous profiles for 1% and 5% probable wind speed at 12-km altitude. Wind direction for these synthetic profiles can be assumed as near the west. These profiles are recommended for *preliminary design;* but no comparisons of maximum missile responses for simulated computer flights through these profiles to responses for flights through a representative sample of actual profiles for Japan are available.

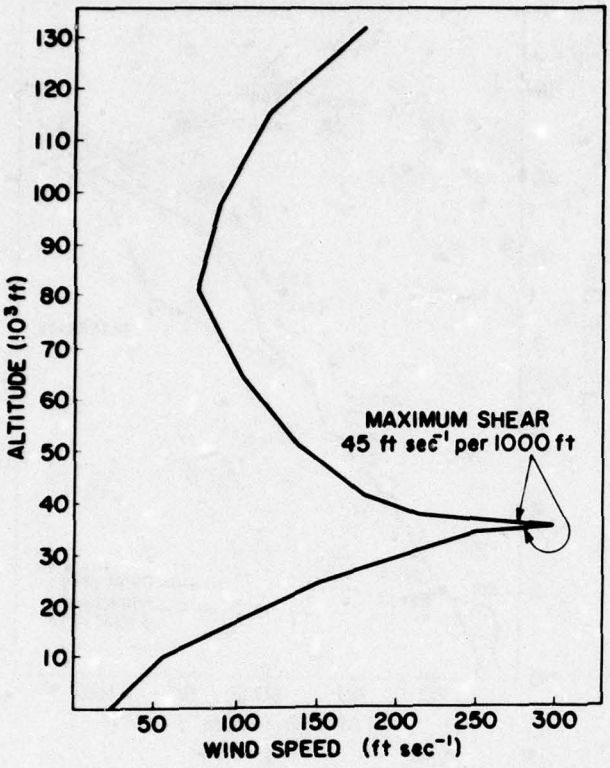


Fig. 4-22. Maximum speed (300 ft sec^{-1}) and associated maximum shear (45 ft sec^{-1} per 1000 ft) are likely to be exceeded only 1% of the wintertime over the northeastern USA. Wind speeds and shears at levels above and below the levels of maximum speed and shear are typical of those likely to be encountered for this 1% probability condition.

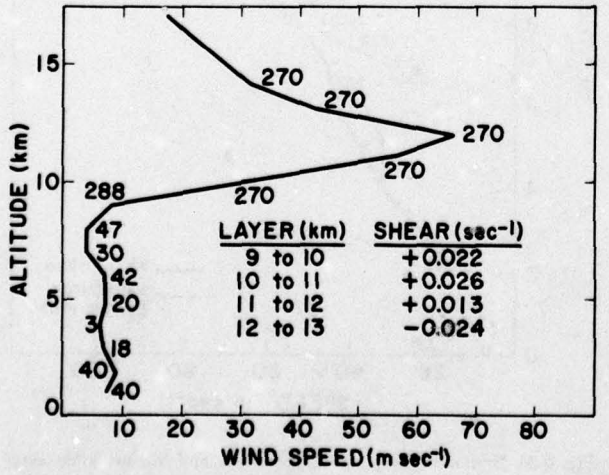
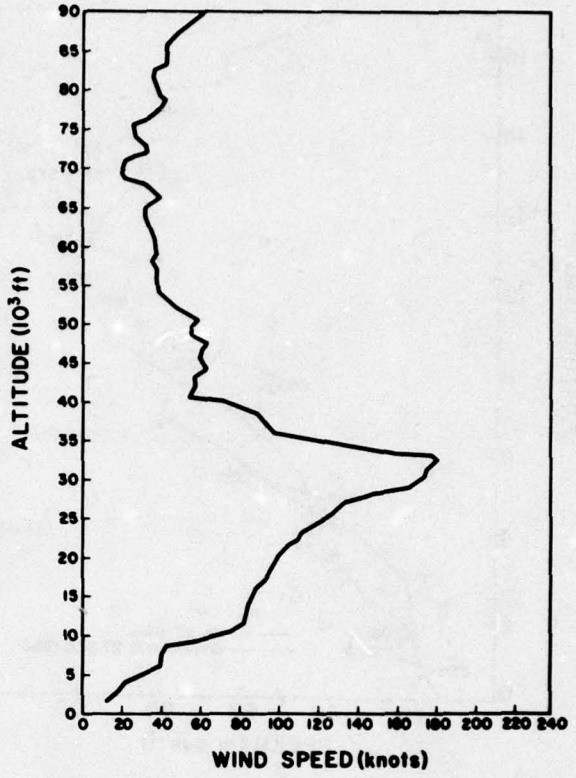


Fig. 4-24. Vandenberg AFB wind sounding, 1735, 2 March 1959.



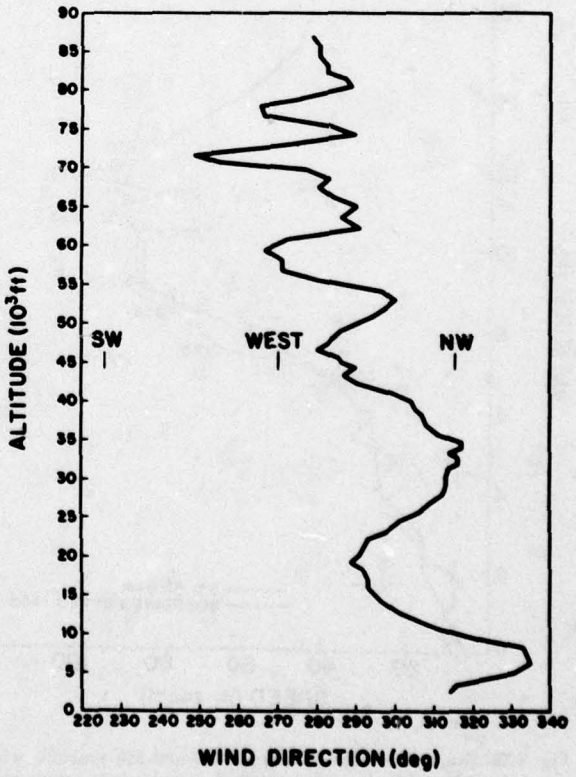
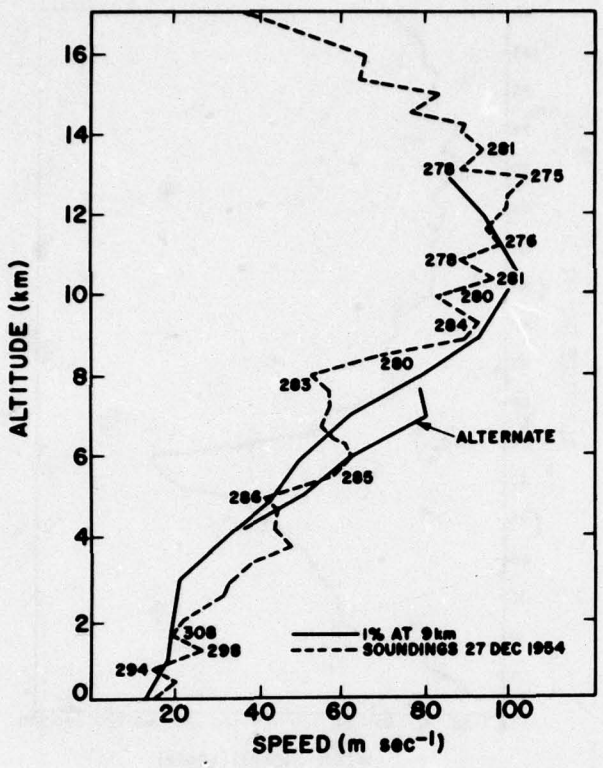
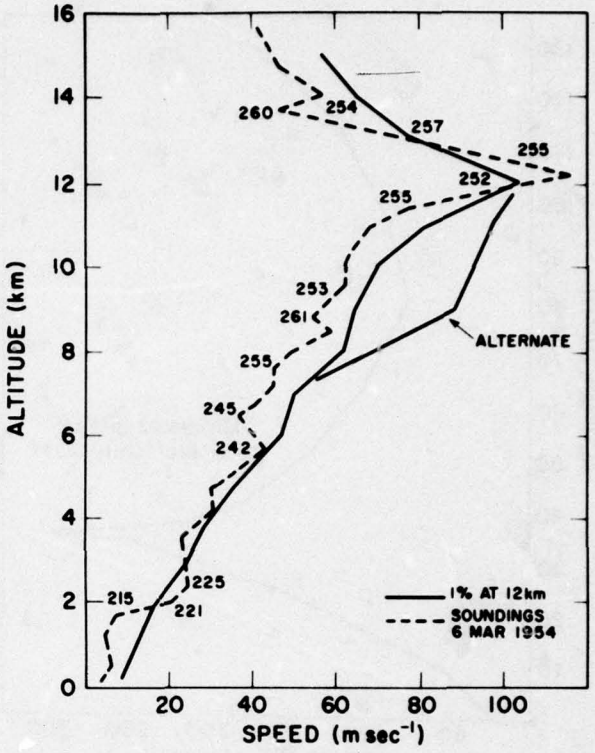
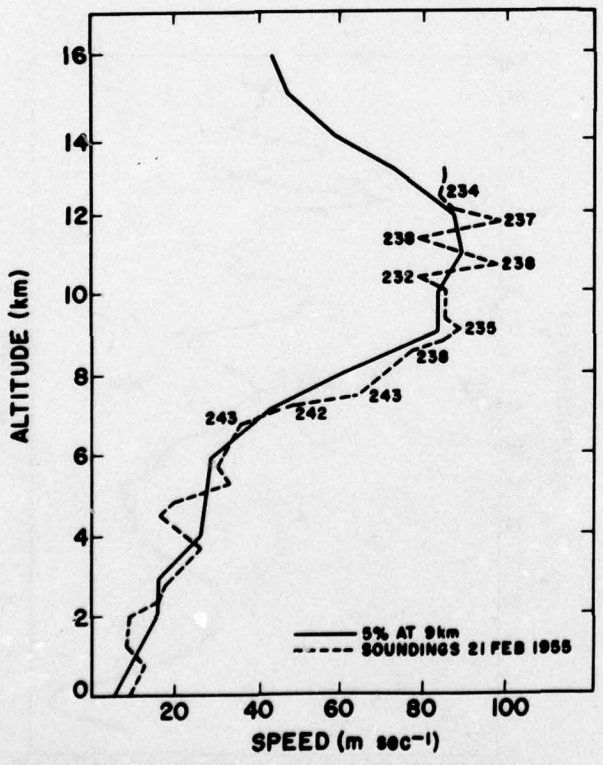


Fig. 4-23. Wind speed and direction profiles from AN/GMD-2 soundings, L. G. Hanscom Field, 3 April 1957.







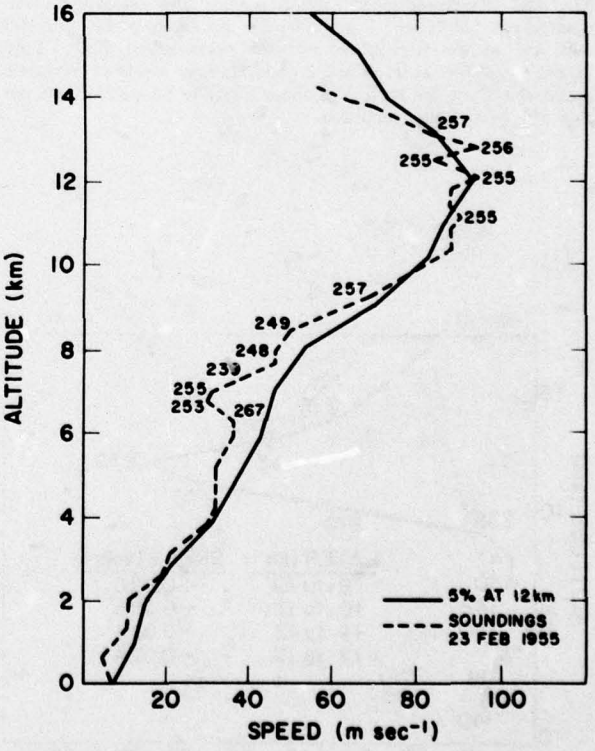


Fig. 4-25. Synthetic design profiles for 1% and 5% probable wind speeds at 9-km altitude and profiles of actual winds which have strong shear at 9 km. Numbers along sounding curves are azimuth directions from which the wind was blowing.

Fig. 4-26. Synthetic design profiles for 1% and 5% probable wind speeds at 12-km altitude and profiles of actual wind which have strong wind shear at 12 km. Numbers along sounding curves are azimuth directions from which the wind was blowing.

Wind stresses may be slightly less over Cape Kennedy than those encountered further north along the east coast. Figure 4-27 provides synthetic wind profiles up to 6, 12, 18, and 24 km developed for flight from Cape Kennedy, utilizing the 95% probable wind speed for the windiest month and the 1% wind build-up for 5 km below each of these four altitudes. Additional wind profiles for intermediate layers can be obtained from the wind build-up data in Fig. 4-28. For example, in Fig. 4-28 the 2-km interval line shows at 12-km altitude a change in wind speed of 48 m sec^{-1}; subtracting this from the speed of 75 m sec^{-1} at 12 km obtained from the 95% probability envelope (Fig. 4-27), gives a wind speed of 27 m sec^{-1}, which is the wind speed for 2 km below 12 km (see 10 km on the synthetic profile for the 12-km curve in Fig. 4-27). Such additional profiles will no doubt require responses for many vehicles which approach extremes to be expected at this location and, hence, may be too restrictive to apply to probes that need not be flown during severest conditions.

A more advanced technique for providing synthetic wind profiles for *preliminary design* is based on a sample of 200 independent (three days apart) winter soundings for each of seven climatically dispersed U.S. locations and for four stations located in other areas of the Northern Hemisphere (considered critical for booster problems because of strong or variable upper-air flow). These are the basic data developed for final design to be considered in Sec. 4.4.3.

Unfortunately, data for the Japanese islands were not available in the appropriate form; consequently, data from nearby, but somewhat less windy Kadena, Okinawa, were used. From each of these 2200 soundings, missile responses at many altitudes and the maximum for each sounding were computed for five different types of vehicles, as were the wind distributions at each level for each of these locations (see Mazzola et al [1963]). The complete distribution of missile response for each altitude by location, and for each sounding by location, was then utilized in investigating synthetic profiles.

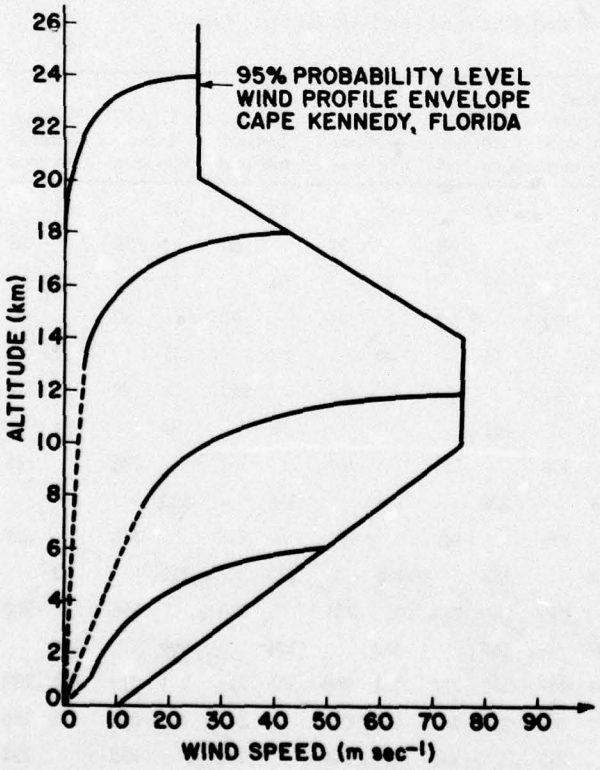


Fig. 4-27. Examples of synthetic wind profiles for the 5 km below the altitudes 6, 12, 18 and 24 km based on 99% probability-of-occurrence wind build-up (see Fig. 4-28), to be associated with the 95% probability-of-occurrence wind profile envelope. (From Scoggins and Vaughan [1962].)

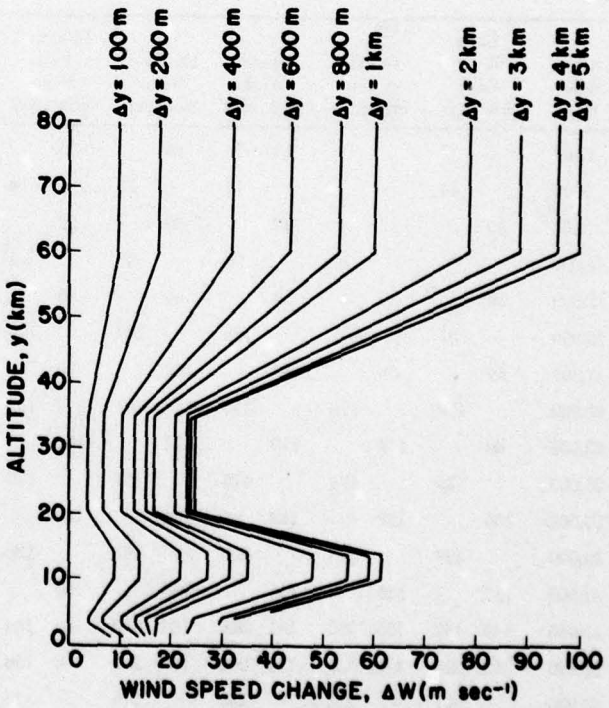


Fig. 4-28. Wind build-up, Cape Kennedy, Florida. The 99% probability-of-occurrence of change in vertical wind speed as a function of altitude for various scale of distance (layer thickness), Δy, below the given altitude, associated with the 95% and 99% probability synthetic wind profiles given in Fig. 4-27. (From Scoggins and Vaughan [1962].)

CHAPTER 4

Sets of discrete profiles for a complete series of altitude levels were systematically prepared from these wind statistics by utilizing the 1% probable maximum east-west wind velocity and the 1% probable 2500-ft thick shear immediately below that altitude. Missile responses computed from "flight" through these profiles approximated 1% extreme bending moments at that altitude for vehicles flown in the most critical direction. To obtain the 1% extreme wind profile response regardless of altitude (the actual design goal), the most severe bending moment obtained from these discrete profiles must be multiplied by a factor of 1.2, an average value. The range in this factor varied from 1.0 up to 1.49 within the combination of 55 missiles and locations, indicating the importance of utilizing this methodology *only for preliminary estimates*. For the vehicles and locations considered, the 1% extreme bending moment obtained in this manner did not differ by more than 20% from that obtained from the complete distribution. Also, 60% of the errors were less than 10% of the overall 1% extreme bending moment.

The data used to make up each of the preliminary design profiles are given in Table 4-11. To obtain the profile for 1% extreme response at a given altitude for each location, simulate a flight for a wind profile with minimum velocity at all altitudes to within 2500 ft of the altitude being investigated. Then move to the 1% probable velocity at that altitude. Responses to all other altitudes are obtained in an analogous manner. Figure 4-29 shows the wind profiles which are to be used to determine the 1% extreme response for Caribou, Maine, for each altitude designated by a capital letter. To obtain the value for 25,000 ft, assume profile s, a, b, c, d, e, E; for 30,000 ft, assume s, a, b, c, d, e, f, F, etc. Profiles must be oriented at the most critical direction.

The seven locations in the U.S., or all 11 locations, should be investigated if the vehicle is designed for either a U.S. or a worldwide operational capability. For single location design, such as for launching from Vandenberg AFB, only the nearest location (Long Beach, California) need be considered.

The highest bending moment obtained from this family of curves for each location can be readily determined by inspection because it will usually be near the altitude of maximum dynamic pressure. It must be multiplied by a factor of 1.2 to provide the first approximation of a 1% extreme response for that location. Of the seven U.S. locations, Caribou was the worst for five designs investigated. For all eleven locations, Caribou was worst for three of

Table 4-11. 1% extremes, minimum and maximum, of East-West wind speed (ft sec^{-1}). Compiled from data of Mazzola et al [1963].

Altitude (ft)	Long Beach Calif. min	Long Beach Calif. max	Denver Colo. min	Denver Colo. max	Seattle Wash. min	Seattle Wash. max	Ft. Worth Texas min	Ft. Worth Texas max	Internat'l Falls Minn. min	Internat'l Falls Minn. max	Montgomery Alabama min	Montgomery Alabama max	Caribou Maine min	Caribou Maine max	Kadena Okinawa min	Kadena Okinawa max	Keflavik Iceland min	Keflavik Iceland max	Tripoli Libya min	Tripoli Libya max	Bitburg Germany min	Bitburg Germany max
2500	1				18		16		26		20		39		−2		23		33		39	
5000		44				72		74		70		75		88		52		88		79		82
7500	36		17		42		40		52		51		63		24		54		48		72	
10,000		74		79		90		87		90		100		99		84		97		82		97
12,500	50		50		54		60		58		69		73		44		68		55		76	
15,000		87		107		115		109		109		127		132		114		122		98		117
17,500	69		66		94		105		89		92		101		77		90		80		93	
20,000		110		125		145		147		137		158		153		167		161		135		138
22,500	89		134		119		114		131		136		120		119		156		127		104	
25,000		136		194		175		161		170		189		187		195		225		178		157
27,500	106		120		148		148		134		162		135		170		140		115		92	
30,000		157		215		208		197		186		229		228		239		220		196		168
32,500	137		136		146		160		120		167		166		162		124		109		136	
35,000	149	192	155	203	131	210	184	232	105	165	203	247	181	251	151	266	156	229	171	219	108	188
37,500	163	214	130	225	136	200	169	238	140	158	179	261	172	267	163	240	92	209	126	245	75	186
40,000		231		230		186		216		174		252		240		255		164		232		154
42,500	122		107		80		140		116		152		154		143		93		87		37	
45,000		176		178		125		204		158		218		238		233		186		190		126
47,500	78		96		72		129		121		100		116		105		75		101		73	
50,000		137		174		124		181		169		214		195		196		167		187		146

the designs and Kadena, Okinawa, for two designs. The 1% extreme stress due to Japanese winds can be expected to be 20% greater than the worst of these eleven locations.

4.4.2 Other Methods of Predicting Winds for Design Purposes

Other methods of applying wind data have been tried, such as utilization of matrices of level-by-level wind statistics (useful in reentry problems, see Sec. 4.4.4) to construct synthetic profiles or to obtain the mean and standard deviation of the responses by level. In another technique, various families of synthetic wind profiles are specified in nomograms involving the area under the wind profile curves. The most promising techniques involve simplification of wind profiles and equations of vehicle motion in order to permit utilization of a desk calculator on a large number of profiles. Hopefully, this method will lead to selection of a wind profile closest to the risk specified in the design philosophy so that the more accurate, detailed calculations of response can be limited to one sounding. Although they are probably acceptable for preliminary design, these techniques cannot be relied upon to depict accurately the response required for the specified risk to which they are supposed to correspond. There is even some question whether the amount of effort involved in some of these indirect approaches is sufficiently less than the effort required in an abbreviated version of the basic approach (Sec. 4.4.3) to warrant utilization for preliminary design.

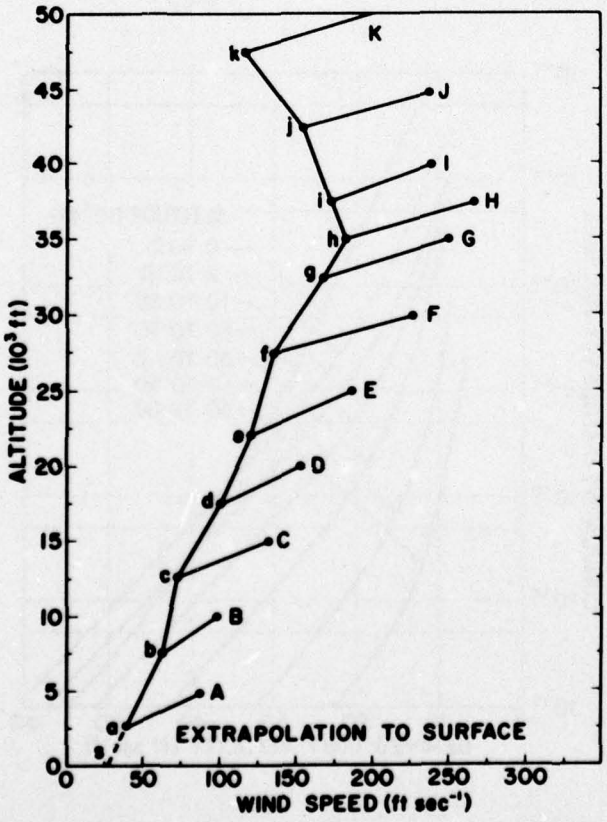


Fig. 4-29. One percent extreme wind profiles for Caribou, Maine.

4.4.3 Final Design Calculations

If a reasonable delay in launching can be tolerated when stresses due to the predicted wind profile (plus those of a reasonably strong gust) exceed the preliminary design stresses, detailed computations are not required. If accuracy in the calculated risk is desired, the basic approach for final design is to subject this design to simulated flights by computers along realistic azimuths through a representative sample of accurately observed and computed wind profiles using equations of motion for as many degrees of vehicle freedom as are feasible. The number of soundings in such a representative sample depends upon the accepted calculated risk in the design, the accuracy required, and the confidence level to be placed in this accuracy. Statistical analyses of the locations listed in Table 4-11 indicate that for locations where wind stresses on missiles have been severest, a sample of about 200 soundings, gathered at intervals of about three days over five windy seasons, are satisfactory for obtaining the 1% extreme yaw bending moment with 10% accuracy and a 0.99 confidence level. For Kadena, Okinawa, an average value of only 70 soundings was required for five different vehicle designs because of the steadiness of the wind. At Caribou, Maine, the requirement was almost 200. At Bitburg, Germany, the upper air flow is so variable from year to year and within the winter season that 400 soundings are required. (Fortunately, this area does not appear particularly critical, at least for the vehicle configurations investigated so far.)

A less costly method than computer flights through 200 soundings is to select from each sample of 200 the 50 soundings that approximate the top 25% of the distribution of missile responses for the typical missile configuration. From these 50 soundings the complete cumulative frequency curve on normal probability paper can be constructed. The complete sample of 11 sets of 200 wind soundings are available on IBM 7090 magnetic tape from the Aeronautics Systems Division, Wright-Patterson Air Force Base, Ohio. Identification of the reduced sample of 50 soundings from each of the 11 locations is provided in Table XIV of the ASD report by Mazzola et al [1963].

In final design, usually only the location which is the most critical in preliminary design need be considered. For design of a vehicle that is to be flown in the U.S., however, the wind sample for Caribou, Maine, should always be investigated even though some other location appears to present more severe conditions during preliminary design. For vehicles to be flown on a worldwide basis, the wind sample for Kadena, Okinawa, should be investigated even if it does not appear to be the most severe during the preliminary design investigations. Furthermore, for worldwide design, an exploratory comparison of approximated 1% extreme bending moment responses for Tateno, Japan, reveals that they exceed Kadena by 16, 10, and 31% for three designs and Caribou

by 8 and 11% for two designs but 8% less for another. For two other designs, Kadena winds are more severe than Caribou (no Tateno comparisons are available). As a best estimate for conservative design, it appears wise to assume the 1% probable wind profile stress will be 20% more severe over Japan than the worst of the locations given in Table 4-11.

The soundings specified for final design were obtained from the standard AN/GMD-1 system. Consequently, they do not provide information on individual gusts which add to the stresses and on detailed fluctuations in the wind profile which create dynamic response of the vehicle. Also, the sample is biased by the fact that the equipment becomes inoperative under extremely strong wind conditions. This bias is offset only in part by the fact that the noise in the instrumentation system tends toward an overestimate of the extremes of responses due to wind profiles. The bias is unimportant when a normal or near normal distribution of the responses can be assumed so that the extremes can be estimated from statistics determined by the central portion of the sample distribution rather than from the sample extremes.

In applying additional load factors due to gustiness, there is no universally acceptable methodology at present. Extremely strong gust spikes of 40 to 50 ft sec^{-1}, developing over vertical distances of about 200 ft (analogous to a 1-cosine shaped gust with a wavelength of 400 ft), are assumed to have a correlation coefficient of 0.5 responses due to the 1% extreme wind profile. (This coefficient was estimated from research flights which revealed 40% likelihood of some turbulence recorded by airplanes in about 30 jet streams which were mostly of moderate strength.) In other cases, independently calculated responses for a light turbulence (gusts of about 10 ft sec^{-1}) or moderately strong gusts (20 to 30 ft sec^{-1}) are added directly to the responses required for strong-wind profiles, implying a correlation coefficient of 1.0. Fortunately, the responses for gusts are considerably smaller than those required by strong-wind profiles of the 1% extreme so that the method of adding the responses required for the general profile and for the gusts is not too critical. For vehicles with nonmilitary missions, gust becomes more important as the design moves toward high risks for profile shear and less severe profiles; the correlation between gusts and profile responses will become more critical. A conservative assumption of 1.0 correlation coefficient is recommended, although a zero correlation is probably more realistic for gustiness with moderate wind profiles. Figure 4-30 presents gust data gathered from aircraft, which are considered most applicable to horizontally moving missiles. Because there are no analogous presentations for vertically moving vehicles, these data have been utilized by assuming isotropy. The probability of encountering such gusts for vertically rising vehicles is difficult to obtain from this; values as low as 10 ft sec^{-1}, based upon assumptions of distance of travel, have been used. No data proven to actually represent the applicable wind details for the problem of dynamic responses of vertically moving vehicles are available for recommendation at this time. A routine program of detailed wind soundings that will depict wind vectors through 100-ft layers on a routine basis is needed.

4.4.4 Ballistic Profiles

Deviations from planned trajectories and impact points will occur because of deviations from the planning models of the integrated wind and density over the trajectory, or deviations from the planned missile response to wind and density. In practice, ballistic effects are analyzed by replacing the integration with a summation so that the effect becomes a weighted average of the conditions at various levels. Wind effects are complicated by the vector nature of wind.

The mean effect of wind on the range and cross range of missiles can be determined from $\Sigma c_i \bar{V}_i$, where c_i is the influence coefficient at the ith level that describes the portion of the total response of the missile that is assignable to the level, and $\bar{V}_i$ represents the mean of the component wind speed for the level. This mean effect can be applicable to a month, season, or the entire year, but seasonal means are preferable.

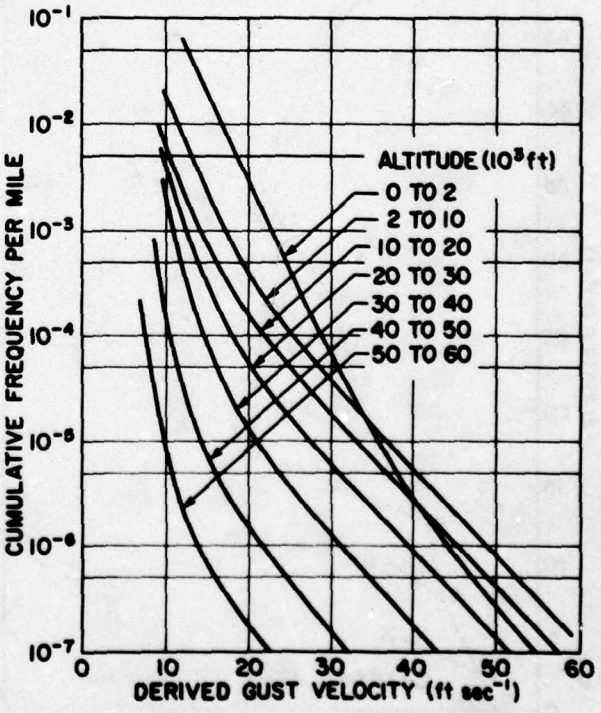


Fig. 4-30. Distribution of overall derived gust velocity for airplanes at various altitudes.

The variation from the mean effect caused by day-to-day fluctuations in the winds is obtained from

$$\sigma = \Sigma_{i,j}\, c_i c_j r_{ij} \sigma_i \sigma_j , \qquad (4\text{-}14)$$

where c_i and c_j are the influence coefficients at the ith and j^{th} levels, σ_i and σ_j are the standard deviations of the component wind at these levels, and r_{ij} is the correlation between the component wind at the ith level and that at the jth level. This yields the standard deviation for each component of the ballistic wind. These can be combined and used to determine the probability of occurrence of deviations of any desired magnitude from the planned trajectory or impact point.

If Eq. 4-14 is applied to the vector ballistic wind instead of to a component, the terms for the deviation of the winds at each level must be expanded to include the correlation between components at the level. The correlation term, r_{ij}, then becomes the correlation between two vectors which involves correlations between all possible pairs of the four components. Because the formula is complex and calculations based on it are lengthy, it is usually assumed that the cross-component correlations are zero at and between levels, and that the wind frequency distributions are essentially circular normal. These assumptions are most valid when the wind data refer to seasons rather than months or the entire year, although they are not perfectly reliable everywhere even for seasonal data.

The wind climatology necessary for determination of ballistic effects consists of the mean wind speed, standard deviation, and correlation between levels for a series of altitudes for each component. This information has been prepared for a number of stations, usually in a matrix form. For targeting purposes, information must pertain to the specific location of interest. For design purposes, a representative sample, including extreme conditions, must be evaluated. Tables 4-12 through 4-18 give the data, including the number of observations, for various stations for the winter season. (Interpretation of statistics on a variate with a circular normal distribution is discussed in Sec. 4.5.3.)

4.5 DESIGN DATA ON WINDS

Wind data can be presented in a variety of ways, each of which is of maximum usefulness for a particular aspect of a design problem. The data presented in this section were selected on the basis of their applicability to a number of different types of problems. Wind velocity is one of the most variable of meteorological elements. The distribution of the vector wind is most difficult to describe and to analyze; this presentation is limited purposely to wind speeds. Tables and figures give wind speeds in mile h^{-1} because the observations were made in these units.

Table 4-12. Means ($\bar{x}$ East to West, and $\bar{y}$ North to South) and standard deviations (s_x, s_y) of wind speed components (knots), and correlations between levels for each component and between components at each level for winter, Wiesbaden, Germany.

No. of Obs.	Level (km)	$\bar{x}$	s_x	Level (km)	0	1	2	4	6	8	10	12	14	16	18	20	22	24	26
				$\bar{y}$	−0.3	−1.1	1.7	5.3	6.3	11.4	15.2	14.0	12.7	11.7	11.0	10.0	11.4	10.5	11.2
				s_y	5.47	12.27	14.60	18.85	26.60	32.94	34.55	26.56	19.80	15.66	15.17	14.97	16.28	17.35	17.44
2392	0	−0.8	7.63		.247	.352	.209	.129	.078	.046	.041	.045	.063	.050	.020	.086	.123	.151	−.072
2358	1	−7.9	17.28		.566	.066	.821	.632	.526	.451	.439	.437	.452	.416	.378	.195	.238	.226	.078
2278	2	−9.5	19.60		.491	.899	.044	.771	.649	.573	.555	.547	.538	.497	.476	.294	.349	.361	.108
2082	4	−11.6	21.03		.419	.761	.851	.109	.859	.770	.734	.703	.650	.589	.518	.360	.403	.430	.233
1873	6	−13.2	26.07		.336	.629	.736	.878	.130	.896	.845	.761	.669	.579	.514	.347	.397	.396	.251
1636	8	−16.3	30.81		.307	.572	.672	.806	.897	.062	.896	.796	.680	.589	.516	.344	.361	.336	.205
1405	10	−18.1	31.93		.310	.560	.664	.791	.853	.906	.068	.856	.723	.654	.570	.382	.395	.403	.272
1111	12	−18.6	24.98		.308	.570	.666	.775	.800	.812	.876	.030	.813	.760	.652	.484	.486	.500	.294
876	14	−19.3	21.68		.272	.534	.625	.692	.705	.712	.759	.824	.025	.798	.689	.565	.515	.483	.404
642	16	−17.7	20.14		.284	.460	.565	.654	.660	.660	.709	.795	.824	.078	.830	.726	.672	.698	.456
447	18	−17.1	21.00		.288	.434	.516	.611	.610	.594	.655	.727	.728	.876	−.071	.787	.740	.764	.575
318	20	−18.7	20.15		.171	.403	.467	.498	.485	.468	.531	.621	.649	.798	.869	.014	.817	.796	.564
240	22	−20.4	22.70		.166	.420	.494	.471	.458	.428	.512	.603	.587	.766	.834	.873	.000	.844	.623
181	24	−23.5	24.16		.172	.436	.526	.476	.445	.408	.504	.599	.559	.719	.791	.855	.917	−.108	.716
114	26	−24.7	27.73		.000	.211	.347	.376	.324	.297	.389	.492	.526	.648	.783	.783	.869	.919	−.059

Table 4-13. Means ($\bar{x}$ East to West, and $\bar{y}$ North to South) and standard deviations (s_x, s_y) of wind speed components (knots), and correlations between levels for each component and between components at each level for winter, Thule, Greenland.

No. of Obs.	Level (km)	$\bar{x}$	s_x	Level (km) / $\bar{y}$ / s_y	0	1	2	4	6	8	10	12	14	16	18	20	22	24	26
				$\bar{y}$	−0.2	−2.8	−4.4	−6.7	−9.9	−10.1	−8.6	−6.9	−5.0	−3.3	0.5	1.1	2.8	−2.4	−24.3
				s_y	2.65	8.91	11.70	16.23	19.96	19.94	14.78	14.00	16.02	19.56	22.64	24.91	23.97	23.90	32.81
934	0	3.6	4.80		−.180	.120	.072	.000	.000	−.010	.032	.062	.048	.144	.000	.032	−.210	.020	−.815
917	1	3.9	6.65		.192	−.394	.714	.425	.227	.151	.207	.183	.273	.221	.186	.072	.261	.095	.712
909	2	1.8	8.88		.093	.593	−.150	.722	.522	.412	.421	.350	.385	.259	.277	.115	.331	.058	.985
906	4	0.9	14.42		−.032	.234	.667	−.017	.836	.727	.635	.487	.415	.264	.230	.104	.125	.485	.970
871	6	0.4	20.69		−.030	.166	.568	.883	.000	.882	.949	.566	.450	.287	.232	.160	.104	.457	.999
776	8	−0.9	22.57		−.028	.092	.465	.804	.904	−.010	.822	.604	.479	.288	.170	.223	.223	.372	.960
664	10	−3.3	18.01		.000	.096	.457	.753	.802	.891	−.088	.815	.719	.564	.401	.269	.249	.178	.987
565	12	−6.1	16.39		.000	.119	.412	.634	.666	.761	.883	−.208	.864	.782	.658	.496	.516	.678	.996
443	14	−9.3	16.37		.058	.124	.313	.542	.570	.684	.823	.902	−.350	.892	.831	.635	.736	.712	.999
319	16	−11.5	17.54		.060	.094	.259	.448	.512	.619	.716	.842	.878	−.407	.907	.718	.814	.908	1.000
180	18	−17.2	18.60		−.041	.017	.186	.376	.431	.525	.637	.752	.811	.863	−.412	.783	.865	.841	.973
91	20	−21.0	22.25		−.154	−.022	.107	.315	.322	.394	.412	.579	.676	.761	.842	−.266	.908	.868	.971
39	22	−21.0	21.80		−.102	.085	.172	.387	.225	.388	.395	.605	.649	.734	.849	.864	−.406	.868	.999
17	24	−16.5	21.71		−.140	.139	.198	.319	.326	.552	.444	.684	.588	.719	.718	.724	.938	−.441	.962
3	26	−2.0	12.23		.115	.974	.999	.918	.983	.918	.918	.918	.000	.803	.235	.487	.803	.999	.669

Table 4-14. Means ($\bar{x}$ East to West, and $\bar{y}$ North to South) and standard deviations (s_x, s_y) of wind speed components (knots), and correlations between levels for each component and between components at each level for winter, Washington, D.C.

No. of Obs.	Level (km)	$\bar{x}$	s_x	Level (km) / $\bar{y}$ / s_y	0	1	2	4	6	8	10	12	14	16	18	20	22	24	26
				$\bar{y}$	−0.0	0.3	1.0	−1.1	−2.6	−4.5	−3.9	−3.3	−2.2	−2.1	−1.1	0.3	0.6	2.4	0.7
				s_y	6.48	17.32	17.54	21.49	29.95	37.88	40.36	30.83	23.19	17.16	13.34	11.20	10.45	10.84	11.85
1314	0	−2.6	5.72		−.125	.610	.358	.276	.185	.137	.032	−.036	−.032	−.017	.017	.025	.010	.071	.017
1285	1	−14.6	12.91		.473	.098	.759	.536	.377	.300	.198	.132	.062	.000	.033	−.114	−.057	.036	.020
1233	2	−21.9	12.75		.237	.667	.078	.726	.587	.523	.407	.326	.246	.160	.152	−.118	−.095	.010	−.066
1113	4	−36.6	16.28		.177	.411	.648	.010	.837	.763	.666	.575	.480	.392	.361	−.039	.000	.110	−.130
923	6	−49.1	22.60		.155	.310	.508	.786	.010	.884	.784	.656	.569	.441	.355	.093	.072	.143	.040
822	8	−60.6	29.40		.118	.244	.445	.686	.832	.044	.874	.729	.621	.505	.396	.130	.093	.183	.000
731	10	−72.6	34.28		.040	.198	.437	.636	.743	.855	.020	.804	.671	.535	.425	.141	.052	.099	−.086
653	12	−72.7	32.03		−.078	.138	.354	.516	.619	.697	.766	.020	.732	.620	.539	.143	.114	.040	−.044
591	14	−64.2	27.39		−.056	.133	.308	.456	.540	.577	.619	.749	.000	.673	.590	.202	.218	.136	−.163
527	16	−48.2	21.85		−.077	.133	.269	.386	.421	.418	.460	.576	.623	−.059	.547	.276	.253	.210	.050
459	18	−32.6	22.36		−.030	.115	.286	.388	.392	.354	.390	.529	.484	.500	.010	.334	.357	.326	.189
402	20	−18.9	22.67		−.041	.075	.153	.253	.270	.297	.354	.368	.328	.460	.405	.014	.463	.254	.239
341	22	−12.6	21.79		−.094	.096	.116	.136	.100	.117	.149	.202	.304	.386	.354	.483	.183	.240	.362
221	24	−9.7	21.94		−.043	−.017	.069	.164	.085	.095	.158	.261	.212	.207	.270	.439	.287	.079	.209
123	26	−8.1	26.69		.020	.120	.172	.194	.051	.121	.180	.333	.365	.358	.458	.388	.545	.424	.310

Table 4-15. Means ($\bar{x}$ East to West, and $\bar{y}$ North to South) and standard deviations (s_x, s_y) of wind speed components (knots), and correlations between levels for each component and between components at each level for winter, Forbes A.F.B., Kansas.

No. of Obs.	Level (km)	$\bar{x}$	s_x	Level (km) / s_y	0	1	2	4	6	8	10	12	14	16	18	20	22	24	26
				$\bar{y}$	0.9	1.8	4.0	3.9	−0.4	−3.8	−7.4	−11.2	−9.2	−4.6	−1.2	3.6	4.5	2.7	4.7
				s_y	7.89	20.34	20.62	25.59	32.45	40.09	45.43	38.10	31.29	24.85	21.19	23.73	16.94	13.62	11.93
567	0	−1.8	5.88		−.105	.720	.472	.203	.099	−.017	−.067	−.087	−.046	−.039	.028	.020	−.139	−.043	.139
559	1	−8.6	12.78		.494	.109	.973	.504	.346	.222	.179	.159	.106	.073	.084	.081	−.141	−.053	.242
559	2	−15.9	12.79		.364	.697	.115	.757	.597	.461	.420	.368	.339	.299	.208	.287	.037	.193	.219
558	4	−27.2	15.20		.138	.329	.583	.199	.893	.793	.756	.681	.660	.580	.487	.454	.352	.400	.359
540	6	−38.3	20.18		.062	.208	.447	.811	.291	.890	.841	.757	.747	.657	.607	.510	.512	.490	.446
503	8	−49.3	29.31		−.020	.161	.345	.686	.824	.284	.911	.785	.764	.693	.544	.583	.589	.488	.259
454	10	−61.3	35.27		−.083	.078	.274	.571	.720	.852	.228	.862	.780	.688	.551	.572	.590	.553	.485
365	12	−64.4	30.43		−.142	.062	.193	.523	.634	.720	.742	.174	.849	.798	.619	.596	.611	.643	.457
271	14	−55.4	25.18		−.146	−.085	.076	.427	.538	.561	.535	.685	.246	.817	.693	.668	.633	.656	.506
182	16	−43.2	24.42		−.136	−.083	.153	.346	.397	.377	.373	.465	.691	.214	.625	.555	.565	.657	.234
115	18	−26.5	20.89		.055	−.037	.207	.352	.290	.175	.067	.209	.488	.492	.372	.599	.559	.696	.513
85	20	−18.4	20.96		.186	.022	.075	.172	.067	.000	−.110	−.081	.319	.427	.656	.041	.673	.647	.459
70	22	−11.0	23.69		.232	.057	.129	.173	.139	.000	−.127	−.112	.220	.445	.590	.717	.358	.573	.478
47	24	−5.4	24.73		.231	−.077	.041	.055	−.041	−.225	−.319	−.181	.247	.203	.707	.714	.735	.563	.234
24	26	−8.6	27.95		.344	−.169	.198	.095	.036	−.058	−.253	−.066	.297	.213	.733	.807	.822	.887	−.129

Table 4-16. Means ($\bar{x}$ East to West, and $\bar{y}$ North to South) and standard deviations (s_x, s_y) of wind speed components (knots), and correlations between levels for each component and between components at each level for winter, Patrick A.F.B., Florida.

No. of Obs.	Level (km)	$\bar{x}$	s_x	Level (km) / s_y	0	1	2	4	6	8	10	12	14	16	18	20	22	24	26
				$\bar{y}$	1.4	−2.4	−1.9	−1.6	−1.2	−0.6	−0.1	0.2	0.2	0.0	0.0	0.1	0.4	0.7	0.8
				s_y	8.03	12.42	12.99	15.30	19.98	24.68	30.14	32.42	27.04	21.11	14.71	9.77	7.43	9.36	10.15
1468	0	−0.3	7.10		−.133	.682	.511	.370	.291	.231	.183	.101	.103	.120	.074	.048	.025	.022	−.093
1452	1	−3.6	13.79		.627	−.083	.775	.520	.397	.281	.168	.101	.083	.141	.066	.105	.032	.129	−.027
1453	2	−10.2	13.89		.565	.833	.000	.685	.554	.465	.359	.271	.223	.251	.252	.127	.076	.063	.025
1435	4	−23.1	16.60		.511	.670	.768	.113	.785	.677	.578	.493	.437	.461	.437	.288	.140	.017	.155
1409	6	−35.8	21.02		.431	.555	.669	.826	.206	.803	.693	.629	.570	.561	.551	.285	.152	−.037	.154
1365	8	−49.1	26.22		.373	.496	.615	.760	.845	.236	.843	.717	.657	.631	.547	.316	.074	−.068	.209
1315	10	−63.1	32.04		.350	.450	.544	.669	.749	.835	.333	.788	.703	.611	.540	.307	.187	−.103	.211
1215	12	−74.5	34.91		.258	.341	.448	.524	.594	.694	.772	.304	.780	.682	.558	.274	.116	.000	.113
978	14	−72.5	32.91		.238	.353	.425	.529	.560	.626	.674	.340	.271	.769	.648	.283	.121	.000	.137
639	16	−55.2	26.73		.218	.296	.410	.489	.515	.594	.585	.646	.706	.228	.688	.368	.188	−.025	−.010
412	18	−33.6	25.63		.010	.109	.215	.314	.331	.432	.424	.460	.495	.601	.144	.372	.239	.000	.052
306	20	−12.0	21.18		.032	.000	.068	.160	.163	.205	.187	.191	.214	.400	.459	.163	.289	.017	.150
251	22	−7.3	21.68		.000	−.010	.017	.095	.127	.092	.191	.163	.098	.260	.210	.448	.055	.193	.068
203	24	−10.1	23.32		−.028	.086	.185	.201	.176	.189	.228	.145	.145	.224	.279	.439	.620	.187	.285
131	26	−15.3	24.70		.076	.089	.203	.234	.237	.224	.206	.199	.118	.224	.281	.430	.585	.721	.048

Table 4-17. Means ($\bar{x}$ East to West, and $\bar{y}$ North to South) and standard deviations (s_x, s_y) of wind speed components (knots), and correlations between levels for each component and between components at each level for winter, Great Falls, Montana.

No. of Obs.	Level (km)	$\bar{x}$	s_x	Level (km) / $\bar{y}$ / s_y	0	1	2	4	6	8	10	12	14	16	18	20	22	24	26
				$\bar{y}$	−7.6	—	−2.2	8.0	12.4	14.2	16.8	11.6	8.7	7.6	7.5	6.6	9.7	15.8	21.8
				s_y	8.95	—	10.59	15.99	26.50	36.45	37.02	26.30	20.36	16.54	15.51	13.39	13.86	14.20	25.51
913	0	−8.7	7.98		.633	—	.223	−.054	−.053	−.092	−.122	−.119	−.082	−.081	.071	.000	.092	−.076	−.283
—	1	—	—		—	—	—	—	—	—	—	—	—	—	—	—	—	—	—
881	2	−19.6	12.80		.555	—	.248	.564	.440	.373	.365	.398	.442	.310	.287	.218	.168	−.054	.124
745	4	−25.9	17.14		.105	—	.546	.193	.773	.682	.700	.686	.608	.374	.252	.125	.082	−.047	−.176
573	6	−31.3	22.53		.014	—	.394	.796	.144	.871	.817	.711	.638	.370	.211	.106	.097	−.084	−.022
417	8	−37.9	30.86		−.078	—	.305	.694	.865	.187	.888	.724	.585	.323	.160	.145	.104	.010	.050
322	10	−41.0	35.01		−.033	—	.336	.670	.781	.845	.167	.808	.636	.413	.322	.167	.070	.022	.074
283	12	−37.3	27.81		−.063	—	.326	.589	.698	.752	.810	.179	.762	.489	.415	.324	.168	.233	.327
254	14	−33.2	23.25		.000	—	.276	.584	.647	.645	.664	.717	.182	.633	.517	.484	.314	.180	.369
244	16	−22.7	22.53		−.070	—	.123	.300	.367	.381	.548	.361	.526	.049	.635	.496	.470	.054	−.119
223	18	−15.2	22.22		.010	—	.169	.364	.380	.406	.404	.513	.561	.342	.162	.505	.428	.135	−.071
186	20	−7.9	24.59		.088	—	.195	.294	.264	.217	.279	.261	.370	.512	.554	.057	.558	.430	.764
119	22	−0.4	24.21		.129	—	.236	.315	.181	.250	.329	.165	.326	.652	.480	.637	.217	.583	.513
58	24	3.9	26.01		.095	—	.111	.353	.175	.174	.329	.385	.514	.354	.669	.651	.727	.320	.887
19	26	10.8	25.61		.238	—	.331	.539	.328	.106	.225	.393	.499	.232	.524	.671	.635	.900	.086

Table 4-18. Means ($\bar{x}$ East to West, and $\bar{y}$ North to South) and standard deviations (s_x, s_y) of wind speed components (knots), and correlations between levels for each component and between components at each level for winter, Shemya, Aleutian Islands, Alaska.

No. of Obs.	Level (km)	$\bar{x}$	s_x	Level (km) / $\bar{y}$ / s_y	0	1	2	4	6	8	10	12	14	16	18	20	22	24	26
				$\bar{y}$	1.6	0.2	−1.5	−5.2	−8.2	−11.2	−13.5	−13.3	−13.9	−14.4	−15.5	−13.8	−14.7	−14.2	−15.5
				s_y	11.85	15.88	15.63	18.57	22.75	26.58	24.98	19.30	17.93	16.48	17.78	17.08	17.86	19.90	20.93
1560	0	0.2	13.43		.119	.817	.762	.603	.470	.349	.367	.365	.365	.301	.249	.253	.221	.240	.277
1535	1	0.2	18.84		.887	.000	.887	.701	.538	.415	.418	.396	.375	.349	.239	.149	.107	.193	.179
1537	2	−1.8	17.74		.827	.911	.027	.797	.627	.504	.505	.474	.433	.388	.318	.210	.166	.237	.272
1494	4	−5.5	20.07		.628	.713	.801	−.022	.830	.718	.673	.638	.544	.507	.358	.319	.184	.282	.321
1374	6	−9.1	25.34		.451	.519	.593	.830	−.047	.863	.788	.703	.576	.542	.365	.347	.184	.310	.359
1129	8	−12.2	31.59		.332	.407	.470	.708	.869	−.107	.866	.765	.644	.629	.427	.361	.251	.298	.337
794	10	−14.2	28.71		.286	.362	.414	.614	.729	.869	.032	.824	.694	.694	.488	.408	.305	.355	.373
560	12	−15.8	22.44		.306	.377	.410	.565	.656	.739	.841	−.022	.828	.761	.592	.477	.414	.496	.493
392	14	−18.7	20.93		.242	.293	.341	.473	.528	.611	.739	.860	−.032	.812	.739	.577	.564	.525	.573
278	16	−20.1	22.62		.223	.325	.353	.486	.540	.586	.707	.837	.867	−.027	.797	.610	.619	.567	.562
224	18	−20.5	23.63		.172	.242	.253	.342	.419	.515	.631	.746	.779	.878	.078	.790	.821	.703	.651
179	20	−18.1	19.99		.109	.181	.214	.327	.325	.395	.548	.653	.705	.780	.831	.254	.843	.776	.737
149	22	−18.6	23.64		.119	.185	.228	.321	.311	.320	.496	.604	.653	.749	.805	.876	.184	.869	.822
106	24	−18.9	24.02		.169	.201	.222	.238	.181	.204	.374	.507	.589	.661	.745	.759	.853	.161	.851
70	26	−19.7	25.07		.155	.179	.185	.217	.151	.178	.338	.437	.522	.546	.647	.691	.828	.922	−.091

4.5.1 Hourly Surface Wind Speeds

Neglecting the diurnal variability, the hourly observations of wind speed have been studied by many investigators whose conclusions differ. Some favor the distribution of wind speeds resulting from the circular bivariate normal distribution of wind components, others the log-normal or the gamma distributions. A historical record covering at least 5 yrs should be used to obtain estimates of wind speeds of 1%, 5%, etc., probability. It is recognized, however, that although there are about 600 city and airport stations in the United States where hourly records are kept, reasonable estimates of calculated risk speeds throughout the country are needed. A location that is close to a weather reporting station should have similar wind characteristics, except that terrain effects (topographic and radiational) superimpose a spatial variability that is difficult to generalize. Figures 4-31 through 4-34 should be useful as preliminary approximations. They are based on published summaries of directly observed distributions of surface wind speeds by months for the United States and Canada.

For estimates of wind speeds, a gamma distribution that works well is

$$f(y) = 0.5\, y^2 \exp(-y), \qquad (4\text{-}15)$$

where y is a reduced variate with mean 3 and standard deviation $\sqrt{3}$. Given the mean ($\bar{V}$) and standard deviation (s_v) of the hourly wind speed at a station, an estimate ($\hat{V}$) of probability (P) can be made by

$$\hat{V} = \bar{V} + s_v\, y_s\,; \qquad (4\text{-}16)$$

y_s is the standardized variate,

$$y_s = (y - 3)/\sqrt{3}\,. \qquad (4\text{-}17)$$

Values of y_s in Eq. (4-16) for estimating wind speeds that will be exceeded (1 — P) percent of the time, the calculated risk, are as follows:

Calculated Risk (%)	y_s
1	3.1
2½	2.45
5	1.9
10	1.4
20	0.7
50	—0.2
75	—0.75
90	—1.1

For example, in the month of January, Logan Airport, Boston, Mass., has a mean hourly wind speed of 13 mile h^{-1}, standard deviation $s_v = 6.4$ mile h^{-1}; using $y_s = 3.1$ in Eq. (4-16), the estimated speed that will be exceeded with only 1% frequency of all hourly observations is 33 mile h^{-1}.

This kind of approximation is good except for several Alaskan stations where calm conditions or very light winds prevail, but in these cases the error of estimate is small because *all* winds are light.

Figures 4-31 to 4-34 show smoothed isopleths of estimated means and standard deviations of the hourly wind speeds during the midseasonal months of January, April, July, and October. The estimations are designed for use in Eq. (4-16) to yield close estimates of the upper quantiles of wind speed. The lines are based on the means and standard deviations at 150 stations having records of five or more years. It was necessary to do much smoothing. Fairbanks, Alaska, for example, has a mean hourly wind in January of 2 mile h^{-1} and standard deviation 3.9 mile h^{-1}, yet Big Delta, approximately 75 miles away, has a mean wind of 12 mile h^{-1} and standard deviation 10.9 mile h^{-1}. Table 4-19 gives some of the largest 1% values of hourly wind speed.

4.5.2 Extreme Surface Wind Speeds

Different kinds of units are used to measure wind speed. The maximum hourly 5-min wind of any day is the greatest averaged speed of the 288 intervals of 5 minutes each. When wind speed multiplied by the time interval equals one mile, there is a mile of wind. The *fastest mile* has the shortest time interval of the day. The *strongest gust* is the highest reading of an instantaneous recording anemometer. There is no direct relation between these units. From Washington, D.C. records, for any period with speeds above 30 mile h^{-1}, the maximum 5-min wind speed is roughly 0.93 times the fastest mile and roughly 0.67 times the strongest gust. Data from the Climatic Center, Air Weather Service, show that the maximum 1-min wind speed is roughly 0.71 times the strongest gust. From data provided by the Meteorological Branch, Department of Transport, Canada, combined with data from the Meteorological Office, London, England, the maximum 1-h wind speed is 0.62 times the strongest gust.

Table 4-19. Some large hourly wind speeds, 1% calculated risk, corrected to 50-ft height above surface.

Stations	Wind Speed (mile h^{-1})			
	January	April	July	October
Shemya, Alaska	52	40	28	46
Stephenville, Nfdld.	47	37	26	39
Rapid City, S. D.	51	38	33	38
Churchill, Manitoba	33	45	28	38
Oklahoma City, Okla.	36	40	29	24
Nome, Alaska	39	37	26	33
Caribou, Maine	43	37	30	31
Cheyenne, Wyoming	40	36	26	34
Tatoosh Island, Wash.	47	38	24	38
Sydney, N .S.	39	38	28	34
Fargo, N. D.	36	40	28	35
Big Delta, Alaska	39	36	26	35

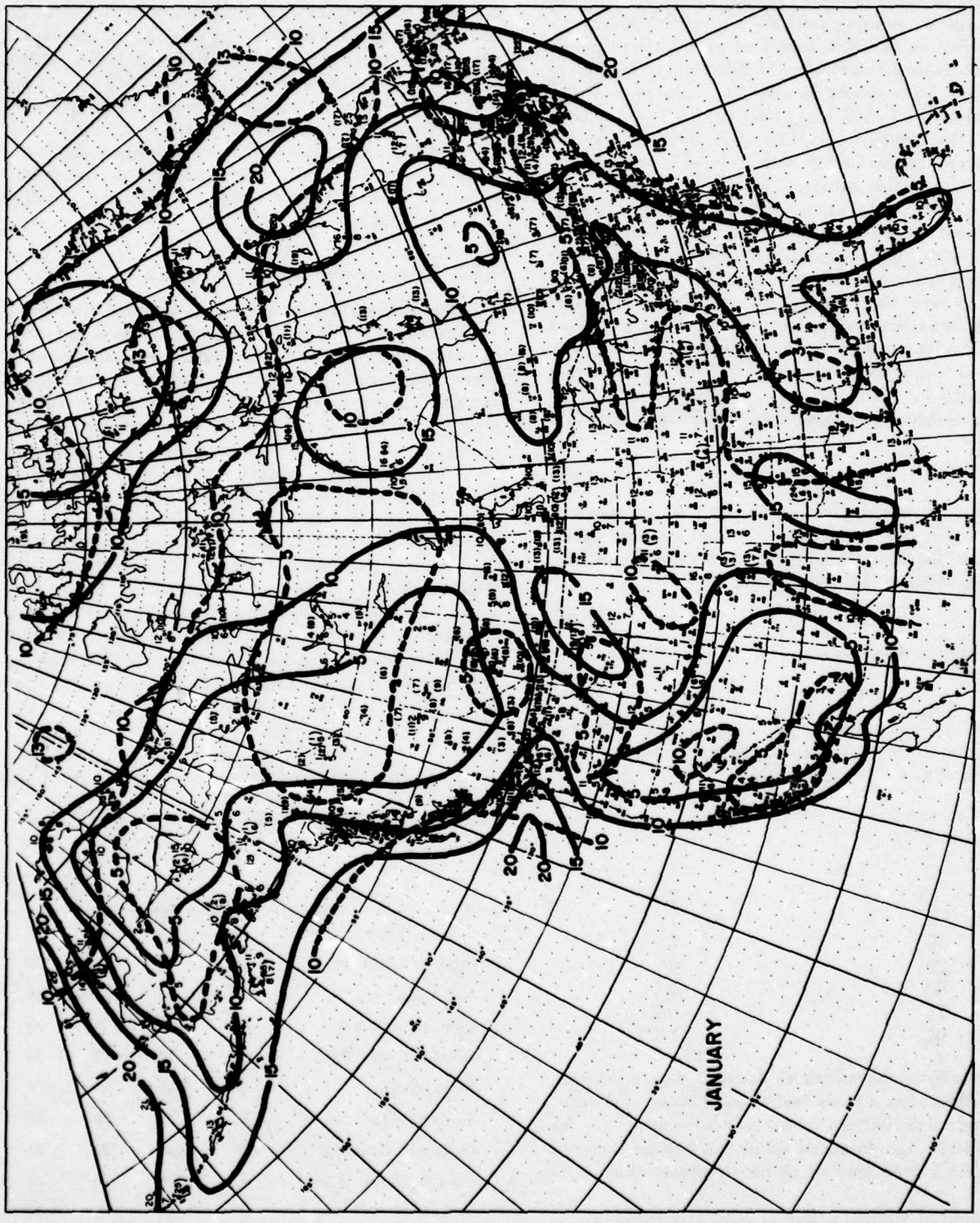


Fig. 4.31. Hourly mean wind speed estimates (mile h^{-1}) for January, corrected to 50 ft above ground. Isopleths of mean speed are in solid lines, standard deviations in broken lines. To obtain quantile estimates of calculated risk see Sec. 4.5.1.

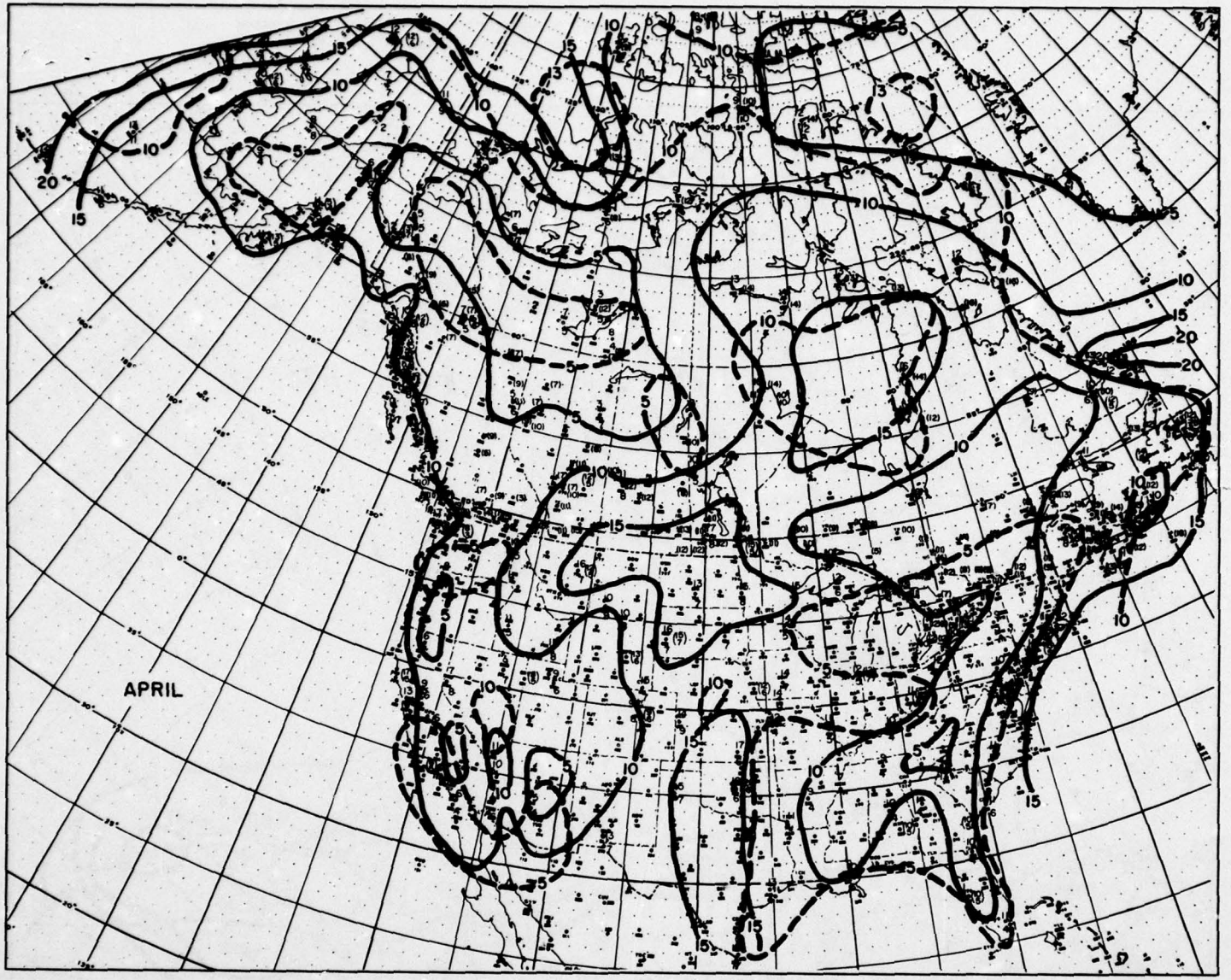


Fig. 4-32. Hourly mean wind speed estimates (mile h^{-1}) for April, corrected to 50 ft above ground. Isopleths of mean speed are in solid lines, standard deviation in broken lines. To obtain quantile estimates of calculated risk see Sec. 4.5.1.

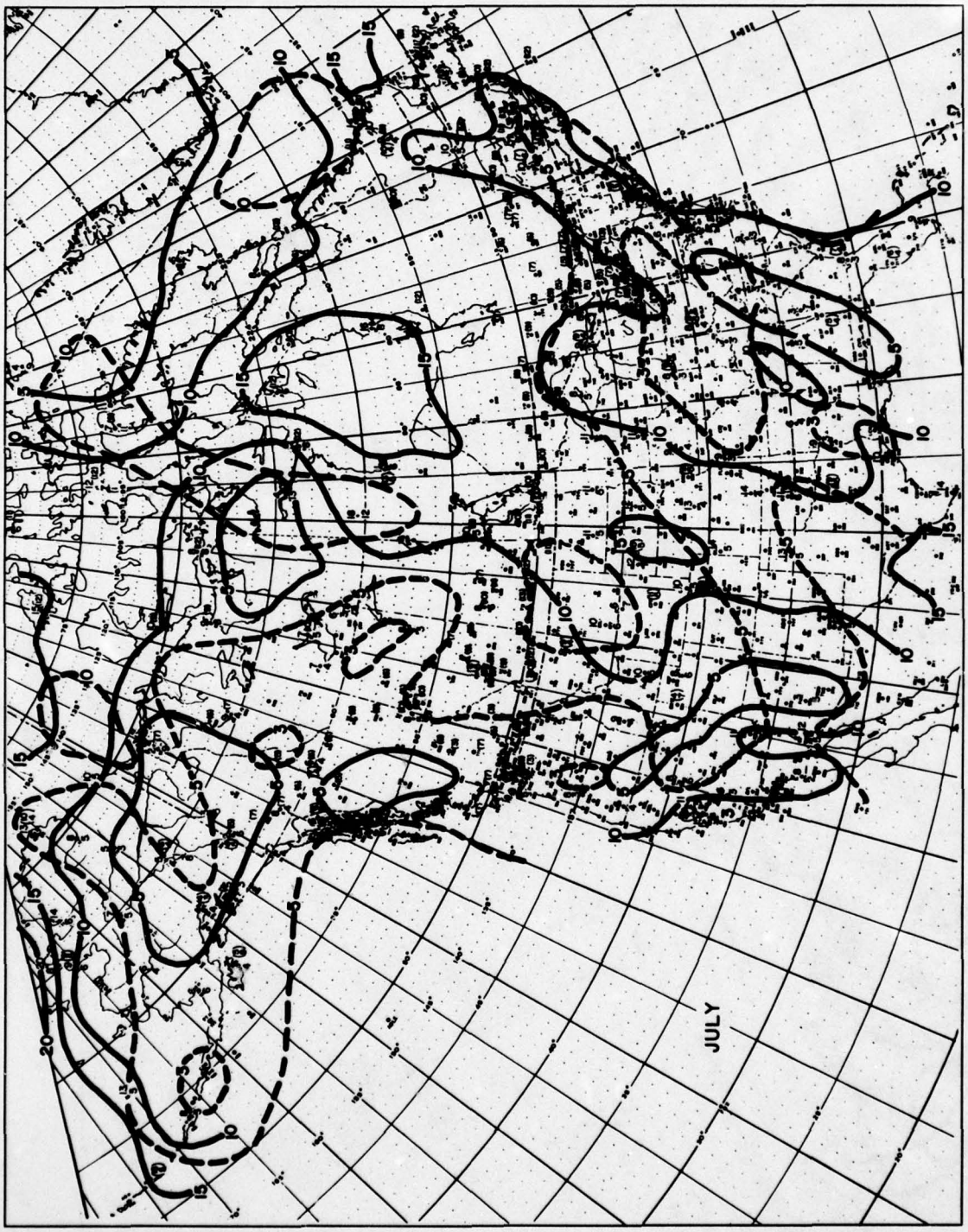


Fig. 4-33. Hourly mean wind speed estimates (mile h^{-1}) for July, corrected to 50 ft above ground. Isopleths of mean speed are in solid lines, standard deviation in broken lines. To obtain quantile estimates of calculated risk see Sec. 4.5.1.

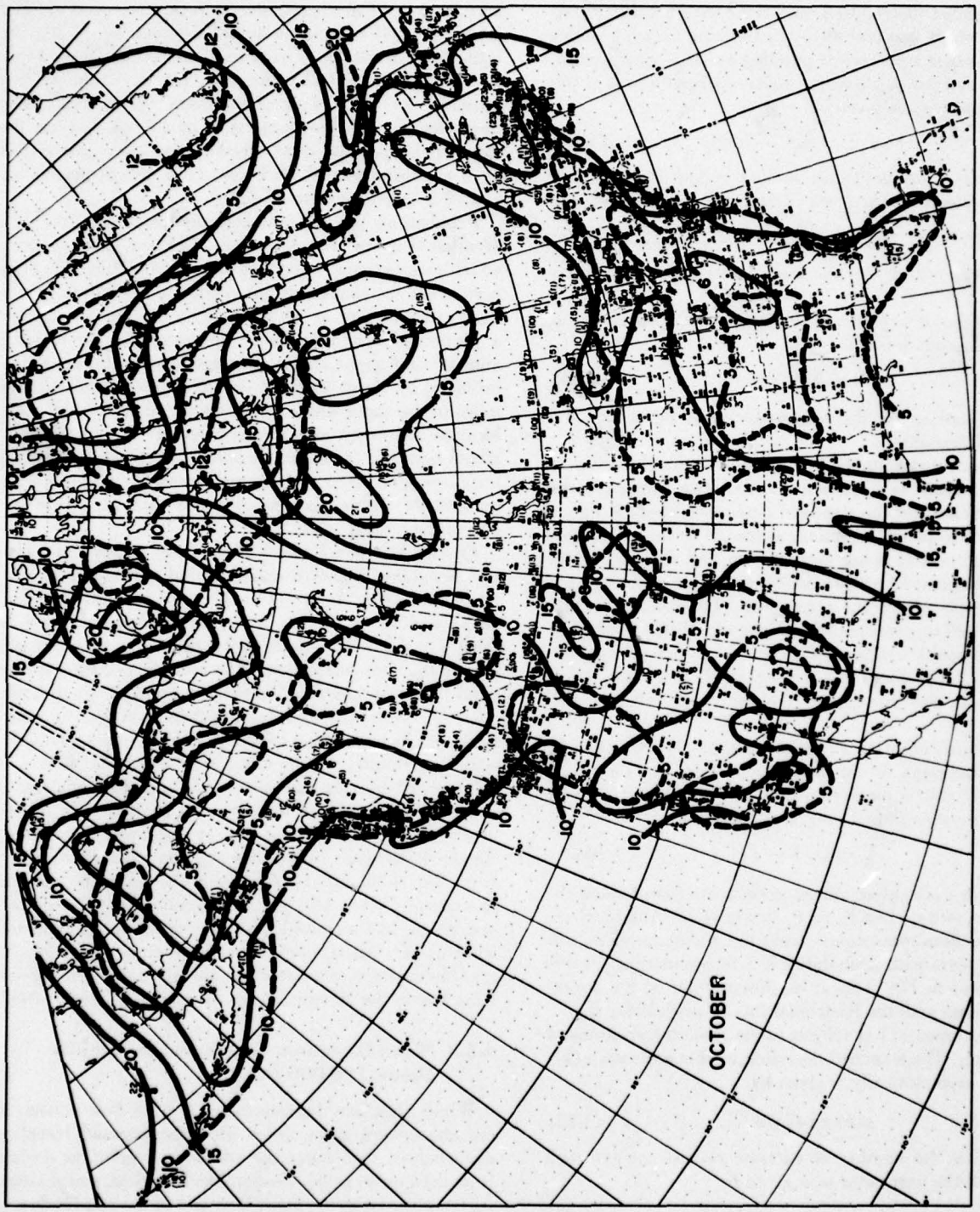


Fig. 4-34. Hourly mean wind speed estimates (mile h^{-1}) for October, corrected to 50 ft above ground. Isopleths of mean speed are in solid lines, standard deviation in broken lines. To obtain quantile estimates of calculated risk see Sec. 4.5.1.

The distribution of annual extreme wind speeds has been the subject of many reports with some conflicting viewpoints. The most favored distribution is the *double exponential distribution* (also called Fisher-Tippett Type I, the Gumbel distribution, and the extreme value distribution) which is useful also in estimating extreme values of many other geophysical parameters. This distribution, which is derived as a limiting form of distributions of the exponential type, is given by

$$F_1(x) = \exp(-e^{-y}). \qquad (4\text{-}18)$$

$F_1(x)$ is the *cumulative probability* of x in any one year with x related to the reduced variate y through the relation

$$[x - E(x)]/\sigma_x = (y - 0.5772)/1.28255 = y_s, \qquad (4\text{-}19)$$

where $E(x)$ and σ_x are the mean and standard deviation of x.

To obtain an estimate, $\hat{x}$, the standardized variate y_s is used in the equation

$$\hat{x} = \bar{x} + s_x y_s, \qquad (4\text{-}20)$$

where $\bar{x}$ and s_x are the observed sample mean and the standard deviation.

The work that is implied by Eq. (4-20) for the estimate of any statistic is to obtain the first two moments, the sample mean, and the standard deviation. There is no requirement to place the sample values in order of increasing magnitude. It is not necessary to find the parameters by successive approximations. Also, this estimate does not depend explicitly on the sample size. The value of y_s can be tabulated or presented graphically in terms of quantile or cumulative probability. Figure 4-35 shows the cumulative probability F_n vs y_s for n equals 1, 5, 10, etc. years (the mean, the mode, and the return period are also shown).

An estimation of an extreme value can be expressed in one of two ways. It can be given in terms of its *return period*, T; this is the period in which it is expected to be exceeded one or more times, and is given by

$$T = 1/(1 - F_1). \qquad (4\text{-}21)$$

Values for y_s for given return periods are found along the line marked $n = 1$ at $F_n = F_1$ in Fig. 4-35. Alternatively, it may be desirable to know what the maximum value will be in n years with probability F_n; its standardized value y_s is found in Fig. 4-35 at the intersection of the appropriate n-line with the horizontal line of probability F_n.

Any estimate ($\hat{x}$) is subject to the random variations of the sample. The standard deviation of this estimate, $s(\hat{x})$, reached asymptotically is given by

$$s(\hat{x}) = s_x \sqrt{\alpha/N}, \qquad (4\text{-}22)$$

where N is the number of extreme values, one for each year, and the parameter α is given by

$$\alpha = 1 + 1.139\, y_s + 1.100\, y_s^2. \qquad (4\text{-}23)$$

For example, a 19-yr record at Denver, Colorado, shows an annual 5-min maximum wind, measured at 50 ft above ground, averaging 38 knots with standard deviation 4.9 knots. If a tower, 50 ft high, is to be built to last for 25 yr, with a calculated risk accepted at the 1% level, it is necessary to know the critical wind speed. From Fig. 4-35 the standardized value at $n = 25$, $F_n = 0.99$ is found to be $y_s = 5.7$. (This corresponds to a return period of 2500 yr which is off scale in the figure.) From Eq. (4-20) the estimated critical 5-min wind speed is thus 66 knots. From Eq. (4-22) and (4-23) the standard deviation of this estimate, for $N = 19$ yr of extremes, is 7.4 knots. The mean for $n = 25$, however, is $y_s = 2.5$, so that on the average the greatest wind speed in the 25-yr period will have a mean value of 50 knots. (The return period for $y_s = 2.5$ corresponds to 45 yr.)

Publications by climatic agencies such as the U. S. Weather Bureau and Canadian Meteorological Service which give extreme values are widely available. Yet, each permanent installation might require a special study for the particular site at which it is to be located and for a particular design problem. For example, the extreme annual wind speed at Boston airport would be an underestimate, by about 33%, of the extreme on Blue Hill, 12 miles to the south southeast. Even the record at the exact location of interest may not be representative of the wind effects on a tall (or short) structure. Furthermore, a brief meteorological record of annual extremes permits estimates only within confidence bands that vary with the size of the record.

Figures 4-36 and 4-37 are isopleths of means and standard deviations of annual extreme wind speeds, drawn with much smoothing, for the United States and Canada; Fig. 4-36 was drawn to fit data at airport stations and Fig. 4-37 to fit city data. The effects of the protection of tall buildings in the cities is apparent. The reduction of the extreme wind might be anything between none to 55%, with the average roughly 25%. Assuming there is a specific structure, such as an antenna tower, to be built in an open field, estimates should be made using the data of Fig. 4-36.

The best statistics are mean and standard deviation of extremes of $n \geq 10$ yr for the exact location, hill, valley or plateau, at which a structure or equipment is to be installed. With these two values and the value y_s obtained from Fig. 4-35, Eq. (4-20) yields the requisite estimate of extreme. Table 4-20 gives the number of years of record, mean, and standard deviation of the extreme annual wind speed (fastest mile) for some stations in the Northern Hemisphere. Similar data are given for the United Kingdom in the Meteorological Magazine, February 1962.

4.5.3 Wind Direction, Speed, and Variability Below 100,000 Ft

Winds aloft may be considered a mean flow pattern in the atmosphere upon which are superimposed traveling disturbances that cause the winds at a point to deviate from their mean value. Geographical, vertical, and seasonal variations exist in the mean flow and in the amplitude and frequency of the disturbances that affect the mean winds and the dispersion of the individual winds about their mean. A jet stream (Sec. 4.5.4) is characteristic of the traveling disturbances in middle latitudes.

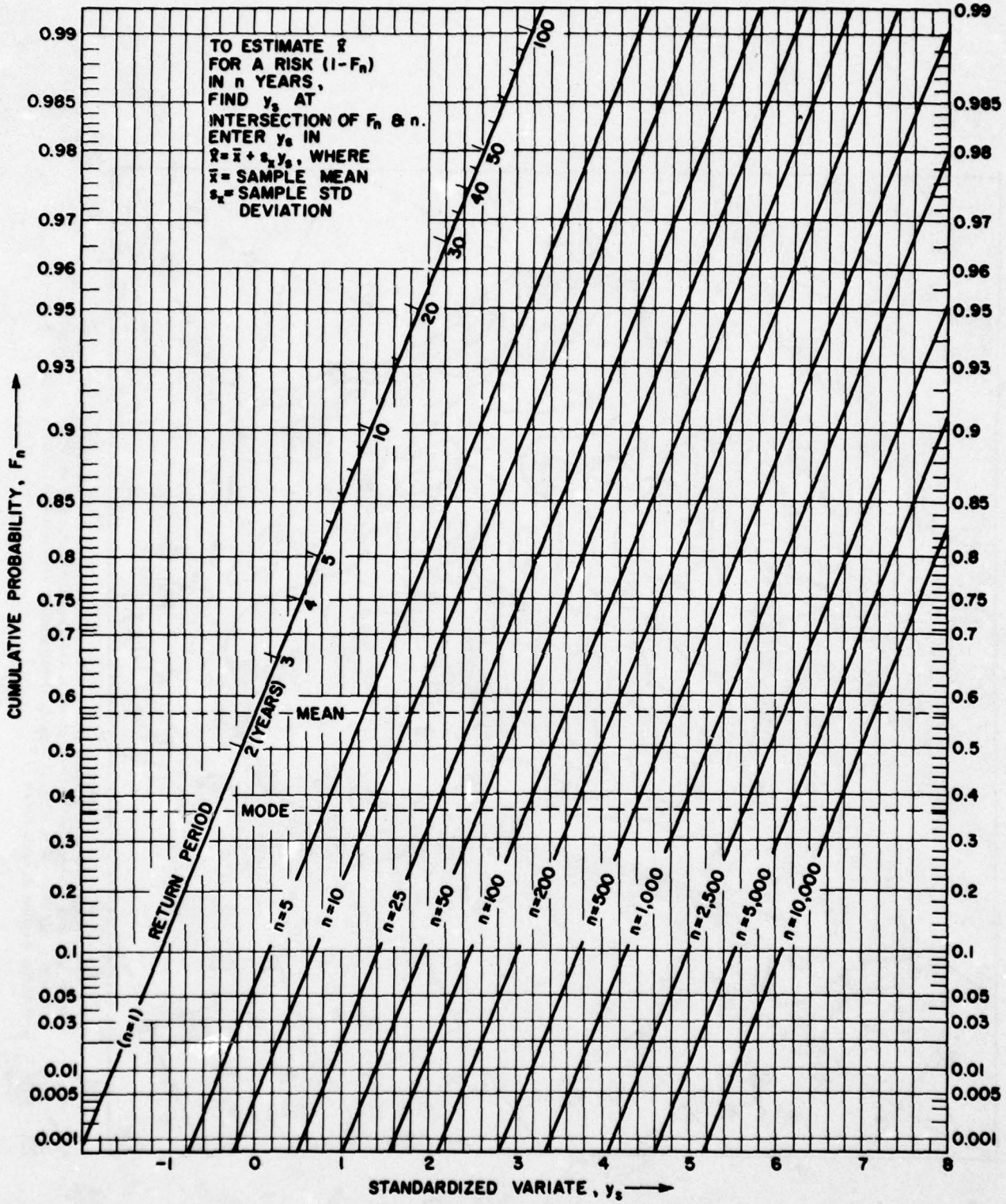


Fig. 4-35. Extreme probability paper with cumulative probability, F_n, as ordinate and standardized variate, y_s, as abscissa. The line $n = 1$ gives the double exponential distribution and shows return period values for y_s. The lines labelled $n = 5, 10, \ldots$ or etc. give the distribution of standardized values of the highest of n observations. Values for y_s for calculating the mean (or the mode) are determined by the intersction of the appropriate n-line with the dashed line labelled mean (or mode), see Sec. 4.5.2.

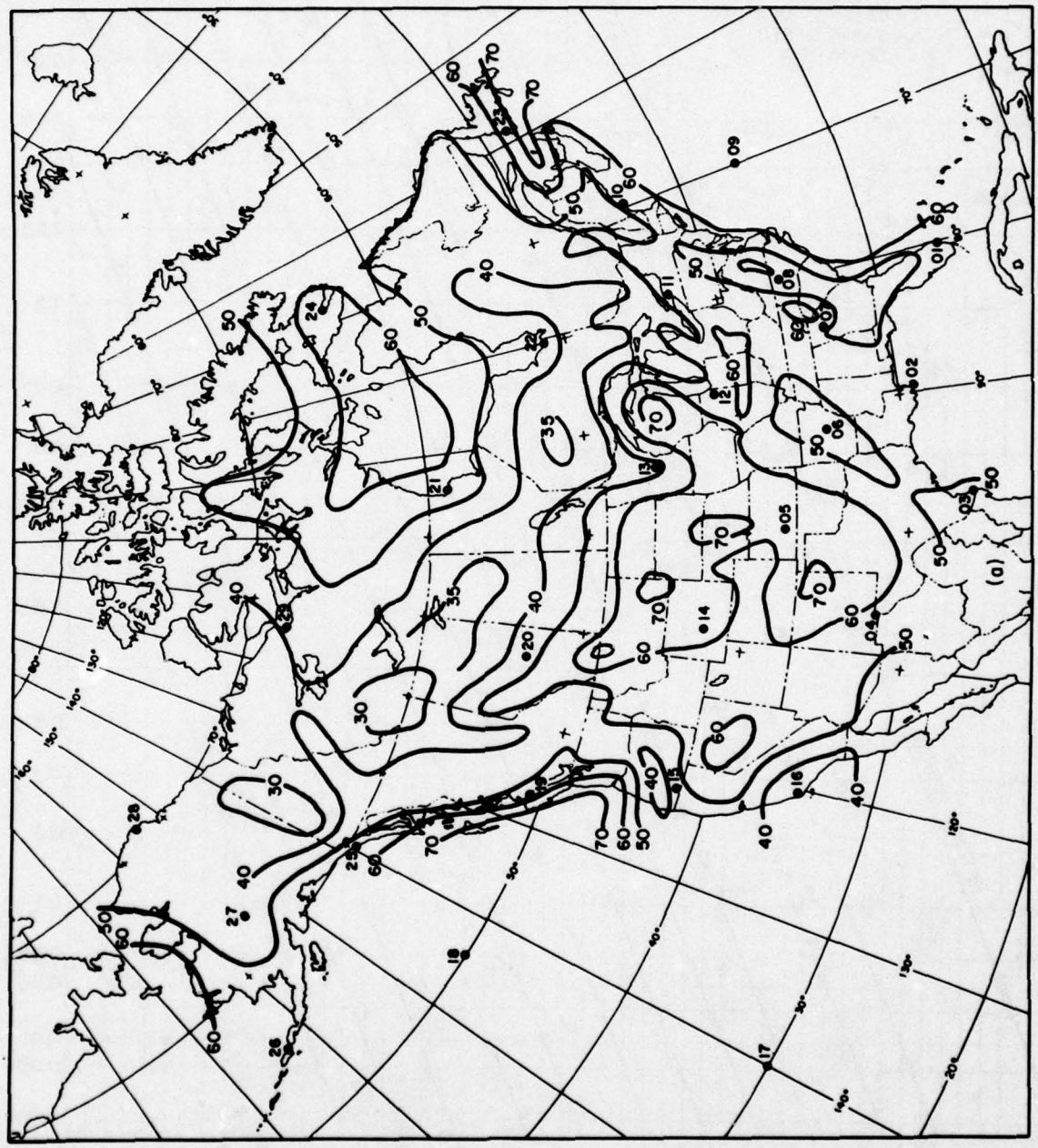


Fig. 4-36. Annual extreme wind speed (fastest mile) at airport stations or stations in open country in the USA and Canada: (a) Isopleths of mean; (b) Isopleths of standard deviation (s_v). (Based on data provided by Meteorological Branch, Department of Transport for Canada and the U. S. National Weather Records Center.)

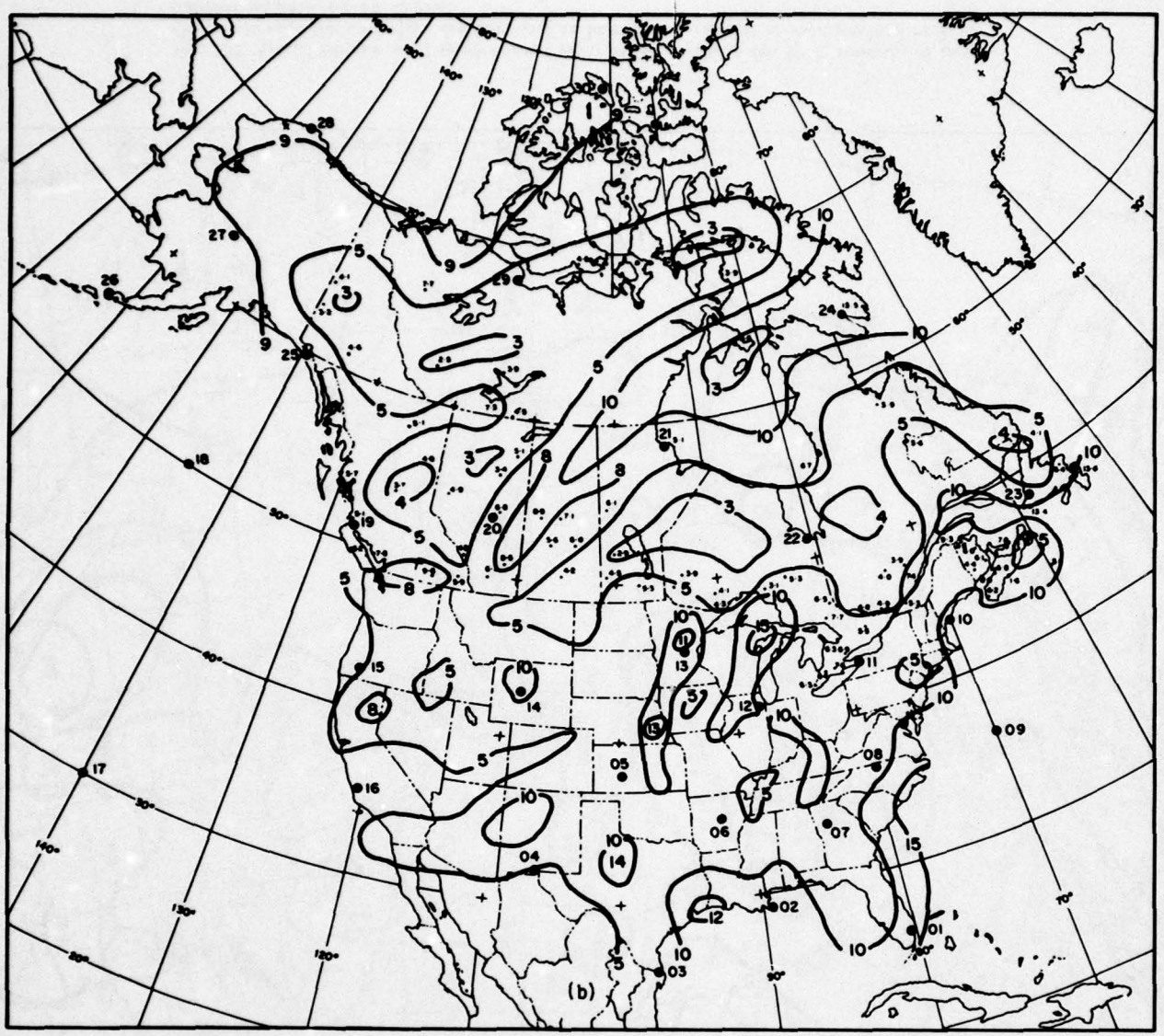


Fig. 4-36. Annual extreme wind speed (fastest mile) at airport stations or stations in open country in the USA and Canada: (a) Isopleths of mean; (b) Isopleths of standard deviation (s_V). (Based on data provided by Meteorological Branch, Department of Transport for Canada and the U. S. National Weather Records Center.)



Fig. 4-37. Annual extreme wind speed (fastest mile) at city offices in the USA. Isopleths of mean ($\bar{V}$) are in solid lines, standard deviation (s_V) in broken lines. (Based on data provided by U. S. National Weather Records Center.)

Table 4-20. Extreme annual wind speed (fastest mile) at 50 ft above ground at the given stations; (A) denotes airport station.

Station	Years of Record	Mean (mile h^{-1})	S.D. (mile h^{-1})	1% Risk in 10 yr (mile h^{-1})
Tampa, Fla. (A)	1941-56	52	8.8	95
Miami, Fla.	1943-58	54	18.0	143
Wilmington, N. C. (A)	1951-58	67	15.9	146
Hatteras, N. C.	1912-57	62	13.4	129
Dallas, Tex. (A)	1941-58	52	6.5	84
Washington, D. C. (A)	1949-58	50	8.5	92
Dayton, Ohio (A)	1944-58	60	8.6	103
Atlanta, Ga. (A)	1933-58	50	7.4	87
Abilene, Tex. (A)	1945-58	63	13.6	131
Columbia, Mo. (A)	1949-58	56	6.2	87
Kansas City, Mo.	1934-58	55	7.0	90
Buffalo, N. Y. (A)	1944-58	58	8.3	99
Albany, N. Y. (A)	1938-58	52	8.4	94
Boston, Mass. (A)	1936-50	59	12.1	119
Chicago, Ill. (A)	1943-58	51	5.6	79
Cleveland, Ohio (A)	1941-58	59	5.8	88
Detroit, Mich. (A)	1934-58	49	5.7	77
Minneapolis, Minn. (A)	1938-58	52	11.1	107
Omaha, Nebraska (A)	1936-58	59	13.1	124
El Paso, Tex. (A)	1943-58	58	4.5	80
Albuquerque, N. M. (A)	1933-58	61	10.2	112
Tucson, Ariz.	1948-58	50	7.1	85
San Diego, Calif.	1940-58	36	6.0	66
Cheyenne, Wyo.	1935-58	63	6.9	97
Rapid City, S. D.	1942-58	66	6.7	99
Bismarck, N. D.	1940-58	66	5.2	92
Great Fall, Mont.	1944-54	65	3.5	82
Portland, Ore.	1950-58	57	6.8	91
New York, N. Y.	1949-58	58	4.8	82
Pittsburgh, Pa.	1935-52	52	6.2	83
	Number of Years of Data			
Fairbanks, Alaska	9	37	8.3	78
Nome, Alaska	11	61	9.1	106
Elmendorf AFB, Alaska	14	45	7.1	81
Shemya Island, Alaska	10	70	6.2	101
Hickam AFB, Hawaii	17	45	8.4	86
Clark AB, Philippines	13	39	12.2	100
Lajes Field, Azores	13	62	16.9	146
Albrook AFB, Canal Zone	18	26	4.1	47
San Pablo, Spain	11	77	15.3	153
Wheelus AB, Libya	14	49	11.8	108
Stuttgart, Germany	15	40	4.8	65
Keflavik, Iceland	9	84	10.8	138
Thule, Greenland	14	80	12.4	142
Tainan, Formosa	39	53	21.2	158
Taipei, Formosa	39	59	21.9	167
Itazuke AB, Japan	14	43	10.0	93
Misawa AB, Japan	11	47	7.2	83
Tokyo Intl. Airport, Japan	15	52	12.2	103
Kimpo AB, Korea	8	43	8.0	82
Bombay, India	6	50	14.2	120
Calcutta, India	6	57	7.4	93
Gaya, India	6	52	6.8	85
Madras, India	6	45	7.5	82
New Delhi, India	6	52	3.8	70
Poona, India	6	39	6.1	69
Central AB, Iwo Jima	17	78	37.9	266
Kadena AB, Okinawa	14	82	25.3	208

Table 4-21 gives the resultant wind direction (degrees), vector mean wind velocity (knots), and the standard vector deviation (knots) for the Northern Hemisphere between 20°N and 80°N at altitudes from 10,000 to 100,000 ft for winter and summer. The resultant wind direction (direction from which the wind blows) is given to the nearest 5° up to 50,000 ft and the nearest 10° above that level. The magnitude of the vector mean wind velocity and its standard vector deviation is given to the nearest knot up to 50,000 ft. Above 50,000 ft, the mean is given to the nearest 5 knots and the deviation is omitted. These conventions were adopted in consideration of the quality and amount of data available at the different levels. Many of the data were obtained from standard AN/GMD-1 soundings, or an equivalent. This equipment becomes inoperative at low-elevation angles of tracking, and increasing error occurs as the angle approaches the critical value. Low-elevation angles are produced by high wind speeds at moderate altitudes or by moderate wind speeds and high altitudes.

Over middle latitudes, where observations are plentiful, the data given in Table 4-21 are reliable except for the ocean areas and the mountainous regions of Asia where observations are sparse. In the low latitudes, reliable observations also are lacking over the ocean areas and the mountains of Asia. Some of the data at 20°N may be affected by the 26-month fluctuation of the zonal winds around the equatorial stratosphere [Ebdon, 1961]. At latitudes 70°N and 80°N, observations are insufficient for the data to be considered very reliable. During winter, explosive warmings of the stratosphere occur over Canada and Northern Europe, frequently during the latter part of January or early February, and the normal westerly flow is weakened or becomes easterly. These periods are included in the data; thus, for a winter month without such a development, the westerly component of the vector mean wind would exceed that given in Table 4-21 by 10% to 20%.

The mean wind velocity vector, $\bar{V}$, is defined by Eq. (4-24), where u and v are the west and the south components at the ith observation. If there are n observations, then

$$\bar{V} = \frac{1}{n}\sqrt{\left(\sum_{i=1}^{n} u_i\right)^2 + \left(\sum_{i=1}^{n} v_i\right)^2}. \qquad (4\text{-}24)$$

The standard vector deviation, σ, is defined in terms of the standard deviations of the components, σ_u and σ_v,

$$\sigma = \sqrt{\sigma_u^2 + \sigma_v^2}. \qquad (4\text{-}25)$$

The standard deviations of the components are defined by

$$\sigma_u^2 = \frac{1}{n}\sum_{i=1}^{n} u_i^2 - \bar{u}^2 \text{ and } \sigma_v^2 = \frac{1}{n}\sum_{i=1}^{n} v_i^2 - \bar{v}^2, \qquad (4\text{-}26)$$

where $\bar{u}$ and $\bar{v}$ are the mean components.

If wind is considered a random variable having two components, its frequency distribution can be represented by the bivariate normal distribution. Its probability density is a function of two variates, x and y, and is represented by a bell-shaped surface such that any plane perpendicular to the x-y plane will cut the surface in a normal distribution curve, and any parallel plane will cut the surface in an ellipse. *Circular normal distribution* is the special case in which there is no correlation between x and y and the standard deviation of x equals that of y; the circular normal distribution is a surface with a circular horizontal cross section and a vertical cross section which has the value $1 - \exp(-r^2/2s^2)$, where r is the radius of the horizontal circle and s the standard deviation. A useful, and usually valid, assumption regarding winds is that they have a circular normal frequency distribution within a season. It is possible to draw circles of probability with the head of the vector mean wind as center. These circles define various probability levels of the wind distribution (i.e., the probability with which all wind vectors drawn from the origin, with end points falling inside a given circle, will occur). The standard vector deviation is the radius of the 63% probability circle. Other probability circles are arrived at by multiplying the standard vector deviation by an appropriate factor to obtain the radius of the desired circle. Factors to be used for various probabilities are:

Factor	0.54	~~0.67~~ 0.83	~~1.15~~ 1.18	~~1.28~~ 1.27	~~1.44~~ 1.38	~~1.65~~ 1.52	~~1.96~~ 1.73	~~2.57~~ 2.15
Probability (%)	25	50	75	80	85	90	95	99

4.5.4 Structure of Jet Streams

Belts of exceptionally strong winds are jet streams. (The term as commonly used applies to the strong westerly winds found at the base of the stratosphere.) Because the disturbances vary in size and intensity and are moving, the jet streams vary in extent, severity, and location. Geographically-oriented descriptions obscure significant features. As Fig. 4-21 shows, this is overcome by relating the features to the position of the core. In winter, the centers (or *cores*) of jet streams are found at altitudes between 30,000 and 40,000 ft in latitudes between 25° to 70° in each hemisphere. In summer, jet streams are weaker, higher (35,000 to 45,000 ft), and farther poleward (35° to 75° latitude). Generally speaking, a jet stream is a few thousand miles in length, a few hundred miles in width, and a few miles in depth.

The average structure of jet streams is shown in Fig. 4-21; this is a cross section showing lines of equal wind speed, *isotachs*, blowing "into the page," labelled in percent of the wind speed at the jet core. Core wind speeds range from 100 knots to as much as 250 knots on rare occasions. Speeds of 140 knots are common in winter. Figure 4-21 also shows the thermal field, the tropopause, and the level of maximum wind. Typical wind and temperature variations across jet streams at a constant altitude or vertically through jet streams may be determined from this figure.

Individual jet streams are variable and may differ considerably from the average. In some cases, two or even three jet cores may be found paralleling each other, separated by distances of a few hundred miles. In addition to these deviations from the average, eddies of various sizes

are present in the wind and temperature fields, as shown in Fig. 4-38. Extreme horizontal changes of wind and temperature are of the order of 40 knots and 5°C in 10-miles distance measured perpendicular to the jet stream. Variations parallel to jet streams are an order of magnitude smaller.

Clear air turbulence is intimately related to jet streams; measurements show that it is more likely in certain regions than in others [McLean, 1961]. At the level of maximum wind (where vertical shear changes sign), turbulence was observed about 14% of the time. From Fig. 4-39 it can be seen that turbulence is most likely to be found north of the jet stream core near the polar tropopause and above the core along the tropical tropopause. Indication of a maximum is also found in the jet stream front.

Other wind currents which exhibit properties similar to those shown in Fig. 4-21 are the low-level jet and the tropical easterly jet stream which is observed in certain areas (e.g., southern India) at an altitude of about 45,000 ft in summer. Although data are sparse, jet streams are believed to exist in the stratosphere at altitudes above 100,000 ft.

Frequently it is too expensive to design equipment to operate under extreme conditions. In such cases, calculated risks are assumed or alternate methods of operation are devised for periods when such conditions exist. If high wind speeds, or strong shears normally associated with them, adversely affect the operation of a particular vehicle that is released vertically into the atmosphere, it may be desirable to select several release sites spaced far enough apart to ensure that operational conditions will exist above one of the stations when the critical wind speed or shear is exceeded above the others. In such cases, Fig. 4-21 will be useful in selecting alternate sites; it indicates the average rate with which wind speed decreases with distance on both sides of the jet stream core. For example, with a 300-ft sec^{-1} wind at the jet stream core, Fig. 4-21 indicates that, on the average, a belt of winds exceeding 225 ft sec^{-1} can be expected to extend 200 miles south and 100 miles north of the core. Consequently, if the maximum wind likely to occur over a region is 300 ft sec^{-1} and the vehicle is only designed to withstand speeds up to 225 ft sec^{-1}, alternate release sites should be selected at least 300 miles apart. As the jet stream axis occasionally approaches a north-south orientation, sites should be selected over 300 miles apart in longitude as well as latitude.

4.5.5 Observed Winds Above 100,000 Ft

Table 4-22 presents statistics on winds above 100,000 ft prepared from the Data Reports of the Meteorological Rocket Network for the period October, 1959 through December, 1963. Six stations with the most consistent observations (Cape Kennedy, White Sands, Point Mugu, Wallops Island, Fort Churchill, and Fort Greeley) were selected to represent the behavior of the wind regimes over North America between 25 and 70 km. The latter two stations, being nearly at the same latitude, were combined in order to provide an adequate data sample.

A natural division of the wind regimes was determined as follows: westerly, 16 October to 31 March; west to east transition, 1 April to 31 May; easterly, 1 June to 15 August; east to west transition, 16 August to 15 October. These seasons are in sufficiently close agreement with the data and analysis given in Sec. 4.2.3. For days with more than one firing, an average was computed to represent that particular day. All days in a season were then pooled to compute the statistics for the season. The number of observations which were used to compute the means and standard deviations decreases rapidly at the higher levels. Values derived from less than 30 observations could be subject to considerable change and should be used with caution.

The natural seasonal groupings are dominated by a long regime of strong westerly winds during the cold season and a shorter regime of strong easterlies during the warm season; these are separated by brief transition regimes of weak and variable winds. The seasonal changes occur first at the highest level and proceed downward. In the westerly and easterly regimes the wind speeds increase with altitude. The wind variability is greater for the westerlies than for the easterlies. The relative variability, based on the average wind speed, decreases with altitude; it is least in the summer and greatest in the transitional regimes.

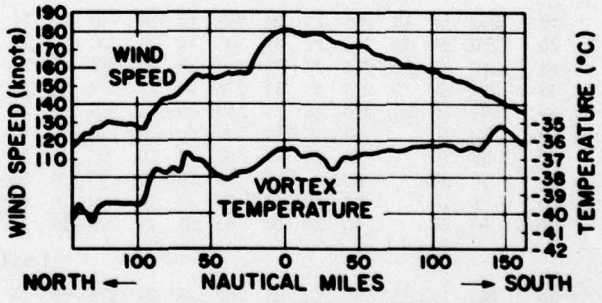


Fig. 4-38. Example of wind and temperature fields near the jet stream.

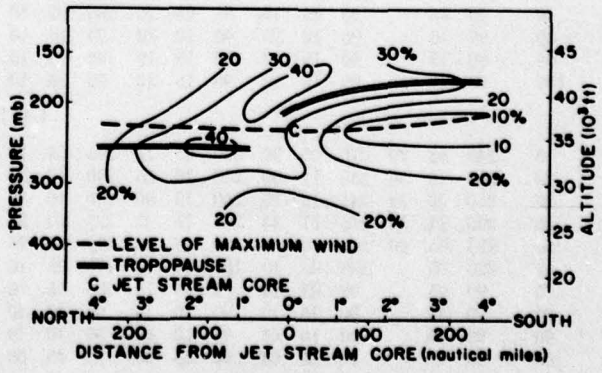


Fig. 4-39. Turbulence in various sectors of a typical jet stream cross section; frequency (%) of occurrence is shown for each contour.

Table 4-21. Resultant wind direction (d in degrees), vector mean wind velocity ($\bar{v}$ in knots), and standard vector deviation (δ in knots) at various altitudes (H) for various latitudes and longitudes in the Northern Hemisphere, summer and winter seasons.

Summer

H	180° W			160° W			140° W			120° W			100° W			80° W			60° W			40° W			20° W		
10^3 ft	d	$\bar{v}$	δ	d	$\bar{v}$	δ	d	$\bar{v}$	δ	d	$\bar{v}$	δ	d	$\bar{v}$	δ	d	$\bar{v}$	δ	d	$\bar{v}$	δ	d	$\bar{v}$	δ	d	$\bar{v}$	δ
LATITUDE 20° N																											
10	80	09	13	80	07	09	115	05	09	115	05	08				120	11	11	130	12	12	65	10	14	90	12	16
20	35	04	14	150	02	13	230	06	12	150	10	12	105	10	10	100	07	12	150	05	12	10	05	14	120	05	14
30	300	04	19	255	12	20	250	16	18	150	14	17	100	08	15	65	06	16	245	05	16	220	08	16	180	10	14
40	300	10	26	270	25	27	245	20	26	140	14	20	95	10	20	30	06	22	270	10	22	225	13	23	160	12	20
50	30	03	20	230	10	20	230	10	20	120	10	15	80	10	20	25	08	18	50	05	20	170	10	20	130	10	20
60	100	15		100	20	10	110	15	10	100	20	10	85	20	10	85	20	10	90	20	10	100	15		90	15	
70	90	30		90	30	10	90	30	10	90	30	10	90	30	10	90	30	10	95	30	10	90	25		90	30	
80	90	35		90	35	10	90	35	10	90	35	10	90	35	15	90	35	15	90	35	15	90	30		90	35	
90	90	35		90	40	10	90	40	10	95	40	15	95	40	15	95	40	15	90	35	15	90	30		90	30	
100	90	45		90	45	12	90	45	15	95	45	15	95	45	15	95	45	15	90	35	15	90	30		90	30	
LATITUDE 30° N																											
10	150	02	15	60	04	13	50	05	13	205	05	12	150	05	14	220	04	13	220	05	14	300	04	16	310	04	16
20	330	08	18	290	05	18	280	04	15	230	10	16	150	02	15	240	04	15	240	06	16	280	05	17	275	08	17
30	325	10	24	275	12	24	260	13	24	240	20	25	360	06	20	300	05	23	280	07	22	280	08	22	255	15	20
40	335	12	32	280	18	30	255	23	30	225	25	30	325	06	30	325	07	28	290	08	25	280	14	28	255	20	25
50	360	08	25	270	10	25	245	20	25	190	10	20	360	06	25	340	08	25	315	05	25	260	10	25	240	10	20
60	40	08		40	10	10	170	10	10	130	05	10	85	10	10	80	10	10	80	10	10	40	10		40	10	
70	90	20		90	20	10	90	20	10	90	20	10	90	20	10	90	20	10	90	20	10	90	20		90	20	
80	90	25		90	25	10	90	25	10	90	25	10	90	25	10	90	25	10	90	25	10	90	25		90	25	
90	90	30		90	30	10	90	30	10	90	30	10	90	30	10	90	30	10	90	25	10	90	25		90	25	
100	90	30		90	35	15	90	35	15	90	35	15	90	35	15	90	35	15	90	30	10	90	25		90	25	
LATITUDE 40° N																											
10	245	18	18	240	13	18	315	10	18	240	07	14	270	10	16	275	16	17	260	16	18	270	14	18	285	10	17
20	270	24	24	265	21	24	300	14	22	250	18	22	270	19	20	275	23	21	265	24	22	270	17	24	280	16	22
30	270	32	30	265	24	32	280	18	30	255	26	34	270	31	28	275	30	29	270	30	29	280	21	32	275	19	28
40	285	35	35	275	23	34	270	22	35	250	32	36	265	40	34	280	35	35	270	30	33	280	25	35	275	24	30
50	295	20	25	270	15	25	260	20	25	245	20	24	250	20	24	280	18	25	280	20	25	275	20	25	280	20	25
60	210	10		190	07	10	180	10	10	180	10	10	190	10	10	220	10	15	200	10	10	200	10		200	10	
70	90	10		90	10	10	90	10	10	95	10	10	90	10	10	85	10	10	80	10	10	90	07		90	10	
80	90	20		90	20	10	90	20	10	90	20	10	90	15	10	90	15	08	90	20	08	90	15		90	15	
90	90	20		90	20	10	90	20	10	90	20	10	90	20	10	90	20	10	90	20	10	90	20		90	20	
100	90	25		90	25	10	90	25	10	90	25	10	90	20	10	90	20	10	90	20	10	90	20		90	20	
LATITUDE 50° N																											
10	260	17	23	245	18	23	260	14	23	275	10	15	285	14	18	285	18	18	270	16	22	260	20	22	265	17	23
20	265	23	29	255	26	30	275	21	29	265	18	25	275	24	23	285	28	25	270	27	29	265	29	30	270	25	30
30	270	31	38	260	32	38	280	30	40	265	25	37	275	36	34	285	38	33	265	40	40	265	40	42	270	31	40
40	270	36	38	260	32	38	275	30	35	270	28	35	270	40	34	280	38	34	265	45	38	265	40	37	265	32	38
50	265	15	25	260	15	25	260	15	25	260	20	25	265	25	20	280	25	25	265	25	25	270	25	25	265	20	25
60	210	10		190	10	10	190	10	10	210	05	10	220	10	15	230	10	10	190	10	10	190	10		200	10	
70	90	05		95	05	10	95	05	10	100	05	10	90	05	10	80	05	10	80	05	10	90	05		100	05	
80	90	10		90	10	10	90	10	10	90	10	10	90	10	10	90	10	10	90	10	10	90	10		90	10	
90	90	15		90	15	10	90	15	10	90	15	10	90	15	08	90	15	08	90	15	08	90	15		90	15	
100	90	15		90	15	10	90	15	10	90	20	10	90	15	08	90	15	08	90	15	08	90	15		90	15	
LATITUDE 60° N																											
10	240	08	20	210	08	20	230	05	18	295	06	14	310	12	18	290	10	20	230	06	20	260	05	21	250	08	24
20	260	10	30	235	11	30	250	10	26	290	12	22	300	17	22	290	18	26	250	10	29	270	13	30	260	14	32
30	260	20	38	245	16	38	260	15	40	280	10	30	295	22	33	290	24	32	255	15	37	260	19	39	265	22	45
40	255	14	34	245	17	33	265	15	32	275	10	28	290	22	30	290	24	29	255	19	30	260	22	35	260	24	35
50	275	05	20	260	10	20	260	10	20	275	10	20	290	15	20	290	15	20	255	10	20	260	15	25	240	15	25
60	220	05		180	05	10	180	05	10	190	05	10	210	10		220	08		200	08		200	10		190	08	
70	90	05		90	05	10	95	05	10	100	05	10	90	05		80	05		80	05		90	05		100	05	
80	90	10		90	10	10	90	10	10	90	10	10	90	10		90	10		90	10		90	10		90	10	
90	90	10		90	10	08	90	10	08	90	10	10	90	10		90	10		90	10		90	10		90	10	
100	90	10		90	15	08	90	15	08	90	15	08	90	15		90	15		90	15		90	15		90	15	

(Continued)

Table 4-21. Resultant wind direction (d in degrees), vector mean wind velocity ($\bar{v}$ in knots), and standard vector deviation (δ in knots) at various altitudes (H) for various latitudes and longitudes in the Northern Hemisphere, summer and winter seasons. (Continued)

	Summer																											
H	180° W			160° W			140° W			120° W			100° W			80° W			60° W			40° W			20° W		
10^3 ft	d	$\bar{v}$	δ	d	$\bar{v}$	δ	d	$\bar{v}$	δ	d	$\bar{v}$	δ	d	$\bar{v}$	δ	d	$\bar{v}$	δ	d	$\bar{v}$	δ	d	$\bar{v}$	δ	d	$\bar{v}$	δ
LATITUDE 70° N																												
10	240	10	18	210	07	17	250	07	16	300	09	13	330	08	18	270	04	18	140	03	17	65	03	16	330	04	18
20	250	12	27	240	11	26	260	11	21	300	15	18	320	13	24	280	07	26	210	06	25	270	04	24	270	04	27
30	240	13	36	230	12	36	260	14	29	290	17	24	320	16	29	280	08	32	235	08	32	250	08	33	270	05	38
40	250	10	28	230	12	28	250	13	24	285	13	22	315	16	24	270	10	23	230	07	25	255	07	25	265	08	25
50	255	05	15	255	05	15	270	05	15	290	10	15	310	10	15	285	05	15	245	05	15	210	03	10	210	05	20
60	210	05		190	03	10	180	03	10	190	03	10	210	03		230	05		230	03		140	02		150	02	
70	90	05		90	05	10	90	05	10	80	05	10	90	05		90	05		90	05		90	05		100	05	
80	90	08		90	08	10	90	08	10	90	08	10	90	08		90	08		90	08		90	08		90	08	
90	90	08		90	08	10	90	10	08	90	08	08	90	08		90	08		90	08		90	08		90	08	
100	90	10		90	10	08	90	10	08	90	10	08	90	10		90	10		90	10		90	10		90	10	
LATITUDE 80° N																												
10	250	07	16	255	06	17	265	06	17	285	06	17	280	04	16	195	03	16	205	04	14	315	04	15	310	05	15
20	250	11	24	260	12	24	280	10	24	290	08	23	285	04	25	235	04	26	230	05	24	265	07	23	285	05	24
30	270	07	32	275	10	32	300	10	30	320	10	30	280	04	30	265	04	30	215	06	30	270	06	34	300	09	32
40	270	10	23	285	10	22	300	10	20	320	10	20	315	05	19	240	04	20	195	04	20	245	04	20	280	05	20
50	220	05	10	270	05	10	305	05	10	310	05	10	280	05	15	260	02	10	170	02	10	180	02	10	240	03	15
60	200	05		200	05		190	05		190	05		30	02		30	02		40	02		150	02		150	02	
70	90	05		90	05		80	05		60	05		70	05		80	05		90	05		100	05		110	05	
80	90	05		90	05		90	05		80	05		90	05		90	05		100	05		90	05		100	05	
90	90	05		90	05		90	05		90	05		90	05		90	05		90	05		90	05		90	05	
100	90	05		90	08		90	08		90	08		90	05		90	05		90	05		90	05		90	05	

	Summer																											
H	0°			20° E			40° E			60° E			80° E			100° E			120° E			140° E			160° E		
10^3 ft	d	$\bar{v}$	δ	d	$\bar{v}$	δ	d	$\bar{v}$	δ	d	$\bar{v}$	δ	d	$\bar{v}$	δ	d	$\bar{v}$	δ	d	$\bar{v}$	δ	d	$\bar{v}$	δ	d	$\bar{v}$	δ
LATITUDE 20° N																												
10	115	15	15	30	10	12	05	10	13	330	03	12	240	05	15	280	07	17	210	05	15	160	05	15	150	08	10
20	115	08	15	25	08	14	05	07	15	70	07	12	110	05	15	115	05	14	165	05	15	170	03	15	130	05	13
30	165	05	15	20	05	17	05	12	15	70	12	12	80	15	15	90	15	15	90	05	15	25	03	15	350	03	18
40	150	10	20	30	05	22	110	22	18	70	28	18	80	25	20	85	25	20	85	10	25	30	05	25	355	05	25
50	120	15	20	110	25	25	110	30	20	90	40	25	80	45	25	75	40	25	75	20	25	65	15	25	60	10	20
60	100	20		100	25		100	35		90	35		90	40		90	40		80	40		90	30		90	20	
70	90	30		90	30		90	30		90	30		90	30		90	30		90	40		90	40		90	30	
80	90	35		90	35		90	35		90	35		90	35		90	35		90	40		90	40		90	40	
90	90	35		90	35														90	45		90	45		90	40	
100	90	35		90	35														90	50		90	55		90	50	
LATITUDE 30° N																												
10	130	03	16	330	10	15	295	08	14	345	04	15							245	06	18	230	07	15	245	10	15
20	200	07	18	315	13	18	270	12	17	360	07	15	175	05	15				245	10	20	250	15	20	250	10	18
30	260	13	19	270	17	20	240	10	21	345	08	18	225	05	20	170	10	25	220	15	30	270	13	27	290	12	23
40	250	20	25	255	25	25	220	17	23	320	07	25	260	08	25	190	15	30	225	15	35	305	20	35	310	15	30
50	245	15	20	220	15	25	195	10	20	180	07	25	30	05	25	60	15	30	340	10	35	340	10	30	345	10	30
60	170	15		150	10		150	15		90	10		90	10		90	20		80	20		70	15		40	10	
70	90	20		90	20		100	20		100	20		90	20		90	20		90	25		90	20		90	20	
80	90	25		90	25		90	25		90	30		90	30		90	30		90	30		90	25		90	25	
90	90	25		90	25		90	25											90	30		90	30		90	30	
100	90	30		90	30		90	30											90	35		90	40		90	40	

(Continued)

Table 4-21. Resultant wind direction (d in degrees), vector mean wind velocity ($\bar{v}$ in knots), and standard vector deviation (δ in knots) at various altitudes (H) for various latitudes and longitudes in the Northern Hemisphere, summer and winter seasons. (Continued)

	Summer																											
H	0°			20° E			40° E			60° E			80° E			100° E			120° E			140° E			160° E		
10^3 ft	d	$\bar{v}$	δ	d	$\bar{v}$	δ	d	$\bar{v}$	δ	d	$\bar{v}$	δ	d	$\bar{v}$	δ	d	$\bar{v}$	δ	d	$\bar{v}$	δ	d	$\bar{v}$	δ	d	$\bar{v}$	δ
LATITUDE 40° N																												
10	265	13	16	315	14	18	255	08	17	330	08	16	250	05	09	290	06	16	285	07	18	260	11	18	265	16	18
20	265	22	20	290	22	23	240	17	20	295	15	20	255	12	20	270	13	20	280	14	25	265	20	25	275	24	24
30	265	30	28	280	32	30	270	38	30	280	33	30	260	34	25	255	20	26	270	23	35	260	37	37	280	34	32
40	265	32	30	265	40	30	255	38	35	275	38	30	260	43	35	275	35	35	275	40	35	265	40	45	280	39	38
50	265	25	25	260	30	25	260	35	25	260	30	25	265	30	30	290	25	25	280	30	30	285	25	35	285	20	30
60	190	15		200	15		200	20		200	20		200	20		200	20		210	20		220	15		220	10	
70	90	10		100	10		100	15		100	10		100	10		90	10		90	10		90	10		80	10	
80	90	20		90	20		90	20		90	20		90	20		90	20		90	20		90	20		90	20	
90	90	20		90	20		90	20											90	20		90	20		90	20	
100	90	25		90	25		90	25											90	20		90	20		90	25	
LATITUDE 50° N																												
10	260	14	20	285	10	20	260	06	19	310	08	18	280	08	17	285	07	16	315	06	17	280	05	19	290	08	20
20	265	20	28	275	14	27	260	08	24	295	13	24	280	14	25	280	13	21	290	13	25	280	12	27	285	16	28
30	270	27	40	270	20	35	260	14	32	290	27	33	275	20	31	275	20	27	275	18	35	285	23	35	285	25	37
40	270	27	35	265	24	35	260	20	35	280	27	35	270	34	32	275	30	30	270	25	36	290	27	35	290	30	40
50	270	15	25	260	20	25	255	25	20	275	25	25	270	25	25	280	20	25	275	20	25	290	20	25	290	20	30
60	200	10		200	10		200	10		200	10		200	10		200	15		200	10		200	10		220	10	
70	100	05		100	05		100	10		100	05		100	05		90	05		90	05		80	05		90	05	
80	90	10		90	10		90	10		90	12		90	12		90	12		90	10		90	10		90	10	
90	90	15		90	15		90	15											90	15		90	15		90	15	
100	90	20		90	20		90	20											90	10		90	10		90	10	
LATITUDE 60° N																												
10	245	12	20	260	08	20	270	07	20	285	08	21	250	07	19	250	05	15	280	05	16	280	05	18	280	05	19
20	250	16	30	260	13	27	275	10	27	290	09	27	270	09	26	270	08	22	280	08	24	275	08	24	280	08	27
30	255	22	45	260	20	40	280	15	32	290	14	34	270	10	35	265	10	30	270	12	27	275	14	30	275	17	34
40	255	22	35	260	20	32	275	20	27	280	17	28	270	18	26	270	15	25	265	16	26	280	16	28	280	12	33
50	255	10	20	260	10	20	270	15	20	270	15	20	270	15	15	270	10	15	270	12	20	290	10	20	300	10	25
60	190	05		200	05		200	05		200	05		190	05		190	05		200	05		200	05		220	05	
70	100	05		100	05		100	05		100	05		90	05		90	05		90	05		90	05		90	05	
80	90	10		90	10		90	10		90	10		90	08		90	08		90	10		90	10		90	10	
90	90	10		90	10		90	10											90	10		90	10		90	10	
100	90	15		90	15		90	15											90	10		90	10		90	10	
LATITUDE 70° N																												
10	255	05	18	225	07	15	235	05	17	225	05	17	210	05	19	210	05	14	240	07	15	250	09	16	250	11	18
20	240	08	26	240	11	22	265	08	23	275	05	23	260	05	24	260	05	22	270	09	24	265	12	23	260	13	25
30	240	14	37	230	16	28	260	08	27	265	05	30	260	04	30	260	04	26	260	08	24	260	12	26	260	14	32
40	245	13	26	240	12	24	260	12	22	265	11	22	260	11	20	255	11	21	255	09	22	255	09	23	255	09	25
50	240	08	15	245	08	15	255	08	15	255	08	15	250	07	15	240	08	13	250	08	15	250	07	15	245	05	15
60	170	05		180	05		200	05		210	05		210	05		190	05		200	05		200	05		210	05	
70	100	05		100	05		100	05		100	05		90	05		90	05		90	05		90	05		90	05	
80	90	08		90	08		90	08		90	08		90	08		90	08		90	08		90	08		90	08	
90	90	08		90	08		90	08											90	08		90	08		90	08	
100	90	08		90	08		90	08											90	05		90	05		90	05	
LATITUDE 80° N																												
10	270	05	15	265	07	14	260	05	15	245	05	15	245	06	15	245	05	14	250	07	15	250	08	14	255	08	16
20	270	05	23	270	06	22	255	05	21	255	05	20	255	08	22	255	05	23	260	09	24	260	10	24	255	11	24
30	270	08	30	235	07	25	240	05	25	245	05	25	250	03	26	250	03	26	260	04	26	265	05	28	265	07	30
40	255	07	20	240	07	19	240	07	18	245	07	18	250	06	18	255	05	18	265	06	20	270	06	20	270	07	20
50	245	05	15	270	05	15	240	05	12	230	05	10	220	04	10	220	05	10	210	03	10	210	03	10	210	03	10
60	160	05		180	05		210	05		210	05		210	02		210	05		210	05		210	05		210	05	
70	110	05		110	05		110	05		110	05		100	05		90	05		90	05		90	05		90	05	
80	100	05		90	05		90	05		90	05		90	05		90	05		80	05		90	05		90	05	
90	90	05		90	05		90	05											90	05		90	05		90	05	
100	90	05		90	05		90	05											90	03		90	03		90	03	

(Continued)

Table 4-21. Resultant wind direction (d in degrees), vector mean wind velocity ($\bar{v}$ in knots), and standard vector deviation (δ in knots) at various altitudes (H) for various latitudes and longitudes in the Northern Hemisphere, summer and winter seasons. (Continued)

Winter

H	180° W			160° W			140° W			120° W			100° W			80° W			60° W			40° W			20° W		
10^3 ft	d	$\bar{v}$	δ	d	$\bar{v}$	δ	d	$\bar{v}$	δ	d	$\bar{v}$	δ	d	$\bar{v}$	δ	d	$\bar{v}$	δ	d	$\bar{v}$	δ	d	$\bar{v}$	δ	d	$\bar{v}$	δ
LATITUDE 20° N																											
10	30	03	18	140	03	17	170	04	15	210	04	15				70	05	14	105	04	17	245	04	18	270	06	17
20	300	16	27	290	08	25	225	05	21	245	14	20	240	13	18	325	05	20	340	09	23	315	05	22	280	18	19
30	290	33	35	280	25	35	260	15	30	255	30	28	250	27	25	275	23	27	295	27	30	290	20	25	280	45	28
40	285	35	35	285	40	35	280	33	35	265	38	30	255	37	28	265	35	30	285	43	33	280	45	30	275	55	32
50	295	25	30	295	30	35	285	30	30	260	30	25	250	33	25	270	30	25	285	30	30	275	30	30	270	40	30
60	190	15		265	15	15	270	15	20	270	15	20	265	15	20	265	15	20	280	15	20	270	15		270	15	
70	80	08		150	08	15	70	05	15	250	08	15	220	05	15	210	05	15	240	03	15	240	03		240	03	
80	90	05		60	08	15	80	05	15	80	08	15	90	02	15	90	03	15	80	05	15	110	03		110	03	
90	90	05		90	05		90	05		90	05		90	05		240	03		90	05		90	05		90	05	
100	90	02		90	02		90	10		90	10		90	03		240	05		90	03		90	10		90	10	
LATITUDE 30° N																											
10	270	20	24	245	12	24	265	07	23	290	11	19	255	20	18	250	17	20	280	13	23	260	08	22	315	07	19
20	270	40	33	270	25	32	275	15	30	280	24	30	260	38	28	275	36	28	290	25	32	285	13	28	300	17	24
30	270	60	40	275	40	42	280	25	40	275	38	40	260	57	40	275	55	35	285	38	40	280	23	35	290	27	33
40	275	70	40	275	55	42	290	37	43	275	48	40	260	70	40	275	65	35	285	48	40	275	35	38	285	35	37
50	280	50	35	285	35	35	290	35	35	270	35	30	260	55	30	270	60	30	285	45	35	280	30	30	280	30	30
60	250	25		265	20	20	270	20	20	285	20	20	265	30	20	270	35	20	270	30	20	280	20		280	20	
70	200	03		150	08	15	30	08	15	300	08	15	270	15	15	270	20	20	270	20	15	270	15		280	15	
80	110	05		90	05	15	60	05	15	330	05	20	280	10	15	270	15	20	250	15	20	260	15		270	10	
90	90	05		85	05	20	90	03		320	08	20	280	10	20	270	15	20	270	20		270	10		270	10	
100	270	10		270	08		270	03		300	10	30	270	15	25	270	20	25	270	25		270	10		270	15	
LATITUDE 40° N																											
10	260	30	25	260	24	28	270	21	29	280	15	23	285	20	23	270	35	25	275	28	27	260	15	28	275	12	24
20	260	47	37	260	37	39	275	32	39	280	29	37	275	37	37	270	53	37	265	47	37	260	30	38	282	18	32
30	260	65	45	265	53	45	275	43	50	285	42	48	270	53	45	270	75	47	265	57	46	260	35	45	280	22	38
40	260	74	45	265	60	45	280	47	45	285	47	43	270	60	45	270	80	40	265	55	48	260	40	43	280	25	38
50	265	55	40	275	40	40	285	35	35	280	35	30	270	45	35	270	60	30	265	50	35	265	35	35	280	25	30
60	250	30		265	20	20	290	20	20	290	25	20	280	30	20	270	35	25	270	35	25	270	35		270	30	
70	210	10		260	20	20	270	15	20	300	15	20	290	20	20	280	30	25	270	30	25	260	30		270	30	
80	240	05		240	10	10	270	10	15	330	10	20	290	20	25	270	25	30	270	30	25	260	30		270	25	
90	270	10		270	10		270	10		330	10	25	300	15	30	270	25	30	270	25	30	270	20		270	20	
100	270	25		270	25		270	20		310	15	30	300	20	35	270	30	35	270	30	35	270	20		270	25	
LATITUDE 50° N																											
10	240	20	28	260	20	30	260	21	31	265	18	20	295	20	20	275	22	25	265	23	27	250	28	33	260	24	32
20	240	26	38	255	32	40	270	32	43	280	31	35	290	33	32	275	37	35	260	40	38	245	43	43	265	34	44
30	240	35	45	255	40	45	270	42	50	285	38	45	285	42	38	270	50	40	255	48	45	250	55	55	265	44	50
40	240	42	45	260	40	40	280	42	40	285	38	35	285	42	33	270	45	35	255	52	40	250	50	45	270	40	45
50	245	30	35	255	30	35	280	30	35	285	30	30	285	35	25	270	45	30	255	45	35	250	35	35	275	30	35
60	230	25		270	25	30	290	20	25	290	25	25	290	35	30	280	40	30	270	40	30	250	40		270	35	
70	230	15		260	20	25	300	15	25	300	25	25	290	30	30	280	35	30	270	40	30	250	40		270	35	
80	230	10		270	15	25	290	20	25	300	20	30	300	30	30	280	30	30	270	40	35	260	35		260	40	
90	260	15		270	15		290	20	30	300	25	30	295	25	35	280	30	35	270	40	35	270	40		270	35	
100	270	30		270	25		290	25	35	300	30	35	295	30	40	280	35	40	270	45		270	40		270	35	
LATITUDE 60° N																											
10	240	07	27	285	08	27	235	08	25	290	13	20	310	14	18	285	13	20	250	12	24	220	14	28	245	20	32
20	240	12	36	260	15	40	270	20	35	290	22	27	305	23	27	275	19	28	245	19	35	230	23	41	250	28	43
30	235	20	40	260	23	42	275	27	42	295	25	33	305	30	32	270	25	33	240	27	40	240	33	47	255	37	55
40	230	20	35	260	27	35	280	30	35	295	25	30	300	30	28	270	25	30	235	30	35	240	38	38	260	40	45
50	240	20	30	255	30	30	280	30	30	295	25	25	300	30	25	270	25	25	240	30	30	240	35	35	270	35	35
60	240	30		270	30	30	280	30	30	290	30	30	300	35		290	35		270	35		250	40		260	40	
70	240	35		270	35	35	290	35	30	280	35	30	300	40		290	40		270	40		250	45		260	40	
80	250	30		270	35	35	280	35	35	280	35	35	270	35		270	45		270	45		250	45		270	45	
90	270	30		270	40	40	275	40	35	285	40	35	270	40		270	45		270	45		270	45		270	45	
100	270	35		270	40	45	275	40	40	285	40	35	270	40		270	45		270	50		270	55		270	55	

(Continued)

Table 4-21. Resultant wind direction (d in degrees), vector mean wind velocity ($\bar{v}$ in knots), and standard vector deviation (δ in knots) at various altitudes (H) for various latitudes and longitudes in the Northern Hemisphere, summer and winter seasons. (Continued)

	Winter																											
H	180° W			160° W			140° W			120° W			100° W			80° W			60° W			40° W			20° W		
10^3 ft	d	$\bar{v}$	δ	d	$\bar{v}$	δ	d	$\bar{v}$	δ	d	$\bar{v}$	δ	d	$\bar{v}$	δ	d	$\bar{v}$	δ	d	$\bar{v}$	δ	d	$\bar{v}$	δ	d	$\bar{v}$	δ
LATITUDE 70° N																												
10	300	03	26	300	04	24	285	07	20	310	08	20	330	08	18	110	02	18	195	07	21	165	08	24	270	09	26
20	280	06	30	280	09	30	290	15	27	310	14	24	325	13	24	190	03	27	195	13	33	215	13	36	245	17	36
30	265	13	34	275	17	35	285	19	33	310	17	27	325	17	28	250	05	29	200	15	36	225	15	40	250	23	46
40	240	17	30	265	23	28	290	20	28	315	18	25	320	17	25	260	15	25	205	15	30	225	20	30	255	25	32
50	240	25	25	260	25	25	285	25	25	305	25	25	310	20	25	275	15	25	225	15	25	230	25	30	260	25	30
60	250	35		270	35	35	290	35	30	300	35	30	310	30		310	20		270	20		250	30		260	30	
70	250	40		270	35	35	290	35	35	310	40	35	310	35		320	30		280	25		250	35		260	35	
80	270	40		270	40	35	280	40	35	290	40	35	290	35		300	35		270	30		270	35		270	40	
90	270	40		270	40	40	275	40	40	280	40	40	280	40		280	40		270	30		270	40		270	45	
100	270	40		270	45	45	275	45	45	280	40	40	270	45		270	45		270	40		270	45		270	50	
LATITUDE 80° N																												
10	330	03	20	330	03	20	330	04	20	355	05	20	30	03	18	95	03	19	155	06	19	180	06	20	220	07	23
20	310	04	25	320	05	25	325	06	25	355	04	25	45	02	25	120	05	25	160	10	29	210	10	32	225	13	30
30	300	08	25	320	10	25	320	10	25	345	07	25	60	03	25	140	05	25	190	10	30	215	10	33	230	15	37
40	265	12	23	295	13	25	325	12	25	360	10	25	60	03	25	160	05	25	180	10	25	210	10	27	240	15	25
50	260	20	20	260	20	25	280	15	25	300	15	25	285	10	25	275	08	25	230	10	25	235	10	25	250	15	25
60	250	20		270	25		280	20		310	20		320	15		340	15		320	15		290	10		260	10	
70	250	25		270	35		280	25		310	20		320	20		330	15		330	15		310	15		250	15	
80	270	30		270	35		270	30		290	25		300	20		300	15		300	20		290	20		260	20	
90	270	30		270	35		270	35		280	25		280	20		290	20		290	20		280	25		270	25	
100	270	35		270	35		270	35		270	30		270	25		270	25		270	25		270	30		270	30	

	Winter																											
H	0°			20° E			40° E			60° E			80° E			100° E			120° E			140° E			160° E		
10^3 ft	d	$\bar{v}$	δ	d	$\bar{v}$	δ	d	$\bar{v}$	δ	d	$\bar{v}$	δ	d	$\bar{v}$	δ	d	$\bar{v}$	δ	d	$\bar{v}$	δ	d	$\bar{v}$	δ	d	$\bar{v}$	δ
LATITUDE 20° N																												
10	240	06	16	265	08	15	290	13	15	250	09	15	270	12	15	290	08	15	200	12	14	210	11	17	210	07	17
20	265	27	21	245	15	25	260	22	22	285	23	23	285	22	20	265	24	20	230	20	17	225	25	20	285	17	20
30	265	55	32	260	35	27	275	40	30	270	45	28	260	40	25	250	45	25	255	40	22	245	32	25	295	30	25
40	265	62	35	260	50	30	275	50	30	265	65	33	250	65	30	250	52	25	250	45	25	240	30	28	280	35	30
50	265	50	25	260	45	30	270	45	25	260	55	30	250	55	32	250	45	25	240	40	25	230	25	25	280	30	25
60	270	40		270	35		270	35		270	35		270	40		270	35		260	30		260	20		150	20	
70	250	10		250	15		210	15		210	25		220	25		230	20		250	10		220	10		90	05	
80	100	05		160	05		30	05		30	05		30	05		30	05		230	05		110	05		70	10	
90	90	05		90	05		90	05											90	10		90	10		90	10	
100	90	10																	90	10		90	15		90	10	
LATITUDE 30° N																												
10	290	14	20	280	16	20	265	20	19	250	18	15							285	28	17	275	30	20	270	30	20
20	280	36	30	270	32	33	255	38	28	265	35	25	270	35	25				270	55	25	270	65	30	265	60	30
30	280	50	45	270	60	45	270	65	40	270	55	35	275	58	35	270	70	35	270	85	35	265	90	35	270	80	40
40	280	55	45	270	65	40	270	75	40	265	75	40	260	80	40	270	80	35	270	90	35	270	10	40	270	95	40
50	280	50	35	270	55	30	270	65	30	265	70	35	260	75	35	265	80	35	265	85	35	265	85	35	275	70	35
60	280	30		280	35		260	35		270	35		270	40		270	50		270	55		250	50		260	35	
70	290	20		280	20		260	25		270	30		270	30		280	30		260	25		240	20		200	15	
80	290	15		280	20		270	20		280	20		280	20		270	15		240	20		220	15		250	05	
90	270	15		270	25		270	20											260	20		260	20		270	08	
100	270	20		270	30														270	25		270	25		270	15	

(Continued)

Table 4-21. Resultant wind direction (d in degrees), vector mean wind velocity ($\bar{v}$ in knots), and standard vector deviation (δ in knots) at various altitudes (H) for various latitudes and longitudes in the Northern Hemisphere, summer and winter seasons. (Continued)

	Winter																											
H	0°			20° E			40° E			60° E			80° E			100° E			120° E			140° E			160° E		
10^3 ft	d	$\bar{v}$	δ	d	$\bar{v}$	δ	d	$\bar{v}$	δ	d	$\bar{v}$	δ	d	$\bar{v}$	δ	d	$\bar{v}$	δ	d	$\bar{v}$	δ	d	$\bar{v}$	δ	d	$\bar{v}$	δ
LATITUDE 40° N																												
10	290	12	23	280	14	24	260	16	21	260	09	15	270	09	11	295	23	17	300	28	18	285	34	23	265	33	24
20	300	18	32	280	20	32	265	27	29	265	16	22	270	27	25	285	40	27	290	44	32	270	54	36	260	52	34
30	305	23	40	280	33	45	265	40	37	270	33	35	270	44	35	285	55	36	285	60	37	270	80	40	260	75	45
40	305	32	40	280	40	40	270	55	38	265	43	37	270	55	35	280	65	40	280	70	40	270	90	40	260	80	45
50	295	30	30	280	35	35	275	45	35	270	45	30	270	50	35	270	60	35	270	65	40	260	80	40	265	70	40
60	290	25		280	35		270	35		270	35		280	45		290	50		270	55		250	50		250	40	
70	290	25		280	30		270	30		260	30		270	35		280	40		260	40		230	40		220	25	
80	290	25		280	30		270	30		270	35		270	35		270	40		250	40		210	25		140	15	
90	270	30		270	30		270	35											270	35		260	30		240	20	
100	270	35		270	40														270	35		270	35		270	30	
LATITUDE 50° N																												
10	290	15	26	280	12	26	260	11	25	260	08	21	275	11	20	295	18	20	315	20	18	290	15	24	250	12	27
20	300	23	36	290	16	34	270	17	30	270	14	28	285	20	30	300	26	27	310	25	30	275	22	35	240	18	35
30	305	30	50	290	20	45	275	20	34	275	18	35	290	30	38	300	35	33	305	25	35	270	26	35	240	27	40
40	305	30	40	290	20	35	275	25	32	270	25	35	280	30	33	295	40	37	300	45	35	270	35	35	240	40	40
50	300	25	30	290	25	35	280	25	30	275	30	25	280	30	30	275	35	35	280	40	35	255	40	35	245	40	35
60	280	30		290	30		270	35		270	40		280	40		290	40		260	40		230	40		230	35	
70	280	30		290	30		270	35		270	40		280	40		280	40		250	40		230	45		230	35	
80	280	35		280	35		270	40		270	50		270	50		270	45		240	40		220	40		230	25	
90	270	40		270	40		270	40											270	40		270	40		270	30	
100	270	50		270	50														270	45		270	40		270	40	
LATITUDE 60° N																												
10	270	16	26	280	09	25	270	07	26	260	08	24	265	12	24	285	13	21	320	09	17	300	04	22	255	03	26
20	280	25	38	290	14	33	285	10	32	280	12	34	290	16	33	310	15	28	320	09	25	290	04	28	225	05	35
30	285	32	50	280	20	45	290	15	38	285	17	35	295	20	38	315	20	32	330	09	30	260	05	31	210	10	35
40	285	35	40	290	25	40	290	20	35	280	20	35	295	20	35	315	20	33	320	15	30	240	08	28	210	10	35
50	280	30	35	290	25	35	290	20	30	285	15	25	290	15	30	290	20	30	290	15	30	245	15	30	220	15	30
60	270	35		280	30		280	30		270	25		280	25		280	25		260	20		220	30		230	20	
70	270	40		280	35		280	35		270	35		280	40		280	40		250	35		220	40		230	30	
80	270	40		270	40		270	35											270	35		230	40		230	35	
90	270	45		270	45		270	40											270	35		270	40		270	35	
100	270	50		270	50														270	40		270	45		270	45	
LATITUDE 70° N																												
10	260	11	23	260	11	22	255	65	23	240	05	23	245	04	23	260	04	20	310	03	17	300	03	20	300	03	23
20	255	18	32	270	13	26	280	07	25	280	06	26	290	06	26	310	06	24	330	03	22	300	03	25	285	04	27
30	260	28	44	270	18	33	280	10	30	290	12	30	300	10	28	320	08	26	50	03	25	210	02	25	250	05	28
40	270	25	32	280	20	30	285	15	30	290	10	30	300	10	30	320	05	28	300	03	25	220	05	25	220	10	25
50	275	25	30	285	20	30	290	15	25	290	10	25	300	05	25	290	05	25	280	03	25	240	10	25	230	15	25
60	270	30		280	35		290	35		280	30		280	30		270	25		220	20		220	30		230	40	
70	270	30		280	40		290	40		280	35		280	35		260	30		220	30		240	35		230	40	
80	270	35		270	35		270	25											270	25		270	35		270	40	
90	270	40		270	40		270	30											270	25		270	35		270	40	
100	270	50		270	50																	270	40		270	45	
LATITUDE 80° N																												
10	245	07	21	250	06	21	240	06	20	230	05	20	230	03	20	250	03	20	300	02	17	315	03	20	330	03	20
20	240	12	28	250	10	26	260	07	20	275	05	25	290	04	22	305	04	23	320	03	22	300	03	25	310	03	25
30	240	18	36	250	16	30	250	10	25	270	10	25	280	07	25	300	04	23	270	03	25	245	03	25	280	05	25
40	255	15	23	270	13	25	280	10	25	290	07	25	300	05	25	295	05	23	270	05	25	250	07	20	260	10	25
50	250	15	25	270	10	25	275	10	25	275	05	25	280	05	25	260	05	20	260	08	25	245	10	20	250	15	20
60	270	15		270	15		280	10		280	10		250	10		230	10		210	15		220	15		230	25	
70	260	15		250	20		270	20		260	15		230	15		230	20		210	20		220	25		230	30	
80	270	20		270	20		270	10											270	20		270	25		270	30	
90	270	20		270	20		270	15											270	25		270	30		270	30	
100	270	40		270	40		270	35														270	40		270	35	

Table 4-22. Seasonal means and standard deviations of wind components (knots); n is the number of observations from which the mean was obtained.

Altitude (km)		Westerly			W to E			Easterly			E to W		
		S	W	n	S	W	n	S	W	n	S	W	n
						CAPE KENNEDY							
25	Mean	5	4	131	0	−13	58	−1	−30	80	−1	−27	42
	S.D.	7	18		6	11		5	12		6	12	
30	Mean	7	12	145	2	−9	70	1	−42	93	1	−26	54
	S.D.	12	28		8	17		6	11		7	16	
35	Mean	6	18	155	0	−5	71	1	−46	101	0	−23	58
	S.D.	17	44		11	20		9	13		8	21	
40	Mean	6	29	159	2	−5	73	2	−60	102	1	−57	57
	S.D.	21	53		12	24		11	15		11	24	
45	Mean	11	45	162	6	−7	71	5	−75	100	3	−22	56
	S.D.	20	55		13	31		12	18		15	33	
50	Mean	17	67	162	9	−6	68	14	−81	97	7	−23	47
	S.D.	23	58		16	41		16	22		16	37	
55	Mean	12	81	139	8	1	54	11	−84	83	12	−13	35
	S.D.	27	52		17	46		18	23		15	38	
60	Mean	8	102	56	7	−8	22	10	−95	54	9	0	18
	S.D.	27	49		18	52		27	31		23	32	
65	Mean							5	−106	9			
	S.D.							30	51				
						WALLOPS ISLAND							
25	Mean	4	18	71	1	−1	34	1	−19	49	1	−2	24
	S.D.	9	20		6	13		7	8		4	13	
30	Mean	8	34	83	4	13	35	2	−24	53	1	−8	29
	S.D.	19	36		7	19		6	12		6	15	
35	Mean	6	60	84	3	19	32	2	−34	55	2	−6	31
	S.D.	24	51		10	26		8	11		7	19	
40	Mean	13	77	83	2	15	30	3	−50	53	−1	−3	30
	S.D.	22	61		11	29		9	14		8	27	
45	Mean	19	95	70	9	9	29	8	−68	49	8	0	29
	S.D.	28	68		10	30		11	14		12	39	
50	Mean	18	106	59	6	10	26	12	−77	42	12	0	25
	S.D.	29	70		15	34		13	20		11	45	
55	Mean	13	117	39	8	−5	18	8	−83	19	12	−3	13
	S.D.	34	56		14	31		19	18		19	50	
60	Mean	14	123	18	10	−6	6	7	−104	4	8	10	6
	S.D.	21	49		6	36		17	15		13	52	
65	Mean	12	119	8									
	S.D.	34	38										
						POINT MUGU							
25	Mean	1	12	159	2	−4	82	1	−27	102	0	−10	73
	S.D.	7	20		6	13		5	12		5	13	
30	Mean	3	26	164	2	8	85	1	−31	101	0	−14	73
	S.D.	12	27		7	19		5	13		7	18	
35	Mean	11	46	160	4	18	84	1	−38	107	7	−3	75
	S.D.	19	35		10	28		8	15		7	27	
40	Mean	7	68	157	−2	18	84	2	−52	105	−1	2	75
	S.D.	26	47		10	36		8	12		10	38	
45	Mean	11	84	148	7	4	80	4	−72	102	3	−26	71
	S.D.	29	49		11	39		13	17		12	43	
50	Mean	19	97	126	12	−1	76	11	−83	93	12	5	61
	S.D.	28	51		12	44		11	18		14	53	
55	Mean	25	109	77	6	−20	47	9	−96	54	19	1	37
	S.D.	26	47		13	49		13	25		14	64	
60	Mean	21	106	25	6	−43	6	−13	−98	7	28	38	5
	S.D.	34	51		8	26		18	25		31	68	
65	Mean	17	115	4	16	−62	2	12	−113	3	45	31	2
	S.D.	13	82		11	11		44	19		50	27	

(Continued)

Table 4-22. Seasonal means and standard deviations of wind components (knots); n is the number of observations from which the mean was obtained. (Continued)

Altitude (km)		Westerly			W to E			Easterly			E to W		
		S	W	n	S	W	n	S	W	n	S	W	n
						WHITE SANDS MISSILE RANGE							
25	Mean	1	15	226	3	−6	74	1	−30	137	1	−17	97
	S.D.	8	19		5	10		5	14		5	13	
30	Mean	6	30	225	2	2	71	3	−36	135	3	−19	95
	S.D.	14	27		7	16		6	11		7	14	
35	Mean	8	54	221	2	15	71	2	−42	131	3	−10	93
	S.D.	20	37		10	22		7	13		7	21	
40	Mean	6	72	214	1	14	70	0	−57	127	4	−10	88
	S.D.	25	41		10	32		10	14		10	30	
45	Mean	16	86	198	10	8	70	10	−74	116	8	−11	84
	S.D.	25	40		11	37		11	18		13	40	
50	Mean	20	102	191	11	7	65	13	−83	109	15	−2	80
	S.D.	24	46		13	45		11	17		15	45	
55	Mean	19	114	162	8	−3	57	12	−92	98	11	6	69
	S.D.	27	44		13	50		15	21		15	45	
60	Mean	18	120	148	15	−13	49	7	−99	67	17	6	45
	S.D.	29	43		16	58		19	30		19	45	
65	Mean	19	114	46	15	−47	21	17	−103	33	11	18	13
	S.D.	37	48		20	41		22	41		18	21	
70	Mean	−2	88	6	8	−67	3	20	−75	4	50	−22	3
	S.D.	40	61		11	20		22	25		47	44	
						FT GREELY AND FT CHURCHILL							
25	Mean	−8	21	140	−1	0	35	1	−9	18	1	21	36
	S.D.	25	24		10	20		7	7		10	12	
30	Mean	−11	24	134	−1	−6	29	−1	−15	17	−1	28	36
	S.D.	31	31		14	27		5	9		15	15	
35	Mean	−17	30	126	−2	−3	23	5	−26	16	−1	35	34
	S.D.	40	33		12	27		7	10		15	19	
40	Mean	−20	38	115	5	−3	17	6	−26	11	−1	45	32
	S.D.	43	39		12	26		6	10		16	24	
45	Mean	−21	45	92	6	−11	9	4	−40	7	3	49	22
	S.D.	36	42		10	17		13	19		17	25	
50	Mean	−18	61	72	10	−22	9	19	−49	5	10	54	17
	S.D.	38	46		15	26		12	23		14	32	
55	Mean	−14	74	36	16	−28	8	25	−72	4	21	51	11
	S.D.	36	45		18	31		15	28		29	39	
60	Mean	−20	74	41	19	−34	6				26	35	4
	S.D.	42	44		15	26					13	31	
65	Mean	−20	36	8									
	S.D.	44	34										

4.6 REFERENCES

Arnold, A., and R. Bellucci, 1957, "Variability of Ballistic Meteorological Parameters," *Tech. Memo. No. M-1913,* Ft. Monmouth, U.S. Army Sig. Eng. Lab.

Durst, C. S., 1954, "Variation of Wind with Time and Distance," *Geophys. Memoirs No. 93,* 584a, Meteorological Office, Air Ministry, London.

Ebdon, R. A., 1961, "Some Notes on the Stratospheric Winds at Canton and Christmas Island," *Quart. J. Royal Meteorol. Soc.*, v. 87, p. 322.

Elford, W. G., 1959, "A Study of Winds Between 80 and 100 Km in Medium Latitudes," *Planet. Space Sci.*, v. 1, p. 94.

Ellsaesser, H. W., 1960, "Wind Variability," *AWS Tech. Rept. No. 105-2,* Hdqtrs., Air Weather Service, Scott AFB, Illinois.

Greenhow, J. S., and E. L. Neufeld, 1961, "Winds in the Upper Atmosphere," *Quart. J. Royal Meteorol. Soc.*, v. 87, p. 472.

Harris, M. F., F. G. Finger, and S. Teweles, 1962, "Diurnal Variation of Wind, Pressure, and Temperature in the Troposphere and Stratosphere over the Azores," *J. Atmos. Sci.*, v. 19, p. 136.

Hines, C. O., 1963, "The Upper Atmosphere in Motion," *Quart. J. Royal Meteorol. Soc.*, v. 89, p. 1.

Kantor, A. J., 1962, "Proceedings of the National Symposium on Winds for Aerospace Vehicle Design," *Air Force Surveys in Geophysics, No. 140,* AFCRL.

Lake, H., 1952, "A Comparison of the Power Law and a Generalized Logarithmic Formula in Micrometeorology," *Trans. Am. Geophys. Union,* v. 33, p. 661.

Lettau, H. H., and B. Davidson, ed., 1957, "Exploring the Atmosphere's First Mile," Pergamon Press.

McLean, G. S., 1961, The Jet Stream and Associated Turbulence, "Proc. Natl. Symp. on Winds for Aerospace Vehicle Design," *Air Force Surveys in Geophysics No. 140,* AFCRL.

Mazzola, L. L., J. Putukian, E. S. Criscione, and N. P. Hobbs, 1963, "Wind, Wind Shear, and Gust Design Criteria for Vertically-Rising Vehicles as Recommended on the Basis of Wind Data from Eleven United States and Foreign Locations," *Rept. No. TDR-62-908,* Aeronautical Systems Division, U.S. Air Force Systems Command.

Rofe, B., 1963, "Australian Sounding Rocket Experiments," *Tech. Note SAD 127,* Australian Defence Scientific Service, Weapons Research Establishment.

Scoggins, J. R., and W. W. Vaughan, 1962, "Cape Canaveral Wind and Shear Data (1 through 80 km) for Use in Vehicle Design and Performance Studies," *Tech. Note D-1274,* National Aeronautics and Space Administration.

Smith, L. B., 1960, "The Measurement of Winds Between 100,000 and 200,000 Feet by Use of Chaff Rockets," *J. Meteorol.*, v. 17, p. 296.

U.S. Weather Bureau, "Climatography of the United States—Summary of Hourly Observations," Dept. of Commerce, Washington, D.C.

Chapter 5

PRECIPITATION, CLOUDS, AND AEROSOLS

Section 5.1 A. E. Cole and R. J. Donaldson
Section 5.2 David Atlas
Section 5.3 A. J. Kantor
Section 5.4 R. K. Soberman
Section 5.5 J. E. Manson

The liquid and particulate content of the atmosphere is discussed in this chapter. Data are provided on the frequency of occurrence of various surface rates of rainfall, the vertical distribution of precipitation intensity, and the particle size distribution in widespread precipitation. Information on the types and limitations of cloud data, the distribution and water content of clouds, and the size, composition, and vertical distributions of aerosols is included.

5.1 PRECIPITATION

The frequency of occurrence of given rates of precipitation and the associated vertical distributions of various precipitation parameters must be considered when designing equipment and weapons systems. For example, in designing a search radar, one must know the frequency of occurrence of the critical rainfall rate over the proposed regions of operation in order to determine the probability of failure due to attenuation by rainfall.

In designing jet engines, one must know the amount of water and ice likely to be ingested at various altitudes. Hail (and associated large raindrops) encountered by an aircraft or missile at high speeds can cause damage. Solving design problems, such as aircraft and radome erosion by precipitation, requires a knowledge of the variation of the rainfall rate and raindrop size distributions with altitude. Such data must be related to surface rates of rainfall so that the probability of occurrence for specific areas can be determined from available data. This section gives examples of the types of precipitation information available.

5.1.1 Surface Rates of Precipitation

Usually, tabulations of occurrences of various rates of precipitation cannot be obtained directly from existing climatological records. Precipitation data for most areas of the world are limited mainly to average monthly, seasonal, and annual totals, and to the number of days on which precipitation fell. *Clock hourly* (totals on the hour every hour) precipitation data are available for numerous stations in the United States and Europe, but for only a few stations elsewhere. Frequencies of occurrence of instantaneous rates of precipitation have been computed for a small number of stations in the United States.

Given below are methods for obtaining the frequencies of occurrence of specific clock hourly and instantaneous rates of precipitation at stations where only the total annual amount of precipitation and number of days on which precipitation occurred are known.

5.1.1.1 *Clock Hourly Rates.* Figures 5-1, 5-2, and 5-3 were prepared by plotting against an index the frequencies of occurrence of clock hourly precipitation rates (0.06, 0.12, and 0.18 in. h^{-1}) determined from climatic data for 22 stations in the United States and Europe. This index is the average per day of measurable precipitation, obtained by dividing the total annual precipitation by the number of days with measurable precipitation (0.01 or more in.). The standard error of estimates (S_y) and the correlation coefficients (γ) given for the regression equaitons (Y) in each figure indicate that a good linear relationship exists between these parameters. Assuming this relationship is valid for other warm temperate to subpolar areas, approximate annual frequency of occurrence of clock hourly precipitation rates at other stations in the temperate zone can be determined from the regression curves shown when only the average annual total precipitation and the number of days with 0.01 or more in. are known. Because data from all North American and European areas used in these correlations fit equally well on the derived curves in Fig. 5-1, 5-2 and 5-3, this assumption appears valid. The standard error of estimate indicates that data obtained from these curves will be within 30, 10, and 8 h yr^{-1}, 68% of the time, for rates $\geq$ 0.06, 0.12, and 0.18 in. h^{-1}, respectively.

Table 5-1 gives approximate frequencies of occurrence of clock hourly precipitation rates, obtained from Fig. 5-1, 5-2, and 5-3, for a few stations.

CHAPTER 5

5.1.1.2 *Instantaneous Rates of Precipitation.* Instantaneous rates of rainfall may vary considerably within one hour. For example, 0.06 in. precipitation may be reported during a clock hour. It could have accumulated in thirty minutes at a rate of 0.12 in. h^{-1}, in twenty minutes at the rate of 0.18 in. h^{-1}, or linearly over the entire hour. Thus, the length of time to be tabulated for computing the frequency of various rates cannot be determined directly from hourly data.

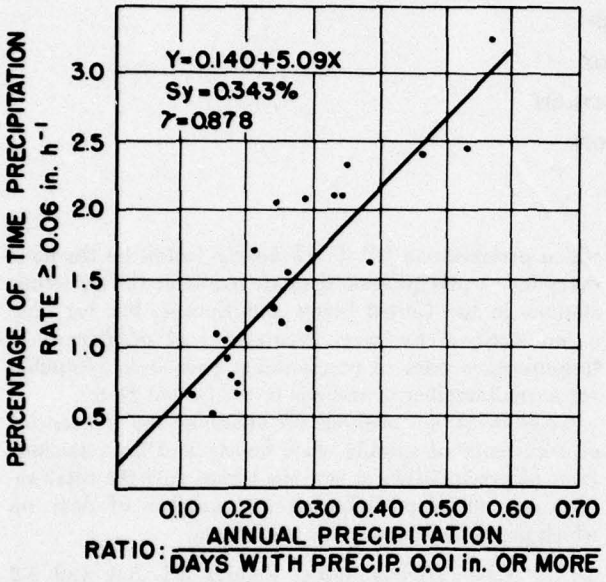


Fig. 5-1. Correlation between annual probability of clock hourly precipitation equal to or exceeding 0.06 in. h^{-1} and usually available precipitation data.

Distribution curves from instantaneous (one-minute periods) and hourly observations for the same station show how the instantaneous rate distributes itself around the clock hourly rate. These instantaneous curves may be used to break down the long-term clock hourly rates into shorter instantaneous segments, and the segments then compounded into a cumulative yearly distribution curve. Figure 5-4 shows cumulative curves and similar curves for two hourly and ½ hourly precipitation rates. A comparison of the frequency curves indicates that it makes little difference in the annual frequency for rainfall rates between 0.06 and 0.18 in. h^{-1} whether these rates are based on two h, one h, ½ h, or instantaneous time increments. The annual frequency of the instantaneous rate is approximately 90% of the mean hourly rate of 0.06 in. h^{-1}, 94% for 0.12 in. h^{-1}, and 100% for 0.18 in. h^{-1}. Because the Washington, D. C. area receives all precipitation types, and because there is nearly a one-to-one relationship for the three rainfall rates, it is considered reliable to adjust hourly frequencies to instantaneous frequencies in other areas on the basis of this analysis. The clock hourly frequencies for stations in Table 5-1 were converted to instantaneous frequencies by using the relationship described above.

Table 5-2 gives the probability of occurrence of given instantaneous rates (hourly rate for one min) of precipitation up to and exceeding 7.50 in. h^{-1} for New Orleans. New Orleans was selected because it is a representative station in an area of heavy rainfall and one for which the frequencies of clock hourly rates, based on 30 years of records, are available. The clock hourly rates were converted to instantaneous frequencies by using the relationship Bussey [1950] found to exist between the two rates in his analysis of rainfall rates at Washington, D.C.

Table 5-3 contains the approximate frequency with which given instantaneous rates of precipitation up to

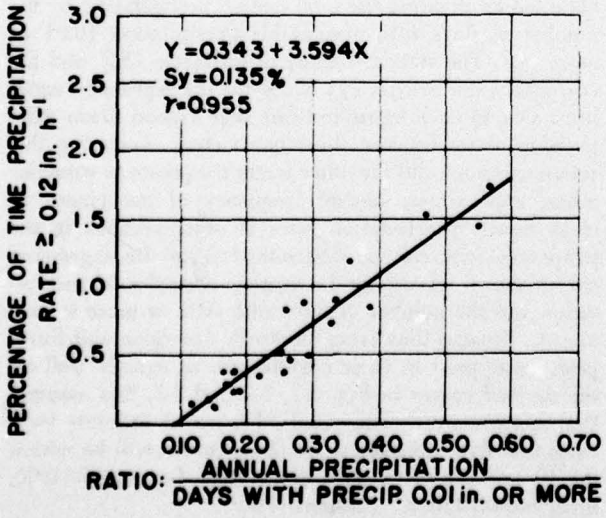


Fig. 5-2. Correlation between annual probability of clock hourly precipitation equal to or exceeding 0.12 in. h^{-1} and usually available precipitation data.

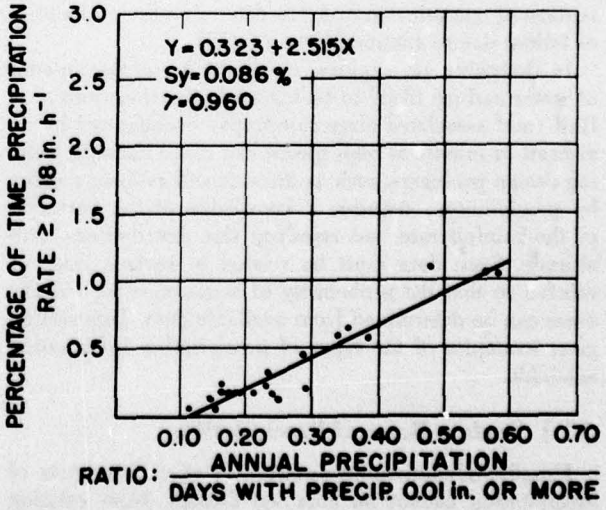


Fig. 5-3. Correlation between annual probability of clock hourly precipitation equal to or exceeding 0.18 in. h^{-1} and usually available precipitation data.

Table 5-1. Percentage of time during an average year in which clock hourly and instantaneous rates of precipitation equal or exceed 0.06, 0.12, and 0.18 in. h^{-1} at selected stations.

Station	Average Annual Precip. (in.)	Number of Days with Measurable Precip.	Clock Hourly Rates			Instantaneous Rates		
			0.06 (%)	0.12 (%)	0.18 (%)	0.06 (%)	0.12 (%)	0.18 (%)
Athens 37° 30′ N 23° 43′ E	15.70	98	0.94	0.24	0.08	0.85	0.23	0.08
Berlin 52° 30′ N 13° 25′ E	22.88	169	0.84	0.16	0.03	0.76	0.15	0.03
Dublin 53° 20′ N 6° 15′ W	27.37	218	0.78	0.13	0.01	0.70	0.12	0.01
London 51° 25′ N 0° 20′ E	24.47	167	0.89	0.20	0.06	0.80	0.19	0.06
Moscow 55° 45′ N 37° 37′ E	24.13	132	1.05	0.30	0.13	0.95	0.29	0.13
Paris 48° 52′ N 2° 20′ E	22.62	160	0.84	0.16	0.03	0.76	0.15	0.03
Rome 41° 45′ N 12° 15′ E	26.70	105	1.45	0.59	0.33	1.31	0.55	0.03
Tokyo 35° 41′ N 139°46′ E	61.40	149	2.22	1.13	0.72	2.00	1.06	0.72
Warsaw 50° 14′ N 21° 00 E	22.21	164	0.84	0.16	0.03	0.76	0.15	0.03
Washington 38° 55′ N 77° 00 W	42.20	124	2.11	0.90	0.60	1.90	0.85	0.60

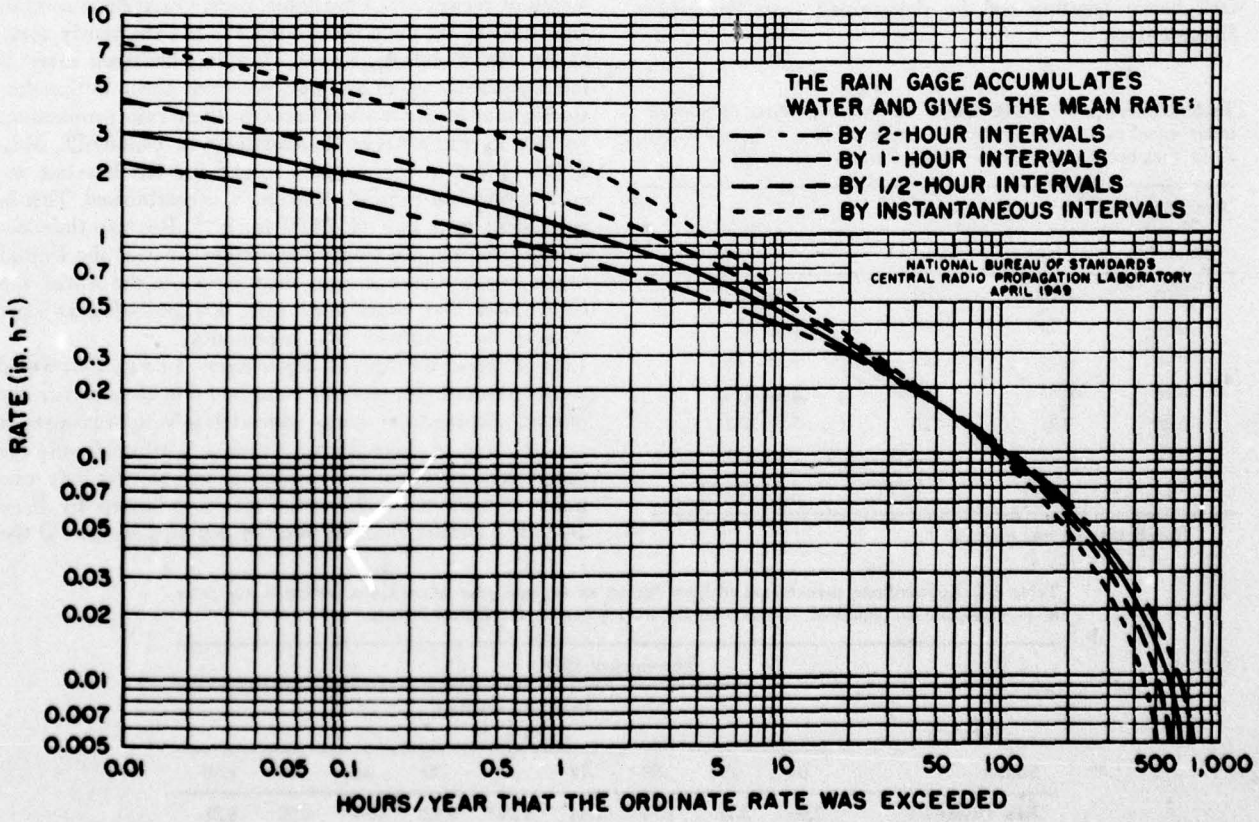


Fig. 5-4. Cumulative distribution of rainfall rates at one location, Washington, D. C. The 1-h curve is based upon observed long-time data. The other three curves are derived from the 1-h curve. (From H. E. Bussy [1950].)

1.50 in. h^{-1} are equalled or exceeded at stations in four climatic areas of the United States. Data for Portland and Washington are representative of conditions found on the northwestern and mideastern coasts, respectively. New Orleans represents an area of heavy rainfall frequently under the influence of tropical maritime air, and Oklahoma City represents the Great Plains.

5.1.1.3 *Separation of Rainfall and Snowfall.* The data considered thus far are for precipitation as a whole, mainly snow and rain. To obtain the frequencies of rates of rainfall, the rates of snowfall $\geq$ 0.06, 0.12, and 0.18 in. h^{-1} must be subtracted from the data in Table 5-1. A detailed examination of the clock hourly rates of precipitation at four stations that have prolonged periods of below freezing weather, such as Bismarck, North Dakota, revealed the following:

(1) 99% to 100% of all precipitation that falls at rates equal to or exceeding 0.12 in. h^{-1} fall as rain and are encountered only at temperatures above freezing.

(2) Roughly 85% of the precipitation falling at rates equal to or exceeding 0.06 in. h^{-1} are encountered at above freezing temperatures as rain, and the remaining 15% occur during the warmer months of the cold season and may be rain or snow.

Periods during which stations experience temperatures well below freezing can be determined from available climatic data.

Table 5-2. Frequencies with which instantaneous rates of precipitation equal or exceed the indicated rates in New Orleans. (After R. D. Fletcher, *Trans. Am. Geophys. Union*, v. 31 p. 344.)

Instantaneous Rate* (in. h^{-1})	Frequency (%)	Frequency (h yr^{-1})	Occurrence Probability
0.06	2.16	189	1 in 46
0.18	1.08	95	1 in 92
0.40	0.56	49	1 in 179
0.80	0.37	32	1 in 274
1.50	0.21	18	1 in 487
3.00	0.044	3.85	1 in 2275
7.50	0.0011	0.096	1 in 91,250

* Hourly rate for one minute.

5.1.1.4 *Extreme Rates of Rainfall.*

(1) *Five Year Expectancy*—Climatic data are not available for computing the maximum rate of rainfall that can be expected to occur anywhere in the world in the next five years. It is necessary to relate the maximum rate of rainfall in a 5-yr period in the United States, where data are available, to the worldwide expectancy.

Information on the maximum rainfall rates to be expected in the United States is contained in U.S. Weather Bureau Technical Paper No. 29 and in a report by Yarnell [1935]. The highest rates of rainfall in the continental United States occur in a relatively narrow region bordering on the Gulf of Mexico. Table 5-4 gives maximum averages rates over 5-min to 1-h time periods with a 5-yr expectancy.

Although greater yearly rainfalls occur in some regions (for example, 70 to 130 in. in the Panama Canal Zone as compared to 57 in. at New Orleans), the 5-yr expectancy on the Gulf Coast appears to be the right order of magnitude for the world. The measured 42-yr maximum 5-min rainfall rate for the Canal Zone of 10.9 in. h^{-1} is only about 10% greater than the expectancy indicated for the same period along the Gulf Coast. Rates as high as 16.1 in. h^{-1} for a 5-min period have been observed at Pensacola, Florida in the past 22 years, but information on length of record is not available. Even Canal Zone rainfall amounts are far from the record 471 in., the yearly average at Mt. Waialeale, Kauai, Hawaii. Maximum rates of fall for periods up to an hour, however, occur in thunderstorms that have physical limits to their rain production. In fact, during a heavy thunderstorm in Unionville, Md., 4 July 1956, a new world's record for the heaviest recorded one-min rainfall, 1.23 in., was established. This is equivalent to a rate of 73.80 in. h^{-1}. Because thunderstorms occurring in tropical maritime air over the United States are as severe as over most places in the world, the Gulf Coast 5-yr expectancy rates are probably at least 80% of the worldwide 5-yr expectancy.

(2) *All Time Worldwide Expectancy.* In Fig. 5-5, world record rainfalls for periods from one min to one year are plotted. From these data, which closely approximate a straight line on logarithmic scales, a worldwide all-time expectancy envelope for rainfall extremes over any one point is computed. This envelope, represented by $R = 14.3\ D^{1/2}$ (where R is the rainfall depth in in. and D the

Table 5-3. Approximate percentages of time during an average year when given instantaneous rates of precipitation are equalled or exceeded at four stations in the United States.

	Percentages (%)								
	Precipitation Rate (in. h^{-1})								
Station	.04	.06	.08	.12	.18	.20	.40	.80	1.50
New Orleans	2.96	2.16	1.74	1.44	1.08	0.92	0.56	0.37	0.21
Oklahoma City	2.04	1.49	1.23	0.81	0.57	0.46	0.20	0.15	0.11
Washington, D.C.	2.58	1.90	1.36	0.84	0.60	0.48	0.17	0.07	0.024
Portland, Oregon	1.84	1.34	1.09	0.57	0.35	0.28	0.11	0.05	0.016

duration in h), is shown in Fig. 5-5. Values taken from this envelope for 1- to 60-min periods are tabulated in Table 5-4. The all time worldwide one-min rate is more than twice the 5-min rate.

5.1.2 Hail

In generic terms, hail is precipitation in the form of round or irregular lumps of ice. In precise meteorological terminology, hail is defined as particles with a diameter of 5 mm (0.2 in.) or more; smaller particles are ice pellets. Ice pellets are, in turn, classified as sleet, which consists of generally transparent and globular grains of ice, or as small hail, which is generally translucent particles consisting of snow pellets (graupel or soft hail) encased in a thin layer of ice. Large hail has a diameter greater than 2 cm (¾ in.).

Large hail is formed only in well-developed thunderstorms whose cloud tops may sometimes extend above 50,000 ft; it is found only in, along, and under such storms. Small hail and soft hail are thought by some meteorologists to be an essential feature of all thunderstorms. However, ice particles less than 1 cm in diameter, which may be present aloft in the cores of thunderstorms, are likely to melt completely before reaching the ground in a typical thunderstorm air mass. Although thunderstorms are most frequent in the tropics and subtropics, occurring up to 180 days per yr in several places, hail is rarely found on the ground in the tropics. Hail that reaches the ground has a maximum frequency over mid-latitude mountainous and adjacent areas (such as Colorado, Wyoming, and Nebraska) where any given location may experience 5 to 10 hailstorms a year in an area where thunderstorms have a probability of occurring 40 to 50 days per yr.

Foster [1961] summarizes the physical properties of hail and its effect on aircraft, and outlines in detail a hail forecasting technique that takes into account low-level convergence, the microphysics of hailstone growth, and buoyancy.

5.1.2.1 *Horizontal Extent.* The diameter of a well-developed thunderstorm cell of the type producing hail is of the order of 5 to 10 miles. Diameters of the areas in which hail is encountered are generally 1 to 3 m. Encounters with several adjacent hailstorm cells in an area are prob-

Table 5-4. Extreme hourly rates.

Period (min)	Gulf Coast 5-Yr Expectancy (in. h^{-1})	Worldwide All-Time (in. h^{-1})
1	15*	112
5	7.2	48
10	6.0	36
30	4.5	22
60	3.2	15

* estimated

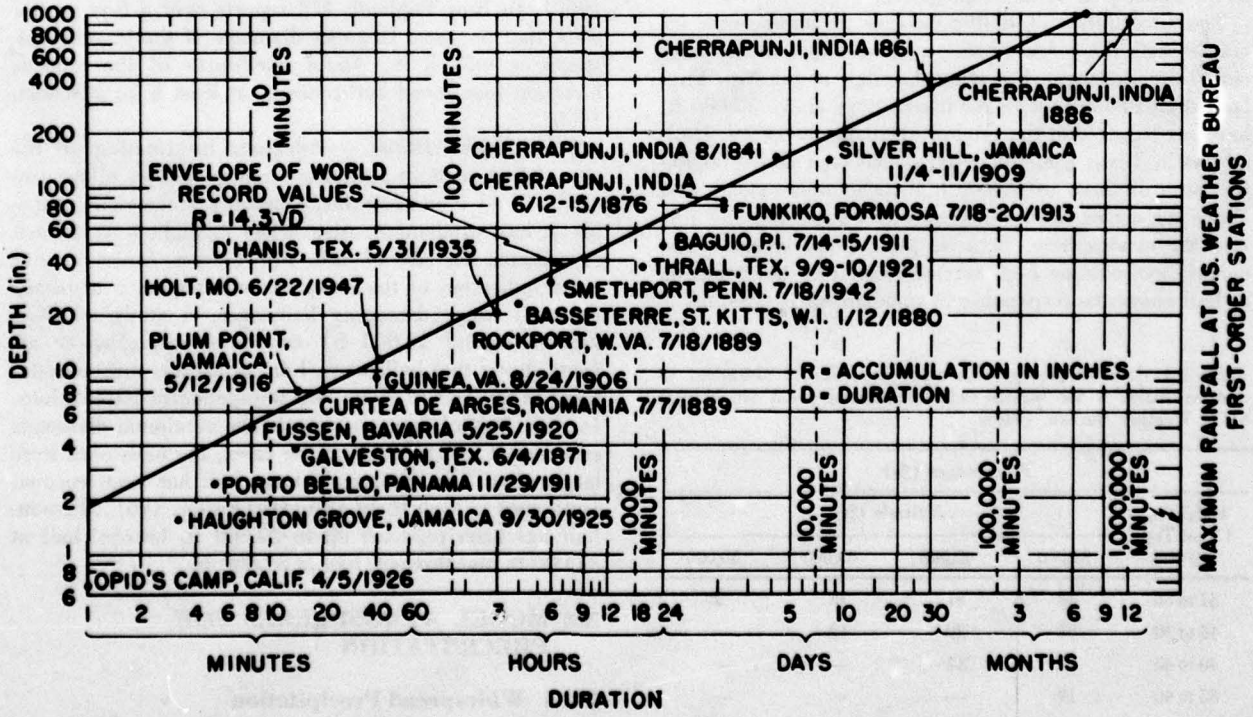


Fig. 5-5. World record rainfalls and an envelope of world record values. (After R. D. Fletchter and D. Sartos, *Air Weather Service Tech. Rept. No. 105-81*, 1951.)

able, and hail paths on the ground nearly 10 miles in width have been observed [Lemons, 1943]. A rough idea of the decrease in horizontal hail path with altitude can be obtained from the radar observations of altitude dependency of precipitation areas in thunderstorms given in Table 5-5.

5.1.2.2 *Vertical Extent.* Although hail can form only at altitudes above the 0°C level, it may be encountered in flights from the surface to very high altitudes. During the Thunderstorm Project [U.S. Weather Bureau, 1949], hail was found at all altitudes up to 26,000 ft, with a maximum occurrence at 15,000 to 16,000 ft in 10% of the traverses made in Florida and Ohio. Unfortunately, no aircraft data were obtained above 26,000 ft. Because the traverses necessarily covered a limited region of the thunderstorm, it is possible that hail was present somewhere in a large proportion of the thunderstorms. Also, the expectancy of hail reaching ground is only about 1 day per yr in Florida, and 2 to 3 days per yr in Ohio. Hail aloft should occur more frequently, and at higher altitudes of maximum occurrence, over areas of greater probability of surface hail.

Analysis of 272 encounters by USAF planes (1951 through 1959) shows that the highest altitude at which large hail was encountered is 44,000 ft. More encounters (29%) occurred at 6000 through 10,000 ft than at any other 5000-ft segment. Over 40% of the encounters occurred above 20,000 ft, and 16% above 30,000 ft. All but three encounters above 20,000 ft were damaging to the aircraft, which suggests that there is a preponderance of large sizes (diameter ¾ in. or greater) when hail is found in the upper part of the troposphere.

The probability of hail occurring at the ground increases with the height of the radar-echo tops of the associated thunderstorm. For about one-half of the New England thunderstorms with radar-echo tops above 50,000 ft, hail was reported at the ground [Donaldson, 1959]. Hailstorms in Texas sometimes have echo tops above 60,000 ft. Some of these extremely high echo tops extend well above the cirrus anvil and penetrate a few thousand feet into the stratosphere. Because these giant storms must contain exceedingly high vertical velocities, the presence of hail above the tropopause in such storms is possible.

Table 5-5. Ratio of precipitation area (at indicated altitudes) to area at 10,000 ft for various radar-determined cloud top heights [U.S. Weather Bureau, 1949].

	Percentages (%)			
Height of Cloud Top (10^3 ft)	Altitude (ft)			
	35,000	40,000	45,000	50,000
51 to 55	84	41	15	2
45 to 50	54	29	10	—
40 to 45	45	11	—	—
35 to 40	19	—	—	—
20 to 55*	6	1.4	0.3	0.01

* all echoes

5.1.2.3 *Size of Hail.*

(1) *At the Ground*

Extreme on record in U.S.A.	5.4 in. (1.5 lb)
Most common:	
India	0.2 to 1.2 in.
France	0.2 to 0.8 in.
Central Europe	up to 1.2 in.
U.S.A.	0.5 to 0.7 in.

Size distribution:

U.S.A. (176 cases with hailstones ½ in. or larger)

in.	%
0.50 to 0.74	39
0.75 to 0.90	20
1.0 to 1.4	14
1.5 to 1.9	11
2.0 to 2.4	6
2.5 to 2.9	4
3.0 to 3.4	4
3.5 to 3.9	1
4 or more	1

India (597 cases)

less than 0.2 in.	27
0.2 to 1.2 in.	51
greater than 1.2 in.	22

Within the United States, hail sizes are larger in the lee of the Rocky Mountains than in the eastern states. In 829 reports covering a ten-yr period in and near Denver, Colorado, the most frequent diameter of the largest hailstones was ½ in.; about one-third of the reports gave maximum hailstone diameters of at least ¾ in. [Beckwith, 1960]. In New England, 472 reports over a 5-yr period show that the most frequent diameter of the largest hailstones is only ¼ in. About one-fourth of the reports, however, mentioned hailstones of at least ¾ in. [Chmela, 1960].

(2) *At Flight Altitudes*—Adequate information on the size of hail at flight altitudes is not available; pilots generally avoid thunderstorms, especially violent ones capable of hail production. Also, when in flight it is difficult to estimate the size of hail. Two studies, however, give some indication of the altitudes and frequency of occurrence of large, damaging hailstones. A study of DC-3 flights (ceiling 12,000 ft) on the Chicago-Denver air route shows that hailstones, 1 in. or larger, were encountered in one out of every 800 thunderstorm penetrations. In about half of these encounters, the maximum diameters exceeded 2 in.; in 10% of the cases, the hailstones were larger than 3 in. Extremely large hail has been encountered even at high flight altitudes [Foster, 1961]. Five-in. hail has been reported up to 29,500 ft, four-in. hail at 31,000 ft, and three-in. hail at 37,000 ft.

5.2 MODEL ATMOSPHERES FOR PRECIPITATION

5.2.1 Widespread Precipitation

Three models of vertical distributions of various precipitation parameters, the result of combinations of em-

pirical and theoretical data, are presented. They indicate approximate conditions in the different types of weather situations.

Case I is representative of summer rain in temperate latitudes and, with a slight increase of temperature, of widespread tropical rains as well.

Case II is associated with rain in the spring and fall months in temperate latitudes and also represents a likely thermal stratification during many orographic rains of temperate climes.

Case III, patterned after the atmospheric structure during severe snowstorms in New England, is representative of a winter snowstorm and, except for the low temperatures, characterizes the winter rains as well.

All cases pertain to widespread uniform precipitation, not to showery conditions. A parabolic distribution of vertical velocity, which is assumed in this study, agrees qualitatively with observed distributions in general storm systems.

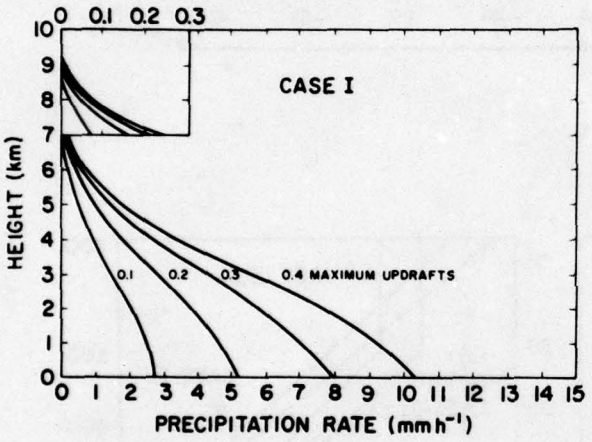


Fig. 5-7. Distribution of precipitation rate with altitude for Case I. Values of maximum updraft in m sec^{-1} are given by each curve.

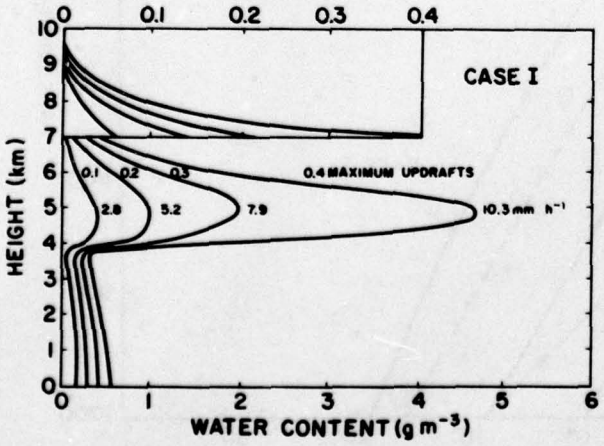


Fig. 5-8. Concentration of precipitation, in g m^{-3}, with height for Case I. Values of maximum updraft in m sec^{-1} (above) and surface precipitation rate in mm h^{-1} (below) are given by each curve.

In the central regions of widespread uniform updrafts in saturated air, the steady-state distribution of condensed water substance (precipitation, not cloud) is given approximately by

$$\frac{\partial M}{\partial z} = \frac{1}{V+w}\left[wG - M\frac{\partial V}{\partial z}\right], \quad (5\text{-}1)$$

where the mass, M, has terminal speed V (negative with respect to w), w is the air speed in the upward (+z) direction, and G is a generation term denoting the amount of water condensed from saturated air per unit vertical distance of air travel. The generation term is a function of the temperature and the pressure, see Kessler [1958]. Equation (5-1) has been solved by finite difference methods to obtain Fig. 5-7 through 5-10. Figure 5-6 and Table 5-6 give the assumed vertical temperature distributions for the three cases studied.

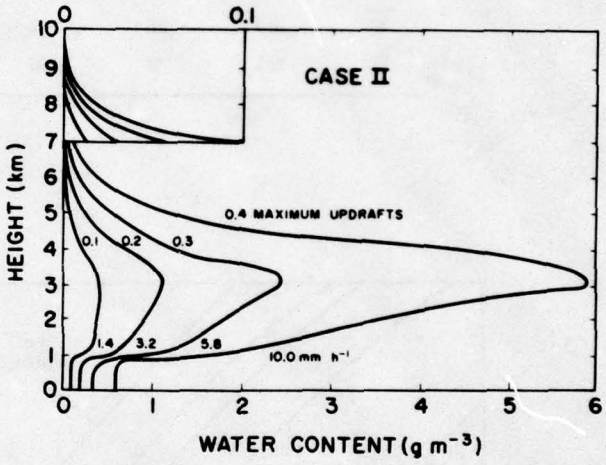


Fig. 5-9. Concentration of precipitation, in g m^{-3}, with height, for Case II. Values of maximum updraft in m sec^{-1} (above) and surface precipitation rate in mm h^{-1} (below) are shown by each curve.

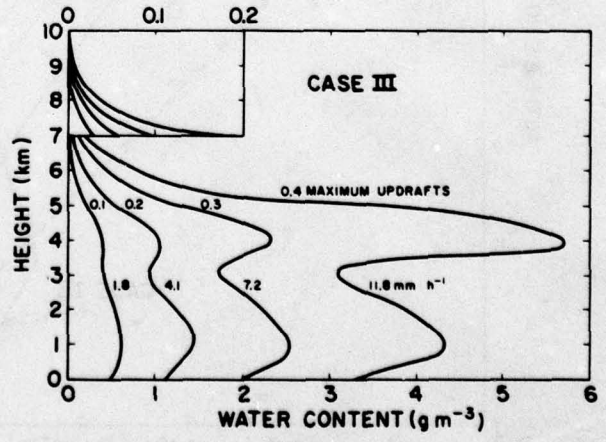


Fig. 5-10. Concentration of precipitation in g m^{-3}, with height, for Case III. Values of maximum updraft in m sec^{-1} (above) and surface precipitation rate in mm h^{-1} (below) are shown by each curve.

Table 5-6. Distributions of vertical air speed (relative updraft) temperature and generating function, G (Eq. 5-1).

Ht (km)	Approx. Pressure (mb)	Relative Updraft ($cm\ sec^{-1}$)	Case I T (°C)	Case I G ($g\ m^{-4}$)	Case II T (°C)	Case II G ($g\ m^{-4}$)	Case III T (°C)	Case III G ($g\ m^{-4}$)
0	1015	0	18	25.8	8	21.2	0	16.8
1	900	36	14	22.5	2	17.3	−7	12.3
2	795	64	9	19.2	−4	13.3	−6	12.0
3	700	84	5	16.0	−10	10.0	−4	12.6
4	615	96	0	13.7	−15	7.3	−9	9.7
5	540	100	−8	9.6	−25	4.1	−17	6.4
6	470	96	−16	6.4	−35	1.5	−26	3.9
7	410	84	−25	4.2	−43	0.8	−35	1.9
8	355	64	−34	1.9	−50	0.4	−43	0.8
9	310	36	−41	1.1	−58	0.2	−50	0.4
10	265	0	−50	0.4	−60	0.2	−53	0.3

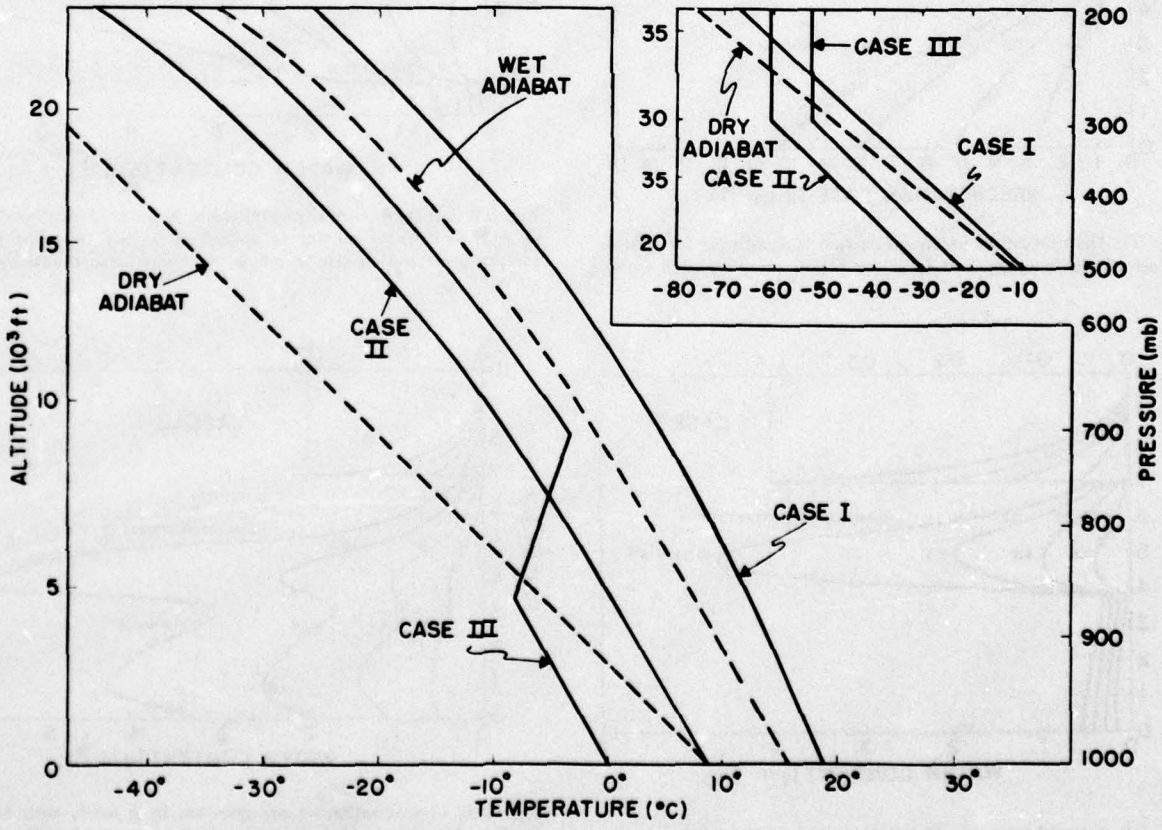


Fig. 5-6. Vertical temperature distribution for situations of widespread precipitation. Case I—summer rain; Case II—spring or fall rain; Case III—winter snowstorm.

In using Eq. (5-1), it is assumed that all particles in the precipitation mass at a given point fall at the same velocity relative to the air. At temperatures below freezing the snow is assumed to fall at the speeds given in Table 5-7. These speeds correspond approximately to those of single crystals at the lower temperatures and to aggregate, wet snowflakes at temperatures near and above melting. Speeds of fall in the liquid phase have been equated to those of the drops of median-volume diameter. The median-volume diameter divides the distribution of sizes that occurs in nature into two parts of equal water content. Combinations of relations [Marshall and Palmer, 1948 and Spilhaus, 1948] give:

$$V = 5.3\, M^{0.12}, \qquad (5\text{-}2)$$

where M is in g m^{-3} and V is in m sec^{-1}.

Figures 5-8 through 5-10 show the surface precipitation rate and vertical distributions of water substance for three cases; the results apply to the interior of widespread precipitation areas. The vertical distribution of precipitation rates for Case I is given in Fig. 5-7. The precipitation rates are $R = M\,(V + w)$, and may be derived for Cases II and III by multiplying each curve by its corresponding values of $V + w$.

Approximate frequencies of occurrence of the surface precipitation rates derived here can be obtained for various stations if it is assumed that rates of precipitation up to and including 0.4 in. h^{-1} (10 mm h^{-1}) normally occur in storms associated with widespread precipitation.

Table 5-7. Assumed variation of the falling speed of snow crystals and flakes with temperature range.

Temperature (°C)	Speed of Fall (cm sec^{-1})
< −8	50
−8 to 0	50 to 100*
0 to 2	100 to 140*

* Increasing linearly from low to high temperature

5.2.1.1 *Water Content of Clouds.* The above computations of the concentration of precipitation with height do not consider water storage in clouds. Under steady conditions, the mass of cloud water per unit volume may be two or three times that of rain in the zone just below the melting level, especially in light precipitation. This factor may be important in some problems. In widespread rainfall, water clouds generally occur with bases at 500 to 1000 ft. The water content normally increases upward to a maximum in the vicinity of the melting level and then, above a temperature level of 1° or 2°C, decreases gradually to zero. Figures 5-11 and 5-12 show steady cloud-water distributions in clouds associated with various surface rates of precipitation occurring under conditions similar to those outlined for Cases I and II.

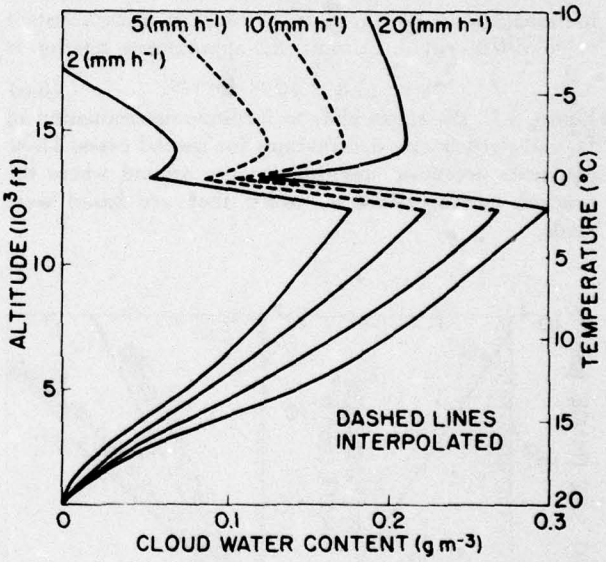


Fig. 5-11. Steady-state water content of clouds for a situation similar to Case I and for surface intensities of 2, 5, 10, and 20 mm h^{-1} (derived from Wexler and Atlas [1958]).

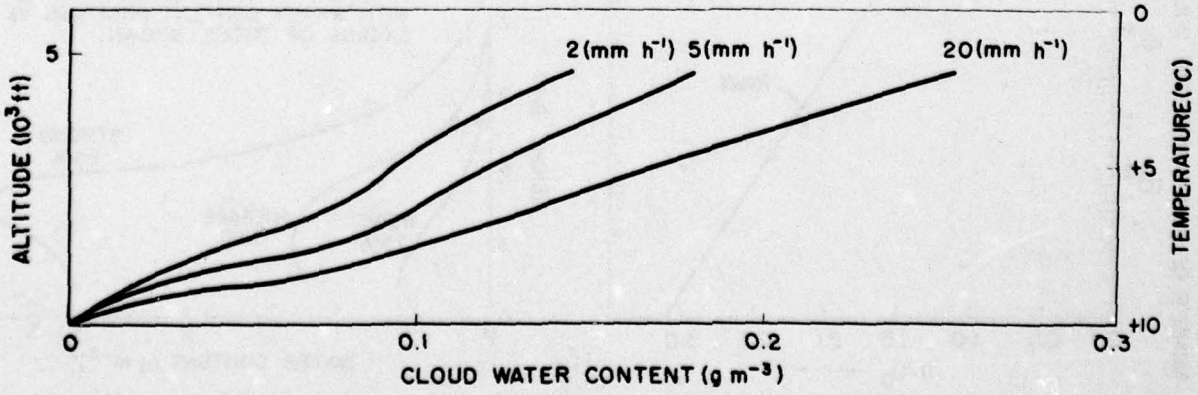


Fig. 5-12. Steady-state water content of clouds for a situation similar to Case II, for surface rain intensities of 2, 5, and 20 mm h^{-1} (derived from Wexler and Atlas [1958]). Curves are cut off at the melting level. From there upward, the liquid water content varies in a manner similar to that for Case I.

5.2.1.2 *Particle Size Distribution.* The distribution of particle sizes in rain and snow may be represented by

$$N_D = N_0 \exp\left(-\frac{3.67\,D}{D_0}\right), \qquad (5\text{-}3)$$

where N_D is the number of particles of unit size-range cm^{-3}, D is the diameter (melted diameter for snow particles) in cm, and D_0 is the diameter of the median volume particles in cm. In rain

$$D_0 = 0.09\,R^{0.21}, \qquad (5\text{-}4)$$

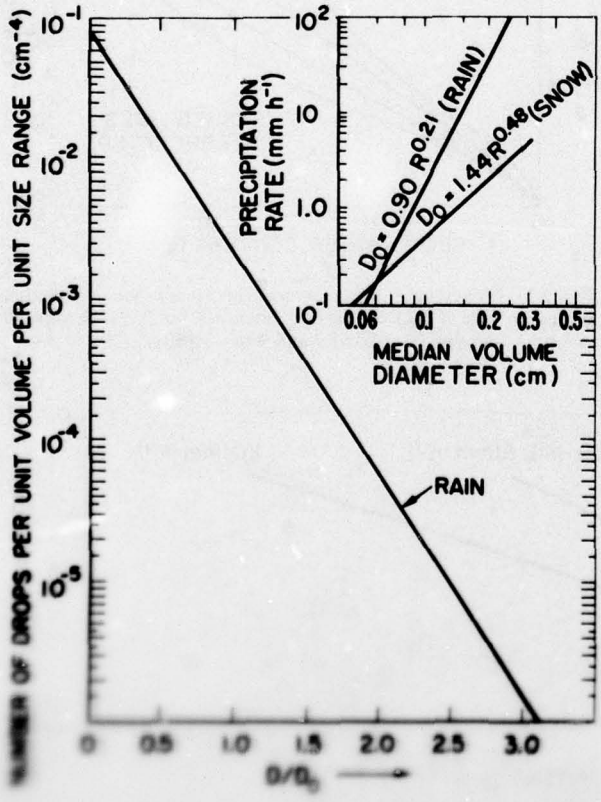
and in snow

$$D_0 = 0.14\,R^{0.48}, \qquad (5\text{-}5)$$

where R is the precipitation rate in mm h^{-1}. Both Eq. (5-4) and (5-5) are approximations, with wide variations in individual cases. In rain, N_0 has a more or less constant value of 0.08 cm^{-4}. In snow, the approximate relation is

$$N_0 = (3.8 \times 10^{-2})R^{-0.87}. \qquad (5\text{-}6)$$

Figure 5-13 illustrates plots to facilitate determination of D_0 and particle size distributions for special cases. These equations are most applicable at the ground where the original measurements on which they are based were made.



5.2.1.3 *Integrals of Diameter over the Size Distribution.* For various applications, it is useful to compute the quantity

$$\sum_{D=0}^{D=D_{max}} (N_D\,D^k) \simeq \int_0^\infty N_0\,e^{-\lambda D}\,D^k\,dD, \qquad (5\text{-}7)$$

where λ is $3.67/D_0$. The general solution of this integral ($\lambda > 0$) is

$$N_0\,\Gamma\,(k+1)/\lambda^{(k+1)},$$

where Γ is the gamma function. For k not an integer, the computations may be made most readily with a table of the gamma function.

5.2.2 Thunderstorm Rainfall

Steady-state conditions with respect to water distributions do not exist when updrafts equal or exceed the fall velocity of the particles. Such strong updrafts exist locally for periods of about 5 to 15 min in thunderstorms or other convective activity and can lead to high local concentrations of water substance. Radar reflectivity distributions associated with thunderstorms provide information on such concentrations. Figure 5-14 shows peak water profiles derived from reflectivity data for the cores of New England thunderstorms [Donaldson, 1961], by use of the approximation

$$M = (6 \times 10^{-4})Z^{0.7}, \qquad (5\text{-}8)$$

where Z is the radar reflectivity factor (see Chapter 9), and M is the liquid content in g m^{-3}. Equation (5-8) is derived by combining Z-R and M-R relations of Jones [1956]. There is evidence that occasional severe thunderstorms may be briefly associated with local water concentrations about ten times larger than the highest values shown in Fig. 5-14.

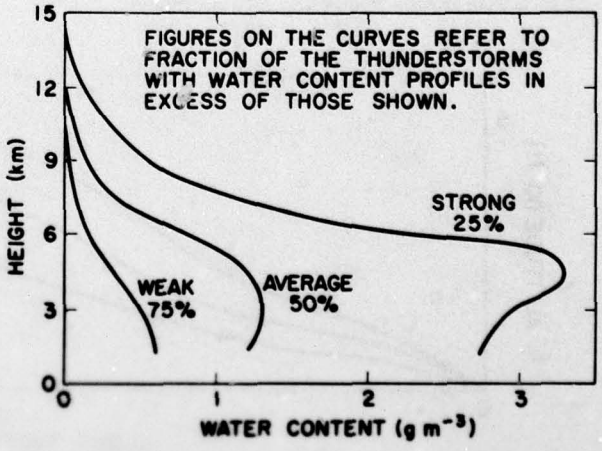


Fig. 5-14. Profiles of concentration of water in the centers of weakly, average, and strongly reflective New England thunderstorms.

5.2.3 Real Precipitation Distributions

The above results are based on idealized or averaged conditions and do not illustrate the small-scale structure characteristic of most real precipitation distributions. Figure 5-15 is an east-west cross section that shows the distribution of precipitation rate in an Ohio thunderstorm believed to be in the early part of the mature stage. The indicated rainfall rates are based on quantitative radar measurements, and may be converted to approximate values of M in $g\,m^{-3}$ by the relation $M = 0.05R$. Figure 5-16 shows east-west cross sections of radar reflectivity during a widespread New England snowstorm. Isopleths on these figures are labeled in dB below an arbitrary base and correspond to values of M that range from about 0.1 to 1.0 $g\,m^{-3}$.

5.3 CLOUDS

This section gives information on the types and limitations of available cloud data. Examples of a few of the standardized cloud summaries prepared on a routine basis by national weather services are provided. Information is also provided on the maximum water content likely to be encountered in clouds from which precipitation is not occurring. Because there are frequently wide variations in the cloud distribution among stations only a few miles apart, particularly in the lower levels, no attempt is made to provide frequency distributions of clouds at various levels. It is recommended that information required for specific design problems should be obtained from meteorologists familiar with the variability and limitations of the data; a detailed description of the problem and the proposed method of application should be provided.

The cloud distribution over a particular region is generally more uniform above 20,000 ft than at lower levels where topographical effects can cause wide variations in stations located a few miles apart; however, little reliable information concerning the amount and frequency of cloud cover is available. Surface visual observations are of limited value. Information in this section is based primarily on aircraft and radar observations, which are more accurate but frequently not available.

5.3.1 Data Available from Surface Observations

Cloud observations taken regularly by ground observers at weather stations throughout the world usually contain the following information:

(1) Visual estimate of total amount of sky covered by clouds;
(2) Cloud ceiling, which is the estimated or measured height above ground of the lowest layer of clouds that cover more than one half of the sky; and
(3) Visual estimates or measurements of amount and height of bases of individual cloud types or layers.

Because low clouds frequently obscure high clouds, it is often impossible to obtain accurate information on the distribution of clouds at higher levels from visual observations at the surface. Studies of the accuracy of visual cloud observations show that the greatest errors occur in estimating cloud amounts when the sky is ⅜ to ⅝ covered.

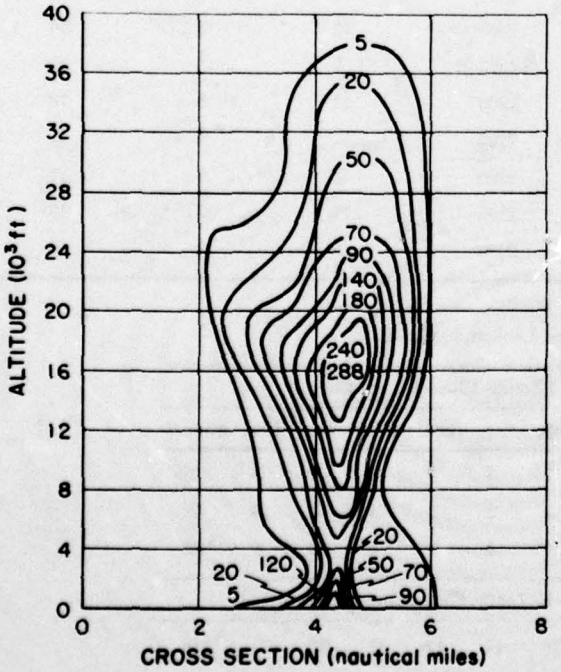


Fig. 5-15. West-east cross section through an Ohio thunderstorm showing the distribution of rainfall rate in mm h^{-1}.

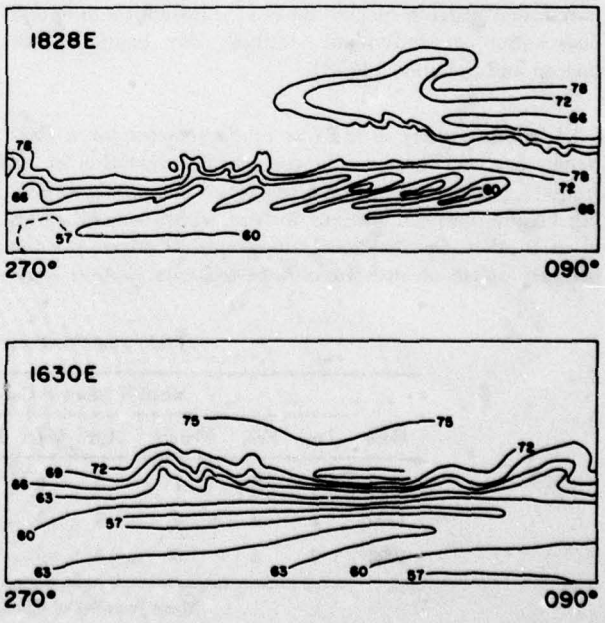


Fig. 5-16. Radar reflectivity distributions observed from Blue Hill, Mass., on 16 March 1956. Horizontal distance is 50 miles and height is 40,000 ft. Isopleths are labeled in dB below an arbitrary base. Corresponding values of water contents range from about 0.1 to 1 $g\,m^{-3}$.

These errors, however, tend to average out over long periods. The average error in visual estimations of cloud heights ranges from 1000 ft for clouds near 2500 ft to 5000 ft for clouds with bases near 23,000 ft. At many observation points, however, particularly airport stations, ceiling heights measured with ceilometers, clinometers, or balloons are available. These measurements are much more accurate than heights based on visual estimates.

Observed values for a particular time give amount of sky covered but not the cloud distribution. For example, if 4/8 cloud cover is reported, one large cloud formation may cover half of the sky or small individual cloud cells may be equally distributed over the entire sky. Thus, there is no indirect way of obtaining the geometry of clouds in the sky from the reported standard observations.

5.3.1.1 *Summaries of Surface Observations.* Tabulations of surface observations of clouds are available for stations in most areas of the world. Summaries similar to Table 5-8 and 5-9, giving the frequency of occurrence of various amounts of cloud cover during different times of the day for each month of the year, are available for most stations. The type of summary given in Table 5-9 is prepared monthly by the U.S. Weather Bureau for each first-order weather station in the United States. Numerous studies providing the frequency of occurrence of various ceiling heights for various times of day, seasons, synoptic situations, and so on, are available for airport stations. Table 5-10, for example, shows the frequency of various ceiling heights during each month of the year at Washington, D. C. In addition to the conventional summaries, other summaries and studies are available, or can be prepared, that provide specific types of information on cloud distribution at individual stations; for example, see Spreen and Solomon [1958].

5.3.1.2 *Limitations in the Use of Summaries for a Particular Station.* There can be considerable variation in the frequency of occurrence of given cloud amounts and ceiling heights between stations located within several miles of each other. Because local topographical effects are the primary cause of such variations, extreme caution must be used in applying climatological data on clouds for one or several stations to an entire region, particularly in mountainous and coastal regions.

Table 5-9. Hourly occurrences of various amounts of sky cover at Duluth, Minnesota during November, 1950.

	Cloud Cover		
Hour	0 to 3/10	4/10 to 7/10	8/10 to 1
0100	11	1	18
0200	11	0	19
0300	10	2	18
0400	9	3	18
0500	5	4	21
0600	10	0	20
0700	6	2	22
0800	7	2	21
0900	9	3	18
1000	9	3	18
1100	7	5	18
1200	8	1	21
1300	8	2	20
1400	8	2	20
1500	5	5	20
1600	8	2	20
1700	10	3	17
1800	10	2	18
1900	9	1	20
2000	12	0	18
2100	11	2	17
2200	12	1	17
2300	11	1	18
2400	9	1	20

Table 5-8. Cloud cover data for London, England.

	Mean Number of Clear (0 to 3 Tenths Cloud Cover) Days												
Hour	Jan.	Feb.	March	Apr	May	June	July	Aug.	Sept.	Oct.	Nov.	Dec.	Annual
0700	5	5	7	6	6	8	7	7	7	6	5	6	75
1300	5	4	5	3	3	4	3	3	3	4	4	4	45
1800	7	6	8	5	6	7	4	8	7	8	8	9	83
	Mean Number of Cloudy (9 to 10 Tenths Cloud Cover) Days												
0700	22	18	19	18	18	15	16	17	17	17	20	21	218
1300	27	17	17	18	19	15	20	14	16	18	20	22	186
1800	19	17	15	16	16	12	15	12	14	15	17	18	210

Table 5-10. Percentage frequency of occurrence of various ceiling heights at Washington, D.C. (From U. S. Weather Bureau Report 1945, "Normal Flying Weather for the United States.")

Ceiling Ht. (ft)	Dec.	Jan.	Feb.	Winter	Mar.	Apr.	May	Spring	June	July	Aug.	Summer	Sept.	Oct.	Nov.	Fall	Annual Mean
0-300	3.1	5.7	2.8	3.9	1.9	1.0	0.8	1.2	0.4	0.5	0.5	0.5	2.1	1.6	2.3	2.0	1.9
301-600	4.6	5.5	4.4	4.8	4.0	3.4	2.4	3.3	1.9	2.0	2.2	2.0	3.8	2.8	3.9	3.5	3.4
601-1000	3.6	4.7	4.0	4.1	5.2	5.6	4.1	5.0	2.9	5.0	3.8	3.9	4.0	3.1	4.7	3.9	4.2
1001-2000	4.6	5.4	4.3	4.8	5.1	4.5	4.6	4.7	4.7	4.7	4.5	4.6	4.7	4.1	5.1	4.6	4.7
2001-5000	13.6	14.0	11.7	13.1	15.2	12.2	10.7	12.7	9.6	9.5	9.6	9.6	9.8	10.0	13.4	11.1	11.6
5000-9750	10.2	10.0	9.5	9.9	9.6	10.0	9.6	9.7	7.1	6.0	8.0	7.0	6.1	7.2	9.0	7.4	8.5
Over 9750	60.3	54.7	63.4	59.5	59.0	63.2	67.9	63.4	73.3	72.5	71.5	72.4	69.5	71.1	61.5	67.4	65.7

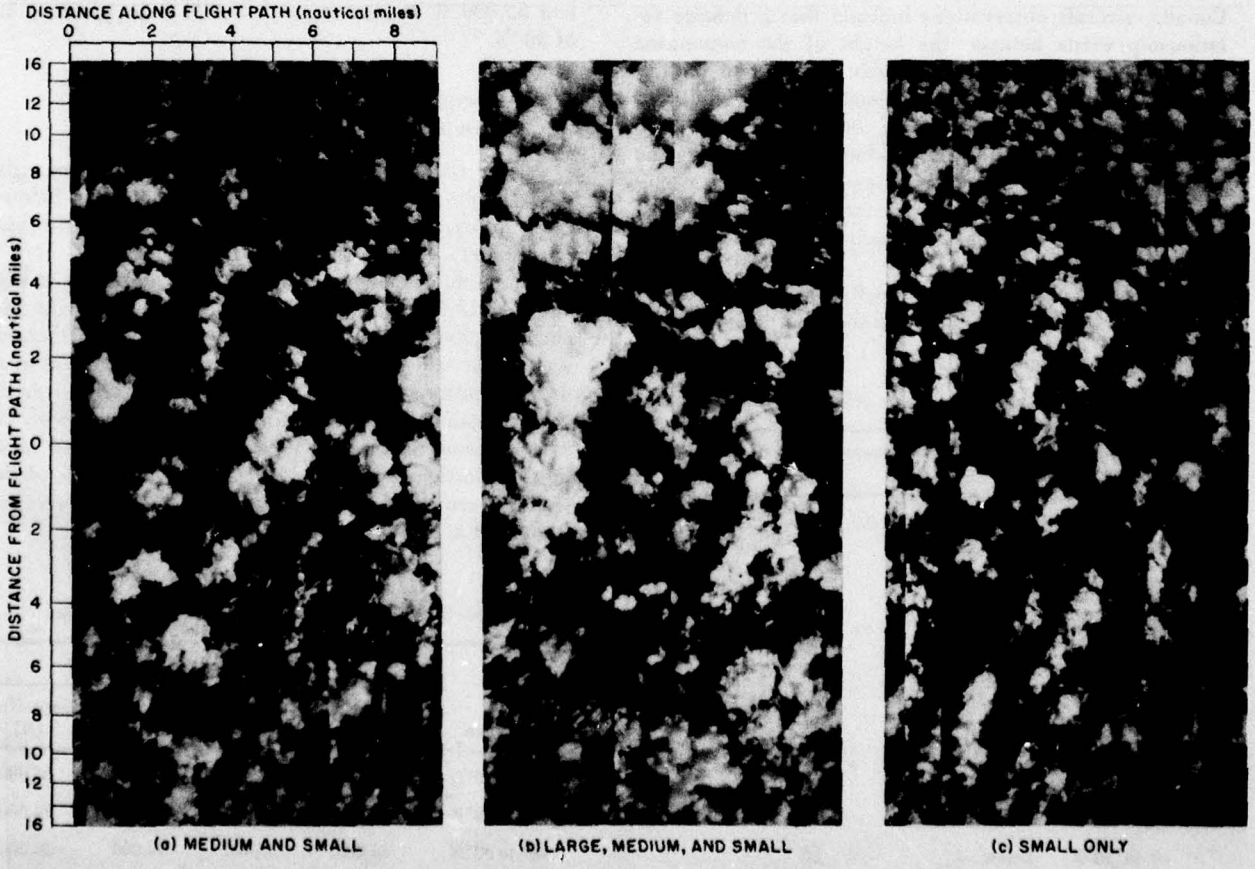


Fig. 5-17. Typical distribution of cumulus cloud types as shown by photograph taken from U-2 aircraft. (Stanford Research Institute.)

5.3.2 Data Available from Aircraft and Radar

Cloud observations taken by reconnaissance aircraft are available over a few areas and routes. Usually summaries of these observations are available only in reports and studies related to specific problems such as aircraft icing, turbulence, and thunderstorm activity; they provide accurate information on the frequency of encountering clouds at particular flight levels. Intervening cloud layers, however, often obscure the cloud distribution at other levels. High-altitude aircraft can provide cloud photographs, such as Fig. 5-17, from which dimensions and distributions of cumulus clouds can be estimated. Weather satellite photographs are providing information on the distribution of clouds over large areas of the earth. From the accumulation of such data, a regional and, eventually, a global cloud climatology will be developed.

Radar observations give accurate information on cloud distribution at all levels, but these data are limited to intermittent observations at a few stations. Experimental vertically pointing radars eventually will provide cloud data for levels on a synoptic basis.

5.3.3 Vertical Extent of Cirrus Clouds

In studies of cirrus clouds over the British Isles and Canada, aircraft observations indicate that a definite relationship exists between the height of the tropopause and the tops of cirrus clouds. Table 5-11, based on 151 aircraft observations of cirrus clouds in the vicinity of the British Isles [James, 1957] and more than 2000 RCAF reports over Canada [Clodman, 1957], gives the frequency distribution of cirrus tops relative to the tropopause. The occurrence of a maximum of cirrus tops just below the tropopause over both regions is consistent with other results.

Although cirrus clouds occasionally are observed above the tropopause, evidence indicates that the probability of encountering extensive cloud formations is negligible. Because there are seasonal, latitudinal, and daily variations in the height of the tropopause, both the latitude and season of the year must be considered in planning minimum flight altitudes above the tropopause. Table 5-12 gives the mean seasonal heights of the tropopause in the Northern Hemisphere; however, mean seasonal heights may be several thousand feet higher than indicated in Table 5-12 on the east side of semistationary lows such as the Icelandic and Aleutian lows during the winter and spring months.

In middle latitudes, the day-to-day variations in the height of the tropopause far exceeds the seasonal variations; large variations in height occur as a result of horizontal oscillations in the tropopause. The arctic tropopause from the north is brought southward in the rear, and the tropical tropopause from the south is projected northward in advance of well-developed migratory cyclones. Although data are not sufficient to define accurately the limits, available data indicate that in middle latitudes (40° to 60°N) the tropopause can fluctuate between about 20,000 and 50,000 ft. North of 60° and south of 30° latitude, the range is much smaller, the order of 3000 to 6000 ft around the seasonal mean heights; 26,000 ft in winter and 34,000 ft in summer north of 60° latitude, and 52,000 ft in summer and 55,000 ft in winter south of 30°N.

Table 5-11. Distribution of cirrus tops relative to the tropopause.

Distance from Tropopause (ft)		Frequency of Occurrence (%)
BRITISH ISLES		
> 4000	above	10
4000 to 0	above	10
0 to 4000	below	50
4000 to 8000	below	16
> 8000	below	14
CANADA		
> 5000	above	1
5000 to 0	above	12
0 to 5000	below	52
5000 to 10,000	below	23
> 10,000	below	12

5.3.4 Frequency of Occurrence of Cloud Formations Above 20,000 Ft

Table 5-13 summarizes the results obtained from radar observations of cloud bases above 20,000 ft at Belmar, New Jersey, for about 17% of the hours in the year (November) 1951 to (October) 1952.

In a study of the frequency of clouds and icing at high altitude, 15,000 weather observations taken at altitudes above 20,000 ft were analyzed. These flight weather observations, taken by the Air Force at regular intervals during routine operations, were made primarily over the United States. They were unevenly distributed with the heaviest concentrations over the Great Plains and along the Pacific Coast. Table 5-14, based on the results of this study, gives the frequency with which clouds were encountered at altitudes above 20,000 ft.

Table 5-12. Mean seasonal heights of the tropopause.

	Altitude			
Latitude	Dec.-Feb. (ft)	Mar.-May (ft)	June-Aug. (ft)	Sept.-Nov. (ft)
60° to 80°N	26,000	28,000	34,000	30,000
50° to 60°N	34,000	34,000	38,000	34,000
40° to 50°N	36,000	38,000	44,000	38,000
30° to 40°N	45,000	45,000	48,000	45,000
10° to 30°N	55,000	52,000	52,000	52,000

Table 5-15 gives the seasonal frequency of occurrence of cirrus formations over southern England as determined from high-altitude aircraft observations during 1949 to 1952. The frequency of occurrence is considerably higher than that reported by radar over Belmar, New Jersey, but the sky coverage may differ considerably and make this comparison invalid. In the study providing the data in Table 5-15, a relationship was found between the air flow at the 300-mb level and the frequency of cirrus cloud occurrence over southern England. Cirrus occurred frequently when the air at 300-mb level had traversed large areas of the Atlantic Ocean, but seldom occurred on air of continental or polar origin. This would account for the relatively large difference between the east coast of the United States, a region where the prevailing flow at 300-mb is normally off the North American continent, and southern England where the prevailing wind is usually off the Atlantic.

Table 5-13. Percentage of time that cloud bases were observed by radar above specific levels.*

Above Level (ft)	Dec. thru Feb. (%)	Mar. thru May (%)	Jun. thru Aug. (%)	Sept. thru Nov. (%)
20,000	18.1	12.0	14.9	14.8
22,000	13.2	8.6	12.2	10.5
24,000	8.5	6.2	9.1	8.8
26,000	5.9	3.6	7.5	7.1
28,000	2.1	2.0	5.9	5.4
30,000	0.2	1.4	2.8	4.3
32,000		0.8	2.0	2.9
34,000			0.4	0.4
Number of Hours of Observation	424	496	256	280

* Tabulations obtained from Evans Signal Laboratory.

Table 5-14. Frequency with which clouds were encountered at various flight levels above 20,000 ft over the U.S.

Altitude Level (ft)	Total Number of Observations*	Number of Observations in Clouds	Time in Clouds (%)
20,000 - 24,980	7257	422	5.8
25,000 - 29,990	5683	292	5.1
30,000 - 34,990	689	13	1.9
35,000 - 39,990	976	2	0.2
40,000 - 44,990	831	0	0
Above 45,000	0	0	0

* These data are listed in terms of number of observations rather than time in hours because the conditions were not recorded continuously but as discrete observations at intervals of approximately one half hour.

An indirect method for estimating the frequency of specific cloud coverage was used to determine the altitudes, above which there is a 95% probability of less than 1/10 sky cover for January and July, that are shown in Fig. 5-18.

5.3.5 Horizontal Extent of Cirrus Clouds

Cirrus cloud formation in midlatitudes can extend over an area up to 1500 miles in length, parallel to frontal systems, and 500 miles in width. Also, the probable extent of cirrus clouds over the United States during the winter months can be estimated from Fig. 5-19. If a flight from Los Angeles to Washington, D.C., a distance of approximately 2500 miles, had been made at 20,000 ft during the period represented by the map in Fig. 5-19, cirrus clouds could have been observed in some amount over practically the entire route.

In a study of high-level clouds in the tropics, based on observations made by Comet aircraft, the presence of extensive sheets of cirrus clouds appears to be the rule rather than the exception [Durst, 1952]. On the African route between Khartoum and Livingston, approximately 15°N to 15°S latitude, continuous sheets of cirrus or cirrostratus clouds were frequently observed with bases between 45,000 and 50,000 ft. These layers frequently extended over 1600 miles of the route.

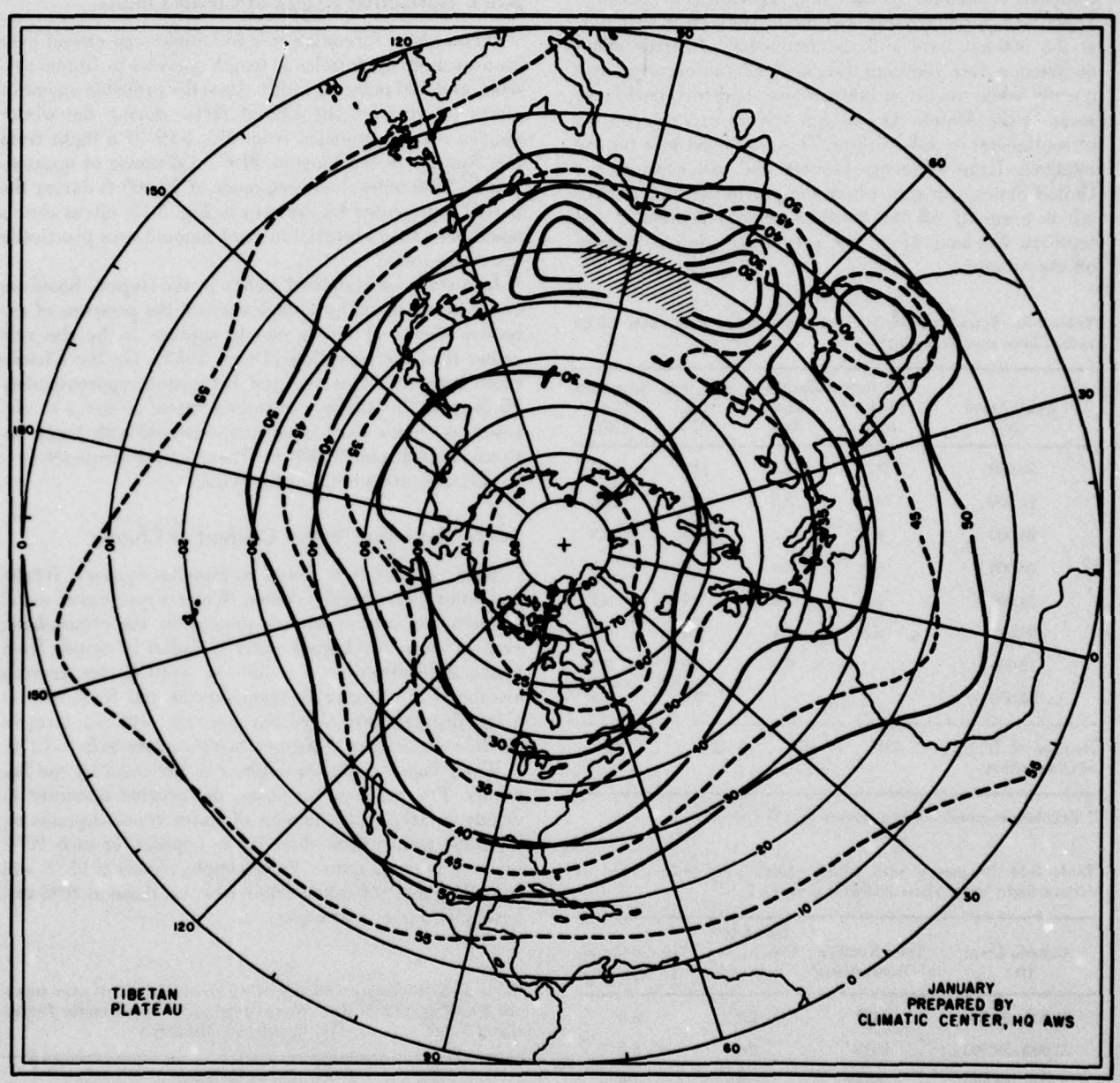
5.3.6 Maximum Water Content of Clouds

Water in clouds is found in gaseous (vapor), liquid, and solid (ice crystals) states. Water vapor exists at all temperatures and is always present in the atmosphere, even in clear air. Liquid water is found in clouds from about 25°C down to a −35° or −40°C. Ice crystals are found at all sub-zero temperatures and frequently at a few degrees above zero but generally will not form in the free atmosphere at temperatures warmer than −12°C.

Water vapor in the atmosphere is indicated by the humidity. For practical purposes, the relative humidity in clouds is 100%. The amount of water vapor depends on the cloud temperature, doubling to tripling for each 10°C increase in temperature. For example, clouds at 25°C will have 23 g m^{-3} of water vapor whereas those at 0°C will have only 5 g m^{-3} of vapor.

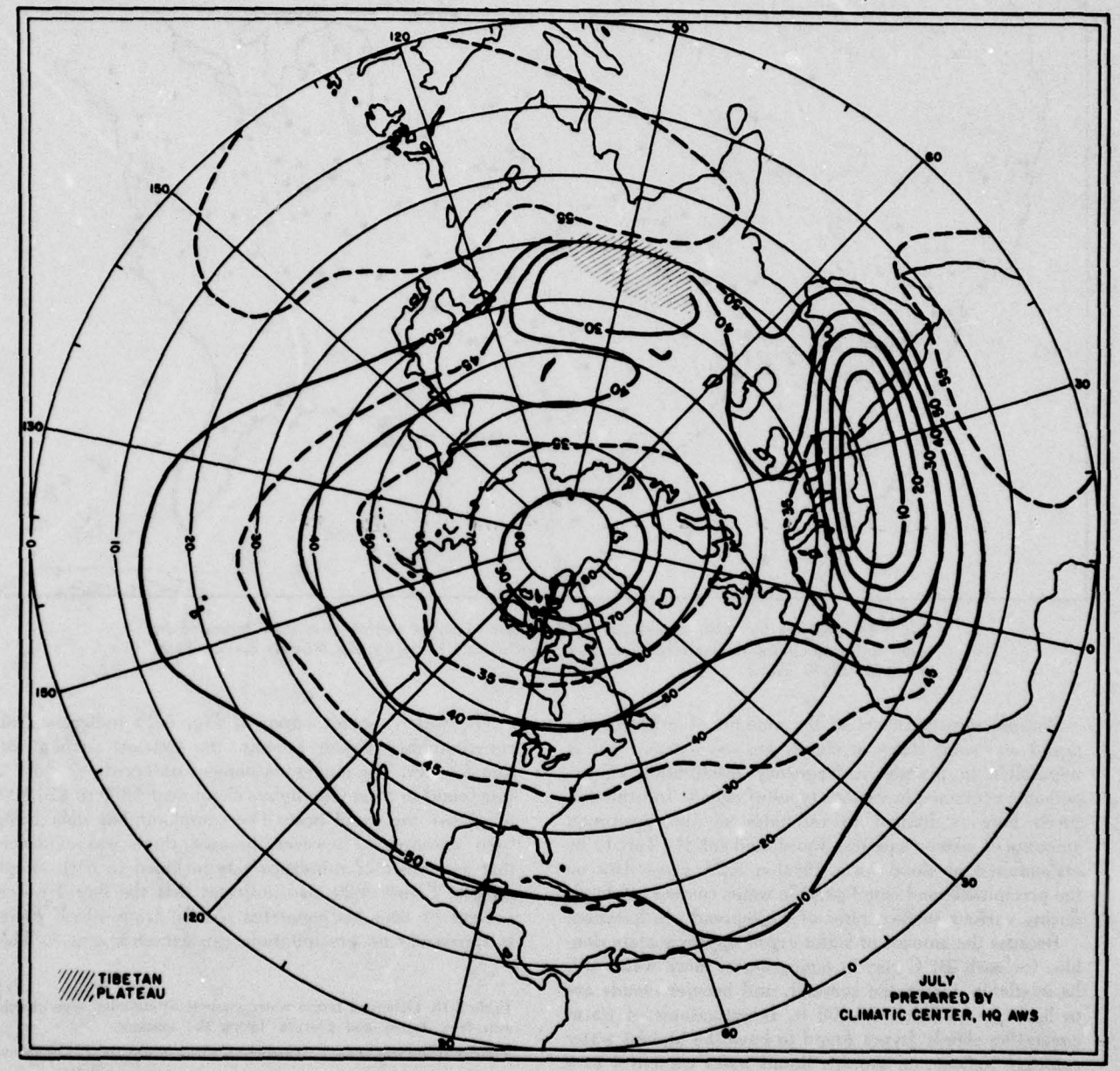
Table 5-15. Seasonal frequency of occurrence of cirrus over southern England. (From R. J. Murgatroyd and P. Goldsmith, *Professional Notes*, v. 7, no. 119, British Air Ministry.)

	Percentage of Occasions			
Season	Cirrus (%)	Distant Cirrus (%)	No Cirrus (%)	No. of Observations
Winter	58	10	32	41
Spring	31	27	42	68
Summer	50	33	17	70
Autumn	47	31	22	64



(a)

Fig. 5-18. Altitudes (10^3 ft) above which there is 95% probability of having 1/10 sky cover. (a) January, (b) July. (From I. Soloman, *Air Weather Service Tech. Rept. No. 159*, 1961.)



(b)

Fig. 5-18. Altitudes (10^3 ft) above which there is 95% probability of having 1/10 sky cover. (a) January, (b) July. (From I. Soloman, *Air Weather Service Tech. Rept. No. 159*, 1961.)

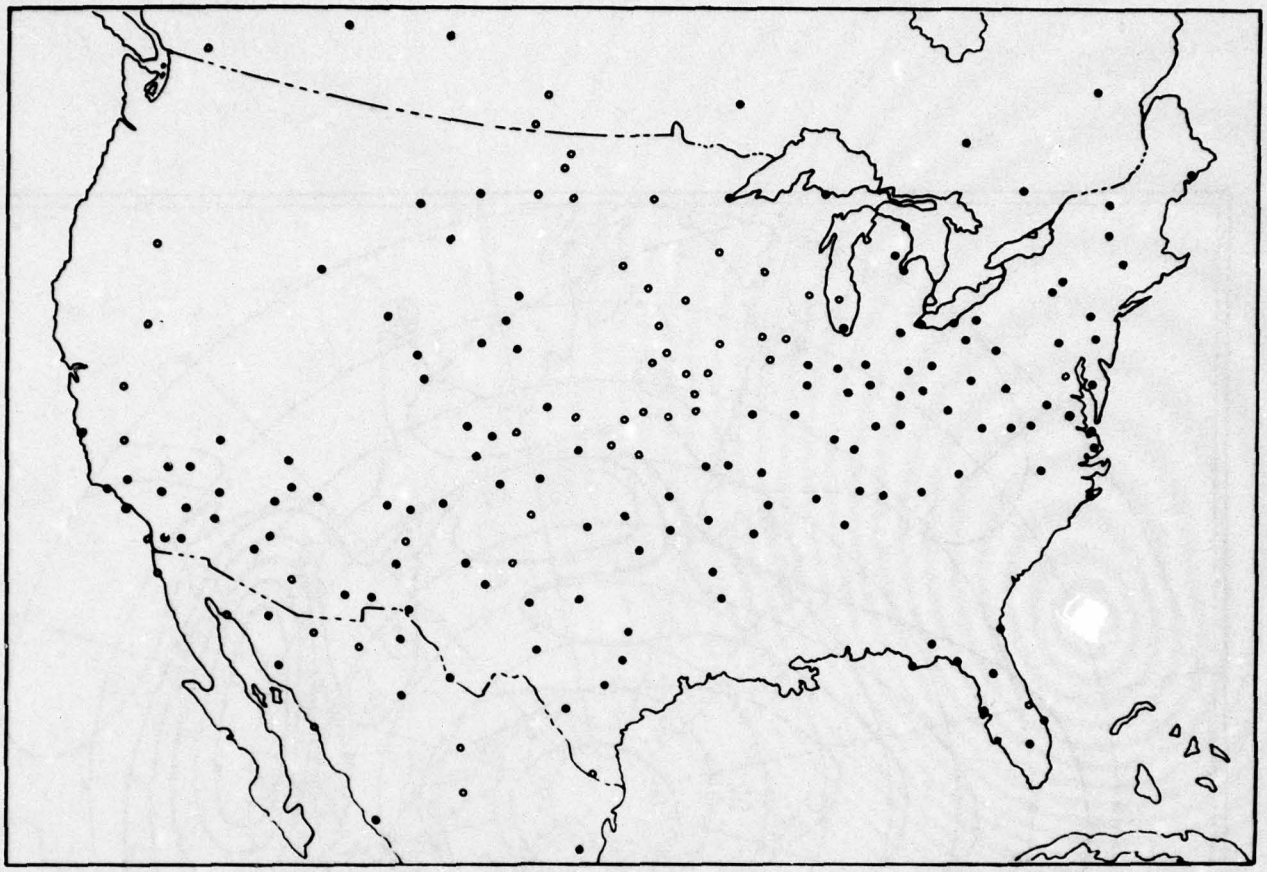


Fig. 5-19. Analyses for 1500, 7 December 1948, reports of cirrus and of clear skies indicated by solid and open circles, respectively. From R. D. Fletcher and D. Sartos, *Air Weather Service Tech. Rept. No. 105-81*, 1951.)

Because measurements of the amount of water in the liquid and solid states in clouds are not extensive, it is impossible to provide a frequency distribution of the amounts contained in various types of clouds. Information given here is limited to estimates of the maximum amounts of water (gaseous, liquid, and solid) likely to be encountered in cloud form. Section 5.2.1 gives data on the precipitable and cloud-particle water content of clouds during various surface rates of widespread precipitation.

Because the amount of water vapor approximately doubles for each 10°C rise in temperature, more water will be available during the summer, and heavier clouds are to be expected below 25,000 ft. Investigations of warm convective clouds (types found to have the highest water content) indicate an average liquid water content 4 to 5 times that observed in the winter, and 5 to 10 times that observed in stratus clouds irrespective of season [aufm Kampe and Weickmann, 1957]. Data from these investigations are shown in Table 5-16 and Fig. 5-20 and 5-21. The droplet size, water content, visibility, and droplet concentration data in Fig. 5-21 represent average values regardless of the altitude at which they were collected, whereas Fig. 5-20 depicts these parameters as functions of thickness in convective type clouds.

The water content curve in Fig. 5-20 indicates that cumulonimbus clouds contain the greatest amount of liquid water. The maximum content observed, 10 g m^{-3}, was found in a cumulonimbus cloud near 4000 m (13,000 ft) above the cloud base. The cumulonimbus data have been questioned, however, because there was evidence that a number of raindrops was included in each cloud sample. Figure 5-20 also indicates that the liquid water content of cumulus congestus clouds, from which there is apparently no precipitation, can exceed 6 g m^{-3}. The

Table 5-16. Observed liquid water content of cumulus type clouds over New Jersey and Florida during the summer.

Clouds		Water Content (g m^{-3})	
Type	Temp (°C)	Average	Maximum
Cumulus Humilis	10 to 24	1.0	3.0
Cumulus Congestus	3 to 11	2.0*	6.6
Cumulonimbus	10 to −8	2.5	10.0

* estimated

formation of precipitation inside a cumulus cloud is a complex function of physical, chemical, and meteorological variables that are poorly understood. Therefore, when precipitation is not actually falling from a cloud, it is difficult to determine what part of the total liquid water content should be classified as cloud particles and what part as suspended precipitable water. Apparently the maximum liquid water content that can exist in a non-precipitating cloud is between 6 and 10 g m^{-3}. A study by the University of Chicago indicates cloud water densities of at least 1.7 g m^{-3} are required before rain is produced.

From Table 5-16, the water content appears to be increasing with decreasing temperature. This can be attributed to the higher flight altitudes at which observations were made in the more developed convective clouds. Theoretically, more moisture is available for condensation at the lower level because of higher temperatures and, there-

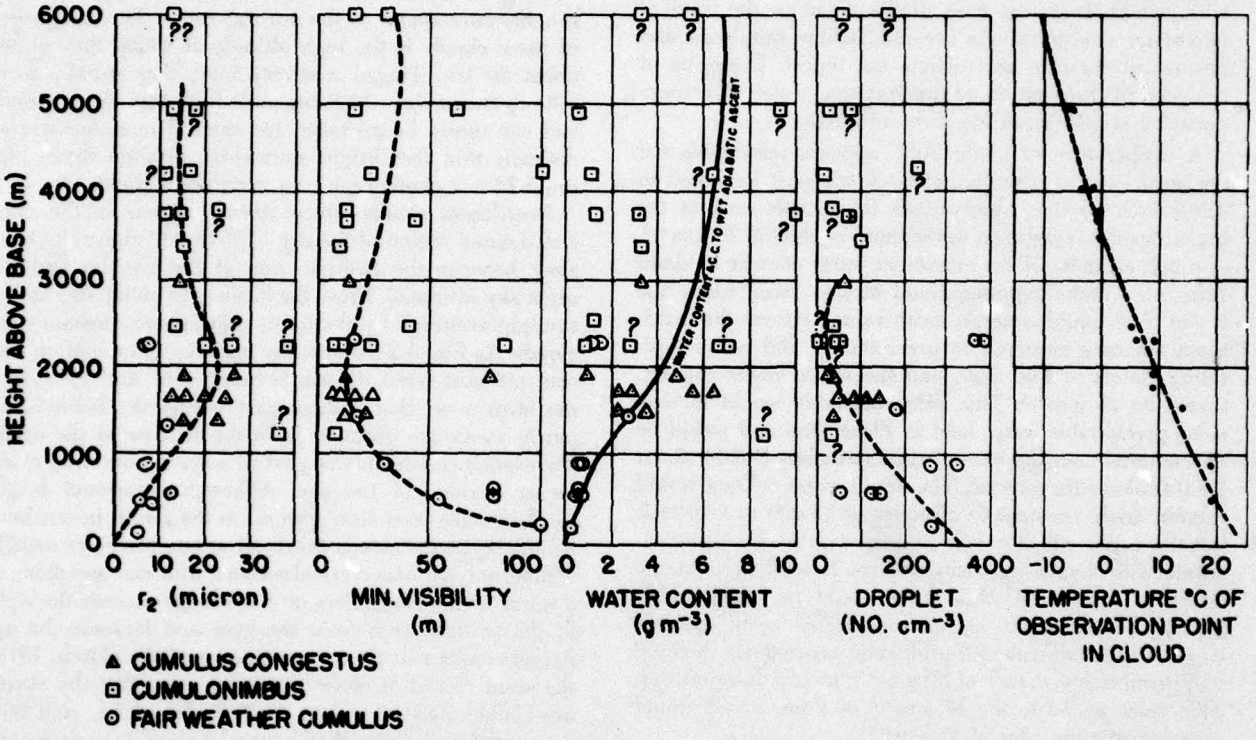


Fig. 5-20. Physical properties in cumuliform clouds vs heights above base of cloud.

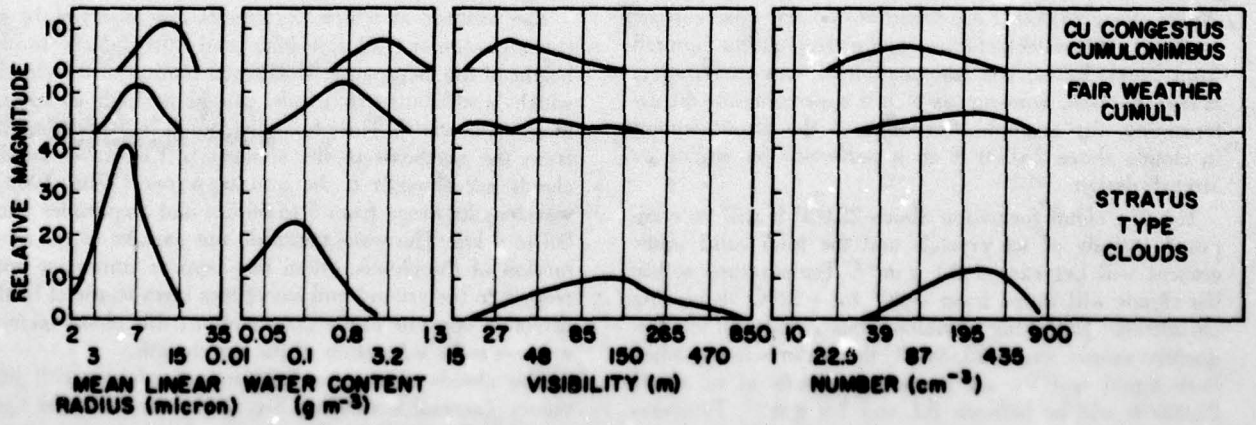


Fig. 5-21. Physical properties of different types of clouds. (From H. J. auln Kampe and H. K. Weickmann [1957] by permission.)

fore, a heavier cloud density would be expected. Strong vertical currents in convective clouds of this type, however, are such that condensed cloud particles originating in the lower levels will be carried aloft. In well-developed convective clouds, with no precipitation, the maximum liquid water content occurs near the top. As the cloud builds to high altitudes and the drop size goes up, down drafts occur. Thus, the maximum liquid concentration will be observed at an altitude corresponding to ½ to ⅞ of the cloud height. After precipitation begins there will be little variation in the amount of liquid (or frozen) water with height, from the base of the cloud to the level of maximum concentration, because falling raindrops and downward currents redistribute the liquid. Examples of the vertical distribution of precipitating water in a thunderstorm are shown in Fig. 5-14 and 5-15.

A temperature of about 20°C appears reasonable for the lower part of cumulonimbus clouds (not indicated in Table 5-16 because observations were made only at the higher levels), yielding a water vapor content of 17 g m^{-3}. A rough estimate of the maximum water content in cloud form of a cumulonimbus cloud at this level, using the 8 g m^{-3} of liquid water, a mean value between the maximum amounts observed in precipitating and nonprecipitating clouds in Fig. 5-20, and the above vapor content, would be 25 g m^{-3}. This value probably would include some precipitable water held in suspension and would be encountered near the base of cumulonimbus clouds, about 2000 ft above the ground. The liquid water content would remain fairly constant to altitudes of 15,000 to 20,000 ft but the vapor will decrease rapidly with height commensurate with decreasing temperature. If total precipitable water is considered, this value could be considerably higher. For example, calculations based upon extreme tropical rains indicate a liquid water content (both cloud and precipitable water) of 30 g m^{-3}, mostly as raindrops. This value added to the 17 g m^{-3} of water vapor would give a maximum value of 47 g m^{-3}.

Few direct observations have been made of the water content of clouds above 25,000 ft. The estimates of the maximum amount of moisture likely to be encountered in clouds above 25,000 ft are based on the few observations available, theoretical studies, and extrapolation upward from lower levels; the information is semiquantitative. It may be used, however, as a first approximation in determining, for example, the effect of the water content in clouds above 25,000 ft on a particular jet engine or aircraft design.

Usually, cloud formation above 25,000 ft will be composed entirely of ice crystals and the total solid water content will not exceed 0.1 g m^{-3}. Temperature within the clouds will range from −20° to −52°C, depending on altitude. Excluding cumulonimbus clouds, which frequently extend above 25,000 ft, the water content when both liquid and ice are present in clouds at or above 25,000 ft will be between 0.1 and 1.0 g m^{-3}. Temperatures at 25,000 ft when this extreme water content is experienced will be near −20°C. Temperature and water content will decrease with increasing altitude.

In cumulonimbus clouds the water content, liquid and ice, may occasionally attain a density of 10 g m^{-3} at 25,000 ft. This value will decrease rapidly at altitudes above 35,000 to 40,000 ft. Temperatures in the clouds above 25,000 ft will range from −15° to −50°C, depending on altitude and latitude.

5.4 NOCTILUCENT CLOUDS

Noctilucent clouds are normally observed during the summer months in northern and southern latitudes which roughly correspond to the auroral zones. The uniqueness of these clouds is the high altitude at which they occur, about 80 km. Tinged a silvery blue, they usually form billows and waves which resemble high thin cirrus clouds and can easily be mistaken for such. The clouds are so optically thin that bright stars shine through them. Figure 5-22 is a photograph of a noctilucent cloud.

Noctilucent clouds almost always appear in the same well-defined region of the sky (10° to 20° above the horizon) between the twilight arch at the horizon and the night sky overhead. From the horizon to about 10° above, sunlight scattered by the lower atmosphere outshines the clouds. As Fig. 5-23 shows, the optimum illumination and contrast exist when the sun is between 6° and 12° below the horizon so that a large part of the sky behind and partly above the observer is in the shadow of the earth. The visible clouds may be part of a system covering much larger regions of the sky. Although occasional bright displays have been seen even up to the zenith in northern Scandinavia, the clouds overhead at one place are usually visible only to observers elsewhere who can see them at a lower angle. Binoculars or a telescope exclude the light of the twilight arch from the eyes and increase the apparent contrast in the wave structure of the clouds. From the scant record of observations, it seems that the clouds are visible mostly between the latitudes of 45° and 80°. Laser studies indicate that it may be possible to detect the presence of the clouds even when they cannot be observed visually and at a latitude where they have never previously been observed [Fiocco and Smullin, 1963].

The altitude at which the clouds are observed is extremely regular (82 ± 4 km) and corresponds to the height of the mesopause. Horizontal motion of the clouds, which is attributed to winds, can be as high as several hundred m sec^{-1}. The gross cloud drift is predominantly from the northeast to the southwest in the Northern Hemisphere. The waves in the clouds are thought to be gravity waves [Witt, 1962]; wavelengths range from 5 to 50 km and amplitudes from 0.5 to 4 km. The wave crests do not partake of the mass motion of the clouds. Often they appear stationary with respect to the ground and sometimes seem to travel in the direction opposite to the mass motion; this phase velocity appears to be a function of the wavelength.

The clouds scatter sunlight in accordance with Mie theory (aerosol scattering, Sec. 7.1); the scattered light is eliptically polarized. The degree of polarization ranges from about 5% at a 20° scattering angle to about 50% at a 60° scattering angle.



Fig. 5-22. Photograph of noctilucent cloud.

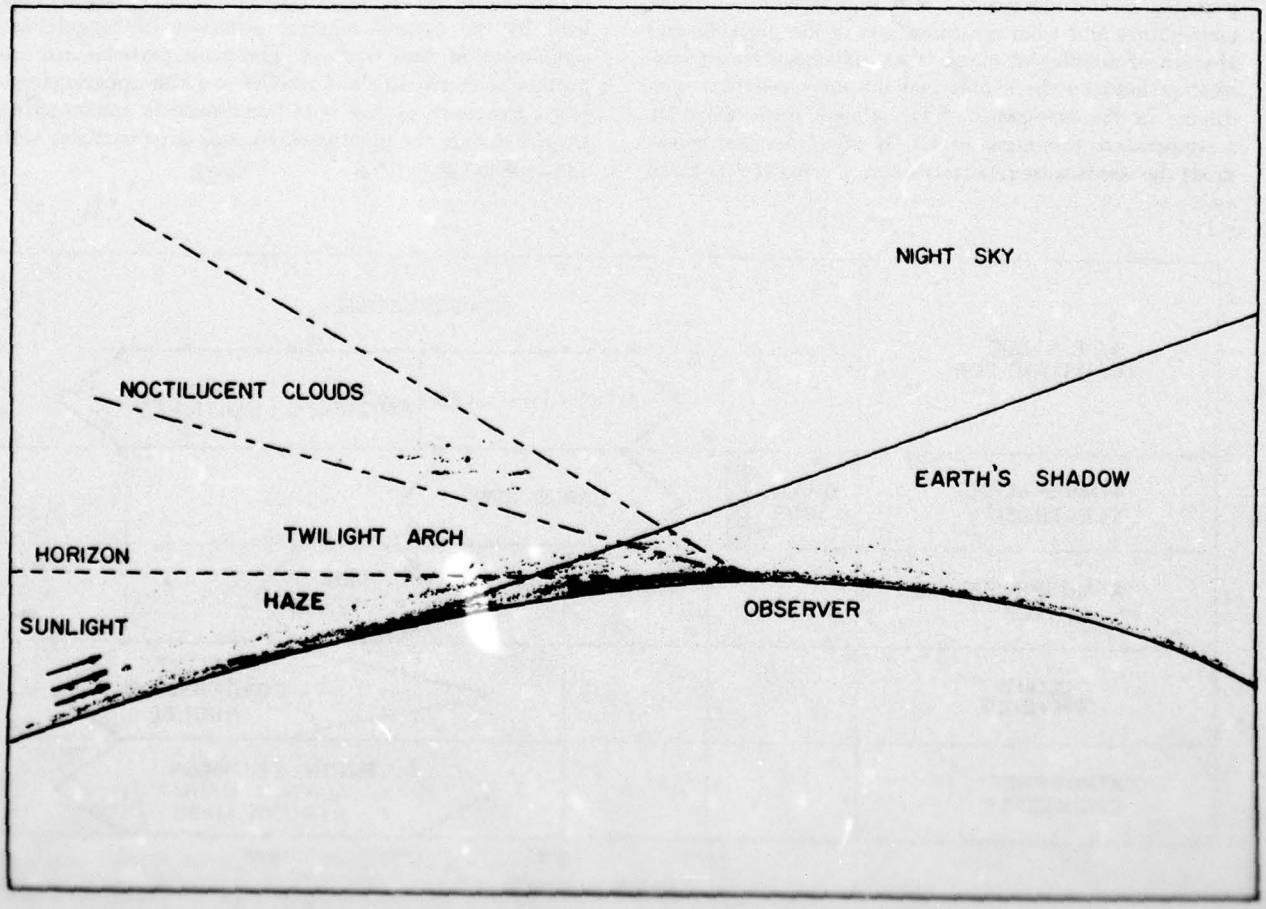


Fig. 5-23. Diagram of twilight conditions associated with noctilucent clouds.

CHAPTER 5

The clouds are composed of particles of which at least the nuclei are extraterrestrial in origin; many of these nuclei are ice-coated. The particle concentration in a vertical column through a cloud sampled during a moderate display was greater than 10^7 cm^{-2}. This is at least 10^3 greater than the particle concentration when no clouds are visible. The nuclei of these particles are not volatile and show evidence of containing iron, nickel, and silicon. The nuclei have a size distribution of the form,

$$\frac{dN}{dr} \propto r^{-p},$$

with a sharp cut off at the lower size limit $r = 0.02\mu$; r is particle radius, and $4 < p < 5$. At least 10% of the particles (mostly larger than $r = 0.1\mu$) show evidence of having been ice-coated; it appears that the ice coating does not increase the particle radius by more than a factor of 10. The clouds are probably not more than several kilometers thick [Hemenway et al, 1964].

The cause of the clouds is still unknown. They may be the result of an enhanced influx of meteoric material such as might be expected during the time of a meteoric shower. On the other hand, they could result from slight vertical updrafts that slow down or stop the normal influx of meteoric matter and thus increase the concentration of particles in the mesopause. Witt and Martin-Löf made temperature and wind measurements in the presence and absence of noctilucent clouds that indicate a strong correlation between the clouds and the meteorological conditions in the mesopause. When clouds were observed, a temperature minimum of 130°K at 84 km was measured; the winds were relatively quiet. During the no-cloud condition, a temperature minimum of 150°K was observed at 81 km and strong winds with shears of 30 m sec^{-1} km^{-1} were measured in the same altitude region.

5.5 AEROSOLS

An aerosol is defined here as a mixture of air and small solid or liquid particles in which the particles follow the motion of the air within certain broad limits. Visible haze is evidence of aerosol content. Fog and clouds are on the borderline. Rain and snow are not aerosol phenomena because they are recognized by the process of separation from, rather than suspension in, the air. The products of *air pollution (smog) and of atmospheric photochemical* reactions may be aerosols.

5.5.1 Size Range and Field of Importance

Natural aerosol particles range in radius from 10^{-3} to $10^2\,\mu$. Figure 5-24 shows the nomenclature. The numerous Aitken particles are important in studies of atmospheric electricity, and are used as a more or less conservative property of tropospheric air in the study of mixing across the tropopause. The large particles are important factors in studies of visibility, cloud physics, and atmospheric chemistry, and in interactions with radioactive debris. These large particles seem to be affected least by the natural removal processes of coagulation, sedimentation, and washout. The giant particles are important primarily in cloud physics and atmospheric chemistry. Processes of fog- and cloud-particle condensation involve mainly the giant particles and large particles with radii greater than 0.5 μ.

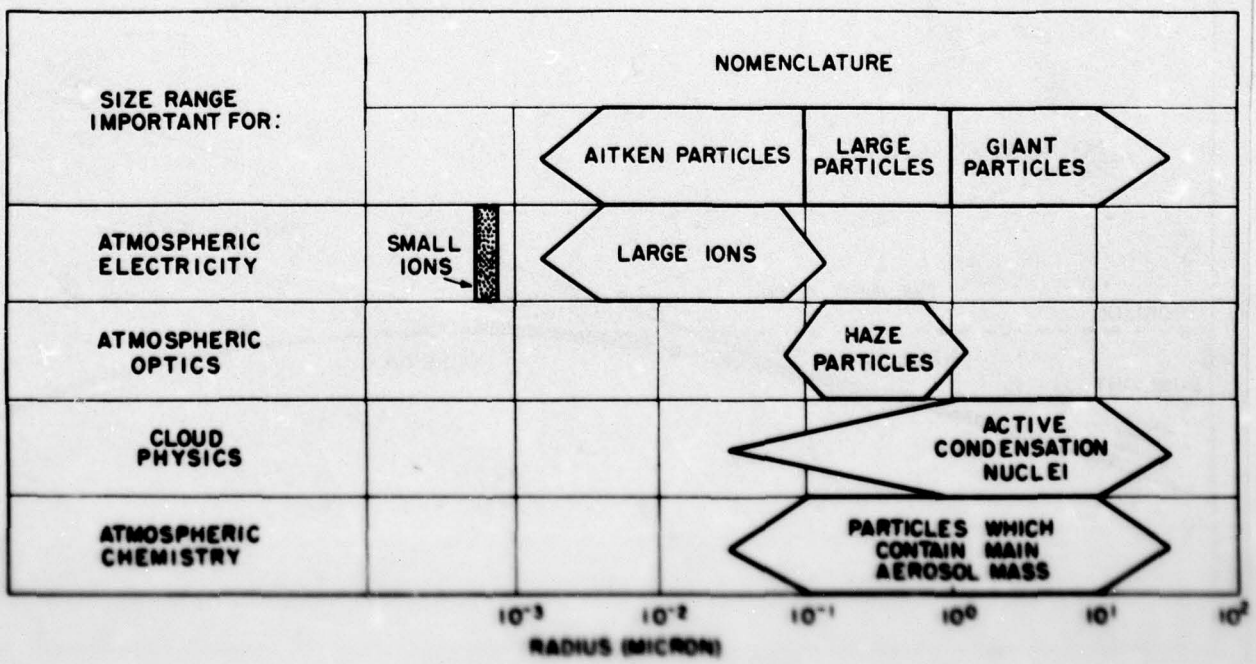


Fig. 5-24. Nomenclature of natural aerosols.

It is necessary to consider very carefully the formulation of any problem involving atmospheric aerosol particles. The various regions of the wide distribution of sizes may vary in importance, depending on the nature of the problem and the local aerosol characteristics; caution is necessary in all problems involving populations made up of individual units having diverse characteristics. The following summary of average characteristics and model populations can be used only as a guide because variations an order of magnitude or more occur in nature. Such fluctuations can easily dominate any particular problem.

5.5.2 Size Distribution

Figure 5-25 shows the average size distribution of natural aerosol particles near the surface in continental air. The number concentration, n, is the total number of particles cm^{-3} with radii from the lower limit of definition of aerosols up to r. Only spherical particles are considered here. The logarithmic derivative $dn/d(\log r)$, is called the number distribution or the size distribution. Number distribution data are plotted in logarithmic coordinates; otherwise, the small particles would dominate. As a result the area under any portion of this curve does not represent the number of particles between corresponding radii. Estimates of the number of particles with radii between any two values can be obtained by using the average value of $dn/d(\log r)$ between r_1 and r_2 ($r_1 < r_2$) and performing the following calculation:

$$\Delta n \Big|_{r_1}^{r_2} = \left\langle dn/d(\log r) \right\rangle_{av} (\log r_2 - \log r_1). \quad (5\text{-}9)$$

The portion of the distribution curve between $-1 < \log r < +1$ (particle radius 0.1 to 10 μ), can be well represented by

$$dn/d(\log r) = cr^{-3}. \quad (5\text{-}10)$$

By direct integration, the number of particles between any two radius values that lie on this portion of the curve is

$$\Delta n \Big|_{r_1}^{r_2} = \frac{1}{3 \ln 10} \left[\frac{dn}{d(\log r)} \right]_{r_2}^{r_1}, \quad (5\text{-}11)$$

where $r_2 > r_1$. For example, the number of particles between 0.1 and 0.2 μ is obtained by substituting values from Fig. 5-25 into Eq. (5-11); thus

$$\Delta n \Big|_{0.1}^{0.2} = \frac{1}{6.9} (4000 - 600) = 490 \text{ cm}^{-3}.$$

The chemical composition of these particles varies considerably with location. Particles with radii less than 0.1 μ are mainly from smoke, and probably consist of carbon. Some soluble and hygroscopic particles, however, also exist in this size range. Windblown mineral dust from the soil is the major source of particles larger than 0.1 μ over land, and sea spray the major source over the ocean. Figure 5-26 shows the average size distribution of aerosols

in maritime air at approximately 80% relative humidity for various wind speeds. No direct measurements of radii less than 1 μ were made, but an estimated extension of the curve for 10 mile h^{-1} is included. Concentration of these smaller particles is expected to be much less in maritime than in continental air because of the characteristics of available sources. Thus, the presence of large concentrations of small particles over the ocean may be considered as evidence of a continental aerosol.

The average continental and maritime aerosol distribution can vary over wide limits, depending on the local conditions. It is expected that the general shape of the distributions will remain as shown in Fig. 5-25 and 5-26. To obtain curves approximating extreme conditions, one may increase the concentrations given in these figures by the factors given in Table 5-17.

The total mass of solid and liquid particles contained in the maritime and continental aerosols, derived from the size distributions, are given in Table 5-18. In comparison, the CO_2 concentration at sea level is close to 600,000 $\mu g\ m^{-3}$. For those chemicals present in the at-

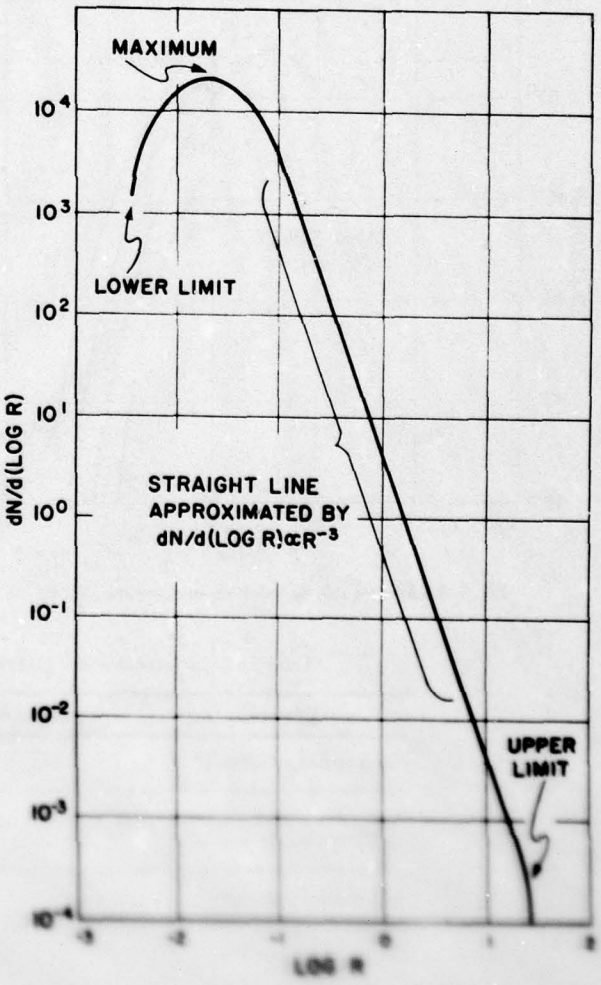


Fig. 5-25. Aerosol size distribution in continental air.

mosphere both as trace gases and related aerosol particles, the mass concentration in the gas phase is generally from 5 to 50 times that of the aerosol particles.

5.5.3 Characteristics of Aerosols at Various Altitudes

Figure 5-27 summarizes present knowledge of the vertical distribution of Aitken particles, large particles, and giant particles. Such curves are called vertical profiles of the quantity plotted as abscissa, in this case the number concentration within a given radius limit. The vertical profile of giant sea-salt particles is different over the source areas than over the continents. Vertical profiles of the large particles and of the Aitken particles are best known. The relative shape of the vertical profiles of the two groups is similar over the first 10 km of altitude. Throughout the range of 10 to 20 km, the Aitken particles decrease in concentration, whereas the large particles increase in concentration. The indicated deep layer of large particles is a worldwide phenomenon. For detailed information on vertical distributions, see Junge [1963 and 1961] and Chagnon and Junge [1961].

The form of the size distribution given in Fig. 5-25 applies to aerosols in the altitude range from 0 to 3 km. The absolute values of the number concentration at any altitude within this range will be approximately proportional to the value of the number concentration of large particles presented in Fig. 5-26. From 3 to 10 km, no direct measurements of the size distribution exist. It is reasonable to assume, however, that the shape of the size distribution remains the same over this altitude range, possibly with a sharper decrease in number concentration of particles with radii greater than 1 μ. Between 10 and 30 km, the size distribution is similar to that in Fig. 5-25 between 0.1 and 1.0 μ. For radii greater than 1 μ, the concentration falls off steeply; it is approximately proportional to r^{-7}. Below 0.1 μ, the concentration drops off to a lower limit at approximately 0.05 μ. The absolute number concentration over this altitude range follows the large particle curve of Fig. 5-27.

The chemical composition of the aerosol material varies markedly in the lower region of the atmosphere. At sea level, 80% of the aerosol material is insoluble. Presumably, this material is made up of windblown mineral dusts from the soil. Although no figures are available, it is rea-

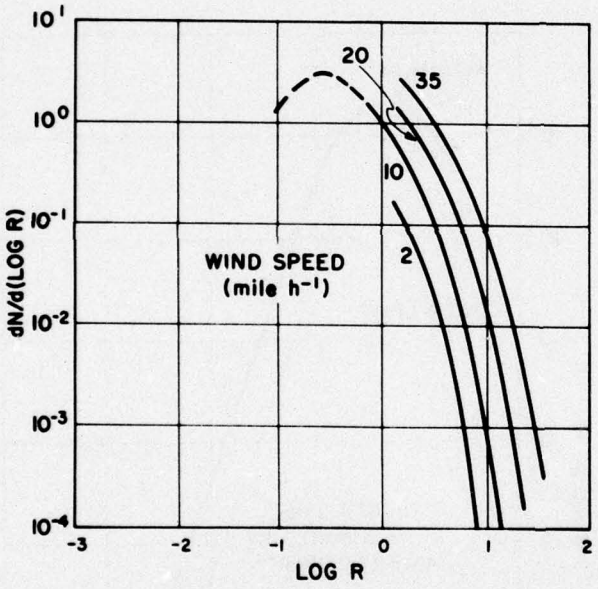


Fig. 5-26. Aerosol size distribution in maritime air.

Table 5-18. Density (μg m^{-3}) of solid and liquid particles.

Environment		Wind Speed (mile h^{-1})	Content (μg m^{-3})
			Sea Spray
		10	4
Maritime Air		20	10
		35	30
		60	100
			Aerosol
	Country		50
Continental Air	Medium-sized Town		100 to 200
	Large City		500 to 1000

Table 5-17. Increase in aerosol concentrations due to various extreme conditions.

Condition	Factor by which Increased	Applicable Size Range
Smog in Large Cities	Up to 30	Whole size range
Dust Clouds over Deserts (Excluding surface layer)	Up to 100	Sizes larger than 0.1 μ
Surf Areas along Coast	Up to 100	All sea spray particles
Storm Areas over Sea	Up to 10	Particles less than 10 μ
	Up to 100	Particles larger than 10 μ

sonable to expect that this surface-generated material decreases in concentration at least as rapidly as the Aitken particles shown in Fig. 5-27. Within the longest lived portion with radii less than 1 μ, the ions SO_4^- and NH_4^+ are the dominant soluble constituents. This is true from sea level to 30 km according to available measurements. In the stratosphere the aerosol is almost entirely soluble. SO_4^- is also the dominant ion present in the ground level aerosol at remote sites on the Greenland icecap at an elevation of 2.3 km [Fenn et al, 1963].

5.5.4 Interaction with Radioactive Material

The natural stratospheric aerosol can act as a primary collection and concentration medium for radioactive material injected into and through the stratosphere. This fact may cause more concern to designers of aircraft for stratospheric operations than the existence of the natural aerosol particles themselves. In the relatively stable air layers between 10 and 30 km, the aerosol particles between 0.05 and 1.0 μ form a stable population. The very finely dispersed radioactive debris will coagulate rapidly with this ambient population of aerosol particles, and will concentrate in the stratosphere aerosol layer. From this point on, the radioactive material will behave dynamically as the large aerosol particles. This fact, together with the altitude concentration implied in the profile of large particles (Fig. 5-27), must be considered in assessing the radioactive hazard as a function of altitude. It should be noted that the possible existence of other aerosol layers at higher altitudes must be considered in estimating the worldwide distribution of debris from high-altitude nuclear tests [Manson, 1961].

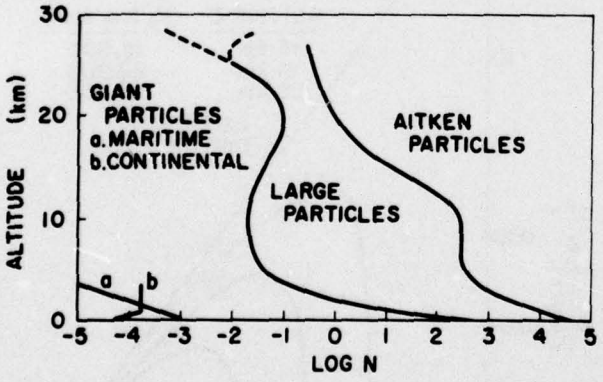


Fig. 5-27. Vertical profiles of the number concentration N(cm^{-3}), for Aitken, large, and giant particles.

5.5.5 Impaction of Aerosol Particles on Aircraft

The large particles in the atmosphere, especially at an altitude of 10 km and above, can be collected on small projections such as ⅛ in. diameter rods and prisms held perpendicular to the air stream. Because the total aerosol particle content of the stratosphere is approximately 10 to 20×10^{-3} $\mu g\ m^{-3}$ at ambient temperature and pressure, such a projection may collect around 10^{-6} g cm^{-2} on the exposed frontal area per hour of flight at a speed of 770 km h^{-1} (415 knots). The high-speed blowers used to pressurize aircraft will efficiently collect these particles in the low-pressure stages; thus, the blowers will also be sites of high residual radioactivity after extended service in the stratosphere.

Figures 5-28, 5-29, and 5-30 present calculated properties of probes used to study the stratospheric particles. The mean impaction efficiency, shown in Fig. 5-28, is $(\eta_c + \eta_r)/2$. η_c and η_r are impaction efficiency functions calculated for right circular cylinders and ribbons, respectively. The impaction efficiency is a measure of the ratio of the number of particles actually striking a collector to the number that would strike if the air stream did not cause some to deviate from their projected trajectories in the absence of the collector. This ratio, which is close to unity for the largest particles and approaches zero for the small particles that follow the air stream closely, depends on the velocity, viscosity, density, and mean free path [Ranz and Wong, 1952]. In Fig. 5-30, the ambient distribution has been extended into the 0.01- to 0.1-μ range to demonstrate the impactor properties. Figures are based on theoretical and experimental studies of particle impaction at ground level, with the necessary corrections for application to use on the Lockheed U-2 aircraft.

Generally, the stratospheric particles adhered equally well to dry and to silicone oil treated surfaces. It appears that these particles are moist as they exist in the stratosphere and, accordingly, any chemical action on exposed surfaces will be accelerated. Although such low concentration will not cause gross effects during currently scheduled high-altitude flights, future design of very long-range stratospheric aircraft may require further examination of the impaction process at high Mach numbers and of the material impacted during such operation, especially at altitudes of 16 to 24 km.

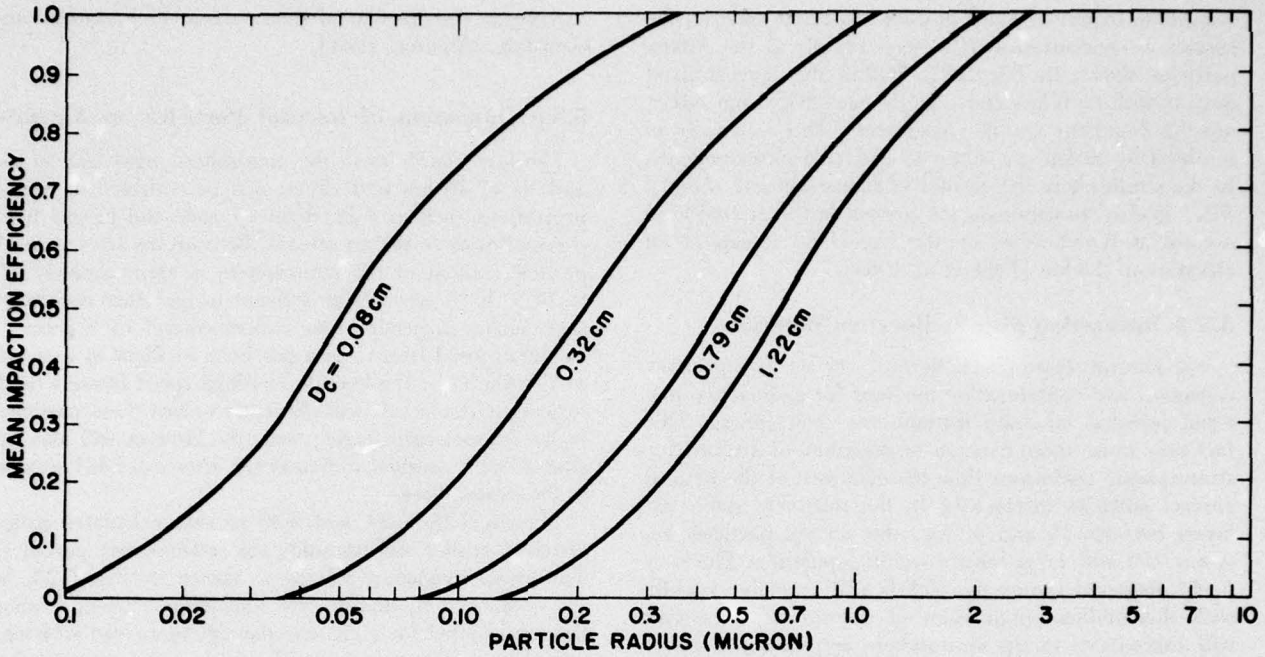


Fig. 5-28. Mean impaction efficiency of collector probes as exposed from U-2 aircraft at 20-km altitude vs radius of particle for various collector diameters, D_c (width of a ribbon or diameter of a cylinder). Air speed is 21,400 cm sec^{-1}. Density of particles is 2 g cm^{-3}.

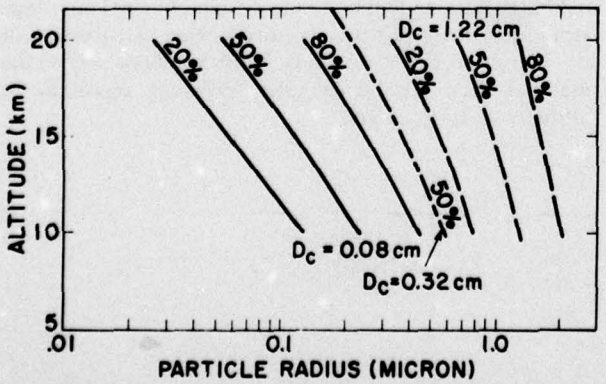


Fig. 5-29. Constant collection efficiency lines for various collector diameters (D_c) as used on U-2 collector probes.

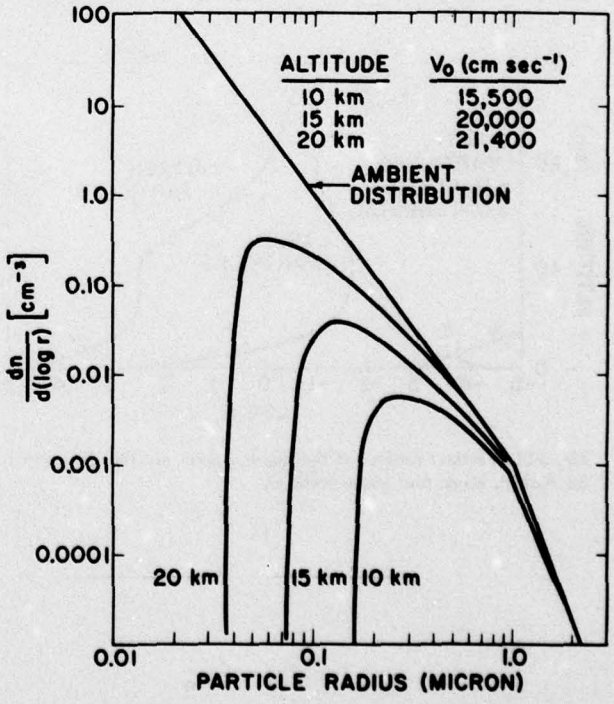


Fig. 5-30. Comparison of assumed ambient size distribution and size distributions collected at several altitudes; collector diameter, 0.32 cm. The ambient distribution, $dn/d(\log r) \propto r^{-3}$, is assumed independent of altitude.

5.6 REFERENCES

aufm Kampe, H. J., and H. K. Weickmann, 1957, "Physics of Clouds," *Meteorol. Monographs*, v. 3, p. 182.

Beckwith, W. B., 1960, Analysis of Hailstorms in the Denver Network, 1949-1958, "Physics of Precipitation," H. Weickmann, ed., American Geophysical Union, Washington, D.C.

Bussey, H. E., 1950, "Microwave Attenuation Estimated from Rainfall and Water Vapor Statistics," *Proc. Inst. Radio Eng.*, v. 38, p. 781.

Chagnon, C. W., and C. E. Junge, 1961, "The Vertical Distribution of Sub-micron Particles in the Stratosphere," *J. Meteorol.*, v. 18, p. 746.

Chmela, A. C., 1960, "Hail Occurrence in New England: Some Relationships to Radar Echo Patterns," *Proc. Eighth Weather Radar Conf.*, American Meteorological Society, Boston, Mass.

Clodman, J., 1957, "Some Statistical Aspects of Cirrus Cloud," *Monthly Weather Rev.*, v. 85, p. 37.

Donaldson, R. J., Jr., 1961, "Radar Reflectivity Profiles in Thunderstorms," *J. Meteorol.*, v. 18, p. 292.

Donaldson, R. J., Jr., 1959, "Analysis of Severe Convective Storms Observed by Radar—II," *J. Meteorol.*, v. 16, p. 281.

Durst, C. S., 1952, "High-Level Clouds in the Tropics," *Meteorol. Res. Paper No. 727*, British Air Ministry, London.

Fenn, R. W., W. E. Gerber, and E. Wasshausen, 1963, "Measurements of the Sulfate and Ammonium Components of the Arctic Aerosol of the Greenland Ice Cap," *J. Atmos. Sci.*, v. 20, no. 5, p. 466.

Fiocco, G., and L. D. Smullin, 1963, "Detection of Scattering Layers in the Upper Atmosphere (60 to 140 Kilometers) by Optical Radar," *Nature*, v. 199, p. 1275.

Foster, D. S., 1961, "Aviation Hail Problem," *Tech. Note 37*, World Meteorological Organization.

Hemenway, C. L., R. K. Soberman, and G. Witt, 1964, "Investigation of Noctilucent Cloud Particles," *Tellus*, v. 16, no. 1.

James, D. G., 1957, "Investigations Relating to Cirrus Clouds," *Meteorol. Mag.*, v. 86, p. 1.

Jones, D. M. A., 1956, "Rainfall Drop Size Distribution and Radar Reflectivity," *Meteorol. Lab. Res. Rept. No. 6*, Illinois State Water Survey, Urbana, Ill.

Junge, C. E., 1963, "Air Chemistry and Radioactivity," Academic Press, New York.

Junge, C. E., 1961, "Vertical Profiles of Condensation Nuclei in the Stratosphere," *J. Meteorol.*, v. 18, p. 501.

Kessler, E., III, 1958, "Use of Radar in Kinematical Studies of Precipitating Weather Systems," *Proc. 7th Weather Radar Conf.*, American Meteorological Society, Boston, Mass.

Lemons, H., 1943, "Semi-Monthly Distribution of Hail in the United States," *Monthly Weather Rev.*, v. 71, p. 115.

Manson, J. E., 1961, "The Interaction of Radioactive and Non-Radioactive Particles in the Stratosphere," *Proc. of the Conf. on Radioactive Fallout from Nuclear Weapons*, U.S. Atomic Energy Commission, Washington, D.C.

Marshall, J. S., and W. M. Palmer, 1948, "The Distribution of Raindrops with Size," *J. Meteorol.*, v. 5, p. 165.

Ranz, W. E., and J. B. Wong, 1952, "Impaction of Dust and Smoke Particles," *Ind. Eng. Chem.*, v. 44, p. 1371.

Spilhaus, A., 1948, "Drop Size Intensity and Radar Echo of Rain," *J. Meteorol.*, v. 5, p. 161.

Spreen, W. C., and I. Solomon, 1958, "An Indirect Method for Estimating the Frequencies of Ceiling below Various Altitudes and Various Altitude Ranges," *Bull. Am. Meteorol. Soc.*, v. 39, p. 261.

U.S. Weather Bureau, 1949, "The Thunderstorm," U.S. Government Printing Office, Washington 25, D.C.

Wexler, R., and D. Atlas, 1958, "Moisture Supply and Growth of Stratiform Precipitation," *J. Meteorol.*, v. 15, p. 531.

Witt, G., 1962, "Height, Structure, and Displacements of Noctilucent Clouds," *Tellus*, v. 14, p. 1.

Yarnell, D. L., 1935, "Rainfall Intensity Frequency Data," *Miscellaneous Publication No. 204*, U.S. Dept. of Agriculture, Washington, D.C.

Chapter 6

ATMOSPHERIC COMPOSITION

Section 6.1	Christos G. Stergis
Section 6.2	Wayne S. Hering
Sections 6.3, 6.5	Robert E. Huffman
Sections 6.4, 6.6, 6.7	W. W. Hunt, Jr.
Section 6.8	John F. Paulson

Table 6-1 gives the composition at the earth's surface of air that contains no water vapor and is free of contaminants; this is the "normal" air of the *U.S. Standard Atmosphere, 1962*. In this standard, the variability below 90 km altitude is neglected. The molecular weight of this standard atmosphere is 28.9644, based on the scale of C^{12} molecular weight equals 12.0000; it is considered constant up to 90 km. Figure 6-1 shows the assumed variation above 90 km, where changes in composition are considered significant.

6.1 PRINCIPAL CONSTITUENTS

The major constituents of the atmosphere up to about 90 km are molecular nitrogen and molecular oxygen. Excluding the small amounts of argon, carbon dioxide, etc. found near the earth's surface, the minor constituents are ozone, atomic oxygen, water vapor, sodium vapor, and nitric oxide.

At about 90 km, the dissociation of molecular oxygen (O_2) by solar ultraviolet radiation begins. The concentration of O_2 then decreases while the concentration of atomic oxygen (O) increases with increasing altitude. At about 200 km, the amount of O is greater than O_2; at 500 km, practically no O_2 remains. Molecular nitrogen (N_2) is much more difficult to dissociate and even at 500 km the concentration of atomic nitrogen (N) is very small. Below 100 km, the predominant process is turbulent mixing of the atmospheric particles, so that the diffusion process is small. Above 100 km, however, the diffusion process becomes important and the lighter gases tend to concentrate in the upper regions and the heavier gases in the lower regions. As a result, the atomic oxygen content increases and the molecular nitrogen decreases with increasing altitude. Figure 6-2 shows the relative proportions of three principal constituents up to 500 km altitude.

As a result of molecular diffusion, helium and hydrogen become the principal constituents in the upper atmosphere. The mass spectrometer experiment on the Explorer

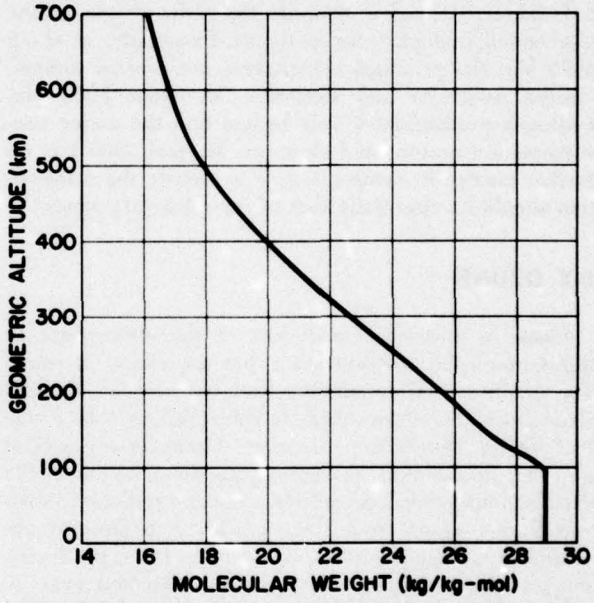


Fig. 6-1. Molecular weight of *U. S. Standard Atmosphere, 1962* as a function of altitude.

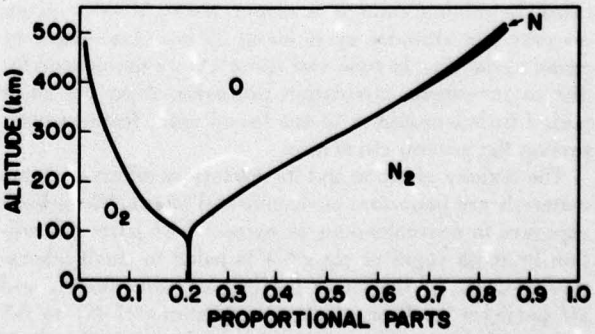


Fig. 6-2. Relative proportions of the principal atmospheric constituents up to 500 km.

* With the exceptions of the paragraph that discusses results of Explorer XVII experiments (Sec. 6.1) and of Sec. 6.2, the information covers data available before June, 1962.

XVII satellite (scientific designation 1963-9) showed helium as a major constituent above 600 km; however, the instrument did not measure hydrogen. Figure 6-3 shows the observed ratios of numbers of helium to oxygen atoms and of oxygen atoms to nitrogen molecules as a function of altitude. Figure 6-4 shows the mean molecular mass of these three constituents derived from the measurements. The mean mass of the atmosphere, particularly at the higher altitudes, is less than the values shown because hydrogen is present in concentrations that increase with altitude.

Positive and negative ions and electrons are formed in the upper atmosphere by photoionization and electron detachment processes with solar radiation providing the energy. Figure 6-5 shows the distribution of the number of ionic particles and total number of particles with altitude. At the peak of the ionosphere (around 300 km), the ion concentration is the order of 10^6 cm^{-3}, but the total number of particles present is several orders of magnitude larger. At higher altitudes the ratio of ions to the total number of particles increases. Eventually, at about 2000 km, the principal constituents are ionized helium, ionized hydrogen and electrons. At about 3000 km, hydrogen predominates over helium and the major constituents are protons and electrons. Beyond 3000 km, no further change in composition is expected; the composition should be essentially that of interplanetary space.

6.2 OZONE

Ozone is a minor constituent of the atmosphere in terms of relative concentration, but the effects of ozone are significant. The radiative heat balance and thermal structure of the stratosphere is controlled to a large extent by the distribution of ozone. Ozone is a principal absorber and emitter of electromagnetic radiation in the earth's atmosphere. Solar electromagnetic radiation in the wavelength region from 3000 to 2300 Å is strongly absorbed in the upper portion of the ozone layer, producing the prominent temperature maximum observed near 50 km. Ozone effectively shields the earth's surface from direct solar radiation of wavelengths shorter than 2900 Å.

Ozone is a natural tracer of atmospheric motion because its mixing ratio is a conservative property of an air parcel at altitudes up to about 25 km. Assessment of ozone variability in time and space allows the meteorologist to investigate circulation processes, from the short period turbulent eddies to the broad scale features comprising the general circulation.

The toxicity of ozone and its deleterious effects on some materials are important environmental effects. Three-hour exposure to concentrations in excess of 15 parts per million by mass (ppm or $\mu g\ g^{-1}$) is lethal to small laboratory animals. Irritation to the human nose, throat, and air passages is observed at concentrations of 0.1 to 0.3 ppm; with increased concentration, tightness in the chest, headache, and drowsiness appear. Severe pneumonia-type illness has been found among men working in an atmosphere which contained 15 ppm of ozone.

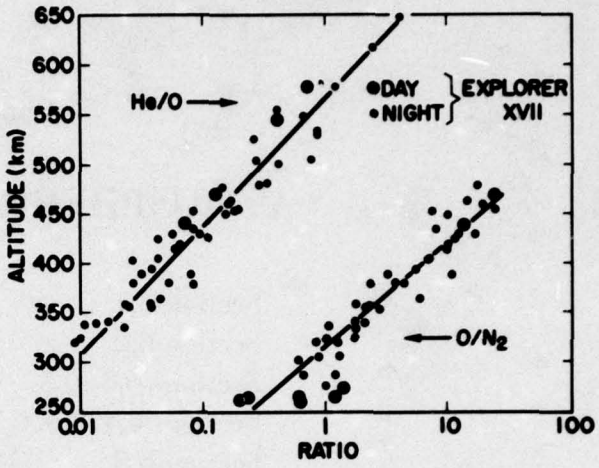


Fig. 6-3. Ratios of numbers of helium atoms to oxygen atoms and of oxygen atoms to nitrogen molecules determined by mass spectrometer experiment on Explorer XVII satellite. (From *IG Bulletin No. 89*, National Academy of Sciences, November 1964.)

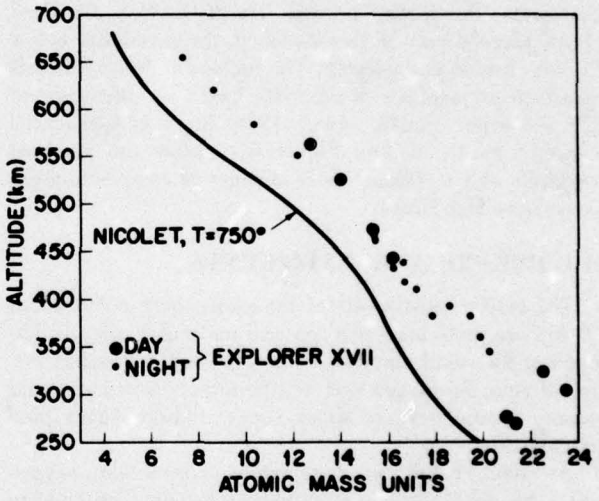


Fig. 6-4. Mean molecular mass of major atmospheric constituents He, O, and N_2 between 250 and 600 km, determined by mass spectrometer experiment on Explorer XVII satellite. (From *IG Bulletin No. 89*, National Academy of Sciences, November 1964.)

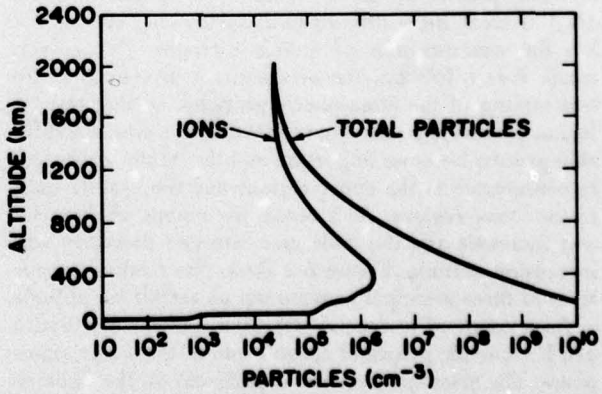


Fig. 6-5. Number of ions and total number of atmospheric particles per cubic centimeter as a function of altitude.

6.2.1 Regions of Ozone Formation

Ozone is continually created in the upper layers of the earth's atmosphere by ultraviolet solar radiation. The primary source is a region 10 to 15 km in depth, centered near 25-km altitude over the equator and sloping upward to 30-km altitude at high latitudes. The concentration above 35 km remains essentially in photochemical equilibrium. Below this source region, ozone is a stable constituent of the atmosphere until it is eventually transported to the ground level where it is destroyed by interaction with organic materials. The concentration of ozone at high levels shows little departure from the values predicted from the chemical and physical reactions, whereas the distribution below about 25 km may exhibit large fluctuations as a result of the mixing history.

Additional sources of atmospheric ozone are in the troposphere [Frankiel, 1958; Reshetov, 1961]. For example, ozone is formed through decomposition of nitrogen dioxide introduced into the atmosphere by factory smoke, forest fires, volcanic eruptions, etc. (The ozone content of smog in the Los Angeles area has exceeded 0.5 ppm.) Ozone is also produced by electrical discharges and the testing of nuclear weapons. Much uncertainty remains concerning the relative importance of sources near the surface and the processes of formation; the amounts introduced are generally considered to be far less than the amounts from photochemical production in the upper atmosphere.

6.2.2 Distribution of Total Ozone

Measurements of the total amount of ozone in a vertical column above the earth's surface have been made for many years at a number of stations by spectrographic methods. Figures 6-6(a) and (b) are contour maps for the seasons of maximum (spring) and minimum (fall) ozone. Values of total ozone are given in units of *atmosphere-centimeters* (atm-cm), which is the height of the resulting volume of ozone if all the ozone in the column of unit area were brought to normal surface pressure and temperature. Total ozone in equatorial regions averages about 0.240 atm-cm and varies only slightly with season. The amount increases to the north, reaching annual average values in excess of 0.380 atm-cm at high latitudes. North of the tropical zone, the variation with season is approximately sinusoidal, with a distinct maximum in early spring and a distinct minimum in the fall; the amplitude increases with latitude.

Average total ozone has significant longitudinal variation. The general features of the ozone distribution conform roughly to the gross features of the mean circulation pattern of the lower stratosphere. Larger amounts of ozone are associated with regions of low pressure and warm temperature above the tropopause; smaller amounts are found in the cold, anticyclonic circulation areas in the lower stratosphere. Similar correspondence of the ozone distribution with circulation features is seen in Fig. 6-6. Average seasonal amounts in the northern regions range from as small as 0.280 atm-cm over Norway in the fall to greater than 0.460 atm-cm over northern Canada and Greenland in the spring.

6.2.3 Vertical Ozone Distribution

In January 1963, the Air Force Cambridge Research Laboratories established an ozonesonde network that provides systematic observations of the vertical ozone distribution by balloon-borne ozonesondes from a network of

Table 6-1. Normal composition of clean, dry atmospheric air near sea level. (From *U. S. Standard Atmosphere, 1962.*)

Constituent Gas	Gas Symbol	Content (% by volume)	Molecular Weight*
Nitrogen	N_2	78.084	28.0134
Oxygen	O_2	20.9476	31.9988
Argon	Ar	0.934	39.948
†Carbon dioxide	CO_2	0.0314	44.00995
Neon	Ne	0.001818	20.183
Helium	He	0.000524	4.0026
Krypton	Kr	0.000114	83.80
Xenon	Xe	0.0000087	131.30
Hydrogen	H_2	0.00005	2.01594
†Methane	CH_4	0.0002	16.04303
Nitrous oxide	N_2O	0.00005	44.0128
†Ozone	O_3	Summer: 0 to 0.000007	47.9982
		Winter: 0 to 0.000002	47.9982
†Sulfur dioxide	SO_2	0 to 0.0001	64.0628
†Nitrogen dioxide	NO_2	0 to 0.000002	46.0055
†Ammonia	NH_3	0 to trace	17.03061
†Carbon monoxide	CO	0 to trace	28.01055
†Iodine	I_2	0 to 0.000001	253.8088

* On basis of C^{12} isotope scale for which C^{12} equals 12.0000.

† The content of these gases may undergo significant variations from time to time or from place to place relative to the normal.

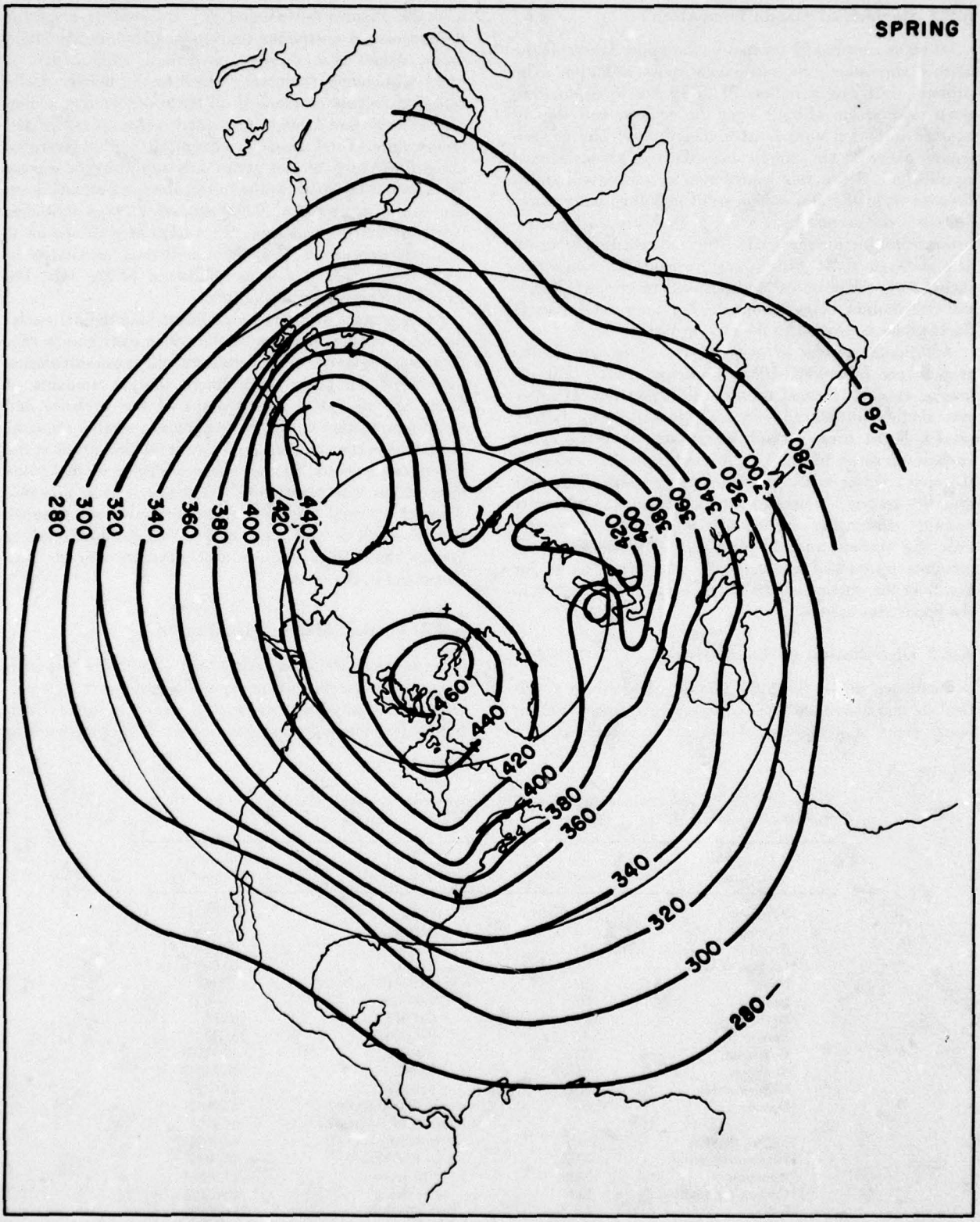


Fig. 6-6(a). Average distribution of total ozone over the Northern Hemisphere in the spring. (Multiply numbers given on contours by 10^{-3} to obtain values in atm-cm.) (From J. London, *Final Rept., New York University, Contract AF19(604)-5492*, 1962.)

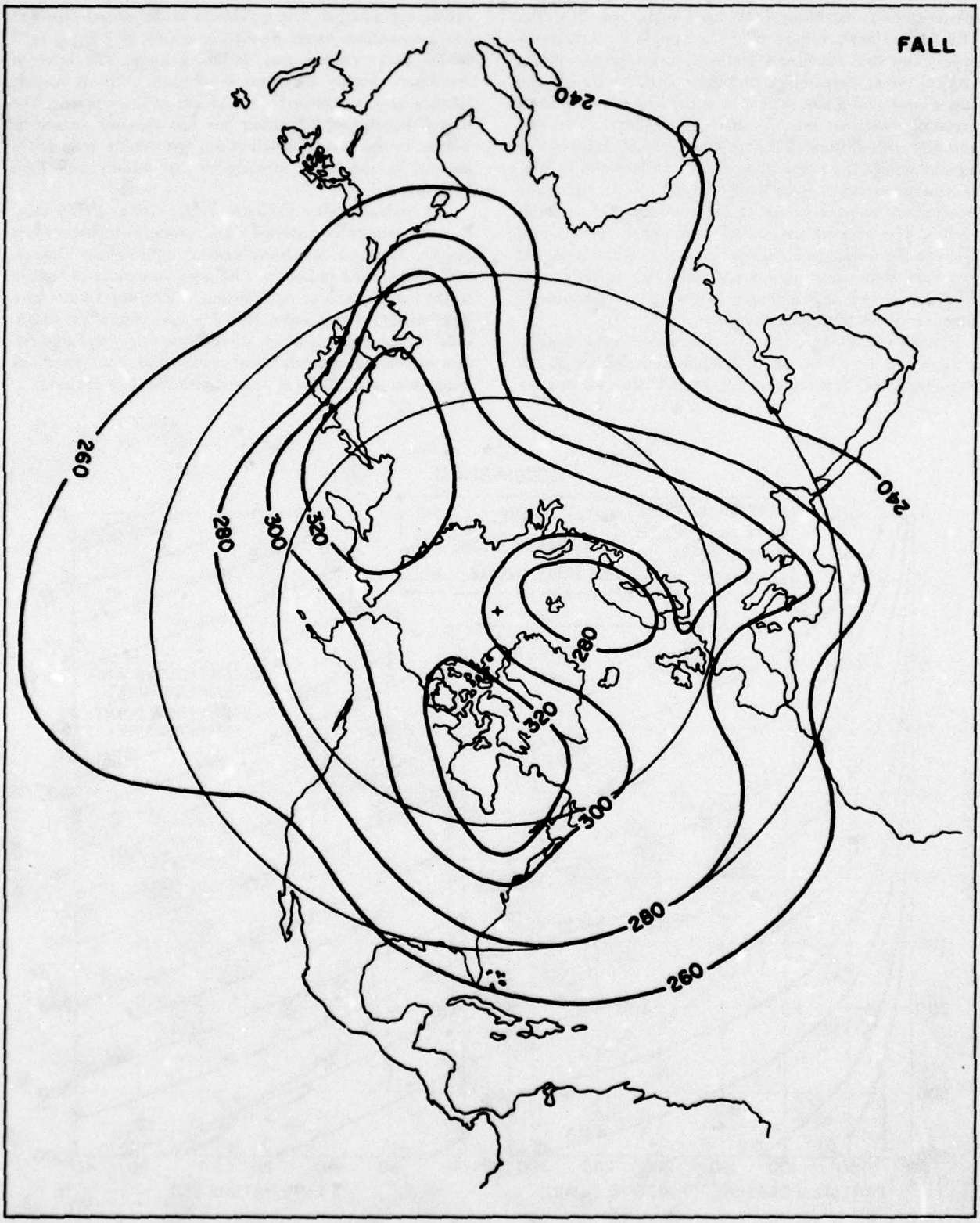


Fig. 6-6(b). Average distribution of total ozone over the Northern Hemisphere in the fall. (Multiply numbers given on contours by 10^{-3} to obtain values in atm-cm.) (From J. London, *Final Rept., New York University, Contract AF19(604)-5492*, 1962.)

eleven stations extending from the Canal Zone to Alaska [Regener, 1960]. Figure 6-7 is a sample of a network ozonogram that illustrates features characteristic of the vertical ozone distribution in middle latitudes during the late winter and early spring months. The ozone partial pressure remains low in the troposphere, increases abruptly with altitude at the tropopause level, and reaches a maximum in the range 20 to 25 km. In terms of mixing ratios, values range from near 0.05 $\mu g\ g^{-1}$ in the lower troposphere to peak values of 10 to 15 $\mu g\ g^{-1}$ at about 35 km. The greatest variability is found in the stratum between the tropopause and the level of maximum partial pressure. Both short-period and seasonal variations in total ozone can be attributed largely to ozone density changes in this atmospheric layer.

Figures 6-8(a) and (b) give the mean ozone density distribution as a function of latitude and altitude as derived from the North American network observations for spring and summer. The maximum ozone season (spring) has a maximum ozone density in excess of 700 $\mu g\ m^{-3}$ in the polar region near 16-km altitude. The level of maximum density increases in altitude with decreasing latitude and is centered near 25 km at the equator. The ozone density configuration for the summer season is similar to the spring distribution, but greatly reduced in amount in the lower stratosphere at middle and high latitudes.

Theoretical studies [Dütsch, 1956; Craig, 1951] show that above approximately 35 km, ozone disturbances are quickly restored to photochemical equilibrium concentrations by solar radiation. Although uncertainties remain in the calculations of equilibrium values, the results provide fairly reliable estimates of actual ozone concentrations in the upper portion of the ozone layer. Table 6-2 lists calculated photochemical equilibrium concentrations in summer and winter at several altitudes and latitudes.

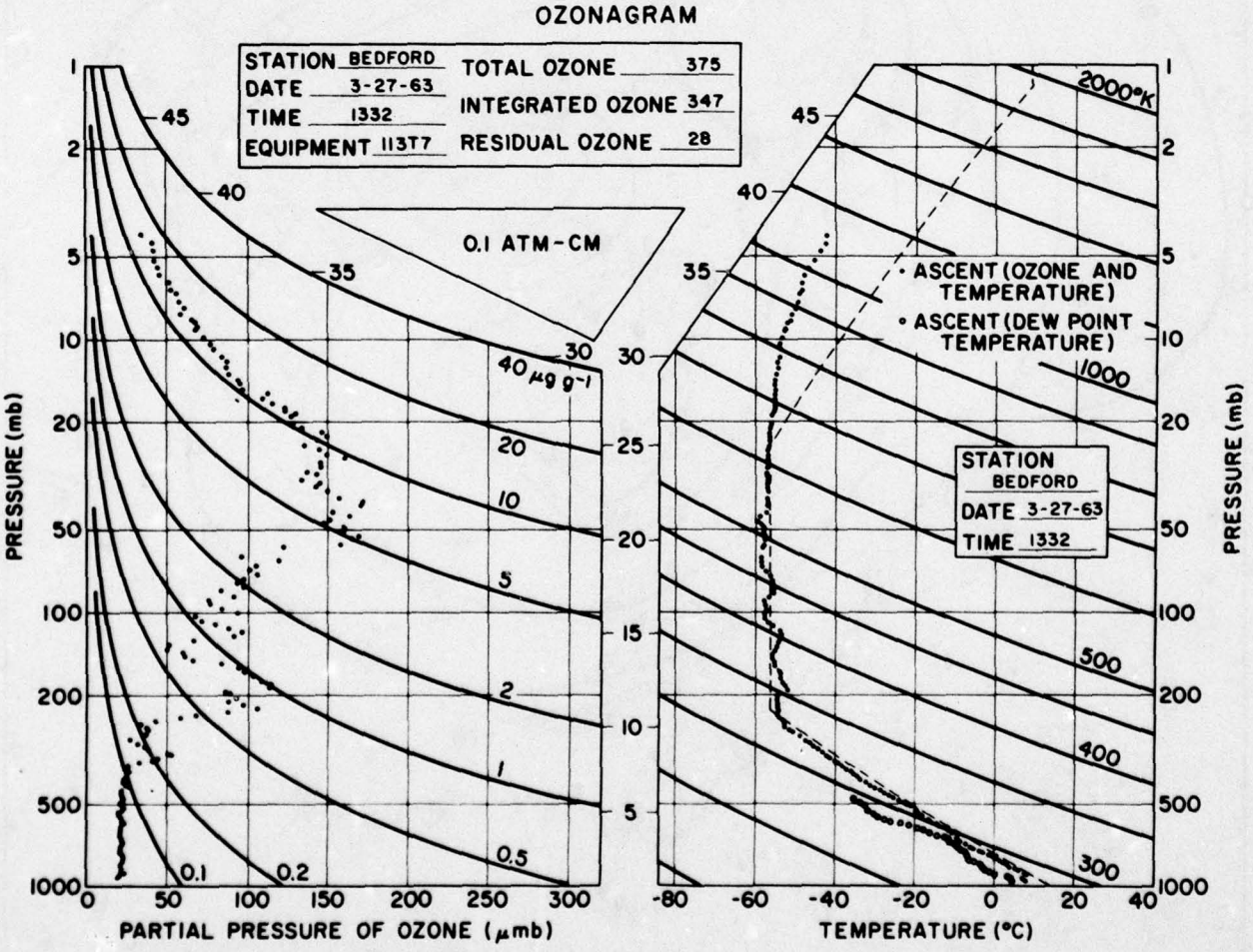


Fig. 6-7. Vertical distribution of ozone and temperature over Bedford, Massachusetts. Loci of points with constant mixing ratios (0.1 up to 40 $\mu g\ g^{-1}$) are given on the left chart, and loci of constant potential temperature (200° to 2000°K) on the right. Numbers between the charts indicate the altitude in kilometers.

6.3 ABSORPTION AND IONIZATION IN THE UPPER ATMOSPHERE

The absorption of solar ultraviolet radiation and x-rays (Sec. 16.2) is one of the predominant factors in determining the composition of the upper atmosphere and its variability. Table 6-3, using molecular oxygen as a typical example, lists the significant processes in which the solar energy is absorbed and the products formed in the reactions. (There are other conceivable processes not listed.) All but the dissociative processes and ion pair formation may occur in atomic as well as molecular absorption.

For any process to occur with radiation of a particular wavelength, the molecule or atom must have an appreciable absorption cross section at that wavelength, the photon must provide the right amount of energy for the reaction, and the process must have a high probability compared to other processes that are also energetically possible. In many cases, information available from studies of atomic and molecular energy levels, absorption spectra, and ionization and excitation potentials can be used to restrict the choice of processes. In other cases, very little quantitative information is available at this time (1962). (Improved data on absorption and ionization coefficients of N_2 and O_2 in the 600-1000 Å region became available after this section was prepared; for measurements at fairly good bandwidths, see Huffman, et al [1964], and Cook and Metzger [1964]. Recent measurements at solar lines down to about 300 Å are given by Samson and Cairns [1964].) Dissociation and direct photoionization are the most important processes in the upper atmosphere. The meager experimental data available indicates that ion pair formation, dissociative ionization, and photoionization plus fluorescence are not as important.

The photoionization cross section and the photoionization efficiency measure the probability of ionization. When plotted as a function of wavelength, the cross section rises sharply at the wavelength corresponding to the ionization potential (in a manner similar to a step function); it rapidly approaches a broad maximum at several volts above the ionization potential and then decreases slowly at higher energies. Vibrational structure, Franck-Condon factors, or higher energy continua may confuse this simple picture, however. This is in contrast to photodissociation continua, which usually begin and end in a diffuse manner and depend more on location of a suitable repulsive potential curve than on energy requirements.

Table 6-4 lists the lowest ionization potential and the wavelength of the photon with corresponding energy ($h\nu$) for the atmospheric atoms and molecules; for extensive tables see Watanabe [1958]. Of the atmospheric molecules, nitric oxide has the lowest ionization potential; the other major constituents lie at much shorter wavelengths, which greatly hampers spectroscopic measurement (good window materials are not available below the lithium fluoride limit at 1030 Å).

Table 6-3. Photon absorption processes.

Process	Example
Dissociation	$O_2 + h\nu \rightarrow O + O$
Photoionization (ground state)	$O_2 + h\nu \rightarrow O_2^+ + e^-$
Photoionization (excited states)	$O_2 + h\nu \rightarrow O_2^{+*} + e^-$
Excitation	$O_2 + h\nu \rightarrow O_2^*$
Preionization	$O_2 + h\nu \rightarrow O_2^* \rightarrow O_2^+ + e^-$
Ion pair formation	$O_2 + h\nu \rightarrow O^+ + O^-$
Dissociative ionization	$O_2 + h\nu \rightarrow O^+ + O + e^-$
Photoionization plus fluorescence	$O_2 + h\nu_1 \rightarrow O_2^{+*} + e^-$
	$O_2^{+*} \rightarrow O_2^+ + h\nu_2 + e^-$

* excitated state

Table 6-4. Ionization potentials and corresponding wavelengths.

Atmospheric Constituent	Energy (eV)	Wavelength (Å)
O	13.614	910.7
O_2	12.075	1026.7
N	14.54	852.7
N_2	15.580	795.7
NO	9.25	1340.3

Table 6-2. Photochemical equilibrium concentrations of atmospheric ozone (calculated by J. London and C. Prabhakara, unpublished data).

Altitude (km)	Concentration (molecules per cubic centimeter)					
	Summer			Winter		
	0°	30°N	60°N	0°	30°N	60°N
70	5×10^9	6.4×10^9	7×10^9	6×10^9	4×10^9	1.7×10^9
60	1.5×10^{10}	1.7×10^{10}	1.7×10^{10}	1.2×10^{10}	1×10^{10}	5×10^9
50	5×10^{10}	6×10^{10}	6×10^{10}	4×10^{10}	6×10^{10}	6×10^{10}
40	6×10^{11}	6×10^{11}	7×10^{11}	7×10^{11}	7×10^{11}	3×10^{11}

CHAPTER 6

The absorption of a monochromatic beam of photons by a gas is given by

$$I(\lambda) = I_o(\lambda) \exp(-k(\lambda)\, x), \qquad (6\text{-}1)$$

where $I(\lambda)$ is the transmitted intensity at wavelength λ, $I_o(\lambda)$ is the incident intensity, $k(\lambda)$ is the *absorption coefficient*, and x is the reduced length of the light path. This *reduced length* is

$$x = l\left(\frac{P}{P_o}\right)\left(\frac{T_o}{T}\right), \qquad (6\text{-}2)$$

where l is the geometric path length, P and T are ambient pressure and temperature, P_o is 1 atmosphere (1013.25 mb, 760 mm Hg), and T_o is 273.2°K. The *total absorption cross section* is defined as,

$$\sigma = k/n_o, \qquad (6\text{-}3)$$

where n_o, the number density of the gas at standard conditions, is Loschmidts number (2.69×10^{19} cm^{-3}) if σ is in cm^2 and k in cm^{-1}. (The megabarn, 10^{-18} cm^2, is often used as a unit for values of cross sections.) The total absorption cross section measures the removal of photons from an incident beam for any feasible process. The terms absorption coefficient and absorption cross section are often used interchangeably; both parameters are extensively used in reporting experimental or theoretical results.

The photoionization cross section measures all ionization processes occurring at a given wavelength and altitude. The radiation flux at the altitude in question, however, is reduced from the flux value at the top of the atmosphere by other absorption processes, as measured by the total absorption cross section. Therefore, experimental determination of both cross sections is necessary to understand reactions in the ionosphere. The *photoionization cross section*, $\sigma_i(\lambda)$, may be less than or equal to the total absorption cross section in the vacuum ultraviolet region (1400 to 100 Å);

$$\sigma_i(\lambda) = f(\lambda)\ \sigma(\lambda), \qquad (6\text{-}4)$$

where $f(\lambda)$ is the ionization efficiency. The ionization efficiency is the average number of ions produced per photon absorbed or the primary quantum yield for ions. Whereas the total absorption cross section may be determined from the ratios of the incident and transmitted intensities, the number of photons absorbed must be known to obtain the ionization cross section. Determination of the absolute intensity is a more difficult experimental problem than measurement of the relative light

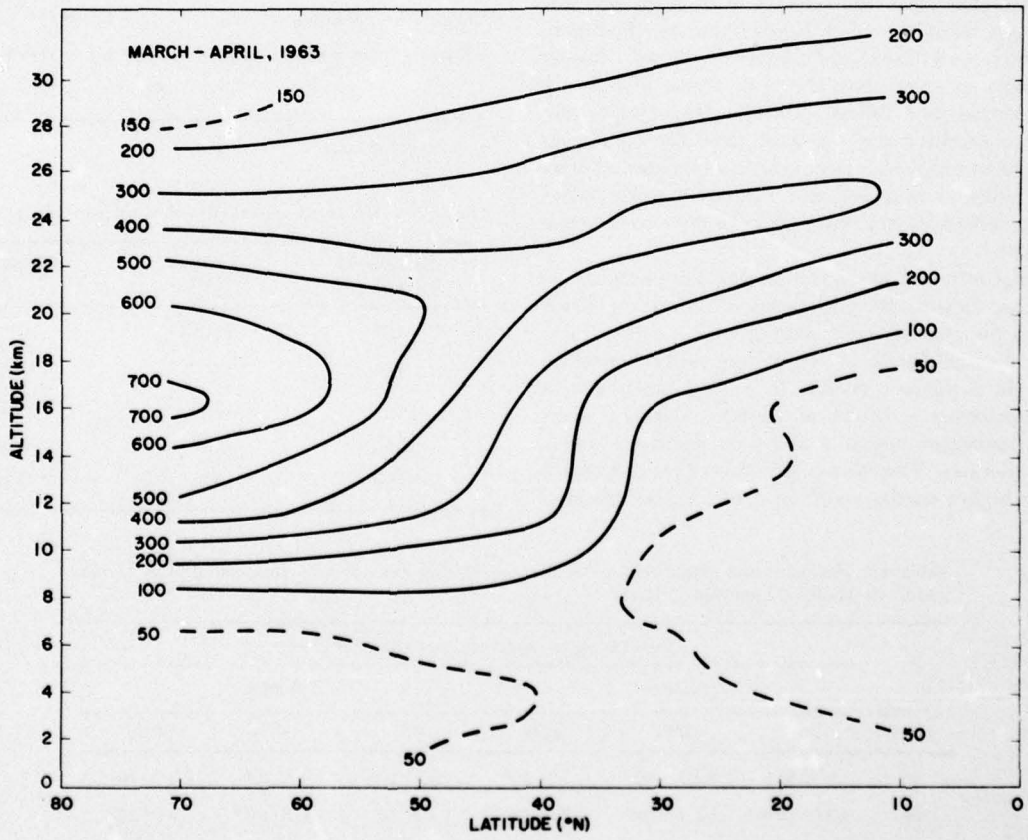


Fig. 6-8(a). Average ozone density over the North American continent derived from ozonesonde network data, for March-April. Values for the contours are $\mu g\ m^{-3}$; divide values by 2.14×10^{-4} for density in atm-cm km^{-1}.

intensity, which explains the lack of photoionization data compared to absorption data.

In contrast to the vacuum ultraviolet range, where the ionization efficiency is never greater than unity, photons in the x-ray region may have a larger ionization yield because of additional secondary ionization from the very high energy electrons resulting from the initial absorption. In this region (roughly below 100 Å), it is assumed that every absorbed photon leads to ionization and that the total number of ions per photon absorbed is approximated by the total photon energy divided by 35 eV, the energy typically required to produce an ion-pair in air.

6.3.1 Molecular Nitrogen

Molecular nitrogen (N_2) is relatively transparent to solar electromagnetic radiation down to about 1000 Å. Absorption coefficient measurements in the 1450 to 1000 Å region involve only the weak Lyman-Birge-Hopfield bands. The absorption coefficients are in the range 0.1 to 0.01 cm^{-1}, and are not considered especially important in atmospheric absorption processes.

Beginning at 1000 Å, however, the spectrum consists of a number of complex and strong bands. Absorption continua resulting in photodissociation are not believed to exist in N_2. The upper limits typically set make them appear to be of no interest for atmospheric problems, but there may possibly be an underlying continuum in the 800 to 950 Å region. At wavelengths below 796 Å, there is strong absorption into the ionization continuum superimposed with band systems of Rydberg states converging to higher molecular ionization potentials. (A similar situation occurs in all of the atmospheric diatomic gases and probably in the atomic oxygen and atomic nitrogen.)

Because of the number and intensity of the bands throughout the region below 1000 Å, high resolution is required for adequate investigation. As a result, the absorption and ionization cross sections are not well known; they are apparently pressure dependent at most wavelengths. All of the studies in the main ionization continua have been done with background light sources that give a series of atomic lines; this results in a widely varying set of absorption coefficients in regions where there are strong molecular bands either with or without an underlying continuum.

From 1000 to 850 Å, the spectrum consists of many strong bands; Watanabe and Marmo [1956] and Clark [1952] give studies of this region. Figure 6-9 shows the regions from 840 to 980 Å at a resolution of 0.2 Å. The solar emission line of the hydrogen Lyman series at 973 Å (H Ly-γ) appears to almost exactly coincide with the

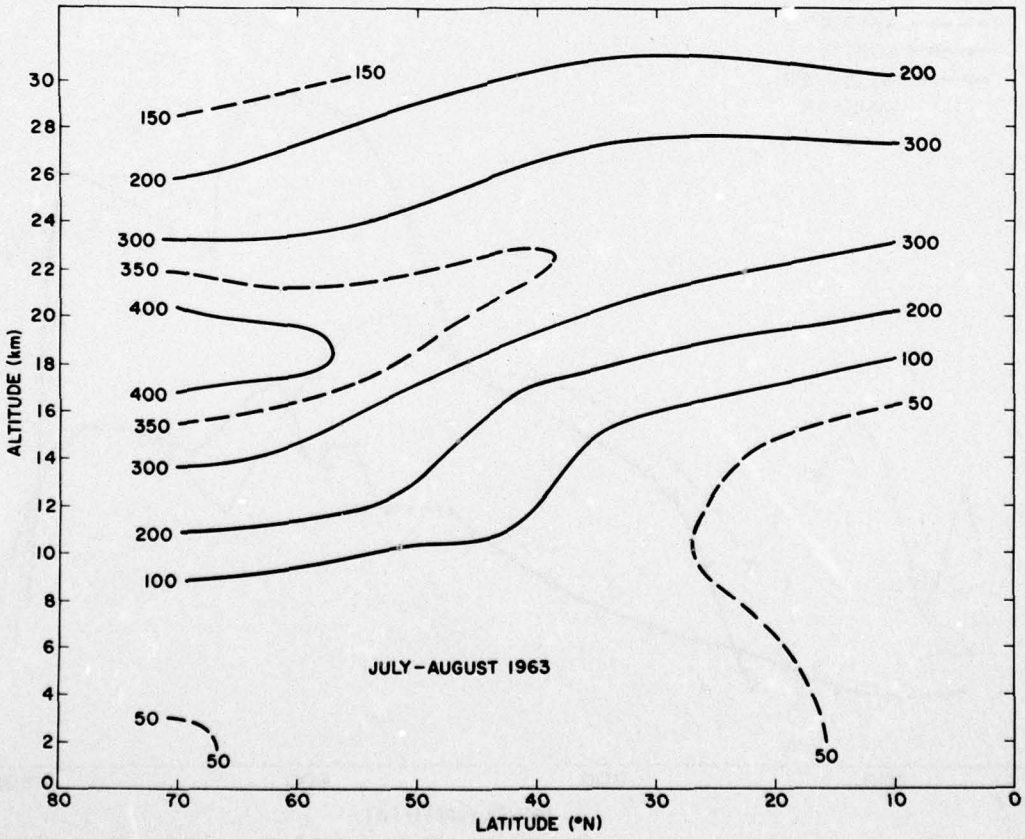


Fig. 6-8(b). Average ozone density over the North American continent derived from ozonesonde network data, for July-August. Values for the contours are $\mu g\ m^{-3}$; divide values by 2.14×10^{-4} for density in atm-cm km^{-1}.

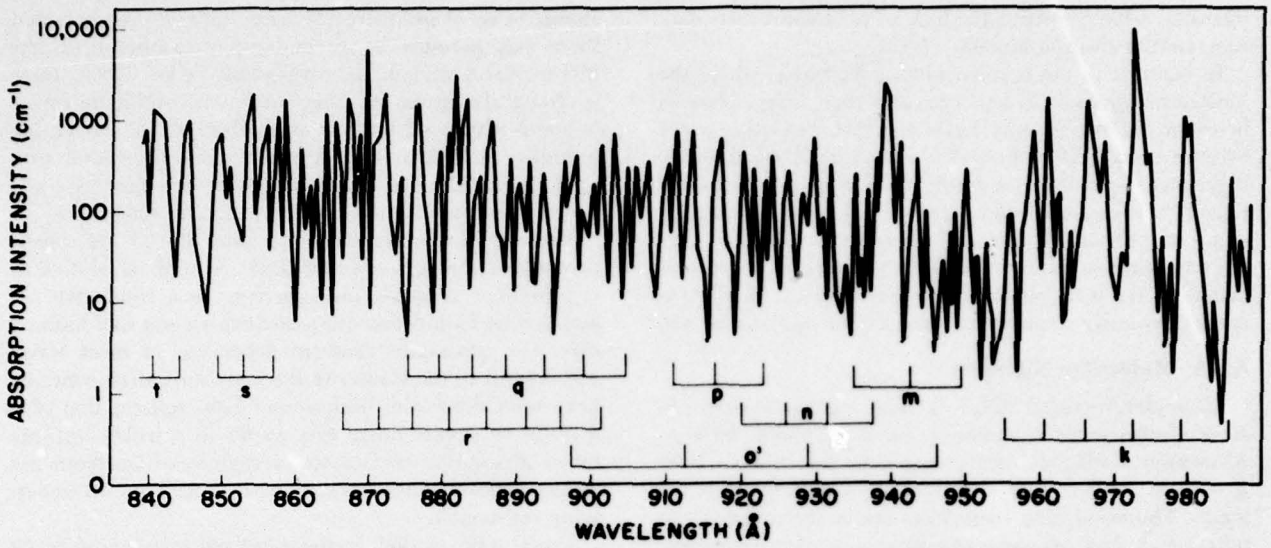


Fig. 6-9. Absorption coefficient curve of N_2. (From F. K. Itamoto, Jr. and H. C. McAllister, *University of Hawaii Scientific Rept. No. 4*, 1961, Contract AF19(604)-4576, AFCRL.)

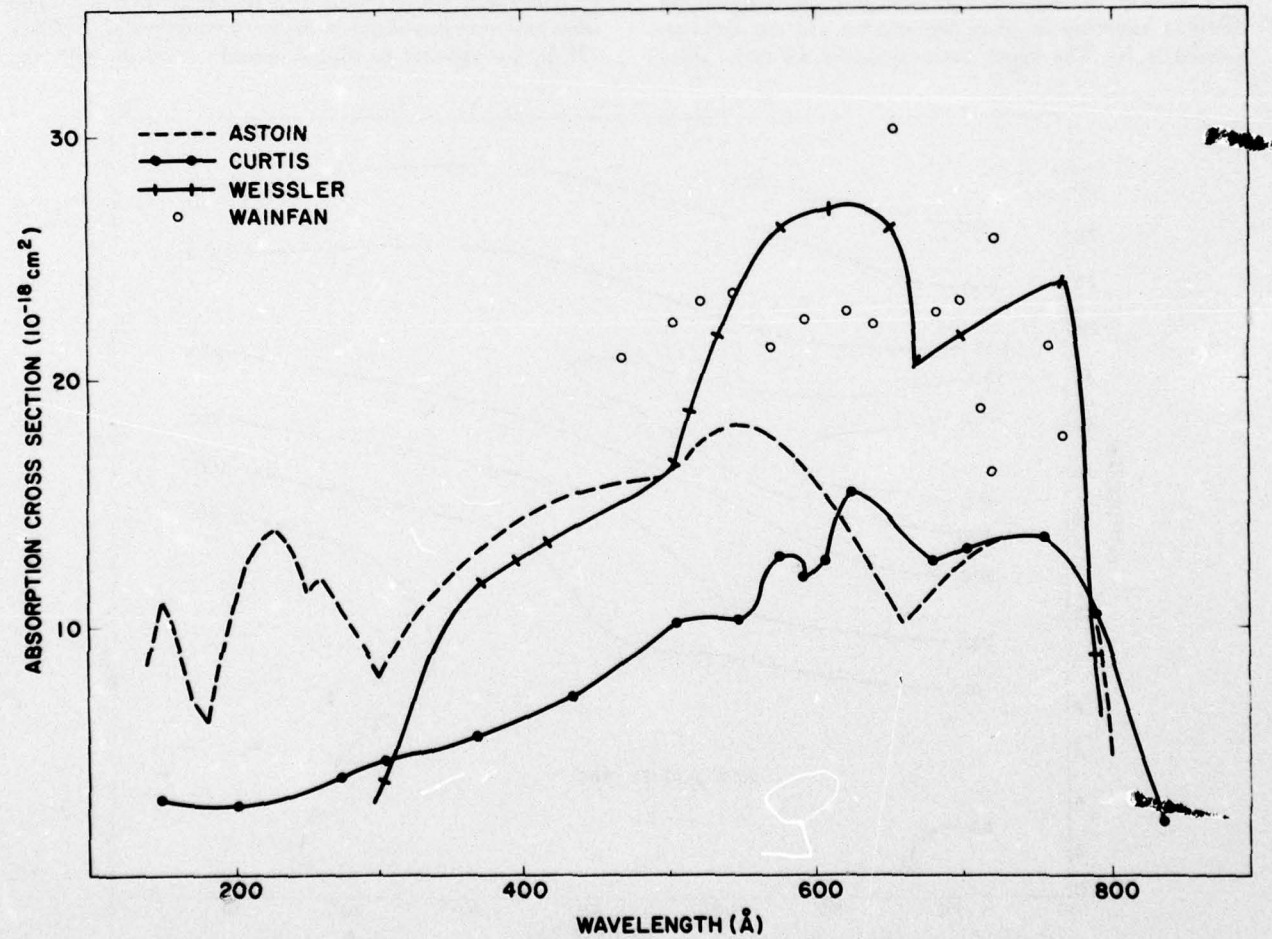


Fig. 6-10. Absorption cross sections of N_2. (Data from: N. Astoin and J. Granier, *Comptes Rendus*, v. 244, p. 1350, 1957; J. P. Curtis, *Phys. Rev.*, v. 94, p. 908, 1954; G. L. Weissler, P. Lee, and E. I. Mohr, *J. Opt. Soc. Am.*, v. 42, p. 84, 1952; and N. Wainfain, W. C. Walker, and G. L. Weissler, *Phys. Rev.*, v. 99, p. 542, 1955.)

peak of what is probably the strongest N_2 band observed. Values of the absorption coefficient as high as 10,000 cm^{-1} are reported. This intense absorption explains the peculiar absence of H Ly-γ in published densitometer traces of the solar spectrum. The superposition of this strong solar emission line with a strong N_2 band illustrates the importance of the total absorption process in determining the ionization processes at lower altitudes. (Due to the strong absorption, this wavelength contributes practically nothing to ionization in the first continua of O_2, which starts at about 1026 Å, and an error in the ion production rate from O_2 would result if this absorption were neglected.)

The region from 850 to about 150 Å is most important for its effect on the ionosphere. Below 796 Å, photoionization of N_2 may occur. Figure 6-10 shows absorption cross sections in this region; it is a plot of the envelopes of the lowest ionization coefficients measured. The agreement is fairly close between Astoin and Curtis down to 600 Å; between 600 and 500 Å all of the curves are different. Below 500 Å the curves of Weissler and Astoin agree fairly well. At many wavelengths there are differences of a factor of two. Only Wainfan carried out ionization cross section measurements. The ionization cross section measurements are in many cases larger than any of the total absorption cross sections, so no firm approximation to the ionization efficiency can be made.

The use of line background sources in experiments generally means that little or no information is obtained about possible preionized bands that conceivably might contribute much to the total ionization. It is apparent from experiments with a continuum background source that the Hopfield series converging to the B $^2\Sigma_u^+$ state are broadened and have a minimum in the continuum on the low wavelength side. Experiments by Comes and Lessman [1961] indicate that many of the bands at wavelengths other than the Hopfield series are also preionized. From the data, however, it is difficult to make exact assignments.

When the absorbed photon is sufficiently energetic, dissociative photoionization must be considered; in N_2 this occurs at 510 Å. Figure 6-11 shows data obtained using a mass spectrometer to detect the masses of the product ions formed by ultraviolet radiation. Although the data are not calibrated in an absolute sense, it is apparent that the dissociative ionization process in N_2 is

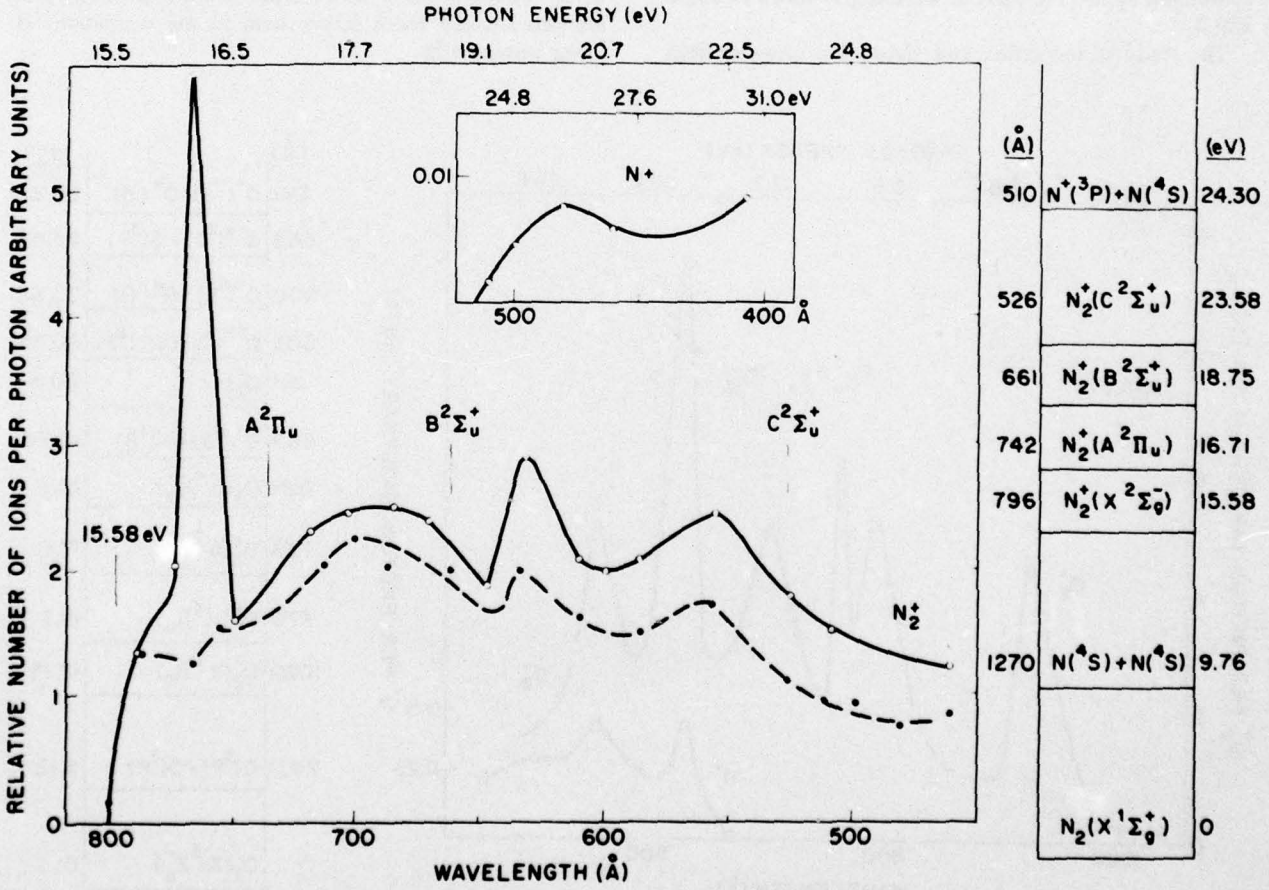


Fig. 6-11. Yield of N_2+ per incident photon from photoionization of N_2; insert shows yield of N+. Solid curve obtained with air-helium mixture, dashed curve with argon, in the light source. (Data from Weissler et al [1959].)

about two orders of magnitude less than the molecular ionization process. On the basis of these results, contributions to ionization from this source can be neglected. Further studies of this type are necessary, however, to rule out spurious effects, such as differences of collection efficiencies of the mass spectrometer at the two mass peaks.

6.3.2 Molecular Oxygen

The strong Schumann-Runge absorption bands of O_2 occur at wavelengths of 2000 Å and below. The bands merge with the intense Schumann-Runge dissociation continuum extending to wavelengths shorter than 1750 Å. Absorption in the region between 1750 and 1250 Å results in a large fraction of all the oxygen above about 110 km altitude being in the atomic state. Between 1250 and 1050 Å, the spectrum of O_2 is complex, making assignments difficult. Seven windows (deep minima in the absorption coefficient curves) allow higher energy photons to penetrate below levels at which the 1250 to 1750 Å radiation is absorbed. (By coincidence, the strong solar emission line of atomic hydrogen, H Ly-α at 1216 Å, coincides with one of the deepest windows.) Below about 1025 Å, O_2 can be photoionized, and a definite continuum appears to exist at wavelengths down to about 150 Å.

The study of ionization and absorption cross sections of O_2 in the region from 1050 to 150 Å is complicated by strong molecular bands superimposed on the ionization continua. The bands are typically more diffuse than in N_2 and are not as numerous. The ionization continuum associated with the ground state of O_2^+ is much weaker than continua associated with higher, excited states of this ion. Strong absorption, apparently leading to ionization, begins in O_2 at about 800 Å, the same wavelength as in N_2.

Watanabe and Marmo [1956] mapped the so-called Hopfield bands and the underlying continuum in the region from 1025 to 850 Å and observed that these bands were strongly preionized. In general, the results of Lee [1955] agree with those of Watanabe and Marmo. At 1026 Å (Lyman β line of atomic hydrogen, which is present in the solar emission spectrum), the ionization cross section is 0.90×10^{-18} cm^2.

Below 850 Å, the measured cross sections give information principally about the envelope of the underlying continuum. Absorption spectra, however, continue to show a number of bands superimposed on the continua; this region should be mapped to obtain a more complete picture of the absorption processes. At wavelengths that appear to correspond to the threshold of the a $^4\Pi_u$ state of O_2 (about 770 Å), the absorption and ionization cross sections become much larger than in the continuum at lower wavelengths.

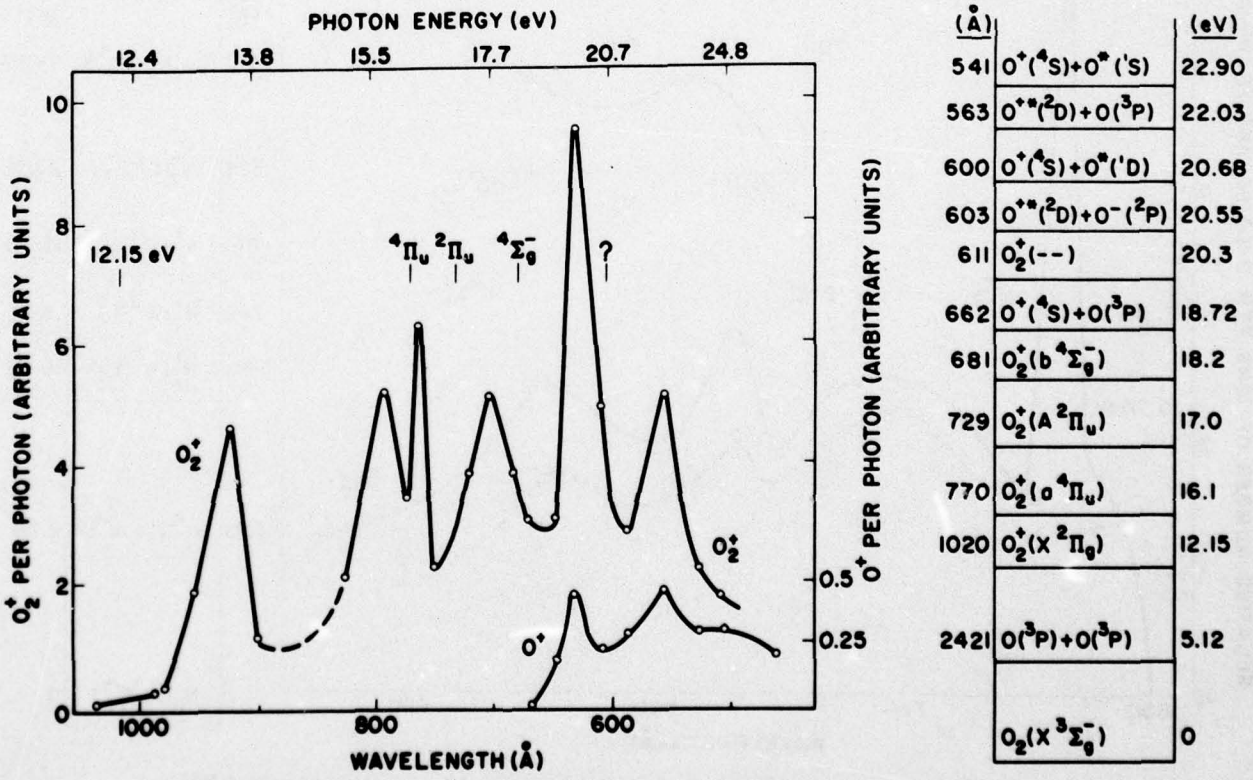


Fig. 6-12. Yields of O_2+ and $O+$ per incident photon from photoionization of O_2 and O. (Data from Weissler et al [1959].)

Dissociative ionization of O_2 is first energetically possible at 662 Å. Figure 6-12 shows that the process is more effective than in the case of N_2; however, the relative scarcity of O_2 at altitudes where radiation of this wavelength is absorbed makes this process relatively unimportant.

6.3.3 Nitric Oxide

Nitric oxide is formed and destroyed by an involved chain of reactions with atomic oxygen and atomic nitrogen. It was predicted to be an atmospheric component in the transition region around 100 km where O_2 is converted to O by photodissociation. The concentration necessary to be significant in forming the D region is very small; Jursa et al [1959] determined an upper limit of 10^{-8} cm^{-3} in the D region atmosphere. The NO^+ ion has been observed with rocket-borne mass spectrometers. Because theoretical calculations indicate that the amount of NO necessary to account for the D region would be very difficult to detect, the lack of definite composition data is not considered to rule out the currently accepted theory. An intense source of ionizing radiation that extends to altitudes of the D region is the solar emission of H Ly-α radiation; it penetrates one of the O_2 windows.

Nitric oxide ionizes at 9.25 eV (about 1340 Å), the lowest ionization potential of any atmospheric diatomic molecule. This is related to the fact that NO^+ has the largest dissociation energy of the atmospheric positive molecular ions, being isoelectronic with the very stable N_2 and CO.

Figure 6-13 shows photoionization and absorption cross sections in the region between 1100 and 1350 Å. In this figure the ionization continuum appears almost like a step function, rising sharply at the ionization potential; this is characteristic of photoionization continua. Other sharp rises in the ionization cross section curve correspond in energy to the vibrational energy spacings of the ground state of the molecular ion. The ionization efficiency starts fairly low, but below 1225 Å attains values close to unity. There are no strongly preionized lines in this wavelength region. There is little indication of the onset of photoionization in the absorption cross section curve. The general structure of the photoionization curve was confirmed [Hurzeler et al, 1958]. Watanabe [1958] gives 2.02×10^{-18} cm^2 as the ionization cross section at 1216 Å (H Ly-α).

Figure 6-14 shows absorption cross section data at wavelengths below 1080 Å. It is apparent from the curves that additional work on the spectrum of NO below 1080 Å is needed. Photoionization cross sections to about 700 Å were determined by Walker and Weissler [1955], and dissociative ionization by Weissler et al [1959].

6.3.4 Atomic Oxygen and Nitrogen

Incoming solar photons in the altitude regions where the ionospheric layers are formed encounter an atmosphere composed primarily of N_2, O, O_2, and perhaps N. Because of the slower recombination processes of atomic ions, photoionization processes with atomic species are likely to contribute more to the steady-state ion concentration. The atomic species, however, are extremely reactive chemically, compared with other neutral atmospheric components. They readily recombine to the molecular form (either in the gas or on the walls of experimental apparatus) and react with other gases present. (They also ionize in the region where laboratory experiments are difficult.)

The treatment of atomic photoionization processes by theoretical methods, however, is more feasible than the treatment of molecular processes, so there are theoretical

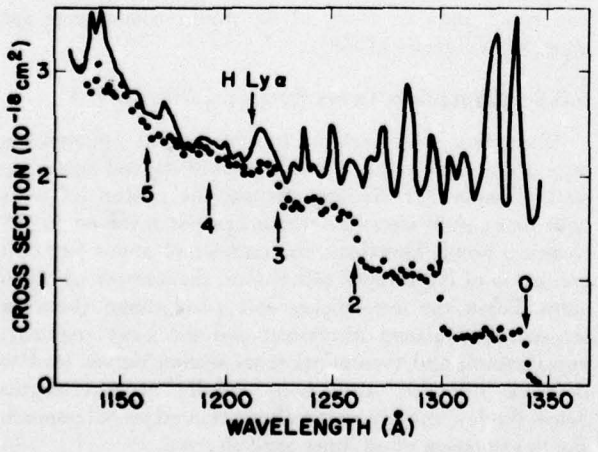


Fig. 6-13. Total absorption cross section (solid curve) and photoionization cross section (dots) of NO. (After K. Watanabe, *J. Chem. Phys.*, v. 22, p. 1564, 1954, and F. F. Marmo, *J. Opt. Soc. Am.*, v. 43, p. 1186, 1953.)

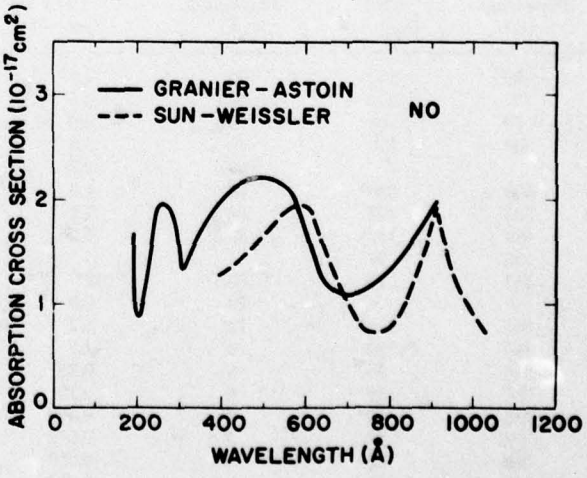


Fig. 6-14. Absorption cross section of NO; the smooth curves indicate the envelope of absorption continua. (Data from J. Granier and N. Astoin, *Compt. Rend.*, v. 242, p. 1431, 1956; H. Sun and G. L. Weissler, *J. Chem. Phys.*, v. 23, p. 1372, 1955.)

Table 6-5. Photoionization coefficients for atomic oxygen. (From A. Dalgarno and D. Parkinson, *J. Atm. Terrest. Phys.*, v. 18, p. 335, 1960.)

Wavelength (Å)	Coeff (cm^{-1})	Wavelength (Å)	Coeff (cm^{-1})
911	70	153	59
769	91	131	40
732	94	115	30
		100	23
732	200*	83	14
665	230	70	35
		52	6.2
665	300*	40	3.2
587	350	34	2.4
525	350	30	1.8
475	350	26	1.1
455	300	22.8	.54
435	260		
		22.8	14*
435	350*	20	11
400	320	15	5.4
365	270	8	0.97
315	220	6	0.43
310	210	5	0.26
		4	0.13
310	270*	3	0.056
290	250	2.5	0.035
270	220	2.0	0.018
245	170	1.5	0.018
220	140	1.0	0.0024
185	91		

* Value for the higher ionization potential.

Table 6-6. Photoionization coefficients for atomic nitrogen. (From A. Dalgarno and D. Parkinson, *J. Atm. Terrest. Phys.*, v. 18, p. 335, 1960.)

Wavelength (Å)	Coeff (cm^{-1})	Wavelength (Å)	Coeff (cm^{-1})
852	240	108	4.0
727	270	96	3.5
634	300	79	3.0
608	270	73	3.0
		63	2.7
608	380*	49	1.9
536	270	34	1.1
480	180	30.3	0.86
396	97		
367	70	30.3	19*
		20	7.0
367	150*	15	3.2
340	120	10	1.1
316	94	6	0.25
278	59	5	0.15
248	40	4	0.078
223	27	3	0.032
203	20	2.5	0.019
166	10	2.0	0.010
141	6.5	1.5	0.0043
122	4.6	1.0	0.0014

* Value for the higher ionization potential.

values for O and N cross sections. Bates and Seaton [1949] computed values for O and N at energies up to 12.5 eV above the ionization potentials; their calculations are thought to be within a factor of two of the correct values. Tables 6-5 and 6-6 list calculated photoionization coefficients of O and N, covering the range from the ionization potentials to 0.1 Å in the x-ray region. These values agree with previous calculations and agree fairly well with experimental data in the x-ray region; there are few experimental results for comparison in the vacuum ultraviolet region. The one experimental study of the absorption cross section of N was by Ehler and Weissler [1955]. The observed values at a few wavelengths agree well with the calculations of Bates and Seaton. At present, there does not appear to be any published experimental work on absorption cross sections of O.

Calculations of this type give information only on the principal ionization continuum and not on superimposed absorption lines that may be preionized or may absorb solar emission lines strongly. This is unfortunate because strongly autoionized lines have been found in the spectra of the vapors of a number of metallic elements in the vacuum ultraviolet and the location of similar cases in the atomic atmospheric gases could have important consequences for ionospheric problems.

6.3.5 Minor Constituents

There are a number of molecular and atomic constituents that might contribute to the primary ionization yield. Such gases may be important in connection with release of chemicals in the upper atmosphere for controlled experiments or as a by-product of the numerous operations carried on in the ionosphere in the course of space exploration and study. A partial list of these species includes ozone, sodium atoms, nitrous oxide, water vapor, carbon dioxide, the rare gases, atomic and molecular hydrogen, carbon monoxide, methane, and ammonia. The observation of significant amounts of Ca^+ and Mg^+ in the atmosphere indicates that other materials also may be important. Data on many of the minor constituents are given by Watanabe [1958].

6.3.6 Absorption Cross Sections, 100 to 1 Å

Absorption cross sections for this region (photon energy about 120 to 12,000 eV) do not depend upon the state of molecular binding, because the photon interacts with inner shell electrons which are not involved in the chemical bond. Therefore, the number of atoms per unit volume is of importance rather than the number of molecules. Below the overlapping soft x-ray range (between the extreme vacuum ultraviolet and the x-ray regions), experimental and theoretical cross section curves tend to decrease smoothly and monotonically at wavelengths below the few sharply rising absorption edges corresponding to excitation of an inner shell electron.

The tremendous energy of each x-ray photon (compared with the lowest ionization energy required) results in secondary processes that follow the initial absorption and yield a number of ion-pairs per photon consumed.

The average value of 35 eV is used in calculations as the quantity of energy required to create one ion-pair in air. The absorption coefficients in the x-ray region are typically smaller than in the vacuum ultraviolet region and the spectrum is simpler. Most of this energy is deposited in the E region of the ionosphere. The region 1 to 10 Å is considered somewhat less important because this radiation has been detected only during the brief periods of solar flares.

Figure 6-15 shows a composite spectrum of the mass absorption coefficient for air in the region 7 to 100 Å. The mass absorption coefficient is k/ρ, where ρ is the density. At wavelengths below 7 Å, the cross section continues to decrease rapidly. Theoretical calculations of k are given in Tables 6-5 and 6-6. The values seem to be adequate for making ionospheric calculations. Minor constituents containing atoms other than nitrogen and oxygen are not thought likely to give rise to special ionospheric phenomena following absorption in this wavelength range.

6.3.7 Average Absorption Coefficients

In making calculations of ion production rates with presently available data on solar flux and neutral specie composition, it is usually permissible to use cross section values averaged over broad wavelength ranges in combination with special values for those solar emission lines in which much of the flux is concentrated (Sec. 16.2). Table 6-7 lists average values of absorption coefficients that are satisfactory for ion production rate calculations in the E and F regions; only N_2, O, and O_2 are known to be important in the wavelength region 1027 to 10 Å. The total absorption above a given altitude must be considered in determining the flux available for photoionization at that altitude. Large amounts of the incident solar flux between 800 and 1026 Å are absorbed by N_2 and are not available to ionize O_2 and O; this is particularly true at 972.5 Å (H Ly-γ emission line). Over many ranges it is not possible to gave an average value for N_2 absorption because of the strength of the molecular bands superimposed on the continuum. This molecular band absorption variation decreases the value of compilations such as Table 6-7; it illustrates the complexity of the total atmospheric absorption problem. When making calculations in these regions, the appropriate averages for N_2 in the 850 to 1000 Å range may be estimated from the data of Watanabe and Marmo [1956]. The absorption and ionization cross sections are considered to be equal for these calculations.

For absorption in the D region, the wavelength range from 1026 to 1400 Å, which causes the ionization of nitric oxide, must be considered. The cross sections may be read from Figure 6-13.

6.4 RECOMBINATION

The recombination of positive ions with free electrons is one of two principal processes by which free electrons are removed from the upper atmosphere; the other process is formation of negative ions by direct attachment. Every electron-ion recombination is the reverse of an ionization process and is exothermic. The recombination energy must be disposed of in some way, and the mechanisms that dissipate this excess energy provide a convenient means of classifying recombination reactions; for an extensive discussion of these processes, see Massey [1952].

On the basis of information currently available (1962), the recombination processes that exert a significant influence in the upper atmosphere are radiative, dissociative, and ion-ion. There is not yet sufficient evidence to justify consideration of differences between recombination coefficients of specific ions. The variation of recombination coefficient with temperature is not yet known for either dissociative or ion-ion recombination. In radiative recombination, where theoretical values are available as a function of temperature, the variations over the temperature range of interest are insignificant for most purposes. Table 6-8 gives the best current values of the three significant recombination coefficients recommended for application to ionospheric dynamics; dielectronic recombination is included in the radiative term. Three-body recombinations are regarded as negligible in comparison with the others for all altitudes above 40 to 50 km.

6.4.1 Radiative Recombination

Radiative recombination, defined as

$$X^+ + e^- = X + h\nu, \qquad (6\text{-}5)$$

is the predominant recombination reaction occurring at very high altitudes, where the probability of three-body

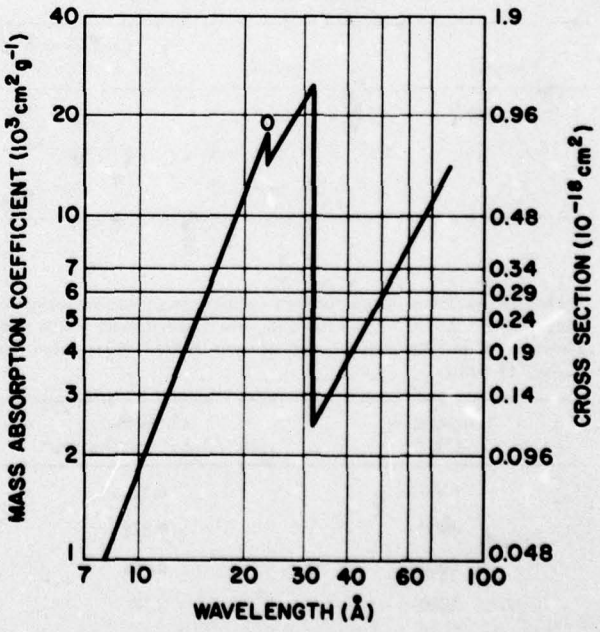


Fig. 6-15. Mass absorption coefficient and absorption cross section for air. (After E. T. Byram, T. A. Chubb, and H. Friedman, *J. Geophys. Res.*, v. 61, p. 251, 1956.)

Table 6-7. Average values of absorption coefficients. (After P. J. Nawrocki and R. Papa, Contract AF19(604)-7405 *AFCRL Rept. No. 595, Geophysics Corporation of America Tech. Rept. No. 61-37-A.*)

Wavelength (Å)	Average Absorption Coefficient (cm^{-1})		
	O	O_2	N_2
1025.7	0	45	0
1011 (lines)	0	30	0
1000-1026	0	40	0
989.8	0	60	20
977.0	0	90	50
972.5	0	1000	7600
949.7	0	200	100
937.8	0	250	200
934, 944	0	100	50
911-1000	0	200	*
850-911	100	250	*
796-850	100	400	*
732-796	100	600	*
500-732	300	600	*
584.3	300	540	520
303.8	270	500	250
300-500	300	500	*
250-300	250	400	300
170-250	150	300	200
100-170	60	150	100
60-100	—	—	30**
30-60	—	—	10**
20-30	—	—	20**
10-20	—	—	30**

* Not averagable
** Mean for air

Table 6-8. Recombination coefficients.

Process	Reaction	Coefficient ($cm^3\ sec^{-1}\ ion^{-1}$)
Radiative	$X^+ + e^- = X + h\nu$	10^{-12}
Dissociative	$XY^+ + e^- = X + Y$	2.5×10^{-7}
Ion-Ion	$X^+ + Y^- = X + Y$	10^{-8}

Table 6-9. Radiative recombination coefficients at various electron temperatures for O^+; values for other atmospheric ions are assumed to be the same order of magnitude. (Calculated by Massey [1952].)

Temperature (°K)	Coefficient ($10^{-12}\ cm^3\ sec^{-1}\ atom^{-1}$)
8000	0.224
4080	0.379
2000	0.683
1020	1.17
500	1.98
222	3.34

processes is low because of the particle densities, and dissociative recombination is minimized by the high abundance ratios of atomic to molecular ions. Table 6-9 lists theoretical values of radiative recombination coefficients of O^+. Massey estimates that these values are accurate to within better than an order of magnitude, and that in no case involving thermal electrons are they likely to exceed $10^{-11}\ cm^3\ sec^{-1}\ atom^{-1}$. A more recent calculation on O^+ [Breene, 1961] gives a coefficient of $2.18 \times 10^{-12}\ cm^3\ sec^{-1}\ atom^{-1}$ at an electron temperature of 500°K, which agrees well with Massey's value. In the absence of any direct experimental determinations, the radiative recombination coefficients for all atmospheric ions are assumed to be around $10^{-12}\ cm^3\ sec^{-1}\ atom^{-1}$.

A special (two step) case of radiative recombination is *dielectronic recombination.* This process is the reverse of autoionization. A positive ion captures an electron and goes into a doubly excited (autoionizing) state of the corresponding neutral atom; then, if the electron is not first reemitted, the atom undergoes transition by radiation into a stable state. The final step is thus a race between radiation and autoionization. Dielectronic recombination needs to be considered only when autoionizing states of the atom lie within a few tenths of an electron volt of the ionization threshold and the absorption cross sections for the particular autoionizing states involved are very large compared with the ionization cross section (as is the case when the autoionizing state has an extremely short radiative lifetime). Theory predicts that, because the available doubly excited states lie too high above the ionization thresholds to be accessible to thermal electrons, rate coefficients greater than $10^{-12}\ cm^3\ sec^{-1}\ atom^{-1}$ are quite improbable for atmospheric ions. Garton et al [1960] determined the dielectronic recombination coefficient of argon to be slightly higher than the estimate, about $5 \times 10^{-11}\ cm^3\ sec^{-1}\ atom^{-1}$. Until more information is available, however, dielectronic recombination coefficients for all atmospheric ions are assumed to be about $10^{-12}\ cm^3\ sec^{-1}\ atom^{-1}$ and are included in the radiative recombination term.

6.4.2 Dissociative Recombination

Dissociative recombination is defined as

$$XY^+ + e^- = X + Y; \qquad (6\text{-}6)$$

X may be the same element as Y. The excess energy released by recombination of molecular ions can be dissipated as radiation or as kinetic and internal energy of dissociating fragments. Theoretically, the dissociative recombination coefficient may be as large as $10^{-7}\ cm^3\ sec^{-1}$ $molecule^{-1}$ [Bates, 1950]; this has been substantiated experimentally. Dissociative recombination is the most significant recombination process at altitudes where molecular ions are prevalent (the D and E, and perhaps the lower F regions of the ionosphere), except where the density is too low for the three-body processes to be controlling.

When the potential curve for a repulsive state of the neutral molecule intersects the curve for the ground state of the ion near its lowest vibration level, and when the colliding electron has little kinetic energy, the ion-electron system is in energy resonance with the repulsive state of the molecule. The electron-ion collision can then induce a radiationless transition to this neutral repulsive state; the resulting neutral can either undergo autoionization back to the stable ion-electron system or dissociate into its neutral fragments to complete the electrical recombination. There is a high probability of recombination with dissociation, because a change of much less than 10^{-8} cm in the nuclear separation should be sufficient to move the system well away from the crossing point of the two potential curves. This reduces the probability of autoionization to negligible levels, and because the time required to accomplish this is ordinarily less than the 10^{-13} sec that is characteristic of autoionization, there is a high probability of recombination with dissociation.

A large number of experimental measurements of dissociative recombination coefficients have been reported in the literature. In most instances, however, there is either some uncertainty as to the identity of the particular ion undergoing recombination, or a question of whether the effects of diffusion might have influenced the data. For example, experimental values reported for the dissociative recombination coefficient of N_2^+ at electron temperatures of about 300°K vary from a high of 1.4×10^{-6} cm^3 sec^{-1} molecule^{-1} to a low of 10^{-10} cm^3 sec^{-1} molecule^{-1}.

The value of 4×10^{-7} cm^3 sec^{-1} molecule^{-1} at 400°K for N_2^+ [Faire and Champion, 1959] is in good agreement with privately communicated (June 1962) revisions of values presented by W. H. Kasner, W. A. Rogers, and M. A. Biondi, *Phys. Rev. Letters*, v. 7, no. 8, p. 321, 1961. The revised values represent the best estimates which these authors are able to make based on corrections of their experimental data using calculations of E. P. Gray and D. G. Kerr, *Ann. Phys.*, v. 17, p. 276, 1962. These values, which were obtained by using an inert gas to reduce diffusion effects and a mass spectrometer to identify the ions, are regarded as the best currently available and probably definitive. They are, in units of cm^3 sec^{-1} molecule^{-1}, $(3.0 \pm 0.5) \times 10^{-7}$ for N_2^+, $(2.0 \pm 0.5) \times 10^{-7}$ for O_2^+, and approximately 1×10^{-6} for N_3^+ and N_4^+ combined. (They also showed that N_3^+ and N_4^+ become significant at nitrogen partial pressures above 0.01 mm Hg and predominant at pressures above 0.1 mm Hg.) Syverson et al [1962] reports the coefficient of NO^+ as 1.3×10^{-7} cm^3 sec^{-1} ion^{-1} at about 3000°K on the basis of shock tube experiments, whereas an earlier report from the same laboratory by Gunton et al [1962] gave a value of about 1×10^{-6} cm^3 sec^{-1} ion^{-1}, based on charge decay experiments and presumably determined at much lower temperature than the first value.

In the absence of more definitive experiments on NO^+, and in view of the uncertainties quoted for O_2^+ and N_2^+, it seems reasonable to use a value of about 2.5×10^{-7} cm^3 sec^{-1} ion^{-1} for the dissociative recombination coefficients of all three major atmospheric molecular ions (N_2^+, O_2^+, and NO^+). Because of a lack of information, the effects of temperature on the rate of dissociative recombination must be neglected at this time (1962).

The excess energy from dissociative recombination goes into internal and kinetic energy of the two neutral fragments, and these energetic neutrals can be the cause of otherwise improbable processes. For example, the 6300 Å oxygen line observed in the night airglow (Sec. 13.1) is widely interpreted to result from dissociative recombination of O_2^+, in which one of the separating atoms is formed in the ^1D state.

6.4.3 Three-Body Recombination

Dissipation of recombination energy by transfer to a third body,

$$X^+ + e^- + M = X + M \qquad (6\text{-}7)$$

is considered to be negligible at altitudes of the E region and above. Massey [1952] concludes that the rate coefficient may be as high as $2 \times 10^{-11} \times P$ (cm^3 sec^{-1} molecule^{-1}), where P is the pressure in mm Hg. On this basis, three-body recombination will be slower than radiative recombination at altitudes above ≈ 60 km (pressures below about 0.1 mm Hg). Throughout the ionosphere, therefore, three-body recombination is now (1962) considered negligible compared with radiative and dissociative recombination.

6.4.4 Ion-Ion Recombination

The net effect of ion-ion recombination is electron removal, and it must be considered in ionospheric dynamics, particularly in those regions where the electron attachment processes are fast and where the ratio of negative ions to free electrons is high. Without regard to the mechanisms of either reaction, the two-step process of electron removal by ion-ion recombination is first electron attachment (Sec. 6.5), then ion-ion recombination,

$$X^- + Y^+ = X + Y. \qquad (6\text{-}8)$$

A large number of specific ion-ion recombinations are recognized as being of possible significance in the upper atmosphere, but very little information is available concerning the rates of these reactions. Massey [1950] concludes that the rate coefficient for the $O^+ + O^-$ reaction is probably as high as 10^{-8} cm^3 sec^{-1} molecule^{-1} at room temperature, and may be an order of magnitude higher. Experiments by Yeung [1958], which yielded two-body mutual neutralization coefficients of 1.47×10^{-8} and 1.85×10^{-8} cm^3 sec^{-1} molecule^{-1} for iodine and bromine, respectively, tend to support this conclusion.

Until more adequate information becomes available, a specific rate constant of about 10^{-8} cm^3 sec^{-1} ion^{-1} is assumed to be characteristic of Eq. 6-8 for ions that occur in the ionosphere. Three-body ion-ion processes are regarded as negligible at all ionospheric altitudes.

6.5 ELECTRON ATTACHMENT

Negative ions may be formed in the ionosphere by attachment of electrons to electronegative atoms and molecules. This process leads to rapid removal of free electrons after sunset, when photodetachment is no longer able to reverse the process. The attaching electrons have low thermal energies. (Most laboratory experiments are done at somewhat higher energies, because measurements are difficult at such low energies.)

The *electron affinity* is the decrease in energy that occurs when a neutral atom or molecule combines with an electron to form a negative ion. The affinity must be positive for the negative ion to be stable. For molecules the electron affinity refers to the ground vibrational states of the lowest electronic states of the molecule and molecular ion. (Applications of the Franck-Condon principle to transitions between potential curves for the molecule and the molecular ion lead to situations where the electron affinity differs from the vertical detachment threshold and the radiative attachment threshold.) Table 6-10 lists the affinities for important constituents of the ionosphere.

Electrons may attach to molecules by a three-body process, in which a third unspecified particle carries away the excess kinetic energy; by dissociative attachment, in which the excess energy is removed by rupturing a molecular bond; and by radiative attachment, in which the excess energy is removed by emission of a photon. For atoms, three-body and radiative attachment can occur. Table 6-11, using O_2 and O as an example, lists these electron attachment processes and gives values for the oxygen rate coefficients.

Table 6-10. Electron affinities of atmospheric constituents.

Atom or Molecule	Electron Affinity (eV)	Reference
O	1.465 ± 0.005	Branscom et al [1958]
O_2	0.15 ± 0.05	Burch et al [1958]
	0.46 ± 0.02	Phelps & Pack [1961]
N	very small or negative	
N_2	very small or negative	
NO_2	> 3.82	Curran [1962]

Because measurements indicate that dissociative attachment occurs only at electron energies above 1 eV, and because the typical electrons have thermal energies around 0.025 eV, the processes to consider for attachment to molecular oxygen are three-body and radiative attachment. The rate of the three-body process varies as the square of the pressure, while the radiative process rate varies as the first power; therefore, the amount of radiative recombination will become larger at higher altitudes, until it finally becomes the only attachment process. On this basis, the three-body process is more important below roughly 100 km, and the radiative process more important above roughly 100 km. In addition, above 100 km there begins to be an appreciable concentration of oxygen atoms, which have a radiative attachment rate coefficient three orders of magnitude larger than the value for molecular oxygen.

Upper atmosphere mass spectrometric experiments revealed a negative ion of mass 46, assumed to be NO_2^-, in greater abundance than any other negative ion [Johnson et al, 1958]. Laboratory observations indicate that NO_2^- is more stable than O_2^-. NO_2^- forms rapidly by charge exchange with O^- and with many other negative ions in the ion source of a higher pressure mass spectrometer [Curran, 1962]. Its mechanism of formation in the upper atmosphere, however, is not known. Experiments [Fox, 1960] indicate that it does not form by direct attachment. It is possible that the ion is the most stable product of a series of charge transfer and other ion reactions, but available data do not yet allow detailed calculations.

6.6 ELECTRON DETACHMENT FROM NEGATIVE IONS

Electron detachment from negative ions is the primary mechanism for the production of free electrons in the upper atmosphere at night; it is also a significant secondary source of free electrons under sunlit conditions where photoionization of neutrals is the primary source. The production of a free electron and a positive ion as products of a reaction between two neutrals (chemionization) may be a significant source of free electrons, but not enough is known at this time (1962) about this proc-

Table 6-11. Electron attachment processes and rate coefficients for oxygen.

Process	Coefficient ($cm^3\ sec^{-1}$)	Reference
Three-body $e^- + 2O_2 = O_2^- + O_2$	2.8×10^{-30} ($T = 300$ °K)	Chanin et al [1959]
Dissociative $e^- + O_2 = O^- + O$	10^{-12} to 10^{-11} (at 1 to 4 V)	Chanin et al [1959]
Radiative $e^- + O_2 = O_2^- + h\nu$	2×10^{-18} ($T = 230$ °K)	Phelps & Pack [1961]
$e^- + O = O^- + h\nu$	1.3×10^{-15}	Haaland [unpublished]

ess in the upper atmosphere to justify its being considered in ionospheric dynamics. The production of negative ions by electron capture from energetic neutrals (such as atomic hydrogen) incident on the upper atmosphere has a very high cross section, and negative ions produced in this way provide electrons in addition to those initially produced by photoionization.

The energy required to detach the excess electron from a negative ion is much less than for ionization. Depending upon the source of this energy, there are two main types of atmospheric electron detachment reactions: photodetachment, in which the energy is supplied by absorption of radiation; and collisional detachment, in which the energy is furnished either by the kinetic energy or by the energy released from chemical reactions involved in collisions between the negative ion and other atmospheric particles.

6.6.1 Photodetachment

Photodetachment of negative ions,

$$X^- + h\nu = X + e^-, \qquad (6\text{-}9)$$

corresponds to photoionization of neutral species. The probability of occurrence per ion (or per molecule) in the upper atmosphere is quite different for the two processes, however. The minimum energy required for photodetachment is low. Almost all solar radiation incident on the atmosphere can photodetach electrons from negative ions. By contrast, photoionization requires so much energy that only solar radiation in the ultraviolet region can photoionize neutral atmospheric particles. Atmospheric photodetachment probabilities per ion (the product of the photodetachment cross section and the radiation flux integrated over the applicable range of wavelengths) are on the order of 1 sec^{-1}, whereas the corresponding photoionization probabilities per molecule are on the order of 10^{-6} to 10^{-8} sec^{-1}. The relative electron production rates of the two processes are a function of these probabilities and of the respective number densities of the negative ions and neutral molecules involved. In full daylight, therefore, the predominating process in electron production is still photoionization.

Experimental values for the photodetachment cross sections of O^- [Branscomb et al, 1958], and O_2^- [Smith et al, 1958] are available over almost all the wavelengths of interest. According to these investigators, the cross section for O^- rises smoothly from a well defined threshold at 8460 Å to a maximum of about 6.3×10^{-18} cm^2 at about 5800 Å, and is then nearly flat down to wavelengths below 4000 Å. For O_2^-, the cross section shows no threshold and no maximum over the range of wavelengths studied, but rises smoothly from about 3.75×10^{-20} cm^2 at 0.5 eV (24,800 Å) to about 2×10^{-18} cm^2 at 3 eV (4100 Å). These cross sections for photodetachment are comparable in magnitude to cross sections for photoionization, about 10^{-18} cm^2. For O^- the atmospheric photodetachment probability is given as 1.4 sec^{-1}, and for O_2^- as 0.44 sec^{-1}, corresponding to mean lifetimes of these ions with respect to photodetachment by solar radiation of about 0.7 and 2.3 sec, respectively.

Experimental data are not available for NO_2^-, but because of its high electron affinity (> 3.8 eV) it is expected to have a mean lifetime with respect to atmospheric photodetachment considerably longer than that for either O_2^- or O^-. (The detachment energy is not necessarily equal to the electron affinity for molecular negative ions, but a higher electron affinity does indicate a higher detachment energy.)

Electrons released in the atmosphere by photodetachment have sufficiently high kinetic energies to excite various other atmospheric processes of interest; for example, the energy distribution curve plotted from calculations of electrons photodetached from O_2^- shows a maximum at electron energies of almost 2 eV.

6.6.2 Collisional Detachment

Pure collisional detachment is defined as

$$X^- + Y = X + Y + e^-. \qquad (6\text{-}10)$$

(Collisional detachment in which the colliding particle is a free electron is regarded as insignificant in the ionosphere.) Data on collisional detachment from atmospheric negative ions are available only for molecular oxygen; however, there is no reason to suppose that pure collisional detachment coefficients for other atmospheric ions would be greater than those for O_2^-. Phelps and Pack [1961] indicate that for O_2^-, the rate coefficient for Eq. (6-10) increases very rapidly with increasing temperature, and the presence of N_2 has little influence on the detachment rate. Their values are 4×10^{-20} (cm^3 sec^{-1} $molecule^{-1}$) at 230°K, 1×10^{-16} at 400°K, and 2.5×10^{-15} at 500°K. Their conclusion that some alternative detachment process must be found to explain the observed nighttime electron densities in the lower ionosphere is widely accepted. Associative detachment that involves species (probably atomic oxygen) not present in their apparatus has been suggested [Whitten and Poppoff, 1962] as the required alternative.

Associative detachment is a special case of Eq. (6-10) in which a chemical bond (XY) is formed as a result of the collision;

$$X^- + Y = XY + e^-. \qquad (6\text{-}11)$$

Information available (1962) on associative detachment is speculative. Bates and Massey [1951] suggested that the rate coefficient may be greater than 5×10^{-14} cm^3 sec^{-1} $molecule^{-1}$ for the reaction

$$O_2^- + O = O_3 + e^-.$$

Reactions of interest in investigations of the upper atmosphere for which there are no definitive data or calculations are:

$$O^- + O = O_2 + e^-,$$
$$O^- + O_3 = O_2 + O_2 + e^-,$$
$$O^- + N = NO + e^-,$$
$$O^- + N_2 = N_2O + e^-.$$

Because estimates of the rate coefficients for Eq. (6-11) are consistently orders of magnitude greater than the experimental values for Eq. (6-10), associative detachment is usually assumed to predominate in the ionosphere, although there is not yet enough reliable information to permit quantitative consideration of associative detachment in ionospheric dynamics.

Bailey's [1959] determination of the effective ionospheric collisional detachment coefficient from ionospheric data was independent of both the identity of the negative ion and of the mechanism assumed. His value, $k = 10^{-17}$ cm^3 sec^{-1} ion^{-1}, is recommended for ionospheric calculations. This value for the effective collisional detachment coefficient, however, will almost certainly prove to be altitude dependent when more data become available. In the meantime, without regard to mechanism or identity of negative ions, collisional detachment can be treated as follows:

$$dN_e/dt = kN_n N_T, \qquad (6\text{-}12)$$

where N_e is the electron number density, N_n is the number density of negative ions, N_T is the total particle number density at the altitude in question, and k, Bailey's effective ionospheric collisional detachment coefficient, is 2×10^{-17} cm^3 sec^{-1} ion^{-1}.

6.7 NON-DETACHMENT REACTIONS OF NEGATIVE IONS WITH NEUTRALS

Negative ion reactions that merely change the identity of the negative ion,

$$X^- + Y \rightarrow X + Y^-, \qquad (6\text{-}13)$$

obviously do not affect the total number of negative ions present in the system. These reactions, however, are potentially important because the rates of the detachment and ion-ion reactions that do affect the total ion and electron concentration in the upper atmosphere depend upon the specific negative ions involved; e.g., compare the photodetachment probabilities for O^- and for O_2^-. Although information on the kinetics of these reactions of negative ions with neutrals is insufficient to justify their inclusion in quantitative treatments of ionospheric dynamics at this time (1962), enough information is available to give a qualitative idea of their probable effects.

Bates and Massey [1951] estimate that at ionospheric temperatures the rate coefficients for the reactions.

$$O_2^- + H \rightarrow O_2 + H^-,$$

and

$$O_2^- + H \rightarrow OH + O^-,$$

are each greater than 5×10^{-13} cm^3 sec^{-1} ion^{-1}. Several other simple charge transfer reactions involving H^- are possible in the upper atmosphere but are of doubtful significance, except perhaps at very high altitudes, because of the low hydrogen concentrations.

For the reaction

$$O^- + O_2 \rightarrow O_2^- + O,$$

which is endothermic, experiments [Thompson, 1959] established that the upper limit for the reaction cross section is 2×10^{-17} cm^2 at ion temperatures corresponding to a mean energy of 0.15 eV. This gives an upper limit to the rate coefficient of 2.7×10^{-12} cm^3 sec^{-1} ion^{-1}.

From quantitative studies of the formation of NO_2^- by charge transfer or ion-atom interchange reactions with O^-, SF_6^-, SF_5^-, and Cl^- in a mass spectrometer, Curran [1962] derived cross sections ranging from 8×10^{-16} to 7×10^{-15} cm^2 for ion kinetic energies less than 0.5 eV plus any kinetic energy of formation. Assuming that the O^- in the experiments was formed with zero kinetic energy and that the value of the cross section for the reaction

$$O^- + NO_2 \rightarrow NO_2^- + O$$

was about 10^{-15} cm^2, the upper and lower limits for the rate coefficient are $5 \times 10^{-11} \leq k \leq 2.4 \times 10^{-10}$ (cm^3 sec^{-1} ion^{-1}) at thermal, or near thermal, energies. The lower limit is obtained by assuming the minimum thermal energy of O^- in the experiment was about 0.025 eV.

For the reaction

$$O_2^- + O \rightarrow O^- + O_2,$$

Bates and Massey [1951] suggest that the rate coefficient is less than 5×10^{-14} cm^3 sec^{-1} ion^{-1}. Other such reactions that were observed in mass spectrometers are regarded as being negligible in the upper atmosphere at this time (1962).

6.8 REACTIONS OF POSITIVE IONS WITH NEUTRALS

In this section, the process

$$WX^+ + YZ \rightarrow WXY^+ + Z \qquad (6\text{-}14)$$

in which a chemical bond is broken and a new bond formed is called an ion-molecule reaction. The term *charge exchange* is restricted to simple transfer of charge, such as

$$X^+ + Y \rightarrow X + Y^+ \text{ or } X^{++} + Y \rightarrow X^+ + Y^+. \qquad (6\text{-}15)$$

These processes are believed to be important in determining the composition of the upper atmosphere. Because of difficulties in producing thermal or nearly thermal ion beams for experimental studies and in calculating theoretical cross sections for thermal energy processes, information on low-energy reactions involving the positive ions of interest (O^+, O_2^+, N^+, N_2^+, and NO^+) is sparse.

The ion-molecule reactions of principal interest, together with the energeticities (assuming reactants and products are in their ground states), are:

(1) $O_2^+ + N_2 \rightarrow NO^+ + NO + 1.2\,eV$
(2) $O_2^+ + N \rightarrow NO^+ + O + 4.3\,eV$
(3) $O^+ + N_2 \rightarrow NO^+ + N + 1.2\,eV$
(4) $O^+ + O_2 \rightarrow O_2^+ + O + 1.4\,eV$
(5) $O^+ + NO \leftrightarrows O_2^+ + N + 0.0\,eV$
(6) $O^+ + NO \rightarrow NO^+ + O + 4.4\,eV$
(7) $N_2^+ + O_2 \rightarrow NO^+ + NO + 4.5\,eV$
(8) $N_2^+ + O \rightarrow NO^+ + N + 3.1\,eV$
(9) $N^+ + O_2 \rightarrow NO^+ + O + 6.7\,eV$
(10) $N^+ + NO \rightarrow NO^+ + N + 5.3\,eV$
(11) $N^+ + NO \rightarrow N_2^+ + O + 2.2\,eV$
(12) $N_2^+ + N \rightarrow N^+ + N_2 + 1.0\,eV$
(13) $N^+ + O_2 \rightarrow NO + O^+ + 2.3\,eV$
(14) $N_2^+ + NO \rightarrow NO^+ + N_2 + 6.3\,eV$
(15) $O_2^+ + NO \rightarrow NO^+ + O_2 + 3.0\,eV$

Of these processes, only reactions (1), (3), (4), (7), and (9) have been studied in the laboratory, and for these there is not good agreement among different investigators.

All conceivable processes between ground state NO^+ and the principal neutral atmospheric constituents except NO itself are endothermic under thermal conditions; thus the disappearance of ground state NO^+ can be due only to ion-electron recombination. Under night conditions, when there can be no photoionization of the products of recombination, the formation of NO^+ by ion-molecule reactions represents an essentially irreversible loss of nitrogen (or oxygen) ions from the atmosphere. For this reason, a knowledge of the rate constants of the ion-molecule reactions producing NO^+ is important in theories of atmospheric dynamics. The restriction to ground state NO^+ is necessary, however, because an internal energy of about 1.2 eV, if it were completely convertible to reaction energy, would make $NO^+ + N \rightarrow N_2 + O^+$, the reverse of reaction no. (3), exothermic.

Reactions (4), (6), (10), (14), and (15) could be either simple charge exchange or ion-molecule reactions; the predominant mechanism may depend upon the energy. The processes might be distinguished by laboratory experiments using isotopic labeling, but this has not yet been done.

Although no exothermic ion-molecule reaction so far investigated is known to have an activation energy, it is probable that the measured rate constants for reactions (3), (4), and (9) are considerably lower than predicted because of such an effect. Rate coefficients measured near 300°K should, therefore, be used with caution in regions of widely different temperature. The available evidence from studies of endothermic ion-molecule reactions indicates a threshold at the ion kinetic energy corresponding to the endothermicity. Under normal atmospheric conditions, then, ion-molecule reactions endothermic to more than about 0.2 eV may be neglected. In missile exhausts, because of the high kinetic energy of the emerging exhaust products, reactions that are endothermic by several volts may occur.

At altitudes below 1000 km, additional species possibly present at very low relative concentrations are H^+, H_2^+, OH^+, H_2O^+, Ar^+, and CO_2^+. Ion-molecule reactions between these species and the major neutral constituents, or between the corresponding rare neutral species and the principal ion constituents, have received little attention.

Table 6-12 is a summary of data on positive ion charge exchange processes of interest in atmospheric physics. These values were collected from a variety of articles, abstracts, and unpublished technical reports for the period 1954 through 1961; space limitations preclude an evaluation and listing of each investigation. Some data on the charge exchange of protons and helium ions with nitrogen and oxygen are included because of the possible importance of such reactions in auroral physics.

Table 6-13 gives selected values of rate constants for several ion-molecule reactions of possible occurrence in the atmosphere and values calculated by the formula [Eyring et al, 1936],

$$k = 2\pi\kappa e\,(\alpha/\mu)^{1/2}, \qquad (6\text{-}16)$$

where e is the electronic charge, α is the polarizability of the reacting neutral, μ is the reduced mass of the reacting ion and neutral system, and κ (taken as unity in the calculations for Table 6-13) is the transmission coefficient. In most instances these calculated values are far greater than the observed rate constants. It is not clear whether or not these differences are due to activation energy requirements. The effect, however, would help to explain why some reactions apparently are faster when the reactant ions have energies in the one volt range than under thermal conditions, as appears to be the case for reaction (3), whereas others may be faster under thermal conditions (e.g., production of CH_5^+ from the reaction between CH_4^+ and CH_4).

Table 6-12. Positive ion-neutral charge exchange reactions.

Reaction	Incident Ion Energy (keV)	Max. Cross Section (10^{-16} cm^2)	Energy* at Max. (KeV)
$H^+ + N_2 \rightarrow H + N_2^+$	0.1-2.5	14.0	>2.5
	3.0-30	12.0	5.0
	3.6-36	16.0	<3.6
	4.0-200	12.0	<4.0
	10.0-1000	10.0	<10.0
$H^+ + O_2 \rightarrow H + O_2^+$	4.0-200	10.0	<4.0
$He^+ + N_2 \rightarrow He + N_2^+$	8.0-200	6.5	30
$He^+ + O_2 \rightarrow He + O_2^+$	8.0-200	8.0	20
$N_2^+ + N_2 \rightarrow N_2 + N_2^+$	0.005-1.0	36	<0.005
	0.01-0.25	25.0	<0.01
	0.05-0.85	25.1	<0.05
$N_2^+ + O_2 \rightarrow N_2 + O_2^+$	0.03-0.25	4.4	—
$N^+ + N_2 \rightarrow N + N_2^+$	0.03-0.25	1.8	>0.25
$N^+ + O_2 \rightarrow N + O_2^+$	0.03-0.25	8.0	—
$NO^+ + NO \rightarrow NO + NO^+$	0.1-0.8	10.3	<0.1
$O_2^+ + N_2 \rightarrow O_2 + N_2^+$	0.03-0.25	2.6	—
$O_2^+ + O_2 \rightarrow O_2 + O_2^+$	0.009-0.25	12.0	<0.009
	0.04-0.85	13.1	<0.04
	0.1-0.8	18.4	<0.1
$O^+ + N_2 \rightarrow O + N_2^+$	0.007-0.85	3.7	<0.85
	0.03-0.25	4.4	—
$O^+ + O_2 \rightarrow O + O_2^+$	0.01-0.2	5.3	—
$O^+ + O \rightarrow O + O^+$	0.0001-1000	100**	<0.0001

* Energy at which maximum cross section occurs
** Theoretical value

Table 6-13. Rate constants for some ion-molecule reactions.

Reaction	Rate Constant (10^{-11} cm^3 sec^{-1})	Remarks
$O_2^+ + N_2 \rightarrow NO^+ + NO$	80	Eq. (6-16)
	<0.021	≈ 2.5 eV (Ref. 1)
$O^+ + N_2 \rightarrow NO^+ + N$	97	Eq. (6-16)
	0.47	thermal (Ref. 2)
$O^+ + O_2 \rightarrow O_2^+ + O$	91	Eq. (6-16)
	0.18	thermal (Ref. 2)
$N_2^+ + O_2 \rightarrow NO^+ + NO$	77	Eq. (6-16)
	<0.021	≈ 2.5 eV (Ref. 1)
$N^+ + O_2 \rightarrow NO^+ + O$	95	Eq. (6-16)
	50	thermal (Ref. 3)
$N_2^+ + N_2 \rightarrow N_3^+ + N$	83	Eq. (6-16)
	1	≈ 4 eV (Ref. 4)
$O_2^+ + O_2 \rightarrow O_3^+ + O$	74	Eq. (6-16)
	≈ 20	(Ref. 5)

Table References:

1. A. Galli, A. Giardini-Guidoni, and G. G. Volpi, *J. Chem. Phys.*, v. 39, p. 518, 1963.

2. G. F. O. Langstroth and J B. Hasted. *Discussions of the Faraday Society*, no. 33, p. 298, 1962.

3. W. L. Fite, J. A. Rutherford, W. R. Snow, and V. A. J. Van Lint, *Discussions of the Faraday Society*, no. 33, p. 264, 1962.

4. C. F. Giese and W. B. Maier, *J. Chem Phys.*, v. 35, p. 1913, 1961.

5. V. Cermak and Z. Herman, *Jaderna Energie*, v. 6, p. 347, 1960.

6.9 REFERENCES

Bailey, D. K., 1959, "Abnormal Ionization in the Lower Ionosphere Associated with Cosmic Ray Flux Enhancements," *Proc. IRE*, v. 47, p. 255.

Bates, D. R. and H. S. W. Massey, 1951, "Negative Ion Concentration in the Lower Atmosphere," *J. Atmos. Terrest. Phys.*, v. 2, p. 1.

Bates, D. R., 1950, "Electron Recombination in Helium," *Phys. Rev.*, v. 77, p. 718.

Bates, D. R., 1950, "Dissociative Recombination," *Phys. Rev.*, v. 78, p. 492.

Bates, D. R. and M. J. Seaton, 1949, "The Quantal Theory of Continuous Absorption of Radiation by Various Atoms in their Ground States. II. Further Calculations on Oxygen, Nitrogen and Carbon," *Monthly Notices Royal Astron. Soc.*, v. 109, p. 698.

Branscomb, L. M., D. S. Burch, S. J. Smith, and S. Geltman, 1958, "Photodetachment Cross Section and the Electron Affinity of Atomic Oxygen," *Phys. Rev.*, v. 111, p. 504.

Breene, Jr., R. G., 1961, "Deionization Cross Section for Oxygen," *J. Chem. Phys.*, v. 35, no. 2, p. 625.

Burch, D. S., S. J. Smith, and L. M. Branscomb, 1958, Photodetachment of O_2^-," *Phys. Rev.*, v. 112, p. 171; Errata (1959), *Phys. Rev.*, v. 114, p. 1652.

Chanin, L. M., A. V. Phelps, and M. A. Biondi, 1959, "Measurement of the Attachment of Slow Electrons in Oxygen," *Phys Rev. Letters*, v. 2, p. 344.

Clark, K. C., 1952, "Ionospheric Absorption by N_2 and O_2 of Certain Extreme Ultraviolet Solar Wavelengths," *Phys. Rev.*, v. 87, p. 271.

Comes, F. J., and W. Lessmann, 1961, "Measurement of Excited States of the Nitrogen Molecule with the Help of Photoionization," *Zeit. Fur Naturforschung*, v. 16, p. 1038.

Cook, G. R., and P. H. Metzger, 1964, "Photoionization and Absorption Cross Section of O_2 and N_2 in the 600 to 1000 Å Wavelength Region," *J. Chem. Phys.*, v. 41, p. 321.

Craig, R. A., 1951, "Radiative Temperature Changes in the Ozone Layer," *Compendium of Meteorology*, American Meteorological Society.

Curran, R. K., 1962, "Formation of NO_2^- by Charge Transfer at Very Low Energies," *Phys. Rev.*, v. 125, p. 910.

Dütsch, H. U., 1956, "Atmospheric Ozone as an Indicator of Currents in the Stratosphere," *Archiv für Meteorologie, Geophysik und Bioklimatologie*, Ser. A, v. 9, p. 87.

Ehler, A. W., and G. L. Weissler, 1955, "Ultraviolet Absorption of Atomic Nitrogen in its Ionization Continuum," *J. Opt. Soc. Am.*, v. 45, p. 1035.

Eyring, H., J. O. Hirschfelder, and H. S. Taylor, 1936, "Theoretical Treatment of Chemical Reactions Produced by Ionization Processes," *J. Chem. Phys.*, v. 4, p. 479.

Faire, A. C., and K. S. W. Champion, 1959, "Measurements of Dissociative Recombination and Diffusion in Nitrogen at Low Pressures," *Phys. Rev.*, v. 113, p. 1.

Fox, R. E., 1960, "Negative Ion Formation in NO_2 by Electron Attachment," *J. Chem. Phys.*, v. 32, p. 285.

Frenkiel, F. N., 1958, "Tropospheric Ozone," *International Association of Meteorology and Atmospheric Physics, Publ. No. 118*, p. 90.

Garton, W. R. S., A. Perry, and K. Codling, 1959, "Spectroscopic Investigation Relating to Autoionization and Dielectronic Recombination," *Proc. 4th International Conf. on Ionization Phenomena in Gases*, N. R. Nilsson, ed., North-Holland Pub. Co., Amsterdam.

Gunton, R. C., E. C. Y. Inn, and T. M. Shaw, 1962, Abstract C-8, *Bull. Amer. Phys. Soc.*, Sec. II, v. 4, p. 132.

Huffman, R. E., Y. Tanaka, and J. C. Larrabee, 1964, "Nitrogen and Oxygen Absorption Cross Sections in the Vacuum Ultraviolet," *Discussions of Faraday Society*, v. 37, p. 159.

Hurzler, H., M. G. Inghram, and J. D. Morrison, 1958, "Photon Impact Studies of Molecules using a Mass Spectrometer," *J. Chem. Phys.*, v. 28, p. 76.

Johnson, C. Y., E. B. Meadows, and J. C. Holmes, 1958, "Ion Composition of the Arctic Ionosphere," *J. Geophys. Res.*, v. 63, p. 443.

Jursa, A. S., Y. Tanaka, and F. LeBlanc, 1959, "Nitric Oxide and Molecular Oxygen in the Earth's Upper Atmosphere," *Planet. Space Sci.*, v. 1, p. 161.

Lee, P., 1955, "Photodissociation and Photoionization of Oxygen as Inferred from Measured Absorption Coefficients," *J. Opt. Soc. Am.*, v. 45, p. 703.

Massey, H. S. W., 1952, "Recombination of Gaseous Ions," *Adv. in Physics*, v. 4, p. 395.

Massey, H. S. W., 1950, *Negative Ions*, Cambridge Univ. Press, Cambridge.

Phelps, A. V., and J. L. Pack, 1961, "Collisional Detachment in Molecular Oxygen," *Phys. Rev. Letters*, v. 6, p. 111.

Regener, V. H., 1960, "On a Sensitive Method of Recording Atmospheric Ozone," *J. Geophys. Res.*, v. 65, no. 12, p. 3975.

Reshetov, V. D., 1961, The Hypothesis of the Aerosol Origin of the Atmospheric Ozone, "Atmospheric Ozone, Results of IGY Work in the USSR, Reports and Resolutions," Moscow University Press, p. 115.

Samson, J. R., and R. Cairns, 1964, "Absorption and Photoionization Cross Sections of O_2 and N_2 at Intense Solar Lines," *J. Geophys. Res.*, v. 69, p. 21.

Smith, S. J., and D. S. Burch, 1959, "Relative Measurements of the Photodetachment Cross Section for H^-," *Phys. Rev.*, v. 116, p. 1125.

Smith, S. J., D. S. Burch, and L. M. Branscomb, 1958, "Experimental Photodetachment Cross Section and the Ionosphere Detachment Rate for O_2^-," *Ann. Geophys.*, v. 14, p. 225.

Syverson, M. W., R. P. Stein, T. M. Shaw, M. Scheibe, and R. C. Gunton, 1962, Abstract F-6, *Bull. Am. Phys. Soc.*, Sec. II, v. 4, p. 378.

Thompson, J. B., 1959, "Negative Ions in the Positive Column of the Oxygen Discharge," *Proc. Phys. Soc. (London)*, v. 73, p. 818.

Walker, W. C., and G. L. Weissler, 1955, "Photoionization Efficiencies and Cross Sections in N_2 and NO," *J. Chem. Phys.*, v. 23, p. 1962.

CHAPTER 6

Watnabe, K., 1958, Ultraviolet Absorption Processes in the Upper Atmosphere, "Advances in Geophysics," v. 5, p. 153, H. E. Landsberg, ed., Academic Press, New York.

Watnabe, K., and F. F. Marmo, 1956, "Photoionization and Total Absorption Cross Section of Gases. II. O_2 and N_2 in the Region 850-1500 Å," *J. Chem. Phys.*, v. 25, p. 965.

Weissler, G. L., J. A. R. Samson, M. Ogawa, and G. R. Cook, 1959, "Photoionization Analysis by Mass Spectroscopy," *J. Opt. Soc. Am.*, v. 49, p. 338.

Whitten, R. C., and I. G. Poppoff, 1962, "Associative Attachment in the D Region," *J. Geophys. Res.* v. 67, no. 3, p. 1183.

Yeung, T. H. Y., 1958, "Recombination Coefficients for Positive and Negative Ions," *Proc. Phys. Soc.* (*London*), v. 71, p. 341.

Chapter 7

ATMOSPHERIC OPTICS

Section 7.1 Louis Elterman
Sections 7.2-7.5 Robert B. Toolin

7.1 ATMOSPHERIC ATTENUATION MODEL

In the ultraviolet, the visible, and the infrared window regions, calculations of attenuation are facilitated by using a model. This model of atmospheric attenuation is based upon the *U.S. Standard Atmosphere, 1962*, augmented by an aerosol content that is characteristic of a meteorological range of about 25 km at sea level; the size distribution of the aerosol is assumed unchanged with altitude. The derivation [Elterman, 1964] of the model is based on a *turbid atmosphere* that is a molecular atmosphere plus aerosol and ozone components. The format of the model is a series of tabulations. (Table 7-4 at end of chapter) for 22 wavelengths from 0.27 to 4.0 μ with parameters arrayed at kilometer intervals of altitude. Horizontal, vertical, and slant-path transmission from sea level, transmission between two altitudes, and transmission to space are readily calculated from the tabulations.

7.1.1 Parameters of Atmospheric Attenuation

Four attenuation coefficients are utilized: the *coefficient for Rayleigh scattering* (β_r), *the coefficient for aerosol scattering* (β_p), the *coefficient for ozone absorption* (β_3), and the *extinction coefficient* (β_t). The defining equations for these coefficients are:

$$\beta_r(h) = \sigma_r n_r(h) \times 10^3 \quad [km^{-1}], \quad (7\text{-}1)$$

$$\beta_p(h) = \beta_p(o)\, n_p(h)/n_p(o) \quad [km^{-1}], \quad (7\text{-}2)$$

$$\beta_3(h) = A_v \times D_3(h) \quad [km^{-1}], \quad (7\text{-}3)$$

and

$$\beta_t(h) = \beta_r(h) + \beta_p(h) + \beta_3(h) \quad [km^{-1}], \quad (7\text{-}4)$$

where h is the altitude (km), σ_r is the Rayleigh scattering cross section (m^2), n_r is the atmospheric number density (m^{-3}), n_p is the aerosol number density (m^{-3}), A_v is the Vigroux [1953] ozone absorption coefficient (cm^{-1}), and D_3 is the ozone concentration (cm km^{-1}). Table 7-1 lists the values of σ_r, $\beta_p(o)$, and A_v used for these calculations.

Figure 7-1 shows the measured values of aerosol attenuation coefficients at sea level [Curcio et al, 1961; Dunkelman, 1952] used for these calculations. Analysis of field measurements shows that up to an altitude of 5 km, the aerosol density relation is

$$n_p(h) = n_p(o) \exp(-h/1.2). \quad (7\text{-}5)$$

Balloon measurements [Chagnon and Junge, 1961] provide additional information concerning the vertical distribution of aerosols between 10 and 25 km. Figure 7-2 shows the vertical distribution of aerosol number density adopted for this clear standard atmosphere. Table 7-2 gives values of aerosol number density used in Eq. (7-2) to compute the aerosol scattering coefficients.

The Rayleigh scattering coefficients were computed using values of n_r from the *U.S. Standard Atmosphere, 1962*. Figure 7-3 shows the ozone concentration profile used to obtain values for $D_3(h)$.

Four *optical thickness* parameters are utilized. The Rayleigh optical thickness from sea level to a given altitude is

$$\tau_r = \sum_{o}^{h} \bar{\beta}_r(h)\, \Delta h, \quad (7\text{-}6)$$

where $\bar{\beta}_r$ is the mean value of β_r for each altitude increment ($\Delta h = 1$ km). The Rayleigh optical thickness from a given altitude to infinity (outward into space) is

$$\tau'_r = \tau_r(\infty) - \tau_r(h). \quad (7\text{-}7)$$

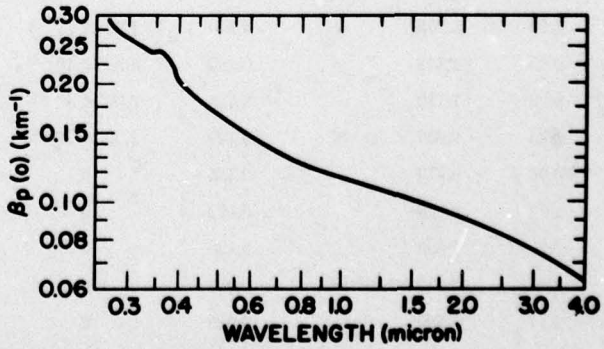


Fig. 7-1. Aerosol attenuation coefficient at sea level, $\beta_p(o)$, vs wavelength, for an average clear day (meteorological range about 25 km).

CHAPTER 7

The extinction optical thickness from sea level to a given altitude is

$$\tau_t = \sum_{o}^{h} \bar{\beta}_t(h)\ \Delta h, \qquad (7\text{-}8)$$

where $\bar{\beta}_t$ is the mean value of β_t for each altitude increment ($\Delta h = 1$ km). The extinction optical thickness from a given altitude to infinity is

$$\tau'_t = \tau_t(\infty) - \tau_t(h). \qquad (7\text{-}9)$$

7.1.2 Applications

Four general cases show the methods of using the parameters in Table 7-4 (at end of chapter) for transmission calculations in a turbid atmosphere and in a Rayleigh atmosphere.

7.1.2.1 *Turbid Atmosphere.*

Case 1, for horizontal transmission over a path length l [km], select the appropriate extinction coefficient for the altitude and wavelength, and use

$$T_h = \exp(-l\beta_t).$$

Case 2, for vertical and slant path transmission from sea level to a given altitude, at a zenith angle θ, select the appropriate extinction optical thickness, and use

$$T_{oh} = \exp(-\tau_t \sec\theta).$$

Case 3, for vertical and slant path transmission between two altitudes above sea level,

$$T_{\Delta h} = \exp[-(\tau_{t2} - \tau_{t1}) \sec\theta],$$

where τ_{t1} is the appropriate extinction optical thickness at the lower altitude and τ_{t2} at the higher altitude.

Case 4 is for vertical or slant path transmission from a given altitude out into space, select the appropriate extinction optical thickness to infinity, and use

$$T_{h\infty} = \exp(-\tau'_t \sec\theta).$$

7.1.2.2 *Rayleigh Atmosphere.* The Rayleigh parameters are used in the equations that correspond to those for a turbid atmosphere.

Case 1 is $T'_h = \exp(-l\beta_r)$;

Case 2 is $T'_{oh} = \exp(\tau_r \sec\theta)$;

Case 3 is $T'_{\Delta h} = \exp[-(\tau_{r2} - \tau_{r1}) \sec\theta]$;

Case 4 is $T'_{h\infty} = \exp(-\tau'_r \sec\theta)$.

Table 7-1. Rayleigh scattering cross sections, σ_r, aerosol scattering coefficient at sea level, $\beta_p(o)$, and ozone absorption coefficient, A_v, at various wave lengths, λ.

λ (μ)	σ_r (m^2)	$\beta_p(o)$ (km^{-1})	A_v (cm^{-1})
0.27	8.959×10^{-30}	0.29	2.10×10^{2}
0.28	7.645	0.27	1.06×10^{2}
0.30	5.676	0.26	1.01×10^{1}
0.32	4.309	0.25	8.98×10^{-1}
0.34	3.334	0.24	6.40×10^{-2}
0.36	2.622	0.24	1.80×10^{-3}
0.38	2.091	0.23	0
0.40	1.689	0.200	0
0.45	1.038	0.180	3.50×10^{-3}
0.50	6.735×10^{-31}	0.167	3.45×10^{-2}
0.55	4.563	0.158	9.20×10^{-2}
0.60	3.202	0.150	1.32×10^{-1}
0.65	2.313	0.142	6.20×10^{-2}
0.70	1.713	0.135	2.30×10^{-2}
0.80	9.989×10^{-32}	0.127	1.00×10^{-2}
0.90	6.212	0.120	0
1.06	3.320	0.113	0
1.26	1.600	0.108	0
1.67	5.210×10^{-33}	0.098	0
2.17	1.800	0.085	0
3.50	2.681×10^{-34}	0.070	0
4.00	1.571	0.063	0

Table 7-2. Aerosol number densities, n_p, at various altitudes, h, for the model of a clear standard atmosphere.

h (km)	n_p (m^{-3})	h (km)	n_p (m^{-3})
0	2.0×10^{8}	16	6.7×10^{4}
1	8.7×10^{7}	17	7.3
2	3.8	18	8.0
3	1.6	19	9.0
4	7.2×10^{6}	20	8.6
5	3.1	21	8.2
6	1.1	22	8.0
7	4.0×10^{5}	23	7.6
8	1.4	24	5.2
9	5.0×10^{4}	25	3.6
10	2.6	26	2.5
11	2.3	27	2.4
12	2.1	28	2.2
13	2.3	29	2.0
14	2.5	30	1.9
15	4.1	31 - 50	neglected

7.2 REFLECTANCE

The spectral reflectance, r_λ, of a surface depends upon the spectral distribution and polarization of the incident flux, the inherent spectral reflectivity of the surface, and the optical condition (i.e., whether it is a Lambertian or Fresnel reflector) of the surface. The evaluation of the spectral reflectance for some natural surfaces is limited because of the restrictions in the experimental geometry. The classical compilation for the spectral reflectances of surfaces is by Krinov [1947]. Duntley et al [1964] give tables of directional luminous reflectance of many different terrain backgrounds.

7.2.1 Ground Reflectance

7.2.1.1 *Water Surfaces.* Figure 7-4 shows that the spectral reflectance of the sea values is low and decreases rapidly with increasing wavelength. There is only a slight increase in the values when the roughness of the sea is greater. Sun glitter (preferred forward angle of scattering) can markedly distort these values. When the solar zenith angle increases beyond 60°, the reflectance increases rapidly (by a factor of three).

7.2.1.2 *Snow, Bare Areas, and Soils.* Figure 7-5 shows the wide variation within this class. Curve 1a is for a fresh snow condition; it shows a rapid decrease in r_λ at the longer wavelengths. Curve 1b is for ice-covered snow; the reflectance is almost independent of wavelength. These two curves indicate the range of values due to the form, state, and age of the snow cover. During the period of melt, the average reflectance is of the order of 0.45. Reflectance decreases with age and greater packing (density) of snow. The variations within this class of surface are so extensive that utilization of these data must be considered carefully for the individual problem. Curves 2, 3, 4, and 5 of Fig. 7-5, all for bare surfaces, demonstrate the effects of the color and condition of the surface. All show a general trend to higher reflectance at longer wavelengths. Curve 2 is characteristic of light-colored but hard-packed surfaces (e.g., clay or limestone). Curve 3 is for light-colored but looser-packed soils, such as desert. Curve 4 is for dark, hard-packed surfaces such as loam and paved roads. Curve 5 is typical of cultivated soils and unpaved roads.

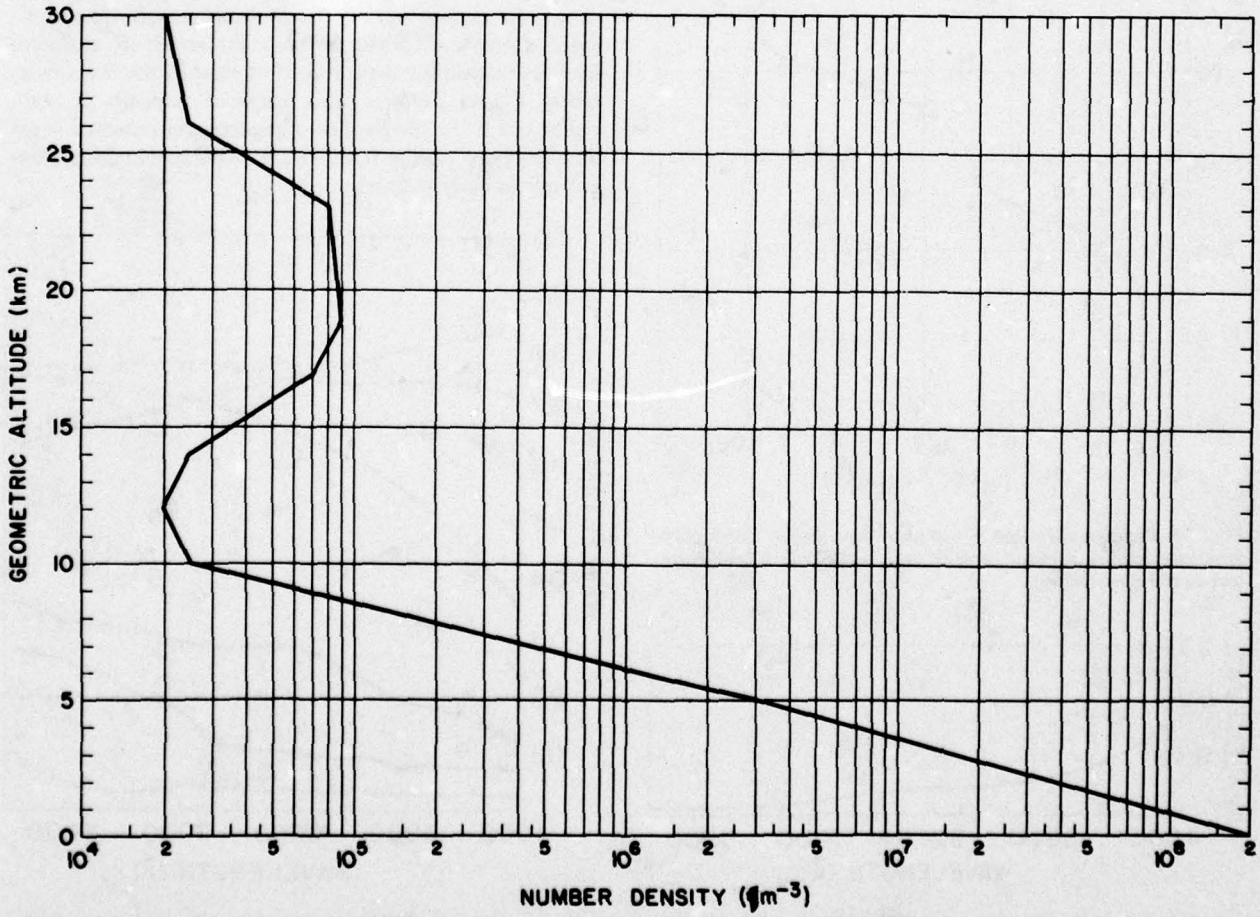


Fig. 7-2. Aerosol number density vs altitude for the atmospheric attenuation model.

7.2.1.3 *Vegetative Formations.* The vertical structure of these formations produce sun-shading effects and limit the interpretation of data. As Fig. 7-6 shows, however, reflectances are low in the visible region, with a steep upswing beyond 7000 Å. Curve a, identified with a wintertime coniferous forest, shows a low and semiflat reflectance (about 0.05) throughout the visible spectrum. Curve b refers to meadows, dry grass, and the same type forest, but during the summer period. Curve c, for deciduous forest and lush grass, shows a characteristic peak at 5500 Å. Curve d, with its almost continuous increase from the ultraviolet to the near infrared, is identified with forests and crops in autumn. Wet formations generally have a lower reflectance than dry surfaces.

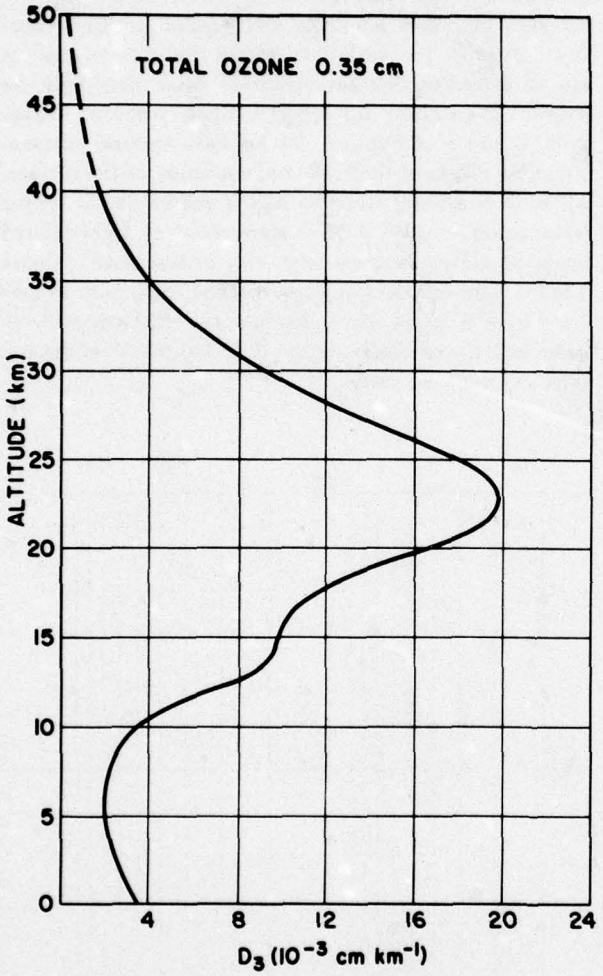


Fig. 7-3. Representative ozone concentration profile. Solid curve developed from ozonesonde network data, dashed curve from chemical equilibrium theory.

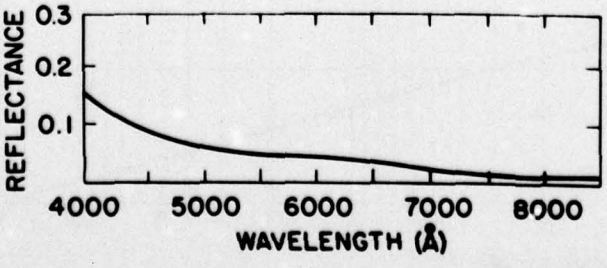


Fig. 7-4. Spectral reflectance for water surfaces (After Krinov [1947].)

7.2.2 Polarization

There are few measurements of the state of polarization of the light reflected from natural surfaces. One study of the radiation from desert terrain showed marked polarization [Coulson, 1959]. The degree of linear polarization at 3700 Å was 0.25 in the azimuth of the sun and decreased very rapidly beyond 90° azimuth. In general, the degree of polarization decreased at longer wavelengths; 0.23 at 3650 Å and 0.12 at 6250 Å, both for an observational angle 54° below the horizontal. As the zenith angle of the sun decreases, this azimuthal distribution becomes more symmetrical.

7.2.3 Observations at High Altitudes

Measurements of spectral reflectance at altitudes well above the natural surface are inadequate. Figure 7-7 shows the change in reflectance from summertime cultivated farm land when a 0.6 cumular cloud structure intruded within the conical field of view of the instrumentation. Figure 7-8 is a polar graph of isopleths of luminance (cd ft^{-2}) for the lower hemisphere measured from an altitude of 98,000 ft (29.8 km) over mountainous desert area in early autumn.

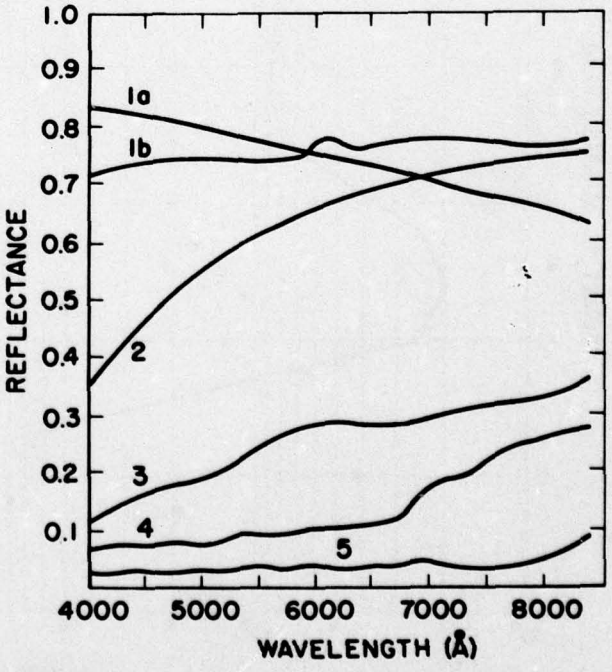


Fig. 7-5. Spectral reflectance for snow and bare soils. (After Krinov [1947].)

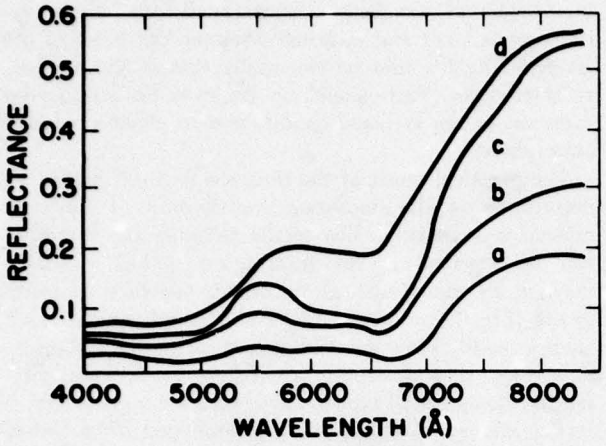


Fig. 7-6. Spectral reflectance for vegetative formation. (After Krinov [1947].)

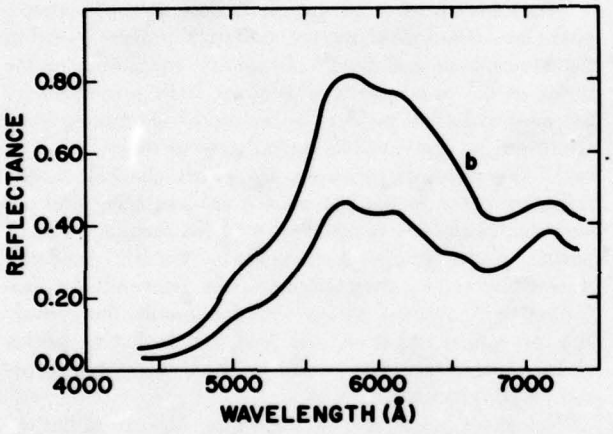


Fig. 7-7. Spectral reflectance, measured at 90,000-ft (27.5 km) altitude above summertime cultivated farmland at 50° solar zenith angle. Curve b shows the effect of the intrusion of 0.6 cumular cloud structure.

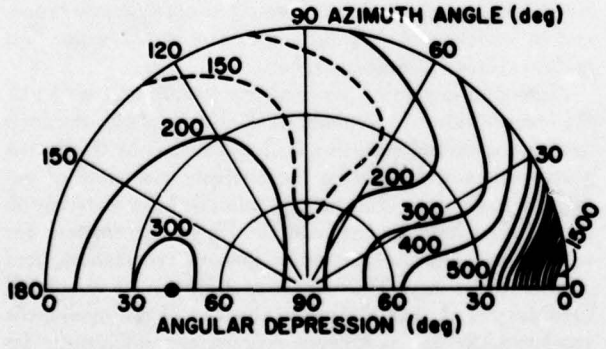


Fig. 7-8. Luminance (cd ft^{-2}) over the downward hemisphere, measured with balloon-borne equipment over mountainous area in early autumn at an altitude of 98,000 ft (29.8 km) in a relatively turbid atmosphere. For results in cd m^{-2}, multiply cd ft^{-2} by 10.764.

7.2.4. Cloud Reflectance

The inevitable consideration of clouds presents an unresolved problem. Fritz [1954] gives some values of average reflectance among the vast range of cloud types, and has developed a relation which agrees fairly well with the few available field measurements. His general values do not indicate either the marked influence of solar zenith angle and internal conditions of the cloud, or modification because of the reflectance properties of underlay surfaces (either another cloud or terrain).

Figure 7-9 shows the variation in total (spectrally integrated) reflectance calculated according to Fritz's relation as a function of the parameter h/L; h is the cloud thickness and L is the mean free path of a light ray. The analysis is restricted to a plane cloud of large drops. The underlay surface has an average reflectance of 0.1, and no absorption is considered. h/L may have values ranging from less than 1.0 (very thin clouds) to perhaps as large as 500 (thick rain clouds). For the thicker ($h/L \geqq 25$), the change in reflectance with solar zenith

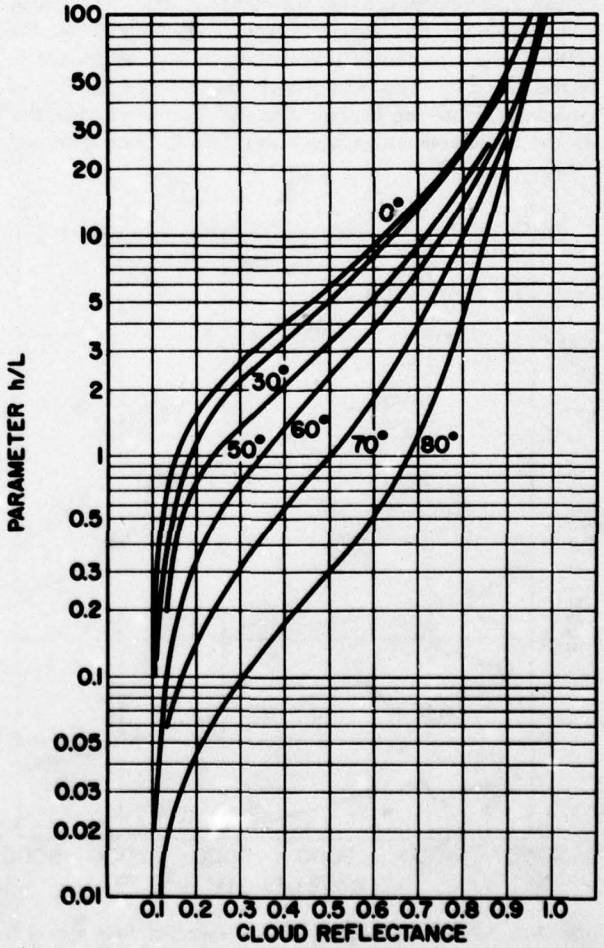


Fig. 7-9. Variation in reflectance as a function of cloud thickness parameter h/L for different solar zenith angles.

angle or with cloud thickness is slight. The cloud condition of small droplets will increase the value of average reflectance, but definite conclusions are not yet possible.

7.3 FLUX EMERGING FROM THE ATMOSPHERE

The few measurements available emphasize that the radiation flux emerging from real atmospheres depends critically on the optical thickness, the zenith angle of the sun, and the zenith angle and azimuth of observation direction, as well as the spectral reflectance of the underlay surface. Coulson [1959] considers this problem for a plane parallel Rayleigh atmosphere, in which there is neither true absorption nor true emission of energy, to determine the intensity and polarization of radiation from the top of a molecular atmosphere. Hughes [1964] discusses the experimental evidence and theoretical predictions, based on a Rayleigh atmosphere, of the variations in sky radiance with altitude.

Figure 7-10 shows the spectral distribution of the emerging flux when the sun is at the zenith; the surface is assumed to be a Lambertian reflector with the reflectance, r, independent of wavelength. The wavelength distribution of flux for light scattered ($r = 0$) by the atmosphere is markedly different from that of the extraterrestrial flux. The wavelength dependence (λ^{-4}) of molecular scattering is evident at the shorter wavelengths. As the reflectance value becomes different from zero, the

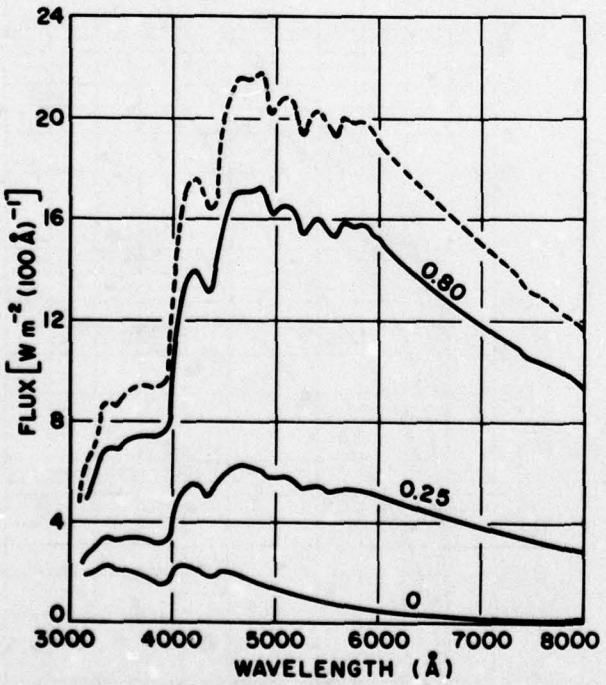


Fig. 7-10. Spectral distribution of flux emerging from top of a model atmosphere for different values of surface reflectance ($r = 0$, 0.25, and 0.80) and the sun at the zenith; dashed curve is the incident extraterrestrial flux. (After Coulson [1959].)

importance of wavelength becomes obvious. If the reflectance is large and r_λ is not constant, the color of the emergent light would be essentially that of the surface-reflected light. Such would be the case for ice-covered snow under the assumed condition of a plane molecular atmosphere.

The practical merit of the theoretical model lies in its description of the important contribution of Rayleigh molecular scattering. The model presents the best that can be expected in the transfer of optical radiation through an atmosphere. However, the few field measurements (Fig. 7-7 and 7-8) and a number of ground-based studies readily show that the aerosol scattering, molecular anisotropy, and absorption are very effective in modifying the fundamental model. More realistic models, which include aerosol distributions, are developed for practical application [Fraser, 1964].

7.4 OPTICAL RADIATION IN THE ATMOSPHERE

The characteristics of optical radiation in the atmosphere are determined by the radiative processes within the atmosphere and by the boundary conditions at the limits of the atmosphere. The upper limit is defined by the solar radiation incident at the top of the atmosphere; the lower, by the variable optical state of the earth's surface. The physical processes by which changes in the radiation occur in the atmosphere are scattering and absorption. *Scattering* is descriptive of the angular redistribution of the energy incident on a material medium. *Absorption* is any thermodynamically irreversible transformation of radiant energy (predominantly the conversion of optical radiation into heat, but including photochemical actions). The combination of these two processes is the *attenuation.*

Permanent gases and water vapor absorb radiation, but for the region 0.3 to 0.8μ, the influence of absorption in the atmosphere may be considered as a minor perturbation. Absorption must be included, however, in calculations of the transfer of optical radiation in industrial areas where the atmosphere contains significant amounts of carbon products. Absorption is a major factor at wavelengths $< 0.29\mu$ because of atmospheric ozone, and at wavelengths $> 0.8\mu$ because of water vapor and carbon dioxide in the atmosphere.

Scattering depends upon both the radiational field and the composition of the medium. Mathematically, the incident and scattered radiation is characterized by the Stokes parameters which describe the intensity and state of polarization. Coulson et al [1960] tabulated the distribution of scattered light in terms of the Stokes parameters for various sun elevations, neutral ground reflectances, and optical thicknesses. This representation can be simplified considerably if: (1) the physical array of the medium is random; (2) the scattering centers are sufficiently far apart so that the scattering is independent; (3) the elements are neither metallic nor absorbing; and (4) other factors such as shape and anisotropy are neglected. Under such conditions, the scattering volume can be described

in terms of N, the number of scatters per unit volume; a, the radius of the scatterers; and μ_λ, the wavelength-dependent real index of refraction of the scatterers. The dimensionless *size parameter*, $\alpha = 2\pi a/\lambda$, delineates the basic types of scattering.

7.4.1 Rayleigh Scattering (Molecular) and Polarization

If the sampled volume contains only molecules of the atmosphere, there is no dependence upon size parameter. The intensity of the scattered radiation is then a function of the intensity, polarization, and wavelength of the incident radiation, the number of molecules and their index of refraction, and the scattering angle ϕ (angle between the direction of the incident and scattered rays). The mathematical formulation is the Rayleigh molecular law of scattering,

$$\beta_{\phi\lambda} = \frac{2\pi^2}{N\lambda^4} (\mu_\lambda - 1)^2 (1 + \cos^2 \phi), \quad (7\text{-}10)$$

where $\beta_{\phi\lambda}$ is the Rayleigh scattering coefficient at angle ϕ and wavelength λ. The intensity of a scattered beam is

$$i_{\phi\lambda} = \beta_{\phi\lambda} i_\lambda, \quad (7\text{-}11)$$

where i_λ is the incident unpolarized intensity. (For a detailed discussion of Rayleigh scattering, see Twersky [1964].)

The assumption, prevailing for this theory and for other more realistic formulations, is that the atmosphere is plane parallel with a stratified density distribution. For measuring vertical distances, the optical thickness parameter is useful for an isotropic medium; if the gaseous composition of the atmosphere is known, the optical thickness of a given height and a given wavelength can be computed (Table 7-4, end of chapter).

The premise of independence of scatterers does not preclude that a light ray which has been scattered once will not be scattered again; each scattering center is exposed to light scattered by other centers and to light reflected from the earth's surface. Figure 7-11 shows the probability of the occurrence of multiple scattering in the forward direction as a function of the optical thickness. With $\tau_r < 0.1$, only single scattering need be considered. For $\tau_r < 0.3$, single and double scattering are effective. When $\tau_r > 0.3$, triple scattering must be considered. In practice, this means that multiple scattering is significant for real path lengths greater than a few hundred meters.

Three neutral points of zero polarization are observed in the plane of the sun's meridian (the vertical circle). The *Arago point*, located on the vertical circle about 20° above the antisolar point, is sensitive to the size parameter; in a turbid atmosphere it is at higher angles above the antisolar point. The *Babinet* (above) and the *Brewster* (below) points are located on the vertical circle 15° to 20° above and below the sun. The simple theory fails to predict the neutral points. Figure 7-12 shows the distribution of the degree of polarization for two solar zenith angles; maximum polarization occurs at an angle of almost 90° from the sun. Figure 7-13 shows the considerable decrease in the maximum degree of polarization, a slight shift of the maximum position toward the zenith, and the increase in angular separation of the neutral points with increasing optical thickness. Figure 7-14 shows the effect of the isotropic neutral reflectance of the underlying surface on the degree of maximum polarization; the neutral points are unchanged.

Neutral points are an integral feature in the complex theory of radiative transfer, but field measurements have seldom agreed with the theory. With due consideration

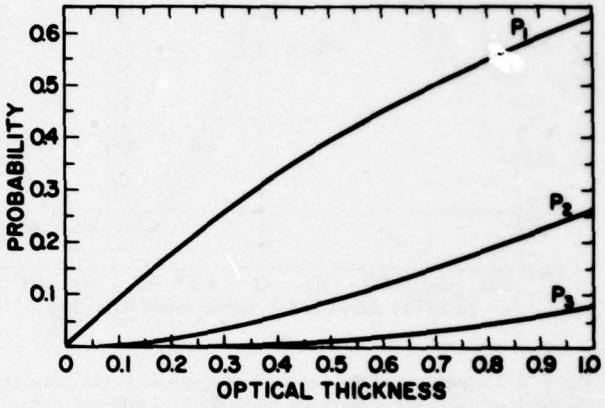


Fig. 7-11. Probability of occurrence of single (P_1), double (P_2) and triple (P_3) scattering as a function of optical thickness. (After D. Bugnolo, *J. Geophys. Res.*, v. 65, no. 3, p. 879, 1960.)

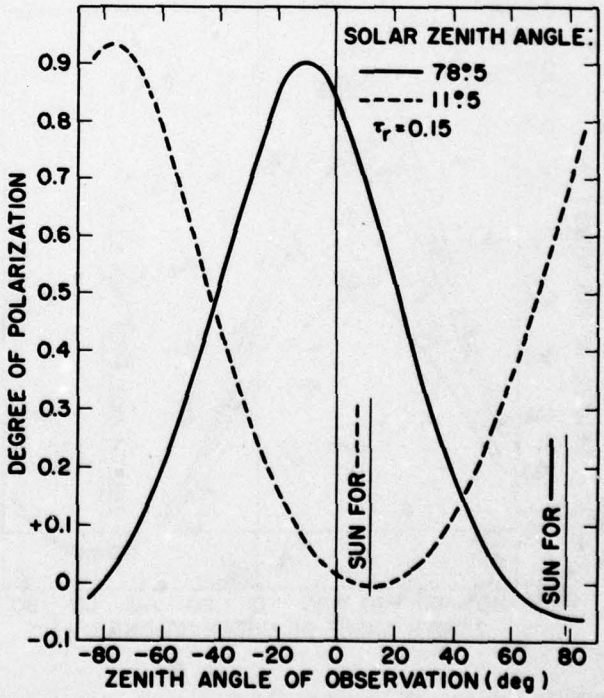


Fig. 7-12. Distribution of the degree of polarization in the plane of the sun's meridian for a Rayleigh atmosphere and optical thickness 0.15 at different solar zenith angles. (After Sekera [1956].)

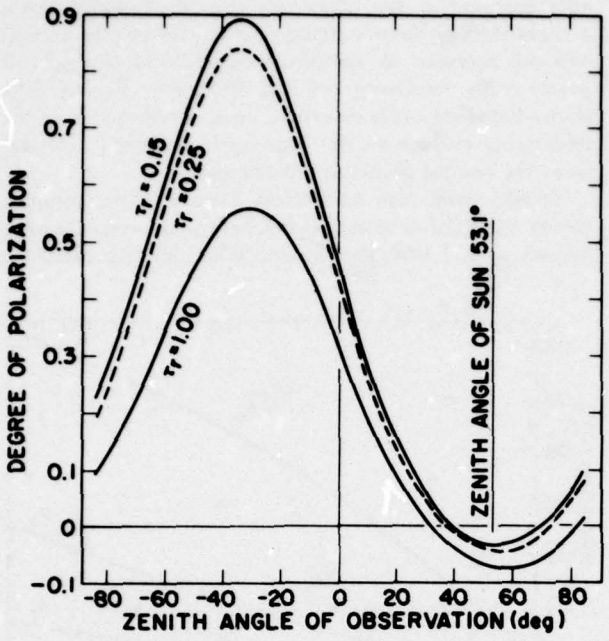


Fig. 7-13. Distribution of the degree of polarization in the plane of the sun's meridian for a Rayleigh atmosphere at different optical thicknesses. (From Sekera [1956] by permission.)

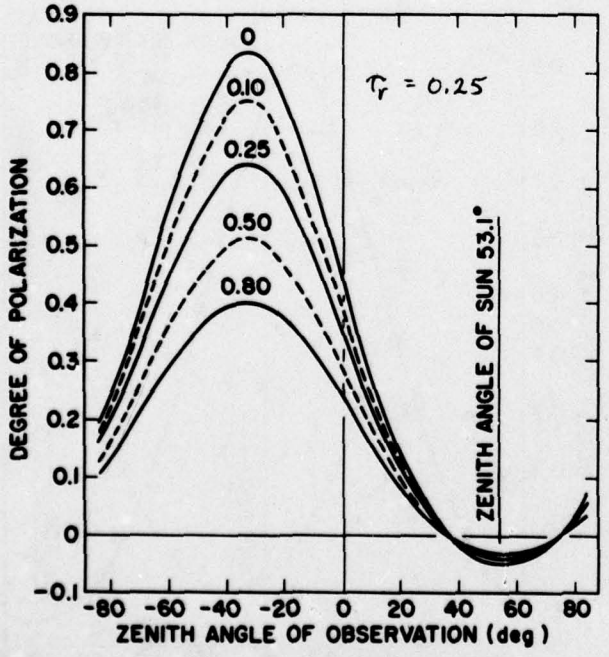


Fig. 7-14. Distribution of the degree of polarization in the plane of the sun's meridian in a Rayleigh atmosphere for the values of diffuse neutral reflectance of the boundary surface given above each curve. (From Sekera [1956] by permission.)

for such factors as optical thickness, ground reflectance, and solar zenith angle, all of which cause variations in the intensity and polarization properties of the molecular atmosphere, the major contribution to real deviations is the variable concentration of particulate matter in suspension in the atmosphere (the aerosols). The dispersion of polarization and its variability are particularly influenced by the aerosols.

7.4.2 Aerosol (Mie) Scattering

The general formulation of the scattering produced by a spherical particle of any size and complex index of refraction derived by Mie was expanded by Van de Hulst [1957]. When the size parameter, α, is < 1 and the particle does not absorb radiation, the solution is identical with the Rayleigh case. Then the intensity of the light scattered from an elemental volume is proportional to λ^{-4} and the scattering pattern is a bilobe symmetrical contour. The transition from the Rayleigh to the Mie region of scattering occurs in the narrow range $1 < \alpha < 2$. For the Mie region, the intensity of the scattered light becomes a complicated function of λ, a, μ_λ, and ϕ. For example, the interaction between the size parameter and the scattering coefficient is oscillatory so that, for a given particle radius and real index of refraction, scattering does not necessarily increase with decreasing values of λ. All Mie particles show common characteristics: forward scattering increases with increasing values of α, and the frequency of the oscillations increases for the larger angles of scattering.

In theoretical computations, the Mie single-particle effects must be integrated over the size distribution of the aerosols in a unit volume of atmosphere. The practical difficulty lies in a correct choice of size-distribution models and in the identification of the basic optical properties of the aerosols. Many computations based upon different choices for μ_λ and different size distributions are available [Penndorf, 1962; Kerker, 1963] in addition to that given in Sec. 17.1.

7.4.3 Atmospheric Scattering

Molecular and aerosol effects are linearly combinable only under the condition of small scattering volume or of small optical path length. Figure 7-15 shows the calculated percentage contribution of single molecular scattering to the total scattered radiation for two conditions of visibility and aerosol size distribution, $N(a) = a^{-2.5}$ and $N(a) = a^{-4}$. The influence of Rayleigh scattering is particularly strong at $\phi = 130°$ and increases with decreasing wavelength. The contribution of Rayleigh scattering also increases with increasing ratio of the large particles to small particles in the size distribution (flatter distribution). Practical utilization of such results, however, should be restricted to either short path lengths or high altitudes because of the supposition that only single scattering occurs; multiple scattering is an unresolved problem in the theoretical formulation of radiative transfer.

Sekera [1956] and Rosenberg [1960] present comprehensive reviews of the theory of radiative transfer as related to these problems. The unfortunate lack of a quantity of well-controlled measurements of the optical and meteorological parameters in real or simulated atmospheres restricts the conclusions to the following qualitative statements:

(1) The presence of aerosols increases the optical thickness and affects the location of the neutral points and of the maximum degree of polarization in the manner indicated by Fig. 7-13.

(2) Increases in scattering intensity for the forward angles (particularly $\phi < 10°$) and for the longer wavelengths are sensitive indicators of increased scattering by aerosols.

(3) For low aerosol content, the degree of polarization at the point of maximum polarization increases with wavelength. As the aerosol content of the atmosphere increases, there is a gradual shift in the point of maximum polarization to shorter wavelengths.

(4) A broad generalization is that the effects of multiple molecular and aerosol scattering produce a variance of 20 to 25% in the visual values of sky radiance and polarization predicted by the elementary theory of scattering for a plane clear atmosphere.

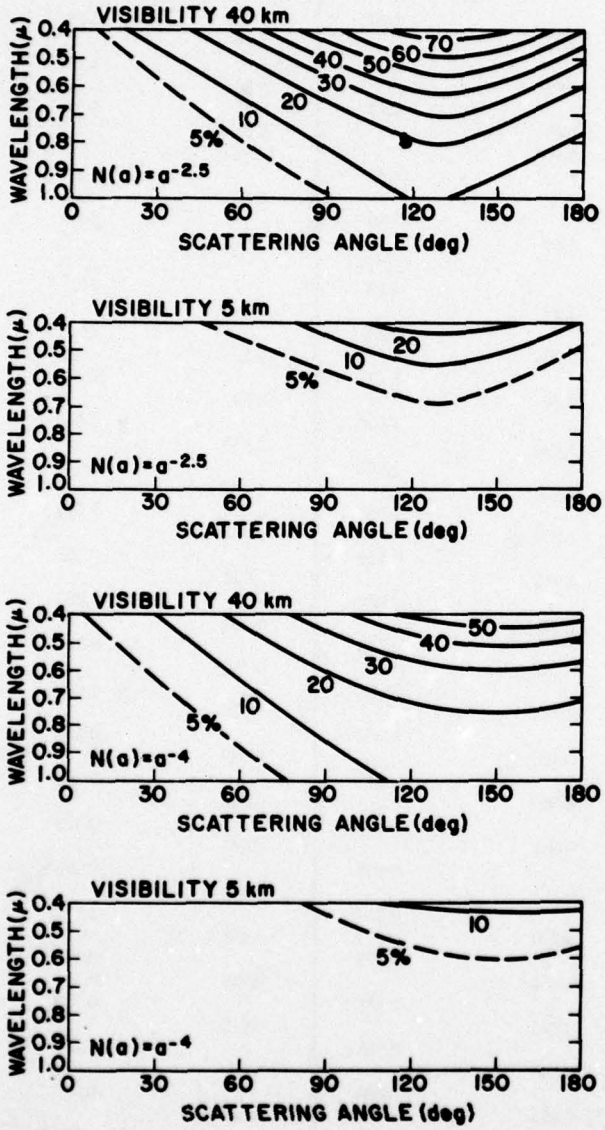


Fig. 7-15. Percentage of single Rayleigh scattering in the total scattering of an air volume for two different aerosol-size distributions and two visibilities; a is the aerosol particle radius. (From K. Bullrich [Kerker, 1963].)

7.4.4 Absorption Coefficients for Ozone

Table 7-3 gives spectral absorption coefficients, A_ν, for ozone in the region from 2987 to 3654 Å; the values refer to an atmosphere-centimeter of pure ozone at normal pressure at different temperatures. A_ν is defined by the relation $I = I_o \exp(-A_\nu d)$, where d is the length in centimeters of a column of unit area at a pressure of 1013 mb (760 mm Hg).

7.5 MEASUREMENTS OF SKYLIGHT

The techniques of direct probing and of optical sampling by searchlights and studies of the sun's aureole give firm evidence of the strong influence of aerosol scattering even at high altitudes. Newkirk and Eddy [1964] found an appreciable aureole due to Mie scattering near the disk of the sun when observations were made at 25-km altitude; the aureole radiance was approximately twice that expected from a pure molecular sky. Figure 7-16 is typical of their observations.

Figure 7-17 is a domical display of sky brightness for an altitude of about 31 km and for two solar zenith angles; calculated values [Koomen, 1959] and observed values are given. The values are comparative except in the forward scattering volume about the sun where incomplete theory makes the computed values suspect, and instrumentation problems invalidate the measurements. It appears that in the antisolar hemisphere of the sky, at this altitude, the scattering approaches that of the simple molecular model. Thus, in star detection problems at such altitudes, it seems justifiable to neglect Mie scattering.

Figure 7-18 shows basically the optical signal-to-noise ratio for stellar detection in a sun-illuminated atmosphere with various angles of view of an optical detection system. A photometric value of 10 cd ft^{-2} (107.6 cd m^{-2}) is assumed to be due entirely to the λ^{-4} distribution of scattered sunlight, and the second magnitude star is assumed to have a spectrum identical to that of the sun.

Table 7-3. Absorption coefficients for pure ozone. Successive maxima (left) and minima (right) are indicated by relative position in the column, and * identifies the principle maxima and minima. Compiled by P. R. Gast from Vigroux [1953] except for values in parentheses, which are estimated.

Wave length (Å)	A_v at 18°C (cm^{-1})	A_v at −44°C (cm^{-1})	A_v at −59°C (cm^{-1})
2987	11.93	11.21	11.09
2998	10.34	9.51	9.41
3004	9.65	8.88	8.78
3016	8.17	7.52	7.43
3021	7.58	(6.97)	(6.82)
3029	6.70	6.16	6.03
3036	6.31	5.80	5.68
3037	6.36	5.91	5.79
3051	4.74	4.31	4.22
3053	4.81	4.42	4.33
3059	4.54	4.13	4.09
3061	4.63	4.30	4.21
3066	4.37	(4.06)	(3.93)
3075	3.66	3.33	3.26
3077	3.73	3.39	3.32
3083	3.36	3.06	2.99
3085	3.34	3.04	3.01
3092	3.11	(2.80)	(2.74)
3098	2.67	2.40	2.35
3100	2.74	2.49	2.41
3104	2.56	2.30	2.25
3106	2.58	(2.35)	(2.27)
3109	2.35	2.12	2.07
3112	2.42	2.20	2.13
3130*	1.727	1.433	1.400
3135*	1.833	1.595	1.540
3146	1.342	1.074	1.047
3148	1.405	1.138	1.110
3151*	1.303	1.068	1.029
3154*	1.451	1.262	1.233
3167*	1.036	0.820	0.787
3170	1.128	0.948	0.925
3173	1.036	0.860	0.839
3176*	1.151	1.001	0.990
3190*	0.714	0.543	0.521
3194	0.886	0.762	0.753
3199	0.792	0.665	0.649
3200*	0.898	0.781	0.772
3209	0.523	0.382	0.356
3210	0.548	0.406	0.389
3216*	0.497	0.373	0.363
3220*	0.691	0.608	0.622
3223	0.583	0.484	0.478
3226	0.675	0.601	0.594
3239*	0.322	0.209	0.193
3242	0.373	0.276	0.272
3245	0.350	0.259	0.252
3248*	0.516	0.470	0.464
3253	0.394	0.319	0.311
3255	0.426	0.354	0.345
3269*	0.212	0.131	0.123
3272	0.279	0.223	0.218
3275	0.244	0.185	0.180
3279*	0.373	0.339	0.339
3292	0.140	0.080	0.071
3295	0.152	0.093	0.087
3299*	0.129	0.079	0.074
3303	0.216	0.184	0.180
3309	0.180	0.139	0.137
3312*	0.249	0.214	0.214
3328*	0.081	0.053	0.049
3332	0.115	0.0736	0.070
3334	0.101	0.068	0.063

(Continued)

Table 7-3. Absorption coefficients for pure ozone. Successive maxima (left) and minima (right) are indicated by relative position in the column, and * identifies the principle maxima and minima. Compiled by P. R. Gast from Vigroux [1953] except for values in parentheses, which are estimated. (Continued)

Wave length (Å)		A_ν at 18°C (cm^{-1})		A_ν at −44°C (cm^{-1})		A_ν at −59°C (cm^{-1})	
3338*		0.177		0.152		0.154	
	3357*		0.046		(0.033)		0.030
3365		0.087		0.070		0.066	
	3369		0.069		0.054		0.049
3372*		0.117		0.103		0.102	
	3391*		0.032		(0.025)		(0.023)
3395		0.051		(0.044)		(0.044)	
	3398		0.039		(0.030)		(0.028)
3401*		0.064		0.055		0.055	
	3417		0.018				
3421		0.021					
	3426*		0.017				
3430		0.025					
	3437		0.022				
3439*		0.035					
	3451		0.015				
3455		0.018					
	3460		0.0137				
3463		0.0154					
	3466*		0.0182				
3472*		0.0139					
	3481		6.68×10^{-3}				
3485		7.6×10^{-3}					
	3489*		6.2×10^{-3}				
3493*		9.79×10^{-3}					
	3499		6.9×10^{-3}				
3501		7.4×10^{-3}					
	3506*		5.41×10^{-3}				
3514*		10.4×10^{-3}					
	3521		6.52×10^{-3}				
3523		7.28×10^{-3}					
	3546		2.05×10^{-3}				
3550		2.37×10^{-3}					
	3554		1.77×10^{-3}				
3556		1.877×10^{-3}					
	3561*		1.54×10^{-3}				
3567*		3.11×10^{-3}					
	3572		2.51×10^{-3}				
3573		2.62×10^{-3}					
	3588*		1.278×10^{-3}				
3594*		1.82×10^{-3}					
	3599		1.59×10^{-3}				
3600		1.761×10^{-3}					
	3604		1.2×10^{-3}				
3606		1.31×10^{-3}					
	3639*		1.77×10^{-4}				
3647*		8.4×10^{-4}					
	3650		6.0×10^{-4}				
3654		8.3×10^{-4}					

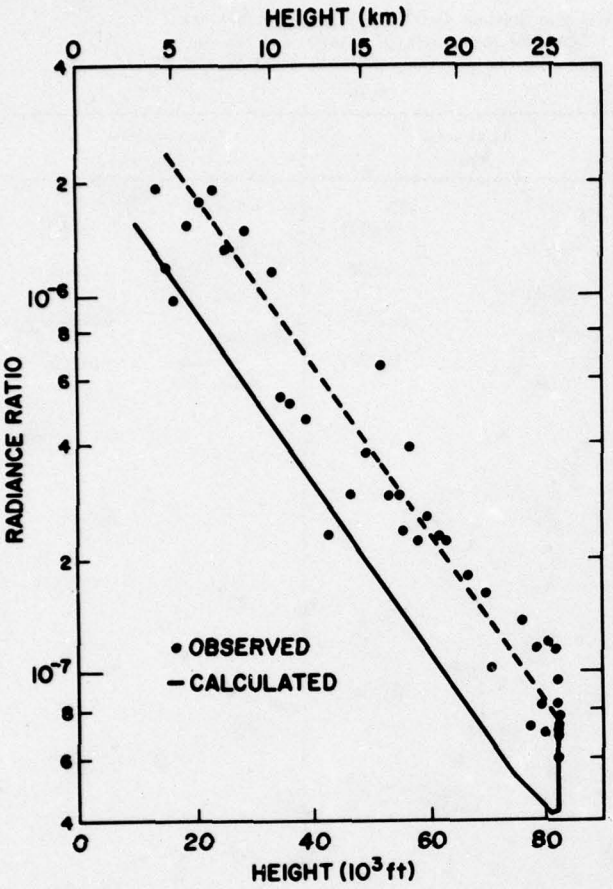


Fig. 7-16. Ratio of daytime sky radiance at 0.44μ to radiance of the mean solar disk at 0.44μ vs altitude. Sky radiance observed at a scattering angle of 2°8 from the sun along that great circle through the sun whose inclination to the vertical plane is the solar zenith angle; the calculated curve is for a pure molecular sky. (From Newkirk and Eddy [1964].)

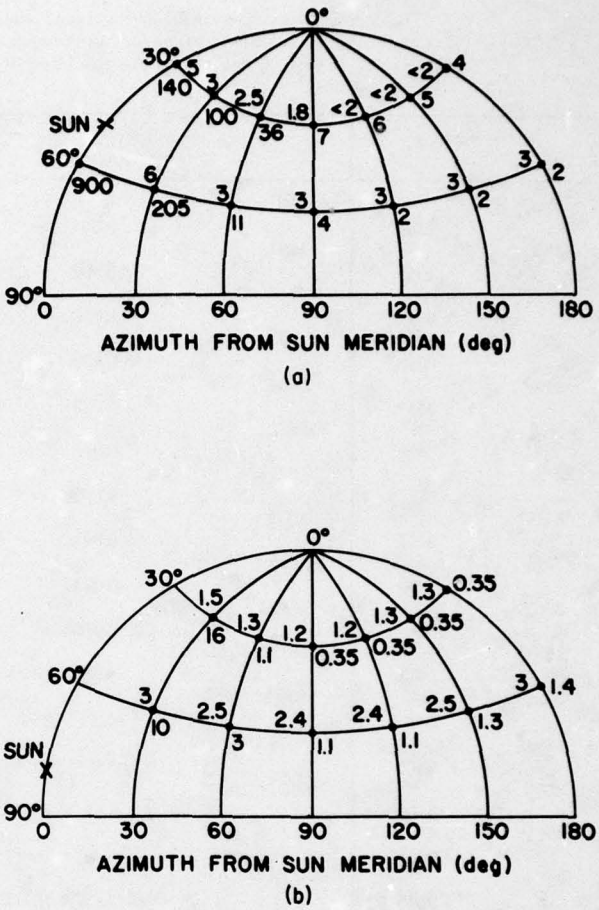


Fig. 7-17. Comparison of computed and measured sky brightness in cd ft^{-2} at 100,000 ft (30.5 km) for solar zenith angle of 50° and 80°. Values to the left of a meridian line are computed, those to the right are measured. For results in cd m^{-2}, multiply by 10.764.

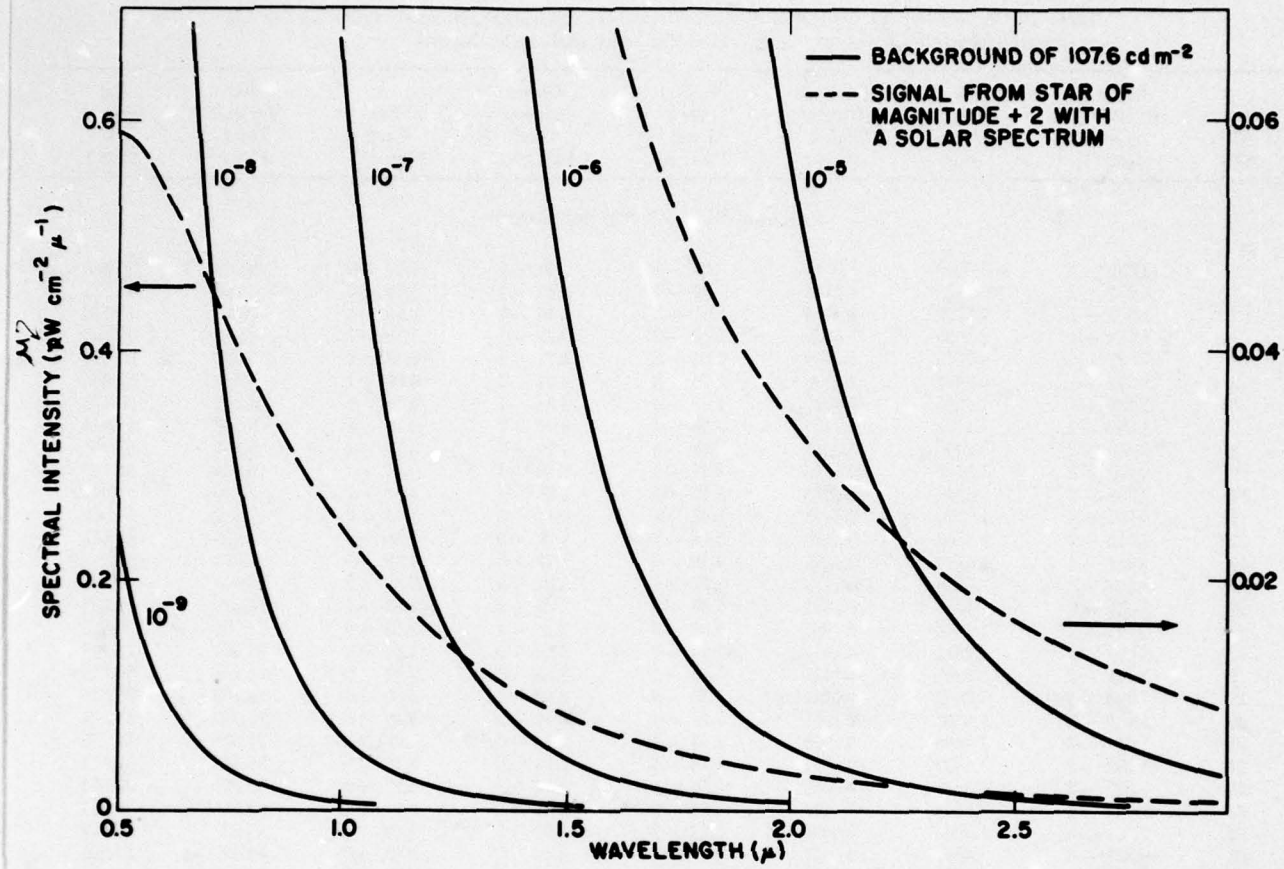


Fig. 7-18. Stellar signal intensity and sky background intensities for various fields of view as a function of wavelength. Solid angle in steradians is given for the background curves; the right-hand scale is for the right-hand stellar intensity curve.

Table 7-4. Parameters for the model of a clear standard atmosphere. Numbers following the plus or minus sign are the power of ten by which that entry shall be multiplied.

Alt (km)	Rayleigh Atten Coeff (km^{-1})	Rayleigh Optical Thick. (0-h)	Rayleigh Optical Thick. (h-∞)	Aerosol Atten Coeff (km^{-1})	Ozone Absorp Coeff (km^{-1})	Ext Coeff (km^{-1})	Ext Optical Thick. (0-h)	Ext Optical Thick. (h-∞)
			PARAMETERS AT 0.27 MICRONS					
0	2.282 −1	0.0000	1.9314	2.90 −1	7.48 −1	1.27 +0	0.000	73.253
1	2.071 −1	0.2177	1.7137	1.28 −1	6.85 −1	1.02 +0	1.143	72.111
2	1.875 −1	0.4150	1.5164	5.51 −2	6.15 −1	8.58 −1	2.081	71.172
3	1.694 −1	0.5935	1.3380	2.32 −2	5.25 −1	7.18 −1	2.869	70.384
4	1.527 −1	0.7545	1.1769	1.04 −2	4.75 −1	6.38 −1	3.547	69.707
5	1.372 −1	0.8994	1.0320	4.64 −3	4.64 −1	6.06 −1	4.168	69.085
6	1.230 −1	1.0295	0.9019	1.60 −3	4.54 −1	5.78 −1	4.761	68.493
7	1.099 −1	1.1460	0.7854	5.80 −4	4.68 −1	5.79 −1	5.339	67.914
8	9.796 −2	1.2499	0.6815	2.03 −4	4.79 −1	5.77 −1	5.917	67.336
9	8.702 −2	1.3424	0.5890	7.25 −5	5.90 −1	6.77 −1	6.544	66.709
10	7.704 −2	1.4245	0.5070	3.77 −5	7.35 −1	8.12 −1	7.289	65.965
11	6.797 −2	1.4970	0.4345	3.48 −5	9.66 −1	1.03 +0	8.212	65.042
12	5.812 −2	1.5600	0.3714	3.19 −5	1.30 +0	1.36 +0	9.410	63.844
13	4.967 −2	1.6139	0.3175	3.48 −5	1.77 +0	1.82 +0	11.003	62.250
14	4.245 −2	1.6600	0.2715	3.77 −5	2.01 +0	2.05 +0	12.941	60.312
15	3.628 −2	1.6993	0.2321	6.09 −5	2.09 +0	2.12 +0	15.029	58.224
16	3.102 −2	1.7330	0.1985	9.86 −5	2.16 +0	2.19 +0	17.188	56.065
17	2.651 −2	1.7617	0.1697	1.07 −4	2.33 +0	2.36 +0	19.464	53.789
18	2.266 −2	1.7863	0.1451	1.16 −4	2.56 +0	2.58 +0	21.935	51.318
19	1.938 −2	1.8073	0.1241	1.30 −4	2.98 +0	3.00 +0	24.728	48.525
20	1.656 −2	1.8253	0.1061	1.25 −4	3.44 +0	3.46 +0	27.959	45.294
21	1.410 −2	1.8406	0.0908	1.19 −4	3.86 +0	3.88 +0	31.629	41.625
22	1.202 −2	1.8537	0.0777	1.16 −4	4.14 +0	4.15 +0	35.643	37.611
23	1.025 −2	1.8648	0.0666	1.10 −4	4.16 +0	4.17 +0	39.801	33.452
24	8.744 −3	1.8743	0.0571	7.54 −5	4.05 +0	4.06 +0	43.916	29.337
25	7.467 −3	1.8824	0.0490	5.22 −5	3.78 +0	3.79 +0	47.841	25.412
26	6.381 −3	1.8894	0.0421	3.77 −5	3.42 +0	3.43 +0	51.449	21.804
27	5.458 −3	1.8953	0.0361	3.48 −5	2.96 +0	2.97 +0	54.647	18.606
28	4.671 −3	1.9003	0.0311	3.19 −5	2.58 +0	2.59 +0	57.425	15.829
29	4.001 −3	1.9047	0.0267	2.90 −5	2.25 +0	2.25 +0	59.844	13.409
30	3.430 −3	1.9084	0.0230	2.75 −5	1.90 +0	1.90 +0	61.919	11.334
31	2.942 −3	1.9116	0.0198	0.00 +0	1.67 +0	1.67 +0	63.703	9.550
32	2.525 −3	1.9143	0.0171	0.00 +0	1.43 +0	1.43 +0	65.255	7.999
33	2.156 −3	1.9167	0.0148	0.00 +0	1.22 +0	1.22 +0	66.584	6.669
34	1.842 −3	1.9187	0.0128	0.00 +0	1.01 +0	1.02 +0	67.705	5.549
35	1.577 −3	1.9204	0.0111	0.00 +0	9.05 −1	9.07 −1	68.666	4.587
36	1.352 −3	1.9218	0.0096	0.00 +0	7.58 −1	7.59 −1	69.499	3.754
37	1.162 −3	1.9231	0.0083	0.00 +0	6.34 −1	6.35 −1	70.196	3.057
38	9.997 −4	1.9242	0.0073	0.00 +0	5.31 −1	5.32 −1	70.780	2.473
39	8.619 −4	1.9251	0.0063	0.00 +0	4.56 −1	4.57 −1	71.275	1.979
40	7.443 −4	1.9259	0.0055	0.00 +0	3.91 −1	3.91 −1	71.699	1.555
41	6.439 −4	1.9266	0.0048	0.00 +0	3.19 −1	3.20 −1	72.054	1.199
42	5.579 −4	1.9272	0.0042	0.00 +0	2.50 −1	2.50 −1	72.339	0.914
43	4.841 −4	1.9277	0.0037	0.00 +0	1.95 −1	1.96 −1	72.563	0.691
44	4.208 −4	1.9282	0.0033	0.00 +0	1.56 −1	1.57 −1	72.739	0.515
45	3.663 −4	1.9286	0.0029	0.00 +0	1.21 −1	1.21 −1	72.878	0.376
46	3.193 −4	1.9289	0.0025	0.00 +0	9.37 −2	9.40 −2	72.985	0.268
47	2.788 −4	1.9292	0.0022	0.00 +0	7.41 −2	7.44 −2	73.070	0.184
48	2.453 −4	1.9295	0.0020	0.00 +0	5.86 −2	5.88 −2	73.136	0.117
49	2.166 −4	1.9297	0.0017	0.00 +0	4.68 −2	4.70 −2	73.189	0.064
50	1.913 −4	1.9299	0.0015	0.00 +0	3.91 −2	3.93 −2	73.232	0.021

(Continued)

Table 7-4. Parameters for the model of a clear standard atmosphere. Numbers following the plus or minus sign are the power of ten by which that entry shall be multiplied. (Continued)

Alt (km)	Rayleigh Atten Coeff (km^{-1})	Rayleigh Optical Thick. (0-h)	Rayleigh Optical Thick. (h-∞)	Aerosol Atten Coeff (km^{-1})	Ozone Absorp Coeff (km^{-1})	Ext Coeff (km^{-1})	Ext Optical Thick. (0-h)	Ext Optical Thick. (h-∞)
			PARAMETERS AT 0.28 MICRONS					
0	1.948 −1	0.0000	1.6481	2.70 −1	3.77 −1	8.42 −1	0.000	37.806
1	1.767 −1	0.1858	1.4624	1.19 −1	3.46 −1	6.41 −1	0.742	37.065
2	1.600 −1	0.3541	1.2940	5.13 −2	3.11 −1	5.22 −1	1.323	36.483
3	1.446 −1	0.5064	1.1417	2.16 −2	2.65 −1	4.31 −1	1.800	36.007
4	1.303 −1	0.6438	1.0043	9.72 −3	2.40 −1	3.80 −1	2.205	35.601
5	1.171 −1	0.7675	0.8806	4.32 −3	2.34 −1	3.56 −1	2.573	35.234
6	1.050 −1	0.8785	0.7696	1.48 −3	2.29 −1	3.35 −1	2.918	34.888
7	9.380 −2	0.9779	0.6702	5.40 −4	2.36 −1	3.31 −1	3.251	34.555
8	8.359 −2	1.0666	0.5815	1.89 −4	2.42 −1	3.25 −1	3.579	34.227
9	7.426 −2	1.1455	0.5026	6.75 −5	2.98 −1	3.72 −1	3.928	33.878
10	6.574 −2	1.2155	0.4326	3.51 −5	3.71 −1	4.37 −1	4.333	33.474
11	5.800 −2	1.2774	0.3707	3.24 −5	4.88 −1	5.46 −1	4.824	32.983
12	4.959 −2	1.3312	0.3170	2.97 −5	6.58 −1	7.08 −1	5.451	32.356
13	4.238 −2	1.3772	0.2710	3.24 −5	8.96 −1	9.38 −1	6.274	31.533
14	3.623 −2	1.4165	0.2317	3.51 −5	1.01 +0	1.05 +0	7.268	30.538
15	3.096 −2	1.4501	0.1981	5.67 −5	1.05 +0	1.08 +0	8.336	29.471
16	2.647 −2	1.4788	0.1693	9.18 −5	1.09 +0	1.12 +0	9.437	28.369
17	2.262 −2	1.5033	0.1448	9.99 −5	1.18 +0	1.20 +0	10.596	27.210
18	1.934 −2	1.5243	0.1238	1.08 −4	1.29 +0	1.31 +0	11.852	25.954
19	1.653 −2	1.5423	0.1059	1.21 −4	1.51 +0	1.52 +0	13.269	24.537
20	1.413 −2	1.5576	0.0906	1.16 −4	1.74 +0	1.75 +0	14.906	22.900
21	1.204 −2	1.5707	0.0775	1.11 −4	1.95 +0	1.96 +0	16.764	21.042
22	1.026 −2	1.5818	0.0663	1.08 −4	2.09 +0	2.10 +0	18.795	19.012
23	8.744 −3	1.5913	0.0568	1.03 −4	2.10 +0	2.11 +0	20.898	16.909
24	7.461 −3	1.5994	0.0487	7.02 −5	2.05 +0	2.05 +0	22.978	14.828
25	6.372 −3	1.6063	0.0418	4.86 −5	1.91 +0	1.91 +0	24.962	12.844
26	5.446 −3	1.6123	0.0359	3.51 −5	1.73 +0	1.73 +0	26.786	11.020
27	4.657 −3	1.6173	0.0308	3.24 −5	1.49 +0	1.50 +0	28.402	9.404
28	3.986 −3	1.6216	0.0265	2.97 −5	1.30 +0	1.31 +0	29.806	8.001
29	3.414 −3	1.6253	0.0228	2.70 −5	1.13 +0	1.14 +0	31.028	6.778
30	2.927 −3	1.6285	0.0197	2.56 −5	9.57 −1	9.60 −1	32.077	5.729
31	2.510 −3	1.6312	0.0169	0.00 +0	8.41 −1	8.43 −1	32.979	4.827
32	2.155 −3	1.6335	0.0146	0.00 +0	7.24 −1	7.25 −1	33.763	4.043
33	1.840 −3	1.6355	0.0126	0.00 +0	6.17 −1	6.19 −1	34.435	3.371
34	1.572 −3	1.6373	0.0109	0.00 +0	5.12 −1	5.14 −1	35.001	2.805
35	1.345 −3	1.6387	0.0094	0.00 +0	4.57 −1	4.58 −1	35.487	2.319
36	1.154 −3	1.6400	0.0082	0.00 +0	3.83 −1	3.84 −1	35.908	1.898
37	9.912 −4	1.6410	0.0071	0.00 +0	3.20 −1	3.21 −1	36.261	1.546
38	8.531 −4	1.6420	0.0062	0.00 +0	2.68 −1	2.69 −1	36.556	1.251
39	7.355 −4	1.6427	0.0054	0.00 +0	2.30 −1	2.31 −1	36.805	1.001
40	6.352 −4	1.6434	0.0047	0.00 +0	1.97 −1	1.98 −1	31.020	0.787
41	5.494 −4	1.6440	0.0041	0.00 +0	1.61 −1	1.62 −1	37.199	0.607
42	4.761 −4	1.6445	0.0036	0.00 +0	1.26 −1	1.27 −1	37.334	0.463
43	4.131 −4	1.6450	0.0032	0.00 +0	9.86 −2	9.90 −2	37.456	0.350
44	3.591 −4	1.6454	0.0028	0.00 +0	7.89 −2	7.92 −2	37.546	0.261
45	3.126 −4	1.6457	0.0024	0.00 +0	6.11 −2	6.14 −2	37.616	0.191
46	2.725 −4	1.6460	0.0022	0.00 +0	4.73 −2	4.75 −2	37.670	0.136
47	2.379 −4	1.6463	0.0019	0.00 +0	3.74 −2	3.77 −2	37.713	0.094
48	2.093 −4	1.6465	0.0017	0.00 +0	2.96 −2	2.98 −2	37.747	0.060
59	1.848 −4	1.6467	0.0015	0.00 +0	2.36 −2	2.38 −2	37.773	0.033
50	1.632 −4	1.6468	0.0013	0.00 +0	1.97 −2	1.99 −2	37.795	0.011

(Continued)

Table 7-4. Parameters for the model of a clear standard atmosphere. Numbers following the plus or minus sign are the power of ten by which that entry shall be multiplied. (Continued)

Alt (km)	Rayleigh Atten Coeff (km^{-1})	Rayleigh Optical Thick. (0-h)	Rayleigh Optical Thick. (h-∞)	Aerosol Atten Coeff (km^{-1})	Ozone Absorp Coeff (km^{-1})	Ext Coeff (km^{-1})	Ext Optical Thick. (0-h)	Ext Optical Thick. (h-∞)
				PARAMETERS AT 0.30 MICRONS				
0	1.446 −1	0.0000	1.2237	2.60 −1	3.60 −2	4.41 −1	0.000	4.968
1	1.312 −1	0.1379	1.0858	1.14 −1	3.29 −2	2.79 −1	0.360	4.608
2	1.188 −1	0.2629	0.9607	4.94 −2	2.96 −2	1.98 −1	0.598	4.370
3	1.073 −1	0.3760	0.8477	2.08 −2	2.52 −2	1.53 −1	0.773	4.194
4	9.671 −2	0.4780	0.7456	9.36 −3	2.28 −2	1.29 −1	0.914	4.053
5	8.693 −2	0.5698	0.6538	4.16 −3	2.23 −2	1.13 −1	1.036	3.932
6	7.792 −2	0.6523	0.5714	1.43 −3	2.18 −2	1.01 −1	1.143	3.825
7	6.964 −2	0.7260	0.4976	5.20 −4	2.25 −2	9.27 −2	1.240	3.728
8	6.206 −2	0.7919	0.4318	1.82 −4	2.30 −2	8.53 −2	1.329	3.639
9	5.513 −2	0.8505	0.3732	6.50 −5	2.84 −2	8.36 −2	1.413	3.555
10	4.881 −2	0.9025	0.3212	3.38 −5	3.53 −2	8.42 −2	1.497	3.471
11	4.306 −2	0.9484	0.2753	3.12 −5	4.65 −2	8.96 −2	1.584	3.384
12	3.682 −2	0.9883	0.2353	2.86 −5	6.27 −2	9.96 −2	1.679	3.289
13	3.147 −2	1.0225	0.2012	3.12 −5	8.53 −2	1.17 −1	1.787	3.181
14	2.690 −2	1.0517	0.1720	3.38 −5	9.67 −2	1.24 −1	1.907	3.061
15	2.299 −2	1.0766	0.1471	5.46 −5	1.00 −1	1.23 −1	2.030	2.937
16	1.965 −2	1.0979	0.1257	8.84 −5	1.04 −1	1.24 −1	2.154	2.814
17	1.680 −2	1.1162	0.1075	9.62 −5	1.12 −1	1.29 −1	2.280	2.687
18	1.436 −2	1.1317	0.0919	1.04 −4	1.23 −1	1.38 −1	2.414	2.554
19	1.228 −2	1.1450	0.0786	1.17 −4	1.43 −1	1.56 −1	2.561	2.407
20	1.049 −2	1.1564	0.0672	1.12 −4	1.66 −1	1.76 −1	2.727	2.241
21	8.936 −3	1.1661	0.0575	1.07 −4	1.86 −1	1.95 −1	2.912	2.056
22	7.614 −3	1.1744	0.0492	1.04 −4	1.99 −1	2.07 −1	3.113	1.855
23	6.492 −3	1.1815	0.0422	9.88 −5	2.00 −1	2.07 −1	3.320	1.648
24	5.540 −3	1.1875	0.0362	6.76 −5	1.95 −1	2.01 −1	3.523	1.445
25	4.731 −3	1.1926	0.0310	4.68 −5	1.82 −1	1.87 −1	3.717	1.251
26	4.043 −3	1.1970	0.0267	3.38 −5	1.65 −1	1.69 −1	3.894	1.073
27	3.458 −3	1.2008	0.0229	3.12 −5	1.42 −1	1.46 −1	4.052	0.916
28	2.960 −3	1.2040	0.0197	2.86 −5	1.24 −1	1.27 −1	4.188	0.780
29	2.535 −3	1.2067	0.0169	2.60 −5	1.08 −1	1.11 −1	4.307	0.661
30	2.173 −3	1.2091	0.0146	2.47 −5	9.12 −2	9.34 −2	4.409	0.559
31	1.864 −3	1.2111	0.0126	0.00 +0	8.01 −2	8.20 −2	4.497	0.471
32	1.600 −3	1.2128	0.0108	0.00 +0	6.89 −2	7.05 −2	4.573	0.395
33	1.366 −3	1.2143	0.0094	0.00 +0	5.88 −2	6.01 −2	4.638	0.329
34	1.167 −3	1.2156	0.0081	0.00 +0	4.88 −2	4.99 −2	4.693	0.274
35	9.989 −4	2.2167	0.0070	0.00 +0	4.35 −2	4.45 −2	4.741	0.227
36	8.566 −4	1.2176	0.0061	0.00 +0	3.65 −2	3.73 −2	4.782	0.186
37	7.359 −4	1.2184	0.0053	0.00 +0	3.05 −2	3.12 −2	4.816	0.152
38	6.334 −4	1.2191	0.0046	0.00 +0	2.56 −2	2.62 −2	4.845	0.123
39	5.461 −4	1.2197	0.0040	0.00 +0	2.19 −2	2.25 −2	4.869	0.099
40	4.716 −4	1.2202	0.0035	0.00 +0	1.88 −2	1.93 −2	4.890	0.078
41	4.079 −4	1.2206	0.0031	0.00 +0	1.54 −2	1.58 −2	4.907	0.060
42	3.534 −4	1.2210	0.0027	0.00 +0	1.20 −2	1.24 −2	4.921	0.046
43	3.067 −4	1.2213	0.0024	0.00 +0	9.39 −3	9.70 −3	4.932	0.035
44	2.666 −4	1.2216	0.0021	0.00 +0	7.51 −3	7.78 −3	4.941	0.027
45	2.321 −4	1.2218	0.0018	0.00 +0	5.82 −3	6.05 −3	4.948	0.020
46	2.023 −4	1.2221	0.0016	0.00 +0	4.50 −3	4.71 −3	4.953	0.014
47	1.766 −4	1.2223	0.0014	0.00 +0	3.57 −3	3.74 −3	4.958	0.010
48	1.554 −4	1.2224	0.0012	0.00 +0	2.82 −3	2.97 −3	4.961	0.007
49	1.372 −4	1.2226	0.0011	0.00 +0	2.25 −3	2.39 −3	4.964	0.004
50	1.212 −4	1.2227	0.0010	0.00 +0	1.88 −3	2.00 −3	4.966	0.002

(Continued)

Table 7-4. Parameters for the model of a clear standard atmosphere. Numbers following the plus or minus sign are the power of ten by which that entry shall be multiplied. (Continued)

Alt (km)	Rayleigh Atten Coeff (km^{-1})	Rayleigh Optical Thick. (0-h)	Rayleigh Optical Thick. (h-∞)	Aerosol Atten Coeff (km^{-1})	Ozone Absorp Coeff (km^{-1})	Ext Coeff (km^{-1})	Ext Optical Thick. (0-h)	Ext Optical Thick. (h-∞)
			PARAMETERS AT 0.32 MICRONS					
0	1.089 −1	0.0000	0.9290	2.50 −1	3.20 −3	3.63 −1	0.000	1.551
1	9.962 −2	0.1047	0.8243	1.10 −1	2.93 −3	2.13 −1	0.288	1.263
2	9.020 −2	0.1996	0.7294	4.75 −2	2.63 −3	1.40 −1	0.464	1.087
3	8.148 −2	0.2854	0.6435	2.00 −2	2.24 −3	1.04 −1	0.586	0.965
4	7.342 −2	0.3629	0.5661	9.00 −3	2.03 −3	8.45 −2	0.680	0.871
5	6.599 −2	0.4326	0.4964	4.00 −3	1.98 −3	7.20 −2	0.759	0.793
6	5.915 −2	0.4952	0.4338	1.38 −3	1.94 −3	6.25 −2	0.826	0.725
7	5.287 −2	0.5512	0.3778	5.00 −4	2.00 −3	5.54 −2	0.885	0.667
8	4.711 −2	0.6012	0.3278	1.75 −4	2.05 −3	4.93 −2	0.937	0.614
9	4.185 −2	0.6457	0.2833	6.25 −5	2.52 −3	4.44 −2	0.984	0.567
10	3.705 −2	0.6851	0.2438	3.25 −5	3.14 −3	4.02 −2	1.026	0.525
11	3.269 −2	0.7200	0.2090	3.00 −5	4.13 −3	3.69 −2	1.065	0.486
12	2.795 −2	0.7503	0.1786	2.75 −5	5.58 −3	3.36 −2	1.100	0.451
13	2.389 −2	0.7762	0.1527	3.00 −5	7.59 −3	3.15 −2	1.133	0.419
14	2.042 −2	0.7984	0.1306	3.25 −5	8.59 −3	2.90 −2	1.163	0.388
15	1.745 −2	0.8173	0.1116	5.25 −5	8.93 −3	2.64 −2	1.191	0.361
16	1.492 −2	0.8335	0.0955	8.50 −5	9.25 −3	2.43 −2	1.216	0.335
17	1.275 −2	0.8473	0.0816	9.25 −5	9.97 −3	2.28 −2	1.239	0.312
18	1.090 −2	0.8592	0.0698	1.00 −4	1.10 −2	2.20 −2	1.262	0.289
19	9.319 −3	0.8693	0.0597	1.13 −4	1.28 −2	2.22 −2	1.284	0.267
20	7.966 −3	0.8779	0.0510	1.08 −4	1.47 −2	2.28 −2	1.306	0.245
21	6.784 −3	0.8853	0.0437	1.02 −4	1.65 −2	2.34 −2	1.329	0.222
22	5.780 −3	0.8916	0.0374	1.00 −4	1.77 −2	2.36 −2	1.353	0.198
23	4.928 −3	0.8969	0.0320	9.50 −5	1.78 −2	2.28 −2	1.376	0.175
24	4.205 −3	0.9015	0.0275	6.50 −5	1.73 −2	2.16 −2	1.398	0.153
25	3.591 −3	0.9054	0.0236	4.50 −5	1.62 −2	1.98 −2	1.419	0.132
26	3.069 −3	0.9087	0.0202	3.25 −5	1.46 −2	1.77 −2	1.438	0.113
27	2.625 −3	0.9116	0.0174	3.00 −5	1.27 −2	1.53 −2	1.454	0.097
28	2.247 −3	0.9140	0.0149	2.75 −5	1.10 −2	1.33 −2	1.469	0.083
29	1.924 −3	0.9161	0.0129	2.50 −5	9.61 −3	1.16 −2	1.481	0.070
30	1.649 −3	0.9179	0.0111	2.38 −5	8.11 −3	9.78 −3	1.492	0.059
31	1.415 −3	0.9194	0.0095	0.00 +0	7.12 −3	8.54 −3	1.501	0.050
32	1.214 −3	0.9207	0.0082	0.00 +0	6.12 −3	7.34 −3	1.509	0.042
33	1.037 −3	0.9219	0.0071	0.00 +0	5.23 −3	6.26 −3	1.516	0.036
34	8.859 −4	0.9228	0.0061	0.00 +0	4.34 −3	5.22 −3	1.521	0.030
35	7.583 −4	0.9236	0.0053	0.00 +0	3.87 −3	4.63 −3	1.526	0.025
36	6.503 −4	0.9243	0.0046	0.00 +0	3.24 −3	3.89 −3	1.531	0.021
37	5.587 −4	0.9249	0.0040	0.00 +0	2.71 −3	3.27 −3	1.534	0.017
38	4.808 −4	0.9255	0.0035	0.00 +0	2.27 −3	2.75 −3	1.537	0.014
39	4.145 −4	0.9259	0.0030	0.00 +0	1.95 −3	2.36 −3	1.540	0.011
40	3.580 −4	0.9263	0.0027	0.00 +0	1.67 −3	2.03 −3	1.542	0.009
41	3.097 −4	0.9266	0.0023	0.00 +0	1.36 −3	1.67 −3	1.544	0.007
42	2.683 −4	0.9269	0.0020	0.00 +0	1.07 −3	1.34 −3	1.545	0.006
43	2.329 −4	0.9272	0.0018	0.00 +0	8.35 −4	1.07 −3	1.546	0.005
44	2.024 −4	0.9274	0.0016	0.00 +0	6.68 −4	8.70 −4	1.547	0.004
45	1.762 −4	0.9276	0.0014	0.00 +0	5.17 −4	6.93 −4	1.548	0.003
46	1.536 −4	0.9277	0.0012	0.00 +0	4.01 −4	5.54 −4	1.549	0.002
47	1.341 −4	0.9279	0.0011	0.00 +0	3.17 −4	4.51 −4	1.549	0.002
48	1.180 −4	0.9280	0.0009	0.00 +0	2.51 −4	3.69 −4	1.550	0.001
49	1.042 −4	0.9281	0.0008	0.00 +0	2.00 −4	3.04 −4	1.550	0.001
50	9.201 −5	0.9282	0.0007	0.00 +0	1.67 −4	2.59 −4	1.550	0.001

(Continued)

Table 7-4. Parameters for the model of a clear standard atmosphere. Numbers following the plus or minus sign are the power of ten by which that entry shall be multiplied. (Continued)

Alt (km)	Rayleigh Atten Coeff (km^{-1})	Rayleigh Optical Thick. (0-h)	Rayleigh Optical Thick. (h-∞)	Aerosol Atten Coeff (km^{-1})	Ozone Absorp Coeff (km^{-1})	Ext Coeff (km^{-1})	Ext Optical Thick. (0-h)	Ext Optical Thick. (h-∞)
			PARAMETERS AT 0.34 MICRONS					
0	8.494 −2	0.0000	0.7188	2.40 −1	2.28 −4	3.25 −1	0.000	1.046
1	7.708 −2	0.0810	0.6378	1.06 −1	2.09 −4	1.83 −1	0.254	0.792
2	6.979 −2	0.1544	0.5643	4.56 −2	1.88 −4	1.16 −1	0.403	0.643
3	6.304 −2	0.2209	0.4979	1.92 −2	1.60 −4	8.24 −2	0.502	0.544
4	5.681 −2	0.2808	0.4380	8.64 −3	1.45 −4	6.56 −2	0.576	0.470
5	5.106 −2	0.3347	0.3840	3.84 −3	1.41 −4	5.50 −2	0.637	0.410
6	4.577 −2	0.3831	0.3356	1.32 −3	1.38 −4	4.72 −2	0.688	0.359
7	4.091 −2	0.4265	0.2923	4.80 −4	1.43 −4	4.15 −2	0.732	0.314
8	3.645 −2	0.4651	0.2536	1.68 −4	1.46 −4	3.68 −2	0.771	0.275
9	3.238 −2	0.4996	0.2192	6.00 −5	1.80 −4	3.26 −2	0.806	0.241
10	2.867 −2	0.5301	0.1887	3.12 −5	2.24 −4	2.89 −2	0.837	0.210
11	2.529 −2	0.5571	0.1617	2.88 −5	2.94 −4	2.56 −2	0.864	0.183
12	2.163 −2	0.5805	0.1382	2.64 −5	3.97 −4	2.21 −2	0.888	0.159
13	1.848 −2	0.6006	0.1182	2.88 −5	5.41 −4	1.91 −2	0.908	0.138
14	1.580 −2	0.6177	0.1010	3.12 −5	6.12 −4	1.64 −2	0.926	0.120
15	1.350 −2	0.6324	0.0864	5.04 −5	6.36 −4	1.42 −2	0.941	0.105
16	1.154 −2	0.6449	0.0739	8.16 −5	6.59 −4	1.23 −2	0.955	0.092
17	9.866 −3	0.6556	0.0631	8.88 −5	7.10 −4	1.07 −2	0.966	0.080
18	8.434 −3	0.6648	0.0540	9.60 −5	7.81 −4	9.31 −3	0.976	0.070
19	7.210 −3	0.6726	0.0462	1.08 −4	9.09 −4	8.23 −3	0.985	0.062
20	6.164 −3	0.6793	0.0395	1.03 −4	1.05 −3	7.32 −3	0.993	0.054
21	5.249 −3	0.6850	0.0338	9.84 −5	1.18 −3	6.52 −3	1.000	0.047
22	4.472 −3	0.6898	0.0289	9.60 −5	1.26 −3	5.83 −3	1.006	0.041
23	3.813 −3	0.6940	0.0248	9.12 −5	1.27 −3	5.17 −3	1.011	0.035
24	3.254 −3	0.6975	0.0212	6.24 −5	1.24 −3	4.55 −3	1.016	0.030
25	2.779 −3	0.7005	0.0182	4.32 −5	1.15 −3	3.97 −3	1.020	0.026
26	2.375 −3	0.7031	0.0157	3.12 −5	1.04 −3	3.45 −3	1.024	0.022
27	2.031 −3	0.7053	0.0135	2.88 −5	9.02 −4	2.96 −3	1.027	0.019
28	1.738 −3	0.7072	0.0116	2.64 −5	7.87 −4	2.55 −3	1.030	0.016
29	1.489 −3	0.7088	0.0100	2.40 −5	6.85 −4	2.20 −3	1.032	0.014
30	1.276 −3	0.7102	0.0086	2.28 −5	5.78 −4	1.88 −3	1.034	0.012
31	1.095 −3	0.7114	0.0074	0.00 +0	5.08 −4	1.60 −3	1.036	0.010
32	9.397 −4	0.7124	0.0064	0.00 +0	4.36 −4	1.38 −3	1.038	0.009
33	8.023 −4	0.7133	0.0055	0.00 +0	3.72 −4	1.17 −3	1.039	0.008
34	6.854 −4	0.7140	0.0048	0.00 +0	3.09 −4	9.95 −4	1.040	0.006
35	5.867 −4	0.7146	0.0041	0.00 +0	2.76 −4	8.63 −4	1.041	0.006
36	5.031 −4	0.7152	0.0036	0.00 +0	2.31 −4	7.34 −4	1.042	0.005
37	4.323 −4	0.7157	0.0031	0.00 +0	1.93 −4	6.26 −4	1.042	0.004
38	3.720 −4	0.7161	0.0027	0.00 +0	1.62 −4	5.34 −4	1.043	0.003
39	3.207 −4	0.7164	0.0024	0.00 +0	1.39 −4	4.60 −4	1.044	0.003
40	2.770 −4	0.7167	0.0021	0.00 +0	1.19 −4	3.96 −4	1.044	0.003
41	2.396 −4	0.7170	0.0018	0.00 +0	9.73 −5	3.37 −4	1.044	0.002
42	2.076 −4	0.7172	0.0016	0.00 +0	7.62 −5	2.84 −4	1.045	0.002
43	1.802 −4	0.7174	0.0014	0.00 +0	5.95 −5	2.40 −4	1.045	0.002
44	1.566 −4	0.7175	0.0012	0.00 +0	4.76 −5	2.04 −4	1.045	0.001
45	1.363 −4	0.7177	0.0011	0.00 +0	3.69 −5	1.73 −4	1.045	0.001
46	1.188 −4	0.7178	0.0009	0.00 +0	2.85 −5	1.47 −4	1.045	0.001
47	1.037 −4	0.7179	0.0008	0.00 +0	2.26 −5	1.26 −4	1.046	0.001
48	9.128 −5	0.7180	0.0007	0.00 +0	1.79 −5	1.09 −4	1.046	0.001
49	8.061 −5	0.7181	0.0006	0.00 +0	1.43 −5	9.49 −5	1.046	0.001
50	7.119 −5	0.7182	0.0006	0.00 +0	1.19 −5	8.31 −5	1.046	0.001

(Continued)

Table 7-4. Parameters for the model of a clear standard atmosphere. Numbers following the plus or minus sign are the power of ten by which that entry shall be multiplied. (Continued)

Alt (km)	Rayleigh Atten Coeff (km^{-1})	Rayleigh Optical Thick. (0-h)	Rayleigh Optical Thick. (h-∞)	Aerosol Atten Coeff (km^{-1})	Ozone Absorp Coeff (km^{-1})	Ext Coeff (km^{-1})	Ext Optical Thick. (0-h)	Ext Optical Thick. (h-∞)
				PARAMETERS AT 0.36 MICRONS				
0	6.680 −2	0.0000	0.5653	2.40 −1	6.41 −6	3.07 −1	0.000	0.872
1	6.062 −2	0.0637	0.5016	1.06 −1	5.87 −6	1.66 −1	0.237	0.635
2	5.489 −2	0.1215	0.4438	4.56 −2	5.27 −6	1.00 −1	0.370	0.502
3	4.958 −2	0.1737	0.3916	1.92 −2	4.50 −6	6.88 −2	0.455	0.417
4	4.468 −2	0.2208	0.3444	8.64 −3	4.07 −6	5.33 −2	0.516	0.356
5	4.016 −2	0.2632	0.3020	3.84 −3	3.98 −6	4.40 −2	0.564	0.308
6	3.599 −2	0.3013	0.2640	1.32 −3	3.89 −6	3.73 −2	0.605	0.267
7	3.217 −2	0.3354	0.2299	4.80 −4	4.01 −6	3.27 −2	0.640	0.232
8	2.867 −2	0.3658	0.1995	1.68 −4	4.10 −6	2.88 −2	0.671	0.201
9	2.547 −2	0.3929	0.1724	6.00 −5	5.06 −6	2.55 −2	0.698	0.174
10	2.255 −2	0.4169	0.1484	3.12 −5	6.30 −6	2.26 −2	0.722	0.150
11	1.989 −2	0.4381	0.1272	2.88 −5	8.28 −6	1.99 −2	0.743	0.129
12	1.701 −2	0.4566	0.1087	2.64 −5	1.12 −5	1.70 −2	0.762	0.110
13	1.454 −2	0.4723	0.0929	2.88 −5	1.52 −5	1.46 −2	0.777	0.095
14	1.242 −2	0.4858	0.0795	3.12 −5	1.72 −5	1.25 −2	0.791	0.081
15	1.062 −2	0.4973	0.0679	5.04 −5	1.79 −5	1.07 −2	0.803	0.069
16	9.077 −3	0.5072	0.0581	8.16 −5	1.85 −5	9.18 −3	0.812	0.060
17	7.759 −3	0.5156	0.0497	8.88 −5	2.00 −5	7.87 −3	0.821	0.051
18	6.633 −3	0.5228	0.0425	9.60 −5	2.20 −5	6.75 −3	0.828	0.044
19	5.671 −3	0.5289	0.0363	1.08 −4	2.56 −5	5.80 −3	0.835	0.037
20	4.847 −3	0.5342	0.0311	1.03 −4	2.95 −5	4.98 −3	0.840	0.032
21	4.128 −3	0.5387	0.0266	9.84 −5	3.31 −5	4.26 −3	0.845	0.027
22	3.517 −3	0.5425	0.0227	9.60 −5	3.55 −5	3.65 −3	0.849	0.023
23	2.999 −3	0.5458	0.0195	9.12 −5	3.56 −5	3.13 −3	0.852	0.020
24	2.559 −3	0.5486	0.0167	6.24 −5	3.47 −5	2.66 −3	0.855	0.017
25	2.185 −3	0.5509	0.0143	4.32 −5	3.24 −5	2.26 −3	0.857	0.015
26	1.868 −3	0.5530	0.0123	3.12 −5	2.93 −5	1.93 −3	0.859	0.013
27	1.597 −3	0.5547	0.0106	2.88 −5	2.54 −5	1.65 −3	0.861	0.011
28	1.367 −3	0.5562	0.0091	2.64 −5	2.21 −5	1.42 −3	0.863	0.009
29	1.171 −3	0.5574	0.0078	2.40 −5	1.93 −5	1.21 −3	0.864	0.008
30	1.004 −3	0.5585	0.0067	2.28 −5	1.63 −5	1.04 −3	0.865	0.007
31	8.609 −4	0.5595	0.0058	0.00 +0	1.43 −5	8.75 −4	0.866	0.006
32	7.390 −4	0.5603	0.0050	0.00 +0	1.23 −5	7.51 −4	0.867	0.005
33	6.310 −4	0.5609	0.0043	0.00 +0	1.05 −5	6.41 −4	0.868	0.004
34	5.391 −4	0.5615	0.0037	0.00 +0	8.69 −6	5.48 −4	0.868	0.004
35	4.614 −4	0.5620	0.0032	0.00 +0	7.76 −6	4.69 −4	0.869	0.003
36	3.957 −4	0.5625	0.0028	0.00 +0	6.50 −6	4.02 −4	0.869	0.003
37	3.399 −4	0.5628	0.0024	0.00 +0	5.44 −6	3.45 −4	0.870	0.002
38	2.926 −4	0.5631	0.0021	0.00 +0	4.55 −6	2.97 −4	0.870	0.002
39	2.522 −4	0.5634	0.0019	0.00 +0	3.91 −6	2.56 −4	0.870	0.002
40	2.178 −4	0.5636	0.0016	0.00 +0	3.35 −6	2.21 −4	0.870	0.002
41	1.884 −4	0.5638	0.0014	0.00 +0	2.74 −6	1.91 −4	0.871	0.001
42	1.633 −4	0.5640	0.0012	0.00 +0	2.14 −6	1.65 −4	0.871	0.001
43	1.417 −4	0.5642	0.0011	0.00 +0	1.67 −2	1.43 −4	0.871	0.001
44	1.232 −4	0.5643	0.0010	0.00 +0	1.34 −6	1.24 −4	0.871	0.001
45	1.072 −4	0.5644	0.0008	0.00 +0	1.04 −6	1.08 −4	0.871	0.001
46	9.345 −5	0.5645	0.0007	0.00 +0	8.03 −7	9.43 −5	0.871	0.001
47	8.159 −5	0.5646	0.0007	0.00 +0	6.35 −7	8.22 −5	0.871	0.001
48	7.179 −5	0.5647	0.0006	0.00 +0	5.02 −7	7.23 −5	0.871	0.001
49	6.339 −5	0.5648	0.0005	0.00 +0	4.01 −7	6.38 −5	0.871	0.001
50	5.598 −5	0.5648	0.0004	0.00 +0	3.35 −7	5.63 −5	0.872	0.000

(Continued)

Table 7-4. Parameters for the model of a clear standard atmosphere. Numbers following the plus or minus sign are the power of ten by which that entry shall be multiplied. (Continued)

Alt (km)	Rayleigh Atten Coeff (km^{-1})	Rayleigh Optical Thick. (0-h)	Rayleigh Optical Thick. (h-∞)	Aerosol Atten Coeff (km^{-1})	Ozone Absorp Coeff (km^{-1})	Ext Coeff (km^{-1})	Ext Optical Thick. (0-h)	Ext Optical Thick. (h-∞)
				PARAMETERS AT 0.38 MICRONS				
0	5.327 −2	0.0000	0.4508	2.30 −1	0.00 +0	2.83 −1	0.000	0.744
1	4.834 −2	0.0508	0.4000	1.01 −1	0.00 +0	1.50 −1	0.216	0.528
2	4.377 −2	0.0969	0.3539	4.37 −2	0.00 +0	8.75 −2	0.335	0.409
3	3.954 −2	0.1385	0.3123	1.84 −2	0.00 +0	5.79 −2	0.408	0.337
4	3.563 −2	0.1761	0.2747	8.28 −3	0.00 +0	4.39 −2	0.459	0.286
5	3.202 −2	0.2099	0.2409	3.68 −3	0.00 +0	3.57 −2	0.498	0.246
6	2.871 −2	0.2403	0.2105	1.27 −3	0.00 +0	3.00 −2	0.531	0.213
7	2.566 −2	0.2675	0.1833	4.60 −4	0.00 +0	2.61 −2	0.559	0.185
8	2.286 −2	0.2917	0.1591	1.61 −4	0.00 +0	2.30 −2	0.584	0.160
9	2.031 −2	0.3133	0.1375	5.75 −5	0.00 +0	2.04 −2	0.605	0.139
10	1.798 −2	0.3325	0.1183	2.99 −5	0.00 +0	1.80 −2	0.625	0.119
11	1.586 −2	0.3494	0.1014	2.76 −5	0.00 +0	1.59 −2	0.642	0.103
12	1.356 −2	0.3641	0.0867	2.53 −5	0.00 +0	1.36 −2	0.656	0.088
13	1.159 −2	0.3767	0.0741	2.76 −5	0.00 +0	1.16 −2	0.669	0.075
14	9.908 −3	0.3874	0.0634	2.99 −5	0.00 +0	9.94 −3	0.680	0.064
15	8.469 −3	0.3966	0.0542	4.83 −5	0.00 +0	8.52 −3	0.689	0.055
16	7.239 −3	0.4045	0.0463	7.82 −5	0.00 +0	7.32 −3	0.697	0.047
17	6.188 −3	0.4112	0.0396	8.51 −5	0.00 +0	6.27 −3	0.704	0.040
18	5.290 −3	0.4169	0.0339	9.20 −5	0.00 +0	5.38 −3	0.710	0.035
19	4.522 −3	0.4218	0.0290	1.03 −4	0.00 +0	4.63 −3	0.715	0.030
20	3.866 −3	0.4260	0.0248	9.89 −5	0.00 +0	3.96 −3	0.719	0.025
21	3.292 −3	0.4296	0.0212	9.43 −5	0.00 +0	3.39 −3	0.722	0.022
22	2.805 −3	0.4326	0.0181	9.20 −5	0.00 +0	2.90 −3	0.726	0.019
23	2.391 −3	0.4352	0.0155	8.74 −5	0.00 +0	2.48 −3	0.728	0.016
24	2.041 −3	0.4375	0.0133	5.98 −5	0.00 +0	2.10 −3	0.731	0.014
25	1.743 −3	0.4394	0.0114	4.14 −5	0.00 +0	1.78 −3	0.733	0.012
26	1.489 −3	0.4410	0.0098	2.99 −5	0.00 +0	1.52 −3	0.734	0.010
27	1.274 −3	0.4424	0.0084	2.76 −5	0.00 +0	1.30 −3	0.736	0.009
28	1.090 −3	0.4435	0.0073	2.53 −5	0.00 +0	1.12 −3	0.737	0.007
29	9.338 −4	0.4445	0.0062	2.30 −5	0.00 +0	9.57 −4	0.738	0.006
30	8.004 −4	0.4454	0.0054	2.18 −5	0.00 +0	8.22 −4	0.739	0.005
31	6.866 −4	0.4462	0.0046	0.00 +0	0.00 +0	6.87 −4	0.740	0.005
32	5.893 −4	0.4468	0.0040	0.00 +0	0.00 +0	5.89 −4	0.740	0.004
33	5.032 −4	0.4473	0.0034	0.00 +0	0.00 +0	5.03 −4	0.741	0.003
34	4.299 −4	0.4478	0.0030	0.00 +0	0.00 +0	4.30 −4	0.741	0.003
35	3.680 −4	0.4482	0.0026	0.00 +0	0.00 +0	3.68 −4	0.742	0.003
36	3.156 −4	0.4485	0.0022	0.00 +0	0.00 +0	3.16 −4	0.742	0.002
37	2.711 −4	0.4488	0.0019	0.00 +0	0.00 +0	2.71 −4	0.742	0.002
38	2.333 −4	0.4491	0.0017	0.00 +0	0.00 +0	2.33 −4	0.742	0.002
39	2.012 −4	0.4493	0.0015	0.00 +0	0.00 +0	2.01 −4	0.743	0.001
40	1.737 −4	0.4495	0.0013	0.00 +0	0.00 +0	1.74 −4	0.743	0.001
41	1.503 −4	0.4497	0.0011	0.00 +0	0.00 +0	1.50 −4	0.743	0.001
42	1.302 −4	0.4498	0.0010	0.00 +0	0.00 +0	1.30 −4	0.743	0.001
43	1.130 −4	0.4499	0.0009	0.00 +0	0.00 +0	1.13 −4	0.743	0.001
44	9.821 −5	0.4500	0.0008	0.00 +0	0.00 +0	9.82 −5	0.743	0.001
45	8.549 −5	0.4501	0.0007	0.00 +0	0.00 +0	8.55 −5	0.743	0.001
46	7.453 −5	0.4502	0.0006	0.00 +0	0.00 +0	7.45 −5	0.744	0.001
47	6.507 −5	0.4503	0.0005	0.00 +0	0.00 +0	6.51 −5	0.744	0.001
48	5.725 −5	0.4503	0.0005	0.00 +0	0.00 +0	5.72 −5	0.744	0.000
49	5.056 −5	0.4504	0.0004	0.00 +0	0.00 +0	5.06 −5	0.744	0.000
50	4.465 −5	0.4504	0.0004	0.00 +0	0.00 +0	4.46 −5	0.744	0.000

(Continued)

Table 7-4. Parameters for the model of a clear standard atmosphere. Numbers following the plus or minus sign are the power of ten by which that entry shall be multiplied. (Continued)

Alt (km)	Rayleigh Atten Coeff (km^{-1})	Rayleigh Optical Thick. (0-h)	Rayleigh Optical Thick. (h-∞)	Aerosol Atten Coeff (km^{-1})	Ozone Absorp Coeff (km^{-1})	Ext Coeff (km^{-1})	Ext Optical Thick. (0-h)	Ext Optical Thick. (h-∞)
			PARAMETERS AT 0.40 MICRONS					
0	4.303 −2	0.0000	0.3641	2.00 −1	0.00 +0	2.43 −1	0.000	0.619
1	3.905 −2	0.0410	0.3231	8.80 −2	0.00 +0	1.27 −1	0.185	0.434
2	3.536 −2	0.0782	0.2859	3.80 −2	0.00 +0	7.34 −2	0.285	0.334
3	3.194 −2	0.1119	0.2522	1.60 −2	0.00 +0	4.79 −2	0.346	0.273
4	2.878 −2	0.1422	0.2219	7.20 −3	0.00 +0	3.60 −2	0.388	0.231
5	2.587 −2	0.1696	0.1946	3.20 −3	0.00 +0	2.91 −2	0.420	0.199
6	2.319 −2	0.1941	0.1700	1.10 −3	0.00 +0	2.43 −2	0.447	0.172
7	2.072 −2	0.2160	0.1481	4.00 −4	0.00 +0	2.11 −2	0.470	0.149
8	1.847 −2	0.2356	0.1285	1.40 −4	0.00 +0	1.86 −2	0.490	0.130
9	1.641 −2	0.2531	0.1110	5.00 −5	0.00 +0	1.65 −2	0.507	0.112
10	1.452 −2	0.2685	0.0956	2.60 −5	0.00 +0	1.46 −2	0.523	0.097
11	1.281 −2	0.2822	0.0819	2.40 −5	0.00 +0	1.28 −2	0.536	0.083
12	1.096 −2	0.2941	0.0700	2.20 −5	0.00 +0	1.10 −2	0.548	0.071
13	9.364 −3	0.3043	0.0599	2.40 −5	0.00 +0	9.39 −3	0.558	0.061
14	8.003 −3	0.3129	0.0512	2.60 −5	0.00 +0	8.03 −3	0.567	0.052
15	6.841 −3	0.3204	0.0438	4.20 −5	0.00 +0	6.88 −3	0.575	0.045
16	5.847 −3	0.3267	0.0374	6.80 −5	0.00 +0	5.92 −3	0.581	0.038
17	4.998 −3	0.3321	0.0320	7.40 −5	0.00 +0	5.07 −3	0.586	0.033
18	4.273 −3	0.3368	0.0274	8.00 −5	0.00 +0	4.35 −3	0.591	0.028
19	3.653 −3	0.3407	0.0234	9.00 −5	0.00 +0	3.74 −3	0.595	0.024
20	3.122 −3	0.3441	0.0200	8.60 −5	0.00 +0	3.21 −3	0.599	0.020
21	2.659 −3	0.3470	0.0171	8.20 −5	0.00 +0	2.74 −3	0.602	0.018
22	2.266 −3	0.3495	0.0147	8.00 −5	0.00 +0	2.35 −3	0.604	0.015
23	1.932 −3	0.3516	0.0126	7.60 −5	0.00 +0	2.01 −3	0.606	0.013
24	1.648 −3	0.3534	0.0108	5.20 −5	0.00 +0	1.70 −3	0.608	0.011
25	1.408 −3	0.3549	0.0092	3.60 −5	0.00 +0	1.44 −3	0.610	0.009
26	1.203 −3	0.3562	0.0079	2.60 −5	0.00 +0	1.23 −3	0.611	0.008
27	1.029 −3	0.3573	0.0068	2.40 −5	0.00 +0	1.05 −3	0.612	0.007
28	8.807 −4	0.3583	0.0059	2.20 −5	0.00 +0	9.03 −4	0.613	0.006
29	7.543 −4	0.3591	0.0050	2.00 −5	0.00 +0	7.74 −4	0.614	0.005
30	6.465 −4	0.3598	0.0043	1.90 −5	0.00 +0	6.66 −4	0.615	0.004
31	5.546 −4	0.3604	0.0037	0.00 +0	0.00 +0	5.55 −4	0.615	0.004
32	4.760 −4	0.3609	0.0032	0.00 +0	0.00 +0	4.76 −4	0.616	0.003
33	4.064 −4	0.3613	0.0028	0.00 +0	0.00 +0	4.06 −4	0.616	0.003
34	3.472 −4	0.3617	0.0024	0.00 +0	0.00 +0	3.47 −4	0.617	0.002
35	2.972 −4	0.3620	0.0021	0.00 +0	0.00 +0	2.97 −4	0.617	0.002
36	2.549 −4	0.3623	0.0018	0.00 +0	0.00 +0	2.55 −4	0.617	0.002
37	2.190 −4	0.3626	0.0016	0.00 +0	0.00 +0	2.19 −4	0.618	0.002
38	1.885 −4	0.3628	0.0014	0.00 +0	0.00 +0	1.88 −4	0.618	0.001
39	1.625 −4	0.3629	0.0012	0.00 +0	0.00 +0	1.62 −4	0.618	0.001
40	1.403 −4	0.3631	0.0010	0.00 +0	0.00 +0	1.40 −4	0.618	0.001
41	1.214 −4	0.3632	0.0009	0.00 +0	0.00 +0	1.21 −4	0.618	0.001
42	1.052 −4	0.3633	0.0008	0.00 +0	0.00 +0	1.05 −4	0.618	0.001
43	9.127 −5	0.3634	0.0007	0.00 +0	0.00 +0	9.13 −5	0.619	0.001
44	7.933 −5	0.3635	0.0006	0.00 +0	0.00 +0	7.93 −5	0.619	0.001
45	6.905 −5	0.3636	0.0005	0.00 +0	0.00 +0	6.91 −5	0.619	0.001
46	6.020 −5	0.3636	0.0005	0.00 +0	0.00 +0	6.02 −5	0.619	0.000
47	5.256 −5	0.3637	0.0004	0.00 +0	0.00 +0	5.26 −5	0.619	0.000
48	4.624 −5	0.3638	0.0004	0.00 +0	0.00 +0	4.62 −5	0.619	0.000
49	4.084 −5	0.3638	0.0003	0.00 +0	0.00 +0	4.08 −5	0.619	0.000
50	3.606 −5	0.3638	0.0003	0.00 +0	0.00 +0	3.61 −5	0.619	0.000

(Continued)

Table 7-4. Parameters for the model of a clear standard atmosphere. Numbers following the plus or minus sign are the power of ten by which that entry shall be multiplied. (Continued)

Alt (km)	Rayleigh Atten Coeff (km^{-1})	Rayleigh Optical Thick. (0-h)	Rayleigh Optical Thick. (h-∞)	Aerosol Atten Coeff (km^{-1})	Ozone Absorp Coeff (km^{-1})	Ext Coeff (km^{-1})	Ext Optical Thick. (0-h)	Ext Optical Thick. (h-∞)
			PARAMETERS AT 0.45 MICRONS					
0	2.644 −2	0.0000	0.2238	1.80 −1	1.25 −5	2.06 −1	0.000	0.455
1	2.400 −2	0.0252	0.1986	7.92 −2	1.14 −5	1.03 −1	0.155	0.300
2	2.173 −2	0.0481	0.1757	3.42 −2	1.03 −5	5.59 −2	0.234	0.220
3	1.963 −2	0.0688	0.1550	1.44 −2	8.75 −6	3.40 −2	0.279	0.175
4	1.769 −2	0.0874	0.1364	6.48 −3	7.91 −6	2.42 −2	0.308	0.146
5	1.590 −2	0.1042	0.1196	2.88 −3	7.73 −6	1.88 −2	0.330	0.125
6	1.425 −2	0.1193	0.1045	9.90 −4	7.56 −6	1.52 −2	0.347	0.108
7	1.274 −2	0.1328	0.0910	3.60 −4	7.80 −6	1.31 −2	0.361	0.093
8	1.135 −2	0.1448	0.0790	1.26 −4	7.98 −6	1.15 −2	0.373	0.081
9	1.008 −2	0.1555	0.0682	4.50 −5	9.83 −6	1.01 −2	0.384	0.070
10	8.926 −3	0.1650	0.0587	2.34 −5	1.22 −5	8.96 −3	0.394	0.061
11	7.875 −3	0.1734	0.0503	2.16 −5	1.61 −5	7.91 −3	0.402	0.052
12	6.734 −3	0.1807	0.0430	1.98 −5	2.17 −5	6.78 −3	0.410	0.045
13	5.755 −3	0.1870	0.0368	2.16 −5	2.96 −5	5.81 −3	0.416	0.039
14	4.919 −3	0.1923	0.0315	2.34 −5	3.35 −5	4.98 −3	0.421	0.033
15	4.204 −3	0.1969	0.0269	3.78 −5	3.48 −5	4.28 −3	0.426	0.029
16	3.593 −3	0.2008	0.0230	6.12 −5	3.60 −5	3.69 −3	0.430	0.025
17	3.072 −3	0.2041	0.0197	6.66 −5	3.88 −5	3.18 −3	0.433	0.021
18	2.626 −3	0.2070	0.0168	7.20 −5	4.27 −5	2.74 −3	0.436	0.018
19	2.245 −3	2.2094	0.0144	8.10 −5	4.97 −5	2.38 −3	0.439	0.016
20	1.919 −3	0.2115	0.0123	7.74 −5	5.74 −5	2.05 −3	0.441	0.013
21	1.634 −3	0.2133	0.0105	7.38 −5	6.44 −5	1.77 −3	0.443	0.012
22	1.392 −3	0.2148	0.0090	7.20 −5	6.90 −5	1.53 −3	0.445	0.010
23	1.187 −3	0.2161	0.0077	6.84 −5	6.93 −5	1.32 −3	0.446	0.008
24	1.013 −3	0.2172	0.0066	4.68 −5	6.76 −5	1.13 −3	0.447	0.007
25	8.651 −4	0.2181	0.0057	3.24 −5	6.30 −5	9.61 −4	0.448	0.006
26	7.394 −4	0.2189	0.0049	2.34 −5	5.70 −5	8.20 −4	0.449	0.005
27	6.323 −4	0.2196	0.0042	2.16 −5	4.93 −5	7.03 −4	0.450	0.005
28	5.412 −4	0.2202	0.0036	1.98 −5	4.31 −5	6.04 −4	0.451	0.004
29	4.636 −4	0.2207	0.0031	1.80 −5	3.74 −5	5.19 −4	0.451	0.003
30	3.973 −4	0.2211	0.0027	1.71 −5	3.16 −5	4.46 −4	0.452	0.003
31	3.408 −4	0.2215	0.0023	0.00 +0	2.78 −5	3.69 −4	0.452	0.002
32	2.926 −4	0.2218	0.0020	0.00 +0	2.39 −5	3.16 −4	0.452	0.002
33	2.498 −4	0.2221	0.0017	0.00 +0	2.04 −5	2.70 −4	0.453	0.002
34	2.134 −4	0.2223	0.0015	0.00 +0	1.69 −5	2.30 −4	0.453	0.002
35	1.827 −4	0.2225	0.0013	0.00 +0	1.51 −5	1.98 −4	0.453	0.001
36	1.566 −4	0.2227	0.0011	0.00 +0	1.26 −5	1.69 −4	0.453	0.001
37	1.346 −4	0.2228	0.0010	0.00 +0	1.06 −5	1.45 −4	0.454	0.001
38	1.158 −4	0.2229	0.0008	0.00 +0	8.86 −6	1.25 −4	0.454	0.001
39	9.986 −5	0.2230	0.0007	0.00 +0	7.59 −6	1.07 −4	0.454	0.001
40	8.624 −5	0.2231	0.0006	0.00 +0	6.51 −6	9.27 −5	0.454	0.001
41	7.460 −5	0.2232	0.0006	0.00 +0	5.32 −6	7.99 −5	0.454	0.001
42	6.464 −5	0.2233	0.0005	0.00 +0	4.16 −6	6.88 −5	0.454	0.001
43	5.609 −5	0.2233	0.0004	0.00 +0	3.25 −6	5.93 −5	0.454	0.000
44	4.875 −5	0.2234	0.0004	0.00 +0	2.60 −6	5.14 −5	0.454	0.000
45	4.244 −5	0.2234	0.0003	0.00 +0	2.02 −6	4.45 −5	0.454	0.000
46	3.700 −5	0.2235	0.0003	0.00 +0	1.56 −6	3.86 −5	0.454	0.000
47	3.230 −5	0.2235	0.0003	0.00 +0	1.24 −6	3.35 −5	0.454	0.000
48	2.842 −5	0.2236	0.0002	0.00 +0	9.77 −7	2.94 −5	0.454	0.000
49	2.510 −5	0.2236	0.0002	0.00 +0	7.80 −7	2.59 −5	0.454	0.000
50	2.216 −5	0.2236	0.0002	0.00 +0	6.51 −7	2.28 −5	0.454	0.000

(Continued)

Table 7-4. Parameters for the model of a clear standard atmosphere. Numbers following the plus or minus sign are the power of ten by which that entry shall be multiplied. (Continued)

Alt (km)	Rayleigh Atten Coeff (km^{-1})	Rayleigh Optical Thick. (0-h)	Rayleigh Optical Thick. (h-∞)	Aerosol Atten Coeff (km^{-1})	Ozone Absorp Coeff (km^{-1})	Ext Coeff (km^{-1})	Ext Optical Thick. (0-h)	Ext Optical Thick. (h-∞)
				PARAMETERS AT 0.50 MICRONS				
0	1.716 −2	0.0000	0.1452	1.67 −1	1.23 −4	1.84 −1	0.000	0.370
1	1.557 −2	0.0164	0.1288	7.35 −2	1.12 −4	8.92 −2	0.137	0.233
2	1.410 −2	0.0312	0.1140	3.17 −2	1.01 −4	4.59 −2	0.204	0.166
3	1.274 −2	0.0446	0.1006	1.34 −2	8.62 −5	2.62 −2	0.240	0.130
4	1.148 −2	0.0567	0.0885	6.01 −3	7.80 −5	1.76 −2	0.262	0.108
5	1.031 −2	0.0676	0.0776	2.67 −3	7.62 −5	1.31 −2	0.278	0.092
6	9.246 −3	0.0774	0.0678	9.18 −4	7.45 −5	1.02 −2	0.289	0.081
7	8.264 −3	0.0862	0.0590	3.34 −4	7.69 −5	8.67 −3	0.299	0.071
8	7.364 −3	0.0940	0.0512	1.17 −4	7.87 −5	7.56 −3	0.307	0.063
9	6.542 −3	0.1009	0.0443	4.17 −5	9.69 −5	6.68 −3	0.314	0.056
10	5.792 −3	0.1071	0.0381	2.17 −5	1.21 −4	5.93 −3	0.320	0.050
11	5.109 −3	0.1125	0.0327	2.00 −5	1.59 −4	5.29 −3	0.326	0.044
12	4.369 −3	0.1173	0.0279	1.84 −5	2.14 −4	4.60 −3	0.331	0.039
13	3.734 −3	0.1213	0.0239	2.00 −5	2.92 −4	4.05 −3	0.335	0.035
14	3.191 −3	0.1248	0.0204	2.17 −5	3.30 −4	3.54 −3	0.339	0.031
15	2.728 −3	0.1277	0.0174	3.51 −5	3.43 −4	3.11 −3	0.342	0.028
16	2.332 −3	0.1303	0.0149	5.68 −5	3.55 −4	2.74 −3	0.345	0.025
17	1.993 −3	0.1324	0.0128	6.18 −5	3.83 −4	2.44 −3	0.348	0.022
18	1.704 −3	0.1343	0.0109	6.68 −5	4.21 −4	2.19 −3	0.350	0.020
19	1.457 −3	0.1359	0.0093	7.51 −5	4.90 −4	2.02 −3	0.352	0.018
20	1.245 −3	0.1372	0.0080	7.18 −5	5.66 −4	1.88 −3	0.354	0.016
21	1.060 −3	0.1384	0.0068	6.85 −5	6.35 −4	1.76 −3	0.356	0.014
22	9.034 −4	0.1394	0.0058	6.68 −5	6.80 −4	1.65 −3	0.358	0.012
23	7.703 −4	0.1402	0.0050	6.35 −5	6.83 −4	1.52 −3	0.359	0.011
24	6.573 −4	0.1409	0.0043	4.34 −5	6.66 −4	1.37 −3	0.361	0.009
25	5.613 −4	0.1415	0.0037	3.01 −5	6.21 −4	1.21 −3	0.362	0.008
26	4.797 −4	0.1420	0.0032	2.17 −5	5.62 −4	1.06 −3	0.363	0.007
27	4.103 −4	0.1425	0.0027	2.00 −5	4.86 −4	9.17 −4	0.364	0.006
28	3.512 −4	0.1429	0.0023	1.84 −5	4.24 −4	7.94 −4	0.365	0.005
29	3.008 −4	0.1432	0.0020	1.67 −5	3.69 −4	6.87 −4	0.366	0.004
30	2.578 −4	0.1435	0.0017	1.59 −5	3.12 −4	5.85 −4	0.366	0.004
31	2.211 −4	0.1437	0.0015	0.00 +0	2.74 −4	4.95 −4	0.367	0.003
32	1.898 −4	0.1439	0.0013	0.00 +0	2.35 −4	4.25 −4	0.367	0.003
33	1.621 −4	0.1441	0.0011	0.00 +0	2.01 −4	3.63 −4	0.368	0.002
34	1.385 −4	0.1442	0.0010	0.00 +0	1.67 −4	3.05 −4	0.368	0.002
35	1.185 −4	0.1444	0.0008	0.00 +0	1.49 −4	2.67 −4	0.368	0.002
36	1.016 −4	0.1445	0.0007	0.00 +0	1.25 −4	2.26 −4	0.369	0.001
37	8.732 −5	0.1446	0.0006	0.00 +0	1.04 −4	1.92 −4	0.369	0.001
38	7.516 −5	0.1447	0.0005	0.00 +0	8.73 −5	1.62 −4	0.369	0.001
39	6.479 −5	0.1447	0.0005	0.00 +0	7.49 −5	1.40 −4	0.369	0.001
40	5.596 −5	0.1448	0.0004	0.00 +0	6.42 −5	1.20 −4	0.369	0.001
41	4.840 −5	0.1448	0.0004	0.00 +0	5.24 −5	1.01 −4	0.369	0.001
42	4.194 −5	0.1449	0.0003	0.00 +0	4.11 −5	8.30 −5	0.369	0.000
43	3.640 −5	0.1449	0.0003	0.00 +0	3.21 −5	6.85 −5	0.369	0.000
44	3.163 −5	0.1450	0.0002	0.00 +0	2.57 −5	5.73 −5	0.370	0.000
45	2.754 −5	0.1450	0.0002	0.00 +0	1.99 −5	4.74 −5	0.370	0.000
46	2.400 −5	0.1450	0.0002	0.00 +0	1.54 −5	3.94 −5	0.370	0.000
47	2.096 −5	0.1450	0.0002	0.00 +0	1.22 −5	3.31 −5	0.370	0.000
48	1.844 −5	0.1450	0.0001	0.00 +0	9.63 −6	2.81 −5	0.370	0.000
49	1.628 −5	0.1451	0.0001	0.00 +0	7.69 −6	2.40 −5	0.370	0.000
50	1.438 −5	0.1451	0.0001	0.00 +0	6.42 −6	2.08 −5	0.370	0.000

(Continued)

Table 7-4. Parameters for the model of a clear standard atmosphere. Numbers following the plus or minus sign are the power of ten by which that entry shall be multiplied. (Continued)

Alt (km)	Rayleigh Atten Coeff (km^{-1})	Rayleigh Optical Thick. (0-h)	Rayleigh Optical Thick. (h-∞)	Aerosol Atten Coeff (km^{-1})	Ozone Absorp Coeff (km^{-1})	Ext Coeff (km^{-1})	Ext Optical Thick. (0-h)	Ext Optical Thick. (h-∞)
				PARAMETERS AT 0.55 MICRONS				
0	1.162 −2	0.0000	0.0984	1.58 −1	3.28 −4	1.70 −1	0.000	0.331
1	1.055 −2	0.0111	0.0873	6.95 −2	3.00 −4	8.04 −2	0.125	0.206
2	9.552 −3	0.0211	0.0772	3.00 −2	2.70 −4	3.98 −2	0.185	0.146
3	8.628 −3	0.0302	0.0681	1.26 −2	2.30 −4	2.15 −2	0.216	0.115
4	7.775 −3	0.0384	0.0599	5.69 −3	2.08 −4	1.37 −2	0.234	0.097
5	6.988 −3	0.0458	0.0526	2.53 −3	2.03 −4	9.72 −3	0.245	0.086
6	6.264 −3	0.0524	0.0459	8.69 −4	1.99 −4	7.33 −3	0.254	0.077
7	5.599 −3	0.0584	0.0400	3.16 −4	2.05 −4	6.12 −3	0.260	0.071
8	4.989 −3	0.0637	0.0347	1.11 −4	2.10 −4	5.31 −3	0.266	0.065
9	4.432 −3	0.0684	0.0300	3.95 −5	2.59 −4	4.73 −3	0.271	0.060
10	3.924 −3	0.0726	0.0258	2.05 −5	3.22 −4	4.27 −3	0.276	0.055
11	3.462 −3	0.0762	0.0221	1.90 −5	4.23 −4	3.90 −3	0.280	0.051
12	2.960 −3	0.0795	0.0189	1.74 −5	5.71 −4	3.55 −3	0.284	0.047
13	2.530 −3	0.0822	0.0162	1.90 −5	7.77 −4	3.33 −3	0.287	0.044
14	2.162 −3	0.0845	0.0138	2.05 −5	8.80 −4	3.06 −3	0.290	0.041
15	1.848 −3	0.0865	0.0118	3.32 −5	9.14 −4	2.80 −3	0.293	0.038
16	1.580 −3	0.0883	0.0101	5.37 −5	9.48 −4	2.58 −3	0.296	0.035
17	1.350 −3	0.0897	0.0086	5.85 −5	1.02 −3	2.43 −3	0.298	0.033
18	1.154 −3	0.0910	0.0074	6.32 −5	1.12 −3	2.34 −3	0.301	0.030
19	9.868 −4	0.0921	0.0063	7.11 −5	1.31 −3	2.36 −3	0.303	0.028
20	8.436 −4	0.0930	0.0054	6.79 −5	1.51 −3	2.42 −3	0.305	0.026
21	7.184 −4	0.0937	0.0046	6.48 −5	1.69 −3	2.48 −3	0.308	0.023
22	6.121 −4	0.0944	0.0040	6.32 −5	1.81 −3	2.49 −3	0.310	0.021
23	5.219 −4	0.0950	0.0034	6.00 −5	1.82 −3	2.40 −3	0.313	0.018
24	4.453 −4	0.0955	0.0029	4.11 −5	1.78 −3	2.26 −3	0.315	0.016
25	3.803 −4	0.0959	0.0025	2.84 −5	1.66 −3	2.06 −3	0.317	0.014
26	3.250 −4	0.0962	0.0021	2.05 −5	1.50 −3	1.85 −3	0.319	0.012
27	2.780 −4	0.0965	0.0018	1.90 −5	1.30 −3	1.59 −3	0.321	0.010
28	2.379 −4	0.0968	0.0016	1.74 −5	1.13 −3	1.39 −3	0.322	0.009
29	2.038 −4	0.0970	0.0014	1.58 −5	9.84 −4	1.20 −3	0.324	0.007
30	1.747 −4	0.0972	0.0012	1.50 −5	8.31 −4	1.02 −3	0.325	0.006
31	1.498 −4	0.0974	0.0010	0.00 +0	7.30 −4	8.79 −4	0.326	0.005
32	1.286 −4	0.0975	0.0009	0.00 +0	6.27 −4	7.56 −4	0.327	0.004
33	1.098 −4	0.0976	0.0008	0.00 +0	5.35 −4	6.45 −4	0.327	0.004
34	9.381 −5	0.0977	0.0007	0.00 +0	4.44 −4	5.38 −4	0.328	0.003
35	8.030 −5	0.0978	0.0006	0.00 +0	3.97 −4	4.77 −4	0.328	0.003
36	6.886 −5	0.0979	0.0005	0.00 +0	3.32 −4	4.01 −4	0.329	0.002
37	5.916 −5	0.0979	0.0004	0.00 +0	2.78 −4	3.37 −4	0.329	0.002
38	5.092 −5	0.0980	0.0004	0.00 +0	2.33 −4	2.84 −4	0.330	0.001
39	4.390 −5	0.0980	0.0003	0.00 +0	2.00 −4	2.44 −4	0.330	0.001
40	3.791 −5	0.0981	0.0003	0.00 +0	1.71 −4	2.09 −4	0.330	0.001
41	3.279 −5	0.0981	0.0002	0.00 +0	1.40 −4	1.73 −4	0.330	0.001
42	2.841 −5	0.0982	0.0002	0.00 +0	1.09 −4	1.38 −4	0.330	0.001
43	2.466 −5	0.0982	0.0002	0.00 +0	8.56 −5	1.10 −4	0.330	0.000
44	2.143 −5	0.0982	0.0002	0.00 +0	6.84 −5	8.99 −5	0.331	0.000
45	1.866 −5	0.0982	0.0001	0.00 +0	5.30 −5	7.16 −5	0.331	0.000
46	1.626 −5	0.0982	0.0001	0.00 +0	4.10 −5	5.73 −5	0.331	0.000
47	1.420 −5	0.0983	0.0001	0.00 +0	3.25 −5	4.67 −5	0.331	0.000
48	1.249 −5	0.0983	0.0001	0.00 +0	2.57 −5	3.82 −5	0.331	0.000
49	1.103 −5	0.0983	0.0001	0.00 +0	2.05 −5	3.15 −5	0.331	0.000
50	9.743 −6	0.0983	0.0001	0.00 +0	1.71 −5	2.69 −5	0.331	0.000

(Continued)

Table 7-4. Parameters for the model of a clear standard atmosphere. Numbers following the plus or minus sign are the power of ten by which that entry shall be multiplied. (Continued)

Alt (km)	Rayleigh Atten Coeff (km^{-1})	Rayleigh Optical Thick. (0-h)	Rayleigh Optical Thick. (h-∞)	Aerosol Atten Coeff (km^{-1})	Ozone Absorp Coeff (km^{-1})	Ext Coeff (km^{-1})	Ext Optical Thick. (0-h)	Ext Optical Thick. (h-∞)
				PARAMETERS AT 0.60 MICRONS				
0	8.157 −3	0.0000	0.0690	1.50 −1	4.70 −4	1.59 −1	0.000	0.305
1	7.402 −3	0.0078	0.0613	6.60 −2	4.30 −4	7.38 −2	0.116	0.189
2	6.703 −3	0.0148	0.0542	2.85 −2	3.87 −4	3.56 −2	0.171	0.134
3	6.055 −3	0.0212	0.0478	1.20 −2	3.30 −4	1.84 −2	0.198	0.107
4	5.456 −3	0.0270	0.0421	5.40 −3	2.98 −4	1.12 −2	0.213	0.092
5	4.904 −3	0.0321	0.0369	2.40 −3	2.92 −4	7.60 −3	0.222	0.083
6	4.396 −3	0.0368	0.0322	8.25 −4	2.85 −4	5.51 −3	0.229	0.076
7	3.929 −3	0.0410	0.0281	3.00 −4	2.94 −4	4.52 −3	0.234	0.071
8	3.501 −3	0.0447	0.0244	1.05 −4	3.01 −4	3.91 −3	0.238	0.067
9	3.110 −3	0.0480	0.0211	3.75 −5	3.71 −4	3.52 −3	0.242	0.063
10	2.753 −3	0.0509	0.0181	1.95 −5	4.62 −4	3.23 −3	0.245	0.060
11	2.429 −3	0.0535	0.0155	1.80 −5	6.07 −4	3.05 −3	0.248	0.057
12	2.077 −3	0.0558	0.0133	1.65 −5	8.20 −4	2.91 −3	0.251	0.054
13	1.775 −3	0.0577	0.0113	1.80 −5	1.12 −3	2.91 −3	0.254	0.051
14	1.517 −3	0.0593	0.0097	1.95 −5	1.26 −3	2.80 −3	0.257	0.048
15	1.297 −3	0.0607	0.0083	3.15 −5	1.31 −3	2.64 −3	0.260	0.045
16	1.109 −3	0.0619	0.0071	5.10 −5	1.36 −3	2.52 −3	0.262	0.043
17	9.476 −4	0.0630	0.0061	5.55 −5	1.47 −3	2.47 −3	0.265	0.040
18	8.100 −4	0.0638	0.0052	6.00 −5	1.61 −3	2.48 −3	0.267	0.038
19	6.925 −4	0.0646	0.0044	6.75 −5	1.87 −3	2.63 −3	0.270	0.035
20	5.920 −4	0.0652	0.0038	6.45 −5	2.16 −3	2.82 −3	0.272	0.033
21	5.041 −4	0.0658	0.0032	6.15 −5	2.43 −3	2.99 −3	0.275	0.030
22	4.295 −4	0.0663	0.0028	6.00 −5	2.60 −3	3.09 −3	0.278	0.027
23	3.662 −4	0.0667	0.0024	5.70 −5	2.61 −3	3.04 −3	0.281	0.024
24	3.125 −4	0.0670	0.0020	3.90 −5	2.55 −3	2.90 −3	0.284	0.021
25	2.669 −4	0.0673	0.0018	2.70 −5	2.38 −3	2.67 −3	0.287	0.018
26	2.281 −4	0.0675	0.0015	1.95 −5	2.15 −3	2.40 −3	0.290	0.015
27	1.951 −4	0.0677	0.0013	1.80 −5	1.86 −3	2.07 −3	0.292	0.013
28	1.670 −4	0.0679	0.0011	1.65 −5	1.62 −3	1.81 −3	0.294	0.011
29	1.430 −4	0.0681	0.0010	1.50 −5	1.41 −3	1.57 −3	0.296	0.009
30	1.226 −4	0.0682	0.0008	1.42 −5	1.19 −3	1.33 −3	0.297	0.008
31	1.051 −4	0.0683	0.0007	0.00 +0	1.05 −3	1.15 −3	0.298	0.007
32	9.025 −5	0.0684	0.0006	0.00 +0	9.00 −4	9.90 −4	0.299	0.006
33	7.705 −5	0.0685	0.0005	0.00 +0	7.68 −4	8.45 −4	0.300	0.005
34	6.583 −5	0.0686	0.0005	0.00 +0	6.38 −4	7.03 −4	0.301	0.004
35	5.635 −5	0.0686	0.0004	0.00 +0	5.69 −4	6.25 −4	0.302	0.003
36	4.832 −5	0.0687	0.0003	0.00 +0	4.77 −4	5.25 −4	0.302	0.003
37	4.151 −5	0.0687	0.0003	0.00 +0	3.99 −4	4.40 −4	0.303	0.002
38	3.573 −5	0.0688	0.0003	0.00 +0	3.34 −4	3.70 −4	0.303	0.002
39	3.080 −5	0.0688	0.0002	0.00 +0	2.86 −4	3.17 −4	0.303	0.001
40	2.660 −5	0.0688	0.0002	0.00 +0	2.46 −4	2.72 −4	0.304	0.001
41	2.301 −5	0.0689	0.0002	0.00 +0	2.01 −4	2.24 −4	0.304	0.001
42	1.994 −5	0.0689	0.0002	0.00 +0	1.57 −4	1.77 −4	0.304	0.001
43	1.730 −5	0.0689	0.0001	0.00 +0	1.23 −4	1.40 −4	0.304	0.001
44	1.504 −5	0.0689	0.0001	0.00 +0	9.82 −5	1.13 −4	0.305	0.000
45	1.309 −5	0.0689	0.0001	0.00 +0	7.60 −5	8.91 −5	0.305	0.000
46	1.141 −5	0.0689	0.0001	0.00 +0	5.89 −5	7.03 −5	0.305	0.000
47	9.964 −6	0.0690	0.0001	0.00 +0	4.66 −5	5.66 −5	0.305	0.000
48	8.766 −6	0.0690	0.0001	0.00 +0	3.68 −5	4.56 −5	0.305	0.000
49	7.742 −6	0.0690	0.0001	0.00 +0	2.94 −5	3.72 −5	0.305	0.000
50	6.837 −6	0.0690	0.0001	0.00 +0	2.46 −5	3.14 −5	0.305	0.000

(Continued)

Table 7-4. Parameters for the model of a clear standard atmosphere. Numbers following the plus or minus sign are the power of ten by which that entry shall be multiplied. (Continued)

Alt (km)	Rayleigh Atten Coeff (km^{-1})	Rayleigh Optical Thick. (0-h)	Rayleigh Optical Thick. (h-∞)	Aerosol Atten Coeff (km^{-1})	Ozone Absorp Coeff (km^{-1})	Ext Coeff (km^{-1})	Ext Optical Thick. (0-h)	Ext Optical Thick. (h-∞)
			PARAMETERS AT 0.65 MICRONS					
0	5.893 −3	0.0000	0.0499	1.42 −1	2.21 −4	1.48 −1	0.000	0.252
1	5.347 −3	0.0056	0.0442	6.25 −2	2.02 −4	6.80 −2	0.108	0.144
2	4.842 −3	0.0107	0.0392	2.70 −2	1.82 −4	3.20 −2	0.158	0.094
3	4.374 −3	0.0153	0.0345	1.14 −2	1.55 −4	1.59 −2	0.182	0.070
4	3.941 −3	0.0195	0.0304	5.11 −3	1.40 −4	9.19 −3	0.195	0.057
5	3.542 −3	0.0232	0.0266	2.27 −3	1.37 −4	5.95 −3	0.202	0.050
6	3.175 −3	0.0266	0.0233	7.81 −4	1.34 −4	4.09 −3	0.207	0.045
7	2.838 −3	0.0296	0.0203	2.84 −4	1.38 −4	3.26 −3	0.211	0.041
8	2.529 −3	0.0323	0.0176	9.94 −5	1.41 −4	2.77 −3	0.214	0.038
9	2.247 −3	0.0347	0.0152	3.55 −5	1.74 −4	2.46 −3	0.216	0.035
10	1.989 −3	0.0368	0.0131	1.85 −5	2.17 −4	2.22 −3	0.219	0.033
11	1.755 −3	0.0386	0.0112	1.70 −5	2.85 −4	2.06 −3	0.221	0.031
12	1.500 −3	0.0403	0.0096	1.56 −5	3.85 −4	1.90 −3	0.223	0.029
13	1.282 −3	0.0417	0.0082	1.70 −5	5.24 −4	1.82 −3	0.225	0.027
14	1.096 −3	0.0429	0.0070	1.85 −5	5.93 −4	1.71 −3	0.227	0.025
15	9.368 −4	0.0439	0.0060	2.98 −5	6.16 −4	1.58 −3	0.228	0.024
16	8.007 −4	0.0447	0.0051	4.83 −5	6.39 −4	1.49 −3	0.230	0.022
17	6.845 −4	0.0455	0.0044	5.25 −5	6.88 −4	1.43 −3	0.231	0.021
18	5.851 −4	0.0461	0.0037	5.68 −5	7.56 −4	1.40 −3	0.233	0.019
19	5.002 −4	0.0467	0.0032	6.39 −5	8.80 −4	1.44 −3	0.234	0.018
20	4.276 −4	0.0471	0.0027	6.11 −5	1.02 −3	1.51 −3	0.236	0.016
21	3.641 −4	0.0475	0.0023	5.82 −5	1.14 −3	1.56 −3	0.237	0.015
22	3.103 −4	0.0479	0.0020	5.68 −5	1.22 −3	1.59 −3	0.239	0.013
23	2.645 −4	0.0481	0.0017	5.40 −5	1.23 −3	1.55 −3	0.240	0.012
24	2.257 −4	0.0484	0.0015	3.69 −5	1.20 −3	1.46 −3	0.242	0.010
25	1.928 −4	0.0486	0.0013	2.56 −5	1.12 −3	1.33 −3	0.243	0.009
26	1.648 −4	0.0488	0.0011	1.85 −5	1.01 −3	1.19 −3	0.244	0.008
27	1.409 −4	0.0489	0.0009	1.70 −5	8.74 −4	1.03 −3	0.245	0.006
28	1.206 −4	0.0491	0.0008	1.56 −5	7.63 −4	8.99 −4	0.246	0.006
29	1.033 −4	0.0492	0.0007	1.42 −5	6.63 −4	7.81 −4	0.247	0.005
30	8.854 −5	0.0493	0.0006	1.35 −5	5.60 −4	6.62 −4	0.248	0.004
31	7.595 −5	0.0494	0.0005	0.00 +0	4.92 −4	5.68 −4	0.249	0.003
32	6.519 −5	0.0494	0.0004	0.00 +0	4.23 −4	4.88 −4	0.249	0.003
33	5.566 −5	0.0495	0.0004	0.00 +0	3.61 −4	4.17 −4	0.250	0.002
34	4.755 −5	0.0495	0.0003	0.00 +0	2.99 −4	3.47 −4	0.250	0.002
35	4.070 −5	0.0496	0.0003	0.00 +0	2.67 −4	3.08 −4	0.250	0.002
36	3.491 −5	0.0496	0.0002	0.00 +0	2.24 −4	2.59 −4	0.251	0.001
37	2.999 −5	0.0496	0.0002	0.00 +0	1.87 −4	2.17 −4	0.251	0.001
38	2.581 −5	0.0497	0.0002	0.00 +0	1.57 −4	1.83 −4	0.251	0.001
39	2.225 −5	0.0497	0.0002	0.00 +0	1.35 −4	1.57 −4	0.251	0.001
40	1.922 −5	0.0497	0.0001	0.00 +0	1.15 −4	1.35 −4	0.251	0.001
41	1.662 −5	0.0497	0.0001	0.00 +0	9.42 −5	1.11 −4	0.251	0.000
42	1.440 −5	0.0498	0.0001	0.00 +0	7.38 −5	8.82 −5	0.252	0.000
43	1.250 −5	0.0498	0.0001	0.00 +0	5.77 −5	7.02 −5	0.252	0.000
44	1.086 −5	0.0498	0.0001	0.00 +0	4.61 −5	5.70 −5	0.252	0.000
45	9.457 −6	0.0498	0.0001	0.00 +0	3.57 −5	4.52 −5	0.252	0.000
46	8.244 −6	0.0498	0.0001	0.00 +0	2.77 −5	3.59 −5	0.252	0.000
47	7.197 −6	0.0498	0.0001	0.00 +0	2.19 −5	2.91 −5	0.252	0.000
48	6.333 −6	0.0498	0.0001	0.00 +0	1.73 −5	2.36 −5	0.252	0.000
49	5.592 −6	0.0498	0.0000	0.00 +0	1.38 −5	1.94 −5	0.252	0.000
50	4.939 −6	0.0498	0.0000	0.00 +0	1.15 −5	1.65 −5	0.252	0.000

(Continued)

Table 7-4. Parameters for the model of a clear standard atmosphere. Numbers following the plus or minus sign are the power of ten by which that entry shall be multiplied. (Continued)

Alt (km)	Rayleigh Atten Coeff (km^{-1})	Rayleigh Optical Thick. (0-h)	Rayleigh Optical Thick. (h-∞)	Aerosol Atten Coeff (km^{-1})	Ozone Absorp Coeff (km^{-1})	Ext Coeff (km^{-1})	Ext Optical Thick. (0-h)	Ext Optical Thick. (h-∞)
			PARAMETERS AT 0.70 MICRONS					
0	4.364 −3	0.0000	0.0369	1.35 −1	8.19 −5	1.39 −1	0.000	0.217
1	3.960 −3	0.0042	0.0328	5.94 −2	7.50 −5	6.34 −2	0.101	0.115
2	3.586 −3	0.0079	0.0290	2.56 −2	6.74 −5	2.93 −2	0.148	0.069
3	3.239 −3	0.0113	0.0256	1.08 −2	5.75 −5	1.41 −2	0.170	0.047
4	2.919 −3	0.0144	0.0225	4.86 −3	5.20 −5	7.83 −3	0.180	0.036
5	2.623 −3	0.0172	0.0197	2.16 −3	5.08 −5	4.83 −3	0.187	0.030
6	2.352 −3	0.0197	0.0172	7.42 −4	4.97 −5	3.14 −3	0.191	0.026
7	2.102 −3	0.0219	0.0150	2.70 −4	5.13 −5	2.42 −3	0.194	0.023
8	1.873 −3	0.0239	0.0130	9.45 −5	5.24 −5	2.02 −3	0.196	0.021
9	1.664 −3	0.0257	0.0113	3.37 −5	6.46 −5	1.76 −3	0.198	0.019
10	1.473 −3	0.0272	0.0097	1.75 −5	8.05 −5	1.57 −3	0.199	0.018
11	1.300 −3	0.0286	0.0083	1.62 −5	1.06 −4	1.42 −3	0.201	0.016
12	1.111 −3	0.0298	0.0071	1.48 −5	1.43 −4	1.27 −3	0.202	0.015
13	9|497 −4	0.0309	0.0061	1.62 −5	1.94 −4	1.16 −3	0.203	0.013
14	8.117 −4	0.0317	0.0052	1.75 −5	2.20 −4	1.05 −3	0.205	0.012
15	6.938 −4	0.0325	0.0044	2.84 −5	2.29 −4	9.51 −4	0.206	0.011
16	5.930 −4	0.0331	0.0038	4.59 −5	2.37 −4	8.76 −4	0.206	0.010
17	5.069 −4	0.0337	0.0032	4.99 −5	2.55 −4	8.12 −4	0.207	0.010
18	4.334 −4	0.0342	0.0028	5.40 −5	2.81 −4	7.68 −4	0.208	0.009
19	3.705 −4	0.0346	0.0024	6.07 −5	3.27 −4	7.58 −4	0.209	0.008
20	3.167 −4	0.0349	0.0020	5.80 −5	3.77 −4	7.52 −4	0.210	0.007
21	2.697 −4	0.0352	0.0017	5.53 −5	4.23 −4	7.48 −4	0.210	0.007
22	2.298 −4	0.0354	0.0015	5.40 −5	4.53 −4	7.37 −4	0.211	0.006
23	1.959 −4	0.0357	0.0013	5.13 −5	4.55 −4	7.03 −4	0.212	0.005
24	1.672 −4	0.0358	0.0011	3.51 −5	4.44 −4	6.46 −4	0.212	0.004
25	1.428 −4	0.0360	0.0009	2.43 −5	4.14 −4	5.81 −4	0.213	0.004
26	1.220 −4	0.0361	0.0008	1.75 −5	3.75 −4	5.14 −4	0.214	0.003
27	1.044 −4	0.0362	0.0007	1.62 −5	3.24 −4	4.45 −4	0.214	0.003
28	8.932 −5	0.0363	0.0006	1.48 −5	2.83 −4	3.87 −4	0.215	0.002
29	7.650 −5	0.0364	0.0005	1.35 −5	2.46 −4	3.36 −4	0.215	0.002
30	6.557 −5	0.0365	0.0004	1.28 −5	2.08 −4	2.86 −4	0.215	0.002
31	5.625 −5	0.0366	0.0004	0.00 +0	1.82 −4	2.39 −4	0.215	0.001
32	4.828 −5	0.0366	0.0003	0.00 +0	1.57 −4	2.05 −4	0.216	0.001
33	4.122 −5	0.0366	0.0003	0.00 +0	1.34 −4	1.75 −4	0.216	0.001
34	3.522 −5	0.0367	0.0002	0.00 +0	1.11 −4	1.46 −4	0.216	0.001
35	3.015 −5	0.0367	0.0002	0.00 +0	9.91 −5	1.29 −4	0.216	0.001
36	2.585 −5	0.0367	0.0002	0.00 +0	8.30 −5	1.09 −4	0.216	0.001
37	2.221 −5	0.0368	0.0002	0.00 +0	6.95 −5	9.17 −5	0.216	0.000
38	1.912 −5	0.0368	0.0001	0.00 +0	5.82 −5	7.73 −5	0.216	0.000
39	1.648 −5	0.0368	0.0001	0.00 +0	4.99 −5	6.64 −5	0.217	0.000
40	1.423 −5	0.0368	0.0001	0.00 +0	4.28 −5	5.70 −5	0.217	0.000
41	1.231 −5	0.0368	0.0001	0.00 +0	3.50 −5	4.73 −5	0.217	0.000
42	1.067 −5	0.0368	0.0001	0.00 +0	2.74 −5	3.80 −5	0.217	0.000
43	9.257 −6	0.0369	0.0001	0.00 +0	2.14 −5	3.06 −5	0.217	0.000
44	8.046 −6	0.0369	0.0001	0.00 +0	1.71 −5	2.52 −5	0.217	0.000
45	7.004 −6	0.0369	0.0001	0.00 +0	1.32 −5	2.03 −5	0.217	0.000
46	6.105 −6	0.0369	0.0000	0.00 +0	1.03 −5	1.64 −5	0.217	0.000
47	5.330 −6	0.0369	0.0000	0.00 +0	8.12 −6	1.34 −5	0.217	0.000
48	4.690 −6	0.0369	0.0000	0.00 +0	6.42 −6	1.11 −5	0.217	0.000
49	4.142 −6	0.0369	0.0000	0.00 +0	5.13 −6	9.27 −6	0.217	0.000
50	3.658 −6	0.0369	0.0000	0.00 +0	4.28 −6	7.94 −6	0.217	0.000

(Continued)

Table 7-4. Parameters for the model of a clear standard atmosphere. Numbers following the plus or minus sign are the power of ten by which that entry shall be multiplied. (Continued)

Alt (km)	Rayleigh Atten Coeff (km^{-1})	Rayleigh Optical Thick. (0-h)	Rayleigh Optical Thick. (h-∞)	Aerosol Atten Coeff (km^{-1})	Ozone Absorp Coeff (km^{-1})	Ext Coeff (km^{-1})	Ext Optical Thick. (0-h)	Ext Optical Thick. (h-∞)
				PARAMETERS AT 0.80 MICRONS				
0	2.545 −3	0.0000	0.0215	1.27 −1	3.56 −5	1.30 −1	0.000	0.187
1	2.309 −3	0.0024	0.0191	5.59 −2	3.26 −5	5.82 −2	0.094	0.093
2	2.091 −3	0.0046	0.0169	2.41 −2	2.93 −5	2.63 −2	0.136	0.051
3	1.889 −3	0.0066	0.0149	1.02 −2	2.50 −5	1.21 −2	0.155	0.032
4	1.702 −3	0.0084	0.0131	4.57 −3	2.26 −5	6.30 −3	0.164	0.022
5	1.530 −3	0.0100	0.0115	2.03 −3	2.21 −5	3.58 −3	0.169	0.017
6	1.371 −3	0.0115	0.0101	6.98 −4	2.16 −5	2.09 −3	0.172	0.015
7	1.226 −3	0.0128	0.0088	2.54 −4	2.23 −5	1.50 −3	0.174	0.013
8	1.092 −3	0.0139	0.0076	8.89 −5	2.28 −5	1.20 −3	0.175	0.011
9	9.702 −4	0.0150	0.0066	3.17 −5	2.81 −5	1.03 −3	0.177	0.010
10	8.590 −4	0.0159	0.0057	1.65 −5	3.50 −5	9.10 −4	0.177	0.009
11	7.578 −4	0.0167	0.0048	1.52 −5	4.60 −5	8.19 −4	0.178	0.009
12	6.480 −4	0.0174	0.0041	1.40 −5	6.21 −5	7.24 −4	0.179	0.008
13	5.538 −4	0.0180	0.0035	1.52 −5	8.45 −5	6.54 −4	0.180	0.007
14	4.733 −4	0.0185	0.0030	1.65 −5	9.57 −5	5.86 −4	0.180	0.006
15	4.046 −4	0.0189	0.0026	2.67 −5	9.94 −5	5.31 −4	0.181	0.006
16	3.456 −4	0.0193	0.0022	4.32 −5	1.03 −4	4.92 −4	0.182	0.005
17	2.956 −4	0.0196	0.0019	4.70 −5	1.11 −4	4.54 −4	0.182	0.005
18	2.527 −4	0.0199	0.0016	5.08 −5	1.22 −4	4.26 −4	0.182	0.004
19	2.160 −4	0.0202	0.0014	5.71 −5	1.42 −4	4.15 −4	0.183	0.004
20	1.847 −4	0.0204	0.0012	5.46 −5	1.64 −4	4.03 −4	0.183	0.004
21	1.573 −4	0.0205	0.0010	5.21 −5	1.84 −4	3.93 −4	0.184	0.003
22	1.340 −4	0.0207	0.0009	5.08 −5	1.97 −4	3.82 −4	0.184	0.003
23	1.142 −4	0.0208	0.0007	4.83 −5	1.98 −4	3.61 −4	0.184	0.002
24	9.749 −5	0.0209	0.0006	3.30 −5	1.93 −4	3.24 −4	0.185	0.002
25	8.325 −5	0.0210	0.0005	2.29 −5	1.80 −4	2.86 −4	0.185	0.002
26	7.115 −5	0.0211	0.0005	1.65 −5	1.63 −4	2.51 −4	0.185	0.002
27	6.085 −5	0.0211	0.0004	1.52 −5	1.41 −4	2.17 −4	0.186	0.001
28	5.208 −5	0.0212	0.0003	1.40 −5	1.23 −4	1.89 −4	0.186	0.001
29	4.461 −5	0.0212	0.0003	1.27 −5	1.07 −4	1.64 −4	0.186	0.001
30	3.824 −5	0.0213	0.0003	1.21 −5	9.03 −5	1.41 −4	0.186	0.001
31	3.280 −5	0.0213	0.0002	0.00 +0	7.93 −5	1.12 −4	0.186	0.001
32	2.815 −5	0.0213	0.0002	0.00 +0	6.82 −5	9.64 −5	0.186	0.001
33	2.404 −5	0.0214	0.0002	0.00 +0	5.82 −5	8.22 −5	0.186	0.000
34	2.054 −5	0.0214	0.0001	0.00 +0	4.83 −5	6.88 −5	0.186	0.000
35	1.758 −5	0.0214	0.0001	0.00 +0	4.31 −5	6.07 −5	0.187	0.000
36	1.507 −5	0.0214	0.0001	0.00 +0	3.61 −5	5.12 −5	0.187	0.000
37	1.295 −5	0.0214	0.0001	0.00 +0	3.02 −5	4.32 −5	0.187	0.000
38	1.115 −5	0.0215	0.0001	0.00 +0	2.53 −5	3.64 −5	0.187	0.000
39	9.610 −6	0.0215	0.0001	0.00 +0	2.17 −5	3.13 −5	0.187	0.000
40	8.299 −6	0.0215	0.0001	0.00 +0	1.86 −5	2.69 −5	0.187	0.000
41	7.179 −6	0.0215	0.0001	0.00 +0	1.52 −5	2.24 −5	0.187	0.000
42	6.220 −6	0.0215	0.0000	0.00 +0	1.19 −5	1.81 −5	0.187	0.000
43	5.398 −6	0.0215	0.0000	0.00 +0	9.30 −6	1.47 −5	0.187	0.000
44	4.692 −6	0.0215	0.0000	0.00 +0	7.44 −6	1.21 −5	0.187	0.000
45	4.084 −6	0.0215	0.0000	0.00 +0	5.76 −6	9.84 −6	0.187	0.000
46	3.560 −6	0.0215	0.0000	0.00 +0	4.46 −6	8.02 −6	0.187	0.000
47	3.108 −6	0.0215	0.0000	0.00 +0	3.53 −6	6.64 −6	0.187	0.000
48	2.735 −6	0.0215	0.0000	0.00 +0	2.79 −6	5.52 −6	0.187	0.000
49	2.415 −6	0.0215	0.0000	0.00 +0	2.23 −6	4.65 −6	0.187	0.000
50	2.133 −6	0.0215	0.0000	0.00 +0	1.86 −6	3.99 −6	0.187	0.000

(Continued)

Table 7-4. Parameters for the model of a clear standard atmosphere. Numbers following the plus or minus sign are the power of ten by which that entry shall be multiplied. (Continued)

Alt (km)	Rayleigh Atten Coeff (km^{-1})	Rayleigh Optical Thick. (0-h)	Rayleigh Optical Thick. (h-∞)	Aerosol Atten Coeff (km^{-1})	Ozone Absorp Coeff (km^{-1})	Ext Coeff (km^{-1})	Ext Optical Thick. (0-h)	Ext Optical Thick. (h-∞)
			PARAMETERS AT 0.90 MICRONS					
0	1.583 −3	0.0000	0.0134	1.20 −1	0.00 +0	1.22 −1	0.000	0.166
1	1.436 −3	0.0015	0.0119	5.28 −2	0.00 +0	5.42 −2	0.088	0.079
2	1.300 −3	0.0029	0.0105	2.28 −2	0.00 +0	2.41 −2	0.127	0.039
3	1.175 −3	0.0041	0.0093	9.60 −3	0.00 +0	1.08 −2	0.145	0.022
4	1.058 −3	0.0052	0.0082	4.32 −3	0.00 +0	5.38 −3	0.153	0.014
5	9.514 −4	0.0062	0.0072	1.92 −3	0.00 +0	2.87 −3	0.157	0.010
6	8.528 −4	0.0071	0.0063	6.60 −4	0.00 +0	1.51 −3	0.159	0.008
7	7.622 −4	0.0079	0.0054	2.40 −4	0.00 +0	1.00 −3	0.160	0.006
8	6.792 −4	0.0087	0.0047	8.40 −5	0.00 +0	7.63 −4	0.161	0.005
9	6.034 −4	0.0093	0.0041	3.00 −5	0.00 +0	6.33 −4	0.162	0.005
10	5.342 −4	0.0099	0.0035	1.56 −5	0.00 +0	5.50 −4	0.162	0.004
11	4.713 −4	0.0104	0.0030	1.44 −5	0.00 +0	4.86 −4	0.163	0.004
12	4.030 −4	0.0108	0.0026	1.32 −5	0.00 +0	4.16 −4	0.163	0.003
13	3.444 −4	0.0112	0.0022	1.44 −5	0.00 +0	3.59 −4	0.164	0.003
14	2.944 −4	0.0115	0.0019	1.56 −5	0.00 +0	3.10 −4	0.164	0.002
15	2.516 −4	0.0118	0.0016	2.52 −5	0.00 +0	2.77 −4	0.164	0.002
16	2.151 −4	0.0120	0.0014	4.08 −5	0.00 +0	2.56 −4	0.165	0.002
17	1.838 −4	0.0122	0.0012	4.44 −5	0.00 +0	2.28 −4	0.165	0.002
18	1.572 −4	0.0124	0.0010	4.80 −5	0.00 +0	2.05 −4	0.165	0.001
19	1.343 −4	0.0125	0.0009	5.40 −5	0.00 +0	1.88 −4	0.165	0.001
20	1.148 −4	0.0127	0.0007	5.16 −5	0.00 +0	1.66 −4	0.165	0.001
21	9.780 −5	0.0128	0.0006	4.92 −5	0.00 +0	1.47 −4	0.166	0.001
22	8.333 −5	0.0129	0.0005	4.80 −5	0.00 +0	1.31 −4	0.166	0.001
23	7.105 −5	0.0129	0.0005	4.56 −5	0.00 +0	1.17 −4	0.166	0.001
24	6.063 −5	0.0130	0.0004	3.12 −5	0.00 +0	9.18 −5	0.166	0.000
25	5.177 −5	0.0131	0.0003	2.16 −5	0.00 +0	7.34 −5	0.166	0.000
26	4.425 −5	0.0131	0.0003	1.56 −5	0.00 +0	5.98 −5	0.166	0.000
27	3.784 −5	0.0131	0.0003	1.44 −5	0.00 +0	5.22 −5	0.166	0.000
28	3.239 −5	0.0132	0.0002	1.32 −5	0.00 +0	4.56 −5	0.166	0.000
29	2.774 −5	0.0132	0.0002	1.20 −5	0.00 +0	3.97 −5	0.166	0.000
30	2.378 −5	0.0132	0.0002	1.14 −5	0.00 +0	3.52 −5	0.166	0.000
31	2.040 −5	0.0133	0.0001	0.00 +0	0.00 +0	2.04 −5	0.166	0.000
32	1.751 −5	0.0133	0.0001	0.00 +0	0.00 +0	1.75 −5	0.166	0.000
33	1.495 −5	0.0133	0.0001	0.00 +0	0.00 +0	1.49 −5	0.166	0.000
34	1.277 −5	0.0133	0.0001	0.00 +0	0.00 +0	1.28 −5	0.166	0.000
35	1.093 −5	0.0133	0.0001	0.00 +0	0.00 +0	1.09 −5	0.166	0.000
36	9.375 −6	0.0133	0.0001	0.00 +0	0.00 +0	9.37 −6	0.166	0.000
37	8.054 −6	0.0133	0.0001	0.00 +0	0.00 +0	8.05 −6	0.166	0.000
38	6.932 −6	0.0133	0.0001	0.00 +0	0.00 +0	6.93 −6	0.166	0.000
39	5.976 −6	0.0133	0.0000	0.00 +0	0.00 +0	5.98 −6	0.166	0.000
40	5.161 −6	0.0134	0.0000	0.00 +0	0.00 +0	5.16 −6	0.166	0.000
41	4.465 −6	0.0134	0.0000	0.00 +0	0.00 +0	4.46 −6	0.166	0.000
42	3.868 −6	0.0134	0.0000	0.00 +0	0.00 +0	3.87 −6	0.166	0.000
43	3.357 −6	0.0134	0.0000	0.00 +0	0.00 +0	3.36 −6	0.166	0.000
44	2.918 −6	0.0134	0.0000	0.00 +0	0.00 +0	2.92 −6	0.166	0.000
45	2.540 −6	0.0134	0.0000	0.00 +0	0.00 +0	2.54 −6	0.166	0.000
46	2.214 −6	0.0134	0.0000	0.00 +0	0.00 +0	2.21 −6	0.166	0.000
47	1.933 −6	0.0134	0.0000	0.00 +0	0.00 +0	1.93 −6	0.166	0.000
48	1.701 −6	0.0134	0.0000	0.00 +0	0.00 +0	1.70 −6	0.166	0.000
49	1.502 −6	0.0134	0.0000	0.00 +0	0.00 +0	1.50 −6	0.166	0.000
50	1.326 −6	0.0134	0.0000	0.00 +0	0.00 +0	1.33 −6	0.166	0.000

(Continued)

Table 7-4. Parameters for the model of a clear standard atmosphere. Numbers following the plus or minus sign are the power of ten by which that entry shall be multiplied. (Continued)

Alt (km)	Rayleigh Atten Coeff (km^{-1})	Rayleigh Optical Thick. (0-h)	Rayleigh Optical Thick. (h-∞)	Aerosol Atten Coeff (km^{-1})	Ozone Absorp Coeff (km^{-1})	Ext Coeff (km^{-1})	Ext Optical Thick. (0-h)	Ext Optical Thick. (h-∞)
				PARAMETERS AT 1.06 MICRONS				
0	8.458 −4	0.0000	0.0072	1.13 −1	0.00 +0	1.14 −1	0.000	0.151
1	7.679 −4	0.0008	0.0064	4.97 −2	0.00 +0	5.05 −2	0.082	0.069
2	6.950 −4	0.0015	0.0056	2.15 −2	0.00 +0	2.22 −2	0.118	0.033
3	6.278 −4	0.0022	0.0050	9.04 −3	0.00 +0	9.67 −3	0.134	0.017
4	5.657 −4	0.0028	0.0044	4.07 −3	0.00 +0	4.63 −3	0.142	0.010
5	5.085 −4	0.0033	0.0038	1.81 −3	0.00 +0	2.32 −3	0.145	0.006
6	4.558 −4	0.0038	0.0033	6.22 −4	0.00 +0	1.08 −3	0.147	0.005
7	4.074 −4	0.0042	0.0029	2.26 −4	0.00 +0	6.33 −4	0.148	0.004
8	3.630 −4	0.0046	0.0025	7.91 −5	0.00 +0	4.42 −4	0.148	0.003
9	3.225 −4	0.0050	0.0022	2.82 −5	0.00 +0	3.51 −4	0.149	0.003
10	2.855 −4	0.0053	0.0019	1.47 −5	0.00 +0	3.00 −4	0.149	0.002
11	2.519 −4	0.0055	0.0016	1.36 −5	0.00 +0	2.65 −4	0.149	0.002
12	2.154 −4	0.0058	0.0014	1.24 −5	0.00 +0	2.28 −4	0.149	0.002
13	1.841 −4	0.0060	0.0012	1.36 −5	0.00 +0	1.98 −4	0.150	0.002
14	1.573 −4	0.0062	0.0010	1.47 −5	0.00 +0	1.72 −4	0.150	0.002
15	1.345 −4	0.0063	0.0009	2.37 −5	0.00 +0	1.58 −4	0.150	0.001
16	1.149 −4	0.0064	0.0007	3.84 −5	0.00 +0	1.53 −4	0.150	0.001
17	9.825 −5	0.0065	0.0006	4.18 −5	0.00 +0	1.40 −4	0.150	0.001
18	8.399 −5	0.0066	0.0005	4.52 −5	0.00 +0	1.29 −4	0.150	0.001
19	7.180 −5	0.0067	0.0005	5.08 −5	0.00 +0	1.23 −4	0.151	0.001
20	6.138 −5	0.0068	0.0004	4.86 −5	0.00 +0	1.10 −4	0.151	0.001
21	5.227 −5	0.0068	0.0003	4.63 −5	0.00 +0	9.86 −5	0.151	0.001
22	4.453 −5	0.0069	0.0003	4.52 −5	0.00 +0	8.97 −5	0.151	0.000
23	3.797 −5	0.0069	0.0002	4.29 −5	0.00 +0	8.09 −5	0.151	0.000
24	3.240 −5	0.0069	0.0002	2.94 −5	0.00 +0	6.18 −5	0.151	0.000
25	2.767 −5	0.0070	0.0002	2.03 −5	0.00 +0	4.80 −5	0.151	0.000
26	2.365 −5	0.0070	0.0002	1.47 −5	0.00 +0	3.83 −5	0.151	0.000
27	2.023 −5	0.0070	0.0001	1.36 −5	0.00 +0	3.38 −5	0.151	0.000
28	1.731 −5	0.0070	0.0001	1.24 −5	0.00 +0	2.97 −5	0.151	0.000
29	1.483 −5	0.0071	0.0001	1.13 −5	0.00 +0	2.61 −5	0.151	0.000
30	1.271 −5	0.0071	0.0001	1.07 −5	0.00 +0	2.34 −5	0.151	0.000
31	1.090 −5	0.0071	0.0001	0.00 +0	0.00 +0	1.09 −5	0.151	0.000
32	9.357 −6	0.0071	0.0001	0.00 +0	0.00 +0	9.36 −6	0.151	0.000
33	7.989 −6	0.0071	0.0001	0.00 +0	0.00 +0	7.99 −6	0.151	0.000
34	6.826 −6	0.0071	0.0000	0.00 +0	0.00 +0	6.83 −6	0.151	0.000
35	5.843 −6	0.0071	0.0000	0.00 +0	0.00 +0	5.84 −6	0.151	0.000
36	5.010 −6	0.0071	0.0000	0.00 +0	0.00 +0	5.01 −6	0.151	0.000
37	4.304 −6	0.0071	0.0000	0.00 +0	0.00 +0	4.30 −6	0.151	0.000
38	3.705 −6	0.0071	0.0000	0.00 +0	0.00 +0	3.70 −6	0.151	0.000
39	3.194 −6	0.0071	0.0000	0.00 +0	0.00 +0	3.19 −6	0.151	0.000
40	2.758 −6	0.0071	0.0000	0.00 +0	0.00 +0	2.76 −6	0.151	0.000
41	2.386 −6	0.0071	0.0000	0.00 +0	0.00 +0	2.39 −6	0.151	0.000
42	2.067 −6	0.0071	0.0000	0.00 +0	0.00 +0	2.07 −6	0.151	0.000
43	1.794 −6	0.0071	0.0000	0.00 +0	0.00 +0	1.79 −6	0.151	0.000
44	1.559 −6	0.0071	0.0000	0.00 +0	0.00 +0	1.56 −6	0.151	0.000
45	1.357 −6	0.0071	0.0000	0.00 +0	0.00 +0	1.36 −6	0.151	0.000
46	1.183 −6	0.0071	0.0000	0.00 +0	0.00 +0	1.18 −6	0.151	0.000
47	1.033 −6	0.0071	0.0000	0.00 +0	0.00 +0	1.03 −6	0.151	0.000
48	9.089 −7	0.0072	0.0000	0.00 +0	0.00 +0	9.09 −7	0.151	0.000
49	8.027 −7	0.0072	0.0000	0.00 +0	0.00 +0	8.03 −7	0.151	0.000
50	7.089 −7	0.0072	0.0000	0.00 +0	0.00 +0	7.09 −7	0.151	0.000

(Continued)

Table 7-4. Parameters for the model of a clear standard atmosphere. Numbers following the plus or minus sign are the power of ten by which that entry shall be multiplied. (Continued)

Alt (km)	Rayleigh Atten Coeff (km^{-1})	Rayleigh Optical Thick. (0-h)	Rayleigh Optical Thick. (h-∞)	Aerosol Atten Coeff (km^{-1})	Ozone Absorp Coeff (km^{-1})	Ext Coeff (km^{-1})	Ext Optical Thick. (0-h)	Ext Optical Thick. (h-∞)
			PARAMETERS AT 1.26 MICRONS					
0	4.076 −4	0.0000	0.0034	1.08 −1	0.00 +0	1.08 −1	0.000	0.141
1	3.699 −4	0.0004	0.0031	4.75 −2	0.00 +0	4.79 −2	0.078	0.063
2	3.349 −4	0.0007	0.0027	2.05 −2	0.00 +0	2.09 −2	0.113	0.029
3	3.025 −4	0.0011	0.0024	8.64 −3	0.00 +0	8.94 −3	0.127	0.014
4	2.726 −4	0.0013	0.0021	3.89 −3	0.00 +0	4.16 −3	0.134	0.007
5	2.450 −4	0.0016	0.0018	1.73 −3	0.00 +0	1.97 −3	0.137	0.004
6	2.196 −4	0.0018	0.0016	5.94 −4	0.00 +0	8.14 −4	0.138	0.003
7	1.963 −4	0.0020	0.0014	2.16 −4	0.00 +0	4.12 −4	0.139	0.002
8	1.749 −4	0.0022	0.0012	7.56 −5	0.00 +0	2.51 −4	0.139	0.002
9	1.554 −4	0.0024	0.0011	2.70 −5	0.00 +0	1.82 −4	0.140	0.002
10	1.376 −4	0.0025	0.0009	1.40 −5	0.00 +0	1.52 −4	0.140	0.001
11	1.214 −4	0.0027	0.0008	1.30 −5	0.00 +0	1.34 −4	0.140	0.001
12	1.038 −4	0.0028	0.0007	1.19 −5	0.00 +0	1.16 −4	0.140	0.001
13	8.871 −5	0.0029	0.0006	1.30 −5	0.00 +0	1.02 −4	0.140	0.001
14	7.582 −5	0.0030	0.0005	1.40 −5	0.00 +0	8.99 −5	0.140	0.001
15	6.480 −5	0.0030	0.0004	2.27 −5	0.00 +0	8.75 −5	0.140	0.001
16	5.539 −5	0.0031	0.0004	3.67 −5	0.00 +0	9.21 −5	0.140	0.001
17	4.735 −5	0.0031	0.0003	4.00 −5	0.00 +0	8.73 −5	0.141	0.001
18	4.048 −5	0.0032	0.0003	4.32 −5	0.00 +0	8.37 −5	0.141	0.001
19	3.460 −5	0.0032	0.0002	4.86 −5	0.00 +0	8.32 −5	0.141	0.001
20	2.958 −5	0.0033	0.0002	4.64 −5	0.00 +0	7.60 −5	0.141	0.000
21	2.519 −5	0.0033	0.0002	4.43 −5	0.00 +0	6.95 −5	0.141	0.000
22	2.146 −5	0.0033	0.0001	4.32 −5	0.00 +0	6.47 −5	0.141	0.000
23	1.830 −5	0.0033	0.0001	4.10 −5	0.00 +0	5.93 −5	0.141	0.000
24	1.562 −5	0.0033	0.0001	2.81 −5	0.06 +0	4.37 −5	0.141	0.000
25	1.334 −5	0.0034	0.0001	1.94 −5	0.00 +0	3.28 −5	0.141	0.000
26	1.140 −5	0.0034	0.0001	1.40 −5	0.00 +0	2.54 −5	0.141	0.000
27	9.747 −6	0.0034	0.0001	1.30 −5	0.00 +0	2.27 −5	0.141	0.000
28	8.343 −6	0.0034	0.0001	1.19 −5	0.00 +0	2.02 −5	0.141	0.000
29	7.146 −6	0.0034	0.0000	1.08 −5	0.00 +0	1.79 −5	0.141	0.000
30	6.125 −6	0.0034	0.0000	1.03 −5	0.00 +0	1.64 −5	0.141	0.000
31	5.254 −6	0.0034	0.0000	0.00 +0	0.00 +0	5.25 −6	0.141	0.000
32	4.510 −6	0.0034	0.0000	0.00 +0	0.00 +0	4.51 −6	0.141	0.000
33	3.850 −6	0.0034	0.0000	0.00 +0	0.00 +0	3.85 −6	0.141	0.000
34	3.289 −6	0.0034	0.0000	0.00 +0	0.00 +0	3.29 −6	0.141	0.000
35	2.816 −6	0.0034	0.0000	0.00 +0	0.00 +0	2.82 −6	0.141	0.000
36	2.415 −6	0.0034	0.0000	0.00 +0	0.00 +0	2.41 −6	0.141	0.000
37	2.074 −6	0.0034	0.0000	0.00 +0	0.00 +0	2.07 −6	0.141	0.000
38	1.785 −6	0.0034	0.0000	0.00 +0	0.00 +0	1.79 −6	0.141	0.000
39	1.539 −6	0.0034	0.0000	0.00 +0	0.00 +0	1.54 −6	0.141	0.000
40	1.329 −6	0.0034	0.0000	0.00 +0	0.00 +0	1.33 −6	0.141	0.000
41	1.150 −6	0.0034	0.0000	0.00 +0	0.00 +0	1.15 −6	0.141	0.000
42	9.963 −7	0.0034	0.0000	0.00 +0	0.00 +0	9.96 −7	0.141	0.000
43	8.646 −7	0.0034	0.0000	0.00 +0	0.00 +0	8.65 −7	0.141	0.000
44	7.515 −7	0.0034	0.0000	0.00 +0	0.00 +0	7.51 −7	0.141	0.000
45	6.542 −7	0.0034	0.0000	0.00 +0	0.00 +0	6.54 −7	0.141	0.000
46	5.703 −7	0.0034	0.0000	0.00 +0	0.00 +0	5.70 −7	0.141	0.000
47	4.979 −7	0.0034	0.0000	0.00 +0	0.00 +0	4.98 −7	0.141	0.000
48	4.380 −7	0.0034	0.0000	0.00 +0	0.00 +0	4.38 −7	0.141	0.000
49	3.868 −7	0.0034	0.0000	0.00 +0	0.00 +0	3.87 −7	0.141	0.000
50	3.416 −7	0.0034	0.0000	0.00 +0	0.00 +0	3.42 −7	0.141	0.000

(Continued)

Table 7-4. Parameters for the model of a clear standard atmosphere. Numbers following the plus or minus sign are the power of ten by which that entry shall be multiplied. (Continued)

Alt (km)	Rayleigh Atten Coeff (km^{-1})	Rayleigh Optical Thick. (0-h)	Rayleigh Optical Thick. (h-∞)	Aerosol Atten Coeff (km^{-1})	Ozone Absorp Coeff (km^{-1})	Ext Coeff (km^{-1})	Ext Optical Thick. (0-h)	Ext Optical Thick. (h-∞)
			PARAMETERS AT 1.67 MICRONS					
0	1.327 −4	0.0000	0.0011	9.80 −2	0.00 +0	9.81 −2	0.000	0.126
1	1.204 −4	0.0001	0.0010	4.31 −2	0.00 +0	4.32 −2	0.071	0.055
2	1.091 −4	0.0002	0.0009	1.86 −2	0.00 +0	1.87 −2	0.102	0.024
3	9.852 −5	0.0003	0.0008	7.84 −3	0.00 +0	7.94 −3	0.115	0.011
4	8.877 −5	0.0004	0.0007	3.53 −3	0.00 +0	3.62 −3	0.121	0.005
5	7.979 −5	0.0005	0.0006	1.57 −3	0.00 +0	1.65 −3	0.123	0.003
6	7.152 −5	0.0006	0.0005	5.39 −4	0.00 +0	6.11 −4	0.125	0.002
7	6.393 −5	0.0007	0.0005	1.96 −4	0.00 +0	2.60 −4	0.125	0.001
8	5.697 −5	0.0007	0.0004	6.86 −5	0.00 +0	1.26 −4	0.125	0.001
9	5.060 −5	0.0008	0.0003	2.45 −5	0.00 +0	7.51 −5	0.125	0.001
10	4.480 −5	0.0008	0.0003	1.27 −5	0.00 +0	5.75 −5	0.125	0.001
11	3.953 −5	0.0009	0.0003	1.18 −5	0.00 +0	5.13 −5	0.125	0.001
12	3.380 −5	0.0009	0.0002	1.08 −5	0.00 +0	4.46 −5	0.125	0.001
13	2.888 −5	0.0009	0.0002	1.18 −5	0.00 +0	4.06 −5	0.125	0.001
14	2.469 −5	0.0010	0.0002	1.27 −5	0.00 +0	3.74 −5	0.126	0.001
15	2.110 −5	0.0010	0.0001	2.06 −5	0.00 +0	4.17 −5	0.126	0.001
16	1.804 −5	0.0010	0.0001	3.33 −5	0.00 +0	5.14 −5	0.126	0.001
17	1.542 −5	0.0010	0.0001	3.63 −5	0.00 +0	5.17 −5	0.126	0.000
18	1.318 −5	0.0010	0.0001	3.92 −5	0.00 +0	5.24 −5	0.126	0.000
19	1.127 −5	0.0011	0.0001	4.41 −5	0.00 +0	5.54 −5	0.126	0.000
20	9.632 −6	0.0011	0.0001	4.21 −5	0.00 +0	5.18 −5	0.126	0.000
21	8.202 −6	0.0011	0.0001	4.02 −5	0.00 +0	4.84 −5	0.126	0.000
22	6.989 −6	0.0011	0.0000	3.92 −5	0.00 +0	4.62 −5	0.126	0.000
23	5.959 −6	0.0011	0.0000	3.72 −5	0.00 +0	4.32 −5	0.126	0.000
24	5.085 −6	0.0011	0.0000	2.55 −5	0.00 +0	3.06 −5	0.126	0.000
25	4.342 −6	0.0011	0.0000	1.76 −5	0.00 +0	2.20 −5	0.126	0.000
26	3.711 −6	0.0011	0.0000	1.27 −5	0.00 +0	1.65 −5	0.126	0.000
27	3.174 −6	0.0011	0.0000	1.18 −5	0.00 +0	1.49 −5	0.126	0.000
28	2.717 −6	0.0011	0.0000	1.08 −5	0.00 +0	1.35 −5	0.126	0.000
29	2.327 −6	0.0011	0.0000	9.80 −6	0.00 +0	1.21 −5	0.126	0.000
30	1.994 −6	0.0011	0.0000	9.31 −6	0.00 +0	1.13 −5	0.126	0.000
31	1.711 −6	0.0011	0.0000	0.00 +0	0.00 +0	1.71 −6	0.126	0.000
32	1.468 −6	0.0011	0.0000	0.00 +0	0.00 +0	1.47 −6	0.126	0.000
33	1.254 −6	0.0011	0.0000	0.00 +0	0.00 +0	1.25 −6	0.126	0.000
34	1.071 −6	0.0011	0.0000	0.00 +0	0.00 +0	1.07 −6	0.126	0.000
35	9.169 −7	0.0011	0.0000	0.00 +0	0.00 +0	9.17 −7	0.126	0.000
36	7.862 −7	0.0011	0.0000	0.00 +0	0.00 +0	7.86 −7	0.126	0.000
37	6.755 −7	0.0011	0.0000	0.00 +0	0.00 +0	6.75 −7	0.126	0.000
38	5.814 −7	0.0011	0.0000	0.00 +0	0.00 +0	5.81 −7	0.126	0.000
39	5.012 −7	0.0011	0.0000	0.00 +0	0.00 +0	5.01 −7	0.126	0.000
40	4.329 −7	0.0011	0.0000	0.00 +0	0.00 +0	4.33 −7	0.126	0.000
41	3.744 −7	0.0011	0.0000	0.00 +0	0.00 +0	3.74 −7	0.126	0.000
42	3.244 −7	0.0011	0.0000	0.00 +0	0.00 +0	3.24 −7	0.126	0.000
43	2.815 −7	0.0011	0.0000	0.00 +0	0.00 +0	2.82 −7	0.126	0.000
44	2.447 −7	0.0011	0.0000	0.00 +0	0.00 +0	2.45 −7	0.126	0.000
45	2.130 −7	0.0011	0.0000	0.00 +0	0.00 +0	2.13 −7	0.126	0.000
46	1.857 −7	0.0011	0.0000	0.00 +0	0.00 +0	1.86 −7	0.126	0.000
47	1.621 −7	0.0011	0.0000	0.00 +0	0.00 +0	1.62 −7	0.126	0.000
48	1.426 −7	0.0011	0.0000	0.00 +0	0.00 +0	1.43 −7	0.126	0.000
49	1.260 −7	0.0011	0.0000	0.00 +0	0.00 +0	1.26 −7	0.126	0.000
50	1.112 −7	0.0011	0.0000	0.00 +0	0.00 +0	1.11 −7	0.126	0.000

(Continued)

Table 7-4. Parameters for the model of a clear standard atmosphere. Numbers following the plus or minus sign are the power of ten by which that entry shall be multiplied. (Continued)

Alt (km)	Rayleigh Atten Coeff (km^{-1})	Rayleigh Optical Thick. (0-h)	Rayleigh Optical Thick. (h-∞)	Aerosol Atten Coeff (km^{-1})	Ozone Absorp Coeff (km^{-1})	Ext Coeff (km^{-1})	Ext Optical Thick. (0-h)	Ext Optical Thick. (h-∞)
				PARAMETERS AT 2.17 MICRONS				
0	4.586 −5	0.0000	0.0004	8.50 −2	0.00 +0	8.50 −2	0.000	0.109
1	4.161 −5	0.0000	0.0003	3.74 −2	0.00 +0	3.74 −2	0.061	0.048
2	3.768 −5	0.0001	0.0003	1.62 −2	0.00 +0	1.62 −2	0.088	0.021
3	3.404 −5	0.0001	0.0003	6.80 −3	0.00 +0	6.83 −3	0.100	0.009
4	3.067 −5	0.0002	0.0002	3.06 −3	0.00 +0	3.09 −3	0.105	0.004
5	2.757 −5	0.0002	0.0002	1.36 −3	0.00 +0	1.39 −3	0.107	0.002
6	2.471 −5	0.0002	0.0002	4.67 −4	0.00 +0	4.92 −4	0.108	0.001
7	2.209 −5	0.0002	0.0002	1.70 −4	0.00 +0	1.92 −4	0.108	0.001
8	1.968 −5	0.0003	0.0001	5.95 −5	0.00 +0	7.92 −5	0.108	0.001
9	1.748 −5	0.0003	0.0001	2.13 −5	0.00 +0	3.87 −5	0.108	0.001
10	1.548 −5	0.0003	0.0001	1.10 −5	0.00 +0	2.65 −5	0.108	0.001
11	1.366 −5	0.0003	0.0001	1.02 −5	0.00 +0	2.39 −5	0.108	0.000
12	1.168 −5	0.0003	0.0001	9.35 −6	0.00 +0	2.10 −5	0.108	0.000
13	9.979 −6	0.0003	0.0001	1.02 −5	0.00 +0	2.02 −5	0.108	0.000
14	8.529 −6	0.0003	0.0001	1.10 −5	0.00 +0	1.96 −5	0.108	0.000
15	7.290 −6	0.0003	0.0000	1.79 −5	0.00 +0	2.51 −5	0.108	0.000
16	6.231 −6	0.0003	0.0000	2.89 −5	0.00 +0	3.51 −5	0.108	0.000
17	5.327 −6	0.0004	0.0000	3.14 −5	0.00 +0	3.68 −5	0.108	0.000
18	4.554 −6	0.0004	0.0000	3.40 −5	0.00 +0	3.86 −5	0.108	0.000
19	3.893 −6	0.0004	0.0000	3.82 −5	0.00 +0	4.21 −5	0.109	0.000
20	3.328 −6	0.0004	0.0000	3.65 −5	0.00 +0	3.99 −5	0.109	0.000
21	2.834 −6	0.0004	0.0000	3.48 −5	0.00 +0	3.77 −5	0.109	0.000
22	2.415 −6	0.0004	0.0000	3.40 −5	0.00 +0	3.64 −5	0.109	0.000
23	2.059 −6	0.0004	0.0000	3.23 −5	0.00 +0	3.44 −5	0.109	0.000
24	1.757 −6	0.0004	0.0000	2.21 −5	0.00 +0	2.39 −5	0.109	0.000
25	1.500 −6	0.0004	0.0000	1.53 −5	0.00 +0	1.68 −5	0.109	0.000
26	1.282 −6	0.0004	0.0000	1.10 −5	0.00 +0	1.23 −5	0.109	0.000
27	1.097 −6	0.0004	0.0000	1.02 −5	0.00 +0	1.13 −5	0.109	0.000
28	9.385 −7	0.0004	0.0000	9.35 −6	0.00 +0	1.03 −5	0.109	0.000
29	8.039 −7	0.0004	0.0000	8.50 −6	0.00 +0	9.30 −6	0.109	0.000
30	6.890 −7	0.0004	0.0000	8.07 −6	0.00 +0	8.76 −6	0.109	0.000
31	5.910 −7	0.0004	0.0000	0.00 +0	0.00 +0	5.91 −7	0.109	0.000
32	5.073 −7	0.0004	0.0000	0.00 +0	0.00 +0	5.07 −7	0.109	0.000
33	4.332 −7	0.0004	0.0000	0.00 +0	0.00 +0	4.33 −7	0.109	0.000
34	3.701 −7	0.0004	0.0000	0.00 +0	0.00 +0	3.70 −7	0.109	0.000
35	3.168 −7	0.0004	0.0000	0.00 +0	0.00 +0	3.17 −7	0.109	0.000
36	2.716 −7	0.0004	0.0000	0.00 +0	0.00 +0	2.72 −7	0.109	0.000
37	2.334 −7	0.0004	0.0000	0.00 +0	0.00 +0	2.33 −7	0.109	0.000
38	2.009 −7	0.0004	0.0000	0.00 +0	0.00 +0	2.01 −7	0.109	0.000
39	1.732 −7	0.0004	0.0000	0.00 +0	0.00 +0	1.73 −7	0.109	0.000
40	1.495 −7	0.0004	0.0000	0.00 +0	0.00 +0	1.50 −7	0.109	0.000
41	1.294 −7	0.0004	0.0000	0.00 +0	0.00 +0	1.29 −7	0.109	0.000
42	1.121 −7	0.0004	0.0000	0.00 +0	0.00 +0	1.12 −7	0.109	0.000
43	9.727 −8	0.0004	0.0000	0.00 +0	0.00 +0	9.73 −8	0.109	0.000
44	8.454 −8	0.0004	0.0000	0.00 +0	0.00 +0	8.45 −8	0.109	0.000
45	7.359 −8	0.0004	0.0000	0.00 +0	0.00 +0	7.36 −8	0.109	0.000
46	6.416 −8	0.0004	0.0000	0.00 +0	0.00 +0	6.42 −8	0.109	0.000
47	5.601 −8	0.0004	0.0000	0.00 +0	0.00 +0	5.60 −8	0.109	0.000
48	4.928 −8	0.0004	0.0000	0.00 +0	0.00 +0	4.93 −8	0.109	0.000
49	4.352 −8	0.0004	0.0000	0.00 +0	0.00 +0	4.35 −8	0.109	0.000
50	3.843 −8	0.0004	0.0000	0.00 +0	0.00 +0	3.84 −8	0.109	0.000

(Continued)

Table 7-4. Parameters for the model of a clear standard atmosphere. Numbers following the plus or minus sign are the power of ten by which that entry shall be multiplied. (Continued)

Alt (km)	Rayleigh Atten Coeff (km^{-1})	Rayleigh Optical Thick. (0-h)	Rayleigh Optical Thick. (h-∞)	Aerosol Atten Coeff (km^{-1})	Ozone Absorp Coeff (km^{-1})	Ext Coeff (km^{-1})	Ext Optical Thick. (0-h)	Ext Optical Thick. (h-∞)
				PARAMETERS AT 3.50 MICRONS				
0	6.830 −6	0.0000	0.0001	7.00 −2	0.00 +0	7.00 −2	0.000	0.089
1	6.198 −6	0.0000	0.0001	3.08 −2	0.00 +0	3.08 −2	0.050	0.039
2	5.612 −6	0.0000	0.0000	1.33 −2	0.00 +0	1.33 −2	0.072	0.017
3	5.070 −6	0.0000	0.0000	5.60 −3	0.00 +0	5.61 −3	0.082	0.007
4	4.568 −6	0.0000	0.0000	2.52 −3	0.00 +0	2.52 −3	0.086	0.003
5	4.106 −6	0.0000	0.0000	1.12 −3	0.00 +0	1.12 −3	0.088	0.002
6	3.680 −6	0.0000	0.0000	3.85 −4	0.00 +0	3.89 −4	0.089	0.001
7	3.290 −6	0.0000	0.0000	1.40 −4	0.00 +0	1.43 −4	0.089	0.001
8	2.931 −6	0.0000	0.0000	4.90 −5	0.00 +0	5.19 −5	0.089	0.000
9	2.604 −6	0.0000	0.0000	1.75 −5	0.00 +0	2.01 −5	0.089	0.000
10	2.305 −6	0.0000	0.0000	9.10 −6	0.00 +0	1.14 −5	0.089	0.000
11	2.034 −6	0.0000	0.0000	8.40 −6	0.00 +0	1.04 −5	0.089	0.000
12	1.739 −6	0.0000	0.0000	7.70 −6	0.00 +0	9.44 −6	0.089	0.000
13	1.486 −6	0.0000	0.0000	8.40 −6	0.00 +0	9.89 −6	0.089	0.000
14	1.270 −6	0.0000	0.0000	9.10 −6	0.00 +0	1.04 −5	0.089	0.000
15	1.086 −6	0.0001	0.0000	1.47 −5	0.00 +0	1.58 −5	0.089	0.000
16	9.281 −7	0.0001	0.0000	2.38 −5	0.00 +0	2.47 −5	0.089	0.000
17	7.934 −7	0.0001	0.0000	2.59 −5	0.00 +0	2.67 −5	0.089	0.000
18	6.782 −7	0.0001	0.0000	2.80 −5	0.00 +0	2.87 −5	0.089	0.000
19	5.798 −7	0.0001	0.0000	3.15 −5	0.00 +0	3.21 −5	0.089	0.000
20	4.956 −7	0.0001	0.0000	3.01 −5	0.00 +0	3.06 −5	0.089	0.000
21	4.221 −7	0.0001	0.0000	2.87 −5	0.00 +0	2.91 −5	0.089	0.000
22	3.596 −7	0.0001	0.0000	2.80 −5	0.00 +0	2.84 −5	0.089	0.000
23	3.066 −7	0.0001	0.0000	2.66 −5	0.00 +0	2.69 −5	0.089	0.000
24	2.617 −7	0.0001	0.0000	1.82 −5	0.00 +0	1.85 −5	0.089	0.000
25	2.235 −7	0.0001	0.0000	1.26 −5	0.00 +0	1.28 −5	0.089	0.000
26	1.910 −7	0.0001	0.0000	9.10 −6	0.00 +0	9.29 −6	0.089	0.000
27	1.633 −7	0.0001	0.0000	8.40 −6	0.00 +0	8.56 −6	0.089	0.000
28	1.398 −7	0.0001	0.0000	7.70 −6	0.00 +0	7.84 −6	0.089	0.000
29	1.197 −7	0.0001	0.0000	7.00 −6	0.00 +0	7.12 −6	0.089	0.000
30	1.026 −7	0.0001	0.0000	6.65 −6	0.00 +0	6.75 −6	0.089	0.000
31	8.803 −8	0.0001	0.0000	0.00 +0	0.00 +0	8.80 −8	0.089	0.000
32	7.556 −8	0.0001	0.0000	0.00 +0	0.00 +0	7.56 −8	0.089	0.000
33	6.452 −8	0.0001	0.0000	0.00 +0	0.00 +0	6.45 −8	0.089	0.000
34	5.512 −8	0.0001	0.0000	0.00 +0	0.00 +0	5.51 −8	0.089	0.000
35	4.718 −8	0.0001	0.0000	0.00 +0	0.00 +0	4.72 −8	0.089	0.000
36	4.046 −8	0.0001	0.0000	0.00 +0	0.00 +0	4.05 −8	0.089	0.000
37	3.476 −8	0.0001	0.0000	0.00 +0	0.00 +0	3.48 −8	0.089	0.000
38	2.992 −8	0.0001	0.0000	0.00 +0	0.00 +0	2.99 −8	0.089	0.000
39	2.579 −8	0.0001	0.0000	0.00 +0	0.00 +0	2.58 −8	0.089	0.000
40	2.227 −8	0.0001	0.0000	0.00 +0	0.00 +0	2.23 −8	0.089	0.000
41	1.927 −8	0.0001	0.0000	0.00 +0	0.00 +0	1.93 −8	0.089	0.000
42	1.669 −8	0.0001	0.0000	0.00 +0	0.00 +0	1.67 −8	0.089	0.000
43	1.449 −8	0.0001	0.0000	0.00 +0	0.00 +0	1.45 −8	0.089	0.000
44	1.259 −8	0.0001	0.0000	0.00 +0	0.00 +0	1.26 −8	0.089	0.000
45	1.096 −8	0.0001	0.0000	0.00 +0	0.00 +0	1.10 −8	0.089	0.000
46	9.556 −9	0.0001	0.0000	0.00 +0	0.00 +0	9.56 −9	0.089	0.000
47	8.342 −9	0.0001	0.0000	0.00 +0	0.00 +0	8.34 −9	0.089	0.000
48	7.340 −9	0.0001	0.0000	0.00 +0	0.00 +0	7.34 −9	0.089	0.000
49	6.482 −9	0.0001	0.0000	0.00 +0	0.00 +0	6.48 −9	0.089	0.000
50	5.724 −9	0.0001	0.0000	0.00 +0	0.00 +0	5.72 −9	0.089	0.000

(Continued)

Table 7-4. Parameters for the model of a clear standard atmosphere. Numbers following the plus or minus sign are the power of ten by which that entry shall be multiplied. (Continued)

Alt (km)	Rayleigh Atten Coeff (km^{-1})	Rayleigh Optical Thick. (0-h)	Rayleigh Optical Thick. (h-∞)	Aerosol Atten Coeff (km^{-1})	Ozone Absorp Coeff (km^{-1})	Ext Coeff (km^{-1})	Ext Optical Thick. (0-h)	Ext Optical Thick. (h-∞)
				PARAMETERS AT 4.00 MICRONS				
0	4.002 −6	0.0000	0.0000	6.30 −2	0.00 +0	6.30 −2	0.000	0.080
1	3.632 −6	0.0000	0.0000	2.77 −2	0.00 +0	2.77 −2	0.045	0.035
2	3.289 −6	0.0000	0.0000	1.20 −2	0.00 +0	1.20 −2	0.065	0.015
3	2.971 −6	0.0000	0.0000	5.04 −3	0.00 +0	5.04 −3	0.074	0.007
4	2.677 −6	0.0000	0.0000	2.27 −3	0.00 +0	2.27 −3	0.077	0.003
5	2.406 −6	0.0000	0.0000	1.01 −3	0.00 +0	1.01 −3	0.079	0.001
6	2.157 −6	0.0000	0.0000	3.46 −4	0.00 +0	3.49 −4	0.080	0.001
7	1.928 −6	0.0000	0.0000	1.26 −4	0.00 +0	1.28 −4	0.080	0.000
8	1.718 −6	0.0000	0.0000	4.41 −5	0.00 +0	4.58 −5	0.080	0.000
9	1.526 −6	0.0000	0.0000	1.57 −5	0.00 +0	1.73 −5	0.080	0.000
10	1.351 −6	0.0000	0.0000	8.19 −6	0.00 +0	9.54 −6	0.080	0.000
11	1.192 −6	0.0000	0.0000	7.56 −6	0.00 +0	8.75 −6	0.080	0.000
12	1.019 −6	0.0000	0.0000	6.93 −6	0.00 +0	7.95 −6	0.080	0.000
13	8.710 −7	0.0000	0.0000	7.56 −6	0.00 +0	8.43 −6	0.080	0.000
14	7.444 −7	0.0000	0.0000	8.19 −6	0.00 +0	8.93 −6	0.080	0.000
15	6.363 −7	0.0000	0.0000	1.32 −5	0.00 +0	1.39 −5	0.080	0.000
16	5.439 −7	0.0000	0.0000	2.14 −5	0.00 +0	2.20 −5	0.080	0.000
17	4.649 −7	0.0000	0.0000	2.33 −5	0.00 +0	2.38 −5	0.080	0.000
18	3.974 −7	0.0000	0.0000	2.52 −5	0.00 +0	2.56 −5	0.080	0.000
19	3.398 −7	0.0000	0.0000	2.84 −5	0.00 +0	2.87 −5	0.080	0.000
20	2.904 −7	0.0000	0.0000	2.71 −5	0.00 +0	2.74 −5	0.080	0.000
21	2.473 −7	0.0000	0.0000	2.58 −5	0.00 +0	2.61 −5	0.080	0.000
22	2.107 −7	0.0000	0.0000	2.52 −5	0.00 +0	2.54 −5	0.080	0.000
23	1.797 −7	0.0000	0.0000	2.39 −5	0.00 +0	2.41 −5	0.080	0.000
24	1.533 −7	0.0000	0.0000	1.64 −5	0.00 +0	1.65 −5	0.080	0.000
25	1.309 −7	0.0000	0.0000	1.13 −5	0.00 +0	1.15 −5	0.080	0.000
26	1.119 −7	0.0000	0.0000	8.19 −6	0.00 +0	8.30 −6	0.080	0.000
27	9.571 −8	0.0000	0.0000	7.56 −6	0.00 +0	7.66 −6	0.080	0.000
28	8.191 −8	0.0000	0.0000	6.93 −6	0.00 +0	7.01 −6	0.080	0.000
29	7.016 −8	0.0000	0.0000	6.30 −6	0.00 +0	6.37 −6	0.080	0.000
30	6.014 −8	0.0000	0.0000	5.98 −6	0.00 +0	6.05 −6	0.080	0.000
31	5.158 −8	0.0000	0.0000	0.00 +0	0.00 +0	5.16 −8	0.080	0.000
32	4.428 −8	0.0000	0.0000	0.00 +0	0.00 +0	4.43 −8	0.080	0.000
33	3.780 −8	0.0000	0.0000	0.00 +0	0.00 +0	3.78 −8	0.080	0.000
34	3.230 −8	0.0000	0.0000	0.00 +0	0.00 +0	3.23 −8	0.080	0.000
35	2.765 −8	0.0000	0.0000	0.00 +0	0.00 +0	2.76 −8	0.080	0.000
36	2.371 −8	0.0000	0.0000	0.00 +0	0.00 +0	2.37 −8	0.080	0.000
37	2.037 −8	0.0000	0.0000	0.00 +0	0.00 +0	2.04 −8	0.080	0.000
38	1.753 −8	0.0000	0.0000	0.00 +0	0.00 +0	1.75 −8	0.080	0.000
39	1.511 −8	0.0000	0.0000	0.00 +0	0.00 +0	1.51 −8	0.080	0.000
40	1.305 −8	0.0000	0.0000	0.00 +0	0.00 +0	1.31 −8	0.080	0.000
41	1.129 −8	0.0000	0.0000	0.00 +0	0.00 +0	1.13 −8	0.080	0.000
42	9.783 −9	0.0000	0.0000	0.00 +0	0.00 +0	9.78 −9	0.080	0.000
43	8.490 −9	0.0000	0.0000	0.00 +0	0.00 +0	8.49 −9	0.080	0.000
44	7.379 −9	0.0000	0.0000	0.00 +0	0.00 +0	7.38 −9	0.080	0.000
45	6.423 −9	0.0000	0.0000	0.00 +0	0.00 +0	6.42 −9	0.080	0.000
46	5.599 −9	0.0000	0.0000	0.00 +0	0.00 +0	5.60 −9	0.080	0.000
47	4.888 −9	0.0000	0.0000	0.00 +0	0.00 +0	4.89 −9	0.080	0.000
48	4.301 −9	0.0000	0.0000	0.00 +0	0.00 +0	4.30 −9	0.080	0.000
49	3.798 −9	0.0000	0.0000	0.00 +0	0.00 +0	3.80 −9	0.080	0.000
50	3.354 −9	0.0000	0.0000	0.00 +0	0.00 +0	3.35 −9	0.080	0.000

7.6 REFERENCES

Chagnon, C. W., and C. E. Junge, 1961, "The Vertical Distribution of Sub-micron Particles in the Stratosphere," *J. Meteorol.*, v. 18, p. 746.

Coulson, K. L., J. V. Dave, and Z. Sekera, 1960, "Tables Related to Radiation Emerging from a Planetary Atmosphere with Rayleigh Scattering," University of California Press.

Coulson, K. L., 1959, "Total Upward Flux and Albedo," *J. Planet. and Space Sci.*, v. 1, p. 277.

Curcio, J. A., G. L. Knestrick, and T. H. Cosden, 1961, "Atmospheric Scattering in the Visible and Infrared," *NRL Report 5567*, and "Atmospheric Attenuation Coefficients in the Visible and Infrared," *NRL Report 5648*, U.S. Naval Research Laboratory, Washington, D.C.

Dunkelman, L., 1952, "Horizontal Attenuation of Ultraviolet and Visible Light by the Lower Atmosphere," *NRL Report 4031*, U.S. Naval Research Laboratory, Washington, D.C.

Duntley, S. Q., et al., 1964, "Visibility," *Appl. Opt.*, v. 3, no. 5, p. 550.

Elterman, L., 1964, "Atmospheric Attenuation Model, 1964, in the Ultraviolet, the Visible, and the Infrared Windows for Altitudes to 50 km," *Environmental Res. Paper No. 46*, AFCRL.

Fraser, R. S., 1964, "Apparent Contrast of Objects on the Earth's Surface as Seen from Above the Earth's Atmosphere," *J. Opt. Soc. Am.*, v. 54, no. 3.

Fritz, S., 1954, "Scattering of Solar Energy by Clouds of 'Large Drops,' " *J. Meteorol.*, v. 11.

Hughes, J. V., 1964, "Sky Brightness as a Function of Altitude," *Appl. Opt.*, v. 3, no. 10, p. 1135.

Kerker, M., 1963, "Proceedings of the Interdisciplinary Conference on Electromagnetic Scattering," Pergamon Press, New York.

Koomen, M. J., 1959, "Visibility of Stars at High Altitude in Daylight," *J. Opt. Soc. Am.*, v. 49, no. 6.

Krinov, E. L., 1947, "Vectoral Reflectance Properties of Natural Formations (trans.)," *Labotoriia Aeormetodov*, Akad. Nauk. SSSR.

Newkirk, G., and J. A. Eddy, 1964, "Light Scattering by Particles in the Upper Atmosphere," *J. Atmos. Sci.*, v. 21, no. 1, p. 35.

Penndorf, R., 1962, "Angular Mie Scattering," *J. Opt. Soc. Am.*, v. 52, no. 4.

Rosenberg, G. V., 1960, "Light Scattering in the Earth's Atmosphere," *Soviet Physics-Uspekhi, Amer. Instit. Phys. Trans.*, v. 3.

Sekera, Z., 1956, "Recent Developments in the Study of the Polarization of Sky Light," *Adv. in Geophys.*, v. 3, Academic Press, New York.

Twersky, V., 1964, "Rayleigh Scattering," *Appl. Opt.*, v. 3, no. 10, p. 1150.

Van de Hulst, H. C., 1957, "Light Scattering by Small Particles," John Wiley and Sons, New York.

Vigroux, E., 1953, "Contributions à l'étude expérimentale de l'absorption de l'ozone," *Annales de Physique*, v. 8, p. 709.

Chapter 8

ATMOSPHERIC ELECTRICITY

Section 8.1 Rita C. Sagalyn
Section 8.2 Donald R. Fitzgerald

8.1 FAIR WEATHER ELECTRICITY

Electric fields, currents, and conductivity as well as positive and negative ions of greatly varying size constitute the principal electrical properties of the atmosphere in fair weather. Air mass motions, pressure systems, winds, turbulence, temperature, and water vapor distributions have an important influence on the electrical properties in the troposphere through their control over the distributions of charged and uncharged aerosols and radioactive particles of terrestrial origin. These influences are greatest in the atmospheric exchange layer. In the altitude region 30 to 70 km, atmospheric electricity studies and ionospheric physics merge.

8.1.1 Electrical Conductivity

The electrical conductivity (quantity of electricity transferred across a unit area per unit potential per unit time) of air, λ, may be expressed as

$$\lambda = \sum_{i=1}^{i=m} n_i e_i k_i, \qquad (8\text{-}1)$$

where m is the number of different ion species present, and n_i, e_i, k_i are the concentration (number per unit volume), charge, and mobility of the ith ion specie, respectively. The *mobility* of an ion is the ratio of its drift velocity to the electric-field strength. In the atmosphere, positive and negative ions have radii ranging from 5×10^{-6} to 5×10^{-8} cm. Small ions, because of their low mass, have a high velocity in the earth's electric field. They contribute over 95% to the total conductivity of the atmosphere, so that the electrical conductivity of the atmosphere depends on the factors influencing the small ion density.

$$\lambda \approx n_+ e k_+ + n_- e k_-, \qquad (8\text{-}2)$$

where n_+ and n_- are the positive and negative small-ion densities, and k_+ and k_- are the mobilities of the positive and negative small ions. At standard temperature and pressure, $k_+ \approx 1.3$ cm^2 V^{-1} sec^{-1} and $k_- \approx 1.6$ cm^2 V^{-1} sec^{-1}. Figure 8-1 shows the variation of k with density of the atmosphere or altitude.

8.1.2 Electric Field

In fair weather areas the horizontal components of the field are negligible so that the atmospheric electric field, E, is defined by

$$E = -\frac{dV}{dZ}, \qquad (8\text{-}3)$$

where V is the electric potential and Z is the altitude. The atmospheric electric field is directed vertically, the potential gradient decreases with increasing altitude, and the field by the electrostatic definition is negative (field vector directed downward). In most of the literature, however, the field is called positive when the potential gradient is positive. Figure 8-2 shows the field as a function of altitude.

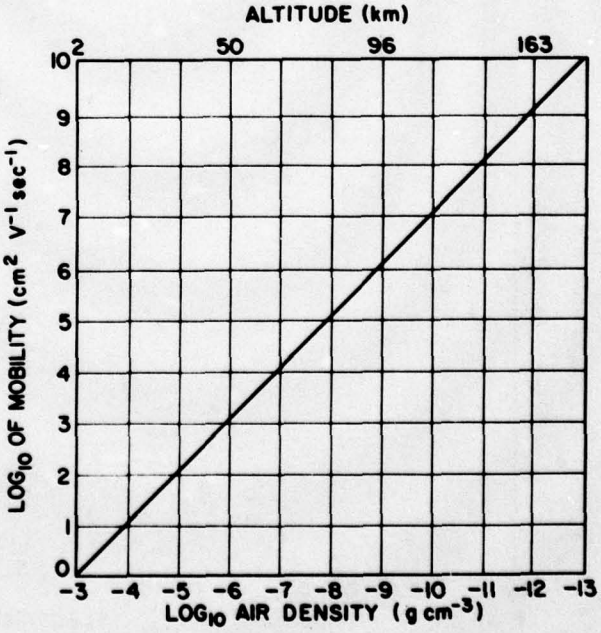


Fig. 8-1. Mobility, k, of small positive or negative ions vs air density or altitude, assuming k = 1.4 cm^2 V^{-1} sec^{-1} at 0°C and 76 cm Hg pressure.

8.1.3 Currents and Space Charge

The vertical *conduction current density*, j, is defined by

$$j = \frac{V}{R_c} = \lambda E. \tag{8-4}$$

The potential difference between the earth and the ionosphere, V, is $-\int_0^\infty E\, dZ$. The resistance of a vertical air column of 1-cm² cross section, R_c, is $\int_0^\infty \frac{dZ}{\lambda}$. Conservation of charge requires that the current along the column be constant. The conduction current density is, therefore, the net vertical current due to positive ions flowing downward and negative ions flowing upward in the atmosphere. The average of conduction current density measurements obtained over land and ocean areas is 2.7×10^{-12} A m^{-2}, with values ranging from 1 to 4×10^{-12} A m^{-2}. The total current flow over the earth is, therefore, approximately 1400 A.

In regions where a space charge exists (excess of ions of one sign), movement of air produces a transfer of charge that can be defined as a *convection current density* j_2;

$$j_2 = \rho v \approx -A_\sigma \partial\rho/\partial Z, \tag{8-5}$$

where ρ is the space charge per unit volume, v is the vertical air velocity, and A_σ is the coefficient of eddy diffusion. Space charge densities and gradients large enough to significantly influence the vertical current are expected to occur primarily in the exchange layer where considerable mixing occurs and greatly varying quantities of charged nuclei are introduced into the atmosphere. (Throughout this chapter, nuclei refer to molecular aggregates that may or may not act as condensation nuclei depending on their chemical composition.) The average convection current is 40% of the total current in the exchange layer. The convection current decreases with altitude. Convection currents comparable to or greater than the conduction current have been observed below 0.015 km [Smith, 1958].

The *space charge density*, ρ, is related to the field and to the potential through Poisson's equation;

$$\frac{dE}{dZ} = \frac{d^2V}{dZ^2} = -4\pi\rho, \tag{8-6}$$

in CGS electrostatic units.

8.1.4 Atmospheric Ions

Atmospheric ions are divided into four main groups according to their size and mobilities: small positive and negative ions, n_+ and n_-, and large positive and negative ions (which are also referred to as charged nuclei), N_1 and N_2. Table 8-1 gives the range of mobilities and radii.

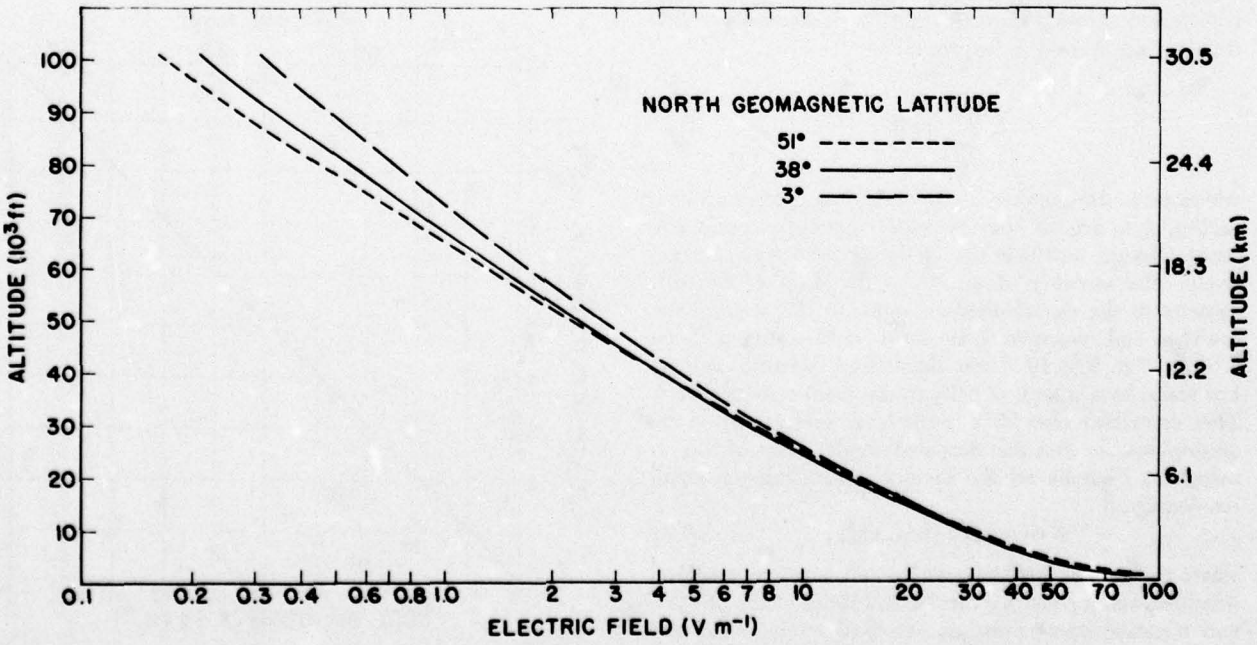


Fig. 8-2. Electric field vs altitude, computed from Eq. (8-4), assuming a conduction current density of 2.7×10^{-12} A m^{-1} and using values of λ from Fig. 8-6.

The continuity equations for the production and destruction of ions are

$$\frac{dn_+}{dt} = q_1 - \alpha n_+ n_- - \eta_{12} n_+ N_2 - \eta_{10} n_+ N_o, \tag{8-7}$$

$$\frac{dn_-}{dt} = q_2 - \alpha n_+ n_- - \eta_{21} n_- N_1 - \eta_{20} n_- N_o, \tag{8-8}$$

$$\frac{dN_1}{dt} = Q_1 + \eta_{10} n_+ N_o - \eta_{21} n_- N_1 - \gamma N_1 N_2, \tag{8-9}$$

$$\frac{dN_2}{dt} = Q_2 + \eta_{20} n_- N_o - \eta_{12} n_+ N_2 - \gamma N_1 N_2, \tag{8-10}$$

where q_1 and q_2 are net production rates of small ions due to radioactive emanations from the earth's surface, cosmic radiation, and diffusion, and Q_1 and Q_2 are net production rates of large ions due to ionizing sources and diffusion ($q_1 \approx q_2$ and $Q_1 \approx Q_2$). N_o is the concentration of neutral nuclei. The *volume recombination coefficient* for small ions is, in $cm^3\ sec^{-1}$,

$$\alpha = 1.75 \times 10^{-5} \left(\frac{273}{T}\right)^{3/2} (M)^{-1/2} f(Y), \tag{8-11}$$

where T is the temperature in °K, M is the molecular weight of the ions in atomic mass units, and f(Y) is the probability function.

$$f(Y) = 1 - 4\,Y^{-4}\,[1 - (Y+1)\,e^{-Y}]^2, \tag{8-12}$$

and

$$Y = 0.81 \left(\frac{273}{T}\right)^2 \left(\frac{P}{760}\right) \left(\frac{L_A}{L}\right). \tag{8-13}$$

P is the pressure in mm Hg and L_A/L is the ratio of the mean free path of a molecule to that of an ion at normal temperature and pressure; for air, $L_A/L = 3$. Table 8-2 gives values of f(Y) for Y between 0 and 2.5. Figure 8-3 shows the variation of α with altitude.

The attachment coefficients are η_{12} for collisions between small positive and large negative ions, η_{21} for collisions between small negative and large positive ions, η_{10} for collisions between a small positive ion and a neutral nucleus, and η_{20} for collisions between a small negative ion and a neutral nucleus. Bricard [1949] derived expressions for these attachment coefficients as a function of the charge and radius of the nuclei and the mobility and diffusion coefficient of the small ion. The diffusion coefficients of small positive and negative ions are approximately equal, and

$$\eta_{12} \approx \eta_{21} = 4\pi\, D\, a/I\ (\zeta, p), \tag{8-14}$$

$$\eta_{20} \approx \eta_{10} = 4\pi\, D\, a/I\ (\zeta, o). \tag{8-15}$$

Table 8-1. Mobility and size range of atmospheric ions.

Ions	Mobility ($cm^2\ sec^{-1}\ V^{-1}$)	Radius (cm)
Small	10^{-2} to 2×10^{-2}	6.6×10^{-8} to 7.8×10^{-7}
Average large	10^{-3} to 10^{-2}	7.8×10^{-7} to 2.5×10^{-6}
Langevin	2.5×10^{-4} to 10^{-3}	2.5×10^{-6} to 5.7×10^{-6}
Ultra large	$< 2.5 \times 10^{-4}$	$> 5.7 \times 10^{-6}$

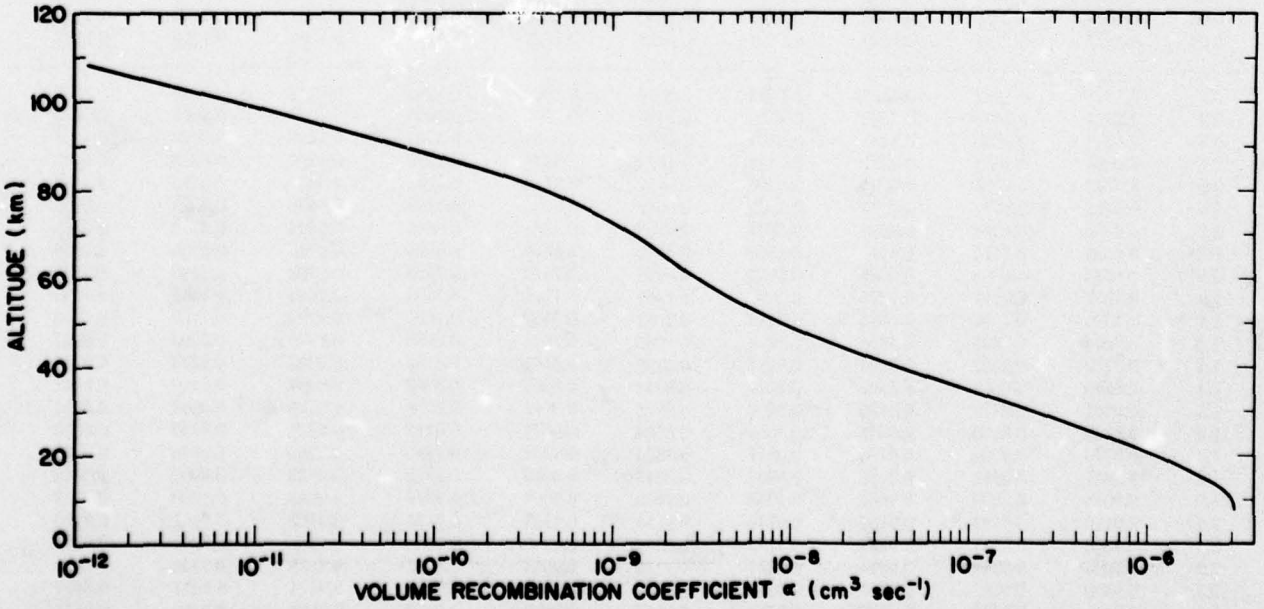


Fig. 8-3. Volume recombination coefficient, α, vs altitude computed from Eq. (8-11).

D is the average value of the small ion diffusion coefficient, a is the radius of the interacting charged or uncharged nucleus, and I (ζ, p) is a dimensionless parameter that contains the dependence of the attachment coefficient on the radius and charge of the nucleus.

$$I(\zeta, p) = \int_1^\infty X^{-2} \exp\left[-\zeta\left(\frac{p}{X} + \frac{1}{2X^2(X^2-1)}\right)\right] dX. \tag{8-16}$$

p is the number of elementary charges on the large ion, $\zeta = ek/Da$ in CGS electrostatic units, or $\zeta = ek/4\pi\epsilon_0 Da$ in MKSA units (k is small-ion mobility), and $X = r/a$, where r is the radius of a sphere of influence centered on the nucleus. Figure 8-4 gives values of $I(\zeta, p)$.

In Eq. (8-9) and (8-10), γ is the combination coefficient for collisions between large ions of opposite sign. It is approximately 10^{-9} cm^3 sec^{-1}, which is three orders of magnitude less than the value of the attachment coefficients. Terms containing γ, therefore, usually may be neglected.

8.1.5 Equilibrium Conditions

Above the exchange layer in fair weather areas, the charged and uncharged nucleus content is low. To a first approximation, ion equilibrium exists. Assuming charge neutrality, Eq. (8-7) and (8-8) reduce to

$$q = \alpha n_\pm^2. \tag{8-17}$$

Measured values of production rate due to cosmic rays at various atmospheric depths and geomagnetic latitude are given in Sec. 17.3. Figure 8-5 shows the variation of small-ion density with altitude calculated from Eq. (8-17) using values of q derived from cosmic ray intensity data [Bowen, 1938] and values of α from Fig. 8-3.

Assuming $k_+ = k_- = k$, then, from Eq. (8-2) and (8-17), the total electrical conductivity above the exchange layer is

$$\lambda = 2ek\sqrt{q/\alpha}. \tag{8-18}$$

Figure 8-6 shows the electrical volume conductivity variations; values of q derived from cosmic ray ionization rates, values of k from Fig. 8-1, and values of α from Fig. 8-3 were used in these calculations.

Under equilibrium conditions in regions of significant nucleus concentration, Eq. (8-7) and (8-8) reduce to

$$q = \alpha n_\pm^2 + n_\pm(\eta_{12} N_\pm + \eta_{10} N_0), \tag{8-19}$$

or

$$n_\pm = -[\beta N_\pm \pm (\beta^2 N_\pm^2 + 4\alpha q)^{1/2}]/2\alpha, \tag{8-20}$$

where $\beta = \eta_{12} + \eta_{10}(N_0/N_\pm)$, and $N_\pm$ is the charged nucleus concentration of either sign. Figure 8-7 shows the

Table 8-2. Probability function f(Y) for Eq. (8-11).

Y	0	1	2	3	4	5	6	7	8	9
0.03	0.03916	0.04044	0.04172	0.04299	0.04426	0.04553	0.04680	0.04806	0.04933	0.05059
0.04	0.05185	0.05311	0.05437	0.05562	0.05688	0.05813	0.05938	0.06063	0.06187	0.06312
0.05	0.06436	0.06560	0.06684	0.6808	0.06932	0.07055	0.07179	0.07302	0.07425	0.07547
0.06	0.07670	0.07792	0.07914	0.08037	0.08158	0.08280	0.08402	0.08523	0.08644	0.08765
0.07	0.08886	0.09007	0.09127	0.09248	0.09368	0.09488	0.09608	0.09727	0.09847	0.09966
0.08	0.1009	0.1020	0.1032	0.1044	0.1056	0.1068	0.1080	0.1091	0.1103	0.1115
0.09	0.1127	0.1138	0.1150	0.1162	0.1174	0.1185	0.1197	0.1209	0.1220	0.1232
0.1	0.1243	0.1358	0.1472	0.1583	0.1694	0.1802	0.1910	0.2015	0.2119	0.2222
0.2	0.2324	0.2423	0.2522	0.2619	0.2715	0.2809	0.2903	0.2994	0.3085	0.3175
0.3	0.3263	0.3350	0.3435	0.3520	0.3603	0.3686	0.3767	0.3847	0.3926	0.4004
0.4	0.4080	0.4156	0.4231	0.4304	0.4377	0.4449	0.4519	0.4589	0.4658	0.4726
0.5	0.4793	0.4859	0.4924	0.4988	0.5051	0.5114	0.5175	0.5236	0.5296	0.5355
0.6	0.5414	0.5471	0.5528	0.5584	0.5639	0.5694	0.5748	0.5801	0.5853	0.5905
0.7	0.5956	0.6006	0.6056	0.6105	0.6153	0.6201	0.6248	0.6294	0.6340	0.6385
0.8	0.6430	0.6474	0.6517	0.6560	0.6602	0.6644	0.6685	0.6726	0.6766	0.6805
0.9	0.6844	0.6883	0.6921	0.6958	0.6995	0.7032	0.7068	0.7103	0.7138	0.7173
1.0	0.7207	0.7241	0.7274	0.7307	0.7339	0.7371	0.7403	0.7434	0.7465	0.7495
1.1	0.7525	0.7555	0.7584	0.7613	0.7641	0.7669	0.7697	0.7724	0.7751	0.7778
1.2	0.7804	0.7830	0.7856	0.7881	0.7906	0.7931	0.7955	0.7979	0.8003	0.8027
1.3	0.8050	0.8072	0.8095	0.8117	0.8139	0.8161	0.8182	0.8203	0.8224	0.8245
1.4	0.8265	0.8285	0.8305	0.8325	0.8344	0.8363	0.8382	0.8401	0.8419	0.8437
1.5	0.8455	0.8473	0.8490	0.8508	0.8525	0.8541	0.8558	0.8574	0.8591	0.8607
1.6	0.8623	0.8638	0.8654	0.8669	0.8684	0.8699	0.8713	0.8728	0.8742	0.8756
1.7	0.8770	0.8784	0.8796	0.8811	0.8824	0.8837	0.8850	0.8863	0.8876	0.8888
1.8	0.8901	0.8913	0.8925	0.8937	0.8948	0.8960	0.8971	0.8983	0.8994	0.9005
1.9	0.9016	0.9027	0.9037	0.9048	0.9058	0.9068	0.9079	0.9089	0.9098	0.9108
2.0	0.9118	0.9127	0.9137	0.9146	9.9154	0.9165	0.9174	0.9182	0.9191	0.9200
2.1	0.9208	0.9217	0.9225	0.9233	0.9242	0.9250	0.9258	0.9266	0.9273	0.9281
2.2	0.9289	0.9296	0.9304	0.9311	0.9318	0.9325	0.9332	0.9339	0.9346	0.9353
2.3	0.9360	0.9367	0.9373	0.9380	0.9386	0.9393	0.9399	0.9405	0.9411	0.9417
2.4	0.9423	0.9429	0.9435	0.9441	0.9447	0.9452	0.9458	0.9464	0.9469	0.9475

dependence of small-ion density and of conductivity on charged nucleus concentration computed for several altitudes. Figure 8-8 gives theoretical relations and experimental data for small ions and charged nuclei at 5000 ft.

8.1.6 Variations in the Exchange Layer

The exchange layer varies in depth between 500 and 10,000 ft above the surface. Large variations in the electrical properties occur in this layer. Meteorologically, the layer is characterized by uniform specific humidity and a nearly adiabatic temperature-lapse rate with a sharp decrease in lapse rate at the top. The horizontal wind velocity differs from the wind velocity in the general circulation due to the frictional influence of the earth's surface. Figures 8-9 and 8-10 show the variations of electrical properties with altitude in a well developed exchange layer.

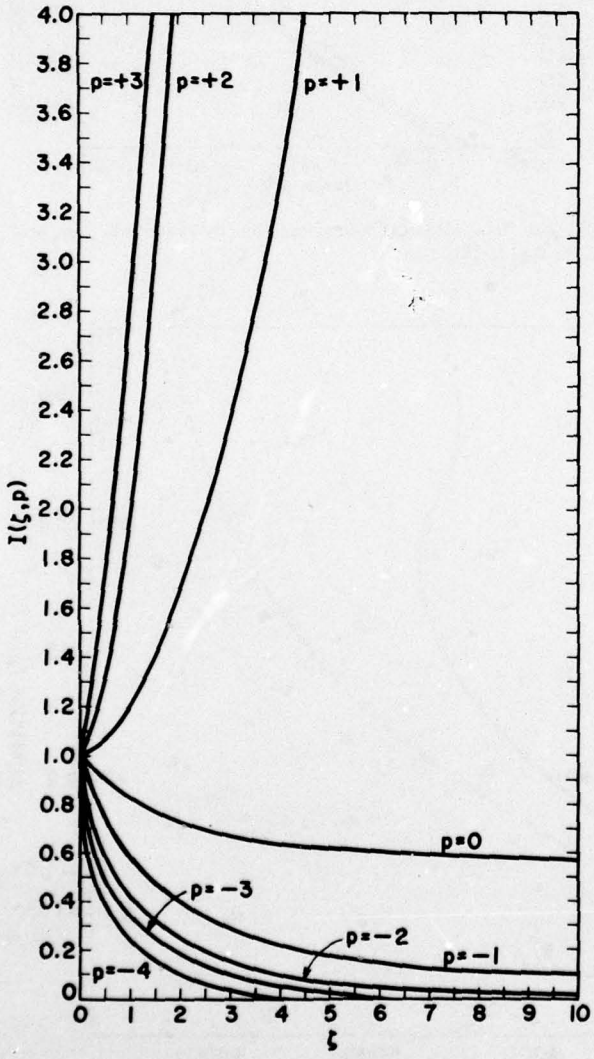


Fig. 8-4. Parameter I (ζ, p) for Eq. (8-14) and (8-15); p is the number of positive or negative elementary charges on the large ion, and ζ is a dimensionless parameter. (After Bricard [1949].)

The distribution and magnitude of the electrical properties vary from day to day and with time of day. At altitudes above 1000 ft during periods of low advection, regular daily variations can be observed. Figures 8-11, 8-12, and 8-13 show the variations observed over southern New Hampshire. This diurnal variation of the electrical properties results from the daily variation of the intensity of atmospheric turbulence and the influx of nuclei from the surface. Figure 8-14 shows the regular variation in the columnar resistance of the atmosphere.

Over land areas, the most complicated distribution of the electrical properties is found between the surface and approximately 1000 ft. In this region, ionization produced by radioactive emanations from the surface of the earth can, particularly in the early morning hours, cause an initial decrease of conductivity with height. This causes the potential gradient to increase with altitude and produces a negative space charge region near the ground. With the onset of turbulence, the concentration of ions in the region between the surface and 1000 ft is greatly reduced, and the conductivity increases or remains constant with altitude. In accordance with Poisson's equation, the potential gradient then decreases with altitude, and a positive or zero space charge exists in this region. The exact nature of the diurnal variation depends upon the radioactive content and porosity of the surface and on the intensity of atmospheric turbulence. Table 8-3 gives the average ion-pair production rates in the lower atmosphere due to radioactivity and to cosmic radiation.

The influence of the exchange layer on the electrical properties is a minimum in regions where air masses are forming, such as the arctic and antarctic. Figure 8-15 shows the vertical distribution of electrical conductivity and the electric field measured on an early morning flight over Greenland. Figures 8-16(a), (b), (c), and (d) show the negligible diurnal variation of the electrical properties over oceans in high-pressure areas where very stable exchange layers are formed. Figure 8-17 shows the influence of the exchange layer on conductivities observed in mountainous regions.

8.1.7 Variations in the Free Atmosphere

Figures 8-18 through 8-20 give measured values of the vertical distribution of electrical conductivity, electric field, and small-ion density (calculated distributions are shown in Fig. 8-2, 8-5, and 8-6). The curves represent average values from about 100 aircraft and balloon flights; the bars indicate limits of variation of the observational data. The variations are due to varying radioactive content, cosmic radiation, and pollution content. Figure 8-21 shows estimated ion pair production rates due to cosmic rays (Neher's data) and to cosmic rays plus atmospheric radioactivity. The pollution content depends strongly upon air mass type and history. Figure 8-22 indicates the extreme variability of the pollution particle content; the data were obtained from about 80 aircraft and balloon flights.

8.1.8 Worldwide Current System and Maintenance of Earth's Charge

Acccording to electrostatic laws, over 90% of the earth's negative charge of about 500,000 C should leak off in about 10 min because of the conductivity of the air. The net charge, however, remains practically constant. It is now generally accepted [Stergis et al, 1957] that thunderstorms and shower clouds act as generators that drive current upward in the reverse direction to the current flow in fair weather areas. The total current due to disturbed weather systems active at any instant approximately balances the conduction current in fair weather areas. The potential gradient in undisturbed fair weather areas has the same diurnal variation all over the earth when referred to universal time [Mauchly, 1923]. This diurnal variation is in phase with the diurnal variation of worldwide thunderstorm activity. The potential gradient in undisturbed areas is proportional to the total potential difference between the earth and ionosphere. The magnitude of this potential difference is 275 $\pm$ 50 kV.

8.2 THUNDERSTORM ELECTRICITY

About 50,000 thunderstorms occur every day throughout the world and, on the average, about 2000 storms are in progress at any time. Charts of the frequency of occurrence of storms over the earth as a function of location and month are published by the World Meteorological Organization, Geneva, Switzerland.

Lightning discharges to ground are usually initiated by *stepped leaders*, which deposit negative charges along the downward path. The main surge is the *return stroke*, which begins when the leader reaches ground; it is characterized by a positive current flowing up the ionized channel. Succeeding return strokes, if any, are preceded by a *dart leader* that again deposits negative charges along the previously ionized channel. Continuing low currents

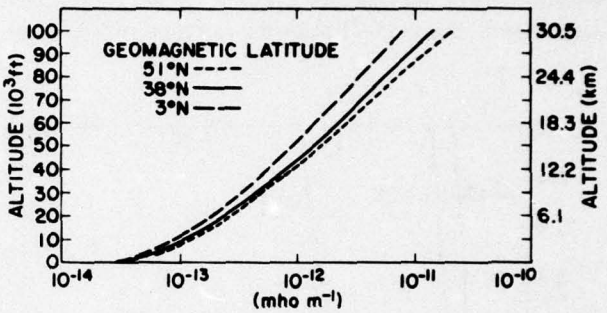


Fig. 8-6. Total electrical volume-conductivity vs altitude, computed from Eq. (8-18).

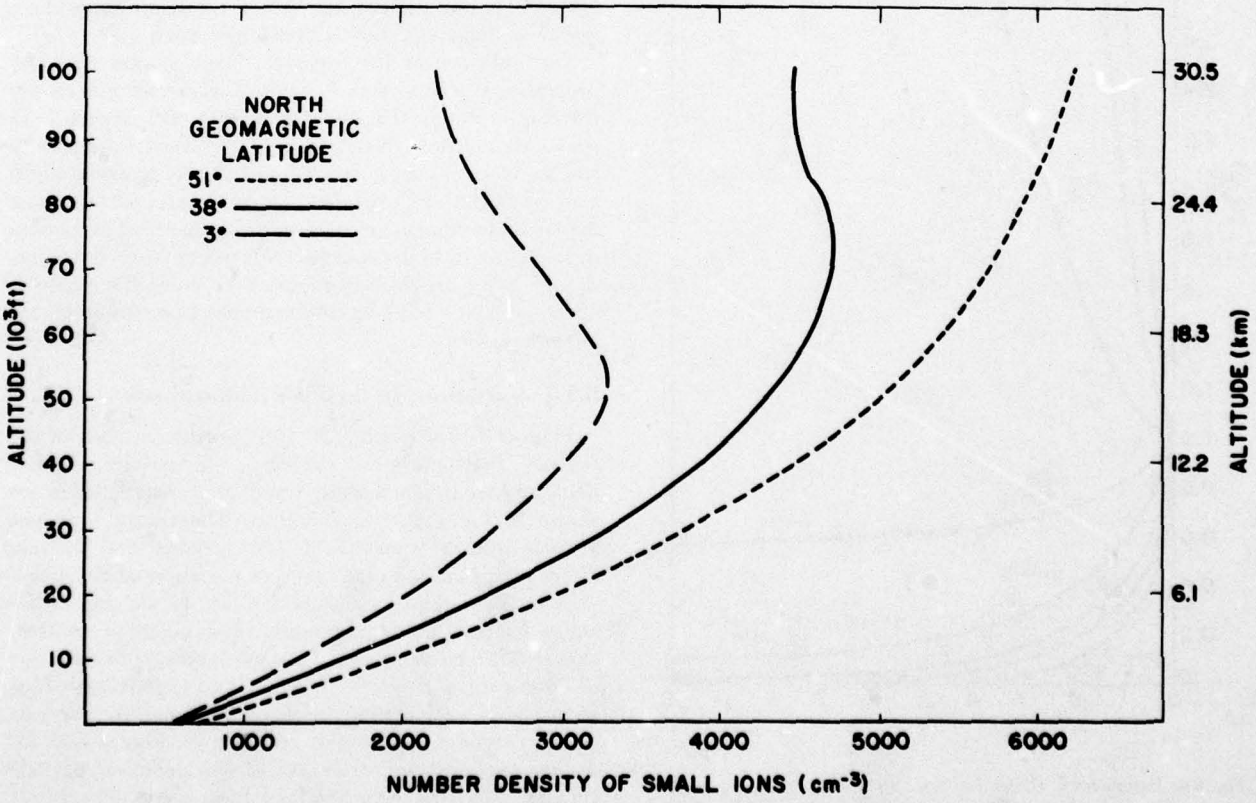


Fig. 8-5. Number density of small positive or negative ions vs altitude, computed from Eq. (8-17).

flow between return strokes and may persist for 0.5 sec or longer. The current changes during discharges produce associated radiation fields; the radiation is most intense in the very low and extremely low-frequency radio spectrum. Smaller within-cloud discharge processes cause significant disturbances extending above 30 Mcps.

8.2.1 Electrostatic Field Patterns

Aircraft penetrations during the growth stage of cumulus congestus clouds are characterized by strong negative charge accumulation on the aircraft at altitudes up to at least 30,000 ft. Electric fields due to the cloud itself rather than aircraft charging are generally weak in and around growing clouds. As the precipitation begins to fall out of these clouds, if the clouds maintain an anvil-like upper portion, then cloud electric fields of several hundred volts per centimeter develop. The fields are oriented so that it appears that the initial precipitation streamers are carrying negative charge toward earth, with positive charge remaining in the lower anvil. Flight through or around the rain sheet at cloud base indicates electric field components up to 2300 V cm^{-1} with a usual excess of negative charge in the rain column. Some regions of cloud base excess positive charge are found in conjunction with mixed phase precipitation.

Clear air flights around large thunderstorm masses show horizontal field components up to 500 V cm^{-1}. The field varies in intensity; higher values occur in the general vicinity of the heavier precipitation areas. Regions of maximum field do not always coincide with regions of maximum radar reflectivity. Figure 8-23 shows the field variation at 31,000 ft along one wall of a large isolated thunderstorm. Figure 8-24 gives the field pattern found on

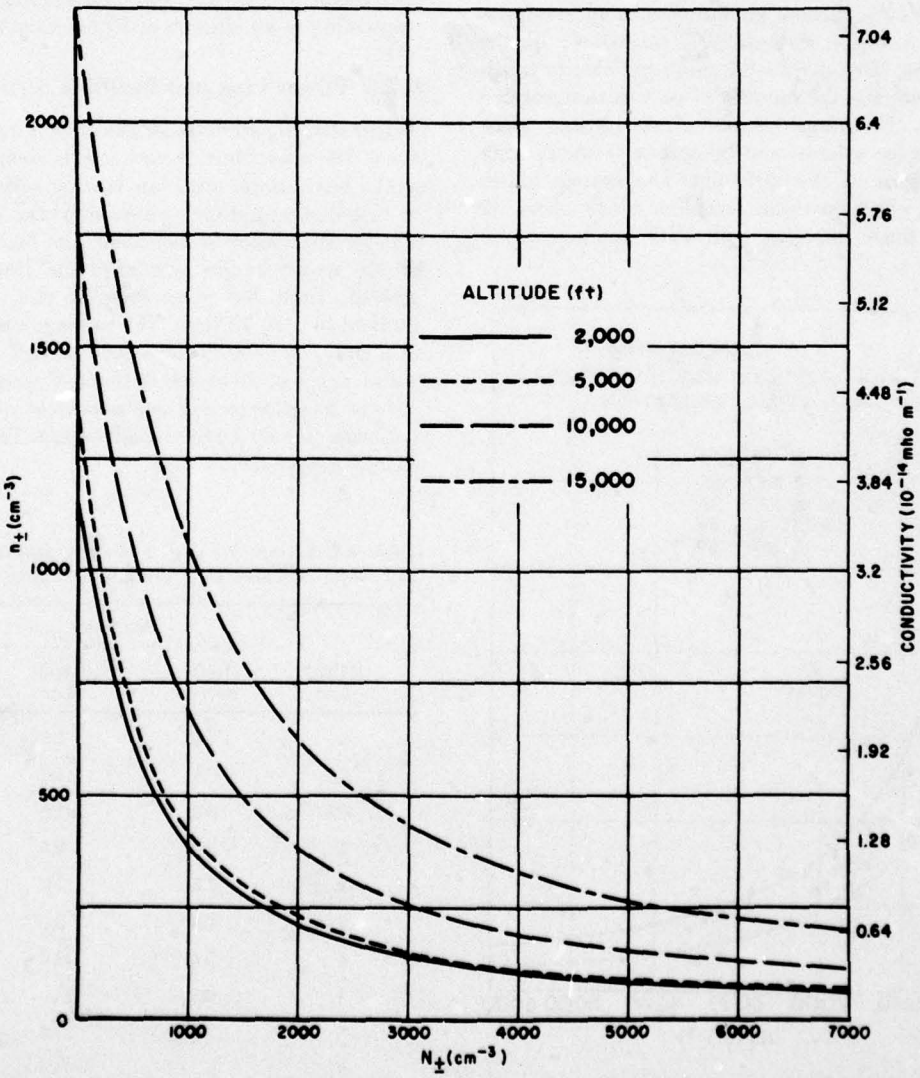


Fig. 8-7. Positive or negative small ion number density, $n_{\pm}$, and electrical conductivity vs positive or negative charged nucleus concentrations, $N_{\pm}$. (From Sagalyn and Faucher [1956].)

flight past a shaft of hail falling from one portion of a line of thunderstorms; the vertical and wingspan-oriented horizontal components have been combined to give direction and magnitude of the two-dimensional field vector. The charge centroid is generally below flight level, but rises to higher altitudes as the hail is approached and the field increases.

The vertical component field patterns in the clear air above large thunderstorms and squall lines, obtained from U-2 aircraft, show that the field at 20 km (about 3 km above the highest part of the storm), is about 50 V cm^{-1} with lightning field changes ranging up to 100 V cm^{-1}.

8.2.2 Precipitation Static

Flight through various haze conditions, rain, and particularly through snow and ice crystal clouds, causes a considerable accumulation of charge and high-aircraft voltage with respect to the environment. Charge accumulation results from collisions of the cloud and precipitation particles with the aircraft. The magnitude of the charging current is related to the mean net charge transferred per impact and the number of particles intercepted per unit time. Discharge of the aircraft takes place through the engine exhaust and by corona from the high curvature portions of the airframe. The corona pulses have a serious effect on radio reception below about 30 Mcps, and at times interfere with VHF equipment. A comprehensive discussion of this phenomenon and the development of corona-resistant antenna sheaths and low-noise dischargers is given in a series of articles by Gunn et al [1946].

High-speed jet aircraft have additional noise problems. At speeds above 250 knots, the noise level may increase at rates up to the sixth power of the speed [Couch, 1960]. Three noise-generating mechanisms are corona pulses, an effect called streamering (flashover to the airframe of charge built up on dielectric surfaces), and an effect due to antenna pickup of sudden changes in the impact-particle voltage. The particle-impact noise is at least 54 dB below the streamering noise level. The spectrum of impact noise decreases inversely with frequency. The streamering spectrum is nearly flat to 160 kcps, rolling off to 3 dB down at 480 kcps. In laboratory tests, corona pulses have rise times as short as 6 nsec with a decay to 50% in 30 nsec at a pressure of 760 mm Hg. Rise and decay times increase to 20 nsec and 100 nsec at reduced pressure corresponding to an altitude of 10 km (200 mm Hg).

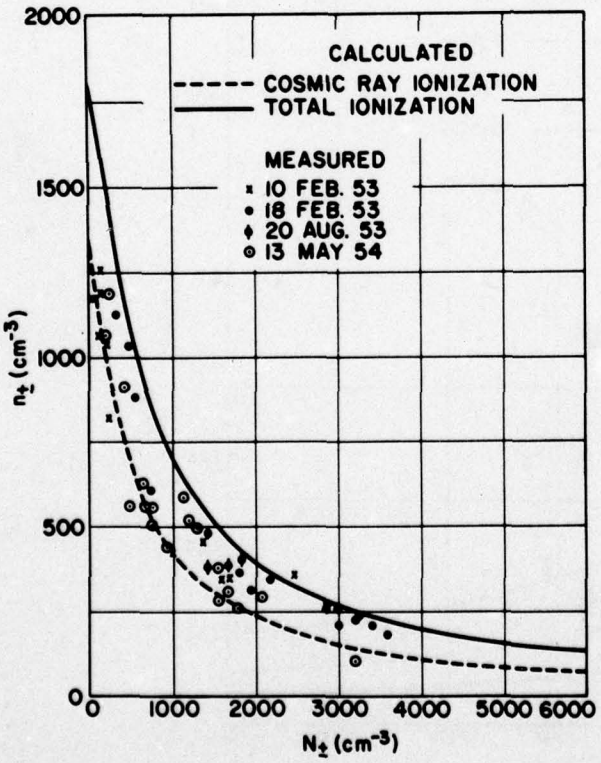


Fig. 8-8. Positive or negative small ion number density, $n_\pm$, vs positive or negative charged nucleus concentration, $N_\pm$, at 5000-ft altitude. (From Sagalyn and Faucher [1956].)

8.2.3 Power Line and Building Strikes

The stroke path has an effective surge impedance of about 500 ohm; thus, the current is about the same if the stroke hits a tower with low footing resistance (10 ohm) or if it strikes mid-span on an overhead ground line with a surge impedance of 250 ohm. The high-current portion of the stroke begins just after the leader contacts the ground. Table 8-4 gives rates of rise. Crest current is reached in 1 to 10 μsec. The average time to crest is 1.5 to 2 μsec, and the average time to half value is 40 μsec with a range of 20 to 200 or more. Currents up to 160,000 A have been measured, and a current of 345,000 A was indicated in a strike to a 585-ft object. Table 8-5 lists total charges transferred.

Table 8-3. Average ion pair production rates due to radioactivity and cosmic radiation as a function of height.

Height (km)	Ion Pairs (cm^{-3} sec^{-1})		
	Radio-activity	Cosmic Rays	Total
0	7.6	1.5	9.1
0.1	5.1	1.6	6.7
0.5	3.8	1.8	5.6
1	2.7	2.6	5.3
2	1.5	5.0	6.5
3	0.9	8.0	8.9
4	0.5	15.0	15.5
5	0.3	23.0	23.3
6	—	37.0	37.0
8	—	75.0	75.0
10	—	125.0	125.0

The number of repetitive flashes in the same or nearly the same channel seems to depend on storm intensity. As determined by photographic methods, the number of strokes range from 1 to 40 or more. Electrical methods, however, show a maximum of 14 discharges with an average of four. The discrepancy may be due to small momentary current increases that are easily mistaken for component strokes on slow camera photographs. Total duration of the discharges in a multiple stroke ranges to above 1.5 sec; 89% of the strokes exceed 1 msec.

Lightning stroke characteristics are given by Harder and Clayton [Byers, 1953], and discussed in considerable detail by Schonland [1956]. A model of the charge distribution in a leader stroke-to-ground [Griscom, 1958] attempts to explain the higher than expected power circuit outages. This model suggests that the advancing tip of the leader contains considerably more charge than the other portions of the leader, so that an initial high-amplitude short-duration current pulse may be experienced prior to

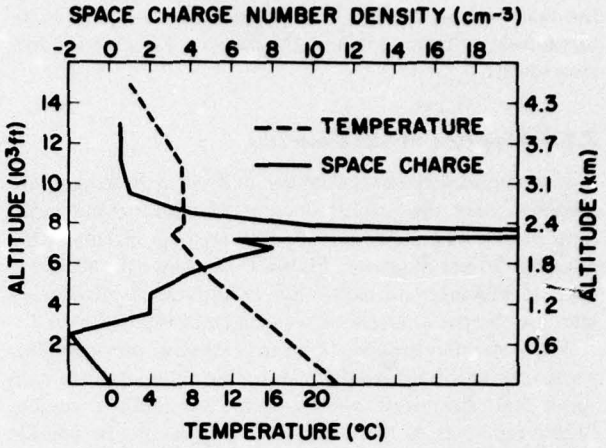


Fig. 8-10. Simultaneous temperature and space charge density vs altitude on 20 August 1953, 1311 to 1416 Eastern Standard Time. (From Sagalyn and Faucher [1954].)

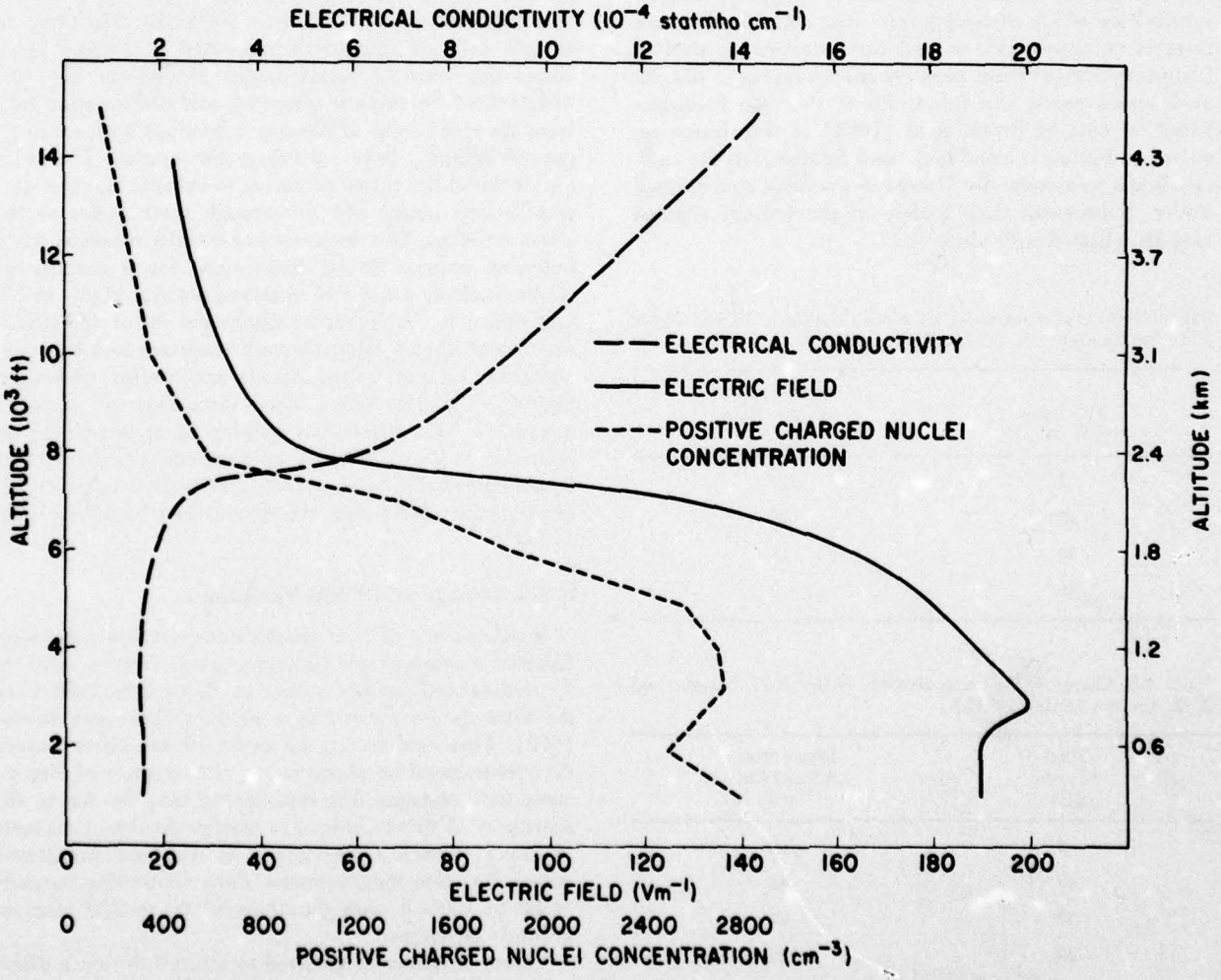


Fig. 8-9. Simultaneous values of electrical conductivity, electric field, and positive charged nuclei concentration vs altitude, observed on 20 August 1953, 1311 to 1416 Eastern Standard Time. (From Sagalyn and Faucher [1954].)

the main return stroke. This pulse would result in high-magnitude voltages spikes at the top of a struck transmission tower.

8.2.4 Possible Strike Patterns

If a cylindrical charge model and vertical strokes are assumed, then the projected point of within-cloud lightning moves in a random-walk fashion in a circular area of about 10-km diameter. Figure 8-25 shows the distribution of distances of successive within-cloud discharges obtained by the analysis of records from three storms.

Most cloud-to-ground lightning strokes progress forward with the interface delineating the thunderstorm rain sheet and downdraft region from the updraft region. Lightning starts as the radar cloud top begins to subside and ends before this interface has reached the forward edge of the cell. The active electrical cell is about 8 km long and contracts as it ages. Strokes appear to occur at random across this whole length of the cell, but with respect to the direction of cloud motion they are usually within 2 km of the advancing rain sheet interface. Because there is no appreciable central concentration of strokes, it appears that the main negative charge region is distributed across nearly the full width of the cell. Estimates based on data of Brook et al [1962] of the charge required to initiate a cloud-to-ground lightning stroke indicate that a minimum of 3 C must be available to a stepped leader. Subsequent dart leaders in the ionized channel may be initiated with about 0.2 C.

Table 8-4. Rate of current rise on fronts of lightning surges. (After E. L. Harder and J. M. Clayton [Byers, 1953].)

Rise Rate (10^9 A sec^{-1})	Direct Strokes ≥ Rise Rate (%)
5	70
10	45
20	15
40	7

Table 8-5. Charge in lightning strokes. (After E. L. Harder and J. M. Clayton [Byers, 1953].)

Total Charge (C)	Direct Strokes ≥ Total Charge (%)
5	60
10	43
20	32
40	20
80*	12

* Total stroke charges exceeding 160 C have been recorded.

Strokes that terminate on the ground have a first leader field-change duration of 10 to 150 msec with a peak from 20 to 30 msec. The period of pulse repetition is most frequently 40 to 60 μsec. The mean pulse interval is 80 μsec, with a range from 10 μsec to above 280 μsec. In contrast to these values associated with a ground stroke, the intracloud strokes have an initial field change duration of 50 to 300 msec, with the most frequent value from 100 to 150 msec. The pulse repetition period varies from 10 μsec to 10 msec with a mean pulse interval of 680 μsec. Detailed information on these characteristic differences is given by Kitagawa and Brook [1960].

The initial breakdown process for a cloud discharge differs from the ground stroke leader process. This differance may arise from differences in the relative concentration of water drops and ice particles as they affect the internal impedance of the cloud charge volumes.

Radar echo and time lapse photographic analysis of 12 storms in the vicinity of Albuquerque, New Mexico, indicate that glaciation of the cloud top is well underway when the radar cloud top reaches altitudes of about 32,000 ft at a temperature of −28° to −30°C. By this time, an electric field disturbance is measured at ground level. About the time the turret begins to descend, the first within-cloud lightning is observed, and precipitation falls from the cloud base. If the storm develops well, cloud-to-ground lightning begins within a few minutes. The radar top of the initial turret continues to subside and new turrets become active and go through their cycles as the storm develops. This sequence is generally observed when lightning occurs. Stroke frequencies for a number of storms indicate a cycle of electrical activity of 10- to 30-min duration. Nonlightning discharges on or to aircraft may occur during flight through moderate to heavy precipitation in nonfreezing clouds and during prolonged flight through haze layers. These discharges are generally associated with differential buildup of static charge on dielectric surfaces. Several independent observations of actual lightning discharges from apparently ice-free clouds are reported; these data are summarized by Moore et al [1960].

8.2.5 Charge and Field Variations

Measurements of total charge transport made by using ballistic magnetograph technique give, from a total of 21 well-defined strokes, values of 20 to over 1000 C as the total charge carried in a stroke [Meese and Evans, 1962]. These values are an order of magnitude larger than those based on observations of current or of electrostatic field changes. The discrepancy may be due to the sensitivity of this technique to smaller persistent currents in many strokes. Observations of magnetic inductance with a flux-gate magnetometer show continuing currents of 80 to 1000 A with durations of 40 to 300 msec in ground discharges.

Values of charge transferred to aircraft during a direct strike, inferred from damage evidence, range up to above 600 C; currents in excess of 200,000 A seem to be experienced. Discharges through the aircraft may cause major

damage to plastic sections and to radio antennas and equipment. Minor damage to flap and control surfaces and hinge bearings may occur and holes may be produced in thin metal skins.

The electromagnetic field associated with a lightning flash is often compared with the field due to a vertical electric monopole antenna situated on a perfectly conducting plane or a free space dipole antenna. At distances large compared with the length of the stroke, but short enough so that ionospheric effects may be neglected (30 to 100 km), standard radiation theory may be applied and expressions for the electric and magnetic fields obtained. At close range ($d << l$ and $d/\tau << l$), the length of the discharge is not important; the magnetic field is a function of current and distance and the electric field a function of current, distance, and frequency [Wait, 1956]. Figure 8-26 indicates the decrease in magnetic and electric field strengths from an oscillating dipole for d/τ ratios less than unity.

Figure 8-27 gives examples of the actual change in magnetic field intensity observed relatively near the storm; one precursor field change is larger than that of the main-stroke field change. The field patterns are typical of those due to essentially vertical flashes to earth. Figure 8-28 shows the variation of magnetic field intensity at distances given by the observed lightning-thunder intervals; the highest value of magnetic field occurring in a multiple discharge was selected.

Table 8-6 lists changes in the vertical component of the electric field with distance from the storm determined from observations taken over a 20-yr period in Cambridge, England. The magnitude, at low frequencies, of the electric field associated with cloud-to-ground strokes is observed to decrease very slowly with distance over ranges comparable with the length of a stroke. According to Watt [1960], the decrease from 4 to 20 km is proportional to d^{-3} and beyond 30 km proportional to d^{-1}. Figure 8-29 indicates the trend and experimental points.

8.2.6 Frequency Characteristics of Radiation

A major portion of the energy radiated in a flash is at frequencies below 100 kcps; hence, most studies of the relation of lightning to *sferics* (radio signals due to atmospheric noise) are concerned with the ELF and VLF frequencies. For example, much work has been done on radio location of distant thunderstorms, the determination of the spectrum of radio noise and the propagation mechanisms at these frequencies.

In the vicinity of 20 cps, the electric field changes shift from a resultant of the worldwide lightning activity to a largely electrostatic variability associated with the movement of atmospheric space charge. It appears that the magnetic field changes at frequencies above about 20 cps are also largely associated with distant lightning activity, but at lower frequencies the main effects are due to ionospheric and earth currents.

For a storm at 10-km distance, the peak power in a flash has an average value of 56 kW in a 300-cps bandwidth at 6 kcps and an average value of 280 mW at 11 Mcps [Horner, 1961]; if one exceptional stroke with a peak power of 3.8 W were neglected, the average power at 11 Mcps would be 110 mW. At 6 kcps the largest pulses are attributed to return strokes from earth, but many of the smaller pulses seem to be associated with within-cloud processes that have characteristics similar to return strokes. At 11 Mcps the return stroke does not radiate appreciably. Stepped leaders radiate to some extent, but it appears that the mean sources of energy at Mcps frequencies have not yet been clearly identified with presently accepted details of the lightning stroke. Brook and Kitagawa [1964] discuss observations at 420 and 850 Mcps and conclude that microwave radiation from lightning is associated primarily with the formation of streamers within the cloud.

Table 8-6. Change in vertical component of electric field, ΔE_v, at approximate distances from the storm. (After E. T. Pierce and T. W. Wormell [Byers, 1953].)

ΔE_v (V cm^{-1})	Distance (km)
> 50	< 6
5 - 50	6 - 12
1 - 5	12 - 20
0.1 - 1	20 - 50
0.01 - 0.1	50 - 100
0.001 - 0.01	100 - 200
< 0.001	> 200

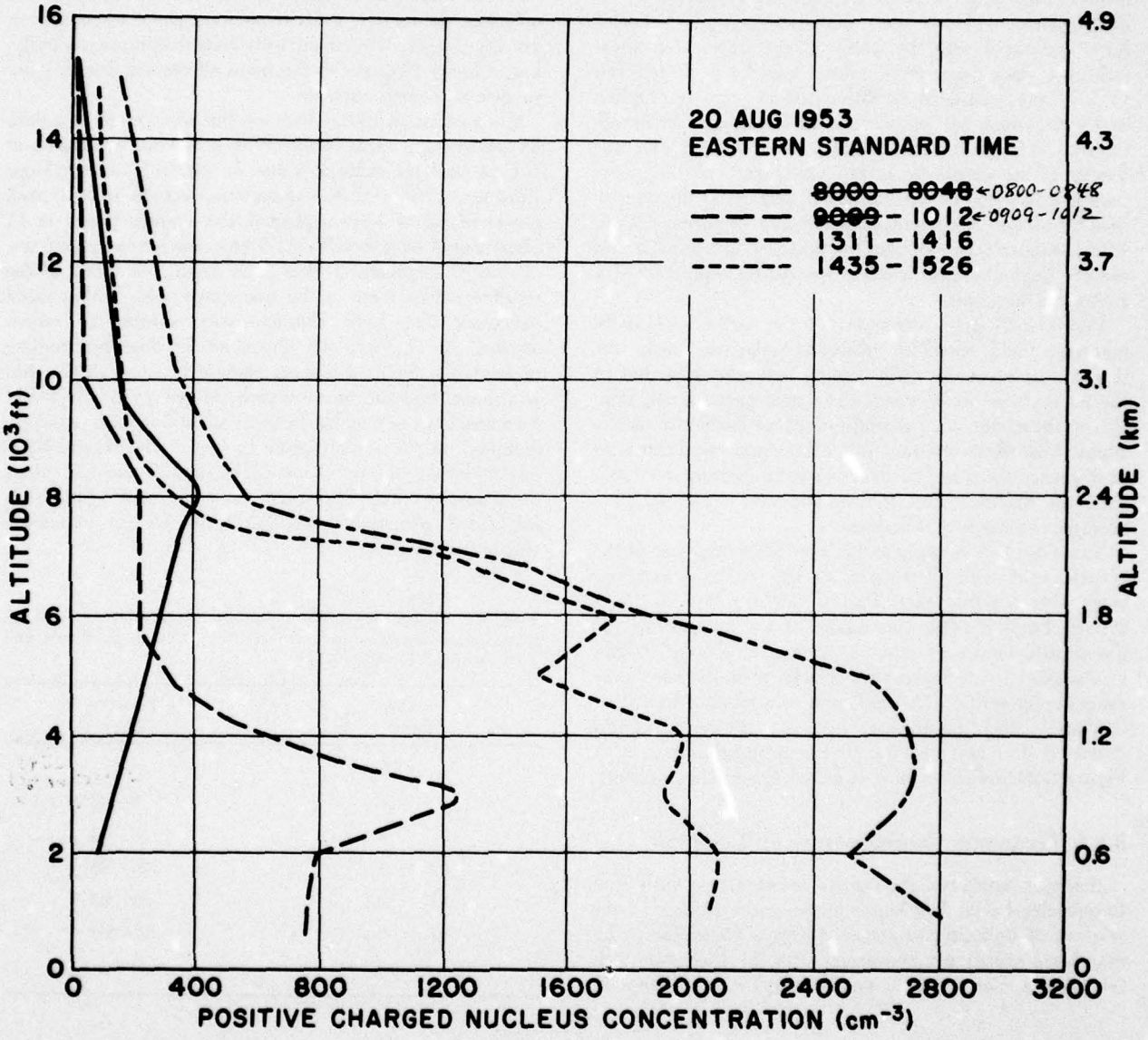


Fig. 8-11. Altitude and time variation of positive charged nucleus concentration during a period of low advection over southern New Hampshire. (From Sagalyn and Faucher [1956].)

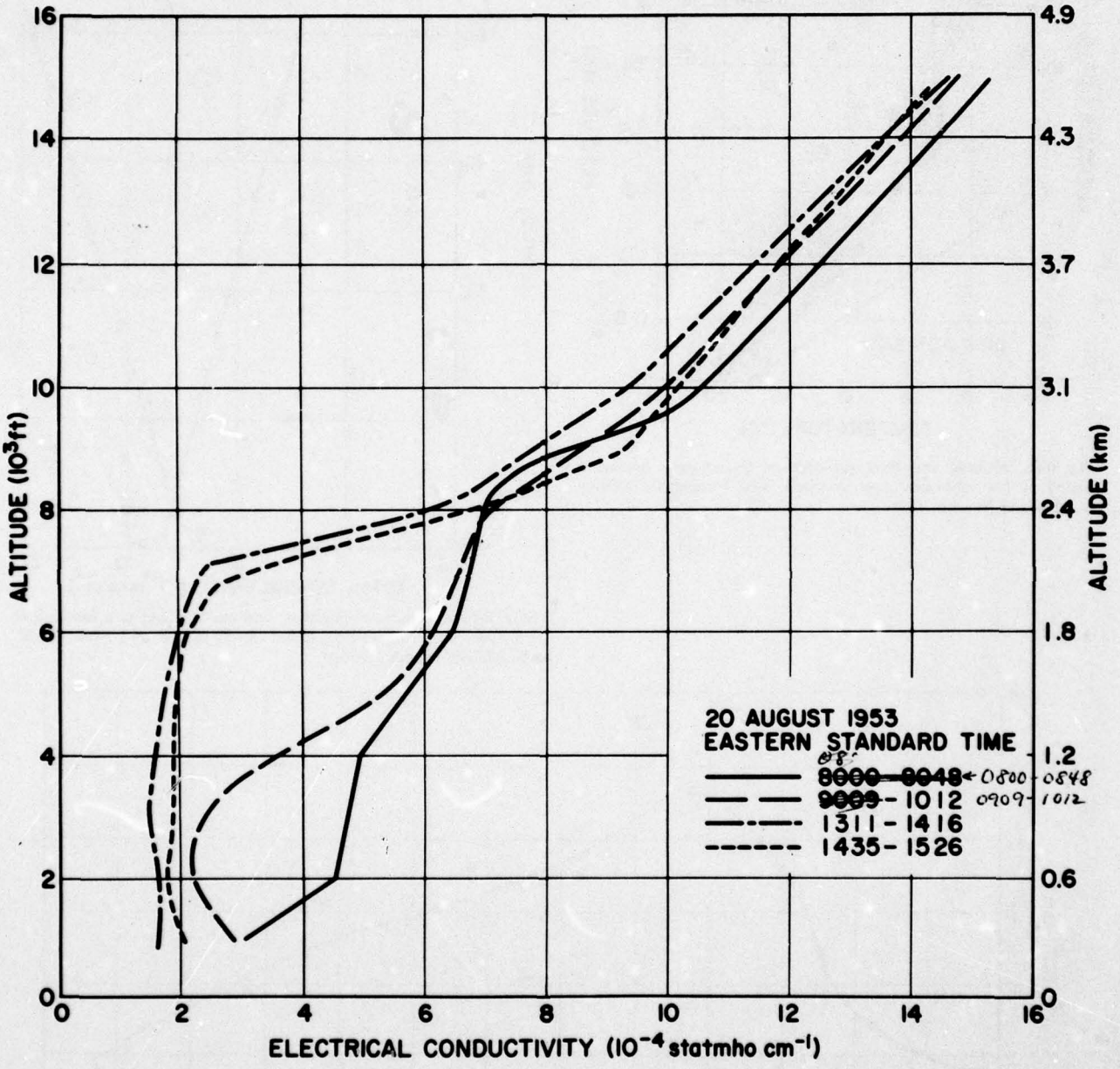


Fig. 8-12. Altitude and time variation of total volume conductivity during a period of low advection over southern New Hampshire. (From Sagalyn and Faucher [1956].)

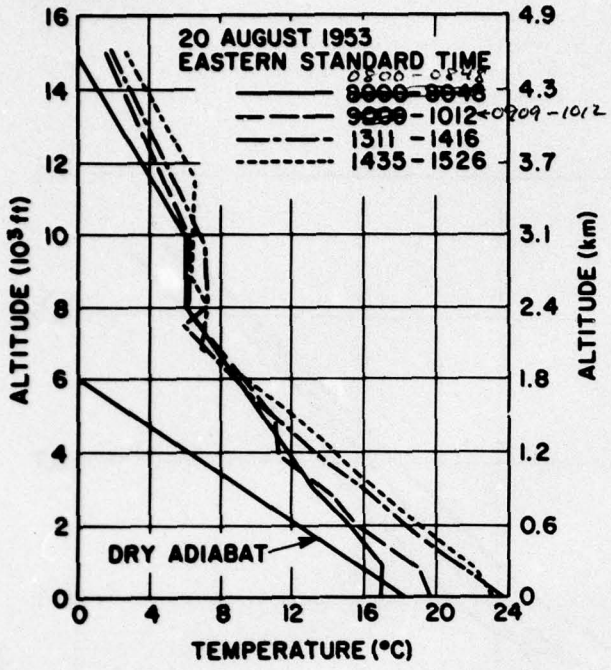


Fig. 8-13. Altitude and time variation of temperature during a period of low advection over southern New Hampshire. (From Sagalyn and Faucher [1956].)

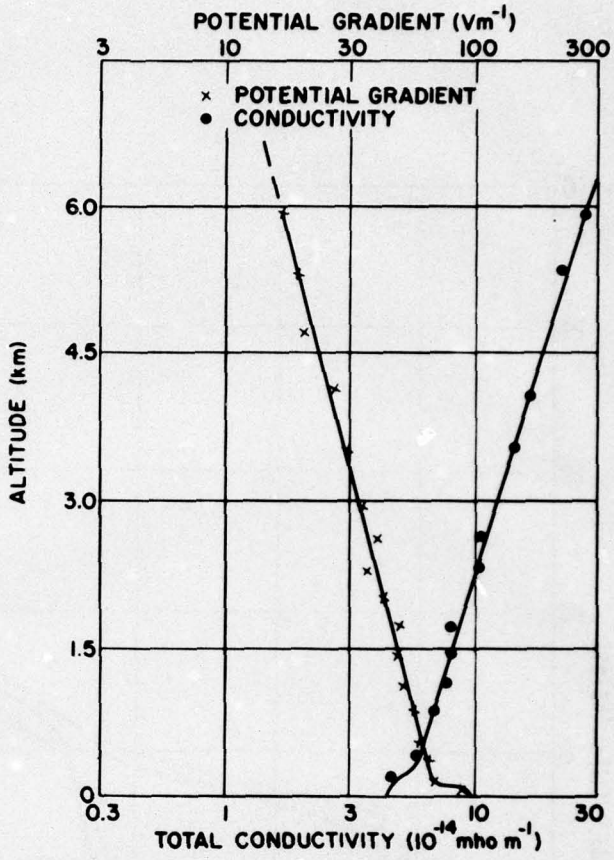


Fig. 8-15. Electrical conductivity and electric field as a function of altitude over Greenland. (After J. F. Clark and after J. M. Kraakevik [Smith, 1958].)

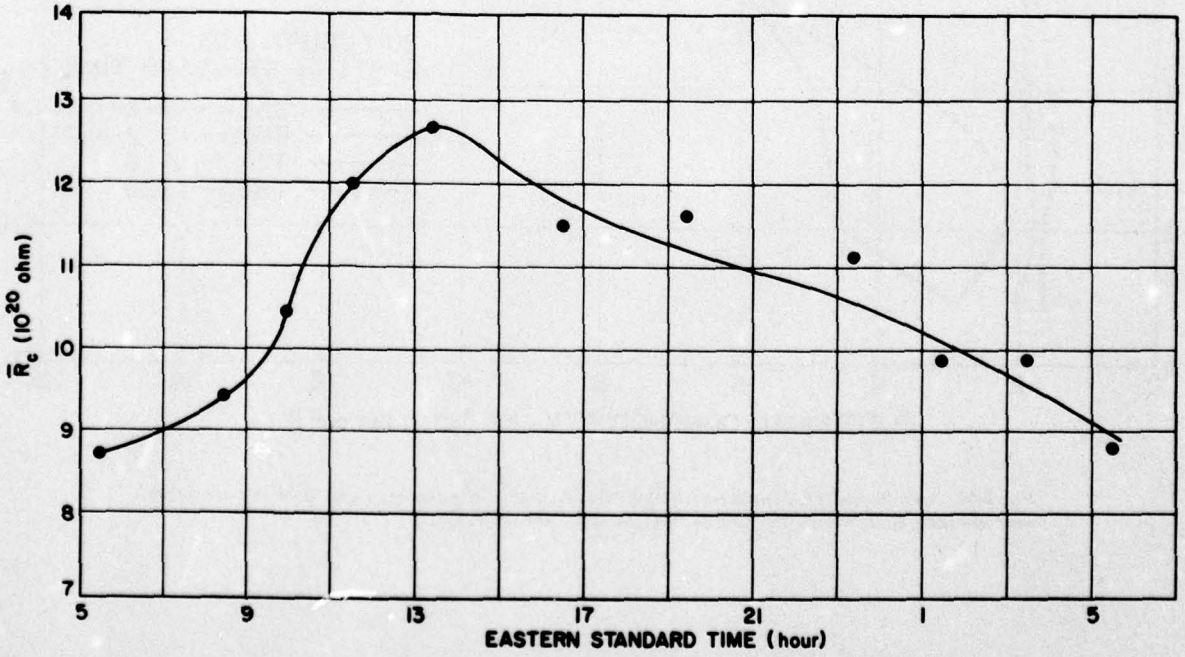
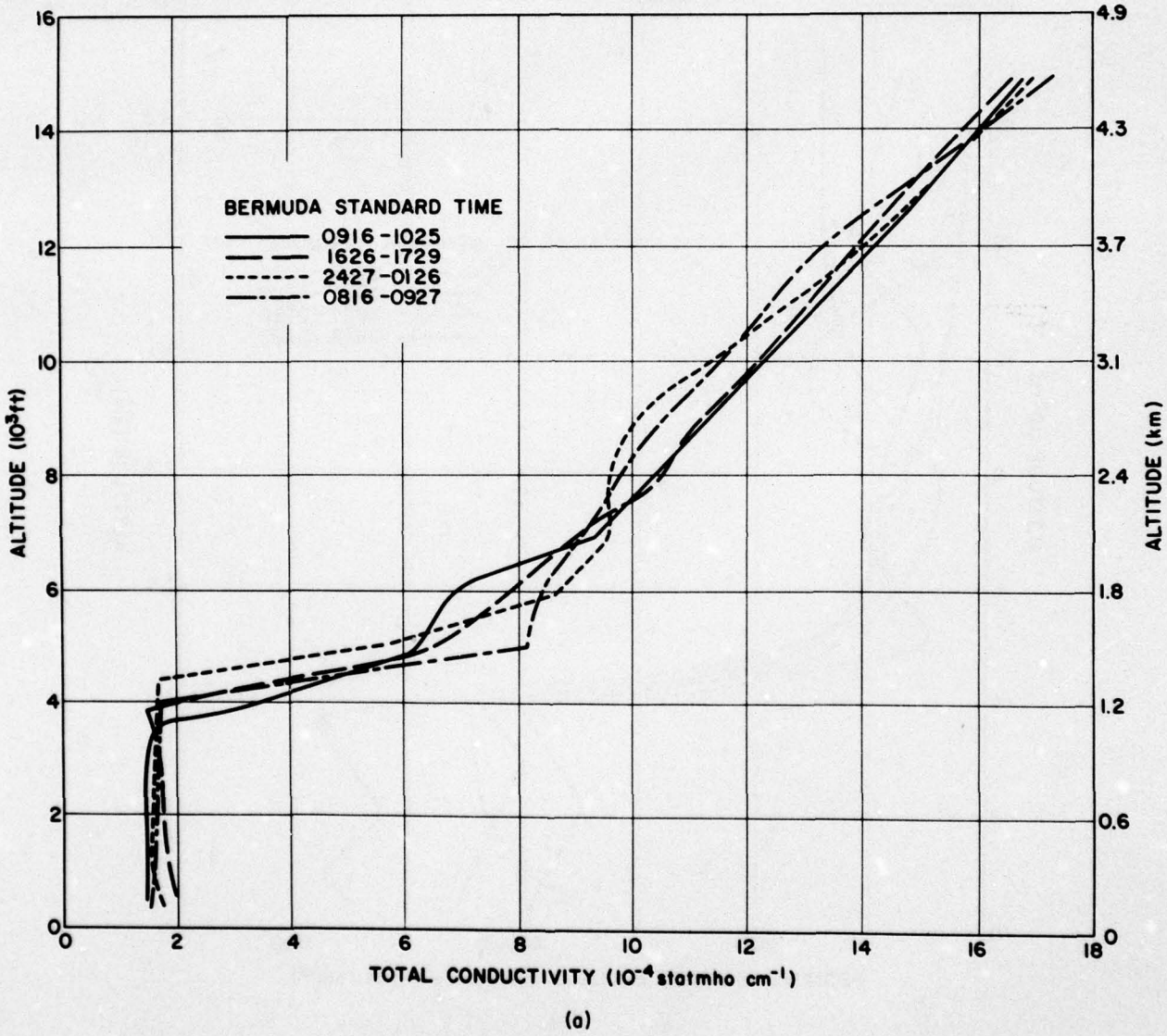
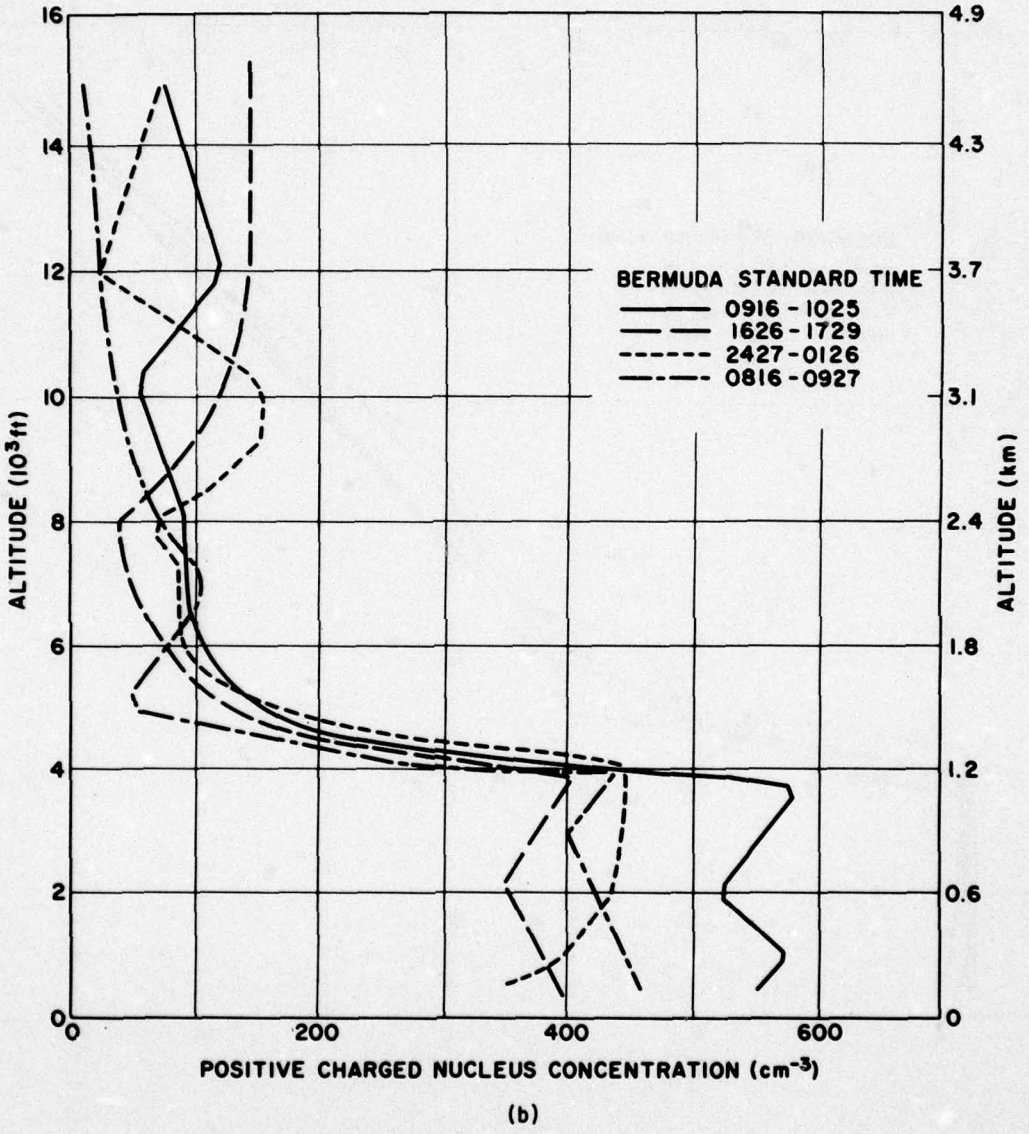


Fig. 8-14. Diurnal variation of average resistance of an air column, R_c, of 1-cm² cross section and 15,000-ft height. (From Sagalyn and Faucher [1956].)



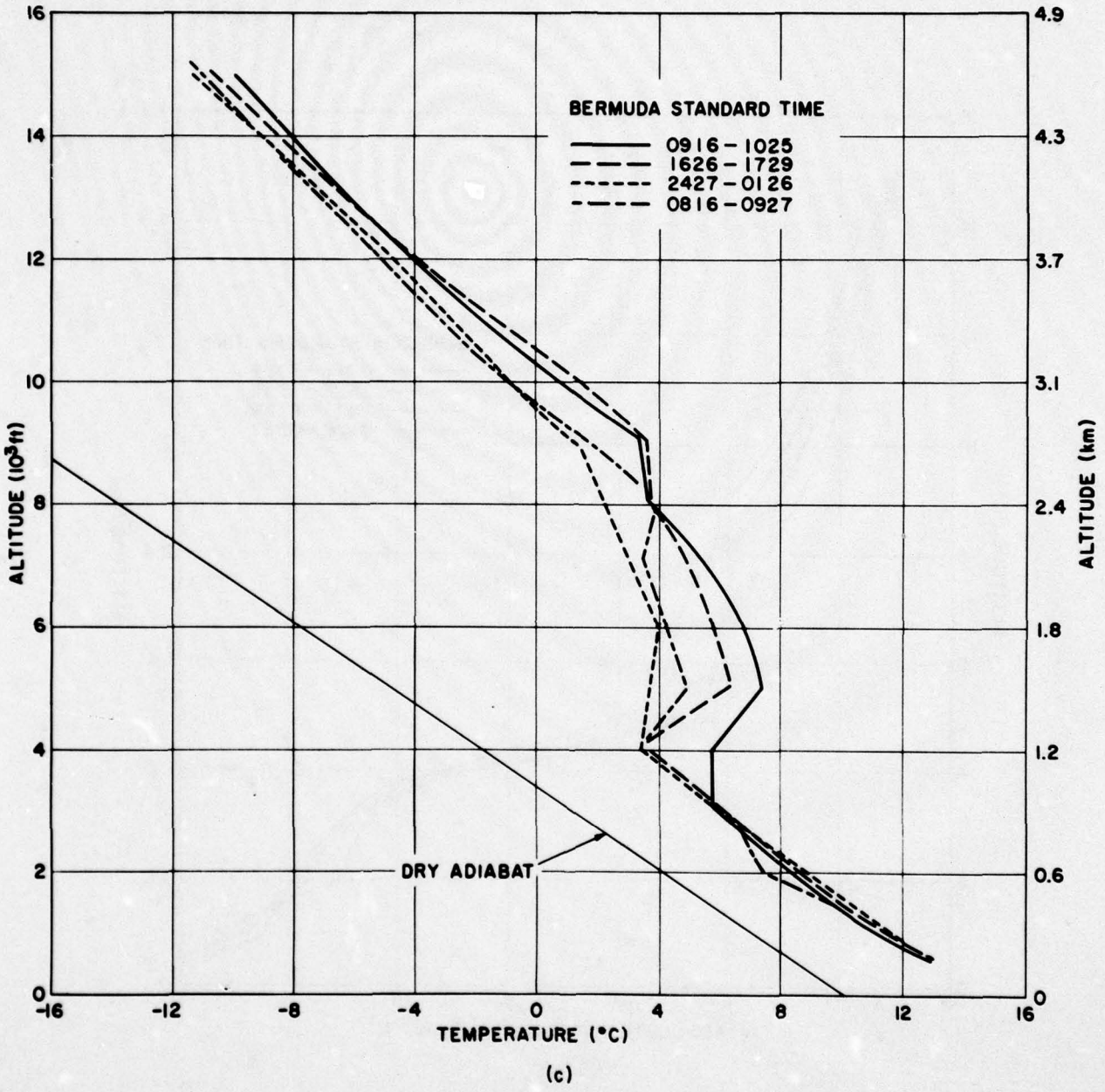
(a)

Fig. 8-16. Time variation of total electrical conductivity, positive charged nucleus concentration, temperature, and absolute humidity over the Atlantic Ocean at latitude 33°, longitude 64° on 13-14 April 1954. (From R. C. Sagalyn [Smith, 1958].)



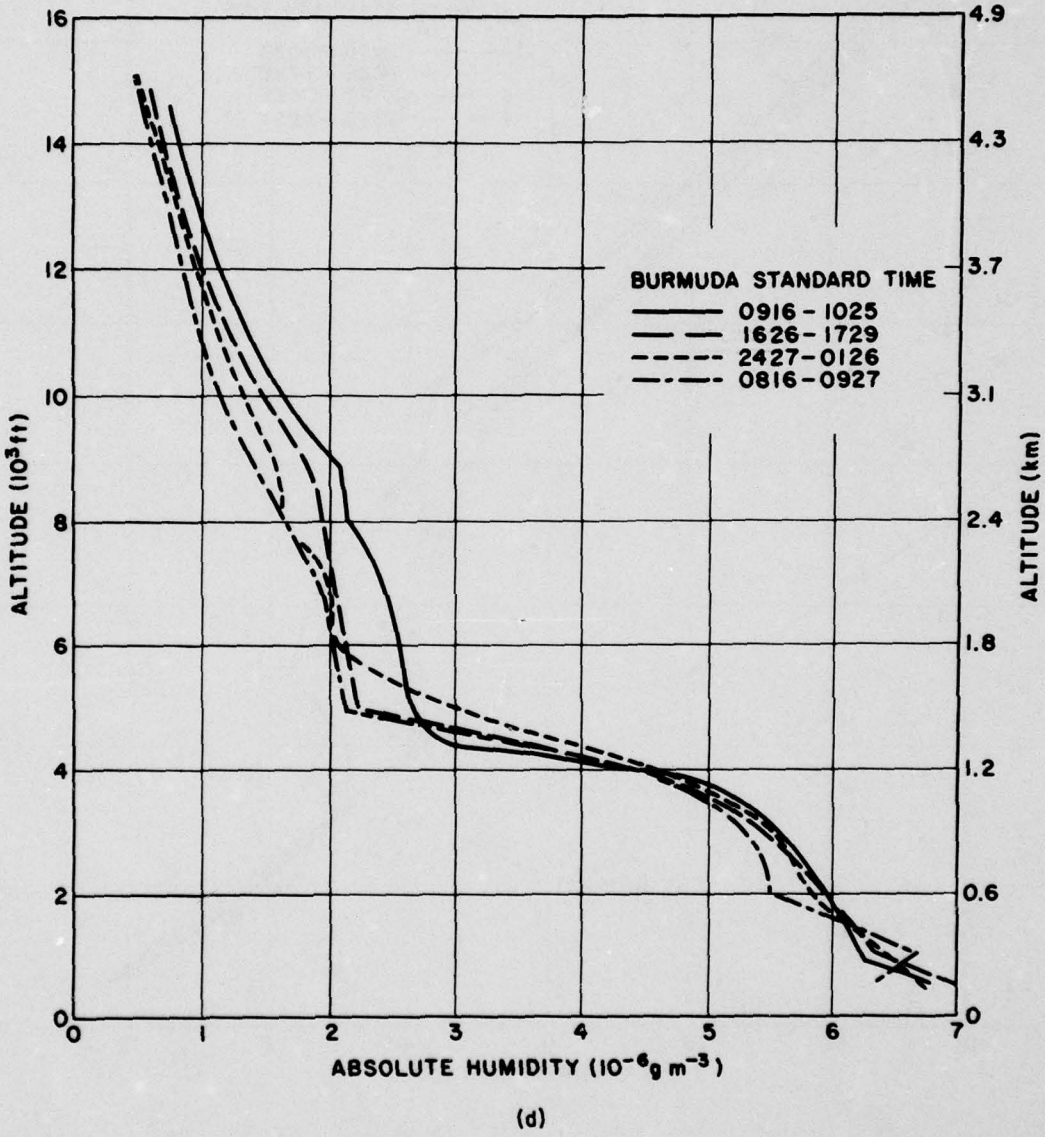
(b)

Fig. 8-16. Time variation of total electrical conductivity, positive charged nucleus concentration, temperature, and absolute humidity over the Atlantic Ocean at latitude 33°, longitude 64° on 13-14 April 1954. (From R. C. Sagalyn [Smith, 1958].)



(c)

Fig. 8-16. Time variation of total electrical conductivity, positive charged nucleus concentration, temperature, and absolute humidity over the Atlantic Ocean at latitude 33°, longitude 64° on 13-14 April 1954. (From R. C. Sagalyn [Smith, 1958].)



(d)

Fig. 8-16. Time variation of total electrical conductivity, positive charged nucleus concentration, temperature, and absolute humidity over the Atlantic Ocean at latitude 33°, longitude 64° on 13-14 April 1954. (From R. C. Sagalyn [Smith, 1958].)

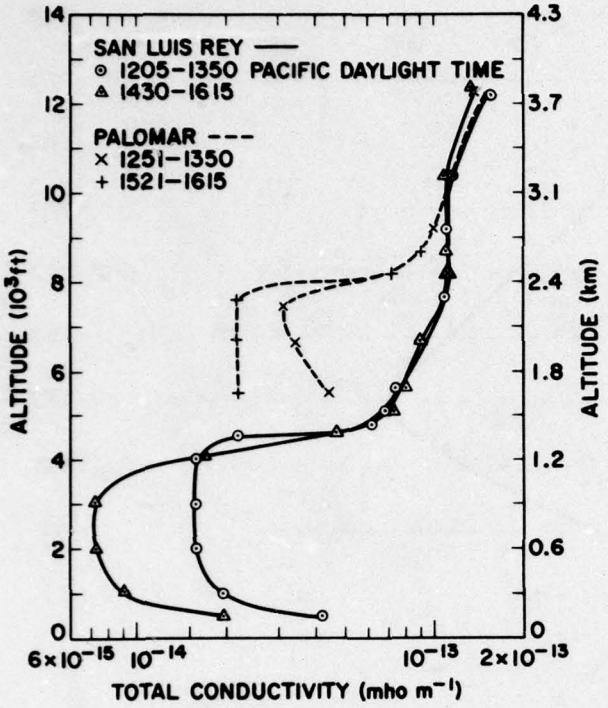


Fig. 8-17. Electrical conductivity vs altitude over San Luis Rey station at 500 ft and Palomar station at 5500 ft on 8 June 1953.

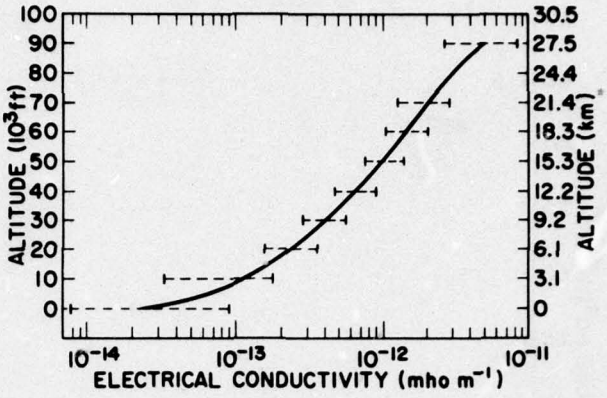


Fig. 8-18. Average value and limits of variation of electrical conductivity observed in the geomagnetic latitude range 33° to 65°N. (Compiled from Callahan et al [1951]), Hatakeyama [1963], Hess [1926], Kraakevik [1958], Sagalyn and Faucher [1954; 1956], and Stergis et al [1955].)

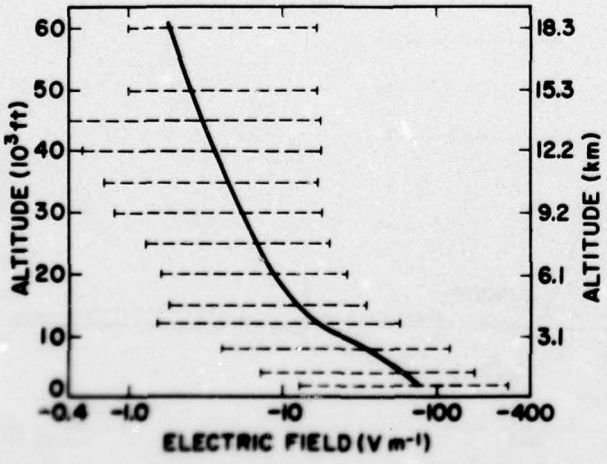


Fig. 8-19. Average value and limits of variation of observed electric field as a function of altitude. (Compiled from Clark [Smith, 1958], [illegible])

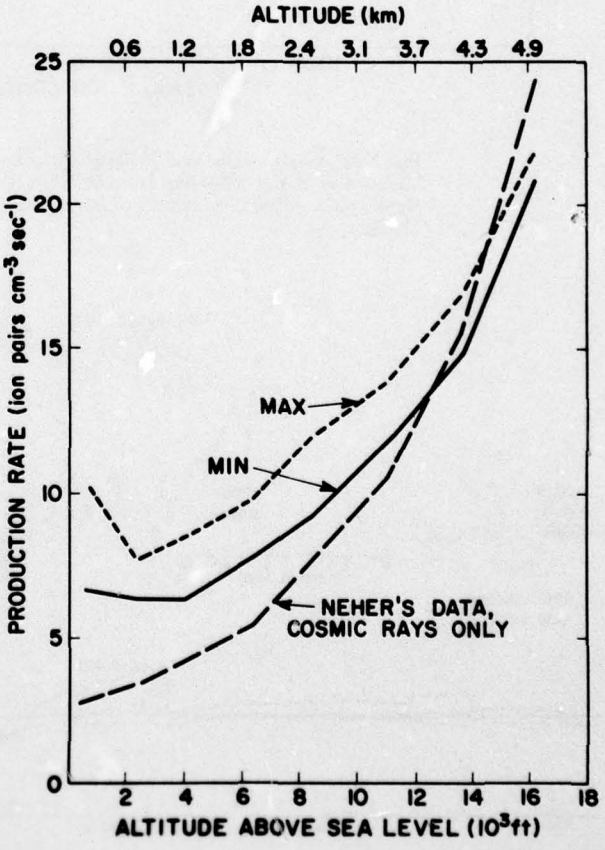


Fig. 8-21. Ion production rate as a function of altitude at geomagnetic latitude 50°N includes the ionization by cosmic rays and radioactive constituents of the atmosphere. (After E. Regener, *Naturwiss*, v. 25, p. 1, 1937; E. Regener and R. Auer, *Physikalische Zeitschrift*, v. 35, 1934.)

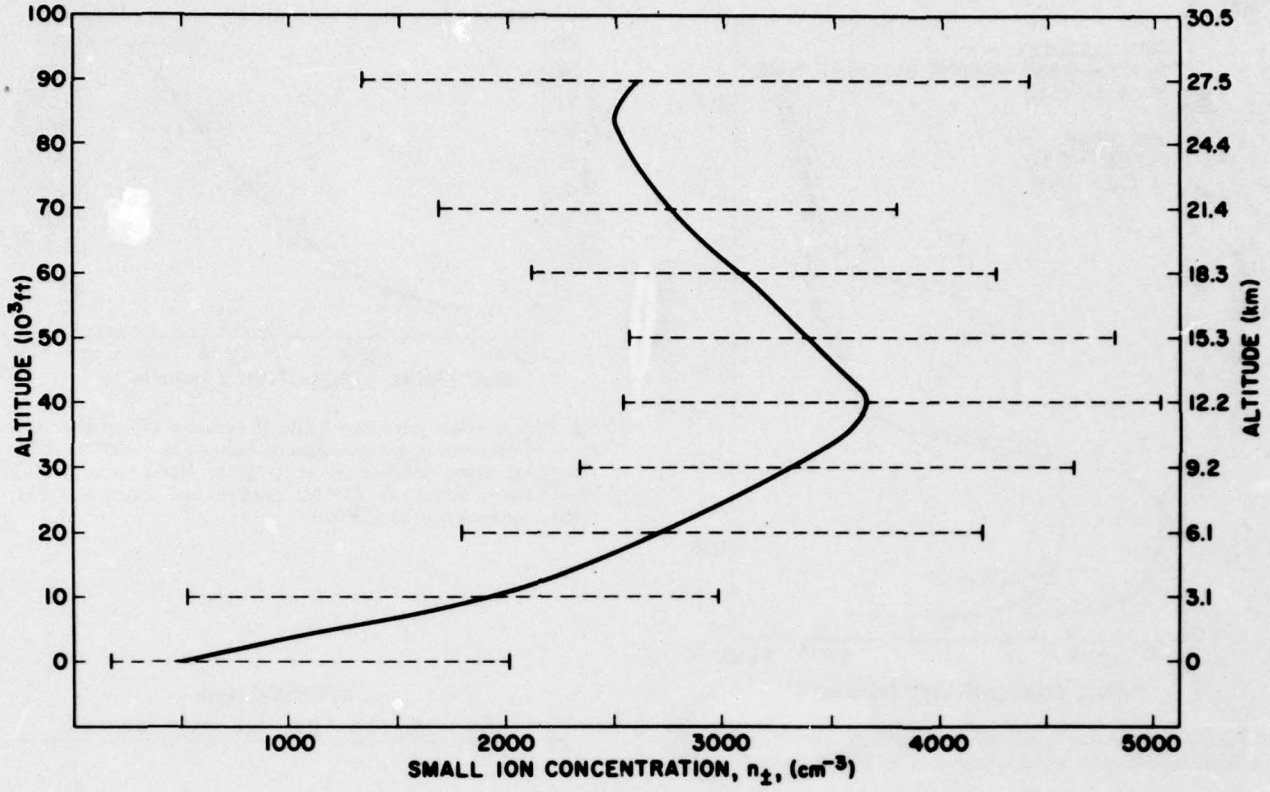


Fig. 8-20. Average value and limits of variation of small ion concentration as a function of altitude observed in the geomagnetic latitude range 33° to 65°N. (Compiled from Callahan et al [1951], Hatakeyama [1963], Kraakevik [1957], Sagalyn and Faucher [1954; 1956], and Stergis et al [1955].)

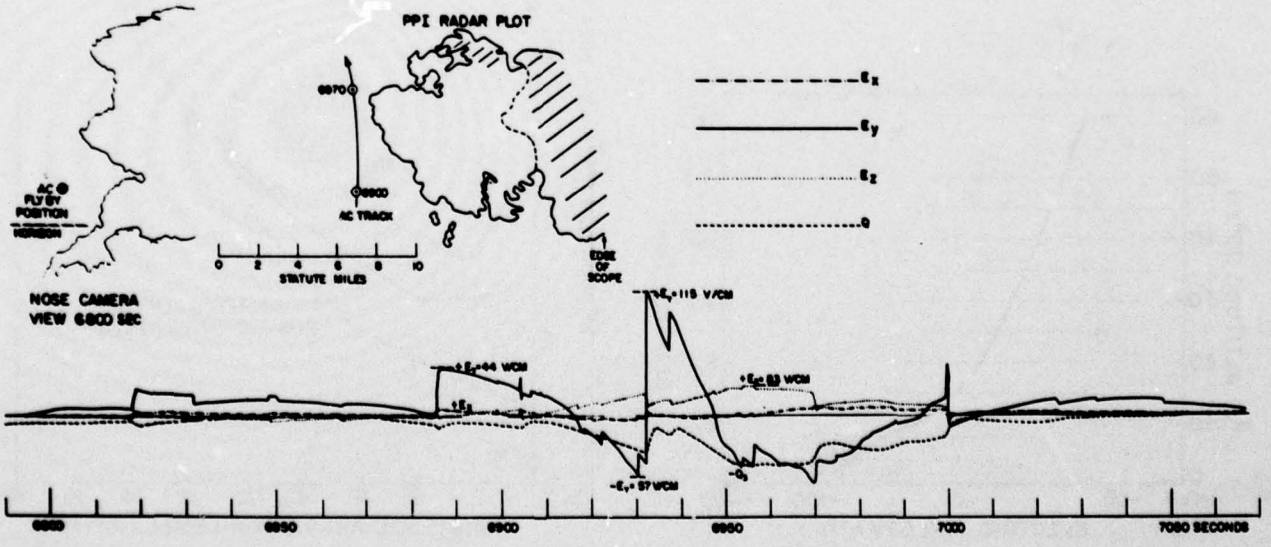


Fig. 8-23. Time variation of electric field components in relation to cloud visual outline (upper left) and Plan Position Indicator map of radar cloud horizontal cross section and aircraft flight track. Ez is vertical field component. Ex is component along direction of flight, and Ey is component along wing.

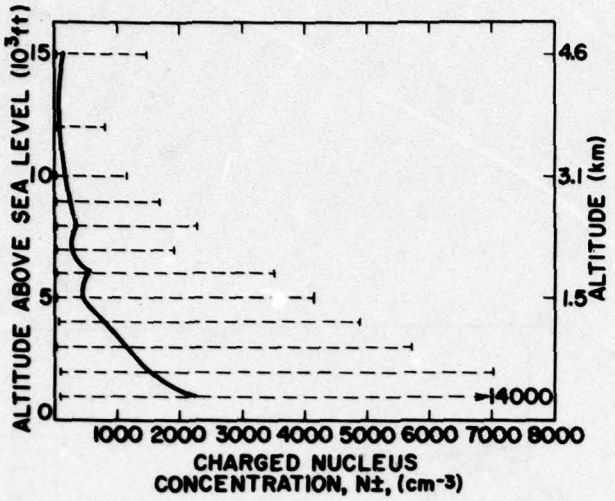


Fig. 8-22. Average value and limits of variation of positive or negative charged nucleus concentration as a function of altitude observed in the geomagnetic latitude range 38° to 50°N. (Compiled from Sagalyn [Smith, 1958] and Sagalyn and Faucher [1954; 1956].)

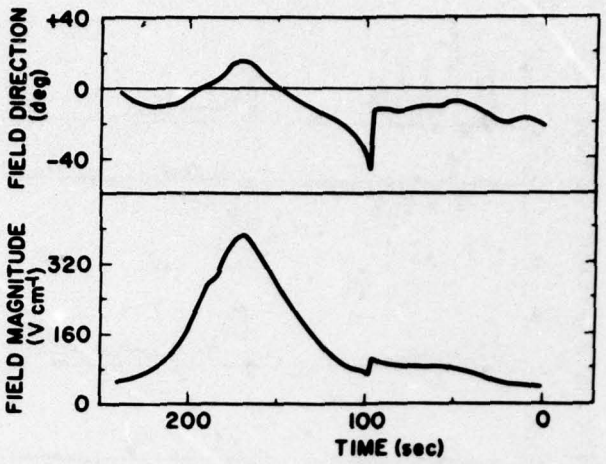


Fig. 8-24. Resultant of vertical and horizontal components of the electric field along a shaft of hail. Angular deviations are with respect to the horizontal plane flight level.

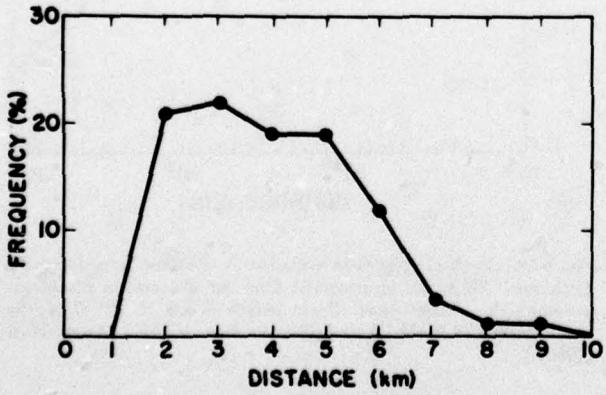


Fig. 8-25. Occurrence frequency vs distance of successive within-cloud discharges. (After Hatakeyama [Smith, 1958].)

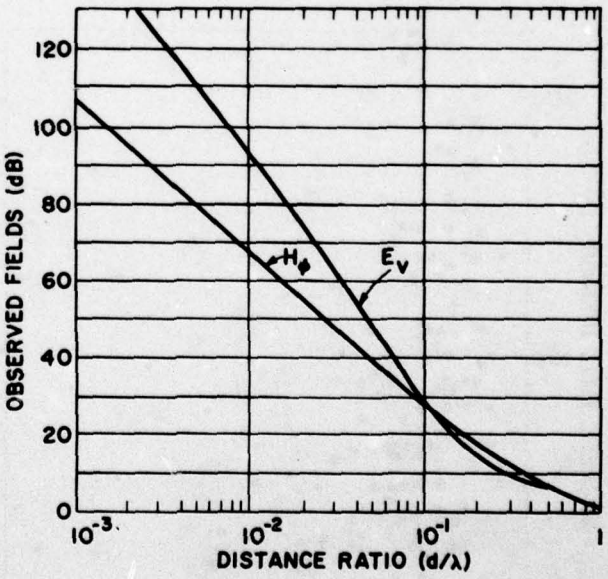


Fig. 8-26. Electric and magnetic fields vs ratio of distance (d) from an oscillatory dipole to the wavelength (λ). H is the magnetic field intensity and E_v the vertical electric field intensity. The ordinate is the ratio, in dB, of the field observed at d/λ to the radiated field at $d/\lambda = 1$. (From Watt [1960].)

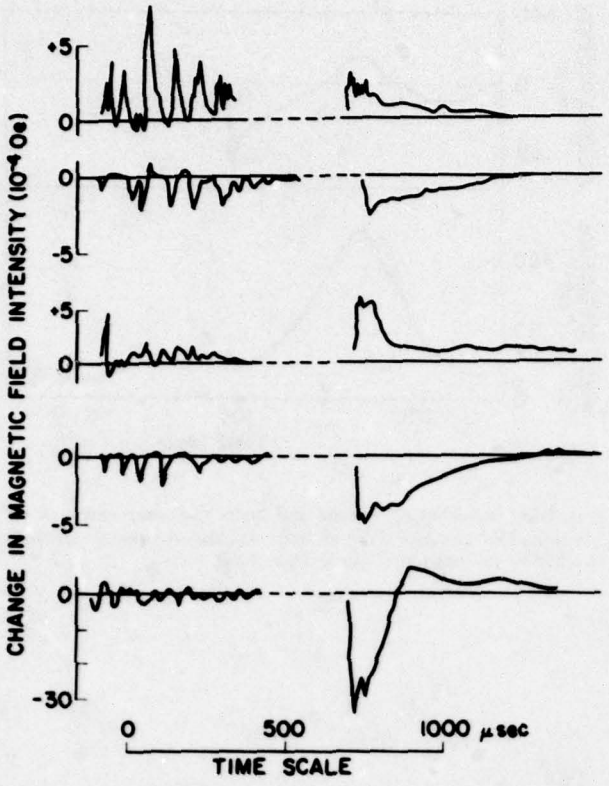


Fig. 8-27. Changes in the magnetic field intensity vs time; pre-discharge is left-hand curve and following stroke is right-hand curve. (From H. Norinder, *Technical Science Report No. 1*, Institute of High Tension Research, University of Uppsala, Sweden, AFCRL-TR-56-288, 1956.)

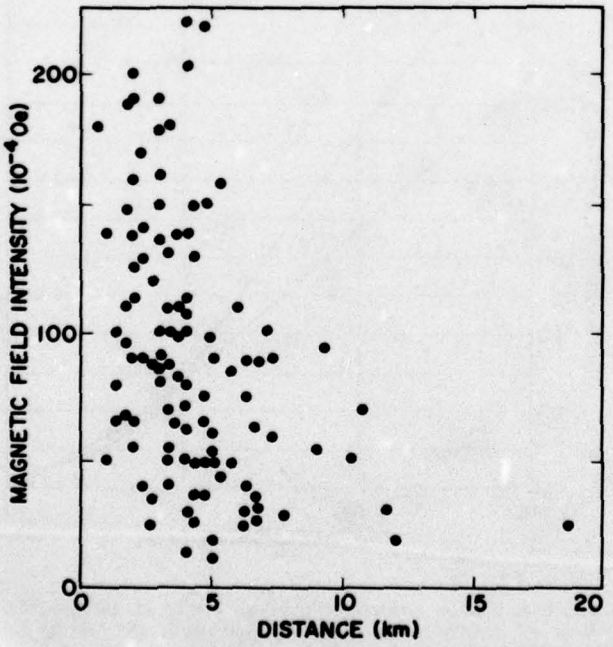


Fig. 8-28. Magnetic field intensity from lightning vs distance. (From H. Norinder, Arkiv for Geofysik, Band 2, Nr. 20, 1956.)

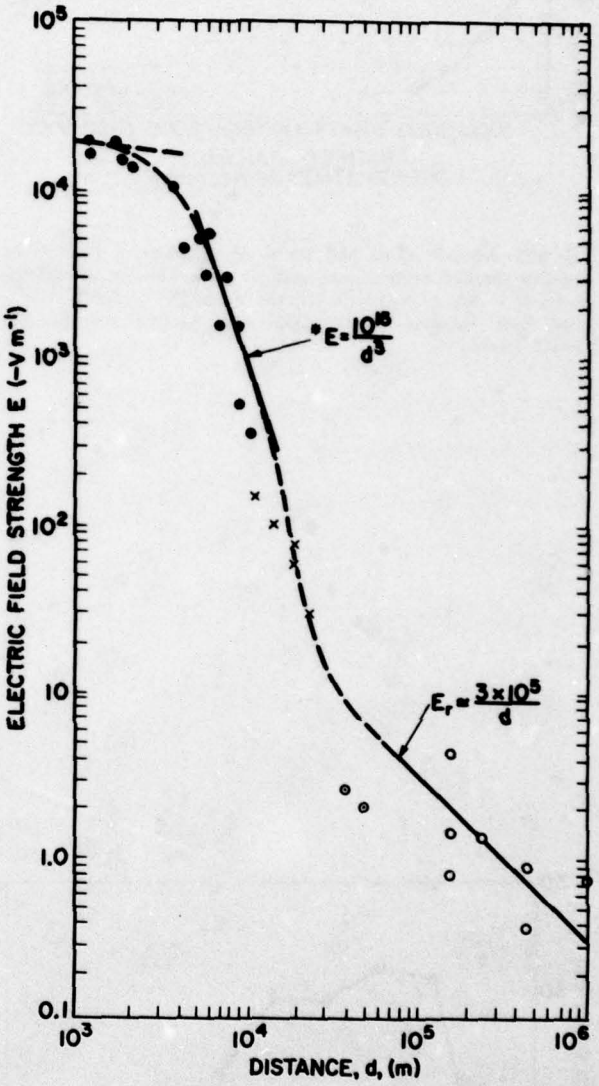


Fig. 8-29. Peak electric field variation vs distance from lightning discharges. *E is the electrostatic field for a complete discharge, assuming the charge times dipole length is 5.6×10^4 C m; E_r is the radiation field assuming a median stroke. (After Watt [1960].)

8.3 REFERENCES

Bowen, I. S., R. A. Millikan, and H. V. Neher, 1938, "New Light on the Nature and Origin of the Incoming Cosmic Rays," *Phys. Rev.*, v. 53, p. 855.

Bricard, P. J., 1949, "L'equilibre Ionique de la Basse Atmosphere," *J. Geophys. Res.*, v. 54, p. 39.

Brook, M., and N. Kitagawa, 1964, "Radiation from Lightning Discharges in the Frequency Range 400 to 1000 Mcps," *J. Geophys. Res.*, v. 69, p. 2431.

Brook, M., N. Kitagawa, and E. J. Workman, 1962, "Quantitative Study of Strokes and Continuing Currents in Lightning Discharges to Ground," *J. Geophys. Res.*, v. 67, p. 649.

Byers, H. R., ed., 1953, "Thunderstorm Electricity," University of Chicago Press, Chicago.

Callahan, R. C., S. C. Coroniti, A. J. Parziale, and R. Patten, 1951, "Electrical Conductivity of Air in the Troposphere," *J. Geophys. Res.*, v. 6, p. 545.

Couch, P. W., 1960, Precipitation Static on Modern Aircraft, "Electromagnetic Wave Propagation," M. Desirant and J. L. Michiels, ed., Academic Press, New York.

Griscom, S. B., 1958, "The Prestrike Theory and Other Effects in the Lightning Stroke," *Trans. Am. Inst. Elect. Engrs.*, III, v. 77.

Gunn, R., W. C. Hall, and G. D. Kinzer, 1946, "Army-Navy Precipitation Static Project," *Proc. Inst. Radio Engrs.*, v. 34, no. 4 and 5.

Hatakeyama, H., 1963, "Atmospheric Electricity Research in the Far East," *Proc. of the Third International Conference on Atmospheric and Space Electricity*, Montreaux.

Hess, V. F., 1926, "Die Electrische Leitfähigkeit der Atmosphäre und Ihre Ursachen," Verlag Vieweg, Braunschweig.

Horner, F., 1961, "Narrow-Band Atmospherics from Two Local Thunderstorms," *J. Atmos. Terrest. Phys.*, v. 21, no. 1.

Kitagawa, N., and M. Brook, 1960, "A Comparison of Intracloud and Cloud-to-Ground Lightning Discharges," *J. Geophys. Res.*, v. 65, no. 4.

Koenigsfeld, L., 1955, "Proceedings of Conference on Atmospheric Electricity," *Geophysical Research Paper No. 42*, AFCRL.

Kraakevik, J. H., 1958, "The Airborne Measurement of Atmospheric Conductivity," *J. Geophys. Res.*, v. 63, p. 161.

Mauchly, S. J., 1923, "On the Diurnal Variation of the Potential Gradient of Atmospheric Electricity," *Terrest. Magnetism Atmos. Elec.*, v. 28, p. 61.

Meese, A. D., and W. H. Evans, 1962, "Charge Transfer in the Lightning Stroke as Determined by the Magnetograph," *J. Franklin Inst.*, v. 273, no. 5.

Moore, C. B., B. Vonnegut, B. A. Stein, and H. J. Survilas, 1960, "Observations of Electrification and Lightning in Warm Clouds," *J. Geophys. Res.*, v. 65, no. 7.

Mühleisen, K., 1962, "Die Elektrische Spannung Zwischen Ionosphäre und Erde," Heinz-Jürgen Fischer.

Rossman, F., 1950, "Berichte des Deutschen Wetterdienstes in der U.S. Zone," no. 15, Bad Kissengen.

Sagalyn, R. C., and G. A. Faucher, 1956, "Space and Time Variations of Nuclei and Electrical Conductivity of the Atmosphere," *Quart. J. Royal Meteorol. Soc.*, v. 82, p. 428.

Sagalyn, R. C., and G. A. Faucher, 1954, "Aircraft Investigation of the Large Ion Content and Conductivity of the Atmosphere and Their Relation to Meteorological Factors," *J. Atmos. Terrest. Phys.*, v. 5, p. 253.

Schonland, B. F. J., 1956, The Lightning Discharge, "Encyclopedia of Physics," S. Flugge, ed., v. 22, Springe-Verlag, Berlin.

Smith, L. G., ed., 1958, "Recent Advances in Atmospheric Electricity," Pergamon Press, New York.

Stergis, C. G., G. C. Rein, and T. Kangas, 1957, "Electric Field Measurements in the Stratosphere" and "Electric Field Measurements above Thunderstorms," *J. Atmos. Terrest. Phys.*, v. 11, pp. 77 and 83.

Stergis, C. G., S. C. Coroniti, A. Nazarek, D. E. Kotas, D. W. Seymour, and J. V. Werne, 1955, "Conductivity Measurements in the Stratosphere," *J. Atmos. Terrest. Phys.*, v. 6, p. 233.

Uchikawa, K., 1961, "Atmospheric Electric Phenomena in the Upper Air over Japan (Part I and II)," *Geophys. Mag.*, v. 30, p. 617.

Venkiteshwaran, S. P., and A. Mani, 1962, "Measurement of Electrical Potential Gradient in the Free Atmosphere over Poona," *J. Atmos. Sci.*, v. 19, p. 226.

Wait, J. R., 1956, "On the Waveform of a Radio Atmospheric at Short Ranges," *Proc. Inst. Radio Engrs.*, v. 44, p. 1052.

Watt, A. D., 1960, "ELF Electric Fields from Thunderstorms," *J. Res. Natl. Bur. Standards*, v. 64D, p. 425.

Chapter 9

SOME ASPECTS OF ELECTROMAGNETIC WAVE PROPAGATION

David Atlas
R. M. Cunningham
R. J. Donaldson, Jr.
Gideon Kantor
Philip Newman

Aspects of electromagnetic wave propagation that are useful in meteorological and other geophysical investigations are discussed in this chapter. No attempt is made to give a comprehensive treatment of the propagation of radio waves. Communication aspects of propagation are beyond the scope of this Handbook.

9.1 REFRACTIVE MODULUS IN THE TROPOSPHERE

The velocity of propagation of electromagnetic radiation within the atmosphere varies with changes in atmospheric composition, pressure, and temperature. In the lower 50,000 feet of the atmosphere, the major contributor to variations in composition is water vapor. Pressure and temperature variations are principally functions of altitude. However, significant variations with time and horizontal distance do occur. From the standpoint of their effect on the velocity of propagation, temperature variations at any given altitude are more significant than pressure variations. At optical wavelengths, the velocity is strongly wavelength dependent but is not affected appreciably by water vapor. On the other hand, at radio wavelengths the velocity is not significantly wavelength dependent but is strongly affected by water vapor.

The phase refractive index, n, is the real part of the complex index of refraction (Sec. 9.3);

$$n = \frac{c}{v}, \tag{9-1}$$

where c is the velocity of propagation in vacuum and v, the phase velocity, is the velocity of propagation in a particular medium. In the troposphere, where the phase refractive index of the atmosphere is very nearly equal to one, it is convenient to define the quantity

$$N = (n - 1) \times 10^6. \tag{9-2}$$

N is called the *refractive modulus* and values are given in N-units.

9.1.1 Optical Wavelengths

An approximate relation between the optical refractive modulus and atmospheric pressure and temperature is

$$N_\infty = 77.6 \frac{P}{T}, \tag{9-3}$$

where N_∞ is the refractive modulus for wavelengths $>>$ 20 μ, P is atmospheric pressure in millibars, and T is atmospheric temperature in degrees Kelvin.

The dispersion formula of Edlen [1953] which has been adopted by the Joint Commission for Spectroscopy is

$$N_s = 64.328 + \frac{29498.10}{146 - 1/\lambda^2} + \frac{255.40}{41 - 1/\lambda^2}, \tag{9-4}$$

where N_s is the refractive modulus at a wavelength λ for a temperature of 288°K and a pressure of 1013.25 mb, and λ is the wavelength in microns. A somewhat less precise but more convenient dispersion formula is

$$N = N_\infty \left[1 + \frac{7.52 \times 10^{-3}}{\lambda^2}\right]. \tag{9-5}$$

Equations (9-3) and (9-5) may be combined to give the refractive modulus as a function of pressure, temperature, and wavelength;

$$N = \frac{77.6\,P}{T} + \frac{0.584\,P}{T\lambda^2}. \tag{9-6}$$

Refractive moduli calculated by using Eq. (9-6) will be in error no more than one N-unit. Figure 9-1 is a nomograph based on Eq. (9-6) that gives values of N accurate to about 5 N-units.

9.1.2 Radio Wavelengths

At radio wavelengths the relationship of refractive modulus to pressure, temperature, and water-vapor pressure may be given by:

$$N = \frac{77.6\,P}{T} + \frac{373000\,P_{wv}}{T^2}, \tag{9-7}$$

where P_{wv} is the partial pressure of water vapor in millibars. Figures 9-2 and 9-3 are nomographs based on Eq. (9-7); these give values accurate to within 5 N-units.

Within an accuracy of 1 part in 10^6, the tropospheric refractive index is independent of frequency for the longest radio wavelengths in use down to 1.25 cm. Absorption by atmospheric constituents begins to rise to significant proportion with decreasing wavelength beyond 1.25 cm. Water vapor content is by far the leading factor in causing changes in N, followed in order of importance by temperature, and pressure. For example, for a temperature of 15°C, pressure of 1013 mb near ground level, and a relative humidity of 60% ($P_{wv} = 10$ mb), the partial derivatives of N become: $\partial N/\partial P_{wv} = 4.5$ (N-units mb^{-1}); $\partial N/\partial T = -1.26$ (N-units $°K^{-1}$); and $\partial N/\partial P = 0.27$ (N-units mb^{-1}).

Under normal conditions, N tends to decrease exponentially with height, Z; an exponential decrease is usually an accurate description for heights greater than 10,000 ft. Below 10,000 ft, N may depart considerably from exponential behavior. The median value for the gradient dN/dZ is typically -0.012 N-units ft^{-1} for the first few thousand feet above ground level.

9.1.3 Standard Profiles of Refractive Modulus

For many purposes it is desirable to have standard refractive-modulus profiles for the atmosphere. By using the equations of the model atmosphere (Chapter 2), an exact analytical expression for the standard optical refractive modulus can be derived. A simplified approximation to this is

$$N_\infty = 273 \exp(-Z/32.2), \quad (Z \leq 25); \qquad (9\text{-}8)$$

Z is the altitude in thousands of feet.

Equation (9-8) can be differentiated to obtain the standard gradient of optical refractive modulus;

$$\frac{dN_\infty}{dZ} = -8.48 \exp(-Z/32.2), \quad (Z \leq 25). \qquad (9\text{-}9)$$

Equations (9-8) and (9-9) may be corrected for dispersion through use of Eq. (9-5).

For the radio wavelengths it is necessary to assume a distribution of water vapor in order to obtain an expression for the refractive modulus. Assuming $P_{wv} = 10.2 (1 - 0.0195 Z)^6$, for $Z \leq 25$, a simplified approximation is

$$N = 316 \exp(-Z/26.5), \quad (Z \leq 25). \qquad (9\text{-}10)$$

The standard gradient of radio-wave refractive modulus is then:

$$\frac{dN}{dZ} = -11.9 \exp(-Z/26.5), \quad (Z \leq 25). \qquad (9\text{-}11)$$

Figures 9-4 and 9-5 are graphs of standard profiles calculated from Eq. (9-9) through (9-11).

9.1.4 Variations of Refractive Moduli

Actual profiles may differ markedly from the standard profiles. Figures 13-6 through 13-9 show some profiles of refractive modulus at microwave frequencies calculated from radiosonde measurements. These are considered typical for the air masses indicated. Average deviations from a model atmosphere refractive index have been studied extensively; for example, see Bean and Thayer [1959].

Cumulus clouds are evidence of the existence of a very inhomogeneous atmosphere. Figure 9-10 shows some measurements of refractive modulus and associated parameters within a fair-weather cumulus cloud. The time response of the instruments from which refractive modulus, temperature, and water-vapor pressure were obtained was such that changes occurring in distances as small as 5 ft could be measured. However, the instrument for measuring liquid water content was much slower responding. Figure 9-11 shows a composite cloud which summarizes data from 30 cloud passes.

Figure 9-12 shows the average ΔN cloud to clear air to be expected in various parts of the United States at the midseason months. The chances of having cumulus clouds at 1500 h local time for these months is also shown. Additional climatological data on ΔN and cumulus clouds is given by Cunningham [1962].

When N decreases with height inside a specific layer much faster than it does above and below the layer, the layer is said to be super-refracting for propagation. One cause of this is temperature inversion (Sec. 3.1.5), often one of only a few degrees in altitude intervals typically of from 50 to a few hundred feet. The temperature change itself may contribute only a small change of a few N-units. However, an inversion usually indicates the presence of a humid air mass under a dry one. The transition from humid to dry air causes a marked change of N in the super-refracting layer, typically of 20 to 50 N-units; changes as pronounced as 80 N-units have been measured. Super-refracting layers may be clear-weather phenomena, or can be accompanied by haze (aerosols) in the lower air mass. Invariably they signify stable weather situations, such as occur when a high pressure center stagnates in an area.

The horizontal and temporal extent of super-refractive layers varies widely. In New England it may be only a few tens of miles. In midwestern states, the layers extend farther and may last from a half hour up to a week. In the trade-wind zones of the world, the climatic regime (manifested by steady wind directions and speeds throughout most of the year) sustains super-refracting layers which extend a few thousand miles both east to west and north to south.

9.2 ATTENUATION AND BACKSCATTERING IN THE TROPOSPHERE

At radio wavelengths $\lambda > 30$ cm, atmospheric absorption and scattering may be considered negligible within the lower atmosphere. In this section, the microwave re-

gion where attenuation is important is discussed. Attenuation at optical wavelengths is discussed in Chapters 7 and 10.

Scattering and attenuation are in general complicated functions of particle size and dielectric properties. The square root of the dielectric constant, m, is

$$\sqrt{m} \equiv n - i\kappa, \tag{9-12}$$

where n is the phase refractive index and κ the absorption index of the medium. Both n and κ depend on the wavelength of the electromagnetic radiation and on the temperature and other characteristics of the medium.

9.2.1 Dielectric Properties

It is convenient to use the parameter K, defined by

$$K \equiv \frac{m-1}{m+2}, \tag{9-13}$$

in describing the dielectric properties of the troposphere; the imaginary part of minus K is written as Im (—K). When the wavelength is long in comparison with the size of the particles (Rayleigh approximation), the backscatter and absorption are relatively simple functions of K. In this special case, backscatter is proportional to $|K|^2$, and attenuation is proportional to Im (—K).

Table 9-1 gives values of n, κ, $|K|^2$ and Im (—K) for water at several temperatures and wavelengths. For ice, the values are practically independent of wavelength in the centimeter band; n and $|K|^2$ are also constant over the temperature range 0 to —20°C. Table 9-2 lists these values and κ and Im (—K) for ice at 0, —10, and —20°C.

Snow is a special case; it may be considered as a mixture of two dielectrics, ice and air. The ratio of K to the mass density, ρ, for a mixture of two dielectrics can be calculated by adding the K/ρ values for the two substances in proportion to the mass of each. The contribution of K/ρ for air may be neglected, so that K/ρ for ice of any density is practically constant. Actual measurements of snow of various densities show that K/ρ varies more or less uniformly from 0.46 for ice of density 0.917 g cm^{-3} (normal ice density, no air spaces) to 0.50 for snow of density 0.22 g cm^{-3}. It follows that $|K|^2$ for normal ice density is 0.176.

9.2.2 Backscattering and Attenuation Cross Sections

The echo power returned by a scattering particle is proportional to its backscattering cross section, σ. The power removed by an attenuating particle is proportional

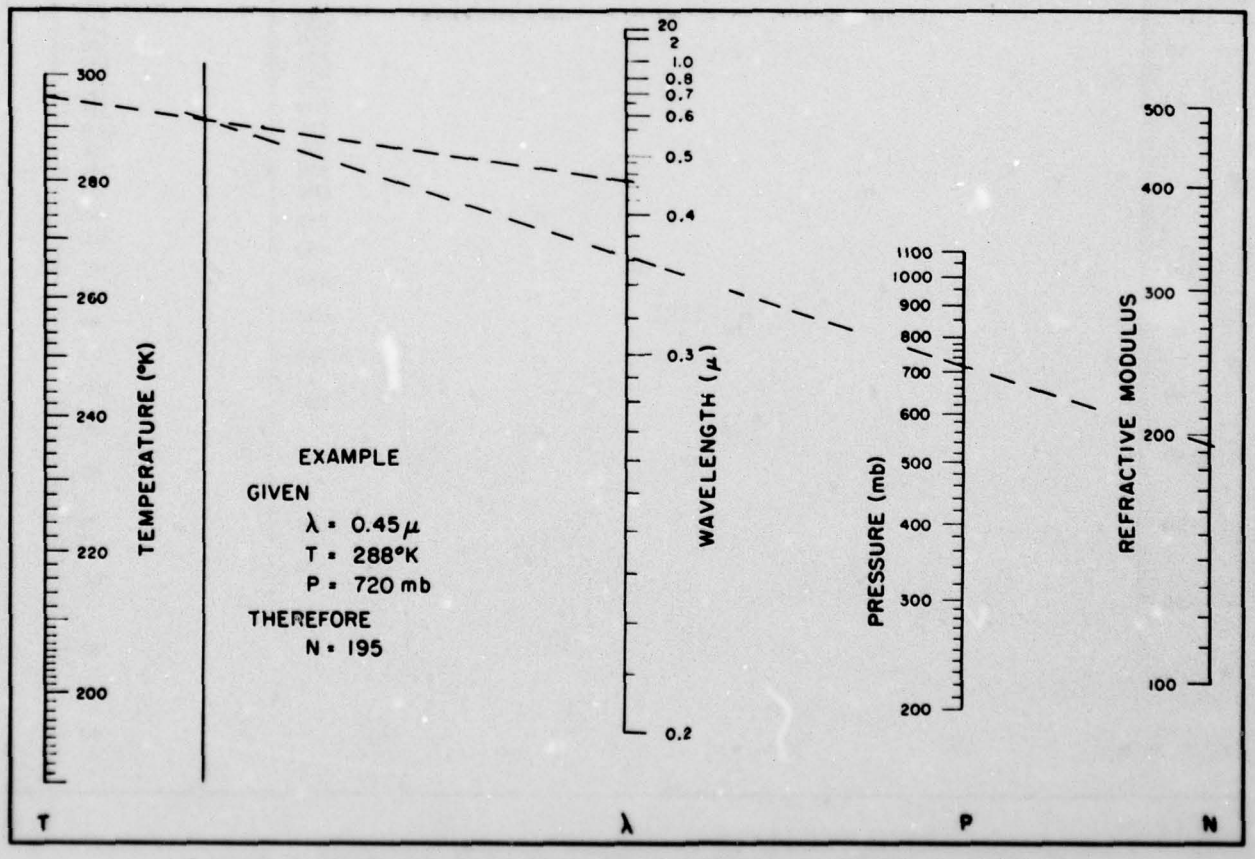


Fig. 9-1. Nomograph for computing refractive modulus at optical wavelengths.

to the total absorption cross section, Q_t. When the scattering or attenuating particle has a diameter D that is small with respect to the wavelength λ of the incident radiation so that $\pi D/\lambda < 0.1$, the backscattering and total absorption cross sections are simple functions of the particle size and dielectric characteristics and may be expressed with sufficient accuracy by the Rayleigh approximations. In this case, for spherical particles,

$$\sigma = \frac{\pi^5 |K|^2 D^6}{\lambda^4} \quad [cm^2], \tag{9-14}$$

and

$$Q_t = \frac{\pi^2 D^3}{\lambda} \text{ Im } (-K) + \frac{2}{3}\sigma \quad [cm^2]. \tag{9-15}$$

The first term in Eq. (9-15) represents the energy loss by absorption and internal dissipation as heat, Q_a; the second term represents the energy loss by scatter in all directions, Q_s. In a lossy dielectric such as liquid water, $Q_s << Q_a$, so that attenuation in the Rayleigh region is given by only the first term in Eq. (9-15). For ice, however, Q_a becomes comparable with Q_s.

Figure 9-13 illustrates the limit of usefulness of the Rayleigh approximations. The ratio of the exact (Mie) solution of the total absorption cross section to the Rayleigh approximation, Q_t (Mie)/Q_t (Rayleigh), is plotted for several wavelengths in the millimeter and centimeter range as a function of the electrical size, $\pi D/\lambda$. The lower part of the diagram is a similar plot of the ratio of the exact to the approximate value of the backscattering cross section. The Rayleigh approximations depart seriously from the exact solutions when $\pi D/\lambda$ exceeds about 0.1 for Q_t and about 0.2 for σ. Thus the Rayleigh approximations are good for cloud particles and all the wavelengths presented on the diagrams. For rain, the Rayleigh approximations are inaccurate except for moderate-size raindrops at 10-cm wavelength and very small drops (no larger than 1 mm) at 3-cm wavelength.

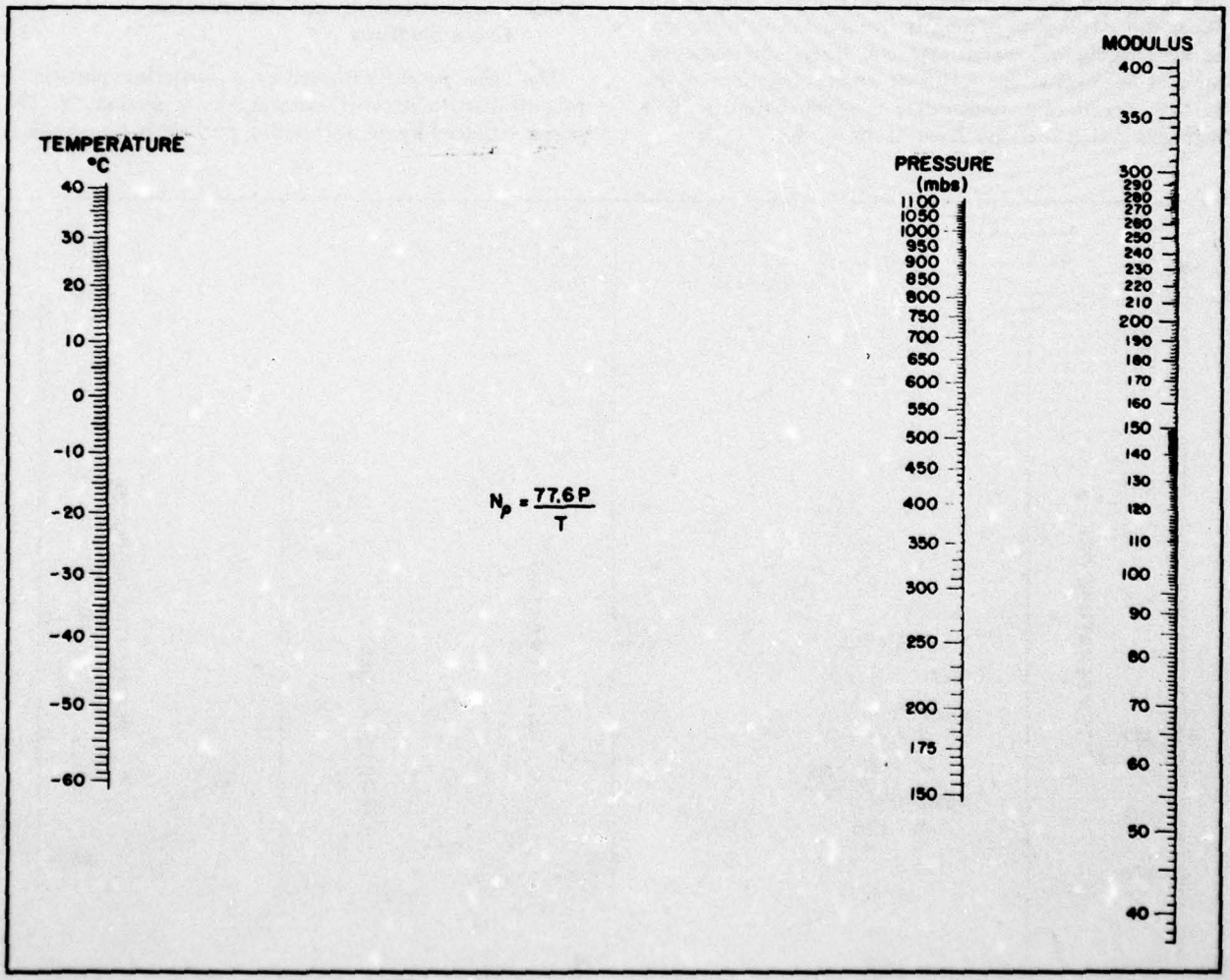


Fig. 9-2. Nomograph for computing contribution to microwave refractive modulus to density of atmospheric gas.

For particles with $D > 0.06\,\lambda$, σ must be computed from the exact Mie equations. Figure 9-14 shows computed normalized cross sections ($4\,\sigma/\pi\,D^2$) versus electrical size for water at 0°C and 3.2-cm wavelength, and for ice in the Mie region. The normalized ice curve is invariant with wavelength in the microwave region because the refractive index of ice is independent of wavelength; however, the 3.2-cm curve in Figure 9-14 is accurate within 9% for all wavelengths between 3 and 10 cm. Experimental measurements [Atlas et al, 1960] show that ice spheres equal to or larger than the wavelength may scatter more than an order of magnitude better than water spheres of the same size.

For water-coated ice with $\pi\,D/\lambda = 0.126$ (near the limit of the Rayleigh region), a water thickness of about one-tenth of the total radius of the sphere will increase σ to about 90% of an all-water sphere. With even a thinner water coating, Q_t rises very rapidly from the low ice-value to a maximum of about twice the water value, and then gradually decreases to the water value as the water coating increases. For $\pi\,D/\lambda = 0.419$, σ rises more slowly, and Q_t does not have such a striking maximum, as the water coating increases. In the case of large ice spheres ($\pi\,D/\lambda > 2.5$), which have a greater backscattering cross section than water spheres of the same mass, a thin water coat might be expected to reduce σ toward the water value. Experiments show that wetting of large ice spheres ($D > 0.8\,\lambda$) causes their cross sections to fall rapidly at 3.3 cm and more slowly at 4.67 cm; the maximum thickness of water coat which could be maintained on a stationary melting hailstone was 10^{-2} cm. Figure 9-15 gives the computed values for ice spheres with 0.01-cm water coat at wavelengths of 3.21 and 4.67 cm.

When $\pi\,D/\lambda$ is approximately greater than 0.1, Q_t must also be computed from the exact Mie equations. Figure 9-16 presents curves of $4\,Q_t/\pi\,D^2$ (the normalized total attenuation cross section) for water at 0°C at several wavelengths. Figure 9-17 shows $4\,Q_t/\pi\,D^2$ for ice.

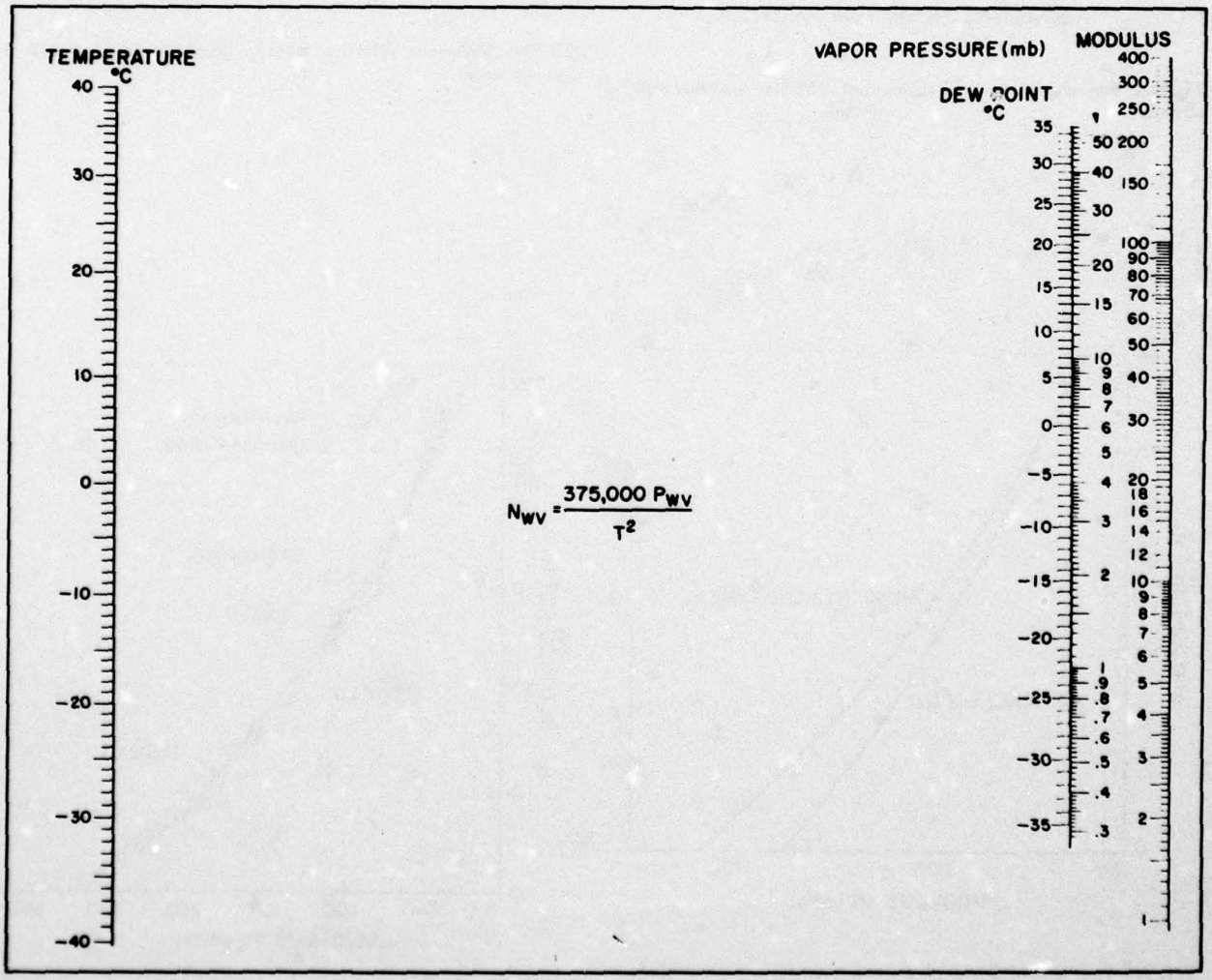


Fig. 9-3. Nomograph for computing contribution to microwave refractive modulus due to water vapor.

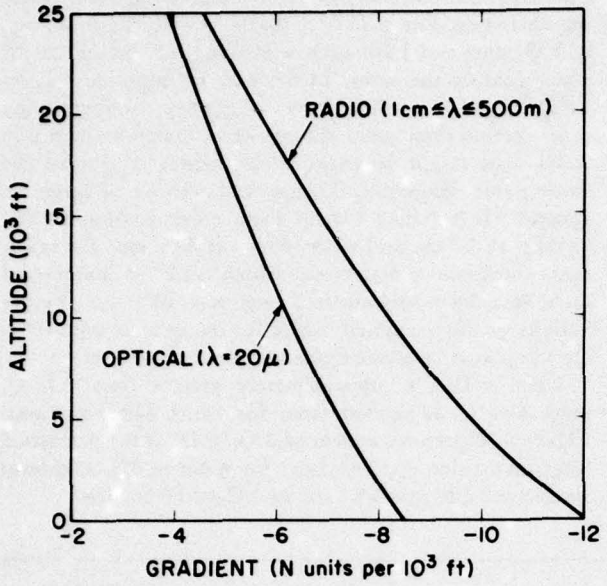


Fig. 9-4. Variation of standard gradient of refractive modulus with altitude.

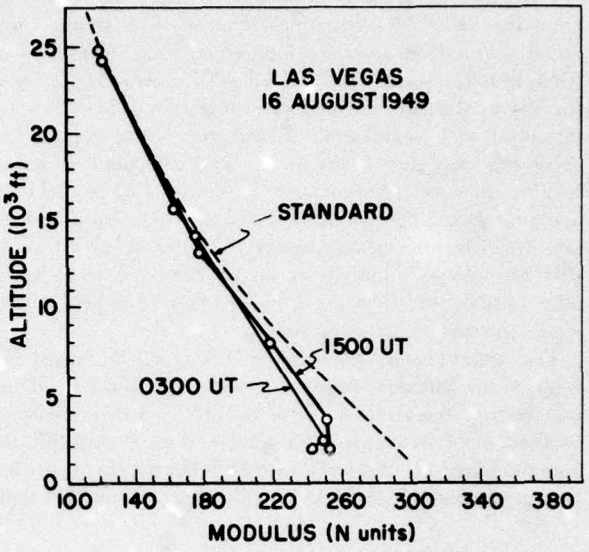


Fig. 9-6. Microwave refractive modulus profile in continental tropical air mass.

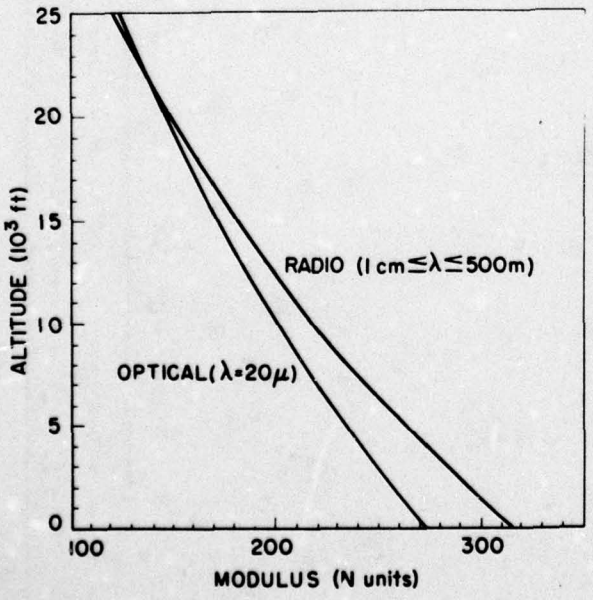


Fig. 9-5. Variation of standard refractive modulus with altitude. Curve for radio wavelengths should approach as a limit the curve for optical wavelengths; the crossing results from the simplified approximations used in calculations.

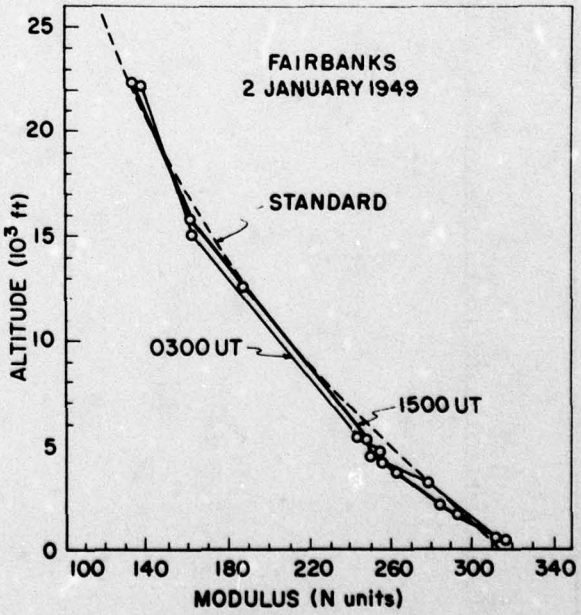


Fig. 9-7. Microwave refractive modulus profile in continental polar air mass.

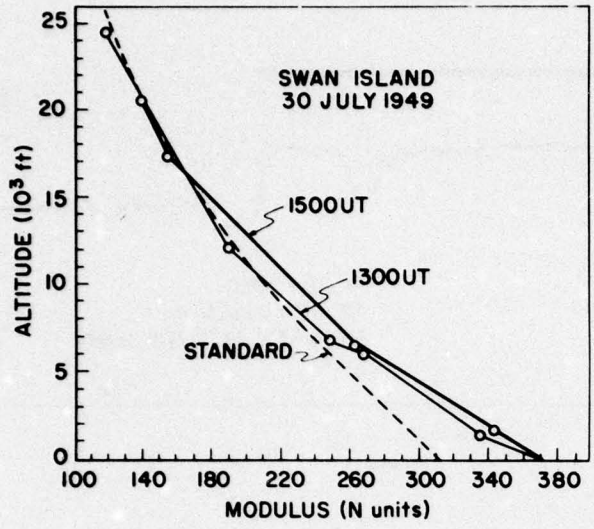


Fig. 9-8. Microwave refractive modulus profile in maritime tropical air mass.

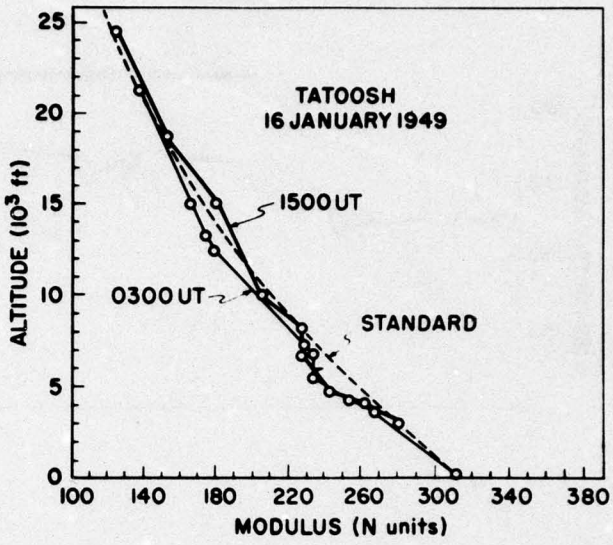


Fig. 9-9. Microwave refractive modulus profile in maritime polar air mass.

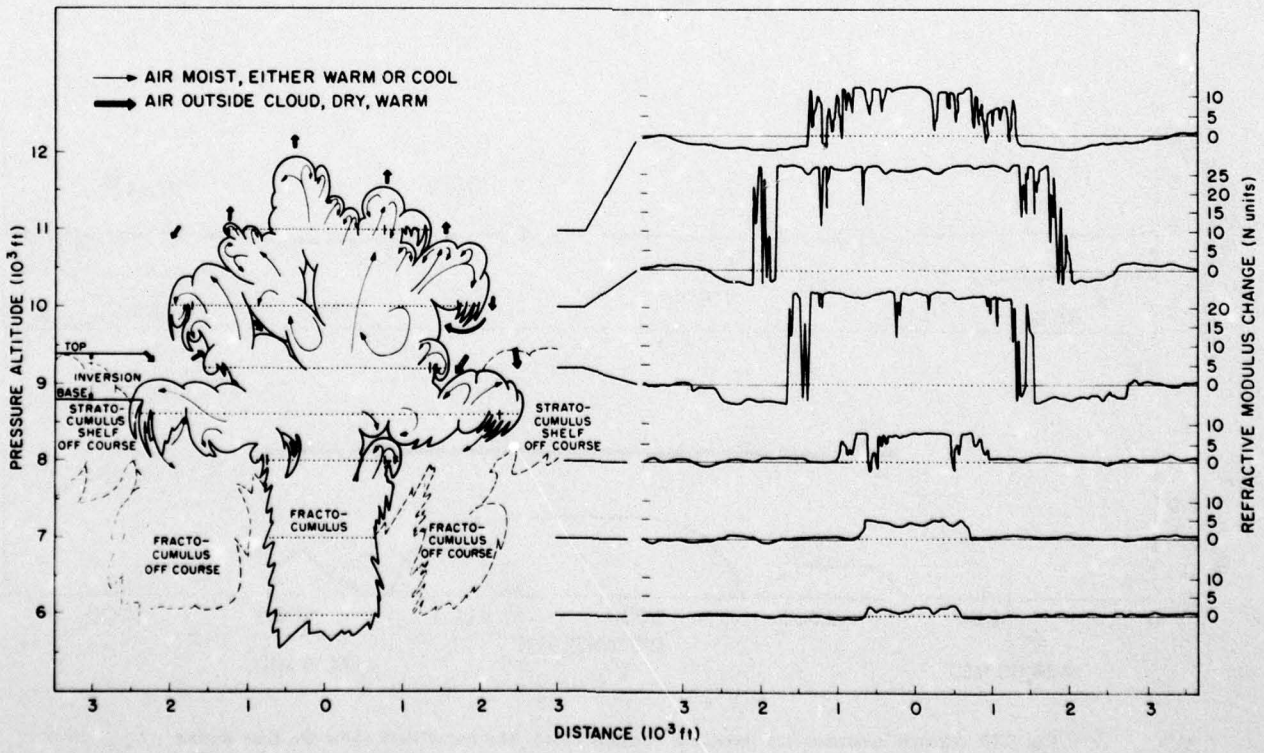


Fig. 9-11. Average cloud shape cross section 90° to wind shear and average refractive modulus changes on June 30, 1955, NW of Boston, Mass. (composite of 30 cloud passes); air motion deduced from temperature and refractive modulus data.

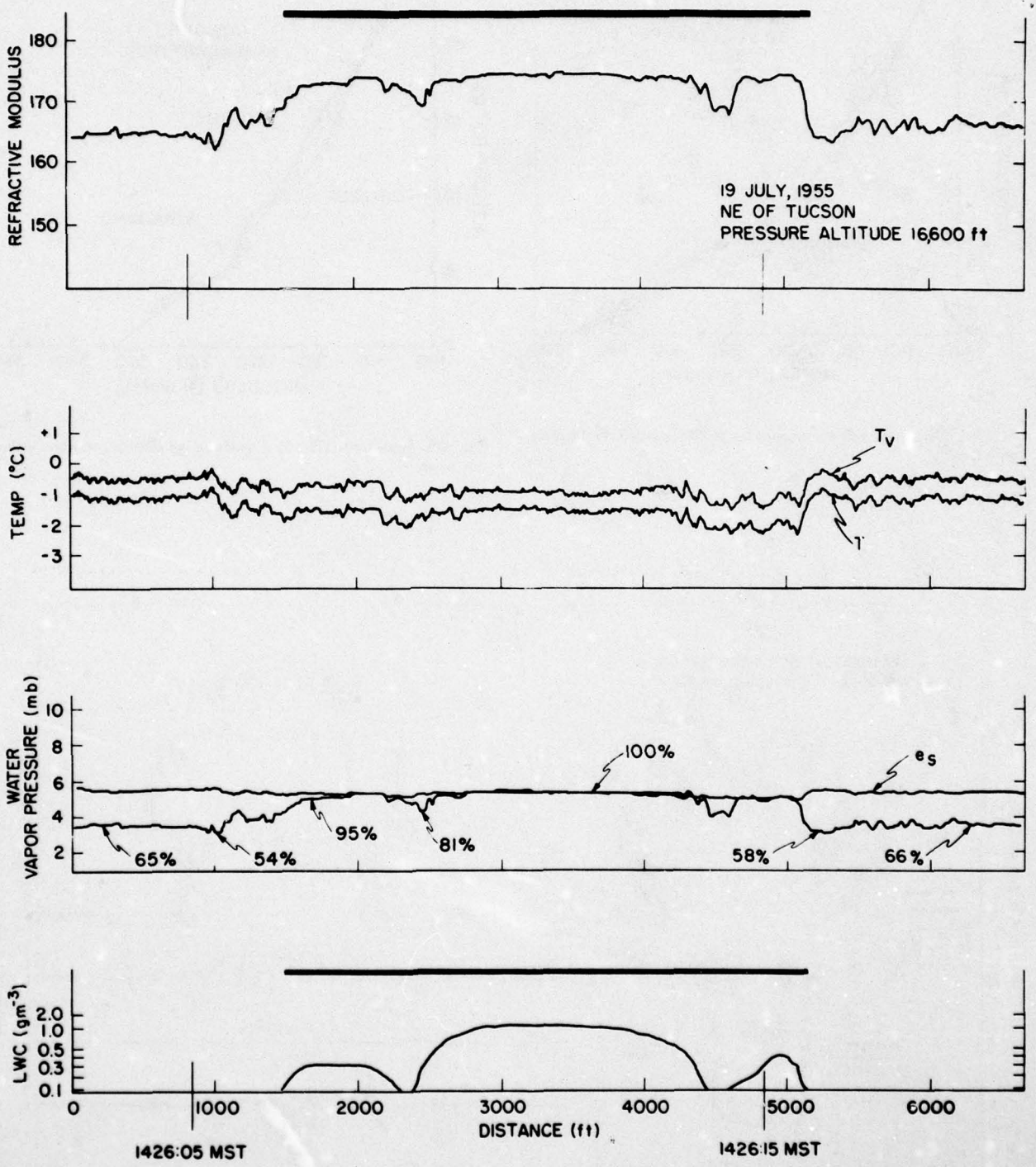


Fig. 9-10. Aircraft measurements through a cumulus cloud. The heavy lines show the time during which an observer in the aircraft indicated that the plane was within the visible cloud. The calculated virtual temperature, T_v, was corrected for liquid water content; T is the measured temperature. Relative humidity in percent is shown on the ambient water-vapor pressure curve; the curve labelled e_s is the calculated saturation water-vapor pressure at the temperature encountered. The bottom curve shows the liquid water content (LWC).

9.2.3 Total Reflectivity

The average echo power returned by a group of randomly distributed scattering particles is proportional to their reflectivity, η. Reflectivity is defined as the summation of the backscatter cross sections of the particles over a unit volume; $\eta \equiv \sum_1 \sigma$. When the backscattering particles are spheres and are small enough with respect to wavelength so that the Rayleigh approximation can be used, the reflectivity is proportional to the *radar reflectivity factor*, Z, which is the summation over a unit volume of the sixth power of the particle diameters; $Z \equiv \sum_1 D^6$. Z is conventionally reported in units of $mm^6\ m^{-3}$. Summation over a unit volume of Eq. (9-14) gives,

$$\sum_1 \sigma = \eta = \frac{\pi^5 |K|^2 Z}{\lambda^4} \times 10^{-6} \quad [cm^2\ m^{-3}]. \tag{9-16}$$

When the particles are larger than Rayleigh size or composed of ice or water-ice mixtures, it is common practice to measure the radar reflectivity and express it in terms of an *equivalent reflectivity factor*, Z_e. By substitution of 0.93 (water in the centimeter wavelength range) for $|K|^2$ in Eq. (9-16),

$$Z_e = 3.5 \times 10^3 \lambda^4 \eta \quad [mm^6\ m^{-3}]. \tag{9-17}$$

Thus Z_e is simply $\sum_1 D^6$ of water drops of Rayleigh size that would have the same reflectivity as that measured.

Because Z is a meteorological parameter that depends only on the particle size distribution and concentration, it is useful to relate Z with the precipitation rate, R. The Marshall-Palmer [1948] distribution is a reasonable and simple description of stratiform-type rainfall. Their regression curve relating Z ($mm^6\ m^{-3}$) with R ($mm\ h^{-1}$) is

$$Z = 200\, R^{1.6}. \tag{9-18}$$

Over a range of R from 0.5 to 70 $mm\ h^{-1}$, Eq. (9-18) may be used to estimate R from Z with an accuracy with $\pm 50\%$ in most stratiform-type rainfall distributions found in nature. In strongly convective storms, a relation more accurate for estimating thunderstorm rainfall rates is

$$Z = 486\, R^{1.37}. \tag{9-19}$$

Figure 9-18 is a plot of reflectivity as a function of rainfall intensity for three different radar wavelengths. The dashed lines, based on the Rayleigh approximation, were computed from Eq. (9-18). At 10-cm wavelength, the exact function would be identical to the Rayleigh curve except at the very highest rainfall rates. At the lower wavelengths, however, the drop sizes are somewhat larger than the limit of the Rayleigh approximation, and a measured Z_e at 0.9 cm would be only one-fifth the true Z at a rainfall rate of 100 $mm\ h^{-1}$. Figure 9-19 illustrates the variation in the Z_e vs R relationship for small λ and large R in the region where the Rayleigh approximation is poor; Wexler applied computed scattering functions for water spheres at 0°C to the Marshall-Palmer raindrop size distribution to obtain these values. For higher wavelengths the relationships are:

$$\begin{aligned} Z_e &= 330\, R^{1.54} \text{ at } 1.87 \text{ cm}, \\ Z_e &= 270\, R^{1.55} \text{ at } 3.2 \text{ cm}, \\ Z_e &= 285\, R^{1.45} \text{ at } 4.67 \text{ and } 5.5 \text{ cm}, \\ Z_e &= 295\, R^{1.45} \text{ at } 10 \text{ cm}. \end{aligned} \tag{9-20}$$

Table 9-1. Variation of dielectric characteristics of water with temperature and wavelength. (From Gunn and East [1954].)

	Temp (°C)	Wavelength 10 cm	3.21 cm	1.24 cm	0.62 cm
n	20	8.88	8.14	6.15	4.44
	10	9.02	7.80	5.45	3.94
	0	8.99	7.14	4.75	3.45
	−8		6.48	4.15	3.10
κ	20	0.63	2.00	2.86	2.59
	10	0.90	2.44	2.90	2.37
	0	1.47	2.89	2.77	2.04
	−8			2.55	1.77
$\lvert K\rvert^2$	20	.928	.9275	.9193	.8926
	10	.9313	.9282	.9152	.8726
	0	.9340	.9300	.9055	.8312
	−8			.8902	.7921
Im(−K)	20	.00474	.01883	.0471	.0915
	10	.00688	.0247	.0615	.1142
	0	.01102	.0335	.0807	.1441
	−8			.1036	.1713

Table 9-2. Variation of dielectric characteristics of ice with temperature. (From Gunn and East [1954].)

n	0 to −20 °C	1.78
κ	0 °C	2.4×10^{-3}
	−10 °C	7.9×10^{-4}
	−20 °C	5.5×10^{-4}
$\lvert K\rvert^2$	0 to −20 °C	0.176* ~~0.197*~~
Im(−K)	0 °C	9.6×10^{-4}
	−10 °C	3.2×10^{-4}
	−20 °C	2.2×10^{-4}

* For ice of normal density (0.917 g cm^{-3}).

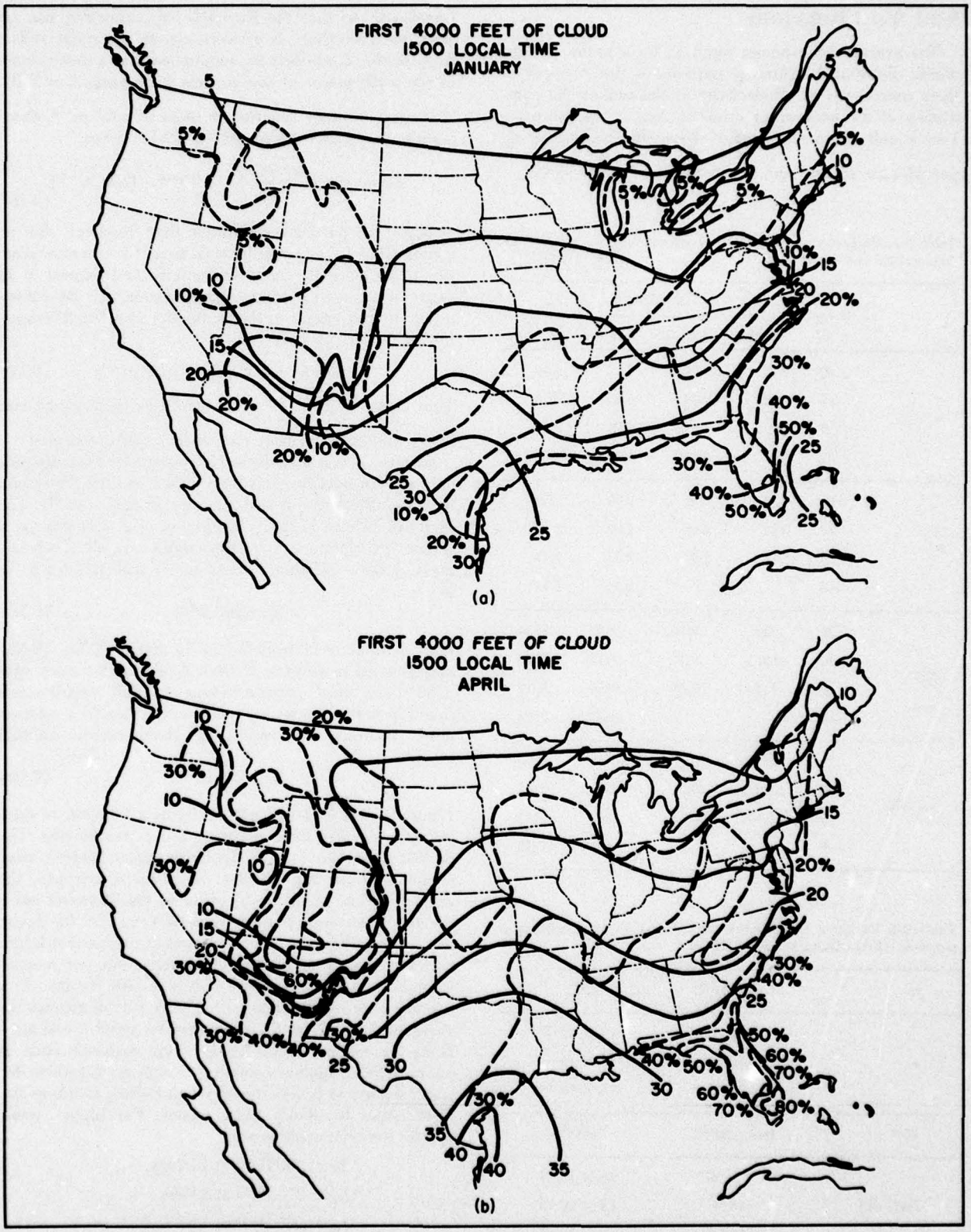


Fig. 9-12. Percent frequency of cumulus and cumulonibus cloud (dashed contours) and ΔN, the average change in refractive modulus (solid contours) for January, April, July and October.

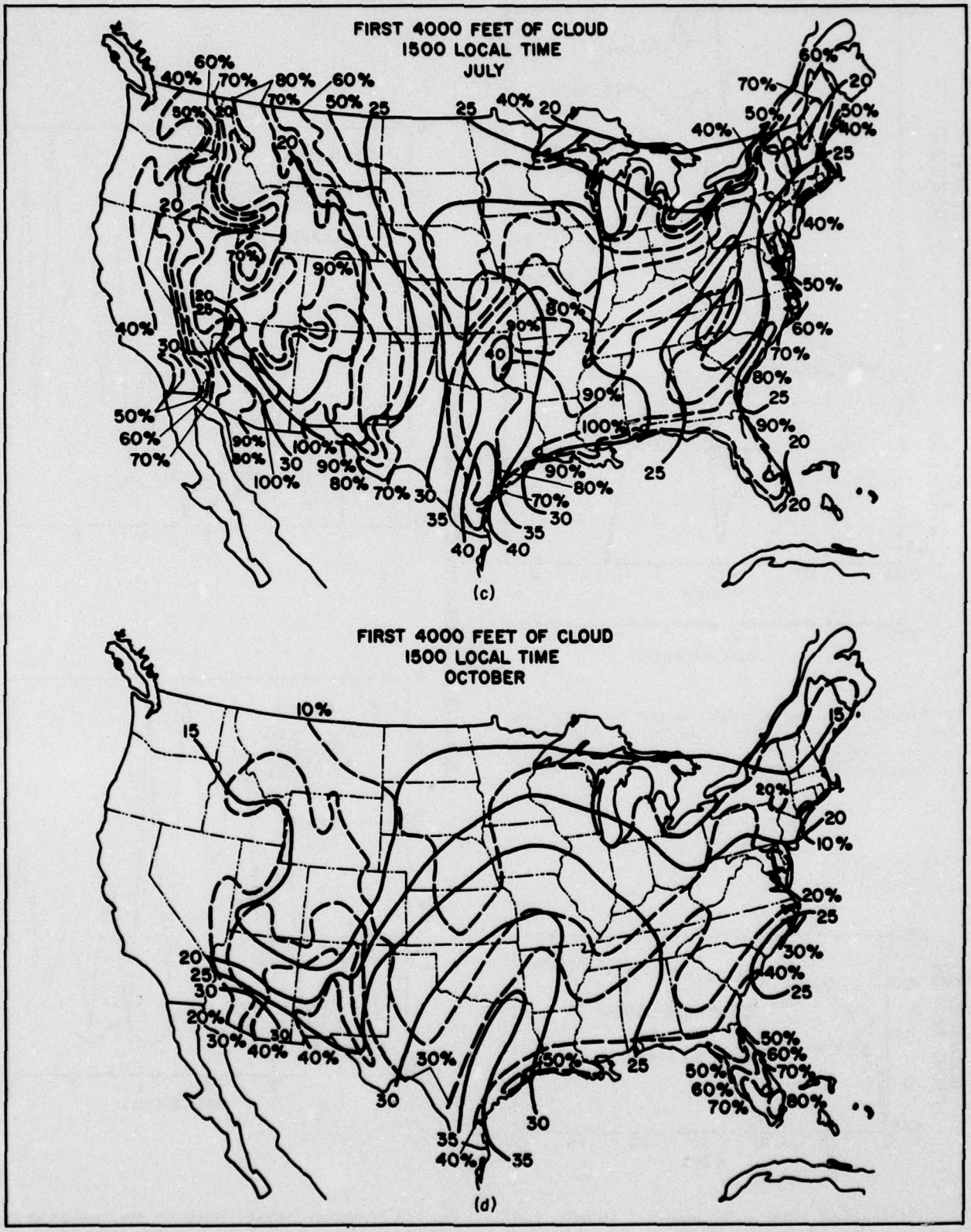


Fig. 9-12. Percent frequency of cumulus and cumulonibus cloud (dashed contours) and ΔN, the average change in refractive modulus (solid contours) for January, April, July and October.

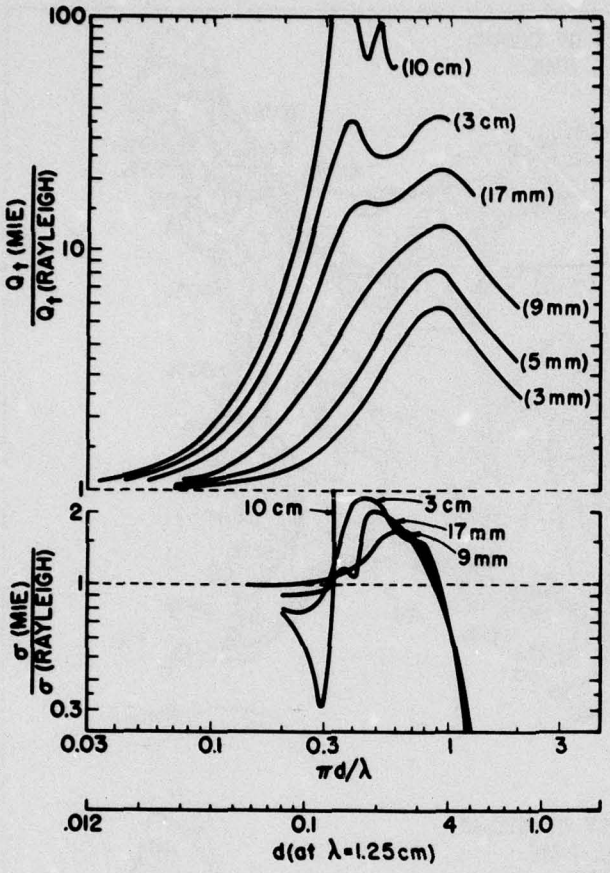


Fig. 9-13. Ratio of actual attenuation (upper) and actual backscattering (lower) to that given by the Rayleigh approximation for water at 18°C. (From F. T. Haddock, U. S. Naval Research Laboratory, unpublished manuscript).

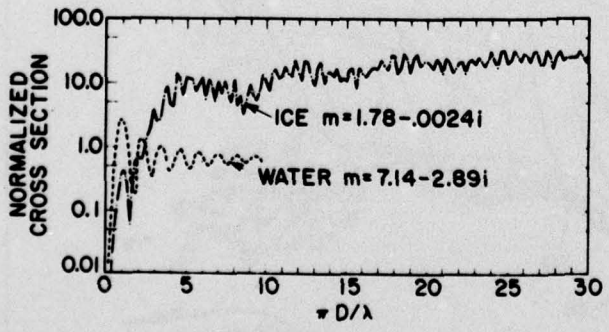


Fig. 9-14. Calculated values of the normalized ($4\sigma/\pi D^2$) backscatter cross section for water at 3.21 cm and 0°C and for ice at wavelengths from 1 to 10 cm. (After B. M. Herman and L. J. Battan, *Quart. J. Royal Meteorol. Soc.* v. 87, p. 223, 1961.)

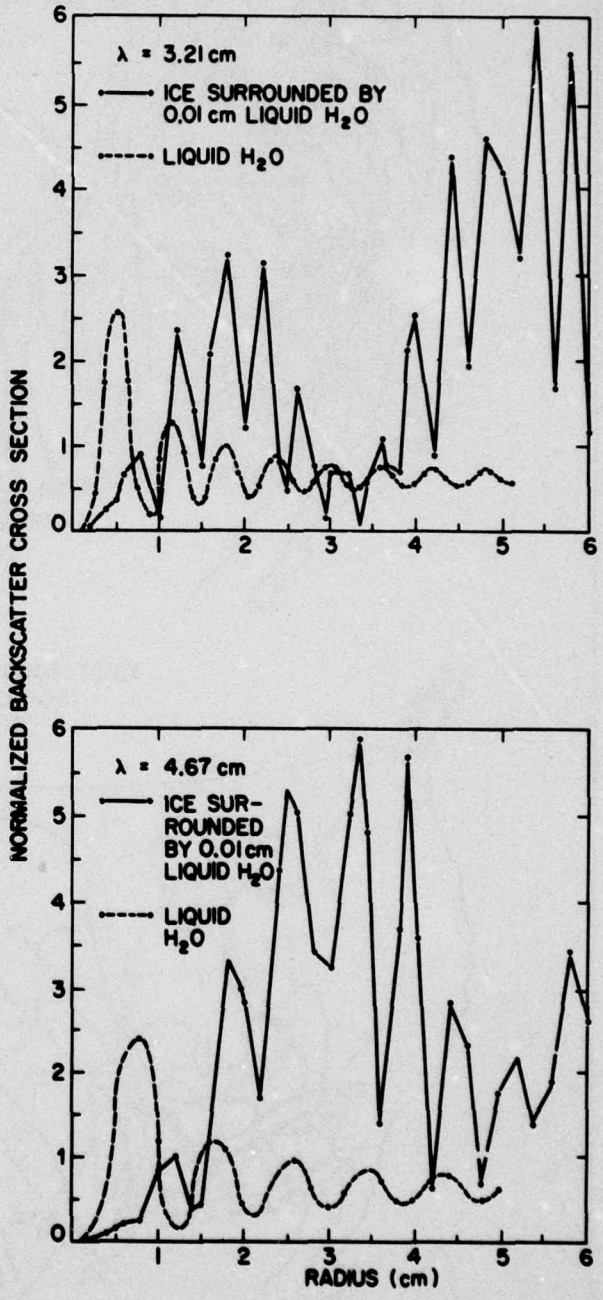


Fig. 9-15. Normalized ($4\sigma/\pi D^2$) backscatter cross sections of ice spheres coated by a water shell of 0.01 cm and of all-water spheres at wavelengths 3.21 cm and 4.67 cm. (After B. M. Herman and L. J. Battan, *J. Meteorol.*, v. 18, p. 468, 1961.)

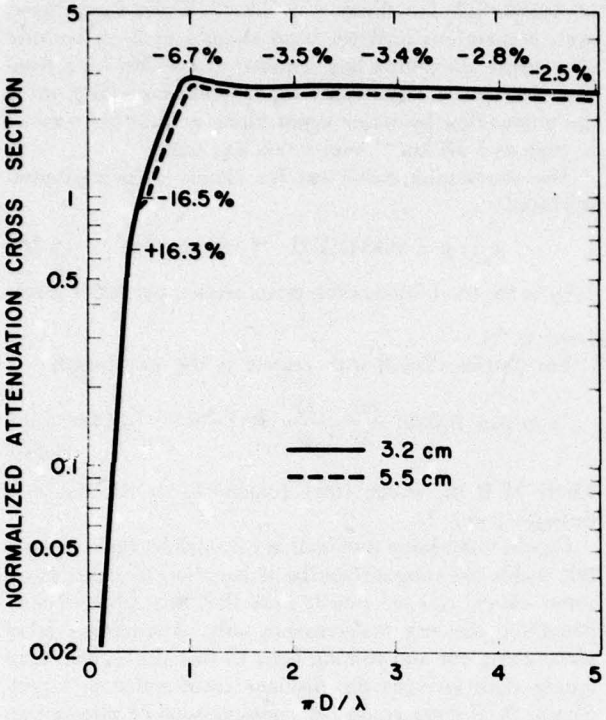


Fig. 9-16. Normalized ($4Q_t/\pi D^2$) attenuation cross sections of water spheres at 0°C and wavelengths of 3.2 and 5.5 cm. Percentages shown by the 3.2-cm curve are the percent differences for 10-cm wavelength; e.g., at $\pi D/\lambda = 2$, the value at 10 cm is minus 3.5% of the value at 3.2 cm. (After B. M. Herman, S. R. Browning and L. J. Battan, Tech. Rept. No. 9, Institute of Atmospheric Physics, University of Arizona, 1961.)

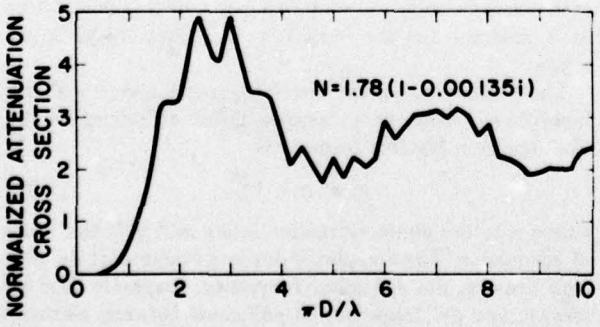


Fig. 9-17. Normalized ($4Q_t/\pi D^2$) attenuation cross sections of ice spheres at wavelengths between 1 and 10 cm. (After B. M. Herman and L. J. Battan, *Proc. Ninth Weather Radar Conference*, Amer. Meteorological Society, p. 259, 1961.)

The Rayleigh relationship, obtained by direct integration of the Marshall-Palmer distribution, is

$$Z = 296\,R^{1.47}. \tag{9-21}$$

The scattering properties of snow are complex. Snow may occur in a great variety of forms of either single ice crystals or aggregates of such crystals. Measurements suggest the following relationships as reasonable:

$$Z_s = 500\,R_s^{1.6}, \text{ for single crystals;} \tag{9-22}$$

$$Z_s = 2000\,R_s^{2}, \text{ for aggregates (flakes).} \tag{9-23}$$

A rough average suitable for characterizing all types of snow is

$$Z_s = 1000\,R_s^{1.6}. \tag{9-24}$$

R_s is the snowfall rate in millimeters of water per hour. The coefficients are greater than those for rain because more of the slower-falling snow particles are required per unit volume to maintain the same rate of precipitation. Z_s corresponds to the diameters which the particles would have if they were compressed to ice of unit density. A corresponding value of $|K|^2$ is used to determine the snow reflectivity; $|K|^2$ for such hypothetical unit-density ice is 0.197. Because this is roughly 1/5 times the corresponding value for water, while the coefficient in Eq. (9-24) is 5 times that for water, the reflectivity of dry snow is roughly equal to that of rain of the same precipitation rate. Wet snow both scatters and attenuates appreciably more than rain. A thin water coating distributed over the *non-spherical shape can scatter a much greater proportion* of incident microwave energy than water spheres of the same mass.

The increased reflectivity in the melting zone over that of the dry snow aloft and the rain below gives rise to an intense echo layer referred to as the "bright band." On the average it occurs in a layer some 1000 to 2000 ft below the 0°C level in the case of non-convective rain which has originated aloft as snow. In some instances the bright band may not occur or may be difficult to observe. It does not occur in the active stages of convective storms in which water particles may be carried up through the 0°C level without freezing; nor when fast falling hailstones, sometimes water coated even at low temperatures, fall through that level. Only a small increase in reflectivity occurs when graupel melts, and the decrease in reflectivity below the melting level may be negligible because the particles have almost reached their final raindrop velocities by the time they have attained a significant water coating.

Clouds composed of water particles scatter very poorly. However, high-power, short-wavelength radars may sometimes detect water clouds at short ranges. An empirical relationship for water clouds is

$$Z = 0.048\,M^2, \tag{9-25}$$

where M, the water content, is in grams per cubic meter.

The reflectivity of ice clouds is not known. However, many so-called ice clouds are really snow crystals falling and evaporating in a dry layer below the cloud base.

Using Eq. (9-22) and a reasonable estimate for the fall velocity of ice crystals (0.3 m sec^{-1}) one obtains

$$Z \approx 570\, M^{1.6}, \qquad (9\text{-}26)$$

where M is the mass concentration in grams per cubic meter. Equation (9-26) is an order-of-magnitude estimate.

Table 9-3 summarizes knowledge on reflectivity of rain, snow, and water cloud. The relation of hailfall rate to reflectivity cannot be approximated by a simple power law, because very little is known about hailstone size and shape spectra. Most hail sizes, however, are in the complex Mie scattering regime even for radar wavelengths as large as 10 cm.

9.2.4 Total Attenuation

Radar power returned by a scatterer is reduced by an attenuation factor k, defined by

$$10 \log k = 2 \int_0^{r_1} (g + c + p)\, dr, \qquad (9\text{-}27)$$

where r_1 is range from radar to target in km and g, c, and p represent the one-way attenuation (dB km^{-1}) by gases, cloud, and precipitation, respectively; the factor 2 accounts for the double path used in radar.

At wavelengths ≥ 3 cm, attenuation by atmospheric gases is negligible. At wavelengths between 0.9 and 3 cm, attenuation by all atmospheric gases except water vapor is considerably less than 0.1 dB km^{-1}. Water vapor, however, is a serious problem from about 1 to 2 cm because of a major absorption line centered at 1.35 cm. In a tropical atmosphere with water vapor content of 20 g m^{-3}, the attenuation by water vapor alone at 1.25 cm may be as high as 1 dB km^{-1} over a two-way path.

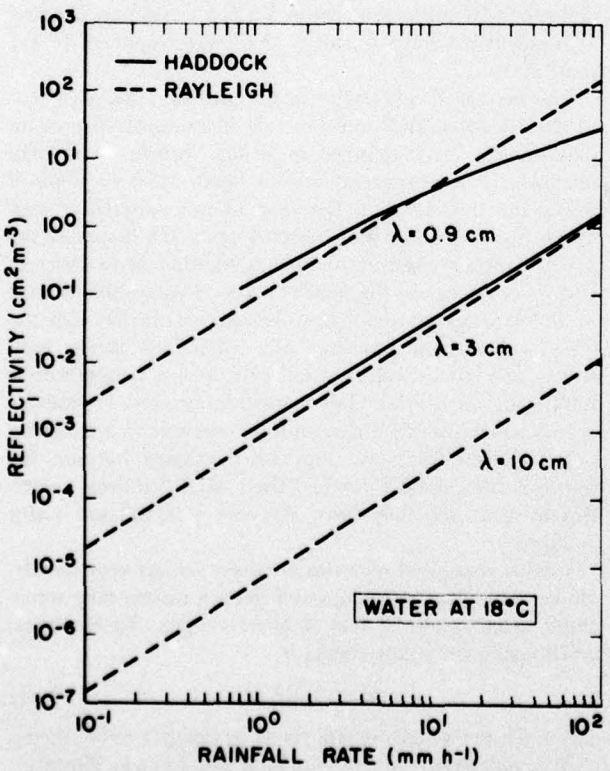


Fig. 9-18. Exact (Haddock) and approximate (Rayleigh) reflectivity as a function of rainfall rate. (After Gunn and East [1954].)

The attenuation coefficient for clouds or precipitation is given by

$$c = p = 0.4343 \sum_1 Q_t \quad [(dB\, km^{-1}]; \qquad (9\text{-}28)$$

$\sum_1 Q_t$ is the total attenuation cross section per cubic meter ($cm^2\, m^{-3}$).

For particles small with respect to the wavelength

$$c = p = 0.4343 \frac{6\pi}{\lambda} \frac{M}{\rho} \operatorname{Im}(-K) \quad [dB\, km^{-1}], \qquad (9\text{-}29)$$

where M is the water (ice) content (g m^{-3}) and ρ is density (g cm^{-3}).

Figure 9-20 shows attenuation for various rates of rainfall. Table 9-4 summarizes the attenuation by rain, snow, water cloud, and ice cloud; note that this table is computed for one-way transmission only. Attenuation takes place going out and coming back so that the actual attenuating path is twice the distance from radar to target. Figure 9-21 gives results of computations of attenuation per unit rainfall rate at $T = 0°C$ over a wide range of wavelengths. The differences between the Wexler data and that of Gunn and East are explainable in part by the temperature difference.

9.3 IONOSPHERIC INTERACTIONS

The propagation of electromagnetic waves less than 1000 Mcps, and especially in the range less than 100 Mcps, is strongly affected by interaction with the ionosphere (see Chapter 12). The ionospheric regions affect different frequency ranges in different ways. In general the F region is of concern primarily to the high frequency (3-30 Mcps) range, and to the lower part of the very high frequency (30-300 Mcps) range. The E region is important for all frequencies below 100 Mcps. The D region acts primarily as an absorber for all frequencies and as a reflector for the very low frequency (3-30 kcps) range.

The interaction of the electromagnetic waves with the ionosphere results in a complex index of refraction, n*. The Appleton-Hartree formula is

$$n^* = n - i\chi, \qquad (9\text{-}30)$$

where n is the phase refractive index and χ is the index of absorption. The complex index is a function of the electron density, the operating frequency, magnetic field intensity, and the frequency of collisions between electrons and neutral molecules. The phase velocity is generally greater than c (the velocity in free space) and the group velocity, v_g, is less than c. χ is related to the absorption coefficient k by $k = 2\pi\chi/\lambda$; k represents the loss of energy caused by collisions. The effect of the magnetic

Table 9-3. Power relations for reflectivity (back-scatter across section per unit volume in cm^2 m^{-3}) as a function of rate of fall of rain or snow (R mm h^{-1}) or of cloud water-content (M g m^{-3}). (From Gunn and East [1954].)

	Temp (°C)	Power	Coefficient at Indicated Wavelength					
			10 cm	5.7 cm	3.2 cm	1.8 cm	1.24 cm	0.9 cm
Rain	18	$R^{1.6}$ $R^{1.56}$ $R^{1.23}$	5.89×10^{-6}	5.59×10^{-5}	~~9.6×10^{-4}~~ 8.14×10^{-4}			0.16
Snow*	All	$R^{1.6}$	6.05×10^{-6}	5.75×10^{-5}	5.75×10^{-4}	5.75×10^{-3}		
Water cloud	20	$M^{1.82}$	8.29×10^{-10}	7.86×10^{-9}	7.91×10^{-8}	7.85×10^{-7}	3.74×10^{-6}	1.24×10^{-5}
	10	$M^{1.82}$	8.32×10^{-10}	7.88×10^{-9}	7.91×10^{-8}	7.83×10^{-7}	3.46×10^{-6}	1.23×10^{-5}
	0	$M^{1.82}$	8.34×10^{-10}	7.89×10^{-9}	7.93×10^{-8}	7.81×10^{-7}	3.42×10^{-6}	1.21×10^{-5}
	−8	$M^{1.82}$		7.92×10^{-9}†	7.95×10^{-8}†	7.78×10^{-7}†	3.36×10^{-6}	1.16×10^{-5}

* R is melted water equivalent of the snow.
† Extrapolated.

Table 9-4. Attenuation (dB km^{-1}) due to precipitation or cloud (one-way); rainfall, or water of melted snow, rate R (mm h^{-1}) and water content M (g cm^{-3}).

	Temp (°C)	Attenuation at Indicated Wavelength					
		10 cm	5.7 cm	3.2 cm	1.8 cm	1.24 cm	0.9 cm
Rain*	18	$0.0003R^{1.00}$	$0.0022R^{1.17}$	$0.0074R^{1.31}$	$0.045R^{1.14}$	$0.12R^{1.05}$	$0.22R^{1.00}$
	0	roughly twice above value	≈ same as above value	slightly < above value	slightly < above value	slightly < above value	slightly < above value
Snow**	0	$0.035 \times 10^{-5}R^{1.6} + 22.0 \times 10^{-5}R$	$0.33 \times 10^{-5}R^{1.6} + 38.5 \times 10^{-5}R$	$3.3 \times 10^{-5}R^{1.6} + 68.6 \times 10^{-5}R$	$33.2 \times 10^{-5}R^{1.6} + 122 \times 10^{-5}R$		
	−10	$0.035 \times 10^{-5}R^{1.6} + 7.3 \times 10^{-5}R$	$0.33 \times 10^{-5}R^{1.6} + 12.9 \times 10^{-5}R$	$3.3 \times 10^{-5}R^{1.6} + 22.9 \times 10^{-5}R$	$33.2 \times 10^{-5}R^{1.6} + 40.6 \times 10^{-5}R$		
	−20	$0.035 \times 10^{-5}R^{1.6} + 5.0 \times 10^{-5}R$	$0.33 \times 10^{-5}R^{1.6} + 8.8 \times 10^{-5}R$	$3.3 \times 10^{-5}R^{1.6} + 15.7 \times 10^{-5}R$	$33.2 \times 10^{-5}R^{1.6} + 28.0 \times 10^{-5}R$		
Water cloud	20	$0.39 \times 10^{-2}M$	$1.36 \times 10^{-2}M$	$4.83 \times 10^{-2}M$	$12.8 \times 10^{-2}M$	$31.1 \times 10^{-2}M$	$64.7 \times 10^{-2}M$
	10	$0.56 \times 10^{-2}M$	$1.96 \times 10^{-2}M$	$6.30 \times 10^{-2}M$	$17.9 \times 10^{-2}M$	$40.6 \times 10^{-2}M$	$68.1 \times 10^{-2}M$
	0	$0.90 \times 10^{-2}M$	$2.72 \times 10^{-2}M$	$8.58 \times 10^{-2}M$	$26.7 \times 10^{-2}M$	$53.2 \times 10^{-2}M$	$99.0 \times 10^{-2}M$
	−8		$3.4 \times 10^{-2}M$†	$11.2 \times 10^{-2}M$†	$34.0 \times 10^{-2}M$†	$68.0 \times 10^{-2}M$	$125 \times 10^{-2}M$
Ice cloud	0	$7.87 \times 10^{-4}M$	$13.8 \times 10^{-4}M$	$24.6 \times 10^{-4}M$	$43.6 \times 10^{-4}M$	$63.5 \times 10^{-4}M$	$87.4 \times 10^{-4}M$
	−10	$2.62 \times 10^{-4}M$	$4.60 \times 10^{-4}M$	$8.19 \times 10^{-4}M$	$14.6 \times 10^{-4}M$	$21.1 \times 10^{-4}M$	$29.3 \times 10^{-4}M$
	−20	$1.80 \times 10^{-4}M$	$3.16 \times 10^{-4}M$	$5.63 \times 10^{-4}M$	$10.0 \times 10^{-4}M$	$14.5 \times 10^{-4}M$	$20.0 \times 10^{-4}M$

* These are empirical relations.
** Values obtained using the Rayleigh approximations, which are not valid for wavelengths less than about 1.5 cm; a value of $R = 10$ or $R^{1.6} = 39$ is an upper limit for snowfall rates.
† Extrapolated.

field is to split the radio wave into waves that are elliptically polarized in opposite senses (Sec. 12.3.2). These waves are reflected at different levels and suffer different degrees of absorption.

While the D, E, and F regions have fairly predictable characteristics, ionospheric propagation is also affected by several less predictable phenomena. The most important is sporadic E (Sec. 12.6) which will reflect frequencies greater than those normally reflected by the E layer. Another phenomenon is the reflection from ionization trails formed by the entry of meteors into the ionosphere (Sec. 9.4). Forward scatter in the very high frequency range by the E and D regions and the forward scatter via the F layer that occurs in the equatorial regions are attributed to ionospheric irregularities or turbulence.

9.3.1 Some Magneto-Ionic Formulas

The *Appleton-Hartree formula*, neglecting both collisions and the effect of the magnetic field, is

$$n^2 = 1 - X, \tag{9-31}$$

where

$$X = f_N^2/f^2, \tag{9-32}$$

and

$$f_N^2 = Ne^2/4\pi^2 \epsilon_o m; \tag{9-33}$$

f_N is the plasma oscillation frequency of the electron, f is the wave frequency, e is the charge of the electron, N is the density of free electrons, m is the mass of electron, and ϵ_o is the permittivity of free space. An approximate value of f_N is $9N^{1/2}$, where N is in m^{-3}. For a frequency propagating vertically upward, reflection ($n = o$) will occur when $f = f_N$, so that at the reflection height where this occurs the electron density can be determined from Eq. (9-33); N for the maximum N of a layer is called the critical (penetration) frequency for that layer.

The effect of the magnetic field, if collisions are neglected, is given by

$$n^2 = 1 - X\left[1 - \frac{Y_T^2}{2(1-X)} \pm \left(\frac{Y_T^4}{4(1-X)^2} + Y_L^2\right)^{1/2}\right]^{-1}. \tag{9-34}$$

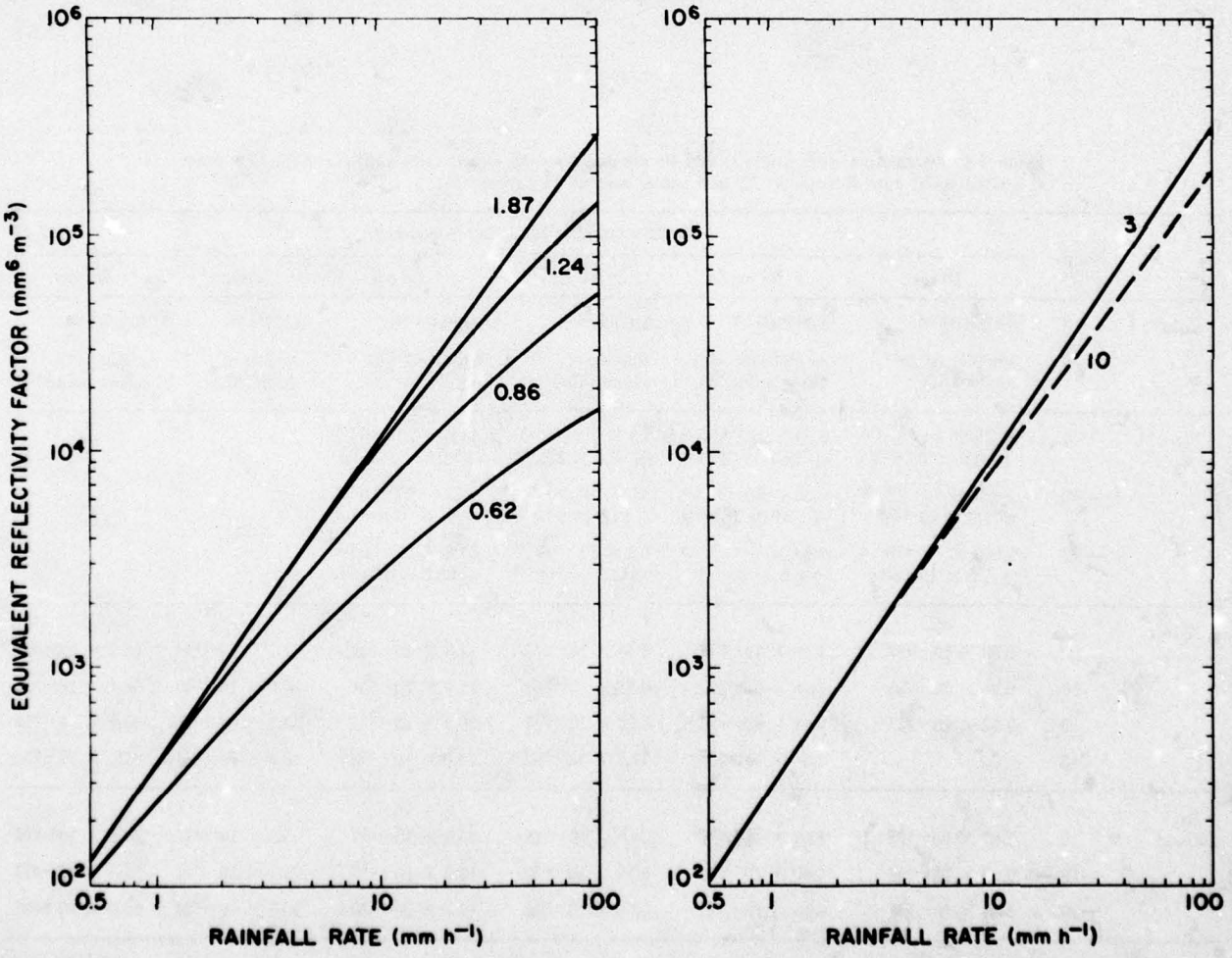


Fig. 9-19. Relationships between equivalent radar reflectivity factor and rainfall rate for 0°C; Marshall-Palmer drop-size distribution assumed for various wavelengths. Numbers by curves are wavelengths in cm. (From R. Wexler, Final Report on Contract AF19(604)-5204, AFCRL.)

The parameter Y is

$$Y = f_H/f. \tag{9-35}$$

The gyrofrequency, f_H, is

$$f_H = \mu_o He/2\pi m = Be/2\pi m, \tag{9-36}$$

where H is the magnetic field intensity, μ_o is the permeability of free space, and $B = \mu_o H$.

$$Y_T = Y \sin \phi, \text{ and } Y_L = Y \cos \phi, \tag{9-37}$$

where ϕ is the angle between the magnetic field and direction of wave propagation. In middle latitudes, f_H is approximately 1.2 Mcps.

For the longitudinal case ($Y_T = 0$) or for the quasi-longitudinal case (Y_T small),

$$n^2 = 1 - \frac{X}{1 \pm Y}. \tag{9-38}$$

Reflection takes place at $X = 1 \pm Y$. (A more careful study of the formula as Y_T approaches zero shows that $X = 1$ will also give $n = 0$, as in the absence of a magnetic field.) The wave represented by $X = 1$ is the *ordinary* wave, while those which involve the gyrofrequency are the *extraordinary* waves.

If the effect of collisions is not neglected, the *absorption coefficient*, k, is not zero. The index of refraction becomes complex [Eq. (9-30)], and the reflection levels and the nature of reflection change. The absorption coefficient for the extraordinary wave is greater than that for the ordinary by $(f + f_H)^2/(f - f_H)^2$ which becomes quite large for wave frequencies, f, in the vicinity of the gyrofrequency. The absorption can be divided into non-deviative (Sec. 12.4), principally in the D region, and deviative in the vicinity where the wave is highly refracted.

For *non-deviative absorption* the formula is approximately

$$k = \frac{1}{2c}(4\pi^2 f_N^2) \frac{\nu}{\nu^2 + 4\pi^2 (f \pm f_H)^2}, \tag{9-39}$$

where ν is the collision frequency (Sec. 12.4.1). For information and discussion of deviative absorption, see for example Buddin [1961] or Ratcliffe [1959].

9.3.2 Ionosondes and Ionograms

Ionosondes transmit sweep frequencies (approximately 1 to 25 Mcps) vertically upward and receive the waves reflected by the ionosphere. Different frequencies are reflected from different heights; the ionogram is a curve showing h′, the virtual height at which the wave appears to be reflected, vs frequency. Figure 9-22 is a schematic diagram illustrating the path of a vertically incident and an obliquely incident wave and the relation between h′ and the true height at which reflection occurs. Ionograms can be converted into true height curves of h vs f or h vs N [Eq. (9-33)], or h vs n [Eqs. (9-31) to (9-34)]. It is possible to convert vertical ionograms into oblique ionograms by employing the Breit-Tuve theorem and Martyn's equivalence theorem. Referring to Fig. 9-22, according to the Breit-Tuve theorem, the transit time for a given frequency, g, along the triangular path is the same as the actual transit along the true curved path. Martyn's theorem states that for $g = f \sec \phi$, the true height and the virtual height of the path of a wave of frequency g are the same as the true height and virtual height at which f is reflected propagating vertically; a flat earth is assumed and the effects of collisional frequency and magnetic field are neglected. The given distance D, and knowing h′ determines ϕ. The result is an oblique ionogram, g versus h′ or g vs t, the travel time. Figure 9-23 is a schematic illustration of oblique and vertical ionograms.

There is a lower cutoff below which frequencies are completely absorbed. This cutoff frequency is f_{min} in the case of the vertical ionogram, and, for transmission between two points, LOF on the oblique ionogram. The separation between the MOF (maximum frequency on the ionogram) and the LOF on the oblique ionogram represents the usable spectrum.

9.4 RADIO REFLECTIONS FROM METEOR TRAILS

Visual meteor trails almost always reflect radio waves, and trails that are not visible frequently reflect radio waves. Most of the ionization of the atmosphere by meteors occurs in the altitude range 80 to 115 km. Like sporadic-E, the ionization produced by meteor bursts supports propagation at frequencies higher than the usual frequencies propagated by the E region. This section is a mere outline of the subject; aspects important in communications, radar operation, etc. are not covered.

9.4.1 Characteristics of a Meteor Trail

The ionization trail initially is considered to be a cylinder with a mean length of 15 km for sporadic meteors and 25 km for shower meteors. Almost immediately after its formation, the cylinder has a cross section of about 2 m at 115 km, decreasing to about 0.03 m at 85 km. The cylinder grows by diffusion of the electrons at an estimated rate of 140 $m^2\ sec^{-1}$ at 115 km down to 1 $m^2\ sec^{-1}$ at 85 km.

The radio magnitude (Sec. 14.3) is related to the number of electrons per meter of path, q, by

$$M_r = 40 - 2.5 \log_{10} q. \tag{9-40}$$

For $q = 10^{14}\ m^{-1}$, M_r is approximately +5. Trails are generally divided into underdense and overdense, the transition occurring at a linear density of approximately 10^{14} electrons m^{-1}.

The maximum likelihood of detection of a meteor ionization trail by radar occurs when the ionization reaches the foot of the normal to the meteor's path from the radar; a visual trail will be seen by eye or camera before the radar detects it. Figure 9-24 is an idealized sketch of radar return from a meteor trail. The amplitude varies as a Fresnel diffraction pattern, caused by the fluctuation in the signal as the ionization trail grows to a Fresnel zone and through several zones.

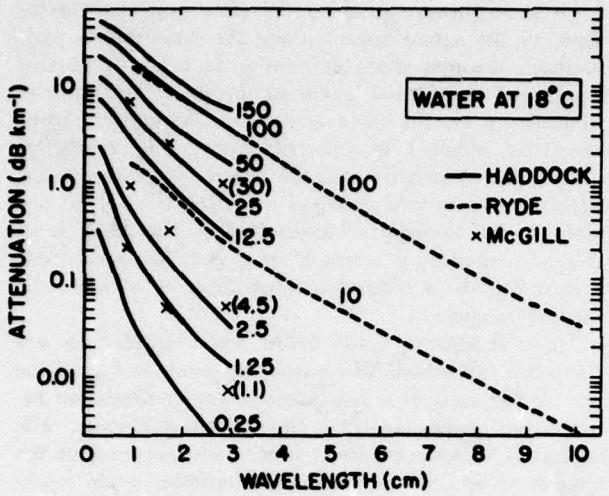


Fig. 9-20. Attenuation versus wavelength for various rain-fall rates; rates in mm h^{-1} are given by each curve. (Data from Gunn and East [1954].)

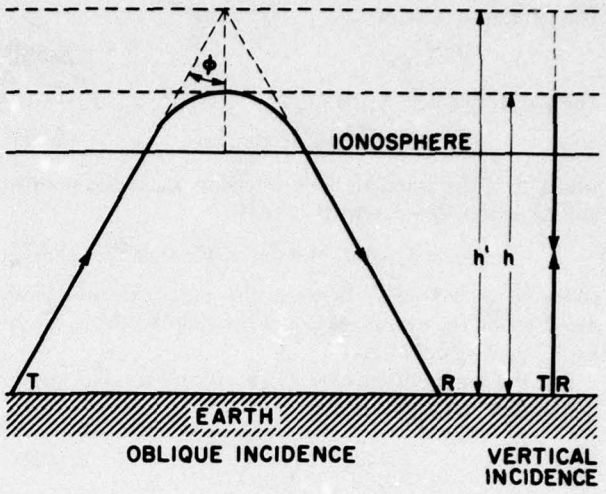


Fig. 9-22. Equivalent path for a plane earth and plane ionosphere; h' is the virtual height and h the true height of reflection.

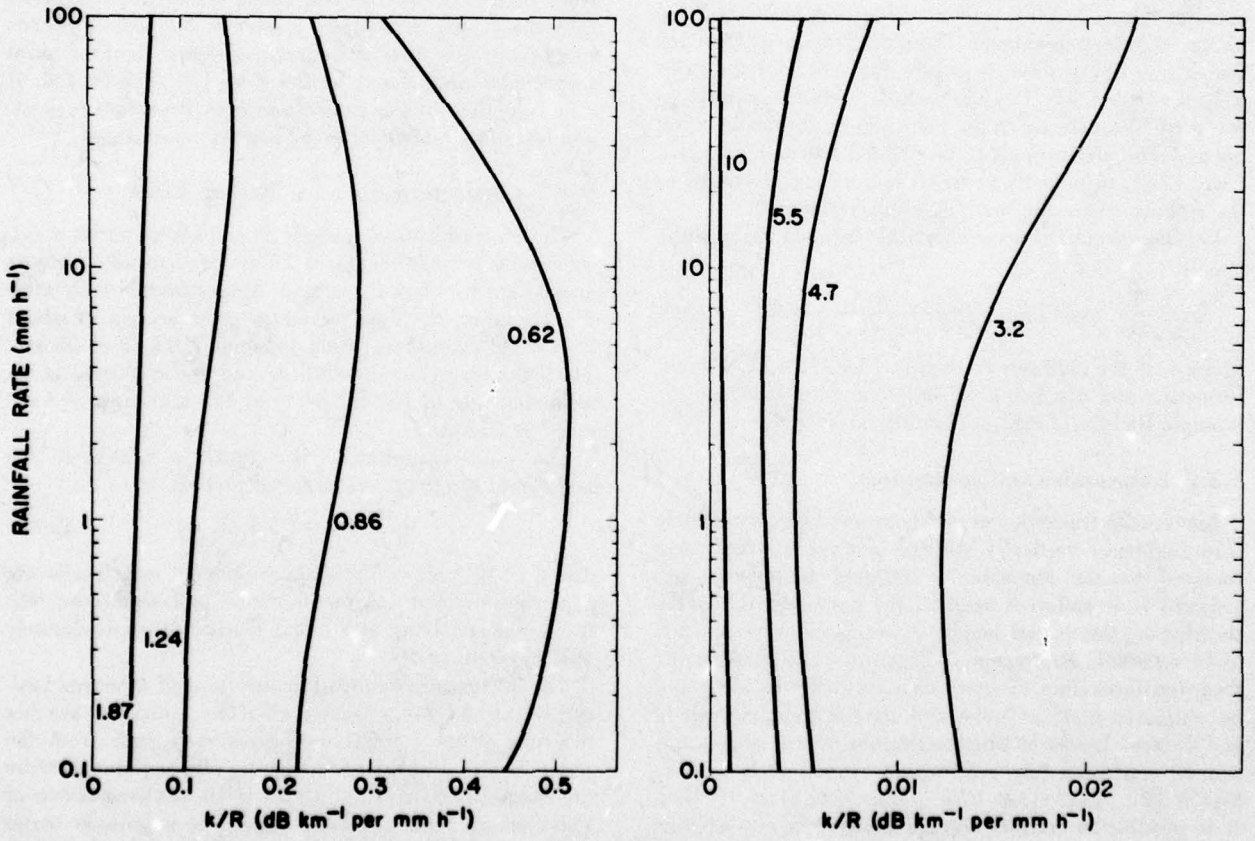


Fig. 9-21. Attenuation per unit rainfall rate (k/R) versus rainfall rate at various wavelengths, for T = 0°C and Marshall-Palmer drop-size distribution; numbers by curves are wavelengths in cm. (From R. Wexler, Final Report on Contract AF19(604)-5204, AFCRL.)

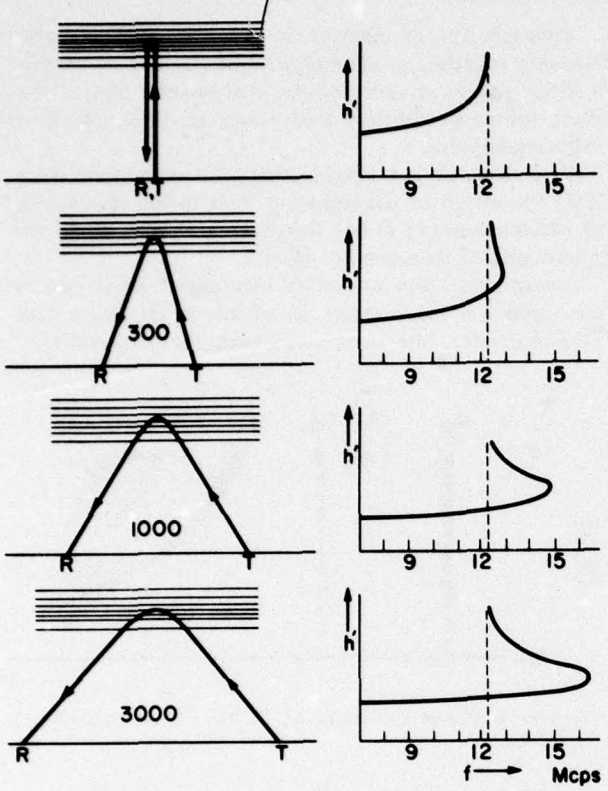


Fig. 9-23. Schematic illustration (not to scale) of the change in shape of the virtual height (h') vs frequency (f) curves for distances between transmitter and receiver of 0, 300, 1000 and 3000 km.

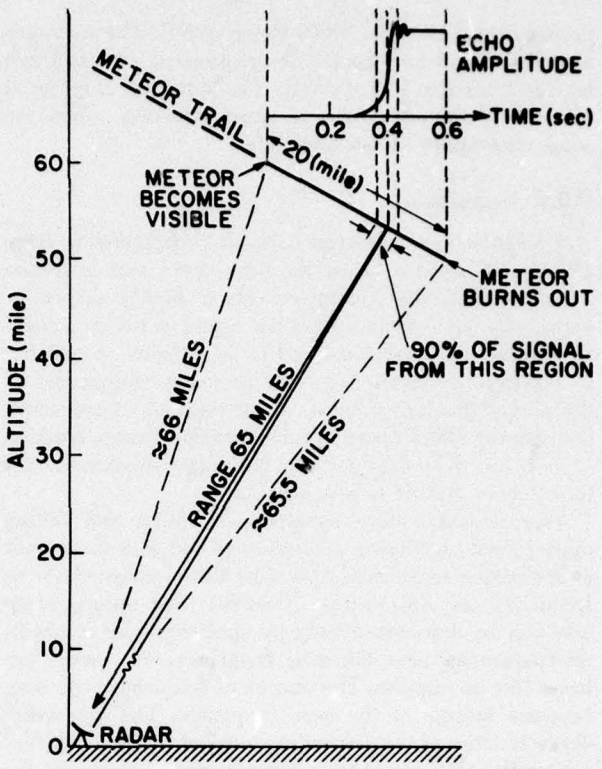


Fig. 9-24. Diagram showing radar range for a meteor trail and the amplitude of the radar echo as a function of time. (After H. S. W. Massey and R. L. F. Boyd, "The Upper Atmosphere," Philosophical Library, New York, 1959.)

9.4.1.1 *The Underdense Trail.* The underdense trail ($q < 10^{14}$ m^{-1}) is supposed to scatter radio waves by the individual free electrons, treating secondary scattering as negligible. The scattering cross section of a single electron is $10^{-28} \sin^2 \gamma$ meters, where γ is the angle between the electric vector incident on the electron and the direction from the electron to the receiver; for radar, $\sin^2 \gamma = 1$. For the underdense trail, the maximum power in watts received by the radar receiver, P_r, is

$$P_r = (2.5 \times 10^{-32})\ P_T\, G_1 G_2\, (\lambda/R_o)^3\, q^2, \quad (9\text{-}41)$$

where P_T is transmitted power, G_1 and G_2 are antenna gains, λ is the radar wavelength in meters, and R_o is the length in meters of the normal from the radar to the meteor path. The lifetime of the trail is controlled by diffusion, so that the decay of the echo amplitude is given by

$$T_u = \frac{\lambda^2}{16\pi^2 D} \sec \phi, \quad (9\text{-}42)$$

where D is the diffusion coefficient (m^2 sec^{-1}) and 2ϕ is the angle between incident and reflected ray. T_u is the time it takes the received power to decay to e^{-2} (8.7 dB) of its maximum value. The actual duration of the return as seen by the receiver will depend on the parameters of the system (power, receiver threshold, antenna gains).

9.4.1.2 *The Overdense Trail.* The overdense trail ($q > 10^{14}$ m^{-1}) is characterized by long enduring echoes. Secondary scattering between electrons is important, the wave does not penetrate freely, and reflection in the early stages is similar to that from a metallic cylinder. In the later stages, the trail is apt to be distorted by winds, and possibly by turbulence, and the ionization then becomes underdense, probably as the result of both diffusion and attachment. Experimental values of duration are generally less than the theoretical value, which is

$$T_{od} \approx 7 \times 10^{-17} \frac{\lambda^2 q}{D} \sec^n \phi; \quad (9\text{-}43)$$

n is about 2 for propagation along the trail and about 0.3 transverse to the trail. The received power is given by

$$P_r = (1.6 \times 10^{-11})\ P_T\, G_1 G_2\, (\lambda/R_o)^3\, q^{1/2}. \quad (9\text{-}44)$$

9.5 WHISTLERS, IONOSPHERICS, AND HYDROMAGNETIC WAVES

This section is a brief presentation of theoretical and experimental results. Extension of magnetoionic theory to take into account the effect of singly charged ions in the audio range is reviewed. This extension serves as an introduction to the discussion of hydromagnetic wave

propagation [Akasofu, 1960; Fejer, 1960]. The summary of whistler and ionspherics observations is obtained primarily from the IGY [1962]. The data are considered statistically reliable, although aural data are subject to some uncertainty of interpretation.

9.5.1 Definitions

A *whistler* is a terrestrial noise that originates in some electrical discharge below the ionosphere and is propagated through the ionosphere along highly dispersive paths. The name derives from the sound heard on a high-gain audio amplifier connected to an antenna. A whistler is usually characterized by one or more components of the nature of gliding tones, which descend in frequency through the audio range in times ranging from a fraction of a second to several seconds. Ordinary whistlers do not have echoes, hybrid traces, noses, etc.

Nose whistlers have simultaneous rising and falling tones joined together in a continuous and smooth manner at the frequency of minimum time delay, called the nose frequency, see Eq. (9-54). Normally, this unique property can be determined only by spectrographic analysis. At frequencies near the nose frequency, the energy behaves like an impulse. The change of frequency with time becomes infinite at the nose frequency. The dispersion characteristics of the descending tones of the nose whistler are similar to those of whistlers which do not exhibit the nose. Figure 9-25 shows nose whistlers. *Multiple* whistlers have two or more components closely associated in time. There are two types, the *multi-path*, where each component appears to originate in the same discharge, and the *multi-source*, where each component appears to originate in a separate discharge. Figure 9-26 shows multi-source whistlers. A *short* whistler is one which has travelled once along its dispersive path. It is often called *one hop*. A *long* or *two hop* whistler has travelled twice along its dispersive path. A *hybrid* is the combination of a long and a short whistler produced by a single discharge. The *echo train* is a succession of whistlers resulting from repeated traverses of the original disturbances through the ionosphere. Usually the time delays of echoes of short whistlers are in the ratios 1:3:5:7: . . ., while for long whistlers the ratios are 2:4:6:8: . . . Echoes of multi-path whistlers sometimes exhibit delays which are combinations of integral multiples of the basic one-hop delays. Figure 9-27 is an idealized presentation of echo trains.

Atmospherics of interest in whistler research are: *ordinary impulse*, an atmospheric with no special characteristic; *tweek*, an atmospheric that sounds like a very short ordinary whistler; and *bonk*, an unusually long ordinary impulse.

Dispersion, D, is a weighted measure of the time delay from the origin of the lightning flash to the appearance of whistler energy; D has the physical dimension of the square root of time, see Eq. (9-53).

Ionospherics, also known as ionospheric noise, are in the same frequency range as whistlers. However, they originate within the outer ionosphere, the ionosphere, or

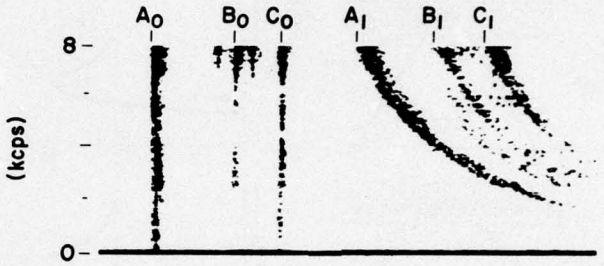


Fig. 9-26. Multi-source whistlers, A_1, B_1, and C_1, and atmospherics, A_o, B_o, C_o.

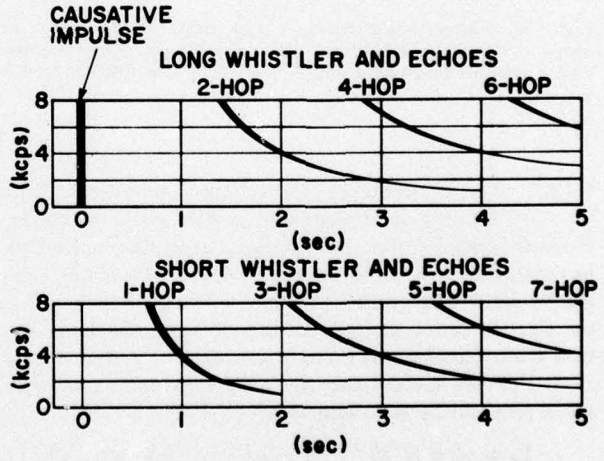


Fig. 9-27. Idealized whistler echo trains.



Fig. 9-25. Two, and possibly more, closely spaced nose whistlers.

possibly the exosphere. They are not associated with whistlers, but are usually associated with magnetic disturbances. Three types of ionospherics are hiss, discrete emissions, and dawn chorus. *Hiss* is a relatively steady noise which has many of the characteristics of thermal-type noise. Usually, the power spectrum of the noise is frequency dependent, and it may change in shape and intensity with time in periods of several seconds or more. *Discrete emissions* are well-defined noises, which may have a tonal quality that have durations on the order of a few tenths to several seconds or more. A definite and repeating frequency-time relation is often observed; these emissions are also referred to as *discrete events*. Examples are the hook and falling tones and the risers. Figure 9-28 shows risers. The *dawn chorus* is a series of many discrete emissions, often overlapping, with time separation of less than one second. Figure 9-29 shows dawn chorus. They are often called simply chorus, since maximum occurrence is not necessarily at dawn; there is, however, a latitude dependence.

Composite noises that have the combined characteristics of whistlers and ionospherics are referred to as *interactions*. They may be initiated by lightning discharges and can involve either the continuous or discrete types of ionospherics. They are often associated with magnetic disturbances.

The magneto-ionic parameters (MKSA units) used for electrons are X and Y, defined by Eq. (9-32) and Eq. (9-35). For singly charged ions the parameters are

$$X_i = F_N^2/f^2 = (m_e/m_i)\ X, \qquad (9\text{-}45)$$

and

$$Y_i = f_i/f = (m_e/m_i)\ Y, \qquad (9\text{-}46)$$

where F_N is the plasma frequency of the ion, $F_N = (N_i e^2/4\pi^2 \epsilon_o m_i)^{1/2}$, f_i is the gyrofrequency of the ion, $f_i = eB/2\pi m_i$, m_i is the mass of the ion, m_e is the mass of the electron, and N_i is the number of ions per unit volume (ion density).

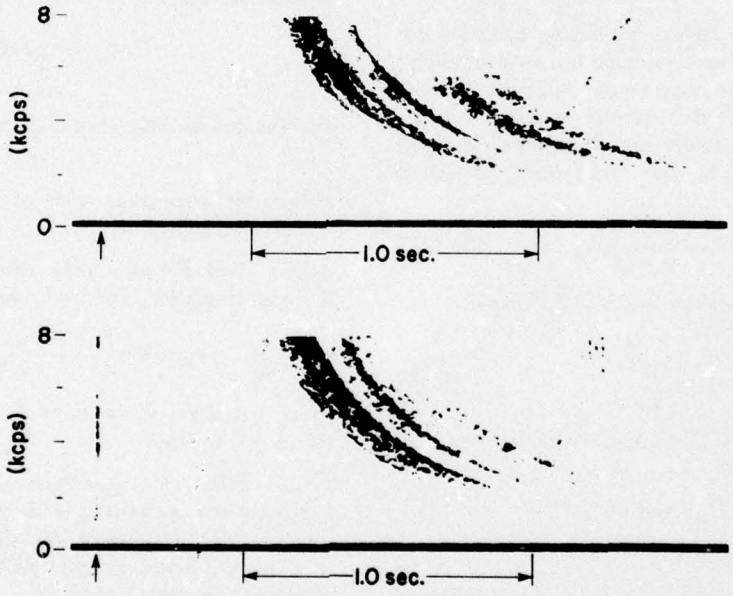


Fig. 9-28. Whistler followed by riser; upper curve observed at Seattle, lower curve at Stanford, 1336:25 UT, 3 April 1959.

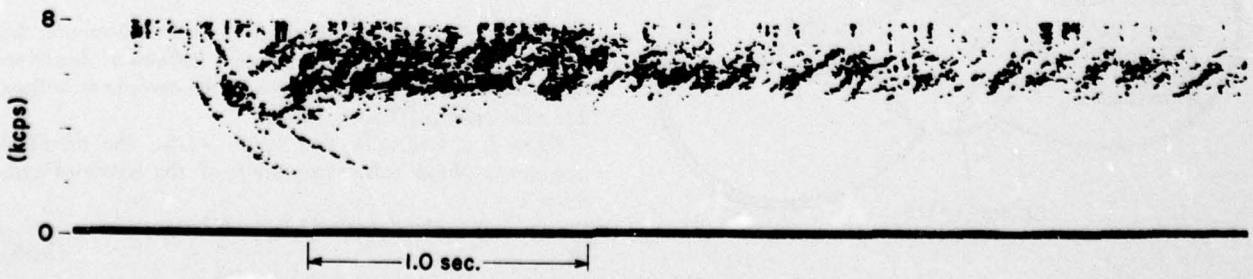


Fig. 9-29. Whistler followed by dawn chorus.

9.5.2 Theory of Whistlers and Ionospherics

Whereas whistlers are excited by lightning discharges below the ionosphere, ionospherics are generated in the ionosphere and possibly in the exosphere. Proposed models for the source of excitation include a traveling-wave amplification model [Gallet, 1959], a Cerenkov radiation model [Ellis, 1959], and a Doppler-shifted radiation model [Dowden, 1962]. Theory assumes that the whistler energy follows the earth's magnetic field lines quite closely. Ray tracing techniques are used to obtain propagation paths for individual whistlers through the ionosphere and exosphere. Figure 9-30 shows an example of whistler guidance by magnetic field lines. The whistler guidance mechanism is assumed to apply to the propagation of ionospherics [Allcock, 1957].

Magneto-ionic theory [Ratcliffe, 1959] applies to the analysis of whistler propagation. Because the effect of the earth's magnetic field has to be taken into account, the medium is anisotropic and, therefore, not only phase but also group refractive index expressions and the corresponding velocities must be considered.

9.5.2.1 *Phase Refractive Index, Neglecting Collision Effects.* The Appleton-Hartree expression has two solutions; the ordinary and extraordinary mode. Although the former cannot propagate in the whistler frequency range, the extraordinary mode usually can. The phase refractive index for propagation in the longitudinal direction (θ equals zero) is

$$n_L^2 = 1 - \frac{X}{1-Y} . \tag{9-47}$$

If Y is very much greater than one, and X/Y is also very much greater than one, then

$$n_L^2 = \frac{X}{Y} . \tag{9-48}$$

Equation 9-48 is applicable to many whistler problems provided the inequalities,

$$f_N^2 >> f f_H, \text{ and } f_H > f,$$

are reasonable assumptions. For medium and low latitudes and at frequencies below 10 kcps, f_H usually is greater than f. At θ equals 90°, the phase refractive index of the extraordinary mode is imaginary for the whistler frequency range so that energy cannot be propagated in a direction perpendicular to the magnetic field.

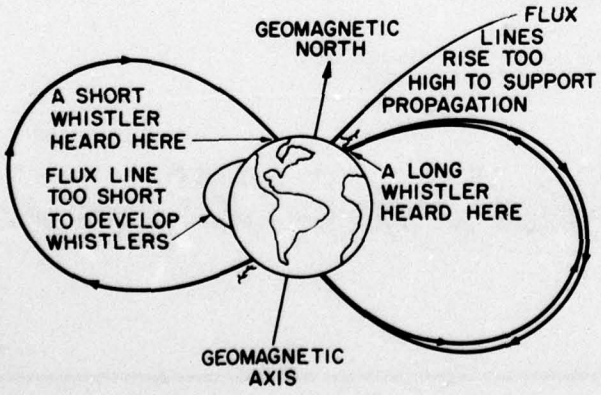


Fig. 9-30. Schematic representation of whistler guidance by the lines of force of the geomagnetic field.

9.5.2.2 *Eckersley Dispersion Law.* The group velocity, v_g is

$$v_g = c\left(n + f\frac{dn}{df}\right)^{-1}. \tag{9-49}$$

From this, if Eq. (9-48) is applicable, one obtains

$$v_g = 2c\,(f f_H)^{1/2}/f_N. \tag{9-50}$$

The time delay, t, from the origin to the appearance of the whistler at a given location is

$$t = \int_{path} \frac{ds}{v_g} . \tag{9-51}$$

By substituting Eq. (9-50) into this and defining D, the dispersion, as

$$D = \frac{1}{2c}\int_{path} f_N f_H^{-1/2}\, ds, \tag{9-52}$$

one obtains the Eckersley dispersion law,

$$t = Df^{-1/2}. \tag{9-53}$$

Hence, for a constant value of D, the plot of t vs $f^{-1/2}$ will be a straight line.

9.5.2.3 *Nose Frequency.* By using Eq. (9-47) instead of the approximation, Helliwell and Morgan [1959] obtain

$$v_g = 2c\left[\frac{f^{1/2}(f_H - f)^{3/2}}{f_H f_N}\right], \tag{9-54}$$

which has a maximum for $f = f_H/4$; this maximum f is the nose frequency.

9.5.2.4 *Effect of Ions, Neglecting Collisions.* The following equations apply to a cold, electrically neutral plasma that has a single kind of ion, singly charged. For $f_i < f << f_H$, the modified longitudinal phase refractive index of the extraordinary mode is

$$n_L^2 = f_N^2/f_H(f_i + f),$$

or

$$n_L^2 = \frac{X}{Y}\left[\frac{1}{Y(m_e/m_i)+1}\right]. \tag{9-55}$$

Because most of the whistler path is in the exosphere, the proton is the significant ion, hence a method of detecting the presence of ionized hydrogen in the exosphere utilizes this relationship [Storey, 1956].

When $f_i < f << f_H$ and $f_N^2 >> f_i f_H$, the modified transverse phase refractive index of the extraordinary mode is

$$n_T^2 = f_N^4/(f_N^2 f_i f_H - f_H^2 f^2),$$

or

$$n_T^2 = X^2/\left(\frac{m_e}{m_i}Y^2X - Y^2\right). \tag{9-56}$$

so that if $f_N^2 f_i f_H > f_H^2 f^2$, transverse propagation is possible. Typical numerical calculations show this to be the case in the 1 to 3 kcps region [Hines, 1957].

9.5.3 Theory of Hydromagnetic Waves

The main purpose of this section is to point out that the magneto-ionic theory can be extended to the subaudio range and the resulting two hydromagnetic modes, provided that the motion of ions is considered although effects of collisions are neglected. Guidance of hydromagnetic waves along the geomagnetic field lines is considered possible for a lower frequency limit of about 1 cps.

The exact solution is available only for the longitudinal case. The equation,

$$n_L^2 = 1 - \frac{f_N^2}{f(f \pm f_H)} - \frac{F_N^2}{f(f \pm f_i)} ,$$

or (9-57)

$$n_L^2 = 1 - \frac{X}{1 \pm Y} - \frac{(m_e/m_i)\, X}{1 \pm (m_e/m_i)\, Y} ,$$

is valid in the whistler-hydromagnetic wave range of frequencies [Booker, 1962].

The theory [Astrom, 1950] shows that the approximation for the ordinary mode can propagate for all angles, while the one for the extraordinary mode cannot propagate for $\theta = 90°$. The following expressions are valid only for wave frequencies well below the gyromagnetic frequency of the particular ion. For the ordinary mode,

$$n^2 = 1 + \frac{c^2}{v_A^2} ,$$

or (9-58)

$$n^2 = 1 + \frac{X}{(m_e/m_i)\, Y^2} .$$

For the extraordinary mode,

$$n^2 = 1 + \frac{c^2}{v_A^2 \cos^2 \theta} ,$$

or (9-59)

$$n^2 = 1 + \frac{X}{(m_e/m_i)\, Y^2 \cos^2 \theta} .$$

The *Alfvén speed*, v_A, is $B/(\rho \mu_o)^{1/2}$, where ρ is the plasma density; $\rho \approx N_i m_i$.

9.5.4 Whistlers, Observations

Many more whistlers are heard during the night than during the day, probably as a result of D region absorption. The overall whistler rate reaches a peak at about 50° geomagnetic latitude; whistlers are virtually unknown at latitudes near the equator. During 1958, stations at geomagnetic latitudes lower than roughly 52° and greater than 62° showed a wintertime maximum in whistler occurrence, whereas stations between 52° and 62° showed a summertime maximum. This may be related to the difference in the behavior of long and short whistlers. Figure 9-31 shows records for four stations. There is a large annual variation in monthly average whistler dispersion with a minimum in June or July and a maximum in November, December or January. Daily whistler rates show little correlation with the daily average magnetic index.

Comparison of the rates of whistler coincidence from many pairs of stations indicates that, when the distance between stations exceeds 1000 km (except for conjugate pairs), the occurrence tends to be independent. However, very strong whistlers are often detected by stations many thousands of kilometers apart. Comparison of whistler components, recorded simultaneously at spaced stations, indicates that a component of average strength spreads over an area with a radius of roughly 500 km before it disappears into the background noise.

Ordinary whistlers constitute the bulk of those included in routine analysis. It should be noted that during a two-minute recording period all short whistlers are similar in appearance. Detailed analysis of two or more whistlers from the same run shows that the delays from source to individual traces are very nearly the same.

The delays of components in whistler echo trains have been studied in some detail. In the frequency range 4 to 8 kcps, the time spacing between successive hops, measured at a fixed frequency, is constant throughout any train. In nearly all cases where both long and short whistlers appear on the same record, an integral relation exists between the delays of the short and long whistlers. Only a few hybrid whistlers have been found. A number of whistlers have been recorded that exhibit types of anomalous characteristics. Although the occurrence rate of nose whistlers is quite low, they are useful because the effective latitude of the propagation path can easily be obtained from the nose frequency. The two commonly used parameters from nose whistlers are the nose frequency and the time delay of the nose.

According to one model of the outer ionosphere that fits the present data satisfactorily, electron densities are proportional to geomagnetic field strength. Figure 9-32 shows this model. An electron density of about 2000, 500, and 100 cm^{-3} at two, three, and five earth radii respectively is indicated for both December and June.

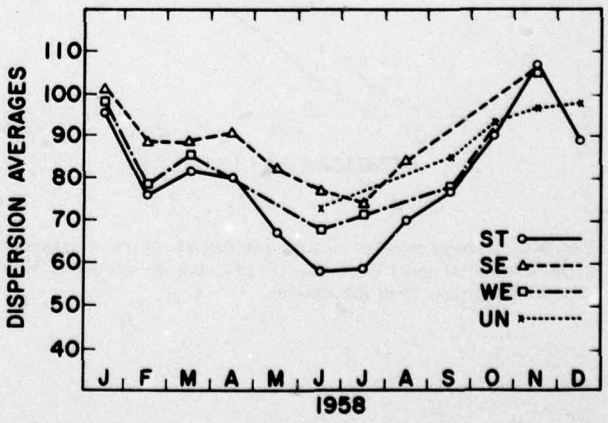


Fig. 9-31. Monthly averages of dispersion (see Eq. 9-53) for Stanford (ST), Seattle (SE), Wellington (WE), and Unalaska (UN) from measurements at 5 kpcs.

Controlled whistler-mode observations at Cape Horn, South America, resulting from a 15.5 kcps transmission at Annapolis, Maryland, demonstrate that audio energy can propagate along the lines of the earth's magnetic field [Helliwell and Gehrels, 1958].

The low frequency portions of experimentally determined dispersion curves of several low-altitude whistlers do not follow the Eckersley dispersion law (Eq. 9-53); the effect of protons could account for this discrepancy [Barrington and Nizhizaki, 1960].

9.5.5 Occurrence Statistics of Ionospherics

Dawn chorus and hiss occur most often near geomagnetic latitudes of 56° and 80° with distribution skewed toward the higher latitudes. Figure 9-33 shows the distribution for disturbed and for quiet days. As a result of the dependence on local magnetic activity it appears that dawn chorus activity, like the aurora, moves toward the equator during geomagnetically disturbed periods. Dawn chorus and hiss occur more frequently on days of low background noise than on days of high noise. A long lasting type of discrete emission has been observed in the auroral zone at Kiruna, Sweden; the maximum intensity occurs near 750 cps which is the proton gyrofrequency at 100 km [Gustafson et al, 1960].

Figure 9-34 shows an Alfvén velocity profile from about 300-km altitude to below 10^5-km altitude. Figure 9-35 is a logarithmic plot of the phase velocities vs angular frequency in the ionosphere; the sub-audio range and the effect of collisions is included.

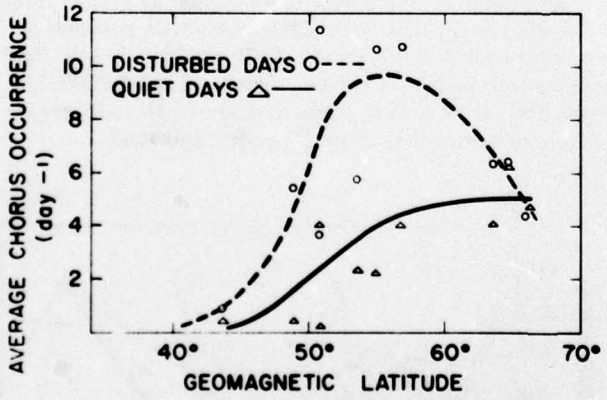


Fig. 9-33. Average number of runs per day of chorus vs geomagnetic latitude on quiet days ($K_p \leq 1.5$) and on disturbed days ($K_p \geq 4.0$); data from ten stations.

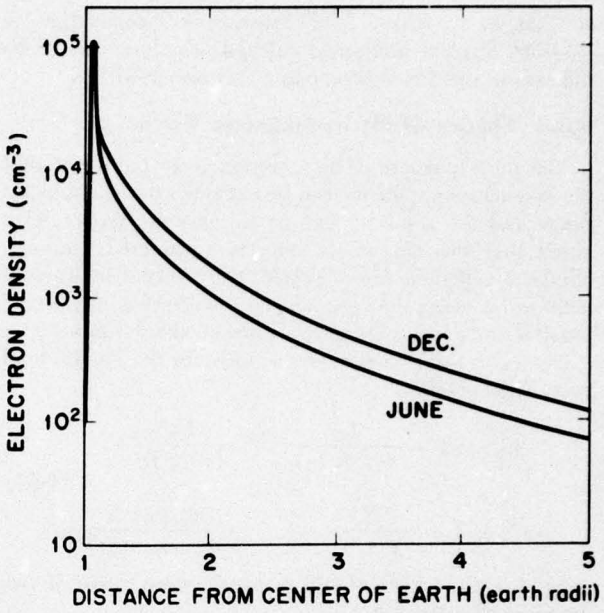


Fig. 9-32. Gyrofrequency model of electron number densities in the outer ionosphere.

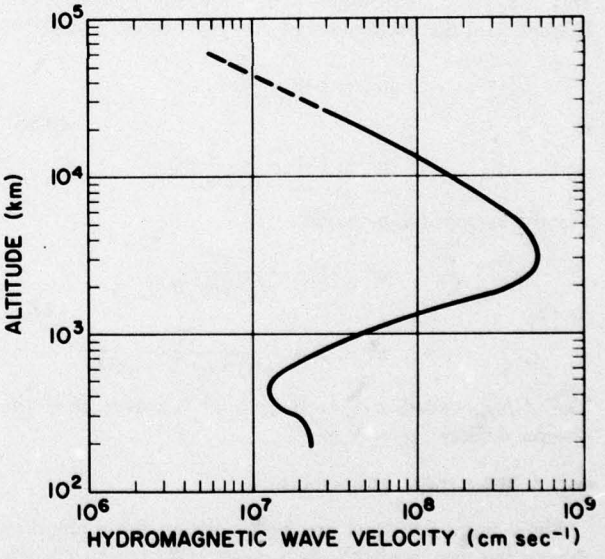


Fig. 9-34. Hydromagnetic wave velocity vs altitude in the geomagnetic equatorial plane, assuming a field of 0.315 gauss at the surface. (From A. J. Dessler, W. E. Francis, and E. N. Parker, *J. Geophys. Res.*, v. 65, p. 2715, 1960, by permission.)

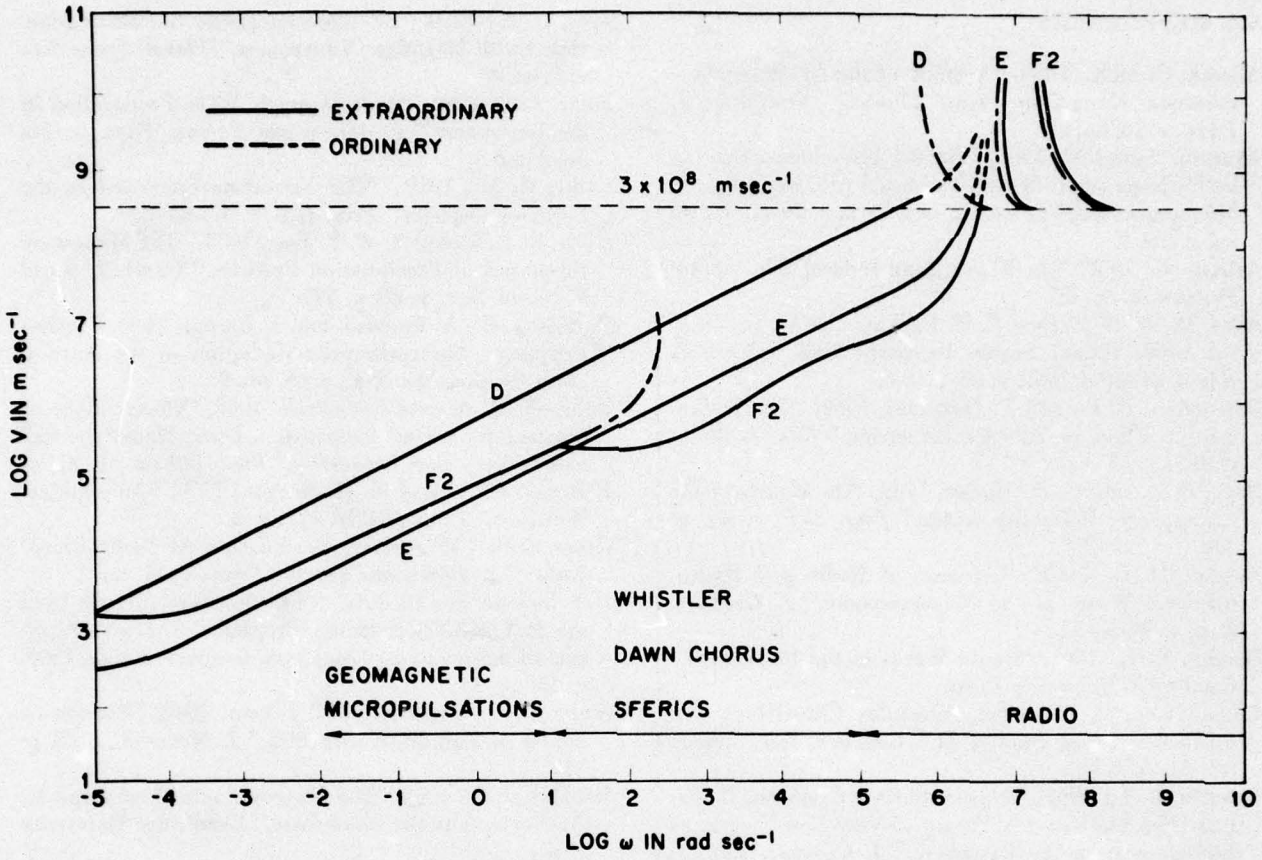


Fig. 9-35. Phase velocity, V, as a function of angular frequency, ω, for hydromagnetic waves in the F2, E, and D regions of the ionosphere. (After Akasofu [1960].)

9.6 REFERENCES

Allcock, G. McK., 1957, "A Study of the AF Radio Phenomenon Known as Dawn Chorus," *Australian J. Phys.*, v. 10, no. 2.

Akasofu, Syun-Ichi, 1960, "On the Ionospheric Heating by Hydromagnetic Waves Connected with Geomagnetic Micropulsations," *J. Atmos. and Terrest. Phys.*, v. 18, no. 2 and 3.

Astrom, E., 1950, "On Waves in an Ionized Gas," *Arkiv Fysik*, v. 2, no. 42.

Atlas, D., W. G. Harper, F. H. Ludlam, and W. C. Macklin, 1960, "Radar Scatter by Large Hail," *Quart. J. Royal Meteorol. Soc.*, v. 86, p. 468.

Barrington, R. E., and T. Nizhizaki, 1960, "The Hydrogen-Ion Effect in Whistler Dispersion," *Can. J. Phys.*, v. 38, no. 12.

Bean, B. R., and G. D. Thayer, 1959, "On Models of the Atmospheric Refractive Index," *Proc. IRE*, v. 47, p. 740.

Booker, M. G., 1962, "Guidance of Radio and Hydromagnetic Waves in the Magnetosphere," *J. Geophys. Res.*, v. 69, no. 11.

Buddin, K. G., 1961, "Radio Waves in the Ionosphere," Cambridge University Press.

Cunningham, R. M., 1962, "Cumulus Climatology and Refractive Index Studies II," *Geophys. Res. Papers No. 51*, AFCRL.

Dowden, R. L., 1962, "Doppler-Shifted Cyclotron Radiation from Electrons: A Theory of Very Low Frequency Emissions from the Exosphere," *J. Geophys. Res.*, v. 67, no. 5.

Edlen, B., "Dispersion of Standard Air," 1953, *J. Opt. Soc. Am.*, v. 43, p. 339.

Ellis, G. R., 1959, "LF Electromagnetic Radiation Associated with Magnetic Disturbances," *Planet. Space Sci.*, v. 1, no. 4.

Fejer, J. A., 1960, "Hydromagnetic Wave Propagation in the Ionosphere," *J. Atmos. and Terrest. Phys.*, v. 18, no. 2 and 3.

Gallet, R. M., 1959, "VLF Emissions Generated in the Earth's Exosphere," *Proc. IRE*, v. 47, no. 2.

Gunn, K. L. S., and T. W. R. East, 1954, "The Microwave Properties of Precipitation Particles," *Quart. J. Royal Meteorol. Soc.*, v. 80, p. 522.

Gustafson, G., A. Egeland, and J. Aarons, 1960, "Audio-Frequency Electromagnetic Radiation in the Auroral Zone," *J. Geophys. Res.*, v. 65, no. 9.

Helliwell, R. A., and E. Gehrels, 1958, "Observations of Magneto-Ionic Duct Propagation Using Man-Made Signals of Very Low Frequency," *Proc. IRE*, v. 46, no. 4.

Helliwell, R. A., and M. G. Morgan, 1959, "Atmospheric Whistlers," *Proc. IRE*, v. 47, no. 2.

Hines, C. O., 1957, "Heavy-Ion Effect in AF Radio Propagation," *J. Atmos. and Terrest. Phys.*, v. 11, no. 1.

IGY Bulletin No. 57, 1962, "Whistlers-West Results from the IGY/IGC-59 Synoptic Program," National Academy of Sciences (see *Trans. Am. Geophys. Union*, 1962, v. 43, no. 1).

Marshall, J. S., and W. McK. Palmer, 1948, "The Distribution of Raindrops with Size," *J. Meteorol.*, v. 5, p. 165.

Ratcliffe, J. A., 1959, "The Magneto-Ionic Theory and Its Applications to the Ionosphere," Cambridge University Press.

Storey, L. R. O., 1956, "A Method to Detect the Presence of Ionized Hydrogen in the Outer Atmosphere," *Can. J. Phys.*, v. 34, no. 11.

Chapter 10

TRANSMISSION AND DETECTION OF INFRARED RADIATION

Sections 10.1, 10.2 John N. Howard
Section 10.3 John S. Garing
Section 10.4 Russell G. Walker

10.1 SOURCES AND DETECTORS

10.1.1 Infrared Radiation Sources

Monochromatic radiation incident on the surface of a substance is either reflected, absorbed, or transmitted; i.e., the sum of the three fractional coefficients of reflectance, absorptance, and transmittance of a given substance equals unity. A substance that neither reflects nor transmits at a given wavelength, but completely absorbs the incident radiation, is *black* at that wavelength; a substance that completely absorbs radiation of all wavelengths is called a *blackbody* (see Appendix B).

For many practical purposes, the source of infrared radiation is a heated object that emits *thermal radiation,* which is assumed to be produced by the agitation of the molecules of the substance. The intensity distribution of thermal radiation is *continuous* (emission at all wavelengths); the spectral distribution depends on the temperature and emissivity of the body. The emissivity of a material is numerically equal to its absorptivity; for a blackbody, the emissivity is unity.

A thermal radiator that emits only a fraction of the total radiation of a blackbody at the same temperature, but has the same efficiency of radiation at all wavelengths (constant emissivity), is called a *gray body.* The emissivity of a gray body is equal to the ratio of its thermal radiation to that of a blackbody at the same temperature. For most engineering applications, either a blackbody or a gray body is assumed. Usually, an actual substance will be neither black nor gray but will have an emissivity that is a function of wavelength.

10.1.2 Infrared Detectors

Table 10-1 lists operating temperatures and approximate useful wavelength ranges of 12 common types of infrared detector.

The photographic detector is most useful for fast recording of spectra in the near infrared region. Although photoemissive detectors, such as the vacuum and gas photocells and the photomultiplier, are capable of fast response, they respond only at wavelengths shorter than about one micron. The lead-salt detectors change resistance in proportion to the intensity and wavelength of the incident radiation; the effect, however, is much larger than a simple thermal change. These detectors have maximum sensitivity in certain narrow spectral regions, usually 1 or 2 μ wide. The wavelength interval, however, can be varied somewhat by a change of temperature of operation of the detector. For sensitivity to wavelengths longer than 5μ, one must choose either a thermal-type detector, such as a bolometer, a pneumatic detector, or a thermocouple, or one of the newer quantum detectors that are produced by doping certain semiconductors with impurities. Both types have disadvantages as infrared detectors; the thermal type is generally slow in response time, and the quantum detector must be cooled to temperatures of liquid nitrogen or even liquid helium. Because of the difficulty of including the required cryogenic accessories, quantum detectors are not used in satellite-borne instruments.

Table 10-1. Characteristics of some infrared detectors.

Type	Operating Temp. (°K)	Approx. Useful Range (μ)
Photographic	—	up to 1.4
Photoemissive	—	up to 1.1
Lead Sulfide	295-0	0.3 - 2.7
	90	0.3 - 3.8
Lead Telluride	90	1.5 - 5.1
Lead Selenide	295-0	1.5 - 5.1
	90	1.5 - 7.1
Pneumatic (Golay)	—	above 0.2
Bolometer—metal strip	—	above 1
Bolometer—thermistor	—	above 1
Thermocouple	—	above 1
Indium Antimonide	78	1 - 5.8
Germanium, copper-doped	4	4 - 29
Germanium, zinc-doped	4	4 - 40

CHAPTER 10

For detailed information on the characteristics of infrared detectors, see Kruse et al [1962]; for a discussion of operating conditions and curves of relative spectral sensitivity, see Potter and Eisenman [1962].

10.1.3 Infrared Window Materials

When sources and detectors of infrared radiation must be enclosed in a vacuum or in a special atmosphere, the enclosure requires windows to transmit the infrared radiation. Some of the optical characteristics of standard infrared prism and window materials are presented in Fig. 10-1.

10.2 ATMOSPHERIC ABSORPTION

The main causes of atmospheric attenuation of infrared radiation are absorption and scattering by molecular constituents and scattering by aerosols such as smoke, fog, and haze particles.

This section is concerned primarily with molecular absorption and the dependence of this absorption on concentration, pressure, and temperature. For a discussion of attenuation by scattering, see Sec. 7.4.

Figure 10-2 presents a typical spectrum (1 to 15 μ) of sunlight at the earth's surface and laboratory spectra of molecules known to be present in the atmosphere. Comparison of the so-called solar spectrum with the molecular spectra shows that all the principal regions of absorption in the atmosphere are due to H_2O, CO_2, and O_3. Because ozone exists chiefly in the stratosphere, the strong absorption band near 9.6 μ can be neglected in problems of transmission along horizontal paths near ground level. For most practical applications, the absorption bands of the other minor constituents are of negligible importance.

The first major problem in computing atmospheric transmission is the estimation in the atmospheric path of water vapor, one of the principal absorbers of infrared radiation. The concentration is usually reported as precipitable centimeters of water, W, which is the thickness of the liquid that would be formed if all the water vapor traversed by a beam of uniform cross section were completely condensed in a container of cross section equal to that of the beam (Sec. 3.4). Figure 10-3 relates the amount of precipitable centimeters of water per kilometer in a horizontal path at ground level to the ambient temperature and relative humidity. In a real atmosphere, the relative amount of water vapor falls off as a function of altitude (Fig. 3-20; Table 3-25). Gutnick [1962] contains tables that facilitate the computation of the amount of water vapor contained in long oblique atmospheric paths.

A measure often used to specify the CO_2 concentration is the atmosphere-centimeter (atm-cm). This is the length in centimeters of a column whose volume would contain the same number of molecules of CO_2 gas at NTP as a column of the same cross section, but of arbitrary length, pressure, and temperature. Because the atmospheric abundance of CO_2 is approximately 0.03% by volume, the absorber concentration of CO_2 at ground level is about 30 atm-cm per kilometer of path.

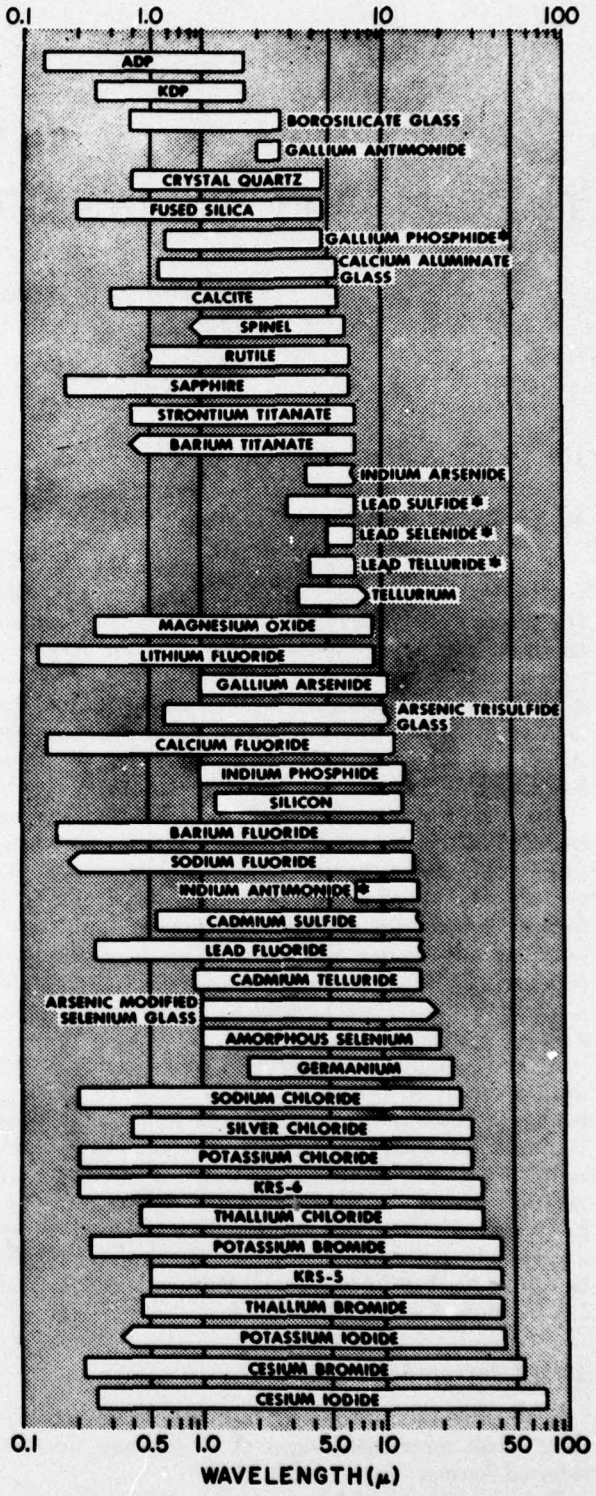


Fig. 10-1. Transmission regions of optical materials. The long and short cutoffs are the wavelengths at which a sample 2-mm thick has 10% transmission. Materials marked with an asterisk have a maximum transmittance (uncorrected for reflection and scattering) less than 10%.

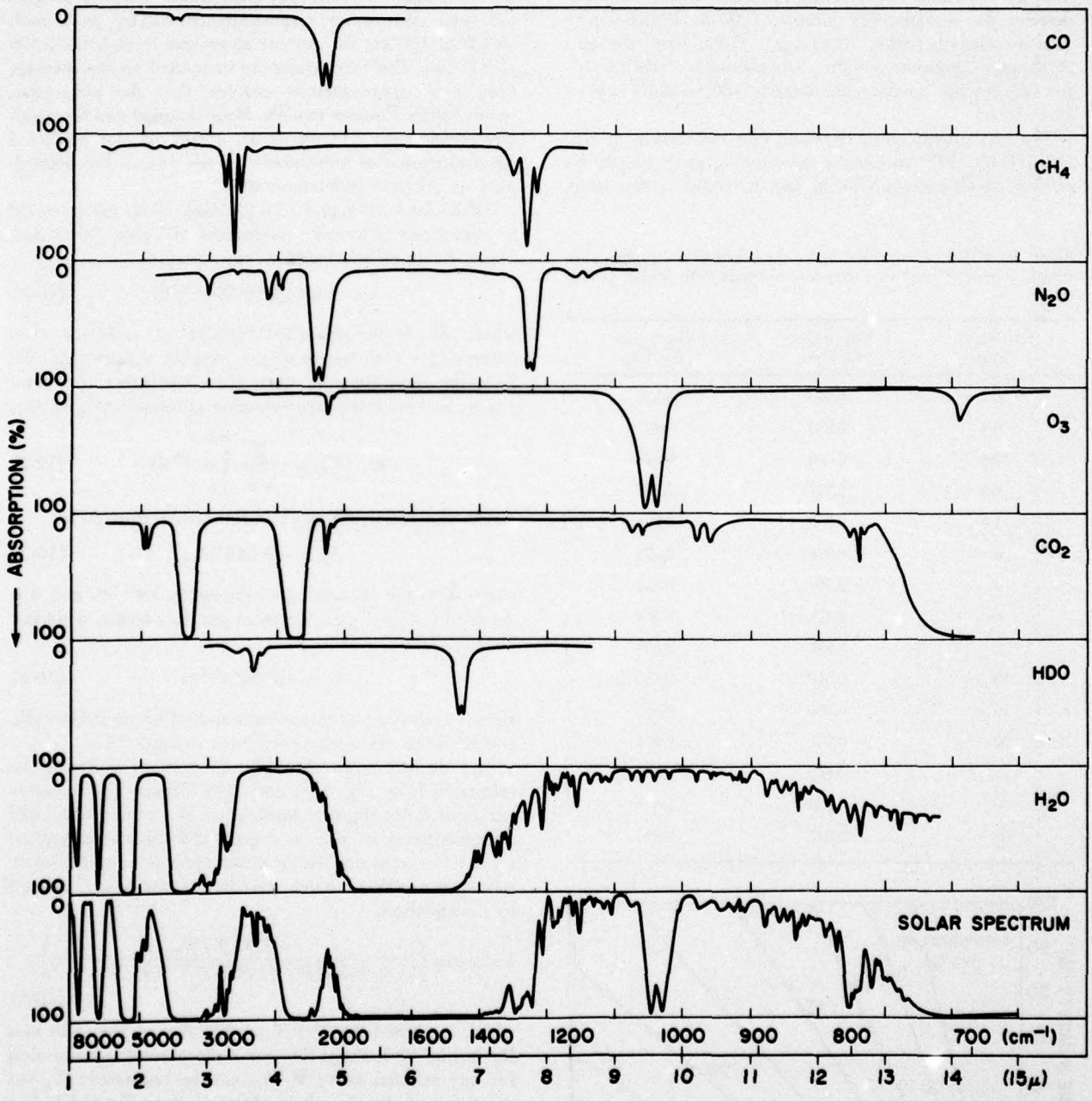


Fig. 10-2. Comparison of the near-infrared solar spectrum with laboratory spectra of various atmospheric gases.

CHAPTER 10

Table 10-13 (at end of chapter) gives the sea-level atmospheric transmittance (ratio of received radiation to source radiation) as a function of the number of precipitable cm of H_2O contained in the total volume occupied by the beam between the radiation source and the detector for wavenumber interval 1000 to 10,000 cm^{-1} (the wavelength region 10 to 1 μ). Table 10-14 (at end of chapter) presents similar data (between 1 and 15 μ) for CO_2 for the wavenumber interval 550 to 10,000 cm^{-1} (1 to 15 μ).

The concentrations of H_2O and CO_2 decrease with altitude. Table 10-2 shows the increase in path length required, at altitudes up to 35 km, to result in the same absorption as at ground level. For example, at a wavelength of 1.34 μ (7450 cm^{-1}) and a path length of 66 km, the transmittance of *dry* air at ground level is 0.816 (Table 10-14). At an altitude of 4 km, the correction for CO_2 is 0.450; therefore, the path length required to give the same absorption (transmittance 0.816) as a path length of 100 km for dry air at ground level is 66/0.450 = 147 km. The corrections are computed on the assumption, only approximately correct, that the absorption bands follow Elsasser models. More detailed and thorough treatments exist [Wyatt et al, 1962] of the predicted spectral profile of atmospheric bands and of the dependence on pressure and temperature.

Table 10-2. Path corrections for various altitudes (divide path length at ground level by correction to obtain path length at altitude).

Altitude (km)	Correction for H_2O	Correction for CO_2
0.2	0.983	0.957
0.4	0.973	0.923
0.6	0.960	0.888
0.8	0.947	0.857
1.0	0.935	0.826
2	0.876	0.676
4	0.767	0.450
6	0.672	0.302
8	0.592	0.204
10	0.518	0.135
15	0.350	0.043
20	0.237	0.014
25	0.160	0.004
30	0.110	0.001
35	0.077	0.0007

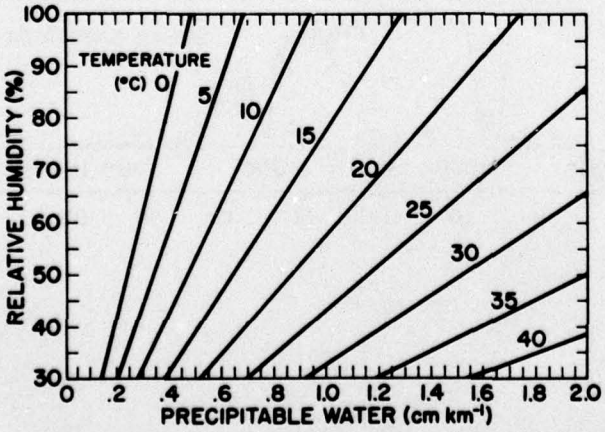


Fig. 10-3. Water-vapor concentration as a function of temperature and relative humidity.

Tables 10-3, 10-4, and 10-5 [McGee, 1962] are intended as extensions to longer wavelengths of Tables 10-13 and 10-14. Table 10-3 is based on the equation,

$$A_W = \text{erf}\,[\beta\,(\pi W)^{1/2}/2], \qquad (10\text{-}1)$$

where A_W is the absorbed fraction of radiation after traversing a path length of precipitable water vapor, W; β is the error-function absorption coefficient for water vapor; and erf is the error function (probability integral),

$$\text{erf}\,(X) = \frac{2}{\sqrt{\pi}}\int_0^X e^{-y^2}\,dy. \qquad (10\text{-}2)$$

The absorption law applied for carbon dioxide is

$$A_c = \text{erf}\,(Kd^{1/2}), \qquad (10\text{-}3)$$

where K is the absorption coefficient in $km^{-1/2}$, and d is the total sea-level path length in km. For ozone, a similar law is assumed,

$$A_z = \text{erf}\,(K'z^{1/2}). \qquad (10\text{-}4)$$

Here, z is the optical thickness in mm of ozone in the path, and K′ is the absorption coefficient in $mm^{-1/2}$.

The transmittance through water vapor can also be estimated from Fig. 10-4 and 10-5. Figure 10-4 presents curves of water vapor concentration, W_o, required to yield a transmittance of 50% as a spectral function. An empirical fit of a large number of measurements of water-vapor spectra shows that the data may be reasonably represented by the equation,

$$T_\lambda = \exp\left\{\frac{-1.97\,W/W_o}{[1 + 6.57\,(P_o/P)\,(T/T_o)^{1/2}\,(W/W_o)\,]^{1/2}}\right\}, \qquad (10\text{-}5)$$

which is plotted for $T = T_o = 273°K$ and $P = 740$ mm Hg in Fig. 10-5. From this curve the percent transmission for any selected ratio, W/W_o, can be estimated; W_o for any selected wavelength is obtained from Fig. 10-4. For example, from curve b, at 5 μ W_o is about 0.4 pr-cm of H_2O. At 5 μ, therefore, the transmissions are 9% for 4 pr-cm ($W/W_o = 10$), 50% for 0.4 pr-cm, and 86% for 0.04 pr-cm. Thus, a plot of transmission vs water-vapor concentration can be constructed for each wavelength of interest.

Engineering calculations that do not require the complete spectral contour use the energy transmitted through

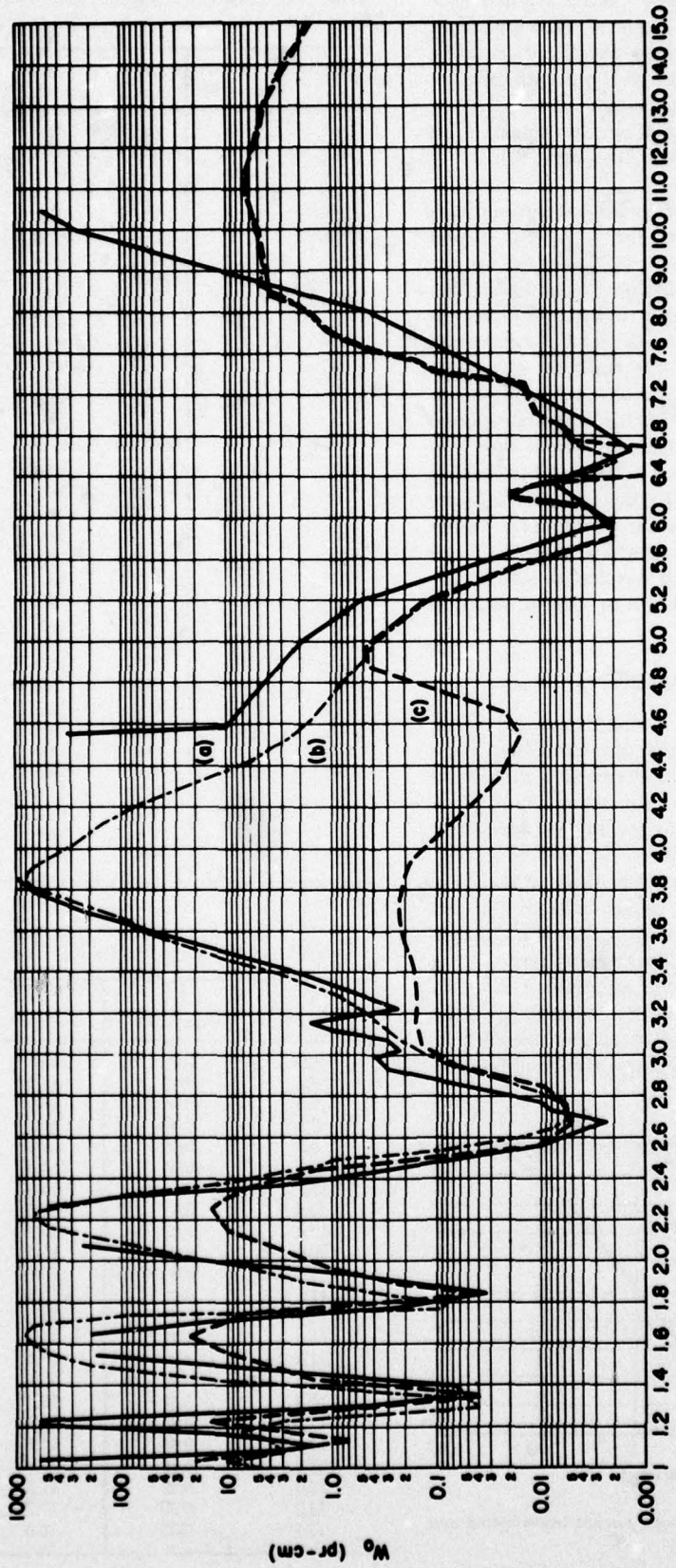


Fig. 10-4. A plot of the amount of H_2O required to yield 50% transmission, according to three different sources. (Curve c includes absorption due to CO_2.)

the entire *windows*, the regions of relative transparency between the strong absorption bands of CO_2 and H_2O. The principal atmospheric windows are listed in Table 10-6. Figure 10-6 gives a measure of the actual radiance (flux density per steradian) transmitted through these windows from blackbody sources at various temperatures for water-vapor concentrations of 0 (dry air), 0.1, 1, 10, 100, and 1000 pr-mm.

The two most important window regions for military and meteorological purposes are the 3- to 5-μ region and the 8- to 13-μ region. The 3- to 5-μ region is the approximate region of sensitivity of PbTe, PbSe, and InSb detectors that are used in many military equipments. This region also contains the strong 4.3 μ fundamental band of CO_2 that is present in the emission spectra of practically all fuels. Operation of many military systems is based on detection of this CO_2 band. The atmospheric infrared transmission in the 3- to 5-μ region is shown in Fig. 10-7, 10-8, and 10-9. Between 4.2 and 4.4 μ there is practically complete absorption by the CO_2 fundamental band. The other important region for atmospheric studies is that bounded on the short wavelength side by the 6.3-μ water-vapor band and on the long wavelength side by the 15-μ CO_2 band. This region is shown in spectral detail in Fig. 10-10 and 10-11.

10.3 ATMOSPHERIC EMISSION

According to Kirchhoff's law, a material or gas which absorbs strongly at some wavelength also has a high emissivity at that wavelength. Thus, as shown in Fig. 10-2, at those wavelengths where there are strong absorption bands, the earth's atmosphere has the highest emissivity and behaves in a manner similar to a 200° to 300°K blackbody. The molecules and aerosols of the atmosphere and clouds scatter the incident radiation from the sun (Sec. 7.4). There is also the emission from the various excited molecules formed in the upper atmosphere.

To calculate the emission of the atmosphere, a fairly complete knowledge of the composition (particularly the distribution of water vapor) and of parameters such as temperature and pressure is necessary. Reasonably accu-

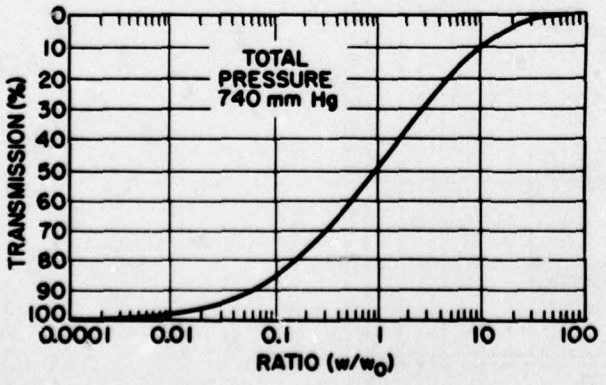


Fig. 10-5. Empirical relationship between percent transmission and water vapor content, see Eq. (10-5).

Table 10-3. Error-function absorption coefficients at sea-level conditions for water vapor, see Eq. (10-1).

λ (μ)	β ($cm^{-1/2}$)	λ (μ)	β ($cm^{-1/2}$)	λ (μ)	β ($cm^{-1/2}$)
7.0	4.96	14.0	0.32	21.0	2.08
7.2	4.76	14.2	0.32	21.2	2.17
7.4	1.70	14.4	0.34	21.4	2.26
7.6	0.84	14.6	0.34	21.6	2.34
7.8	0.51	14.8	0.35	21.8	2.41
8.0	0.41	15.0	0.36	22.0	2.46
8.2	0.35	15.2	0.45	22.2	2.62
8.4	0.26	15.4	0.48	22.4	2.73
8.6	0.23	15.6	0.52	22.6	2.85
8.8	0.23	15.8	0.57	22.8	2.91
9.0	0.23	16.0	0.61	23.0	2.97
9.2	0.23	16.2	0.64	23.2	3.10
9.4	0.23	16.4	0.70	23.4	3.17
9.6	0.23	16.6	0.74	23.6	3.31
9.8	0.23	16.8	0.78	23.8	3.39
10.0	0.22	17.0	0.84	24.0	3.55
10.2	0.22	17.2	0.90	24.2	3.64
10.4	0.22	17.4	0.92	24.4	3.73
10.6	0.21	17.6	0.97	24.6	3.88
10.8	0.21	17.8	1.02	24.8	3.93
11.0	0.21	18.0	1.06	25.0	3.93
11.2	0.21	18.2	1.11	25.2	4.04
11.4	0.22	18.4	1.15	25.4	4.16
11.6	0.22	18.6	1.20	25.6	4.22
11.8	0.22	18.8	1.25	25.8	4.42
12.0	0.22	19.0	1.32	26.0	4.76
12.2	0.23	19.2	1.40	26.2	4.96
12.4	0.23	19.4	1.47	26.4	5.21
12.6	0.23	19.6	1.55	26.6	5.51
12.8	0.24	19.8	1.60	26.8	5.92
13.0	0.26	20.0	1.66	27.0	6.20
13.2	0.26	20.2	1.74		
13.4	~27	20.4	1.82		
13.6	0.29	20.6	1.91		
13.8	0.29	20.8	1.99		

Table 10-4. Error-function absorption coefficients at sea-level conditions for carbon dioxide, see Eq. (10-3).

λ (μ)	K ($km^{-1/2}$)	λ (μ)	K ($km^{-1/2}$)
9.0	0.0	13.6	0.93
9.2	0.03	13.8	1.75
9.4	0.04	14.0	2.32
9.6	0.05	14.2	3.48
9.8	0.01	14.4	5.66
10.0	0.0	14.6	11.9
10.2	0.0	14.8	100+
10.4	0.0	15.0	100+
10.6	0.0	15.2	100+
10.8	0.0	15.4	11.9
11.0	0.0	15.6	4.88
11.2	0.0	15.8	3.48
11.4	0.0	16.0	2.47
11.6	0.0	16.2	1.58
11.8	0.0	16.4	1.02
12.0	0.01	16.6	0.64
12.2	0.02	16.8	0.38
12.4	0.03	17.0	0.22
12.6	0.06	17.2	0.13
12.8	0.10	17.4	0.08
13.0	0.18	17.6	0.05
13.2	0.30	17.8	0.03
13.4	0.55	18.0	0.0

rate calculations require machine computation, but for very rough calculations the atmosphere can be considered as a blackbody at about 250°K for wavelengths longer than about 2.7 μ. At shorter wavelengths, scattered sunlight begins to predominate, and the background radiation increases rapidly toward the visible. At night, there is no scattered sunlight but the OH emission and airglow become important sources at wavelengths below 2.7 μ.

10.3.1 Measurements from the Ground

Several sets of measurements of the atmosphere from the ground are available [Bell at al, 1960; Bennett et al, 1960; Bolle, 1963].

Figure 10-12 illustrates the effect of the angle of elevation and ambient temperature upon the spectral radiance of a clear sky. Near the horizon, where the atmospheric paths are large, the emissivity of the windows approaches unity and the radiation at all wavelengths is nearly that of a blackbody at ambient temperature. As the elevation angle is increased and the path length decreased, the regions of low spectral emissivity are no longer black. In the spectral regions of the 6.3-μ water-vapor band and 15-μ carbon dioxide band, where the spectral emissivity is very high, the sky remains black even at the zenith. The envelopes of the curves correspond closely to the radiation from a blackbody at the ambient temperature indicated. Figure 10-12 also shows the effect of the amount of the emitting molecular species. The increase of water vapor and carbon dioxide in the zenith sky at Florida (humid, sea level) over that at the Elk Park Station (dry, 11,000 ft) causes a greater emissivity in the 8- to 12-μ wavelength region and almost unit emissivity at wavelengths greater than 15 μ. The elevation dependence of the emissivity for a clear sky in the 4.6-μ and 8- to 13-μ spectral region can be approximated by the equation

$$\epsilon = 1 - \exp\left(-0.44 \csc^{1/2}\theta\right), \qquad (10\text{-}6)$$

where ϵ is the emissivity at elevation angle θ; emissivity at the zenith, $\theta = 90°$.

The variation of the radiance values with azimuthal angle is negligible in the high-emissivity regions of the spectrum near 6 and 15 μ. In the poorly emitting regions, generally the azimuthal angle variations for clear sky are almost negligible except for low-elevation angles ($< 30°$). At 7.5°, a smooth asymmetry of about 15% was observed when no visible cloud structure was apparent.

Figure 10-13 shows the sky's spectral radiance for the 1- to 5-μ range, which includes the region of strong scattering ($\lambda < 3\mu$). The emission is strongly dependent on temperature and elevation angle. The scattered radiation increases greatly as the elevation angle decreases and the length of the scattering path increases. (The decreases at 0.94, 1.1, 1.4, 1.9, and 2.7 μ are caused by the absorption of the water-vapor bands at these wavelengths.) The amount of scattered radiation also depends upon the position of the sun relative to the area of the sky observed as well as the amount of atmosphere producing the scattering.

Figure 10-14 shows a detailed example of the emission in the 8- to 13-μ window as a function of zenith angle. These curves were obtained at sea level at S. Agata, Italy. The ozone emission around 9.6 μ is evident.

Continuum absorption coefficients measured for the atmosphere in the 8- to 26-μ spectral region are shown in Fig. 10-15. This continuum absorption (the nonzero absorption between the absorption lines of the atmospheric constituents) appears to be due primarily to the wings of the 6.3-μ and pure rotational water-vapor lines. The continuum transmission $T(\lambda)$ at a wavelength λ can be found approximately from the equation

$$T(\lambda) = \exp\left[-Nk(\lambda)m\right], \qquad (10\text{-}7)$$

where N is the air mass (relative to zenith), $k(\lambda)$ is the value from Fig. 10-15 at λ, and m is the mass of water vapor in the vertical atmospheric column above unit area in g cm^{-2}. CO_2 absorption becomes important from about 12.6 to 17.9 μ. The extinction due to particulate matter is small compared to that due to water vapor throughout the range, 8 to 26 μ, except under very hazy dry conditions.

Table 10-5. Error-function absorption coefficients for ozone, see Eq. (10-4).

λ (μ)	K′ (mm$^{-1/2}$)	λ (μ)	K′ (mm$^{-1/2}$)
8.6	0.0	13.2	0.03
8.8	0.04	13.4	0.06
9.0	0.11	13.6	0.07
9.2	0.07	13.8	0.04
9.4	0.39	14.0	0.03
9.6	0.48	14.2	0.03
9.8	0.39	14.4	0.03
10.0	0.20	14.6	0.03
10.2	0.06	14.8	0.03
10.4	0.0	15.0	0.02
		15.2	0.02
12.2	0.0	15.4	0.02
12.4	0.01	15.6	0.01
12.6	0.01	15.8	0.01
12.8	0.01	16.0	0.01
13.0	0.02	16.2	0.0

Table 10-6. Designation of atmospheric windows.

Window Number	Wavelength Limits (μ)
I	0.72 - 0.94
II	0.94 - 1.13
III	1.13 - 1.38
IV	1.38 - 1.90
V	1.90 - 2.70
VI	2.70 - 4.30
VII	4.30 - 6.00
VIII	6.00 - 15.00
IX	15.00 - 25.00

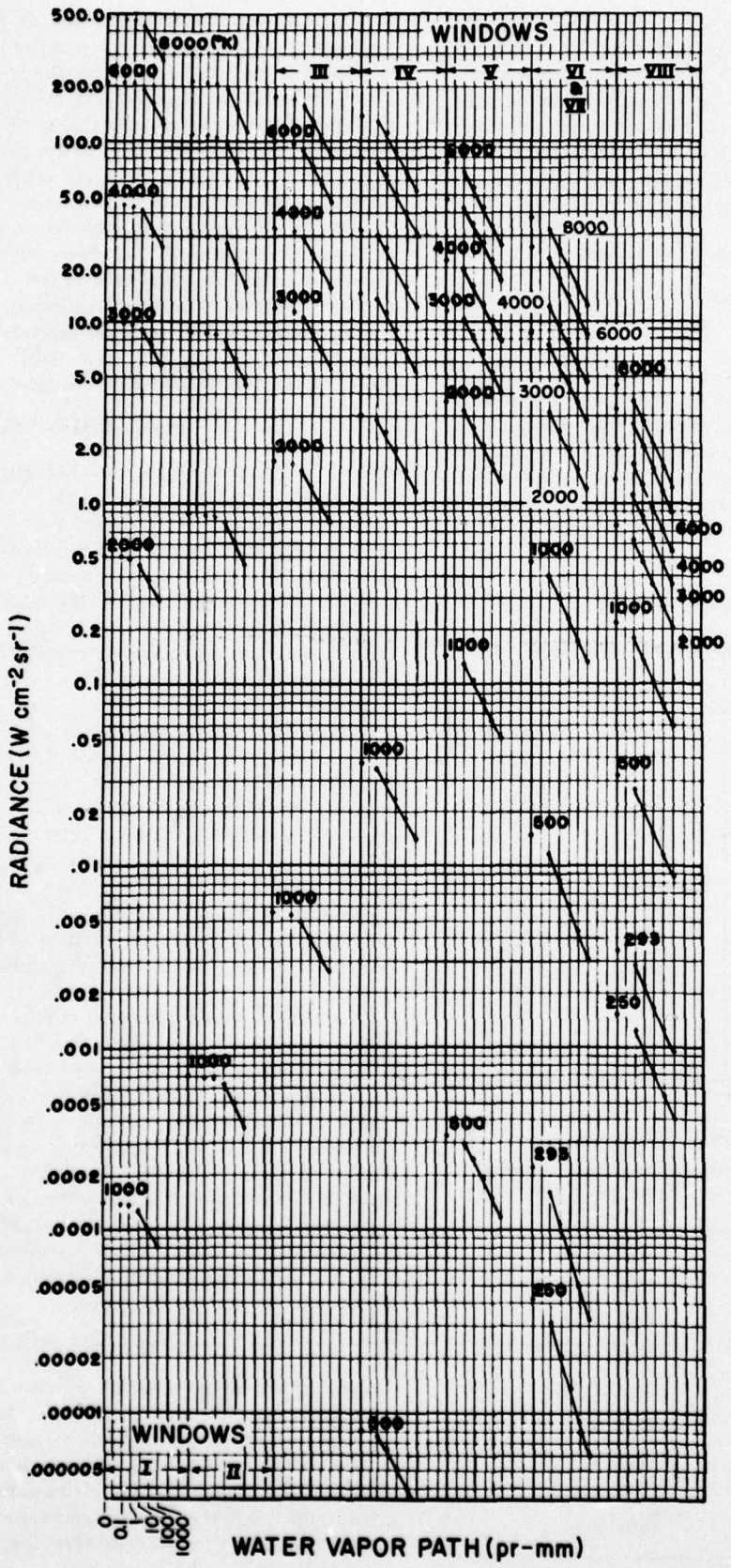


Fig. 10-6. Radiance transmitted through the various atmospheric windows as a function of blackbody source temperature and atmospheric water-vapor content. (Temperature in °K is by each group of plotted points, water-vapor concentration in precipitable millimeters is given by key at bottom left of figure.)

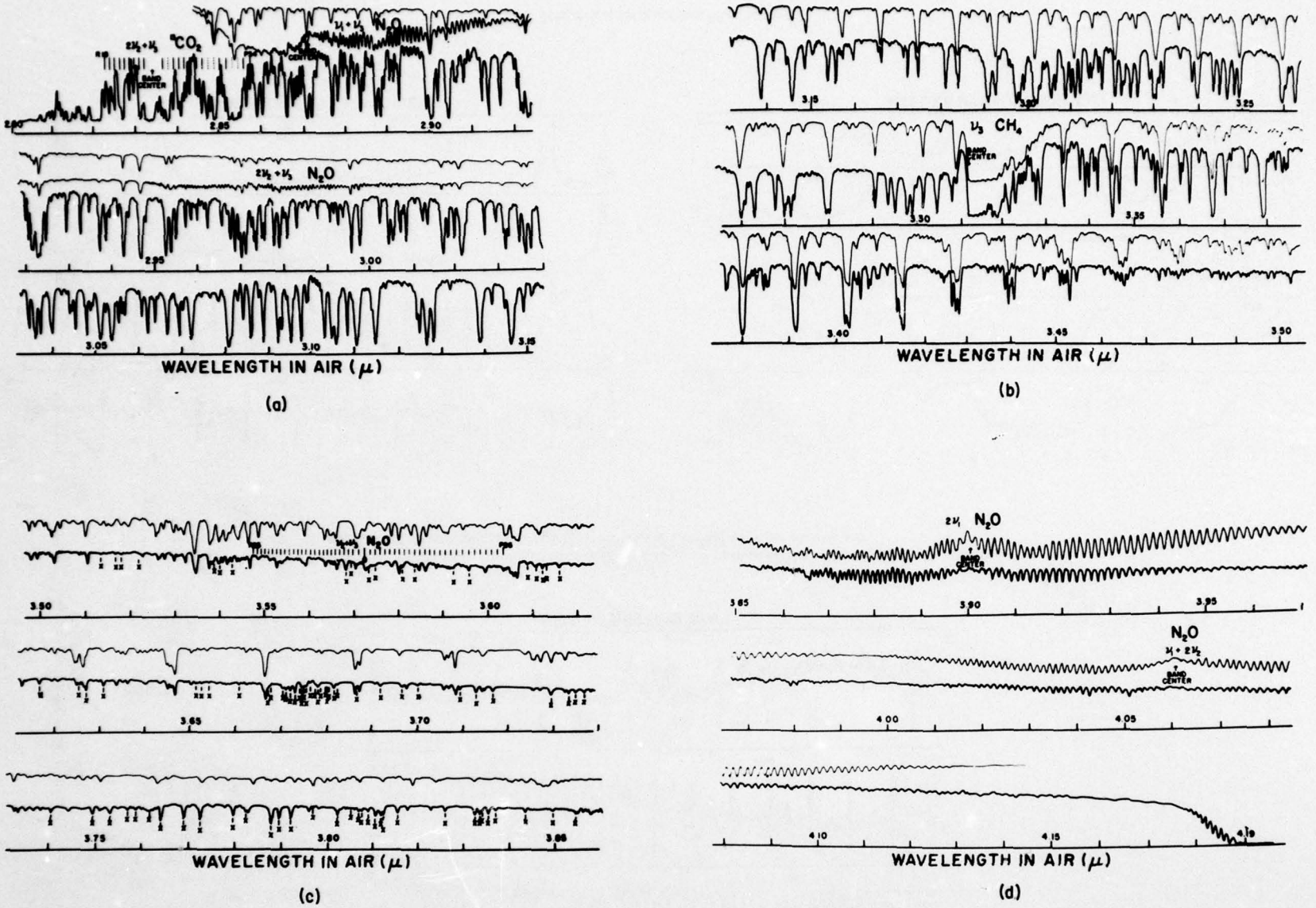


Fig. 10-7. Infrared solar spectrum (heavy curve) from 2.8 to 4.19 μ. (a) Upper curve laboratory air containing H_2O; intermediate curve laboratory air plus N_2O. (b) Upper curve laboratory spectrum of CH_4. (c) X indicates HDO identification. (d) Upper curve laboratory spectrum of N_2O.

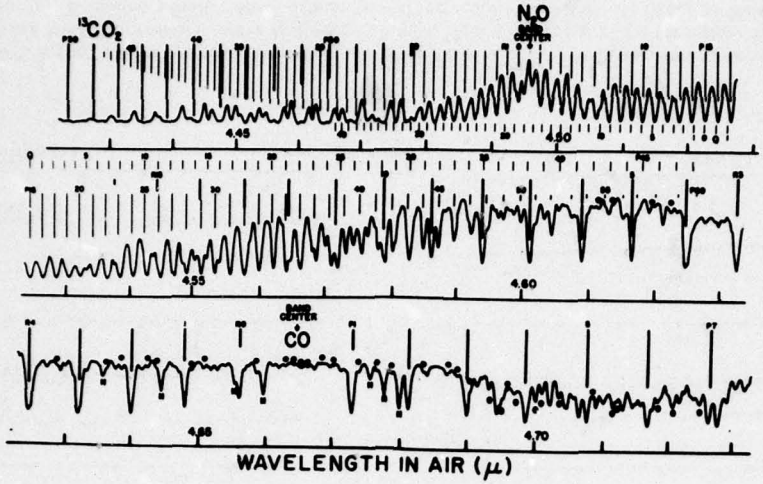


Fig. 10-8. Infrared solar spectrum from 4.43 to 4.73 μ; H indicates H_2O identification, O indicates O_3 identification, and dot above spectrum indicates CO line of solar atmosphere.

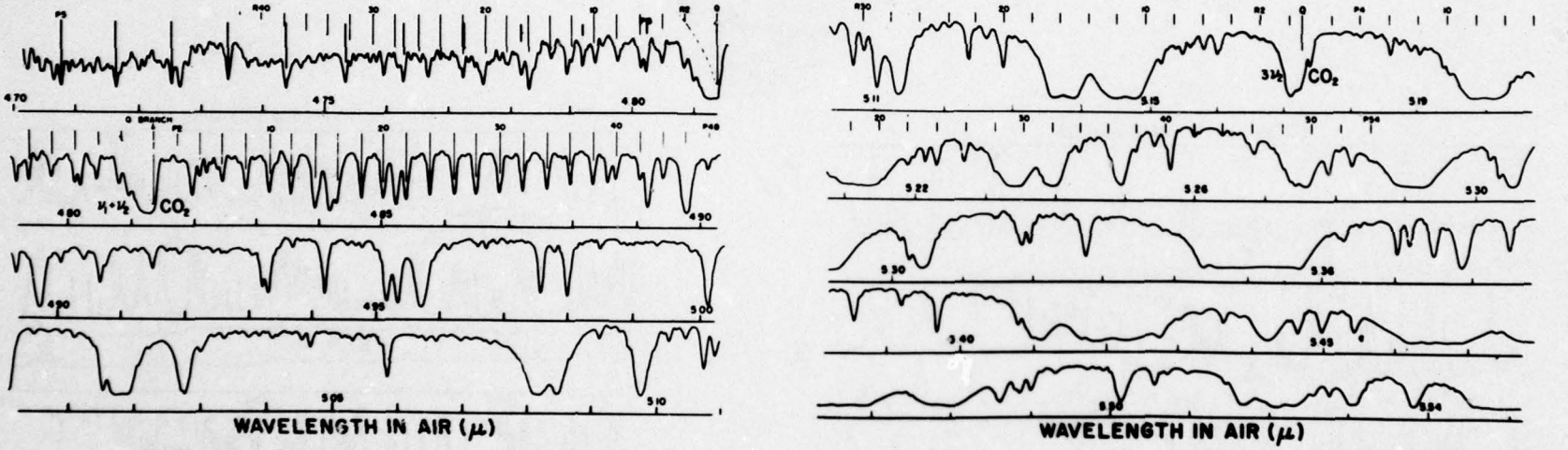


Fig. 10-9. Infrared solar spectrum from 4.7 to 5.55 μ.

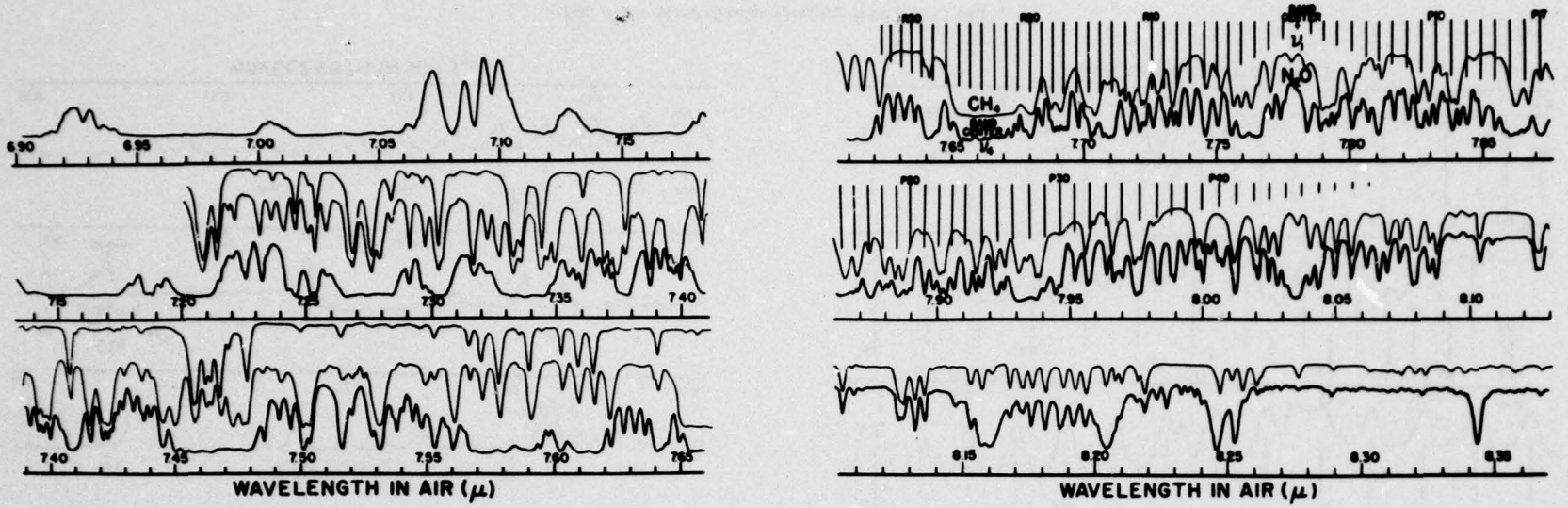


Fig. 10-10. Infrared solar spectrum from 6.9 to 8.45 μ. (a) Upper curve laboratory air containing H_2O; intermediate curve laboratory air plus CH_4. (b) Light curve laboratory air plus CH_4.

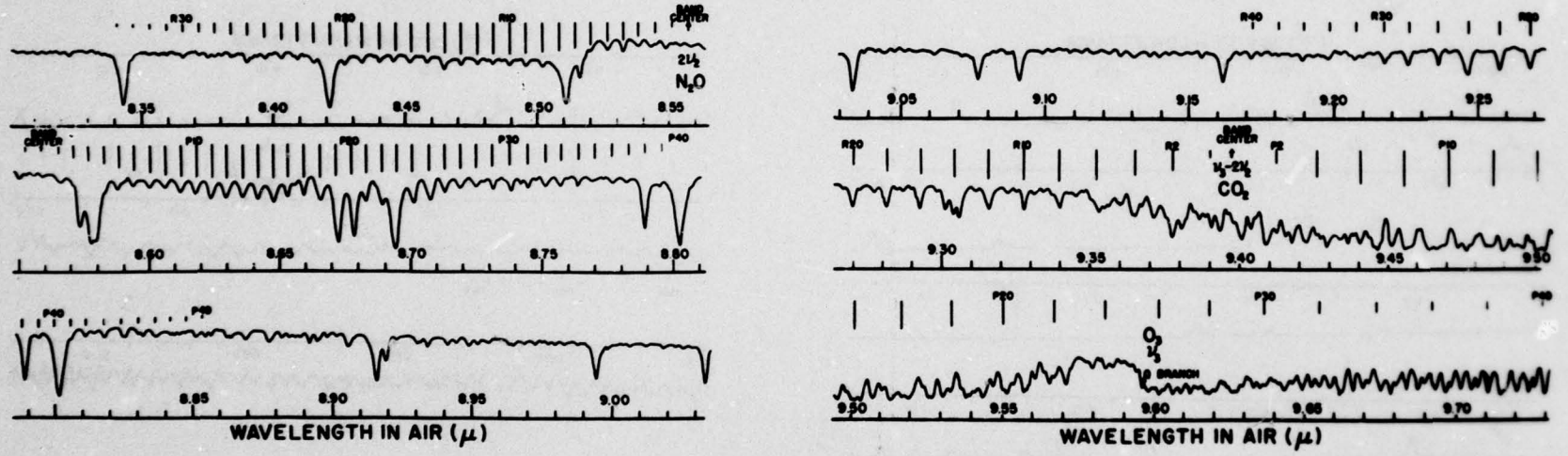


Fig. 10-11. Infrared solar spectrum from 8.35 to 14.2 μ.

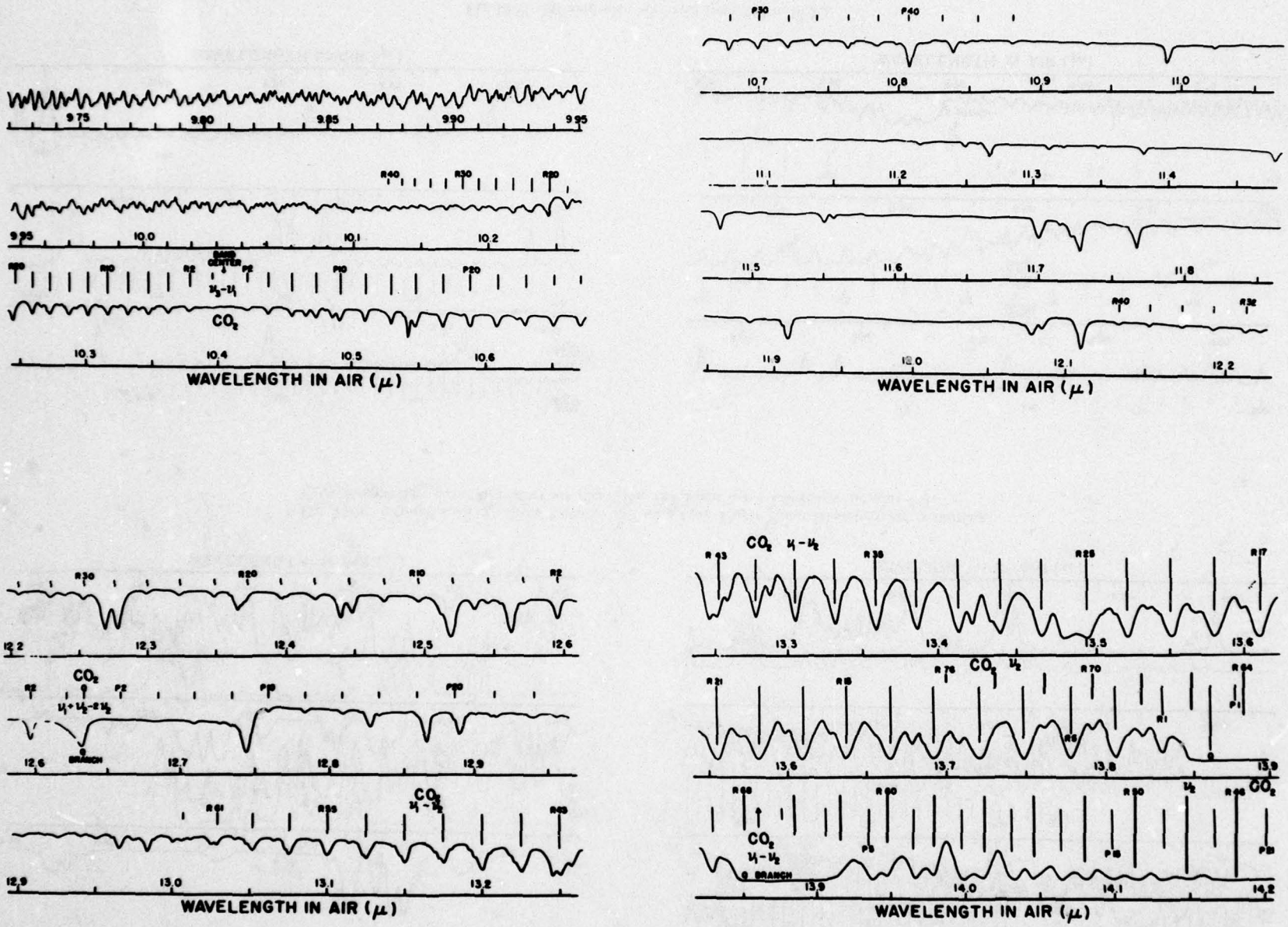


Fig. 10-11. Infrared solar spectrum from 8.35 to 14.2 μ.

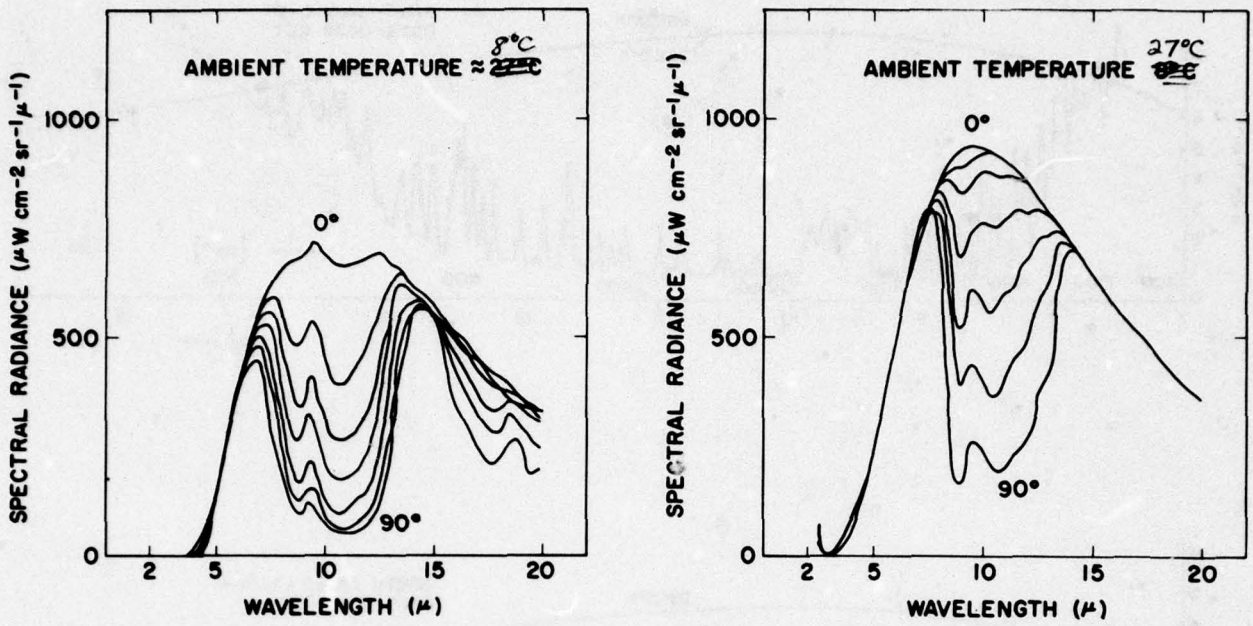


Fig. 10-12. Spectral radiance of a clear sky for angles of elevation 0°, 1.8°, 3.6°, 7.2°, 14.5°, 30°, and 90° above the horizon. Ambient temperature 8°C; measured at night in September from Elk Park Station, Colorado, 11,000 ft above sea level. Ambient temperature about 27°C; measured in June from Cocoa Beach, Florida. (From Bell et al [1960] by permission.)

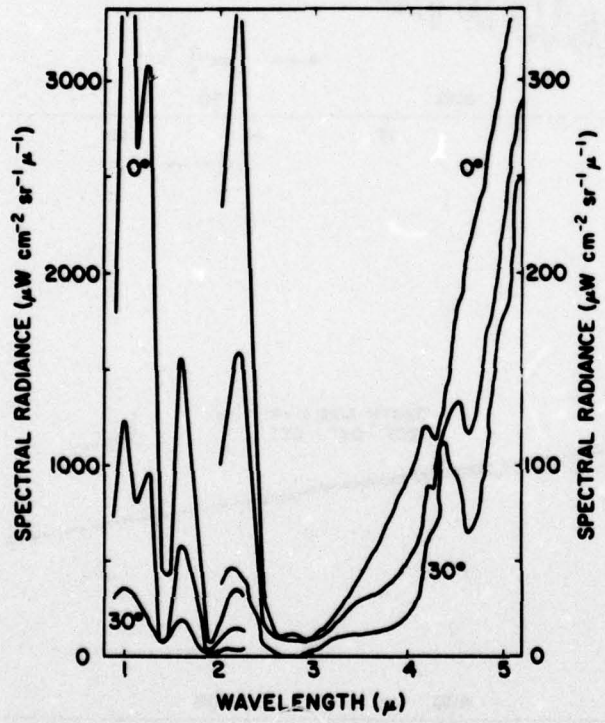


Fig. 10-13. Spectral radiance of a clear sky, showing the dependence of the scattered radiation on elevation angle. Measurements made from Colorado Springs, Colorado, near noon in September; elevation angles 0° (top curve), 7.2° and 30° (lowest curve). Note that the ordinate scale for the short-wavelength set of curves is 10 times larger than the scale of the longer-wavelength curves. (From Bell et al [1960] by permission.)

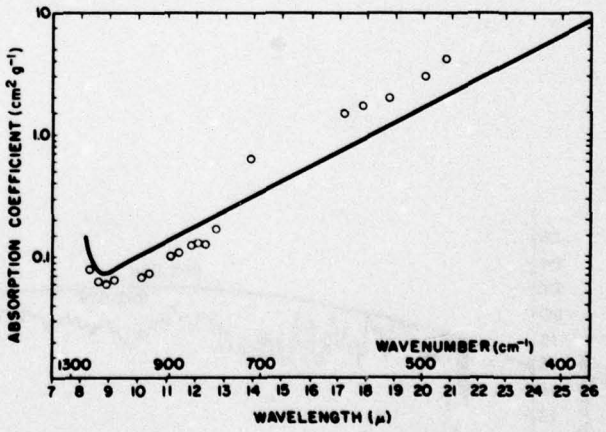


Fig. 10-15. Continuum absorption coefficient for the atmosphere. The solid line is from H. J. Bolle, H. Quenzel, and W. Zdunkowski, *Geofisicia e Meterologia*, v. 11, p. 3, 1963. The circles are values from K. Bignell, F. Saiedy, and P. A. Sheppard, *J. Opt. Soc. Am.*, v. 53, p. 466, 1963.

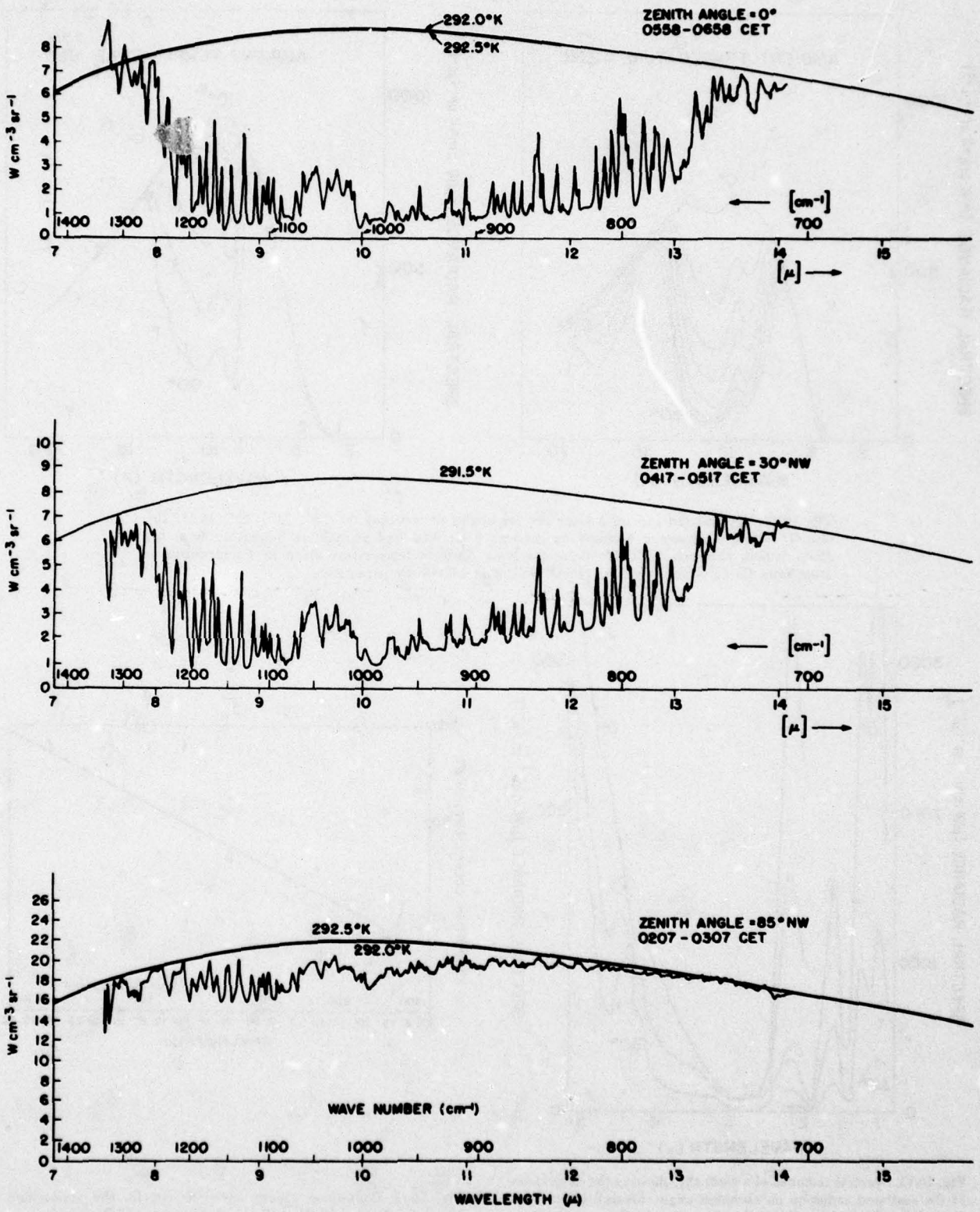


Fig. 10-14. Examples of emission spectra in the 7- to 14-μ region, 24 August 1961; zenith angle 0°, 30°, and 85°. Total amount of precipitable H_2O in vertical column: 2.1 g cm^{-2}. Ground conditions at S. Agata, Italy: air temperature 19°C, pressure 965 mb, absolute humidity 12 g m^{-3}.

10.3.2 Balloon Measurements

At their normal float altitude of approximately 30 km, balloons are above essentially the total atmosphere as far as most infrared properties are concerned. Thus they can be used to measure the outgoing infrared radiation of the atmosphere.

Figure 10-16 shows the radiation for the region 1.2 to 1.8 μ as seen in the early morning from a balloon at 28-km altitude in all downward directions. There were no clouds, so that the effect of forward and back scattering of the sunlight is evident. The field of view of the radiometer was 1/2° by 1/2°. Similar plots of data obtained at longer wavelengths ($> 5\,\mu$) show a more random spatial distribution, but with a definite limb darkening (Sec. 10.3.4). At these longer wavelengths ($> 5\,\mu$), the measurements are primarily of the thermal radiation of the atmosphere, but in the 8- to 13-μ window they are of the ground. The random distribution is probably related to the chance distribution of the temperature and humidity structure of the atmosphere below the balloon. Figure 10-17 gives the measured and calculated values of the spectral distribution of the upward radiation in the atmosphere as a function of altitude, obtained from interferometric measurements from a balloon.

10.3.3 Clouds

Since the presence of clouds considerably changes the radiation characteristics of the atmosphere, either by absorbing or reflecting the radiation from the earth, atmosphere, and sun, or by emitting thermal radiation, it is necessary to know the IR properties of the clouds themselves as well as their distribution in time, geography, type, and altitude.

There is still doubt as to the albedo or reflectance of clouds for all wavelengths. For the near IR, the values quoted range from less than one percent to about 85%. Meteorologists usually assume that in the far IR region, the cloud layers (except for thin cirrus) behave as blackbodies at about the ambient temperature at the surface of the cloud. Figure 10-18 presents an empirical scattering curve for cloud radiances compiled for engineering purposes. The model applies to visible radiation and ice particles and to IR radiation for either water drops or ice. The curve is described by

$$I_\theta / I_{40^\circ} = 0.084 \exp\,(15.7\,\theta^{-1/2}), \qquad (10\text{-}8)$$

where θ is the scattering angles in degrees (for $\theta = 0°$, the detector, cloud, and sun are in a straight line in that order).

Figure 10-19 illustrates the mean radiance values obtained from a U-2 flying within 2000 ft above cumulus, stratus, and cirrus clouds, with a minimum cloud top altitude of 30,000 ft. The spectrometer line-of-sight is directed vertically downward. The main features of the cloud profiles are very similar but are shifted in wavelength with respect to each other. The spectral contour for cumulus clouds shown in the figure was typical of all cumulus systems studied and, presumably, with relatively small variations of any thick optically dense clouds. The spectral contour appears to be related to the optical properties of bulk water and ice [Kislovski, 1959]. The back-

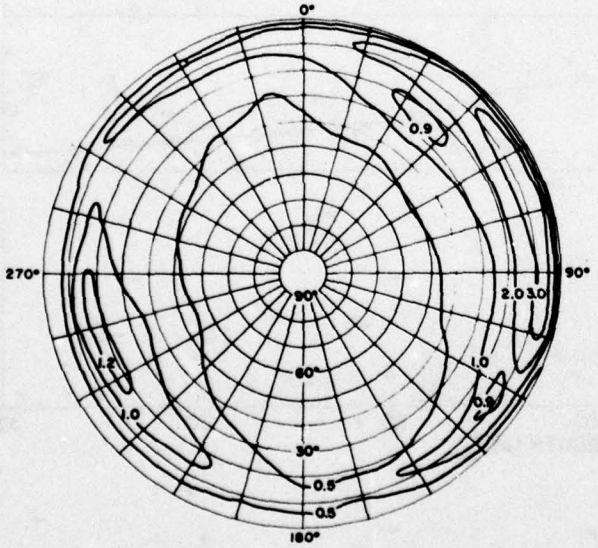


Fig. 10-16. Isoradiance plot for 1.2- to 1.8-μ region, 0750-0755 h MST, 8 May 1959. Isoradiance values are in mW cm^{-2} sr^{-1} as seen through the filter; multiply values by 2.6 to convert to radiance. Altitude 85,000 ft; sun azimuth from magnetic north 77°. Sun elevation, 32°. (From D. Murcray, J. N. Brooks, N. J. Sible, and H. C. Westdal, *Appl. Opt.*, v. 1, no. 2, p. 121, 1962, by permission.)

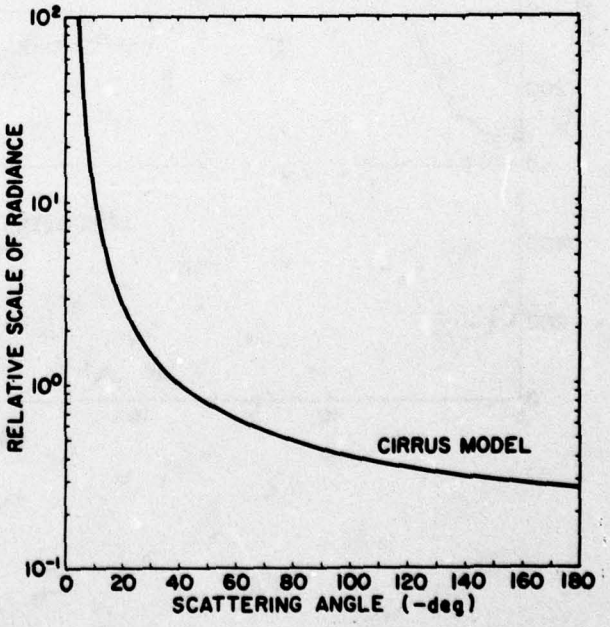


Fig. 10-18. An empirical scattering curve for cloud radiances compiled for engineering purposes. (After R. K. McDonald and R. W. Deltenre, *J. Opt. Soc. Am.*, v. 53, p. 860, 1963.)

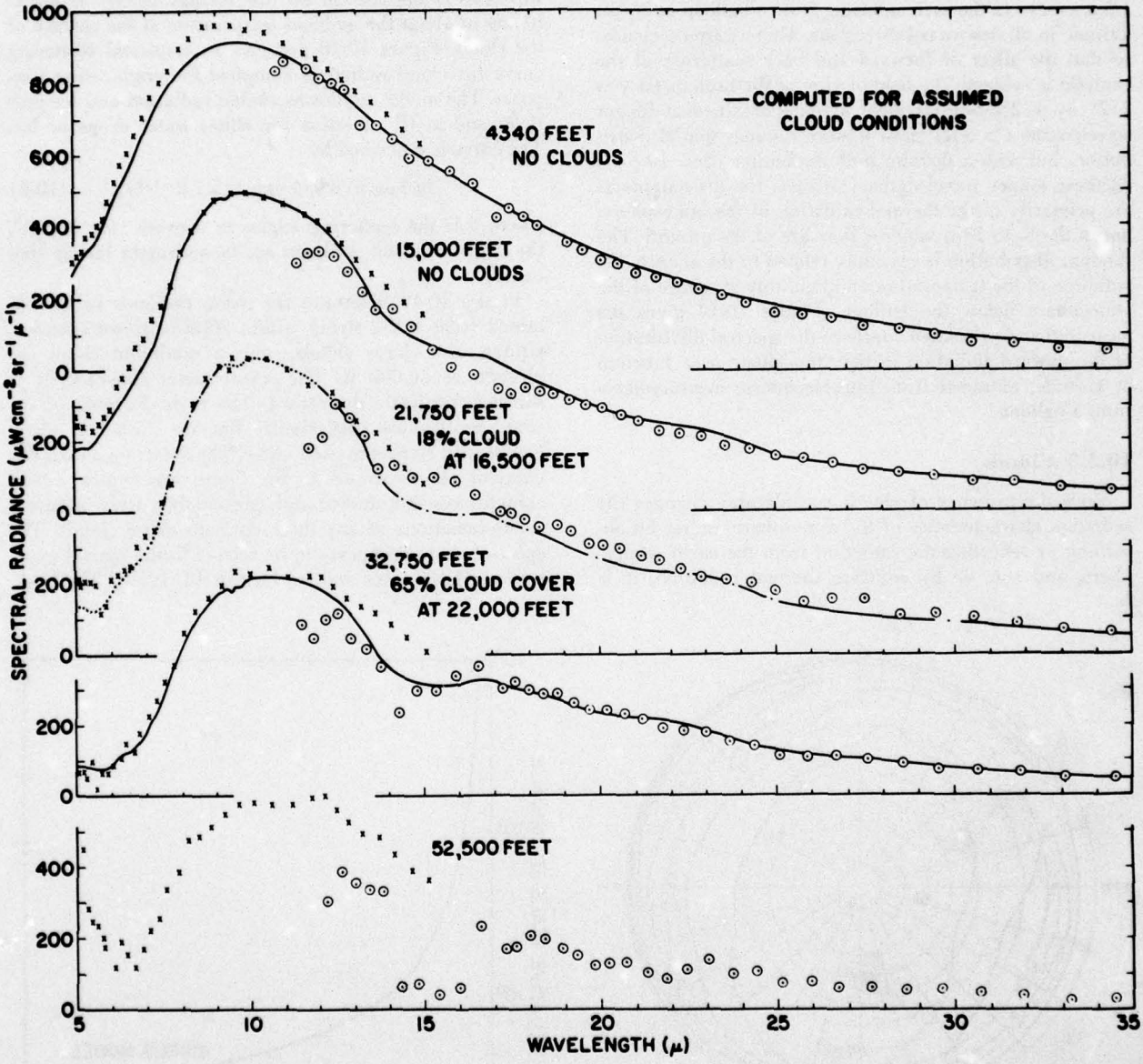


Fig. 10-17. Measurements of the upward atmospheric radiation at various altitudes. The crosses and the circles denote specific spectral radiance values observed by two different interferometer spectrometers. The computed spectra are shown by the solid curves except for 21,750 ft, where each point denotes a computed value.

scattering efficiency or diffuse reflectance, on the order of a few percent in the 2.3- to 2.7-μ region, falls to values as low as a few thousandths of a percent at 2.87 μ, and rises to a few tenths of a percent from 3.1 to 3.7 μ.

Both stratus and cirrus clouds scatter less effectively than cumulus clouds in the 2.3- to 2.7-μ region and more effectively in the 3.2- to 3.7-μ region. The most probable explanation for the difference observed between cumulus clouds and stratus or cirrus clouds is that the latter are semitransparent to infrared radiation and thus the observed cloud radiance is modified by the terrain emission as seen through the clouds. The minimum in the terrain spectrum is due to the atmospheric absorption by water vapor and carbon dioxide. Similar data were obtained with a radiometer flown in a U-2. The radiation from a cloud top in the 8- to 13-μ window was measured. Figure 10-20 shows the results of one flight. The time-scale factor for the radiometric data is plotted relative to the photographs of the cloud top. Average height of the cloud top was estimated to be about 52,000 ft (15.8 km). The data given are the equivalent blackbody temperatures, T_{BB}, assuming an emissivity of unity. The insert diagram is a plot of decreasing T_{BB} that illustrates the correlation between temperature and cloud topography (i.e., the colder the temperature, the higher the cloud height).

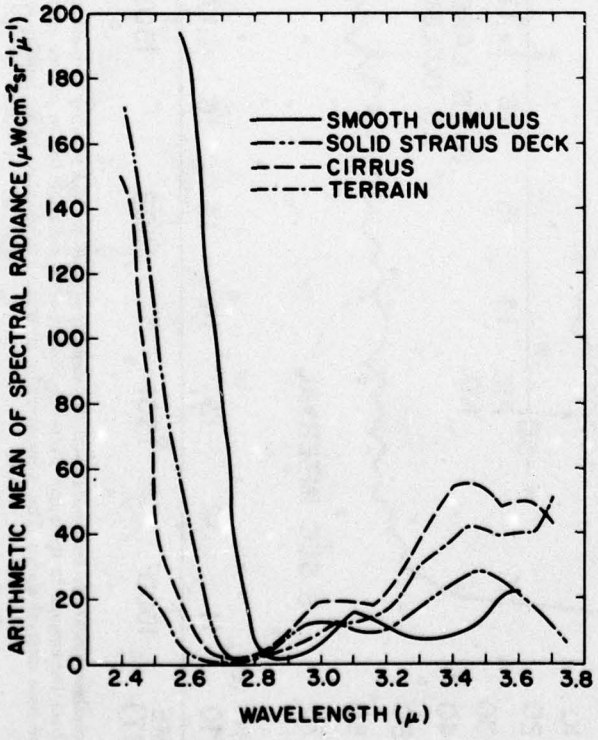


Fig. 10-19. Mean radiance values of cloud tops above 30,000 ft. (From H. H. Blau, Jr., E. M. Duchane, R. P. Espinola, E. C. Reifenstein, III, P. C. von Thüna, and E. A. Vrablik, *Tech. Rept. No. 2, Nonr 3556 (00)*, December 1963.)

10.3.4 Horizon Gradient (Limb Darkening)

More experimental information is needed on how the IR radiation from the atmosphere, as seen from a satellite, decreases or increases as one looks toward the horizon, particularly for satellite guidance systems utilizing IR horizon seekers and for computing the atmosphere's radiative flux (radiance integrated over a hemisphere) from the data obtained with relatively narrow-field-of-view radiometers which measure radiance, not flux.

Figures 10-21 through 10-25 give the radiance values calculated for the 10.5- to 11.0-μ window and for narrow intervals in each of the principal infrared bands. Other detailed calculations of the infrared horizon for several wavelengths and meteorological conditions are given by Hanel et al [1963], and Kondratiev and Yakushevskaya [1962]. Figure 10-26 gives the geometry for the calculations and defines the height parameter Z_o used in Fig. 10-21 through 10-25. ($Z_o = 3$ km corresponds to the refracted ray just grazing the earth's surface. $Z_o = -6371$ km corresponds to zero zenith angle of the emerging ray.) The curves for the window, the 9.6-μ ozone band, and the 6.3-μ H_2O band show a great range of radiance over the disc for even the limited sample of atmospheres. In certain cases there is limb brightening. The uniformity of the gradients and the relatively narrow range of radiance over the disc in the 15-μ CO_2 band and the H_2O rotation band would indicate that these spectral regions should be the most suitable for horizon seekers. There is little experimental data, however, to corroborate these conclusions. Some measurements from satellites in the 15-μ band with a 2-μ bandwidth filter show a small amount of limb darkening. Observations with 1-μ bandwidth filter in one channel of the radiometer carried on TIROS VII showed some limb brightening [Bandeen et al, 1963]. This is more nearly in agreement with Fig. 10-25.

10.3.5 Satellite Measurements

Several TIROS satellites carried a five-channel medium resolution (field of view about 5° by 5°) radiometer. The nominal bandwidths were usually 5.9 to 6.7 μ (the water-vapor absorption band); 7.5 to 13.5 μ (the atmospheric window); 0.2 to 7.0 μ (for measuring reflected solar radiation); 7.0 to 32.0 μ (for measuring terrestrial radiation); and 0.5 to 0.75 μ (equivalent to the response of the TV system). Infrared data for several orbits have been published [NASA, 1961 and 1962; Nordberg et al, 1962].

Wark computed the outgoing intensity for 106 model atmospheres using 77 wavenumber intervals from 0 to 2500 cm^{-1} and five zenith angles. Figure 10-27 shows computed outgoing spectral intensities at zero zenith angle for three of these atmospheric models. The influence of the strong absorption bands is evident at 600 to 800 cm^{-1} (CO_2), 950 to 1100 cm^{-1} (ozone), and 1300 to 1900 cm^{-1} (water vapor).

Figure 10-28 is a single scan of the TIROS III radiometer; it shows the oscillogram of the three thermal channels corresponding to the scan path indicated on the photograph. A large cloud mass is prominent near the center of the picture, with a clear area over the Great Lakes and

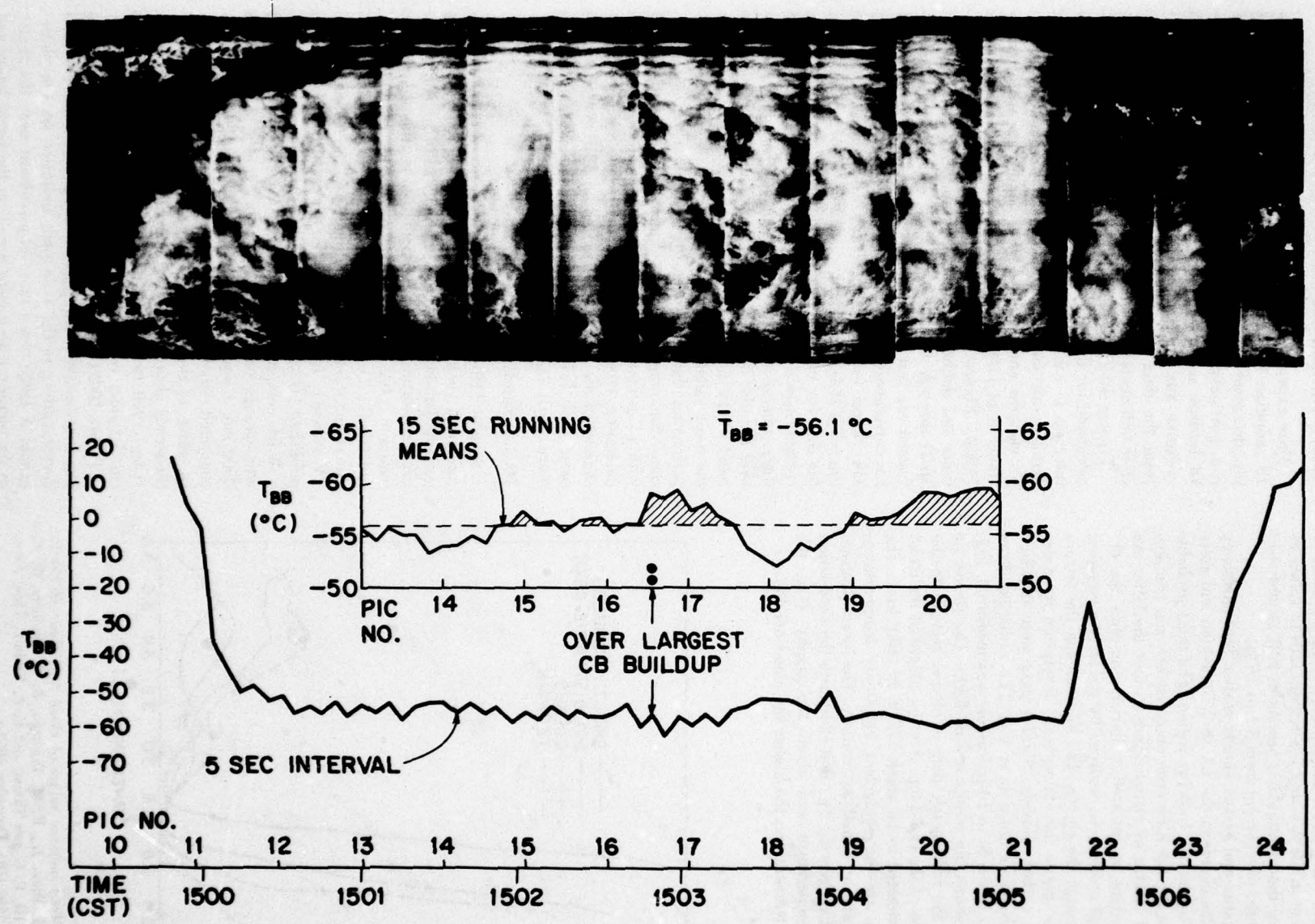


Fig. 10-20. Equivalent blackbody temperatures of the cloud tops in 8- to 13-μ window as measured from a U-2 flying over the cloud (pictured above). In the lower curve, the data were averaged over 5-sec increments. In the upper curve the time scale is indicated by the picture number: each point is the average of three points on the lower curve. $\bar{T}_{BB}$ is the mean temperature for the time interval shown. The point over the largest cumulonimbus (CB) buildup is also indicated.

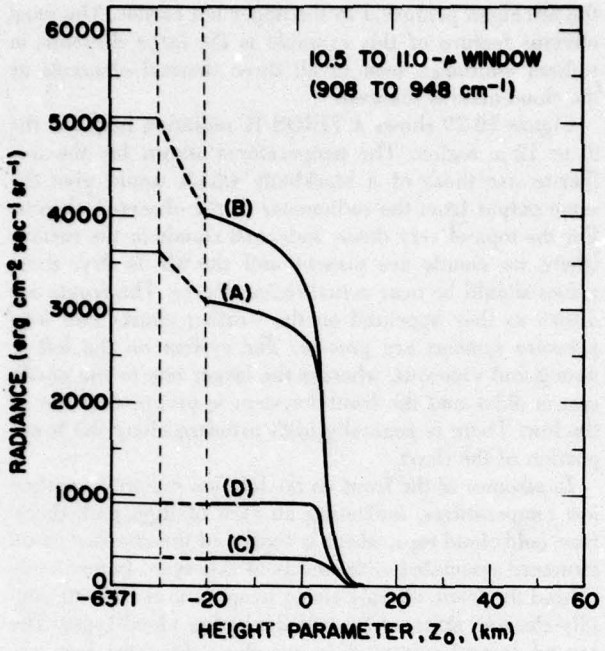


Fig. 10-21.

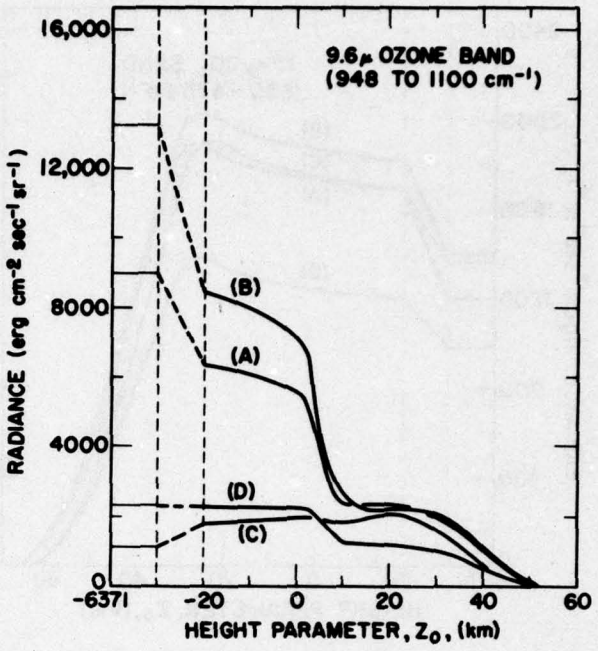


Fig. 10-22.

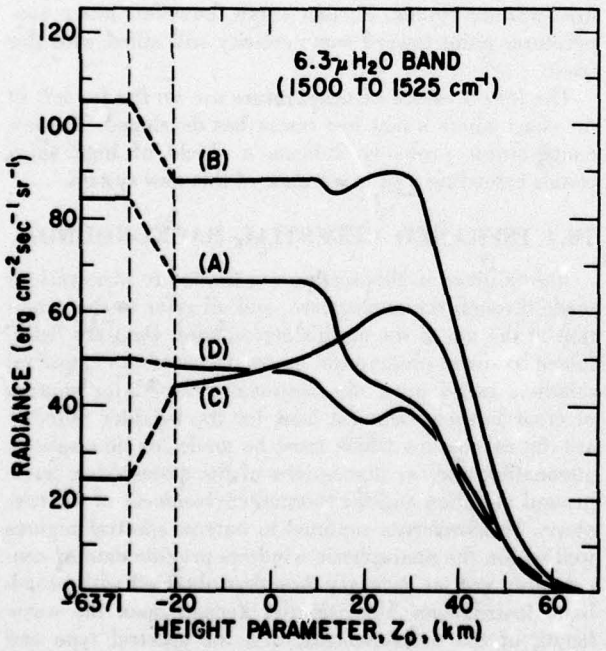


Fig. 10-23.

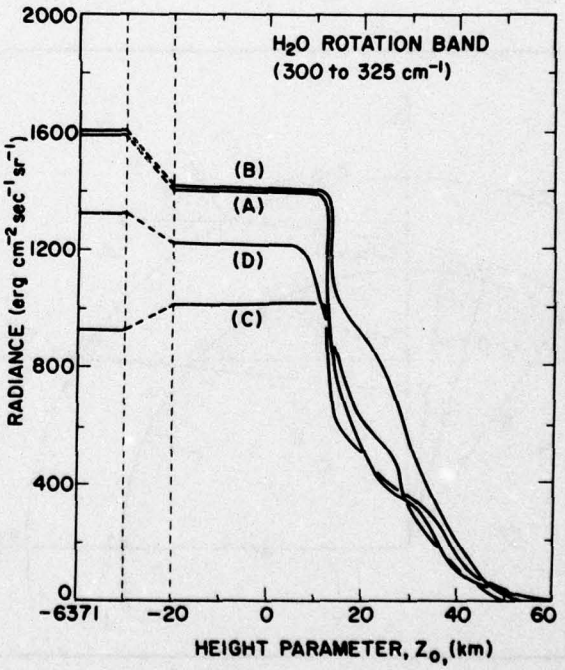


Fig. 10-24.

Figs. 10-21 through 10-25. Variation of radiance with minimum height, Z_o, of unrefracted ray for four atmospheric models in the indicated spectral interval. The four atmospheres are: (A) ARDC model atmosphere, 1959, with clear sky; (B) Albuquerque, N. M., 0000 GCT, 11 July 1958, clear sky; (C) Ponape, Caroline Is., 1200 GCT, 17 May 1958, overcast top at 100 mb; (D) Resolute, N.W.T., Canada, 1200 GCT, 31 December 1958, overcast top at 400 mb. The radiance for the vertical beam ($Z_o = -6371$ km, see Fig. 10-26) is shown by solid line to the left of the dashed line; the radiance near the horizon is to the right of the dashed lines. (From D. Q. Wark, J. Alishouse, and G. Yamamoto, *Appl. Opt.*, v. 3, p. 221, 1964, by permission.)

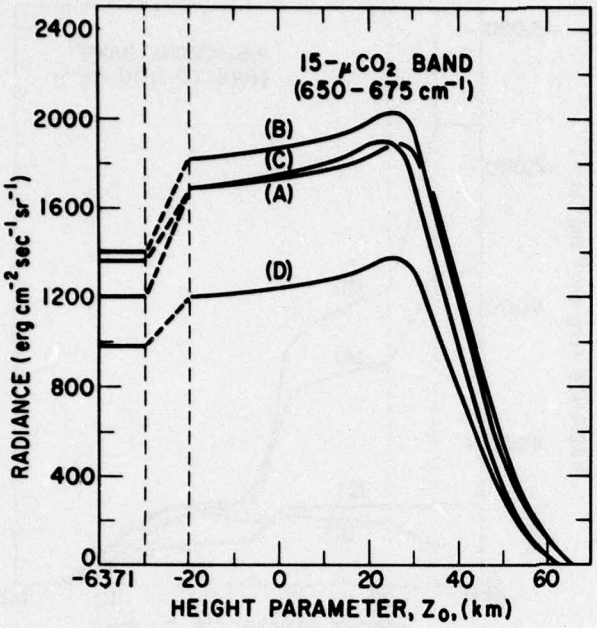


Fig. 10-25.

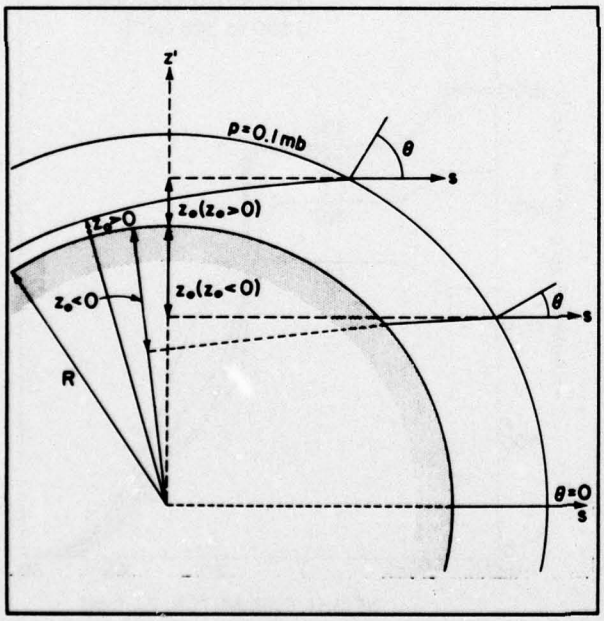


Fig. 10-26. Geometry of optical paths through the atmosphere. The direction of the ray is indicated by s. Positive Z_0 is the minimum height of the unrefracted ray; negative Z_0 is the minimum projection of the intersection of the unrefracted ray with the earth onto the perpendicular radius. θ is the zenith angle of the ray emerging at the atmospheric level of 0.1 mb pressure.

the Michigan peninsula in the upper left corner. The most obvious feature of this example is the large decrease in radiant emittance seen in all three thermal channels as the cloud mass is scanned.

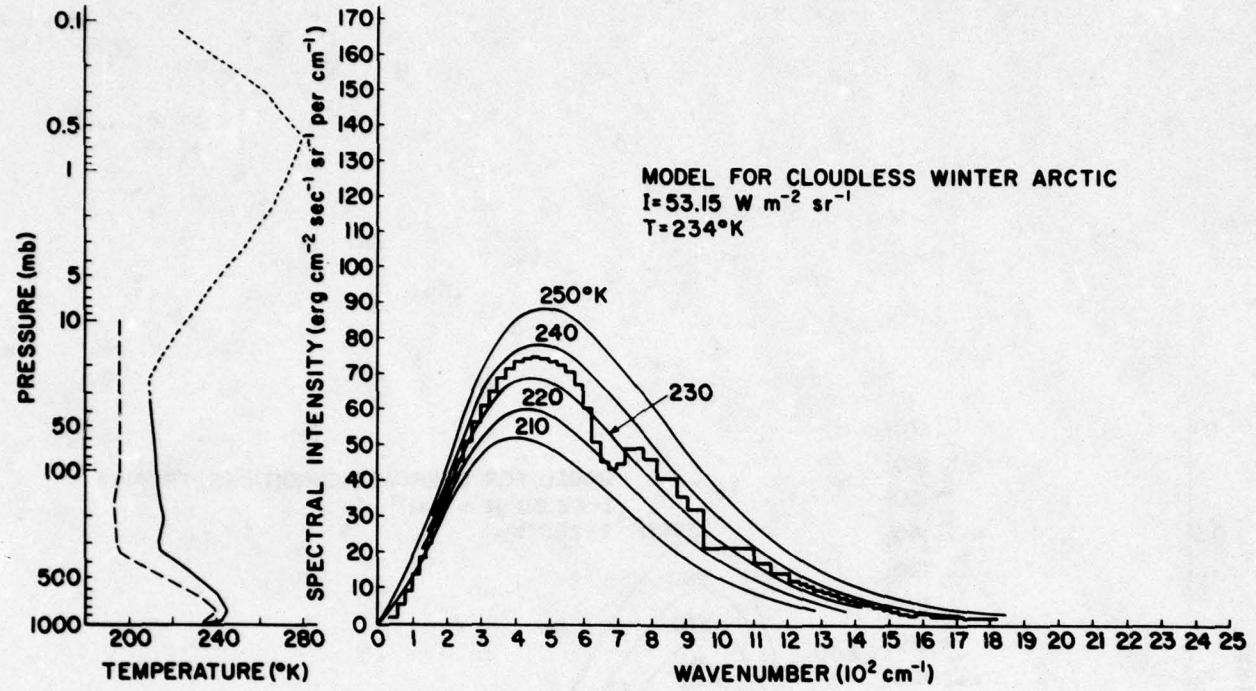
Figure 10-29 shows a TIROS II radiation map for the 8- to 12-μ region. The temperatures shown for the isotherms are those of a blackbody which would give the same output from the radiometer as the observed objects. For the tops of very dense undercast clouds or the surface where no clouds are present and the air is dry, these values should be near actual temperatures. The fronts are drawn as they appeared on the weather chart. Two low-pressure systems are present. The system on the left is young and vigorous, whereas the larger one to the northeast is older and the frontal system is progressing out of the low. There is generally high pressure along the lower portion of the chart.

In advance of the front on the left is a region of marked low temperatures, indicating an area of high and, therefore, cold cloud tops, which is typical of the classical cloud structure associated with storms of this type. Immediately behind the front, sharply rising temperatures indicate rapidly clearing skies, at least of the higher cloud types. The second frontal system does not show the same features. It lies through a region of high temperature (off the coast of Spain) giving evidence of a very weak and dissipating front. It no longer has much cloudiness associated with it; the radiation comes from the ocean or from the tops of low, warmer clouds. Further south, however, lower temperatures point toward some activity still allied with this front.

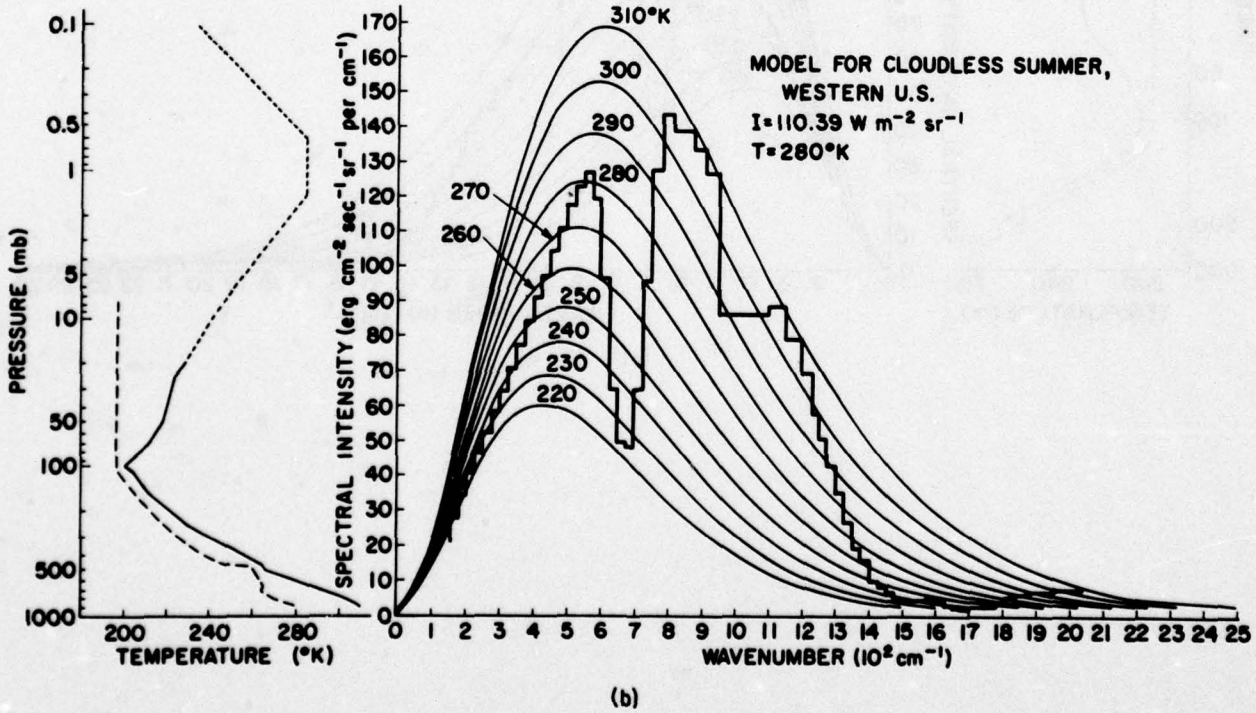
The lowest values of temperature are on the far left of the chart where a new low center has developed. The low temperatures probably indicate a shield of high thick clouds extending well in advance of this new system.

10.4 INFRARED CELESTIAL BACKGROUNDS

Values given in this section are limited to observations made through the atmosphere, and all refer to the condition at the top of the earth's atmosphere. Data are determined by direct observation or are derived from empirical relations based upon observational data. Major sources of error in these data (at least for the brighter objects) are the corrections which must be made for atmospheric attenuation and for fluctuations of the atmospheric background radiation and the thermal environment of the telescope. Measurements confined to narrow spectral regions well within the atmospheric windows provide data of considerably greater accuracy than that obtained with broadband instruments. Uncertainties depend upon the wavelength of the measurements, and the spectral type and visual magnitude of the celestial object. For objects which have temperatures greatly exceeding that of the sun, the uncertainties increase rapidly with wavelength and temperature. For objects of temperature less than the sun, the uncertainties tend to decrease with wavelength and temperature in the near infrared region until low enough temperatures are reached to permit the existence of a high abundance of molecular species in the object's atmosphere.

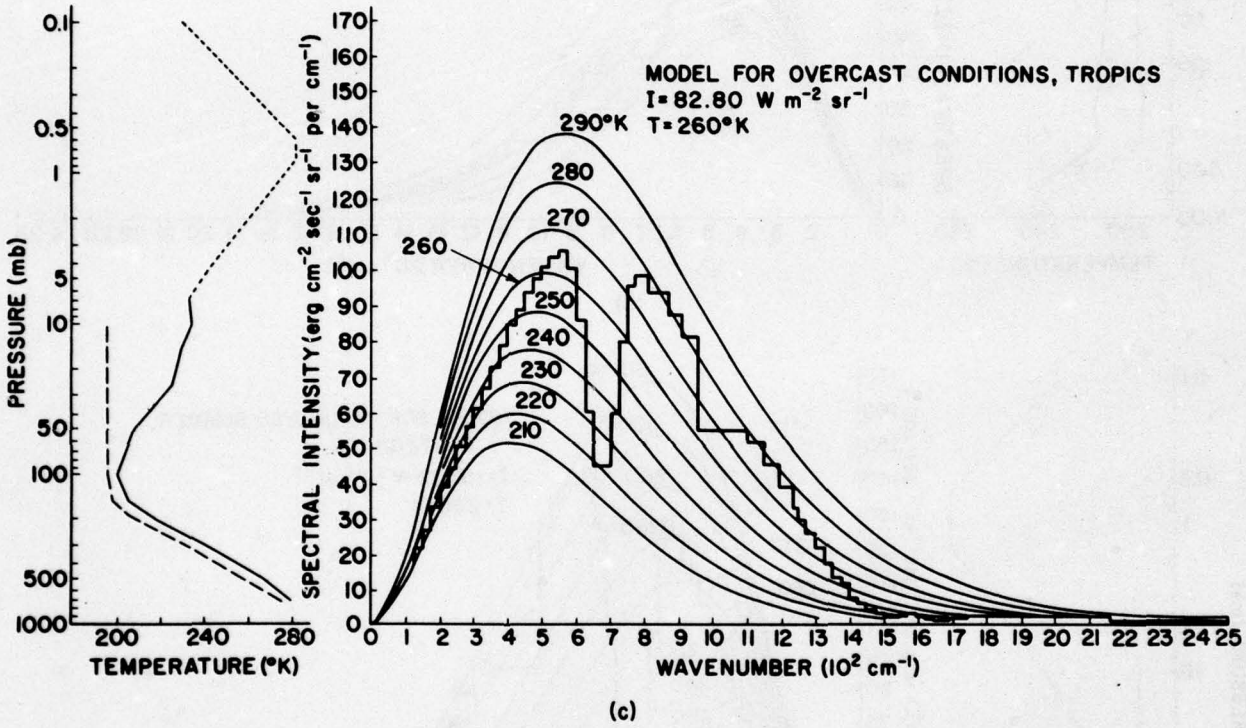


(a)



(b)

Fig. 10-27. The computed spectral intensities at zero zenith angle for 3 atmospheric models. At the left, pressure vs temperature is the solid line, with the upper portion in short dashes to indicate estimated values; pressure vs dew point is the long-dashed line. At the right, intensity per unit wavenumber vs wavenumber is the stepped curve. Smooth curves are for blackbody radiation at the indicated temperatures. I is the total integrated intensity and T is the corresponding blackbody temperature. (From D. Q. Wark, G. Yamamoto, and J. Lienesch, *Meteorol. Satellite Lab. Rept. No. 10*, U. S. Weather Bureau, 1962.)



(c)

Fig. 10-27. The computed spectral intensities at zero zenith angle for 3 atmospheric models. At the left, pressure vs temperature is the solid line, with the upper portion in short dashes to indicate estimated values; pressure vs dew point is the long-dashed line. At the right, intensity per unit wavenumber vs wavenumber is the stepped curve. Smooth curves are for blackbody radiation at the indicated temperatures. I is the total integrated intensity and T is the corresponding blackbody temperature. (From D. Q. Wark, G. Yamamoto, and J. Lienesch, *Meteorol. Satellite Lab. Rept. No. 10*, U. S. Weather Bureau, 1962.)

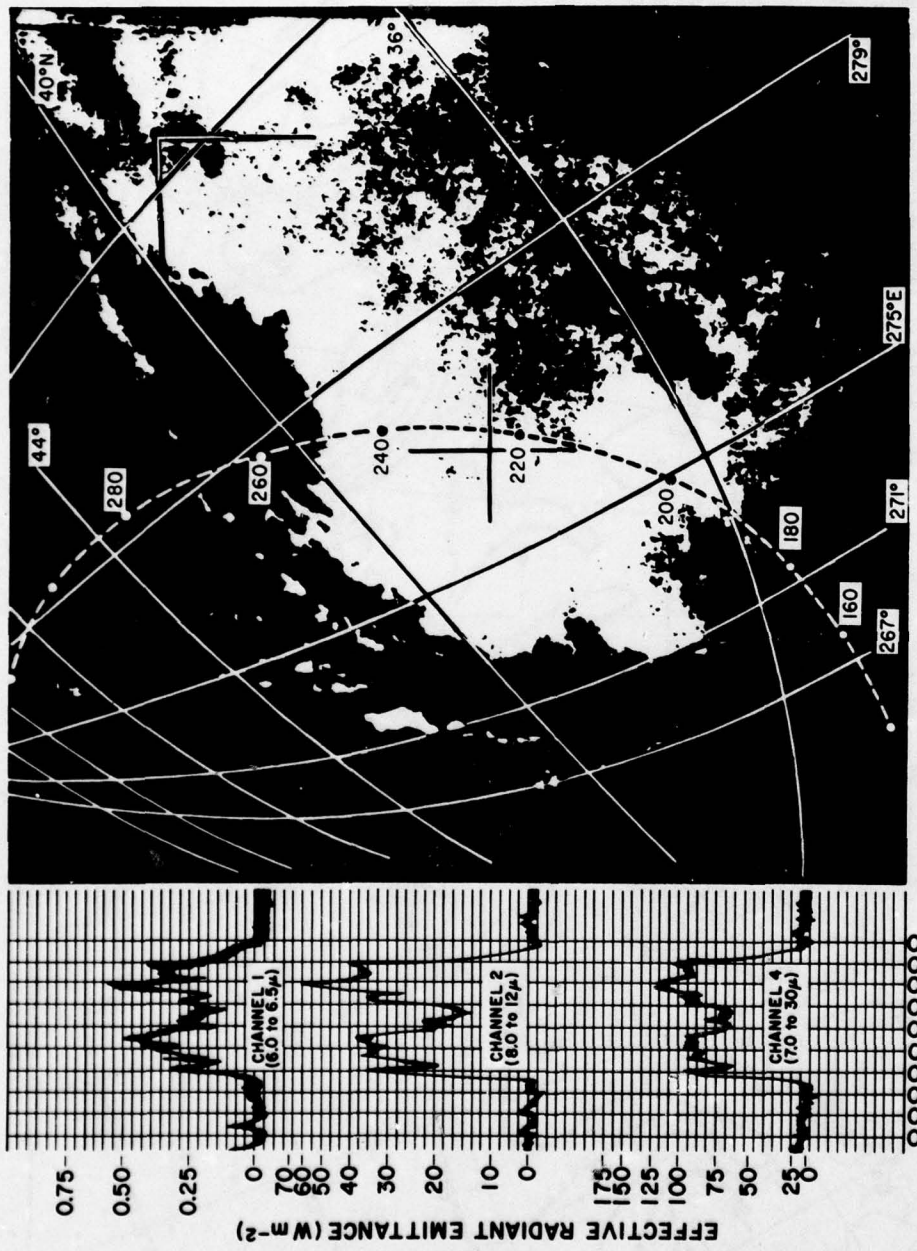


Fig. 10-28. On the left are the analog oscillograms of the outputs of the three thermal channels corresponding to the radiometer scan path (dashed and with arbitrary satellite rotation angles), shown in the photograph on the right taken by TIROS III at about 1735 GMT on 12 July 1961. (From B. J. Connath, *NASA Tech. Note D-1341*, 1962.)

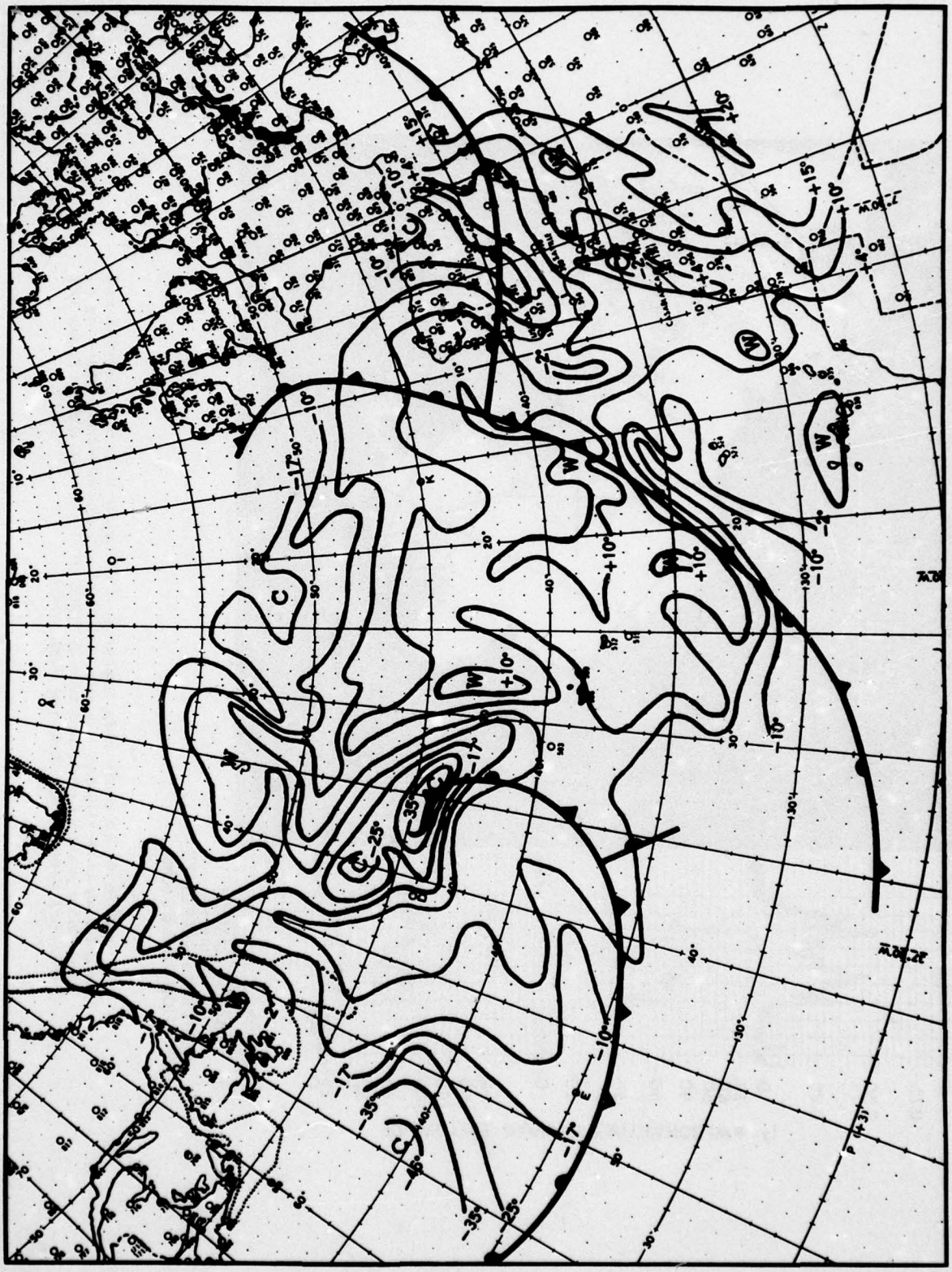


Fig. 10-29. TIROS II radiation map for the 8- to 12-μ channel, pass 30, 25 November 1960. Equivalent blackbody temperatures in °C are given for the isotherms. (From R. A. Hanel and D. Q. Wark, *J. Opt. Soc. Am.*, v. 51, p. 1394, 1961, by permission.)

10.4.1 Stellar Backgrounds

Table 10-7 presents best estimates of the irradiance received from stellar objects at selected wavelengths. For the observational basis of these values, see Johnson [1962]. The table also lists the spectral type (Sec. 21.2.8) and luminosity class (MK system, see Sec. 21.4.1.1), and the photoelectrically measured apparent magnitude V (UBV color system, see Sec. 21.2.5). The values of spectral irradiances, H_λ, are obtained from interpolation of stellar spectral energy distributions and reduced to absolute energy units through the calibration of the magnitude V made by Willstrop [1958]. The tabulation of the total irradiance, H, was obtained by integration of the spectral energy distributions for stars of spectral type later than G0 and from the bolometric corrections derived from model atmospheres for stars of earlier spectral type. Determination of the total irradiance in terms of the magnitude V of the star and the bolometric correction, BC, is made through the relation

$$\log H = -11.62 - 0.4\ (V + BC), \qquad (10\text{-}9)$$

where H is in W cm^{-2}, and

$$H = \int_0^\infty H_\lambda\, d\lambda. \qquad (10\text{-}10)$$

Table 10-8 gives bolometric corrections for stars of late spectral type. For a detailed discussion of the bolometric correction, see Walker [1964]. Application of Eq. (10-9) to stars of known visual magnitude will, in the majority of cases, provide accurate upper limits to the infrared stellar irradiance.

Table 10-9 lists stars suitable for use as a photometric standard (tentative) together with the wavelengths and values of irradiance recommended for standardization of photometric data.

If all stars fainter than $V > +8.0$ magnitude are assumed to contribute a general continuous stellar background, and if the number density of stars along any given galactic coordinate and their distribution among the various spectral types are known, order-of-magnitude estimates of the radiance of the Milky Way can be derived. Table 10-10 gives such an estimate for the wavelength interval 0.8 to 3.0 μ (lead sulfide region).

Table 10-8. Bolometric correction, BC, for stars of late spectral type.

Spectral Type	BC*
K0 II	−0.43
K3 II	−0.85
G8 III	(−0.12)
K0 III	−0.28
K2 III	−0.47
K3 III	−0.50
K4 III	−0.77
K5 III	−0.98
M0 III	−1.14
M2 III	−1.52
M3 III	−1.68
M4 III	(−2.18)
M6 III	(−2.68)
G0 V	−0.06
G2 V	−0.07
K0 V	−0.08
K2 V	−0.11
K7 V	−0.87
M2 V	−1.20
M5 V	−2.35

* Values in parentheses are less reliable.

Table 10-10. Estimated radiance of the celestial sphere in the wavelength interval 0.8 to 3.0 μ (lead sulfide detector); averages over all galactic longitudes.

Galactic Latitude	Radiance (W cm^{-2} sr^{-1})	Remarks
0°	1.5×10^{-10}	
10°	6.9×10^{-11}	
40°	2.4×10^{-11}	
90°	1.5×10^{-11}	
0° to 360°	8.9×10^{-11}	Average over 4π sr
0°	1.2×10^{-10}	Due to K and M stars only
0°	3×10^{-9}	Toward the galactic nucleus (longitude 0°)

Table 10-9. Stars suitable for photometric standards.

Star	Spectral Type	V (mag)	Spectral Irradiance (10^{-14} W cm^{-2} μ^{-1}) 0.556 μ	1.00 μ	2.20 μ	3.73 μ	10.20 μ
α Lyrae	A0V	0.03	371.0	62.9	3.63	0.501	0.019
α Aurigae	G8III	0.09	350.0	163.0	19.5	3.46	0.108
ϵ Cygni	K0III	2.45	40.1	21.9	2.99	0.459	—
α Arietis	K2III	1.99	60.9	39.5	6.19	0.630	—
α Tauri	K5III	0.86	186.0	206.0	49.4	8.85	0.289

Table 10-7. Spectral irradiance at selected wavelengths and the total irradiance, H, in the infrared region; for 0.28-14 read 0.28×10^{-14}. Values in parentheses are less reliable than others. (For spectral type classification symbols, see Sec. 21.2.8 and Sec. 21.4.1; additional symbols are prefix c for supergiant, suffix p for peculiar spectrum.)

Star	Spectral Type	V (mag)	Spectral Irradiance ($W\ cm^{-2}\ \mu^{-1}$)									H ($W\ cm^{-2}$)	w*
			10 μ	5 μ	3.33 μ	2.5 μ	2.00 μ	1.67 μ	1.25 μ	1.0 μ	0.566 μ		
α Tau	K5III	+0.86	0.28-14	0.33-13	0.13-12	0.33-12	0.62-12	0.98-12	0.17-11	0.22-11	0.19-11	0.32-11	4
α Ser	K3III	2.66	(0.14-15)	(0.19-14)	0.78-14	0.20-13	0.41-13	0.69-13	0.15-12	0.21-12	0.33-12	0.31-12	3
α Sco	Me+A	0.92	(0.70-14)	(0.85-13)	0.32-12	0.79-12	0.14-11	0.24-11	0.39-11	0.50-11	0.16-11	0.76-11	2
α Peg	F5Ib	1.80	0.17-15	0.94-15	0.45-14	0.14-13	0.32-13	0.61-13	0.15-12	0.26-12	0.73-12	0.44-12	3
χ Peg	M2II	4.80		(0.85-15)	0.44-14	0.12-13	0.28-13	0.41-13	0.67-13	0.76-13	0.46-13	0.11-12	1
ε Peg	K2Ib	2.40	(0.43-15)	(0.57-14)	0.22-13	0.54-13	0.11-12	0.17-12	0.31-12	0.40-12	0.42-12	0.55-12	3
γ Ori	B2III	1.64	0.39-16	0.31-15	0.14-14	0.38-14	0.84-14	0.16-13	0.46-13	0.10-12	0.84-12	0.36-11	2
α Ori	M2II-III	0.10	0.75-14	0.15-12	0.58-12	0.13-11	0.23-11	0.35-11	0.55-11	0.66-11	0.35-11	0.10-10	2
β Oph	K2III	2.78	(0.13-15)	(0.17-14)	0.73-14	0.19-13	0.37-13	0.63-13	0.13-12	0.19-12	0.29-12	0.27-12	3
α Lep	F0Ib	2.56		(0.36-15)	0.14-14	0.40-14	0.89-14	0.17-13	0.43-13	0.89-13	0.36-12	0.25-12	2
γ Leo	K0III	1.95	(0.29-15)	(0.40-14)	0.16-13	0.44-13	0.85-13	0.15-12	(0.30-12)	(0.45-12)	0.63-12	0.60-12	2
Lal 21185	M2V	7.47	(0.48-17)	(0.77-16)	0.31-15	0.75-15	0.15-14	0.24-14	0.43-14	0.63-14	0.39-14	0.80-14	2
α Hya	K4III	1.97			0.34-13	0.86-13	0.17-12	0.26-12	0.48-12	0.66-12	0.62-12	0.87-12	3
30g Her	M6III	5.00		(0.26-13)	0.89-13	0.17-12	0.26-12	0.36-12	0.45-12	0.41-12	0.38-13	0.85-12	2
ζ Her	G0IV	2.82		(0.59-15)	0.26-13	0.71-14	0.15-13	0.27-13	0.62-13	0.11-12	0.28-12	0.20-12	3
γ Gem	A0IV	1.95	(0.19-16)	(0.28-15)	0.14-14	0.51-14	0.93-14	0.18-13	0.51-12	0.11-12	0.63-12	0.53-12	3
β Gem	K0III	1.15	0.63-15	0.63-14	0.26-13	0.66-13	0.14-12	0.23-12	0.46-12	0.71-12	0.13-11	0.11-11	3
α Gem	A1V	1.59				0.59-14	0.13-13	0.25-13	0.72-13	0.17-12	0.88-12	0.73-12	3
ε Eri	K2V	3.73		(0.45-15)	0.19-14	0.50-14	0.10-13	0.18-13	0.35-13	0.57-13	0.12-12	0.92-13	2
σ Dra	K0V	4.68		(0.15-15)	0.64-15	0.17-14	0.35-14	0.61-14	0.14-13	0.23-13	0.51-13	0.37-13	3
γ Dra	K5III	2.22	0.57-15	0.78-14	0.31-13	0.75-13	0.14-12	0.23-12	0.41-12	0.54-12	0.49-12	0.78-12	3
61 Cyg B	K7V	6.02	(0.14-16)	(0.17-15)	0.72-15	0.19-14	0.37-14	0.61-14	0.10-13	0.15-13	0.15-13	0.23-13	3
ε Cyg	K0III	2.45	(0.12-15)	(0.16-14)	0.69-14	0.19-13	0.39-13	0.66-13	0.14-12	0.22-12	0.40-12	0.35-12	4
β Cyg	gK1p	3.07		(0.17-14)	0.70-14	0.19-13	0.42-13	0.66-13	0.13-12	0.19-12	0.23-12	0.22-12	3
α Cyg	A2Ia	1.26	(0.48-16)	0.72-15	0.35-14	0.10-13	0.24-13	0.46-13	0.12-12	0.26-12	0.12-11	0.94-12	3
ε Cr B	K3III	4.15	(0.49-16)	(0.64-15)	0.27-14	0.67-14	0.13-13	0.21-13	(0.44-13)	(0.67-13)	0.83-13	0.91-13	1
β Com	G0V	4.30		(0.16-15)	0.73-15	0.20-14	0.41-14	0.73-14	0.17-13	0.29-13	0.73-13	0.53-13	3
δ Cep	cF4	3.70			0.63-15	0.22-14	0.47-14	0.87-14	0.21-13	0.38-13	0.13-12	0.10-12	1
θ Cen	K0III-IV	1.98		(0.27-14)	0.11-13	0.30-13	0.60-13	0.10-12	0.22-12	0.35-12	0.61-12	0.53-12	1
β Cas	F2IV	2.25	(0.25-16)	(0.44-15)	0.22-14	0.65-14	0.15-13	0.28-13	0.67-13	0.12-12	0.47-12	0.34-12	3
α CMa	A1V	−1.47	0.59-15	0.65-14	0.30-13	0.84-13	0.19-12	0.39-12	0.10-11	0.22-11	0.15-10	0.14-10	3
β Aur	A2IV	+1.90			(0.17-14)	0.44-14	0.11-13	0.20-13	0.50-13	0.11-12	0.66-12	0.56-12	3
α Eri	B9V	0.06		(0.44-15)	(0.26-14)	0.82-14	0.22-13	0.56-13	0.16-12	0.94-12	0.36-11	0.81-11	1
α Leo	B7V	1.33	0.41-16	0.35-15	0.16-14	0.50-14	0.12-13	0.24-13	0.74-13	0.16-12	0.11-11	0.14-11	3
α Aql	A7IV	0.75			0.72-14	0.19-13	0.46-13	0.84-13	0.20-12	0.41-12	0.19-11	0.14-11	3
α And	A0p	2.13				0.30-14	0.60-14	0.13-13	0.35-13	0.77-13	0.54-12	0.68-12	3
β Ori	B8Ia	0.08	(0.98-16)	0.14-14	0.67-14	0.20-14	0.48-13	0.92-13	0.25-12	0.62-12	0.35-11	0.45-11	3
α Lyr	A0V	0.03	0.11-15	0.17-14	0.79-14	0.23-13	0.53-13	0.11-12	0.29-12	0.64-12	0.37-11	0.31-11	4
ζ Pup	O5	2.25			0.37-15	0.13-14	0.32-14	0.65-14	0.22-13	0.52-13	0.48-12	0.13-10	3
SUN	G2V	−26.73		0.41-03	0.18-02	0.49-02	0.10-01	0.19-01	0.44-01	0.71-01	0.19-00	0.13-00	4
δ And	K3III	+3.25		(0.12-14)	0.53-14	0.14-13	0.28-13	0.51-13	0.12-12	0.18-12	0.19-12	0.22-12	1
ζ Cep	K1Ib	3.36		(0.17-14)	0.69-14	0.22-13	0.45-13	0.75-13	0.14-12	0.21-12	0.17-12	0.25-12	1
δ Sge	M2	3.80		(0.18-14)	0.12-13	0.43-13	0.75-13	0.11-12	0.18-12	0.22-12	0.11-12	0.37.12	1
μ Cep	M2Ia	3.99	0.38-15	0.11-13	0.56-13	0.13-12	0.21-12	0.31-12	0.50-12	0.61-12	0.96-13	0.64-12	2

(Continued)

Table 10-7. Spectral irradiance at selected wavelengths and the total irradiance, H, in the infrared region; for 0.28-14 read 0.28×10^{-14}. Values in parentheses are less reliable than others. (For spectral type classification symbols, see Sec. 21.2.8 and Sec. 21.4.1; additional symbols are prefix c for supergiant, suffix p for peculiar spectrum.) (Continued)

Star	Spectral Type	V (mag)	Spectral Irradiance (W cm^{-2} μ^{-1}) (Continued)									H (W cm^{-2})	w*
			10 μ	5 μ	3.33 μ	2.5 μ	2.00 μ	1.67 μ	1.25 μ	1.0 μ	0.566 μ		
18 Cep	gM5	5.5		(0.12-14)	0.80-14	0.22-13	0.44-13	0.67-13	0.11-12	0.14-12	0.24-13		1
α Her	M5II	3.04	0.39-14	0.50-13	0.21-12	0.64-12	0.12-11	(0.19-12)	(0.23-11)	0.23-11	0.23-12	0.35-11	2
η Gem	M3III	3.10		0.46-14	0.24-13	0.66-13	0.13-12	0.23-12	(0.39-12)	(0.57-12)	0.22-12	0.70-12	2
μ Gem	M3III	2.91		(0.81-14)	0.47-13	0.14-12	0.26-12	(0.42-12)	(0.80-12)	0.10-11	0.26-12	0.87-12	2
2 Cen	cM6	4.20		0.14-13	0.51-13	0.11-12	(0.17-12)	(0.24-12)	(0.30-12)	(0.29-12)	0.80-13	0.63-12	1
β Peg	M2II	2.60		0.14-13	0.76-13	0.19-12	0.35-12	0.50-12	0.82-12	0.97-12	0.35-12	0.13-11	3
δ Lyr	M4	4.50	0.66-15	0.80-14	0.33-13	0.77-13	0.16-12	0.23-12	0.37-12	0.39-12	0.60-13	0.52-12	2
α Cet	M2II	2.52	0.77-15	0.99-14	0.39-13	0.97-13	0.18-12	0.27-12	0.47-12	0.62-12	0.37-12	0.90-12	3
Barnard's	M5V	9.54			(0.23-15)	0.45-15	0.83-15	0.11-14	0.17-14	0.20-14	0.58-15	0.34-14	1
HR 5299	gM4	5.13		(0.31-14)	0.12-13	(0.32-13)	0.60-13	(0.77-13)	(0.11-12)	(0.10-12)	0.34-13	0.17-12	1
HR 483	G2V	4.94		(0.89-16)	(0.39-15)	0.11-14	0.22-14	0.40-14	0.92-14	0.16-13	0.40-13	0.30-13	3
γ Vir	F0V	2.74		(0.30-15)	0.13-14	0.38-14	0.89-14	0.17-13	0.40-13	0.76-13	0.31-12	0.21-12	2
α Vir	B2V	0.98		0.34-15	0.15-14	0.49-14	0.12-13	0.23-13	0.73-13	0.16-12	0.15-11	0.14-10	3
μ UMa	M0III	3.00	0.47-15	0.61-14	0.23-13	0.57-13	0.10-12	0.16-12	0.27-12	0.34-12	0.24-12	0.45-12	3
α UMa	K0IV	1.79	0.36-15	0.40-14	0.17-13	0.44-13	0.88-13	0.15-12	0.30-12	0.45-12	0.73-12	0.71-12	3
δ Tau	K0III	3.73	(0.76-16)	(0.61-15)	0.25-14	0.61-14	0.12-13	0.21-13	0.45-13	0.70-13	0.12-12	0.11-12	2
α Cas	K0II	2.47		0.29-14	(0.12-13)	0.30-13	0.60-13	0.10-12	0.20-12	0.30-12	0.39-12	0.39-12	1
α CMi	F5IV	0.34	0.41-15	0.36-14	0.16-13	0.46-13	0.10-12	0.19-12	0.45-12	0.77-12	0.28-11	0.19-11	3
β Cnc	K4III	3.53	(0.15-15)	(0.19-14)	0.76-14	0.23-13	0.43-13	0.61-13	0.99-13	0.13-12	0.15-12	0.20-12	2
η Boo	G0IV	2.70		0.49-15	0.22-14	0.63-14	0.13-13	0.24-13	0.58-13	0.10-12	0.32-12	0.22-12	2
α Boo	K2IIIp	−0.06		0.42-13	0.17-12	0.44-12	0.85-12	0.14-11	0.26-11	0.32-11	0.40-11	0.45-12	3
i Aur	K3II	+2.70	0.68-15	0.50-14	0.20-13	0.48-13	0.93-13	0.15-12	0.26-12	0.36-12	0.32-12	0.51-12	3
α Aur	G8III+F	0.09	0.11-14	0.11-13	0.49-13	0.13-12	0.26-12	0.47-12	0.10-11	0.16-11	0.35-11	0.26-11	4
α Ari	K2III	1.99	(0.26-15)	(0.35-14)	0.15-13	0.38-13	0.78-13	0.13-12	0.26-12	0.40-12	0.61-12	0.59-12	4
γ Aql	K3III	2.64	(0.34-15)	(0.45-14)	0.18-13	0.46-13	0.88-13	0.14-12	0.25-12	0.33-12	0.33-12	0.45-12	3
γ And	K2III	2.30	(0.32-15)	(0.44-14)	0.18-13	0.45-13	0.87-13	0.14-12	0.27-12	0.40-12	0.46-12	0.56-12	3
β And	M0III	2.06	(0.11-14)	(0.13-13)	0.54-13	0.12-12	0.23-12	0.35-12	0.60-12	0.81-12	0.57-12	0.11-11	3

* weighing factor: 1 is poor, 2 is fair, 3 is good, and 4 is suitable as a tentative standard

10.4.2 IR Backgrounds Originating in the Solar System

Table 10-11 briefly summarizes the irradiance of the earth's atmosphere by the principal members of the solar system; for details see Ramsey [1962]. The irradiance received from planets and satellites is the sum of two components, the reflected solar radiation and the thermal emission due to the temperature of the object. In Table 10-11, the irradiance in the lead sulfide region includes both components, whereas the peak spectral irradiance is for the thermal emission component.

There are no intensive studies of the dependence of the reflected component of the infrared irradiance on the planet's phase. It is probable that this component obeys the same phase laws as the visible radiation. The phase effect for the thermal component depends strongly upon the extent of the planetary atmosphere. Thermal emission from the moon shows a strong phase effect. The temperature of the lunar surface at the subsolar point may be as high as 374°K while that of the dark side may be as low as 120°K. Mercury shows a strong phase effect, primarily due to the variation of the temperature at the subsolar point from about 688°K at perihelion to 558°K at aphelion. For both Mercury and the moon, the phase effect observed is more pronounced than that calculated for blackbody radiation. Measurements of Mars in the region 8 to 13 μ indicate a strong dependence of surface temperature on the color of the surface feature being observed. Dawn to noon temperatures typically vary over the range from 200 to 293°K. The heavily clouded atmosphere of Venus shows strong phase effects in the visible region, but measurements of 8- to 13-μ emission indicate that day to night temperature differences are less than 10°K. For Jupiter and Saturn, no complete phase information is available. Because of the apparently high opacity of their atmospheres and the rapid rotations of these planets, it is expected that any phase variations would be small. The extremely low temperatures of Neptune, Uranus, and Pluto preclude their contributing more than a negligible amount to the background radiation.

The infrared radiation from the zodiacal light and the gegenschein constitute a source of large spatial extent. Table 10-12 presents order-of-magnitude estimates of the expected radiance in the lead sulfide region. These values are based upon the distribution of particle density and the scattering properties observed in the visible region. The elongation is the angle in the plane of the ecliptic measured from the earth-sun line; zero degrees is taken as toward the sun.

Table 10-12. Radiance from the zodiacal light and gengenschein, wavelength region 0.8 to 3.0 μ.

Elongation (deg)	Radiance (W cm^{-2} sr^{-1})	Angular Width* (deg)
10	1.5×10^{-8}	
20	3.1×10^{-9}	
30	1.1×10^{-9}	25
50	4.6×10^{-10}	
70	2.5×10^{-10}	
90	1.6×10^{-10}	50
130	9.9×10^{-11}	70
150	1.0×10^{-10}	
180	1.5×10^{-10}	40

* Perpendicular to the plane of the ecliptic.

Table 10-11. Irradiance of earth's atmosphere by sun, moon, and planets.

Object	Irradiance in Region 0.8 to 3 μ (W cm^{-2})	Self Emission Component: Peak Spectral Irradiance (W cm^{-2} μ^{-1})	Self Emission Component: Peak Wavelength (μ)	Self Emission Component: Effective Temp (°K)	Remarks
Sun	0.119	1.98×10^{-1}	0.54	5778	see Table 10-7
Moon	2.6×10^{-7}	2.51×10^{-7}	7.24	374	full moon
Mercury	1.20×10^{-11}	5.84×10^{-11}	4.20	613	elongation
Venus	1.78×10^{-10}	6.04×10^{-12}	8.7	241	elongation
Mars	3.67×10^{-12}	7.76×10^{-13}	10.16	293	quadrature
Mars		3.75×10^{-12}	10.16	293	opposition
Jupiter	8.18×10^{-12}	3.49×10^{-13}	21.46	150	*
Saturn	8.4×10^{-13}	3.26×10^{-14}	24.14	125	*
Uranus	1.0×10^{-15}	1.96×10^{-16}	32.19	90	opposition
Neptune	8.0×10^{-15}	—	—	—	opposition

* Total irradiance at quadrature and peak spectral irradiance at opposition.

Table 10-13. Infrared transmittance of water vapor at 1-atm pressure, 300°K, and averaged over 100 cm^{-1} intervals. (From P. J. Wyatt et al [1962].)

Wave-number (cm^{-1})	Water Vapor Amount (pr-cm)														
	50	20	10	5	2	1	0.5	0.2	0.1	0.05	0.02	0.01	0.005	0.002	0.001
1050.0	0.317	0.615	0.784	0.895	0.966	0.986	0.993	0.997	0.999	0.999	1.000	1.000	1.000	1.000	1.000
1100.0	0.205	0.494	0.685	0.824	0.926	0.963	0.981	0.992	0.996	0.998	0.999	1.000	1.000	1.000	1.000
1150.0	0.099	0.333	0.533	0.702	0.854	0.919	0.955	0.978	0.988	0.994	0.998	0.999	0.999	1.000	1.000
1200.0	0.031	0.171	0.343	0.525	0.727	0.832	0.899	0.950	0.972	0.985	0.994	0.997	0.998	0.999	1.000
1250.0	0.005	0.055	0.150	0.290	0.502	0.648	0.764	0.870	0.920	0.954	0.979	0.989	0.994	0.998	0.999
1300.0	0.000	0.006	0.033	0.097	0.241	0.377	0.522	0.686	0.781	0.852	0.918	0.951	0.972	0.988	0.994
1350.0	0.000	0.001	0.006	0.022	0.070	0.137	0.234	0.393	0.518	0.636	0.765	0.840	0.897	0.946	0.969
1400.0	0.000	0.000	0.000	0.000	0.003	0.016	0.054	0.168	0.299	0.445	0.620	0.727	0.812	0.893	0.935
1450.0	0.000	0.000	0.000	0.000	0.000	0.001	0.009	0.064	0.155	0.280	0.462	0.590	0.699	0.812	0.876
1500.0	0.000	0.000	0.000	0.000	0.000	0.000	0.000	0.011	0.047	0.122	0.276	0.411	0.544	0.699	0.793
1550.0	0.000	0.000	0.000	0.000	0.000	0.003	0.016	0.062	0.118	0.201	0.346	0.469	0.588	0.725	0.809
1600.0	0.000	0.000	0.000	0.000	0.000	0.003	0.020	0.083	0.165	0.279	0.453	0.579	0.687	0.797	0.858
1650.0	0.000	0.000	0.000	0.000	0.000	0.001	0.005	0.028	0.073	0.154	0.310	0.441	0.564	0.703	0.788
1700.0	0.000	0.000	0.000	0.000	0.000	0.000	0.001	0.016	0.052	0.124	0.269	0.396	0.520	0.668	0.762
1750.0	0.000	0.000	0.000	0.000	0.000	0.000	0.002	0.026	0.082	0.177	0.342	0.475	0.598	0.736	0.819
1800.0	0.000	0.000	0.000	0.000	0.000	0.001	0.007	0.048	0.123	0.238	0.420	0.557	0.678	0.802	0.871
1850.0	0.000	0.000	0.000	0.000	0.001	0.011	0.049	0.163	0.289	0.429	0.604	0.714	0.801	0.884	0.926
1900.0	0.000	0.000	0.000	0.000	0.006	0.037	0.117	0.287	0.435	0.573	0.721	0.804	0.866	0.923	0.952
1950.0	0.000	0.000	0.000	0.006	0.048	0.129	0.250	0.430	0.557	0.668	0.783	0.849	0.898	0.943	0.965
2000.0	0.000	0.000	0.005	0.030	0.129	0.257	0.402	0.581	0.691	0.780	0.865	0.911	0.943	0.971	0.983
2050.0	0.000	0.002	0.020	0.079	0.234	0.383	0.524	0.681	0.773	0.844	0.910	0.943	0.966	0.984	0.991
2100.0	0.000	0.010	0.056	0.158	0.357	0.512	0.645	0.778	0.850	0.902	0.947	0.968	0.981	0.991	0.995
2150.0	0.012	0.078	0.183	0.325	0.525	0.657	0.763	0.863	0.915	0.949	0.975	0.987	0.993	0.997	0.999
2200.0	0.041	0.183	0.342	0.505	0.690	0.791	0.864	0.928	0.957	0.976	0.990	0.995	0.997	0.999	1.000
2250.0	0.106	0.330	0.518	0.677	0.823	0.891	0.935	0.968	0.982	0.991	0.996	0.998	0.999	1.000	1.000
2300.0	0.197	0.490	0.685	0.825	0.926	0.961	0.979	0.991	0.995	0.998	0.999	1.000	1.000	1.000	1.000
2350.0	0.272	0.581	0.759	0.879	0.953	0.975	0.987	0.994	0.997	0.998	0.999	1.000	1.000	1.000	1.000
2400.0	0.327	0.638	0.802	0.904	0.962	0.978	0.988	0.994	0.997	0.999	0.999	1.000	1.000	1.000	1.000
2450.0	0.378	0.687	0.840	0.929	0.974	0.986	0.993	0.997	0.998	0.999	1.000	1.000	1.000	1.000	1.000
2500.0	0.412	0.719	0.865	0.947	0.983	0.992	0.997	0.999	0.999	1.000	1.000	1.000	1.000	1.000	1.000
2550.0	0.398	0.708	0.858	0.944	0.983	0.993	0.997	0.999	1.000	1.000	1.000	1.000	1.000	1.000	1.000
2600.0	0.340	0.646	0.808	0.909	0.966	0.983	0.992	0.997	0.999	0.999	1.000	1.000	1.000	1.000	1.000
2650.0	0.296	0.593	0.764	0.876	0.949	0.974	0.987	0.995	0.998	0.999	1.000	1.000	1.000	1.000	1.000
2700.0	0.208	0.469	0.647	0.781	0.891	0.939	0.967	0.987	0.993	0.997	0.999	0.999	1.000	1.000	1.000
2750.0	0.157	0.400	0.582	0.727	0.860	0.920	0.957	0.982	0.991	0.995	0.998	0.999	1.000	1.000	1.000
2800.0	0.143	0.391	0.584	0.738	0.875	0.932	0.965	0.986	0.993	0.997	0.999	0.999	1.000	1.000	1.000
2850.0	0.087	0.308	0.510	0.683	0.841	0.909	0.950	0.979	0.989	0.994	0.998	0.999	1.000	1.000	1.000
2900.0	0.041	0.188	0.361	0.534	0.717	0.811	0.876	0.933	0.959	0.976	0.989	0.994	0.997	0.999	0.999
2950.0	0.007	0.074	0.200	0.364	0.573	0.697	0.790	0.874	0.917	0.947	0.973	0.985	0.992	0.997	0.998
3000.0	0.002	0.036	0.120	0.249	0.439	0.569	0.677	0.788	0.851	0.899	0.946	0.969	0.983	0.993	0.996
3050.0	0.001	0.017	0.063	0.153	0.315	0.442	0.559	0.694	0.778	0.846	0.914	0.949	0.972	0.988	0.994
3100.0	0.000	0.003	0.022	0.077	0.199	0.314	0.437	0.596	0.703	0.792	0.882	0.929	0.960	0.983	0.991
3150.0	0.000	0.009	0.043	0.113	0.243	0.360	0.482	0.636	0.736	0.817	0.897	0.938	0.965	0.985	0.992
3200.0	0.000	0.008	0.041	0.113	0.261	0.392	0.520	0.668	0.759	0.831	0.901	0.938	0.964	0.984	0.992
3250.0	0.000	0.000	0.004	0.030	0.127	0.245	0.379	0.553	0.668	0.765	0.862	0.915	0.951	0.978	0.989

(Continued)

Table 10-13. Infrared transmittance of water vapor at 1-atm pressure, 300°K, and averaged over 100 cm^{-1} intervals. (From P. J. Wyatt et al [1962].) (Continued)

Wave-number (cm^{-1})	Water Vapor Amount (pr-cm)														
	50	20	10	5	2	1	0.5	0.2	0.1	0.05	0.02	0.01	0.005	0.002	0.001
3300.0	0.000	0.000	0.002	0.022	0.114	0.238	0.383	0.566	0.683	0.780	0.875	0.924	0.957	0.981	0.990
3350.0	0.000	0.000	0.001	0.011	0.086	0.209	0.366	0.565	0.688	0.783	0.873	0.919	0.952	0.977	0.988
3400.0	0.000	0.000	0.000	0.003	0.040	0.124	0.256	0.457	0.596	0.711	0.822	0.881	0.923	0.960	0.978
3450.0	0.000	0.000	0.000	0.001	0.015	0.055	0.138	0.305	0.450	0.587	0.736	0.821	0.883	0.937	0.963
3500.0	0.000	0.000	0.000	0.000	0.002	0.016	0.055	0.168	0.296	0.440	0.619	0.732	0.821	0.902	0.941
3550.0	0.000	0.000	0.000	0.000	0.000	0.002	0.012	0.064	0.148	0.267	0.448	0.579	0.694	0.814	0.880
3600.0	0.000	0.000	0.000	0.000	0.000	0.000	0.001	0.014	0.063	0.160	0.340	0.483	0.612	0.751	0.831
3650.0	0.000	0.000	0.000	0.000	0.000	0.000	0.000	0.007	0.039	0.118	0.285	0.428	0.564	0.714	0.801
3700.0	0.000	0.000	0.000	0.000	0.000	0.000	0.000	0.001	0.012	0.049	0.151	0.260	0.381	0.540	0.649
3750.0	0.000	0.000	0.000	0.000	0.000	0.000	0.000	0.007	0.034	0.093	0.214	0.324	0.436	0.573	0.665
3800.0	0.000	0.000	0.000	0.000	0.000	0.000	0.000	0.011	0.052	0.139	0.307	0.445	0.571	0.703	0.778
3850.0	0.000	0.000	0.000	0.000	0.000	0.000	0.000	0.006	0.029	0.091	0.238	0.377	0.517	0.676	0.769
3900.0	0.000	0.000	0.000	0.000	0.000	0.000	0.004	0.030	0.078	0.160	0.318	0.453	0.583	0.727	0.810
3950.0	0.000	0.000	0.000	0.000	0.003	0.017	0.056	0.157	0.266	0.392	0.561	0.674	0.767	0.859	0.908
4000.0	0.000	0.000	0.001	0.013	0.071	0.155	0.268	0.438	0.565	0.676	0.792	0.857	0.906	0.948	0.969
4050.0	0.000	0.006	0.043	0.137	0.327	0.482	0.619	0.762	0.840	0.896	0.943	0.966	0.980	0.991	0.995
4100.0	0.001	0.040	0.167	0.371	0.639	0.784	0.878	0.949	0.975	0.988	0.995	0.998	0.999	1.000	1.000
4150.0	0.006	0.115	0.330	0.572	0.807	0.902	0.957	0.989	0.996	0.999	1.000	1.000	1.000	1.000	1.000
4200.0	0.021	0.208	0.459	0.685	0.872	0.940	0.976	0.995	0.998	1.000	1.000	1.000	1.000	1.000	1.000
4250.0	0.046	0.295	0.550	0.751	0.902	0.958	0.985	0.996	0.999	1.000	1.000	1.000	1.000	1.000	1.000
4300.0	0.083	0.376	0.622	0.799	0.923	0.969	0.990	0.997	1.000	1.000	1.000	1.000	1.000	1.000	1.000
4350.0	0.121	0.439	0.672	0.831	0.937	0.975	0.992	0.998	1.000	1.000	1.000	1.000	1.000	1.000	1.000
4400.0	0.140	0.455	0.674	0.827	0.931	0.971	0.988	0.996	0.999	0.999	1.000	1.000	1.000	1.000	1.000
4450.0	0.119	0.395	0.602	0.758	0.882	0.936	0.965	0.984	0.992	0.996	0.998	0.999	0.100	1.000	1.000
4500.0	0.070	0.271	0.459	0.624	0.781	0.860	0.910	0.954	0.973	0.985	0.994	0.997	0.998	0.999	1.000
4550.0	0.064	0.249	0.430	0.591	0.753	0.836	0.891	0.941	0.964	0.980	0.991	0.995	0.998	0.999	1.000
4600.0	0.058	0.228	0.390	0.534	0.688	0.775	0.843	0.909	0.944	0.968	0.986	0.993	0.996	0.999	0.999
4650.0	0.073	0.246	0.399	0.531	0.674	0.758	0.827	0.899	0.938	0.965	0.984	0.992	0.996	0.998	0.999
4700.0	0.111	0.325	0.496	0.629	0.758	0.826	0.877	0.929	0.956	0.975	0.989	0.994	0.997	0.999	0.999
4750.0	0.095	0.298	0.472	0.617	0.757	0.829	0.882	0.932	0.958	0.975	0.989	0.994	0.997	0.999	0.999
4800.0	0.059	0.223	0.384	0.533	0.689	0.775	0.841	0.906	0.941	0.965	0.984	0.992	0.996	0.998	0.999
4850.0	0.064	0.242	0.413	0.571	0.728	0.809	0.869	0.924	0.952	0.971	0.987	0.993	0.996	0.999	0.999
4900.0	0.067	0.251	0.429	0.595	0.758	0.838	0.895	0.942	0.964	0.978	0.990	0.995	0.997	0.999	0.999
4950.0	0.039	0.184	0.352	0.524	0.706	0.802	0.870	0.930	0.958	0.976	0.989	0.994	0.997	0.999	1.000
5000.0	0.019	0.116	0.253	0.416	0.614	0.731	0.819	0.899	0.938	0.965	0.984	0.992	0.996	0.998	0.999
5050.0	0.003	0.040	0.120	0.249	0.454	0.598	0.716	0.830	0.891	0.934	0.969	0.983	0.991	0.997	0.998
5100.0	0.000	0.009	0.040	0.107	0.253	0.389	0.527	0.688	0.785	0.858	0.925	0.956	0.976	0.990	0.995
5150.0	0.000	0.000	0.003	0.015	0.071	0.159	0.285	0.473	0.607	0.720	0.832	0.891	0.933	0.967	0.981
5200.0	0.000	0.000	0.000	0.000	0.010	0.045	0.124	0.289	0.433	0.571	0.722	0.807	0.871	0.929	0.957
5250.0	0.000	0.000	0.000	0.000	0.009	0.041	0.114	0.273	0.416	0.554	0.707	0.794	0.858	0.918	0.948
5300.0	0.000	0.000	0.000	0.000	0.008	0.035	0.093	0.219	0.337	0.456	0.597	0.685	0.760	0.839	0.807
5350.0	0.000	0.000	0.000	0.000	0.002	0.014	0.055	0.171	0.289	0.411	0.560	0.657	0.740	0.828	0.881
5400.0	0.000	0.000	0.000	0.000	0.005	0.027	0.088	0.238	0.380	0.520	0.678	0.771	0.841	0.907	0.940
5450.0	0.000	0.000	0.000	0.002	0.025	0.080	0.173	0.337	0.472	0.599	0.735	0.812	0.869	0.922	0.949
5500.0	0.000	0.000	0.000	0.007	0.060	0.150	0.271	0.447	0.571	0.679	0.791	0.853	0.901	0.945	0.967

(Continued)

Table 10-13. Infrared transmittance of water vapor at 1-atm pressure, 300°K, and averaged over 100 cm^{-1} intervals. (From P. J. Wyatt et al [1962].) (Continued)

Wave-number (cm^{-1})	Water Vapor Amount (pr-cm)														
	50	20	10	5	2	1	0.5	0.2	0.1	0.05	0.02	0.01	0.005	0.002	0.001
5550.0	0.000	0.004	0.023	0.069	0.180	0.297	0.424	0.586	0.692	0.779	0.866	0.912	0.945	0.973	0.985
5600.0	0.001	0.023	0.082	0.186	0.365	0.505	0.633	0.768	0.844	0.899	0.948	0.970	0.984	0.993	0.996
5650.0	0.053	0.180	0.314	0.458	0.633	0.744	0.830	0.908	0.946	0.970	0.987	0.993	0.997	0.999	0.999
5700.0	0.119	0.338	0.522	0.679	0.826	0.898	0.943	0.975	0.987	0.993	0.997	0.999	0.999	1.000	1.000
5750.0	0.196	0.433	0.607	0.742	0.864	0.920	0.956	0.981	0.990	0.995	0.998	0.999	1.000	1.000	1.000
5800.0	0.339	0.595	0.749	0.851	0.931	0.963	0.981	0.992	0.996	0.998	0.999	1.000	1.000	1.000	1.000
5850.0	0.428	0.684	0.822	0.905	0.962	0.982	0.991	0.996	0.998	0.999	1.000	1.000	1.000	1.000	1.000
5900.0	0.493	0.731	0.851	0.922	0.968	0.985	0.993	0.997	0.998	0.999	1.000	1.000	1.000	1.000	1.000
5950.0	0.481	0.705	0.819	0.893	0.949	0.973	0.986	0.994	0.997	0.999	0.999	1.000	1.000	1.000	1.000
6000.0	0.373	0.600	0.733	0.828	0.908	0.946	0.969	0.986	0.993	0.996	0.999	0.999	1.000	1.000	1.000
6050.0	0.387	0.615	0.745	0.834	0.910	0.945	0.968	0.985	0.992	0.996	0.998	0.999	1.000	1.000	1.000
6100.0	0.345	0.559	0.685	0.779	0.869	0.917	0.950	0.977	0.988	0.994	0.997	0.999	1.000	1.000	1.000
6150.0	0.329	0.529	0.654	0.752	0.851	0.905	0.943	0.974	0.986	0.993	0.997	0.999	0.999	1.000	1.000
6200.0	0.354	0.558	0.682	0.776	0.869	0.916	0.950	0.977	0.988	0.994	0.997	0.999	1.000	1.000	1.000
6250.0	0.262	0.478	0.623	0.738	0.850	0.907	0.946	0.975	0.987	0.993	0.997	0.999	0.999	1.000	1.000
6300.0	0.181	0.386	0.545	0.683	0.822	0.892	0.938	0.972	0.986	0.993	0.997	0.998	0.999	1.000	1.000
6350.0	0.112	0.282	0.441	0.599	0.772	0.862	0.922	0.965	0.982	0.991	0.996	0.998	0.999	1.000	1.000
6400.0	0.093	0.244	0.394	0.553	0.739	0.840	0.909	0.959	0.979	0.989	0.996	0.998	0.999	1.000	1.000
6450.0	0.071	0.199	0.336	0.492	0.689	0.806	0.887	0.950	0.794	0.987	0.995	0.997	0.999	1.000	1.000
6500.0	0.056	0.189	0.335	0.497	0.694	0.809	0.890	0.951	0.975	0.987	0.995	0.997	0.999	1.000	1.000
6550.0	0.071	0.222	0.376	0.534	0.716	0.820	0.894	0.952	0.975	0.987	0.995	0.997	0.999	1.000	1.000
6600.0	0.081	0.243	0.399	0.553	0.725	0.823	0.892	0.949	0.972	0.986	0.994	0.997	0.998	0.999	1.000
6650.0	0.070	0.218	0.367	0.519	0.693	0.794	0.869	0.934	0.963	0.980	0.992	0.996	0.998	0.999	1.000
6700.0	0.027	0.111	0.221	0.357	0.543	0.669	0.773	0.874	0.925	0.957	0.981	0.990	0.995	0.998	0.999
6750.0	0.005	0.043	0.118	0.234	0.422	0.564	0.687	0.814	0.881	0.928	0.966	0.982	0.990	0.996	0.998
6800.0	0.004	0.047	0.129	0.248	0.432	0.568	0.687	0.809	0.876	0.924	0.963	0.980	0.990	0.996	0.998
6850.0	0.002	0.031	0.090	0.180	0.336	0.464	0.587	0.726	0.809	0.873	0.932	0.960	0.978	0.991	0.995
6900.0	0.001	0.011	0.045	0.117	0.264	0.395	0.524	0.675	0.769	0.843	0.915	0.950	0.973	0.988	0.994
6950.0	0.000	0.008	0.041	0.116	0.273	0.411	0.546	0.702	0.796	0.867	0.932	0.962	0.980	0.992	0.996
7000.0	0.000	0.003	0.017	0.060	0.172	0.296	0.438	0.619	0.735	0.827	0.911	0.950	0.973	0.989	0.994
7050.0	0.000	0.000	0.002	0.015	0.077	0.173	0.303	0.493	0.628	0.744	0.858	0.916	0.953	0.980	0.989
7100.0	0.000	0.000	0.001	0.008	0.052	0.129	0.243	0.424	0.563	0.687	0.815	0.883	0.931	0.968	0.983
7150.0	0.000	0.000	0.000	0.003	0.027	0.085	0.187	0.366	0.510	0.642	0.782	0.860	0.914	0.959	0.978
7200.0	0.000	0.000	0.000	0.000	0.008	0.034	0.089	0.209	0.327	0.458	0.627	0.737	0.826	0.908	0.947
7250.0	0.000	0.000	0.000	0.004	0.033	0.082	0.155	0.281	0.392	0.510	0.662	0.761	0.842	0.916	0.952
7300.0	0.000	0.000	0.000	0.005	0.041	0.109	0.213	0.389	0.527	0.652	0.785	0.859	0.912	0.957	0.976
7350.0	0.000	0.000	0.000	0.001	0.015	0.056	0.137	0.300	0.443	0.580	0.735	0.826	0.892	0.947	0.971
7400.0	0.000	0.000	0.000	0.004	0.033	0.093	0.195	0.374	0.516	0.648	0.790	0.868	0.922	0.964	0.981
7450.0	0.000	0.000	0.001	0.007	0.052	0.134	0.256	0.447	0.589	0.713	0.838	0.903	0.945	0.976	0.988
7500.0	0.000	0.002	0.018	0.061	0.170	0.281	0.408	0.576	0.690	0.784	0.877	0.925	0.957	0.981	0.990
7550.0	0.000	0.006	0.039	0.123	0.302	0.448	0.581	0.722	0.803	0.864	0.921	0.950	0.970	0.986	0.993
7600.0	0.000	0.009	0.048	0.139	0.323	0.470	0.600	0.736	0.812	0.869	0.922	0.950	0.970	0.986	0.993
7650.0	0.006	0.043	0.112	0.221	0.402	0.539	0.657	0.779	0.846	0.897	0.943	0.966	0.981	0.992	0.996
7700.0	0.057	0.174	0.296	0.426	0.589	0.695	0.782	0.867	0.913	0.946	0.974	0.985	0.992	0.997	0.998
7750.0	0.245	0.440	0.581	0.698	0.813	0.875	0.919	0.958	0.976	0.987	0.995	0.997	0.999	0.999	1.000

(Continued)

Table 10-13. Infrared transmittance of water vapor at 1-atm pressure, 300°K, and averaged over 100 cm^{-1} intervals. (From P. J. Wyatt et al [1962].) (Continued)

Wavenumber (cm^{-1})	Water Vapor Amount (pr-cm)														
	50	20	10	5	2	1	0.5	0.2	0.1	0.05	0.02	0.01	0.005	0.002	0.001
7800.0	0.554	0.737	0.830	0.892	0.944	0.968	0.983	0.993	0.996	0.998	0.999	1.000	1.000	1.000	1.000
7850.0	0.724	0.868	0.922	0.953	0.977	0.987	0.993	0.997	0.999	0.999	1.000	1.000	1.000	1.000	1.000
7900.0	0.781	0.897	0.939	0.963	0.981	0.989	0.994	0.998	0.999	0.999	1.000	1.000	1.000	1.000	1.000
7950.0	0.845	0.933	0.963	0.979	0.990	0.995	0.997	0.999	0.999	1.000	1.000	1.000	1.000	1.000	1.000
8000.0	0.815	0.910	0.947	0.969	0.986	0.992	0.996	0.998	0.999	1.000	1.000	1.000	1.000	1.000	1.000
8050.0	0.710	0.832	0.891	0.932	0.966	0.982	0.990	0.996	0.998	0.999	1.000	1.000	1.000	1.000	1.000
8100.0	0.597	0.747	0.827	0.887	0.940	0.965	0.981	0.992	0.996	0.998	0.999	1.000	1.000	1.000	1.000
8150.0	0.547	0.708	0.798	0.866	0.927	0.957	0.976	0.989	0.995	0.997	0.999	1.000	1.000	1.000	1.000
8200.0	0.361	0.528	0.643	0.743	0.848	0.905	0.944	0.975	0.987	0.993	0.997	0.999	0.999	1.000	1.000
8250.0	0.192	0.369	0.509	0.637	0.776	0.854	0.911	0.957	0.977	0.988	0.995	0.997	0.999	1.000	1.000
8300.0	0.210	0.390	0.527	0.650	0.780	0.853	0.907	0.954	0.974	0.986	0.994	0.997	0.999	0.999	1.000
8350.0	0.154	0.320	0.452	0.575	0.712	0.794	0.859	0.920	0.952	0.973	0.988	0.994	0.997	0.999	0.999
8400.0	0.127	0.290	0.426	0.551	0.690	0.774	0.841	0.908	0.944	0.968	0.986	0.993	0.996	0.999	0.999
8450.0	0.143	0.319	0.462	0.592	0.731	0.812	0.873	0.931	0.960	0.978	0.991	0.995	0.998	0.999	1.000
8500.0	0.177	0.356	0.494	0.620	0.755	0.832	0.890	0.943	0.968	0.983	0.993	0.996	0.998	0.999	1.000
8550.0	0.220	0.394	0.524	0.642	0.772	0.849	0.906	0.955	0.975	0.987	0.995	0.997	0.999	1.000	1.000
8600.0	0.189	0.355	0.488	0.614	0.755	0.839	0.902	0.954	0.976	0.987	0.995	0.997	0.999	1.000	1.000
8650.0	0.089	0.231	0.371	0.516	0.688	0.790	0.867	0.932	0.962	0.979	0.991	0.995	0.998	0.999	1.000
8700.0	0.047	0.167	0.303	0.454	0.639	0.750	0.834	0.909	0.945	0.968	0.986	0.993	0.996	0.999	0.999
8750.0	0.036	0.138	0.260	0.401	0.584	0.702	0.796	0.884	0.928	0.958	0.981	0.990	0.995	0.998	0.999
8800.0	0.028	0.107	0.205	0.326	0.496	0.616	0.721	0.828	0.887	0.930	0.966	0.981	0.990	0.996	0.998
8850.0	0.031	0.120	0.229	0.356	0.525	0.638	0.734	0.832	0.887	0.928	0.965	0.981	0.990	0.996	0.998
8900.0	0.030	0.127	0.249	0.392	0.578	0.697	0.792	0.881	0.926	0.957	0.980	0.990	0.995	0.998	0.999
8950.0	0.040	0.140	0.261	0.400	0.583	0.702	0.799	0.892	0.937	0.965	0.985	0.992	0.996	0.998	0.999
9000.0	0.082	0.215	0.348	0.490	0.663	0.770	0.854	0.927	0.960	0.979	0.991	0.996	0.998	0.999	1.000
9050.0	0.190	0.366	0.507	0.636	0.777	0.857	0.915	0.961	0.979	0.989	0.996	0.998	0.999	1.000	1.000
9100.0	0.322	0.517	0.648	0.752	0.854	0.908	0.944	0.974	0.986	0.993	0.997	0.998	0.999	1.000	1.000
9150.0	0.413	0.605	0.721	0.809	0.889	0.928	0.955	0.978	0.988	0.994	0.997	0.999	0.999	1.000	1.000
9200.0	0.472	0.654	0.760	0.836	0.905	0.938	0.962	0.982	0.990	0.995	0.998	0.999	0.999	1.000	1.000
9250.0	0.560	0.720	0.808	0.871	0.927	0.955	0.973	0.988	0.994	0.997	0.999	0.999	1.000	1.000	1.000
9300.0	0.693	0.810	0.872	0.915	0.954	0.973	0.985	0.993	0.997	0.998	0.999	1.000	1.000	1.000	1.000
9350.0	0.824	0.897	0.934	0.959	0.980	0.989	0.994	0.998	0.999	0.999	1.000	1.000	1.000	1.000	1.000
9400.0	0.903	0.947	0.969	0.982	0.992	0.996	0.998	0.999	1.000	1.000	1.000	1.000	1.000	1.000	1.000
9450.0	0.942	0.973	0.986	0.993	0.997	0.999	0.999	1.000	1.000	1.000	1.000	1.000	1.000	1.000	1.000
9500.0	0.934	0.970	0.985	0.992	0.997	0.998	0.999	1.000	1.000	1.000	1.000	1.000	1.000	1.000	1.000
9550.0	0.903	0.953	0.974	0.986	0.994	0.997	0.999	0.999	1.000	1.000	1.000	1.000	1.000	1.000	1.000
9600.0	0.843	0.915	0.950	0.972	0.988	0.994	0.997	0.999	0.999	1.000	1.000	1.000	1.000	1.000	1.000
9650.0	0.720	0.832	0.895	0.938	0.972	0.985	0.992	0.997	0.998	0.999	1.000	1.000	1.000	1.000	1.000
9700.0	0.627	0.767	0.847	0.905	0.953	0.974	0.986	0.994	0.997	0.999	0.999	1.000	1.000	1.000	1.000
9750.0	0.604	0.747	0.828	0.887	0.940	0.966	0.981	0.992	0.996	0.998	0.999	1.000	1.000	1.000	1.000
9800.0	0.571	0.716	0.800	0.864	0.923	0.953	0.973	0.988	0.994	0.997	0.999	0.999	1.000	1.000	1.000
9850.0	0.525	0.676	0.766	0.837	0.904	0.940	0.965	0.984	0.992	0.996	0.998	0.999	1.000	1.000	1.000
9900.0	0.500	0.661	0.755	0.829	0.899	0.937	0.963	0.984	0.992	0.996	0.998	0.999	1.000	1.000	1.000
9950.0	0.493	0.662	0.760	0.836	0.907	0.944	0.968	0.986	0.993	0.996	0.999	0.999	1.000	1.000	1.000

Table 10-14. Infrared transmittance of carbon dioxide at 1-atm pressure, 300°K, and averaged over 50 cm^{-1} intervals. (From V. R. Stull, P. J. Wyatt, and G. N. Plass, *Appl. Opt.*, v. 3, no. 2, p. 243, 1964, by permission.)

Wavenumber (cm^{-1})	CO_2 Concentration Reduced to 273°K (atm-cm)														
	10,000	5,000	2,000	1,000	500	200	100	50	20	10	5	2	1.0	0.5	0.2
550.0	0.143	0.294	0.526	0.685	0.809	0.914	0.956	0.978	0.992	0.996	0.998	0.999	1.000	1.000	1.000
600.0	0.000	0.000	0.005	0.023	0.063	0.165	0.282	0.421	0.596	0.707	0.797	0.888	0.934	0.964	0.985
650.0	0.000	0.000	0.000	0.000	0.000	0.000	0.002	0.009	0.039	0.088	0.171	0.335	0.476	0.603	0.737
700.0	0.000	0.000	0.000	0.000	0.000	0.003	0.013	0.039	0.107	0.189	0.303	0.492	0.633	0.750	0.860
750.0	0.001	0.010	0.053	0.115	0.199	0.341	0.466	0.594	0.740	0.824	0.886	0.941	0.967	0.982	0.993
800.0	0.147	0.310	0.549	0.705	0.824	0.921	0.959	0.979	0.992	0.996	0.998	0.999	1.000	1.000	1.000
850.0	0.170	0.329	0.540	0.672	0.775	0.875	0.927	0.960	0.983	0.991	0.996	0.998	0.999	1.000	1.000
900.0	0.563	0.697	0.823	0.885	0.929	0.966	0.981	0.990	0.996	0.998	0.999	1.000	1.000	1.000	1.000
950.0	0.598	0.727	0.847	0.909	0.949	0.978	0.989	0.994	0.998	0.999	0.999	1.000	1.000	1.000	1.000
1000.0	0.736	0.829	0.910	0.948	0.972	0.988	0.994	0.997	0.999	0.999	1.000	1.000	1.000	1.000	1.000
1050.0	0.326	0.483	0.668	0.775	0.856	0.927	0.960	0.979	0.991	0.996	0.998	0.999	1.000	1.000	1.000
1100.0	0.640	0.717	0.815	0.874	0.919	0.960	0.978	0.988	0.995	0.998	0.999	0.999	1.000	1.000	1.000
1150.0	1.000	1.000	1.000	1.000	1.000	1.000	1.000	1.000	1.000	1.000	1.000	1.000	1.000	1.000	1.000
1200.0	1.000	1.000	1.000	1.000	1.000	1.000	1.000	1.000	1.000	1.000	1.000	1.000	1.000	1.000	1.000
1250.0	1.000	1.000	1.000	1.000	1.000	1.000	1.000	1.000	1.000	1.000	1.000	1.000	1.000	1.000	1.000
1300.0	1.000	1.000	1.000	1.000	1.000	1.000	1.000	1.000	1.000	1.000	1.000	1.000	1.000	1.000	1.000
1350.0	1.000	1.000	1.000	1.000	1.000	1.000	1.000	1.000	1.000	1.000	1.000	1.000	1.000	1.000	1.000
1400.0	1.000	1.000	1.000	1.000	1.000	1.000	1.000	1.000	1.000	1.000	1.000	1.000	1.000	1.000	1.000
1450.0	1.000	1.000	1.000	1.000	1.000	1.000	1.000	1.000	1.000	1.000	1.000	1.000	1.000	1.000	1.000
1500.0	1.000	1.000	1.000	1.000	1.000	1.000	1.000	1.000	1.000	1.000	1.000	1.000	1.000	1.000	1.000
1550.0	1.000	1.000	1.000	1.000	1.000	1.000	1.000	1.000	1.000	1.000	1.000	1.000	1.000	1.000	1.000
1600.0	1.000	1.000	1.000	1.000	1.000	1.000	1.000	1.000	1.000	1.000	1.000	1.000	1.000	1.000	1.000
1650.0	1.000	1.000	1.000	1.000	1.000	1.000	1.000	1.000	1.000	1.000	1.000	1.000	1.000	1.000	1.000
1700.0	1.000	1.000	1.000	1.000	1.000	1.000	1.000	1.000	1.000	1.000	1.000	1.000	1.000	1.000	1.000
1750.0	1.000	1.000	1.000	1.000	1.000	1.000	1.000	1.000	1.000	1.000	1.000	1.000	1.000	1.000	1.000
1800.0	0.995	1.000	1.000	1.000	1.000	1.000	1.000	1.000	1.000	1.000	1.000	1.000	1.000	1.000	1.000
1850.0	0.968	0.994	0.999	0.999	1.000	1.000	1.000	1.000	1.000	1.000	1.000	1.000	1.000	1.000	1.000
1900.0	0.610	0.741	0.866	0.921	0.956	0.981	0.990	0.995	0.998	0.999	1.000	1.000	1.000	1.000	1.000
1950.0	0.481	0.618	0.760	0.841	0.897	0.949	0.972	0.986	0.994	0.997	0.999	1.000	1.000	1.000	1.000
2000.0	0.655	0.801	0.916	0.965	0.987	0.995	0.997	0.999	1.000	1.000	1.000	1.000	1.000	1.000	1.000
2050.0	0.138	0.264	0.472	0.618	0.737	0.842	0.896	0.935	0.969	0.983	0.991	0.996	0.998	0.999	1.000
2100.0	0.019	0.087	0.272	0.440	0.593	0.754	0.840	0.899	0.951	0.974	0.986	0.994	0.997	0.999	0.999
2150.0	0.036	0.168	0.465	0.674	0.820	0.926	0.969	0.991	0.997	0.999	0.999	1.000	1.000	1.000	1.000
2200.0	0.001	0.022	0.157	0.340	0.537	0.752	0.861	0.930	0.979	0.992	0.996	0.998	0.999	1.000	1.000
2250.0	0.000	0.000	0.000	0.001	0.008	0.042	0.096	0.174	0.318	0.455	0.595	0.752	0.837	0.898	0.950
2300.0	0.000	0.000	0.000	0.000	0.000	0.000	0.000	0.000	0.005	0.024	0.068	0.168	0.271	0.293	0.567
2350.0	0.000	0.000	0.000	0.000	0.000	0.000	0.000	0.000	0.000	0.000	0.000	0.000	0.003	0.020	0.114
2400.0	0.000	0.000	0.000	0.000	0.003	0.042	0.131	0.262	0.441	0.552	0.638	0.725	0.778	0.825	0.879
2450.0	0.000	0.000	0.014	0.084	0.244	0.532	0.720	0.847	0.939	0.973	0.991	0.999	1.000	1.000	1.000
2500.0	0.004	0.045	0.250	0.484	0.691	0.963	0.931	0.970	0.994	0.999	1.000	1.000	1.000	1.000	1.000
2550.0	0.107	0.310	0.617	0.785	0.887	0.957	0.984	0.997	1.000	1.000	1.000	1.000	1.000	1.000	1.000
2600.0	0.383	0.615	0.824	0.910	0.957	0.991	0.999	1.000	1.000	1.000	1.000	1.000	1.000	1.000	1.000
2650.0	0.649	0.806	0.920	0.963	0.988	1.000	1.000	1.000	1.000	1.000	1.000	1.000	1.000	1.000	1.000
2700.0	0.817	0.905	0.966	0.990	0.999	1.000	1.000	1.000	1.000	1.000	1.000	1.000	1.000	1.000	1.000
2750.0	0.903	0.954	0.990	0.999	1.000	1.000	1.000	1.000	1.000	1.000	1.000	1.000	1.000	1.000	1.000
2800.0	0.950	0.981	0.999	1.000	1.000	1.000	1.000	1.000	1.000	1.000	1.000	1.000	1.000	1.000	1.000
2850.0	0.977	0.996	1.000	1.000	1.000	1.000	1.000	1.000	1.000	1.000	1.000	1.000	1.000	1.000	1.000
2900.0	0.994	1.000	1.000	1.000	1.000	1.000	1.000	1.000	1.000	1.000	1.000	1.000	1.000	1.000	1.000
2950.0	1.000	1.000	1.000	1.000	1.000	1.000	1.000	1.000	1.000	1.000	1.000	1.000	1.000	1.000	1.000
3000.0	1.000	1.000	1.000	1.000	1.000	1.000	1.000	1.000	1.000	1.000	1.000	1.000	1.000	1.000	1.000
3050.0	1.000	1.000	1.000	1.000	1.000	1.000	1.000	1.000	1.000	1.000	1.000	1.000	1.000	1.000	1.000
3100.0	1.000	1.000	1.000	1.000	1.000	1.000	1.000	1.000	1.000	1.000	1.000	1.000	1.000	1.000	1.000
3150.0	1.000	1.000	1.000	1.000	1.000	1.000	1.000	1.000	1.000	1.000	1.000	1.000	1.000	1.000	1.000
3200.0	1.000	1.000	1.000	1.000	1.000	1.000	1.000	1.000	1.000	1.000	1.000	1.000	1.000	1.000	1.000
3250.0	1.000	1.000	1.000	1.000	1.000	1.000	1.000	1.000	1.000	1.000	1.000	1.000	1.000	1.000	1.000
3300.0	0.997	0.998	0.999	1.000	1.000	1.000	1.000	1.000	1.000	1.000	1.000	1.000	1.000	1.000	1.000
3350.0	0.936	0.965	0.985	0.992	0.996	0.999	0.999	1.000	1.000	1.000	1.000	1.000	1.000	1.000	1.000
3400.0	0.719	0.838	0.927	0.962	0.981	0.992	0.996	0.998	0.999	1.000	1.000	1.000	1.000	1.000	1.000
3450.0	0.282	0.436	0.635	0.756	0.848	0.927	0.961	0.980	0.992	0.996	0.998	0.999	1.000	1.000	1.000

(Continued)

Table 10-14. Infrared transmittance of carbon dioxide at 1-atm pressure, 300°K, and averaged over 50 cm^{-1} intervals. (From V. R. Stull, P. J. Wyatt, and G. N. Plass, *Appl. Opt.*, v. 3, no. 2, p. 243, 1964, by permission.) (Continued)

Wavenumber (cm^{-1})	CO_2 Concentration Reduced to 273°K (atm-cm)														
	10,000	5,000	2,000	1,000	500	200	100	50	20	10	5	2	1.0	0.5	0.2
3500.0	0.004	0.025	0.112	0.240	0.406	0.625	0.756	0.849	0.927	0.960	0.979	0.991	0.996	0.998	0.999
3550.0	0.000	0.000	0.002	0.013	0.045	0.138	0.254	0.404	0.163	0.746	0.845	0.928	0.961	0.980	0.992
3600.0	0.000	0.000	0.000	0.000	0.000	0.001	0.010	0.045	0.167	0.313	0.474	0.663	0.772	0.853	0.927
3650.0	0.000	0.000	0.000	0.000	0.003	0.034	0.103	0.217	0.408	0.554	0.680	0.806	0.873	0.920	0.961
3700.0	0.000	0.000	0.000	0.000	0.000	0.001	0.009	0.035	0.131	0.259	0.414	0.610	0.729	0.820	0.905
3750.0	0.004	0.029	0.112	0.191	0.264	0.345	0.396	0.444	0.512	0.576	0.655	0.764	0.835	0.891	0.942
3800.0	0.153	0.335	0.587	0.734	0.841	0.928	0.964	0.982	0.993	0.997	0.998	0.999	1.000	1.000	1.000
3850.0	0.472	0.624	0.784	0.867	0.921	0.963	0.980	0.990	0.996	0.998	0.999	1.000	1.000	1.000	1.000
3900.0	0.900	0.949	0.982	0.992	0.996	0.998	0.999	1.000	1.000	1.000	1.000	1.000	1.000	1.000	1.000
3950.0	0.988	0.998	1.000	1.000	1.000	1.000	1.000	1.000	1.000	1.000	1.000	1.000	1.000	1.000	1.000
4000.0	0.999	1.000	1.000	1.000	1.000	1.000	1.000	1.000	1.000	1.000	1.000	1.000	1.000	1.000	1.000
4050.0	1.000	1.000	1.000	1.000	1.000	1.000	1.000	1.000	1.000	1.000	1.000	1.000	1.000	1.000	1.000
4100.0	1.000	1.000	1.000	1.000	1.000	1.000	1.000	1.000	1.000	1.000	1.000	1.000	1.000	1.000	1.000
4150.0	1.000	1.000	1.000	1.000	1.000	1.000	1.000	1.000	1.000	1.000	1.000	1.000	1.000	1.000	1.000
4200.0	1.000	1.000	1.000	1.000	1.000	1.000	1.000	1.000	1.000	1.000	1.000	1.000	1.000	1.000	1.000
4250.0	1.000	1.000	1.000	1.000	1.000	1.000	1.000	1.000	1.000	1.000	1.000	1.000	1.000	1.000	1.000
4300.0	1.000	1.000	1.000	1.000	1.000	1.000	1.000	1.000	1.000	1.000	1.000	1.000	1.000	1.000	1.000
4350.0	1.000	1.000	1.000	1.000	1.000	1.000	1.000	1.000	1.000	1.000	1.000	1.000	1.000	1.000	1.000
4400.0	1.000	1.000	1.000	1.000	1.000	1.000	1.000	1.000	1.000	1.000	1.000	1.000	1.000	1.000	1.000
4450.0	1.000	1.000	1.000	1.000	1.000	1.000	1.000	1.000	1.000	1.000	1.000	1.000	1.000	1.000	1.000
4500.0	1.000	1.000	1.000	1.000	1.000	1.000	1.000	1.000	1.000	1.000	1.000	1.000	1.000	1.000	1.000
4550.0	1.000	1.000	1.000	1.000	1.000	1.000	1.000	1.000	1.000	1.000	1.000	1.000	1.000	1.000	1.000
4600.0	0.999	1.000	1.000	1.000	1.000	1.000	1.000	1.000	1.000	1.000	1.000	1.000	1.000	1.000	1.000
4650.0	0.992	0.996	0.999	0.999	1.000	1.000	1.000	1.000	1.000	1.000	1.000	1.000	1.000	1.000	1.000
4700.0	0.890	0.939	0.973	0.986	0.993	0.997	0.999	0.999	1.000	1.000	1.000	1.000	1.000	1.000	1.000
4750.0	0.551	0.698	0.844	0.913	0.954	0.981	0.990	0.995	0.998	0.999	1.000	1.000	1.000	1.000	1.000
4800.0	0.133	0.271	0.489	0.644	0.770	0.884	0.935	0.965	0.985	0.993	0.996	0.998	0.999	1.000	1.000
4850.0	0.009	0.042	0.165	0.311	0.469	0.652	0.759	0.843	0.920	0.956	0.977	0.990	0.995	0.998	0.999
4900.0	0.131	0.267	0.489	0.646	0.770	0.877	0.927	0.958	0.981	0.990	0.995	0.998	0.999	1.000	1.000
4950.0	0.015	0.050	0.147	0.265	0.411	0.605	0.727	0.819	0.903	0.943	0.969	0.987	0.993	0.997	0.999
5000.0	0.121	0.179	0.265	0.352	0.462	0.619	0.726	0.813	0.896	0.939	0.966	0.986	0.993	0.996	0.999
5050.0	0.393	0.550	0.723	0.816	0.881	0.936	0.962	0.978	0.991	0.995	0.998	0.999	1.000	1.000	1.000
5100.0	0.020	0.077	0.233	0.388	0.541	0.709	0.806	0.880	0.943	0.969	0.984	0.994	0.997	0.998	0.999
5150.0	0.530	0.629	0.754	0.836	0.899	0.952	0.974	0.986	0.994	0.997	0.999	0.999	1.000	1.000	1.000
5200.0	0.984	0.992	0.997	0.998	0.999	1.000	1.000	1.000	1.000	1.000	1.000	1.000	1.000	1.000	1.000
5250.0	0.987	0.993	0.997	0.999	0.999	1.000	1.000	1.000	1.000	1.000	1.000	1.000	1.000	1.000	1.000
5300.0	0.999	0.999	1.000	1.000	1.000	1.000	1.000	1.000	1.000	1.000	1.000	1.000	1.000	1.000	1.000
5350.0	1.000	1.000	1.000	1.000	1.000	1.000	1.000	1.000	1.000	1.000	1.000	1.000	1.000	1.000	1.000
5400.0	1.000	1.000	1.000	1.000	1.000	1.000	1.000	1.000	1.000	1.000	1.000	1.000	1.000	1.000	1.000
5450.0	1.000	1.000	1.000	1.000	1.000	1.000	1.000	1.000	1.000	1.000	1.000	1.000	1.000	1.000	1.000
5500.0	1.000	1.000	1.000	1.000	1.000	1.000	1.000	1.000	1.000	1.000	1.000	1.000	1.000	1.000	1.000
5550.0	0.998	0.999	1.000	1.000	1.000	1.000	1.000	1.000	1.000	1.000	1.000	1.000	1.000	1.000	1.000
5600.0	0.997	0.998	0.999	1.000	1.000	1.000	1.000	1.000	1.000	1.000	1.000	1.000	1.000	1.000	1.000
5650.0	0.997	0.998	0.999	1.000	1.000	1.000	1.000	1.000	1.000	1.000	1.000	1.000	1.000	1.000	1.000
5700.0	0.994	0.997	0.999	0.999	1.000	1.000	1.000	1.000	1.000	1.000	1.000	1.000	1.000	1.000	1.000
5750.0	1.000	1.000	1.000	1.000	1.000	1.000	1.000	1.000	1.000	1.000	1.000	1.000	1.000	1.000	1.000
5800.0	1.000	1.000	1.000	1.000	1.000	1.000	1.000	1.000	1.000	1.000	1.000	1.000	1.000	1.000	1.000
5850.0	1.000	1.000	1.000	1.000	1.000	1.000	1.000	1.000	1.000	1.000	1.000	1.000	1.000	1.000	1.000
5900.0	1.000	1.000	1.000	1.000	1.000	1.000	1.000	1.000	1.000	1.000	1.000	1.000	1.000	1.000	1.000
5950.0	0.998	0.999	1.000	1.000	1.000	1.000	1.000	1.000	1.000	1.000	1.000	1.000	1.000	1.000	1.000
6000.0	0.992	0.996	0.998	0.999	1.000	1.000	1.000	1.000	1.000	1.000	1.000	1.000	1.000	1.000	1.000
6050.0	0.935	0.964	0.984	0.992	0.996	0.998	0.999	1.000	1.000	1.000	1.000	1.000	1.000	1.000	1.000
6100.0	0.919	0.955	0.981	0.990	0.995	0.998	0.999	1.000	1.000	1.000	1.000	1.000	1.000	1.000	1.000
6150.0	0.958	0.978	0.991	0.996	0.998	0.999	1.000	1.000	1.000	1.000	1.000	1.000	1.000	1.000	1.000
6200.0	0.675	0.783	0.882	0.930	0.961	0.983	0.991	0.996	0.998	0.999	1.000	1.000	1.000	1.000	1.000
6250.0	0.697	0.791	0.882	0.929	0.960	0.982	0.991	0.995	0.998	0.999	1.000	1.000	1.000	1.000	1.000
6300.0	0.877	0.920	0.958	0.976	0.987	0.995	0.997	0.999	0.999	1.000	1.000	1.000	1.000	1.000	1.000
6350.0	0.510	0.651	0.795	0.873	0.926	0.968	0.983	0.991	0.996	0.998	0.999	1.000	1.000	1.000	1.000
6400.0	0.942	0.965	0.984	0.992	0.996	0.998	0.999	1.000	1.000	1.000	1.000	1.000	1.000	1.000	1.000

(Continued)

Table 10-14. Infrared transmittance of carbon dioxide at 1-atm pressure, 300°K, and averaged over 50 cm^{-1} intervals. (From V. R. Stull, P. J. Wyatt, and G. N. Plass, *Appl. Opt.*, v. 3, no. 2, p. 243, 1964, by permission.)

Wavenumber (cm^{-1})	CO_2 Concentration Reduced to 273°K (atm-cm)														
	10,000	5,000	2,000	1,000	500	200	100	50	20	10	5	2	1.0	0.5	0.2
6450.0	0.978	0.988	0.995	0.998	0.999	1.000	1.000	1.000	1.000	1.000	1.000	1.000	1.000	1.000	1.000
6500.0	0.856	0.915	0.961	0.980	0.990	0.996	0.998	0.999	1.000	1.000	1.000	1.000	1.000	1.000	1.000
6550.0	0.973	0.986	0.994	0.997	0.999	0.999	1.000	1.000	1.000	1.000	1.000	1.000	1.000	1.000	1.000
6600.0	1.000	1.000	1.000	1.000	1.000	1.000	1.000	1.000	1.000	1.000	1.000	1.000	1.000	1.000	1.000
6650.0	1.000	1.000	1.000	1.000	1.000	1.000	1.000	1.000	1.000	1.000	1.000	1.000	1.000	1.000	1.000
6700.0	0.996	0.998	0.999	1.000	1.000	1.000	1.000	1.000	1.000	1.000	1.000	1.000	1.000	1.000	1.000
6750.0	0.949	0.973	0.988	0.994	0.997	0.999	0.999	1.000	1.000	1.000	1.000	1.000	1.000	1.000	1.000
6800.0	0.944	0.969	0.987	0.993	0.997	0.999	0.999	1.000	1.000	1.000	1.000	1.000	1.000	1.000	1.000
6850.0	0.982	0.991	0.996	0.998	0.999	1.000	1.000	1.000	1.000	1.000	1.000	1.000	1.000	1.000	1.000
6900.0	0.701	0.808	0.903	0.946	0.971	0.988	0.994	0.997	0.999	0.999	1.000	1.000	1.000	1.000	1.000
6950.0	0.284	0.446	0.641	0.756	0.841	0.917	0.953	0.975	0.989	0.995	0.997	0.999	0.999	1.000	1.000
7000.0	0.672	0.720	0.787	0.837	0.883	0.933	0.960	0.978	0.991	0.995	0.998	0.999	1.000	1.000	1.000
7050.0	0.999	1.000	1.000	1.000	1.000	1.000	1.000	1.000	1.000	1.000	1.000	1.000	1.000	1.000	1.000
7100.0	1.000	1.000	1.000	1.000	1.000	1.000	1.000	1.000	1.000	1.000	1.000	1.000	1.000	1.000	1.000
7150.0	0.999	0.999	1.000	1.000	1.000	1.000	1.000	1.000	1.000	1.000	1.000	1.000	1.000	1.000	1.000
7200.0	0.995	0.998	0.999	1.000	1.000	1.000	1.000	1.000	1.000	1.000	1.000	1.000	1.000	1.000	1.000
7250.0	0.963	0.980	0.992	0.996	0.998	0.999	1.000	1.000	1.000	1.000	1.000	1.000	1.000	1.000	1.000
7300.0	0.931	0.963	0.984	0.992	0.996	0.998	0.999	1.000	1.000	1.000	1.000	1.000	1.000	1.000	1.000
7350.0	0.969	0.984	0.993	0.997	0.998	0.999	1.000	1.000	1.000	1.000	1.000	1.000	1.000	1.000	1.000
7400.0	0.886	0.937	0.973	0.986	0.993	0.997	0.999	0.999	1.000	1.000	1.000	1.000	1.000	1.000	1.000
7450.0	0.545	0.682	0.816	0.887	0.935	0.971	0.985	0.992	0.997	0.998	0.999	1.000	1.000	1.000	1.000
7500.0	0.773	0.847	0.915	0.948	0.971	0.987	0.993	0.997	0.999	0.999	1.000	1.000	1.000	1.000	1.000
7550.0	0.687	0.780	0.873	0.920	0.952	0.978	0.988	0.994	0.998	0.999	0.999	1.000	1.000	1.000	1.000
7600.0	0.275	0.436	0.631	0.748	0.837	0.918	0.955	0.976	0.990	0.995	0.997	0.999	0.999	1.000	1.000
7650.0	0.926	0.954	0.977	0.987	0.993	0.997	0.999	0.999	1.000	1.000	1.000	1.000	1.000	1.000	1.000
7700.0	0.771	0.843	0.910	0.945	0.968	0.986	0.993	0.996	0.999	0.999	1.000	1.000	1.000	1.000	1.000
7750.0	0.575	0.704	0.830	0.895	0.940	0.974	0.986	0.993	0.997	0.999	0.999	1.000	1.000	1.000	1.000
7800.0	0.968	0.983	0.993	0.996	0.998	0.999	1.000	1.000	1.000	1.000	1.000	1.000	1.000	1.000	1.000
7850.0	0.997	0.999	1.000	1.000	1.000	1.000	1.000	1.000	1.000	1.000	1.000	1.000	1.000	1.000	1.000
7900.0	0.995	0.976	0.990	0.995	0.997	0.999	0.999	1.000	1.000	1.000	1.000	1.000	1.000	1.000	1.000
7950.0	0.955	0.975	0.990	0.995	0.997	0.999	1.000	1.000	1.000	1.000	1.000	1.000	1.000	1.000	1.000
8000.0	0.998	0.999	1.000	1.000	1.000	1.000	1.000	1.000	1.000	1.000	1.000	1.000	1.000	1.000	1.000
8050.0	1.000	1.000	1.000	1.000	1.000	1.000	1.000	1.000	1.000	1.000	1.000	1.000	1.000	1.000	1.000
8100.0	1.000	1.000	1.000	1.000	1.000	1.000	1.000	1.000	1.000	1.000	1.000	1.000	1.000	1.000	1.000
8150.0	0.997	0.999	0.999	1.000	1.000	1.000	1.000	1.000	1.000	1.000	1.000	1.000	1.000	1.000	1.000
8200.0	0.994	0.997	0.999	0.999	1.000	1.000	1.000	1.000	1.000	1.000	1.000	1.000	1.000	1.000	1.000
8250.0	0.996	0.998	0.999	1.000	1.000	1.000	1.000	1.000	1.000	1.000	1.000	1.000	1.000	1.000	1.000
8300.0	0.990	0.995	0.998	0.999	1.000	1.000	1.000	1.000	1.000	1.000	1.000	1.000	1.000	1.000	1.000
8350.0	1.000	1.000	1.000	1.000	1.000	1.000	1.000	1.000	1.000	1.000	1.000	1.000	1.000	1.000	1.000
8400.0	1.000	1.000	1.000	1.000	1.000	1.000	1.000	1.000	1.000	1.000	1.000	1.000	1.000	1.000	1.000
8450.0	1.000	1.000	1.000	1.000	1.000	1.000	1.000	1.000	1.000	1.000	1.000	1.000	1.000	1.000	1.000
8500.0	1.000	1.000	1.000	1.000	1.000	1.000	1.000	1.000	1.000	1.000	1.000	1.000	1.000	1.000	1.000
8550.0	1.000	1.000	1.000	1.000	1.000	1.000	1.000	1.000	1.000	1.000	1.000	1.000	1.000	1.000	1.000
8600.0	1.000	1.000	1.000	1.000	1.000	1.000	1.000	1.000	1.000	1.000	1.000	1.000	1.000	1.000	1.000
8650.0	1.000	1.000	1.000	1.000	1.000	1.000	1.000	1.000	1.000	1.000	1.000	1.000	1.000	1.000	1.000
8700.0	1.000	1.000	1.000	1.000	1.000	1.000	1.000	1.000	1.000	1.000	1.000	1.000	1.000	1.000	1.000
8750.0	1.000	1.000	1.000	1.000	1.000	1.000	1.000	1.000	1.000	1.000	1.000	1.000	1.000	1.000	1.000
8800.0	0.996	0.998	0.999	1.000	1.000	1.000	1.000	1.000	1.000	1.000	1.000	1.000	1.000	1.000	1.000
8850.0	0.994	0.997	0.999	0.999	1.000	1.000	1.000	1.000	1.000	1.000	1.000	1.000	1.000	1.000	1.000
8900.0	1.000	1.000	1.000	1.000	1.000	1.000	1.000	1.000	1.000	1.000	1.000	1.000	1.000	1.000	1.000
8950.0	0.994	0.997	0.999	0.999	1.000	1.000	1.000	1.000	1.000	1.000	1.000	1.000	1.000	1.000	1.000
9000.0	0.995	0.997	0.999	1.000	1.000	1.000	1.000	1.000	1.000	1.000	1.000	1.000	1.000	1.000	1.000
9050.0	1.000	1.000	1.000	1.000	1.000	1.000	1.000	1.000	1.000	1.000	1.000	1.000	1.000	1.000	1.000
9100.0	1.000	1.000	1.000	1.000	1.000	1.000	1.000	1.000	1.000	1.000	1.000	1.000	1.000	1.000	1.000
9150.0	0.999	1.000	1.000	1.000	1.000	1.000	1.000	1.000	1.000	1.000	1.000	1.000	1.000	1.000	1.000
9200.0 thru 9950.0	1.000	1.000	1.000	1.000	1.000	1.000	1.000	1.000	1.000	1.000	1.000	1.000	1.000	1.000	1.000

10.5 REFERENCES

Bandeen, W. R., B. J. Conrath, and R. A. Hanel, 1963, "Preliminary Results from the TIROS VII Radiation Experiment," *J. Atmos. Sci.*, v. 20, p. 609.

Bell, E. E., L. Eisner, J. Young, and R. A Oetjen, 1960, "Spectral Radiance of Sky and Terrain at Wavelengths between 1 and 20 Microns. II. Sky Measurements," *J. Opt. Soc. Am.*, v. 50, p. 1313.

Bennett, H. E., J. M. Bennett, and M. R. Nagel, 1960, "Distribution of Infrared Radiance over a Clear Sky," *J. Opt. Soc. Am.*, v. 50, p. 100.

Bolle, H. J., 1963, "The 15-26 Micron Sky Emission Spectrum at Jungfraujoch (3570 m)," *Appl. Opt.*, v. 2, p. 571.

Gutnick, M., 1962, "Mean Atmospheric Moisture Profiles to 31 km for Middle Latitudes," *Appl. Opt.*, v. 1, p. 670.

Hanel, R. A., W. R. Bandeen, and B. J. Conrath, 1963, "The Infrared Horizon of the Planet Earth," *J. Atmos. Sci.*, v. 20, no. 2, p. 73.

Johnson, H. L., 1962, "Infrared Stellar Photometry," *Astrophys. J.*, v. 135, p. 69.

Kislovski, L., 1959, "Optical Characteristics of Water and Ice in the Infrared and Radiowave Regions of the Spectrums," *Optics and Spectroscopy*, v. 7, p. 201.

Kondratiev, K. Ya., and K. E. Yakushevskaya, 1962, "The Angular Distribution of the Outgoing Thermal Radiation in the Different Regions of the Spectrum," *Artificial Earth Satellites*, v. 14, p. 13, Academy of Sciences, USSR.

Kruse, P. W., L. D. McGauchlin, and R. B. McQuistan, 1962, "Elements of Infrared Technology," John Wiley, New York.

McGee, R. A., 1962, "Transmission Tables for H_2O, CO_2, and O_3," *Proc. IRIS*, v. 7, no. 2, p. 211.

NASA, Goddard Space Flight Center, 1961, "TIROS II Radiation Data Catalog and Radiation Data Users' Manual."

NASA, Goddard Space Flight Center, 1961, "TIROS II Radiation Data Catalog."

Nordberg, W., W. R. Bandeen, B. J. Conrath, V. Kunde, and I. Persano, 1962, "Preliminary Results of Radiation Measurements from the TIROS III Meteorological Satellite," *J. Atmos. Sci.*, v. 19, p. 20.

Potter, R. F., and W. L. Eisenman, 1962, "Infrared Photodetectors: A Review of Operational Detectors," *Appl. Opt.*, v. 1, p. 567.

Ramsey, R. C., 1962, "Spectral Irradiance from Stars and Planets above the Atmosphere from 0.1 to 100.0 microns," *Appl. Opt.*, v. 1, p. 465.

Walker, R. G., 1964, "Celestial Background Radiation 1. Revised Scale of Bolometric Corrections," *Air Force Surveys in Geophys. No. 155 (1)*, AFCRL.

Willstrop, R. V., 1958, "Narrow Band Photometry of Southern Stars," *Monthly Notices Astro. Soc., South Africa*, v. 17, p. 40.

Wyatt, P. J., V. R. Stull, and G. N. Plass, 1962, "Quasi-Random Model of Band Absorption," *J. Opt. Soc. Am.*, v. 52, p. 1209.

Chapter 11

THE GEOMAGNETIC FIELD

Edwin J. Chernosky
Paul F. Fougere
Robert O. Hutchinson

This chapter is a survey of present knowledge of the magnetic fields in the space immediately surrounding the earth, the *magnetosphere*. The outer limit of this volume of space, which varies considerably with time, is the inner boundary of the transition region where interactions with the interplanetary magnetic fields and solar plasmas predominate.

The *main field* is that portion of the geomagnetic field that originates inside the earth; it is often called the permanent field. The main field is roughly equivalent to the field of a centered dipole with a moment $8.05 \pm 0.02 \times 10^{25}$ gauss cm^3, or $3.114 \times 10^{-5}\,T\,R_E^3$ (T is tesla and R_E is the radius of earth); this dipole is inclined at an angle of about 11° to the axis of rotation. The field strength at the surface is about 0.6 gauss in the polar regions and about 0.3 gauss in the equatorial regions. The main field has a slow secular change that is about 0.1% per year or less, although it may be as much as 0.3% a year in particular regions.

Fields originating outside the earth are much more variable and are weaker; in general, they have durations of a few days or less. Electric current systems in the lower ionosphere are the major sources of the time-varying component of the geomagnetic field. During great magnetic storms, the field variations due to this source may amount to 0.035 gauss in the auroral zones (more than 5% of the main field). At low latitudes, the fluctuations are much smaller. The largest fluctuations last from 15 min to a few hours. Between the earth's surface and the lower ionosphere, the only significant source is electrical discharge in thunderstorms; these produce small fluctuations at frequencies of about 0.1 cps and higher. The extremely small current density of fair weather currents (opposite polarity to lightning discharges) is negligible for most purposes. Above the lower ionosphere, the major sources of magnetic field variations are hydromagnetic wave phenomena and a postulated ring current; direct observational evidence of either is scarce.

The main field at the surface is the most accurately known; in principle, it can be extrapolated upward to give the field, due to sources inside the earth, at great altitudes. This requires first an analytic specification of the field at the surface and then the analytic continuation of the field outward. At altitudes up to several thousand km, the extrapolated values of the main field may be considered correct (within the limitations of the knowledge of the surface fields), and the time-varying fields from other sources may be superposed on the main field. (Extrapolation is strictly accurate only in the space between the surface and the ionosphere, where the conductivity is negligible and no appreciable sources exist.) At altitudes of several earth radii, interactions between the main field and the corpuscular radiation from the sun become more important and eventually become comparable with the computed, undisturbed main field itself. At such altitudes, using the linear superposition of fields is inadequate; more direct observational evidence is required before the estimates of field configurations and variations can be accepted with confidence.

At present, the advance prediction of the time of occurrence of a geomagnetic disturbance is uncertain, and the prediction of the magnitude of a given disturbance is not possible. The description of disturbances is statistical, indicating the probability of disturbance as a function of amplitude, latitude, altitude, and time.

11.1 UNITS, DEFINITIONS, AND MEASUREMENTS

The mixed electrostatic and electromagnetic CGS system of units is used throughout this chapter. The customary unit of measurement is the gamma, regarded interchangeably as a unit of induction (gauss) or of magnetic intensity (oersted); 1 γ is 10^{-5} G (10^{-9} tesla) or 1 γ is 10^{-5} Oe [$(10^{-2}/4\pi)$ ampere-turn per meter].

11.1.1 Elements of the Geomagnetic Field

Figure 11-1 shows the various components, called *elements*, of the geomagnetic field and their associated angles. The magnetic induction at any point is the vector *F* (vector *B* of Maxwell's equations); the scalar F is called the *intensity*, or the *total field*. X, Y, and Z are the Cartesian components of the field; X and Y are positive to the north and east, respectively. Z is called the *vertical intensity* of the field and is positive in the downward direction. H is the *scalar intensity of the horizontal component* of

the field. The *declination*, D (also called the *magnetic variation* and the *variation of the compass*) is the angle between X and H; D is positive measured eastward (clockwise) from north, so that D is positive when Y is positive. I, the *inclination* or *dip*, is the angle between H and F; it is positive directed downward from H to F, so that I is positive when Z is positive.

F may be determined by any one of several triads; those most commonly used are (H, D, Z), (H, I, D), (F, I, D), and (X, Y, Z). The trigonometric relationships among the elements is determined by Fig. 11-1.

11.1.2 Magnetic Coordinates

The *geomagnetic poles* of the earth are defined as the intersections with the surface of the earth of the axis of the best-fit centered dipole (Sec. 11.2.2.1). For epoch 1945 [Vestine, 1947], they were about 79°N, 290°E (near Thule, Greenland) and 79°S, 110°E (in Antarctica). The geomagnetic coordinate system is based on the geomagnetic poles which are defined as ±90° geomagnetic latitude; plus is geomagnetic north. The *prime geomagnetic meridian* is the Greenwich half of the great circle that passes through both geomagnetic and geographic poles; it lies along a geographic meridian at about 290°E (70°W) over most of its length. *Geomagnetic longitude* is measured eastward from this prime geomagnetic meridian (0° geomagnetic longitude). *Geomagnetic hour* is determined by geomagnetic longitude; local geomagnetic noon is the time at which the mean sun (Sec. 21.2.1) crosses the local geomagnetic meridian. Magnetic elements given in geomagnetic coordinates are usually primed; X′ and Y′ indicate the components of field in the geomagnetic north and geomagnetic east direction, respectively.

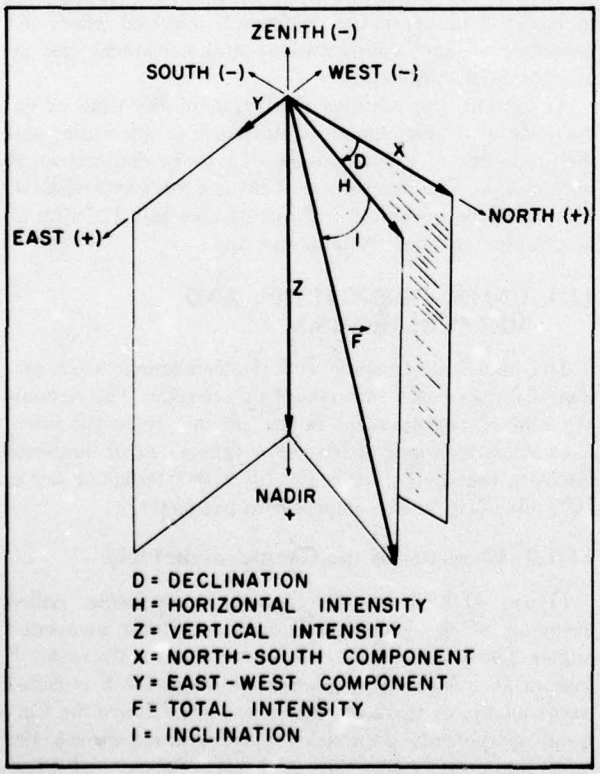


Fig. 11-1. The magnetic force, *F*, and the elements of the earth's magnetic field.

The geomagnetic coordinate system describes the simplest mathematical approximation to the main field of the earth. It is widely used in studies of magnetic disturbance, the ionosphere, cosmic rays, etc.; but for precise studies higher order approximations of the main field may be required (Sec. 11.2.2).

Figure 11-2 shows the geomagnetic coordinate system superposed on a Mercator projection in geographic coordinates. Figure 11-3 is a Mercator projection of the earth drawn in geomagnetic coordinates, showing the locations of magnetic observatories. Figure 11-4 shows polar projections centered on the north and south geomagnetic poles.

The geomagnetic poles must be distinguished from the dip poles, which are often indicated as "magnetic poles" on maps and charts. Magnetic *dip poles* are the points on the surface of the earth where $I = 90°$ (zero horizontal component); they are located asymmetrically at geographic coordinates about 75°N, 259°E, and 67°S, 143°E for epoch 1960. The *magnetic dip equator* is the locus of points where the magnetic field is parallel to the earth's surface ($I = 0$). The dip, geomagnetic, and other equators and poles are discussed in detail by Chernosky et al [1964].

The *magnetic latitude* (also called dip latitude) is a hybrid parameter which has recently come into use. It is based on the formula $\tan \theta = \frac{1}{2} \tan I$. The value of θ when the actual value of I from Fig. 11-5 is used in the formula is the magnetic latitude, see Fig. 11-13. This parameter is easily obtained, varies more smoothly with geographic latitude than I, and at the surface and comparatively low altitudes is more closely related to the actual field than is the dipole approximation. It is useful in the study of ionospheric phenomena at altitudes up to a few hundred km.

11.1.3 Geomagnetic Measurements

The principal source of measurements of the absolute value of the vector magnetic field and of the time variations of its components is the standard magnetic observatory. There are over one hundred of these observatories in operation throughout the world, including about eighty that make their data regularly available to the world scientific community (Fig. 11-3). Observatory data are most frequently presented in the form of hourly values of D, H, and Z (or X, Y, and Z). These data together with hourly values for the 5 and 10 most quiet days and the 5 most disturbed days and reproductions of the daily magnetograms are usually published annually; publication may lag some years behind the observational period. For details of the operation of an observatory and of observatory instruments, see McComb [1952]. An extensive discussion of the instruments and the capabilities and limi-

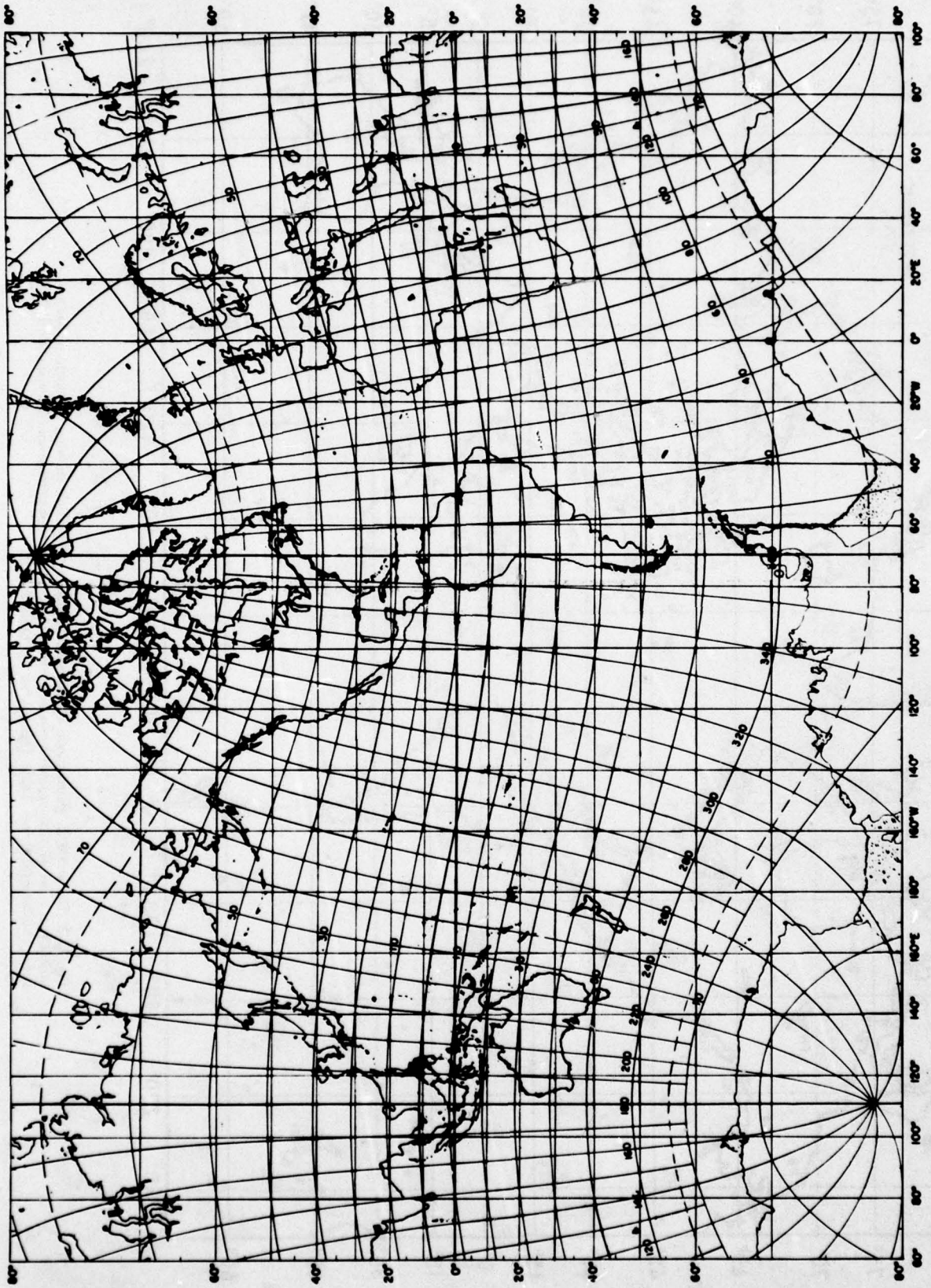


Fig. 11-2. The geomagnetic coordinates (centered dipole field) superposed on geographic Mercator projection. (After Vestine et al [1947].)

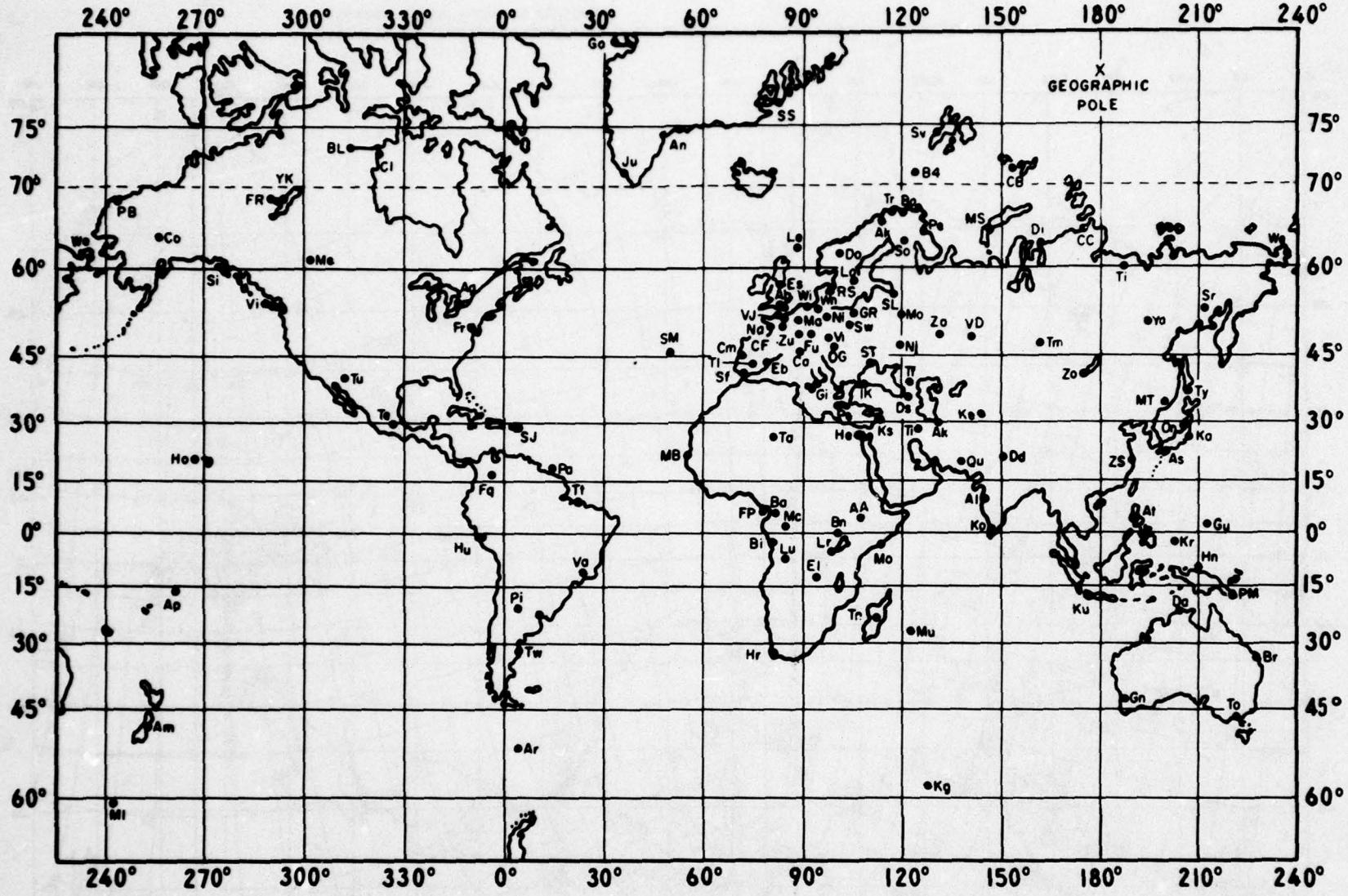


Fig. 11-3. The world in geomagnetic coordinates, Mercator projection, showing magnetic observatories. For a list of some magnetic observatories and their exact geographic and geomagnetic latitudes and longitudes, see Table 11-2. (After N. Fukushima.)

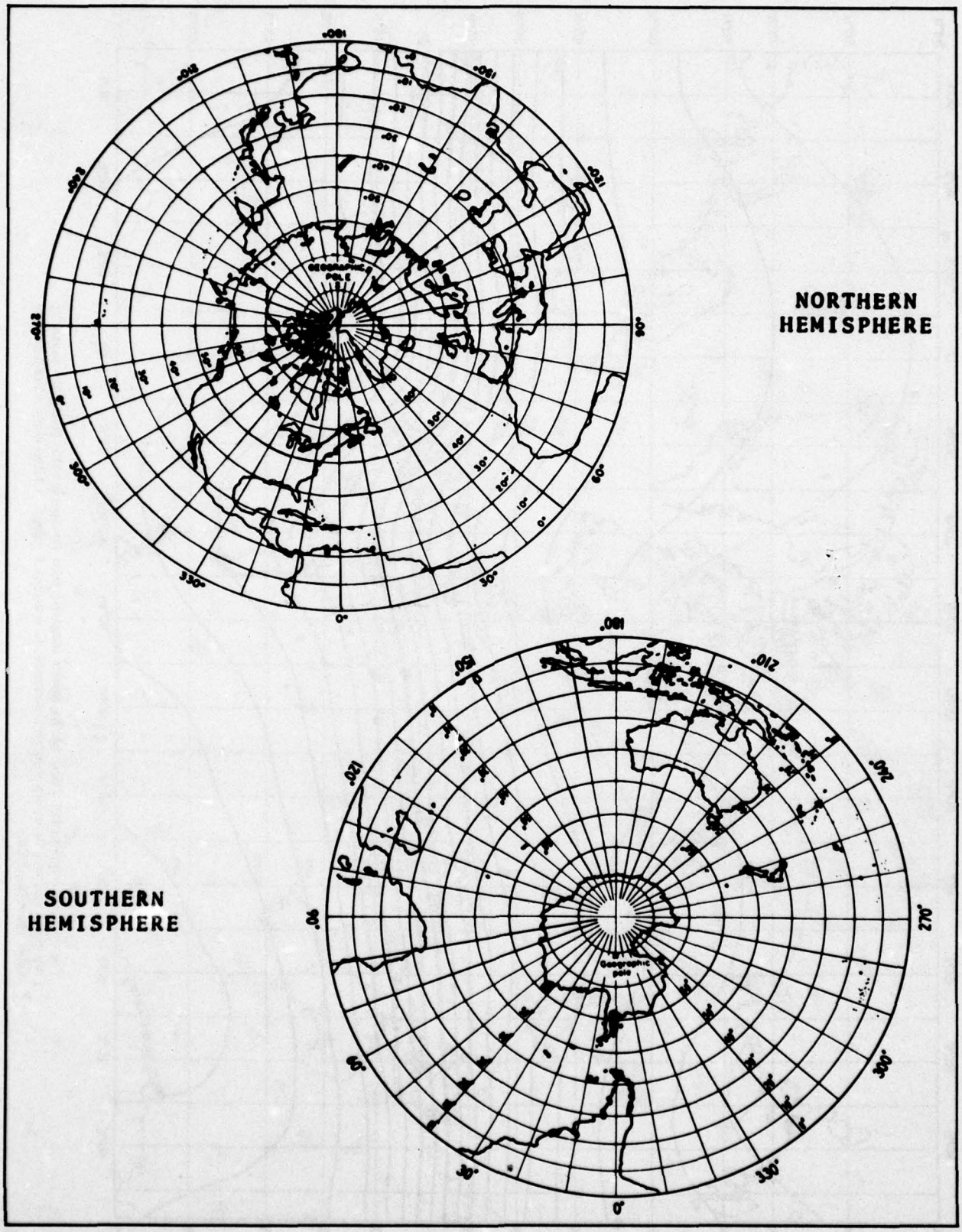


Fig. 11-4. The world in geomagnetic coordinates, polar projections. (After N. Fukushima.)

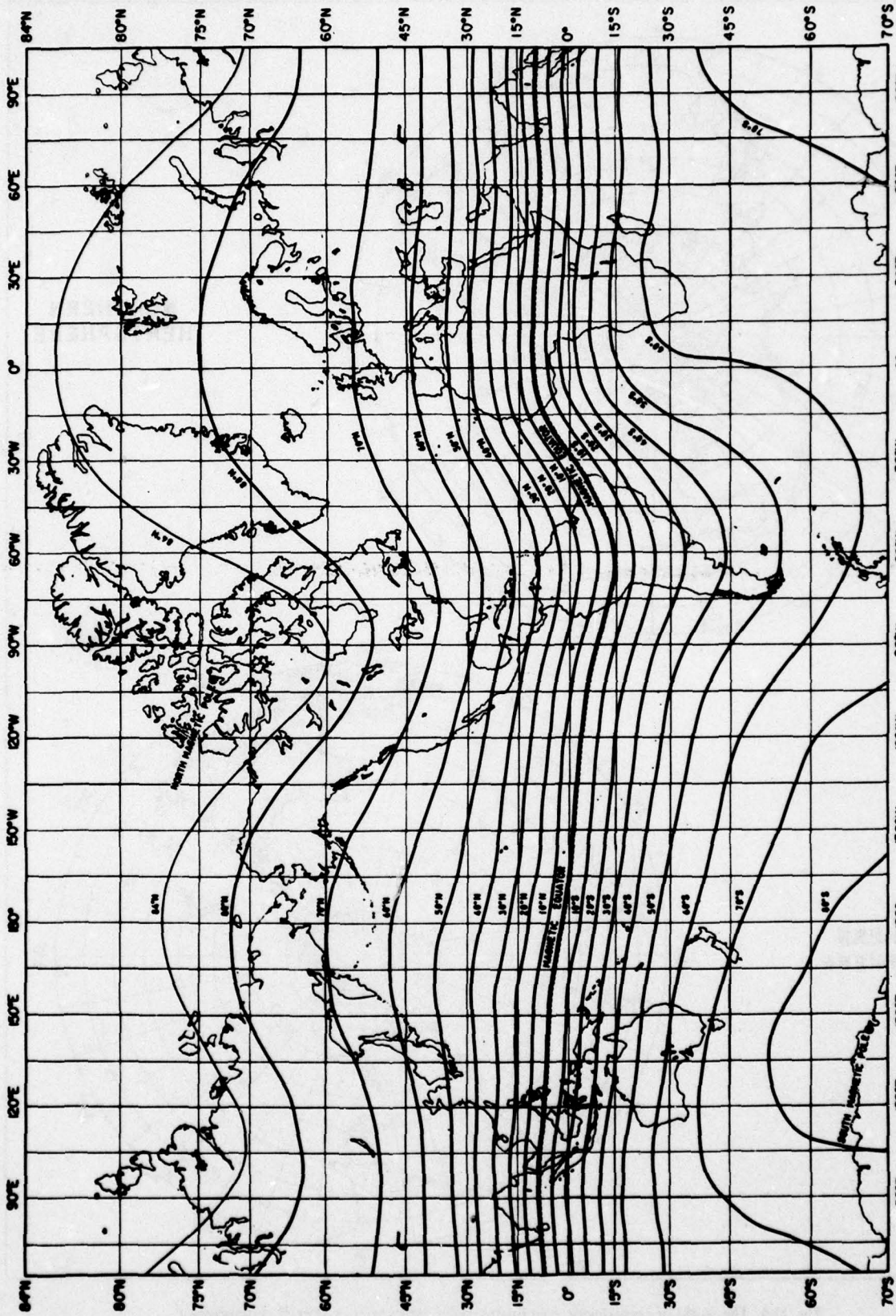


Fig. 11-5. The inclination (dip) of the earth's magnetic field for epoch 1955, giving the magnetic dip poles and magnetic dip equator; contours of constant I (deg). (After Navy Oceanographic Office chart No. 1700.)

tations of the various techniques by which the observational data on the geomagnetic field are obtained is given by Whitham [1960].

Observatory instruments are of two basic types: variometers that continuously record the time changes of three components of the field (usually D, H, and Z) with respect to fixed base lines; and absolute instruments used periodically to measure three field quantities (usually D, H, and I) and establish the absolute values of the variometer base lines. (For details see Hazard [1947].) The standard magnetogram includes traces from each of the D, H, and Z variometers recorded on a single sheet together with base lines for each component, a temperature trace, and a system of time marks. Sensitivities vary from about 2 γ mm^{-1} for lower-middle latitude stations to about 25 γ mm^{-1} for auroral-zone stations. The determination of D has a maximum accuracy of about 15 or 30 sec of arc. H absolute may be measured to an accuracy of about 1 γ by means of the best sine galvanometers or about 5 to 20 γ with the theodolite magnetometer, depending upon observational location. With the best instruments, the accuracy of I is about 0.1 min of arc. Variation instruments available for field use are less sensitive.

The proton precession magnetometer and the alkali-vapor magnetometer are useful for rapid measurements of the absolute value of the total scalar magnetic intensity; for a discussion of applications and limitations, see Sonett [1960]. Other electronic instruments are: second harmonic, heliflux, or saturable core type, used in airborne and space vehicles; the variable-mu or field-varied inductance type, best suited for sensing small rapid changes; and Hall effect devices, used for measuring magnetic field configurations in small areas.

11.2 THE MAIN FIELD OF THE EARTH

Although present knowledge cannot definitely exclude a contribution of about 0.1% to the surface field from sources outside the earth, it is accepted that the sources of the main field lie inside the earth. Most of the main field is believed to arise from electric currents flowing in a molten, metallic core which has a radius about one-half that of the earth. The currents are attributed to a self-exciting dynamo action in this core [Elsasser, 1950]. Present theory and the evidence of paleomagnetism suggest that the strength and distribution of the currents may have changed drastically during geologic time; the resulting field may, in fact, have reversed in direction one or more times.

The configuration of these internal currents is such that the field at the surface of the earth resembles that of a dipole, but there are appreciable departures from the dipole field which are called anomalies. The large or *regional anomalies* affect areas of thousands of square miles; they are attributed to irregularities or eddies in the internal current system, probably near the boundary between the core and the mantle, so that their effect is most pronounced at that portion of the surface immediately above them. These large anomalies are very slowly moving westward, which indicates that the rates of rotation of the core and the crust of the earth are slightly different. Anomalies of lesser geographic extent, called *surface anomalies*, are irregularities in the field caused by deposits of ferromagnetic materials in the crust; such deposits contribute little to the main field except in localized areas. The slow secular change of the main field is attributed to changes in the strength and distribution of the internal current system as well as to the westward drift.

11.2.1 Magnetic Charts

Figures 11-5 through 11-12 are charts of the magnetic field and its components; the magnetic poles on these charts are the dip poles. The charts prepared by the U.S. Navy Oceanographic Office show more detail (scale 1:39,000,000 at the equator for world charts) and contours of the rate of the secular change. For the United States and Europe, present charts are probably accurate to about one percent (declination accurate to about 1/2 degree), but for other areas the error may be considerably larger, particularly at high latitudes. Small surface anomalies extending about 100 miles or less are not indicated on the charts; locally they can amount to as much as a few percent of the total field. The effects of the time variations that arise from sources outside the earth are eliminated as far as possible. In preparing the charts, the measurements, which may be made over a period of several years, are converted to a common time, the epoch, by making corrections for the secular change. Because the secular change is only partially predictable, magnetic charts must be revised periodically. U.S. Navy Oceanographic Office charts are published every ten years (every five years for the declination charts). Additional data now available for oceans and polar areas will result in considerable improvements of the charts for the 1965 epoch.

Figure 11-13 shows the magnetic latitude in geographic coordinates. Figure 11-14 shows the magnetic meridians that indicate the direction of the horizontal component of field over the earth's surface.

The best information presently available on the main field lacks the desired accuracy. The World Magnetic Survey (WMS), sponsored by the International Association of Geomagnetism and Aeronomy of the International Union of Geodesy and Geophysics, was initiated in recognition of the need for more accurate knowledge of the geomagnetic field. The WMS is being conducted during a minimum of the sunspot cycle when measurements of the undisturbed main field can be obtained more readily. All nations are enhancing their magnetic survey efforts for the period 1962-1965 and will supply the data to the World Data Centers so that improved magnetic charts can be prepared for Epoch 1965.

11.2.2 Analysis of the Main Field

A complete analysis of the main field consists of two steps; first an *analytic specification* (mathematical repre-

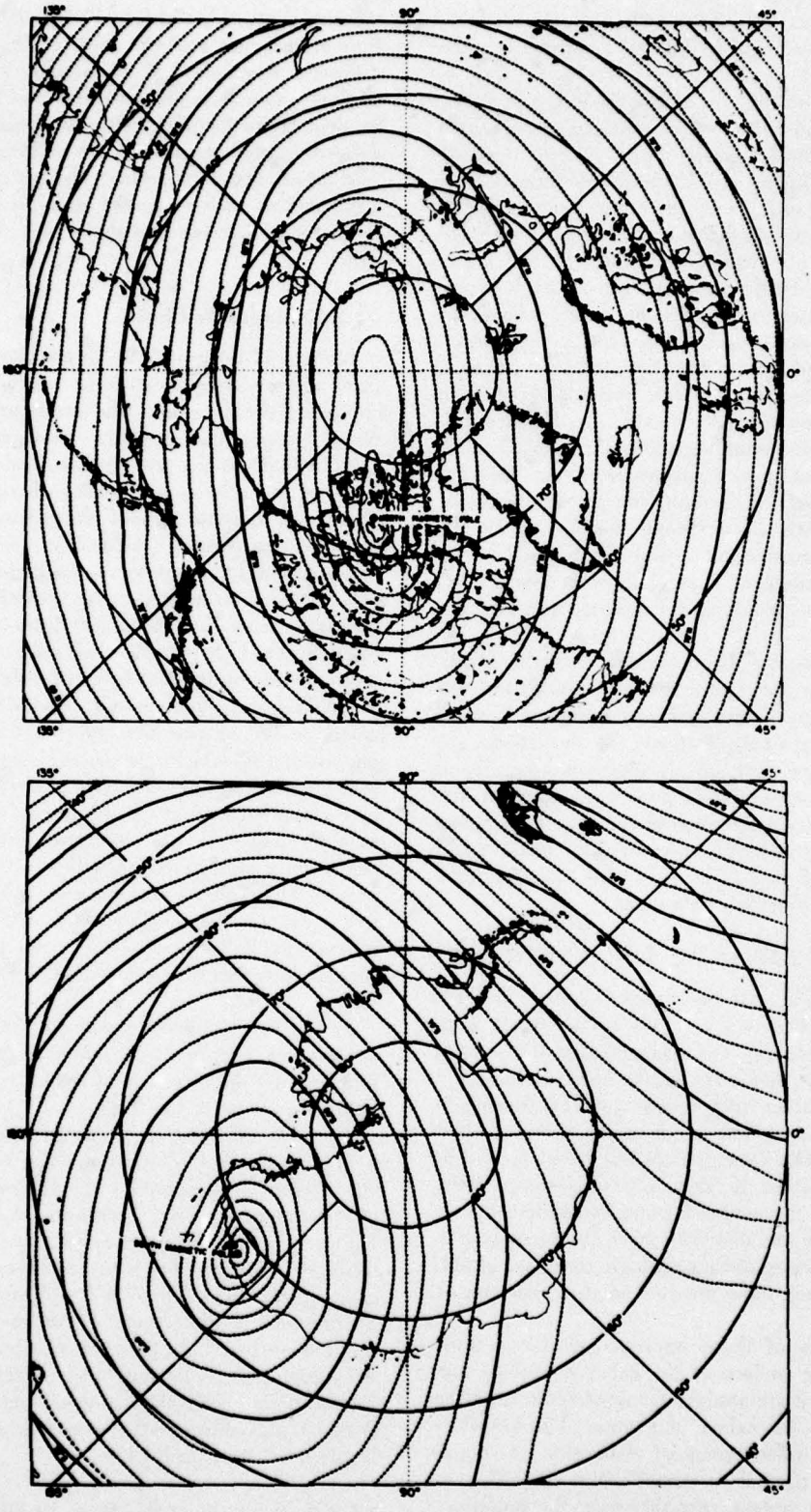


Fig. 11-6. The inclination (dip) of the earth's magnetic field, north and south polar areas, for epoch 1955; contours of constant I (deg). (After Navy Oceanographic Office Charts Nos. 1700N and 1700S.)

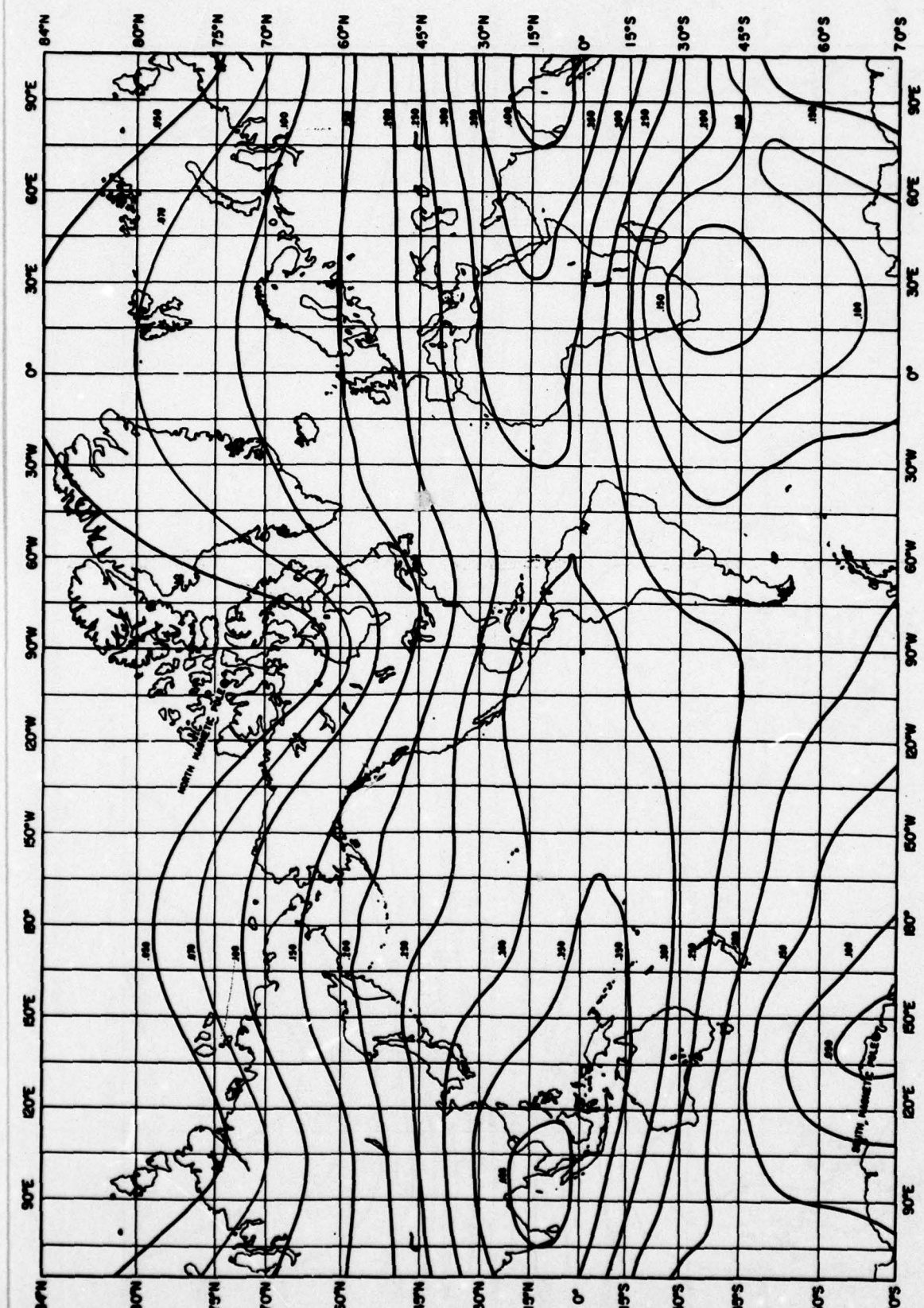


Fig. 11-7. The horizontal intensity of the earth's magnetic field for epoch 1955; contours of constant H (gauss). (After Navy Oceanographic Office Chart No. 1701.)

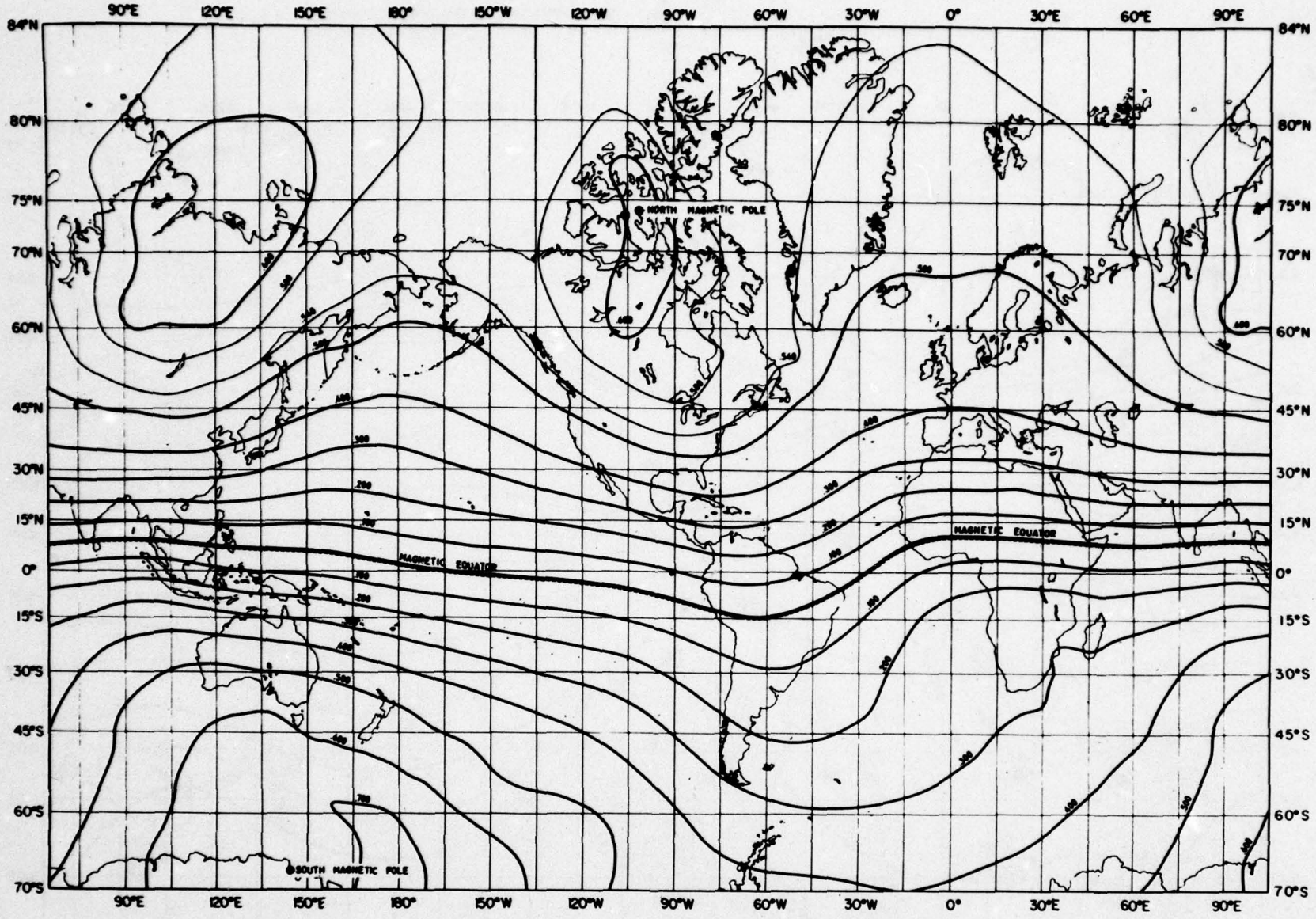


Fig. 11-8. The vertical intensity of the earth's magnetic field for epoch 1955; contours of constant Z (gauss). (After Navy Oceanographic Office Chart No. 1702.)

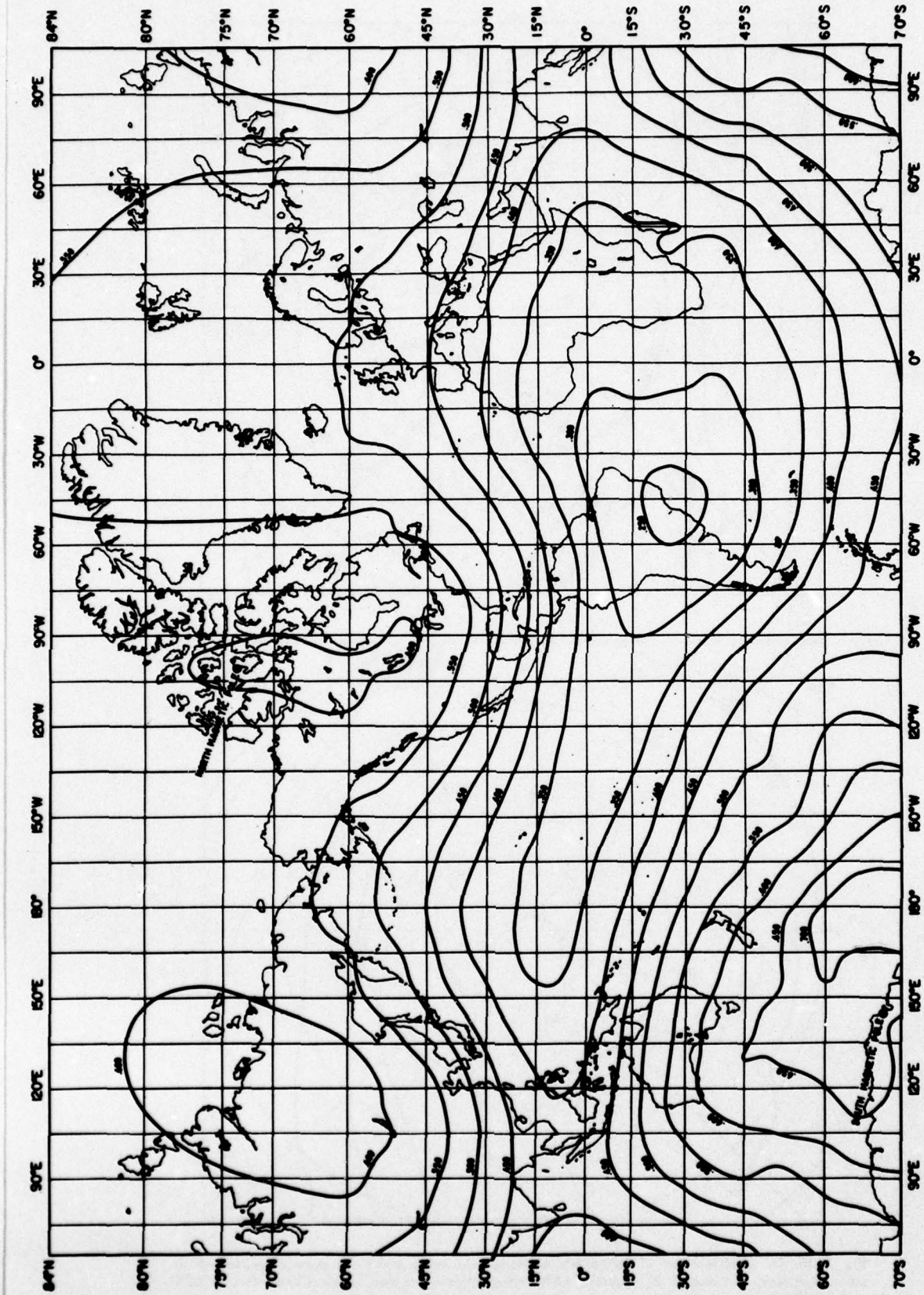


Fig. 11-9. The total intensity of the earth's magnetic field for epoch 1955; contours of constant F (gauss). (After Navy Oceanographic Office Chart No. 1703.)

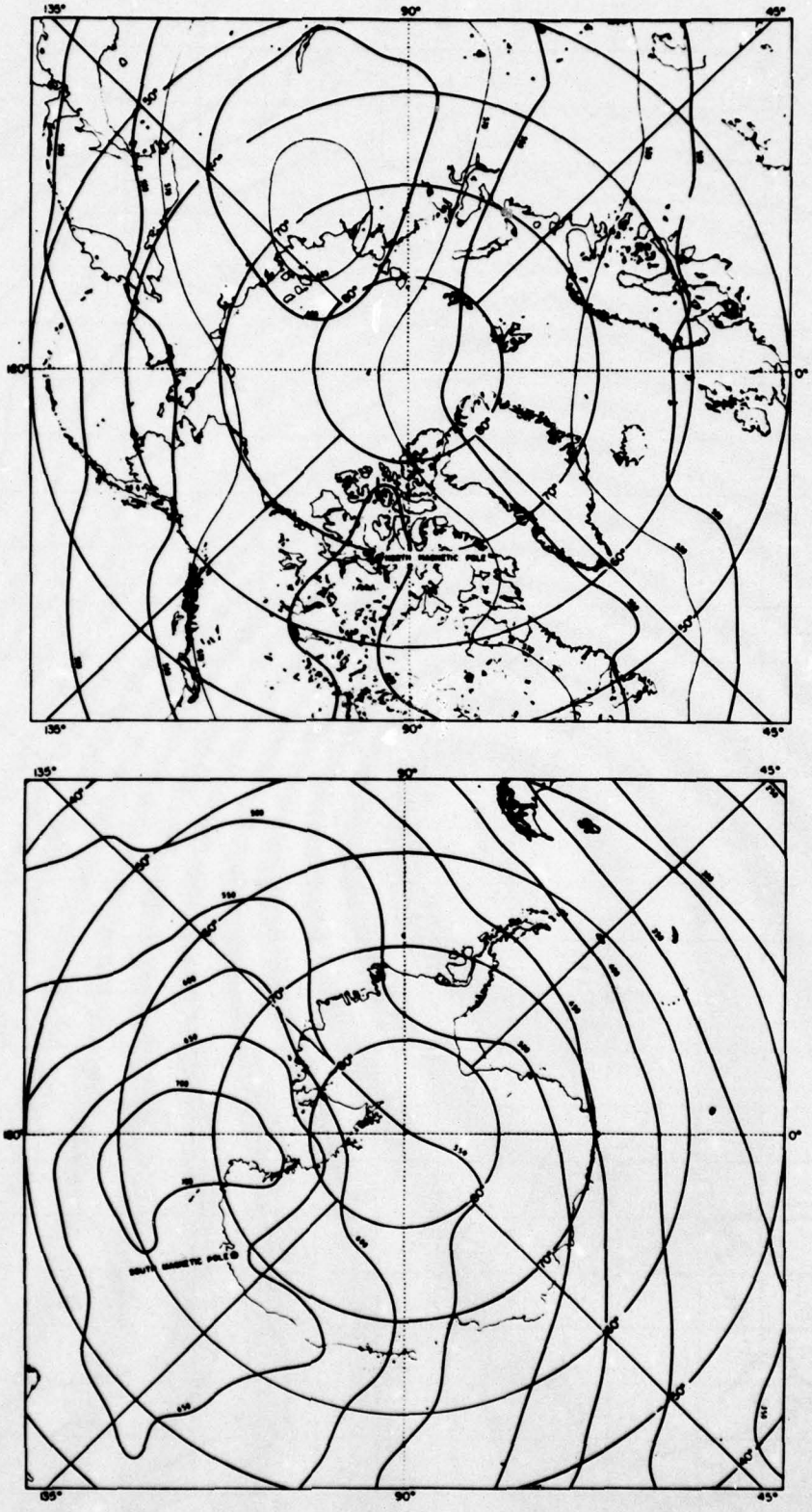


Fig. 11-10. The total intensity of the earth's magnetic field, north and south polar areas, for epoch 1955; contours of constant F (gauss). (After Navy Oceanographic Office Charts Nos. 1703N and 1703S.)

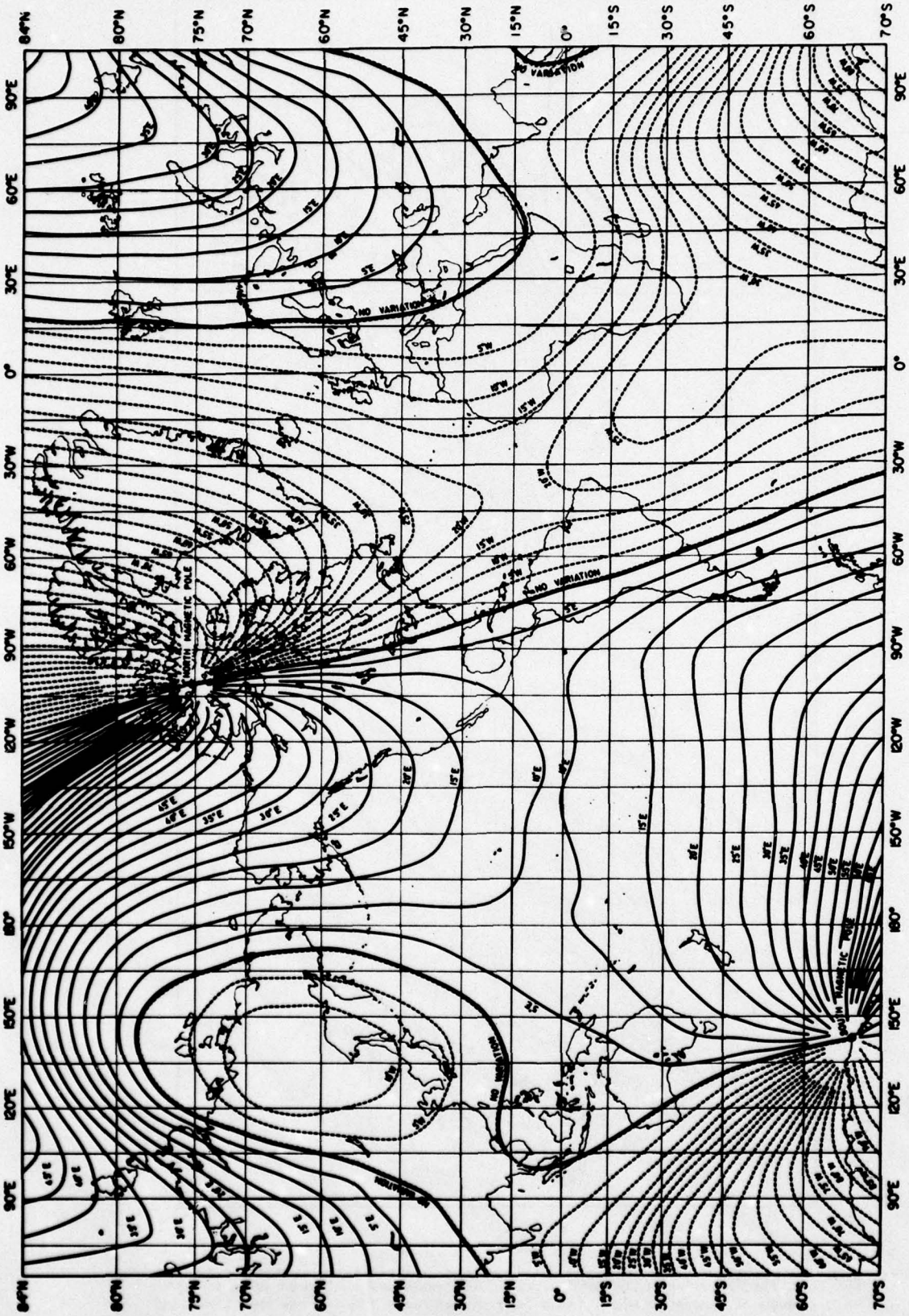


Fig. 11-11. The declination of the earth's magnetic field for epoch 1960; contours of constant D (deg). (After Navy Oceanographic Office Chart No. 1706.)

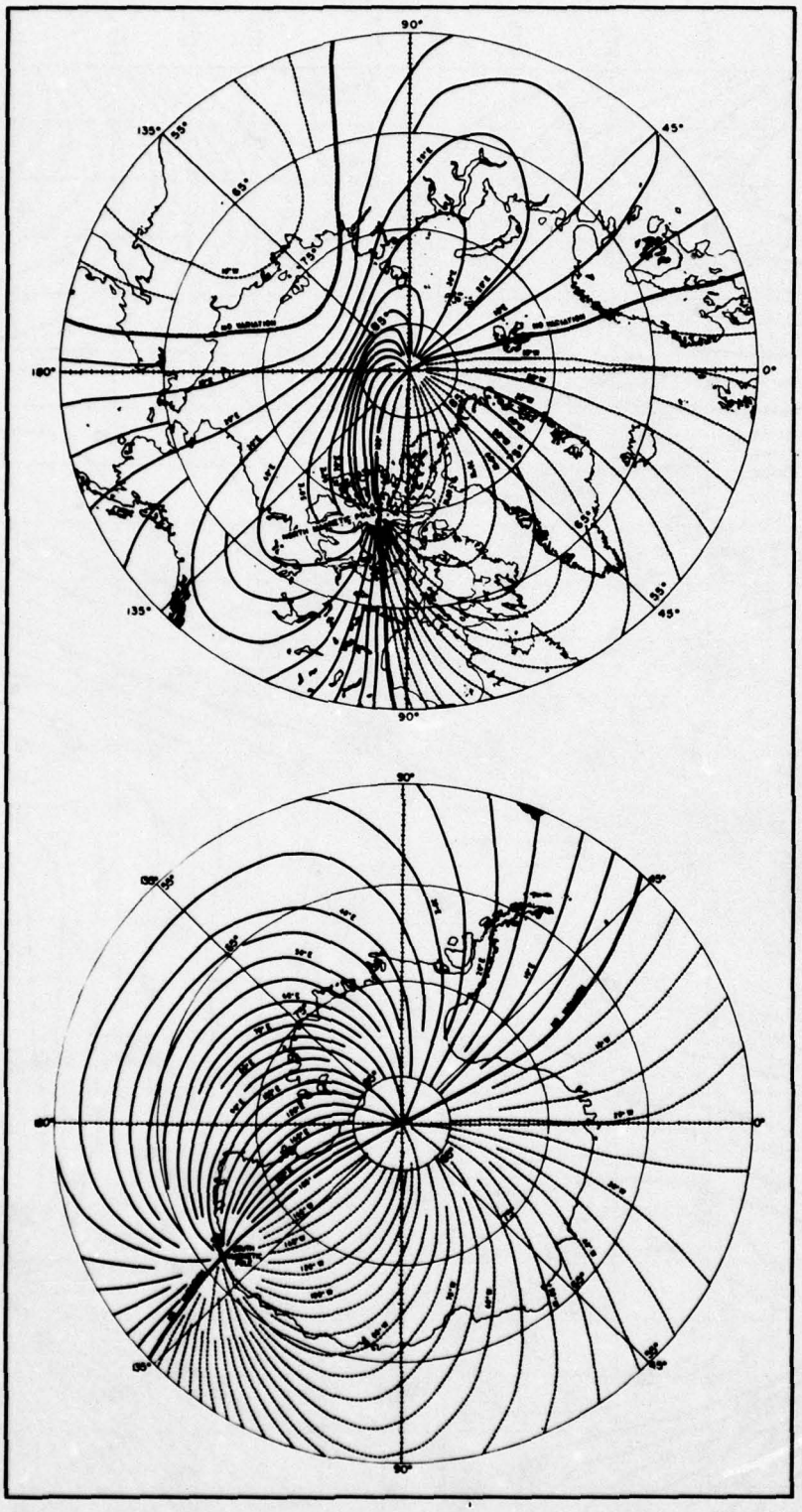


Fig. 11-12. The declination of the earth's magnetic field, north and south polar areas, for epoch 1960; contours of constant D (deg). (After Navy Oceanographic Office Charts Nos. 1706N and 1706S.)

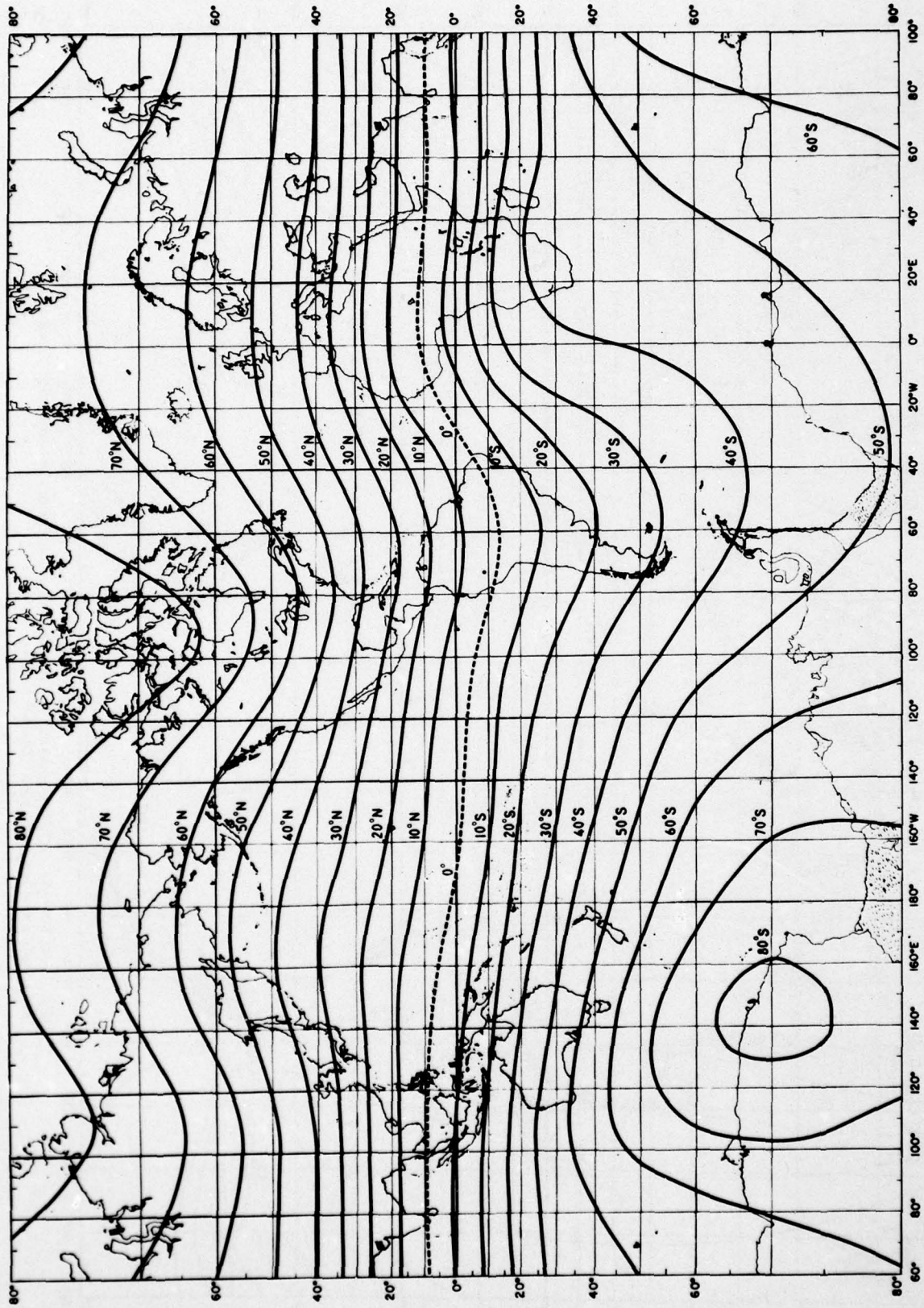


Fig. 11-13. Magnetic latitude, θ; the dashed line is the dip equator. (Derived from Fig. 11-5 by dipole equation $\tan \theta = \frac{1}{2} \tan I$.)

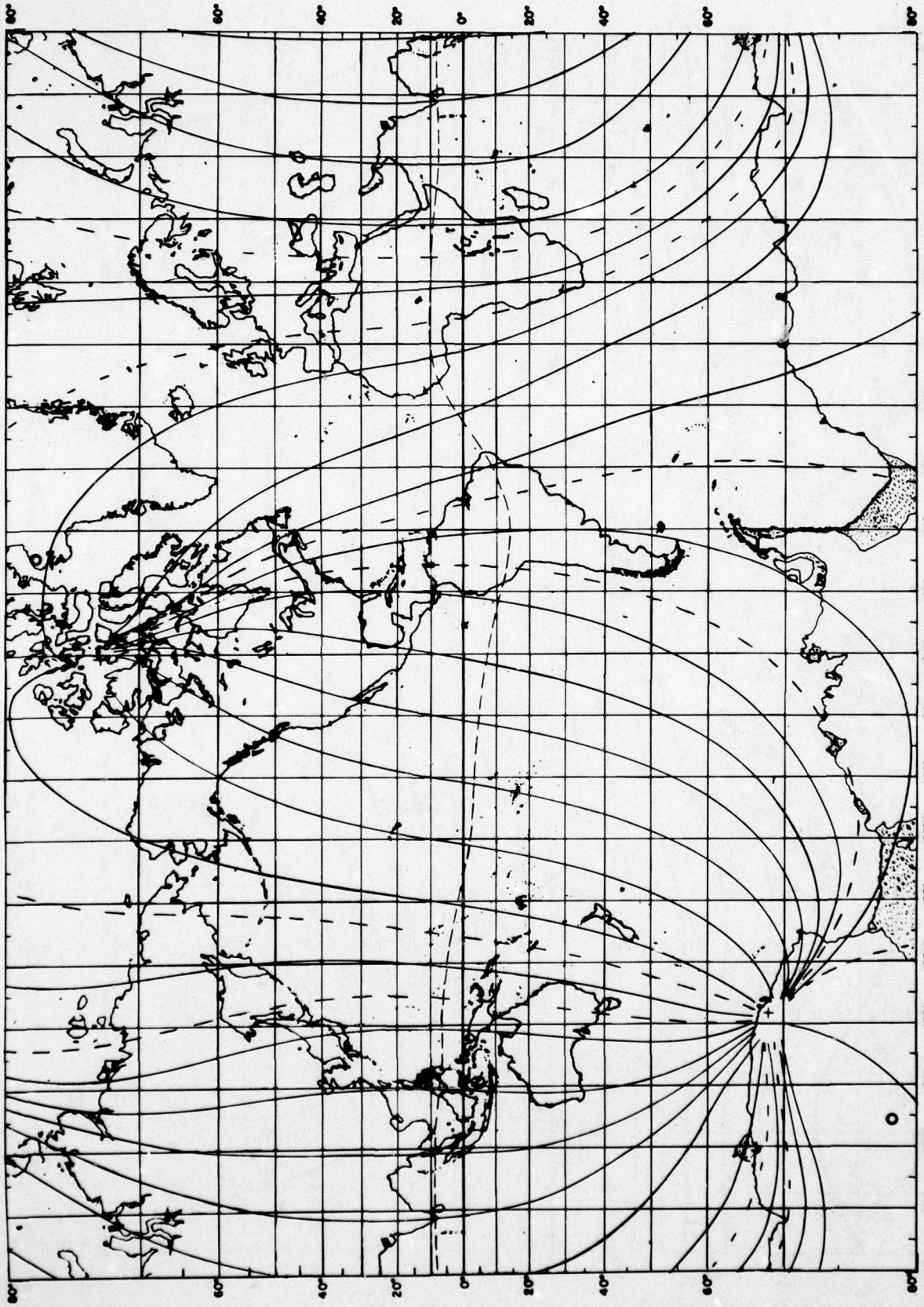


Fig. 11-14. Magnetic meridians showing the direction of the horizontal intensity. The dashed horizontal curve is the dip equator. (Derived from Fig. 11-11.)

sentation) of the magnetic field over the surface is derived from the geomagnetic data, then the analytic continuation (extrapolation) is computed from the analytic specification to give the field values at points outside the surface of the earth. When data over the entire surface of the earth are to be analyzed, spherical harmonics are used to obtain an analytic specification. When more detailed data covering a limited area of the earth are to be analyzed, the Taylor series method is preferable.

11.2.2.1 *Spherical Harmonic Analysis and Magnetic Dipoles.* The important equations for the earth's magnetic field are:

$$\nabla \times \boldsymbol{F} = 0 \qquad (11\text{-}1a)$$

and Maxwell's equation,

$$\nabla \cdot \boldsymbol{F} = 0. \qquad (11\text{-}1b)$$

Equation (11-1a) is an excellent approximation which stems from the extremely small current densities present immediately above and on the surface of the earth; Eq. (11-1b) is rigorously true. Equation (11-1a) implies the existence of a potential function V for which

$$\boldsymbol{F} = -\nabla V. \qquad (11\text{-}2)$$

Equation (11-1b) then gives

$$\nabla^2 V = 0. \qquad (11\text{-}3)$$

Thus, if information is available for the entire surface of the earth, the analytic specification problem becomes a boundary value problem in potential theory. In the absence of an external source of the main field, the solution of Laplace's equation suitable for a spherical boundary at $r = a$ gives as the potential function at $r \geqq a$,

$$V = a \sum_{n=1}^{\infty} \sum_{m=0}^{n} P_n^m (\cos\theta) \left(\frac{a}{r}\right)^{n+1} \times (g_n^m \cos m\phi + h_n^m \sin m\phi). \qquad (11\text{-}4)$$

In this equation, θ, ϕ, and r are geographic coordinates (colatitude, east longitude, and radial distance); the $P_n^m (\cos\theta)$ are ~~the Schmidt functions~~, multiples of the associated Legendre functions,

$$P_n^m (\cos\theta) = N_n^m P_{n,m} (\cos\theta),$$

where for the Schmidt functions,

$$N_n^m = \left[\frac{(n-m)!\,(2-\delta_{0m})}{(n+m)!}\right]^{1/2}$$

(δ is the Kronecker delta, equal to one if $m = 0$, and zero if $m \neq 0$); and g_n^m and h_n^m are ~~Gaussian~~ the Schmidt coefficients. Substituting Eq. (11-4) into Eq. (11-2) and differentiating, gives for the spherical components of the field

$$X = \sum_{n=1}^{\infty} \sum_{m=0}^{n} \left(\frac{a}{r}\right)^{n+2} \frac{d}{d\theta} [P_n^m (\cos\theta)] \times (g_n^m \cos m\phi + h_n^m \sin m\phi),$$

$$Y = \sum_{n=1}^{\infty} \sum_{m=0}^{n} \left(\frac{a}{r}\right)^{n+2} \frac{m}{\sin\theta} P_n^m (\cos\theta) \times (g_n^m \sin m\phi - h_n^m \cos m\phi),$$

$$Z = -\sum_{n=1}^{\infty} \sum_{m=0}^{n} \left(\frac{a}{r}\right)^{n+2} (n+1)\, P_n^m (\cos\theta) \times (g_n^m \cos m\phi + h_n^m \sin m\phi). \qquad (11\text{-}5)$$

For the Gaussian Functions,

$$N_n^m = \frac{2^m n!\,(n-m)!}{(2n)!}$$

and g_n^m and h_n^m are the Gaussian coefficients.

Thus, given a set of coefficients (g_n^m, h_n^m), the field at any point (r, θ, ϕ) can be computed.

Table 11-1 gives the values of the Gaussian coefficients g_n^m and h_n^m; it shows that g_1^0 is certainly the dominant term in the spherical harmonic expansion. The potential due to this dominant term is $g_1^0 \cos\theta\ (a^3/r^2)$, which is the potential due to a dipole of moment $g_1^0\, a^3$ lying along the earth's rotation axis pointing south. The next two terms are also dipoles. They lie in the plane of the geographic equator; $g_1^1\, a^3$ points toward 180° geographic longitude, and $h_1^1\, a^3$ points toward longitude 90°E. The resultant, $H_o a^3$, of these three mutually orthogonal dipoles has a magnitude (units of earth radii cubed) $H_o = [(g_1^0)^2 + (g_1^1)^2 + (h_1^1)^2]^{1/2}$ and a polar angle $\Theta_o = \cos^{-1}(g_1^0/H_o)$. The two equatorial dipoles have a resultant of magnitude $[(g_1^1)^2 + (h_1^1)^2]^{1/2}$ pointing toward east longitude $\Phi_o = \tan^{-1}(h_1^1/g_1^1)$. The point (a, Θ_o, Φ_o) is the South geomagnetic pole; its antipode, the North geomagnetic pole, is situated at about 11° colatitude (79°N) and 69°W longitude.

The resultant dipole is the basis of the geomagnetic coordinate system; longitude is measured eastward from the prime magnetic meridian. In geomagnetic coordinates the potential of the dipole term, V_1, becomes

$$V_1 = H_0\, (a^3/r^2) \cos\mu, \qquad (11\text{-}6)$$

so

$$X' = H_0 \left(\frac{a}{r}\right)^3 \sin\mu,$$

$$Z' = 2\, H_0 \left(\frac{a}{r}\right)^3 \cos\mu, \qquad (11\text{-}7)$$

where μ is geomagnetic colatitude. A further refinement, brought about by considering the first three quadripole terms, is to remove the dipole to a slightly eccentric position; for detailed discussion of this refinement and for formulas to convert from geographic to geomagnetic coordinates, see Chapman and Bartels [1940]. Such simplifications as the centered dipole and eccentric dipole are qualitatively useful for many purposes, but for accurate quantitative work, recourse must be made to a full set of spherical harmonics.

For worldwide data, a method for performing a spherical harmonic analysis was devised and programmed for digital computer [Fougere, 1963]. The program accepts data at the locations where the measurements are actually made rather than requiring an equally spaced grid of input data; it thus bypasses the intermediate step of subjective, hand-drawn charts, necessary in previous work. Table 11-1 gives the resulting Gaussian coefficients for epoch 1960.0 derived from observations of X, Y, and Z at 82 magnetic observatories [Fougere, 1965].

11.2.2.2 *Taylor Series Analysis.* If a set of magnetic observations covering a limited portion of the earth's surface is made at a given epoch and altitude, a polynomial, in Taylor series form, may be used to represent these observations. For example, if the north component (X) has been measured at a set of points, colatitude θ_v and east longitude ϕ_v, ($v = 1, 2, \ldots\ldots n$), then the polynomial representation $X(\theta, \phi)$ of degree D about the point (θ_0, ϕ_0) is

$$X(\theta, \phi) = \sum_{i=0}^{D} \sum_{j=0}^{D-i} X_{ij} \alpha^i \beta^j, \qquad (11\text{-}8)$$

where $\alpha = \theta - \theta_0$, $\beta = \phi - \phi_0$, and

$$X_{ij} = \frac{1}{(i+j)!} \left[\frac{\partial^{i+j} X(\theta, \phi)}{\partial \theta^i \partial \phi^j} \right]_{\substack{\theta=\theta_0 \\ \phi=\phi_0}}$$

If X_v is the observed value of X at θ_v and ϕ_v and $X(\theta_v, \phi_v)$ is the value of the polynomial at the same point, then the coefficients, X_{ij}, are determined from the expressions,

$$X_v = X(\theta_v, \phi_v) + R_v, \qquad (11\text{-}9)$$

where R_v, the residual, is the difference between measured and computed value of X at v. A straightforward (but numerically difficult) method of finding the X_{ij} from Eq. (11-9) is the method of least squares; i.e., minimizing $\sum_{v=1}^{n} R_v^2$ with respect to variations in the coefficients X_{ij}. A superior method (programmed for the digital computer) consists in first finding orthogonal functions of (α, β), representing X by a linear combination of these functions, and then finding the unknown coefficients using the method of least squares. The final expression in then transformed back to the Taylor series form.

If the observational material is vector in nature; e.g., if X, Y, and Z are measured, and if each of these components is represented independently by its own Taylor series, then the radial component of the curl of the computed field will not vanish as it should. A method, which fits the observations to coupled Taylor series in such a way that the radial component of the curl of the computed field vanishes identically, was recently improved [Fougere, 1964] by utilizing orthogonal functions and programmed for digital computer. Another computer program utilizes any given set of Taylor series coefficients and produces sufficient output for an automatic digital data plotter to yield contour charts of the function represented by the Taylor series.

11.3 THE MAIN FIELD AT HIGH ALTITUDES

The two methods used for predicting field values at high altitudes from analytic specifications of the field at low altitudes correspond to the spherical harmonic and Taylor series methods discussed previously. The first is suitable for application to the whole earth (or large portions), while the latter is useful for small areas over which the vector field is known in more detail.

Table 11-1. Coefficients for spherical harmonic analysis for epoch 1960.0. For each (n, m) pair the upper entry is g_n^m, the lower entry h_n^m, see Eq. (11-4). Units are gamma (10^{-5} gauss), and coefficients are rounded off to nearest gamma using Gaussian normalization [Fougere, 1963].

n \ m	0	1	2	3	4	5	6	7	8
1	−30509	−2181							
	——	5841							
2	−2196	5145	1448						
	——	−3443	172						
3	2867	−6161	2229	657					
	——	−1194	563	−138					
4	4360	4775	2280	−652	175				
	——	956	−1141	145	−152				
5	−2103	2763	1929	−245	−250	−6			
	——	−397	1241	−598	−326	62			
6	693	2485	−227	−2234	70	−166	−45		
	——	12	925	375	101	9	−38		
7	2781	−2257	227	−374	−516	337	−16	−21	
	——	−2438	191	758	266	51	149	2	
8	−815	407	729	−190	884	−155	−47	154	——
	——	−372	−1176	−42	−1868	81	−75	——	——

11.3.1 Spherical Harmonic Extrapolation

This method makes use of the inherent radial dependence of the spherical harmonic expansion which is a unique solution of a boundary value problem. Only the lack of an adequate analytic specification of the surface field limits the accuracy of the results. An Air Force Cambridge Research Laboratories computer program, given any set of coefficients and a position, finds all seven field elements (F, D, I, H, X, Y, X); if an observed value of one of the elements (such as a rocket measurement of F) is also given, it finds the difference between observed and computed values [Hutchinson and Shuman, 1961]. Another AFCRL program, given any set of Gaussian coefficients, produces sufficient data to determine contour charts of any element of the field, at any altitude for the earth or any chosen portion thereof. The contour interval can be $\geq 6\gamma$ for X, Y, Z, H, and F, or for D and I ≥ 6 min of arc. Figures 11-15 through 11-22 are world total-intensity charts at various altitudes prepared from this program, using the set of Gaussian coefficients given in Table 11-1.

11.3.2 Taylor Series Extrapolation

This method [Zmuda and McClung, 1955] is especially useful for small areas if accurate, detailed data (such as the vector field and a set of its horizontal derivatives at a point) are known. Such information is easily obtained from an analytic specification of the field over a surface of constant altitude. (From the usual magnetic charts only the values of the field components and their very low-order derivatives are obtainable.) Equations (11-1a and 1b), expanded in spherical coordinates, give

$$\frac{\partial}{\partial\theta}(F_2 \sin\theta) - \frac{\partial}{\partial\phi} F_1 = 0, \qquad (11\text{-}10)$$

$$\frac{\partial}{\partial\phi} F_3 - \sin\theta \frac{\partial}{\partial r}(r F_2) = 0, \qquad (11\text{-}11)$$

$$\frac{\partial}{\partial\theta} F_3 - \frac{\partial}{\partial r}(r F_1) = 0, \qquad (11\text{-}12)$$

$$\sin\theta \frac{\partial}{\partial r}(r^2 F_3) + r \frac{\partial}{\partial\theta}(F_1 \sin\theta) + r \frac{\partial}{\partial\phi} F_2 = 0, \qquad (11\text{-}13)$$

where F_1, F_2, F_3 (the ordinary spherical components) are $-X$, Y, and $-Z$ respectively. Equation (11-10) is used in preparing F_1 and F_2 specifications, while Eq. (11-11, 12 and 13) can be used to obtain the vertical derivatives of F_1, F_2, and F_3 in terms of the values and the horizontal derivatives of F_1, F_2, and F_3 on a surface of constant altitude.

A recurrence formula [Zmuda, 1956] from which radial derivatives of any order may be obtained is

$$F_{\beta,j} \equiv \frac{\partial^j}{\partial r^j} F_\beta \Big]_{r=a}. \qquad (11\text{-}14)$$

Zmuda's formula, valid for $j \geq 0$, is

$$F_{1,j+1} = \frac{1}{r}\left[\frac{\partial}{\partial\theta} F_{3,j} - (j+1) F_{1,j}\right],$$

$$F_{2,j+1} = \frac{1}{r}\left[\frac{1}{\sin\theta}\frac{\partial}{\partial\phi} F_{3,j} - (j+1) F_{2,j}\right],$$

$$F_{3,j+1} = -\frac{1}{r}\left[\left(\frac{\partial}{\partial\theta} + \cot\theta\right) F_{1,j} + \frac{1}{\sin\theta}\times \frac{\partial}{\partial\phi} F_{2,j} + (j+2) F_{3,j}\right]. \qquad (11\text{-}15)$$

Using these vertical derivatives, the extrapolation formula is an ordinary Taylor series:

$$F_\beta \Big]_{r=a+h} = \sum_{j=0} \frac{h^j}{j!} F_{\beta,j}, \qquad (11\text{-}16)$$

where h is the altitude above the surface $r = a$.

11.3.3 Comparison of Predicted and Observed Values

The Taylor series method of extrapolation has been directly verified for small areas and limited altitude ranges (up to 6 km) by airborne magnetometer measurements. All other comparisons with observed field values are based on harmonic analysis.

The major portion of the surface field represented by the centered dipole terms ($n = 1$) decreases with increasing altitude as the inverse cube of the radial distance, whereas those portions of the surface field represented by the successively higher order terms (representing the departures from the centered dipole field) decrease as successively higher inverse powers of the radial distance. It might be expected that, as the altitude increases and the higher order terms become less important, the spherical harmonic extrapolation will yield more accurate values of the main field. This is true only to the extent that the assumption that the main field at the surface is produced entirely by internal sources is valid.

At altitudes between about 100 and 20,000 km, external sources of transient field are encountered, but the field at any point may be considered to be a linear superposition of the main field and the fields due to such transient external phenomena. Although it is difficult in practice to separate these effects in satellite data, an accurate comparison with predicted main field values is, in principle, feasible. At distances of several earth radii, the main field interacts with the solar wind and the linear superposition theory is no longer applicable.

Vanguard III magnetic measurements were used to verify the applicability of spherical harmonic extrapolation techniques and to compare several sets of Gaussian coefficients. It is concluded from the results that the present technique for the extrapolation of the geomagnetic field to satellite altitudes is capable of high accuracy (the order of 0.2% for the best sets of Gaussian coefficients). The outer radiation zone fits the centered dipole approximation of the geomagnetic field over a wide range of geomagnetic latitudes; that is, the observed locations of the

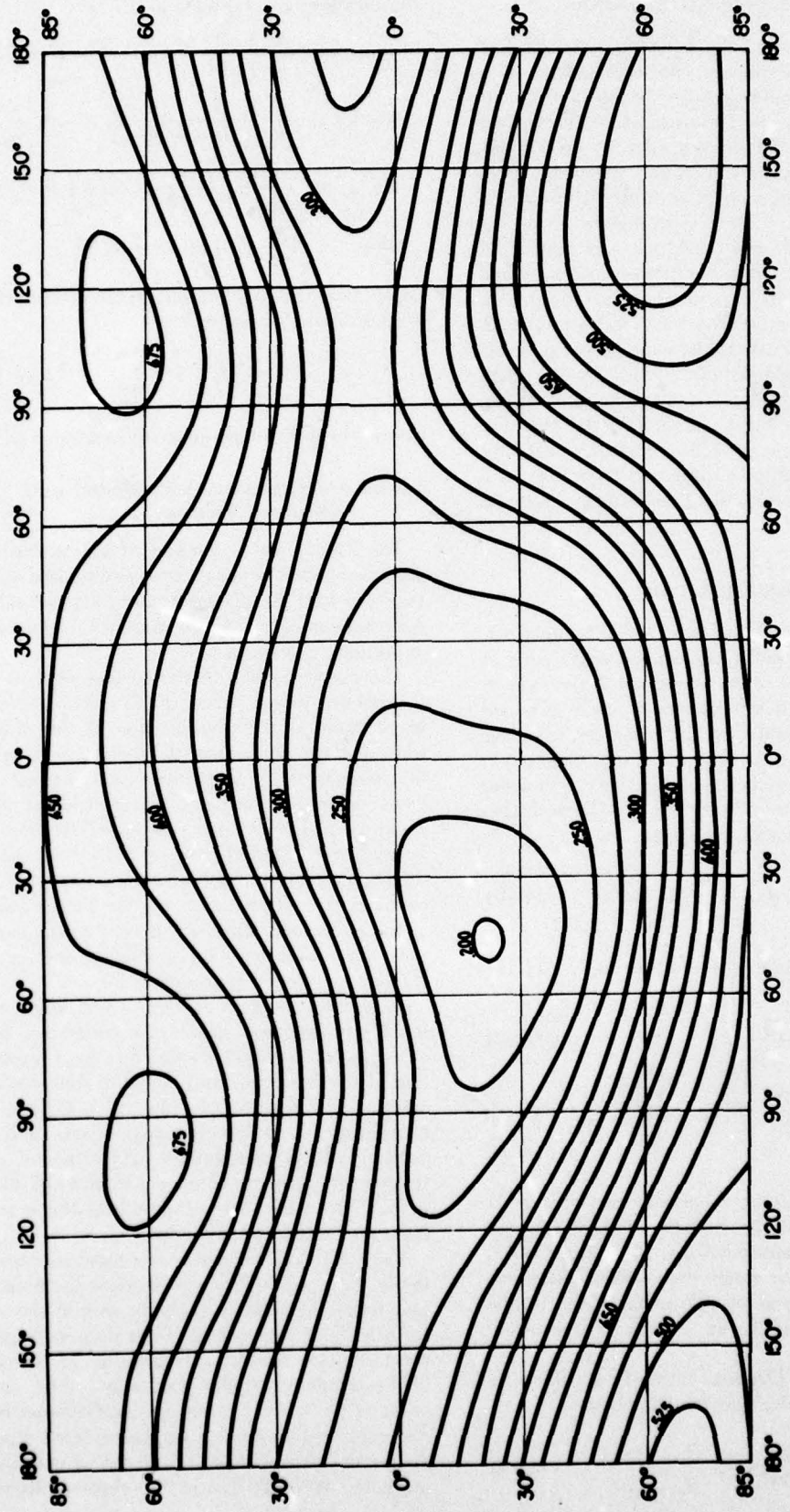


Fig. 11-15. Total intensity of the earth's magnetic field, F, in gauss, epoch 1960, altitude 500 km. (Spherical harmonic analysis of Fougere.)

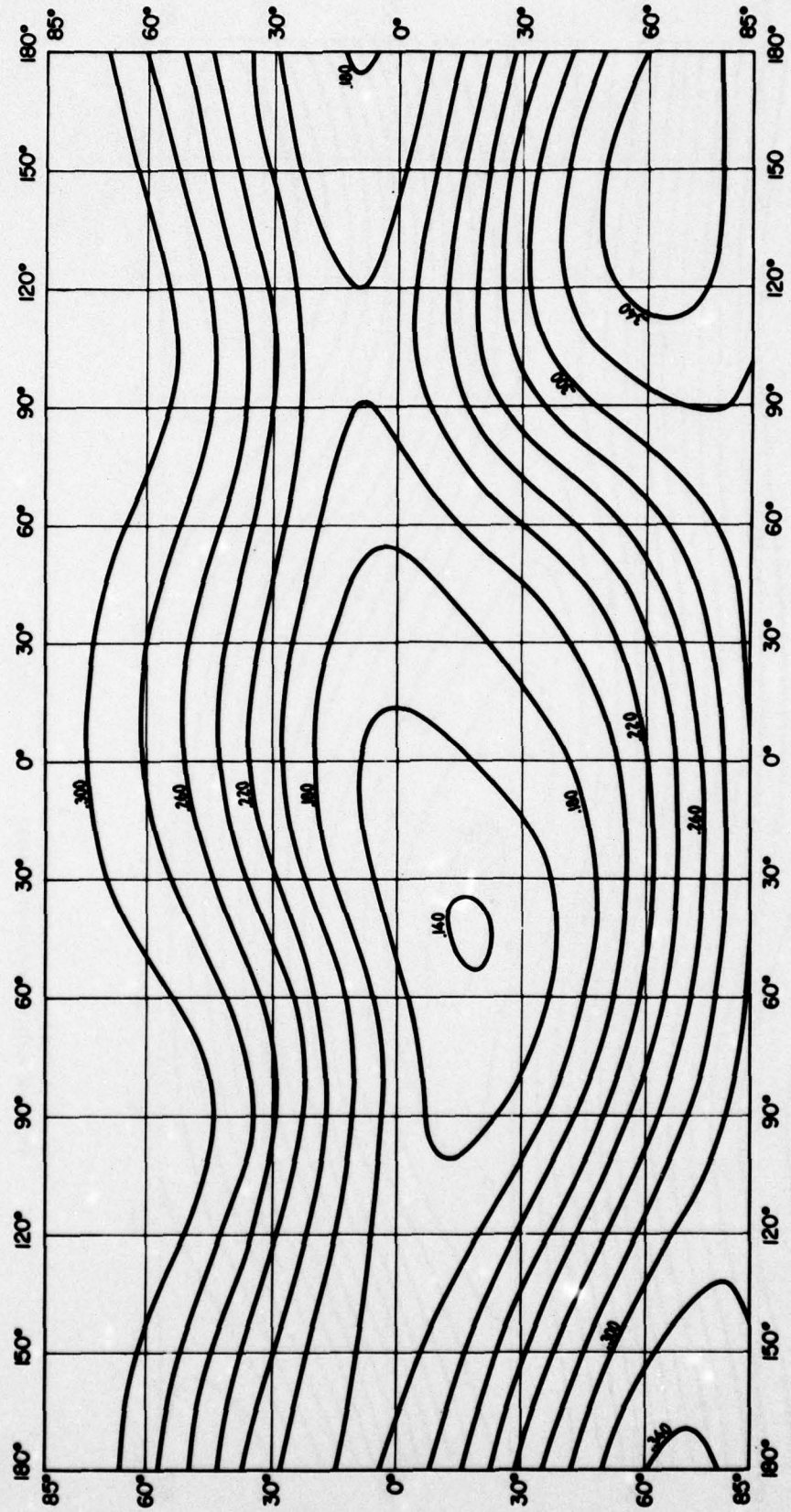


Fig. 11-16. Total intensity of the earth's magnetic field, F, in gauss, epoch 1960, altitude 1500 km. (Spherical harmonic analysis of Fougere.)

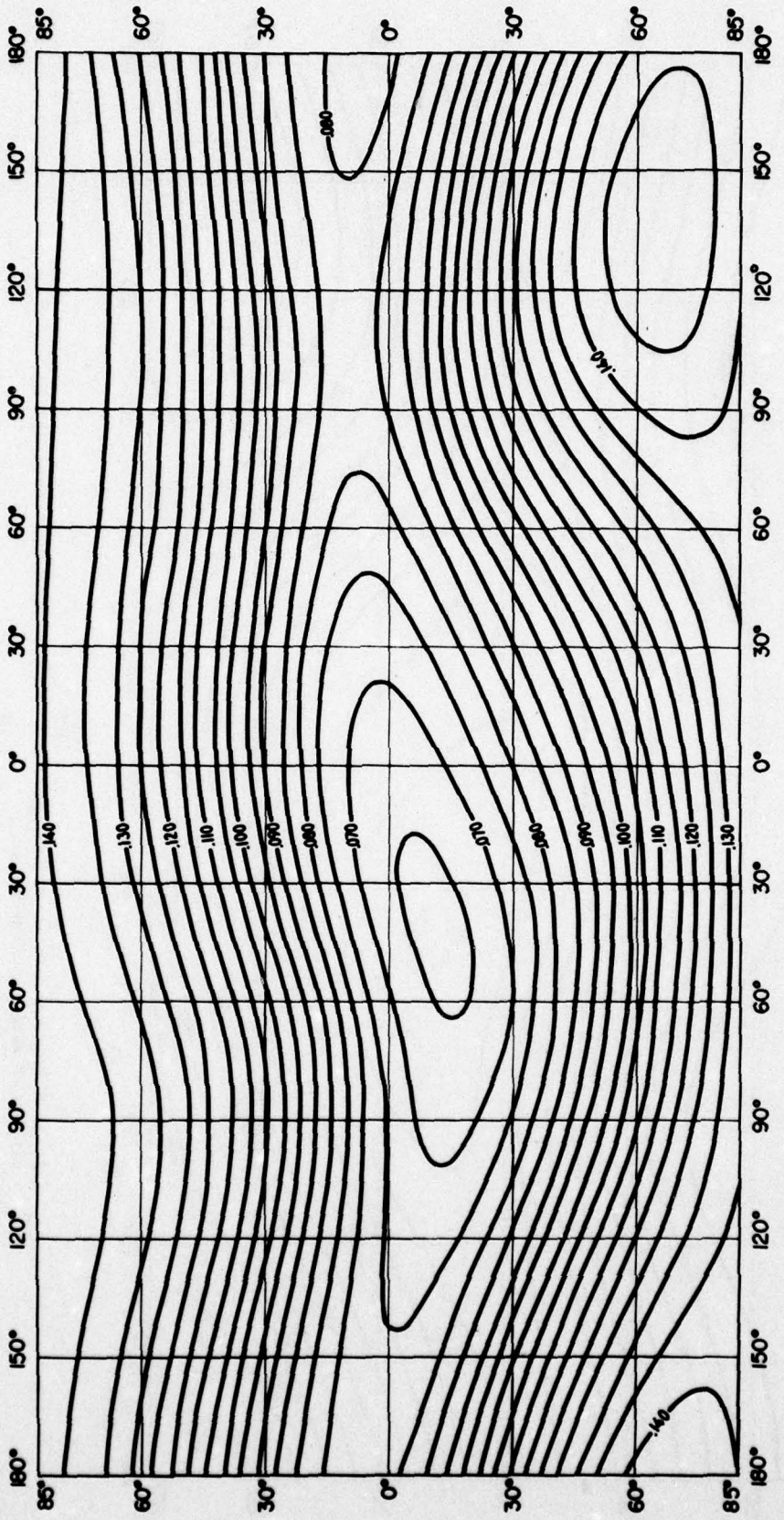


Fig. 11-17. Total intensity of the earth's magnetic field, F, in gauss, epoch 1960, altitude 4000 km. (Spherical harmonic analysis of Fougere.)

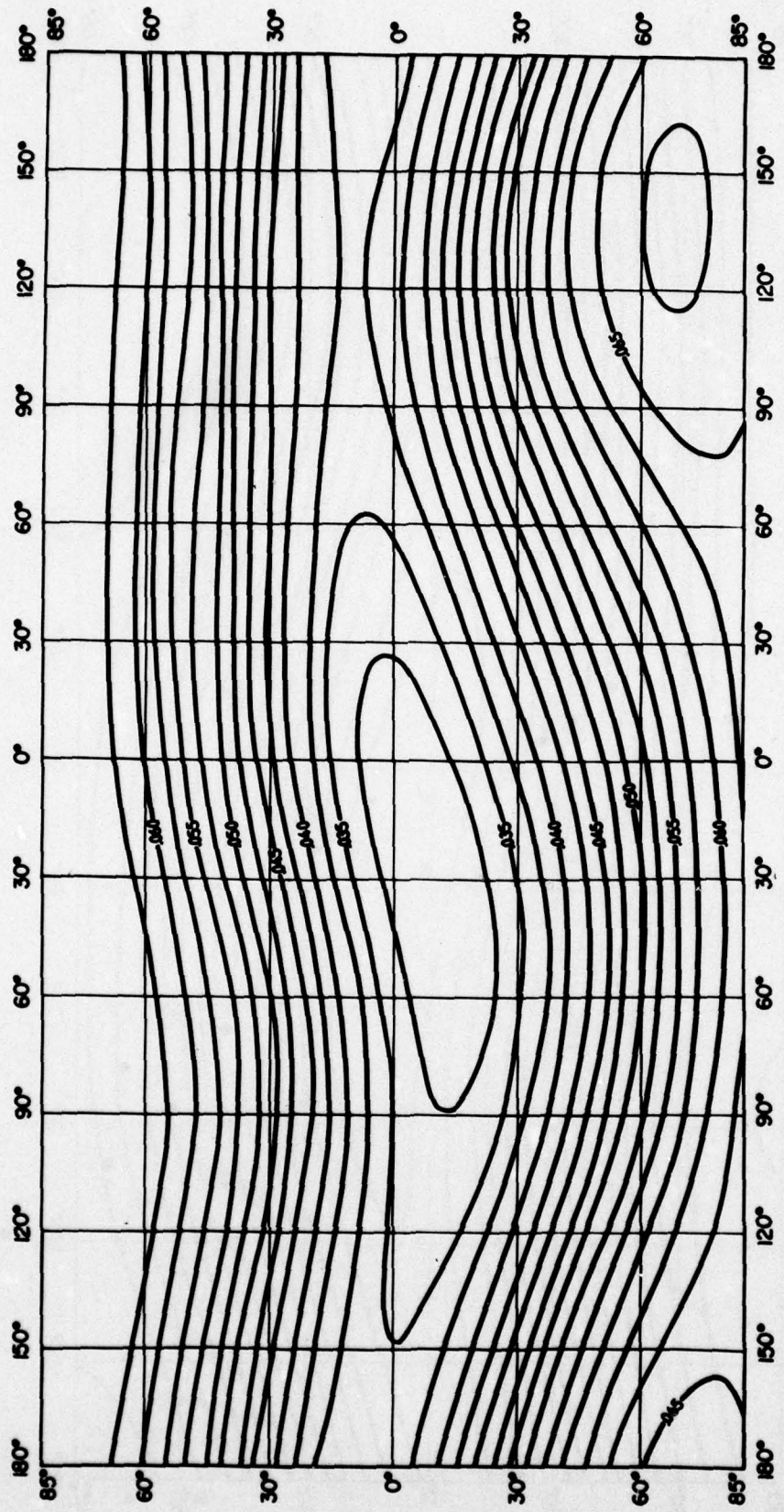


Fig. 11-18. Total intensity of the earth's magnetic field, F, in gauss, epoch 1960, altitude 7000 km. (Spherical harmonic analysis of Fougere.)

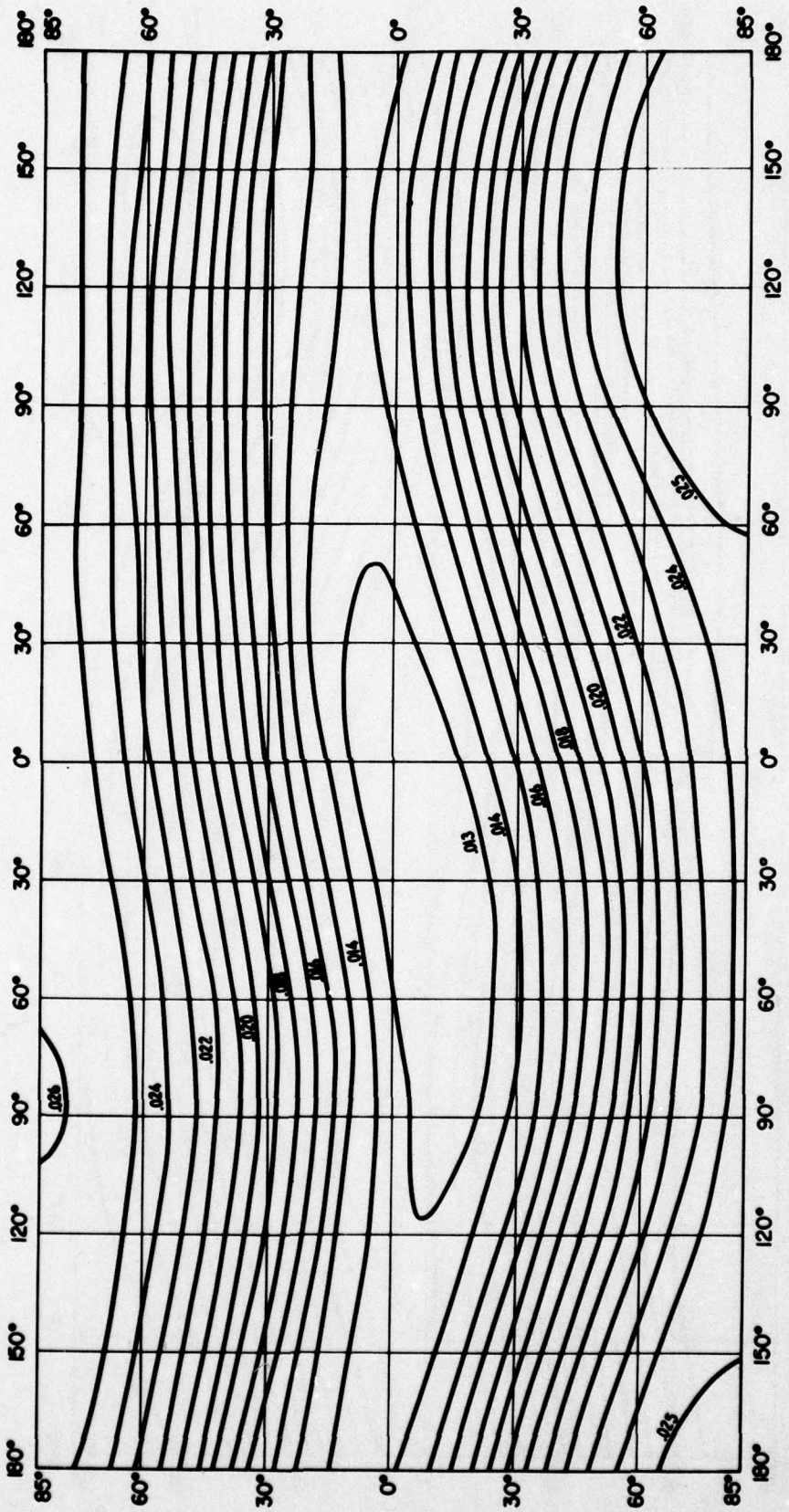


Fig. 11-19. Total intensity of the earth's magnetic field, F, in gauss, epoch 1960, altitude 12,000 km. (Spherical harmonic analysis of Fougere.)

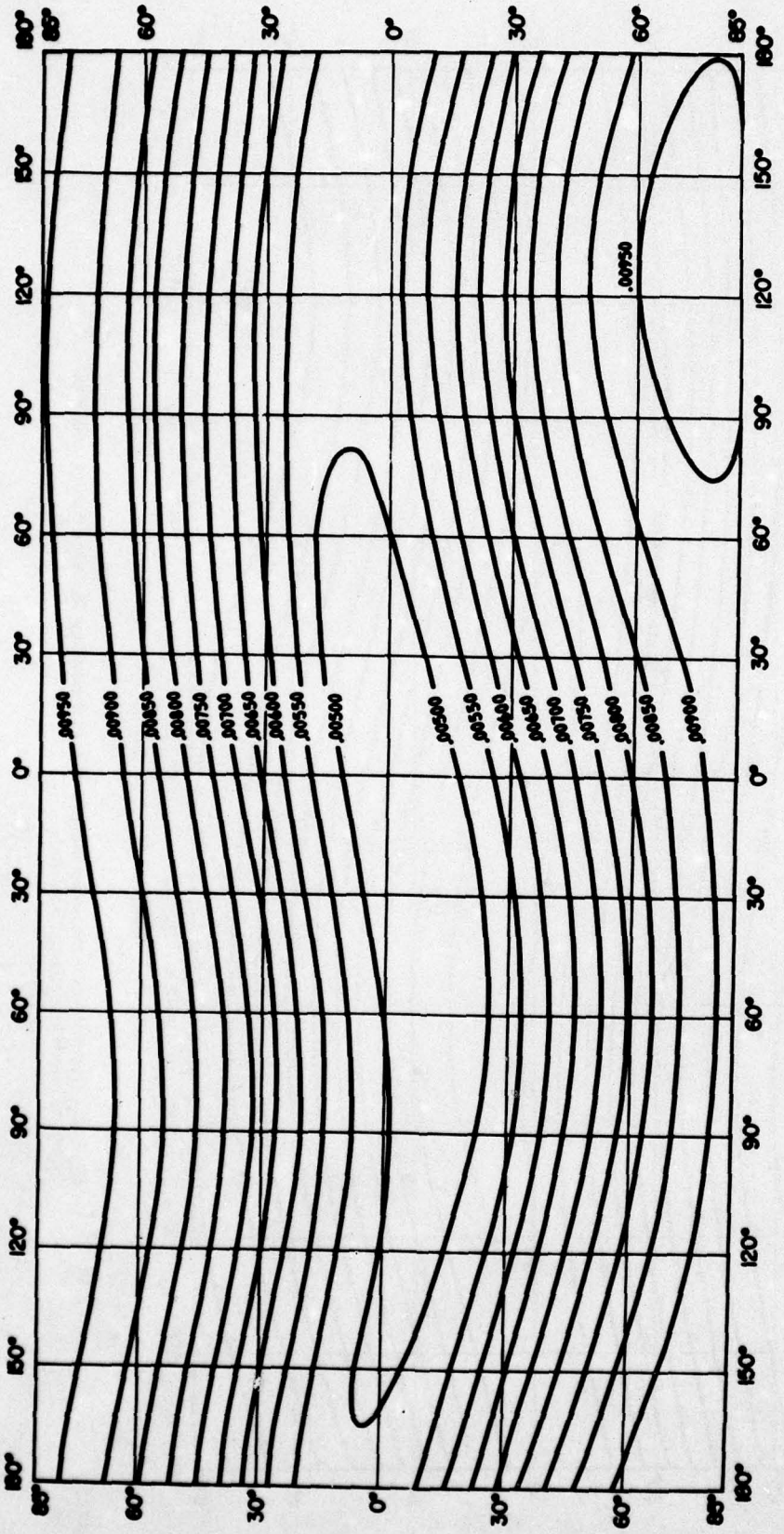


Fig. 11-20. Total intensity of the earth's magnetic field, F, in gauss, epoch 1960, altitude 3 earth radii. (Spherical harmonic analysis of Fougere.)

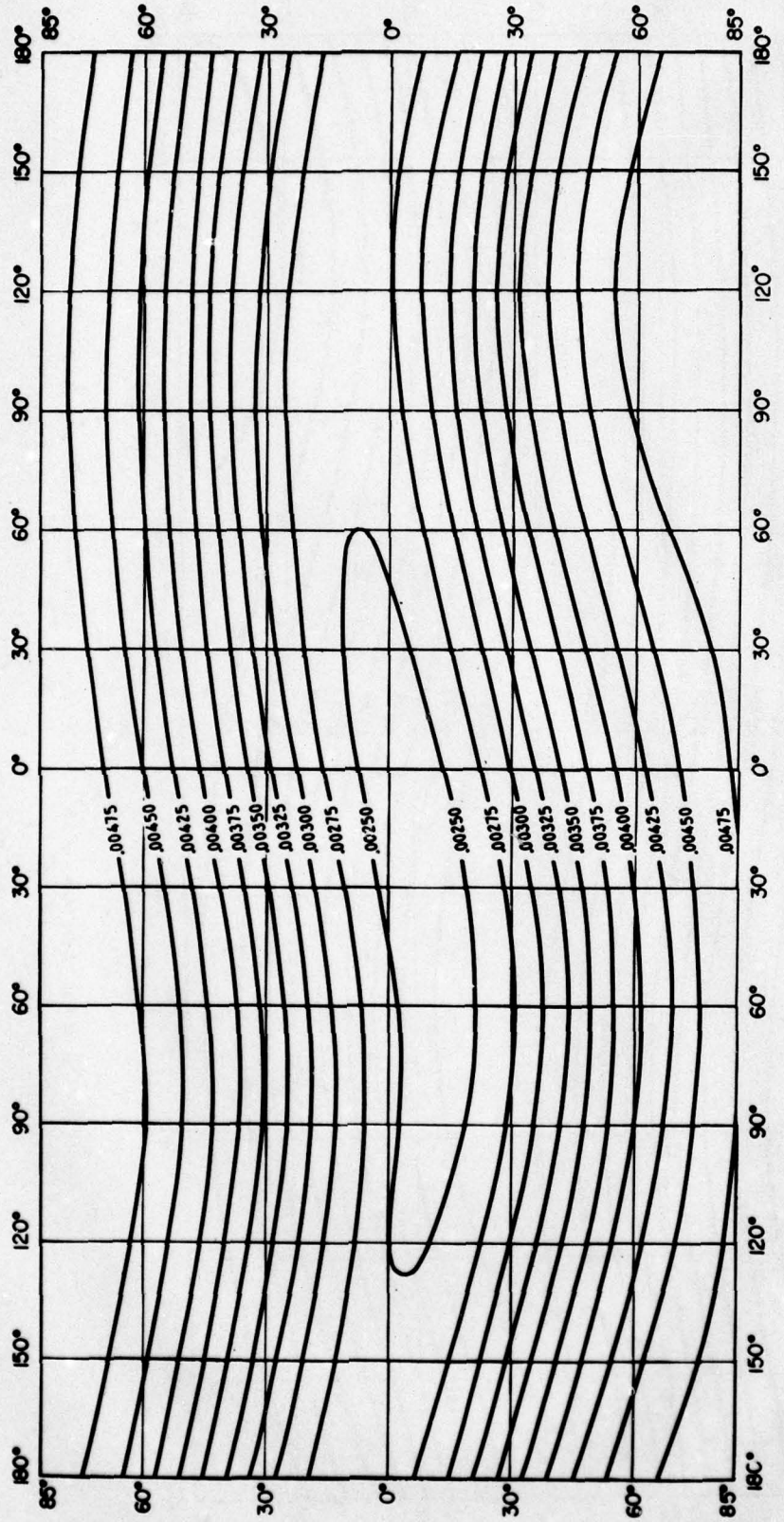


Fig. 11-21. Total intensity of the earth's magnetic field, F, in gauss, epoch 1960, altitude 4 earth radii. (Spherical harmonic analysis of Fougere.)

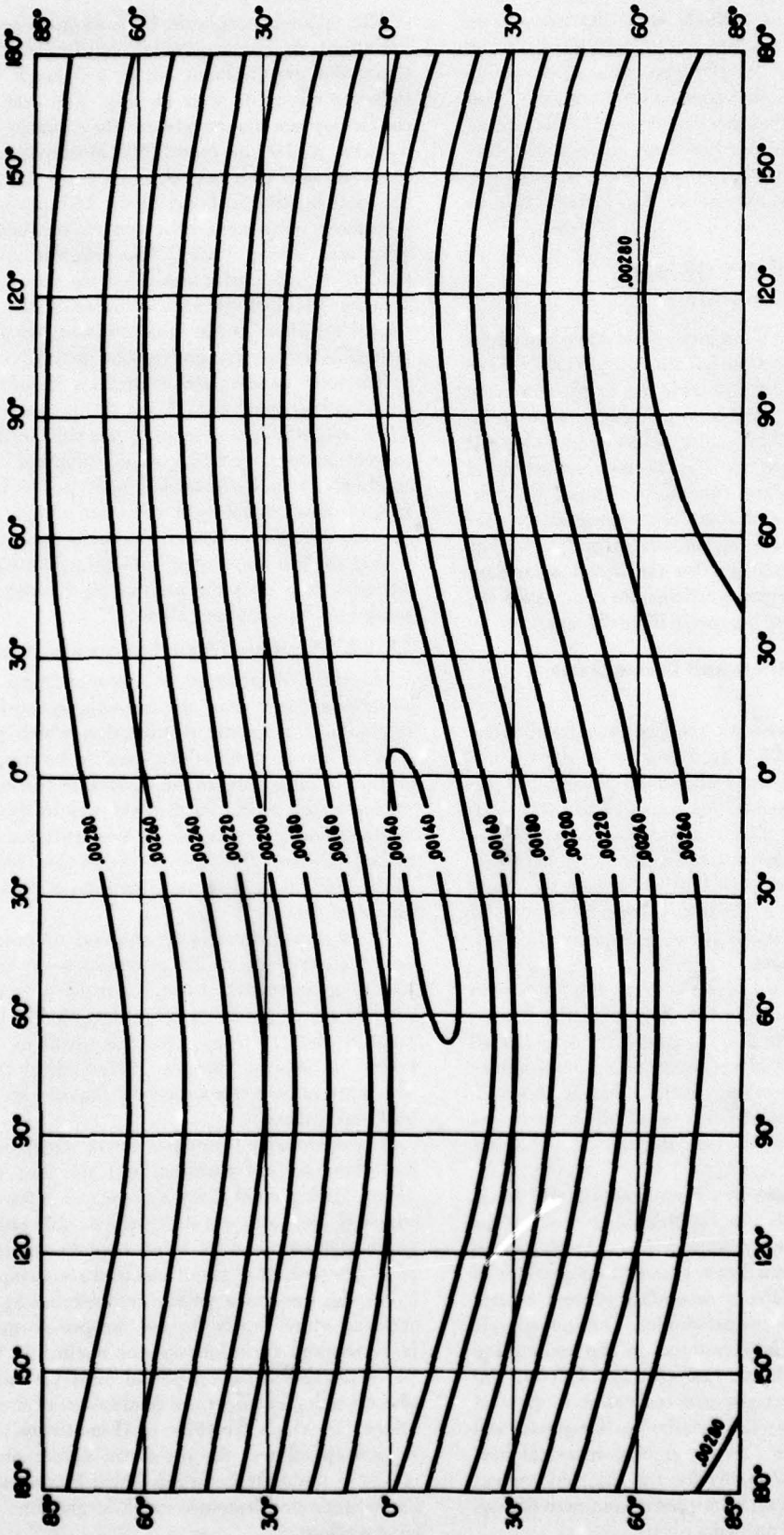


Fig. 11-22. Total intensity of the earth's magnetic field, F, in gauss, epoch 1960, altitude 5 earth radii. (Spherical harmonic analysis of Fougere.)

outer-belt peak intensities, which were determined on successive passes of the satellite through the zone, lay on a surface defined by the set of dipole field lines having the same altitude above the geomagnetic equator [Fan et al, 1961]. This confirms the conclusion that the accuracy of predicted field values based on surface measurements increases with altitude and also indicates that the contribution of external sources to the surface field is negligible.

11.4 TIME VARIATIONS OF THE GEOMAGNETIC FIELD

Variations of the earth's magnetic field have durations ranging from several days to less than a second. These transient variations originate outside the earth, chiefly in the ionosphere, and are attributed primarily to solar influences. Both solar electromagnetic radiation and charged particles from the sun are involved in the production of the variations. Although the two effects cannot be completely separated, in general solar electromagnetic radiation is the energy source for the smooth diurnal variations of field during quiet times and for the direct solar-flare effects, whereas solar charged particles are considered the chief source of energy for magnetic disturbances.

11.4.1 Diurnal Variations and Direct Solar Flare Effect

On a succession of quiet days, regular patterns of variations which repeat each 24 h are observed in the various magnetic elements. Variations attributed to solar effects are designated by the letter S; the smooth quiet-day variations are Sq. There is also a lunar component of the daily variation of field, designated by the letter L, whose amplitude is less than one-tenth that of S. Both the amplitude and shape of L vary drastically over the course of a lunar month, and careful analysis is required to separate L from the S variations.

Figure 11-23 is an example of average curves for Sq from several stations, showing the change in the X′, Y′, and Z components. At the June solstice, Sq is enhanced in the Northern Hemisphere and reduced in the Southern Hemisphere; at the December solstice, this is reversed. Sq increases at sunspot maximum. In addition, there are variations that occur over intervals of a few days that are less predictable.

Harmonic analysis shows that both external and internal sources contribute to the Sq field observed at the earth's surface. The primary source is a current system in the ionosphere that contributes about three-quarters of the surface field and induces a secondary current system in the earth that produces the remainder. The ionospheric current systems are usually computed on the assumption that they flow in a thin sheet at an altitude of about 100 km, and the induced currents are estimated to flow at a depth of about 300 km; for details, see Chapman and Bartels [1940] and Fejer [1964]. A new spherical harmonic analysis and a new model for the external current systems that utilizes ideas on ionospheric conductivities as a function of altitude are needed.

The upper-atmospheric tidal motions producing the L variations are due to gravitational forces. For the S variations, the gravitational forces are much less important than the effects of solar heating. The tidal circulation in the ionosphere can be greater than that at the surface by a factor of 100 or more. The atmosphere is sufficiently resonant at a 12-h period to suppress the 24-h period of the solar heating in favor of the 12-h period which is the dominant component observed in the magnetic records [Sen and White, 1955]. The different amplitude variations of S and L with sunspot cycle are unexplained phenomena. Conductivity theory indicates that the two effects should originate at the same altitude and should be similarly affected by changes in solar activity.

Magnetic effects are sometimes observed simultaneously with a visual solar flare; this is the *direct solar flare effect, sfe,* which is essentially an enhancement of the Sq current system, resulting from enhanced ionization and conductivity in the lower ionosphere. The increased emission of short wavelength radiation during the flare may be such that the enhanced ionization and current system during the sfe may extend downward to somewhat lower altitudes than does the normal Sq current system [Veldkamp and Van Sabben, 1960].

11.4.2 Magnetic Disturbances and Storms

Magnetic disturbance is a general term used for field variations other than the smooth, quiet-day variations. Intervals of magnetic disturbance, which may last from a few hours to a few days, tend to be more or less concurrent at all points on the surface of the earth; however, there may be moderate disturbances in the auroral zones that are hardly noticeable at low latitudes. During a disturbed interval, the time at which the largest variations of the field occur is more a function of local time than of universal time.

A *magnetic storm* is an interval of pronounced magnetic activity observable everywhere on earth. A *storm sudden commencement, ssc,* is a rapid increase in H occurring in about 1 to 6 min and appearing simultaneously (within about 1 min) over the world as an abrupt increase of several gammas on standard magnetograms. The more intense storms usually have an ssc; other storms build up gradually.

A typical sudden-commencement magnetic storm shows five characteristic features: (1) the ssc; (2) an *initial phase,* lasting from a few minutes to a few hours during which H decays to pre-storm value (this phase is not generally characterized by large random variations); (3) a *main phase,* lasting about one to three days, in which H is below the pre-storm value, first decreasing and then increasing more slowly toward the pre-storm value (many large random variations appear during the main phase); (4) a *post-perturbation* period after the end of the main phase (as indicated by the diminution of the random variations) in which the value of H continues to rise toward, or perhaps above, the pre-storm value; and (5) an increase in the daily variation which increases with increasing latitude and becomes much larger than Sq at auroral zone stations.

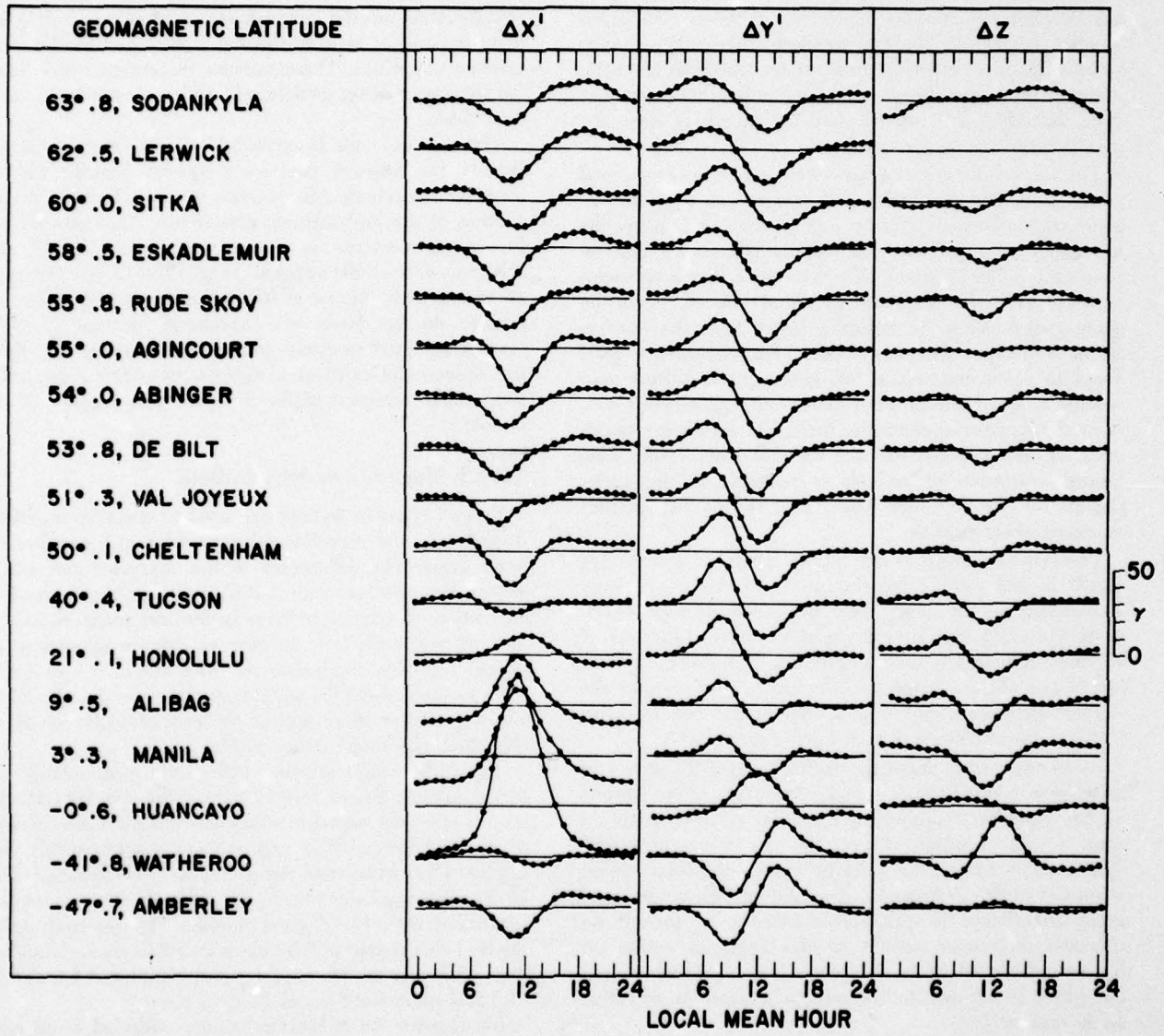


Fig. 11-23. Average solar quiet day (Sq) variations of geomagnetic components for years 1922-1933. (After Vestine et al [1947].)

The main phase for intense storms tends to show a greater rate of change than the main phase for weaker storms; i.e., a larger variation but shorter duration. In spite of the similarities, there are many differences from one storm to another; for any particular storm, significant departures from the average trends are not unusual.

The intensity of the storm is usually rated according to the maximum range of the variations of the field components during the storm; however, a rating according to the maximum storm-time depression of the H component is often preferred. The two methods give rather similar results. The most intense storms are termed great magnetic storms; their occurrence averages only about one per year, but they are concentrated in the years near the maximum of the sunspot cycle.

The largest disturbance variations occur in the auroral zones; these are about 10° wide centered at about ± 67° geomagnetic latitude. During a great magnetic storm, the maximum range of the field components at an auroral zone station will be about 2500 γ or more. The amplitudes decrease at higher latitudes to about one-half near the geomagnetic poles. At latitudes lower than the auroral zones, a sharper decrease occurs; the disturbance level drops to about one-fifth at 50° geomagnetic latitude and reaches a broad minimum of about one-eighth below 30°. Near the equatorial electrojet there is a secondary maximum of about one-fourth the auroral zone value. This latitude variation of activity is reflected in the scales chosen for the K index (Sec. 11.4.3) for the various magnetic observatories.

The largest variations are highly irregular and do not repeat in any predictable fashion from one day or one disturbance to the next; they are called *random variations*. Generally the largest variations have durations of about 15 min to 3 h, with amplitudes decreasing for both longer and shorter durations. At auroral zone stations the random variations tend to be of shorter duration but with higher rates of change than at lower latitudes.

Recurrence of a magnetic disturbance in 27 days can often be attributed to long-lived, observable active regions on the sun that reappear at the solar central meridian after a solar rotation. There are also many occasions (particularly during the quiet portion of the solar cycle) when the 27-day recurrence of weak-to-moderate geomagnetic disturbance is quite pronounced even though no corresponding solar activity is observable. A region on the sun whose effect on the geomagnetic field is evident but which is not detected by other observations, is called an *M region*.

The *disturbance field* (D field) in any component is defined as the difference between the instantaneous value and the long-term (for a month or more) average value minus the computed values of the quiet-day S and L fields for the particular instant of time. The D field may be separated into three parts, SD, Dst, and Di (different symbols are used by different authors). The *disturbance daily variation*, SD, is the part which varies with local time. SD may be computed as $\bar{S} - S_q$, where $\bar{S}$ is the average daily variation derived for all days. An alternate and probably preferable, method is to computed SD as Sd — Sq, where Sd is the daily variation derived for disturbed days only. Figure 11-24 shows average SD curves of the change in the X′, Y′, and Z components at various latitudes for a sunspot minimum year. The *storm-time variation*, Dst, is that part of D which depends upon time computed from the initial onset or the ssc of the storm. The amplitude of the Dst variation in the H component is large enough at low latitudes so that it is often readily recognizable on the magnetograms showing individual disturbances; at high latitudes it is obscured by the large random variations. These random variations, which form the third part of the D field, are Di, *the irregular disturbance field*.

The sources of the D variations are not yet firmly established; the various theories proposed require further observational checks. At present, it seems that the major portion of the high-latitude disturbance field arises from ionospheric currents, as a comparison of the X′, Y′, and Z components of SD suggests (Fig. 11-24). The Dst variation, which is largest at low latitudes, is less easily explained on the basis of ionospheric currents; a ring current centered over the geomagnetic equator and flowing around the earth at a distance of a few earth radii is a widely accepted explanation for this portion of the D field.

11.4.3 Magnetic Activity Indices

Several types of indices are used to describe magnetic disturbance and its relationship to solar and geophysical phenomena. The differences in the character and intensity of the variations with latitude influence the choice and derivation of activity indices. In auroral zones, measures derived over periods of an hour or less are important. In middle latitudes, the indices for intervals of 3 h to 1 day are most used. Near the equator, indices based on an interval of a day or more appear to be suitable for study of the equatorial ring current effects.

The *daily ranges* are the earliest and most readily obtained indices. These designate the difference between the largest and smallest momentary (or hourly mean) values of the declination (R_D) and of the horizontal (R_H) and vertical (R_Z) intensities during the day. The letters Q and D are often used to indicate the intervals of minimum or maximum activity of each month. The internationally selected five quietest (5Q) days and five most disturbed days (5D) per month are frequently employed for definition and studies of Sq and Di variations.

Information on magnetic activity collected from contributing observatories is incorporated into the International Association of Geomagnetism and Aeronomy (IAGA) Bulletin 12, issued annually. Each issue contains: three-hour values of K for each station, K_p, and a_p; the daily values of K_p, A_p, C_p, and C_i; lists of the quiet and disturbed days; and information on rapid variations. A collection of K_p, A_p, and C_p values for the years 1932-1961 is given in IAGA Bulletin 18. The K_p, C_p, A_p, and preliminary C figures are also published monthly in the Journal of Geophysical Research.

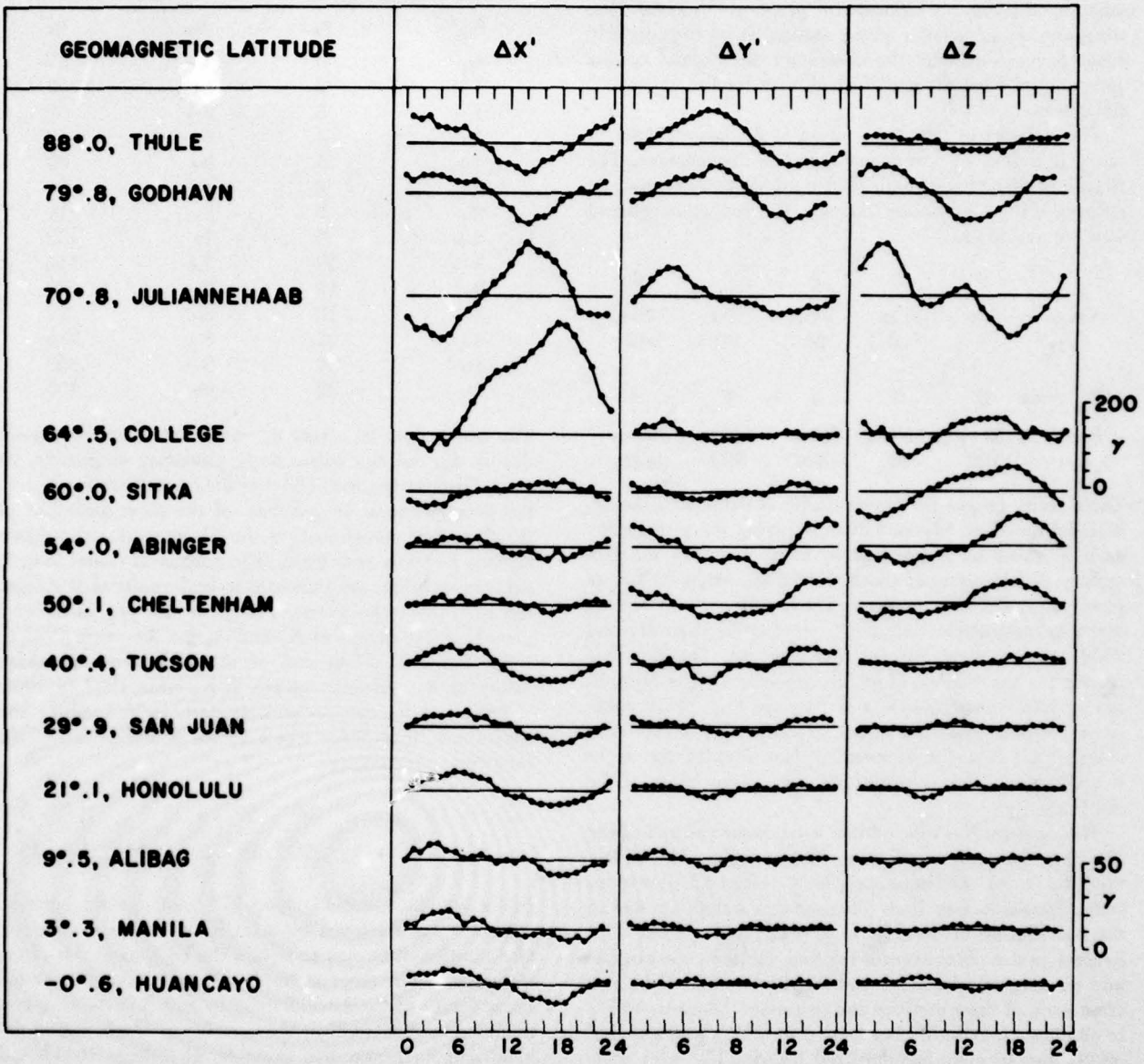


Fig. 11-24. Average disturbance daily variation (disturbed minus quiet days) of geomagnetic components for polar yr 1932-1933. Note that the intensity scale (γ) for 60° and higher stations is reduced. (After Vestine et al [1947].)

11.4.3.1 *Indices K, a, and A.* The *K index* evaluates the activity during each 3-h interval of the Greenwich day on the basis of the sum of the maximum positive and negative deviations of the trace of the most disturbed component from its undisturbed or quiet-day configuration. The intent is to separate magnetic disturbance from the smooth, diurnal variations. In practice, however, the diurnal variations at a given station vary considerably from day to day, and the observer must depend on his judgment of what the undisturbed trace for the day would have been.

The K index of 9 at any station is the largest disturbance; K indices of 3 or 4 are moderate disturbances. The K scale is quasi-logarithmic. For a middle-latitude station, such as Wingst or Fredericksburg, the ranges of gamma in a 3-h period are:

K =	0	1	2	3	4
Range = (γ)	0 to 5	5 to 10	10 to 20	20 to 40	40 to 70

K =	5	6	7	8	9
Range = (γ)	70 to 120	120 to 200	200 to 320	320 to 500	500 or more

The activity ranges for observatories at different geomagnetic latitudes are adjusted by multiplying the γ range for each K value by a constant in order to make the frequency distributions of the K values the same, as far as possible, at different stations. Thus, a K of 9 represents 300 γ or more at low latitudes (except at the equator) and 2500 γ or more at auroral zone stations. The K scales chosen for the various observatories indicate the latitudinal variation in magnetic activity; see Fig. 11-25. Data from a single observatory are identified by a two-letter suffix; e.g., K_{Hu} for Huancayo. The sum of the eight K values for a day is sometimes used as an index of the daily activity.

The measure K_w, now seldom used, is an average of the K values from all contributing observatories. The widely used K_p index was developed in an effort to obtain an index relatively free from geographical weighting due to the distribution of observatories (Fig. 11-3). Table 11-2 lists the twelve observatories selected and their geographic and geomagnetic latitudes and longitudes. The K indices from each of these stations are processed [Bartels, 1957] to eliminate longitudinal or local time effects and seasonal effects and to yield standardized indices, K_s, on a scale with finer gradations in which −, o, or + is added to the K number. The average of the K_s indices from the 12 observatories is the planetary 3-h range index K_p, also in thirds of scale steps. The K_p values are available for the years beginning with 1932; some stations have scaled K values for earlier years. Figures 11-26 and 11-27 show the K_p values for 1958 and 1963 by the bar charts (called musical diagrams by Bartels). They give the levels of magnetic activity for years of low (1963) and high (1958) sunspot number and also illustrate the tendency for magnetic disturbance to recur at 27-day intervals.

Because a linear scale of disturbance values is preferable for studies of the correlation of magnetic activity with other phenomena, the a and A measures were generated from the K indices. The *equivalent 3-h planetary amplitude*, a_p, is derived from K_p by the following conversion:

K_p	a_p	K_p	a_p
0o	0	5−	39
0+	2	5o	48
1−	3	5+	56
1o	4	6−	67
1+	5	6o	80
2−	6	6+	94
2o	7	7−	111
2+	9	7o	132
3−	12	7+	154
3o	15	8−	179
3+	18	8o	207
4−	22	8+	236
4o	27	9−	300
4+	32	9o	400

The average of the eight a_p values for each Greenwich day is A_p, the *equivalent daily planetary amplitude.* At a standard station with 500 γ as the lower limit for K = 9, the average range, in gammas, of the most disturbed of the three field components in the 3-h interval with a given K_p may be taken as twice a_p. The numerical values in such conversion tables are thus said to be in units of 2 γ (e.g., for $K_p = 3+$, the average range is 36 γ). Table 11-3 gives monthly means of K_p and A_p for the years 1932 to 1962. Table 11-6 (at end of chapter) gives the daily values of A_p and daily means of K_p from 1957 to 1962.

The a and A measures may similarly be derived for any individual observatory which scales K indices from the following conversion:

K =	0	1	2	3	4	5	6	7	8	9
a_k =	0	3	7	15	27	48	80	140	240	400

For a standard station, near 50° geomagnetic latitude, with 500 γ as the lower limit for K = 9, the a_k values are also multiplied by two to obtain the equivalent 3-h range in gammas. For other stations, the gamma values for the lower limit of K = 9 are divided by 250, and the resultant numbers used to multiply the a_k value to obtain the equivalent gamma range. For example, at College (64°.5 and 255°.1 geomagnetic latitude and longitude), with a lower limit for K = 9 of 2500 γ, a K of 6 would indicate an equivalent range of 800 γ. (For any particular 3-h interval, the actual gamma range at College for K = 6 might be any value between 600 and 1000 γ.)

The A_k measure for any observatory is the average of the eight a_k for the Greenwich day. Use of the daily A_p (planetary) or A_k (local) is recommended in preference to the sum of the indices K_p or K. The daily quasi-logarithmic range index C9 is also sometimes used; it is derived from the K_p indices, via the A_p indices.

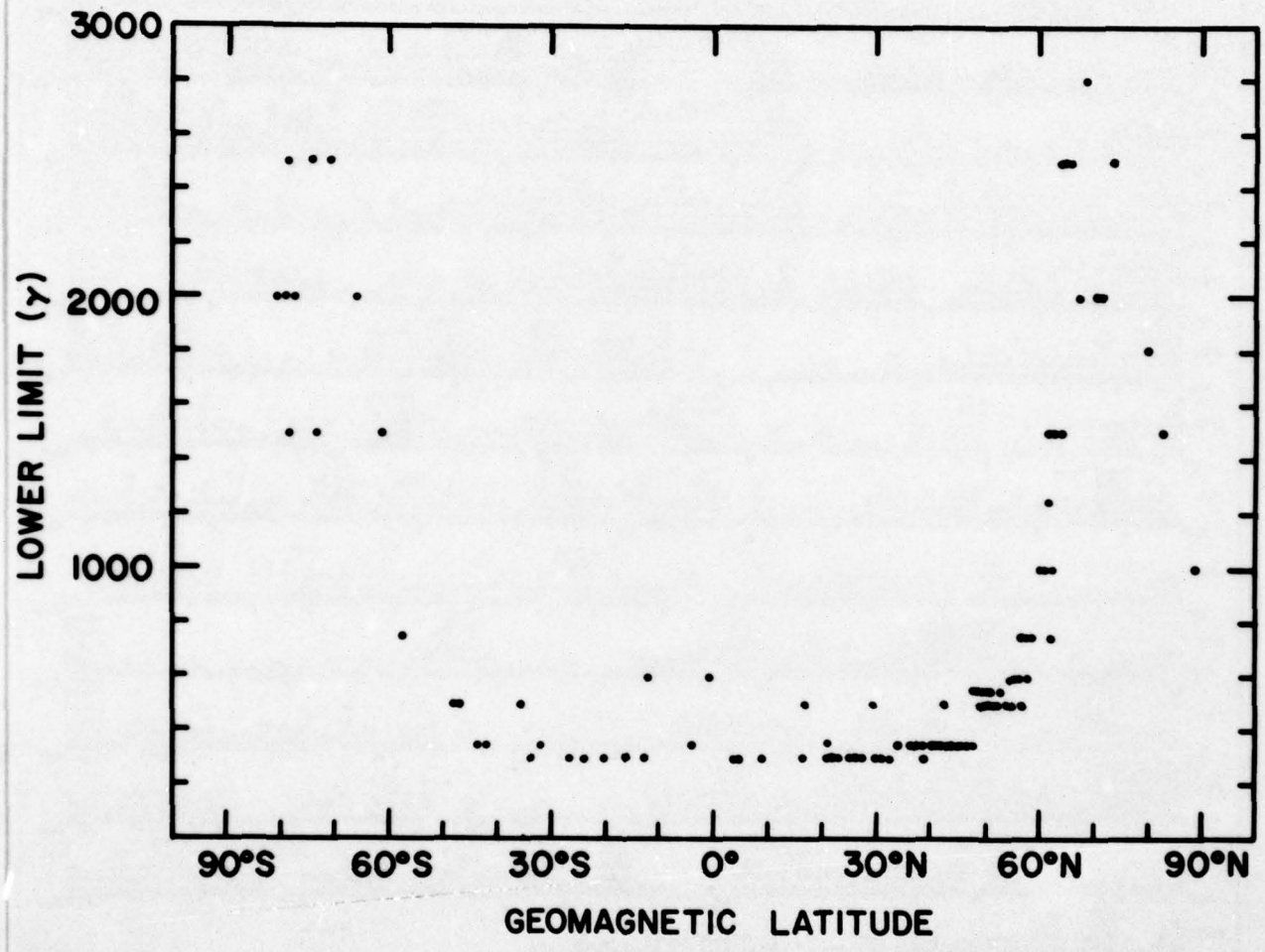


Fig. 11-25. The variation of the intensity of magnetic activity vs latitude as indicated by the lower limit for K = 9 for reporting stations; 1959 data.

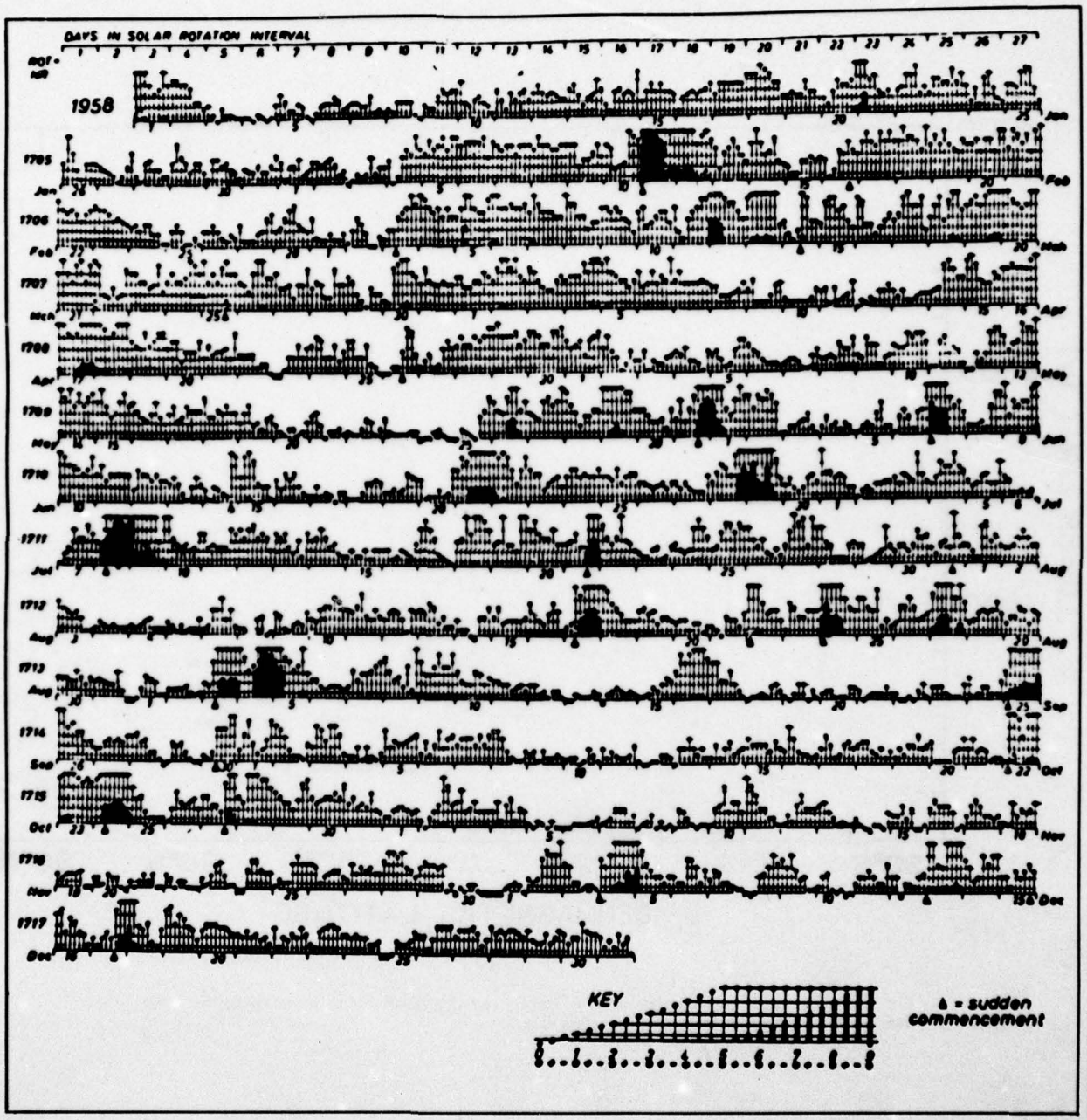


Fig. 11-26. Planetary magnetic three-hour range indices K_p for 1958, a year of high solar activity. (After J. Bartels.)

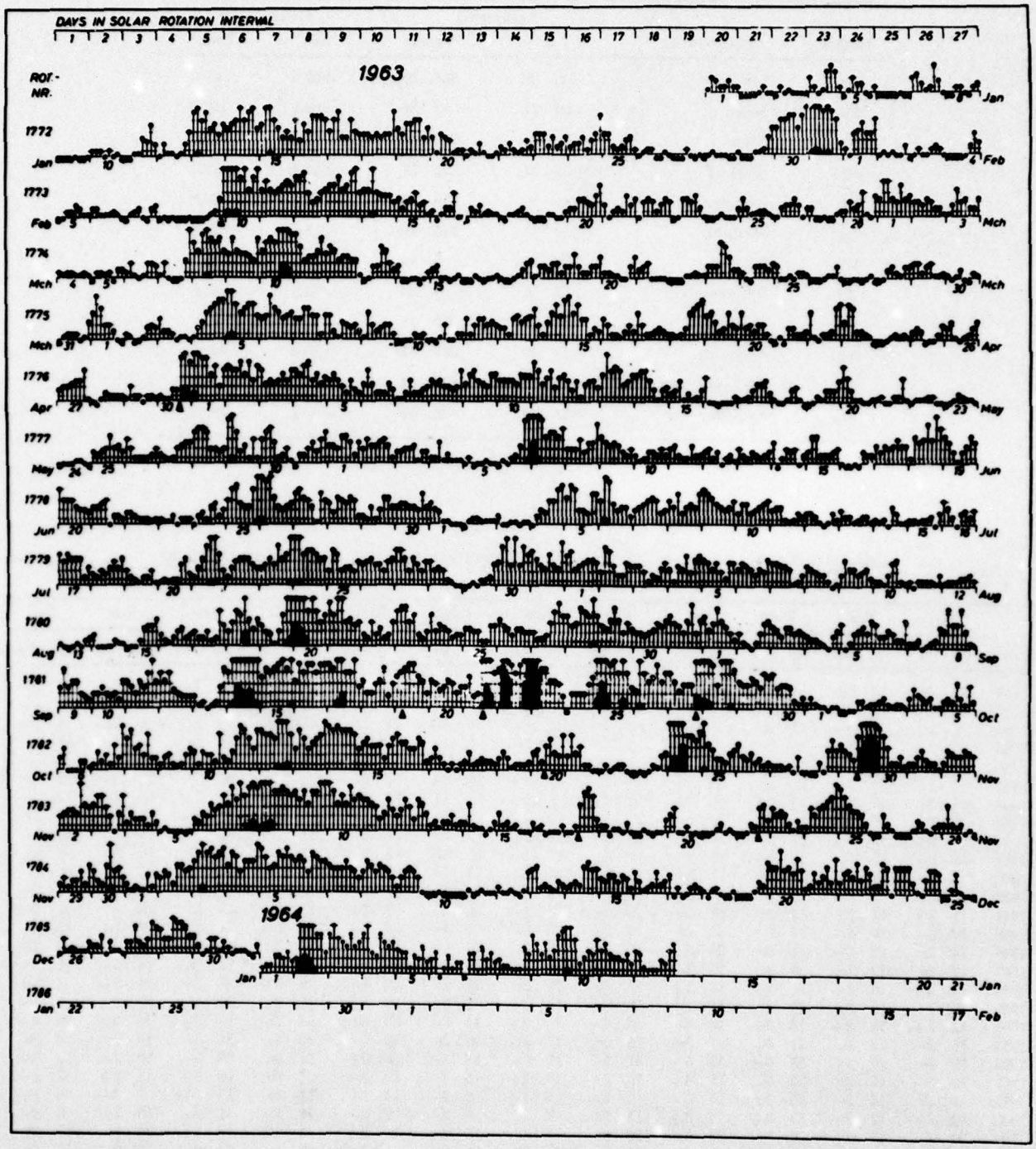


Fig. 11-27. Planetary magnetic three-hour range indices K_p for 1963, a year of low solar activity. (After J. Bartels.)

Table 11-2. Magnetic observatories selected for determining K_p indices. (For a complete list of magnetic observatories, see International Association of Geomagnetism and Aeronomy Bulletin No. 12 series.)

Symbol	Observatory	Geographic		Geomagnetic	
		Lat	Long.	Lat	Long.
Le	Lerwick	+60 08	358 49	+62.5	88.6
Lo	Lovö	+59 21	17 50	+58.1	105.8
Si	Sitka	+57 04	224 40	+60.0	275.4
RS	Rude Skov	+55 51	12 27	+55.8	98.5
Es	Eskdalemuir	+55 19	356 48	+58.5	82.9
Me	Meanook	+54 37	246 40	+61.8	301.0
Wn	Wingst	+53 45	9 04	+54.5	94.0
Wi	Witteveen	+52 49	6 40	+54.2	91.0
Ha	Hartland	+51 00	355 31	+54.6	79.0
Ag	Agincourt	+43 47	280 44	+55.0	347.0
Fr	Fredericksburg	+38 12	282 38	+49.6	349.9
Am	Amberley	−43 09	172 43	−47.7	252.5

Table 11-3. Monthly means of equivalent daily planetary amplitude, A_p, and planetary 3-h range index, K_p, 1932-1962.

	Jan		Feb		Mar		Apr		May		June		July		Aug		Sept		Oct		Nov		Dec	
Year	A_p	K_p	A_p	K_p	A_p	K_p	A_p	K_p	A_p	K_p	A_p	K_p	A_p	K_p	A_p	K_p	A_p	K_p	A_p	K_p	A_p	K_p	A_p	K_p
1932	11	2o	12	2+	18	3−	17	3−	14	2+	7	1+	7	1+	12	2o	12	2+	10	2o	8	2−	9	2−
1933	10	2o	11	2o	12	2o	13	2+	12	2o	8	2−	7	2−	9	2−	12	2o	10	2o	9	2o	7	1+
1934	6	1+	8	2−	11	2o	6	1+	7	1+	5	1o	6	1+	9	2o	10	2o	6	1+	5	1o	8	2−
1935	9	2−	10	2o	10	2o	8	1+	6	1+	10	2−	7	1+	5	1+	13	2o	12	2o	8	2−	10	2o
1936	9	2o	11	2o	9	2−	15	2+	10	2o	12	2o	11	2o	5	1o	5	1o	9	2−	8	2−	5	1o
1937	7	1+	13	2+	12	2o	20	2+	13	2o	12	2+	12	2+	10	2−	9	2−	20	3−	12	2o	10	2o
1938	28	3o	16	3−	13	2o	18	3−	18	2+	9	2−	13	2o	12	2o	17	2+	16	2+	10	2o	11	2o
1939	7	2−	16	2+	19	3o	28	3+	21	3o	15	3−	19	3−	19	2o	13	2+	22	3−	9	2−	11	2o
1940	15	2+	12	2+	37	3−	18	2+	13	2+	16	2+	12	2o	11	2o	14	2+	14	2+	16	3−	15	3−
1941	14	2+	18	3o	33	3+	15	2+	11	2o	11	2o	19	2+	16	2+	27	3−	11	2o	16	2+	11	2o
1942	9	2o	12	2o	22	3o	17	2+	8	2−	8	2+	13	2+	13	2+	17	3−	22	3o	15	3−	11	2o
1943	11	2o	9	2o	13	2+	14	2+	14	2+	12	2+	15	3−	31	4−	26	3+	24	3o	20	3−	14	2+
1944	13	2+	12	2o	18	3−	15	2+	9	2−	8	2−	6	1+	9	2o	10	2o	11	2o	6	1+	14	2o
1945	10	2−	10	2o	17	2+	13	2o	9	2o	7	2−	9	2−	7	1+	10	2−	11	2o	8	1+	13	2o
1946	13	2o	22	3−	33	3o	20	3−	17	3−	16	3−	22	3−	11	2o	34	3+	13	2+	13	2+	9	2o
1947	12	2o	12	2o	31	4−	18	3−	14	2+	16	3−	16	3−	26	3+	32	4−	23	3o	14	2+	11	2o
1948	12	2+	13	2+	17	2+	13	2+	19	3o	10	2o	10	2o	20	3−	15	3−	27	3+	16	3−	13	2+
1949	20	3−	15	2+	19	3−	14	2+	18	2+	14	2+	8	2−	13	2+	13	2+	25	3o	15	2+	9	2o
1950	12	2+	18	2+	14	2+	18	3o	16	3−	14	2+	14	2+	25	3o	22	3o	28	3+	20	3−	16	3−
1951	16	3−	22	3o	21	3o	27	3+	20	3o	17	3−	20	3o	22	3+	40	4o	24	3o	18	3o	20	3o
1952	19	3o	26	3+	33	4−	34	4−	27	3+	18	3−	15	3−	13	2+	23	3o	20	3−	12	2+	15	2+
1953	15	3−	15	2+	22	3o	16	3−	16	2+	13	2+	16	3−	19	3−	21	3o	16	2+	13	2+	7	2−
1954	9	2o	16	3−	16	3o	14	3−	7	2−	6	1+	8	2−	10	2o	17	3o	15	2+	9	2−	6	1+
1955	12	2o	12	2+	15	2+	14	2+	11	2o	9	2o	8	2−	9	2−	13	2+	11	2o	13	2o	8	2−
1956	18	3−	15	2+	20	3−	27	3o	26	3o	17	3o	13	2+	16	2+	18	2+	13	2+	24	3o	10	2o
1957	17	2+	17	3−	26	3+	21	3o	11	2+	22	3−	16	2+	14	2+	49	4−	14	2+	18	3−	18	3o
1958	15	3−	27	3+	26	4−	20	3o	17	3−	24	3o	25	3o	18	3−	20	2+	16	3−	8	2−	15	2+
1959	14	2+	24	3+	24	3−	17	3−	19	3−	15	3−	32	3+	23	3o	28	4−	19	3−	22	3o	19	3o
1960	15	2+	14	2+	18	3−	42	4−	24	3o	20	3o	20	3−	20	3−	20	3−	36	3+	32	3o	21	3o
1961	12	2o	16	2+	14	2+	14	2+	13	2+	14	2+	28	3o	11	2o	13	2o	16	2o	10	2−	12	2o
1962	7	1+	10	2o	8	2−	14	2+	7	1+	9	2o	12	2+	15	3−	19	3o	10	3o	13	2+	13	2o
1963	11	2−	9	2−	8	2−	10	2o	11	2o	11	2o												

11.4.3.2 *Polar Range Index Q.* The quarter-hourly range index is a quasi-logarithmic measure for use at high-latitude stations (above about 58° geomagnetic latitude) to provide a more detailed comparison with other phenomena such as aurora [Bartels, 1957]. Because of the great amount of scaling required and the quantity of tabular data developed, it has not been widely used. The gamma ranges for the Q scale proposed for use at all stations (i.e., not to be adjusted for latitude) are as follows:

Q	0	1	2	3	4	5
Range (γ)	0	10	20	40	80	140
	10	20	40	80	140	240
Q	6	7	8	9	T	E
Range (γ)	240	400	660	1000	1500	2200
	400	660	1000	1500	2200	inf.

Q is scaled for the most disturbed of the two horizontal components; the vertical component is not used. Q is intended to indicate the intensity of ionospheric currents above the station, and not the intensity of more distant line-currents which might be up to 1000 miles away. The four Q indices for each hour of the Greenwich day are for the four 15-min intervals *centered* on the hour and on 15, 30, and 45 min after the hour.

11.4.3.3 *Variability Indices C, C_i, and C_p.* The *magnetic character figure, C,* is a subjectively obtained index for a 24-h interval. Participating observatories evaluate the magnetograms for each Greenwich day and assign one of three values: 0 for quiet, 1 for moderately disturbed, and 2 for very disturbed days. (Individual observatories sometimes also assign C indices to the local day.) Averages of the Greenwich-day values reported by contributing stations around the world are given to the first decimal place (0.0 to 2.0) and are designated C_i, or C_{int}, to indicate their international nature. While the individual C figures are subjective and on a coarse scale, the averaging of values from many observatories reduces the effects of these shortcomings.

Table 11-4 gives monthly and annual means of the C_i values for the years 1884 to 1962. Table 11-7 (at end of chapter) gives the daily values of C_i for 1957 to 1962. Because the C_i figures are available as far back as 1884, they are useful in many studies of the relationship between magnetic and solar activity. The C_i figures, for example, demonstrate the 27-day recurrent magnetic activity due to the solar rotation period. The C_i figure, however, is determined from a group of observatories whose geographical distribution may change during the years. A value C_p, derived from K_p, with a range of 0.0 to 2.4 has been proposed but not extensively used.

Table 11-4. Monthly and annual means of the magnetic character figure, C_i, 1884-1962.

Year	Jan	Feb	Mar	Apr	May	June	July	Aug	Sept	Oct	Nov	Dec	Annual
1884	0.37	0.58	0.78	0.73	0.44	0.60	0.69	0.52	0.52	0.63	0.73	0.57	0.59
1885	0.62	0.69	0.52	0.68	0.82	0.85	0.56	0.67	0.84	0.65	0.49	0.47	0.66
1886	0.66	0.64	0.84	0.76	0.86	0.82	0.74	0.70	0.61	0.83	0.82	0.87	0.76
1887	0.68	0.88	0.61	0.81	0.67	0.52	0.48	0.66	0.75	0.51	0.53	0.61	0.64
1888	0.68	0.66	0.55	0.57	0.70	0.53	0.52	0.49	0.60	0.58	0.60	0.53	0.58
1889	0.36	0.41	0.62	0.47	0.38	0.32	0.49	0.51	0.53	0.49	0.65	0.42	0.47
1890	0.61	0.59	0.52	0.53	0.49	0.48	0.53	0.53	0.69	0.76	0.64	0.49	0.57
1891	0.54	0.71	0.85	0.85	0.83	0.56	0.55	0.68	0.83	0.76	0.59	0.63	0.70
1892	0.76	0.95	1.03	0.70	0.85	0.69	0.91	0.73	0.78	0.90	0.71	0.80	0.82
1893	0.76	0.76	0.73	0.69	0.63	0.76	0.67	0.72	0.81	0.83	0.75	0.61	0.72
1894	0.75	1.01	0.77	0.78	0.76	0.80	0.86	0.72	0.81	0.73	0.80	0.59	0.78
1895	0.72	0.93	0.95	0.83	0.72	0.66	0.75	0.51	0.61	0.93	0.87	0.65	0.76
1896	0.97	0.94	0.84	0.71	0.70	0.51	0.57	0.72	0.70	0.65	0.58	0.60	0.70
1897	0.59	0.68	0.70	0.87	0.73	0.62	0.49	0.58	0.62	0.68	0.67	0.77	0.67
1898	0.68	0.68	0.80	0.65	0.67	0.64	0.64	0.70	0.78	0.68	0.65	0.65	0.69
1899	0.69	0.74	0.74	0.71	0.71	0.57	0.56	0.60	0.66	0.49	0.48	0.63	0.63
1900	0.63	0.49	0.58	0.44	0.45	0.29	0.31	0.37	0.40	0.38	0.33	0.32	0.42
1901	0.44	0.42	0.48	0.43	0.46	0.51	0.48	0.47	0.43	0.41	0.38	0.44	0.45
1902	0.36	0.51	0.39	0.48	0.43	0.45	0.45	0.43	0.45	0.49	0.46	0.43	0.44
1903	0.43	0.35	0.45	0.57	0.52	0.62	0.57	0.67	0.73	0.80	0.75	0.62	0.59
1904	0.69	0.55	0.42	0.62	0.61	0.50	0.57	0.46	0.53	0.58	0.54	0.50	0.55
1905	0.68	0.74	0.63	0.55	0.47	0.57	0.48	0.69	0.67	0.47	0.68	0.42	0.59
1906	0.45	0.90	0.68	0.63	0.58	0.56	0.69	0.63	0.79	0.59	0.55	0.71	0.65
1907	0.69	0.83	0.58	0.55	0.72	0.67	0.67	0.66	0.68	0.71	0.61	0.53	0.66
1908	0.64	0.71	0.87	0.68	0.82	0.66	0.49	0.77	0.89	0.53	0.60	0.47	0.68
1909	0.76	0.63	0.79	0.49	0.59	0.54	0.53	0.65	0.70	0.69	0.49	0.58	0.62

(Continued)

Table 11-4. Monthly and annual means of the magnetic character figure, C_i, 1884-1962. (Continued)

Year	Jan	Feb	Mar	Apr	May	June	July	Aug	Sept	Oct	Nov	Dec	Annual
1910	0.58	0.71	0.81	0.68	0.72	0.53	0.55	0.81	0.80	0.96	0.77	0.76	0.72
1911	0.78	0.89	0.78	0.76	0.70	0.53	0.61	0.53	0.50	0.59	0.49	0.45	0.63
1912	0.42	0.49	0.45	0.45	0.47	0.47	0.41	0.49	0.47	0.46	0.45	0.43	0.46
1913	0.51	0.53	0.53	0.54	0.45	0.45	0.42	0.46	0.58	0.57	0.42	0.36	0.49
1914	0.46	0.50	0.62	0.50	0.37	0.52	0.61	0.61	0.53	0.64	0.60	0.46	0.54
1915	0.53	0.64	0.68	0.61	0.58	0.61	0.47	0.60	0.59	0.77	0.82	0.54	0.62
1916	0.61	0.56	0.86	0.68	0.75	0.67	0.62	0.75	0.75	0.76	0.83	0.65	0.71
1917	0.81	0.69	0.59	0.63	0.66	0.55	0.61	0.85	0.61	0.74	0.53	0.72	0.67
1918	0.63	0.78	0.73	0.79	0.68	0.56	0.69	0.77	0.88	0.85	0.77	0.88	0.75
1919	0.78	0.81	0.89	0.70	0.82	0.55	0.54	0.70	0.83	0.91	0.52	0.66	0.73
1920	0.62	0.52	0.78	0.65	0.57	0.43	0.51	0.61	0.87	0.65	0.58	0.65	0.62
1921	0.54	0.51	0.68	0.67	0.83	0.55	0.54	0.58	0.50	0.63	0.62	0.65	0.61
1922	0.65	0.74	0.79	0.75	0.57	0.62	0.66	0.71	0.69	0.68	0.47	0.42	0.65
1923	0.48	0.61	0.53	0.44	0.47	0.50	0.42	0.36	0.52	0.55	0.42	0.50	0.48
1924	0.64	0.56	0.64	0.43	0.54	0.64	0.55	0.41	0.67	0.52	0.54	0.40	0.54
1925	0.44	0.42	0.42	0.52	0.47	0.74	0.55	0.61	0.71	0.82	0.48	0.57	0.56
1926	0.84	0.85	0.85	0.75	0.60	0.53	0.49	0.50	0.75	0.67	0.46	0.54	0.64
1927	0.62	0.66	0.80	0.60	0.65	0.47	0.56	0.61	0.77	0.84	0.35	0.63	0.63
1928	0.44	0.62	0.48	0.52	0.75	0.72	0.72	0.56	0.75	0.83	0.65	0.54	0.63
1929	0.47	0.82	0.85	0.54	0.61	0.56	0.66	0.55	0.75	0.85	0.71	0.71	0.67
1930	0.69	0.89	0.90	1.04	0.93	0.87	0.87	0.88	0.85	0.88	0.61	0.54	0.83
1931	0.54	0.62	0.59	0.45	0.54	0.65	0.55	0.68	0.82	0.95	0.83	0.74	0.66
1932	0.76	0.76	0.95	0.89	0.80	0.43	0.49	0.67	0.73	0.73	0.58	0.67	0.70
1933	0.65	0.65	0.71	0.76	0.62	0.55	0.54	0.60	0.77	0.65	0.63	0.53	0.64
1934	0.52	0.65	0.76	0.45	0.51	0.44	0.43	0.68	0.68	0.50	0.39	0.66	0.56
1935	0.69	0.72	0.73	0.55	0.51	0.68	0.56	0.51	0.86	0.86	0.65	0.73	0.67
1936	0.69	0.78	0.64	0.82	0.70	0.69	0.73	0.45	0.46	0.69	0.70	0.47	0.65
1937	0.55	0.89	0.78	0.83	0.74	0.74	0.78	0.53	0.61	0.98	0.73	0.63	0.73
1938	1.08	0.79	0.65	0.80	0.76	0.57	0.73	0.73	0.83	0.81	0.67	0.66	0.76
1939	0.51	0.86	0.96	1.01	0.93	0.78	0.83	0.66	0.66	0.87	0.47	0.63	0.76
1940	0.82	0.68	0.81	0.70	0.69	0.72	0.63	0.64	0.70	0.72	0.84	0.79	0.73
1941	0.72	0.81	1.01	0.65	0.58	0.63	0.66	0.66	0.80	0.58	0.73	0.58	0.70
1942	0.52	0.62	0.88	0.72	0.40	0.48	0.66	0.66	0.73	0.87	0.70	0.56	0.65
1943	0.52	0.50	0.66	0.62	0.65	0.64	0.69	1.01	0.90	0.87	0.79	0.64	0.71
1944	0.63	0.54	0.83	0.64	0.47	0.44	0.35	0.50	0.52	0.54	0.31	0.60	0.53
1945	0.48	0.51	0.69	0.55	0.41	0.31	0.44	0.39	0.42	0.53	0.34	0.60	0.47
1946	0.56	0.71	0.85	0.59	0.63	0.63	0.69	0.41	0.84	0.50	0.54	0.42	0.61
1947	0.57	0.52	0.98	0.63	0.61	0.66	0.60	0.85	1.00	0.78	0.57	0.54	0.69
1948	0.63	0.70	0.71	0.64	0.78	0.54	0.56	0.79	0.73	0.97	0.74	0.69	0.71
1949	0.68	0.71	0.75	0.59	0.68	0.61	0.47	0.62	0.61	0.89	0.74	0.49	0.65
1950	0.68	0.70	0.66	0.75	0.75	0.65	0.66	0.82	0.85	0.91	0.76	0.73	0.74
1951	0.77	0.90	0.90	1.00	0.85	0.82	0.84	0.92	1.13	0.84	0.82	0.84	0.89
1952	0.82	0.94	1.04	1.02	0.91	0.75	0.65	0.65	0.87	0.75	0.61	0.68	0.81
1953	0.70	0.61	0.83	0.74	0.62	0.54	0.70	0.77	0.85	0.66	0.60	0.40	0.67
1954	0.47	0.78	0.82	0.70	0.43	0.37	0.50	0.60	0.86	0.72	0.52	0.35	0.60
1955	0.62	0.69	0.76	0.70	0.56	0.54	0.44	0.44	0.63	0.58	0.59	0.48	0.59
1956	0.94	0.68	0.89	0.89	0.89	0.78	0.63	0.67	0.67	0.62	0.92	0.54	0.76
1957	0.67	0.70	0.96	0.89	0.56	0.76	0.63	0.65	1.02	0.72	0.85	0.82	0.77
1958	0.78	0.96	1.09	0.83	0.75	0.80	0.85	0.69	0.62	0.68	0.42	0.75	0.77
1959	0.74	0.95	0.72	0.71	0.79	0.76	0.95	0.88	1.06	0.78	0.83	0.81	0.83
1960	0.69	0.69	0.76	1.07	0.88	0.82	0.82	0.83	0.76	0.97	0.91	0.92	0.84
1961	0.55	0.66	0.65	0.65	0.69	0.62	0.94	0.59	0.55	0.51	0.43	0.52	0.61
1962	0.32	0.58	0.45	0.72	0.36	0.57	0.68	0.80	0.85	0.95	0.64	0.63	0.63
1963*	0.51	0.44	0.44	0.54	0.69	0.59	0.63	0.72	1.02	0.65	0.57	0.53	0.61
1964*	0.57	0.66	0.64	0.69	0.58	0.46	0.54	0.41	0.55	0.54	0.40	0.29	0.53

* Preliminary means based on C_p.

For the years that both C_i and A_p are available, the two indices show a reasonably good correlation. Prior to 1932, A_p is not available, but approximate values can be obtained from C_i by the following conversion:

C_i	A_p	C_i	A_p
0.0	2	1.0	19
0.1	4	1.1	22
0.2	5	1.2	26
0.3	6	1.3	31
0.4	8	1.4	37
0.5	9	1.5	44
0.6	11	1.6	52
0.7	12	1.7	63
0.8	14	1.8	80
0.9	16	1.9	110
		2.0	160

11.4.3.4 *Difference Indices U, u, u_1, and* Δ. The U figure is obtained directly from the arithmetic difference of two consecutive daily means of the horizontal intensity H. Each daily value is derived from the 48-h interval covering two Greenwich days and is assigned to the second day of the pair. Because two days are involved in deriving a daily value, the mean U figure for a month is usually used. The *equatorial value*, u, is derived from the relation

$$u = U\ (\sin \mu \cos B)^{-1}, \qquad (11\text{-}17)$$

where μ is the geomagnetic colatitude and B is the angle between the direction of H and the geomagnetic meridian through the observing station. The basis for u is the component of H which is parallel to the axis of the centered geomagnetic dipole. The u values can be modified by a nonlinear conversion to obtain the u_1 values which proportionally de-emphasize larger values of u. Table 11-5 gives monthly and annual means of u for the years 1872 to 1949; annual values back to 1835 are available.

The delta indices are also derived from the differences of consecutive means of a magnetic field component [Chernosky, 1956]. The differences of consecutive hourly means of H are termed Δh_1, hourly differences for declination are designated Δd_1, etc. The delta indices assigned to Greenwich days are designated by capital letters; they are obtained by averaging the 24 individual difference values. ΔH_1, for example, is obtained from the 24 Δh_1 values for the day (23 differences in one day and the difference involving the last hour of the preceding day). Table 11-8 (at end of chapter) lists monthly and annual means of the ΔH_1 index at Huancayo, Peru, for 1932 to 1944.

When basic intervals of n hours length are used, the delta index of H for the Greenwich day is defined by

$$\Delta H_n \equiv \frac{1}{24} \sum_{i=1}^{24} \Delta h_n^i, \qquad \Delta h_n^i \equiv \left| \overline{H}_n^i - \overline{H}_n^{i-n} \right| \qquad (11\text{-}18)$$

where $\overline{H}_n^i$ is the mean value of H for the n-hour interval starting with the ith hour of the Greenwich day and $\overline{H}_n^{i-n}$ is the mean value for the preceding n-hour interval (the interval starting n hours before the ith hour of the Greenwich day under consideration). The ΔH_{24} value is similar to the U figure in that differences of consecutive 24-h intervals are utilized. However, ΔH_{24} is the average of 24 values of Δh_{24} covering a three-day interval, whereas U is computed from only one difference for two consecutive Greenwich days. U is dependent upon the phase relationship of any long-period change to the Greenwich day, while ΔH_{24} is not.

11.4.3.5 *Examples of the Activity Indices.* Figures 11-28 through 11-31 are plots of activity indices with the Zurich sunspot numbers included for comparison. Figure 11-28 shows that fairly good agreement exists between the daily indices A_p and C_i and the daily averages of K_p. The storm-time depressions of the daily means of H at the Fredericksburg station correspond to high activity indices. The good agreement between A_p and the daily range R_Z (computed in this case from hourly mean values) at Fredericksburg may be a fortuitous occurrence in this particular example. Daily means and ranges for the other components show weaker relationships to the activity indices. A poor correlation (if any) is shown between the daily indices of magnetic activity and the Zurich sunspot number.

Figure 11-29 shows monthly means; the correlation between A_p, K_p, and C_i is improved, but the correlation between these indices and ΔH_1 for Huancayo (−0°.6, 353°.8 geomagnetic latitude and longitude) and u computed for various observatories is not good. The monthly means, for quiet days only, of R_H and R_D at Greenwich show reasonable agreement with the Zurich sunspot number, but none of these three quantities show much correlation with the other activity indices.

Although the magnetic activity is not closely related to solar activity as measured by sunspot number on a day-to-day or a month-to-month basis, when longer periods are examined, the correlation between the Zurich sunspot number and u, ΔH_1, and the quiet-day ranges at Greenwich is good. A less pronounced correlation with a sunspot number also appears for A_p, K_p, and C_i. Figure 11-30 shows the annual means and Fig. 11-31 the 11-yr means. In the 11-yr means, the individual sunspot cycles are averaged out, and the long-term trend of activity with a low at about 1900 appears. In particular, the equatorial activity indices u and ΔH_1 exhibit one of the strongest statistical relationships to solar activity.

11.4.4 Rapid Geomagnetic Variations

Rapid variations of magnetic field with durations ranging from a few minutes down to about 0.1 sec are called micropulsations; for an extensive review, see Jacobs and Westphal [1963]. In addition to specific events such as the ssc's and sfe's, there are the *random fluctuations*, a continuous spectrum of broad-frequency bandwidth, and a wide variety of quasi-sinusoidal variations representing energy in narrow bandwidths that are called oscillations.

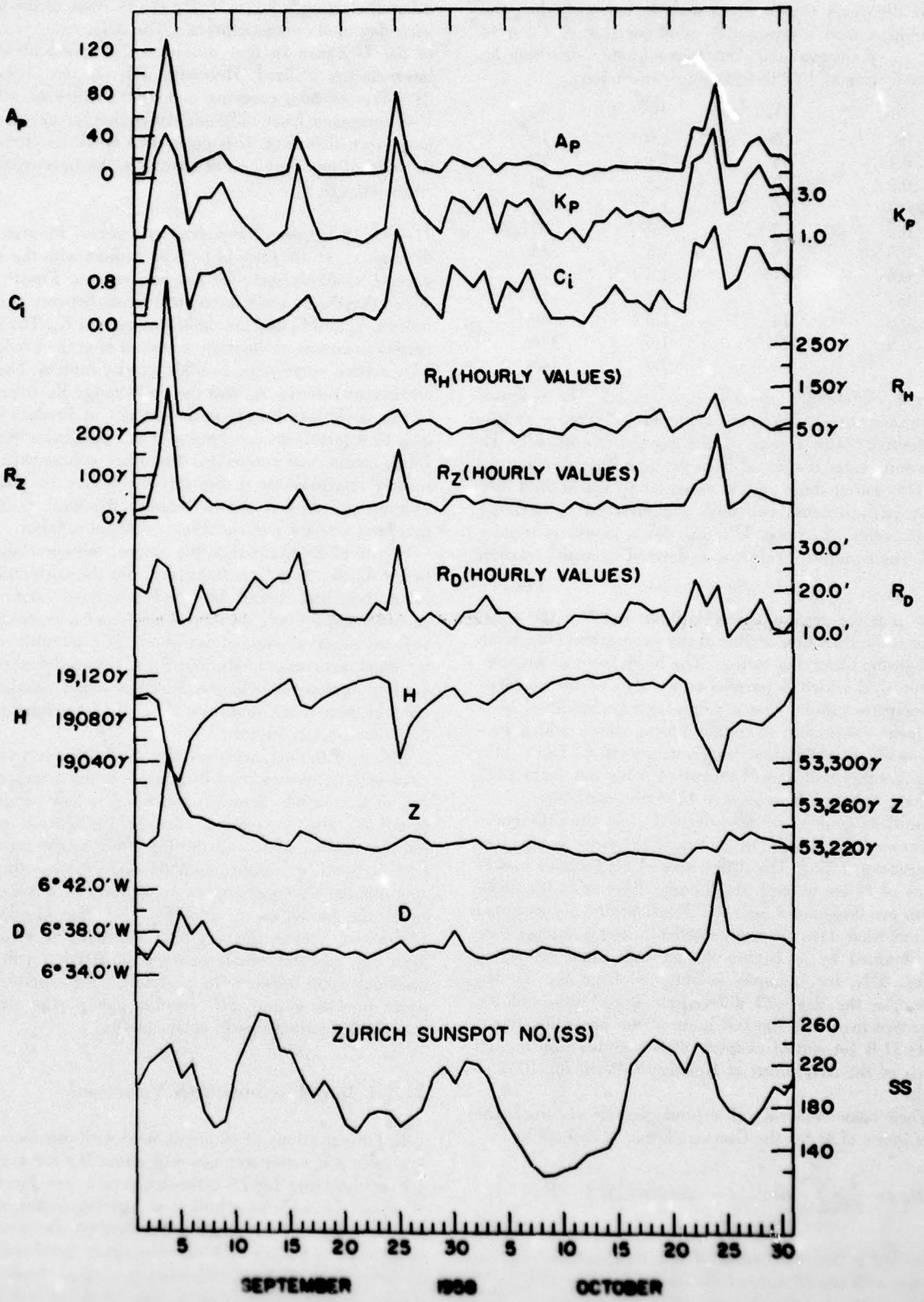


Fig. 11-28. Example of day-to-day changes in magnetic field, activity indices, and sunspot numbers at a middle-latitude station (Fredericksburg).

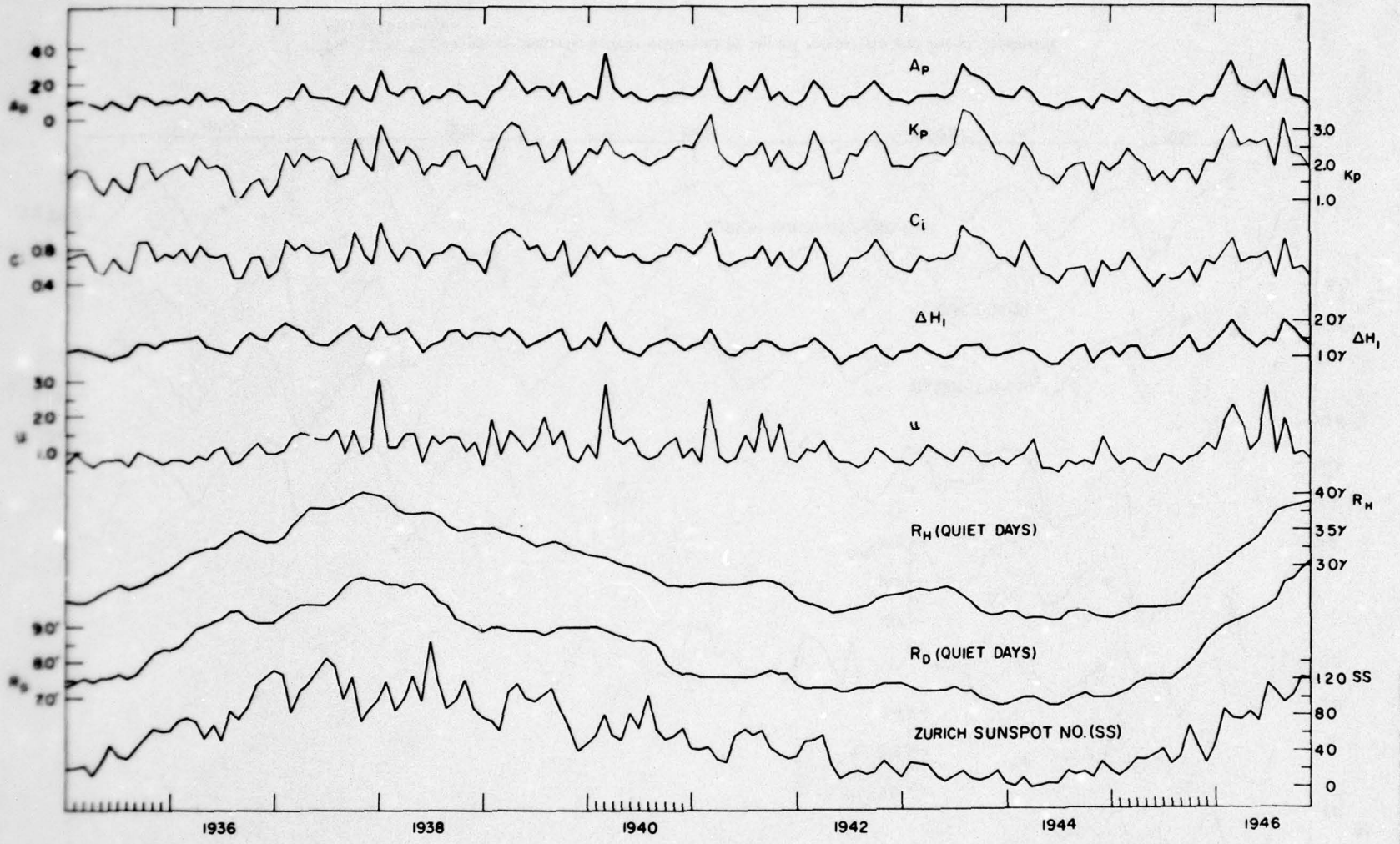


Fig. 11-29. Example of monthly variation in magnetic activity and sunspot numbers; R_D and R_H at Greenwich, ΔH_1 at Huancayo.

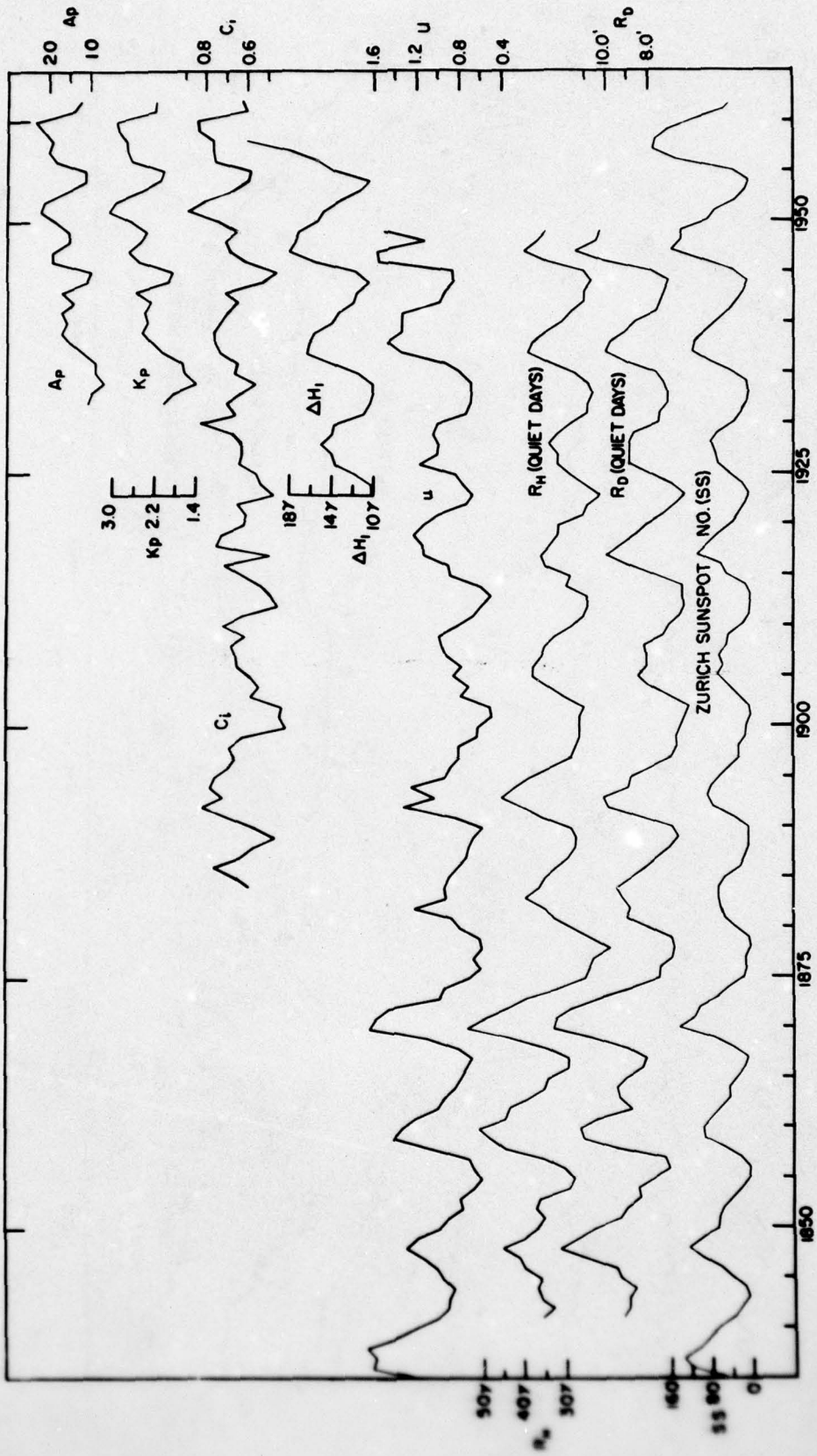


Fig. 11-30. The change in magnetic activity evidenced by annual means; R_D and R_H at Greenwich, ΔH_I at Huancayo.

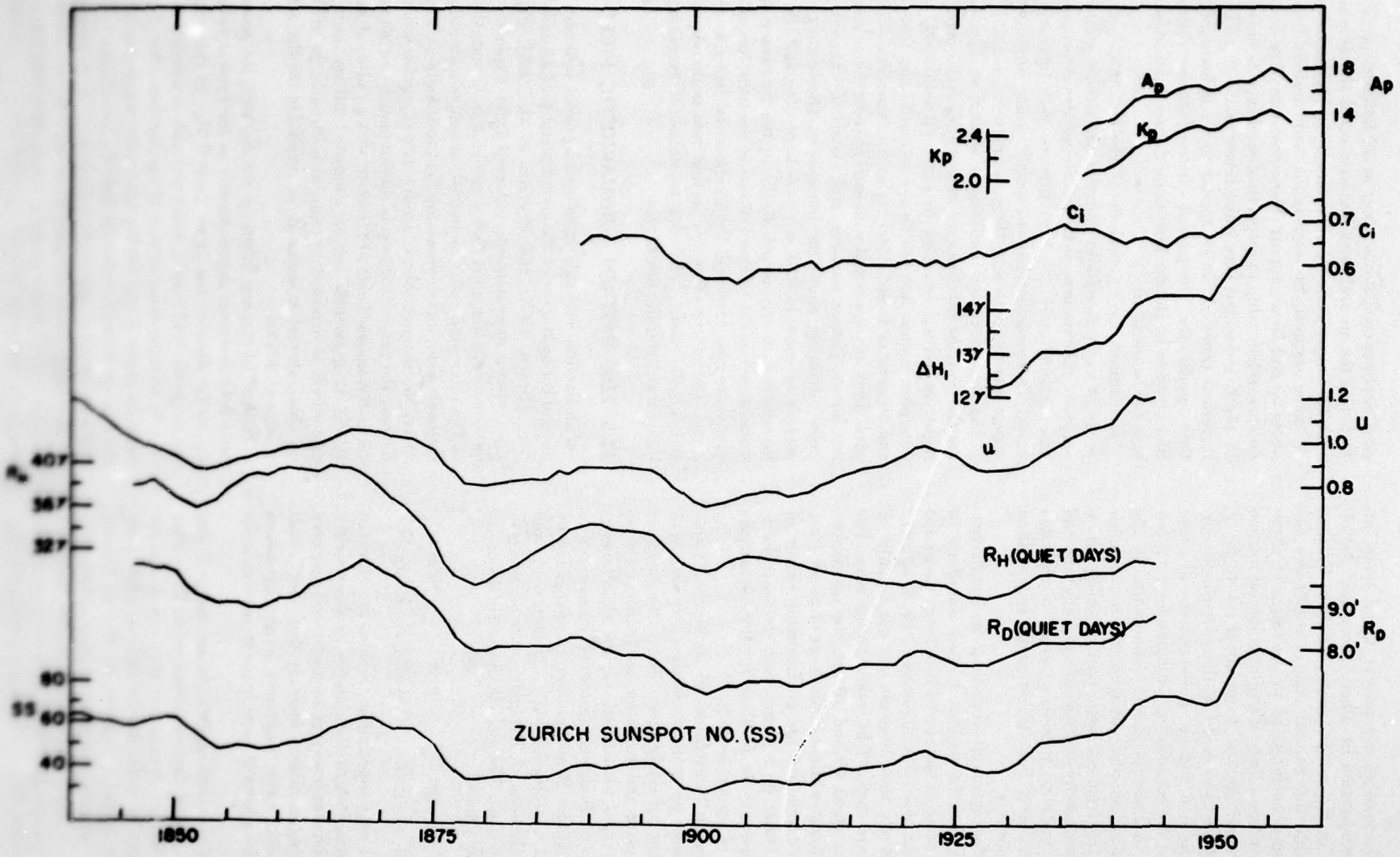


Fig. 11-31. The long-term variation in magnetic activity shown by 11-yr means; R_D and R_H at Greenwich, ΔH_1 at Huancayo.

The random fluctuations are present at all times, although sometimes obscured by other phenomena. Amplitudes are largest in the auroral zones. At Point Barrow, Alaska (just inside the auroral zone), amplitudes are directly proportional to durations in the range of about 1 sec to 3 min; average values of the three largest fluctuations per 3-h interval increase from about 0.1 to 25 γ. The amplitudes of the random fluctuations are closely correlated with the local K indices. For durations of about 2 min, the largest fluctuations have amplitudes of a few hundred gamma at times of strong disturbance. In the auroral zone, ionization and conductivity in the lower ionosphere resulting from energetic particle precipitation are probably rather patchy and variable in both time and space. These fluctuations, therefore, could result from statistical fluctuations of both the strength and position of the overhead currents.

At lower latitudes the amplitudes of the random fluctuations decrease. Those fluctuations having durations of about 1 min and longer continue to be closely associated with magnetic disturbance (as measured by the K index); for shorter durations these fluctuations are usually so small that they are masked by other phenomena. For durations between about 60 and 10 sec, the oscillations are often predominant, while for durations of about 1 sec and less, thunderstorms are the predominant source of the fluctuations. Other phenomena, such as ionospheric turbulence, perhaps may be involved for the fluctuations having durations of several seconds.

The quasi-sinusoidal waveforms of oscillations imply resonant mechanisms for their production, but the physical mechanisms are not established. Observations suggest that separate resonant and excitation mechanisms are required for many types of oscillations; the simultaneous occurrence of two mechanisms would then be required to produce the oscillations. A terminology recommended by the International Association of Geomagnetism and Aeronomy for pulsations of a regular and mainly continuous character is *pc*. The period range (in seconds) is divided into five groups:

pc 1	*pc 2*	*pc 3*	*pc 4*	*pc 5*
0.2-5	5-10	10-45	45-150	150-600

The largest and longest-period oscillations are observed in the auroral zones. Polarization studies of these oscillations occurring simultaneously at northern and southern geomagnetic conjugate points indicate that they result from hydromagnetic waves generated in the exosphere and propagated along lines of force in the transverse mode [Sugiura, 1961].

The most often observed oscillations are the pc 3 and pc 4, which are common daytime phenomena. They often start before local sunrise or continue after sunset, but are usually less common at night. Amplitudes are a few gammas or less except in the auroral zones. The pc 4 occur principally at sub-auroral and auroral geomagnetic latitudes (about 50° to 65°) and seldom at low latitudes; they sometimes have amplitudes of 20 γ or more in the auroral zones and are then called giant pulsations. The pc 3 daytime oscillations occur at all latitudes up to and including the auroral zone, and may occur simultaneously with the longer period oscillations at the higher latitudes. At some stations, no oscillations with periods between about 35 and 55 sec appear. The occurrence of pc 3 shows no close relationship to magnetic disturbance as measured by the K index, but very quiet times ($K \leq 1$) or highly disturbed times ($K \geq 6$) appear to be unfavorable for their appearance. The periods observed during disturbed times tend to be shorter than those during quiet times and may fall below 10 sec.

Oscillations having periods of about 2 to 8 sec that occur at night at middle latitudes are closely related to magnetic disturbance; both the frequency of occurrence and the amplitudes ($\leq 1\ \gamma$) increase with increasing K index. These oscillations are usually quite sinusoidal in appearance, more so than the pc 3 and pc 4 groups.

The shortest-period oscillations studied in any detail are the pc 1. At low latitudes they are observed chiefly at night; at auroral latitudes they are predominantly daytime phenomena. Amplitudes are normally less than 1 γ, and occurrence is not closely related to magnetic disturbance. They are associated with such phenomena as cosmic-ray bursts, meteor showers, and clouds of charged particles mirroring above the ionosphere. Oscillations with periods as short as 0.02 sec have been observed but not investigated in any detail. Peaks in the frequency spectrum caused by the resonant modes of the earth-ionosphere cavity are also observed, the fundamental being at about 8 cps. The source of energy in this case is thunderstorm activity, the peaks being due to statistical averaging of individual lightning discharges.

11.5 THE DISTANT GEOMAGNETIC FIELD

Information available from space probes indicates the general configuration of the geomagnetic field at its boundary [Beard, 1964; and Heppner et al, 1963]. Figure 11-32 shows measurements obtained from Explorer XII on a magnetically quiet and a moderately disturbed day.

The solar wind (see Chapter 18) interacts with the geomagnetic field, and confines the field to a finite volume of space, the magnetosphere. Under average quiet sun conditions, the magnetosphere is approximately hemispherical on the sunward side of the earth with a radius of about 10 R_E. It apparently has an elongated tail on the night side which is expected to close at a distance $> 40\ R_E$; no observational evidence is yet available on the actual closure of this tail.

Within the magnetosphere on the day side, the geomagnetic field decreases approximately as the inverse cube of the radial distance out to to about 5 R_E; in this region the magnetic field may be predicted with reasonable accuracy by suitable extrapolation of surface data (Sec. 11.3). Between about 5 and 10 R_E (the outer magnetosphere), the field decreases less rapidly than the inverse cube of the distance. At the magnetosphere boundary, the direction of the field may change abruptly by about 180° in a distance of a few hundred km. In quiet times, there may be little change in the magnitude of the field, which at this point

is about 50 γ. There is a transition region of turbulent fields between the magnetosphere and the region of the true interplanetary field that lies beyond the shock front (about 15 R_E) formed by the interaction of the solar wind and the geomagnetic field.

At times of magnetic disturbance both the particle density and velocity of the solar wind increase, and there is greater compression of the magnetosphere. The field just inside the boundary is increased, not just because the boundary is closer to the earth, but also because the geomagnetic field is more highly compressed. Under these conditions, there is an abrupt decrease in the magnitude of the field at the boundary as well as a 180° change in direction.

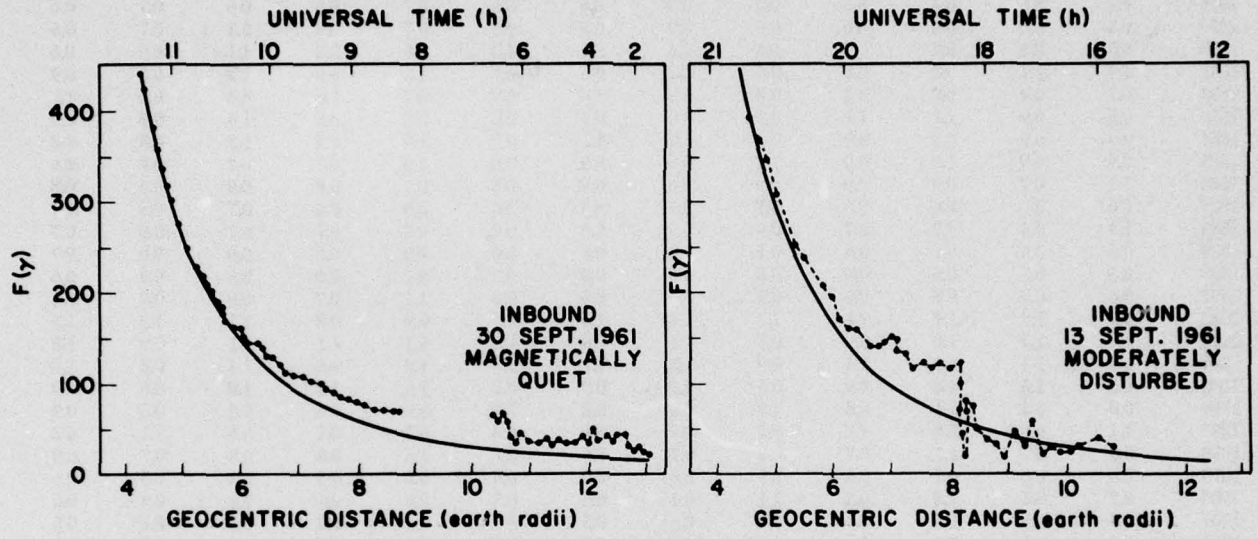


Fig. 11-32. Measurements of the magnetic field from Explorer XII; smooth curve is calculated from theory. (After L. J. Cahill and P. G. Amazeen, *J. Geophys. Res.*, v. 68, p. 1835, 1963.)

Table 11-5. Monthly and annual means of the difference index, u, 1872-1949.

Year	Jan	Feb	Mar	Apr	May	June	July	Aug	Sept	Oct	Nov	Dec	Annual
1872	1.1	1.9	1.4	1.2	1.1	1.2	1.8	2.1	1.5	1.9	1.3	1.0	1.5
1873	1.4	0.9	1.5	1.3	0.8	1.0	0.8	0.9	0.8	0.8	1.0	0.8	1.0
1874	1.0	1.3	1.2	1.3	0.7	0.7	0.8	0.8	0.8	1.4	0.8	0.6	1.0
1875	0.7	1.1	0.9	0.8	0.7	0.7	0.7	0.6	0.9	0.7	0.7	0.5	0.7
1876	0.6	0.9	0.8	0.5	0.5	0.6	0.5	0.5	0.6	0.6	0.6	0.6	0.6
1877	0.7	0.6	0.6	0.5	0.9	0.7	0.6	0.7	0.6	0.7	0.8	0.6	0.7
1878	0.7	0.5	0.4	0.5	0.5	0.8	0.5	0.6	0.7	0.6	0.6	0.7	0.6
1879	0.4	0.5	0.6	0.6	0.6	0.9	0.5	0.5	0.7	0.6	0.5	0.7	0.6
1880	0.5	0.4	0.7	0.7	0.6	0.6	0.7	1.4	1.0	0.8	1.1	0.9	0.8
1881	0.9	1.1	0.8	0.8	0.6	0.7	0.8	0.7	1.2	0.9	1.2	0.8	0.9
1882	0.7	0.9	0.8	2.2	0.8	0.9	1.0	0.9	0.7	1.8	3.0	0.9	1.2
1883	0.5	0.9	1.1	1.1	0.7	0.8	0.9	0.8	1.3	0.8	1.4	0.8	0.9
1884	0.9	0.9	0.8	0.9	0.8	0.9	1.1	0.7	1.0	1.1	1.3	0.8	0.9
1885	0.9	0.9	1.0	0.9	1.2	0.9	0.9	0.8	1.0	0.7	0.8	0.8	0.9
1886	1.1	0.7	0.9	0.9	0.9	0.6	0.9	0.8	0.7	0.8	0.9	0.5	0.8
1887	0.6	0.6	0.6	0.8	0.7	0.7	0.8	0.8	0.9	0.6	0.7	0.8	0.7
1888	1.1	0.4	0.7	0.7	0.9	0.9	0.6	0.8	0.6	0.7	0.7	0.6	0.7
1889	0.6	0.6	0.7	0.6	0.7	0.8	0.5	0.6	0.8	0.6	0.9	0.6	0.7
1890	0.5	0.5	0.5	0.5	0.6	0.5	0.5	0.5	0.7	0.9	0.8	0.4	0.6
1891	0.6	0.8	0.8	0.9	0.9	0.6	0.9	0.9	1.1	0.7	0.8	0.9	0.8
1892	1.0	1.7	1.7	1.1	1.7	1.4	1.6	1.7	0.9	0.8	1.2	1.3	1.3
1893	0.9	1.2	1.0	0.9	0.7	1.1	0.8	1.6	1.1	1.1	1.1	0.9	1.0
1894	0.8	1.7	1.4	1.4	0.9	1.2	1.7	1.9	1.2	0.8	1.4	0.8	1.3
1895	0.9	1.4	1.0	0.9	0.6	0.9	0.9	0.8	1.0	1.1	1.0	0.8	0.9
1896	0.8	0.8	1.1	0.8	1.2	0.8	0.8	1.0	0.9	0.8	0.8	0.8	0.9
1897	1.1	0.8	0.8	1.0	0.8	0.7	0.8	0.6	0.7	0.7	0.6	1.1	0.8
1898	0.5	0.7	1.2	0.7	0.7	0.7	0.6	0.7	1.5	0.8	0.8	0.7	0.8
1899	0.6	1.0	0.7	0.6	0.9	0.6	0.5	0.6	0.6	0.5	0.4	0.5	0.6
1900	0.7	0.6	1.2	0.5	1.1	0.4	0.4	0.5	0.5	0.6	0.4	0.4	0.6
1901	0.5	0.5	0.6	0.4	0.4	0.6	0.5	0.5	0.4	0.4	0.5	0.5	0.5
1902	0.4	0.5	0.5	0.6	0.5	0.5	0.5	0.6	0.4	0.6	0.6	0.4	0.5
1903	0.4	0.6	0.4	0.8	0.5	0.5	0.6	0.8	0.6	1.7	1.3	1.1	0.8
1904	0.9	0.5	0.5	1.0	0.9	0.9	0.6	0.7	0.6	0.7	0.8	0.6	0.7
1905	0.7	0.9	1.0	0.7	0.5	0.8	0.7	0.9	0.9	0.8	1.4	0.9	0.9
1906	0.5	1.1	0.7	0.7	0.9	0.7	0.8	0.7	0.7	0.5	0.8	1.1	0.8
1907	0.8	1.7	0.9	0.6	0.9	0.8	0.8	0.6	1.0	1.0	1.1	0.7	0.9
1908	0.7	0.6	1.0	0.8	0.9	0.6	0.8	1.0	2.1	1.0	1.1	0.9	1.0
1909	1.1	0.8	1.1	0.6	1.3	0.7	0.7	0.7	1.9	1.2	0.8	0.9	1.0
1910	0.7	0.6	1.1	1.1	0.8	0.6	0.6	1.2	0.7	1.0	0.6	0.7	0.8
1911	0.5	0.5	0.7	0.8	0.9	0.6	0.7	0.6	0.6	0.7	0.5	0.9	0.7
1912	0.5	0.5	0.6	0.7	0.5	0.5	0.6	0.6	0.6	0.6	0.8	0.5	0.6
1913	0.5	0.5	0.5	0.6	0.5	0.5	0.4	0.5	0.5	0.6	0.4	0.4	0.5
1914	0.5	0.5	0.5	0.7	0.5	0.5	0.7	0.5	0.8	0.7	0.7	0.6	0.6
1915	0.6	0.7	0.8	0.8	0.6	1.3	0.7	0.7	0.8	1.4	1.2	0.9	0.9
1916	0.8	0.6	1.4	1.2	0.8	0.8	0.7	1.4	1.0	0.9	0.7	0.5	0.9
1917	1.1	0.9	0.9	1.0	0.8	1.1	1.3	2.4	1.0	1.2	0.8	1.1	1.1
1918	0.7	0.2	1.2	1.5	1.1	0.9	0.8	1.1	1.1	1.5	1.2	1.5	1.2
1919	1.0	1.0	1.2	1.0	1.5	1.0	0.9	1.5	1.6	1.6	1.3	1.1	1.2
1920	0.8	1.0	2.5	1.2	1.1	0.9	0.9	1.0	1.3	1.0	0.9	0.9	1.1
1921	0.7	0.8	0.9	1.1	2.7	0.8	0.6	0.8	0.8	0.9	0.9	0.8	1.0
1922	0.7	0.9	1.1	0.8	0.7	0.6	0.6	0.6	1.0	0.8	0.5	0.5	0.7
1923	0.6	0.7	0.8	0.5	0.6	0.6	0.7	0.6	0.8	0.8	0.7	0.5	0.7
1924	0.8	0.6	0.6	0.6	1.0	1.0	0.7	0.5	0.9	0.8	0.9	0.6	0.7
1925	0.6	0.7	0.7	0.6	0.9	0.8	0.7	0.8	1.1	1.1	0.8	1.1	0.8
1926	1.4	1.4	1.3	1.4	0.9	1.1	0.8	0.8	1.5	1.7	0.8	1.0	1.2
1927	1.1	0.8	1.2	1.4	1.0	0.6	0.9	1.1	0.7	1.6	0.8	1.0	1.0
1928	0.6	0.6	0.8	0.6	1.3	0.8	1.8	1.0	1.3	1.4	1.0	0.7	1.0
1929	0.8	1.5	1.7	0.8	0.9	0.8	1.0	1.0	0.9	1.0	1.0	1.2	1.1
1930	0.8	0.8	0.9	0.8	1.1	1.0	0.7	0.8	1.4	1.3	1.0	1.3	1.0
1931	0.6	0.7	0.6	0.7	0.8	0.8	0.6	0.7	0.9	1.1	0.8	0.5	0.7
1932	0.5	0.6	0.9	0.7	0.9	0.6	0.6	0.7	0.7	0.8	0.6	0.7	0.7
1933	0.7	0.6	0.7	0.5	1.0	0.6	0.6	0.8	0.9	0.6	0.5	0.6	0.7
1934	0.6	0.7	0.8	0.6	0.9	0.7	0.6	0.6	0.8	0.5	0.6	0.8	0.7
1935	0.7	1.0	0.7	0.6	0.8	0.8	0.8	0.6	1.0	0.9	0.8	0.7	0.8
1936	0.8	0.8	0.7	0.9	0.8	1.1	1.2	0.7	0.8	1.1	1.3	1.0	0.9
1937	1.0	1.1	1.5	1.6	1.5	1.4	1.4	1.7	1.0	1.7	1.0	1.2	1.3
1938	3.1	1.2	1.2	1.6	1.6	0.8	1.5	1.3	1.5	1.5	1.1	1.4	1.5

(Continued)

Table 11-5. Monthly and annual means of the difference index, u, 1872-1949. (Continued)

Year	Jan	Feb	Mar	Apr	May	June	July	Aug	Sept	Oct	Nov	Dec	Annual
1939	0.7	2.0	1.0	1.7	1.4	1.1	1.4	2.1	1.3	1.7	0.9	0.8	1.3
1940	1.3	0.9	3.0	1.5	1.3	1.5	1.0	0.9	1.0	1.3	1.5	0.9	1.3
1941	1.2	0.8	2.6	1.0	0.8	0.9	1.6	1.1	2.2	1.1	1.9	0.9	1.3
1942	0.8	1.2	1.1	1.4	1.0	0.8	0.8	0.7	0.8	1.2	1.0	0.8	1.0
1943	0.8	0.7	0.9	1.3	1.1	0.9	0.8	1.2	1.1	0.8	0.8	0.9	0.9
1944	0.7	0.9	1.0	1.4	0.6	0.6	0.5	0.8	0.7	0.8	0.7	1.5	0.9
1945	1.0	0.7	0.9	0.8	0.6	0.5	1.0	0.9	0.7	0.9	1.0	1.3	0.9
1946	1.1	1.9	2.4	1.9	1.1	1.4	2.9	1.0	2.0	1.0	1.1	0.9	1.6
1947	1.2	1.2	2.6	1.4	1.6	1.7	1.2	1.4	3.4	1.3	1.2	0.8	1.6
1948	0.9	0.9	1.3	0.9	1.2	1.2	0.8	1.1	1.0	1.9	1.2	1.1	1.1
1949	2.6	1.6	1.6	1.4	2.0	1.4	0.8	1.2	1.0	2.1	1.8	0.8	1.5

Table 11-6. Daily values of equivalent daily planetary amplitude, A_p, and daily means of planetary 3-h range index K_p, 1957-1962.

	Jan		Feb		Mar		Apr		May		June		July		Aug		Sept		Oct		Nov		Dec	
Day	Ap	Kp	Ap	Kp	Ap	Kp	Ap	Kp	Ap	Kp	Ap	Kp	Ap	Kp	Ap	Kp	Ap	Kp	Ap	Kp	Ap	Kp	Ap	Kp
												1957												
1	8	2−	7	2−	16	3−	23	4−	16	3o	5	1+	83	5+	6	2−	28	4−	21	3+	8	2o	29	4o
2	25	3+	9	2+	132	7o	15	3o	10	2+	5	1+	55	4o	9	2o	102	6o	12	3−	7	2o	16	3o
3	10	2+	12	2+	32	4o	20	3+	11	2+	33	4o	30	4−	27	3+	135	7−	19	3o	13	3−	13	3−
4	5	1+	31	4o	14	3−	19	3+	10	2+	38	4+	12	2o	12	2o	145	6o	12	3−	4	1o	10	2+
5	4	1o	39	4+	17	3+	37	4+	8	2o	29	4o	56	5−	10	2o	112	6o	10	2+	4	1o	26	4o
6	6	2−	10	2+	14	3−	27	3+	13	3−	33	4+	16	3o	31	4o	36	4+	2	1−	24	2+	28	4o
7	7	2o	5	1+	9	2+	4	1o	11	2+	9	2−	9	2+	8	2o	11	2+	6	2−	31	3+	21	3+
8	14	3o	7	2o	15	3o	12	3−	11	2+	8	2o	9	2+	7	2o	7	2−	3	1−	18	3o	11	2+
9	13	3−	7	2−	16	3o	25	4−	22	3+	4	1o	6	2−	16	3o	13	3−	7	2o	29	4o	18	3+
10	31	4+	5	1+	73	6−	58	5o	10	2+	3	1−	4	1o	9	2−	8	2o	18	3+	26	4o	22	4−
11	15	3+	9	2+	9	2o	17	3o	8	2o	4	1o	5	1o	4	1o	6	2−	19	3+	21	4−	41	5−
12	7	2−	15	3o	8	2−	11	2+	5	1+	7	2−	9	2+	19	3+	7	2o	13	3−	17	3o	29	4o
13	5	1+	43	5−	10	2o	11	2+	11	3−	9	2o	3	1−	33	4o	160	7−	26	4−	11	3−	22	3+
14	4	1o	8	2−	4	1o	4	1o	6	2−	7	2−	6	1+	8	2o	38	4+	50	5o	22	4−	8	2o
15	7	2o	12	2+	11	2+	18	3−	5	1+	19	3+	5	1o	9	2o	14	3−	12	3−	21	3+	22	3+
16	8	2o	7	2o	37	4+	17	3o	4	1o	5	1+	16	3o	5	1+	12	2+	4	1o	10	2+	13	3−
17	6	2−	11	2+	15	3o	55	5−	7	2−	17	3o	8	2o	4	1o	12	3−	7	2−	6	1+	20	3+
18	3	1−	17	3+	13	3−	42	4+	6	2−	23	4−	13	3−	7	2−	12	2+	6	2−	25	4−	11	3−
19	7	2−	23	4−	11	3−	60	5+	12	2+	26	4−	25	4−	13	2+	4	1o	9	2o	10	2+	20	3+
20	4	1o	17	3o	13	3−	14	3o	17	3+	14	3−	11	2+	10	2+	6	2−	11	2+	10	2+	20	3+
21	82	5o	35	4+	20	3o	17	3+	13	3−	13	3−	6	2−	19	3o	74	5o	28	3+	4	1o	14	3−
22	70	5o	24	4−	23	4−	4	1o	6	2−	16	3o	26	4−	4	1o	104	6o	19	3+	6	2−	4	1o
23	26	4o	32	4−	19	3+	11	2+	8	2o	8	2o	11	2o	2	1−	164	7+	20	3+	7	2−	4	1o
24	27	4−	62	5−	11	2+	27	4o	6	1+	14	3−	12	3−	3	1−	33	4o	9	2o	12	3−	7	2
25	22	3+	9	2o	31	4−	10	2+	12	3−	41	5−	6	2−	7	2−	18	3o	8	2o	30	4o	16	3o
26	12	3−	4	1o	13	3−	23	4−	28	4o	84	6o	4	1o	8	2o	8	2o	8	2o	64	5+	18	3+
27	12	3−	6	1+	44	5−	20	3+	8	2o	17	3o	8	1+	19	3+	4	1o	12	3−	47	5−	6	2−
28	7	2−	3	1o	58	5−	18	3o	6	2−	18	3+	6	2−	10	2+	10	2o	14	3−	28	4o	4	1o
29	24	3+			77	6−	13	3−	5	1+	5	1+	12	3−	28	3−	139	6+	18	3+	16	3o	6	1+
30	36	4+			21	3o	12	3−	28	4−	150	7o	5	1+	38	4o	56	5+	16	3o	10	2+	18	3o
31	12	3−			20	3+			10	2+			7	2−	36	4−			8	2−			53	5+
												1958												
1	48	5−	9	2o	6	2−	19	3+	21	4−	60	5o	17	3o	15	3−	5	1+	15	3−	7	2o	2	1−
2	20	3+	9	2o	7	2−	34	4+	11	2+	26	4−	6	2−	12	3−	5	1+	11	2+	16	2+	23	3+
3	4	1o	6	2−	21	3+	18	3+	7	2−	6	1+	15	3o	10	2+	64	5o	18	3o	12	3−	7	2−
4	3	1−	17	3−	28	4o	36	4+	8	2o	5	1+	21	3+	4	1+	131	6o	5	1+	10	2+	54	5o
5	6	2−	30	4o	39	4+	26	4−	12	2+	8	2−	11	2+	5	1+	71	5o	13	3−	3	1−	28	3o
6	7	2o	30	4+	36	4+	23	4−	8	2o	15	3−	6	1+	5	1+	6	2−	12	2+	3	1−	12	2+
7	6	2−	25	4o	26	4o	17	3+	6	2−	77	5+	17	3o	12	2+	16	3o	14	3o	6	2−	6	1+
8	5	1+	27	4o	22	3+	9	2+	11	2+	13	2+	200	7o	4	1o	20	3o	10	2o	3	1−	10	2o
9	12	3−	18	3+	20	3+	9	2o	10	2+	32	4o	75	6−	7	2−	25	4−	5	1+	4	1o	12	2+
10	10	2+	24	3+	18	3+	5	1+	20	3+	31	4o	17	3o	16	3o	12	3−	4	1o	12	3−	4	1o
11	12	3−	199	7+	22	3+	7	2−	10	2o	18	3+	15	3o	15	3o	7	2o	6	1+	17	3−	8	2o
12	14	3o	59	5+	64	5o	6	1+	14	2+	15	3o	21	4−	10	2+	5	1+	3	1−	9	2o	6	2−
13	16	3o	18	3+	48	5o	6	2−	29	4o	9	2o	15	3o	12	2+	3	1−	7	2−	6	2−	50	5o
14	15	3−	23	4−	20	3−	20	3+	38	5−	15	2+	14	3−	7	2−	4	1o	7	2−	3	1−	19	3+
15	15	3o	8	2o	23	4−	25	4−	27	4o	21	3o	6	2−	9	2+	6	2−	10	2+	6	1+	10	2+
16	13	3−	14	3−	16	3o	32	4+	16	3o	10	2+	7	2−	12	3−	40	5−	9	2o	9	2o	16	3o
17	22	4−	31	4+	27	4−	54	5o	17	3+	4	1+	16	3−	82	5+	13	3−	9	2o	9	2o	30	3o
18	30	4o	32	4+	34	4+	44	5o	18	3+	7	2−	34	4+	20	3+	4	1o	8	2o	8	2o	33	3+
19	12	3−	25	4−	44	5−	24	4−	10	2+	9	2o	25	4−	11	3−	4	1o	8	2o	5	1+	21	3+
20	20	3+	26	4o	38	5−	15	3o	5	1+	8	2−	22	4−	6	2−	4	1o	6	2−	4	1o	15	3o
21	33	4−	31	4o	33	4+	14	3−	6	1+	66	5+	53	4+	6	2−	4	1o	6	2−	4	1o	8	2o
22	19	3+	25	4o	24	3o	6	2−	5	1+	38	4+	20	3+	34	4o	4	1o	47	5−	3	1−	9	2+
23	22	4−	21	4−	21	3+	7	2−	4	1o	13	3−	6	2−	13	3−	5	1+	44	5o	7	2−	12	3−
24	12	2+	8	2o	27	4o	15	3o	2	1−	18	3+	18	3o	84	6−	6	2−	89	6o	8	2o	7	2o
25	19	3+	5	1+	33	4+	11	2+	10	2−	16	3o	23	4−	18	3o	82	6o	10	2o	10	2o	4	1o
26	16	3−	7	2−	27	4−	13	2o	39	4+	8	2o	11	2+	14	3o	25	4−	11	2+	8	2o	13	3−
27	8	2o	10	2o	17	3o	10	2o	24	4−	8	2o	28	4o	64	5+	10	2+	30	4−	9	2+	12	3−
28	7	2−	15	3o	15	3o	24	4−	18	3o	55	4+	10	2o	13	3−	8	2o	37	4+	18	3+	14	3o
29	14	3−			10	2+	31	4+	52	5o	103	6o	9	2o	11	3−	5	1+	20	3+	12	2+	10	2+
30	9	2o			32	4−	29	4o	12	3−	9	2+	12	3−	9	2+	20	3o	19	3+	2	0+	12	3−
31	8	2o			18	3+			72	5−			15	3−	7	2−			12	3−			7	2−

(Continued)

Table 11-6. Daily values of equivalent daily planetary amplitude, A_p, and daily means of planetary 3-h range index K_p, 1957-1962. (Continued).

	Jan		Feb		Mar		Apr		May		June		July		Aug		Sept		Oct		Nov		Dec	
Day	A_p	K_p	A_p	K_p	A_p	K_p	A_p	K_p	A_p	K_p	A_p	K_p	A_p	K_p	A_p	K_p	A_p	K_p	A_p	K_p	A_p	K_p	A_p	K_p
										1959														
2	3	1o	23	4−	31	4+	6	2−	7	2−	19	3+	14	2+	16	3o	34	4+	23	3+	69	6−	30	4+
3	6	2−	22	4−	23	4+	12	3−	7	2−	16	3o	5	1+	20	3+	39	4o	46	4o	48	5o	50	5o
4	7	2−	36	4+	14	3o	7	2−	16	3o	22	4−	15	2+	19	3o	103	6+	51	5−	36	4+	12	3−
5	25	3+	24	4−	12	3−	6	2−	29	3+	15	3o	16	3o	9	2+	34	4+	37	4+	28	4o	68	4+
6	24	4−	18	3+	6	1+	6	2−	3	1−	12	3−	11	2+	22	3+	18	3−	53	5+	23	4−	16	3o
7	19	3+	11	2+	6	2−	8	2o	6	1+	8	2o	14	3o	14	3o	7	2−	15	3o	11	2+	6	2−
8	18	3+	12	3−	11	2o	22	3+	33	4+	11	2+	11	3o	14	3−	10	2+	8	2o	13	3−	7	2−
9	38	4o	23	3+	4	1o	44	4+	16	3o	19	3+	18	3+	22	3+	6	2−	6	2−	9	2o	8	2o
10	45	5o	6	1+	2	1−	98	6o	14	3o	12	3−	13	3−	14	3−	8	2−	4	1o	10	2+	6	1+
11	14	3−	36	4o	4	1o	23	4−	26	4−	24	3o	44	4+	8	2o	15	3o	3	1−	5	1+	6	2−
12	13	3−	24	4−	18	3+	10	2+	108	6+	6	1+	24	3+	5	1+	14	3−	7	1+	7	2−	16	3o
13	9	2o	21	3+	12	3−	9	2+	14	3−	4	1o	11	2+	6	2−	14	2+	4	1o	12	3−	18	3o
14	8	2−	30	4o	8	2o	11	2+	5	1+	9	2o	16	3o	6	2−	18	3+	13	3−	28	4o	40	5−
15	8	2o	37	4+	6	2−	10	2o	33	4o	8	2o	236	8−	27	4−	18	3+	15	3o	5	1+	26	4o
16	17	3o	61	5+	4	1o	6	2−	36	4o	6	2−	47	5−	130	7−	16	3o	4	1o	8	2o	17	3o
17	18	3+	24	3o	6	2−	7	2−	13	3−	6	1+	110	5+	114	6+	23	3+	17	3o	12	2+	8	2o
18	19	3+	4	1+	7	1+	5	1+	24	4−	8	2o	119	6+	28	4o	27	4o	36	5−	14	3−	14	2+
19	10	2+	12	3−	6	2−	4	1+	14	3o	7	2o	31	4o	21	3+	36	4o	15	3o	11	2+	14	3−
20	4	1o	4	1o	5	1+	5	1+	10	2+	8	2o	18	3+	38	4+	61	5+	8	2−	4	1o	6	2−
21	3	1−	6	2−	6	2−	8	2o	13	3−	8	2o	16	3o	34	4+	86	6o	6	1+	16	3o	4	1o
22	7	2−	17	3o	5	1+	3	1−	15	3o	11	3−	13	3−	27	4o	73	6−	19	3+	17	3+	6	1+
23	8	2o	15	2+	11	2+	40	3+	12	3−	15	3−	13	3−	28	4o	24	4−	10	2o	40	4+	28	4−
24	4	1o	4	1o	8	2o	27	4o	52	5o	26	3o	28	4−	20	3+	24	4−	6	2−	8	2o	15	3−
25	18	3−	69	5+	31	4o	22	4−	25	3+	6	2−	38	5−	15	3o	37	4+	22	4−	10	2+	8	2o
26	22	3−	48	5o	81	5o	18	3+	7	2−	14	3−	33	4+	8	2o	23	4−	26	4o	13	3−	26	4o
27	9	2o	30	4o	178	8−	14	3−	5	1+	31	3+	25	4−	5	1o	21	4−	11	2+	15	3−	38	5−
28	9	2+	44	5−	87	6−	12	3−	3	1−	34	4+	13	3−	3	1−	18	3+	4	1o	82	6−	40	5−
29	17	3o			73	6−	24	4−	3	1−	51	5o	10	2+	13	3−	9	2o	6	1+	15	3o	18	3o
30	11	2+			20	3+	21	3+	6	1+	38	4+	4	1o	9	2+	12	3−	28	4−	43	5−	14	3−
31	14	3−			19	3+			22	3+			15	3o	9	2+			38	4+			7	2−
1	1	0+	11	2+	42	5−	11	2o	9	2+	7	2o	5	1+	20	3+	20	3+	44	5−	43	5−	28	4o
										1960														
1	4	1o	8	2o	19	3+	241	8+	49	5−	28	4−	26	4−	14	3−	3	1−	48	5o	12	3−	93	6o
2	5	1+	15	3−	23	4−	62	5o	15	3o	5	1+	16	3o	18	3+	20	3o	49	5o	16	3o	26	4o
3	6	2−	19	3+	21	4−	68	5o	8	2o	8	2−	13	3−	7	2o	35	4o	15	3−	18	3+	9	2o
4	10	2+	18	3+	16	3o	26	4−	5	1+	52	5o	20	3+	7	2−	95	6o	36	4−	52	5o	6	1+
5	24	4−	19	3o	14	3o	34	4o	10	2+	34	4+	16	3o	3	1−	118	7−	34	4o	11	2o	10	2+
6	9	2o	19	3o	13	3−	17	3o	60	5o	25	4−	12	3−	7	2−	28	4−	203	8o	6	2−	21	3+
7	6	2−	5	1+	4	1o	22	3+	55	5+	15	3o	5	1+	7	2−	27	4−	186	7+	6	1+	25	3+
8	5	1+	10	2o	13	3−	16	3o	128	7−	24	4−	3	1−	16	3o	19	3+	33	4+	3	1o	22	3o
9	4	1o	6	1+	11	3−	14	3−	16	3o	19	3+	4	1o	22	3+	16	3o	38	5−	5	1+	20	3+
10	43	4+	6	1+	22	3+	33	4o	12	3−	6	2−	8	2o	14	3−	13	3−	10	2o	6	1+	10	2+
11	27	4o	8	2−	34	4+	25	4−	42	4+	5	1+	10	2+	23	4−	15	3−	17	3o	18	3o	9	2+
12	15	3o	6	1+	8	2o	35	4o	20	3+	5	1+	10	2+	24	4−	11	2+	6	1+	67	4+	18	3+
13	10	2+	11	2o	5	1+	28	4−	11	3−	6	2−	12	3−	8	2o	21	3+	4	1o	280	8+	14	3−
14	42	5−	29	4o	8	2o	14	3o	13	3−	14	3−	40	4+	14	3−	13	2o	3	1−	49	5−	6	1+
15	30	4−	9	2o	21	3−	24	3+	10	2o	11	2+	93	6−	8	2o	4	1o	17	3o	69	5+	43	4+
16	6	1+	27	4−	52	5o	29	4o	42	4o	6	1+	77	6−	52	4−	4	1o	6	2−	94	6−	33	4−
17	14	3−	23	4−	21	4−	30	4o	14	3−	7	2−	24	4−	106	6+	8	2−	7	2−	18	3+	7	2−
18	23	3+	28	4o	12	2+	21	3+	6	2−	14	3o	14	3−	16	3−	16	3−	27	4o	5	1+	26	4−
19	8	2o	21	3+	10	2+	4	1o	5	1+	16	3o	35	4o	21	3o	4	1o	10	2+	6	1+	17	3+
20	17	3o	19	3o	4	1o	2	0+	4	1o	8	2o	26	4−	26	4−	5	1+	10	2+	9	2+	24	4−
21	50	5o	22	4−	7	2−	3	1−	6	1+	16	3o	10	2+	28	4o	8	2o	8	2−	45	5−	25	4−
22	20	3+	10	2+	5	1+	5	1+	5	1+	13	3−	10	2+	14	3−	10	2+	2	0+	30	4o	20	3+
23	18	3+	10	2+	5	1+	15	2+	26	3o	11	2+	9	2−	7	2o	14	3−	3	1−	10	2+	14	3o
24	18	3+	4	1o	16	3o	66	5+	31	4o	13	3−	10	2+	6	1+	27	4−	21	3−	16	3−	15	3o
25	10	2+	4	1o	6	2−	57	5+	19	3+	26	4−	4	1o	3	1−	5	1+	76	5+	39	5−	9	2o
26	7	2o	6	1+	7	2−	18	3+	19	3+	22	3+	8	2o	4	1o	10	2o	63	5+	17	3o	16	3o
27	9	2o	22	4−	6	1+	31	3+	16	3−	65	5+	6	1+	16	3o	17	3−	38	5−	21	3+	50	5−
28	6	2−	6	2−	17	3o	84	6o	18	3−	36	4+	6	2−	14	2+	7	2−	45	5−	21	3o	23	4−
29	12	3−	16	3o	18	3o	55	5o	54	5o	36	4o	29	4o	45	5−	14	3−	40	5−	9	2+	19	3+
30	2	0+			20	3+	174	7+	18	3o	55	5−	29	4o	58	5−	28	4o	34	4+	17	3−	17	3o
31	3	1−			129	7−			13	3−			37	4+	16	3o			29	4o			15	3o

(Continued)

Table 11-6. Daily values of equivalent daily planetary amplitude, A_p, and daily means of planetary 3-h range index K_p, 1957-1962. (Continued).

	Jan		Feb		Mar		Apr		May		June		July		Aug		Sept		Oct		Nov		Dec	
Day	A_p	K_p	A_p	K_p	A_p	K_p	A_p	K_p	A_p	K_p	A_p	K_p	A_p	K_p	A_p	K_p	A_p	K_p	A_p	K_p	A_p	K_p	A_p	K_p
										1961														
1	7	2−	3	1−	8	2o	17	3o	15	3−	30	4o	10	2o	8	2o	28	4o	114	5+	5	1+	54	4+
2	4	1o	2	0+	8	2−	14	3o	19	3−	28	4−	12	3−	42	5−	13	3−	6	1+	4	1o	66	6−
3	5	1+	13	2+	5	1o	27	4−	4	1o	10	2o	16	3o	18	3+	12	2+	5	1+	4	1o	55	5o
4	3	1−	43	4−	3	1−	6	1+	8	2−	8	2o	16	3−	18	3+	5	1+	7	2−	4	1o	10	2+
5	4	1o	29	3+	14	2o	5	1+	20	3+	9	2o	45	5−	9	2o	12	3−	4	1o	19	3+	11	2+
6	6	1+	23	3+	37	4−	9	2−	30	4o	17	3−	16	3o	7	2o	5	1o	5	1+	16	3−	15	3−
7	8	2o	11	2+	3	1o	8	2−	20	3+	24	4−	14	3−	4	1o	4	1o	6	1+	42	5−	6	1+
8	22	4−	9	2+	5	1+	6	1+	11	3−	16	3o	10	2+	17	3−	4	1o	6	1+	23	3+	2	0+
9	30	4o	7	2−	13	3−	24	3+	15	3−	6	2−	9	2o	4	1o	8	2−	3	1−	12	3−	3	1o
10	5	1+	4	1o	46	4o	18	3+	8	2o	4	1o	14	3o	11	3−	7	2−	2	1−	5	1o	6	2−
11	1	0+	9	2o	6	2−	26	4−	19	3+	2	1−	9	2o	24	4−	12	2+	12	2+	3	1−	14	3−
12	5	1+	2	0+	7	2−	10	2+	15	3o	8	2−	5	1+	7	2−	17	3−	20	3+	15	3o	6	1o
13	9	2+	23	3+	10	2+	15	3−	22	3−	3	1−	102	5o	2	1−	8	2−	14	3−	4	1o	4	1o
14	5	1o	8	2−	26	4o	54	5−	10	2o	4	1o	98	6o	8	2−	28	4−	6	2−	13	2+	4	1o
15	19	3o	7	2−	24	4−	61	5−	4	1o	11	2+	25	4−	8	2o	6	2−	3	1−	1	0+	7	2−
16	12	2+	27	4−	20	3o	13	3−	28	4o	10	2+	23	3+	5	1o	7	2o	1	0o	3	1−	4	1o
17	8	2o	29	3+	14	3−	4	1+	8	2o	6	1+	26	4o	5	1+	11	2o	1	0+	16	3−	4	1o
18	17	3o	51	5−	12	2+	5	1+	3	1−	14	3−	93	6o	5	1+	7	2−	3	1−	49	5o	2	0+
19	26	3+	18	3+	38	4+	7	2o	8	2o	7	2−	18	2+	9	2o	3	1−	6	1+	11	2o	1	0+
20	41	4+	30	4o	17	3+	7	2−	13	3−	10	2+	19	3o	6	2−	9	2+	18	2+	13	3−	3	1−
21	18	3o	23	4−	11	2+	2	1−	5	1+	58	5+	35	4o	5	1+	2	1−	8	2o	7	2−	3	1−
22	21	3+	18	3+	13	2+	8	2−	11	2+	58	5+	12	2+	2	0+	6	1+	5	1+	2	1−	6	1+
23	6	2−	11	2+	10	2+	8	2o	14	3−	9	2o	17	3−	3	1−	2	1−	6	1+	2	0+	12	2+
24	18	3+	10	2−	8	2o	11	2+	8	2o	6	2−	13	3−	4	1o	42	4o	5	1+	3	1−	10	2+
25	18	3+	3	1o	5	1+	8	2−	34	4o	9	2o	14	3−	9	2+	35	4o	8	2−	4	1o	2	0+
26	12	3−	4	1o	9	2o	14	3−	7	2−	6	1+	23	3o	11	2+	18	3+	31	4o	5	1+	4	1o
27	8	2o	9	2o	22	3o	12	3−	6	1+	7	2−	114	6+	8	2−	26	4−	30	4o	4	1o	9	2o
28	12	3−	12	3−	17	3o	7	2−	10	2o	4	1o	18	3+	5	1+	5	1o	128	6o	3	1−	18	3o
29	9	2+			6	2−	5	1+	5	1o	25	3+	8	2o	16	2+	6	2−	32	3+	3	1−	13	3−
30	4	1o			10	2o	9	2+	9	2o	4	1o	8	2o	37	4+	36	3o	6	2−	2	0+	16	3o
31	4	1o			6	1+			22	4−			6	2−	30	4o			5	1o			7	2−
										1962														
1	6	1+	1	0+	7	2−	11	2+	9	2−	9	2+	9	2+	38	4+	29	4o	43	5−	8	2o	7	2−
2	9	2o	4	1o	7	2o	9	2−	9	2+	5	1+	8	2o	10	2+	34	4+	23	4−	15	3−	3	1o
3	2	0+	4	1o	7	2−	13	3−	7	2−	5	1o	8	2o	11	2+	47	5−	11	2+	14	3o	4	1o
4	1	0+	20	3o	6	2−	12	3−	2	0+	13	3−	19	3+	6	2−	36	4+	10	2+	19	3+	17	3o
5	1	0+	7	2−	17	3−	7	1+	4	1−	10	2+	16	3o	8	2o	16	3o	12	2o	6	1+	7	2−
6	3	1−	6	1+	31	4o	27	4−	23	3+	10	2+	12	3−	18	3+	22	3+	17	3−	24	4−	3	1−
7	3	1−	20	3+	8	2o	58	5+	7	2−	9	2o	8	2o	21	3+	14	3−	12	2+	15	3−	4	1o
8	4	1o	3	1−	2	1−	32	4o	6	1+	3	1−	10	2+	32	4+	14	3−	35	4+	8	2o	7	2--
9	6	2−	6	1+	2	0+	12	2+	2	1−	22	4−	6	2−	19	3+	11	2+	32	4+	5	1o	7	1+
10	52	5o	3	1−	12	3−	30	4o	6	1+	17	3o	8	2o	10	2+	11	2o	22	4−	4	1o	7	2−
11	12	3−	13	2+	12	3−	22	4−	9	2o	6	2−	9	2+	2	1−	9	2o	25	4−	11	2+	25	4−
12	4	1o	20	3+	16	3o	9	2o	3	1−	8	2o	7	2o	4	1o	58	5o	9	2o	4	1o	11	2+
13	5	1+	13	3−	8	2−	5	1+	13	3−	5	1+	11	2+	5	1o	23	4−	11	2+	3	1−	16	3o
14	11	2o	15	3−	4	1o	3	1−	15	3o	8	2o	9	2o	9	2o	11	2+	30	4o	7	1+	13	3−
15	10	2+	12	2+	10	2o	9	2o	15	3−	11	2+	6	1+	22	3+	15	3o	10	2+	26	4−	11	2+
16	12	3−	38	4+	4	1o	7	2−	8	2o	6	1+	3	1−	21	3o	10	2+	20	3o	27	4o	5	1+
17	4	1o	14	3−	4	1o	8	2o	3	1−	2	0+	2	0+	24	4−	7	2o	7	2−	8	2−	36	4−
18	2	1−	6	1+	8	2o	12	3−	2	1−	2	1−	4	1o	21	3+	5	1+	17	3−	1	0+	44	5−
19	15	3o	3	1−	13	3−	7	1+	10	2+	4	1+	10	2+	17	3o	39	4+	29	3+	4	1o	42	5−
20	4	1o	3	1−	13	3−	10	2o	5	1+	4	1o	16	3o	5	1+	13	2+	11	2+	4	1o	35	4+
21	7	2−	7	2−	15	3o	20	3o	3	1−	12	2+	12	3−	7	2−	12	3−	14	3−	19	3+	22	4−
22	1	0+	13	3−	4	1o	30	4o	3	1−	10	2+	7	2−	31	4o	21	4−	22	4−	35	5−	11	3−
23	1	0+	10	2+	4	1o	12	3−	2	1−	15	3o	8	2o	17	3+	13	3−	23	4−	20	3+	4	1o
24	1	0+	9	2o	7	2−	4	1o	2	0+	6	2−	16	3−	20	3+	6	1+	27	4o	16	3o	4	1+
25	4	1+	8	2−	9	2o	13	2+	2	0+	6	2−	15	3−	13	3−	7	2−	34	4+	19	3+	4	1o
26	8	2o	17	3o	4	1o	11	2+	4	1o	7	2−	46	5−	8	2o	32	4o	33	4+	6	2−	17	3o
27	10	2+	17	3o	4	1o	7	2o	12	3−	19	3+	28	4o	5	1+	9	2o	29	4o	9	2+	6	2−
28	3	1−	2	1−	4	1o	8	2o	6	2−	17	3o	18	3+	4	1+	9	2o	18	3+	7	2o	4	1+
29	7	2−			8	2−	6	2−	6	2−	14	3o	10	2o	15	3o	19	3o	12	3−	8	2o	5	1+
30	7	2o			3	1−	5	1+	3	1−	13	3−	5	1+	13	3−	14	3−	14	3o	32	4o	4	1o
31	1	0+			4	1o			22	3+			11	2o	25	3+			9	2+			12	2+

Table 11-7. Daily values of magnetic character figure, C_i, 1957-1963.

Day	Jan	Feb	Mar	Apr	May	June	July	Aug	Sept	Oct	Nov	Dec
						1957						
1	0.3	0.3	1.0	1.0	0.7	0.2	1.8	0.3	1.2	1.1	0.4	1.2
2	1.3	0.5	2.0	0.8	0.4	0.2	1.5	0.7	1.8	0.8	0.4	0.9
3	0.6	0.9	1.2	1.0	0.7	1.3	1.2	1.2	1.9	1.0	0.7	0.8
4	0.1	1.4	0.7	0.8	0.5	1.3	0.8	0.9	1.9	0.8	0.1	0.5
5	0.1	1.3	0.8	1.3	0.4	1.1	1.6	0.6	1.9	0.7	0.2	1.1
6	0.3	0.4	0.9	1.1	0.8	1.2	0.9	1.3	1.3	0.1	1.3	1.1
7	0.3	0.2	0.6	0.1	0.7	0.6	0.4	0.4	0.7	0.2	1.2	1.1
8	0.9	0.2	0.8	0.6	0.9	0.3	0.6	0.4	0.3	0.0	1.5	0.5
9	1.0	0.2	0.9	1.1	1.0	0.2	0.2	0.9	0.6	0.5	1.3	1.0
10	1.4	0.2	1.9	1.5	0.6	0.0	0.1	0.5	0.4	1.0	1.2	1.1
11	0.6	0.7	0.4	0.8	0.6	0.1	0.3	0.2	0.2	1.1	1.1	1.4
12	0.3	0.9	0.3	0.8	0.2	0.2	0.5	1.1	0.4	0.9	1.0	1.1
13	0.1	1.6	0.6	0.5	0.6	0.5	0.0	1.2	2.0	1.2	0.8	1.0
14	0.1	0.4	0.0	0.1	0.3	0.4	0.2	0.5	1.3	1.5	1.1	0.3
15	0.4	0.6	0.7	1.0	0.2	0.9	0.1	0.5	0.8	0.8	1.0	1.1
16	0.3	0.3	1.4	1.0	0.2	0.2	0.9	0.2	0.7	0.1	0.6	0.8
17	0.1	0.7	0.8	1.6	0.4	0.9	0.6	0.2	0.8	0.4	0.2	1.0
18	0.0	1.0	0.7	1.5	0.2	1.1	0.8	0.5	0.5	0.2	1.2	0.5
19	0.4	1.2	0.7	1.6	0.6	1.0	1.1	0.5	0.1	0.5	0.6	1.1
20	0.1	0.9	0.7	0.7	0.9	0.8	0.7	0.7	0.3	0.7	0.7	1.1
21	1.9	1.3	1.0	0.9	0.8	0.8	0.2	0.9	1.7	1.3	0.2	0.7
22	1.8	1.0	1.2	0.2	0.4	0.9	1.1	0.2	1.9	1.1	0.2	0.1
23	1.3	1.4	0.9	0.6	0.4	0.4	0.7	0.1	2.0	1.1	0.4	0.1
24	1.2	1.5	0.6	1.1	0.2	0.9	0.7	0.0	1.2	0.5	0.8	0.4
25	1.1	0.3	1.2	0.4	0.8	1.5	0.4	0.3	1.0	0.4	1.3	1.0
26	0.6	0.0	0.8	1.1	1.2	1.7	0.1	0.4	0.4	0.4	1.8	1.0
27	0.6	0.1	1.5	0.9	0.4	1.0	0.6	1.0	0.2	0.7	1.5	0.4
28	0.2	0.1	1.6	0.9	0.4	1.0	0.2	0.6	0.3	0.7	1.2	0.1
29	1.4		1.8	0.8	0.2	0.1	0.8	1.2	2.0	1.0	0.9	0.4
30	1.3		1.0	0.8	1.3	2.0	0.2	1.3	1.7	0.9	0.6	1.0
31	0.6		1.0		0.5		0.3	1.3		0.5		1.6
						1958						
1	1.6	0.4	0.3	1.0	1.0	1.5	0.8	0.9	0.2	0.9	0.3	0.1
2	1.0	0.4	0.2	1.2	0.7	1.1	0.2	0.6	0.2	0.7	1.1	1.3
3	0.1	0.2	1.2	1.0	0.2	0.2	0.8	0.5	1.6	1.0	0.8	0.4
4	0.1	1.1	1.2	1.3	0.3	0.1	1.0	0.1	1.9	0.2	0.4	1.8
5	0.4	1.4	1.4	1.1	0.7	0.4	0.7	0.2	1.7	0.8	0.1	1.3
6	0.5	1.3	1.4	1.2	0.3	0.7	0.1	0.2	0.3	0.6	0.1	0.8
7	0.3	1.2	1.1	0.8	0.2	1.5	0.9	0.6	1.0	1.0	0.2	0.2
8	0.2	1.2	1.0	0.4	0.8	0.7	2.0	0.2	1.0	0.5	0.0	0.8
9	0.8	1.0	1.0	0.3	0.7	1.2	1.7	0.3	1.1	0.1	0.1	0.7
10	0.8	1.2	0.9	0.1	1.0	1.2	1.0	0.8	0.6	0.1	1.0	0.0
11	0.8	2.0	1.1	0.4	0.5	1.0	0.9	0.8	0.3	0.1	0.9	0.5
12	0.8	1.8	1.6	0.1	0.8	0.7	1.1	0.6	0.1	0.0	0.6	0.3
13	0.9	1.0	1.5	0.2	1.3	0.4	0.8	0.7	0.0	0.3	0.2	1.6
14	1.0	1.2	1.2	1.0	1.4	0.7	0.7	0.4	0.1	0.4	0.1	1.2
15	1.0	0.5	1.2	1.0	1.2	1.0	0.2	0.5	0.2	0.7	0.2	0.7
16	0.8	0.9	0.8	1.3	0.9	0.5	0.2	0.8	1.5	0.4	0.5	1.0
17	1.2	1.3	1.2	1.5	0.9	0.1	0.8	1.8	0.6	0.4	0.3	1.4
18	1.2	1.3	1.3	1.4	1.0	0.4	1.3	1.1	0.1	0.2	0.5	1.3
19	0.8	1.1	1.5	1.1	0.6	0.6	1.1	0.6	0.1	0.6	0.1	1.1
20	1.3	1.2	1.4	0.9	0.2	0.3	1.0	0.1	0.1	0.3	0.1	0.8
21	1.3	1.3	1.3	0.8	0.2	1.6	1.5	0.2	0.2	0.2	0.1	0.4
22	1.0	1.1	1.0	0.2	0.1	1.8	1.0	1.4	0.2	1.5	0.1	0.6
23	1.1	0.9	1.1	0.4	0.1	0.7	0.2	0.7	0.1	1.4	0.4	0.8
24	0.6	0.3	1.2	0.7	0.1	0.9	0.9	1.8	0.4	1.8	0.5	0.2
25	1.1	0.2	1.4	0.5	0.6	0.7	1.0	1.0	1.8	0.6	0.8	0.2
26	0.9	0.2	1.1	0.8	1.3	0.3	0.6	0.8	1.1	0.8	0.5	0.9
27	0.5	0.5	0.9	0.6	1.1	0.3	1.2	1.7	0.6	1.4	0.6	0.7
28	0.3	0.8	0.7	1.1	1.0	1.6	0.6	0.8	0.4	1.4	1.1	0.8
29	0.8		0.4	1.2	1.6	1.7	0.5	0.5	0.1	1.0	0.8	0.4
30	0.5		1.3	1.2	0.8	0.6	0.6	0.4	1.1	1.0	0.1	0.7
31	0.5		0.8		1.7		0.8	0.3		0.8		0.2

(*Continued*)

Table 11-7. Daily values of magnetic character figure, C_i, 1957-1963. (Continued)

Day	Jan	Feb	Mar	Apr	May	June	July	Aug	Sept	Oct	Nov	Dec
						1959						
1	0.0	0.7	1.4	0.6	0.5	0.3	0.2	1.0	1.1	1.3	1.3	1.1
2	0.1	1.1	1.2	0.3	0.3	1.0	0.8	0.9	1.2	1.0	1.6	1.2
3	0.2	1.2	1.1	0.6	0.4	1.0	0.1	1.0	1.4	1.5	0.4	1.5
4	0.5	1.3	0.9	0.2	1.0	1.1	0.8	1.0	1.8	1.3	1.3	0.7
5	1.3	1.1	0.8	0.1	1.2	0.8	0.9	0.6	1.3	1.3	1.1	1.7
6	1.2	1.0	0.1	0.2	0.1	0.7	0.6	1.1	0.9	1.5	1.1	0.9
7	1.1	0.6	0.4	0.6	0.2	0.5	0.8	1.0	0.4	0.9	0.7	0.3
8	1.1	0.9	0.6	1.1	1.3	0.7	0.8	0.8	0.6	0.3	0.6	0.3
9	1.5	1.1	0.1	1.5	0.9	1.0	0.9	1.1	0.2	0.3	0.7	0.3
10	1.6	0.2	0.1	1.9	1.0	0.7	0.8	0.8	0.4	0.2	0.6	0.2
11	1.0	1.4	0.2	1.3	1.3	1.1	1.4	0.4	0.9	0.2	0.1	0.2
12	0.9	1.1	1.0	0.5	1.9	0.2	1.1	0.2	0.8	0.4	0.2	1.0
13	0.5	1.2	0.7	0.5	0.8	0.1	0.6	0.3	0.7	0.2	0.8	1.1
14	0.5	1.3	0.4	0.7	0.2	0.4	0.9	0.3	1.1	0.8	1.2	1.4
15	0.3	1.3	0.2	0.6	1.2	0.4	2.0	1.2	1.1	1.0	0.1	1.1
16	1.2	1.7	0.1	0.2	1.3	0.2	1.4	2.0	0.9	0.1	0.5	1.0
17	1.0	1.0	0.2	0.4	0.8	0.3	1.9	1.8	1.2	1.0	0.5	0.3
18	1.0	0.1	0.4	0.2	1.2	0.6	2.0	1.2	1.2	1.2	0.9	0.5
19	0.4	0.7	0.2	0.2	0.8	1.4	1.2	1.1	1.2	0.9	0.5	0.8
20	0.1	0.1	0.1	0.1	0.7	0.4	1.0	1.4	1.6	0.4	0.1	0.3
21	0.1	0.2	0.2	0.4	0.8	0.4	0.9	1.3	1.9	0.4	1.0	0.1
22	0.4	0.8	0.2	0.0	0.9	0.8	0.8	1.1	1.7	1.2	1.0	0.4
23	0.5	0.3	0.7	1.5	0.7	0.9	0.7	1.2	1.2	0.5	1.4	1.3
24	0.1	0.2	0.5	1.4	1.6	1.1	1.2	1.1	1.2	0.3	0.2	0.9
25	1.3	1.9	1.3	1.1	1.3	0.4	1.2	0.9	1.2	1.2	0.6	0.4
26	1.2	1.5	1.8	1.1	0.4	0.8	1.1	0.4	1.2	1.2	0.7	1.2
27	0.6	1.3	1.9	0.9	0.2	1.3	1.1	0.2	1.1	0.7	0.8	1.4
28	0.5	1.5	1.8	0.9	0.1	1.3	0.7	0.1	0.9	0.0	1.7	1.4
29	1.2		1.6	1.2	0.0	1.5	0.5	0.7	0.5	0.2	0.8	0.9
30	0.7		1.1	1.1	0.3	1.4	0.1	0.6	0.9	1.3	1.4	0.8
31	0.8		1.0		1.1		0.9	0.6		1.5		0.4
						1960						
1	0.0	0.4	1.1	2.0	1.4	1.2	1.2	0.7	0.0	1.5	0.6	1.8
2	0.1	1.1	1.1	1.5	0.7	0.2	0.9	0.9	1.2	1.4	0.8	1.2
3	0.1	1.0	1.1	0.5	0.3	0.6	0.8	0.4	1.3	0.7	1.0	0.3
4	0.6	0.9	1.1	1.1	0.2	1.5	1.0	0.4	1.8	1.4	1.5	0.3
5	1.1	1.1	0.9	1.2	0.5	1.3	0.9	0.1	1.9	1.3	0.5	0.5
6	0.5	0.9	0.8	0.9	1.6	1.2	0.6	0.4	1.3	2.0	0.2	1.2
7	0.2	0.2	0.1	1.1	1.5	0.8	0.2	0.5	1.2	2.0	0.2	1.3
8	0.2	0.6	0.8	0.9	1.9	1.1	0.0	1.0	1.0	1.1	0.1	0.9
9	0.1	0.2	0.7	0.7	1.0	1.0	0.1	1.1	0.7	1.3	0.1	1.1
10	1.6	0.1	1.1	1.2	0.7	0.2	0.5	0.8	0.8	0.5	0.3	0.6
11	1.2	0.4	1.3	1.0	1.3	0.2	0.8	1.2	0.8	0.8	1.0	0.4
12	1.0	0.2	0.3	1.2	1.0	0.2	0.7	1.1	0.4	0.2	1.7	1.1
13	0.8	0.8	0.1	1.0	0.7	0.2	0.7	0.5	1.0	0.1	2.0	0.6
14	1.6	1.2	0.4	0.8	0.7	0.8	1.4	1.0	0.7	0.0	1.6	0.3
15	1.2	0.6	1.2	1.0	0.6	0.4	1.8	0.5	0.1	1.1	1.7	1.5
16	0.5	1.3	1.6	1.2	1.3	0.1	1.7	1.4	0.1	0.3	1.6	1.2
17	0.9	1.2	1.1	1.1	0.9	0.2	1.2	1.8	0.4	0.3	1.0	0.2
18	1.2	1.1	0.6	1.0	0.2	0.8	0.9	1.0	0.7	1.3	0.2	1.3
19	0.5	1.2	0.5	0.1	0.2	0.8	1.4	1.2	0.0	0.5	0.4	0.9
20	1.1	0.9	0.0	0.0	0.1	0.4	1.2	1.3	0.2	0.6	0.6	1.2
21	1.7	1.1	0.4	0.1	0.2	0.8	0.6	1.2	0.5	0.4	1.5	1.2
22	1.1	0.4	0.2	0.2	0.3	0.7	0.6	0.8	0.6	0.0	1.3	0.9
23	1.0	0.4	0.2	0.8	1.1	0.7	0.6	0.4	0.7	0.1	0.5	0.7
24	0.9	0.1	0.9	1.6	1.2	0.9	0.7	0.2	1.2	1.2	0.9	1.0
25	0.6	0.1	0.3	1.4	1.1	1.2	0.0	0.1	0.2	1.7	1.4	0.3
26	0.2	0.2	0.3	1.0	1.1	1.2	0.5	0.1	0.7	1.5	0.9	0.8
27	0.3	1.1	0.2	1.3	0.9	1.6	0.3	1.1	0.8	1.4	1.2	1.6
28	0.2	0.2	1.0	1.7	0.9	1.3	0.4	0.8	0.3	1.5	1.0	1.1
29	0.7	0.9	1.0	1.4	1.6	1.4	1.3	1.5	0.9	1.4	0.4	1.0
30	0.0		1.1	2.0	1.1	1.6	1.2	1.4	1.3	1.3	1.0	0.9
31	0.1		2.0		0.9		1.3	0.8		1.2		1.0

(Continued)

Table 11-7. Daily values of magnetic character figure, C_i, 1957-1963. (Continued)

Day	Jan	Feb	Mar	Apr	May	June	July	Aug	Sept	Oct	Nov	Dec
						1961						
1	0.2	0.0	0.3	1.0	0.9	1.3	0.4	0.5	1.2	1.8	0.3	1.7
2	0.1	0.0	0.2	0.9	0.9	1.3	0.7	1.4	0.8	0.3	0.1	1.8
3	0.1	0.9	0.1	1.2	0.0	0.6	0.9	1.0	0.6	0.2	0.2	1.6
4	0.1	1.5	0.1	0.2	0.6	0.4	1.0	1.1	0.3	0.4	0.3	0.6
5	0.2	1.2	0.9	0.2	1.1	0.4	1.4	0.7	0.6	0.1	1.1	0.9
6	0.2	1.2	1.3	0.6	1.2	1.0	0.9	0.5	0.1	0.3	0.8	1.0
7	0.5	0.6	0.2	0.5	0.9	1.1	0.8	0.2	0.0	0.3	1.6	0.3
8	1.2	0.4	0.2	0.2	0.7	1.0	0.5	0.8	0.0	0.1	1.1	0.0
9	1.2	0.2	0.9	1.2	0.8	0.3	0.5	0.1	0.5	0.0	0.6	0.1
10	0.1	0.0	1.4	1.0	0.5	0.1	0.8	0.7	0.4	0.0	0.1	0.4
11	0.0	0.3	0.3	1.3	1.0	0.0	0.4	1.2	0.7	0.8	0.1	0.8
12	0.2	0.0	0.2	0.6	0.8	0.6	0.4	0.4	0.8	1.0	0.9	0.1
13	0.4	1.3	0.4	0.8	1.1	0.1	1.8	0.2	0.5	0.8	0.0	0.2
14	0.2	0.6	1.2	1.5	0.5	0.2	1.8	0.6	1.3	0.4	0.7	0.1
15	1.1	0.3	1.2	1.5	0.2	0.7	1.2	0.6	0.3	0.0	0.0	0.4
16	0.7	1.2	1.1	0.9	1.3	0.6	1.1	0.3	0.4	0.0	0.2	0.2
17	0.4	1.3	0.6	0.1	0.5	0.3	1.4	0.3	0.5	0.0	1.0	0.0
18	1.0	1.4	0.8	0.1	0.0	0.8	1.8	0.3	0.2	0.0	1.5	0.0
19	1.3	1.0	1.3	0.5	0.6	0.3	0.8	0.4	0.0	0.3	0.5	0.0
20	1.4	1.2	0.9	0.3	0.9	0.7	1.1	0.4	0.5	0.8	0.8	0.1
21	0.9	1.1	0.6	0.0	0.3	1.7	1.3	0.2	0.0	0.6	0.4	0.1
22	1.0	0.8	0.7	0.6	0.7	1.6	0.6	0.0	0.3	0.2	0.1	0.3
23	0.3	0.5	0.6	0.5	0.9	0.4	0.9	0.2	0.1	0.3	0.0	0.9
24	1.1	0.3	0.4	0.7	0.5	0.3	0.7	0.3	1.5	0.1	0.0	0.5
25	0.8	0.1	0.1	0.4	1.3	0.5	0.7	0.7	1.3	0.6	0.1	0.0
26	0.8	0.0	0.5	0.6	0.3	0.4	1.1	0.8	0.9	1.4	0.2	0.1
27	0.3	0.3	1.2	0.8	0.3	0.4	1.9	0.6	1.1	1.3	0.1	0.7
28	0.8	0.7	1.0	0.4	0.8	0.1	1.0	0.2	0.2	1.9	0.1	1.2
29	0.5		0.4	0.3	0.1	1.4	0.5	1.0	0.2	1.3	0.0	0.8
30	0.1		0.6	0.6	1.6	0.1	0.6	1.4	1.3	0.3	0.0	0.8
31	0.0		0.4		1.1		0.3	1.3		0.1		0.4
						1962						
1	0.2	0.0	0.4	0.6	0.6	0.7	0.6	1.5	1.3	1.5	0.5	0.4
2	0.5	0.1	0.4	0.7	0.6	0.2	0.5	0.8	1.3	1.1	0.9	0.0
3	0.0	0.1	0.7	0.8	0.4	0.3	0.5	0.8	1.5	0.7	0.8	0.2
4	0.0	1.4	0.3	0.7	0.0	1.0	1.2	0.4	1.3	0.6	1.0	1.2
5	0.0	0.4	1.1	0.4	0.2	0.8	1.0	0.5	1.0	0.8	0.1	0.3
6	0.0	0.4	1.4	1.3	1.2	0.7	0.8	1.0	1.0	0.8	1.2	0.1
7	0.2	1.1	0.3	1.6	0.4	0.8	0.5	1.1	0.8	0.8	0.8	0.1
8	0.1	0.1	0.0	1.4	0.2	0.1	0.7	1.3	0.8	1.5	0.5	0.3
9	0.4	0.1	0.0	0.8	0.0	1.2	0.3	1.1	0.7	1.3	0.3	0.3
10	1.8	0.0	0.8	1.4	0.2	1.0	0.5	0.7	0.5	1.2	0.1	0.4
11	0.7	0.9	0.8	1.1	0.6	0.3	0.6	0.0	0.5	1.1	0.8	1.4
12	0.1	1.0	1.1	0.5	0.1	0.4	0.5	0.1	1.6	0.4	0.1	0.8
13	0.1	0.9	0.3	0.2	0.8	0.2	0.6	0.3	1.2	0.7	0.0	1.1
14	0.9	0.9	0.3	0.1	0.8	0.3	0.7	0.7	0.6	1.3	0.6	0.8
15	0.6	0.9	0.6	0.7	0.8	0.8	0.3	1.1	0.9	0.5	1.3	0.4
16	0.6	1.5	0.1	0.5	0.4	0.3	0.1	1.1	0.7	1.1	1.2	0.1
17	0.1	0.8	0.1	0.3	0.1	0.0	0.1	1.2	0.3	0.3	0.4	1.5
18	0.1	0.4	0.6	0.7	0.0	0.1	0.2	1.1	0.2	0.8	0.1	1.5
19	1.1	0.0	1.0	0.4	0.6	0.2	0.8	1.0	1.5	1.4	0.2	1.5
20	0.1	0.0	0.8	0.7	0.3	0.2	1.0	0.2	0.7	0.6	0.1	1.5
21	0.5	0.4	1.0	1.3	0.0	0.7	0.8	0.4	0.7	0.7	1.2	1.3
22	0.0	0.8	0.2	1.3	0.0	0.6	0.4	1.4	1.0	1.1	1.4	0.6
23	0.0	0.6	0.2	0.7	0.0	1.0	0.6	1.0	0.7	1.0	1.0	0.0
24	0.0	0.6	0.2	0.2	0.0	0.4	1.0	1.1	0.1	1.3	0.9	0.2
25	0.2	0.5	0.5	0.8	0.0	0.3	1.0	0.9	0.4	1.4	0.9	0.1
26	0.4	1.2	0.1	0.9	0.1	0.4	1.6	0.4	1.4	1.3	0.2	1.2
27	0.6	1.0	0.1	0.5	0.8	1.1	1.4	0.1	0.4	1.3	0.5	0.5
28	0.0	0.0	0.2	0.4	0.4	1.2	1.1	0.2	0.6	0.9	0.2	0.4
29	0.2		0.3	0.3	0.3	0.8	0.7	1.1	1.1	0.7	0.7	0.2
30	0.4		0.0	0.2	0.1	0.9	0.2	1.0	0.8	0.7	1.2	0.2
31	0.0		0.1		1.1		0.9	1.2		0.7		0.9

(Continued)

Table 11-7. Daily values of magnetic character figure, C_i, 1957-1963. (Continued)

Day	Jan	Feb	Mar	Apr	May	June	July	Aug	Sept	Oct	Nov	Dec
						1963*						
1	0.2	0.8	0.8	0.5	1.5	0.6	0.2	1.1	0.8	0.0	0.6	0.2
2	0.0	0.1	0.2	0.2	1.3	0.7	0.2	0.9	0.5	0.1	0.9	0.9
3	0.0	0.2	0.6	1.1	1.0	0.4	0.0	0.5	0.6	0.2	0.8	1.4
4	0.5	0.3	0.0	1.1	1.2	0.2	0.8	0.8	0.3	0.3	0.3	1.2
5	0.1	0.1	0.2	1.4	0.6	0.0	1.0	0.8	0.6	0.6	0.0	1.3
6	0.0	0.0	0.2	1.2	0.6	1.1	1.1	0.7	0.5	0.2	1.0	1.2
7	0.5	0.1	0.9	0.8	0.4	1.5	0.8	0.6	0.2	0.7	1.5	0.8
8	0.0	0.0	1.4	0.4	0.9	0.8	0.8	0.3	0.8	0.8	1.5	0.8
9	0.0	0.9	1.1	0.3	1.0	0.6	0.8	0.6	0.9	0.4	1.4	0.3
10	0.0	1.6	1.6	0.0	1.0	0.4	0.6	0.5	0.5	0.7	1.2	0.0
11	0.5	1.1	1.1	0.2	1.1	0.4	0.2	0.2	1.1	1.2	1.0	0.0
12	0.4	1.1	0.6	0.6	0.8	0.1	0.2	0.2	0.7	1.5	0.8	0.1
13	1.4	1.4	0.6	0.7	1.3	0.3	0.1	0.0	0.7	1.3	0.2	0.3
14	1.4	1.0	0.0	1.1	0.9	0.2	0.2	0.0	1.8	1.3	0.2	0.7
15	1.1	0.4	0.0	0.9	0.3	0.6	0.2	0.6	1.4	0.9	0.1	0.3
16	1.2	0.3	0.0	0.3	0.2	0.1	0.3	0.3	1.3	0.8	0.0	0.3
17	1.0	0.1	0.5	0.3	0.5	0.8	1.0	0.7	1.4	0.2	1.0	0.1
18	0.9	0.2	0.6	0.9	0.3	1.1	0.8	1.2	0.9	0.2	0.0	0.0
19	1.0	0.0	0.6	0.8	0.4	0.7	0.2	1.2	1.2	0.2	0.0	0.3
20	0.3	0.7	0.3	0.6	0.4	0.9	0.4	1.5	0.8	0.8	0.1	1.2
21	0.1	0.4	0.1	0.1	0.4	0.4	1.2	1.2	1.5	0.5	0.0	0.8
22	0.2	0.5	0.1	0.7	0.1	0.1	0.8	0.6	1.9	0.1	0.5	0.8
23	0.6	0.3	0.8	0.4	0.1	0.1	1.1	1.0	1.7	0.3	0.4	0.9
24	0.7	0.0	0.2	0.1	0.0	0.3	1.3	0.7	1.0	1.7	1.2	0.6
25	0.5	0.2	0.1	0.1	0.7	1.1	0.7	0.6	1.6	0.8	0.7	0.0
26	0.0	0.3	0.1	0.3	0.4	1.3	0.8	0.6	1.2	0.4	0.0	0.1
27	0.0	0.0	0.0	0.7	0.5	0.9	0.9	1.0	1.3	0.3	0.1	0.1
28	0.0	0.3	0.2	0.2	1.0	0.7	0.3	1.3	1.6	0.5	0.2	0.7
29	0.4		0.2	0.1	1.0	0.6	0.2	0.9	1.0	1.6	0.5	1.0
30	1.4		0.1	1.2	0.7	0.8	1.3	0.8	0.7	1.3	1.0	0.3
31	1.5		0.4		0.8		1.1	1.0		0.3		0.1

* Preliminary values

Table 11-8. Daily values and monthly means of the ΔH_1 index for Huancayo, Peru, (—0°.6, 353°.8 geomagnetic latitude and longitude), 1933-1944.

Day	Jan	Feb	Mar	Apr	May	June	July	Aug	Sept	Oct	Nov	Dec
						1933						
1	15.9	13.9	13.1	10.2	18.2	7.9	4.8	4.3	10.2	10.5	8.5	8.4
2	11.6	11.0	12.9	9.9	12.4	5.9	5.1	6.5	12.4	10.0	15.5	11.1
3	8.3	9.7	13.5	11.8	11.1	6.1	6.5	9.0	11.6	10.0	15.2	12.9
4	13.3	9.4	11.0	10.1	10.2	8.4	5.9	5.6	10.0	13.7	13.2	11.1
5	7.7	7.3	9.5	8.3	11.8	6.4	5.9	18.6	7.7	17.6	11.0	9.3
6		7.7	5.6	9.5	10.6	8.5	6.4	11.6	10.5	12.2	14.5	8.8
7		9.1	9.2	9.5	9.4	6.7	9.2	6.4	6.7	18.0	10.1	9.0
8	10.3	1.6	9.8	8.7	7.3	11.4	8.8	9.3	9.5	14.3	14.0	8.0
9	10.9	9.2	10.3	11.1	7.5	8.2	10.4	7.2	17.4	16.2	7.1	12.2
10	7.7	10.7	11.7	10.3	10.7	7.0	8.1	7.7	13.1	15.9	7.3	12.5
11	6.1	13.1	8.3	10.6	6.5	6.0	9.1	6.9	9.8	13.4	10.5	6.6
12	10.9	14.9	8.2	10.6	9.0	6.9	7.3	7.9	9.7	11.6	8.2	8.4
13	14.5	14.1	9.7	11.2	10.5	11.9	7.4	10.9	10.7	13.5	4.8	11.1
14	10.2	14.3	11.7	11.8	11.6	10.5	5.7	9.2	11.1	11.3	6.0	5.9
15	15.3	12.7	12.6	15.3	8.5	5.8	5.6	6.7	11.2	9.6	7.2	8.0
16	12.3	10.1	9.7	12.1	9.0	6.9	7.6	9.4	12.1	10.2	6.7	7.7
17	13.8	9.9	8.5	11.0	9.0	5.4	8.8	12.5	8.7	9.3	6.4	8.5
18	10.0	8.5	17.0	12.5	14.1	6.5	9.8	10.7	13.2	9.0	12.3	10.2
19	8.6	12.0	16.4	10.1	7.7	6.1	5.5	14.8	11.0	9.8	10.5	9.0
20	12.4	14.8	12.1	9.2	8.3	9.9	8.2	9.5	13.5	10.1	12.2	12.0
21	7.8	14.0	11.5	13.7	5.2	7.2	7.6	11.5	12.6	9.6	10.2	10.9
22	13.8	11.5	10.9	14.4	8.5	9.0	5.5	10.1	11.0	12.1	8.6	10.4
23	13.5	11.3	12.9	9.8	6.2	7.2	10.2	10.8	12.2	14.7	6.9	9.4
24	8.8	12.5	13.3	12.5	7.2	7.6	11.7	11.4	9.7	14.0	5.5	6.1
25	12.0	15.0	14.0	10.5	8.2	11.5	8.8	8.2	10.8	8.3	6.3	9.0
26	12.8	14.9	11.2	11.7	7.7	6.5	8.1	10.5	12.6	7.6	6.0	7.0
27	18.8	12.9	12.9	8.5	9.0	7.8	9.4	7.7	11.5	7.2	7.5	9.9
28	13.9	12.7	9.7	10.9	7.7	7.5	6.1	9.3	11.3	8.9	8.9	7.9
29	13.1		10.9	8.5	7.7	6.7	4.5	9.7	13.1	9.3	10.1	9.1
30	15.9		11.8	17.5	11.3	4.9	3.2	7.5	10.8	10.0	7.9	10.3
31	14.4		12.5		12.6		4.2	8.6		8.4		8.8
Mean	11.9	11.7	11.4	11.1	9.5	7.6	7.3	9.4	11.2	11.5	9.3	9.3
					ANNUAL MEAN = 10.1							
						1934						
1	17.0	12.8	9.1	13.9	13.6	7.5	6.4	8.9	12.7	12.7	8.2	12.6
2	10.2	11.1	12.5	13.6	13.6	6.3	5.9	7.2	7.8	9.7	8.0	9.0
3	10.0	13.2	8.5	14.9	10.9	10.5	11.0	13.0	10.7	11.8	8.1	9.0
4	11.5	12.3	18.0	16.4	9.0	7.4	5.9	9.9	10.3	8.3	7.7	11.8
5	13.4	12.9	15.0	12.3	10.1	14.1	7.4	7.1	10.1	8.2	8.3	8.0
6	10.0	7.2	11.0	13.7	11.0	11.0	8.8	9.2	12.7	12.0	7.7	4.9
7	14.4	7.4	10.5	10.2	9.1	6.0	7.0	9.3	11.7	13.1	15.1	9.8
8	11.1	9.3	10.7	9.9	7.2	9.0	6.3	7.5	11.0	12.7	10.9	9.3
9	9.4	17.0	8.4	11.2	6.2	9.5	9.4	8.7	10.6	8.9	12.6	8.5
10	8.9	7.5	9.7	11.9	7.5	6.7	8.0	8.2	8.1	11.0	8.5	11.5
11	6.2	10.5	11.6	11.5	9.7	7.4	9.5	11.2	8.8	11.8	7.7	12.0
12	4.9	11.0	8.0	10.5	11.6	14.2	7.1	13.1	10.5	12.3	6.2	5.8
13	10.2	14.7	8.9	10.9	8.7	5.1	7.0	9.3	10.2	10.6	6.1	8.4
14	11.9	9.8	10.4	13.3	6.6	10.5	9.0	8.0	10.2	14.0	8.7	7.1
15	9.3	18.2	13.0	13.2	8.8	8.5	8.6	9.8	8.3	9.7	7.0	9.3
16	16.9	17.8	16.5	13.1	7.8	8.0	9.0	7.5	9.6	9.9	6.9	4.4
17	12.7	13.7	12.4	10.5	8.8	6.5	7.2	12.0	15.7	7.8	6.5	8.0
18	13.3	13.8	12.3	11.1	11.4	10.8	9.4	10.3	7.7	8.1	7.7	4.9
19	10.4	9.4	11.6	9.7	11.7	6.9	4.5	11.0	10.7	10.7	7.7	9.7
20	10.7	9.9	10.7	9.5	10.5	7.6	7.9	6.6	9.7	12.8	7.2	9.3
21	11.4	8.5	9.5	9.1	11.5	6.2	5.4	7.0	9.8	12.4	7.0	14.5
22	14.9	6.8	13.2	7.5	8.7	6.4	7.3	8.8	9.5	13.8	8.9	11.3
23	8.8	6.7	12.2	8.4	9.9	8.4	5.0	7.8	8.5	11.9	12.2	14.5
24	9.4	7.0	10.8	10.7	9.1	5.2	7.1	11.6	12.4	14.5	16.2	15.5
25	9.3	7.7	17.5	9.4	8.4	10.9	6.6	11.2	14.4	13.5	6.2	20.2
26	9.7	6.9	8.9	6.6	7.5	7.1	8.8	12.2	14.0	11.5	9.1	15.6
27	6.0	9.2	12.4	9.9	8.7	6.4	11.0	13.7	13.5	7.9	12.7	11.7
28	10.2	10.7	14.7	8.5	9.5	6.5	10.2	10.9	9.8	8.5	13.9	8.7
29	9.5		12.5	11.2	9.1	7.2	9.0	11.8	10.2	8.4	13.2	26.0
30	10.0		12.7	12.4	8.7	4.4	14.8	8.4	12.2	6.6	9.0	7.5
31	17.0		12.3		6.3		9.1	9.4		8.8		12.3
Mean	10.9	10.8	11.8	11.2	9.4	8.1	8.0	9.7	10.7	10.8	9.2	10.7
					ANNUAL MEAN = 10.1							

(*Continued*)

Table 11-8. Daily values and monthly means of the ΔH_1 index for Huancayo, Peru, (−0°.6, 353°.8 geomagnetic latitude and longitude), 1933-1944. (Continued)

Day	Jan	Feb	Mar	Apr	May	June	July	Aug	Sept	Oct	Nov	Dec
						1935						
1	11.7		11.4	8.1	17.0	6.7	8.9	15.1	10.0	14.8	14.5	19.1
2	7.3	12.3	9.5	10.9	12.2	5.1	7.9	9.4	9.8	15.1	14.3	15.4
3	8.9	11.5	8.3	10.7	10.8	8.4	5.5	6.9	7.6	14.5	9.1	13.5
4	12.7	10.7	10.2	14.9	10.7	6.7	4.7	11.7	14.1	13.0	7.6	13.5
5	11.7	12.1	8.7	12.1	9.9	8.7	5.2	9.0	14.2	12.2	11.6	11.7
6	12.2	11.5	11.1	11.2	10.7	8.1	9.1	8.6	13.0	12.0	11.9	10.2
7	10.6	12.7	11.3	9.7	9.1	14.3	8.0	10.0	11.6	16.6	9.2	7.7
8	11.5	13.3	9.4	12.4	9.1	13.9	12.5	9.2	9.3	11.9	8.1	12.8
9	11.1	11.0	10.2	12.3	8.8	17.0	6.8	12.0	12.2	7.3	11.7	10.5
10	7.2	11.7	8.5	16.2	14.0	6.8	9.0	9.5	12.0	11.5	9.7	16.8
11	10.1	13.1	8.0	15.4	10.5	9.7	6.5	5.1	25.8	12.5	15.9	9.7
12	9.9	10.5	11.3	10.5	10.2	6.2	8.6	7.4	14.8	12.2	20.8	15.7
13	8.2	17.4	18.8	12.0	10.8	8.2	7.2	7.2	11.1	12.6	17.1	16.5
14	8.8	15.7	16.2	9.5	9.7	8.2	10.7	8.5	12.7	15.9	15.9	20.3
15	11.7	15.1	13.2	9.5	10.7	5.9	8.0	10.2	9.1	16.8	10.6	16.6
16	8.2	12.2	13.9	13.0	12.6	5.3	9.8	12.7	13.0	12.6	9.7	13.0
17	11.5	13.7	10.9	10.4	9.4	10.9	9.7	13.9	17.1	16.7	9.2	12.7
18	11.0	14.4	12.7	13.0	11.0	13.3	11.4	14.9	14.8	16.4	13.7	10.5
19	11.1	6.0	12.0	11.8	11.3	12.1	15.2	14.4	16.4	12.2	13.5	8.3
20	13.0	14.4	11.1	9.8	13.2	10.0	14.2	13.9	11.3	15.7	10.9	9.7
21	13.4	13.5	16.8	11.7	10.6	7.2	13.5	10.6	9.6	14.5	9.0	8.2
22	11.9	11.9	14.9	11.0	9.7	7.2	16.2	8.6	10.5	10.4	7.1	7.7
23	16.2	14.4	13.8	12.5	8.9	7.4	13.0	10.5	17.2	11.6	11.2	9.2
24	13.9	14.5	13.0	12.1	6.2	7.1	12.7	9.0	12.3	17.6	10.7	10.2
25	13.6	10.0	10.5	7.0	9.0	7.3	17.3	10.5	16.2	15.6	11.4	15.3
26	12.5	10.8	11.5	7.2	8.6	8.3	7.0	9.4	14.7	12.6	10.6	15.2
27	21.7	6.3	9.9	7.2	8.2	9.7	10.1	12.9	15.5	12.4	20.6	18.6
28	17.4	6.6	9.9	6.1	7.1	8.8	9.5	10.1	13.3	13.2	13.4	19.1
29	9.6		10.4	7.4	8.2	11.4	8.2	11.2	13.7	12.0	16.0	20.0
30			13.5	10.2	5.6	9.5	8.1	11.7	15.5	8.3	18.0	21.5
31			7.9				8.5	11.3		14.3		
Mean	11.7	12.1	11.6	10.9	10.1	9.0	9.8	10.5	10.3	13.4	12.4	14.0
						ANNUAL MEAN = 11.6						
						1936						
1	22.5	11.5	13.6	18.4	12.0	12.8	13.1	12.7	12.0	19.8	18.7	15.2
2	16.4	15.2	8.5	13.0	13.1	18.1	18.2	10.8	15.6	16.1	20.7	15.0
3	16.9	9.9	9.7	15.7	10.5	14.0	11.5	8.0	16.2	16.5	19.8	17.5
4	8.7	13.5	11.2	12.3	16.7	9.8	10.0	10.2	17.3	18.9	17.0	23.2
5	7.5	8.5	11.2	13.2	9.2	8.8	13.5	11.5	15.6	19.2	17.1	17.1
6	6.9	12.7	15.7	16.8	10.4	9.7	10.5	14.0	13.5	20.5	16.9	13.0
7	7.9	9.4	10.0	15.6	13.4	7.5	13.7	6.9	12.2	20.3	10.5	12.4
8	12.0	12.6	14.7	19.1	14.7	15.1	8.7	11.2	13.5	14.2	14.2	14.8
9	12.2	15.8	13.5	11.7	13.5	23.2	8.4	11.0	12.0	13.0	11.8	12.5
10	13.5	17.7	14.3	11.6	22.7	13.3	17.2	11.3	11.1	16.0	15.5	10.6
11	16.2	16.5	17.5	15.7	15.2	11.5	18.8	6.0	8.7	11.8	13.2	8.0
12	16.2	15.0	18.8	19.7	16.8	8.7	8.8	9.5	12.5	12.4	14.5	11.5
13	14.0	12.5	20.0	19.0	11.1	13.5	12.4	9.3	16.6	14.5	17.4	9.9
14	17.5	20.5	14.7	17.9	12.4	11.1	12.0	8.9	13.7	12.2	15.3	12.1
15	12.5	19.1	14.2	17.9	13.1	15.0	9.3	12.2	13.0	18.0	18.4	10.9
16	8.1	15.9	11.3	12.5	11.9	12.0	12.1	11.3	15.7	26.7	15.7	10.5
17	13.7	14.6	15.2	14.3	11.2	9.5	11.8	10.0	15.0	18.8	16.7	10.2
18	15.5	12.9	18.6	22.2	12.3	13.7	13.6	7.2	19.7	19.7	17.6	11.5
19	13.6	17.5	15.0	20.2	15.2	22.2	8.9	10.5	15.7	19.2	16.3	16.1
20	10.8	13.4	14.7	19.0	13.7	11.9	9.4	10.3	16.5	19.4	10.7	14.2
21	12.0	15.6	14.8	19.0	13.7	10.9	9.6	13.4	14.7	13.2	11.5	15.5
22	13.8	13.2	14.3	21.8	11.6	9.6	4.7	14.0	15.2	16.3	9.1	13.1
23	15.6	16.2	22.7	19.6	10.7	11.0	9.4	9.1	14.2	16.7	10.6	13.5
24	22.9	16.3	17.5	17.1	12.7	12.4	6.0	10.7	12.2	20.7	10.5	7.0
25	15.3	17.7	19.5	14.2	13.2	10.0	9.3	15.0	14.4	13.4	11.7	13.1
26	19.8	16.4	20.9	14.8	12.9	15.1	9.6	9.7	11.8	14.7	15.9	18.2
27	16.3	16.0	16.8	12.5	10.0	6.8	9.0	13.8	14.2	11.9	11.2	20.7
28	14.7	17.7	13.1	11.5	10.0	9.8	9.5	12.9	18.7	13.9	15.7	21.7
29	17.7	14.3	13.9	10.5	14.3	10.0	16.1	12.0	20.3	14.9	28.6	20.5
30	16.9		13.7	10.2	10.0	9.2	12.4	20.6	17.8	13.2	17.5	29.5
31	17.1		13.0		9.7		10.9	10.6		23.4		23.7
Mean	14.3	14.8	14.9	15.9	12.8	12.2	11.2	11.1	14.7	16.8	15.3	14.8
						ANNUAL MEAN = 14.1						

(Continued)

Table 11-8. Daily values and monthly means of the ΔH_1 index for Huancayo, Peru, (−0°.6, 353°.8 geomagnetic latitude and longitude), 1933-1944. (Continued)

Day	Jan	Feb	Mar	Apr	May	June	July	Aug	Sept	Oct	Nov	Dec
						1937						
1	23.3	24.1	27.7	20.0	17.3	11.8	10.6	10.0	12.8	22.5	14.9	14.7
2	22.5	25.0	19.0	25.3	12.8	12.3	8.0	20.0	13.4	19.5	19.4	15.9
3	18.9	47.7	16.7	24.2	10.7	8.5	11.8	16.1	17.8	17.0	15.0	14.0
4	16.4	21.7	16.1	12.0	13.8	10.8	9.8	14.7	15.0	31.8	15.1	12.8
5	18.1	19.1	29.5	12.5	18.7	14.6	13.2	15.3	19.3	22.7	16.7	11.2
6	15.7	15.2	17.5	15.8	12.5	12.8	11.3	11.7	18.7	27.0	15.6	12.7
7	23.4	8.2	15.7	10.5	10.5	10.2	14.1	18.1	17.8	24.5	21.5	20.2
8	14.0	11.2	13.4	13.9	11.5	14.1	11.7	14.8	19.5	28.8	18.7	14.1
9	19.7	17.3	17.5	12.2	12.8	10.5	17.9	16.5	12.1	33.0	13.8	15.3
10	17.5	11.4	15.6	12.8	14.0	14.9	16.6	17.2	20.5	23.4	12.5	13.4
11	15.4	19.3	15.3	19.1	15.5	12.5	15.5	13.5	18.0	28.9	13.6	14.0
12	16.7	19.5	14.9	18.5	15.5	11.7	10.0	17.5	16.0	23.7	10.0	10.7
13	22.4	21.5	22.1	17.2	14.7	19.5	13.7	19.2	17.7	16.0	12.2	10.6
14	16.2	22.0	22.2	15.1	17.1	14.6	13.8	18.3	15.6	15.7	6.7	12.0
15	16.2	15.5	23.2	14.8	15.0	12.3	14.1	15.1	14.0	14.5	10.0	7.0
16	17.6	19.7	17.2	15.5	15.2	14.7	13.2	11.5	15.4	14.7	9.7	13.0
17	15.8	23.2	16.6	11.7	12.2	17.2	13.8	13.2	16.7	15.5	16.7	15.2
18	16.3	16.9	17.3	15.3	13.3	14.1	9.6	13.1	18.9	14.9	21.5	22.6
19	17.4	20.9	19.0	13.2	14.8	11.4	19.1	14.0	16.3	14.9	16.5	21.6
20	17.3	15.5	13.5	10.5	10.3	16.6	14.7	13.3	15.9	13.5	19.2	20.3
21	22.0	16.2	14.6	14.3	16.7	16.3	14.2	16.5	18.1	11.6	19.3	21.1
22	14.4	17.3	20.6	13.0	12.5	15.3	13.5	25.7	14.0	17.8	22.2	20.6
23	13.6	15.9	14.7	12.9	14.5	15.2	16.2	12.7	18.7	22.4	18.4	21.7
24	10.0	22.6	18.1	27.1	12.5	11.9	24.2	10.8	20.6	19.4	22.6	20.8
25	15.8	21.6	17.4	32.0	19.8	14.6	16.8	16.3	16.5	16.8	17.9	14.7
26	14.2	21.6	19.4	34.9	16.4	11.5	14.3	20.7	18.7	17.6	14.7	16.2
27	18.7	22.2	24.0	26.3	18.7	18.7	9.6	18.0	15.3	15.7	12.2	11.9
28	16.1	20.2	19.1	17.9	15.7	12.9	12.4	19.9	15.0	15.5	14.5	12.7
29	22.6		16.0	15.1	15.7	8.9	11.6	16.0	15.2	12.6	21.8	12.2
30	30.5		20.3	15.1	15.0	13.3	12.2	9.1	37.1	13.7	14.6	12.0
31	23.7		23.1		12.5		13.0	11.9		13.2		12.8
Mean	18.1	19.7	18.6	17.3	14.5	13.5	13.6	15.5	17.4	19.3	15.9	15.1
					ANNUAL MEAN = 16.5							
						1938						
1	13.0	13.0	15.7	19.8	15.6	9.8	20.5	12.7	13.8	25.5	14.4	10.5
2	12.9	16.3	13.4	16.6	15.7	15.8	12.8	16.5	14.3	20.5	14.5	12.7
3	15.4	22.1	16.1	15.2	19.0	10.1	12.3	20.8	15.1	21.4	13.2	17.8
4	20.3	15.0	17.1	17.5	29.2	9.9	22.9	22.2	15.4	15.5	15.7	12.5
5	17.0	14.1	20.6	16.5	14.7	10.0	11.7	18.2	14.6	16.5	15.0	14.8
6	18.4	33.1	18.8	22.0	17.3	9.0	13.1	10.7	11.3	21.2	15.6	8.8
7	17.1	16.4	11.1	20.8	11.7	9.0	12.4	16.4	19.2	18.0	14.0	12.7
8	19.9	32.2	12.5	14.3	15.5	13.7	10.6	14.9	17.8	26.0	17.3	22.0
9	13.1	23.7	9.9	13.9	13.6	9.2	13.6	14.0	15.1	17.4	17.1	23.4
10	10.5	15.6	8.5	10.9	11.9	12.8	17.7	14.2	14.3	15.4	16.9	31.2
11	14.7	18.4	12.9	17.2	34.7	14.2	9.5	18.4	15.0	18.7	17.6	17.5
12	18.5	13.3	19.0	18.0	19.2	17.2	12.1	10.4	9.4	19.7	15.6	14.4
13	23.5	19.0	12.6	21.6	14.0	18.0	10.2	12.6	19.9	19.2	18.0	15.6
14	12.0	16.7	16.9	21.5	21.5	10.5	14.8	11.8	24.6	16.2	18.2	14.1
15	15.4	16.4	18.5	15.7	22.2	11.3	21.0	10.6	23.0	16.7	13.0	14.1
16	21.9	13.2	16.5	57.3	17.3	9.0	17.7	9.7	20.1	14.7	11.1	25.5
17	38.7	16.7	21.8	18.3	15.0	9.2	14.1	11.7	12.7	14.1	20.0	22.0
18	23.1	15.5	17.5	22.0	13.1	9.2	10.1	11.2	15.2	13.5	15.5	25.1
19	28.2	15.4	19.7	21.7	11.0	12.2	11.7	13.2	11.4	14.0	14.8	14.0
20	25.6	15.3	19.5	18.4	12.6	9.9	13.8	11.2	16.8	14.3	12.5	18.2
21	21.9	16.8	16.6	16.1	11.2	10.1	13.1	15.2	16.6	15.9	15.0	9.0
22	40.1	11.2	27.0	21.7	12.3	12.7	9.5	22.6	16.4	17.6	14.0	23.3
23	22.4	15.3	22.5	15.8	9.4	11.7	13.7	16.3	19.1	18.8	14.0	14.0
24	22.0	9.3	20.4	15.3	17.9	11.0	11.2	14.6	16.9	14.4	20.0	21.4
25	47.8	16.1	16.7	15.6	10.7	8.9	14.8	12.5	19.6	21.7	15.9	16.5
26	28.0	11.5	15.3	14.0	9.2	11.7	8.5	17.0	24.7	21.2	15.5	27.3
27	12.8	9.4	11.2	13.6	9.9	10.6	9.5	11.8	23.1	21.8	13.8	18.0
28	8.4	17.0	12.2	14.7	18.4	12.9	11.5	15.6	31.8	17.9	12.2	15.8
29	9.5		20.2	14.8	17.3	10.8	13.5	18.9	21.5	16.5	15.3	13.7
30	13.9		15.9	13.5	10.5	12.8	19.2	14.4	25.1	18.8	10.0	16.4
31	28.2		18.1		15.2		15.2	11.8		14.2		9.0
Mean	20.5	16.7	16.6	18.5	15.7	11.4	13.6	14.6	17.8	18.0	15.2	17.1
					ANNUAL MEAN = 16.3							

(Continued)

Table 11-8. Daily values and monthly means of the ΔH_1 index for Huancayo, Peru, (—0°.6, 353°.8 geomagnetic latitude and longitude), 1933-1944. (Continued)

Day	Jan	Feb	Mar	Apr	May	June	July	Aug	Sept	Oct	Nov	Dec
						1939						
1	11.4	20.2	21.1	15.2	16.1	16.4	14.0	15.1	11.5	23.3	14.1	12.9
2	13.2	15.0	17.8	11.7	26.5	15.7	11.6	12.8	16.1	23.3	13.6	11.5
3	13.0	13.1	15.9	16.1	17.2	13.0	16.1	11.7	26.4	34.1	12.8	10.0
4	9.5	14.5	22.4	20.9	17.8	15.3	19.9	14.4	15.3	25.0	9.9	11.8
5	14.1	16.1	17.3	16.9	21.5	14.1	22.9	11.6	14.1	21.6	11.0	8.0
6	16.3	19.3	14.0	13.8	23.1	10.8	13.3	14.5	17.1	20.8	8.3	14.0
7	18.2	19.5	15.5	17.9	20.3	10.8	11.7	15.3	13.7	21.2	14.0	17.9
8	23.8	23.2	17.2	16.0	18.7	9.5	11.5	16.7	14.2	18.8	9.3	13.4
9	24.4	23.6	15.1	15.0	15.2	9.5	11.8	14.4	14.0	14.9	11.3	11.6
10	22.4	19.0	17.3	16.5	15.1	11.5	10.0	19.9	15.3	13.8	12.5	10.8
11	21.7	19.0	17.8	18.3	10.3	9.9	17.6	15.7	15.3	13.5	14.6	13.6
12	17.3	11.4	14.2	11.8	10.1	12.3	10.7	27.9	13.5	15.7	16.0	18.3
13	24.1	11.1	12.2	12.5	12.8	15.8	9.7	17.5	16.5	35.8	15.8	11.7
14	22.8	9.2	13.3	14.0	9.3	16.9	18.2	17.3	12.7	22.5	14.7	14.4
15	14.6	11.8	13.0	12.3	11.4	13.5	12.6	14.3	18.1	19.4	11.4	12.7
16	16.3	13.9	14.3	14.7	15.0	12.2	16.8	23.6	18.4	23.5	12.0	13.2
17	12.8	10.9	10.2	37.3	13.9	10.6	17.0	13.2	26.1	13.9	15.6	10.0
18	11.6	17.1	10.5	18.0	14.1	15.3	13.8	17.8	14.5	16.6	10.8	8.6
19	16.0	14.7	10.6	14.2	16.9	15.5	16.5	17.4	19.7	19.1	12.5	9.5
20	16.6	17.3	16.1	21.7	16.2	11.1	16.2	7.7	18.2	14.8	9.8	9.0
21	23.0	14.5	17.9	28.6	15.7	12.9	19.3	10.8	16.4	14.3	7.3	15.5
22	16.4	16.3	18.9	18.7	18.6	11.2	16.8	29.4	19.3	16.5	8.3	13.1
23	17.5	16.3	15.5	26.1	18.7	15.0	13.4	18.3	12.0	12.0	8.4	12.8
24	18.9	31.8	14.0	40.1	14.5	10.9	12.8	13.4	12.8	13.0	16.3	10.2
25	19.3	28.4	17.2	21.9	15.7	11.1	11.3	12.3	20.4	14.8	18.5	6.8
26	17.1	17.4	18.5	16.3	13.8	14.3	15.5	14.6	18.6	14.4	11.8	10.4
27	15.4	14.9	23.5	16.1	17.3	12.5	10.4	14.0	21.0	17.0	11.5	16.9
28	17.7	17.1	21.7	16.6	15.8	13.4	13.6	15.8	16.4	17.8	11.8	22.7
29	16.6		18.8	19.1	21.3	13.5	14.5	12.8	18.9	15.1	10.2	17.3
30	12.5		15.4	14.0	11.5	15.9	14.2	12.6	22.2	15.3	13.3	16.8
31	12.4		14.9		15.0		11.0	16.0		13.4		17.8
Mean	17.0	21.4	16.2	18.4	16.1	13.1	14.3	15.8	17.0	18.6	12.2	13.0
					ANNUAL MEAN = 15.7							
						1940						
1	18.8	17.9	13.1	20.7	11.0	8.4	9.8	14.5	14.5	21.0	14.6	11.9
2	14.8	13.0	10.6	16.5	15.4	11.2	6.3	11.0	16.0	17.7	15.8	13.5
3	27.5	10.5	10.3	23.0	11.0	8.8	11.5	16.8	19.3	17.8	12.8	11.7
4	16.6	14.3	13.5	17.0	10.3	10.3	11.7	14.1	19.9	17.9	17.5	11.6
5	11.5	12.7	12.2	16.9	10.9	11.2	10.8	14.0	15.3	16.5	13.9	11.5
6	7.5	15.2	13.8	13.3	12.5	18.8	11.9	16.0	15.3	16.7	12.5	14.4
7	12.2	11.2	11.4	12.6	12.0	11.2	9.3	10.8	14.8	15.4	10.1	.90
8	15.4	17.9	13.0	13.8	9.8	14.7	7.3	15.7	11.5	19.4	7.3	11.2
9	20.4	12.4	12.8	13.0	12.5	12.3	12.6	21.5	14.0	14.6	11.9	13.4
10	25.2	19.3	16.0	13.9	11.0	8.8	11.5	13.0	10.8	15.7	9.0	17.7
11	24.5	14.6	17.8	14.9	9.1	7.8	12.0	10.0	10.5	16.4	12.8	10.3
12	20.3	14.6	19.8	13.1	14.7	10.8	8.2	10.4	9.5	16.3	21.6	9.1
13	17.8	16.0	14.7	12.6	14.1	7.5	19.0	8.6	10.4	14.8	22.0	10.2
14	18.2	12.0	13.7	16.7	11.1	17.8	9.9	12.2	13.1	14.1	18.7	11.7
15	13.1	12.3	14.5	14.6	11.5	14.7	9.5	12.5	15.1	17.0	13.0	11.3
16	14.6	12.8	12.1	15.5	7.6	11.0	11.8	12.3	14.0	16.4	15.5	14.0
17	16.1	13.3	12.6	11.9	13.8	11.3	9.3	13.3	15.4	16.1	19.5	7.5
18	19.1	9.6	12.1	12.7	17.4	11.1	7.9	15.9	14.5	18.3	10.8	13.7
19	12.1	10.3	19.1	14.9	13.3	9.9	8.3	15.5	14.7	13.5	12.7	10.8
20	11.0	12.7	18.3	15.8	12.3	12.0	9.6	11.9	19.9	15.5	15.4	11.7
21	10.8	12.8	12.0	14.7	8.5	9.8	13.3	12.8	14.0	17.5	15.2	12.5
22	11.3	9.7	13.3	15.6	12.7	8.6	12.1	14.1	13.3	13.3	20.1	14.2
23	10.1	10.7	24.3	14.1	15.1	9.8	9.4	12.0	10.1	14.0	15.4	9.0
24	16.3	12.9	54.0	12.7	19.5	11.3	12.0	15.4	12.3	15.7	12.7	6.8
25	14.9	19.5	39.3	24.5	12.6	29.1	12.5	10.5	17.2	17.5	24.9	9.4
26	16.0	12.5	26.5	19.6	14.8	12.0	8.4	12.1	28.4	16.9	11.3	10.1
27	16.6	13.0	30.8	13.7	10.0	11.5	10.6	12.9	18.4	10.0	7.9	6.2
28	14.3	12.5	18.5	10.8	11.0	9.0	8.9	12.9	14.2	10.6	9.2	12.0
29	14.4	12.4	57.8	11.9	12.0	11.1	8.1	14.5	11.8	11.0	15.7	16.5
30	21.8		32.1	12.7	12.3	9.2	12.0	11.9	13.5	14.9	11.9	19.6
31	12.0		36.7		9.4		11.4	14.9		16.5		20.5
Mean	16.0	13.3	20.2	15.1	12.2	11.7	10.5	13.4	14.7	15.7	14.4	12.1
						ANNUAL MEAN = 14.1						

(Continued)

Table 11-8. Daily values and monthly means of the ΔH_1 index for Huancayo, Peru, (−0°.6, 353°.8 geomagnetic latitude and longitude), 1933-1944. (Continued)

Day	Jan	Feb	Mar	Apr	May	June	July	Aug	Sept	Oct	Nov	Dec
						1941						
1	13.3	16.6	95.7	13.5	13.1	7.9	11.9	10.0	17.2	13.0	23.7	24.8
2	12.7	21.8	22.8	13.5	10.5	8.5	7.6	11.5	9.9	11.0	11.7	9.9
3	14.0	18.6	19.4	12.1	9.0	7.9	11.2	10.0	12.1	11.7	11.4	17.9
4	12.6	10.9	18.4	13.9	13.0	9.7	16.2	24.6	12.5	15.4	10.8	13.4
5	11.1	11.2	16.5	12.0	9.7	10.1	50.4	11.4	9.9	14.9	15.2	16.5
6	20.2	14.2	14.1	12.3	9.6	6.4	12.2	12.8	9.9	13.5	14.0	15.1
7	14.7	10.0	12.9	13.5	10.3	6.3	13.8	16.4	12.0	13.1	14.0	12.9
8	13.5	9.4	12.0	10.0	14.3	6.2	10.5	12.0	14.8	17.7	10.9	11.3
9	11.7	10.0	16.6	9.1	11.8	9.6	11.7	11.6	10.6	16.3	8.8	13.5
10	8.1	10.9	11.1	16.0	11.3	15.5	13.4	10.5	9.5	18.8	13.9	12.0
11	9.2	16.6	17.6	12.7	12.8	12.7	11.7	9.5	11.2	27.7	11.5	6.1
12	12.7	12.3	12.8	14.4	14.8	11.1	8.8	8.0	11.0	18.5	7.6	8.9
13	17.1	17.0	13.7	12.4	13.6	17.7	7.8	10.5	17.7	14.1	6.3	9.1
14	13.2	16.5	21.3	12.3	11.2	12.3	8.3	13.5	13.3	14.9	6.5	14.2
15	17.5		17.2	14.8	12.0	13.2	9.5	5.8	15.8	12.7	6.2	9.6
16	12.8	17.1	18.4	16.6	11.7	8.1	13.6	11.4	13.2	12.7	9.2	14.5
17	23.3	15.5	17.1	14.4	10.5	11.4	11.4	8.7	11.2	10.0	14.5	16.2
18	18.1	11.3	16.7	11.7	11.2	13.3	11.0	9.3	45.9	9.6	15.5	15.5
19	16.3	10.6	17.8	13.7	8.3	8.8	7.7	13.1	32.2	12.6	19.1	12.4
20	14.6	11.3	13.7	11.0	7.4	11.0	12.3	7.5	17.7	12.8	13.6	11.3
21	14.2	11.9	17.2	10.4	17.9	9.7	18.2	13.2	17.6	14.5	16.8	9.4
22	14.2	15.7	15.0	11.5	15.4	11.3	12.7	11.7	16.2	23.4	15.2	12.8
23	10.9	16.1	13.7	10.0	11.1	6.7	13.6	11.4	14.0	12.8	13.7	14.6
24	11.3	13.8	11.5	16.1	11.0	11.9	13.6	12.6	20.9	14.0	13.2	11.8
25	11.7	13.2	11.3	22.2	9.2	11.6	9.1	10.2	15.0	16.7	14.5	11.2
26	14.2	13.7	15.0	10.7	11.0	11.9	11.5	14.4	14.4	21.9	9.0	9.1
27	10.8	21.8	12.1	11.2	7.9	12.4	10.7	21.3	13.9	11.9	11.7	12.5
28	14.5	15.7	19.6	19.0	9.3	12.0	12.2	22.1	15.4	8.5	24.6	8.1
29	13.3		17.4	13.2	8.8	12.7	11.5	14.5	10.2	10.5	9.0	11.2
30	13.7		26.2	12.7	7.4	9.0	10.6	14.5	12.7	9.2	6.5	6.6
31	12.7		25.9		9.5		10.4	12.1		19.3		8.6
Mean	13.8	14.2	19.0	13.2	11.1	10.6	12.7	12.5	15.3	14.6	12.6	12.3
					ANNUAL MEAN = 13.5							
						1942						
1	9.2	11.5	31.7	14.7	15.2	10.4	12.5	9.5	8.0	12.4	8.0	8.3
2	11.9	13.3	15.0	13.3	15.3	8.3	8.0	10.5	12.4	15.2	12.3	6.5
3	15.3	10.8	15.0	15.2	15.1	8.7	8.0	10.5	12.5	12.9	6.7	8.8
4	19.7	12.2	15.3	20.6	16.5	7.1	6.7	9.4	11.8	10.7	9.7	8.5
5	16.9	12.8	24.3	12.2	10.5	8.5	8.1	6.5	10.8	11.0	11.5	7.0
6	14.5	21.8	17.9	9.8	10.6	7.4	7.0	10.4	11.9	9.4	7.5	10.6
7	8.2	16.7	15.6	9.0	8.2	5.6	9.0	13.5	10.0	10.2	8.8	10.2
8	13.1	18.4	18.2	16.7	12.6	6.9	12.3	7.9	7.7	12.7	14.2	11.7
9	11.9	16.1	16.9	9.2	7.7	5.7	8.7	8.0	11.1	13.9	13.8	13.6
10	15.5	14.2	14.5	10.9	8.8	5.6	8.1	16.3	10.8	15.9	14.5	10.0
11	18.2	13.9	10.3	13.0	9.7	8.6	11.5	8.6	13.2	17.5	10.7	8.5
12	15.1	9.3	11.5	9.0	12.3	8.5	9.5	9.7	19.7	18.8	8.8	9.8
13	15.7	8.6	16.5	13.8	12.2	12.4	9.0	9.1	17.2	15.9	9.5	7.0
14	11.4	7.1	9.7	18.7	14.0	10.8	10.5	8.5	18.0	15.8	10.2	8.1
15	8.5	13.2	10.6	11.8	13.8	9.1	12.4	12.5	12.3	16.3	8.4	8.2
16	12.2	9.7	12.3	16.4	12.8	8.7	11.7	15.4	12.7	14.6	5.8	6.9
17	17.7	16.4	16.5	22.0	10.9	9.3	7.6	8.7	15.0	14.2	6.3	7.9
18	17.5	16.6	17.8	13.2	10.2	9.1	7.6	15.6	11.6	12.5	8.5	7.1
19	17.1	15.3	20.7	19.2	13.9	13.2	5.5	11.8	13.1	11.3	8.1	6.4
20	14.9	16.4	18.7	15.4	15.5	7.5	13.5	12.6	9.5	9.9	10.5	11.5
21	20.8	16.3	20.3	10.7	12.0	6.5	10.3	9.6	11.2	12.7	11.0	14.0
22	10.6	11.5	17.0	9.1	9.0	5.5	6.9	11.9	16.3	14.0	6.6	12.5
23	12.5	20.4	14.6	22.0	9.1	7.7	7.7	19.1	11.5	10.6	17.3	6.7
24	10.4	16.3	13.0	13.7	9.6	8.0	8.2	12.6	14.0	9.3	10.8	8.0
25	13.6	17.7	13.7	10.0	7.8	8.6	12.3	10.5	13.7	9.1	12.7	10.9
26	9.5	14.1	18.7	9.3	7.8	5.4	9.8	8.4	8.6	11.4	14.5	13.0
27	7.4	14.1	13.3	13.2	13.7	8.2	15.2	13.0	11.7	14.1	12.8	11.2
28	7.6	27.2	10.7	16.3	7.2	7.5	14.0	9.8	14.2	19.2	16.0	9.5
29	11.1		14.9	12.3	8.4	7.9	13.4	8.8	14.7	22.8	10.7	10.0
30	12.5		12.9	9.3	7.2	9.4	16.4	14.2	15.5	12.4	9.2	4.3
31	8.9		12.8		8.3		11.7	6.8		9.2		7.5
Mean	13.2	14.7	15.8	13.7	11.2	8.2	10.1	11.0	12.7	13.4	10.5	9.1
					ANNUAL MEAN = 12.0							

(Continued)

Table 11-8. Daily values and monthly means of the ΔH_1 index for Huancayo, Peru, (—0°.6, 353°.8 geomagnetic latitude and longitude), 1933-1944. (Continued)

Day	Jan	Feb	Mar	Apr	May	June	July	Aug	Sept	Oct	Nov	Dec
						1943						
1	11.4	6.4	10.0	12.9	11.7	9.2	6.3	12.4	14.2	18.8	10.8	15.0
2	7.9	7.6	14.2	9.5	11.4	8.4	6.6	12.2	12.4	18.2	10.6	16.2
3	11.7	9.7	12.1	15.7	10.1	9.7	12.8	17.2	11.4	23.5	11.0	10.9
4	13.2	10.5	12.3	13.3	12.7	11.3	16.4	10.5	13.2	14.2	9.4	7.9
5	9.6	11.7	13.2	19.6	11.7	12.8	14.2	12.8	12.9	15.3	12.3	5.4
6	12.7	15.0	10.4	13.7	11.0	14.7	12.8	11.2	8.4	12.8	11.4	5.4
7	8.4	14.6	10.5	9.6	10.6	11.6	9.1	13.6	9.7	14.4	9.4	5.3
8	8.0	16.2	11.5	13.2	7.8	12.1	12.0	14.5	12.2	18.0	9.6	6.9
9	8.8	15.5	13.6	11.6	5.8	11.8	12.6	11.3	15.0	16.1	6.5	7.3
10	15.0	10.5	12.6	16.4	9.0	9.0	8.6	10.0	13.2	11.4	11.1	6.0
11	11.7	13.2	17.6	11.0	10.8	9.6	11.8	10.0	16.2	11.4	8.5	13.6
12	10.5	8.3	9.5	8.7	8.7	6.0	11.3	10.9	16.0	11.2	7.8	10.6
13	6.0	10.9	7.9	6.5	10.3	8.0	10.0	16.4	12.1	14.4	9.5	10.3
14	5.7	8.4	11.5	10.0	10.5	9.2	7.5	10.5	13.0	12.6	9.2	15.9
15	7.6	7.4	12.3	11.1	10.2	10.9	7.3	8.8	13.4	11.9	12.5	14.9
16	5.7	9.2	21.5	12.4	9.7	7.5	9.0	11.5	9.6	9.7	10.7	11.8
17	19.6	19.5	12.4	7.2	11.5	5.3	11.5	13.9	15.1	15.6	10.5	14.1
18	7.2	11.7	8.5	9.0	14.0	6.7	11.5	14.9	13.4	10.9	9.4	11.6
19	9.4	12.1	14.5	8.8	10.7	9.1	11.8	13.6	10.9	12.9	16.5	13.7
20	18.4	9.8	18.3	10.0	10.8	13.2	8.7	15.5	11.2	18.3	9.1	14.3
21	8.5	12.7	19.2	12.9	10.9	11.6	10.0	15.6	13.3	10.2	10.8	9.1
22	16.6	6.0	19.9	10.0	7.6	9.8	12.0	9.0	11.5	11.4	7.7	8.5
23	14.1	13.1	17.9	11.7	10.8	11.7	8.3	7.7	12.9	12.5	8.7	5.8
24	15.7	10.9	9.5	12.1	11.7	10.4	10.2	14.6	13.0	13.8	9.5	9.3
25	11.2	16.7	9.9	14.2	15.0	7.9	9.5	11.7	11.0	13.8	10.5	8.5
26	17.3	18.3	13.7	20.0	11.6	5.8	8.4	13.1	9.8	12.8	13.9	7.1
27	12.5	7.5	14.1	10.1	11.5	6.6	9.2	10.0	14.4	13.0	14.2	7.4
28	15.4	10.0	12.6	11.5	10.8	9.3	8.1	13.7	18.7	9.8	16.0	10.3
29	12.7		24.1	11.7	9.9	9.4	7.7	12.4	14.6	12.7	12.4	17.4
30	10.1		14.8	10.9	6.9	7.2	11.0	16.2	24.7	11.2	9.8	9.9
31	8.8		13.7		6.5		10.4	29.7		15.2		14.2
Mean	11.3	11.6	13.7	11.8	10.4	9.5	10.2	13.1	13.2	13.8	10.7	10.5
					ANNUAL MEAN = 11.7							
						1944						
1	11.3	9.1	10.7	12.2	9.5	8.2	9.6	8.8	12.4	16.6	10.9	8.8
2	8.6	10.1	10.7	23.9	10.5	9.2	6.0	9.6	15.8	13.3	11.0	14.1
3	9.7	4.4	5.5	13.5	9.0	4.7	6.9	15.0	8.2	13.7	10.0	7.3
4	8.1	10.1	10.0	9.7	14.7	6.8	6.9	8.1	12.4	15.2	14.5	10.5
5	11.8	11.6	9.9	10.0	11.2	9.1	8.5	10.2	12.3	16.7	12.7	8.6
6	7.3	7.7	10.7	10.7	10.5	8.3	7.9	9.6	10.8	22.1	8.0	7.2
7	9.6	11.3	9.8	12.7	9.2	7.7	5.5	10.1	14.4	16.5	8.6	5.9
8	9.0	15.1	10.5	11.1	9.4	9.4	6.9	9.4	13.6	12.6	8.9	7.4
9	9.8	12.0	11.3	17.0	9.7	7.4	9.7	12.5	8.6	11.7	9.1	8.5
10	15.2	16.0	10.9	15.5	11.0	6.6	7.5	8.7	9.0	11.3	11.4	9.8
11	20.2	12.5	14.5	15.0	11.0	7.4	9.9	10.5	6.7	20.7	5.6	6.2
12	11.7	11.8	13.6	9.3	11.3	7.2	7.9	10.2	9.7	8.0	7.6	7.0
13	15.1	14.4	10.9	7.8	6.9	6.3	7.5	5.7	11.5	8.0	6.4	15.8
14	12.8	16.7	14.2	10.2	7.5	8.8	7.7	10.9	11.9	13.8	7.3	7.5
15	13.5	16.7	10.7	14.0	7.8	10.5	11.3	11.0	13.5	16.9	8.3	11.7
16	12.6	13.7	9.1	12.7	9.3	8.5	8.5	8.1	11.7	13.2	6.1	30.1
17	9.8	10.7	9.2	9.7	9.3	7.2	7.9	8.7	13.4	13.5	8.0	17.3
18	12.5	9.4	15.4	10.9	6.1	7.1	6.9	12.7	12.1	14.7	9.0	13.2
19	8.7	6.5	15.7	7.4	4.6	6.6	8.2	11.0	12.1	16.2	9.6	13.3
20	7.4	8.4	10.2	9.0	5.3	7.7	9.9	10.9	14.2	16.2	10.4	14.1
21	9.1	8.7	9.4	8.2	7.9	9.1	10.0	10.5	13.4	13.1	5.8	13.8
22	5.4	9.8	11.8	11.7	10.2	10.4	7.0	8.9	12.1	10.4	8.6	11.0
23	4.7	10.0	12.7	10.3	7.5	9.6	6.0	9.9	17.2	14.7	7.5	5.8
24	6.1	12.2	13.7	14.7	10.0	5.7	7.2	10.2	15.2	13.7	4.1	5.6
25	6.1	14.7	21.1	10.3	7.1	6.4	8.1	9.5	12.7	13.8	5.8	5.6
26	17.2	13.8	15.4	11.6	9.6	11.1	6.2	8.1	12.1	16.5	8.3	9.6
27	18.0	11.3	21.1	12.2	9.0	7.9	7.3	9.9	13.6	8.7	6.6	11.2
28	11.8	12.7	13.2	11.7	9.7	6.8	6.6	9.0	9.0	9.2	6.1	15.6
29	12.3	13.8	17.1	10.2	12.8	8.8	7.7	7.3	12.2	6.5	7.7	14.2
30	10.7		11.9	11.2	10.3	7.1	7.3	8.7	13.5	10.0	7.9	17.0
31	13.0		12.2		9.2		7.4	12.3		12.8		14.0
Mean	10.9	11.6	12.4	11.8	9.3	7.9	7.8	9.9	12.2	13.6	8.4	11.2
					ANNUAL MEAN = 10.6							

11.6 REFERENCES

Bartels, J., 1957, The Technique of Scaling Indices K and Q of Geomagnetic Activity, "Annals of the IGY, Vol. IV," parts 4-7, Pergamon Press, London.

Beard, D. B., 1964, "Solar Wind Geomagnetic Field Boundary," *Rev. Geophys.*, v. 2, p. 335.

Chapman, S., and J. Bartels, 1940, "Geomagnetism," Oxford University Press, London.

Chernosky, E. J., J. M. Collins, and M. P. Hagan, 1964, "Equatorial Loci of the Earth's Magnetic Field and Cosmic Ray Parameters," *Environ. Res. Papers No.* 5, AFCRL.

Chernosky, E. J., 1956, "The Delta Measure of Geomagnetic Activity," *Trans. Am. Geophys. Union*, v. 37, p. 339.

Elsasser, W. M., 1950, "The Earth's Interior and Geomagnetism," *Revs. Modern Phys.*, v. 22, p. 1.

Fan, C. Y., P. Meyer, and J. A. Simpson, 1961, "Dynamics and Structure of the Outer Radiation Belt," *J. Geophys. Res.*, v. 66, p. 2607.

Fejer, J. A., 1964, "Atmospheric Tides and Associated Magnetic Effects," *Rev. Geophys.*, v. 2, p. 275.

Fougere, P. F., 1965, "Spherical Harmonic Analyses, Part II: A New Model Derived from Magnetic Observatory Data for Epoch 1960.0," *J. Geophys. Res.*, v. 70, no. 9.

Fougere, P. F., 1964, "Mutually Consistent Magnetic Charts Based on Orthogonal Functions," *J. Geophys. Res.*, v. 69, no. 12, p. 2641.

Fougere, P. F., 1963, "Spherical Harmonic Analysis, Part I: A New Method and Its Verifications," *J. Geophys. Res.*, v. 68, no. 4, p. 1131.

Hazard, D. L., 1947, Directions for Magnetic Measurements, "U.S. Coast and Geodetic Survey Serial 166, 3rd ed.," U.S. Government Printing Office, Washington, D.C.

Heppner, J. P., N. F. Ness, C. S. Scearce, and T. L. Skillman, 1963, "Explorer 10 Magnetic Field Measurements," *J. Geophys. Res.*, v. 68, p. 1.

Hutchinson, R., and B. Shuman, 1961, "Rocket Measurements of the Magnetic Field Above New Mexico," *J. Geophys. Res.*, v. 66, p. 2687.

Jacobs, J. A., and K. O. Westphal, 1963, Geomagnetic Micropulsations, "Physics and Chemistry of the Earth, Vol. V," p. 253.

McComb, H. E., 1952, Magnetic Observatory Manual, "U.S. Coast and Geodetic Survey Special Publication No. 283," U.S. Government Printing Office, Washington, D.C.

Sen, H. K., and M. L. White, 1955, "Thermal and Gravitational Excitation of Atmospheric Oscillations," *J. Geophys. Res.*, v. 60, p. 483.

Sonett, C. P., 1960, Experimental Physics Using Space Vehicles, "Advances in Space Science, Vol. 2," Academic Press, New York.

Sugiura, M., 1961, "Evidence of Low-Frequency Hydromagnetic Waves in the Exosphere," *J. Geophys. Res.*, v. 66, p. 4087.

Veldkamp, J., and D. Van Sabben, 1960, "On the Current System of Solar-Flare Effects," *J. Atmos. Terrest. Phys.*, v. 18, p. 192.

Vestine, E. H., 1947, "The Geomagnetic Field, Its Description and Analysis," *Carnegie Institution of Washington Publication, No. 580.*

Whipple, K., 1960, "Methods and Techniques in Geophysics, Vol. I," S. K. Runcorn, ed., Interscience Publishers, Inc., New York.

Zmuda, A. J., 1956, "Limiting Form of Taylor Series Used in Extrapolating Components of the Geomagnetic Intensity," *Trans. Am. Geophys. Union*, v. 37, p. 9.

Zmuda, A. J., and L. McClung, 1955, "Vertical Extrapolation of Geomagnetic Field Components," *Trans. Am. Geophys. Union*, v. 36, p. 939.

Chapter 12

IONOSPHERIC PHYSICS

Section 12.1	R. J. Cormier
Section 12.2	James C. Ulwick
Section 12.3	J. A. Klobuchar
Section 12.4	Wolfgang Pfister
Sections 12.5, 12.6	T. J. Keneshea

Ionization of the upper atmosphere depends primarily on the sun and its activity. The major part of the ionization is produced by solar ultraviolet and x radiation and by corpuscular radiation from the sun. Cosmic rays may make a very minor contribution. As the earth rotates with respect to the sun, ionization increases in the sunlit atmosphere, and decreases on the darkened side.

12.1 IONOSPHERIC REGIONS AND DISTURBANCES

The *D region* is present only during daylight hours. Its peak altitude is normally around 90 km but this may decrease considerably, especially during solar flares. This region has the lowest electron density of all the regions. The *E region* occurs at a peak altitude in the vicinity of 110 km. The daytime electron density is about one magnitude greater than that of the D region. At night, the electron density is very much lower than during the day.

The F region is a combination of two regions with somewhat different characteristics. The *F_1 region* has a peak altitude of about 200 km in daytime, but is absent at night. The *F_2 region* is erratic and is especially sensitive in its relation to the sunspot cycle. The peak is generally at approximately 300 km; it has the highest electron density in the ionosphere. The F_2 region does not disappear at night, but the electron density decreases by an order of magnitude under normal conditions.

During disturbed conditions caused by solar flares (Sec. 15.4.3) and magnetic disturbances (Sec. 11.4.2), the ionospheric regions behave in various ways depending upon the latitude. At the time of the flare, a *sudden ionospheric disturbance (SID)* is observed on the sunlit side of the earth. The magnitude of the associated absorption depends on latitude [Warwick, 1963]. Within one to three hours later, a *polar cap absorption (PCA)* event is observed only at latitudes greater than 65°N. Twenty-five to forty hours later, an *auroral zone absorption (AZA)* event is observed coincident with geomagnetic storms and also with changes in the F-region maximum electron density, which either decreases or increases depending on the latitude. For detailed information regarding individual storms, see Hill [1962].

12.1.1 Sudden Ionospheric Disturbance

The SID is associated with solar flares, usually of importance 2 or greater. The various ways of observing an SID are:

(a) sudden enhancement of atmospherics (SEA),
(b) sudden phase anomaly (SPA),
(c) sudden cosmic noise absorption (SCNA),
(d) short wave fadeout (SWF), and
(e) sudden frequency deviation (SFD).

The first four conditions are associated with abnormal ionization in the lower D region caused by an increase in ~~x radiation in the decimeter wavelength.~~ the flux of solar x-rays. The fifth is associated with ionization in the upper E and lower F_2 regions caused by solar ultraviolet radiation.

It was formerly thought that the SID was the result of enhancement of ionization existing in the D region and was caused by an increase in solar Lyman-α radiation. Rocket flights and satellite data, however, show no increase in Lyman-α radiation during flares, but do show that the x-ray flux increases by as much as 100 times normal conditions. The current belief is that an entirely new region is formed in the lower D region by x radiation [Nicolet and Aiken, 1960]. SIDs are correlated with the centimeter bursts on the sun rather than with the optical Hα flares. The x-ray flux below 8 Å is also clearly related to SIDs.

The observations of increased ionization in the upper E and lower F_1 regions during flares, and the disappearance of increased E-region ionization after the disappearance of the increased D-region ionization, support the current view that no single monochromatic radiation is effective in ionizing both the D and E regions, but rather radiation at several wavelengths is involved.

Changes in the F-region ionization associated with solar flares are found to be more sensitive indicators of solar flares than the D-region indicators [Chan and Villard, 1963].

12.1.2 High Latitude Absorption Events

Polar cap absorption events are associated with charged particles ejected during an intense solar flare. The influx of protons with energies between approximately 10 MeV and 100 MeV lasts for several days after the cessation of the flare. The PCAs are independent of magnetic activity and are correlated with Type IV radio bursts (Sec. 16.3.4). PCAs are distinguishable by their high intensity smoothly varying with time. They are observed only on the polar cap and have never been found to descend below 65°N latitude.

Auroral zone absorption events are associated with aurora particles, particularly with pulsating and flaming auroral displays (Sec. 13.2) and geomagnetic disturbances. An AZA, unlike a PCA, is not uniform but will show different amounts of absorption at various times depending upon local regions. The auroral zone absorption, like visual aurora, is the effect of bombardment of the upper atmosphere by charged particles guided into auroral latitudes by the earth's magnetic field. The AZA has a tendency to move to lower latitudes during magnetic disturbances and the southernmost extent is proportional to the depression of the geomagnetic field. This is explained by the change in the geomagnetic cutoff rigidity (Sec. 17.3) for incoming particles due to the distorted outer geomagnetic field.

Another high latitude absorption event observed is the *sudden commencement absorption* (SCA), which is associated with the sudden commencement of a magnetic disturbance.

12.1.3 F-Region Effects

Ionospheric disturbances are characterized by the deviation of the F-region maximum electron density for a particular day from the mean of that particular month. For details concerning individual storms, see Somayajulu [1963]. The variations are associated with magnetic disturbances and show various deviations depending on latitude. In middle and high latitudes, the F-region maximum electron density decreases for approximately three days and then returns to normal. The electron density sometimes decreases by a factor of 10 to 15. In equatorial and low latitudes, the maximum electron density of the F region decreases on the initial storm day, then increases above the normal mean for the next two days before returning to normal. Middle latitude stations exhibit both types of disturbances.

During ionospheric disturbances, a subsidiary electron density peak is observed at low latitudes below the F_2 region that is often reported as the normal F_1-region returns. This subsidiary peak, however, does not behave like a region directly controlled by the sun. It does not show strong dependence upon the sun's zenith distance as does the normal F_1 region. In studies made during 1960 at Concord, Massachusetts, it was observed that ionospheric storms characterized by increased F-region electron density did not show a pronounced F_1 region. The disturbances regarded as the normal midlatitude type did show this region.

Solar ultraviolet radiation produces an ionization maximum at about 160-km height corresponding to the F_1-region peak. The loss of ionization at this height is by recombination.

Many hypotheses are proposed to explain the latitudinal behavior of the F-region electron density variations during ionospheric disturbances, but none successfully explain all observed effects. The suggestion that vertical transport of O_2, due to enhanced turbulence below the F_2 region, could cause the decreased F-region electron density fails to explain the increase of F-region electron density at the low latitudes. Another suggestion is that changes in the auroral zone are caused by thermal expansion. Particles from the solar plasma precipitating into the auroral zone provide a means of heating the ionosphere. Satellite drag perturbations show that a general heating of the atmosphere from 200 to 700 km occurs during a geomagnetic storm. The total electron content determined from balloon measurements reveals that the density at 1000-km height decreases by a substantial amount during disturbed conditions. The reduction in the electron-density maximum is believed to be not just a redistribution of ionization, but also a removal of ionization at all levels, possibly associated with an increased loss rate.

12.2 ELECTRON AND ION DENSITY AND TEMPERATURE

The ionosphere has a geographical, diurnal, seasonal, and solar cycle variation; but because of the limited number of observations, it is not yet possible to produce models of the charged-particle density or temperature distribution for all these conditions.

12.2.1 Densities

The major exploratory tool for determining the electron density in the ionosphere has been the vertical incidence sounders. Ionosonde data are easy to obtain from stations scattered throughout the world and from these ionograms profiles of electron density above the observing station up to the peak of the F_2 region are obtained. However, uncertainties arise from the low-frequency limitations of the equipment and from ambiguities, if there are valleys in the regions. In addition, the vertical incidence sounder cannot give results below approximately 200 km at night because the electron density is too low. Positive ion densities cannot be measured directly by this technique but only inferred from the electron density measurements when the number of negative ions may be assumed to be relatively small. Studies of lunar radar reflections provide data on the total electron content in a column of the ionosphere above the peak of the F_2 region (Sec. 12.3). Rocket and satellite investigations provide basic information and aid ionosonde interpretation. These studies also reveal that the ionosphere does not consist of discrete layers as originally supposed, but is a continuum with an almost monotonic increase in electron density up to the F_2 maximum. Figure 12-1 shows distributions of electron density obtained from NRL rocket-flight

experiments. Pfister and Ulwick [1958], using a different propagating technique, show a continuous increase in electron density with a fine structure about every 6 km. There is a strong tendency for the peaks to appear at preferred altitudes such as 85, 94, 100, 105, 111, 117 and 129 km. Figure 12-2 shows the results of two rocket experiments flown at White Sands, New Mexico (June 1956), and the results of a resonance probe flown at Michikawa, Japan (March 1961), all at roughly the same local time. The NRL experiment shows a sporadic-E condition (the sharp spike in the electron density profile) at 101 km, approximately 1-km thick, with a peak value of 4.5×10^5 electrons cm^{-3}. The resonance probe results show a fine structure similar to the propagation results although the peaks are not at the same altitudes.

Figure 12-3 shows nighttime and daytime positive ion densities obtained by an ion-trap probe on a rocket. Figure 12-4 shows measurements of nighttime and daytime electron densities in the D and E regions obtained by Langmuir probes in rocket experiments.

Measurements above the F_2 layer by ground instrumentation can be made with incoherent back scatter sounders. Figure 12-5 is an electron density profile obtained by this method. Figure 12-6 shows the ion density profile above the F_2 layer obtained from a daytime rocket flight carrying a retarding potential probe. Figure 12-7 shows simultaneous measurements at night of electron density from an RF impedance probe and positive ion density from an ion trap probe on a rocket flight from Cape Kennedy, Florida. The two slopes above the F_2 layer peak in Fig. 12-7(b) are attributed to O^+ and H^+ ions; there was no evidence for He^+ ions.

Figure 12-8 shows electron densities to high altitudes measured by a standing wave impedance probe on a satellite. With satellite data one does not get a vertical profile as with rockets but obtains instead a variation of density with respect to altitude, magnetic latitude, and local time. The data are plotted as a function of altitude with the latitude and time given on the right hand ordinate. A two-frequency (3 and 7.2 Mcps) switched impedance probe was flown to cover a range of electron density from 5×10^2 to 5×10^6 electrons cm^{-3}. Because there was excellent agreement between the two results, the 7.2 Mcps data were used for the higher densities (5×10^4 to 10^6) and the 3.0 Mcps data for the lower densities (10^3 to 5×10^4) in plotting this figure. The sample rate was

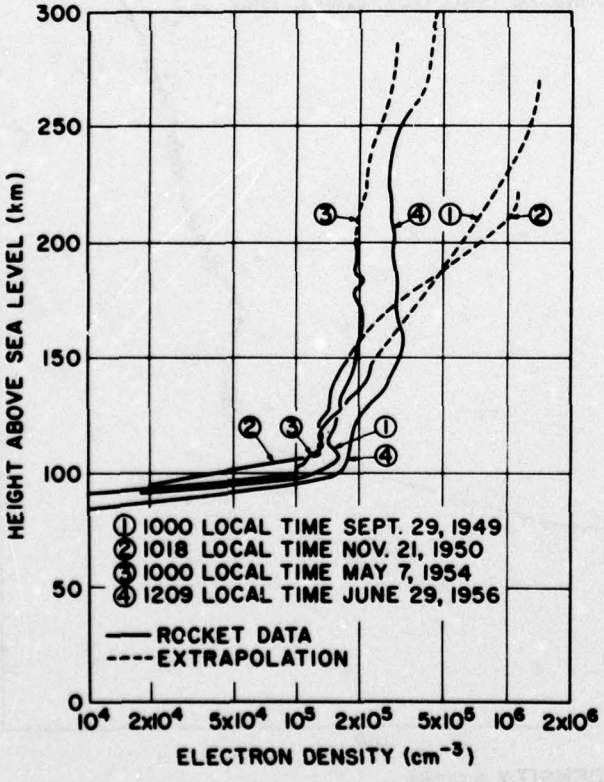


Fig. 12-1. Electron densities from NRL experiments, using Seddon's propagation method, at White Sands, New Mexico. (From H. Freidman, 1959, *Proc. Inst. Radio Engrs.*, v. 47, no. 2, by permission.)

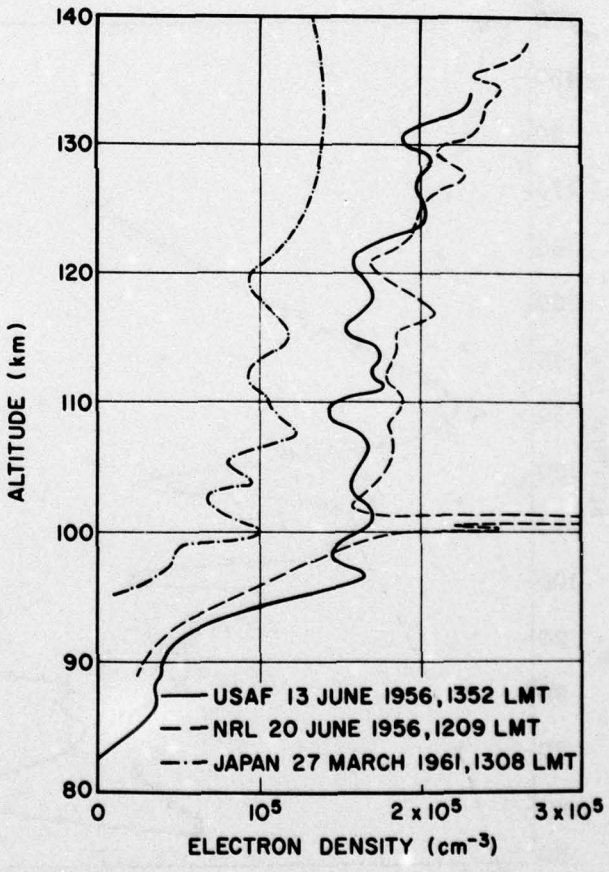


Fig. 12-2. Electron density profiles over White Sands, N. M. (USAF and NRL) and over Michikawa, Japan. USAF curve, Pfister and Ulwick [1958]; NRL curve, J. Jackson and J. C. Seddon (from *J. Geophys. Res.*, v. 63, no. 1, 1958); Japan curve, T. Yunezawa (from *Report of Japanese Rocket Observations*, Radio Research Laboratories, Kuchubunji, Tokyo, Japan.)

a measurement approximately every 2 sec. The increase in electron density at apogee is due to the change in latitude. To illustrate this, the reciprocal of L, the magnetic shell parameter (Sec. 17.2.1), is also shown.

Figure 12-9 shows the electron and positive ion densities obtained from the impedance probe and the ion trap probe flown together on a satellite. The orbit of the satellite and the magnetometer output, showing a stable orbit, are included. The electron density results show a striking similarity, even in the fine structure, between the two orbits with a 22° difference in longitude. Evidence of the auroral zone occurs only in the southern hemisphere.

Figure 12-10 shows the results from another satellite where more orbits are available; irregularities in the F region are more visible. The orbit perigee was 220 km. Examination of the structure shows that the distance between irregularity peaks is about 400 km, with small scale fluctuations between 5% and 10%. A 1200-km wide irregularity is also evident. Data from this satellite were used for the study of the electron density in the southern auroral zone. Here the fluctuations were much larger than those shown in Fig. 12-10. Figure 12-11 shows contours of equal electron density in the southern auroral zone. The orbit number (data are missing on orbits 4 and 13), the latitude, local time, and the corresponding altitude of the satellite are given, as well as the longitude of the southernmost point for the corresponding orbit. In general, the electron density decreases with increasing height of the satellite and with the transition from day to night. Two interesting features are evident. A ridge of maximum intensity on the day side at 70° geographic latitude, and a system of ridges and valleys parallel to the magnetic latitude.

When the interest is the gross structure of the ionosphere, the topside sounder (a special ionosonde in a satellite) is the best method of obtaining electron density profiles above the F layer. Figure 12-12 shows contours of equal electron densities in the orbital plane for just one portion of the orbit obtained from the Alouette satellite by this technique.

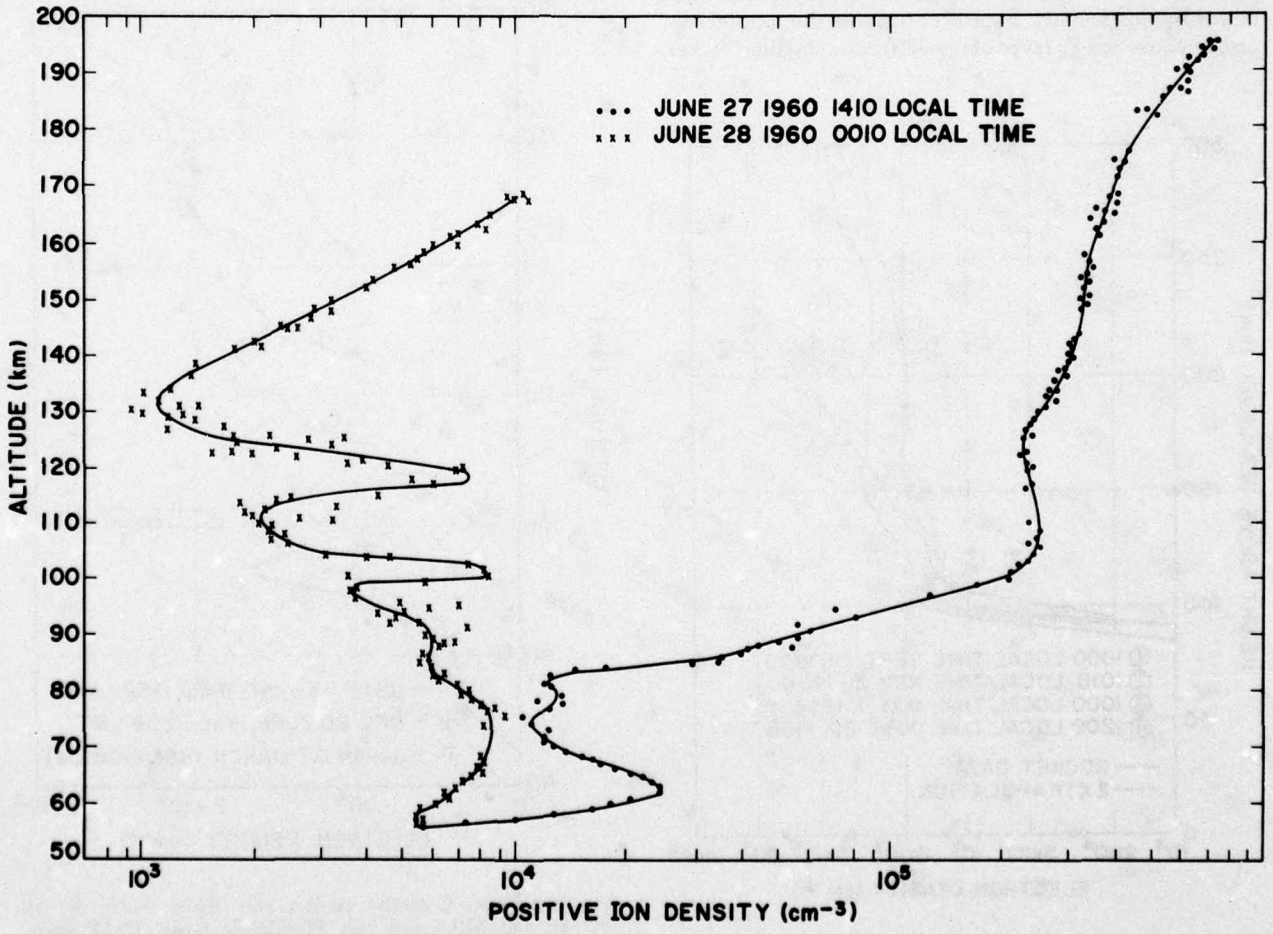


Fig. 12-3. Positive ion densities for daytime and nighttime ionosphere. Data from ion-trap probe on a rocket. (From R. C. Sagalyn and M. Smiddy, *Space Research IV, COSPAR*, North-Holland Publishing Co., Amsterdam, Holland, 1964, by permission.)

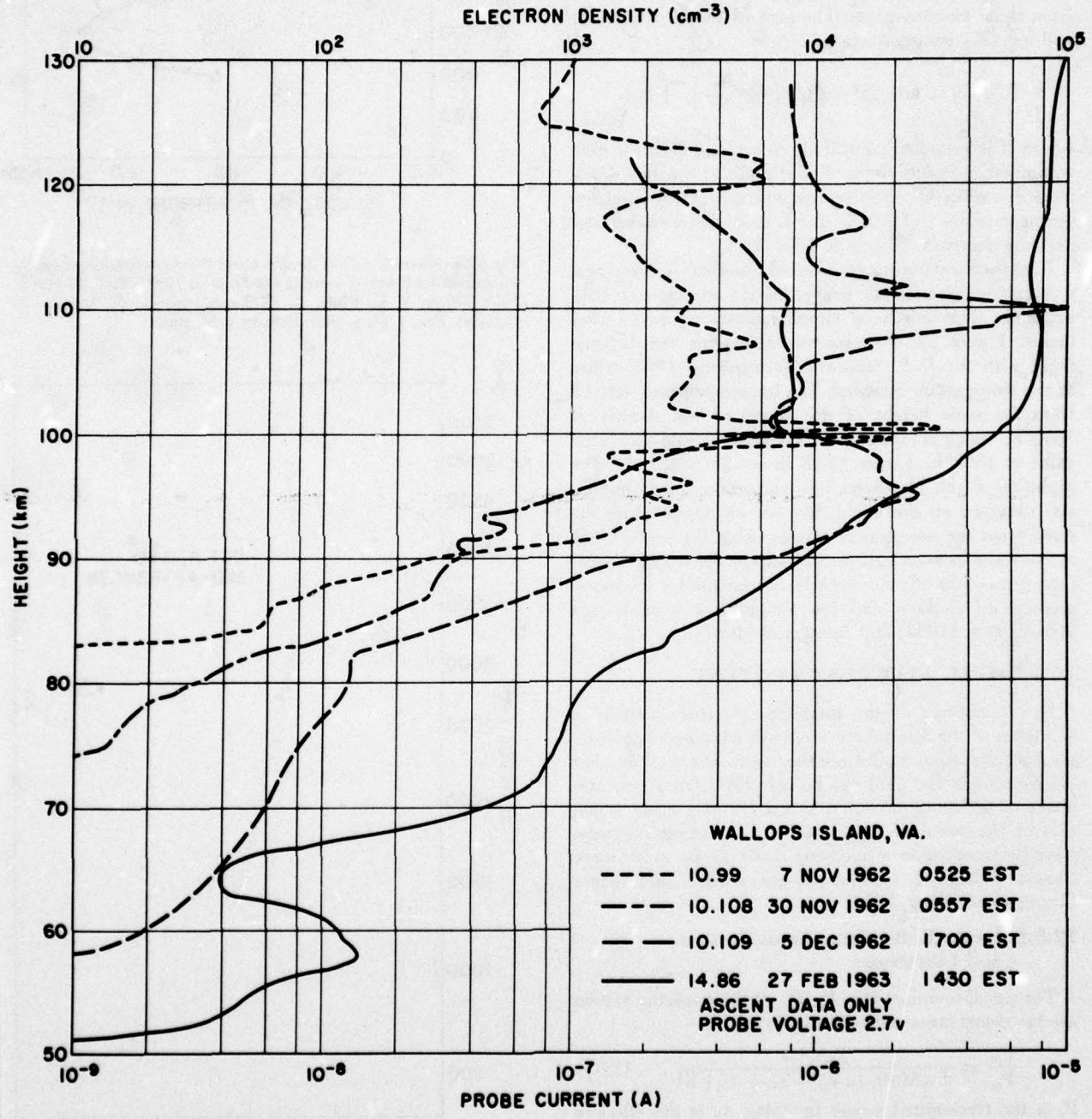


Fig. 12-4. Profiles of probe current in the D and lower E region. Measurements by L. G. Smith using Langmuir probes on rockets. (Courtesy of Geophysics Corporation of America.)

12.2.2 Electron and Ion Temperatures

Figure 12-13 shows the geopotential altitude of the intersection of a satellite orbit with magnetic shell parameters and the electron density distribution observed for that orbit. If diffusive equilibrium for protons along magnetic field lines is assumed, the temperature can be computed from these measurements. The sum of the electron (T_e) and ion (T_i) temperatures is

$$T_e + T_i = 1.17\ (H - H_o)\left(\ln \frac{N_o}{N}\right)^{-1}\ [°K], \qquad (12\text{-}1)$$

where H is geopotential altitude in km and N is the electron number-density in cm^{-3}. For shells of L values 4 and 5 earth radii, the effective temperature of the electron-proton mixture is 1200°K; for L = 2, the effective temperature decreases slightly to 1000°K.

In experiments using an injected spherical ion trap and a cylindrical electrostatic probe, the ion and electron temperatures were measured simultaneously on two rocket flights. Figure 12-14 shows the results for the daytime flight with the *U.S. Standard Atmosphere, 1962* values of gas temperature included. The ion temperature derived from the scale height of the measured ion density is 1650°K, which compares well with the directly measured value of 1500°K. Figure 12-15 shows the results for the nighttime flight. No direct ion temperatures information was obtained on this flight, but the ion temperature derived from the ion density results using the scale-height method was in exact agreement with the electron temperature. For results of other rocket experiments for the measurement of electron and ion temperature profiles, see Spencer et al [1962] and Auno et al [1961].

12.3 TOTAL ELECTRON CONTENT

Determinations of the total free electron content in a column of the ionosphere are made by observing radio signals reflected to earth from the moon. The total number of electrons in the path can be calculated from measurements of the rotation caused by the *Faraday effect* (rotation of the plane of polarization of an electromagnetic wave propagating in a magnetic field) as the radio wave travels through a column of the earth's atmosphere [Daniels and Bauer, 1959].

12.3.1 Lunar Reflections, Cross Section, and Libration

The signal-to-noise ratio, P_A/P_n, of the receiving system used to detect lunar reflected signals is

$$\frac{P_A}{P_n} = \frac{P_t A_e^2\, \sigma}{4\pi \Delta f \lambda^2 k\ (n T_o - T_o + T_A)\ R^4}. \qquad (12\text{-}2)$$

P_t is the transmitted power in watts, A_e is the effective area of the receiving antenna in m^2, σ is the effective lunar scattering cross section in m^2, λ is the operating wavelength of the transmitter in m, n is the noise figure of the receiver, T_o is the ambient temperature in °K, and R is the distance to the moon in m. The other symbols are defined in Sec. 22.1.

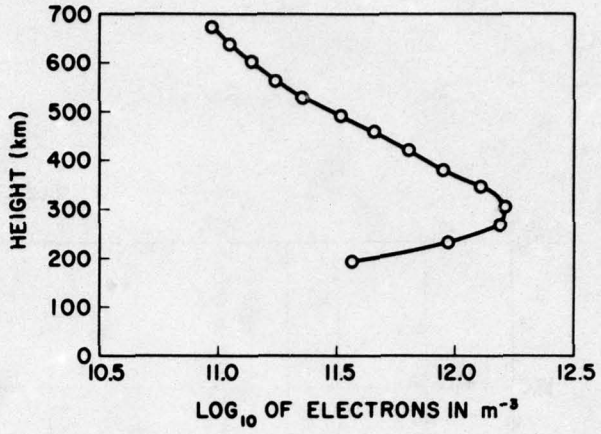


Fig. 12-5. Electron density profile above the F_2 region obtained by incoherent back-scatter method 140 Mcps at 1420 h EST, 18 March 1960. (From V. C. Pineo, L. G. Kraft, and H. W. Briscoe, *J. Geophys. Res.*, v. 65, p. 2629, 1960, by permission.)

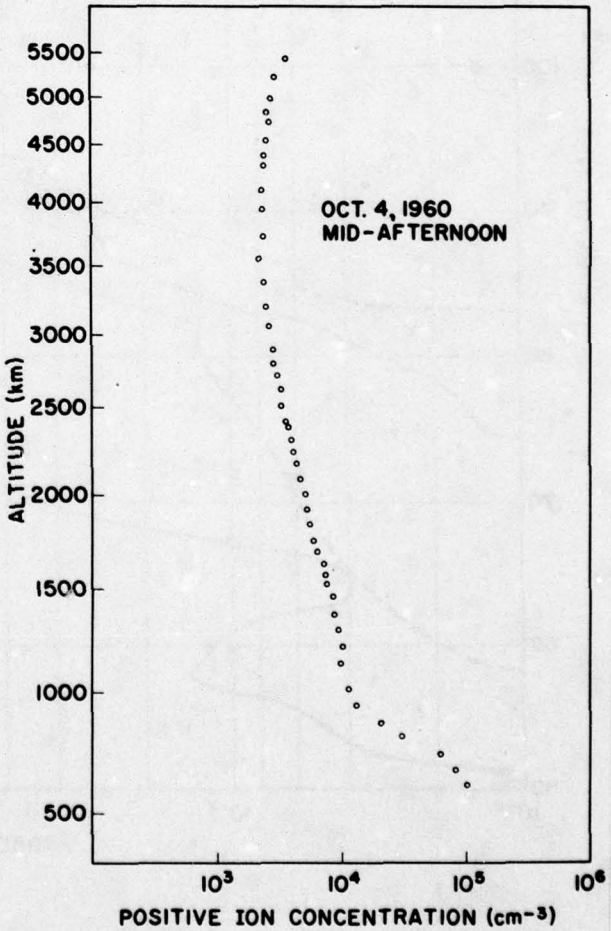
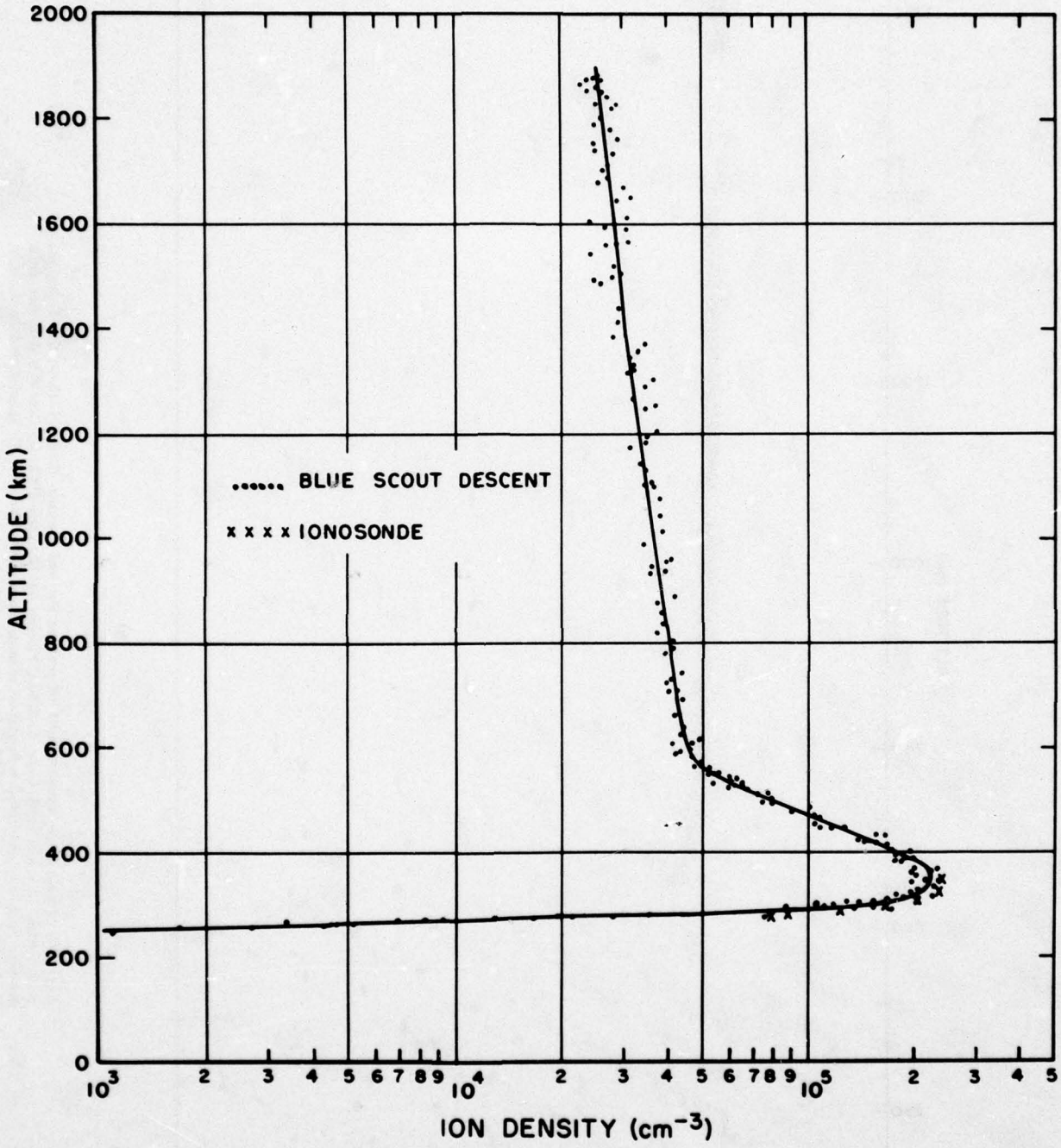
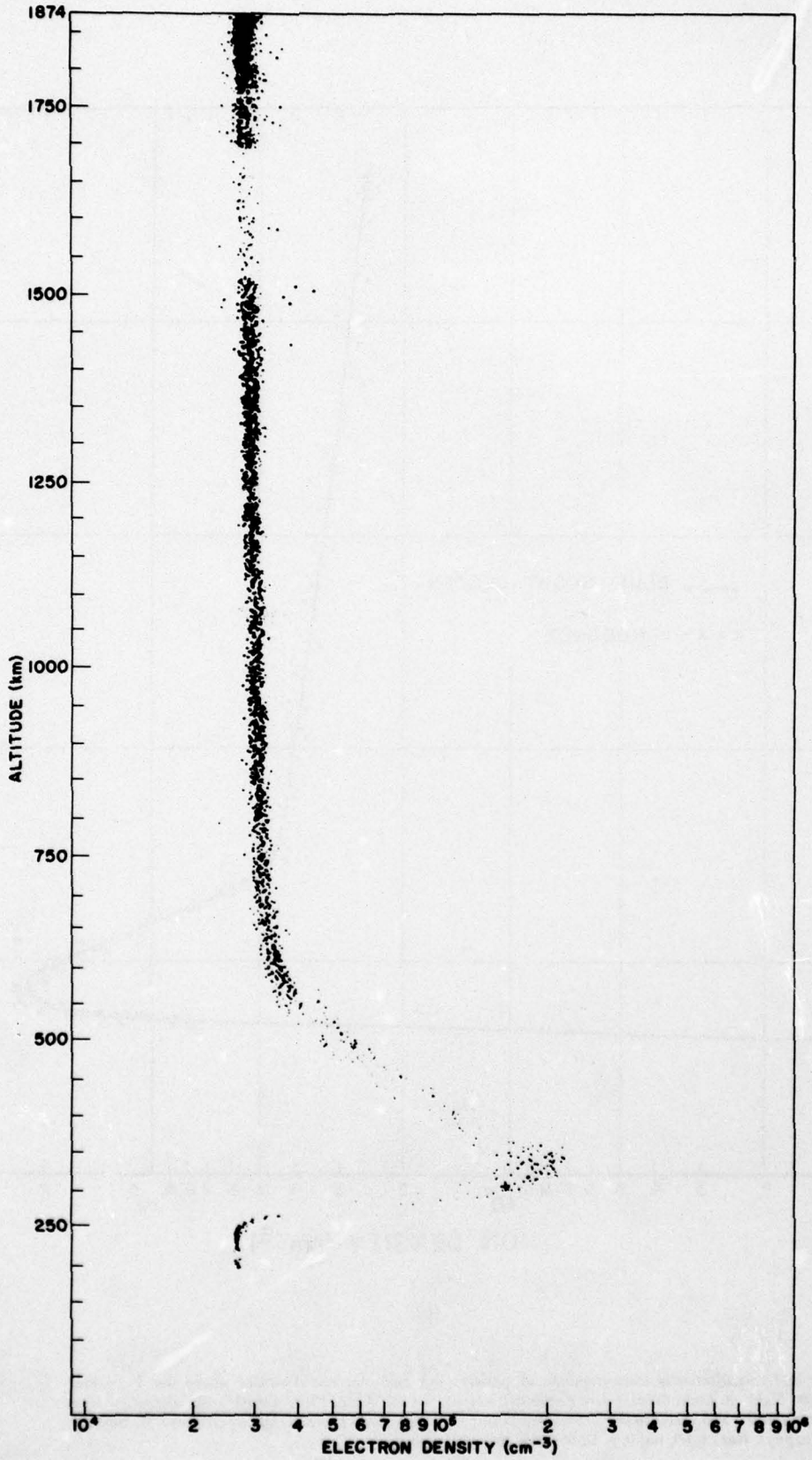


Fig. 12-6. Positive ion density above the F_2 region; measurements made by L. C. Hale with a retarding-potential probe on a daytime rocket flight. (From W. B. Hanson, *J. Geophys. Res.*, v. 67, no. 1, 1962, by permission.)



(a)

Fig. 12-7. Simultaneous measurements of positive ion and electron densities above the F region; rocket flight at night from Cape Kennedy, Florida on 12 April 1961. Positive ion densities from ion-trap probe and electron densities from rf impedance probe. (From R. C. Sagalvn and M. Smiddy, *J. Geophys. Res.*, v. 69, no. 9, p. 1809, 1964, by permission.)



(b)

Fig. 12-7. Simultaneous measurements of positive ion and electron densities above the F region; rocket flight at night from Cape Kennedy, Florida on 12 April 1961. Positive ion densities from ion-trap probe and electron densities from rf impedance probe. (From R. C. Sagalyn and M. Smiddy, *J. Geophys. Res.*, v. 69, no. 9, p. 1809, 1964, by permission.)

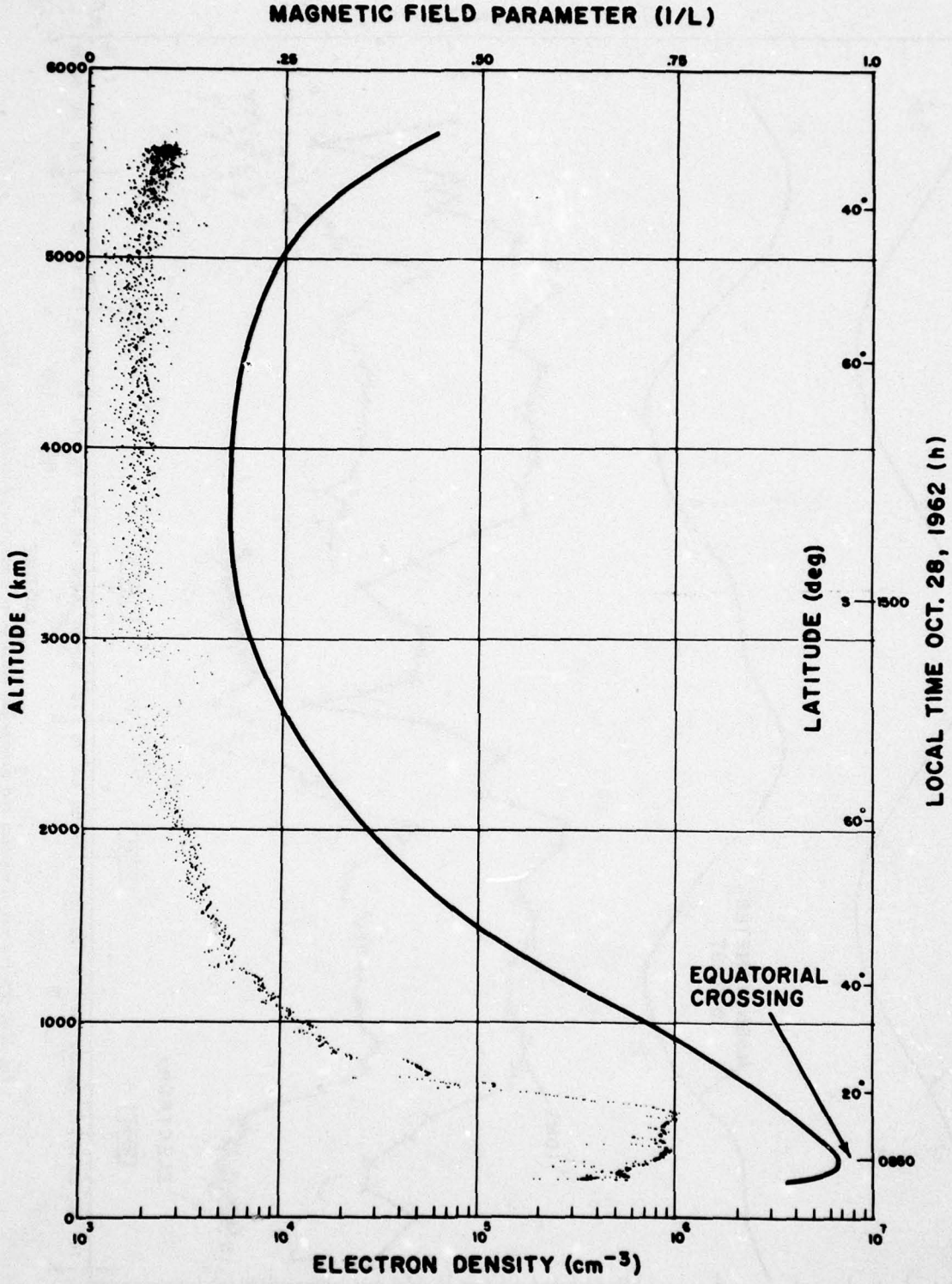


Fig. 12-8. Electron densities above the F region from impedance probes on a satellite ascent; the increase in density at apogee is due to the change in latitude. The solid curve is a plot of the reciprocal of the magnetic shell parameter (L) vs altitude.

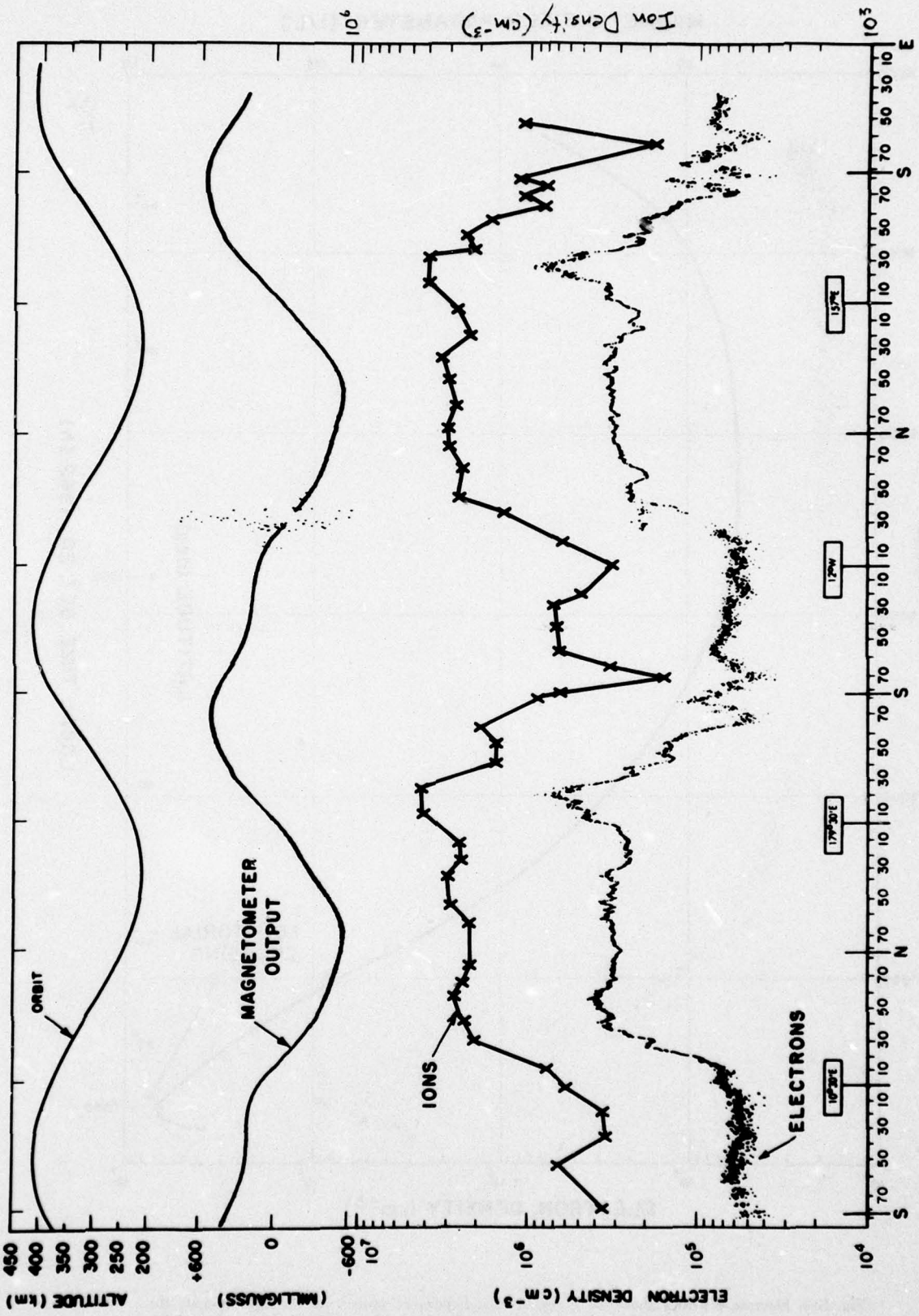


Fig. 12-9. Observations of electron and positive ion densities as a function of latitude; impedance probe and ion trap probe measurements from a satellite. The longitudes are given at equator crossings; the local time for north to south equator crossing was 1715 h and for south to north equator crossing 0515 h.

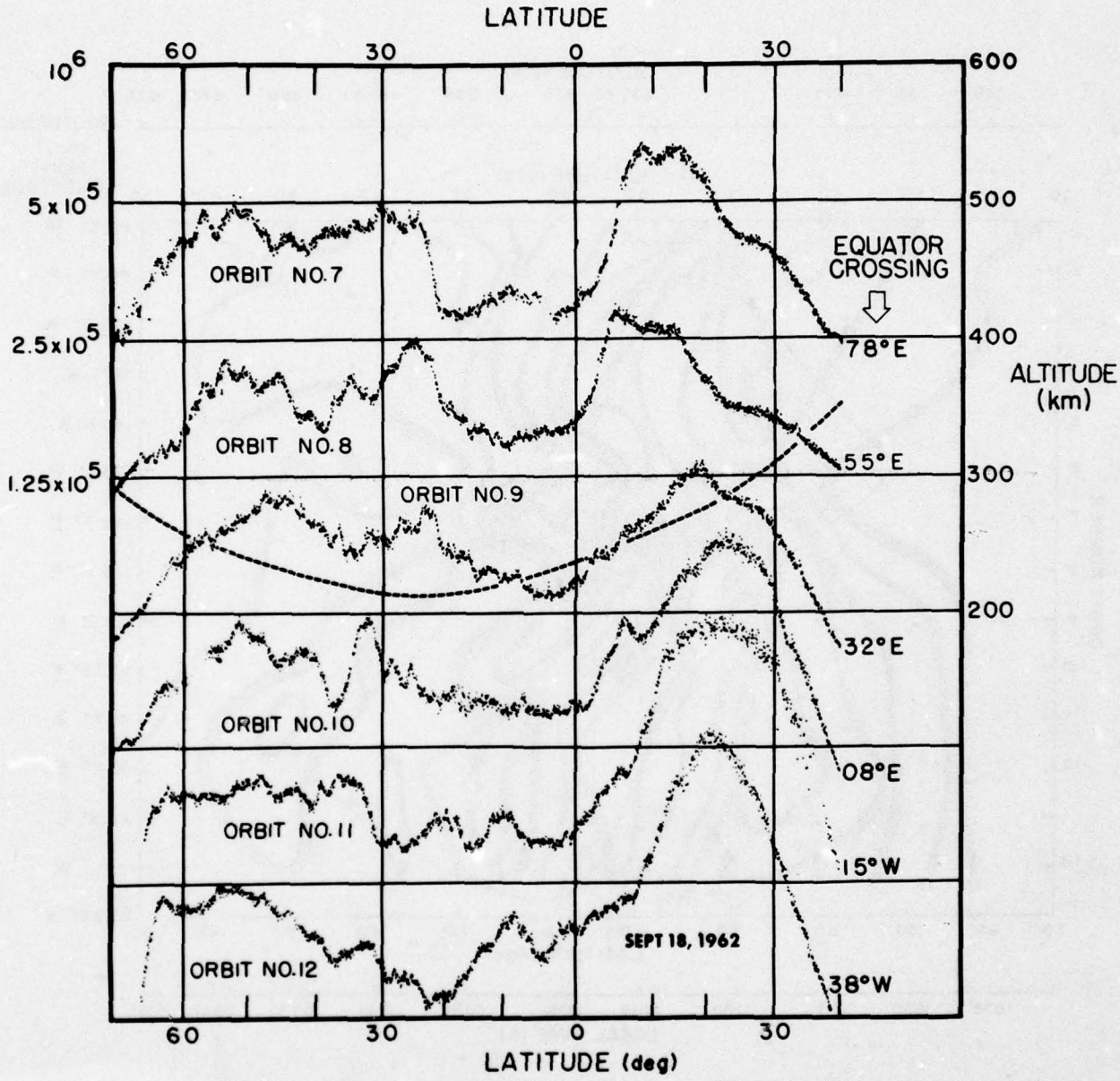


Fig. 12-10. Fine structure of electron density in the F region from impedance probe measurements; the dashed curve shows orbit altitudes. Longitudes at equator crossings are given for each orbit. Local time of equator crossings 1630h. The electron density (cm^{-3}) scale is for orbit no. 7. Curves for other orbits are shifted progressively by a factor of 2; e. g., for orbit no. 8, read 5×10^5 for ordinate labeled 2.5×10^5. For orbit no. 9, read 5×10^5 for ordinate labeled 1.25×10^5, and so on.

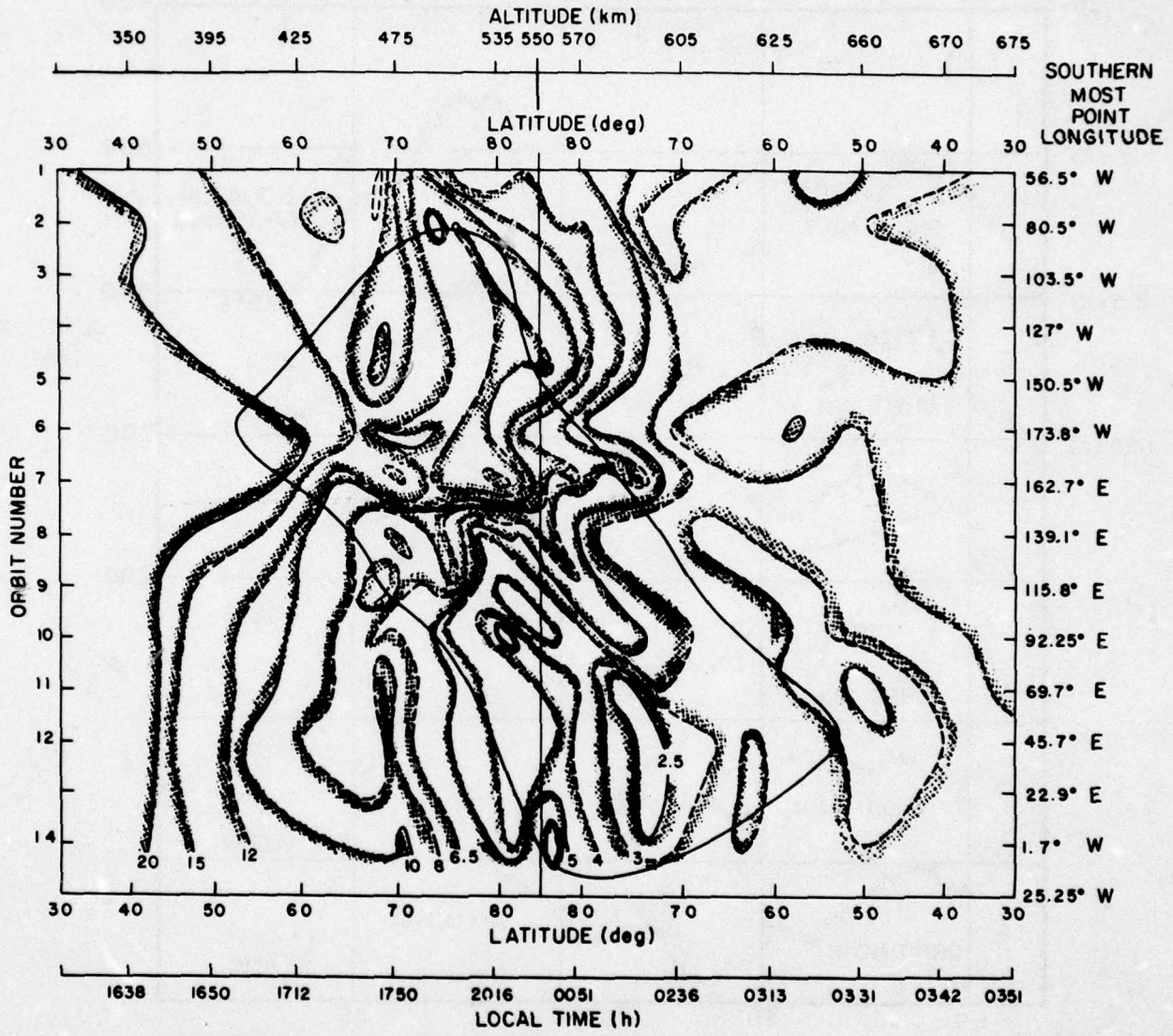


Fig. 12-11. Contours of equal electron density from impedance probe measurements. The southern auroral zone is shown as a solid line. Values of density given for the contours are in units of 10^4 electrons cm^{-3}.

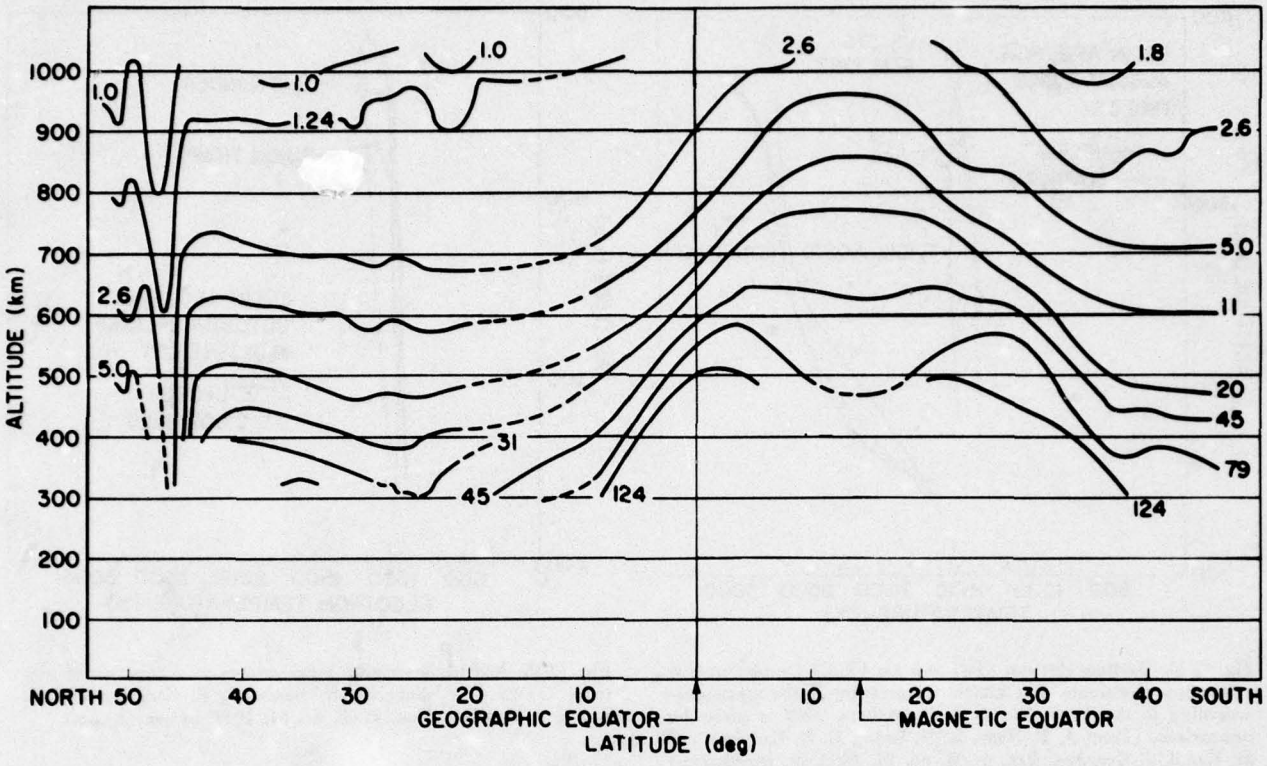


Fig. 12-12. Contours of equal electron density in the orbital plane of an Alouette satellite; measurements by a topside sounder during one portion of the orbit. Density in units of 10^4 electrons cm^{-3}.

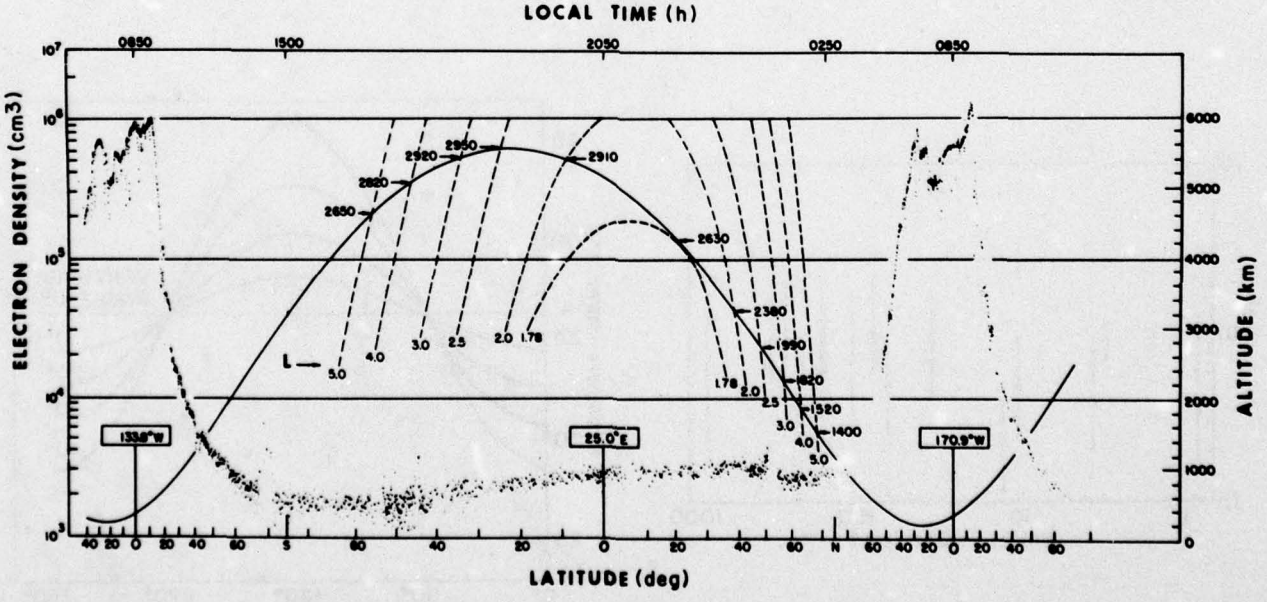


Fig. 12-13. Electron density from a standing wave impedance probe on 1962 beta kappa satellite, orbit no. 23. Solid curve shows orbit altitudes. Dashed curves show the magnetic shell parameter, L. Geopotential altitudes of the satellite at crossings of the shells are given in kilometers. Longitudes at equatorial crossings are shown on the latitude scale.

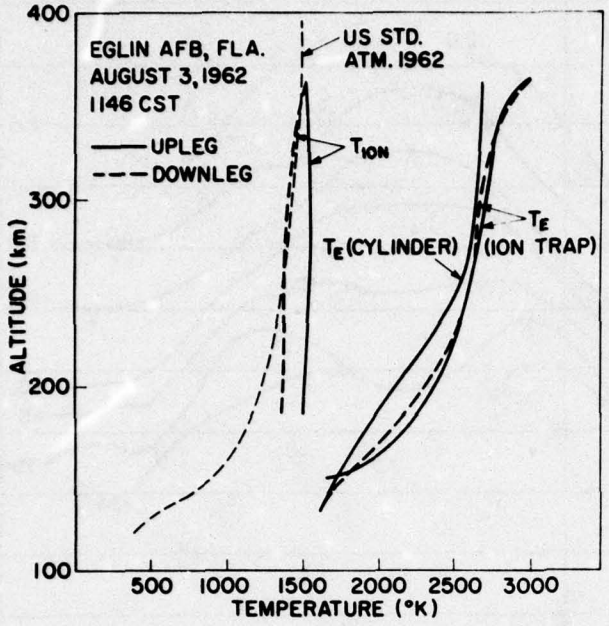


Fig. 12-14. Daytime electron (T_E) and ion (T_{ion}) temperatures as a function of altitude. The kinetic temperature of the atmosphere according to the *U. S. Standard Atmosphere, 1962* is given for comparison. (From A. F. Nagy, L. H. Brace, G. R. Carignan and M. Kanal, *J. Geophys. Res.*, v. 68, no. 24, 1963, by permission.)

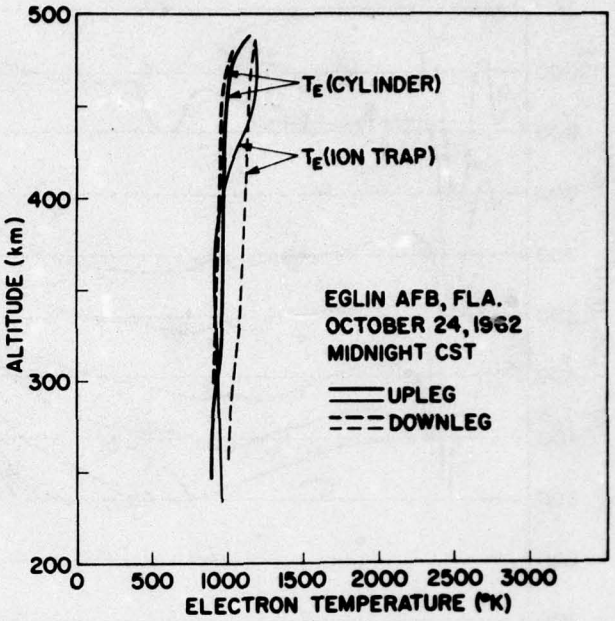


Fig. 12-15. Nighttime electron temperatures as a function of altitude. (From A. F. Nagy, L. H. Brace, G. R. Carignan and M. Kanal, *J. Geophys. Res.*, v. 68, no. 24, 1963, by permission.)

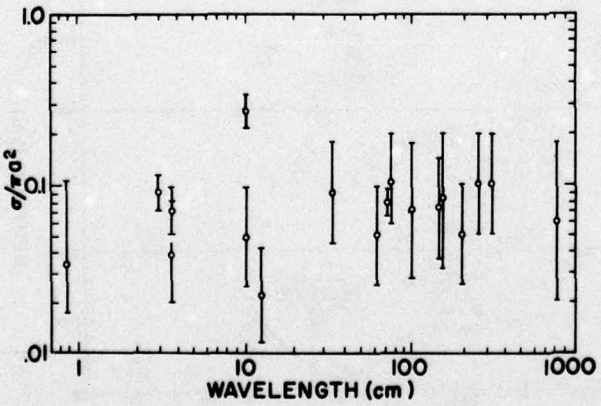


Fig. 12-16. Values observed at various wavelengths of the ratio of the effective lunar scattering cross section, σ, to the area of the projected lunar disk, πa^2. (From J. V. Evans and G. H. Pettengill, *J. Geophys. Res.*, v. 68, no. 17, p. 5098, 1963, by permission.)

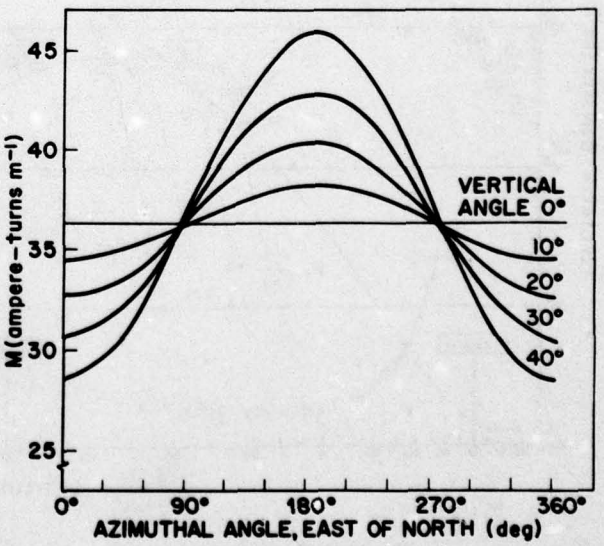


Fig. 12-17. The variation of M at an ionospheric height of 350 km, observed at longitude 88°, latitude 40°. (From K. C. Yeh and V. H. Gonzales, *J. Geophys. Res.*, v. 65, pp. 3209-3214, 1960.)

Figure 12-16 shows observations at various wavelengths of the ratio ($\sigma/\pi a^2$) of the effective lunar scattering cross section to the area of the projected lunar disk. No clear dependence of σ on wavelength is apparent over the wavelength range from 8.6 mm to 7.8 m, but the experimental errors are large.

Lunar libration (Sec. 19.7) produces amplitude fading of the reflected radio waves, and it can sometimes be confused with the Faraday polarization rotation. At frequencies above approximately 40 Mcps, however, the Faraday fading is usually much slower than the libration fading. The total angular rate of lunar libration is:

$$\begin{aligned} L &= (L_l^2 + L_B^2)^{1/2} \quad [\text{rad sec}^{-1}]; \\ L_l &= 12 \times 10^{-7} \cos\phi \cos t + L_{le}, \\ L_B &= 12 \times 10^{-7} \cos\phi \sin t \sin\delta + L_{be}. \end{aligned} \tag{12-3}$$

ϕ is the observer's latitude, t is the local hour angle of the moon, and δ is the declination of the moon. L_{le} and L_{be} are computed from daily selenographic coordinates given in the *American Emphemeris and Nautical Almanac.*

12.3.2 Faraday Rotation of Plane of Polarization

The amount of rotation, in radians, as the wave travels through the earth's ionosphere is proportional to the product of electron density and the component of the geomagnetic field strength along the direction of propagation. For a one-way path,

$$\Omega = \frac{K}{f^2} \int_o^{\text{moon}} N H \cos\theta \sec i \, dh. \tag{12-4}$$

The proportionality constant, K, is 2.97×10^{-2} [rad m^3 amp-turn^{-1} sec^{-2}], f is transmitted frequency in cps, N is electron density in electrons m^{-3}, H is magnetic field intensity in ampere turns m^{-1}, θ is the angle between the geomagnetic field and the direction of propagation, i is the zenith angle of the moon, and sec i dh is the element of path length. The value, $K = 9.47 \times 10^{-3}$, is sometimes used. In this case, Ω is the amount of polarization rotation expressed in complete number of turns for a two-way lunar path. Equation (12-4) requires that the mode of propagation be quasi-longitudinal so that the inequality

$$\left(\frac{f_H \sin\theta}{f}\right)^4 << 4\left(1 - \frac{f_N^2}{f^2}\right)\left(\frac{f_H \cos\theta}{f}\right)^2$$

must be satisfied; f_H is the gyromagnetic frequency of the electron and f_N is the electron plasma frequency (Sec. 9.3.1). At frequencies above 100 Mcps, this inequality is satisfied for $\theta \leq 89°$; and from midlatitude stations the propagation angle to the moon is always less than 89°. The geomagnetic field intensity near the earth is reasonably well known; therefore, Eq. (12-4) is usually expressed as

$$\Omega = \frac{KM}{f^2} \int_o^{\text{moon}} Ndh, \tag{12-5}$$

where M is the mean value of H cos θ sec i. M is computed using an assumed distribution of Ndh; the mean value equals the actual value at ionospheric heights ranging from 340 to 400 km. Figure 12-17 shows the variation of M for various azimuthal and vertical directions from a midlatitude station.

The rotation is usually greater than 180°; thus, Eq. (12-2 or 12-3) is ambiguous by $n\pi$. From Eq. (12-4),

$$d\Omega/df = -2\Omega_1/f_1. \tag{12-6}$$

Thus, if two closely-spaced frequencies are used, the ambiguity in Ω_1 (the angle measured at f_1) can be resolved by measuring $\Delta\Omega$, the angular difference in received polarization at the two frequencies. N can be calculated from Eq. (12-4 or 12-5). At 100 Mcps a typical amount of angular rotation for a one-way ionospheric path varies from 450°, as a predawn minimum, to about 3600° as a noon maximum. A five-degree polarization change can be seen readily, so the sensitivity of the measurement is better than 0.1%. Because of this sensitivity to small changes in electron content, Faraday rotation data are useful for studies of ionospheric irregularities.

12.3.3 Variations in Electron Content

The ratio of the columnar electron content above the height of maximum density to that below is determined by the joint use of lunar reflections and ionosonde data. This ratio varies from about 3 in the daytime to a mean of about 5 at night.

Figure 12-18 shows the diurnal variation of $\int$ Ndh over a period of one lunar month in winter. Large differences occur in day-to-day values, except that near sunrise all days show nearly the same total electron content. Small, short-duration, irregular changes in total content are the order of 1% to 2% and have a maximum frequency of occurrence near noon.

In the summer, the northern midlatitude total electron content increases near sunrise, remains fairly constant throughout the daytime period, and decreases slowly at about sunset. Day-to-day variations are somewhat smaller than in the winter. While the total columnar electron content is generally lower during periods of low sunspot activity, more work needs to be done to determine the dependence on solar activity.

12.4 NON-DEVIATIVE ABSORPTION

Radio waves propagating through the ionosphere undergo a varying amount of absorption. Electrons and ions that oscillate in the electromagnetic field of the wave and then collide with other particles (mainly neutral atoms and molecules) absorb energy from the wave, transferring it to thermal energy of the atmospheric constituents. An exact numerical treatment that includes all possible cases of absorption is excessively complicated. Thus, it is an established practice to distinguish between the deviative and the non-deviative absorption. If the refractive index in the medium differs appreciably from unity, absorption is called deviative (in the presence of gradients

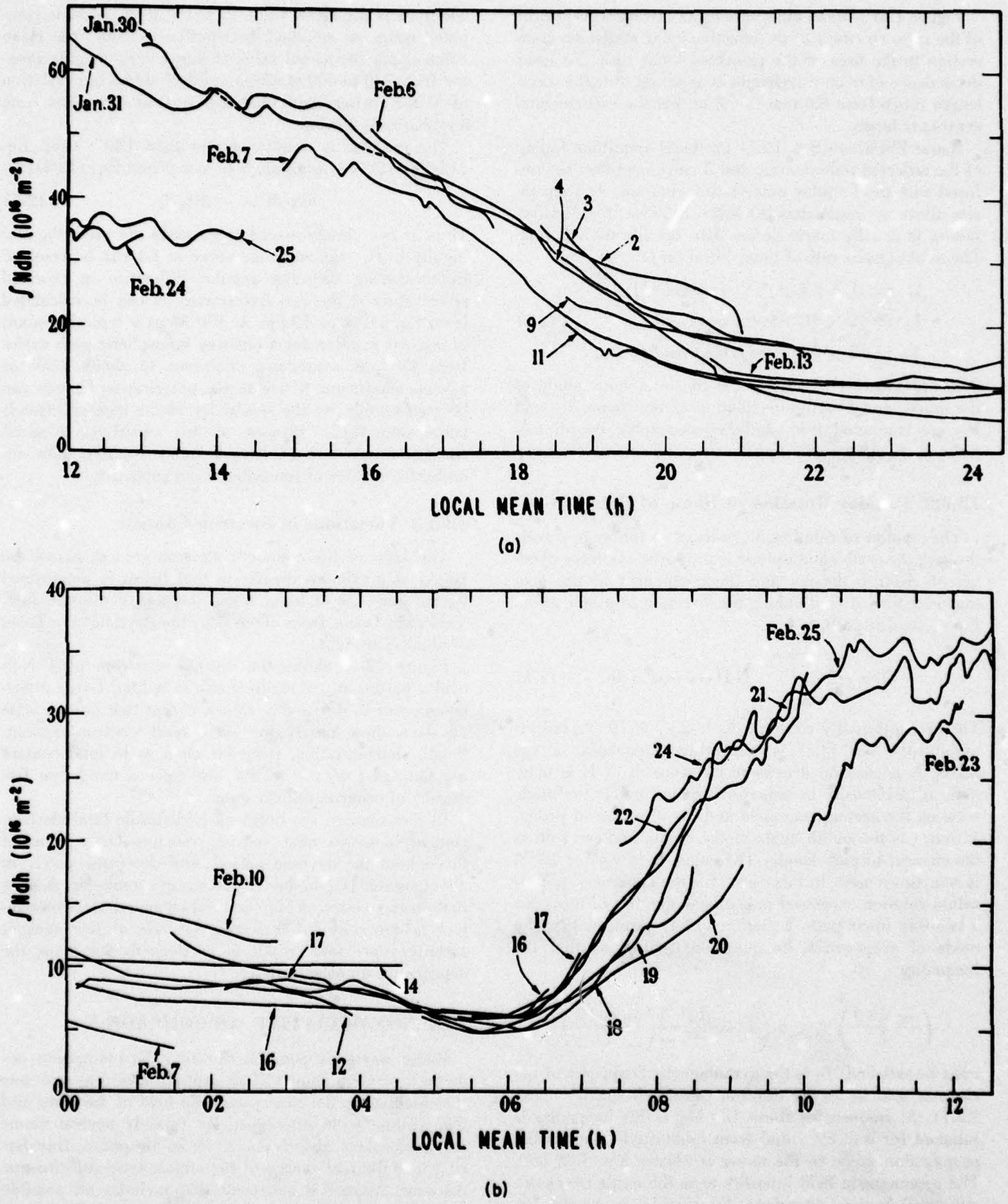


Fig. 12-18. Diurnal variation of ∫ Ndh; observations made at Manchester, England, in January and February 1960. (From J. V. Evans and G. N. Taylor, *Proc. of Royal Soc., A.*, v. 263, pp. 189-211, 1963, by permission.)

of the refractive index, a ray deviates from a straight propagation path). Non-deviative absorption is the limiting case of absorption when, for small enough electron or ion densities, the real part of the refractive index does not deviate appreciably from unity. The ray may deviate slightly from the straight path, but the absorption along the ray path can be determined independently of the deviations of the ray paths. Non-deviative absorption is applicable to all problems where the frequency of the radio wave is high enough not to approach reflection conditions.

12.4.1 Absorption in an Isotropic Medium

If effects due to the geomagnetic field and other perturbing factors are neglected, the non-deviative absorption along a given path of propagation can be computed provided the electron density along the path is known. The absorption per unit path length, ρ, is

$$\rho = \frac{\omega}{c}\,\chi, \tag{12-7}$$

where ω is the angular operating frequency ($2\pi f$) of the wave, c is the light velocity, and χ is the imaginary part of the refractive index. The usual simple formula for the refractive index in an ionized medium is

$$(n^*)^2 = (n - j\chi)^2 = 1 - \frac{\omega_N^2}{\omega^2}\,\frac{\omega}{\omega - j\nu} \tag{12-8}$$

where ω_N is the plasma angular frequency and ν is the collision frequency of the electrons with neutral particles. The electron plasma frequency is related to the electron density

$$\omega_N^2 = N_e\, e^2/m_e\, \epsilon_o, \tag{12-9}$$

where N_e is number of electrons (m^{-3}), and charge (e) and rest mass (m_e) of the electron, and the permittivity (ϵ_o) are in rationalized MKSA units. In cgs units,

$$\omega_N^2 = 3.19 \times 10^9\ [\mathrm{cm^3\ rad^2\ sec^{-2}}] \times N_e\ [\mathrm{cm^{-3}}]. \tag{12-10}$$

Combining Eq. (12-7) and (12-8), the formula for non-deviative absorption

$$\rho = \frac{\omega_N^2}{2c}\,\frac{\nu}{\omega^2 + \nu^2}, \tag{12-11}$$

is obtained. Equation (12-11) would be valid if the collision frequency were independent of the speed of the individual electrons. The electron collision frequency, however, is proportional to the energy of the electrons. A corrected formula [Huxley, 1957] for the non-deviative absorption is

$$\rho = \frac{\omega_N^2}{2c}\,\overline{\frac{\nu}{\omega^2 + \nu^2}\left(1 + \frac{2}{3}\,\frac{\omega^2 - \nu^2}{\omega^2 + \nu^2}\right)}; \tag{12-12}$$

the mean value is taken over the velocity distribution of the electrons.

In the lower ionosphere the electrons reach thermal equilibrium with the gas in a very short time. Therefore, for most cases of practical interest, a Maxwellian distribution can be assumed and the non-derivative absorption written as

$$\rho = \frac{\omega_N^2}{2c\omega}\left[\frac{5}{2}\,\frac{\omega}{\nu_p}\,C_{5/2}\left(\frac{\omega}{\nu_p}\right)\right], \tag{12-13}$$

where ν_p is the most probable collision frequency in the distribution curve. For a Maxwellian distribution,

$$\nu_p = \frac{2}{3}\,\bar{\nu}, \tag{12-14}$$

where $\bar{\nu}$ is the mean collision frequency. For tabulations of the functions $C_p(x) = \frac{1}{p!}\int_0^\infty e^p\, e^{-\epsilon}\,\frac{d\epsilon}{\epsilon^2 + x^2}$, see Dingle et al [1957]. Equation (12-13) is in agreement with the derivation accepted by most of the recent workers [Sen and Wyller, 1960; Shkarofsky, 1961]. Figure 12-19 is a plot of the term in the braces of Eq. (12-13) as a function of ω/ν_p and of $\omega/\bar{\nu}$. For comparison, the term $\frac{\omega\,\bar{\nu}}{\omega^2 + \bar{\nu}^2}$ is also plotted. For high values of $\bar{\nu}$, this term agrees with the term in braces, whereas for small values of $\bar{\nu}$, it is lower by a factor of 5/3.

The mean collision frequency of thermal electrons in air is proportional to the product of air density and temperature, or simply to the pressure. Phelps measured collisional cross sections and derived

$$\frac{5}{3}\,\bar{\nu} = 2.3 \times 10^8\, P, \tag{12-15}$$

where P is pressure in mm of mercury. This is in satisfactory agreement with rocket measurements of collision frequencies [Kane, 1959].

Different definitions of the collision frequency are in use. In addition to most probable collision frequency and the mean collision frequency, there is an effective collision frequency $<\nu>$ [Shkarofsky, 1961]. If introduced into Eq. (12-8), $<\nu>$ gives the right absorption for high operating frequencies. For the special case of air,

$$<\bar{\nu}> = \frac{5}{3}\,\bar{\nu} = \frac{5}{2}\,\nu_p. \tag{12-16}$$

In the following numerical analysis, Phelps' value of ν has been adopted together with the ARDC Model Atmosphere 1959.

Figures 12-20 and 21 are families of curves showing the parameter

$$A = \frac{1}{2c\omega}\left[\frac{5}{2}\,\frac{\omega}{\nu_p}\,C_{5/2}\left(\frac{\omega}{\nu_p}\right)\right] \tag{12-17}$$

as a function of height for different angular operating frequencies. To obtain the non-deviative absorption in neper km^{-1}, multiply the value of A (obtained from Fig. 12-20 or 12-21) by the square of the angular plasma

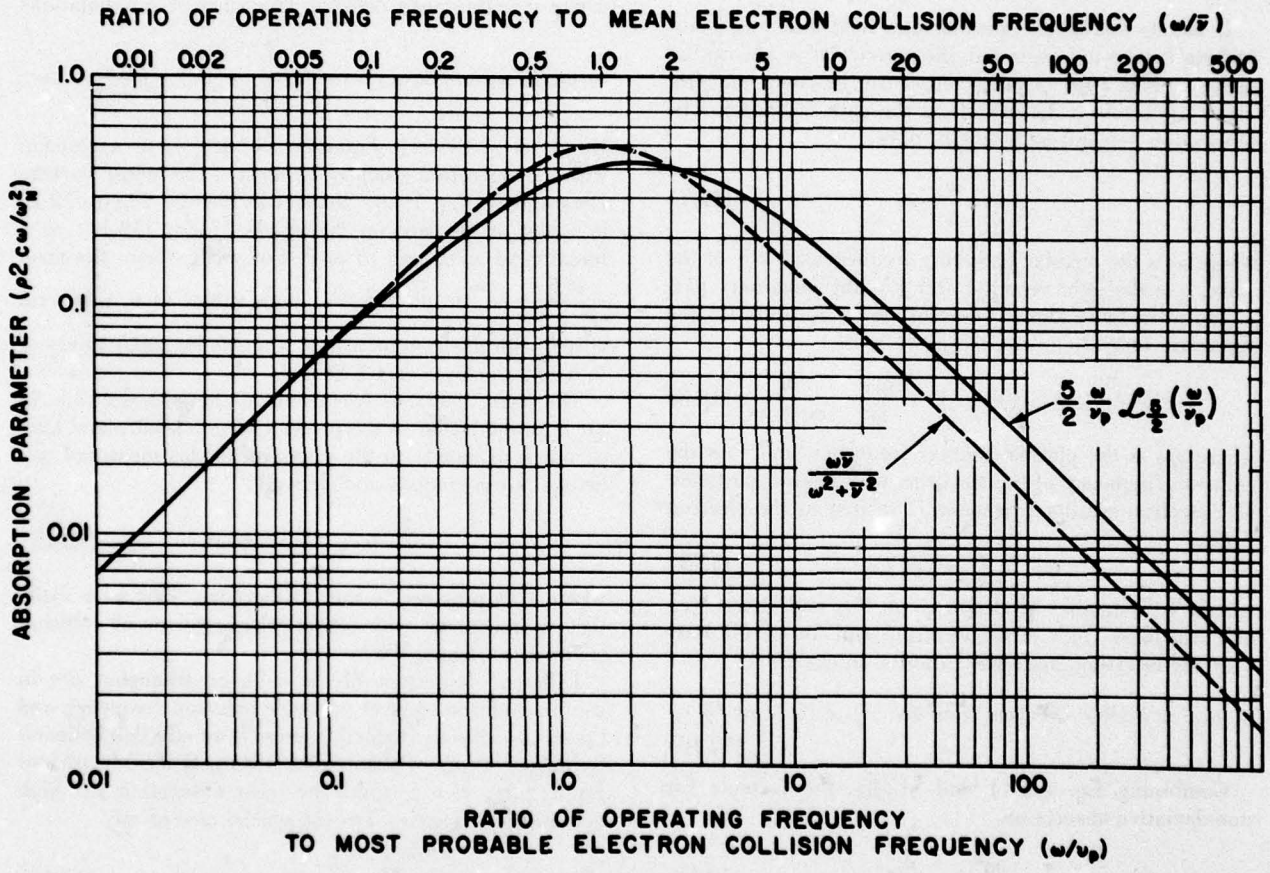
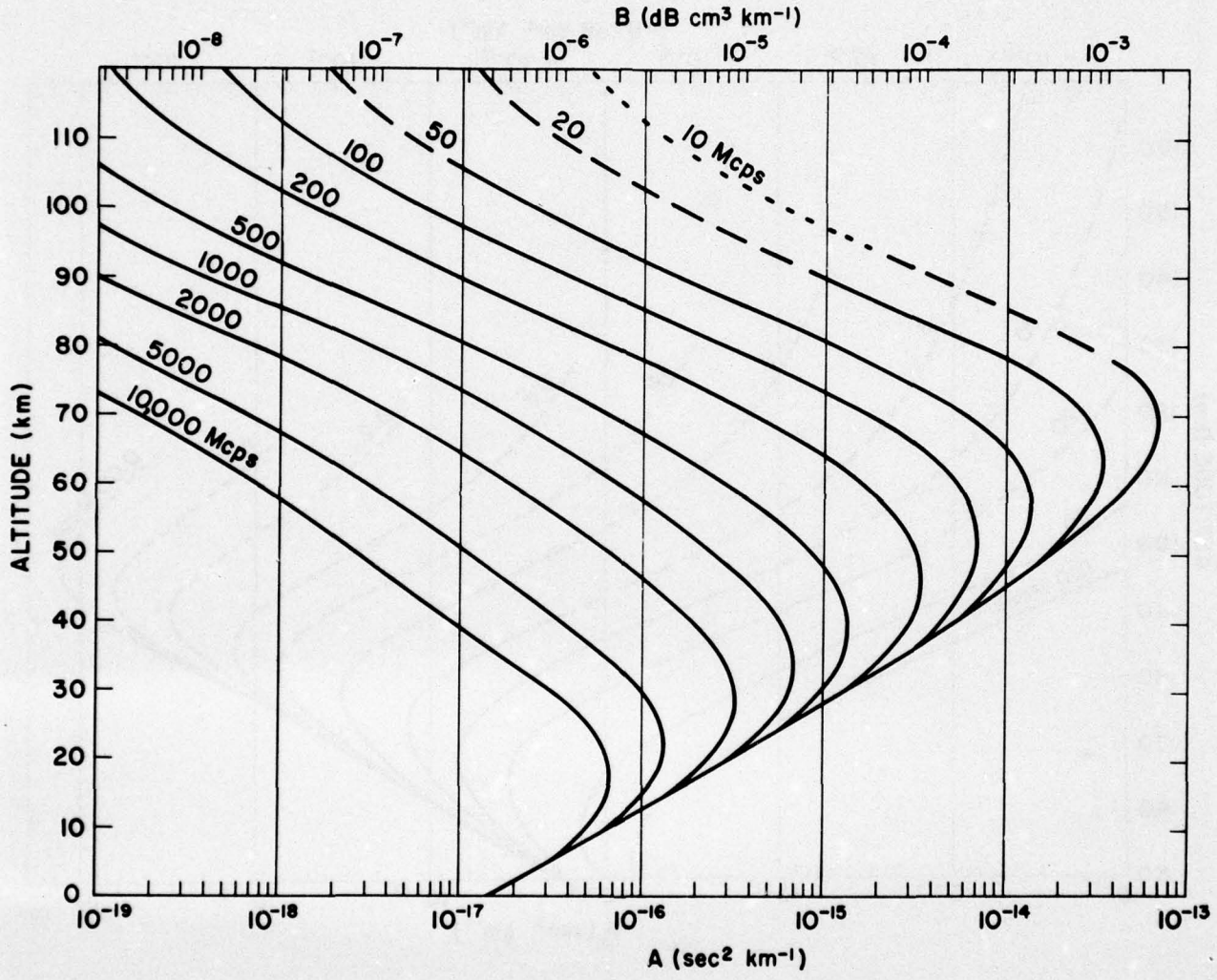
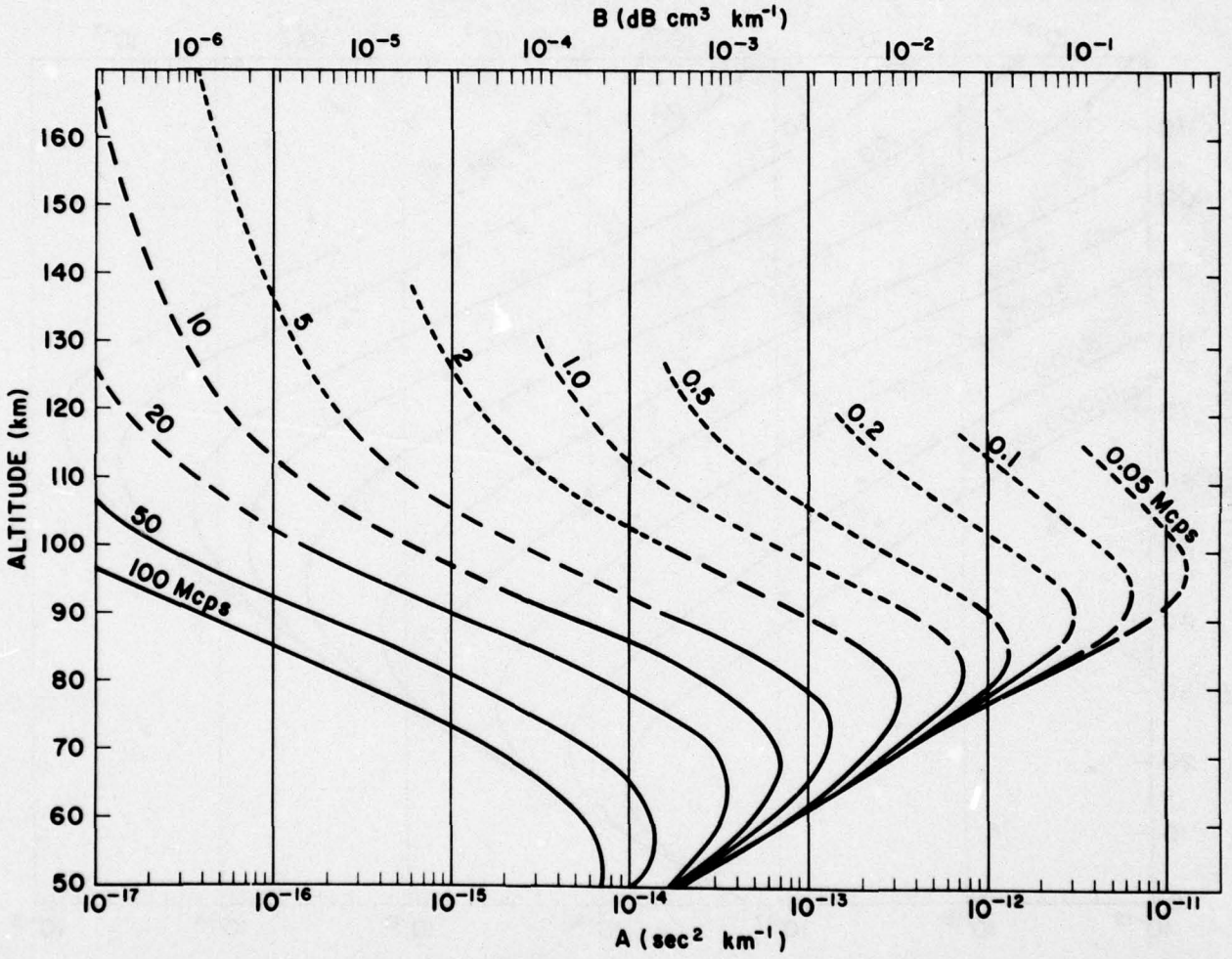


Fig. 12-19. Values of parameters in Eq. (12-11) and (12-13).



Figs. 12-20 and 12-21. Parameters A and B, for use in Eq. (12-18) and (12-19) as a function of altitudes for the various operating angular frequencies (rad Mcps) given on each curve. Dashed and dotted portions of the curves indicate non-applicability under various conditions, see Sec. 12.4.2.



Figs. 12-20 and 12-21. Parameters A and B, for use in Eq. (12-18) and (12-19) as a function of altitudes for the various operating angular frequencies (rad Mcps) given on each curve. Dashed and dotted portions of the curves indicate non-applicability under various conditions, see Sec. 12.4.2.

frequency in radians sec^{-1};

$$\rho\ [km^{-1}] = A\ [sec^2\ km^{-1}]\ \times \omega_N{}^2\ [sec^{-2}]. \quad (12\text{-}18)$$

For convenience, a second scale has been drawn (parameter B) for use when the absorption is to be measured in dB km^{-1} and electrons densities per cubic centimeter are used rather than angular frequency;

$$\rho_b\ [dB\ km^{-1}] = B\ [dB\ cm^3\ km^{-1}]\ \times N_e\ [cm^{-3}]. \quad (12\text{-}19)$$

The magnitude of B is 2.77×10^{10} A. Correction for the collision frequency due to oxygen dissociation is incorporated in the curves given in Fig. 12-20 and 12-21. In the model atmosphere used, oxygen dissociation increases very slowly starting at 90-km altitude, so that the correction is still below 10% even at 160 km.

12.4.2 Effect of the Geomagnetic Field

If the magnetic field of the earth is included in the analysis, the ionized atmosphere must be treated as an anisotropic, double-refractive medium. The refractive index, and hence the non-deviative absorption, depends on the angle θ between the direction of the magnetic field and the direction of propagation. There are two values: one for the ordinary and one for the extraordinary mode of propagation.

The situation is relatively simple when $\theta = 0$ or in the case of longitudinal propagation. The shape of the curves in Fig. 12-20 and 12-21 remains unchanged if, instead of the angular operating frequency, the parameter used is the equivalent frequency, $\omega_q = \omega \pm \omega_H$; the plus is used for the ordinary wave and the minus for the extraordinary wave. ω_H is the angular gyrofrequency of the electrons around the geomagnetic field, B. $\omega_H = eB/m_e$ (MKSA units), or in mixed cgs units, $\omega_H = eB/m_e c$ (e in statcoulomb and B in gauss). Based on the geomagnetic dipole field at a height of 100 km, the electron gyrofrequency can be found from the formula,

$$\omega_H \approx 5.55\ (1 + 3\ \sin^2 \lambda)^{1/2} \quad [rad\ Mcps], \quad (12\text{-}20)$$

where λ is the geomagnetic latitude. For more accurate values, the local magnetic field must be used. For middle latitudes, a reasonable average value of ω_H is 10 rad Mcps.

For the ordinary wave of the longitudinal propagation, Fig. 12-20 may be used with $\omega_q = \omega + \omega_H$ as parameter of the curves. For high operating frequencies ($\omega >> \omega_H$), the absorption approaches the value of the non-magnetic field case. For low frequencies ($\omega << \omega_H$), the absorption is independent of the operating frequency and determined only by the gyrofrequency, showing a maximum effectiveness of electrons around 70 km in middle latitudes. In Fig. 12-20 and 12-21 the dotted and dashed parts of the curves indicate a warning for application of the limiting case of non-deviative absorption. If it is assumed that this condition is violated when $\omega\ (\omega + \omega_H) > 5\ \omega_N{}^2$, the dotted part of the curves cannot be used for the normal nighttime ionosphere and both the dotted and dashed parts of the curves cannot be used for the normal daytime ionosphere.

Figure 12-21 may be used for the extraordinary wave of longitudinal propagation with the parameter $\omega_q = |\ \omega - \omega_H\ |$. It especially shows the behavior around the gyrofrequency. The gyrofrequency itself (i.e., $\omega_q = 0$) is not shown because the condition of non-deviative absorption is violated above 85 or 90 km. The dotted and dashed parts of the curves are plotted for frequencies above the gyrofrequency. The criterion for the validity of the non-deviative absorption is more complex. However, for the gyrofrequency itself, it can be stated as $\nu^2 > 5\ \omega_N{}^2$. It is obvious from the graphs that close to the gyrofrequency the absorption should not be calculated with the formula for non-deviative absorption.

For the case of transverse propagation ($\theta = 90°$), the ordinary mode of propagation is not affected by the presence of the geomagnetic field; therefore, Fig. 12-20 and 12-21 can be used in the original sense with $\omega_q = \omega$ as parameter.

However, for the extraordinary mode of propagation, not only the parameters but also the curves change. This can be seen from Fig. 12-22, which is a plot of an absorption factor defined by $\rho \dfrac{2\ c\omega_H}{\omega_N{}^2}$ versus the ratio $<\nu>/\omega_H$. The curve for the ordinary wave is a replot of the function $\dfrac{5}{2} \dfrac{\omega}{\nu_p} C_{5/2}\left(\dfrac{\omega}{\nu_p}\right)$ from Fig. 12-19. The two curves for the extraordinary wave were computed according to an exact formula. The asymptotic behavior of the curves is the same, approaching a 45° line for low collision frequencies as well as for high collision frequencies. The difference lies in the curvature at the maximum. The maximum is slightly less pronounced in the curves for the extraordinary wave. The curvature is expected to change somewhat with a change in frequency. Since the change of shape is relatively minor, using the curves of Fig. 12-20 and 12-21 appears justified. An appropriate equivalent frequency, ω_q, may be used as a parameter so that the asymptotic value for low collision frequencies is matched. This means that, in general, the curves are correct for the limiting cases of low and high altitudes, and that in the transition region (the region most effective for absorption) the curves will be approximately correct.

One should have this in mind when Fig. 12-20 and 12-21 are used for propagation with an arbitrary angle against the magnetic field of the earth. For convenience, an equivalent frequency for non-deviative absorption is plotted in Fig. 12-23 for the ordinary wave and in Fig. 12-24 for the extraordinary wave. Note that for operating frequencies sufficiently above the gyrofrequency, the equivalent frequency can be represented with good accuracy by $\omega_q = \omega \pm \omega_L$; ω_L is the longitudinal component of ω_H. The behavior of the curves for the extraordinary wave is somewhat complicated below the gyrofrequency. However, in this frequency range, the concept of an equivalent frequency has only limited application because of the restrictive conditions for non-deviative absorption (too high electron density in the critical height range).

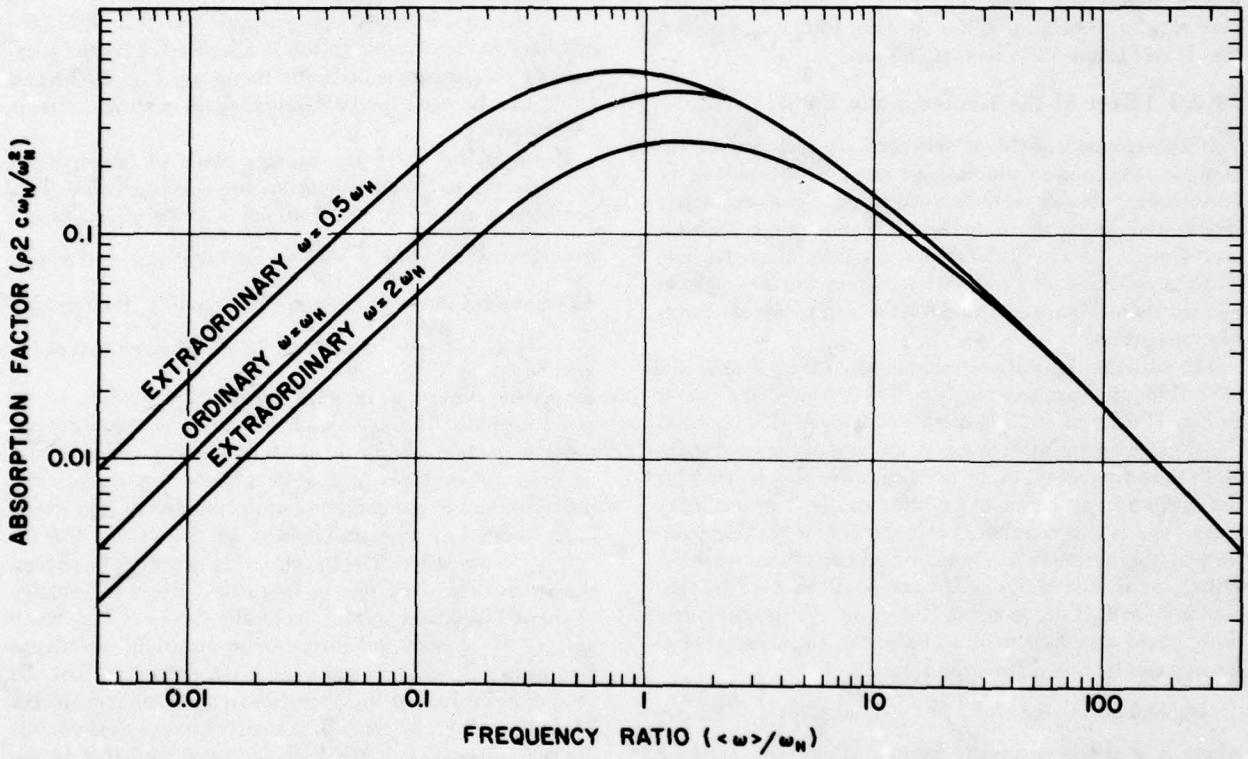


Fig. 12-22. Absorption factor versus the ratio of effective collision frequency to gyromagnetic angular frequency of electrons.

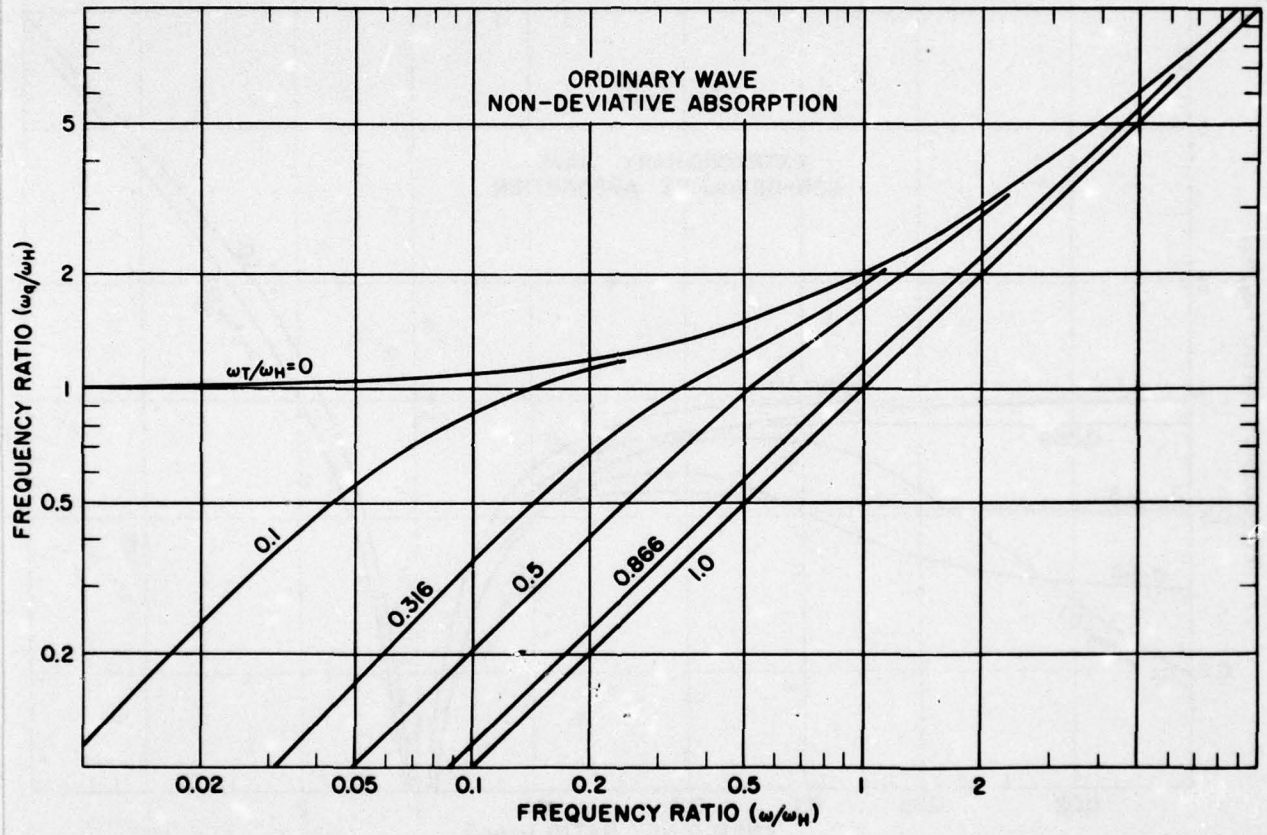


Fig. 12-23. Ratio of operating frequency to electron gyromagnetic frequency vs ratio of equivalent frequency to electron gyromagnetic frequency, for ordinary wave and various values of ω_T/ω_H.

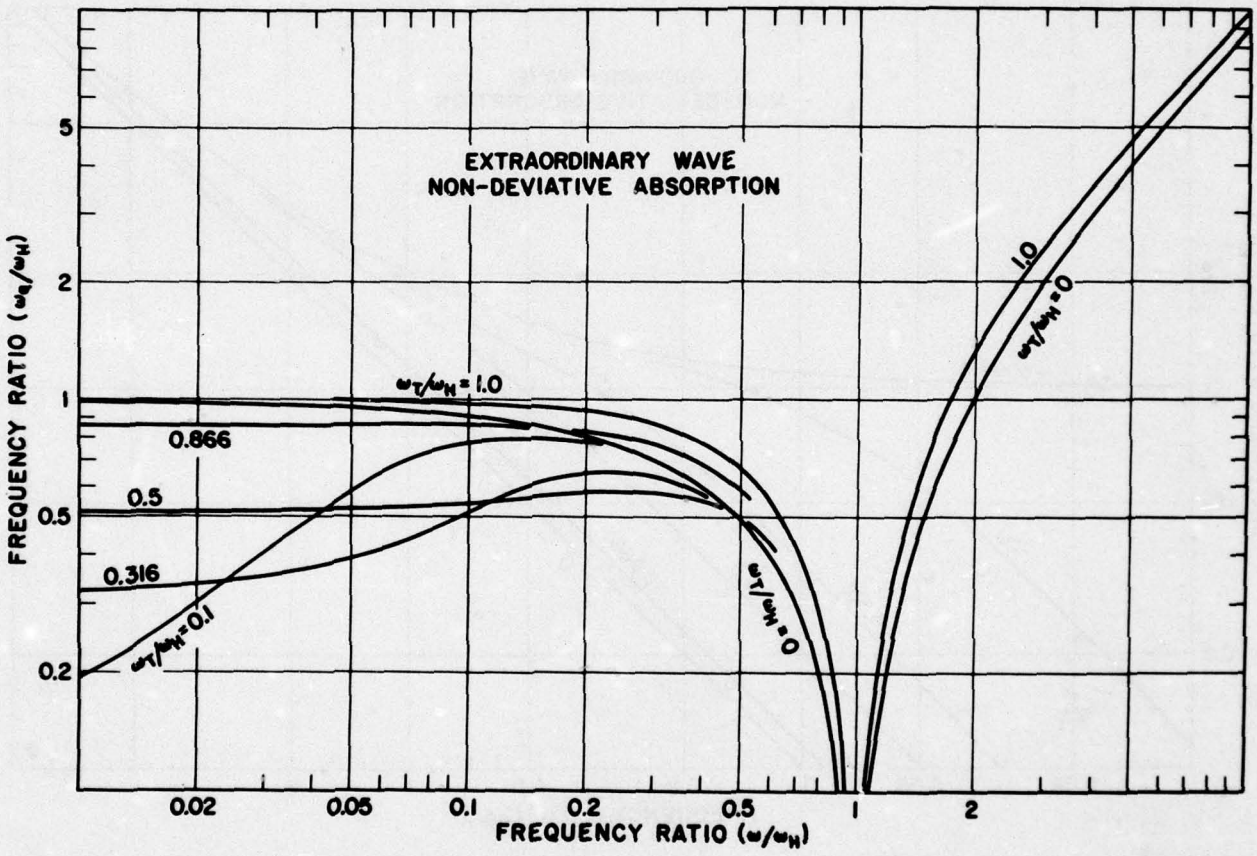


Fig. 12-24. Ratio of operating frequency to electron gyromagnetic frequency vs ratio of equivalent frequency to electron gyromagnetic frequency, for extraordinary wave and various values of ω_T/ω_H.

The procedure for determining the absorption in the case of propagation at an arbitrary angle against the magnetic field is as follows:

(1) From Fig. 12-23 or 12-24, select an equivalent frequency ω_q depending on the angular operating frequency ω and on the transverse component of ω_H.

(2) Find the appropriate curve for the absorption factor from Fig. 12-20 or 12-21.

(3) Make sure that the criterion for non-deviative absorption, which in analogy to the case of longitudinal propagation may be stated as $\omega_N^2 << \omega\omega_q + <\nu>^2$, is met for values of the effective collision frequency shown in Fig. 12-25.

(4) Multiply the absorption factor of Fig. 12-23 or 12-24 by the square of the plasma frequency or by the electron density, respectively, to obtain the absorption per unit path length.

12.4.3 Effect of Electron Collisions With Ions

So far only collisions with neutral particles have been considered. Collisions with ions must be considered in the upper altitudes, where the number density of neutral particles becomes small enough, or in the special case of extremely high ion densities.

Several formulas are available in the literature. They vary slightly depending on the assumed maximum distance for the Coulomb force, which is limited by the interaction of ions and electrons in the neutral plasma. For numerical purposes, a formula for the effective collision frequency of electrons with ions [Nicolet, 1953] slightly modified by considering the total number of ions ($N_i = N_+ + N_-$) is adopted.

$$<\nu_{ei}> = N_i\, T^{-3/2}\, [33.9 + 5.44 \ln (T/N_i^{1/3})], \qquad (12\text{-}21)$$

where T is the electron temperature in °K and N_i is in cm^{-3}.

Figure 12-25 is a plot of Eq. (12-21) for different densities together with the collision frequency with neutrals, $<\nu_{eo}>$. The shape of the curves is mainly determined by the temperature dependence, showing a maximum at the height of the temperature minimum.

In the natural ionosphere the collisions with ions can be neglected up to the height of the E layer maximum. Above about 120 km the effect of the ions can be taken into account by adding the effective collision frequencies with neutrals and with ions; $<\nu> = <\nu_{eo}> + <\nu_{ei}>$. The absorption can then be computed from the formula for small collision frequencies ($<\nu> << \omega_q$),

$$\rho = \frac{\omega_N^2}{2c}\,\frac{<\nu_{eo}> + <\nu_{ei}>}{\omega_q}\,. \qquad (12\text{-}22)$$

In the range where this formula holds, another method would be to use the curves of Fig. 12-21 and 12-22 and to multiply the value found by the factor

$$\frac{<\nu_{eo}> + <\nu_{ei}>}{<\nu_{eo}>}\,.$$

This factor can be taken from Fig. 12-25 provided the ion density, which in this height range is normally equal to the electron density, is known.

Equations (12-15), (12-21), and (12-22) are applicable also for the non-deviative absorption in the F layer. However, the curves have not been extended to these heights because of the uncertainties in the electron temperature values.

Conceivably, under conditions of abnormal modifications of the ionosphere, cases of higher electron-ion collision frequencies might be encountered. Such cases are rare, however. A detailed treatment of the absorption in such a general case is given by Shkarofsky [1961].

12.4.4 Absorption Due to Collisions of Ions With Neutral Particles

Under normal ionospheric conditions, the absorption is due to collisions of electrons wth neutral particles or with ions. Collisions between molecular particles can be safely neglected for the propagation of radio waves because of the much higher mobility of the electrons. A measure of the electromagnetic effect is the square of the plasma frequency of the ion. In cgs units

$$\omega_{Ni}^2 = 4\pi e^2 N_i/m_i,$$

or in rationalized MKSA units, (12-23)

$$\omega_{Ni}^2 = e^2 N_i/m_i\epsilon_o;$$

where N_i is the number of singly charged ions of mass m_i per unit volume. The effect of the ions is, therefore, reduced by the ratio of mass of electrons to mass of ions (m_e/m_i) and can only be compensated by a higher number density N_+. Unless the negative ion ratio N_-/N_e approaches the order of magnitude of the mass ratio m_i/m_e (about 50,000 in air), the ions can be neglected. In the atmosphere, such a high ion density can be expected only in the lower part of the D region under severely disturbed conditions. We can assume, therefore, that due to the high density of the air, only collisions with neutral particles have to be considered, and simply add the contributions of the different kinds of ions. The formula for the non-deviative absorption is

$$\rho = \rho_e + \Sigma\,\rho_i, \qquad (12\text{-}24)$$

where ρ_e is the absorption due to electrons as computed previously. ρ_i depends on the collision cross section of the particular kind of ion in air.

In view of the uncertainties of the kind of ion and of the exact value of the collision cross section, the collision frequency between neutral air particles is a good approximation to use. According to the ARDC Model Atmosphere 1959, it follows the formula

$$\bar{\nu} = 2.775 \times 10^{-10} \times \sqrt{T/300} \times N. \qquad (12\text{-}25)$$

Figure 12-26 is a family of curves of parameters A_i or B_i for ion collisions corresponding to Fig. 12-20 for electron collisions.

$$\rho_i\,[km^{-1}] = A_i\,\Sigma\,\omega_{Ni}^2, \qquad (12\text{-}26)$$

where $\Sigma\,\omega_{Ni}^2$ is the sum of the squares of the ion plasma

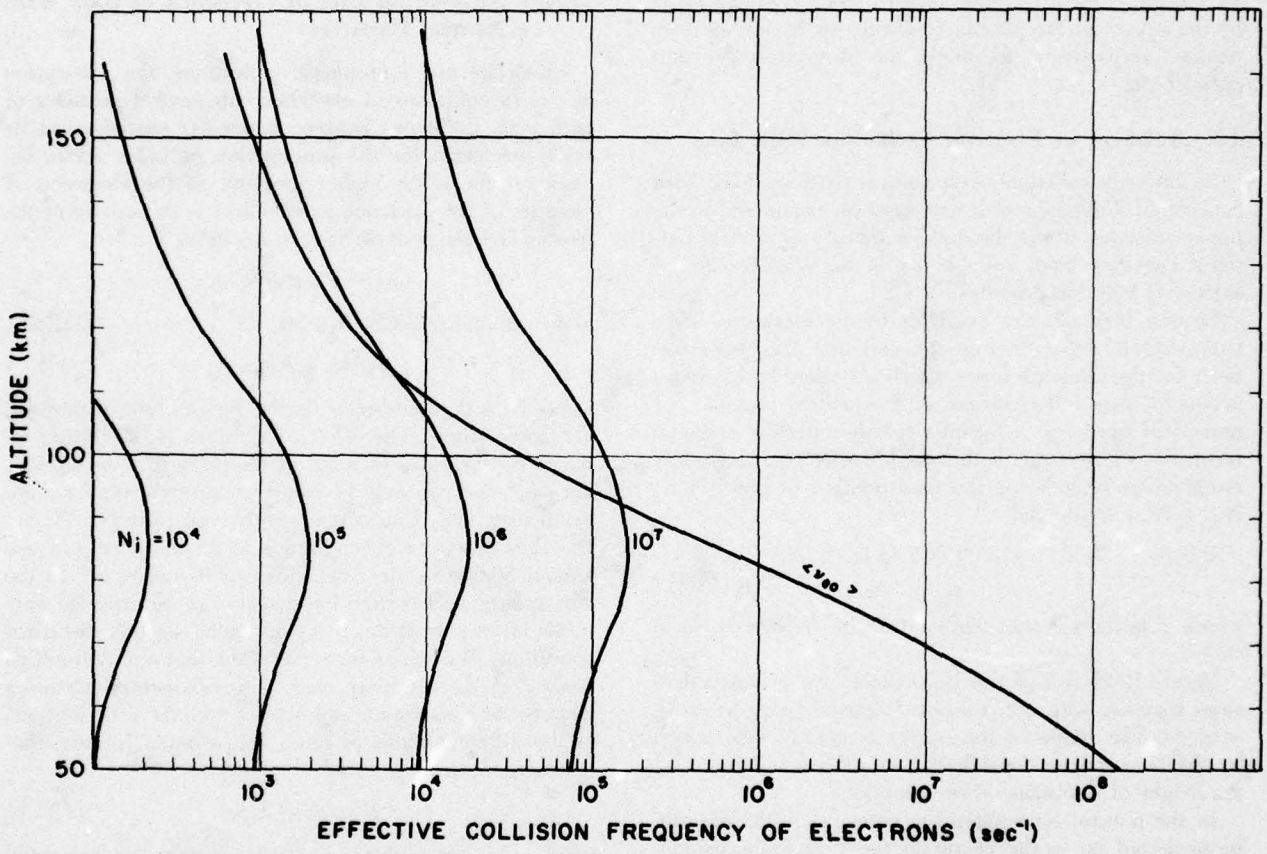


Fig. 12-25. Effective collision frequency, $<\nu>$, with ions for different ion densities (N_I), and with neutrals ($<\nu_{eo}>$) as a function of altitude.

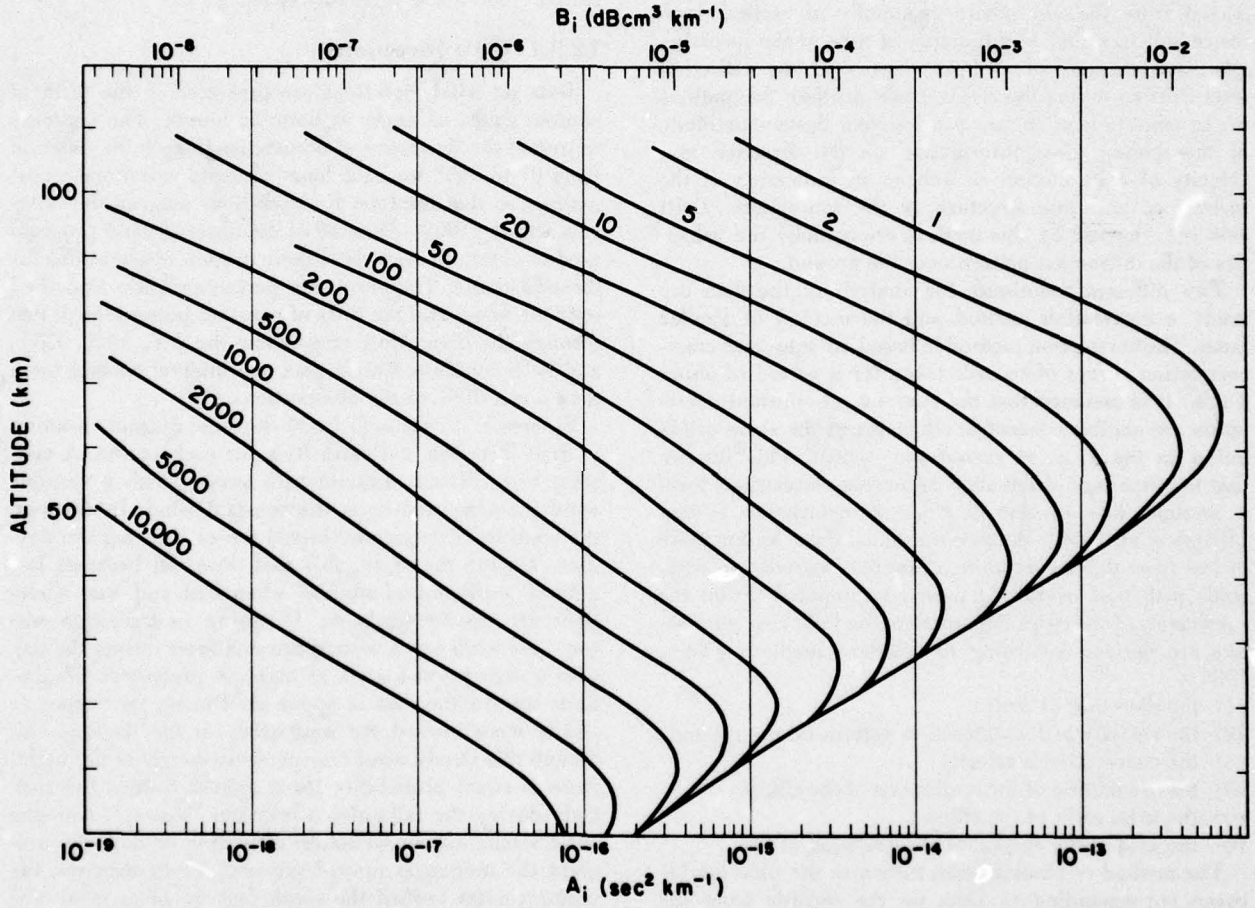


Fig. 12-26. Parameters A_i and B_i for use in Eq. (12-26) and (12-27) as a function of altitude for the operating angular frequencies (rad Mcps) given on each curve.

frequencies. Another possibility is to use the scale for B_i and to compute the absorption with the formula

$$\Sigma \rho_i \left[\frac{dB}{km}\right] = B_i \Sigma N_i m_e/m_i. \qquad (12\text{-}27)$$

The summations must be over the total number of positive and negative ions.

12.5 IONOSPHERIC WINDS

Data in this section are from observations by radio wave fading techniques. With this method, a signal is reflected from the ionosphere essentially at vertical incidence and recorded as a function of time at the receiving site. Irregularities of electron density at the reflection level drifting across the receiver site produce fluctuations in the amplitude of the recorded signal. Systematic study of this fading gives information on the direction and velocity of drift motion as well as an indication of the turbulence and fine structure in the ionosphere. Drift velocities derived by this method are actually the velocities of the diffraction pattern over the ground.

Two different techniques for analysis of the data are used: a correlation method and the method of similar fades. The correlation method is based on auto- and cross-correlation curves of records taken for a period of about 3 min. It is assumed that the contours of constant correlation are similar concentric ellipsoids of the same orientation in the x, y, vt coordinate system. This implies that the time lags of the auto- and cross-correlations form a straight line in the τ, $\tau'^2 - \tau^2$ coordinate system [Briggs et al, 1950]. Because the actual data deviate more or less from this assumption, a family of correlation ellipsoids with best overall fit must be computed. From the coefficients of the ellipsoid equation, the following parameters are derived according to standard methods [Yerg, 1955]:

(1) the direction of drift;
(2) the velocity of the diffraction pattern on the ground;
(3) the characteristic velocity;
(4) the orientation of the major axis of the ellipse;
(5) the axial ratio of the ellipse;
(6) the area of the ellipse for a correlation of 0.5.

The method of similar fades measures the time lag between corresponding maxima on the records from the three spaced receivers. From the receiver separation and the time lags, the drift velocity and drift direction are derived [Mitra, 1949].

Sufficient stations are not available to obtain data on global circulation patterns. The information on the drift direction and drift velocity was selected from three locations: Puerto Rico; Freiburg, Germany; and Rostov, Russia. The geomagnetic latitudes of these stations are about 30°N, 50°N and 45°N, respectively. The transmitted frequencies used are 2.33 Mcps, 2 to 4 Mcps, and 2.2 Mcps, respectively. Thus the reflections must occur from the E region (around 110 km). It is not possible to state precisely the height of reflection, because the reflection level is constantly changing. The variation in the level could be anywhere between 10 and 20 km. At night all reflections at these frequencies must occur from sporadic E since these operating frequencies are too low for E-region reflection at night. Because of the nature of the variation of the parameters being studied, the months were grouped into seasons: Winter (Nov., Dec., Jan., Feb.), Spring (Mar., April), Summer (May, June, July, Aug.), and Fall (Sept., Oct.).

The Puerto Rico data represent observations taken from March 1958 through February 1959. The Freiburg data are selected observations taken from 1957 through 1961. The Rostov observations [Pozigun, 1960] are from September 1958 through August 1959.

12.5.1 Drift Directions

Data on wind directions are presented in the form of contour maps of angle vs hour or month. The contours represent the frequency of occurrence in each 30° interval from 0° to 360° for each hour (diurnal variations), normalized so that the total for each hour over all the intervals adds to 100%. Because of the observational program used to obtain the raw data, there are few observations for the odd hours. Therefore, the percentages are smoothed over the hours and the lines of constant percentage drawn through the data. Most maps show the 5%, 10%, 15%, and 20% contours. Rarely does any interval contain more than about 20% of the observations.

Figures 12-27 through 12-30 show the diurnal variation of drift direction at Puerto Rico for each season. A constant wind direction varies with season, with a variable wind superimposed upon the constant wind. In summer, the wind is fairly steady toward the east during the daytime. During the night, this east direction becomes less defined until around sunrise, when east and west directions are equally probable. In spring (a transition season), the tendency is toward the southwest during the day with a shift toward south at night. A preference for motions toward the east is apparent. During the winter, a steady wind toward the west exists in the daytime. Although this steady wind may persist throughout the night, there is equal probability for a motion toward the east. Only during the fall (also a transition season), does the wind vector appear to rotate with time of day. At midnight the motion is toward the east. From then on, the vector rotates toward the south and by noon is toward the west. The rotation continues, but during the hours before midnight the motion toward the west seems to persist.

Figures 12-31 through 12-34 show the diurnal variation in the drift direction at Freiburg for each season. Here the wind direction shows a strong tendency toward the east during a summer day with a shift toward south during a summer night. In the winter months, the direction is not so well defined as it is in Puerto Rico, although there is a strong tendency toward the southwest during most of the hours. Around sunset, the wind vector appears to rotate rapidly from southwest to west, to north, to east, and back to southwest. At Freiburg, the equinoctial months display a marked semi-diurnal variation that is

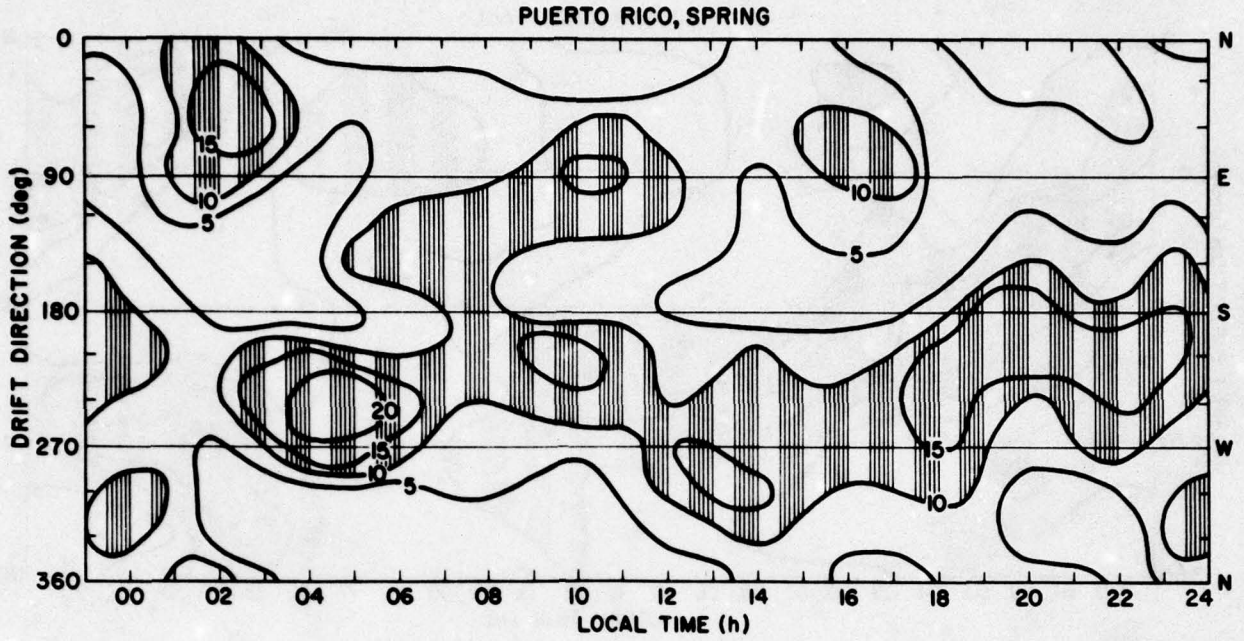


Fig. 12-27. Diurnal variation of drift direction at Puerto Rico, spring.

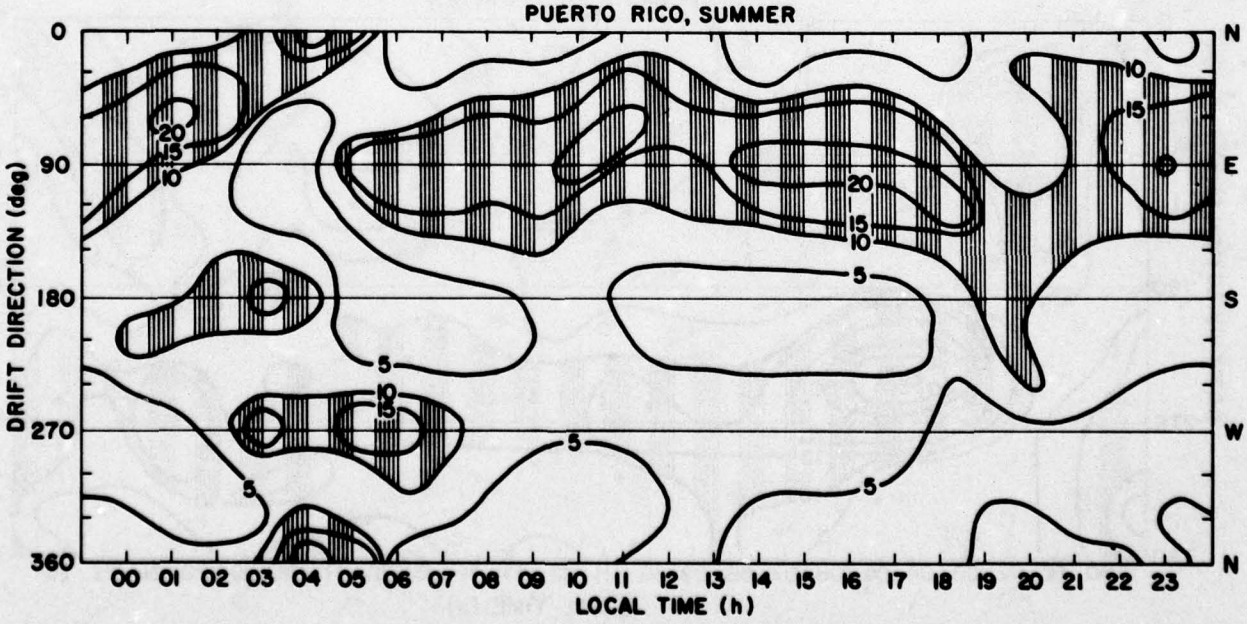


Fig. 12-28. Diurnal variation of drift direction at Puerto Rico, summer.

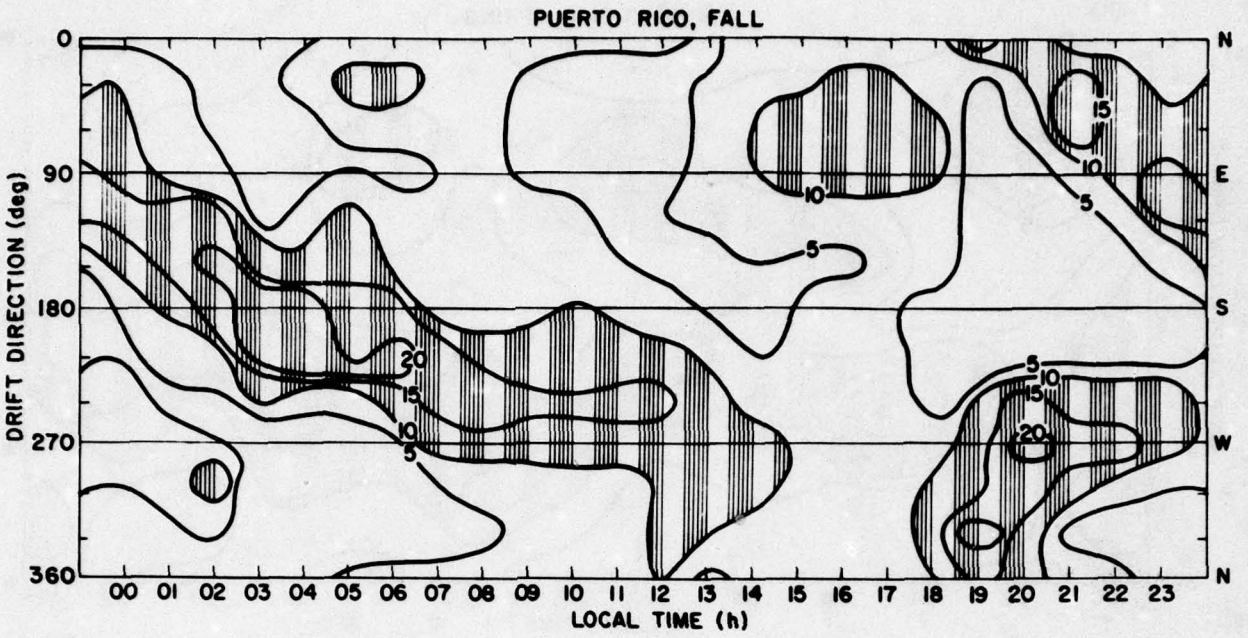


Fig. 12-29. Diurnal variation of drift direction at Puerto Rico, fall.

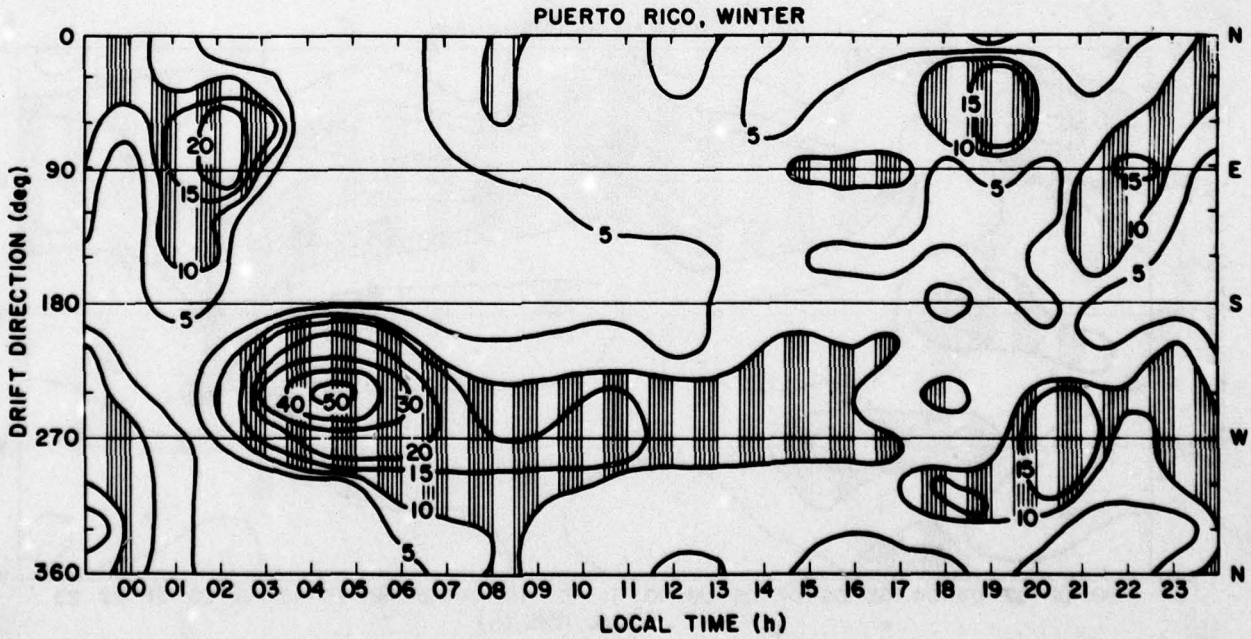


Fig. 12-30. Diurnal variation of drift direction at Puerto Rico, winter.

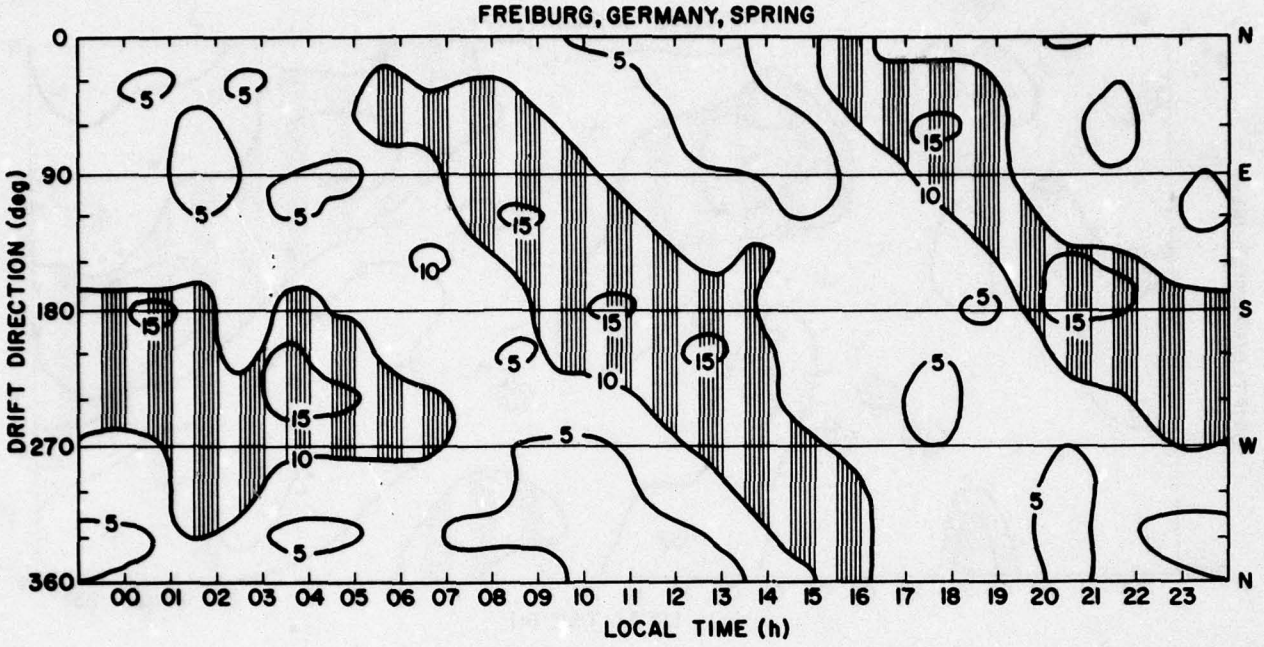


Fig. 12-31. Diurnal variation of drift direction at Freiburg, Germany, spring.

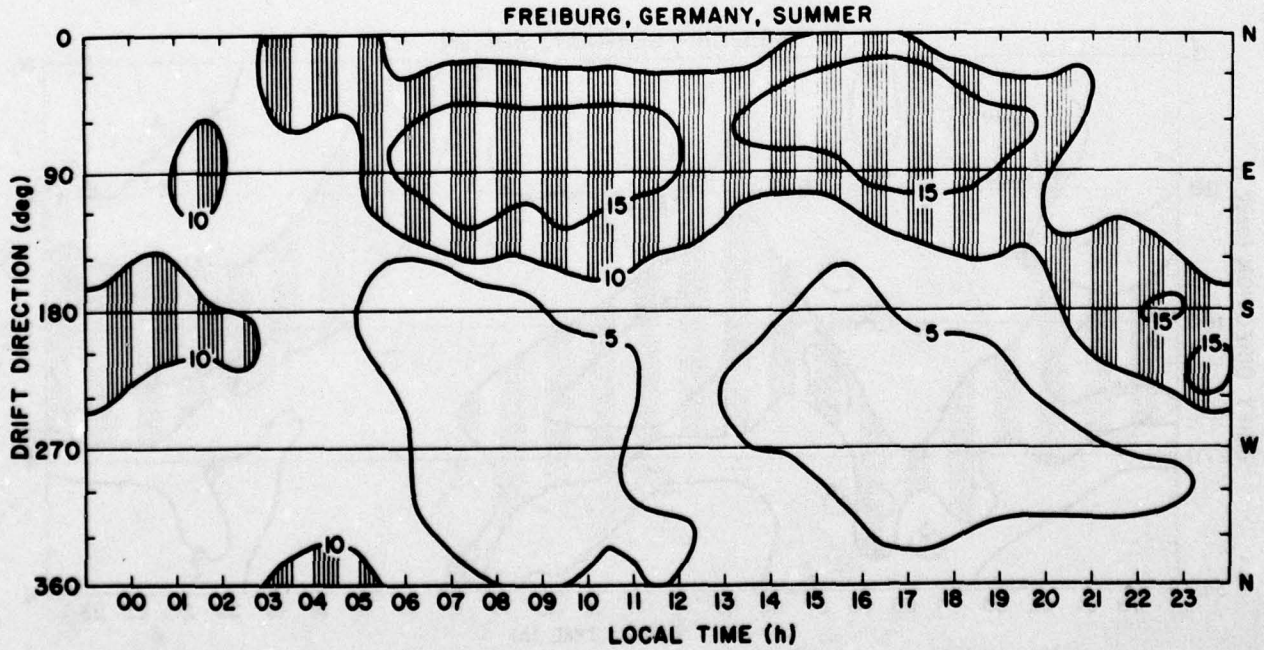


Fig. 12-32. Diurnal variation in drift direction at Freiburg, Germany, summer.

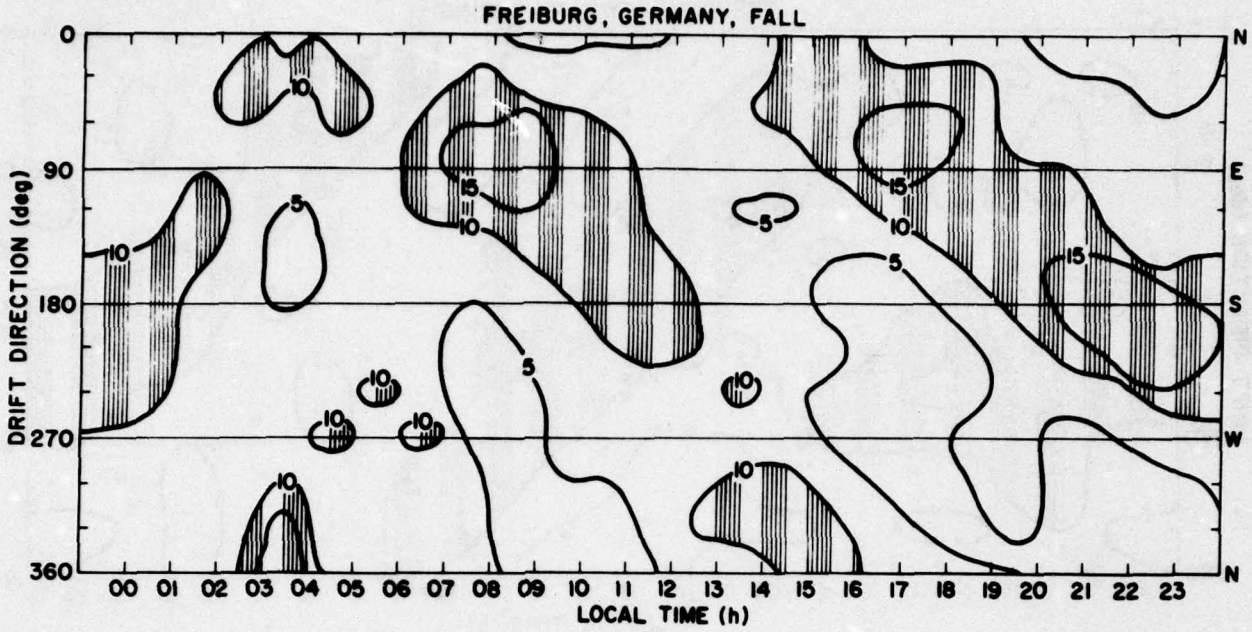


Fig. 12-33. Diurnal variation in drift direction at Freiburg, Germany, fall.

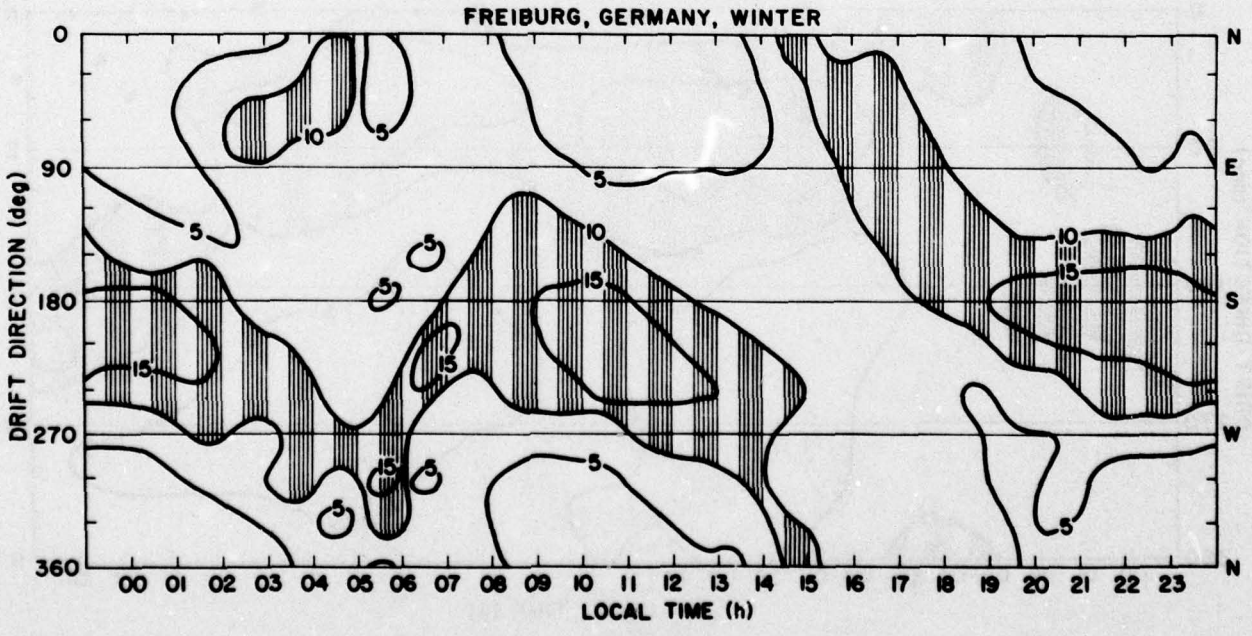


Fig. 12-34. Diurnal variation in drift direction at Freiburg, Germany, winter.

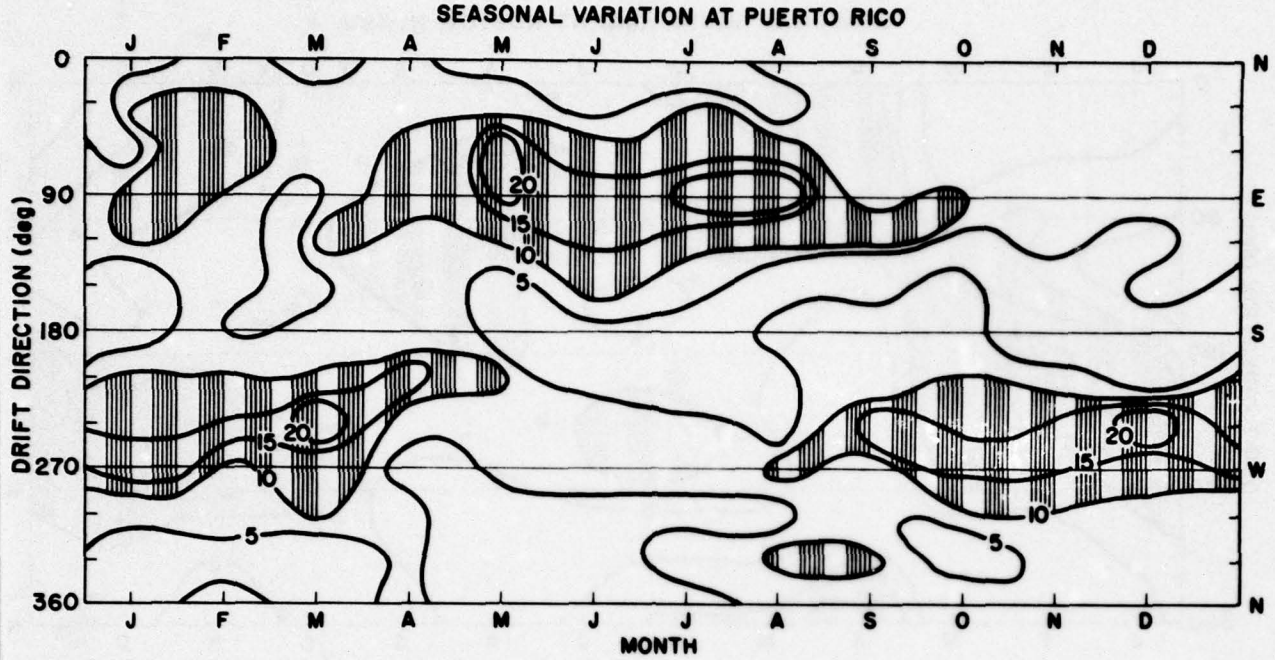


Fig. 12-35. Seasonal variation of drift direction at Puerto Rico.

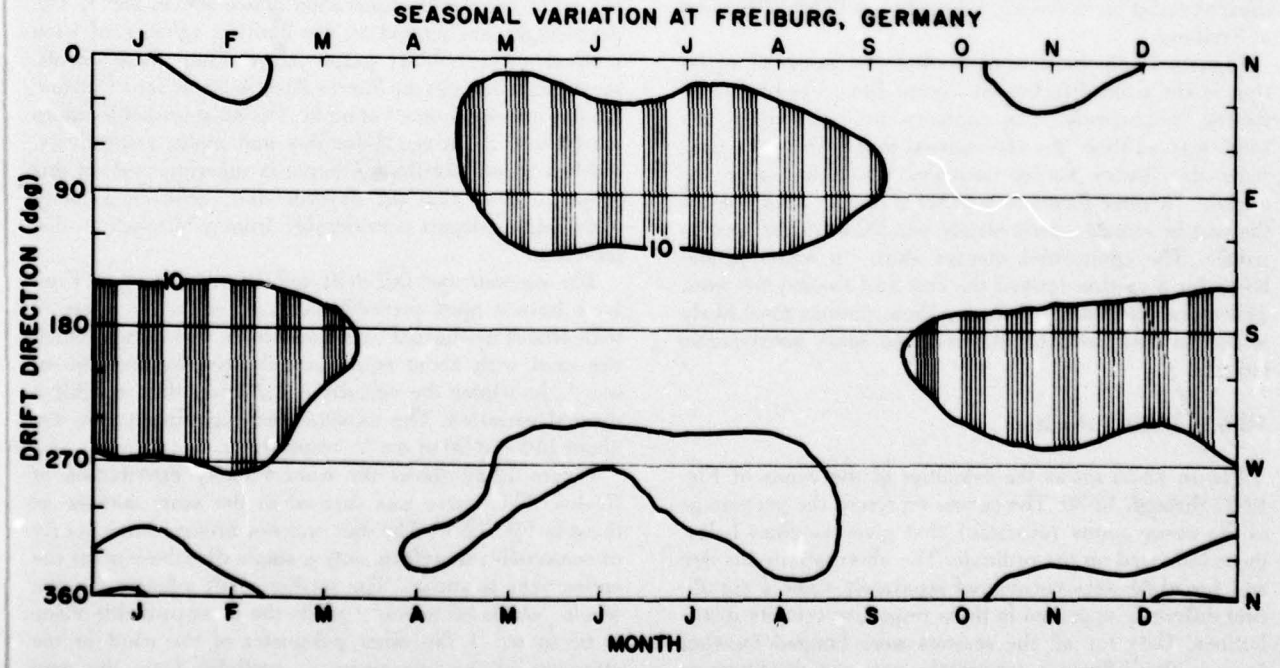


Fig. 12-36. Seasonal variation in drift direction at Freiburg, Germany.

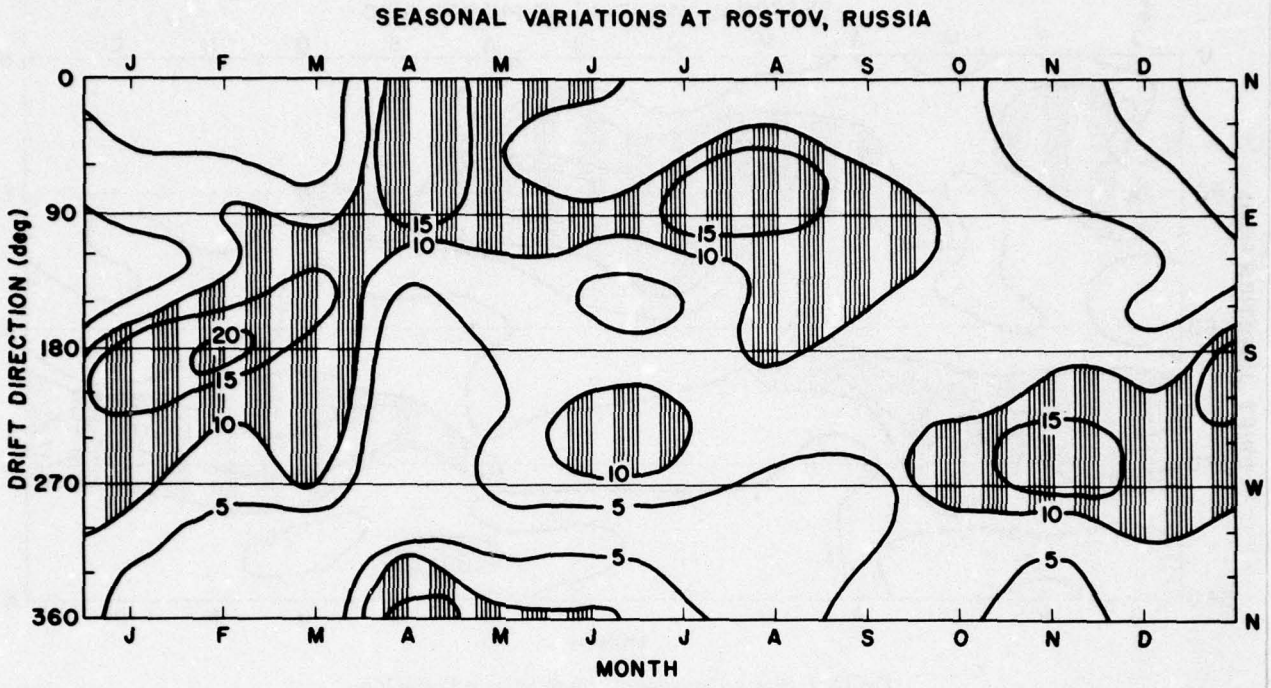


Fig. 12-37. Seasonal variation in drift direction at Rostov, Russia.

not apparent at Puerto Rico. The wind vector undergoes a complete rotation during the day and again during the night. In general, there is considerable similarity in the diurnal variation in the wind direction at Puerto Rico and at Freiburg.

Figures 12-35 through 12-37 show the seasonal variation in the wind direction at Puerto Rico, Freiburg, and Rostov, respectively. The contours were drawn in the same way as those for the diurnal maps. Only the data from the Rostov station required smoothing over the angles. All three locations exhibit a steady wind toward the east in summer and a steady wind toward the west in winter. The equinoctial months show an equal probability for a motion toward the east and toward the west. The similarity that exists among these stations most likely is due to their location at about the same geomagnetic latitude.

12.5.2 Drift Velocities

Figure 12-38 shows the velocities of the winds of Fig. 12-27 through 12-30. The curves represent the percentage of the observations (abscissa) that give velocities below those indicated on the ordinate. The observations for day and for night were considered separately since a significant difference appeared in these respective velocity distributions. Data for all the seasons were lumped together because the difference among the seasonal distributions was insignificant. The curves include the total number of observations with velocities within the range of 0 to 80 m sec^{-1} (increments of 10 m sec^{-1}); 80 to 200 m sec^{-1} (increments of 20 m sec^{-1}); one range from 200 to 300 m sec^{-1}; and every observation above 300 m sec^{-1}. The percentages are plotted at the limiting velocity of each interval on probability graph paper. From these curves, the median velocity at Puerto Rico is 75 m sec^{-1} during the day and 45 m sec^{-1} at night. The most probable values are 65 and 24 m sec^{-1} for day and night, respectively. A Maxwellian distribution curve is superimposed on this graph to show that the daytime and nighttime velocity distributions depart considerably from a Maxwellian distribution.

The summer and fall drift velocities recorded at Freiburg have a most probable value of about 50 m sec^{-1} with almost no diurnal variation. In the spring two velocities exist with about equal probability: 50 and 100 m sec^{-1}. In winter the velocity distribution does exhibit a diurnal variation. The daytime and nighttime values are about 110 and 90 m sec^{-1}, respectively.

Figure 12-39 shows the wind velocity distribution at Rostov. This curve was derived in the same manner as those in Fig. 12-38. The data was not broken down hourly or seasonally; therefore, only a single distribution for the entire year is shown. The median drift velocity for the whole year is 80 m sec^{-1} while the most probable value is 65 m sec^{-1}. No other parameter of the wind or the structure of the ionosphere is available from the data recorded at Rostov.

12.5.3 Characteristic Velocity

The characteristic velocity gives a quantitative measure of the amount of random change taking place in the medium. The correlation method employed to reduce the Puerto Rico data allows for the computation of this parameter. (The method of similar fades used to reduce the Freiburg data cannot give this velocity.)

Figures 12-40 and 12-41 were constructed in the same manner as the drift velocity curves. Figure 12-40 shows that the characteristic velocity distribution for summer was sufficiently different from that for the other three seasons to require a separate curve. From Fig. 12-40, the median velocity for daytime is 59 m sec^{-1} and for nighttime is 54 m sec^{-1}. The most probable value for day is 51 m sec^{-1} and for night is 50 m sec^{-1}. In the daytime distribution, about 11.5% of the observations are above 100 m sec^{-1}, while 4.5% of the nighttime velocity distributions are above 100 m sec^{-1}.

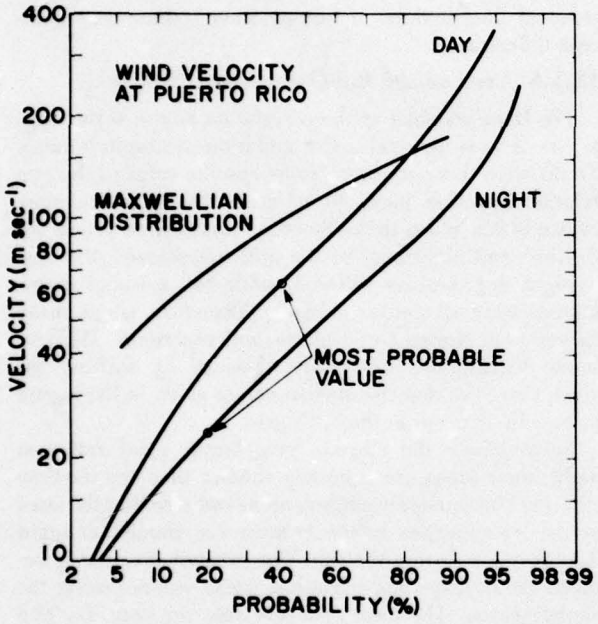


Fig. 12-38. Wind velocity distribution at Puerto Rico.

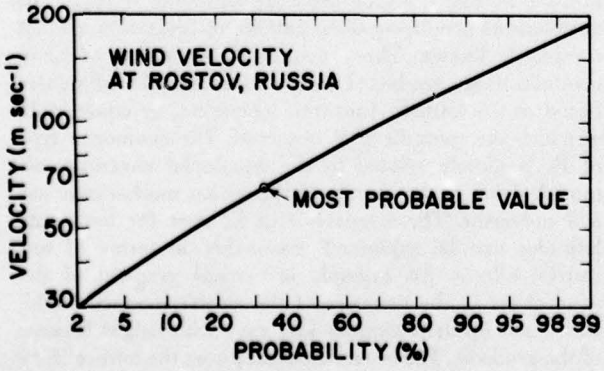


Fig. 12-39. Wind velocity distribution at Rostov, Russia.

Figure 12-41 shows the characteristic velocity distributions for fall, winter, and spring. One curve combining all three seasons is drawn for daytime and one for nighttime. To obtain the curve for any one of the seasons, the given curve is shifted parallel to itself until the median value (given in the legend) falls on the 50% grid. The daytime curve requires almost no shifting since the median values for the three seasons are about equal, but the nighttime medians vary over a 30 m sec^{-1} range.

The ratio of the drift velocity to the characteristic velocity is referred to as the turbulence ratio. Figure 12-42 is a scatter diagram of a plot of the drift velocity versus the characteristic velocity. From the distribution of the observations, a definite correlation exists between these two parameters of the winds. When the drift velocity is small, the characteristic velocity is also small. When the drift velocity is large, the characteristic velocity also tends to be large.

12.5.4 Orientation of the Correlation Ellipse

The orientation of the correlation ellipse is one of the parameters that describes the characteristics of the diffraction pattern on the ground. In the correlation analysis, the correlation surfaces are assumed to be concentric ellipsoids. This parameter is the tilt angle of the ellipses, which are the cross sections of these ellipsoids cut out by planes of constant time.

Figure 12-43 is a histogram showing the distribution of this angle for day and night at Puerto Rico. It includes a plot of all the observations that occurred in 30° intervals from 0° to 180°. The length of the bar corresponds to the number of observations within the interval. The most probable angle in the daytime is in the range 50° to 65° east of north, or the equivalent, 230° to 245° east of north. The nighttime values appear to be fairly evenly distributed over all the angles with only a slight preference for a N-NE or S-SW orientation.

Figure 12-44 is a scatter diagram of a plot of the drift direction versus the orientation angle of the ellipse. The two preferred directions of the drift are obvious: one around east and one around west. The preponderance of ellipse orientation angles around 60° is also apparent. When the drift direction is not in one of the preferred directions, however, the ellipse orientation angle is scattered over the entire range from 0° to 180°. From the Freiburg data, the most probable orientation of the major axis of the ellipse is about 10° west of north.

12.5.5 Axial Ratio of Correlation Ellipses

The axial ratio of the correlation ellipse is another parameter that gives some information on the structure. Figure 12-45 is a probability plot of this quantity. Day and night curves are presented because of the significant difference between the two distributions of this parameter.

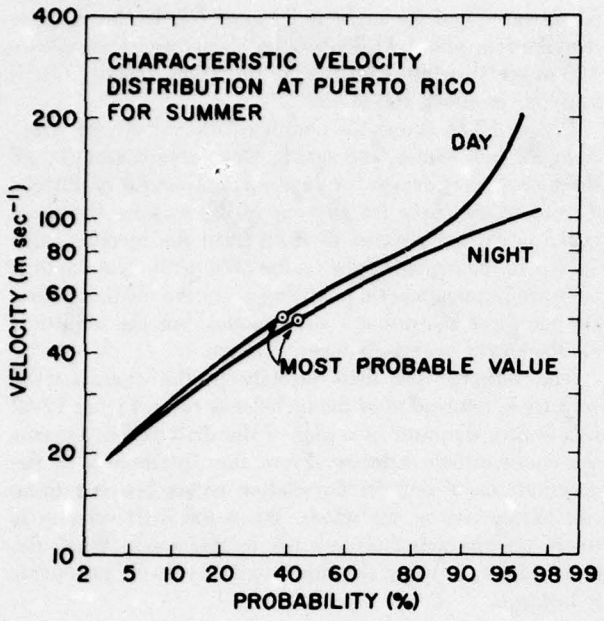


Fig. 12-40. Characteristic velocity distribution at Puerto Rico for summer.

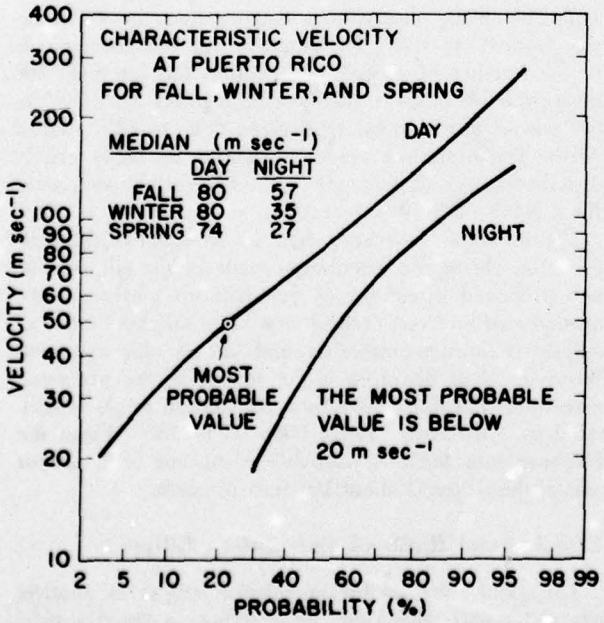


Fig. 12-41. Characteristic velocity distribution at Puerto Rico for fall, winter, and spring.

All the data for the year at Puerto Rico were combined to obtain these plots. The percentages were derived in the same manner as the preceding probability plots with 0.25 increments used. Both curves in Fig. 12-45 approach unity asymptotically since this is the limiting value of this ratio. The figure shows that the ellipses are longer at night than they are in the daytime. The median value for night is 2.35 and for day it is 2.00. The most probable value for both day and night is 1.35.

Figures 12-40 and 12-41 show that the characteristic velocity is smaller during the night than it is during the day, but that the axial ratio is larger during the night than during the day. This implies that the less the turbulence, the more elliptical is the correlation function. There is no apparent correlation between the axial ratio and the drift velocity, although a definite inverse correlation does exist between the axial ratio and the characteristic velocity. The seasonal distributions of this parameter show no significant differences.

12.5.6 Area of the 0.5-Correlation Ellipse

The last parameter of the correlation ellipse is the area, $\pi \cdot a \cdot b$ (a is the semi-major and b the semi-minor axis). To describe this parameter, some specific value of the correlation function must be selected. The most common choice is 0.5. When the probability curves were drawn for daytime and nighttime for the different seasons, the day-to-night distributions differed, while the seasonal distributions were all similar in shape. Therefore, single mean curves were drawn for daytime and nighttime. The seasonal distributions are easily obtained by shifting the given curves so that the median values given in the legend in Fig. 12-46 occur at the 50% grid.

Even though the ellipses have larger axial ratios at night, their areas are generally smaller than the daytime ellipses. The smaller nighttime areas indicate that the sizes of the irregularities in the E layer are smaller at night than they are during the day. The greatest divergence between the daytime and nighttime areas occurs during the winter season. The most probable area for both day and night is somewhat smaller than 0.08 km^2.

12.6 SPORADIC E

Localized regions of increased ionization introduced into the normal E region are called sporadic E (E_s). The mechanisms producing these patches of ionization are not completely known. Three general classifications of E_s in common usage are based on the characteristic differences found at the latitude (auroral, temperate, or equatorial) at which the sporadic E is observed. The equatorial type of E_s is closely related to the equatorial electrojet, although some of the details of the actual mechanisms are still unknown. The occurrence of E_s over the temperate latitudes can be explained reasonably in terms of terrestrial effects. An example is vertical gradient of the wind shear in the presence of the earth's magnetic field, which sets up drift motions that vary with height because of the gradient. The occurrence of E_s over the auroral zone is strongly linked to the bombardment of the atmosphere by extraterrestrial charged particles.

12.6.1 Worldwide Occurrence of E_s

Studies of the worldwide occurrence of E_s are available for the years 1948-1957 [Smith, 1957] and the IGY years 1957-1958. Figures 12-47 through 12-52 are world maps for 1958. Day (0600-1800 h local time) and night (1800-0600 h) distributions are presented separately for the summer (May, June, July, Aug.), winter (Nov., Dec., Jan., Feb.) and the equinoxes (March, April, Sept., Oct.). The values given beside each station in these figures represent the percent of the time period during which the critical frequency of E_s (fE_s) on an ionogram exceeds 5 Mcps.

12.6.2 Results of Analysis of Radio Amateur Data

Data for the single-hop sporadic E statistics are for observers operating at 50 Mcps. The percentage of each hour that the E_s mode was observed during the two years of the IGY was calculated from the data, but only for the continental United States over areas 25° to 50°N latitude. Table 12-1 gives the geographical distribution of sporadic E over the United States for summer, winter, and the equinoxes. In each 2.5° block there are four entries. The first number is the total number of possible midpoints occurring in each 2.5° by 2.5° block. These were computed using the coordinates of all the reporting radio amateurs, which, when taken in all possible pairs, produced midpoints that were located over continental United States. These numbers represent the geographical coverage possible in this program. The second number in each block is the total of the average daily percentages for the summer months for the two years. The third number is the total of the average daily percentages for the winter months for two years, and the fourth number is this same quantity for the equinoctial months. In order to obtain the average percentage of time per season that E_s occurred over any area for the two IGY years, these average daily percentages must be divided by 240 (30 days × 8 months).

Figure 12-53 shows the geographical distribution of the average percentage of time for the two summer seasons that E_s occurred. The area outlined in black is where the largest number of midpoints occur. The amateur coverage is probably sufficient here to observe all the E_s present. Over other areas of the United States, the coverage is considered *inadequate to observe every* E_s occurrence.

The geographical distribution of sporadic E clouds over the United States is not uniform. The highest local activity occurs over Missouri and Arkansas, with 1.25% of the time during the summer months. In general, the local activity is below 0.5% except over the area covering the state of Illinois and the surrounding states. This is not believed to be caused by the lack of coverage, although such a lack is evident near the boundaries of the continental United States.

Figure 12-54 shows the average percentage of time per hour sporadic E was present over the whole United States in each month for the two IGY years. Apparently the E_s activity over the continental United States has a pronounced peak in the summer months (May, June, July and Aug.). Thus, during 20% of that time, at least one sporadic-E cloud reflecting 50 Mcps over a distance between 200 and 2000 km can be observed. The percentage for the winter months (Dec. and Jan.) is only 4% and even lower (2%) for the remainder of the months. The activity measured in percentage of time was somewhat higher in 1957. There is also a diurnal distribution of E_s activity with a broad maximum in the evening hours amounting to 40% of the time between 1800 and 2300 h. A second maximum with 40% occurs in the noon hours between 0900 and 1400.

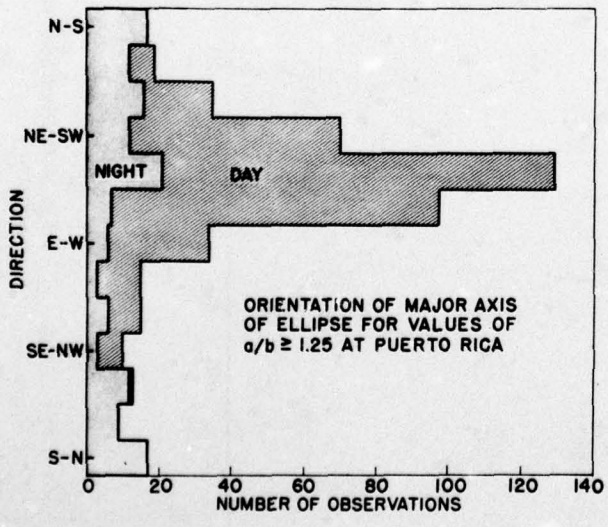


Fig. 12-43. Orientation of major axis of ellipse for values of $a/b \geq 1.25$ at Puerto Rico.

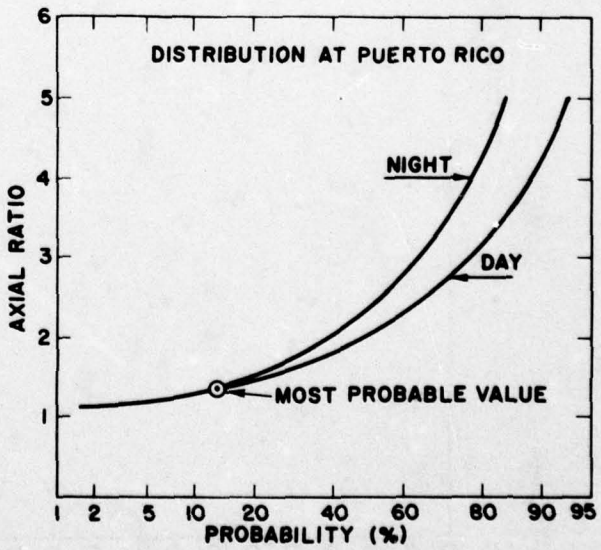


Fig. 12-45. Distribution of axial ratio at Puerto Rico.

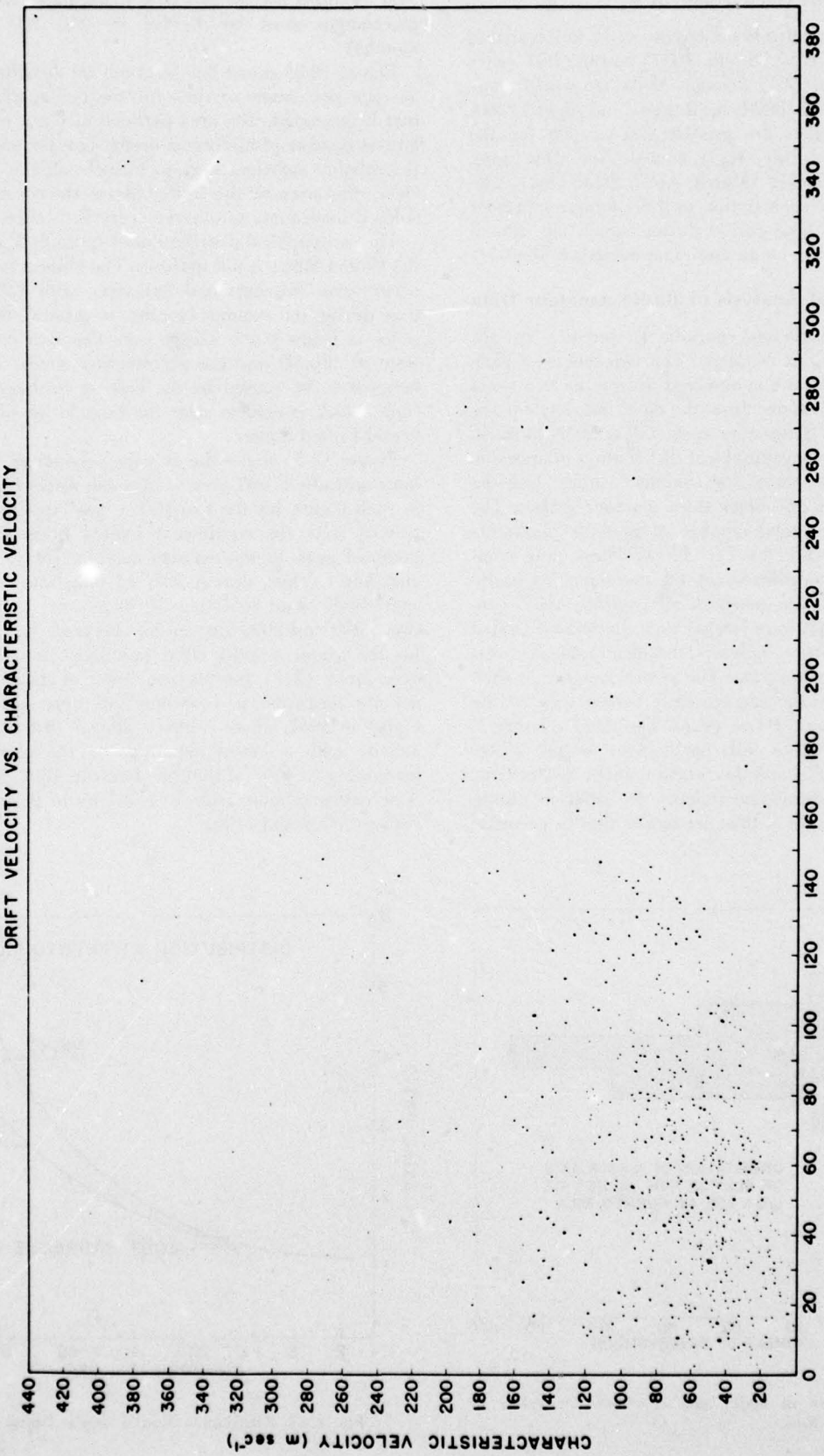


Fig. 12-42. Distribution of individual observations for Puerto Rico, drift velocity vs characteristic velocity.

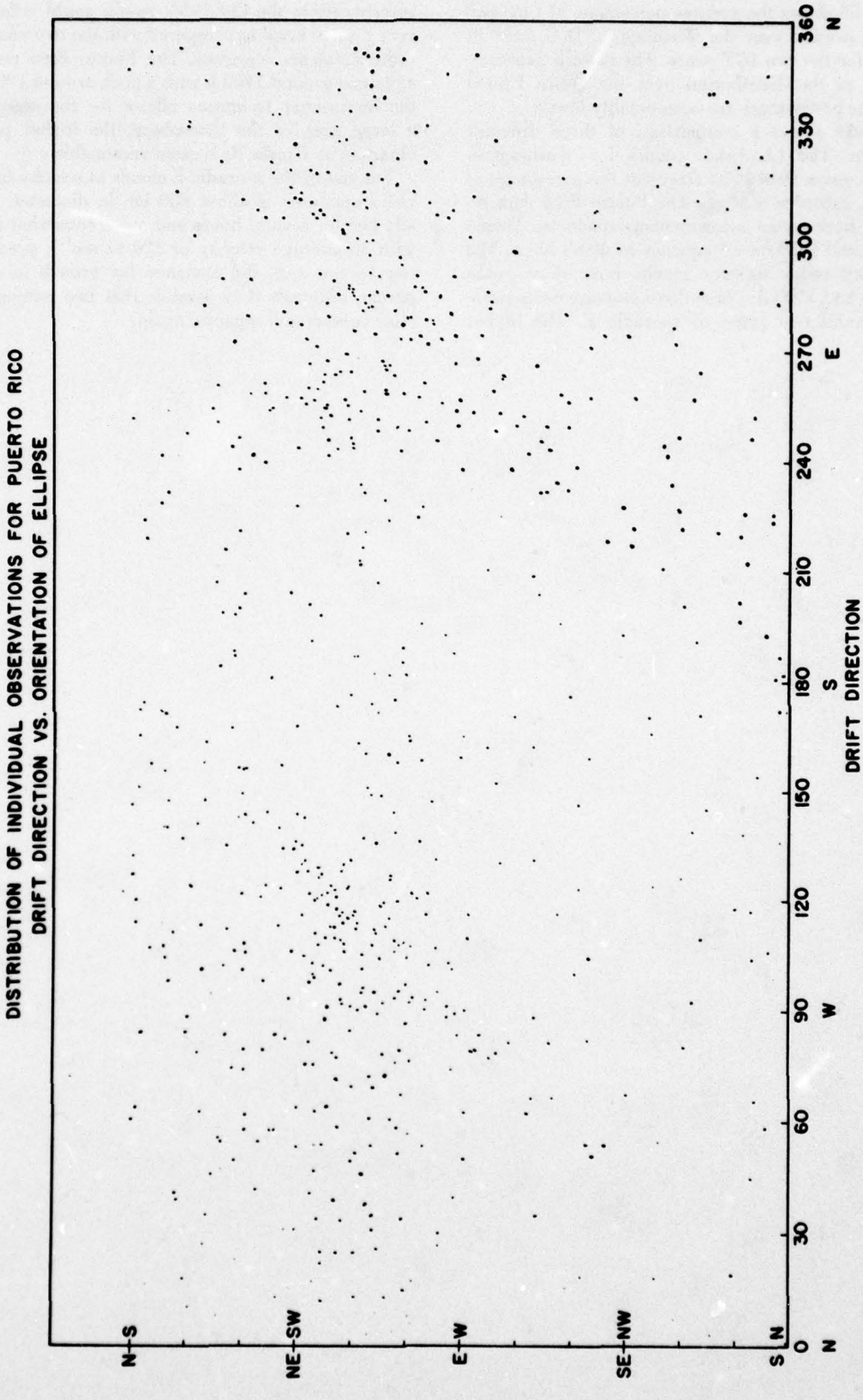


Fig. 12-44. Distribution of individual observations for Puerto Rico, drift direction vs orientation of ellipse.

Figure 12-55 shows the average percentage of time per hour E_s was present over the Washington, D.C. area in each month for the two IGY years. The pattern generally is the same as the distribution over the entire United States, but the percentages are considerably lower.

Figure 12-56 shows a comparison of three different measurements. The Chadwick results for Washington, D. C. for the years 1949-1959 represent the percentage of time that fE_s exceeded 5 Mcps. The Puerto Rico data resulted from backscatter measurements made by Dueño during 1958 and 1959 on a frequency of 40.68 Mcps. The Chadwick and radio amateur results both show peaks around 1000 and 1900 h. These three measurements probably involve different types of sporadic E. The higher percentages in the Chadwick results could reflect his ten-year time interval as compared with the two years that the radio amateurs observed. The Puerto Rico results show a plateau around 1100 h with a peak around 1700 h. Since the backscatter technique allows for the observation of a large area of the ionosphere, the higher percentages obtained at Puerto Rico seem reasonable.

The size of the sporadic-E clouds as seen by the amateur radio operators is about 600 km in diameter. They usually last for several hours and move somewhat irregularly with an average velocity of 100 m sec^{-1}, predominantly toward the west. No tendency for growth in size is apparent, although it is possible that two patches come in close contact and separate again.

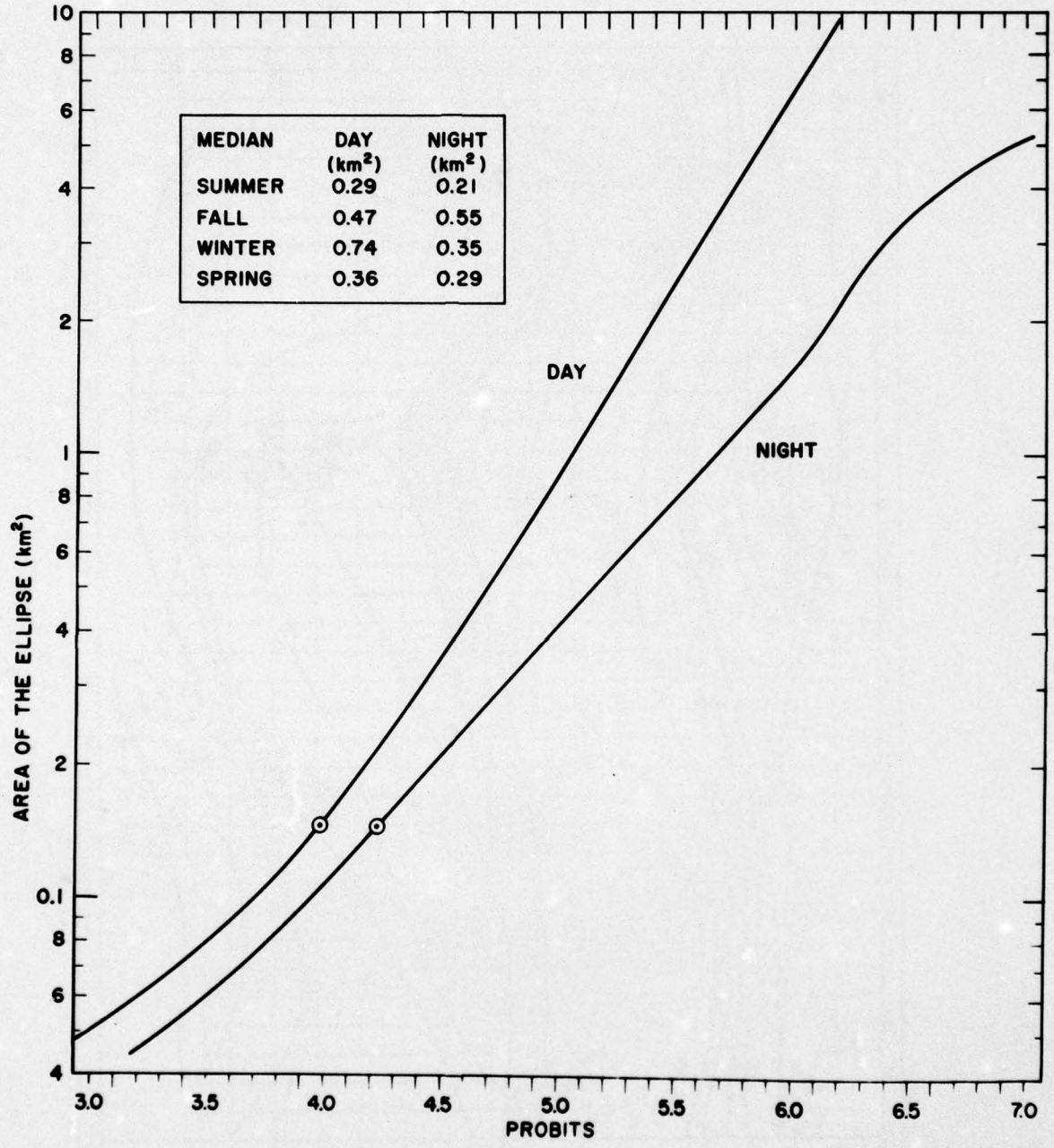


Fig. 12-46. Area of the 0.5 correlation ellipse.

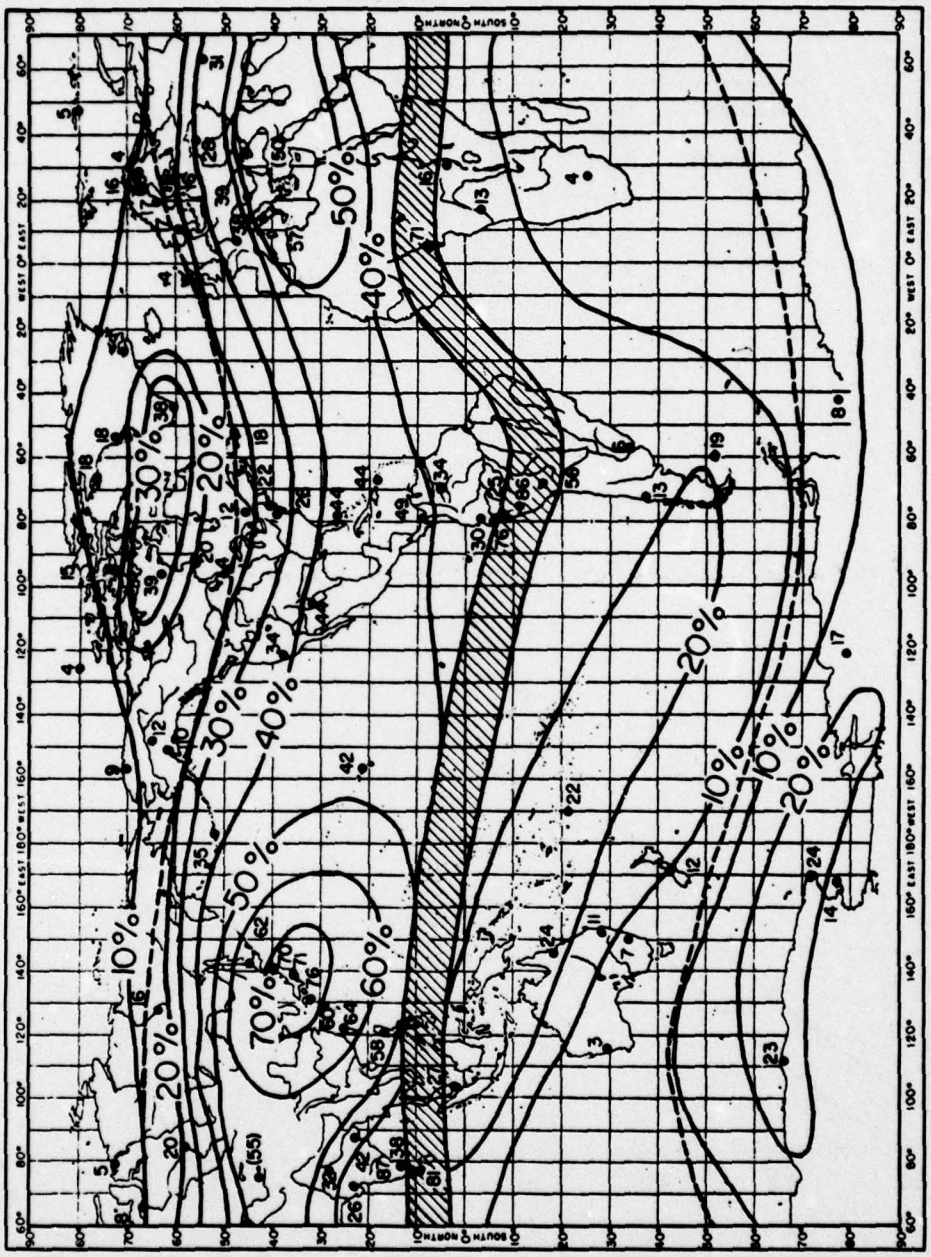


Fig. 12-47. Map showing percent of time that fE_s exceeded 5 Mcps during daytime hours of the June solstice, 1958. (Courtesy of H. I. Leigton, A. H. Shapley, and E. K. Smith, CRPL, National Bureau of Standards.)

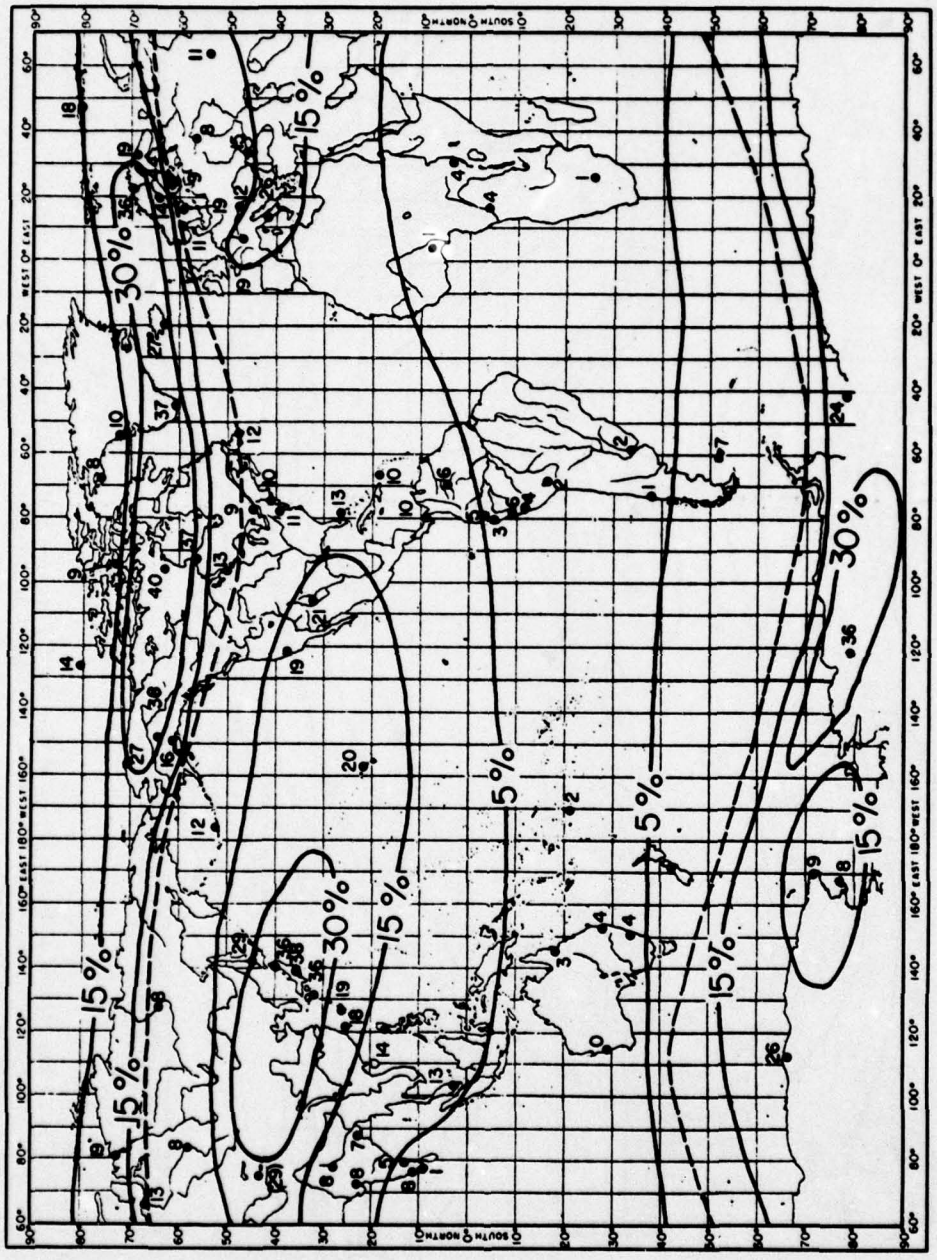


Fig. 12-48. Map showing percent of time that that fE_s exceeded 5 Mcps during nighttime hours of the June solstice, 1958. (Courtesy of H. I. Leighton, A. H. Shapley, and E. K. Smith, CRPL, National Bureau of Standards.)

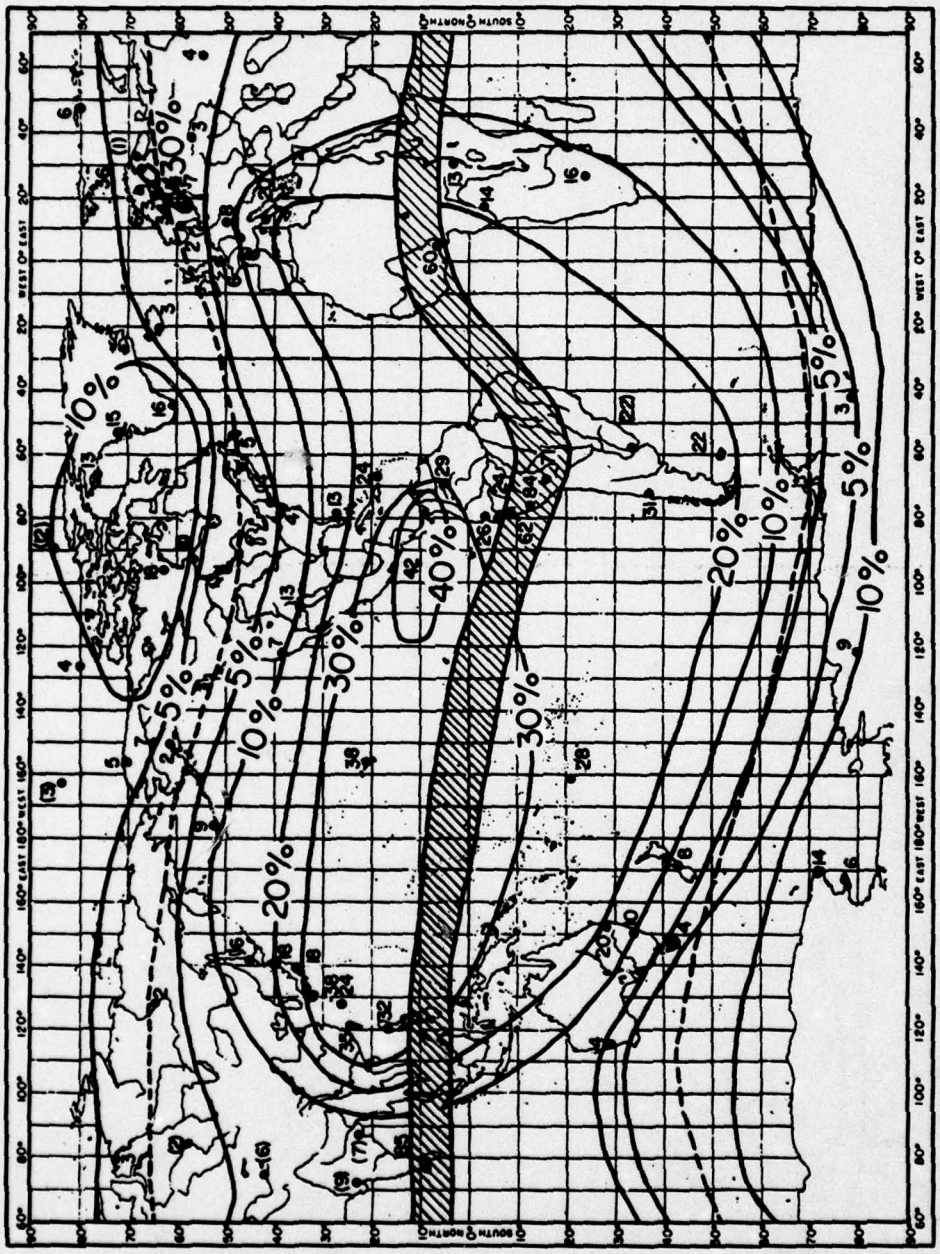


Fig. 12-49. Map showing percent of time that fE_s exceeded 5 Mcps during daytime hours of the equinoctial months, 1958. (Courtesy of H. I. Leighton, A. H. Shapley, and E. K. Smith, CRPL, National Bureau of Standards.)

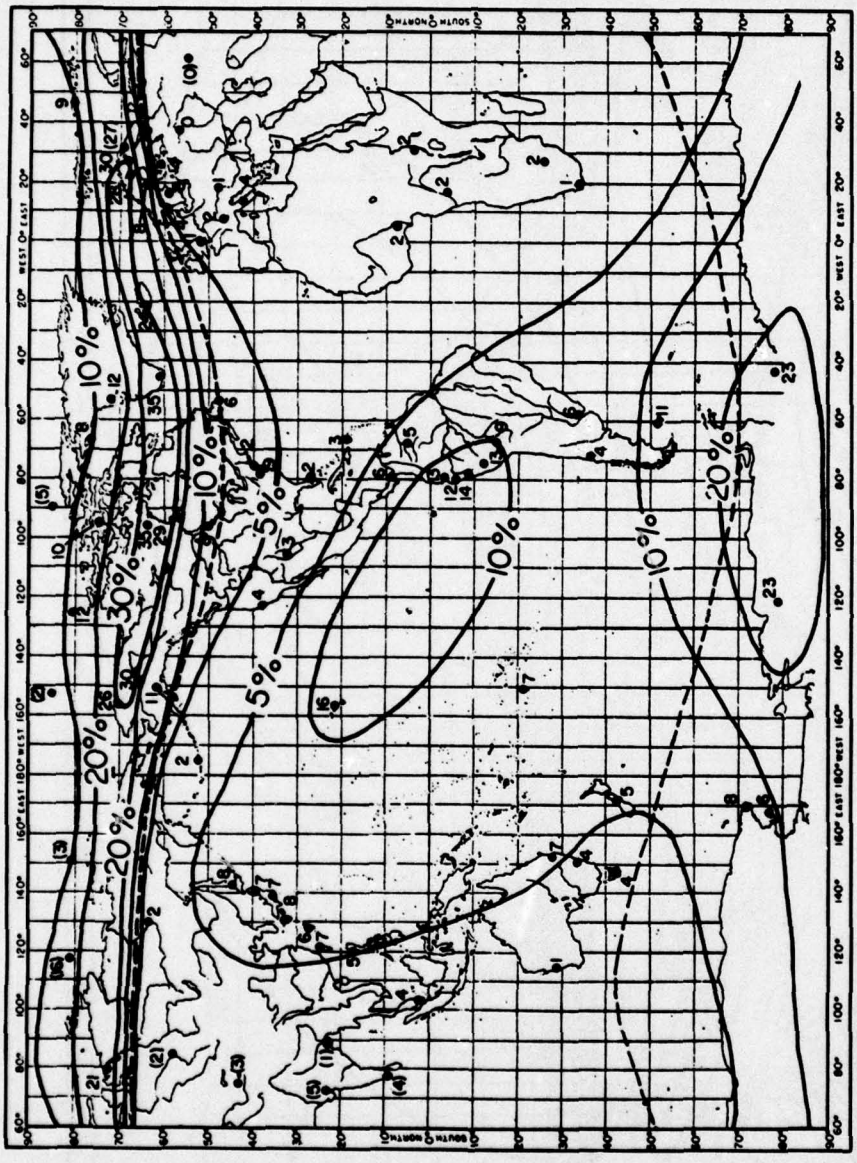


Fig. 12-50. Map showing percent of time that fE_s exceeded 5 Mcps during nighttime hours of the equinoctial months, 1958. (Courtesy of H. I. Leighton, A. H. Shapley, and E. K. Smith, CRPL, National Bureau of Standards.)

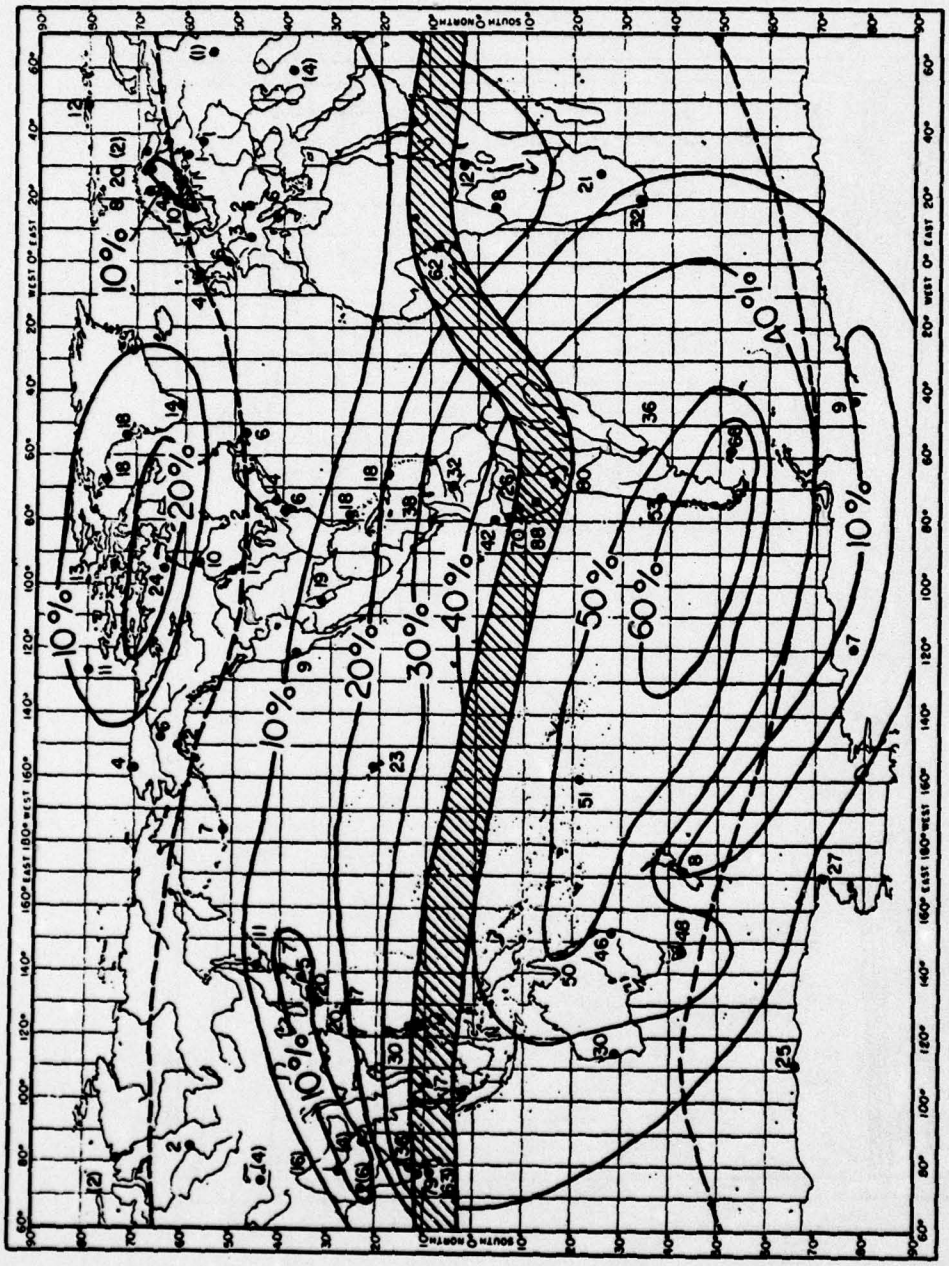


Fig. 12-51. Map showing percent of time that fE_s exceeded 5 Mcps during daytime hours of the December solstice, 1958. (Courtesy of H. I. Leighton, A. H. Shapley, and E. K. Smith, CRPL, National Bureau of Standards.)

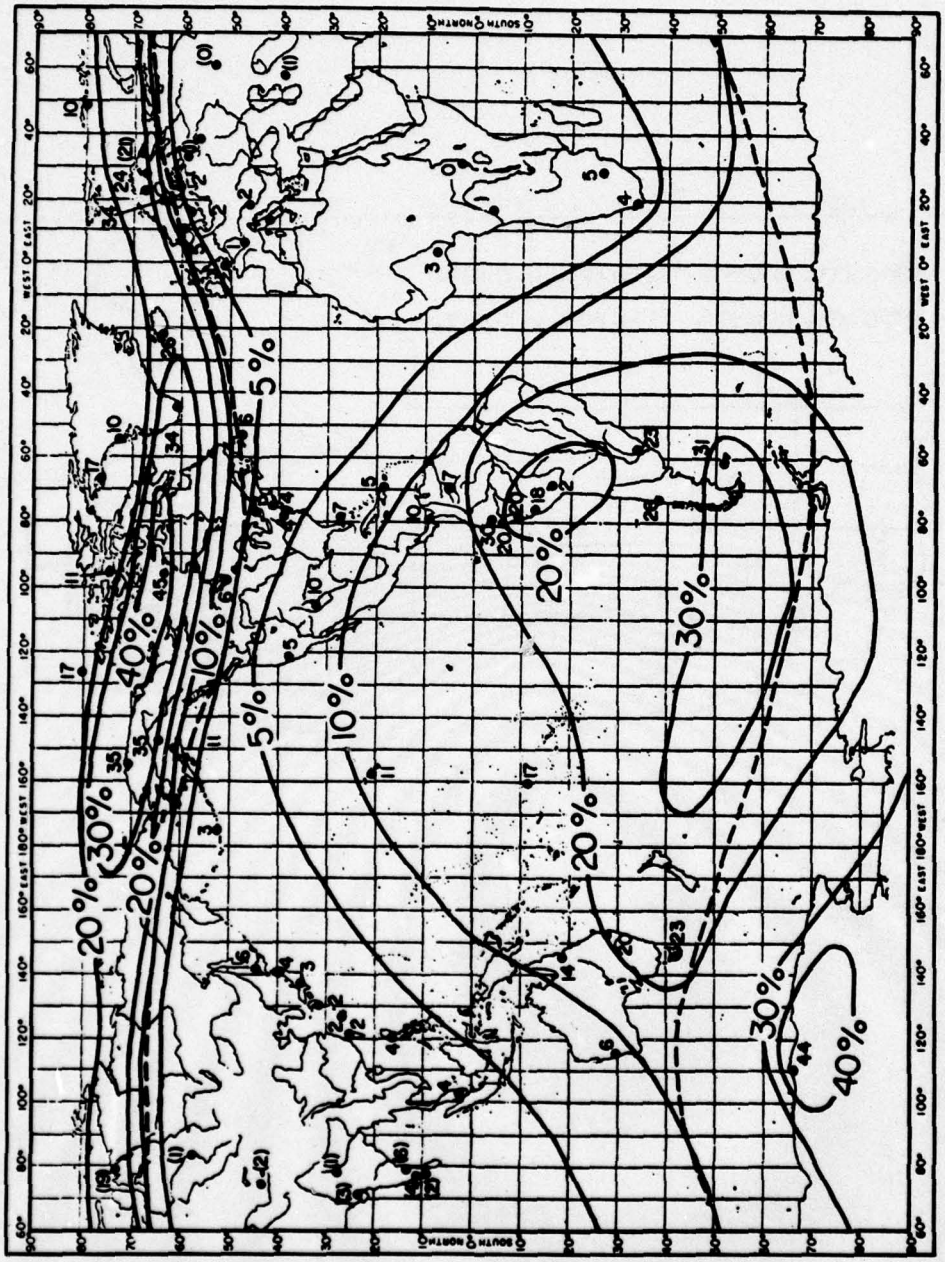


Fig. 12-52. Map showing percent of time that fE_s exceeded 5 Mcps during nighttime hours of the December solstice, 1958. (Courtesy of H. I. Leighton, A. H. Shapley, and E. K. Smith, CRPL, National Bureau of Standards.)

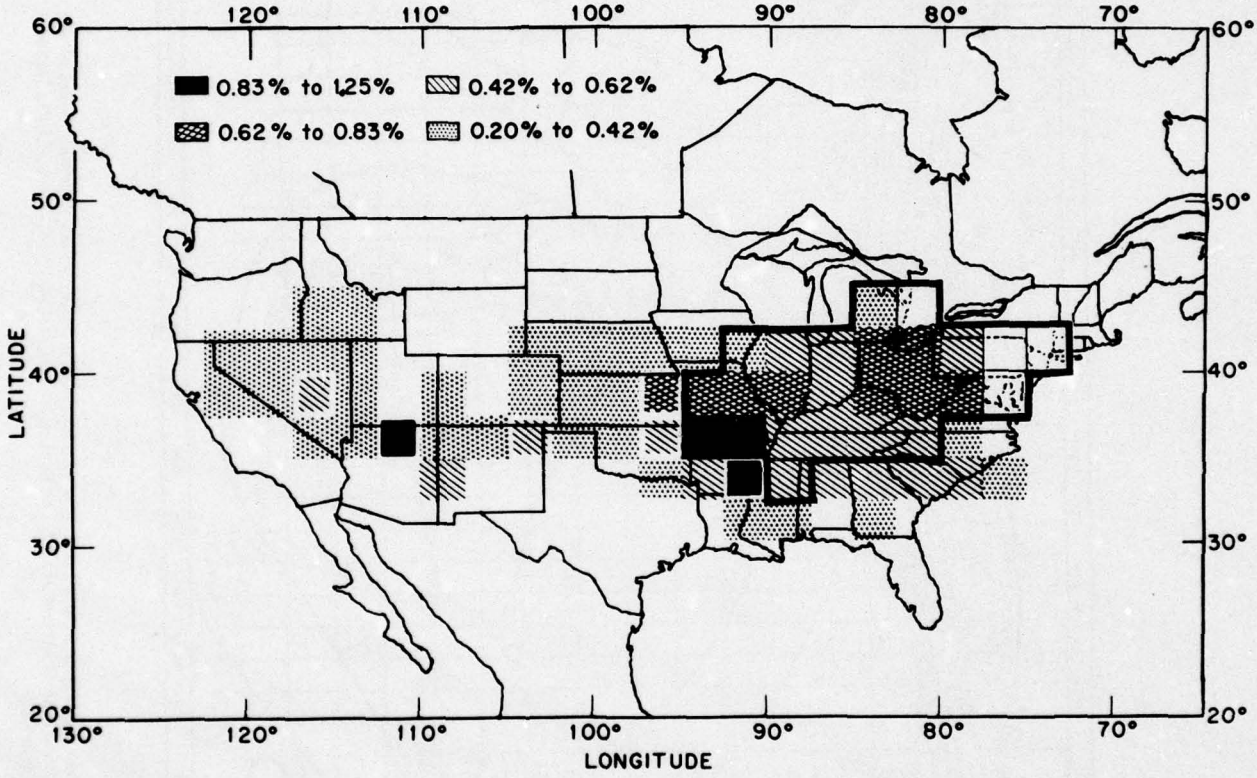


Fig. 12-53. Geographical distribution of the average percentage of time E_s occurred during the summer months of IGY. Over the black areas, the average percentage of time that E_s is observed exceeds 0.83%; over the hatched areas, it exceeds 0.42%; and over the dotted areas; it exceeds 0.20%. The average percentage of time over other areas is less than 0.20%.

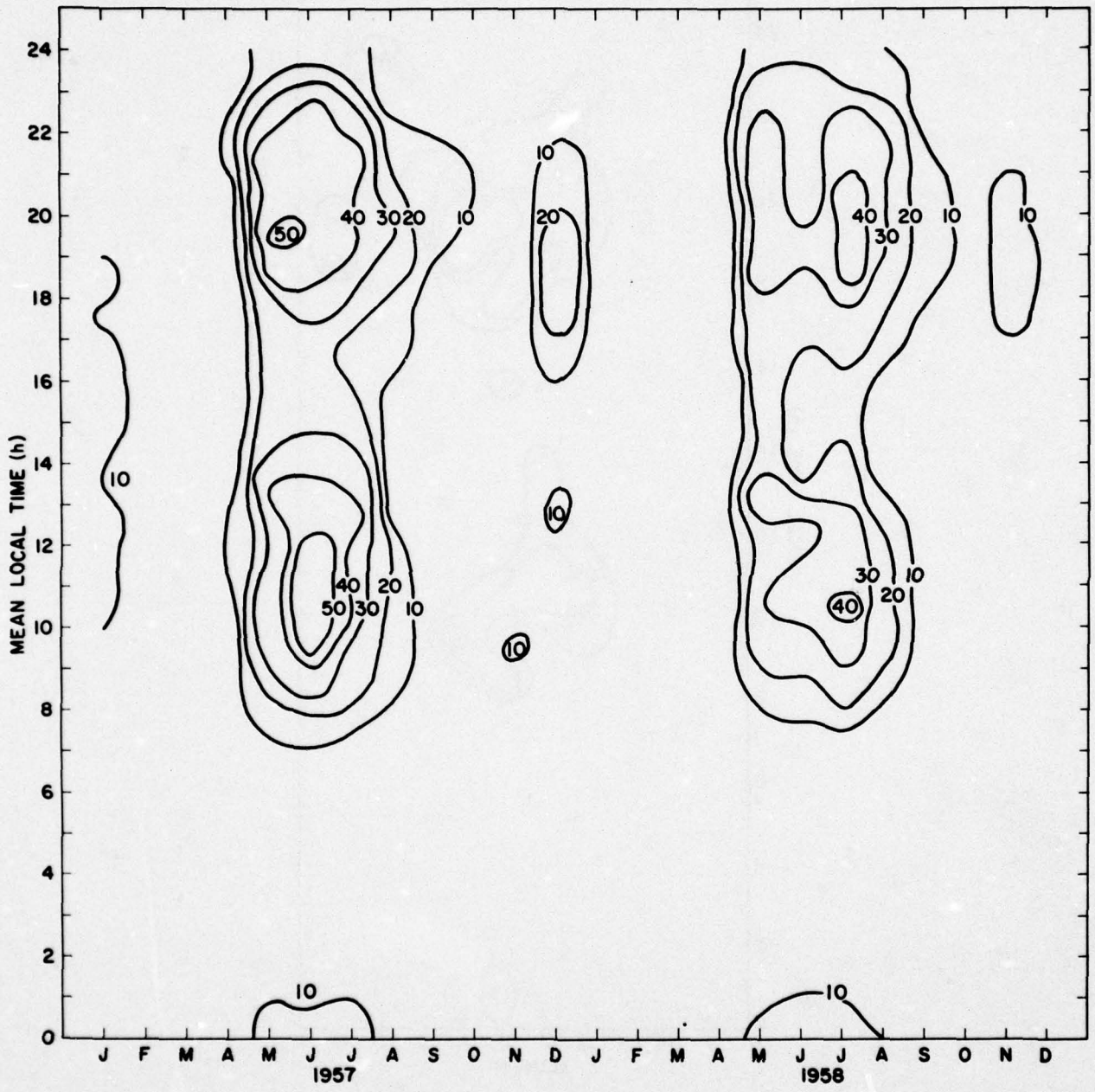


Fig. 12-54. Diurnal distribution of E_s over the United States, 1957-1958, radio amateur data on 50 Mcps. Contours represent average monthly percent of time E_s present.

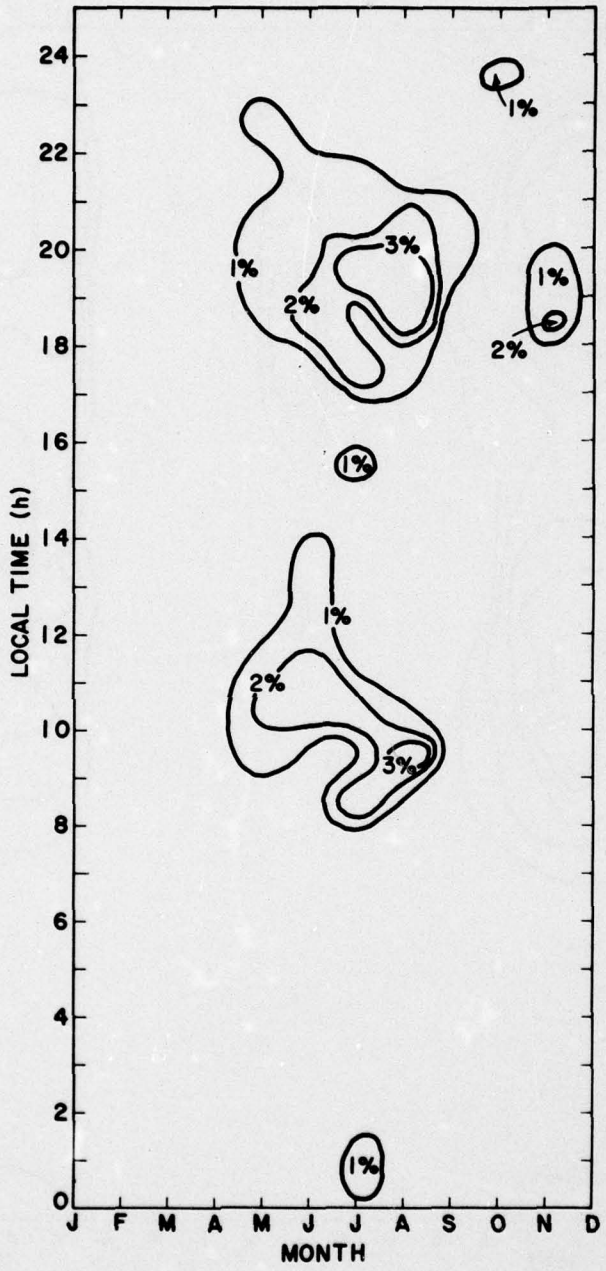


Fig. 12-55. Percent of time sporadic E present Washington, D. C., 1957-1958, radio amateur data.

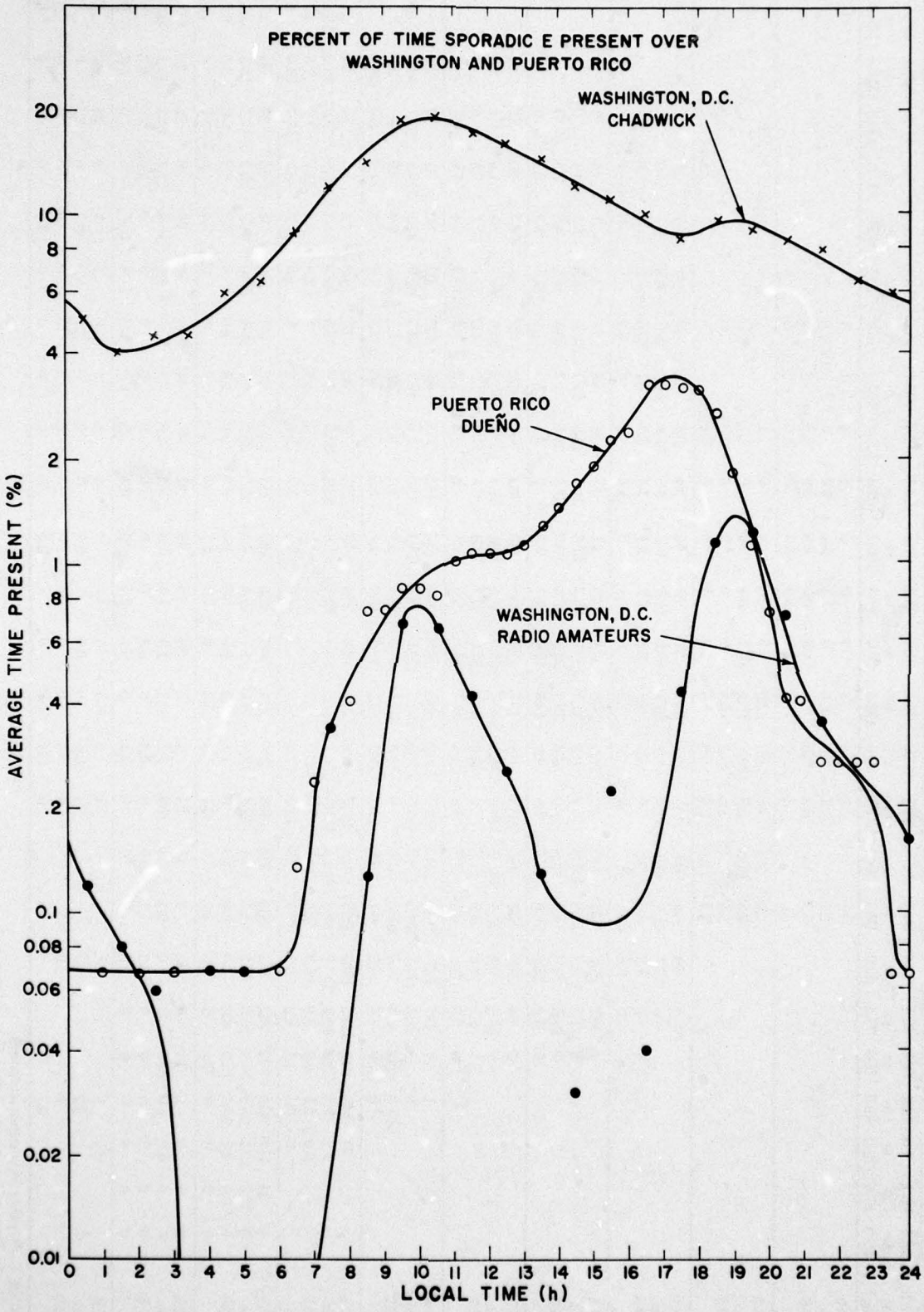


Fig. 12-56. Percent of time sporadic E is present over Washington, D. C., and over Puerto Rico. For Chadwick and Dueño data, see Smith and Matsushita [1962].

Table 12-1. Total percent of time sporadic E present over the continental United States during 1957-1958.* (From radio amateur data.)

North Lat (deg)	West Longitude (deg)																							
	62.5 to 65.0	65.1 to 67.5	67.6 to 70.0	70.1 to 72.5	72.6 to 75.0	75.1 to 77.5	77.6 to 80.0	80.1 to 82.5	82.6 to 85.0	85.1 to 87.5	87.6 to 90.0	90.1 to 92.5	92.6 to 95.0	95.1 to 97.5	97.6 to 100.0	100.1 to 102.5	102.6 to 105.0	105.1 to 107.5	107.6 to 110.0	110.1 to 112.5	112.6 to 115.0	115.1 to 117.5	117.6 to 120.0	120.1 to 122.5	122.6 to 125.0
25.0 to 27.5								19		1	4	3	19	8	6	4	4	2	1					
								2.1		1.1	3.5	2.6	0	1.3	3.4	2.0	0	0	0					
								0.2		0.6	0	1.6	1.0	0.9	8.5	2.9	0.2	0	0					
								0		0	0	0	1.7	3.0	3.3	0	3.1	0	0					
27.6 to 30.0								22	3.4	44	115	20	15	36	14	4	4							
								5.5	31.3	2.5	40.3	17.1	12.1	0.6	0	0	1.7							
								1.8	1.4	1.6	16.7	4.1	0	0	0	0	0.5							
								2.9	11.9	7.4	5.9	4.6	1.0	0	0	0	2.4							
30.1 to 32.5						5	90	149	168	104	123	117	77	61	45	24	18	16	22	1	1	1		
						0	35.3	41.9	87.1	32.4	66.4	88.9	48.6	16.0	9.3	8.3	43.8	17.2	46.7	0.9	0.7	0		
						0	1.9	6.9	9.2	5.4	13.5	8.8	2.0	2.1	1.1	3.3	7.9	7.1	20.6	0	0	0		
						0	8.6	18.7	15.3	0	3.2	1.2	0	0.3	0	1.3	0	0	0.5	0	0	0		
32.6 to 35.0					1	187	352	331	440	369	508	380	273	183	81	55	36	98	56	23	17	14	9		
					0	71.6	134.3	121.8	147.8	110.2	138.3	237.3	139.7	58.7	27.4	34.9	45.5	24.7	103.0	35.3	26.3	46.4	0	
					0	29.8	15.8	6.4	22.5	22.0	24.8	23.9	23.9	10.8	10.0	22.2	24.5	11.2	18.6	16.3	4.0	3.5	0	
					0	5.4	18.0	16.0	10.8	4.0	4.9	12.4	3.0	0.1	0.5	0	0.7	1.5	21.6	12.5	4.2	2.3	0	
35.1 to 37.5					5	84	366	577	845	1112	968	814	566	326	159	132	107	132	81	48	32	23	25	46	
					0	28.9	79.4	136.4	146.9	148.7	186.4	299.8	226.0	143.4	7.32	69.2	123.9	50.2	84.6	216.3	62.5	61.4	7.4	3.0	
					2.1	6.1	5.8	7.3	11.7	0	40.0	45.9	56.0	30.1	13.4	19.6	17.0	8.1	6.8	42.1	11.4	5.3	0	0	
					0	3.3	11.7	8.5	7.4	9.8	21.4	22.3	14.5	5.8	3.3	1.2	2.2	1.2	5.2	13.5	9.4	6.9	0.4	0	
37.6 to 40.0				1	77	737	1269	1648	1714	1761	1270	941	528	380	183	181	134	89	172	52	52	81	12	25	
				0	0	11.3	175.5	169.5	173.8	138.5	188.9	158.7	154.5	159.4	75.4	54.2	73.5	49.7	57.7	33.7	85.1	119.1	55.1	93.3	
				0	0.2	3.5	16.0	22.6	31.0	0	63.8	37.9	46.0	29.5	9.9	3.7	3.7	2.2	3.7	8.7	9.0	9.0	6.7	3.2	
				0	0	1.4	15.8	8.7	15.3	23.2	29.2	10.9	10.4	10.7	2.6	2.5	7.6	1.6	1.1	1.4	7.6	11.8	6.0	23.5	
40.1 to 42.5			20	141	843	1254	1982	2153	1975	1937	1174	767	469	264	318	233	47	34	82	40	33	43	50	74	31
			1.7	18.3	23.8	47.2	118.5	182.2	162.3	131.5	130.1	54.6	50.1	82.4	80.0	93.1	88.2	8.9	12.9	29.2	51.3	83.0	98.3	93.6	15.6
			0.6	2.5	6.8	3.9	26.9	41.5	29.1	0	38.0	13.7	27.1	6.9	4.5	3.9	3.3	1.0	0	2.9	0.2	13.7	1.7	7.3	1.7
			0	3.7	1.1	2.2	6.4	17.0	13.2	13.7	17.4	1.6	1.7	4.3	8.5	5.2	0.4	0	0	0	8.2	2.8	15.4	20.0	0
42.6 to 45.0	1	44	117	116	372	288	362	607	732	408	237	276	148	136	185	131	111	22	161	32	32	55	24	24	21
	0	7.5	22.1	30.6	36.9	14.0	27.2	41.6	64.1	35.2	18.9	4.8	5.7	13.4	19.5	32.5	38.5	9.4	23.0	15.0	64.2	58.2	15.7	35.2	33.5
	0	0.6	2.7	14.3	15.8	3.2	8.9	8.9	13.4	0	1.1	1.8	0.3	0.3	1.0	0.3	0	1.4	0	0	1.2	0	0	3.9	0.7
	0	0	0	0	2.4	0	1.6	3.1	5.1	2.7	1.0	2.3	0	0.2	2.1	3.8	1.0	0	0	0	2.0	0	0	3.2	0
45.1 to 47.5	2	4	5	2	15	9	12	1	41	24	4	4	14	10	18	42	43	34	90	10	26	38	25	17	19
	0	0	0.5	0	18.8	0	0	0.3	7.3	2.9	3.2	11.5	1.9	1.6	1.8	3.2	2.9	3.9	13.0	4.9	14.0	21.1	14.2	13.2	2.5
	0	0	0	0	0	0	0.2	1.2	0.9	0	0.3	0	0.2	0	0	0	0	0	0	0	0	0.3	0	0.3	0
	0	0	0	0	0	0	0	0	0	0	0.2	0	0.5	0.6	0	0.4	0	0.8	2.2	0	10.5	0	0	2.8	0
47.6 to 50.0				2			3			4	4	4	5		7	5	9	4	8	6	3	9	14	2	15
				5.2			0			0.3	0.6	0	0.9		0.6	0	0	0	0.6	6.8	2.2	0	2.7	0	2.5
				0			0			0	0	0	0		0	0	0	0	0	0	0	0	0	0	0
				0.7			0			0	0.4	0	0		0.6	0	0	0	0	0	0.6	0	0	0	0

* Entry No. 1—Number of possible midpoints.
No. 2—Percent for summer (May, June, July, Aug.).
No. 3—Percent for winter (Nov., Dec., Jan., Feb.).
No. 4—Percent for equinoctial (Mar., April, Sept., Oct.).

12.7 REFERENCES

Auno, Y., K. Hiruo, and S. Miyazaki, 1961, "Positive Ion Density, Electron Density, and Electron Temperature in the Ionosphere by the Kappa-8, -5, and -6 Rockets," *J. Rad. Res. Labs. Japan*, v. 8, p. 453.

Briggs, B. H., G. J. Phillips, and D. H. Shinn, 1950, "The Analysis of Observations on Spaced Receivers of the Fading of Radio Signals," *Proc. Phys. Soc. B*, v. 63.

Chan, K. L., and O. G. Villard, Jr., 1963, "Sudden Frequency Deviations Induced by Solar Flares," *J. Geophys. Res.*, v. 68, no. 10, p. 3197.

Daniels, F. G., and S. J. Bauer, 1959, "The Ionospheric Faraday Effect and Its Applications," *J. Franklin Inst.*, v. 267, no. 3.

Dingle, R. B., D. Arndt, and S. K. Roy, 1957, "Semiconductor Integrals," *Appl. Sci. Res.*, v. 6B, p. 158.

Hill, G. E., 1962, "Polar Cap and Auroral Zone Absorption Events during the First Six Months of the I.G.Y.," *J. Phys. Soc. Japan*, no. 17, suppl. A-1, International Conf. Cosmic Rays and the Earth Storm.

Huxley, L. G. H., 1957, "Free Path Formulae for the Electric Conductivity of a Weakly Ionized Gas in the Presence of a Uniform and Constant Magnetic Field and a Sinusoidal Electric Field," *Australian J. Phys.*, v. 10, p. 240.

Kane, J. A., 1959, "Arctic Measurements of Electron Collision Frequencies in the D Region of the Ionosphere," *J. Geophys. Res.*, v. 64, p. 133.

Mitra, S. N., 1949, "Radio Method of Measuring Winds in the Ionosphere," *Proc. Inst. Elec. Engrs.*, v. 96, part III.

Nicolet, M., 1953, "The Collision Frequency of Electrons in the Ionosphere," *J. Atmos. Terrest. Phys.*, v. 3, p. 200.

Nicolet, M., and A. C. Aiken, 1960, "The Formation of the D Region of the Ionosphere," *J. Geophys. Res.*, v. 65, no. 5.

Pfister, W., and J. C. Ulwick, 1958, "The Analysis of Rocket Experiments in Terms of Electron-Density Distributions," *J. Geophys. Res.*, v. 63, no. 2.

Pozigun, V. L., 1960, "Drift of Inhomogeneities in the Ionosphere According to Observations at Rostov-on-the-Don," *Researches of the Irregularities in the Ionosphere*, IGY Program, sect. V, Publishing House of the Academy of Sciences of the USSR, Moscow.

Sen, H. K., and A. A. Wyller, 1960, "On the Generalization of the Appleton-Hartree Magneto-Ionic Formation," *J. Geophys. Res.*, v. 65, p. 3961.

Shkarofsky, J. P., 1961, "Values of the Transport Coefficients in a Plasma for Any Degree of Ionization Based on a Maxwellian Distribution," *Can. J. Phys.*, v. 39, p. 1619.

Smith, E. K., Jr., 1957, "Worldwide Occurrence Sporadic E," National Bureau of Standards Circular No. 582, U.S. Government Printing Office, Washington, D.C.

Smith, E. K., Jr., and S. Matsushita, eds., 1962, "Ionospheric Sporadic E," Pergamon Press Inc., New York.

Somayajulu, Y. V., 1963, "Changes in the F Region During Magnetic Storms," *J. Geophys. Res.*, v. 68, no. 7.

Spencer, N., L. Brace, and G. R. Carignan, 1962, "Electron Temperature Evidence for Nonthermal Equilibrium in the Ionosphere," *J. Geophys. Res.*, v. 67, pp. 157-175.

Warwick, C. S., 1963, The Sudden Ionospheric Disturbance, "Radio Astronomical and Satellite Studies of the Atmosphere," J. Aarons, ed., North Holland Publishing Co., Amsterdam.

Yerg, D. G., 1955, "Notes on Correlation Methods for Evaluating Ionospheric Winds from Radio Fading Records," *J. Geophys. Res.*, v. 60.

Chapter 13

AIRGLOW AND AURORAE

S. M. Silverman
G. J. Hernandez
A. L. Carrigan
T. P. Markham

Airglow radiation is mainly the effect of chemical reactions of upper atmospheric constituents. Nightglow, twilight glow, and dayglow are sometimes used for descriptive convenience.

Auroral radiation is caused mainly by direct excitation of upper atmospheric constituents by particles. Northern Hemisphere aurorae are called aurora borealis or northern lights; those in the Southern Hemisphere, aurora australis or southern lights. In general, both airglow and auroral radiations are emitted at heights greater than 75 km.

Excellent books on the airglow and aurora with related fields are available; for example, Chamberlain [1961], Ratcliffe [1960], Störmer [1955], Harang [1951], and Dalgarno and Armstrong [1957]. These should be consulted for more details than can be given in this chapter.

13.1 AIRGLOW

The airglow normally occurs in layers at varying altitudes above the earth's surface. The spectrum consists of a continuum plus emission lines and bands. The spatial distribution of emission for certain lines may be patchy in nature, with patches on the order of thousands of kilometers in diameter. It is estimated that about forty percent of the total night-sky light in the direction of the celestial pole is due to airglow. The unit of intensity used most commonly is the Rayleigh, defined as

$$1\ \mathrm{R} = 10^6 \text{ quanta cm}^{-2} \text{ (column) sec}^{-1}.$$

13.1.1 Spectrum

Atomic emission lines and molecular bands found in the airglow are listed in Tables 13-1 and 13-2. (Square brackets enclosing the atomic species are used to identify lines originating from forbidden transitions.) These lines and bands are not necessarily the only ones found, but are those for which general agreement now exists. Studies with high-sensitivity and high-resolution spectroscopic instruments may lead to positive identification of other lines and bands. The night-sky spectrum also has a continuum extending from about 4000 Å into the infrared, with a spectral intensity in the visible region of the order of 2 to 3 R Å^{-1}. Figure 13-1 shows the airglow spectrum from 3000 to 12,400 Å. Figure 13-2 shows the airglow spectrum in the near infrared (wavenumber 4400 to 8400 cm^{-1}).

13.1.2 Intensity

The intensities of airglow emissions are extremely variable. Values given should be treated as guides to the approximate magnitudes rather than as definitive and conclusive. In general, the intensities show diurnal, seasonal, and secular variations and, for many emissions, are sensitive to magnetic activity. Table 13-3 gives some intensities for night airglow and twilight airglow emissions. For a discussion of twilight metallic emissions, see Vallance Jones [1963].

13.1.3 Altitudes

The most reliable results for the altitudes at which the night airglow occurs appear to be the direct determinations by rocket probes (primarily work of the Naval Research Laboratory). The altitude of the 6300 Å [OI] emission was determined by a comparison of the intensity variations in the east and west. Theoretical considerations [Lagos et al, 1963] indicate a thick luminosity profile which should show marked seasonal changes for the peak luminosity. The altitudes for the sodium, lithium, and potassium emissions were determined from measurements of the twilight intensities. The results are listed in Table 13-4. Almost all of the measurements refer to midlatitudes during a period of a few years centered on IGY-IGC. Very little information is available on possible changes of these altitudes with season or with sunspot cycle.

13.1.4 Latitude Variation

The latitude dependency of the airglow emissions is not known with certainty at present, and the following comments should be considered as only tentative. Table 13-5 shows the latitude dependency of the 5577 Å [OI] line based on IGY-IGC data. In the neighborhood of the auroral zone, the uncertainty of the mean intensities is greater because of the dependence on magnetic activity. Figure 13-3 shows the mean intensities for the 5577 Å and 6300 Å [OI] emissions for the two cases of no magnetic

activity (K = 0) and the average for all K-values. The mean intensity for the 3914 Å N_2^+ emission is shown for the average of all K-values.

The curves for the 5577 Å and 6300 Å [OI] emissions are considered to be moderately reliable; those for the 3914 Å N_2^+ emission are not considered very reliable. Evidence exists of large variations along different geomagnetic meridians, a strong dependence on local K-index, and considerable diurnal variations at some stations. These data should be considered as tentative. In Fig. 13-4, the latitude variations are shown for several airglow emissions determined from shipboard measurements.

13.1.5 Diurnal, Annual, and Secular Variations

To determine the diurnal and annual variations, sufficient data exist only for the 5577 Å [OI], 6300 Å [OI], and 5893 Å NaI lines, and for the secular variation only for the 5577 Å [OI]. For the other airglow emissions, the data are too sparse to allow definite conclusions to be drawn.

Table 13-1. Atomic emission lines in airglow.

Wavelength (Å)	Element	Transition	Found In*	References**
1215	H Ly-α	$2p\ ^2P^o_{3/2} - 1s\ ^2S_{1/2}$	N	[Kupperian et al 1959]
3933.7 3968.7	CaII	$4p\ ^2P^o_{3/2,\ 1/2} - 4s\ ^2S_{1/2}$	T	[Vallance Jones, 1963]
5199.92 5202.29	[NI]	$2p^3\ ^2D_{3/2,\ 5/2} - 2p^3\ ^4S_{3/2}$	T, N	[Turtle, 1963]
5577.345	[OI]	$2p^4\ ^1S_o - 2p^4\ ^1D_2$	N, T	
5889.953 5895.923	NaI	$3p\ ^2P^o_{3/2,\ 1/2} - 3s\ ^2S_{1/2}$	N, T, D	[Vallance Jones, 1963]
6300.308 6363.790	[OI]	$2p^4\ ^1D_2 - 2p^4\ ^3P_{2,\ 1}$	N, T, D	
6562.817	H-α	$3p\ ^2P^o_{3/2} - 2s\ ^2S_{1/2}$ $3s\ ^2S_{1/2} - 2p\ ^2P^o_{3/2}$ $3d\ ^2D_{5/2} - 2p\ ^2P^o_{3/2}$	N	[Ingham, 1962]
6707.912 6707.761	LiI	$2p\ ^2P^o_{1/2,\ 3/2} - 2s\ ^2S_{1/2}$	T	[Vallance Jones, 1963]
7664.907 7698.979	KI	$4p\ ^2P^o_{3/2,\ 1/2} - 4s\ ^2S_{1/2}$	T	[Vallance Jones, 1963]
8446.26 8446.38 8446.76	OI	$3p\ ^3P_{0,\ 2,\ 1} - 3s\ ^3S_1$	T	[Shefov, 1963]
10829.081 10830.250 10830.341	HeI	$2p\ ^3P^o_{0,\ 1,\ 2} - 2s\ ^3S_1$	T	[Shefov, 1963]

* N, T, and D refer to nightglow, twilight glow, and dayglow, respectively.
** In general, refer to Radcliffe [1960] and Chamberlain [1961]; additional references are supplementary and are to be used in conjunction with the particular line.

Table 13-2. Molecular bands in airglow.

Molecule	System	Transition	Found In*	References**
O_2	Herzberg	$A^3\Sigma_u^+ \rightarrow X^3\Sigma_g^-$	N	[Ingham 1962]
O_2	Atmospheric Kaplan-Meinel	$b^1\Sigma_g^+ \rightarrow X^3\Sigma_g^-$	N	
O_2	Infrared Atmospheric	$a^1\Delta_g \rightarrow X^3\Sigma_g^-$	T	
N_2^+	First Negative	$B^2\Sigma_u^+ \rightarrow X^2\Sigma_g^+$	N, T	
OH	Meinel	$X^2\pi$	N	

* N, T, and D refer to nightglow, twilight glow, and dayglow, respectively.
** In general, refer to Radcliffe [1960] and Chamberlain [1961]; additional references are supplementary and are to be used in conjunction with the particular band.

13.1.5.1 *Diurnal Variation.* The diurnal variation at any station shows considerable variability from night to night. Table 13-6 gives the average intensity ratio relative to the midnight value for the 5577 Å [OI] emission observed for several stations. The large variability can be seen from the standard deviations listed. If sufficient data from enough stations are available, the intensity variations during the night are found to be strongly dependent on the latitude of the station. Figure 13-5 shows the typical average behavior for the 5577 Å [OI], 6300 Å [OI], and 5893 Å NaI lines. Although Fig. 13-5 is based on observations, it is designed to be illustrative and considerable variation from these curves must be expected for individual nights at different seasons and sunspot epochs.

13.1.5.2 *Annual Variation.* In northern temperate latitudes the 5577 Å [OI] line shows a maximum at almost all stations in October and one or more maxima in the spring between March and May; the spring maximum varies from station to station and from year to year. In the equatorial zone the behavior appears to be similar, but sufficient data are not available to allow a definitive con-

Table 13-3. Airglow emission intensities. (After Chamberlain [1961].)

Element		Intensity (R)
	NIGHT AIRGLOW	
5577 Å	[OI]	50 to 500
6300 Å	[OI]	30 to 250
5893 Å	NaI	< 30 (summer) 200 (winter)
6563 Å	H-α	5 to 20
5200 Å	[NI]	< 5
8645 Å	O_2 Atmospheric (0-1)	1.5×10^3
observable range	O_2 Herzberg	430
1.58 μ	OH (4-2)	175×10^3
(estimated total)	OH	4500×10^3
	TWILIGHT AIRGLOW	
3914 Å	N_2+	1×10^3 (quiet magnetic conditions)
5893 Å	NaI	1×10^3 (summer)
		5×10^3 (winter)
6300 Å	[OI]	1×10^3
3933 Å	CaII	150
6708 Å	LiI	200
5200 Å	[NI]	10
8446 Å	[OI]	13
10,830 Å	HeI	1×10^3
1.58 μ	O_2 Atmospheric (0-1)	20×10^3

Table 13-4. Altitudes and airglow emissions. (After Barbier [1961], Vallance Jones [1963], Delsemme and Delsemme [1960] and Chamberlain [1961].

Emission	Altitude	
	Maximum (km)	≈ Limits (km)
5577 Å [OI]	95-100	80-120
5893 Å NaI	85-95*	70-110*
6300 Å [OI]	250-275	Variable
Herzberg O_2		
2600-2900 Å	100	90-100
2400-2800 Å	97	85-120
Atmospheric O_2	97	75-120
OH		
6300 Å	85	56-100
7280 Å	83	50-135
7600-10,400 Å	90	
Continuum		
5335 Å	105	90-110
5200-5500 Å	100	85-110
5420 Å	103-105	73-145
6708 Å LiI	80*	65-105*
7665 Å, 7699 Å KI	95*	80-130*

* Altitudes for twilight emissions.

Table 13-5. Latitude dependence of 5577 Å [OI] emission line. (After F. E. Roach, *J. Geophys. Res.*, v. 68, p. 1015, 1963.)

Latitude (deg.)	Median Intensity (R)
5	200
10	220
15	230
20	220
25	220
30	250
35	260
40	280
45	275
50	315
55	570
60	1300
65	2500

clusion. The 5893 Å NaI lines show the most pronounced seasonal variation with a maximum in the winter that may be as large as 30 times the minimum in the summer.

13.1.5.3 *Secular Variation.* The only airglow emission for which sufficient data are available to determine a secular variation is the 5577 Å [OI] emission. As shown in Fig. 13-6 and 13-7, observations indicate a definite dependence of the intensity on sunspot cycle. Figure 13-6 also indicates a latitude dependent hysteresis loop, the statistical significance of which is in doubt. The 6300 Å [OI] line may also be expected to show a correlation with sunspot cycle; however, additional data are required to establish this.

13.2 AURORAE

Since the International Geophysical Year, it has become clear that several types of aurorae are latitude dependent. The *polar-glow aurora* is an extensive glow covering the polar cap, whose most important feature is the presence of first negative bands of N_2^+. It is produced by protons originating in solar flares and is closely associated with polar cap absorption events [Sandford, 1963].

The *low-latitude aurora* is characterized by the preponderance of the 6300 Å and 6364 Å [OI] emissions with, at times, a much smaller enhancement of the 5577 Å [OI] emission. A review of low-latitude aurorae is given by Roach and Roach [1963].

The *classical aurora* is found in the regions surrounding the zone of maximum auroral frequency. Most studies of aurorae refer to the classical aurora, unless otherwise stated. The existence of daytime aurora has recently been confirmed by measurements of the 5577 Å and 6300 Å [OI] lines and the accompanying increase of magnetic activity [Noxon, 1963].

There is an atmospheric phenomenon called *radio-aurora*; for details, see Collins and Forsyth [1959], Ratcliffe [1960], and Chamberlain [1961]. Radio-aurora may be described briefly as the ionization giving rise to certain characteristic types of radio reflections. Optical aurora is not always accompanied by observable radio-aurora and the radio-aurora may occur without visible aurora.

Processes involved in the formation of aurorae are related to corpuscular radiation originating primarily at the sun. It is believed that charged particles (electrons and, to a lesser extent, protons) interacting with the earth's magnetic field and atmosphere excite the atmospheric gases which then emit visible radiation. This is known as visual aurorae. At the present time, a generally accepted theory of aurorae formation is not available. The interaction mechanisms involved between the solar particles and the geomagnetic field and atmosphere are not fully understood and the role played by the radiation belts which surround the earth is not clear.

13.2.1 Forms, Brightness, and Color

Nomenclature used to describe the general shape or form of visible aurorae is found in the *International Auroral Atlas*, published for the International Union of Geodesy and Geophysics, University Press, Edinburgh, 1963, to which the reader is referred for further details. In general the notation is summarized and defined as follows:

Qualifying Symbols and Condition	*Structure*	*Form*	*Brightness Index*	*Color Class*
q = quiet	H = homogeneous	A = arc	0	a
$a_{(1,2,3,4)}$ = active	S = striated	B = band	1	b
$p_{(1,2,3,4)}$ = pulsing	$R_{(1,2,3)}$ = rayed	P = patch	2	c
$m_{(2,3,\ldots)}$ = multiple		V = veil	3	d
f = fragmentary		R = rays	4	e
c = coronal		N = not identifiable		f

Table 13-6. Diurnal variation of the 5577 Å (OI) airglow emission.

Local Civil Time	Tonanzintla Feb. 1959-May 1962			Huancayo June 1958-Nov. 1961			San Juan May 1960-March 1962			Sacramento Peak July 1957-Sept. 1959		
	Intensity Ratio	N	σ	Intensity Ratio	N	σ	Intensity Ratio	N	σ	Intensity Ratio	N	σ
20	2.10	43	1.25	1.15	34	0.39				0.82	81	0.31
21	1.69	84	1.04	1.08	45	0.38				0.87	116	0.25
22	1.26	121	0.53	1.04	71	0.30				0.92	130	0.22
23	1.21	161	0.53	1.03	90	0.19	1.32	22	0.72	0.99	138	0.17
00	1.00	206	—	1.00	103	—	1.00	71	—	1.00	146	—
01	0.94	190	0.39	1.03	92	0.19	0.86	63	0.35	0.98	135	0.17
02	0.90	168	0.41	1.10	82	0.27	0.85	57	0.41	0.98	121	0.28
03	0.96	145	0.67	1.16	75	0.35	1.02	53	0.62	0.96	111	0.33
04	0.88	120	0.50	1.23	72	0.51	1.14	35	0.75	0.86	74	0.30
05	0.99	73	0.57	1.31	57	0.60	1.52	11	0.68	0.77	41	0.27

Note: The intensity ratio is taken relative to the midnight value. N represents the number of observations and σ the standard deviation.

Detailed description of an aurora should be given using one or more symbols from the first column, followed in order by one symbol from each of the other columns, for example, $a_3 f R_3 B$ 3c. For many purposes a more limited description is adequate: RB 3c or merely RB.

13.2.1.1 *Form, Condition, and Structure.* The forms are fundamental in the identification and reporting of aurorae. *Band-like forms* (Fig. 13-8 through 13-13) are characterized by a continuous lower border. When the form appears as a simple slightly curving arch, or as part of an arch with a regular lower border, it is called an *arc* (A). When the lower border is irregular and contains kinks or folds, the form is called a *band* (B).

Diffuse forms are a patch or a veil. The *patch* (P) is a splotch of luminosity with no discernible continuous lower border and is usually like a diffuse patch of cloud. The *veil* (V) is a rather extensive uniform luminosity, often covering a large portion of the sky, that may occur alone or as a background to other forms.

Rays (R) (Fig. 13-14 through 13-16) are shafts of luminosity aligned in the direction of the geomagnetic field. The form may consist of a single ray, a small bundle of rays, or many scattered rays.

The *forms not identifiable* (N) are aurorae that are difficult to identify because of adverse observing conditions, such as clouds, moonlight, and twilight, or because the identifiable parts are below the horizon and only a diffuse glow appears above the horizon.

The condition, *quiet* (q), describes an aurora that undergoes only very slow changes in position or shape. *Active* (a) describes an aurora that moves or changes its shape rapidly. The four subclasses of activity are:

a_1, the movement of folds or irregularities along the boundary of bands at speeds up to about 500 m sec^{-1};

a_2, the individual forms in which the shape of the lower border changes rapidly;

a_3, the appearance of rapid movement of rays horizontally along the form; and

a_4, a display as a whole in which forms fade rather quickly while new, similar, or different forms appear in other parts of the sky.

The *pulsing* (p) condition shows fairly rapid and often rhythmic fluctuations in brightness. Four subclasses are:

p_1 (pulsating) for those conditions where the phase of the variation of brightness is uniform throughout the form;

p_2 (flaming) for a large area of the sky rather than an individual form (sky appears lit by surges of luminosity sweeping upwards, or occasionally downwards, towards the magnetic zenith);

p_3 (flickering) for a condition of a large part of a display which undergoes rapid, irregular changes in brightness as if lit by flickering flames;

p_4 (streaming) for an irregular variation of brightness which progresses rapidly along the horizontal extent of homogeneous forms.

Qualifying symbols are used to describe other conditions. *Multiple* ($m_{2,3}$) is used when two or more associated and roughly parallel forms of the same kind occur. *Fragmentary* (f) means only a portion of an arc or band is present. If a rayed form is situated around the magnetic zenith and is viewed along the direction of the magnetic field lines, the rays appear to converge and assume the shape of a fan or crown; this is the *coronal* (c) condition.

Homogeneous (H) implies a lack of internal structure; the brightness is uniform or changes only gradually across the form. *Striated* (S) describes rather irregular fine striations or filaments, usually the order of 10 km long within the form, aligned roughly parallel with the lower border. It is observed occasionally in patches and more often in arcs and bands at high elevations. *Rayed* structures ($R_{1,2,3}$) are characterized by the appearance within them of rays aligned along the lines of force of the earth's magnetic field. R_1 refers to short rays about 10 km long; they are usually bright near the bottom ends and fade rapidly with height. R_2 refers to rays a few hundred kilometers in length and rather uniform in brightness. R_3 refers to very long rays several hundreds to 1000 km in length; their brightness is rather faint and changes gradually with height.

13.2.1.2 *Brightness Index.* Brightness index is a visual estimate (order of magnitude) of auroral intensity (luminance $\times 4\pi$ sr^2) in the region of maximum intensity. For the green atomic oxygen emission 5577 Å, a scale of intensity index is defined in Table 13-7.

Distinguishing between strong airglow and very weak aurorae is difficult because both appear colorless. Bright aurorae, with intensity above the eye's color threshold, generally appear green as a result of excitation of atomic oxygen at a wavelength of 5577 Å. Occasionally red or bluish-purple colors are also visible. The red is attributed to excitation of the atomic oxygen doublet at 6300 and 6364 Å, and possibly to ionized molecular oxygen. The bluish-purple is attributed to the excitation of ionized molecular nitrogen. If green, red, and bluish-purple are combined in a bright aurora, a white or yellow color may occasionally be apparent.

Table 13-7. Intensities and index intensities of the 5577 Å [OI] line.

(10^3 R)	Index	Visual Appearance of Typical Aurora
< 0.1	0	subvisual
1	1	comparable with Milky Way; green color not perceived
10	2	comparable with moonlit cirrus cloud; green color sometimes perceived
10^2	3	comparable with brightly moonlit cirrus cloud or moonlit cumulus cloud
10^3	4	much brighter than 3; sometimes casts easily discernible shadows

13.2.1.3 *Color Class.* Aurorae are observed in a variety of colors and color combinations. Rough estimates by eye of color may be indicated as follows:

Color Class	*Description*
a	red upper region
b	red lower border
c	white, green or yellow
d	red
e	red and green
f	blue or purple dominant

13.2.2 Spectrum

The many atomic lines and molecular bands which have been identified in auroral spectra are listed in Tables 13-8 and 13-9. However, not all of these necessarily appear in a particular aurora. Figures 13-17 through 13-20 show an auroral spectrum from 1100 to 11,000 Å and from 14,000 to 16,500 Å.

13.2.3 Altitudes

The apparent sharp lower border of auroral arcs and bands has been measured by various observers in an effort to determine the heights at which aurorae occur. Height measurements [Störmer, 1955] of Northern Hemisphere aurorae occurring in Norway from 1911 to 1944 revealed a concentration of auroral heights within the band 90 to 110 km. Similarly, W. M. Aitken measured auroral photographs taken simultaneously in the Southern Hemisphere at the South Pole and Ellsworth Stations, Antarctica, during 1961. These measurements showed that most of the lower borders were around 100 km with an occasional deeper penetration to 90 km. The upper limit of auroral rays, found in some sunlit rays, can be higher than 1000 km.

13.2.4 Occurrences and Variations

The maximum auroral frequency occurs within circular bands approximately 20° to 25° from each geomagnetic pole. This band of maximum auroral occurrence is called the *auroral zone* in each hemisphere. Aurorae are observed occasionally at midlatitudes and very rarely at tropical latitudes.

Figure 13-21 shows the *isoaurorae*, which represent regions of equal frequency of occurrence of overhead aurorae. These should be distinguished from the *isochasms* which represent regions of equal frequency of occurrence of aurorae in any part of the sky. Details on the locations of the auroral zones are given by Hultquist [1962].

The influence of solar activity causes a maximum in auroral events about two years after the maximum of the 11-yr solar cycle. Auroral events have a seasonal variation with maximum activity in the spring and fall, and a 27-day recurrence tendency because of the sun's rotation.

Table 13-8. Atomic lines in auroral spectra; value in parentheses below multiplet is excitation potential in eV. Wavelengths marked * are uncertain. (From Chamberlain [1961] by permission of Academic Press, N. Y.)

Forbidden Atomic Lines			
Transition	Multiplet	J	λ (Å)
[OI]$_{32}$ Auroral	$2p^4\ ^1D - 2p^4\ ^1S$ (4.17)	2 - 0	5577.345
[OI]$_{31}$ Transauroral	$2p^4\ ^3P - 2p^4\ ^1S$ (4.17)	1 - 0	2972.325
[OI]$_{21}$ Nebular	$2p^4\ ^3P - 2p^4\ ^1D$ (1.96)	2 - 2	6300.308
		1 - 2	6363.790
[OII]$_{32}$ Auroral	$2p^3\ ^2D^o - 2p^3\ ^2P^o$ (5.00)	2½ - ½	7318.6
		2½ - 1½	7319.4
		1½ - ½	7329.9
		1½ - 1½	7330.7
[OII]$_{21}$ Nebular	$2p^3\ ^4S^o - 2p^3\ ^2D^o$ (3.31)	1½ - 1½	3726.16
		1½ - 2½	3728.91
[NI]$_{32}$ Auroral	$2p^3\ ^2D^o - 2p^3\ ^2P^o$ (3.56)	2½ -	10,395.4
		1½ -	10,404.1
[NI]$_{31}$ Transauroral	$2p^3\ ^4S^o - 2p^3\ ^2P^o$ (3.56)	1½ -	3466.4
[NI]$_{21}$ Nebular	$2p^3\ ^4S^o - 2p^3\ ^2D^o$ (2.37)	1½ - 1½	5199.42
		1½ - 2½	5202.29
[NII]$_{32}$ Auroral	$2p^2\ ^1D - 2p^2\ ^1S$ (4.04)	2 - 0	5754.8
[NII]$_{21}$ Nebular	$2p^2\ ^3P - 2p^2\ ^1D$ (1.89)	2 - 2	6583.6*

Permitted Atomic Lines			
No.	Multiplet	J	λ (Å)
	OI		
1	$3s\ ^5S^o - 3p\ ^5P$ (10.69)	2 -	7774.
3	$3s\ ^5S^o - 4p\ ^5P$ (12.23)	2 -	3947.5
4	$3s\ ^3S^o - 3p\ ^3P$ (10.94)	1 -	8446.5
5	$3s\ ^3S^o - 4p\ ^3P$ (12.31)	1 -	4368.30
6	$3s\ ^3S^o - 5p\ ^3P$ (12.82)	1 -	3692.44
9	$3p\ ^5P - 5s\ ^5S^o$ (12.61)	- 2	6455.*
10	$3p\ ^5P - 4d\ ^5D^o$ (12.70)	—	6157.
11	$3p\ ^5P - 6s\ ^5S^o$ (12.96)	- 2	5436.
12	$3p\ ^5P - 5d\ ^5D^o$ (13.01)	—	5330.
14	$3p\ ^5P - 6d\ ^5D^o$ (13.18)	—	4968.
19	$3p\ ^5P - 3s'\ ^3D^o$ (12.49)	2 - 3	7995.12
		- 2	7987.
20	$3p\ ^3P - 5s\ ^3S^o$ (12.64)	- 1	7254.4*
22	$3p\ ^3P - 6s\ ^3S^o$ (12.98)	- 1	6046. *

Permitted Atomic Lines (Continued)			
No.	Multiplet	J	λ (Å)
	OII		
1	$3s\ ^4P - 3p\ ^4D^o$ (25.54)	2½ - 3½	4649.139
		1½ - 2½	4641.811
		½ - 1½	4638.854
		2½ - 2½	4676.234
		1½ - 1½	4661.635
		½ - ½	4650.841
2	$3s\ ^4P - 3p\ ^4P^o$ (25.74)	2½ - 2½	4349.426
		1½ - 1½	4336.865
		1½ - ½	4345.562
		1½ - 2½	4319.631
		½ - 1½	4317.139
3	$3s\ ^4P - 3p\ ^4S^o$ (26.19)	2½ - 1½	3749.49
		1½ - 1½	3727.33*
		½ - 1½	3712.75*
5	$3s\ ^2P - 3p\ ^2D^o$ (26.14)	1½ - 2½	4414.909
		½ - 1½	4416.975
		1½ - 1½	4452.377
6	$3s\ ^2P - 3p\ ^2P^o$ (26.45)	1½ - 1½	3973.263
		½ - ½	3954.372
		1½ - ½	3982.719
		½ - 1½	3945.048*
10	$3p\ ^4D^o - 3d\ ^4F$ (28.58)	3½ - 4½	4075.868
		2½ - 3½	4072.164
		1½ - 2½ }	4069.8
		½ - 1½ }	
		3½ - 3½	4092.940*
		1½ - 1½	4078.862*
11	$3p\ ^4D^o - 3d\ ^4P$ (28.71)	1½ - ½	3872.45*
		1½ - 1½	3882.45*
12	$3p\ ^4D^o - 3d\ ^4D$ (28.73)	3½ - 2½	3883.15*
13	$3p\ ^4D^o - 3d\ ^2F$ (28.74)	2½ - 2½	3857.18*
		3½ - 2½	3875.82*
15	$3s'\ ^2D - 3p'\ ^2F^o$ (28.24)	2½ - 3½	4590.971*
		1½ - 2½	4596.174*
16	$3s'\ ^2D - 3p'\ ^2D^o$ (28.39)	2½ - 2½	4351.269
		1½ - 1½	4347.425
17	$3s'\ ^2D - 3p'\ ^2P^o$ (28.71)	2½ - 1½ }	3912.0*
		1½ - 1½ }	
		1½ - ½	3919.287*
19	$3p\ ^4P^o - 3d\ ^4P$ (28.70)	2½ - 2½	4169.230*
		½ - ½	4121.48*
20	$3p\ ^4P^o - 3d\ ^4D$ (28.73)	2½ -	4120. *
21	$3p\ ^4P^o - 3d\ ^2F$ (28.74)	2½ - 2½	4112.029*
26	$3p\ ^2D^o - 3d\ ^2D$ (28.94)	1½ - 1½	4369.28*
28	$3p\ ^4S^o - 3d\ ^4P$ (28.71)	1½ - 2½	4924.60*
		1½ - ½	4890.93*
33	$3p\ ^2P^o - 3d\ ^2D$ (28.94)	½ - 1½	4941.12*
36	$3p'\ ^2F^o - 3d'\ ^2G$ (31.18)	3½ - 4½	4189.788
		2½ - 3½	4185.456

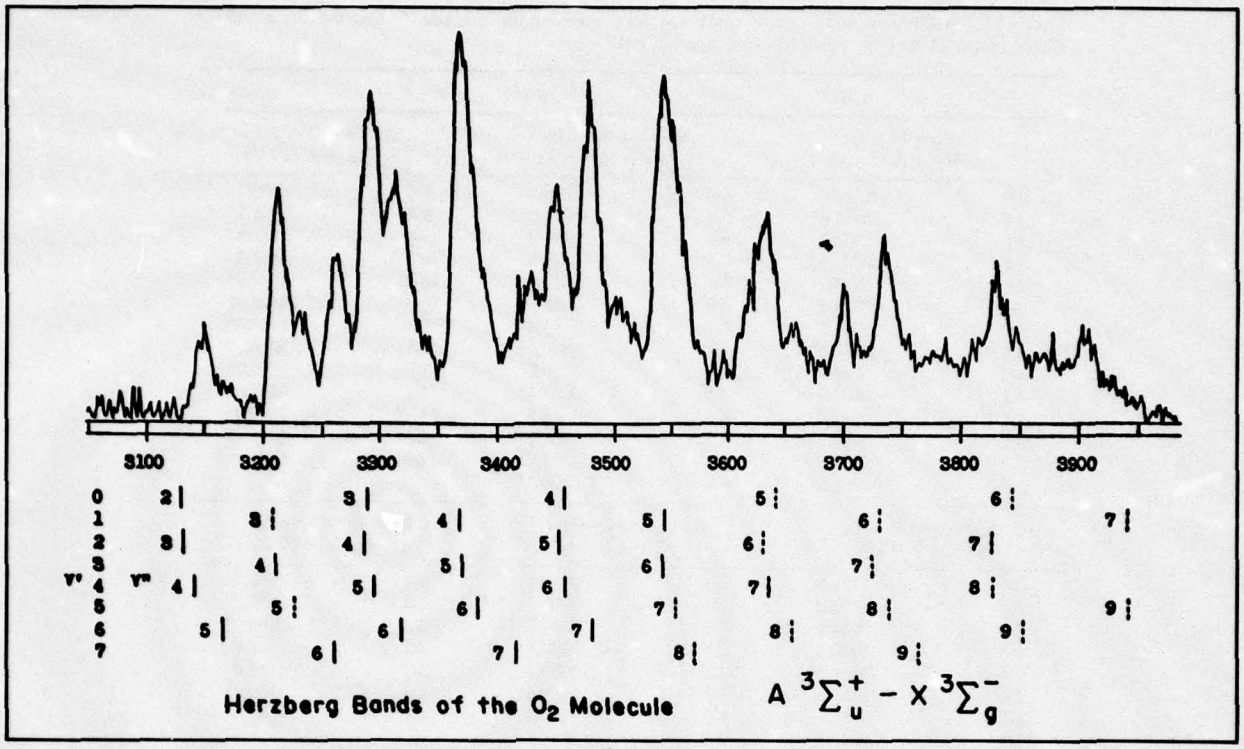
Table 13-8. Atomic lines in auroral spectra; value in parentheses below multiplet is excitation potential in eV. Wavelengths marked • are uncertain. (From Chamberlain [1961] by permission of Academic Press, N. Y.) (Continued)

Permitted Atomic Lines (Continued)			
No.	Multiplet	J	λ (Å)
	NI		
1	$3s\ ^4P - 3p\ ^4D^o$ (11.71)	2½ - 3½	8680.24
		1½ - 2½	8683.38
		2½ - 2½	8718.82
		1½ - 1½	8711.69
		½ - ½	8703.24
2	$3s\ ^4P - 3p\ ^4P^o$ (11.79)	2½ - 2½	8216.28
		2½ - 1½	8242.34
		1½ - ½	8223.07
		1½ - 2½	8184.80
		½ - 1½	8187.95
5	$3s\ ^4P - 4p\ ^4P^o$ (13.21)	2½ - 2½	4223.04•
6	$3s\ ^4P - 4p\ ^4S^o$ (13.26)	2½ - 1½	4151.46•
8	$3s\ ^2P - 3p\ ^2P^o$ (12.07)	1½ - 1½	8629.24
9	$3s\ ^2P - 4p\ ^2S^o$ (13.14)	1½ - ½	4935.03
		½ - ½	4914.90
15	$3p\ ^2S^o - 3d\ ^2P$ (12.91)	½ - 1½	9060.6•
	NII		
1	$2p^3\ ^1D^o - 3p\ ^1P$ (20.32)	2 - 1	4895.20•
3	$3s\ ^3P^o - 3p\ ^3D$ (20.57)	2 - 3	5679.56
		1 - 2	5666.64
		0 - 1	5676.02
		2 - 2	5710.76
		1 - 1	5686.21
		2 - 1	5730.67
4	$3s\ ^3P^o - 3p\ ^3S$ (20.85)	2 - 1	5045.098
		1 - 1	5010.620
		0 - 1	5002.692
5	$3s\ ^3P^o - 3p\ ^3P$ (21.07)	2 - 2	4630.537
		1 - 0	4621.392
		1 - 2	4601.478
		0 - 1	4607.153
6	$3s\ ^3P^o - 3p\ ^1D$ (21.51)	1 - 2	3955.851
8	$3s\ ^1P^o - 3p\ ^1P$ (20.32)	1 - 1	6482.07
9	$3s\ ^1P^o - 3p\ ^3D$ (20.56)	1 - 2	5747.29•
		1 - 1	5767.43•
12	$3s\ ^1P^o - 3p\ ^1D$ (21.51)	1 - 2	3994.996
14	$3p\ ^1P - 3d\ ^3F^o$ (23.02)	1 - 2	4564.78•
19	$3p\ ^3D - 3d\ ^3F^o$ (23.04)	3 - 4	5005.140
		2 - 3, 1 - 2	5001.3
		3 - 3	5025.665
		2 - 2	5016.387

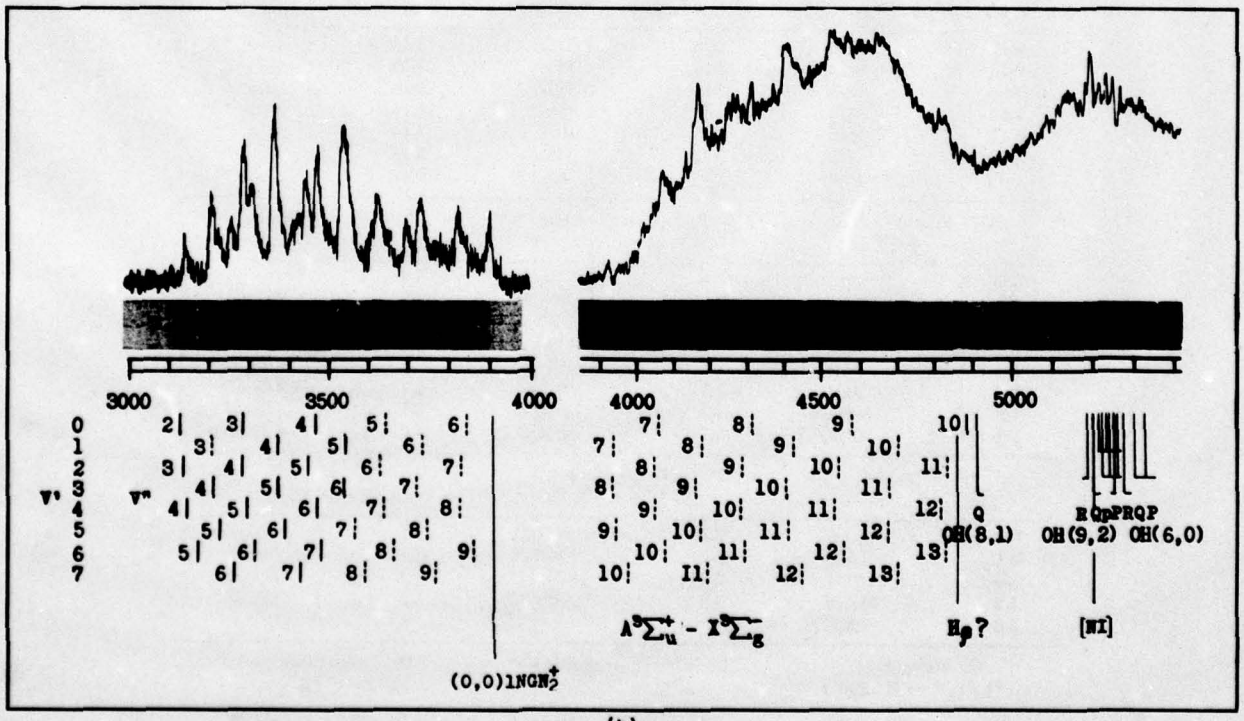
Permitted Atomic Lines (Continued)			
No.	Multiplet	J	λ (Å)
	NII		
20	$3p\ ^3D - 3d\ ^3D^o$ (23.14)	3 - 2	4810.286•
		2 - 1, 2 - 2	4791. •
		2 - 3, 1 - 1	4780.5•
21	$3p\ ^3D - 3d\ ^3P^o$ (23.31)	2 - 2	4488.15•
		3 - 2	4507.559•
24	$3p\ ^3S - 3d\ ^3P^o$ (23.32)	1 - 0	4987.377•
28	$3p\ ^3P - 3d\ ^3D^o$ (23.14)	2 - 1	5960.93•
29	$3p\ ^3P - 3d\ ^3P^o$ (23.32)	1 - 0	5454.26•
39	$3d\ ^3F^o - 4f\ ^3G$ (26.10)	4 - 5	4041.321
		3 - 4	4043.537
		2 - 3	4035.087
		4 - 4	4057.00•
		3 - 3	4044.75•
40	$3d\ ^3F^o - 4f\ ^1G$ (26.10)	3 - 4	4026.080
42	$3d\ ^1D^o - 4f\ ^1F$ (26.05)	2 - 3	4176.164
43	$3d\ ^1D^o - 4f\ ^3F$ (26.05)	2 - 3	4171.608
47	$3d\ ^3D^o - 4f\ ^1F$ (26.05)	2 - 3	4241.787
48	$3d\ ^3D^o - 4f\ ^3F$ (26.05)	3 - 4	4241.787
		2 - 3, 1 - 2	4237.0•
	H		
1	$2p\ ^2P^o - 3d\ ^2D$ et al. (12.04)	—	6562.817 (Hα)
1	$2p\ ^2P^o - 4d\ ^2D$ et al. (12.69)	—	4861.332 (Hβ)
1	$2p\ ^2P^o - 5d\ ^2D$ et al. (13.00)	—	4340.468 (Hγ)
	He I		
1	$2s\ ^3S - 2p\ ^3P^o$ (20.87)	1 -	10,830. •
	Na I		
1	$3s\ ^2S - 3p\ ^2P^o$ (2.10)	½ - 1½	5889.953
		½ - ½	5895.923

Table 13-9. Molecular bands in auroral spectra; wavelengths marked • are uncertain. (From Chamberlain [1961] by permission of Academic Press.)

$v' - v''$	λ (Å)	$v' - v''$	λ (Å)	$v' - v''$	λ (Å)
N_2 First Positive ($B\,^3\Pi_g \rightarrow A\,^3\Sigma_u^+$)		N_2 First Positive ($B\,^3\Pi_g \rightarrow A\,^3\Sigma_u^+$)		N_2 First Positive ($B\,^3\Pi_g \rightarrow A\,^3\Sigma_u^+$)	
0-0	10,510.	6-2	6069.7	9-6	6394.7
1-0	8912.4	6-3	6623.6	9-7	6957.7
2-0	7753.7	6-4	7274.0	9-8	7612.9•
2-1	8723.0	6-5	8047.9•	10-6	5854.4
3-0	6875.2	7-3	6013.6	10-7	6322.9•
3-1	7626.8	7-4	6544.8	10-8	6859.3•
3-2	8542.5	7-5	7164.8	11-8	6253.0•
4-0	6186.8•	7-6	7896.9•	11-7	5804.3•
4-1	6788.6	8-4	5959.0	11-8	6253.0•
4-2	7504.7	8-5	6468.5	11-9	6764.0•
5-1	6127.4	8-6	7059.5•	11-10	7349.8•
5-2	6704.8	8-7	7752.0•	12-8	5755.2•
5-3	7387.2	9-4	5478.2•	12-9	6185.2•
5-4	8205.5•	9-5	5906.0•		
N_2 Second Positive ($C\,^3\Pi_u \rightarrow B\,^3\Pi_g$)		N_2 Second Positive ($C\,^3\Pi_u \rightarrow B\,^3\Pi_g$)		N_2 Second Positive ($C\,^3\Pi_u \rightarrow B\,^3\Pi_g$)	
0-0	3371.3	1-3	3755.4	3-2	3116.7
0-1	3576.9	1-4	3998.4	3-3	3285.3
0-2	3804.9	1-6	4574.3	3-4	3469. •
0-3	4059.4	2-1	3136.0	3-5	3671.9
0-4	4343.6•	2-2	3309.	3-7	4141.8
1-0	3159.3	2-3	3500.5•	4-4	3268.1•
1-1	3339.	2-4	3710.5	4-8	4094.8•
1-2	3536.7	2-5	3943.0		
N_2 Vegard-Kaplan ($A\,^3\Sigma_u^+ \rightarrow X\,^1\Sigma_g^+$)		N_2 Vegard-Kaplan ($A\,^3\Sigma_u^+ \rightarrow X\,^1\Sigma_g^+$)		N_2 Vegard-Kaplan ($A\,^3\Sigma_u^+ \rightarrow X\,^1\Sigma_g^+$)	
0-10	3602.	1-16	5752. •	3-14	4169. •
0-12	4218. •	2-10	3268. •	3-15	4534.
1-9	3198.	2-11	3502. •	3-18	6068. •
1-10	3425.	2-12	3767.	4-11	3192. •
1-11	3683.	2-13	4072.	4-14	3948. •
1-12	3978.	2-14	4425.	5-15	4045. •
1-13	4320. •	2-15	4837. •	5-17	4771. •
N_2^+ First Negative ($B\,^2\Sigma_u^+ \rightarrow X\,^2\Sigma_g^+$)		N_2^+ First Negative ($B\,^2\Sigma_u^+ \rightarrow X\,^2\Sigma_g^+$)		N_2^+ First Negative ($B\,^2\Sigma_u^+ \rightarrow X\,^2\Sigma_g^+$)	
0-0	3914.4	1-4	5148.8	3-4	4166.8
0-1	4278.1	2-1	3563.9	3-5	4554.1
0-2	4709.2	2-2	3857.9	4-6	4515.9•
0-3	5228.3	2-3	4199.1	4-7	4957.9
1-0	3582.1	2-4	4599.7	5-6	4121.3•
1-1	3884.3	2-5	5076.6	5-7	4485.9•
1-2	4236.5	3-2	3548.9	6-7	4110.9•
1-3	4651.8	3-3	3835.4•	6-8	4466.6•
N_2^+ Meinel ($A\,^2\Pi \rightarrow X\,^2\Sigma_g^+$)		N_2^+ Meinel ($A\,^2\Pi \rightarrow X\,^2\Sigma_g^+$)		N_2^+ Meinel ($A\,^2\Pi \rightarrow X\,^2\Sigma_g^+$)	
0-0	11,036.2	2-1	9431.2•	3-1	8053.6
0-1	14,523.	2-2	11,820.2•	4-1	7036.8
1-0	9145.3	2-3	15,748.	4-2	8293.4
1-2	15,114.	3.0	6853.0	5-2	7239.9
2-0	7825.7				
O_2 Atmospheric ($b\,^1\Sigma_g^+ \rightarrow X\,^3\Sigma_g^-$)		O_2 Infrared Atmospheric $a\,^1\Delta_g \rightarrow X\,^3\Sigma_g^-$		O_2^+ First Negative ($b\,^4\Sigma_g^- \rightarrow a\,^4\Pi_u$)	
0-1	8598.	0-1	14,663. •	0-0	6026.4
1-1	7684.			0-1	6418.7•
				1-0	5631.9
				1-1	5973.4•
				2-0	5295.7

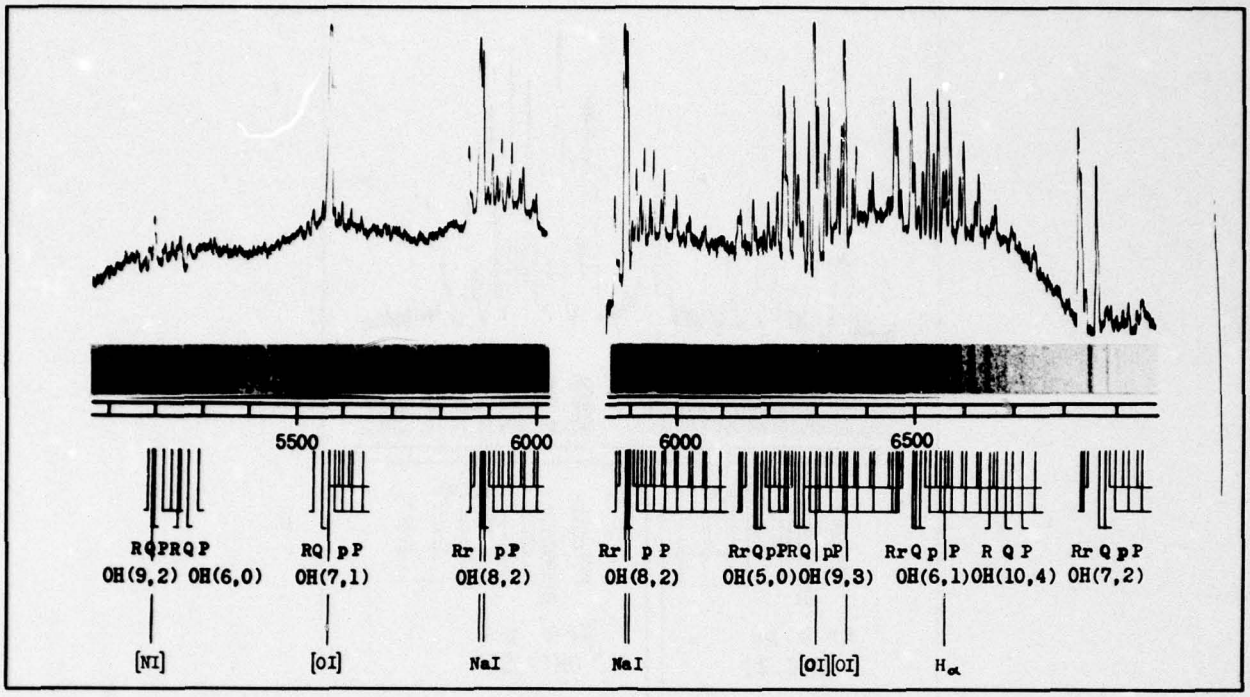


(a)

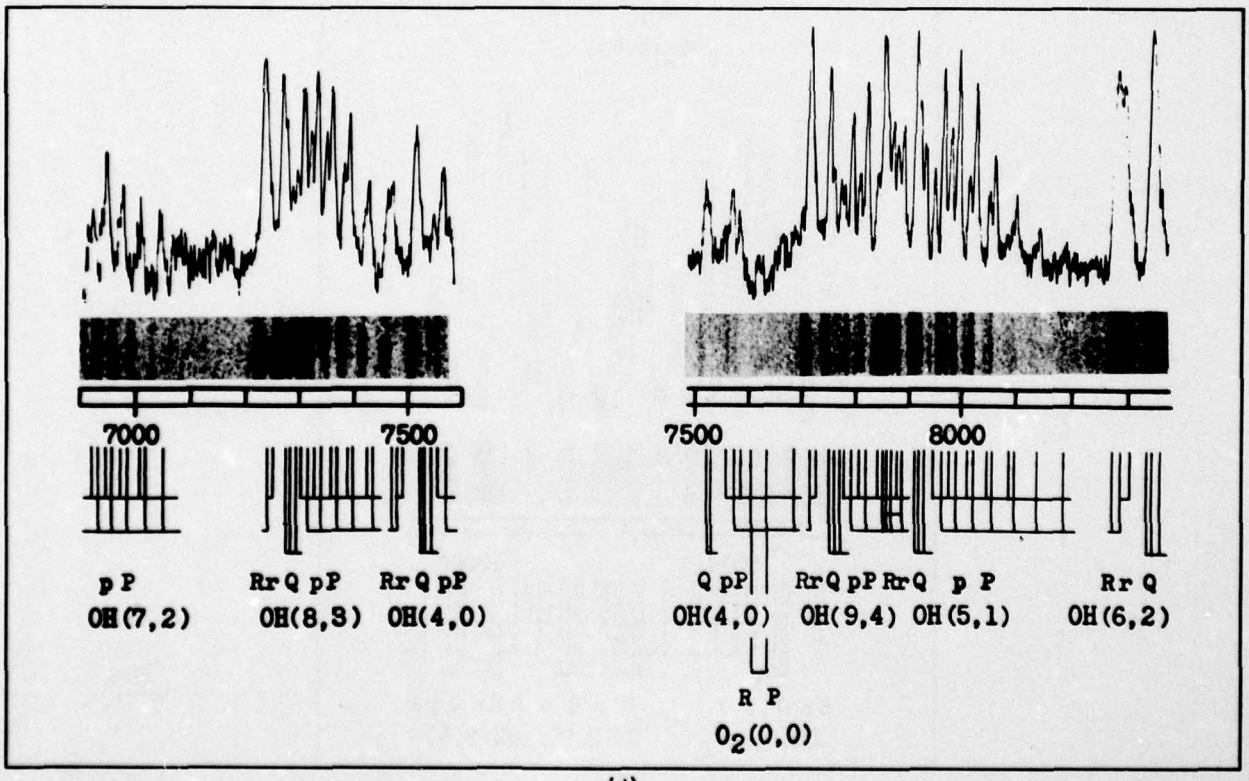


(b)

Fig. 13-1. Night-sky spectrum in the wavelength range 3000 to 12,400 Å: (a) 3050 to 3950 Å, (b) 3000 to 5400 Å, (c) 5100 to 7000 Å, (d) 6900 to 8400 Å, (e) 8200 to 10,100 Å, (f) 9800 to 11,400 Å, and (g) 11,300 to 12,400 Å. (From V. I. Krassovsky, N. N. Shefov, and V. I. Yarin, *Planetary Space Sci.*, v. 9, p. 883, 1962 by permission.)

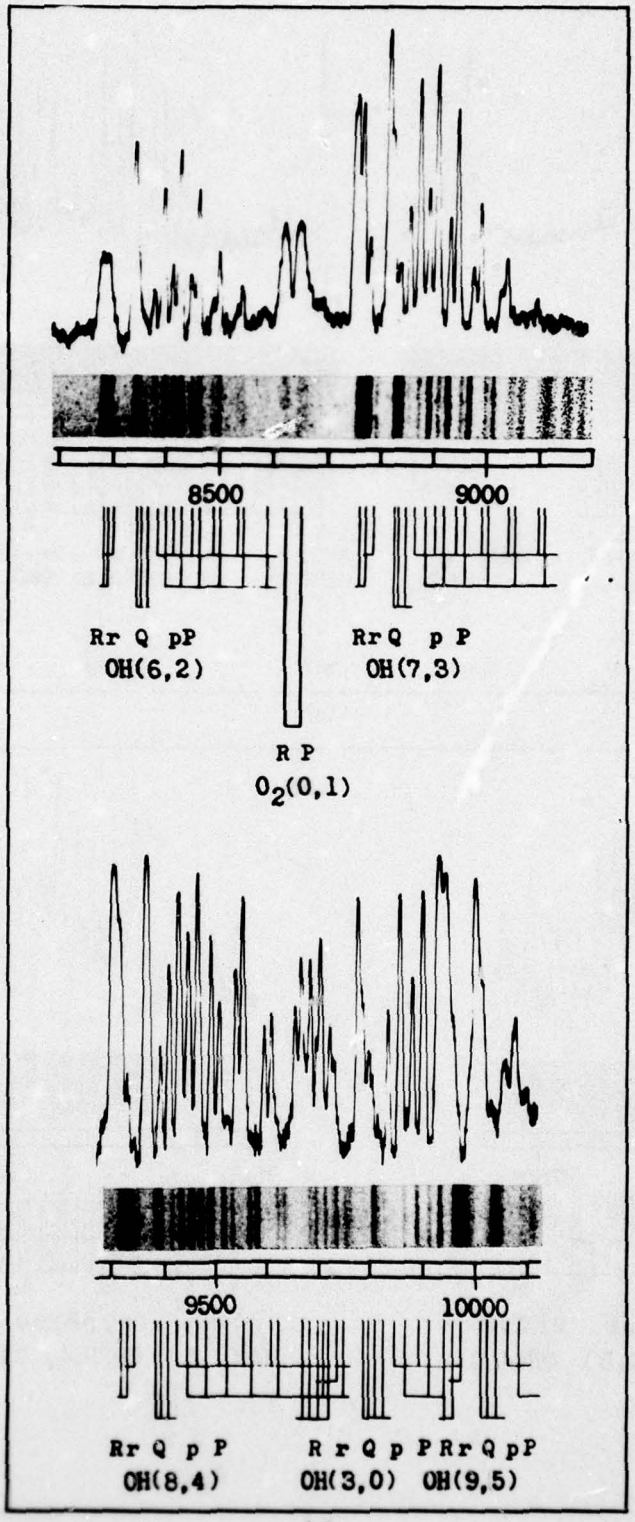


(c)



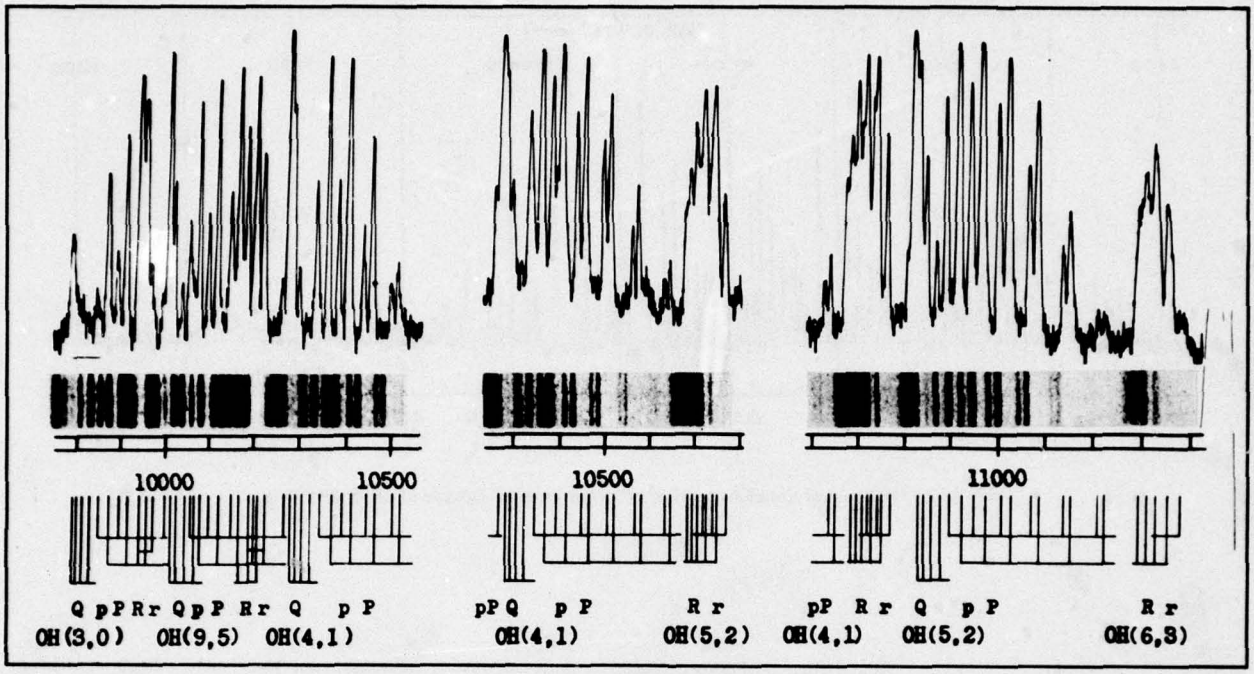
(d)

Fig. 13-1. Night-sky spectrum in the wavelength range 3000 to 12,400 Å; (a) 3050 to 3950 Å, (b) 3000 to 5400 Å, (c) 5100 to 7000 Å, (d) 6900 to 8400 Å, (e) 8200 to 10,100 Å, (f) 9800 to 11,400 Å, and (g) 11,300 to 12,400 Å. (From V. I. Krassovsky, N. N. Shefov, and V. I. Yarin, *Planetary Space Sci.*, v. 9, p. 883, 1962 by permission.)

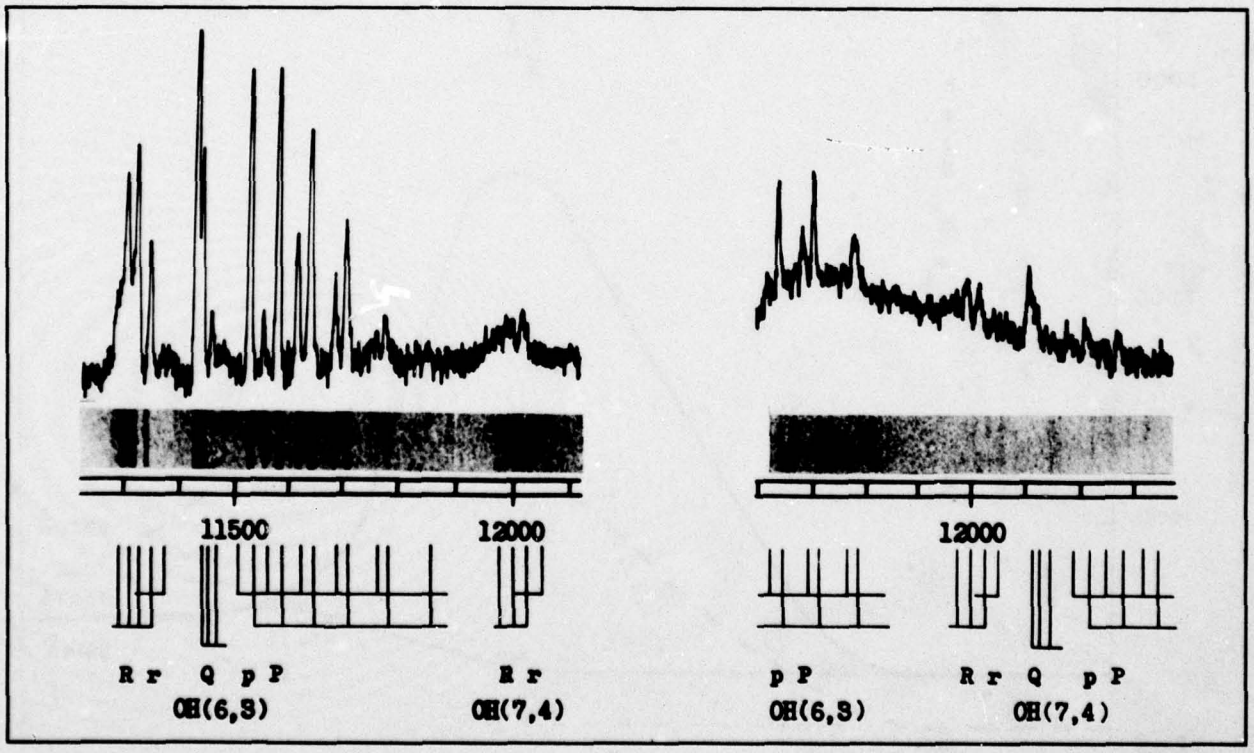


(e)

Fig. 13-1. Night-sky spectrum in the wavelength range 3000 to 12,400 Å; (a) 3050 to 3950 Å, (b) 3800 to 5400 Å, (c) 5100 to 7000 Å, (d) 6900 to 8400 Å, (e) 8200 to 10,100 Å, (f) 9800 to 11,400 Å, and (g) 11,300 to 12,600 Å. (From V. I. Krasovsky, N. N. Shefov, and V. I. Yarin, *Planetary Space Sci.*, v. 9, p. 883, 1962 by permission.)



(f)



(g)

Fig. 13-1. Night-sky spectrum in the wavelength range 3000 to 12,400 Å; (a) 3050 to 3950 Å, (b) 3000 to 5400 Å, (c) 5100 to 7000 Å, (d) 6900 to 8400 Å, (e) 8200 to 10,100 Å, (f) 9800 to 11,400 Å, and (g) 11,300 to 12,400 Å. (From V. I. Krassovsky, N. N. Shefov, and V. I. Yarin, *Planetary Space Sci.*, v. 9, p. 883, 1962 by permission.)

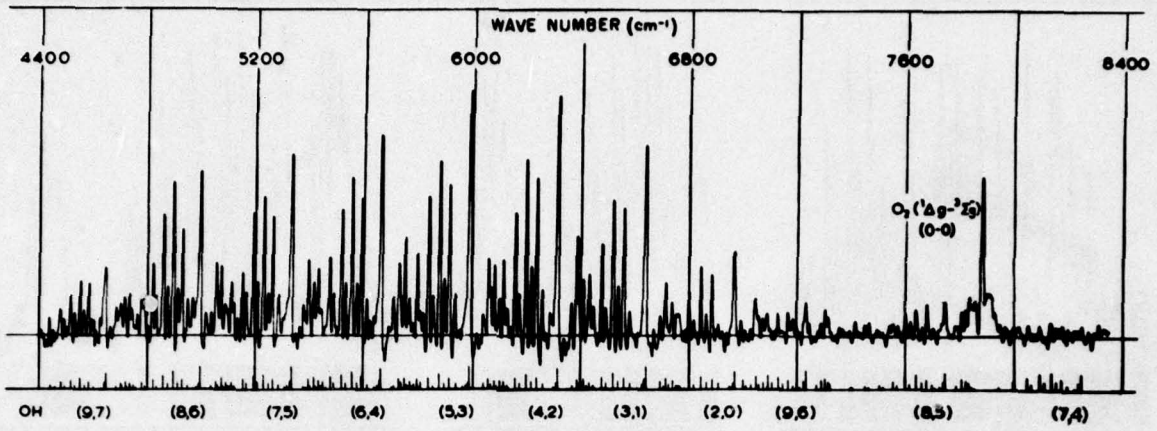


Fig. 13-2. Spectrum of the night airglow observed from an altitude of about 80,000 ft.

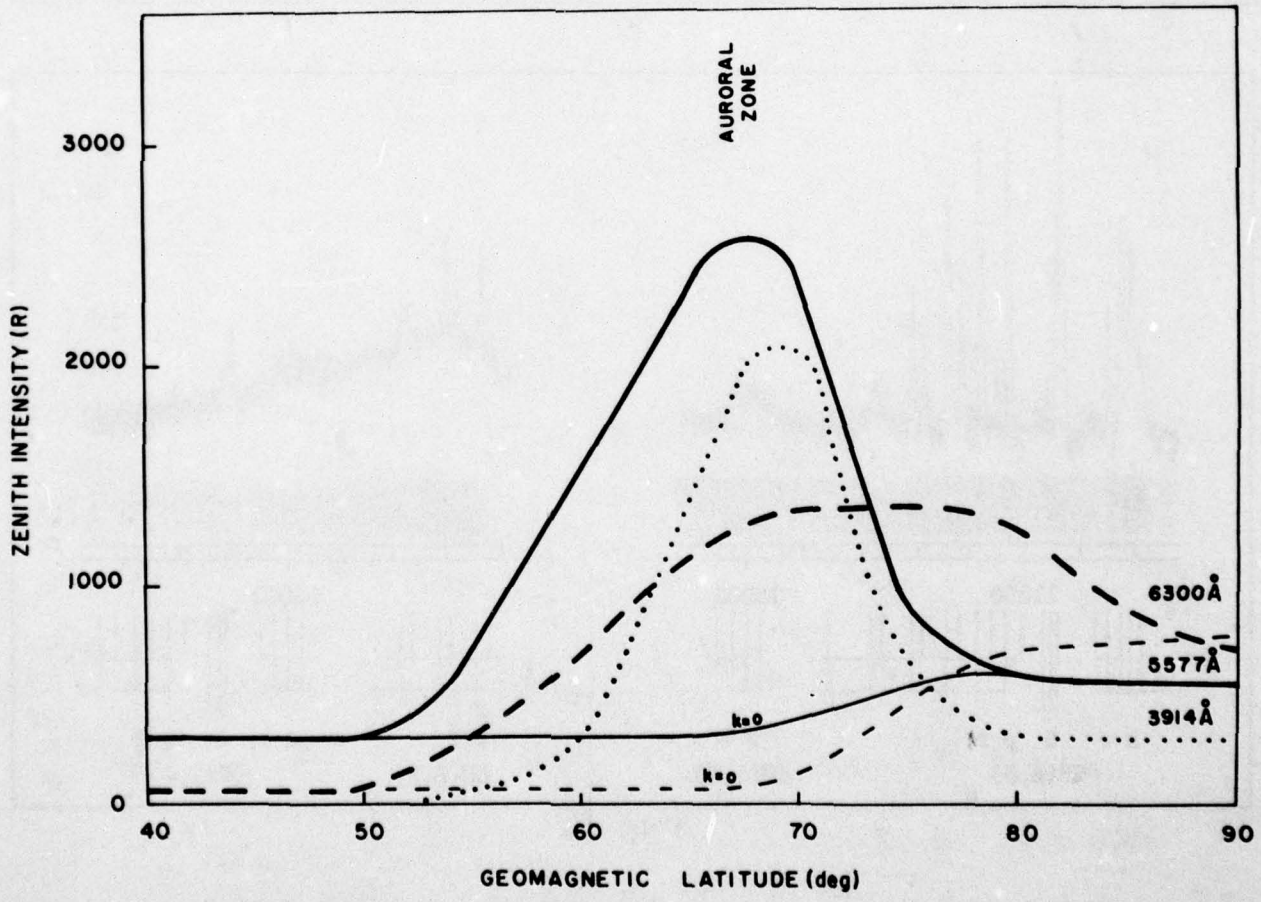


Fig. 13-3. Mean intensity, all K-indices vs geomagnetic latitude. (After B. P. Sandford, private communication, 1963.)

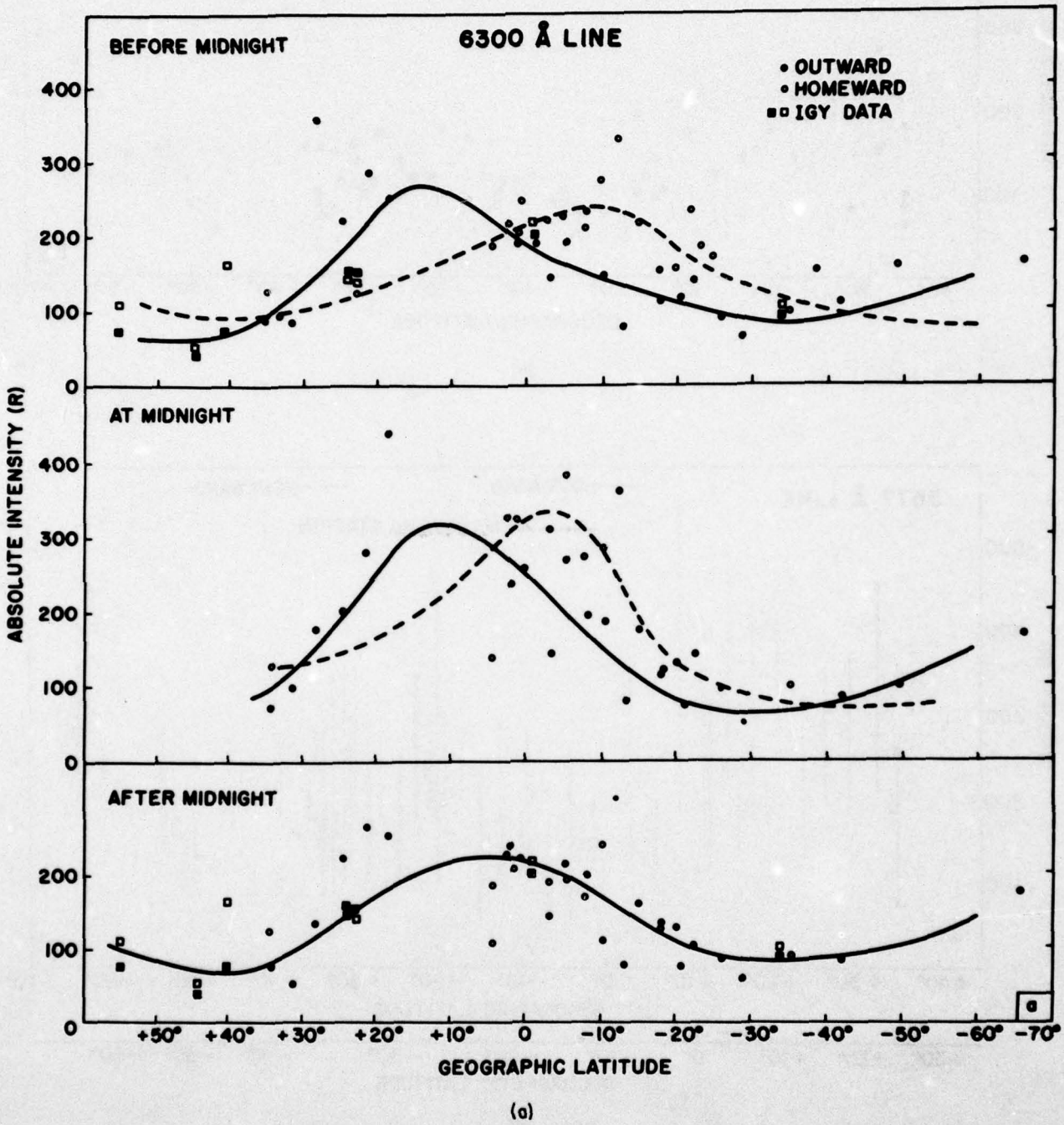
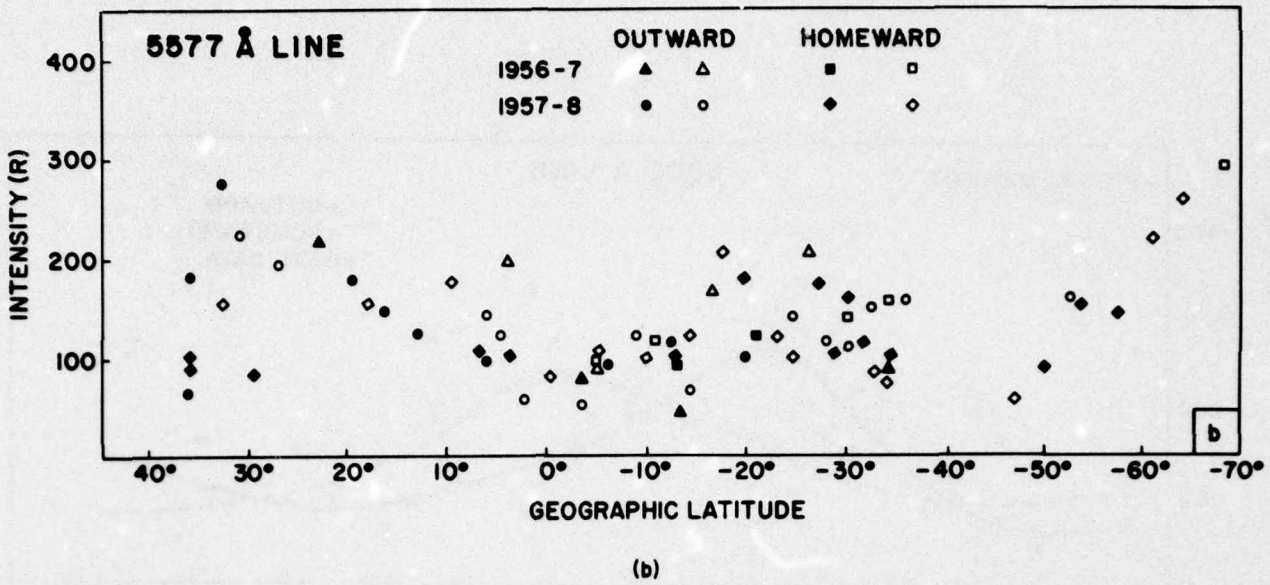
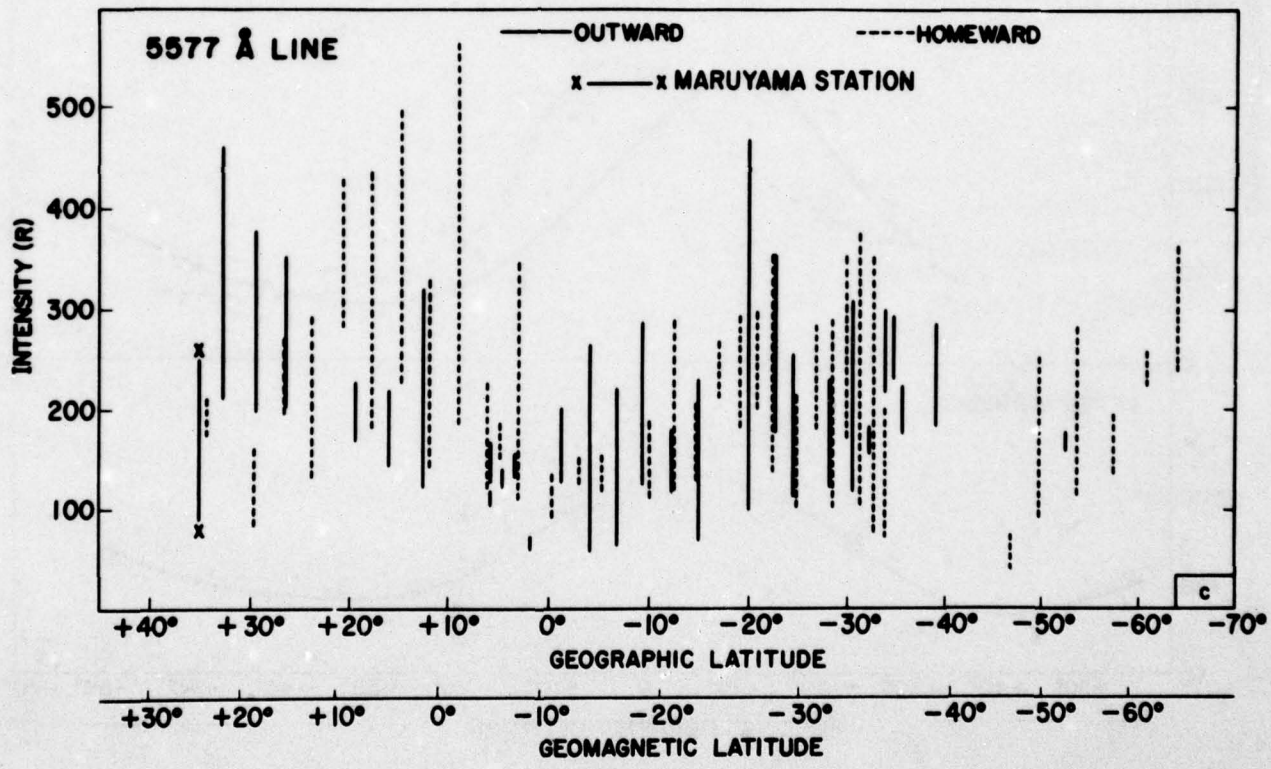


Fig. 13-4. Latitude variations for airglow emissions; (a) latitude dependence of the 6300 Å line, (b) intensities of 5577 Å emission observed in 1956-1957 and 1957-1958 Soya expeditions, and (c) zenith intensity of 5577 Å emission observed during the 1957-1958 Soya expeditions. (a) from T. Nakamura, 1961, v. 15, p. 245, and (b) and (c) from J. Nakamura, 1958, v. 12, p. 419, *Report of Ionosphere Research in Japan* by permission.)

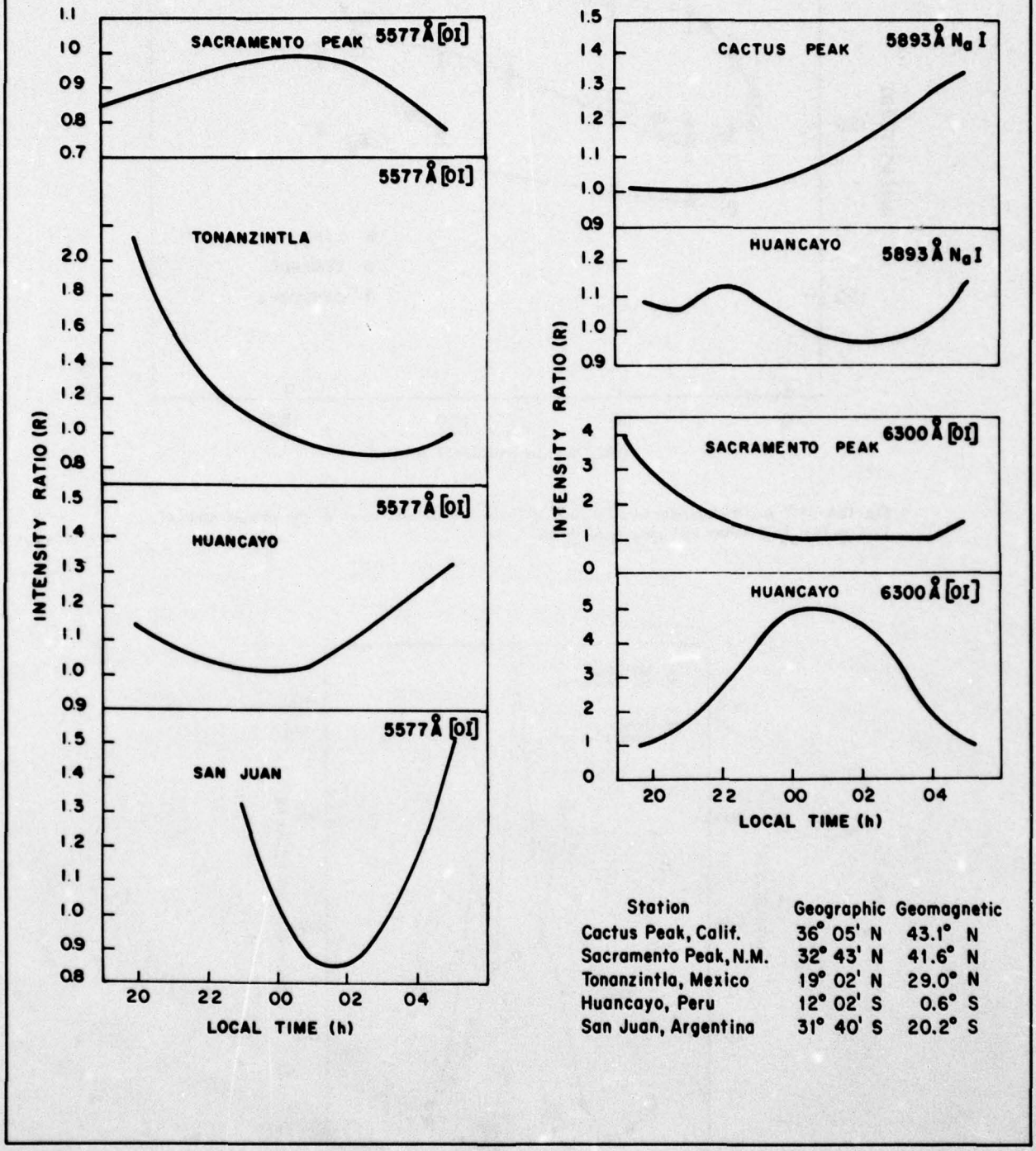


(b)



(c)

Fig. 13-4. Latitude variations for airglow emissions; (a) latitude dependence of the 6300 Å line, (b) intensities of 5577 Å emission observed in 1956-1957 and 1957-1958 Soya expeditions, and (c) zenith intensity of 5577 Å emission observed during the 1957-1958 Soya expeditions. (a) from T. Nakamura, 1961, v. 15, p. 245, and (b) and (c) from J. Nakamura, 1958, v. 12, p. 419, *Report of Ionosphere Research in Japan* by permission.)



Station	Geographic	Geomagnetic
Cactus Peak, Calif.	36° 05' N	43.1° N
Sacramento Peak, N.M.	32° 43' N	41.6° N
Tonanzintla, Mexico	19° 02' N	29.0° N
Huancayo, Peru	12° 02' S	0.6° S
San Juan, Argentina	31° 40' S	20.2° S

Fig. 13-5. Typical diurnal variations of the 5577 Å, 6300 Å, and 5893 Å emissions. (From data of H. B. Pettit et al, *Ann. Geophys.*, v. 10, p. 326, 1954, for Cactus Peak; for the other stations, S. M. Silverman, *Planetary Space Sci.*, v. 12, no. 3, p. 247, 1964.)

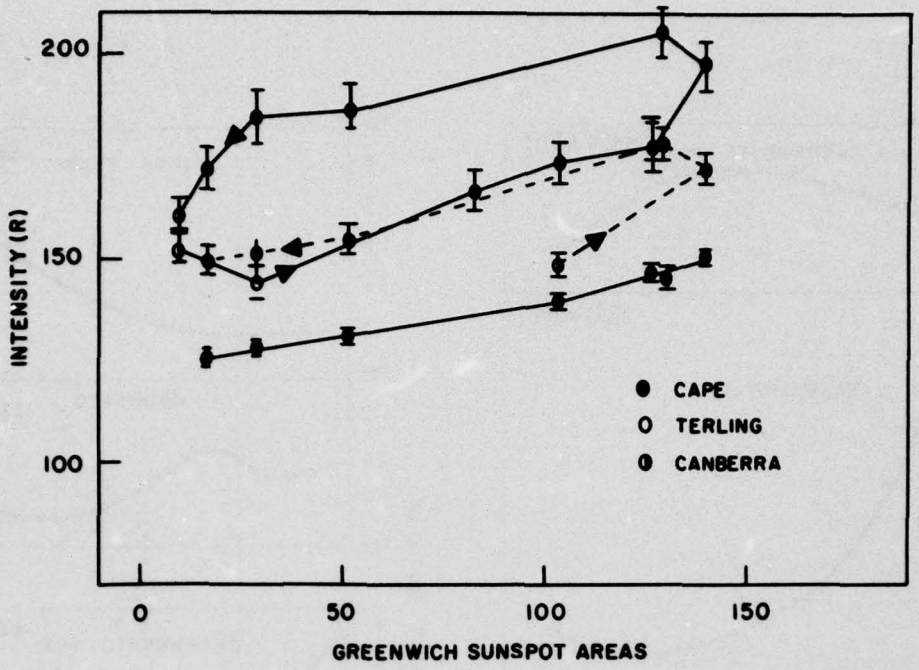


Fig. 13-6. 5577 Å [OI] intensity as a function of Greenwich sunspot areas for the sunspot cycle of 1923 to 1934 [Hernandez and Silverman, 1964].

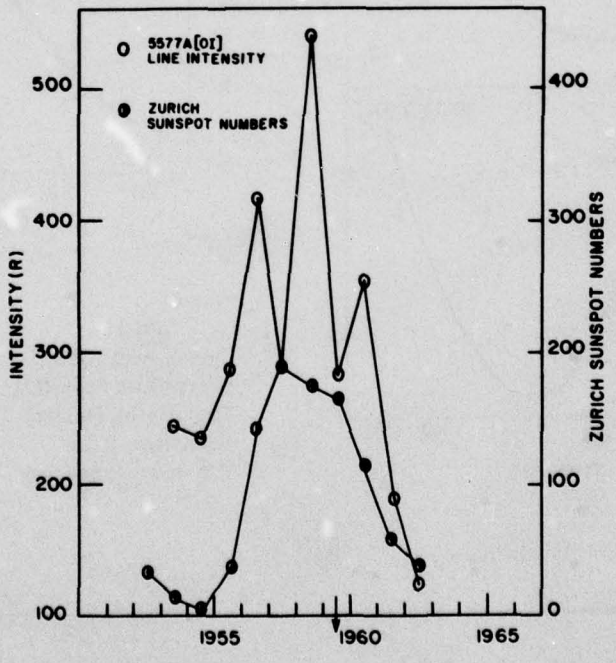


Fig. 13-7. 5577 Å [OI] intensity at Sacramento Peak, N. M., and Zurich sunspot numbers for the period 1953 through 1962 [Hernandez and Silverman, 1964].



Fig. 13-8. Homogeneous arc with main arc below the horizon and diffuse second arc above it (qm_2HA).

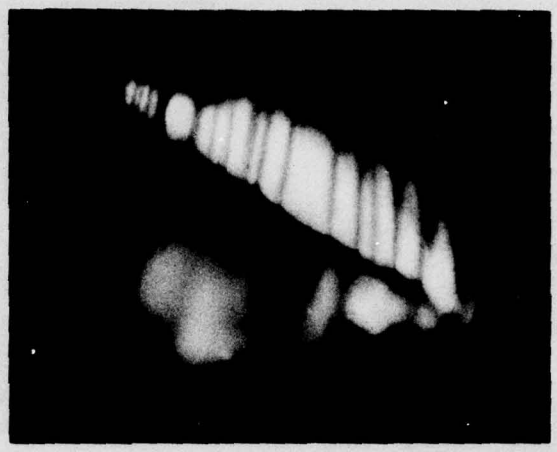


Fig. 13-11. Series of rays arranged close to each other along the band (R_2B).

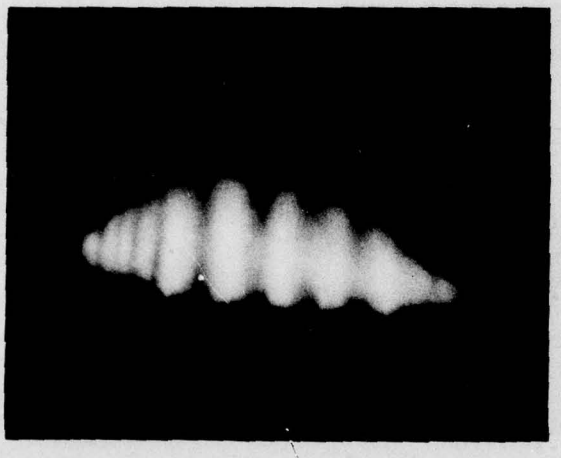


Fig. 13-9. Arc with ray structure-luminosity of quiet homogeneous arc increased suddenly, then rapidly changed into arc of long rays (a_3R_1A).

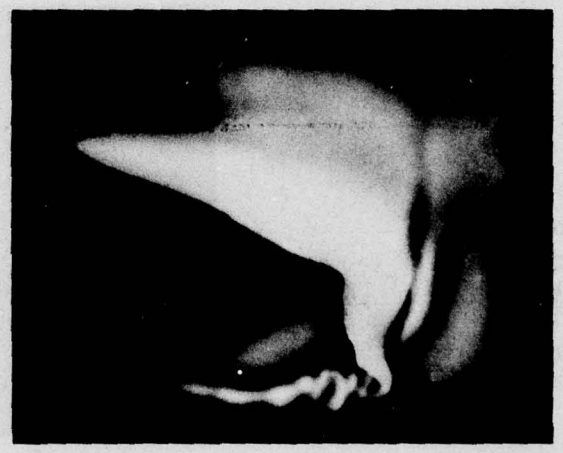


Fig. 13-12. Rapidly moving homogeneous band with sharp lower border and luminosity varying according to angle of view (a_1HB).

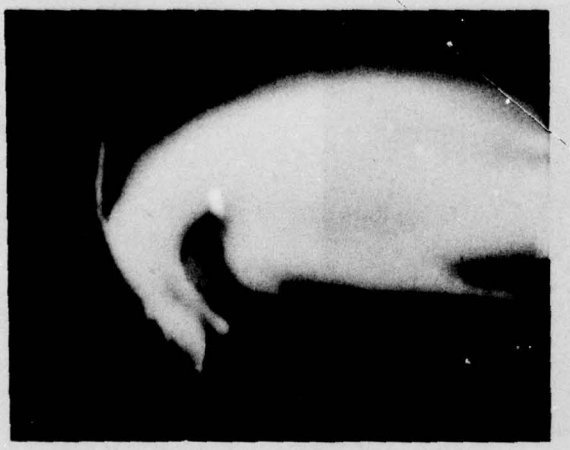


Fig. 13-10. Typical homogeneous band showing sharp lower border with ellipsoidal shape and folds (qHB).



Fig. 13-13. Coronal-rayed band with rays occurring at magnetic zenith and appearing to converge (cR_2B).



Fig. 13-14. Bundle of rays (a_2mR_3R).



Fig. 13-15. Narrow isolated rays of low intensity (mR_3R).

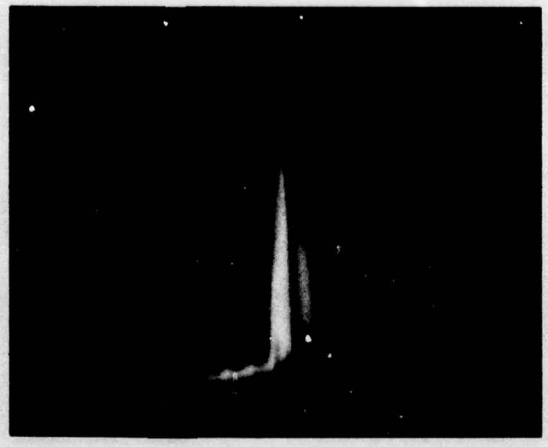


Fig. 13-16. Ray (top of 300 km) protruding out of faint rayed arc (qfR_2A).

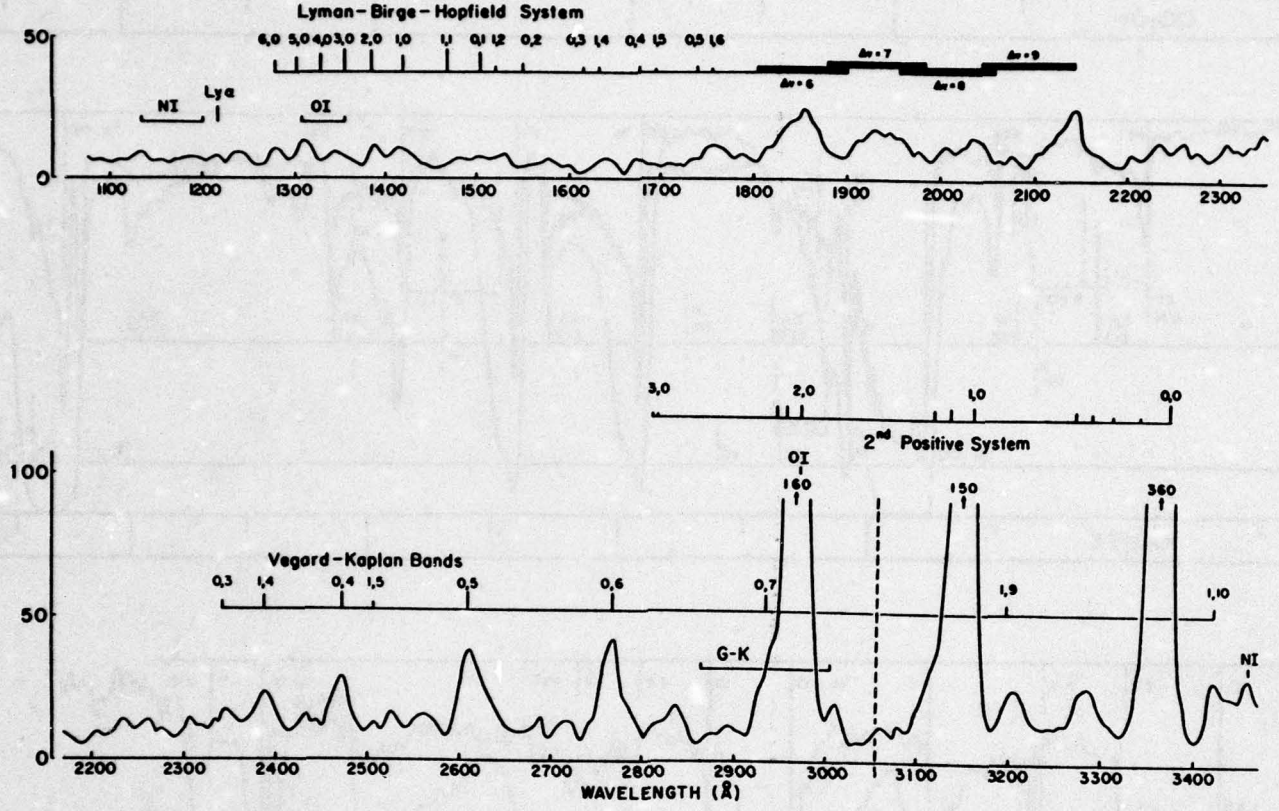


Fig. 13-17. Composite of four brightest auroral spectra. (From H. M. Crosswhite, E. C. Zipf, and W. G. Fastie, *Scientific Rpt. No. 2*, AFCRL No. 1058, Johns Hopkins University, 1961.)

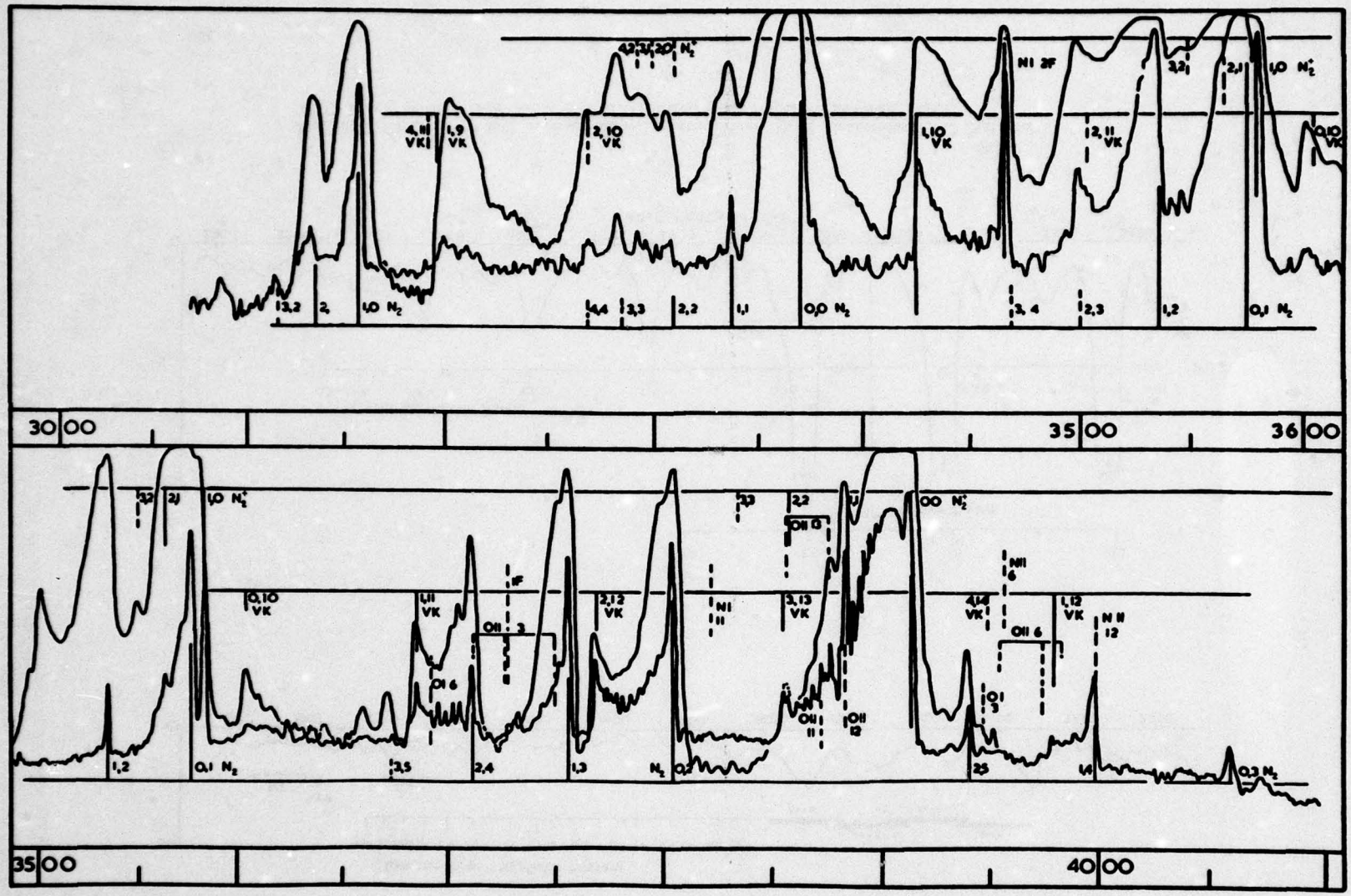


Fig. 13-18. Photometric tracings of auroral spectra. (From A. Vallance Jones, *Scientific Rept. No. AR-20*, University of Saskatchewan, Contract AF19(122)-152, 1955, by permission.)

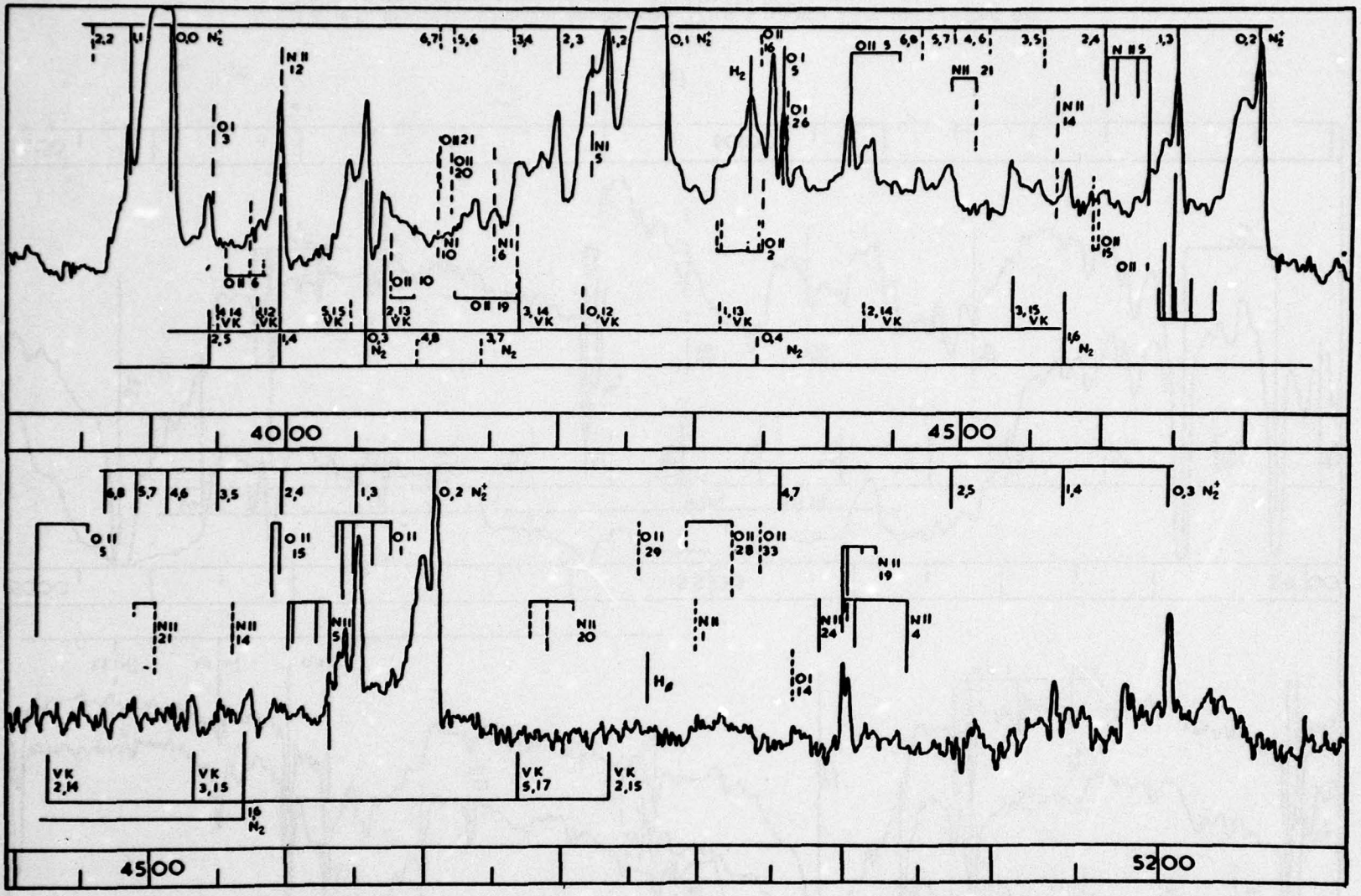
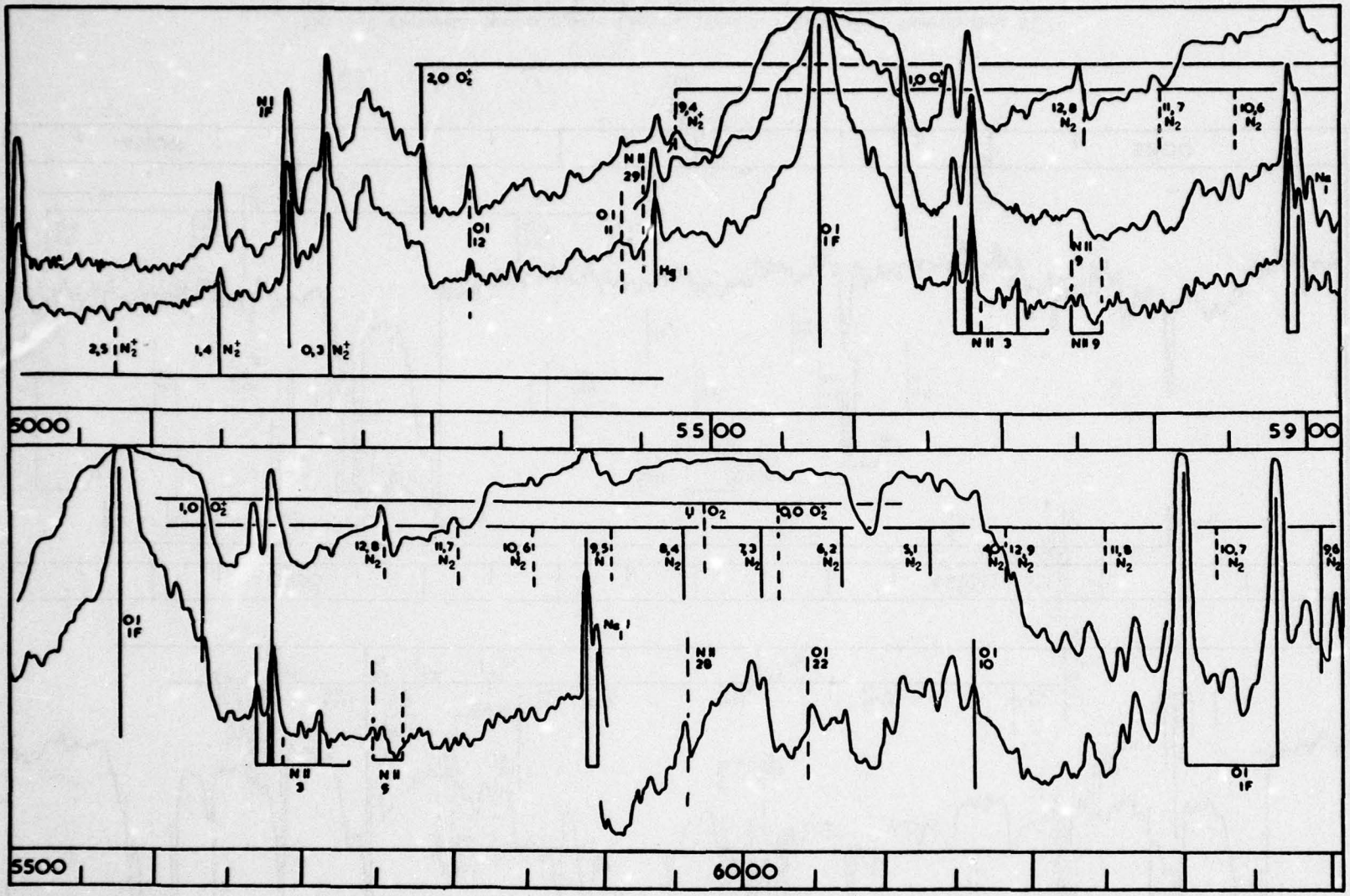


Fig. 13-18. Photometric tracings of auroral spectra. (From A. Vallance Jones, *Scientific Rept. No. AR-20*, University of Saskatchewan, Contract AF19(122)-152, 1955, by permission.)



(c)

Fig. 13-18. Photometric tracings of auroral spectra. (From A. Vallance Jones, *Scientific Rept. No. AR-20*, University of Saskatchewan, Contract AF19(122)-152, 1955, by permission.)

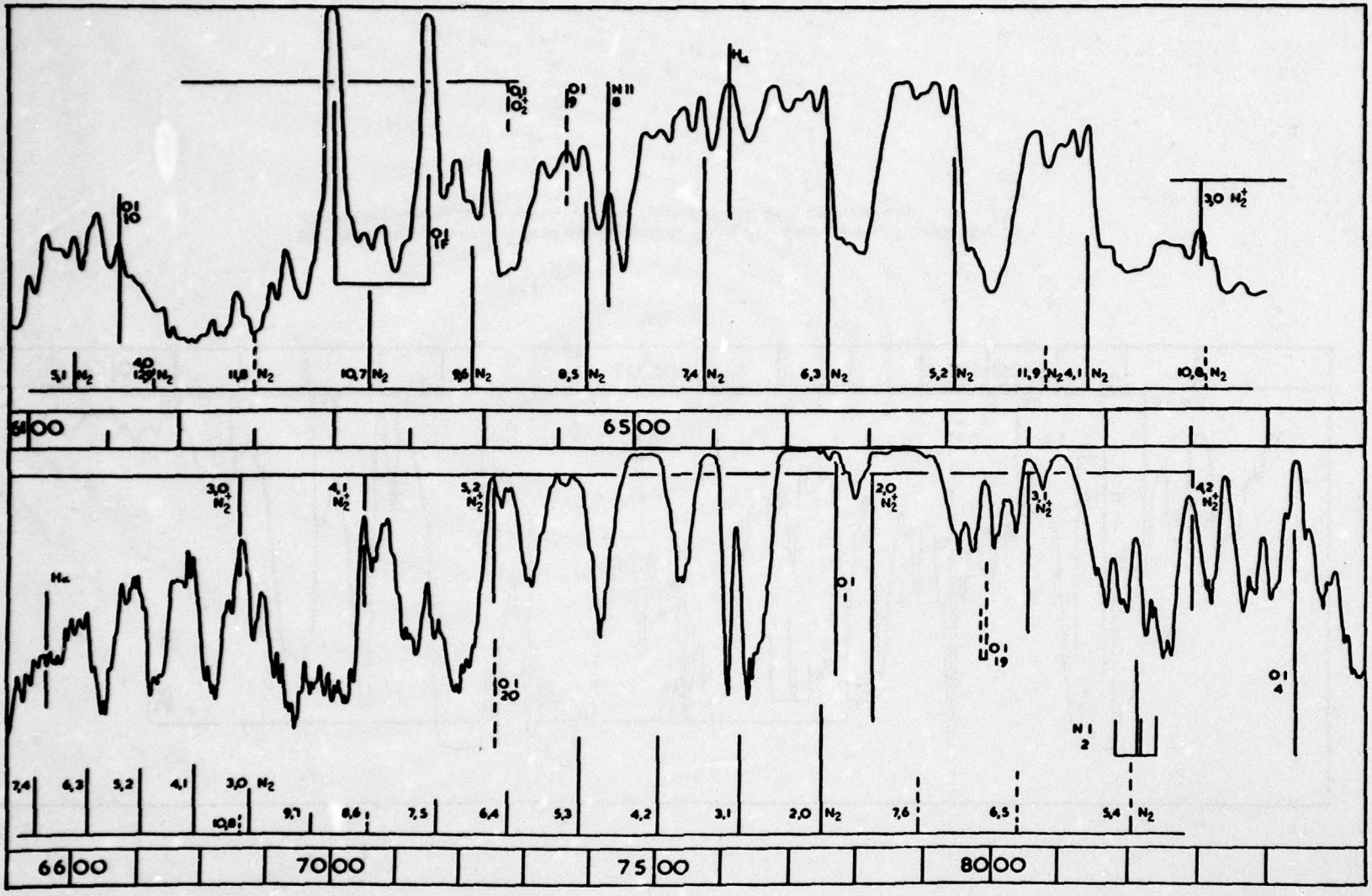


Fig. 13-18. Photometric tracings of auroral spectra. (From A. Vallance Jones, *Scientific Rept. No. AR-20*, University of Saskatchewan, Contract AF19(122)-152, 1955, by permission.)

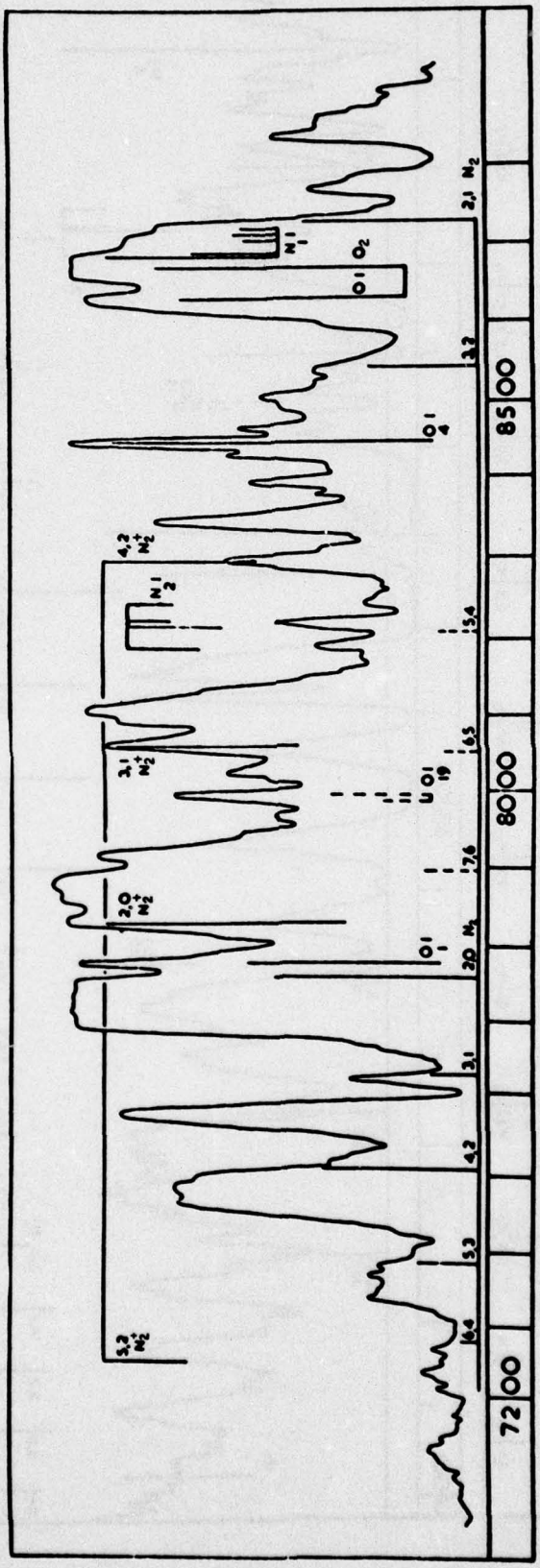


Fig. 13-18. Photometric tracings of auroral spectra. (From A. Vallance Jones, *Scientific Rept. No. AR-20*, University of Saskatchewan, Contract AF19(122)-152, 1955, by permission.)

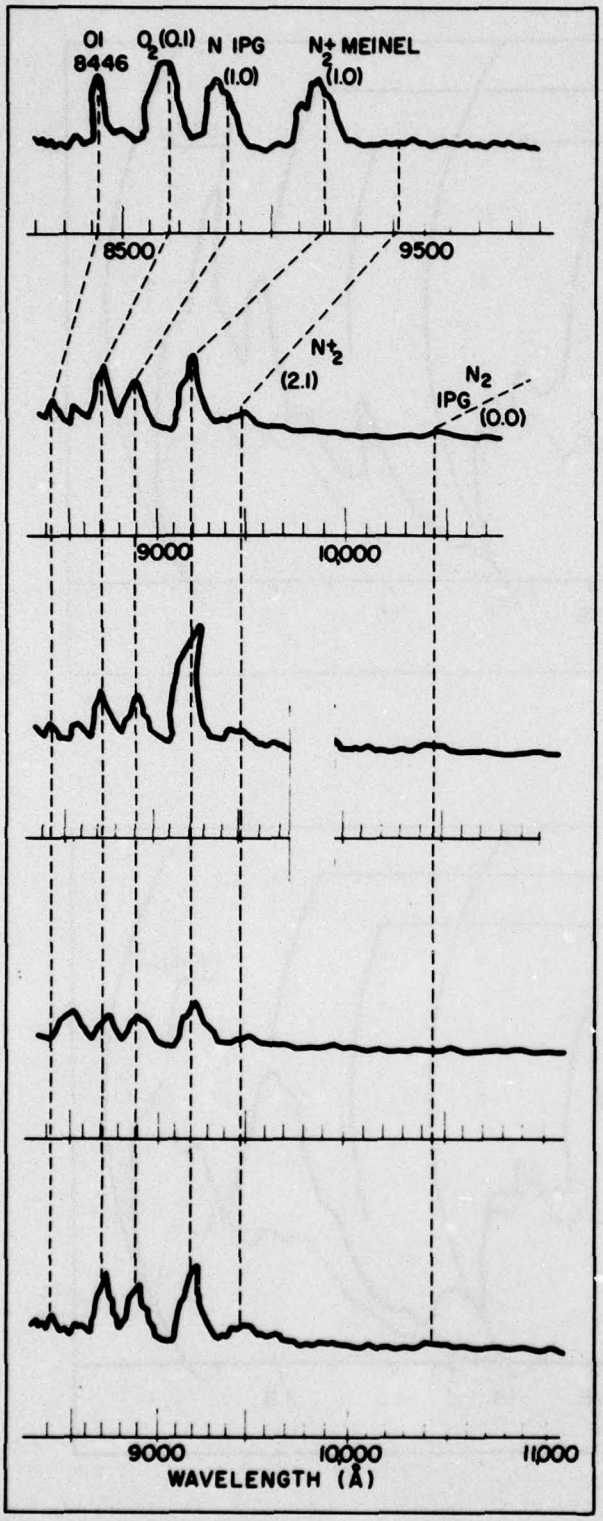
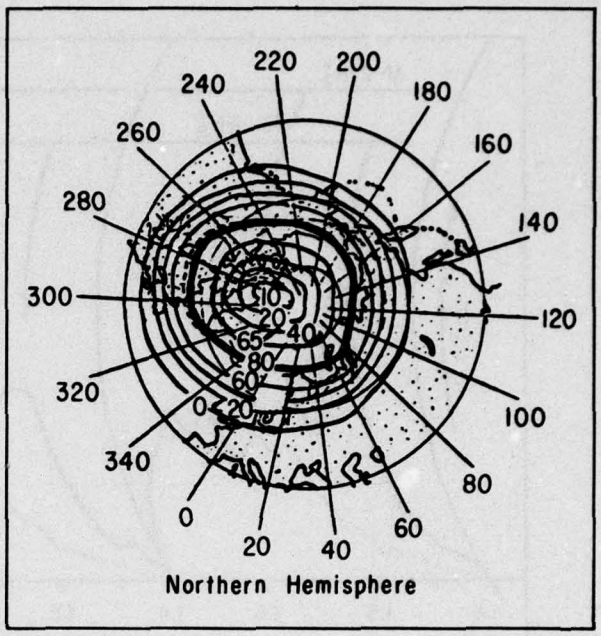


Fig. 13-19. Auroral spectra in the 8400 to 11,000 Å region. They illustrate the more prominent features and their variations in relative intensity. (From D. M. Hunten, *Ann. de Geophys.*, v. 14, p. 167, 1958, by permission.)



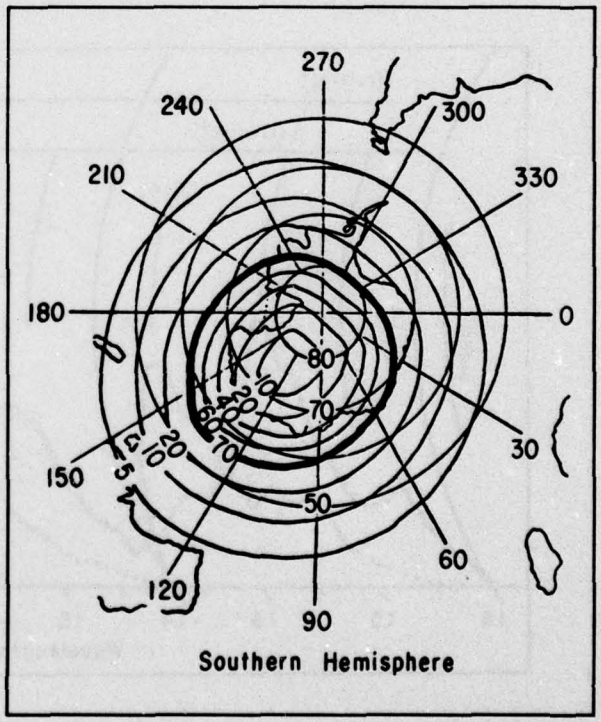


Fig. 13-21. Isoaurorae of aurora appearance frequency. Figures in the isolines gaps represent aurora appearance frequency in percentage. (From J. I. Feldstein, O. V. Khorosheva and A. I. Lebedinsky, *J. Phys. Soc. Japan*, v. 17, Supp. A-I, 250, 1962, by permission.)

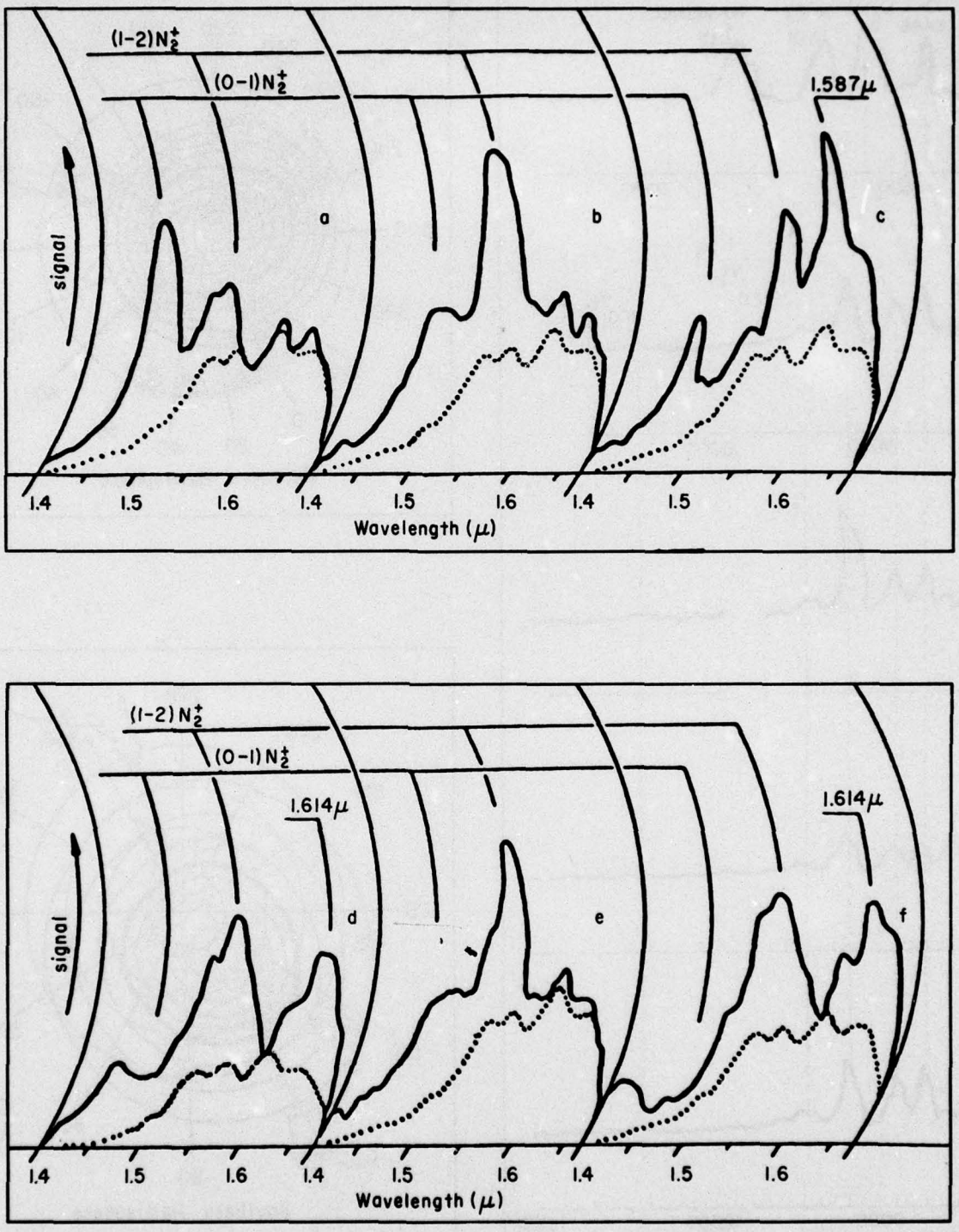


Fig. 13-20. Auroral spectra in the 14,000 to 16,500 Å region. The dotted curve is the airglow spectrum fitted to the auroral spectrum in a region where the auroral emission appeared feeble. Spectra a, b, and c were made in consecutive scans, with a total time of 3 min. The relative intensities of features on a single scan are not significant since the aurora fluctuates in brightness during the scanning period. (From A. W. Harrison and A. Vallance Jones, *Atmos. Terrest. Phys.*, v. 13, p. 291, 1959, by permission.)

13.3 REFERENCES

Barbier, D., 1961, "Les Variations d'Intensité de la Raie 6300 Å de la Luminescence Nocturne," *Ann. Geophys.*, v. 17, p. 3.

Chamberlain, J. W., 1961, "Physics of the Aurora and Airglow," Academic Press, N.Y.

Collins, C., and P. A. Forsyth, 1959, "Bistatic Radio Investigation of Auroral Ionization," *J. Atmos. Terrest. Phys.*, v. 13, p. 315.

Dalgarno, A., and E. B. Armstrong, eds., 1957, "The Airglow and the Aurorae," Pergamon Press, London.

Delsemme, A., and D. Delsemme, 1960, "La Raie Rouge du Ciel Nocturne a l'Equateur," *Ann. Geophys.*, v. 16, p. 507.

Harang, L., 1951, "The Aurorae," Wiley and Sons, Inc., New York.

Hernandez, G. J., and S. M. Silverman, 1964, "A Reexamination of Lord Rayleigh's Data on the Airglow 5577 Å [OI] Emission," *Planetary Space Sci.*, v. 12, p. 97.

Hultquist, B., 1962, "On Auroral Isochasms and the Orientation of Auroral Arcs," *J. Phys. Soc. Japan*, Supp. A-I, Part I, p. 78.

Ingham, M. F., 1962, "The Nightglow Spectrum," *Monthly Notices Royal Astron. Soc.*, v. 124, p. 505.

Kupperian, J. E., E. T. Byram, T. A. Chubb, and H. Friedman, 1959, "Far Ultraviolet Radiation in the Night Sky," *Planetary Space Sci.*, v. 1, p. 3.

Lagos, P., W. Bellew, and S. M. Silverman, 1963, "The Airglow 6300 Å [OI] Emission Theoretical Considerations on the Luminosity Profile," *J. Atmos. Terrest. Phys.*, v. 25, p. 581.

Noxon, J. F., 1963, "Observations of Daytime Aurora," *J. Atmos. Terrest. Phys.*, v. 25, p. 637.

Ratcliffe, J. R., ed., 1960, Chaps. 5-7, "Physics of the Upper Atmosphere," Academic Press, New York.

Roach, F. E., and J. Roach, 1963, "Stable 6300 Å Auroral Arcs in Mid-latitudes," *Planetary Space Sci.*, v. 11, p. 523.

Sandford, B. P., 1963, "Optical Studies of Particle Bombardment in Polar Cap Absorption Events," *Planetary Space Sci.*, v. 10, p. 195.

Shefov, N. N., 1963, "Helium in the Upper Atmosphere," *Planetary Space Sci.*, v. 10, p. 73.

Störmer, C., 1955, "The Polar Aurora," Oxford Press, London.

Turtle, J. P., 1963, "Observations of the NI 5200 Å Auroral Doublet at Byrd Station, Antarctica," *Planetary Space Sci.*, v. 11, p. 1375.

Vallance Jones, A., 1963, "Metallic Emissions in the Twilight and Their Bearing on Atmospheric Dynamics," *Planetary Space Sci.*, v. 10, p. 117.

Chapter 14

METEORITIC PHENOMENA

Robert K. Soberman

Meteoroids are extraterrestrial particulate matter larger than molecular scale in size. There is evidence that all meteoroids are moving in closed orbits in the solar system. They are thought to originate in the asteroid belt between Mars and Jupiter and in the debris from comets. Because of limitations of the observational techniques, infrequency of the phenomena, and scatter in available data, data contained in this chapter are intended to serve only as a guide and must be used with discretion.

14.1 DEFINITIONS

The following nomenclature for meteoroid phenomena, although not universal, is generally accepted by investigators in the field. The streak of light observed when a meteoroid enters the atmosphere is known as a *meteor*. This term applies to the results of the interaction with the atmosphere and is sometimes extended to cover more than the light emanations; e.g., ionization. If the event is spectacularly brilliant, it is called a *fireball*, and if it appears to explode, a *bolide*. A portion of a meteoroid which survives to reach the ground is called a *meteorite*. The very small particles which, because of a large surface area relative to their mass, can undergo atmospheric entry without vaporizing are *micrometeorites*. The terms *cosmic dust* and *meteoric dust* include micrometeorites and other debris of meteoric origin.

The immediate vicinity of a vaporizing meteoroid is known as the head of the meteor. A brighter meteor sometimes leaves a glowing train or wake along its path in the atmosphere; this is the *meteor trail*, although the term is also used sometimes to denote the projection of the visible path on the observer's celestial sphere. The *radiant* of a meteor is the point where the extrapolated meteor path intersects the celestial sphere. *Shower meteors* (meteor streams) are those which have the same radiant; a *sporadic meteor* is one which is not a member of a recognized shower. The words visual, photographic, telescope, and radio, when applied to meteors, indicate the particular observing technique, although some size information may be intended because of the different sensitivities of these techniques.

14.2 METEOROID COMPOSITION AND DENSITY

Meteoroid composition has been investigated through the chemical analysis of meteorites found on the earth. Because this is the best information available for the composition of interplanetary debris, there is a tendency to extend such results to cover all meteoroids. There is good evidence, however, that the meteorites which do reach the ground are atypical, being of asteroidal origin; whereas, most meteoroids are generally associated with a cometary origin. Although some data on the composition of meteors are available from spectral analysis, these data are more qualitative than quantitative. In addition, there is some information available from the analysis of cosmic dust samples.

Meteoric matter is generally classified as stone or iron, according to the relative abundance of elements. Table 14-1 gives the average composition of iron and stone meteorites. The ratio of the number of stone to the number of iron meteoroids has been placed as high as 13 to 1. Elements identified in meteor spectra are Al, Ca, Cr, Fe, H, Mg, Mn, Na, Ni, Si, Sr, O, and N (the oxygen and nitrogen are felt to be due to our atmosphere). Fe, Ni, FeO and Fe_2O_3 have been identified in cosmic dust samples. One study of micrometeorites has shown evidence of Si, Fe, Ti, Ca, Mg, and Cu.

The density of meteoroids is thought to vary within broad limits. Meteorite specific gravities measured directly yield a mean value of approximately 3 for stone and 8 for iron types. From the extremely low aerodynamic drag ($\approx$10 dyn cm^{-2}) at the height where some meteors fragment, it was concluded that such meteoroids are agglomerates or dust balls with a specific gravity of 0.1. There is evidence that low-density agglomerates extend even down to the micrometeorite size [Hemenway and Soberman, 1962]. Whipple [1963] uses a mean specific gravity of 0.44 as typical for stony meteoroids of ground-observable meteors.

14.3 METEOROID MAGNITUDE

Meteors are generally characterized by the relative brilliance of their interaction with the atmosphere. The unit

of measurement is astronomical magnitude (Sec. 21.2.4); the observer compares the brilliance of the meteor with that of nearby stars. The comparison is largely subjective and depends on many factors (e.g., speed and color of the meteor), but trained observers can usually agree on apparent visual magnitudes. The relation between the luminosities, L, and apparent visual magnitudes, m_v, of meteors (or stars) is

$$m_v - m'_v = 2.5\,(\log_{10} L' - \log_{10} L). \qquad (14\text{-}1)$$

An arbitrary zero of apparent visual magnitude is selected for $L = 1.944 \times 10^{-7}$ foot-candle (lumen ft^{-2}). This corresponds closely to the luminosity of the star Vega (α Lyrae), which has an apparent visual magnitude of +0.04. (At a distance of 1 meter, one standard candle has an apparent visual magnitude of −14.2.) Meteors of apparent visual magnitude +6 may be detected with the unaided eye; those as faint as +11 may be detected with optical telescopes. Radio methods can detect signals returned from the ionized trail of meteors as faint as +11 and also cover a much larger portion of the sky.

The absolute visual magnitude, M_v, is defined as the magnitude the meteor would have if observed at a distance of 100 km in the direction of the zenith. Figure 14-1 shows the two corrections to the apparent visual magnitude of a meteor that are necessary to convert it to absolute magnitude: the *distance correction* for attenuation of the radiation with distance (inverse square law), and the *absorption correction* for attenuation by absorption and scattering in the atmosphere. The latter is a function of the meteor's zenith angle, Z, which is the angle between the observer's vertical and his line of sight to the meteor.

Öpik [1958] derives a relation between the absolute visual magnitude of a meteor and the power radiated that can be detected by the human eye;

$$M_v = 6.8 - 2.5 \log_{10} I_w, \qquad (14\text{-}2)$$

where I_w is the luminous power in watts.

Table 14-1. Average composition (percent by weight) of iron and stone meteorites.

Iron		Stone			
Element	(%)	Element	(%)	Element	(%)
Fe	90.66	O	36.40	C	0.15
Ni	8.48	Fe	23.38	Cr	0.03
Co	0.59	Si	18.20	Mn	0.24
P	0.17	Mg	13.80	Co	0.17
S	0.04	S	1.80	K	0.17
C	0.03	Ca	1.70	Ti	0.11
Ca	0.02	Al	1.50	P	0.11
Cr	0.01	Ni	1.50	Cl	0.08
		Na	0.65	Cu	0.01

The absolute photographic meteor magnitude, M_p, is determined by comparison of the intensity of a meteor with intensities of star images on the same photographic plate. Photographic and visual magnitudes are not identical. The difference $M_p - M_v$ is defined as the color index of the meteor. For bright meteors photographed on blue-sensitive plates, the color index is usually taken as −1.8 magnitudes. The radio magnitude, M_r, is based on the echo duration detected from the meteor and is correlated with visual magnitudes by simultaneous radio and visual observations. McKinley [1961] derives the relation

$$M_r = 36 - 2.5 \log_{10} q + 2.5 \log_{10} V, \qquad (14\text{-}3)$$

where V is the meteor velocity in km sec^{-1}, and q is the number of electrons liberated per meter of meteor path.

14.4 INTERACTION WITH ATMOSPHERE

Because most meteoroids vaporize before reaching the ground, their mass, density, and shape are not directly measurable. The ground observables are the deceleration, or drag, and the energy of interaction with the atmosphere. The drag equation usually is written as

$$\frac{dV}{dt} = -\Gamma A \rho_a V^2 / m^{1/3} \rho_m^{2/3}. \qquad (14\text{-}4)$$

V is the velocity of the meteoroid. Γ is the dimensionless *drag coefficient*; it depends chiefly upon the shape of the meteoroid and, somewhat, on velocity, height, and rotation. Values for Γ vary from 0.5 to 1.0. A is the dimensionless shape factor, defined so that the expression $A(m/\rho_m)^{2/3}$ is the effective cross-sectional area of the meteoroid; m and ρ_m are the mass and density of the meteoroid. ρ_a is the ambient air density.

Whatever the mechanism for meteoroid ablation in the atmosphere, the mass loss is taken as proportional to the kinetic energy transferred to the intercepted air mass. The differential mass equation is

$$\frac{dm}{dt} = -\frac{\Lambda A}{2\zeta}\left(\frac{m}{\rho_m}\right)^{2/3} \rho_a V^3. \qquad (14\text{-}5)$$

Λ is the dimensionless *heat transfer coefficient* which is a measure of the efficiency of the collision process in converting kinetic energy to heat; values in the range 0.6 down to 0.1 or less have been proposed. ζ is the *heat of ablation* of the meteoroid material; it usually lies in the range 0.2 to 1.0×10^{10} erg g^{-1}.

It is generally assumed that the luminous power radiated by a meteor is proportional to the rate of loss of kinetic energy:

$$I = -\frac{\tau}{2}\frac{dm}{dt} V^2. \qquad (14\text{-}6)$$

τ, the luminous efficiency factor, is a function of the meteoroid velocity and usually is taken as equal to $\tau_o V$, where τ_o is the *luminosity coefficient*. Because I is determined in units of magnitude (rather than power) referred to a meteor of zero magnitude 100 km up at the zenith, the customary unit for τ_o is zero magnitude g^{-1} cm^{-3}

sec^4, sometimes abbreviated cgs and M_v (or M_p). Values of τ_o determined from an artificial meteoroid are: $\tau_o = 1.4 \times 10^{-19}$ zero magnitude (visual) g^{-1} cm^{-3} sec^4 for iron meteoroids, and $\tau_o = 2.3 \times 10^{-20}$ zero magnitude (visual) g^{-1} cm^{-3} sec^4 for stone meteoroids. Values in good agreement with these were obtained from three photographic meteors showing evidence of being asteroidal iron or stone meteorites; hence, these values should be useful for asteroidal meteors, but care should be exercised in applying them to cometary meteors of unknown composition. Whipple [1963] adopts a mean value for all meteors of

$$\tau_o = 3.8 \times 10^{-20} \text{ zero magnitude (visual) g}^{-1}\text{ cm}^{-3}\text{ sec}^4 \qquad (14\text{-}7)$$

and obtains a mean meteoroid density of $\rho = 0.44$ g cm^{-3}.

The power going into ionization is also assumed to vary as the rate of loss of kinetic energy;

$$qV\eta = -\frac{1}{2}\,\tau_q\,\frac{dm}{dt}\,V^2, \qquad (14\text{-}8)$$

where η is the mean ionization potential per atom involved (units of energy per electron liberated), and τ_q is the dimensionless *ionization-efficiency* factor. The ratio τ_q/τ appears to have a value of about unity for $V = 35$ km sec^{-1} and nearly three for $V = 60$ km sec^{-1}. From such data it is generally concluded that τ_q/τ varies approximately as V^2.

Another method of describing meteoric ionization is based upon the probability factor β, which is the probability that an ablated meteor atom will produce a free electron on collision with an air molecule. The mass of the ions produced per second is assumed proportional to the meteoroid mass loss; that is,

$$qV\mu = -\beta\,\frac{dm}{dt}\,, \qquad (14\text{-}9)$$

where μ is the mass of a single meteor atom. From Eq. (14-8) and (14-9),

$$\tau_q = 2\,\eta\beta/\mu\,V^2. \qquad (14\text{-}10)$$

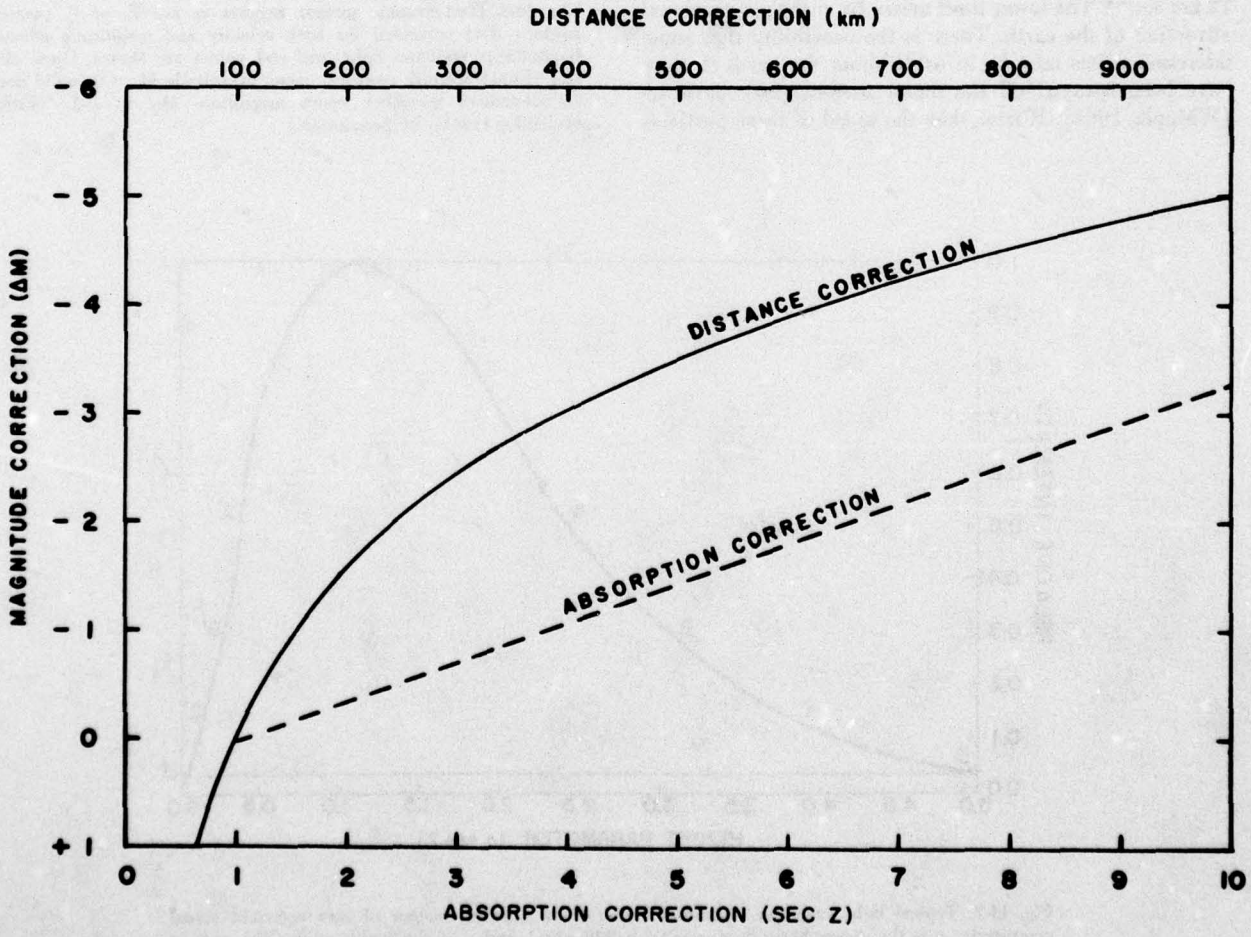


Fig. 14-1. Corrections to be added to observed magnitude to yield absolute magnitude. (From McKinley [1961], by permission.)

Figure 14-2 shows a typical light curve or ionization curve for a meteor. Intensities relative to the maximum are plotted against the height parameter, $(H - H_e)/a$, in units of a sec Z; H_e is the altitude of the end point, a is the atmospheric density scale height (Chapter 3) and Z is the zenith angle. According to Öpik, the maximum intensity occurs when approximately 1/3 of the meteoroid mass remains.

The heights at which meteors occur depend upon mass, velocity, and zenith angle, as well as on the density of the atmosphere. Figure 14-3 shows the beginning points, maximum luminosity points, and end points for two sets of data on photographic meteors as a function of Z and cos Z. Faint radio meteors often extend up to altitudes of 110 km, or slightly higher, and large meteorites can be luminous down to ground level.

14.5 SPEED

No definite evidence exists for any meteoroids having come from outside the solar system; therefore, it is possible to express limits on meteoroid speed. With respect to the earth, a meteoroid approaching from a great distance can enter the atmosphere with speeds ranging from 11 to 72 km sec^{-1}. The lower limit arises from the gravitational attraction of the earth. There is the possibility that some micrometeorites may be in orbit about the earth or may have been sprayed off the moon as secondary particles [Whipple, 1961]. If true, then the speed of these particles

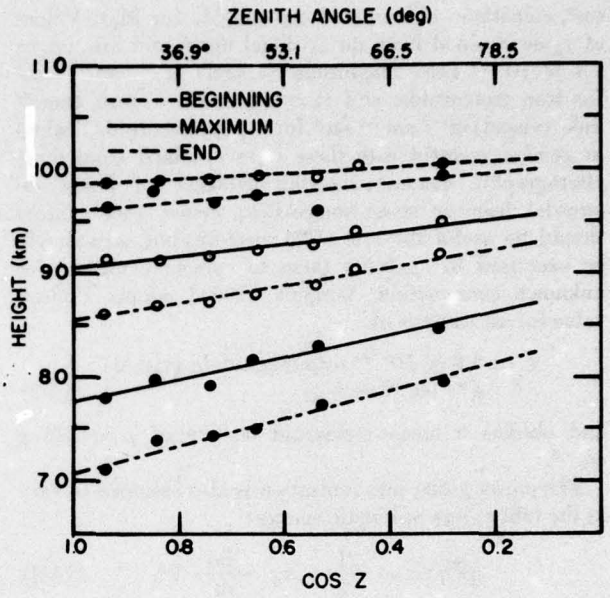


Fig. 14-3. Photographic meteor heights vs cos Z, or Z (zenith angle); data corrected for both velocity and magnitude effects. Beginning, maximum light, and end points are shown. Open circles (Super-Schmidt meteors) mean magnitude M = 0; solid dots (small-camera meteors) mean magnitude $M_p = -5$. (From McKinley [1961], by permission.)

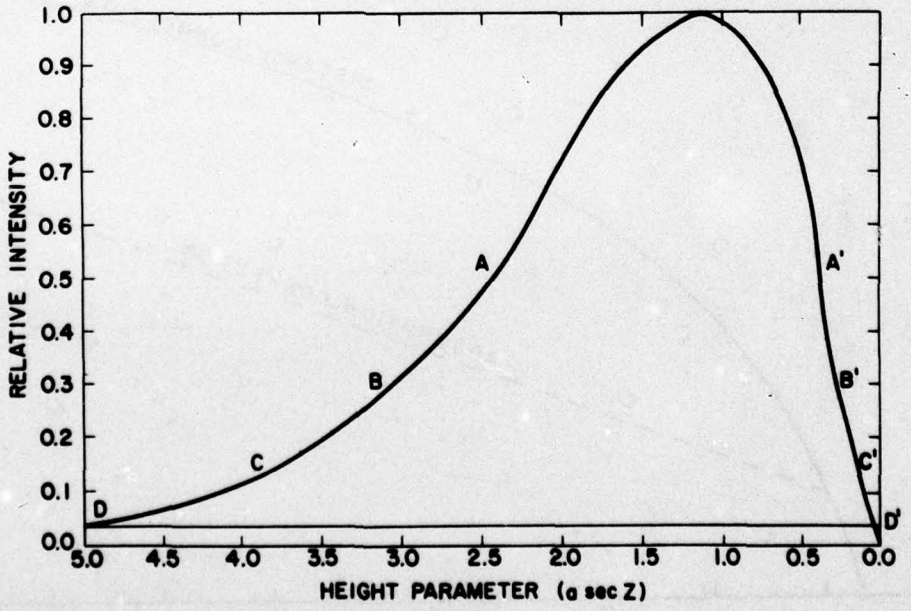


Fig. 14-2. Typical light curve, or ionization curve, of an ablating meteor of *zero apparent visual* magnitude; a is the atmospheric density scale height (km) and Z is the zenith angle. The portion of the trajectory between A and A′ is observed as an integrated brightness of $+4m_v$; that between B and B′ as $+3m_v$; that between C and C′ as $+1.5m_v$. (From Öpik [1958], by permission.)

may be somewhat less than 11 km sec^{-1}. The upper limit, 72 km sec^{-1}, is for a meteoroid approaching the earth with a relative velocity equal to the sum of the earth's velocity in its orbit about the sun ($\approx$ 30 km sec^{-1}) and the maximum velocity which a body could have at the distance of the earth's orbit from the sun and still be trapped in the solar system ($\approx$ 42 km sec^{-1}). Figure 14-4 shows a normalized distribution of speeds, before atmospheric slowdown, of meteoroids entering the earth's atmosphere. The data are taken from 621 photographic meteors.

For a vehicle on an interplanetary mission there would be no lower limit for the speed of encounter with a meteoroid. The upper limit could be calculated by summing the vehicle's heliocentric velocity with the heliocentric escape velocity at the point of encounter.

14.6 METEOROID MASS AND FLUX

The conversion from magnitude to mass of a meteoroid is still far from being straightforward; uncertainties result from the wide range of physical properties of meteoroids as well as from limitations of the observations. Estimates of the mass of a zero magnitude meteoroid have differed by several orders of magnitude. A new estimate, which rests on a more certain foundation of experimental work, is that a 1-g stony-type cometary meteoroid entering the atmosphere at 30 km sec^{-1} would have zero visual magnitude, so that

$$-2.5 \log_{10} m = M_v, \qquad (14\text{-}11)$$

when m is in grams. Dependence upon other variables, such as velocity, is omitted because the exact form of such dependence is still in question, and inclusion of other variables might tend to delude the user as to the precision of the relationship. If the speed differs greatly from $V_o =$ 30 km sec^{-1}, however, the term $-7.5 \log_{10} V/V_o$ should be added to the left-hand side of Eq. (14-11).

Estimates of mean meteoroid flux have undergone many changes, resulting in part from changes in the mass-magnitude conversion but also from the increasing amount of data from rockets and satellites. The present values are still very uncertain, however, even with this new data. Much of this uncertainty stems from the limited amount of data collected by a single experiment which often necessitates averaging over long periods of time and large volumes of space.

Figure 14-5 presents current estimates of the mean near-earth meteoroid flux. The curves due to Whipple and Watson are the result of radio, visual, and photographic meteor data extrapolated to smaller masses; Watson's estimate was corrected in accord with the new mass-magnitude conversion. The curve labeled McCracken et al is from rocket and satellite micrometeorite experiments. The divergence of the different curves should serve as a caution against too much reliance upon a single estimate of the meteoroid flux, particularly in the range $-8 < \log m < -4$, where all curves are extrapolations. A single relationship is not expected to be valid over such a large range of masses, particularly when some of the material originates from different sources (asteroidal vs cometary), and certain forces (e.g., radiation pressure) that are negligible at one end of the mass scale play dominant roles at the other. Curves presented here undoubtedly will be revised, and it would be advisable to consult the most recent literature before choosing a particular flux value as a final design criteria.

Figure 14-6 is an estimate of the meteoroid flux decrease with distance from the earth. This curve is highly uncertain, although recent data from deep space probes tend to confirm the existence of a geocentric concentration. The manner in which the flux decreases, and the

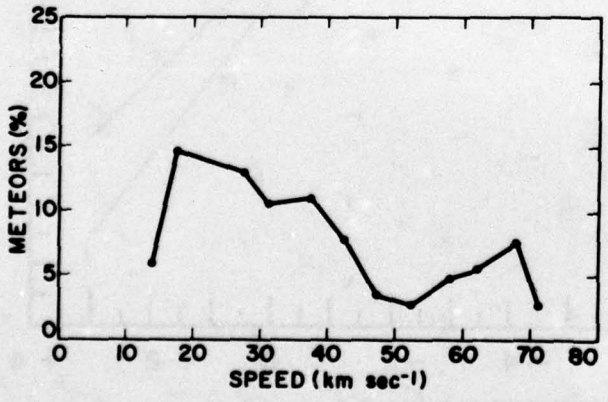


Fig. 14-4. Normalized distribution of speeds of photographic meteors before slowdown by the atmosphere. (From McKinley [1961], by permission.)

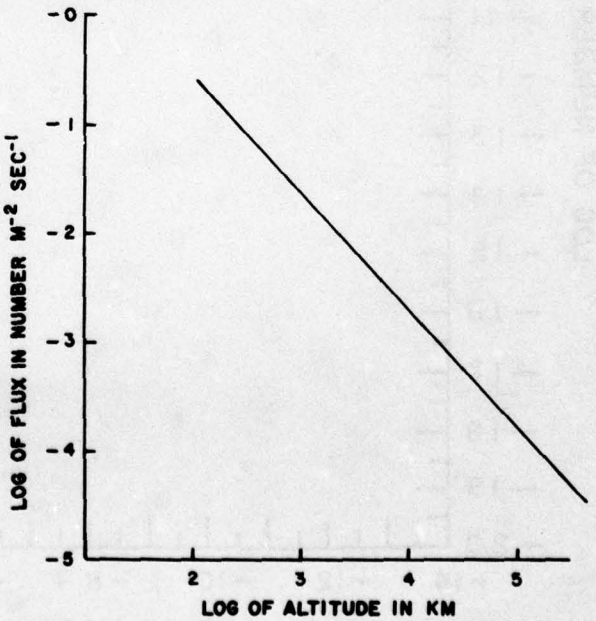


Fig. 14-6. Estimate of meteoroid flux in number per second in one square meter area as a function of distance (km) from earth.

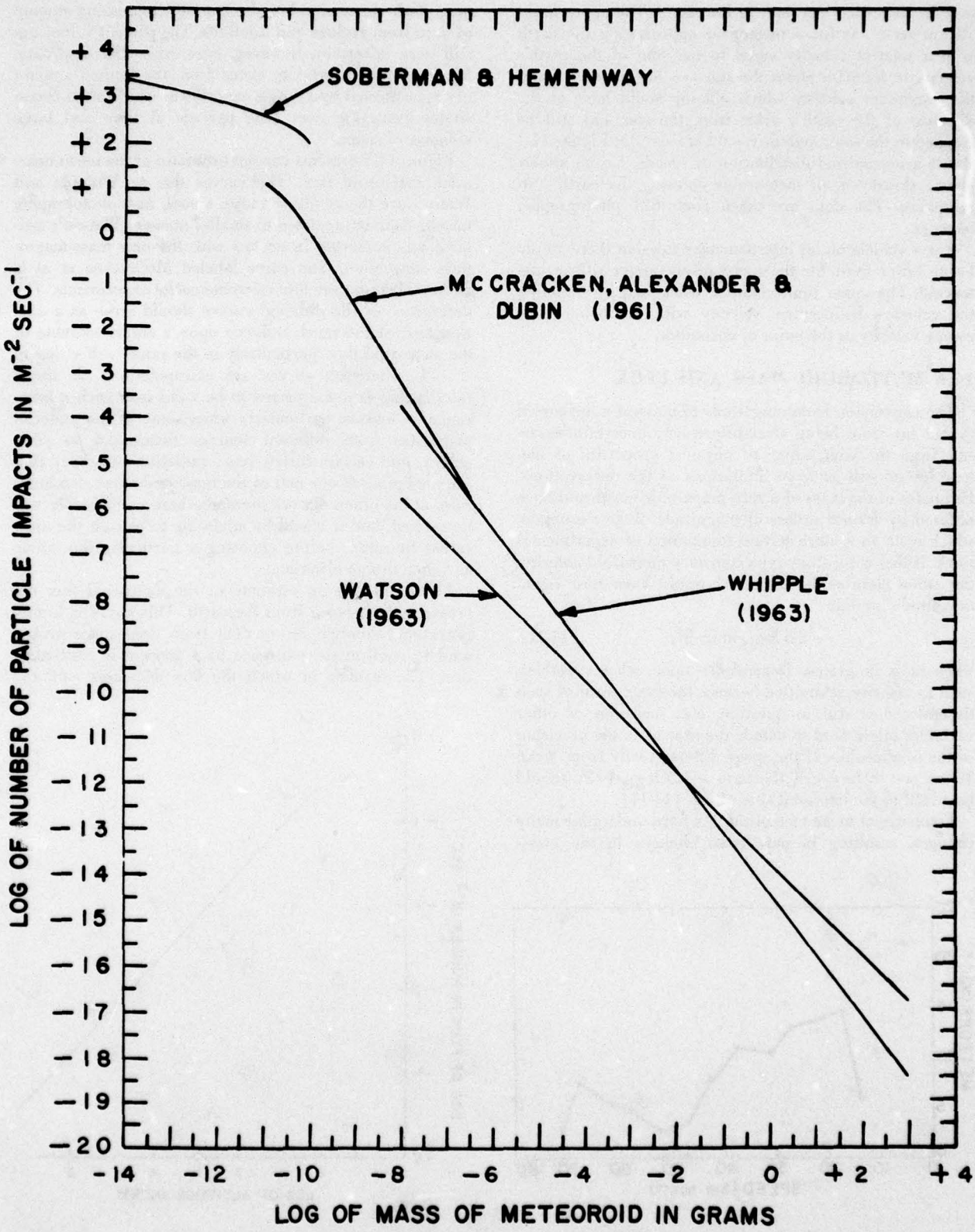


Fig. 14-5. Recent estimates of mean near-earth meteoroid flux in number of particle impacts per second in one square meter area as a function of mass of meteroid in grams.

mass range over which such a relation is applicable, are highly debatable. In interplanetary space, large departures from a normal meteoroid flux should exist in the vicinities of the asteroid belts and of cometary orbits. In the immediate vicinity of the earth, the concentration of meteoric matter is enhanced by atmospheric interactions. High concentrations of such matter can be accumulated in the upper atmosphere; meteoric matter can be seen from the ground in the form of noctilucent clouds (Sec. 5.4).

14.7 TEMPORAL VARIATIONS AND SHOWERS

There can be large excursions from the mean values of meteoroid fluxes. Temporal variations in the sporadic meteor flux occur on a daily and annual time base. Large variations occur at the time of the meteor showers.

The normal high-to-low ratio in the daily cycle is between 3 and 5. The low normally comes during local early evening hours, and the high during early morning hours. The annual high-to-low ratio is between 2 and 3, with the low rates occurring during early months of the calendar year and the high occurring during the last part. It should be noted that these numbers refer only to the change in the sporadic rate; the major meteor streams (showers) are not included. However, it is not clear that minor streams do not contribute in some measure to the annual variation. The daily cycle is probably due to the earth's rotation; the side of the earth facing the direction of the earth's orbital motion intercepts more meteoroids than the opposite side. The mean relative velocity on this forward side should also be higher.

Meteor streams or showers are increases in the flux of meteors entering the atmosphere. In most cases these showers are associated with the earth's passage through the orbit of a comet. Presumably, debris from the comet is dispersed over its orbit, and when the earth passes through this zone, it sweeps out some of the cometary debris. Where the two orbits intersect regularly, we have a recurring meteor shower. Most of the better known meteor showers recur annually. There is some evidence that there is a corresponding increase in the micrometeorite flux during the time of meteor showers [Alexander et al, 1961], although mechanisms such as the Poynting-Robertson effect should remove most of the small ($< 100\,\mu$) particles from the older cometary orbits. Table 14-2 lists data for the more prominent annually recurring meteor showers. A shower is usually named after the constellation in which the radiant appears. If more than one radiant happens to occur within a given constellation, the name is prefixed in each case by the Greek letter designation of the nearest prominent star. The right ascension and declination (see Fig. 21-4) of the radiant at the time of maximum activity are given. The duration listed is the interval between the times when the shower activity is one-quarter of the maximum. This duration may not be symmetrically

Table 14-2. Major meteor showers; values in parentheses are less reliable. (From McKinley [1961].)

Shower	Date of Peak Activity	Radiant Coordinates (deg) α	Radiant Coordinates (deg) δ	Dates of Detectable Meteors	Duration of Peak (days)	Radiant Transit (approx. local time)	Speed Before Slowdown (km/sec)	Equivalent Visual Rates (h^{-1})
†Quadrantids	Jan. 3	231	+50	1-4 Jan.	0.5	0835	41	50
Corona Australids	Mar. 16	245	−48	14-18 Mar.	(5)	0445	—	(5)
Virginids	Mar. 20	190	00	Mar. 5-Apr. 2	(20)	0050	30	(5)
Lyrids	Apr. 21	272	+32	19-24 Apr.	2	0410	48	5
†Eta Aquarids	May 4	336	00	Apr. 21-May 12	10	0735	64	20
†Arietids*	June 7	45	+23	May 29-June19	20	1000	39	60
†Zeta Perseids*	June 9	62	+24	1-17 June	15	1100	29	40
Ophiuchids	June 20	260	−20	17-26 June	(10)	2325	—	(20)
†Beta Taurids*	June 29	87	+20	June 24-July 5	10	1115	31	20
Capricornids	July 25	315	−15	July 10-Aug. 5	(20)	0050	—	(20)
†Southern Delta Aquarids	July 29	339	−17	July 21-Aug. 15	15	0210	41	20
†Northern Detal Aquarids	July 29	339	00	July 15-Aug. 18	20	0210	41	10
Pisces Australids	July 30	340	−30	July 15-Aug. 20	(20)	0210	—	(20)
Alpha Capricornids	Aug. 1	309	−10	July 15-Aug. 20	(25)	0000	23	5
Southern Iota Aquarids	Aug. 5	338	−15	July 15-Aug. 25	(25)	0410	35	(10)
Northern Iota Aquarids	Aug. 5	331	−6	July 15-Aug. 25	(25)	0110	30	(10)
†Perseids	Aug. 12	46	+58	July 25-Aug. 17	5	0540	60	50
Kappa Cygnids	Aug. 20	290	+55	18-22 Aug.	(3)	2125	26	(5)
Orionids	Oct. 21	95	+15	18-26 Oct.	5	0420	66	20
Southern Taurids	Nov. 1	52	+14	Sept. 15-Dec. 15	(45)	0045	29	(5)
Northern Taurids	Nov. 1	54	+21	Oct. 15-Dec. 1	(30)	0055	30	(5)
Leonids	Nov. 16	152	+22	14-20 Nov.	4	0026	72	(5)
Phoenicids	Dec. 5	15	−55	(Dec. 5)	(0.5)	2000	(13)	(50)
†Geminids	Dec. 13	113	+32	7-15 Dec.	6	0205	35	50
†Ursids	Dec. 22	217	+80	17-24 Dec.	2	0825	34	15

† Stronger and more consistent showers.
* Daylight showers detected by radio observation.

disposed within the period of detectable meteors because the activity of many showers displays a slow rise and a rapid fall. The observed speed listed is before slowdown by the atmosphere. The equivalent visual rates are the number per hour at maximum activity that a single naked-eye observer would see assuming a clear dark night and a radiant elevation of 45°. These rates are for the shower meteors and are, in addition to the normal background rates, characteristic of the time of day and the date (normal background is in the range 5 to 15 h^{-1}). The equivalent rates are intended to indicate long term coverage only; there are appreciable deviations from these average rates from year to year and from hour to hour.

14.8 METEOROID DAMAGE

To estimate the depth of penetration of a single meteoroid which impacts a surface, or the number of penetrations which a surface will experience in a given time, relationships developed from theoretical and experimental studies of hypervelocity terminal ballistics must be used. This branch of technology has taken large forward strides in recent years, but much still remains to be done. In particular, experimental data on cratering by individual projectiles of known mass at velocities in excess of 10 km sec^{-1} are sparse. Extrapolations of existing data to meteoroid impact conditions differ by factors of 2 or 3 in the estimates of depth of penetration. Although there is general agreement that hypervelocity craters in thick uniform targets are hemispherical in shape and that the volume of the crater varies linearly with the mass of the projectile, little data exists on the penetration of thin targets, laminated targets, and spallation from such targets.

One estimate of the meteoroid damage that might be anticipated is, in cgs units,

$$d = 0.6 \left(\frac{6 \rho m}{\pi \rho_t^2} \right)^{1/3} \ln \left(1 + \frac{K^{2/3} B}{4} \right), \quad (14\text{-}12)$$

where d is the depth of penetration into a semi-infinite homogeneous solid of density ρ_t by a projectile of mass m and density ρ, $K = \rho/\rho_t$, and B, the best number, is $\rho_t V^2/H$, where H is the Brinell hardness. Comparison with other empirical relationships of the same type indicates that Eq. (14-12) yields a penetration depth somewhat less than estimates used previously. There appears to be general agreement that a projectile will penetrate a target which is 1.5 times as thick as the crater depth in a semi-infinite target.

Figure 14-7 gives an estimate of the mean penetration flux for aluminum and steel surfaces in the near-earth environment, based on the penetration relation for thin targets (1.5d thickness), and the estimated meteoroid flux values (Sec. 14.6). The data from the penetration experiments carried by Explorer XVI are plotted for comparison. One expects meteoroid punctures to follow a Poisson distribution,

$$P(n) = \frac{(\phi\, At)^n}{n!} \exp(-\phi\, At), \quad (14\text{-}13)$$

where (P) n is the probability of exactly n punctures during time t in an area A. The appropriate flux value, ϕ, is obtained from Fig. 14-7. From this, one can calculate a reliability factor for design thicknesses, bearing in mind the limitations of the estimates on which such a reliability factor is based.

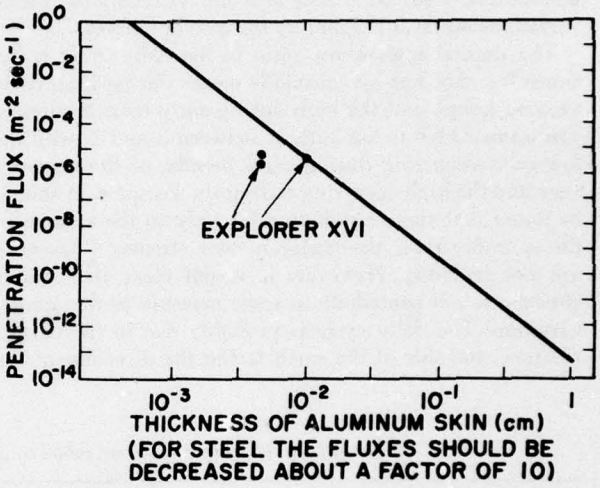


Fig. 14-7. Estimate of meteoroid penetration of thin metal target in space.

14.9 REFERENCES

Alexander, W. M., C. W. McCracken, and H. E. LaGow, 1961, "Interplanetary Dust Particles of Micron Size Probably Associated with the Leonid Meteor Stream," *J. Geophys. Res.*, v. 66, no. 11, p. 3970.

Hemenway, C. L., and R. K. Soberman, 1962, "Studies of Micrometeorites Obtained from a Recoverable Sounding Rocket," *Astron. J.*, v. 67, no. 5, p. 256.

McKinley, D. W. R., 1961, "Meteor Science and Engineering," McGraw-Hill Book Co., Inc., New York.

Öpik, E. J., 1958, "Physics of Meteor Flight in the Atmosphere," Interscience Pub., New York.

Whipple, F. L., 1963, "On Meteoroids and Penetration," *J. Geophys. Res.*, v. 68, no. 17, p. 4929.

Whipple, F. L., 1961, "The Dust Cloud about the Earth," *Nature*, v. 189, no. 4759, p. 127.

Chapter 15

THE SUN

John W. Evans

Radiant energy from the sun determines the surface temperature of the earth and supplies virtually all the energy for natural processes on the surface and in the atmosphere. Geological and paleontological evidence indicates that the sun has shone with about its present intensity for at least a billion years. The solar radiation, however, is not absolutely constant. There are short-period fluctuations in ultraviolet and x radiation and in corpuscular emission that induce complex responses in interplanetary space and in the earth's atmosphere. In this chapter, solar characteristics and activities are described and phenomena responsible for abnormal emissions are identified; other chapters deal with the responses themselves.

15.1 BASIC CHARACTERISTICS OF THE SUN

The sun is a relatively small faint cool star. Its average distance from the earth is 149.6×10^6 km, slightly less than 93 million miles. Its mass is 333,400 times the mass of the earth or 1.989×10^{30} kg. The rotation period of the sun, as seen from the orbiting earth, is a function of solar latitude, varying from about 26 days at the equator to 34 days at the pole. An effective period of 27 days is usually satisfactory for predicting rotational recurrences of solar-terrestrial disturbances. Because the axis of rotation is inclined only 7° to the plane of the earth's orbit, most of the solar surface can be seen in the course of one rotation. Most of the transient disturbances that affect the earth's atmosphere emanate more or less radially from low solar latitudes, and because the earth is never far from the plane of the solar equator, the earth is exposed to disturbances throughout the year.

The sun is essentially a sphere of gas heated by a nuclear reaction at its center (Sec. 21.6.1). Although the sun has no distinct phase boundaries, it does have boundaries that are defined by differences in temperature, density, magnetic field strength, state of ionization, or other conditions that affect the observable characteristics of the solar gas. These boundaries exist in a dynamic sense only; generally, they are not barriers to the flow of material. Figure 15-1 indicates the principal features of the sun's structure.

15.2 STEADY-STATE FEATURES OF THE SOLAR ATMOSPHERE

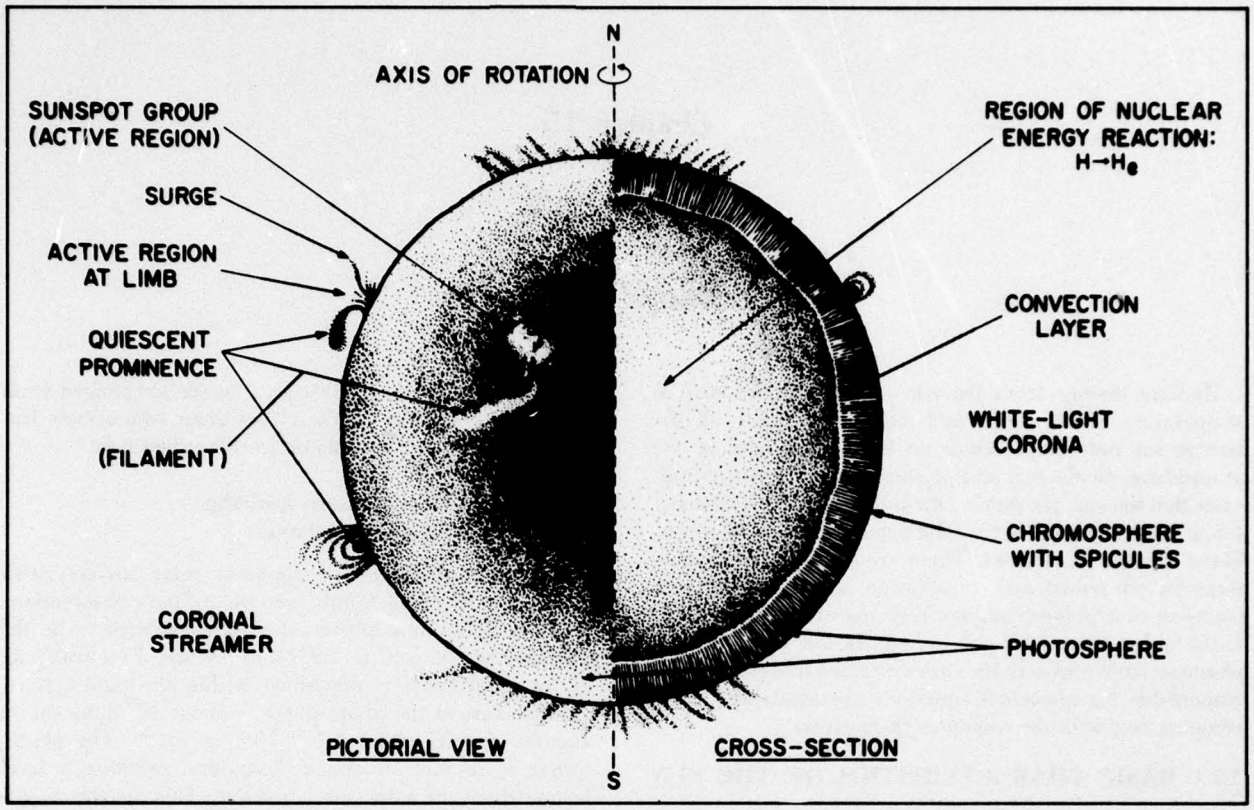
All observable features of the solar atmosphere are in a state of constant visible change. The statistical description of many features, however, remains unchanged from one time to another. These steady-state (quiescent) features of the solar atmosphere are described here.

15.2.1 The Photosphere and the Line Absorbing Layer

The *photosphere* is the apparent solar surface, with a very sharply defined limb, seen by ordinary observations in white light. Its diameter, usually considered to be the diameter of the sun, is 1.3914×10^6 km. Practically all of the solar mass is contained within the photosphere. The pressure at the photosphere is about 10^5 dyne cm^{-2}, and the density about 3.3×10^{-7} g cm^{-3}. The photosphere is in fact an optical boundary, marking a level below which the solar gas is opaque. This opacity is primarily due to a small concentration of negative hydrogen ions in the region immediately below the photosphere. These negative ions act as continuous absorbers over a great range of wavelengths, absorbing most of the intense radiation from the interior. The resulting accumulation of thermal energy in this layer sets up a system of convection currents that transports the excess energy through the negative hydrogen barrier. This energy is then reradiated into the relatively transparent gases above the photosphere and, hence, into space. The sharply defined level at which convective transport of energy gives way to the radiative process is the visible surface of the photosphere. The system of convective cells of ascending and descending gases existing in the photosphere gives the surface the granular appearance shown in Fig. 15-2.

Because the opaque gas composing the photosphere absorbs and reradiates approximately as a blackbody, the photosphere emits an essentially continuous spectrum. When corrections are made for selective absorptions in the earth's atmosphere, the total energy and its distribution in the visible spectrum of the photosphere correspond approximately to that in the radiation from a blackbody at about 6000°K (see Fig. 16-1).

Sharply tuned absorptions by the various atoms in and above the photosphere give rise to thousands of dark lines (Fraunhofer lines) in the continuous emission spectrum of the photosphere. This line absorption spectrum, shown in Fig. 15-3(a), is the source of most information on the abundances of the various elements, as well as the physical state (temperature, density, magnetic field strength, dynamics, etc.) of the solar atmosphere. Although the lines



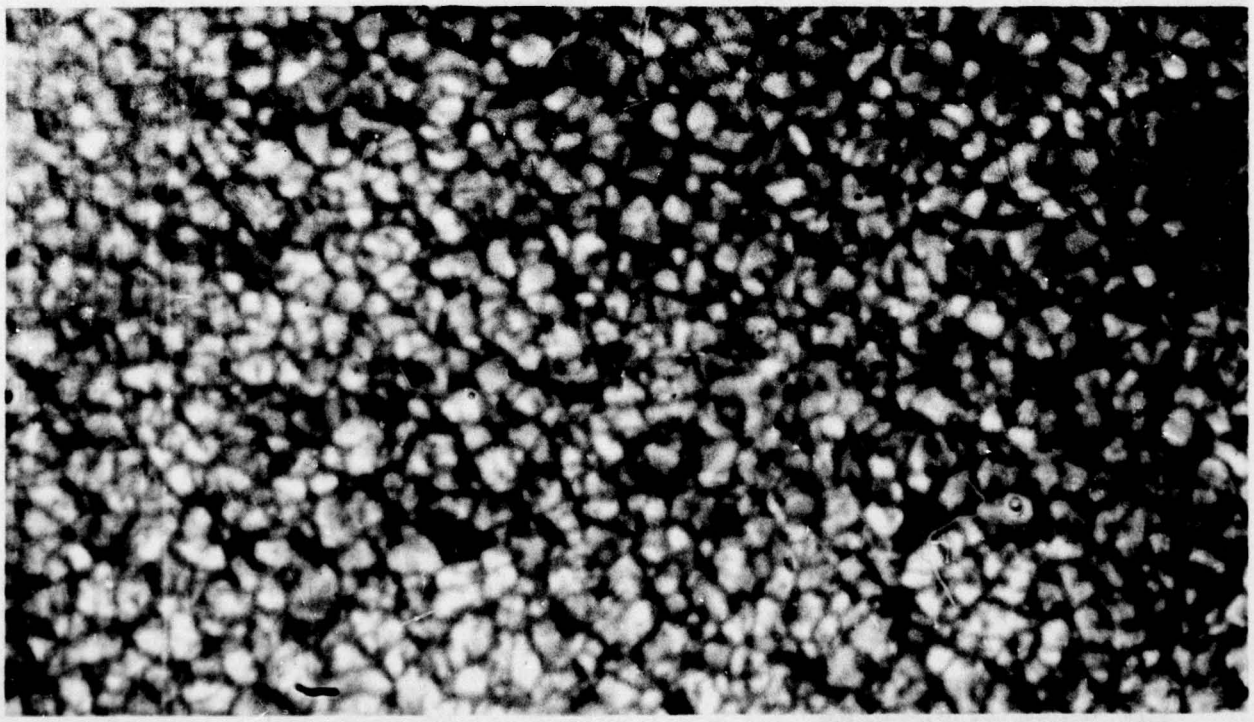


Fig. 15-2. Photospheric granulation and sunspot structure photographed with a balloon-borne telescope at an altitude of 80,000 ft. (Sacramento Peak Observatory.)

of a number of atoms are unobservable through the terrestrial atmosphere, all the natural chemical elements known on earth probably exist in the sun. Their relative abundances, however, differ radically. The sun's mass consists of approximately two-thirds hydrogen and one-third helium. All other elements combined constitute less than one percent of the total.

The granules of Fig. 15-2 are evidence of convection from below. Bright areas are the tops of hot rising columns of gas, which cool and sink through the relatively dark interstices. The root-mean-square temperature fluctuation in the visible surface is about 92°K. Granule diameters vary from about 2000 km to some limit below the resolving power of existing observational equipment. Their mean life time is about 8.6 min.

The principal region of line absorption is a layer about 350 km thick above the visible surface of the photosphere. High resolution spectra such as those of Fig. 15-3(b) show small scale "line wiggles" due to Doppler shifts; these are induced by mass motions in the higher line-absorbing layer of elements comparable in size to the granules. The vertical motions are composed largely of short-lived resonant oscillations with periods of about 300 sec, and with amplitudes, which increase with height, from about 60 to 150 km. The line intensities fluctuate in phase with this quasi-periodic motion, presumably as a result of the pressure changes. The motions and intensity fluctuations persist with decreasing regularity up through the chromosphere. Thus the inhomogeneities and the constant fluctuations seen in the white photosphere and in the chromosphere are also characteristic of the intervening layers.

At the line-absorbing level, the sun shows evidence of a general dipole magnetic field similar to that of the earth, with a field strength near the poles of a few gauss. During the sunspot maximum of 1957-1958, the dipole field reversed sign; this reversal may well be one more cyclical activity of the sun with a period of about 23 yr in conformity with the 11.4-yr cycle of magnetic activity in sunspots. Superimposed on the general magnetic field is a strong background of random magnetic "noise" of about 0.5 gauss when measured over areas the order of 100 square sec of arc (about 5000 km^2). It is probable, however, that much larger fluctuations in field strength exist in smaller surface elements that are comparable in size to photospheric granulation. The strong fields in sunspots are of a different order of magnitude.

15.2.2 The Chromosphere

The *chromosphere* is a 10,000-km thick layer of transparent glowing gas above the photosphere. Its continuous spectrum is extremely faint, and, like all solar features above the photosphere, it can be observed normally only by isolating the light of one of its strong lines, usually the red H_α line at 6563 Å (Fraunhofer C line) or the line of CaII at 3934 Å (Fraunhofer K). It is also beautifully visible for a few seconds as a brilliant red arc at the solar limb when the moon has just covered the photosphere at a total eclipse. These few seconds afford the best possible conditions for observing the chromospheric spectrum, which is then seen as a bright line emission spectrum. Figure 15-4 shows a small section of this "flash spectrum" taken at the eclipse of 5 February 1962 in New Guinea. The relative intensities of the lines and the faint continuum indicate that the chromospheric temperature ranges from about 10,000°K to perhaps 60,000°K, increasing with height. The density decreases with height roughly from 5×10^{-13} to 5×10^{-15} g cm^{-3}.

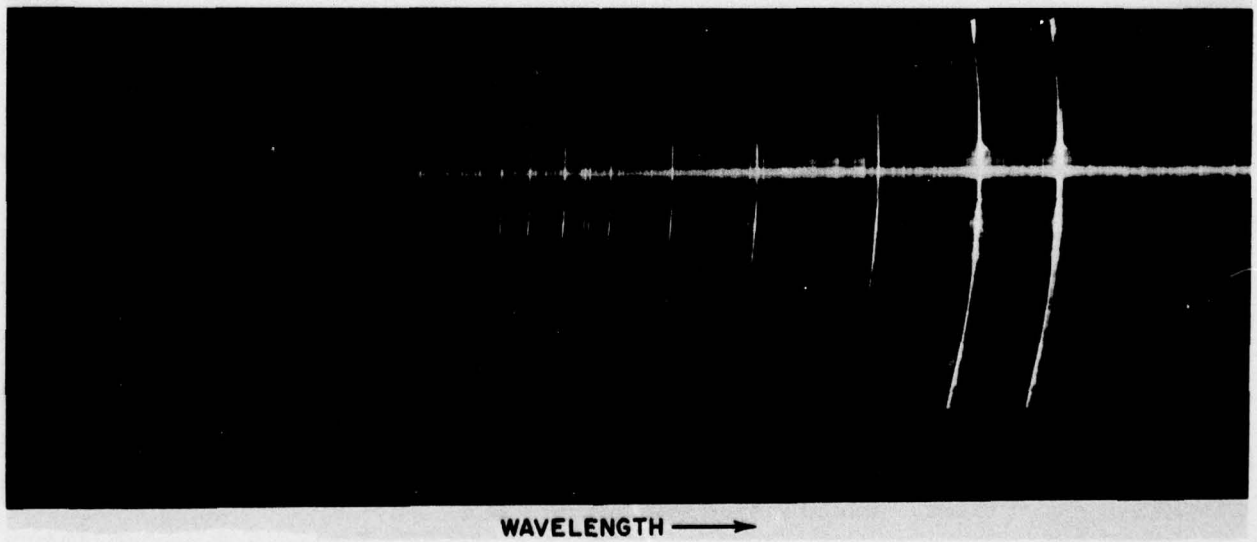


Fig. 15-4. Flash spectrum of chromosphere taken at eclipse of 5 February 1962 with slitless spectrograph in New Guinea. The very strong K and H_α lines of CaII (3934 and 3968 Å) are at the right. The convergence of the Balmer series of hydrogen extends past the middle toward the left. (Sacramento Peak Observatory.)

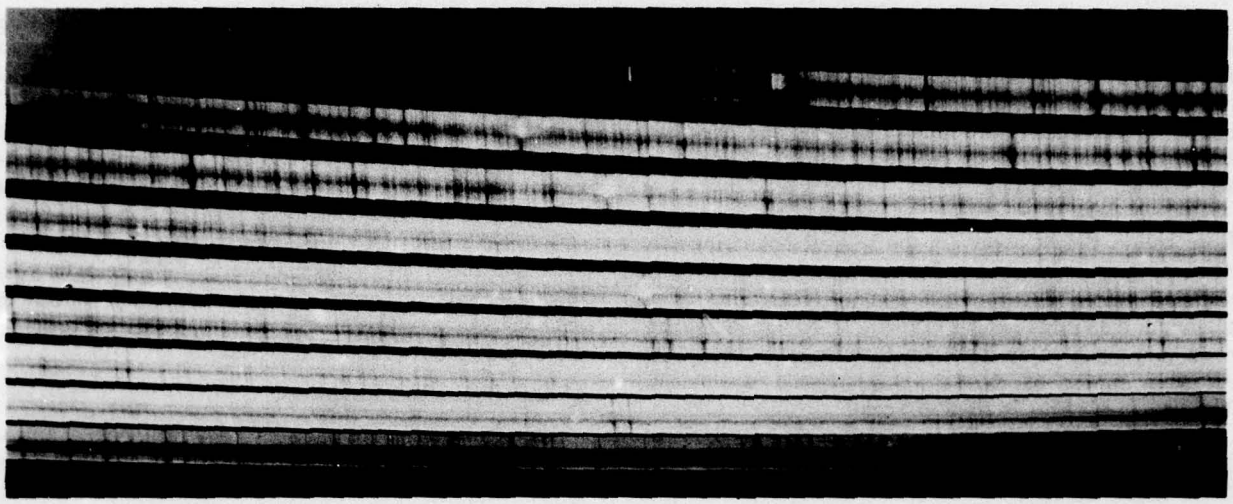


Fig 15-3(a). Solar spectrum from about 3900 Å to 6800 Å. Successive strips overlap somewhat. Note the strong emission lines where the slit crossed a large flare. (Sacramento Peak Observatory.)

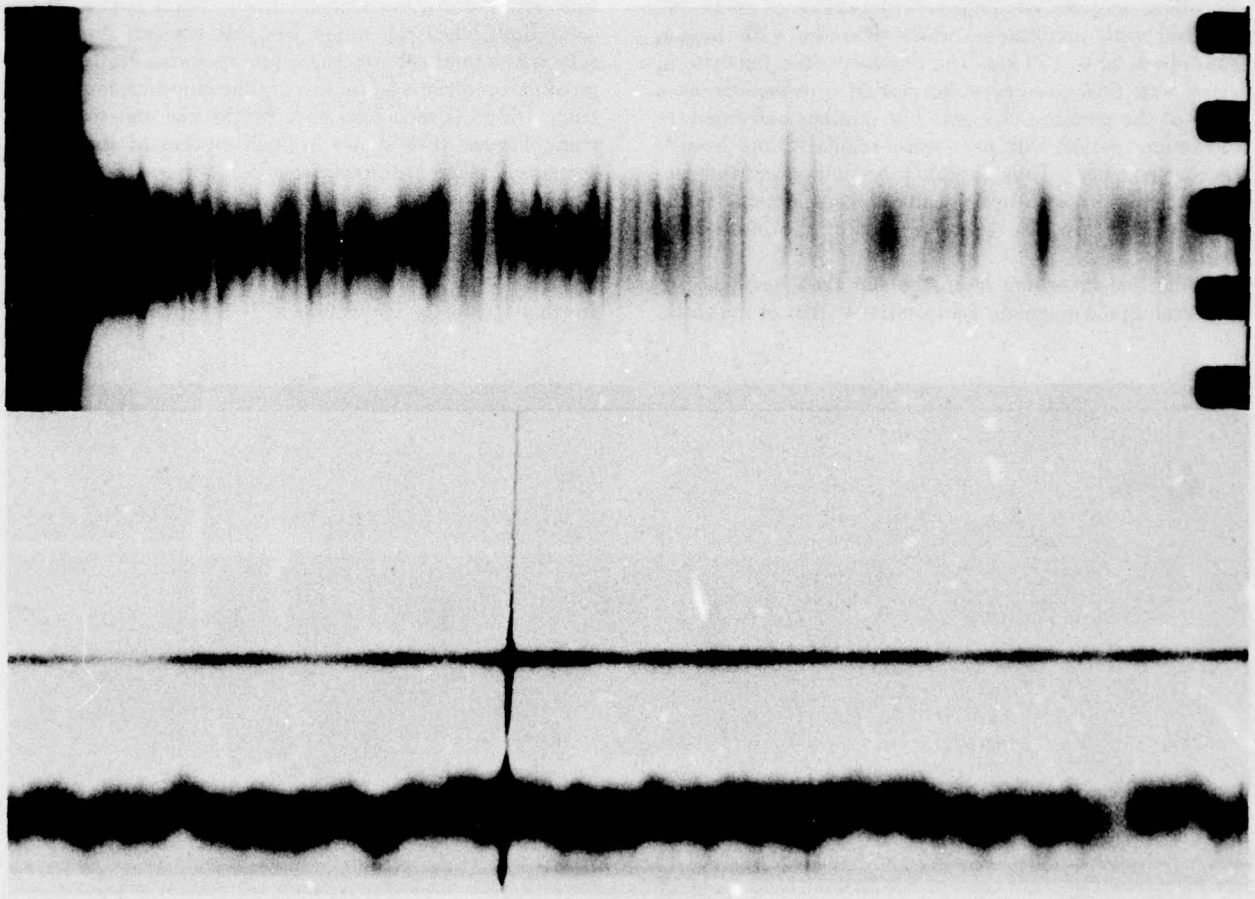


Fig. 15-3(b). Fine detail in the chromospheric H_a line (above), and the D_2 line of sodium (below), originating near the photosphere-chromosphere boundary. Intensity fluctuations and Doppler-shifted "line wiggles" in different elements of the solar surface imaged along the slit are distinctly different at the levels of formation of these lines. The narrow structureless lines shown are due to terrestrial water vapor. (Sacramento Peak Observatory.)

The top of the chromosphere is in continual small scale eruption. Over most of the sun, thousands of small spike-like jets, the *spicules*, project upward from the chromosphere. Figure 15-5 shows their appearance at the limb. Each spicule has a lifetime of at most a few minutes. They are probably related to the convective activity in the photosphere.

Photographs taken in the light of the H_α (or of the K) line, such as Fig. 15-6, show the intricate structure of the chromosphere over the solar disk. The physical differences between the bright and dark elements are not yet known. Large vertical velocity fluctuations in both space and time are present, but appear to be unrelated to brightness in H_α light.

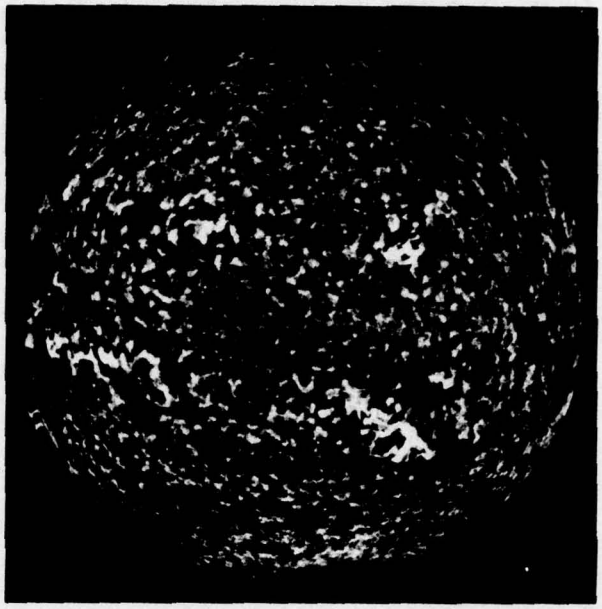


Fig. 15-6. Chromosphere, in H_α light, seen in projection against the solar disk. (Sacramento Peak Observatory.)

15.2.3 The Corona

During a total eclipse, when the glare of the photosphere is excluded, a faint white halo in the region beyond the chromosphere becomes visible. This halo is caused by two superposed sources of light. One source, the F-corona, is sunlight scattered by the zodiacal dust particles. These particles are at great distances from the sun and are not properly a part of the sun's atmosphere. The second source, the true *corona,* is an extension of the sun's atmosphere. The most prominent visible features of the corona are the irregular halo that surrounds the sun to a mean distance of roughly its radius and the long rays of streamers that sometimes extend several solar diameters into space.

There are two components of the light of the true corona: the emission lines and the white light. A small fraction of the light at lower levels is concentrated in the bright emission lines of highly ionized iron, nickel, calcium, and other elements. The fact that 9 to 15 of the electrons are stripped from these atoms is convincing evidence of the high coronal temperature, around 1 to 2 $\times 10^6$ °K. Figure 15-7 was taken, without an eclipse, by the light of the green line (5303 Å) of Fe XIV. Most coronal radiation is light from the photosphere scattered by free electrons; this is the *white light corona.* The high



Fig. 15-7. The emission corona, photographed 9 March 1956 in the green line of Fe XIV (5303 Å). The black disk entirely eclipses the photosphere and chromosphere. (Sacramento Peak Observatory.)

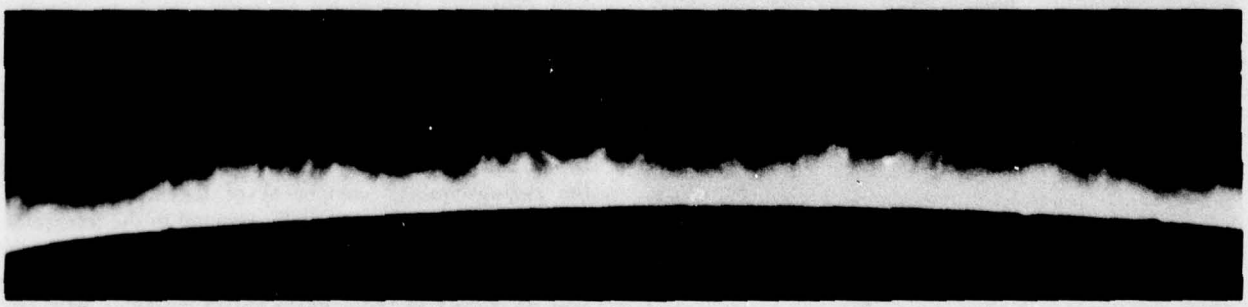


Fig. 15-5. Profile of the chromosphere at the limb of the artificially eclipsed sun in the light of the H_α line showing the minute spicule structure. (Sacramento Peak Observatory.)

kinetic velocities of the electrons (caused by the high coronal temperature) introduce large random Doppler shifts in the scattering process, which smear out the Fraunhofer lines to such an extent that they are no longer detectable. Thus the white light spectrum is a smooth continuum with no absorption lines. Figure 15-8, a photograph of the white light corona, shows the streamers characteristic of sunspot minimum. Because the white light corona has not been satisfactorily photographed except during an eclipse, little is known about its day-to-day variations. Photoelectric methods promise a means for detecting large changes, but some years of observation will be required to determine the nature of these changes.

The general form of the corona, and particularly the development of the long streamers, is related to the sunspot cycle. During spot maxima, streamers are absent and the corona is a round, compact halo with intricate local structures induced by underlying active regions. Near spot minima, the internal structure is simpler and the streamers are well developed.

The coronal density is the order of 5×10^{-16} g cm^{-3} at the base. The density decreases steadily with distance from the sun, but is still appreciable at the earth and probably extends far beyond. At present there is no real distinction between the outer corona and the interplanetary medium. Thus the corona can be considered as diminishing outward until the density of local interstellar space ($\approx 10^{-24}$ g cm^{-3}) is reached. The physical conditions in the outer corona (or the interplanetary medium) are uncertain. Space probe experiments indicate that the corona has an outward flux of material (the solar wind) that streams past the earth with an estimated mean velocity of 300 km sec^{-1} and a density of about 10^{-23} g cm^{-3} (see Chapter 18).

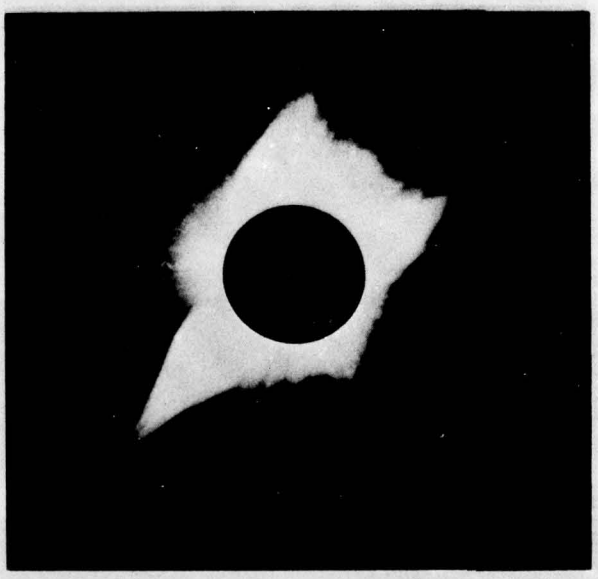


Fig. 15-8. The white corona during total eclipse. (Yerkes Observatory.)

The temperature along the solar radius drops from a maximum of about 1.5×10^7 °K at the center to a minimum of about 4300°K just below the boundary between the photosphere and chromosphere. The temperature rises again through the chromosphere to a maximum of about 1.5×10^6 °K in the lower corona. The rate of temperature decrease outward through the corona is apparently quite slow, at least through a distance of the first few solar radii.

The heating of the corona and chromosphere through the relatively cool photosphere is apparently the result of the upward transport of mechanical energy that originates in the strong convective motions which produce photospheric granulations. Recent observations of velocity shifts in the Fraunhofer lines show that the line-absorbing layer consists of elements 3000 to 6000 km in diameter which are in vertical oscillation with a sharp resonance at periods around 300 sec. These oscillations could be induced by upward surges of the convecting granulation layer; they are sufficient to transport the energy necessary for heating the chromosphere and corona. The exact nature of the conversion of the kinetic energy of the oscillations into heat is obscure.

15.3 ENERGY OF THE SUN

Energy leaves the sun as electromagnetic radiation and corpuscular radiation (high-speed protons and other charged particles). The intensities of both forms of emission are subject to transient variation, but the percentage variation in electromagnetic radiation appears much smaller than that of the corpuscular.

The solar radiant energy flux is often expressed as the total radiant energy incident per unit surface area normal to the flux at the earth's mean distance from the sun. This is the *solar constant*, which is about 1400 Wm^{-2} (see Sec. 16.1). The steady power of the electromagnetic radiation from the sun, subject to the present uncertainty in the true value of the solar constant, is about 3.8×10^{23} kW. This radiation results from the thermonuclear conversion of 4.2×10^6 tons of mass per second into energy. The total energy of corpuscular emission is unknown, but must be a very small fraction of that of the electromagnetic radiation.

A blackbody the size of the photosphere would radiate energy at the same rate as the sun if it were at a temperature of about 5750°K. The distribution of energy in the solar spectrum through the near ultraviolet, visible, and near infrared, however, is similar to that of radiation from a blackbody at about 6000°K. The sun is not a true blackbody; the discrepancy is primarily because in the different wavelength regions, we see layers at different depths of the solar atmosphere and, therefore, at different temperatures. This is particularly significant in observations of the radio-frequency component of the sun's radiation, because radio telescopes usually respond to the integrated emission over the entire sun and corona of radiation in a given frequency band. The corona is highly ionized, so that its opacity to radio waves varies markedly with frequency. The height from which the radio emission can escape increases from the level of the chromosphere for

the highest frequency to many solar radii for the lowest detectable frequency. Because coronal temperatures are of the order 10^6 °K, the observed intensity of radio emission is far greater than from a blackbody at the temperature of the photosphere. A detailed discussion is given in Chapter 16.

15.4 TRANSIENT SOLAR PHENOMENA

Superimposed on the predominantly steady-state condition of the sun are numerous, but relatively minor disturbances known as solar activity. The degree of such transient activity varies cyclically. The most prominent periodicity is that of sunspot numbers and related activity, averaging about 11.4 yr. The *relative sunspot number* (also known as the *Wolf number*, the *Zurich sunspot number*, or the *mean sunspot number*) is 10 times the number of spot groups plus the number of individual spots visible at a given time, averaged for the various contributing observatories and corrected for systematic differences between the stations. The cycle seems to derive from a more fundamental magnetic periodicity at twice the period of the sunspot number, about 23 yr. Figure 15-9 shows the relative sunspot number by years from 1700 to 1963 inclusive; the cyclic character is apparent.

Transient dark sunspots and associated bright faculae visible in white light are the obvious manifestations of solar activity; most disturbances are detectable by special instruments only. Most features of solar activity occur in restricted regions, usually surrounding sunspots, known as active centers. Figure 15-10 shows the photosphere during high activity. The active centers include such slowly changing quiescent features as sunspots, plages, coronal brightenings in emission lines, and, probably, the white light coronal streamers. They also include a class of eruptive features, lasting typically a few hours, that comprises flares, certain types of prominences, coronal hot spots, and outbursts of radio noise. All of these share in the sunspot cycle.

15.4.1 Prominences

Prominences are large clouds of gas high above the chromosphere, visible as bright flamelike objects with emission spectra against the sky background at the limb, or as long ropy dark *filaments* with absorption spectra against the solar disk (see Fig. 15-6). They appear over both undisturbed and active regions. Despite their variety, prominences can be classified by certain distinctive characteristics. Figure 15-11 shows three types.

Quiet region prominences differ sharply from those attending active regions. They may appear as a branching shape, suggesting a bush or tree, that often persists for weeks, or as a massive pillar that lasts a few hours. Against the solar disk they are the largest of the dark filaments, sometimes as long as 400,000 km. Several such

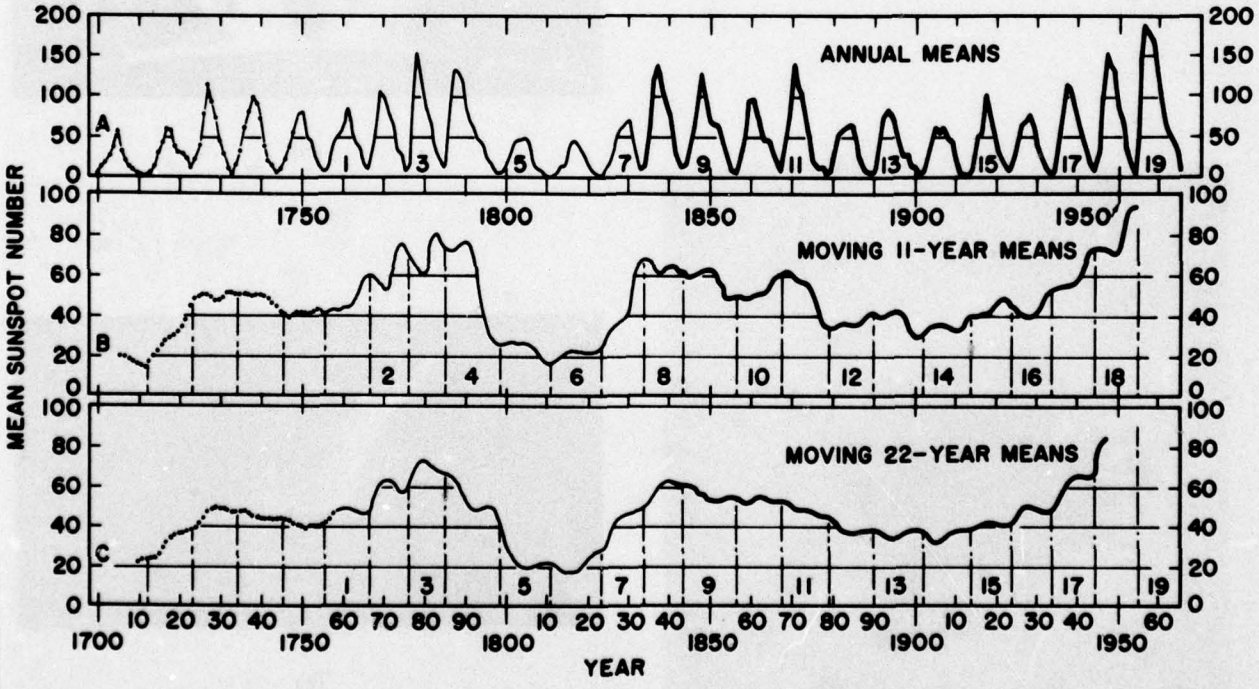


Fig. 15-9. Means of relative sunspot numbers, 1700 to 1960. Annual means show the 11-yr cycle, with numbered periods. The moving means are derived for each year by averaging the relative sunspot numbers over the 11- or 22-yr interval centered on that particular year. These moving means deliberately smooth out the 11- and 22-yr cycles, and reveal only the slower variations, which may or may not be periodic.

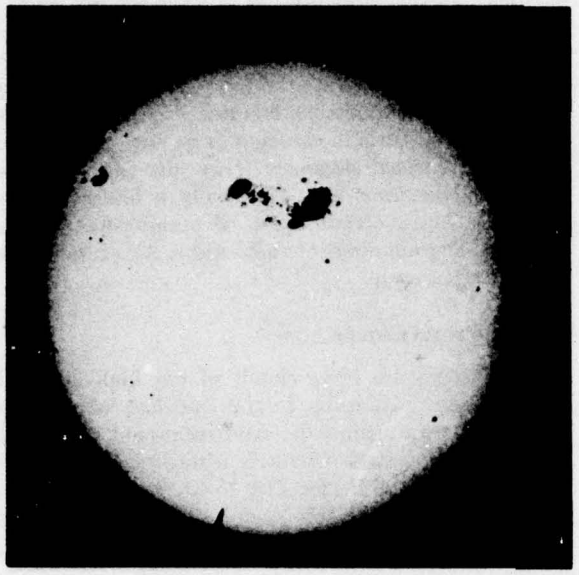


Fig. 15-10(a). Photosphere of the sun during a period of high sunspot activity. Pointed inserts near top and bottom of disk mark the rotational axis.

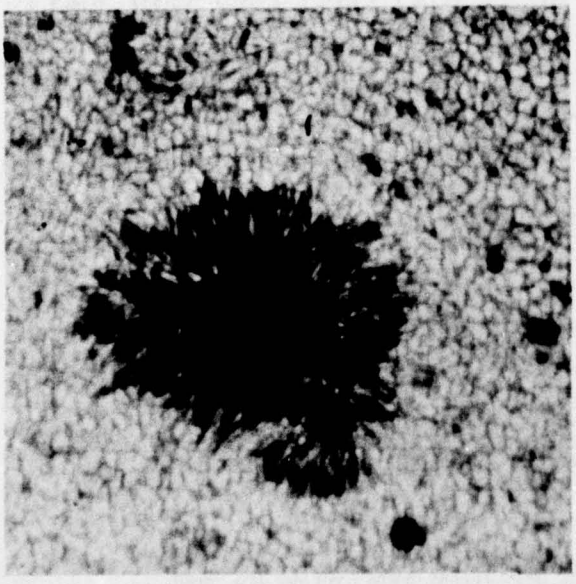
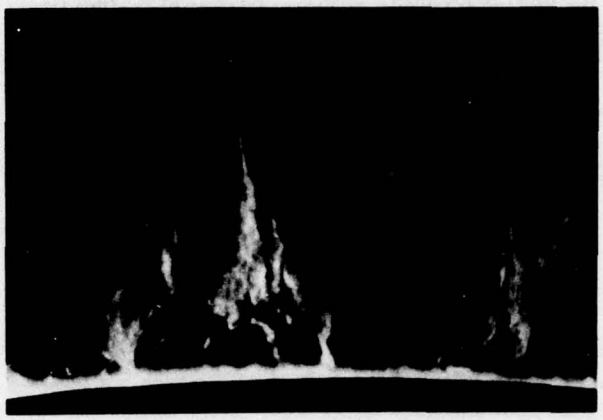
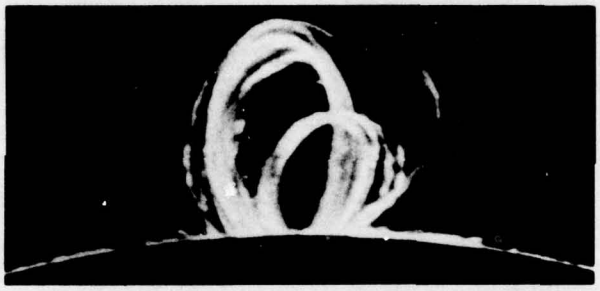


Fig. 15-10(b). Sunspot structure photographed on Project Stratoscope flight 11 Aug 1959. (Princeton Observatory.)



(a)



(b)



(c)

Fig. 15-11. Three types of prominences photographed in H_α light: (a) typical quiet region prominence, (b) loop prominences over an active center (c) surge prominence over an active center. (Sacramento Peak Observatory.)

filaments are visible in Fig. 15-6. At any one time several prominences can usually be observed at the limb and are the most spectacular features on the sun. Typically, they are like a curtain 150,000 km long, 35,000 km high, and 5000 km thick.

When a large quiescent prominence is seen at the limb during total eclipse, it usually is situated beneath a system of alternating dark and light arches in the white corona. At a distance of perhaps half a solar radius from the limb these arches merge into a broad, tapering streamer that extends far into space. Evidence tends to identify these streamers with the particle streams (corpuscular radiation) that are potent agents of the 27-day recurring magnetic disturbances known as M-region storms (Sec. 15.6).

Among active center prominences, the most significant are the loops and surges. The *loops* appear to originate in a seemingly inexhaustible nucleus, perhaps 75,000 km high. For 2 or 3 h, material pours from the nucleus down into the chromosphere along a pair of well-defined arcs, which together form a nearly complete circle resting in the chromosphere with the nucleus at the top. *Surges* are spike-shaped tongues of gas originating in the chromosphere. They have velocities of hundreds of kilometers per second; the slightly curved trajectory that is usually inclined to the solar radius. After reaching its maximum extension (normally in 5 to 15 min), the surge either retracts along its original trajectory or fades out.

Because prominences are embedded in the corona, there must necessarily be marked interactions between the two; some interactions are observable, especially at eclipses. Both quiet and active region prominences are relatively cool, dense condensations in the coronal medium. The prominence temperature in the densest part probably varies from 6000°K to 20,000°K. This temperature is only about one percent that of the coronal temperature, but the prominence density is about one hundredfold greater than the coronal density, and pressure equilibrium usually appears to be maintained between the two. Most prominences are composed of a fine, threadlike internal structure. The motions tend to be downward, but with a velocity much less than that of a free-falling body. Important exceptions are the eruptive prominences, which are formerly quiet prominences that are suddenly blown to great heights in the corona, and spray prominences, which are upward ejections of material from the most active regions with velocities as high as 1500 km sec^{-1}. Figure 15-12 shows the development of a spray prominence.

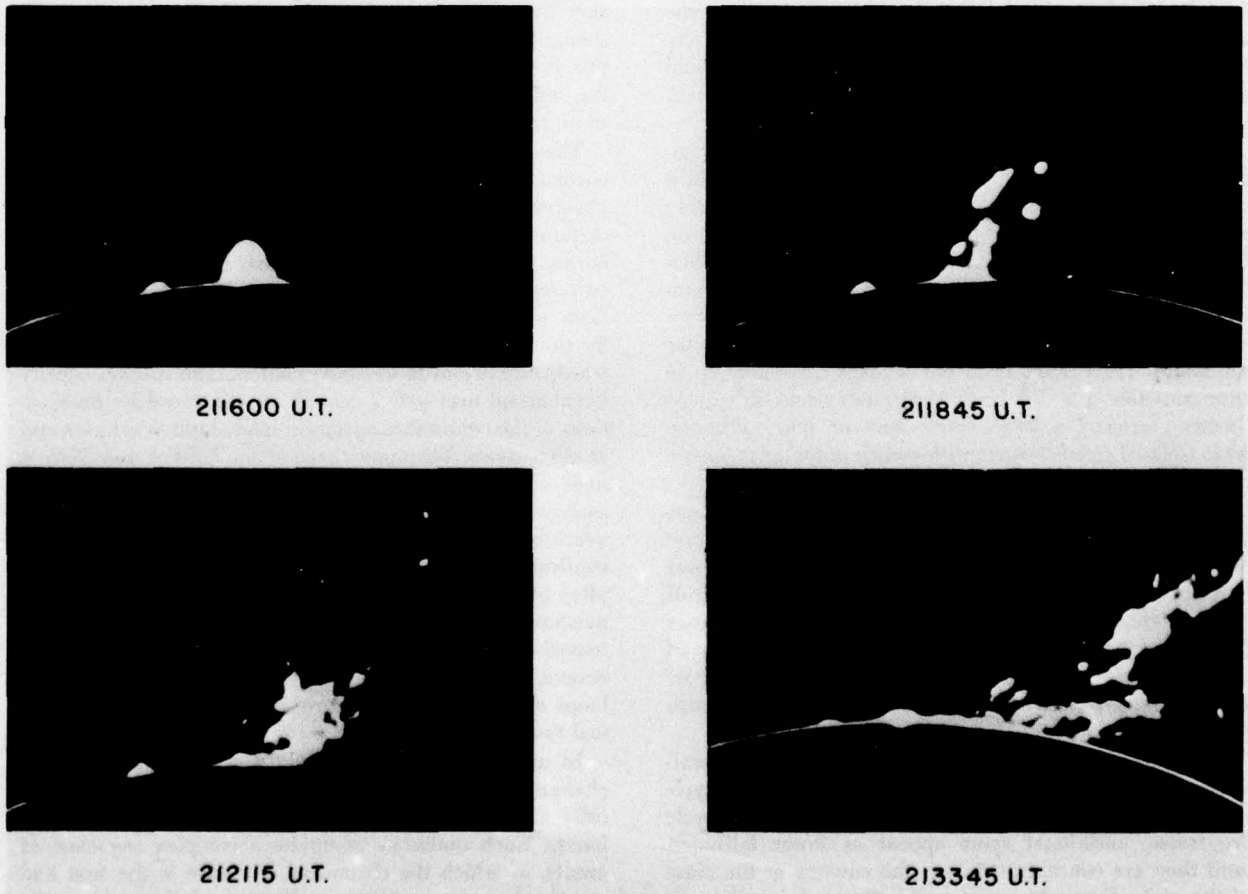


Fig. 15-12. Sequence showing development of a spray prominence associated with a flare, 10 February 1956. (Sacramento Peak Observatory.)

15.4.2 Active Centers

The basic cause of an active center and the driving agent for all forms of solar activity is a strong magnetic field that pervades the whole active center and may endure for a period of a few hours to a few months. If the fields are stronger than about 500 gauss, they form dark sunspots by inhibiting the normal convection that transfers heat into the photosphere. Thus the surface cools off by about 2000°K and appears relatively dark. All sunspots are centered on the strongest vertical magnetic fields in active centers. Field strengths are typically 1000 to 2000 gauss, but occasionally go to 4000 gauss. The structure of the magnetic fields in different centers varies enormously, from simple single poles to irregular distributions of opposite poles that are dominated usually by one large pair. The degree of eruptive activity in a center increases with the complexity of the field. Eruptive activity is presumably due to relatively small fluctuations in the field because the energies of even the most violent eruptive features are small compared with the energy stored in the magnetic field. The process by which the magnetic energy is converted is not yet established. One promising qualitative picture of the relation between solar magnetism, the sunspot cycle, and solar activity is that proposed by H. Babcock, "The Topology of the Sun's Magnetic Field and the 22-Year Cycle," *Astrophys. J.*, v. 133, p. 572, 1961; another is presented in Sec. 18.3 and 18.5.

Figure 15-10(b) shows the complex structure of a typical medium-size sunspot. It normally consists of a dark center, or umbra, surrounded by a sharply bounded gray area of intermediate brightness known as the penumbra. The penumbra is composed of generally radial, bright filaments on a darker background. In small spots the penumbra is usually absent, whereas very large spots will often have several umbrae in a single enormous and irregular penumbra. Sizes range from the smallest detectable up to approximately 3×10^9 km^2. Most spots occur in groups clustered around a large single spot or pair, although large isolated circular spots with simple unipolar magnetic fields are not uncommon.

Typically, a spot begins with the development of a large, nearly circular spot that leads the group in the direction of the solar rotation. Sometimes a single small follower spot appears. More commonly, the follower is a group of smaller irregular spots. Lifetimes of spot groups range from a few hours to several months, with an average of about a day. The conspicuous phenomena of active regions, however, are largely due to the minority of groups that persist for weeks.

Spots occur in both the northern and southern hemispheres of the sun. The first spots of a new 11-yr cycle typically appear at latitudes of 20° to 25°. As the cycle progresses, additional spots appear at lower latitudes, until they are concentrated near the equator at the close of the cycle. Few spots appear at latitudes lower than 5° or higher than 35°. During a particular 11-yr cycle, all leader spots in the northern hemisphere are of one magnetic polarity, and all of their follower spots of the opposite polarity. In the southern hemisphere the polarities of leaders and followers are opposite those in the northern hemisphere. This pattern persists throughout the rise and decline of spot activity. During the next 11-yr cycle the entire pattern of magnetic polarity in sunspots is reversed. Thus, the fundamental cycle of solar activity appears to be about 23 yr rather than 11.4 yr.

Faculae are regions of enhanced white light brightness in the high photosphere, visible around spots near the limb. They appear to be about 900°K hotter than the normal photosphere. Faculae are among the first intimations of the development of an active region, and they often persist for weeks after the spots have disappeared.

Plages are bright clouds in the lower chromosphere above sunspot groups. They are conspicuous in the light of the K and H_α lines and quite irregular in outline and brightness (see Fig. 15-6). Ordinarily, a plage is comparatively quiet, changing noticeably only in several hours. A bright plage often precedes the appearance of a sunspot and persists after the spot is gone.

The emission lines of highly ionized elements in the corona are brighter over active regions than over the undisturbed photosphere. This brightening of coronal emission lines is particularly noticeable in the two relatively strong lines of iron, the red line at 6374 Å and the green line at 5303 Å. The brightening of these coronal lines at the east limb is often the first indication of the appearance of an active region rotating onto the disk.

The influence of active regions upon the white light corona cannot be specified because of the limitation of observations to eclipses. Inadequate data indicate that certain raylike structures are characteristic of the white corona over active regions, and that the brightness of the corona is anomalously high over such regions. The directions of conspicuous long streamers may be determined by the combined effects of magnetic fields reaching upward from two or more active centers. The coronal density is enhanced over active centers, as evidenced by observations of the continuous spectrum made both at eclipses and at other times. The appearance of the 5694 Å and 5445 Å lines of CaXV (ionization potential, 821 eV) over some centers indicates that these particular centers excite the overlying corona to abnormally high temperature. This is confirmed by the radio observations. Surge prominences often occur in the corona over an active region. The high nucleus of a loop is usually in a CaXV hot spot. Coronal material appears to condense at the tops of loop prominences, providing the downward flowing material. The loops and the associated coronal activities emit nonthermal radio noise.

In an active region marked by complex and rapidly changing magnetic fields, the quiescent phenomena typically are punctuated by sudden and violent eruptive outbursts. Such outbursts comprise a complex sequence of events, of which the chromospheric flare is the first and usually the most conspicuous. Flares and abrupt increases in bright coronal line emission almost always occur in the vicinity of the plage and spot that mark an active region.

15.4.3 Flares

A flare is a transient, localized brightening of the chromosphere, usually involving the plage of an active center. *Flare importance* is assigned primarily by maximum area. Table 15-1 indicates relative sizes, durations, and frequencies of the importance classes. A flare is not rare, except in the years near solar minimum. Excluding those of importance 1— (subflares), the average incidence rate is about 0.4 h^{-1} at sunspot maximum. The greatest flares, however, occur at the rate of only 20 to 30 yr^{-1} in peak years of solar activity. The light from a typical flare shows a rise to maximum intensity in 2 to 12 min, then a slower decline. The peak amplitude ranges from 2 to 20 times the normal brightness of the chromospheric environment. Like its total duration, the intensity of a flare correlates loosely with its area; the dispersion, however, is very large. Small flares usually have simple convex shapes (hemispheres), but the largest are invariably complex (see Fig. 15-13). Normally, a flare projects only slightly above the chromosphere; typical heights range from 10^4 to 4×10^4 km.

The flare visible in hydrogen or calcium light is only part of a complex phenomenon. Often a flare ejects material into the corona, as a flare surge or spray (see Fig. 15-12). Usually the material moves at a few hundred kilometers per second in a curved trajectory, and falls back along the same path after reaching out to a solar radius or less. More rarely the ejected gases travel at 2 to 3 times the velocity of escape (638 km sec^{-1}) from solar gravity. Another frequent side effect is the activation of quiescent prominences at distances up to a solar radius from the eruption. Some normally invisible disturbance is propagated from the flare, at a few hundred kilometers per second, which sets in motion some of the filaments it encounters. Sometimes the filament may disappear abruptly for a few minutes and reappear. Occasionally, the filament is invisible for a day or two before re-forming in its original position. The characteristic radio-frequency emissions of flares are discussed in Sec. 16.3. Many flares including even subflares emit a strong x-ray flux. The important ionospheric effects due to x-rays from flares are described in Sec. 15.6.

Table 15-1. Flare classification.

Importance (Class)	Area (Sq. deg*)	Duration (min)	Relative Frequency of Occurrence
1—	2.06	17	0.75
1	2.06 to 5.15	32	0.196
2	5.15 to 12.4	69	0.048
3	12.4 to 24.7	145	0.0055
3+	> 24.7	145	0.0055

* Units of heliographic equatorial square degrees; 1 deg^2 = [illegible] 4.85 $\times$ 10^{-5} of the solar hemisphere.

A small fraction of flares (usually of importance 3 or 2) eject streams of charged particles (corpuscular radiation) into the interplanetary medium. The energy spectrum varies widely. When the modal energy is a few keV, the entry of the particles into the geomagnetic field may produce a sudden commencement geomagnetic storm. More rarely (about 40 events, 1956 to 1960), a flare may produce considerable flux of particles with energies of 0.1 to 100 MeV. When such particles enter the geomagnetic field, they are guided to the magnetic poles and are absorbed by the atmosphere. The resulting enhancement of ionization produces a *polar cap absorption* (PCA) event, in which extraterrestrial radio sources become severely attenuated in polar regions. Even more rarely (12 cases, 1942 to 1961), a flare will emit particles with energies of 1 to 50 GeV. (Because this is comparable to the lower energy of cosmic rays, these particles are often, but imprecisely, called "solar cosmic rays.") Protons with such relativistic energies can penetrate the earth's magnetic field in temperate and even equatorial latitudes, where they can be detected as *ground level events* (GLE). Energetic particles are emitted by flares in a discrete direction, so that the earth does not always intercept them. When the corpuscular solar flux is of sufficient density, however, it can modulate the influx of galactic cosmic radiation. (Forbush decrease, see Sec. 17.3.3.) The practical significance of the proton emission of flares is discussed in Sec. 15.5.5.



Fig. 15-13. Great chromospheric flare of 28 August 1956, photographed in H_α light with 16-inch coronagraph. (Sacramento Peak Observatory.)

CHAPTER 15

The origin and physical processes of flares are not understood. Quasi-equilibrium models of classical astrophysics fail completely to explain their radio-frequency, x-ray and corpuscular emissions. Energy arguments point clearly to the presence of magnetic fields in active centers as the necessary condition for a flare; observations indicate that complex fields are particularly effective. Theoretical explanations of the catastrophic processes of energy conversion, however, are only partially successful, and far from complete. Optical spectra of flares resemble those of very dense prominences; in addition, the emission lines of the hydrogen Balmer series are extraordinarily wide. This observation supports the suggestion that a hydromagnetic pinch effect plays a role in the energy conversion.

15.5 PROTON SHOWERS IN SPACE NEAR EARTH

The proton showers originating in large flares and passing the neighborhood of the earth with appreciable fluxes of particles constitute a hazard to certain kinds of equipment (solid-state devices and photographic materials, in particular) and to living organisms in space. Although the hazard to man in space is currently the subject of considerable controversy, there can be no doubt that space travellers will desire to avoid proton showers if possible. The characteristics of the showers themselves are considered in Sec. 17.4. Their relation with associated solar phenomena and the problem of predicting them in a useful fashion are discussed here.

All fast proton showers are associated with flares of importance 3+, 3, and occasionally 2+. Only about 1/3 of these flares, however, produce showers that hit the earth. As they leave the sun, the protons usually produce a radio burst (see Sec. 16.3), which is the only means available at present for detecting them before they arrive at the earth. Arrival is detected usually by the polar cap absorption they produce; some showers are observed directly from balloons and space vehicles. Effects caused by the arrival of relativistic energy particles are registered on cosmic ray counters at ground level (GLE).

The time of flight, sun to earth, varies from about 1/2 h to 10 or 12 h for fast proton showers, and appears to have little relation to the energy spectrum. Presumably the delays result from the structure of the interplanetary magnetic fields. This hypothesis is supported by the fact that the delays are significantly longer near sunspot maximum than at minimum, presumably because the interplanetary fields, which originate mainly in the solar fields, are stronger and more chaotic at the time of maximum.

Because only in a minority of major flares are proton showers observed, investigators are looking for the associated solar conditions that appear to favor the production of proton showers. Results up to the present indicate that the following conditions in an active center favor proton showers:

a) a sunspot of large penumbral area;
b) age of calcium plages not less than two weeks;
c) production of many small flares and other observable indicators of great activity;
d) complex magnetic fields;
e) location in the northern solar hemisphere for proton showers in general, and in the northwestern quadrant for the relativistic energy showers (this unexpected preference is statistically beyond doubt, see Sec. 17.4.2 and 18.3.3);
f) presence in the active center of systems of large loop prominences just before the flare; and
g) the flare covering a major portion of the umbra of the dominant sunspot. All but indicators (f) and (g) are useful for selecting short intervals (up to about 5 days) that can be reliably expected to be free of proton showers, and have been so used quite effectively, during the period of declining solar activity. They will not, however, be sufficient indicators during periods of sunspot maximum because many of these conditions will be present continuously.

It appears likely that more definitive indicators, if any exist, may be found in the study of the small details, particularly those of magnetic fields and mass motions, in the active centers. It is in the small scale phenomena that the large gradients of temperature, velocity, and field strength are expected. These gradients should be the most significant symptoms of an approaching instability that results in the catastrophic energy release of a large flare, and the associated ejection of fast protons.

15.6 TERRESTRIAL EFFECTS OF SOLAR EMISSIONS

The electromagnetic and corpuscular emissions from the sun differ in their total energies, penetrating power, degree of fluctuation, and intensity distributions over the earth. Each produces characteristic and generally diverse effects on the earth's atmosphere. These effects may best be considered in terms of the conditions induced by the quiet sun emission with superimposed disturbances induced by transients.

The temperature of the earth's surface and atmosphere is maintained almost entirely by solar electromagnetic radiation, principally that in the infrared and visible regions. Most of this energy is absorbed at the surface. The detailed absorption characteristics of the atmosphere for various wavelengths and the resulting thermal condition are given in Chapter 7 and Sec. 3.1.1. Various photochemical processes are induced by absorption of sunlight. At the surface, photosynthesis in plants is the most important. In the atmosphere, dissociation of oxygen, nitrogen, and water vapor, and the formation of ozone are important. These atmospheric processes are treated in Chapters 3 and 6. Because of the low energy and intensity, the radio-frequency component has no significant influence on the natural environment. It is, however, a significant factor in radio communications.

Above a height of about 60 km are regions of atmospheric ionization known as the ionosphere. They are maintained by photochemical and photoelectric processes en-

ergized by solar ultraviolet radiation of wavelength shorter than 1300 Å. The E and F regions are relatively stable, and, although they have large, regular, diurnal and seasonal variations in ion concentration, they are usually affected little by transient solar activity. The D region (at about 65 km), however, reacts strongly to the short wavelength ultraviolet radiation from some solar flares.

The corpuscular emission from the sun, in contrast to the electromagnetic radiation, consists largely of transients. The direct effects of electromagnetic radiation are confined to the sunlit hemisphere of earth and are most marked when the sun is at the zenith. Because the corpuscular emission is strongly influenced by the earth's magnetic field, the principal effects appear in the regions that surround the geomagnetic poles. The geomagnetic field also distributes the incoming particles almost uniformly in longitude, thus obliterating the diurnal variation that would otherwise occur.

When a large solar flare occurs, highly characteristic terrestrial responses are initiated. These fall into two principal groups (exclusive of fast-proton showers): the effects induced by electromagnetic radiation that occurs simultaneously with the flare, and those induced by the low-energy corpuscular radiation that arrives about 16 h later. Aurorae, geomagnetic disturbances, anomalies in cosmic radiation, and localized heating of the atmosphere result from the corpuscular emission.

The passage of an active, rapidly evolving sunspot region across the visible face of the sun is accompanied by a general intensification of the atmospheric effects attributed to ultraviolet radiation of the quiet sun. The atmospheric ionization is intensified and geomagnetic disturbances increase. The largest spots produce solar-radio-noise storms that continue for hours or days at levels of intensity thousands of times greater than normal.

The immediate effect of the x rays from a flare is an abrupt increase of ionization in the D region, known as a sudden ionospheric disturbance (SID). Ionization at this level, where the mean free path of free electrons is small, is responsible for several observable effects. Radio waves at medium frequencies are strongly absorbed, and long-distance communications fade out. Cosmic radio noise at 15 to 25 Mcps is absorbed and also fades. At very low frequencies (15 to 40 kcps), however, the D region becomes a reflector. Atmospheric radio noise is enhanced, and phase anomalies in low-frequency radio signals are observed. An SID is marked also by a sharp, brief geomagnetic disturbance that behaves like an intensification of the usual quiet day magnetic pattern, rather than a general magnetic storm.

An SID is invariably caused by a flare, although many small flares and some of the large ones fail to produce an SID. The reason for this is not known, although there is some evidence that the SID potential of a flare is a function of the absorbing power of the overlying layers in the solar atmosphere; i.e., the height of the flare in the chromosphere.

A large flare, or series of flares, is characteristically followed in about 10 to 30 h by a very sudden, worldwide geomagnetic storm and enhanced auroral activity. Such magnetic storms are accompanied by weakening of the F_2-region ionization and freakish fluctuations of the E region. These disturbances sometimes last for many hours and even several days, and interfere with communications much more seriously than do the brief fadeouts that accompany an SID. Formation of the sporadic E region is particularly effective in producing freakish radio conditions. Large magnetic storms are generally nonrecurrent, because the flare-producing phase of an active region seldom persists through a complete rotation of the sun.

A magnetic and auroral phenomenon known as an *M-region* disturbance or storm recurs at approximately 27-day intervals during several months or even years. An example of this recurrence is shown in Fig. 15-14. The solar source of these recurrent storms is called an M region, but it has not been identified with any observable solar feature. The portion of the solar disk that faces the earth during a recurrent storm is always free of active spot regions. Also, these storms are prevalent during the last 3 or 4 yr of an 11-yr cycle when sunspot activity is low. The terrestrial effects of the recurrent M-region storms are similar to those of the corpuscular bombardment from active regions, but are much less vigorous. These recurrent storms are of moderate intensity with a gradual onset; they often last several days. They differ further from storms produced by active regions in that the average intensities of the recurrent disturbances reach seasonal maxima near the times when the earth is at its greatest distance above or below the plane of the sun's equator. The reason for this seasonal maximum has not been established.

Although the recurrent storms are negatively correlated with sunspot number, their aggregate effect is so much less than that of large storms from active regions that the predominant correlation is between sunspot numbers and geomagnetic disturbances (Sec. 11.4). Large sunspots in their later phases tend to inhibit corpuscular emission. When a spot region has ceased to produce flares and has reached an inactive state, emissions from the regions are likely to be lower than from an average undisturbed region of the sun. Conditions for radio communications then tend to be better than usual.

15.7 SOLAR TRANSIENTS AND WEATHER

Weather is a complex system of energy transformation for which virtually all the energy involved comes ultimately from the sun. Long-period correlation of weather parameters with the sunspot cycle are suggested by records of river and lake levels, annual growth rings in contemporary and petrified trees, the advance and retreat of glaciers, periodicities in the spacings of glacial varves, and direct weather records from some restricted localities. Many of the detailed changes in the meteorological pattern, ranging from local day-to-day weather to worldwide secular variation in climate, may possible originate in or be triggered by transient variations in the solar radiation. Investigations in this field are impeded by the complexity

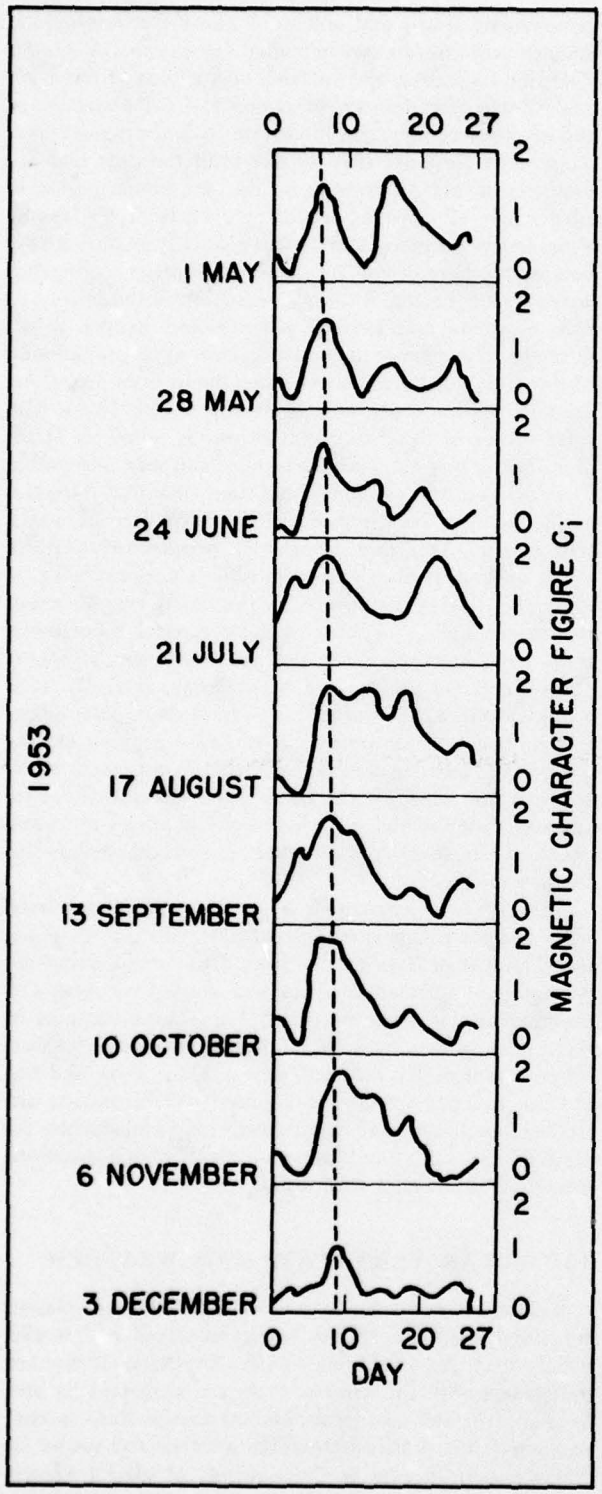


Fig. 15-14. Example of recurrence of geomagnetic disturbance (M region) at approximately 27-day intervals in 1953, near sunspot minimum. The magnetic character figure, C_i, is an index of the degree of geomagnetic disturbance each day. The curves are plotted from 3-day running means.

of meteorological phenomena and the lack of adequate records of either weather or solar activity; no clear-cut responses such as those found in the ionosphere have been established.

The distribution pattern of barometric pressure over the world appears to be slightly but significantly associated with solar activity. The solar effect on pressure could be just one readily observable aspect of a more general effect on the global circulation pattern. This supposition is reinforced by apparent correlations between the patterns of high-altitude (30,000 ft) wind shears over the central Pacific and the presence of visible active regions on the sun, accompanied by transient bursts in solar radio emission.

The most serious difficulties are the problems of how energy changes induced in the upper atmosphere are transferred to meteorological levels and the comparatively minute energies involved. Solar variations in the ultraviolet radiation and in corpuscular emission cannot exceed 10^{-5} of the steady flow of energy received from the sun. This is, of course, totally inadequate as a source of energy for large-scale meteorological changes, but it is possibly enough to upset a delicate energy balance and trigger such changes.

Chapter 16

SOLAR ELECTROMAGNETIC RADIATION

Section 16.1 P. R. Gast
Section 16.2 A. S. Jursa
Section 16.3 J. Castelli
S. Basu
J. Aarons

16.1 SOLAR IRRADIANCE

The sun is a source of electromagnetic radiation subtending ≈ 32.0 min of arc (0.00931 rad) at a distance of one astronomical unit (mean distance from the sun of the earth's orbit). At this distance and outside the atmosphere of the earth, Johnson [1945] gives a value of 1396 ± 27 W m^{-2} (uncertain within $\pm 2\%$) for the total irradiance. A value of 1390 W m^{-2} for the total irradiance, however, is used here (the reasons for selecting this lower value are discussed by Gast in a paper to be published in 1965); for the whole disk, this is equivalent to a brightness temperature of 5750°K.

The total irradiance is essentially constant. Aldrich and Hoover [1954] state: "The record indicates a surprisingly small, irregular variation, seldom exceeding a range of 2%, with a gradual trend toward larger values. The total increase in the means of successive 5-yr intervals is 0.3% since 1925." Their data for monthly means show a root-mean-square deviation of 0.6%. The greatest root-mean-square deviation for 10-day mean values is $\pm 0.17\%$ [Sterne and Dieter, 1958].

There is a seasonal variation in the total irradiance amounting to -3.27% at aphelion and $+3.42\%$ at perihelion. The seasonal variation in the apparent diameter of the sun is ≈ 4 sec of arc between aphelion and perihelion. In 1965 the perihelion (radius vector is 0.98332, see annual American Ephemeris and Nautical Almanac) is on 3 January. On this date the irradiance would be 1438 W m^{-2} if the solar constant is 1390 W m^{-2}. Similarly at aphelion on 3 July (radius vector is 1.016722) the irradiance would be 1345 W m^{-2}. The time variation in solar emission in the far ultraviolet and x-ray regions and in the radio-frequency region does not contribute to a significant change in the total irradiance.

Figure 16-1 shows the distribution of spectral irradiance outside the earth's atmosphere and at sea level for the sun at the zenith. Solar spectral irradiance cannot be characterized by any single blackbody temperature distribution (see Appendix B). The brightness temperature of the whole disk approximates 4500°K in the ultraviolet at 2000 Å, 5900°K in the yellow green at 5600 Å, and in the infrared, 5600°K at 4.0 μ, 5300°K at 5.0 μ, and 5040°K at 11.1 μ. With increasing wavelengths in the microwave region, the brightness temperature of emission by the corona reaches 1 to 2×10^6 °K (Sec. 18.2).

16.1.1 Irradiance Outside the Earth's Atmosphere

The *solar constant*, H_o, is defined as the total irradiation per unit area normal to the direction of the sun, at one astronomical unit (Sec. 21.2.1) and outside the earth's atmosphere. The spectral irradiance, $H_{\Delta\lambda}$, is the irradiance per wavelength interval. Total irradiance is

$$H_o = \sum_{\lambda=0}^{\lambda=\infty} H_{\Delta\lambda}. \qquad (16\text{-}1)$$

The difference between Johnson's value of 1396 W m^{-2} (2.00 g cal cm^{-2} min^{-1}) for H_o and the Aldrich and Hoover (Smithsonian) value of 1357 W m^{-2} (1.946 g cal cm^{-2} min^{-1}) only slightly exceeds the 2% fiducial uncertainty adopted by Johnson. (Johnson is preparing a revision of his 1954 values in which $H_{\Delta\lambda}$ is increased in the region 0.2 to 0.4 μ; his value of H_o, however, remains unchanged.) The difference results from the larger estimates Johnson derives for $H_{\Delta\lambda}$ in the ultraviolet (0.2 to 0.25 μ) and infrared regions, which account for an increase of about 2.7% in the solar constant. The value 1390 W m^{-2}, on which Tables 16-1 are based, is obtained by computer summation of the same basic data used by Johnson.

CHAPTER 16

Table 16-1a is a tabulation of spectral irradiances from the x-ray into the radio region, and gives the percentage contribution of each wavelength interval to the solar constant. It shows that 99% of the total irradiance is included in the interval 0.22 to 11 μ. Table 16-1b is a breakdown into smaller wavelength intervals of values given in Table 16-1a. Table 16-1c lists cumulative values of spectral irradiance over the limits from 1 Å to the given wavelength. The values are not known with the accuracy implied by the significant figures which are used in summing over the wider intervals; errors of 3 to 5 percent are possible over a 100 Å interval.

These values are based on the Smithsonian Scale of Pyrheliometry. The Smithsonian Scale, which is conserved by standard silver disk pyrheliometers, differs from another pyrheliometric scale conserved by standard Ångström pyrheliometers. (Neither exactly agrees with calibrations derived from the tungsten lamps used as laboratory standard sources.) For international use it has been recommended that an International 1936 Pyrheliometric Scale [IGY, 1958] be used. This implies a reduction of 2.0% from the Smithsonian Scale of 1913. In 1954, Aldrich and Hoover suggested a reduction by 2.4%. The net effect is that on the International Pyrheliometric Scale the estimate of 1396 W m^{-2} should be increased by about 0.4% to 1401 W m^{-2}.

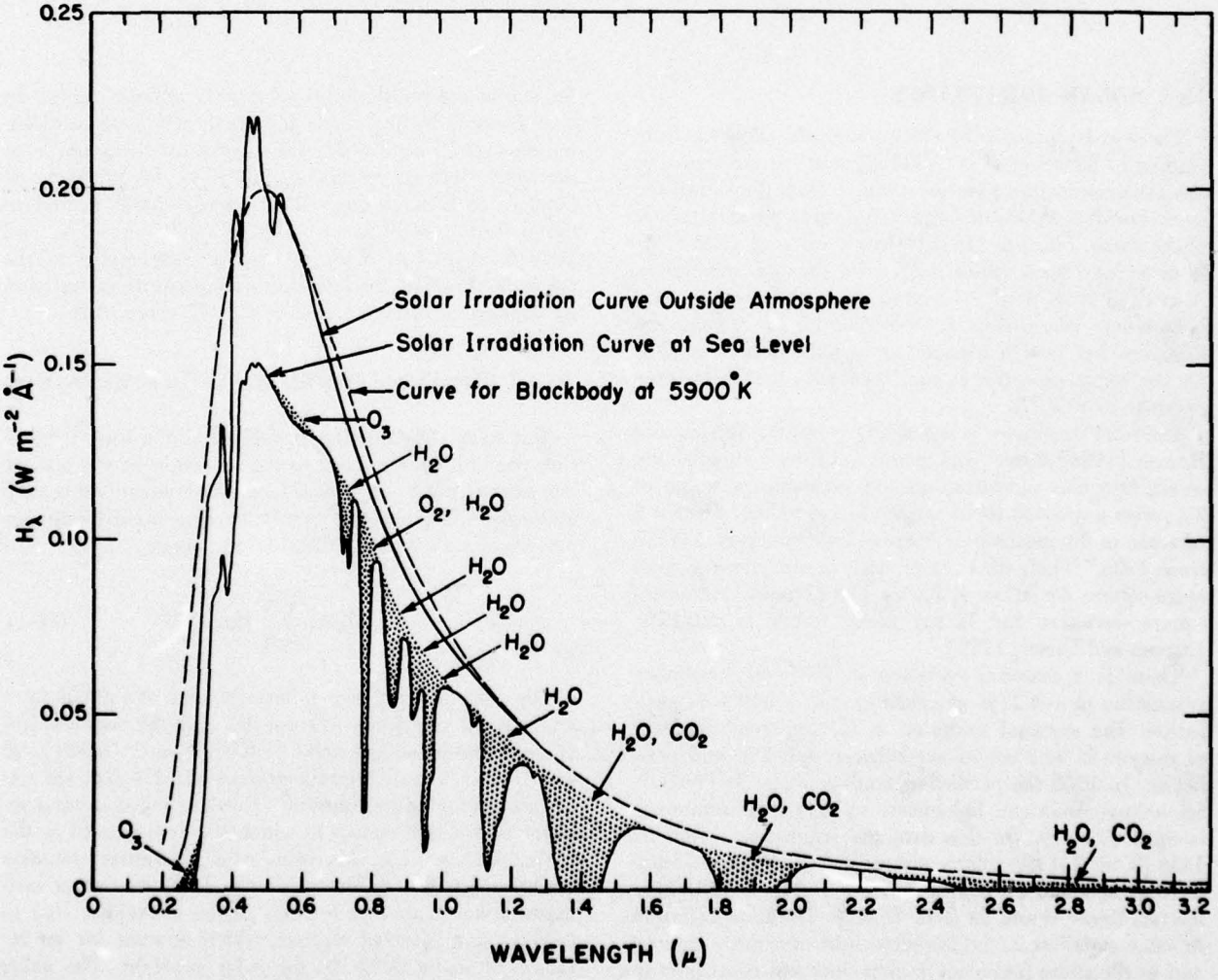


Fig. 16-1. Spectral distribution curves related to the sun; shaded areas indicate absorption, at sea level, due to the atmospheric constituents shown.

Table 16-1a. Solar spectral irradiance for quiet sun, outside the earth's atmosphere at the mean sun-to-earth distance; $H_o = 1390$ W m^{-2}.

Wavelength Interval	$H_{\Delta\lambda}$ (W m^{-2} $\Delta\lambda^{-1}$)	$H_{\Delta\lambda}/H_o$ (%)	Wavelength Interval	$H_{\Delta\lambda}$ (W m^{-2} $\Delta\lambda^{-1}$)	$H_{\Delta\lambda}/H_o$ (%)
(Å)			(μ)		
1-8	$< 10^{-9}$*	$< 10^{-11}$*	0.5-0.6	193	13.9
8-31	10^{-7}**	7×10^{-9}**	0.6-0.7	162	11.7
31-165	0.70×10^{-3}†	4.9×10^{-5}†	0.7-0.8	128	9.2
165-303	1.18×10^{-3}	8.3×10^{-5}	0.8-0.9	101	7.2
304	0.25×10^{-3}	1.8×10^{-5}	0.9-1.0	81	5.8
305-460	3.15×10^{-3}	2.2×10^{-4}	1.0-1.1	66	4.8
460-1215	1.74×10^{-3}	1.2×10^{-4}	1.1-1.2	55	4.0
1216	4.40×10^{-3}	3.1×10^{-4}	1.2-1.3	45	3.2
1216-1800	3.30×10^{-2}	2.3×10^{-3}	1.3-1.5	66	4.7
1800-2250	0.9	6.5×10^{-2}	1.5-2.0	84	6.1
(μ)			2.0-3.0	54	3.9
0.225-0.3	17	1.3	3.0-11.0	27	1.9
0.3-0.4	110	7.9	11.0-30.0	0.7	0.05
0.4-0.5	200	14.4	1 cm-30 m	10^{-11}††	$< 10^{-13}$††

* Increases 10^3 and 10^5 for disturbed sun and for Class 3 flare respectively.
** Increases by factor of at least 50 for disturbed sun.
† Increases by factor of 7 for disturbed sun.
†† Increases by factor of 10^3 for disturbed sun.

Table 16-1c. Cumulative solar spectral irradiance outside the earth's atmosphere at the mean sun-to-earth distance; $H_o = 1390$ W m^{-2}.

Wavelength (μ)	$\sum_o^\lambda H_{\Delta\lambda}$ (W m^{-2})	$\sum_o^\lambda H_{\Delta\lambda}/H_o$ (%)	Wavelength (μ)	$\sum_o^\lambda H_{\Delta\lambda}$ (W m^{-2})	$\sum_o^\lambda H_{\Delta\lambda}/H_o$ (%)
0.225	0.90	0.065			
0.230	1.26	0.091	0.355	71.2	5.12
0.235	1.60	0.115	0.360	76.8	5.53
0.240	1.93	0.139	0.365	82.9	5.96
0.245	2.29	0.165	0.370	90.0	6.47
0.250	2.67	0.192	0.375	96.2	6.92
0.255	3.14	0.226	0.380	103.2	7.42
0.260	3.77	0.271	0.385	109.2	7.85
0.265	4.62	0.332	0.390	115.1	8.28
0.270	5.74	0.413	0.395	121.0	8.70
0.275	6.92	0.498	0.400	127.3	9.15
0.280	8.07	0.581	0.405	136.6	9.82
0.285	9.52	0.685	0.410	146.1	10.50
0.290	11.67	0.840	0.415	155.7	11.20
0.295	14.55	1.046	0.420	165.2	11.88
0.300	17.65	1.269	0.425	174.8	12.57
0.305	20.8	1.50	0.430	183.3	13.2
0.310	24.4	1.76	0.435	191.8	13.8
0.315	28.3	2.04	0.440	201.2	14.5
0.320	32.5	2.33	0.445	211.5	15.2
0.325	36.7	2.64	0.450	222.2	16.0
0.330	42.4	3.05	0.455	232.9	16.8
0.335	48.1	3.46	0.460	243.6	17.5
0.340	53.6	3.86	0.465	254.1	18.3
0.345	59.4	4.27	0.470	264.6	19.0
0.350	65.0	4.68	0.475	275.4	19.8

(Continued)

Table 16-1c. Cumulative solar spectral irradiance outside the earth's atmosphere at the mean sun-to-earth distance; $H_o = 1390$ Wm^{-2}. (Continued).

Wavelength (μ)	$\sum_{o}^{\lambda} H_{\Delta\lambda}$ (W m^{-2})	$\sum_{o}^{\lambda} H_{\Delta\lambda}/H_o$ (%)	Wavelength (μ)	$\sum_{o}^{\lambda} H_{\Delta\lambda}$ (W m^{-2})	$\sum_{o}^{\lambda} H_{\Delta\lambda}/H_o$ (%)
0.480	286.2	20.6	0.960	961.8	69.2
0.485	296.7	21.3	0.970	969.5	69.7
0.490	306.8	22.1	0.980	977.2	70.2
0.495	317.1	22.8	0.990	984.6	70.8
0.500	327.4	23.5	1.000	992.0	71.3
0.505	337.2	24.2	1.010	999.1	71.7
0.510	347.0	25.0	1.020	1006.2	72.4
0.515	356.6	25.6	1.030	1013.1	72.9
0.520	366.2	26.3	1.040	1020.0	73.4
0.525	375.9	27.0	1.050	1026.7	73.8
0.530	385.6	27.7	1.060	1033.2	74.3
0.535	395.5	28.4	1.070	1039.7	74.8
0.540	405.4	29.2	1.080	1046.0	75.2
0.545	415.3	29.9	1.090	1052.3	75.7
0.550	425.0	30.6	1.100	1058.4	76.1
0.555	434.8	31.3	1.200	1113.6	80.07
0.560	444.3	32.0	1.300	1158.8	83.33
0.565	453.8	32.6	1.400	1195.2	85.94
0.570	463.4	33.3	1.500	1224.5	88.05
0.575	472.9	34.0	1.600	1248.4	89.77
0.580	482.5	34.7	1.700	1268.0	91.18
0.585	492.0	35.4	1.800	1284.2	92.35
0.590	501.5	36.1	1.900	1297.8	93.32
0.595	511.0	36.8	2.000	1309.1	94.14
0.600	520.4	37.4	2.100	1318.7	94.83
0.610	538.3	38.7	2.200	1325.9	95.42
0.620	555.8	40.0	2.300	1333.9	95.90
0.630	573.0	41.2	2.400	1350.0	96.35
0.640	589.9	42.4	2.500	1345.1	96.73
0.650	606.3	43.6	2.600	1349.6	97.08
0.660	622.4	44.8	2.700	1353.6	97.37
0.670	638.1	45.9	2.800	1357.1	97.62
0.680	653.4	47.0	2.900	1360.1	97.84
0.690	668.4	48.1	3.000	1362.8	98.03
0.700	683.0	49.1	3.100	1365.20	98.201
0.710	697.3	50.1	3.200	1367.33	98.354
0.720	711.2	51.1	3.300	1369.23	98.491
0.730	724.8	52.1	3.400	1370.93	98.613
0.740	738.0	53.1	3.500	1372.46	98.723
0.750	750.9	54.0	3.600	1373.84	98.822
0.760	763.5	54.9	3.700	1375.08	98.912
0.770	775.8	55.8	3.800	1376.20	98.992
0.780	787.8	56.6	3.900	1377.22	99.066
0.790	799.4	57.5	4.000	1378.15	99.133
0.800	810.8	58.3	4.100	1378.99	99.193
0.810	822.2	59.1	4.200	1379.74	99.247
0.820	832.8	59.9	4.300	1380.42	99.296
0.830	843.5	60.6	4.400	1381.03	99.340
0.840	853.9	61.4	4.500	1381.60	99.381
0.850	864.0	62.1	4.600	1382.12	99.418
0.860	873.9	62.8	4.700	1382.60	99.453
0.870	883.6	62.5	4.800	1383.05	99.485
0.880	893.1	64.2	4.900	1383.46	99.515
0.890	902.4	64.9	5.000	1383.84	99.542
0.900	911.4	65.5	6.000	1386.39	99.725
0.910	920.3	66.2	7.000	1387.73	99.822
0.920	928.9	66.8	11.0	1389.48	99.948
0.930	937.4	67.4	30.0	1390.21	> 99.999
0.940	945.7	68.0			
0.950	953.8	68.6			

Table 16-1b. Solar spectral irradiance, outside the earth's atmosphere at the mean sun-to-earth distance; $H_o = 1390\ Wm^{-2}$.

Wavelength $\Delta\lambda$ (μ)	$H_{\Delta\lambda}$ ($W\ m^{-2}\ \Delta\lambda^{-1}$)	$H_{\Delta\lambda}/H_o$ (%)	Wavelength $\Delta\lambda$ (μ)	$H_{\Delta\lambda}$ ($W\ m^{-2}\ \Delta\lambda^{-1}$)	$H_{\Delta\lambda}/H_o$ (%)
0.001-0.225	0.9	0.065	0.425-0.450	47.41	3.41
0.225-0.230	0.36	0.026	0.450-0.455	10.75	0.77
0.230-0.235	0.34	0.024	0.455-0.460	10.65	0.77
0.235-0.240	0.33	0.024	0.460-0.465	10.51	0.76
0.240-0.245	0.36	0.026	0.465-0.470	10.56	0.76
0.245-0.250	0.38	0.027	0.470-0.475	10.71	0.77
0.225-0.250	1.77	0.127	0.450-0.475	53.18	3.82
0.250-0.255	0.47	0.034	0.475-0.480	10.80	0.78
0.255-0.260	0.63	0.045	0.480-0.485	10.55	0.76
0.260-0.265	0.85	0.061	0.485-0.490	10.10	0.73
0.265-0.270	1.12	0.081	0.490-0.495	10.30	0.74
0.270-0.275	1.18	0.085	0.495-0.500	10.25	0.74
0.250-0.275	4.25	0.306	0.475-0.500	52.00	3.74
0.275-0.280	1.15	0.083	0.500-0.505	9.80	0.70
0.280-0.285	1.45	0.104	0.505-0.510	9.80	0.70
0.285-0.290	2.15	0.155	0.510-0.515	9.65	0.69
0.290-0.295	2.88	0.207	0.515-0.520	9.60	0.69
0.295-0.300	3.10	0.223	0.520-0.525	9.65	0.69
0.275-0.300	10.73	0.772	0.500-0.525	48.50	3.49
0.300-0.305	3.20	0.230	0.525-0.530	9.75	0.70
0.305-0.310	3.58	0.257	0.530-0.535	9.85	0.71
0.310-0.315	3.95	0.284	0.535-0.540	9.90	0.71
0.315-0.320	4.08	0.293	0.540-0.545	9.90	0.71
0.320-0.325	4.28	0.308	0.545-0.550	9.75	0.70
0.300-0.325	19.09	1.373	0.525-0.550	49.15	3.53
0.325-0.330	5.66	0.41	0.550-0.555	9.74	0.70
0.330-0.335	5.73	0.41	0.555-0.560	9.58	0.69
0.335-0.340	5.49	0.39	0.560-0.565	9.52	0.68
0.340-0.345	5.74	0.41	0.565-0.570	9.50	0.68
0.345-0.350	5.66	0.41	0.570-0.575	9.57	0.69
0.325-0.350	28.28	2.03	0.550-0.575	47.91	3.45
0.350-0.355	6.17	0.44	0.575-0.580	9.57	0.69
0.355-0.360	5.66	0.41	0.580-0.585	9.52	0.68
0.360-0.365	6.07	0.44	0.585-0.590	9.52	0.68
0.365-0.370	7.06	0.51	0.590-0.595	9.48	0.68
0.370-0.375	6.26	0.45	0.595-0.600	9.35	0.67
0.350-0.375	31.22	2.25	0.575-0.600	47.44	3.41
0.375-0.380	6.99	0.50	0.600-0.610	17.93	1.29
0.380-0.385	5.93	0.43	0.610-0.620	17.56	1.26
0.385-0.390	5.96	0.43	0.620-0.630	17.19	1.24
0.390-0.395	5.85	0.42	0.630-0.640	16.83	1.21
0.395-0.400	6.32	0.45	0.640-0.650	16.44	1.18
0.375-0.400	31.05	2.23	0.600-0.650	85.95	6.18
0.400-0.405	9.27	0.67	0.650-0.660	16.07	1.16
0.405-0.410	9.52	0.68	0.660-0.670	15.70	1.13
0.410-0.415	9.66	0.69	0.670-0.680	15.34	1.10
0.415-0.420	9.50	0.68	0.680-0.690	14.97	1.08
0.420-0.425	9.53	0.69	0.690-0.700	14.62	1.05
0.400-0.425	47.48	3.41	0.650-0.700	76.70	5.52
0.425-0.430	8.49	0.61	0.700-0.710	14.27	1.03
0.430-0.435	8.56	0.62	0.710-0.720	13.95	1.00
0.435-0.440	9.38	0.67	0.720-0.730	13.57	0.98
0.440-0.445	10.31	0.74	0.730-0.740	13.23	0.95
0.445-0.450	10.67	0.77	0.740-0.750	12.90	0.93

(Continued)

Table 16-1b. Solar spectral irradiance, outside the earth's atmosphere at the mean sun-to-earth distance; $H_o = 1390\ Wm^{-2}$. (Continued)

Wavelength $\Delta\lambda$ (μ)	$H_{\Delta\lambda}$ ($W\ m^{-2}\ \Delta\lambda^{-1}$)	$H_{\Delta\lambda}/H_o$ (%)
0.700-0.750	67.92	4.88
0.750-0.760	12.57	0.90
0.760-0.770	12.26	0.88
0.770-0.780	12.00	0.86
0.780-0.790	11.67	0.84
0.790-0.800	11.40	0.82
0.750-0.800	59.90	4.31
0.800-0.810	11.13	0.80
0.810-0.820	10.88	0.78
0.820-0.830	10.63	0.76
0.830-0.840	10.40	0.75
0.840-0.850	10.15	0.73
0.800-0.850	53.19	3.82
0.850-0.860	9.92	0.71
0.860-0.870	9.69	0.70
0.870-0.880	9.47	0.68
0.880-0.890	9.26	0.67
0.890-0.900	9.06	0.65
0.850-0.900	47.40	3.41
0.900-0.910	8.85	0.64
0.910-0.920	8.66	0.62
0.920-0.930	8.47	0.61
0.930-0.940	8.29	0.60
0.940-0.950	8.12	0.58
0.900-0.950	42.39	3.05
0.950-0.960	7.95	0.57
0.960-0.970	7.78	0.56
0.970-0.980	7.62	0.55
0.980-0.990	7.47	0.54
0.990-1.000	7.32	0.53
0.950-1.000	38.14	2.74
1.000-1.010	7.19	0.52
1.010-1.020	7.06	0.51
1.020-1.030	6.94	0.50
1.030-1.040	6.82	0.49
1.040-1.050	6.70	0.48
1.000-1.050	34.71	2.50
1.050-1.060	6.58	0.47
1.060-1.070	6.46	0.46
1.070-1.080	6.35	0.46
1.080-1.090	6.23	0.45
1.090-1.100	6.12	0.44
1.050-1.100	31.74	2.28
1.100-1.200	55.16	3.97
1.200-1.300	45.23	3.25
1.300-1.400	36.38	2.62
1.400-1.500	29.34	2.11
1.100-1.500	166.11	11.95
1.500-1.600	23.88	1.72
1.600-1.700	19.61	1.41
1.700-1.800	16.22	1.17
1.800-1.900	13.53	0.97
1.900-2.000	11.37	0.82
1.500-2.000	84.63	6.09
2.000-2.100	9.61	0.69
2.100-2.200	8.18	0.59
2.200-2.300	7.00	0.50
2.300-2.400	6.02	0.43
2.400-2.500	5.21	0.37
2.000-2.500	36.02	2.58
2.500-2.600	4.53	0.33
2.600-2.700	3.95	0.28
2.700-2.800	3.47	0.25
2.800-2.900	3.05	0.22
2.900-3.000	2.70	0.19
2.500-3.000	17.71	1.27
3.000-3.100	2.39	0.172
3.100-3.200	2.13	0.153
3.200-3.300	1.90	0.137
3.300-3.400	1.70	0.122
3.400-3.500	1.53	0.110
3.000-3.500	9.65	0.694
3.500-3.600	1.38	0.099
3.600-3.700	1.24	0.089
3.700-3.800	1.12	0.081
3.800-3.900	1.02	0.073
3.900-4.000	0.93	0.067
3.500-4.000	5.69	0.409
4.000-4.100	0.84	0.060
4.100-4.200	0.75	0.054
4.200-4.300	0.68	0.049
4.300-4.400	0.61	0.044
4.400-4.500	0.57	0.041
4.000-4.500	3.45	0.248
4.500-4.600	0.52	0.037
4.600-4.700	0.48	0.035
4.700-4.800	0.45	0.032
4.800-4.900	0.41	0.030
4.900-5.000	0.38	0.027
4.500-5.000	2.24	0.161
5.000-6.000	2.55	0.183
6.000-7.000	1.34	0.096
7.0 - 11.0	1.75	0.126
11.0 - 30.0	0.73	0.052
1 cm to 30 m	$\approx 10^{-11}$	$< 10^{-13}$

16.1.2 Irradiance Within the Earth's Atmosphere

The spectral irradiance within the atmosphere depends upon the density of the air in the path of the beam. *Optical air mass*, m, is the ratio of the path length of radiation through the atmosphere (l_m) at any given angle, z^o, to the path length toward the zenith, (l_z);

$$m = l_m/l_z \cong \sec z^o, \text{ for } z^o \leq 62°. \qquad (16\text{-}2)$$

(The intersection of l_m and l_z, the place at which observations are made, may be either at sea level or some greater elevation. It is desirable that the equivalent attenuating atmosphere be taken as based at sea level; unfortunately this is not an invariable practice.)

Table 16-2 gives the optical air mass for an observer at sea level and the sun at increasing zenith angles. With a zenith angle of 60°, the slant path through the atmosphere is doubled. When the zenith angle exceeds $\approx 62°$ and the slant path between source and observer passes through the denser part of the atmosphere, the light path is refracted and the mass of air traversed is no longer simply proportional to the secant of the zenith angle. Refraction is wavelength dependent so the effective air mass must be calculated by tracing the ray through the atmosphere. Table 16-3 gives results of such calculations of optical air masses at several wavelengths for a dry (zero relative humidity), clear (pure Rayleigh scattering) atmosphere with the ambient temperature 288°K and pressure 760 mm Hg; they differ from values for the same angle in Table 16-2.

Figure 16-2 shows the depletion of the solar beam in passing through the atmosphere to sea level as a function of optical air mass. The irradiance outside the atmosphere (zero optical air mass) is included for comparison. Table 16-4 gives values for the irradiance at sea level for an optical air mass of two.

For use with attenuation coefficients, a dimensional quantity related to the optical air mass is needed. The *atmospheric reduced equivalent thickness* is defined as the depth of the atmosphere, l_z, reduced to equivalent thickness at 15°C and 1013 mb (STP) or the equivalent thickness at 0°C and 1013 mb (NTP). The reduced equivalent thickness for an isothermal atmosphere is 8.434 atm-km (STP) and 7.995 atm-km (NTP).

Table 16-5 gives the reduced equivalent thickness of the atmosphere with varying altitude equivalent to the optical thickness reduced to normal temperature (0°C) and pressure (1013 mb, or 760 mm Hg).

A statistical summary of the records of 27 stations over 11 yr (July 1952 through June 1963) may be ordered from the National Weather Records Center, U.S. Weather Bureau, Asheville, N. C. 28801. The report, "Summary of Solar Radiation Observations," is in two parts; a descriptive section (D2-90577-1), and a volume containing the 13 summary tables (D2-90577-2) which list means and frequencies of values of solar intensity by hours, days, months, and seasons, percentage of possible intensity, and correlations of transmissivity with zenith angle, cloud cover, and horizontal visibility.

Table 16-3. Optical air mass at sea level for selected wavelengths and large apparent zenith angles, z°, of the sun.

z° (deg)	Wavelength (μ)					
	0.3	0.4	0.55	0.7	1.0	3.0
86	12.33	12.32	12.32	12.32	12.32	12.32
87	15.18	15.17	15.17	15.16	15.16	15.16
88	19.47	19.45	19.44	19.43	19.43	19.42
89	26.34	26.29	26.27	26.26	26.25	26.24
90	38.28	38.17	38.11	38.08	38.06	38.05

Table 16-2. Optical air mass for various apparent zenith angles, z°, of the sun; values by Bemporad. (From "Smithsonian Meteorological Tables," 6th revised edition, Smithsonian Institution, Washington, D. C., 1951.)

z° (deg)	0	1	2	3	4	5	6	7	8	9
0	1.00	—	—	—	—	—	1.01	—	—	—
10	1.02	—	—	1.03	—	1.04	—	1.05	—	—
20	1.06	1.07	1.08	1.09	1.09	1.10	1.11	1.12	1.13	1.14
30	1.15	1.17	1.18	1.19	1.20	1.22	1.23	1.25	1.27	1.28
40	1.30	1.32	1.34	1.37	1.39	1.41	1.44	1.46	1.49	1.52
50	1.55	1.59	1.62	1.66	1.70	1.74	1.78	1.83	1.88	1.94
60	2.00	2.06	2.12	2.19	2.27	2.36	2.45	2.55	2.65	2.77
70	2.90	3.05	3.21	3.39	3.59	3.82	4.07	4.37	4.72	5.12
80	5.60	6.18	6.88	7.77	8.90	10.39	12.44	15.36	19.79	26.96

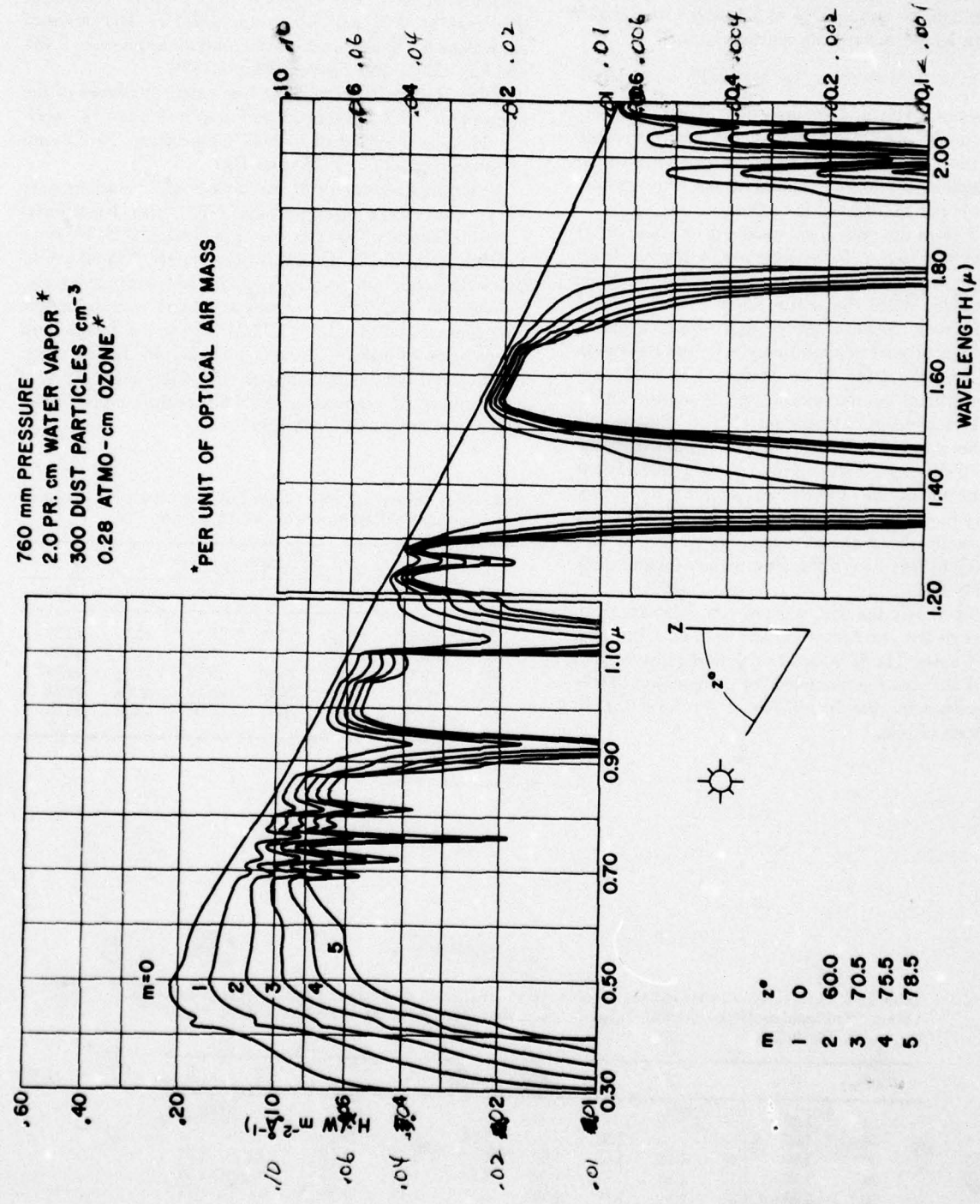


Fig. 16-2. Solar spectral irradiance curves at sea level for various optical air masses; the value of the solar constant used in this calculation was 1322 W m^{-2}. (After P. Moon, *J. Franklin Institute*, v. 230, no. 5, p. 583, 1940.)

Table 16-4. Solar irradiance at sea level on an area normal to the sun for $m = 2$, $H_o = 1322$ W m^{-2}. (After P. Moon, *J. Franklin Institute*, v. 230, no. 5, 1940.)

λ (μ)	$H_{\Delta\lambda}$ (W m^{-2} μ^{-1})	λ (μ)	$H_{\Delta\lambda}$ (W m^{-2} μ^{-1})	λ (μ)	$H_{\Delta\lambda}$ (W m^{-2} μ^{-1})	λ (μ)	$H_{\Delta\lambda}$ (W m^{-2} μ^{-1})
.301	.177	.61	1168	1.11	126	1.61	198
.302	.342	.62	1165	1.12	69.9	1.62	194
.303	.647	.63	1176	1.13	98.3	1.63	189
.304	1.16	.64	1175	1.14	164	1.64	184
.305	1.91	.65	1173	1.15	216	1.65	173
.306	2.89	.66	1166	1.16	271	1.66	163
.307	4.15	.67	1160	1.17	328	1.67	159
.308	6.11	.68	1149	1.18	346	1.68	145
.309	8.38	.69	978	1.19	344	1.69	139
.310	11.0	.70	1108	1.20	373	1.70	132
.311	13.9	.71	1070	1.21	402	1.71	124
.312	17.2	.72	832	1.22	431	1.72	115
.313	21.0	.73	965	1.23	420	1.73	105
.314	25.4	.74	1041	1.24	387	1.74	97.1
.315	30.0	.75	867	1.25	328	1.75	80.2
.316	34.8	.76	566	1.26	311	1.76	58.9
.317	39.8	.77	968	1.27	381	1.77	38.8
.318	44.9	.78	907	1.28	382	1.78	18.4
.319	49.5	.79	923	1.29	346	1.79	5.70
.32	54.0	.80	857	1.30	264	1.80	.920
		.81	698	1.31	208	1.81	—
		.82	801	1.32	168	1.82	—
.33	101	.83	863	1.33	115	1.83	—
.34	151	.84	858	1.34	58.1	1.84	—
.35	188	.85	839	1.35	18.1	1.85	—
.36	233	.86	813	1.36	.660	1.86	—
.37	279	.87	798	1.37	—	1.87	—
.38	336	.88	614	1.38	—	1.88	—
.39	397	.89	517	1.39	—	1.89	—
.40	470	.90	480	1.40	—	1.90	—
.41	672	.91	375	1.41	1.91	1.91	.705
.42	733	.92	258	1.42	3.72	1.92	2.34
.43	787	.93	169	1.43	7.53	1.93	3.68
.44	911	.94	278	1.44	13.7	1.94	5.30
.45	1006	.95	487	1.45	23.8	1.95	17.7
.46	1080	.96	584	1.46	30.5	1.96	31.7
.47	1138	.97	633	1.47	45.1	1.97	37.7
.48	1183	.98	645	1.48	83.7	1.98	22.6
.49	1210	.99	643	1.49	128	1.99	1.58
.50	1215	1.00	630	1.50	157	2.00	2.66
.51	1206	1.01	620	1.51	187	2.01	19.5
.52	1199	1.02	610	1.52	209	2.02	47.6
.53	1188	1.03	601	1.53	217	2.03	55.4
.54	1198	1.04	592	1.54	226	2.04	54.7
.55	1190	1.05	551	1.55	221	2.05	38.3
.56	1182	1.06	526	1.56	217	2.06	56.2
.57	1178	1.07	519	1.57	213	2.07	77.0
.58	1168	1.08	512	1.58	209	2.08	88.0
.59	1161	1.09	514	1.59	205	2.09	86.8
.60	1167	1.10	252	1.60	202	2.10	85.6
						2.11	84.4
						2.12	83.2
						2.13	20.7
						2.14	—

CHAPTER 16

16.2 SOLAR ULTRAVIOLET AND X RAYS

Absorption by ozone and other atmospheric constituents make direct measurement of the solar spectrum in the region below 3000 Å impossible at the earth's surface. Studies of this region are made with instruments carried on rockets, and the data are not as detailed as those accumulated in the visible region by ground-based instrumentation. Rocket-borne instruments have been severely limited in dispersion and resolution because of restrictions on size and weight. Another limiting factor is the relatively short time available for actual measurement; the observation time is determined by the flight time of the rocket. Solar emission of x rays and Lyman-α radiation varies in intensity with solar disturbances and with the solar cycle. Until many observations for continuous periods of time and under varying solar conditions are available, the short wavelength spectrum cannot be described with the accuracy that is possible in the visible region.

Solar electromagnetic energy which lies below 3000 Å comprises less than 2% of the sun's total electromagnetic energy. The significance of the radiation in this region is not in the total energy emitted, but in the effect these high-energy photons have on materials and on the physics and chemistry of the earth's upper atmosphere. This is particularly true of the spectrum below 2000 Å.

Table 16-5. Atmospheric reduced equivalent thickness, l_r, for various altitudes, h, at NTP (0°C, 1013 mb). Minus numbers indicate power of ten by which the entry and succeeding entries should be multiplied.

h (km)	l_r (km)	h (km)	l_r (km)
0	7.995	40	2.395^{-2}
1	7.094	42	1.856
2	6.277	44	1.447
3	5.538	46	1.134
4	4.872	48	8.929^{-3}
5	4.272	50	7.042^{-3}
6	3.733	52	5.555
7	3.251	54	4.381
8	2.820	56	3.439
9	2.437	58	2.681
10	2.098	60	2.076^{-3}
11	1.797	62	1.595
12	1.537	64	1.215
13	1.314	66	9.183^{-4}
14	1.123	68	6.876
15	9.603^{-1}	70	5.098^{-4}
16	8.210	72	3.741
17	7.021	74	2.714
18	6.003	76	1.947
19	5.134	78	1.388
20	4.391^{-1}	80	9.899^{-5}
21	3.755	82	7.062
22	3.212	84	5.038
23	2.747	86	3.596
24	2.350	88	2.567
25	2.010^{-1}	90	1.832^{-5}
26	1.721	92	1.309
28	1.270	94	9.443^{-6}
30	9.443^{-2}	96	6.884
32	7.078	98	5.069
34	5.344	100	3.769^{-6}
36	4.063		
38	3.110		

16.2.1 Solar Spectrum, 3000 to 1800 Å

The structure of the solar spectrum between 3000 Å and approximately 1800 Å resembles closely that of the spectrum above 3000 Å. The radiation originates in the solar photosphere and consists of a blackbody continuum superimposed with numerous Fraunhofer lines. Figure 16-3 is a plot of solar irradiance vs wavelength over the region 1800 to 3000 Å. The horizontal dashes represent averaged values of irradiance over narrow wavelength regions, 5 to 25 Å wide. The smooth curve represents an average value of the irradiance. The circles are examples of a few of the strong absorption lines, or of narrow groups of lines, which occur in this region. They are indicative of the large excursions from the average curve that appear in the detailed spectrum; this is also indicated by the distribution of dashes. When relatively large regions, 200 Å or more in width, are being considered, the smooth curve can be used to represent the solar energy distribution with reasonable accuracy. More detailed information concerning this portion of the spectrum is given in the Photometric Atlas [McAllister, 1960].

The intensity of the continuum decreases from about 100 erg cm^{-2} sec^{-1} $Å^{-1}$ at 3000 Å toward shorter wavelengths. At 2090 Å, a pronounced and abrupt drop in intensity occurs. Below 2085 Å, the Fraunhofer lines appear much weaker, and the continuum decreases relatively smoothly to 1936 Å where two strong absorption lines (at 1936 and 1932 Å, attributed to aluminum) occur. Below 1932 Å, the continuum falls rapidly to approximately 0.3 erg cm^{-2} sec^{-1} $Å^{-1}$ at 1800 Å. Figure 16-4 shows the changes in intensity at 2085 and 1936 Å. There is no conclusive explanation at this time for these apparent increases in absorption within the solar atmosphere.

16.2.2 Solar Emission Lines, 1900 to 60 Å

The blackbody continuum declines rapidly below 1900 Å. It is detectable, although weak, to about 1550 Å. Measurements indicate that at 1800 and 1720 Å the intensity is not more than 75% and 15%, respectively, of 5800°K blackbody radiation at these wavelengths [Aboud et al, 1959]. Fraunhofer lines are not observed below 1700 Å. Below 1900 Å emission lines appear; first superimposed on the diminishing blackbody continuum, then superimposed on another weak continuum that begins at about 1500 Å and extends to about 1000 Å, finally standing alone, for the most part, from 1000 Å to the x-ray region.

Features of special interest are: the weak continuum between 1500 and 1000 Å, whose origin has been suggested as the lower chromosphere; the hydrogen Lyman-α

line and hydrogen Lyman series with its associated continuum; the He I line at 584 Å, the He II line at 303.8 Å, and the He II continuum beginning at about 228 Å; and lines from highly ionized atoms such as Ne VIII, Mg X, Si XII, Fe XV, and Fe XVI.

Over 200 solar emission lines have been observed and measured in the region between 2000 and about 60 Å. Most of these lines have been identified with hydrogen, helium, oxygen, nitrogen, carbon, silicon, neon, magnesium, and iron in various states of ionization; the lines are produced in the chromosphere and corona. Hydrogen Lyman-α is the most intense emission line; its intensity is of the order of 6 erg cm^{-2} sec^{-1}. The half-width of this line is approximately 1 Å. High-resolution spectrograms show broad wings extending to more than 1 Å on each side of the center and a shallow but broad absorption dip across the peak as well as a narrow, deep absorption core at the center that has been attributed to absorption by interplanetary hydrogen. There is agreement among investigators concerning the existence of many of the solar emission lines; however, there are uncertainties in determining the presence of lines in some observations and discrepancies among other observations. Therefore no attempt has been made to prepare a single comprehensive table of emission lines. Two tables are presented as reported by the investigators so that the results may be compared.

Table 16-6 lists solar emission lines with measured intensities in the region 1817 to 1207 Å; these observations were made in 1957. Table 16-7 lists some of the observed lines from excellent spectrograms showing about 200 emission lines that were obtained in 1960. The intensities given in Table 16-6 are higher by factors of 2 to 8 for 14 of the 18 lines common to both tables. Violett and Rense [1959] give an extensive list of lines and relative intensities observed in 1958 and 1959.

Fig. 16-5 shows numerous solar emission lines in the region from 1300 to 260 Å. Line intensities may be read from the traces with the help of the variable ordinate scale.

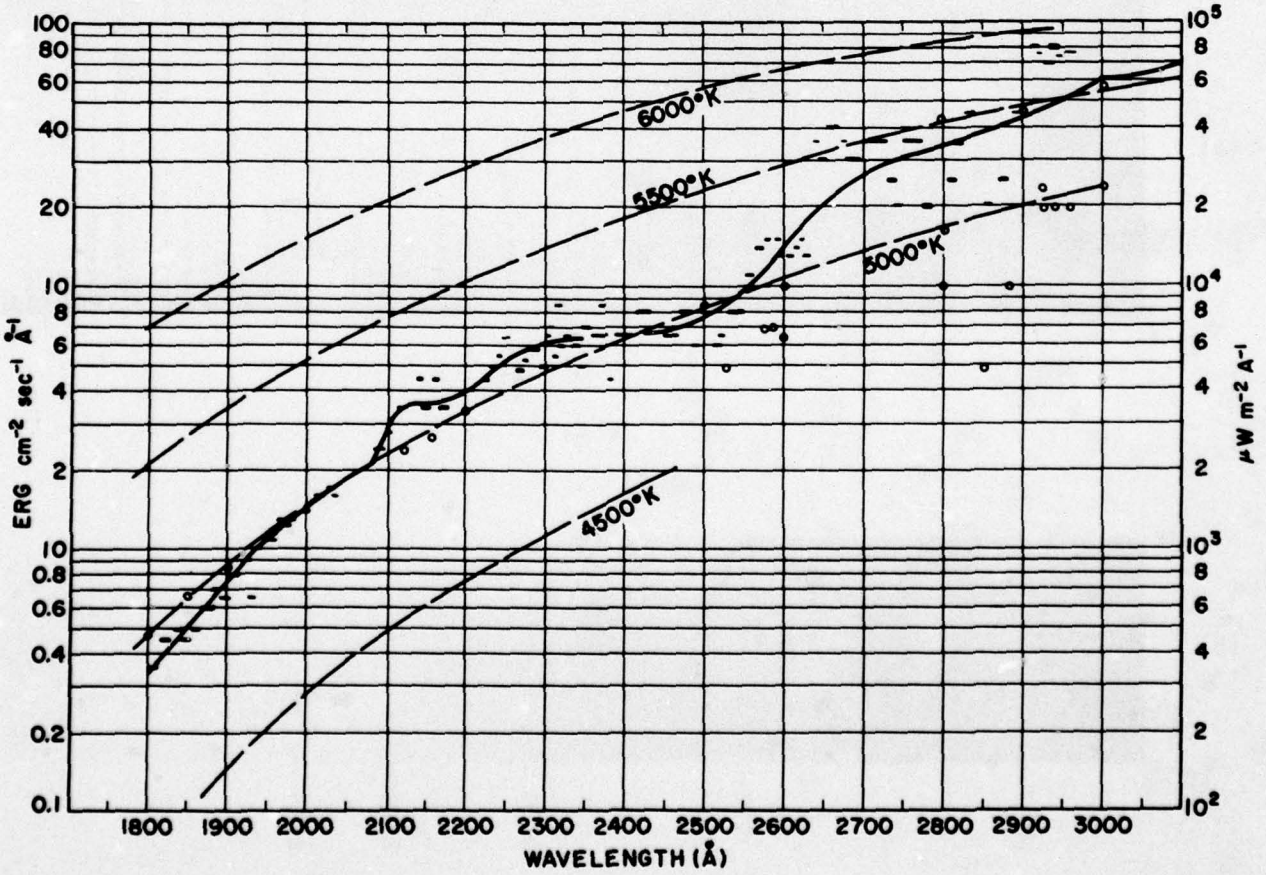


Fig. 16-3. Solar irradiance in the wavelength region 1800 to 2965 Å compared with blackbody curves. The solar intensity varies from point to point, as shown by the dashes and circles. The smooth curve can be considered as a reasonably accurate representation of the intensity of the solar radiation in this region. (After McAllister [1960].)

16.2.3 Solar X-Ray Emission

X-rays originate in the solar corona and are most intense in the vicinity of active regions which are identified by the presence of flares, plages and sunspots (see Chapter 15). The intensity also depends upon general solar conditions. In the absence of flares, total emission below about 60 Å varies from an average value of 0.13 to 1.0 erg cm^{-2} sec^{-1} over a solar cycle [Friedman, 1961]. Measurements at the solar minimum, with a quiet sun, show that the short wavelength limit is of the order of 10 Å while at solar maximum, with a quiet sun, the limit is extended to about 6 Å. During solar disturbances photon energies as high as 125 keV (0.1 Å), were observed. The solar disk was photographed in the 20 to 60 Å region with an x-ray pin-hole camera [Chubb et al, 1961]. The photograph showed that the intensity of x-ray emission in the most active region of the sun at that particular time (12 October 1958) was 70 times greater than that from the quiet background.

16.2.4 Intensity of Radiation Below 3000 Å

Table 16-8 presents the most recent evaluation of fluxes in the region 1775 to 1 Å for a quiet sun. X-ray intensities fluctuate greatly, and the values given in Table 16-8 are only representative.

Figure 16-6 illustrates the variation of photon flux of a few selected emission lines with respect to altitude. For a detailed report on absorption of solar radiation below 1300 Å by atmospheric constituents, see Hall et al [1962] and Hinterreger and Hall [1965]. When the solar spectrum in the region above approximately 1500 Å but below 3000 Å is photographed under proper experimental conditions, the effect of atmospheric absorption on the resulting spectra can be observed. Figure 16-7 shows the spectrum in the region 1750 to 2125 Å photographed by a rocket-borne instrument through long atmospheric pathlengths at sunset. The effect of absorption by molecular oxygen in the atmosphere is very pronounced, as the Schumann-Runge bands (1926 to 1760 Å) show.

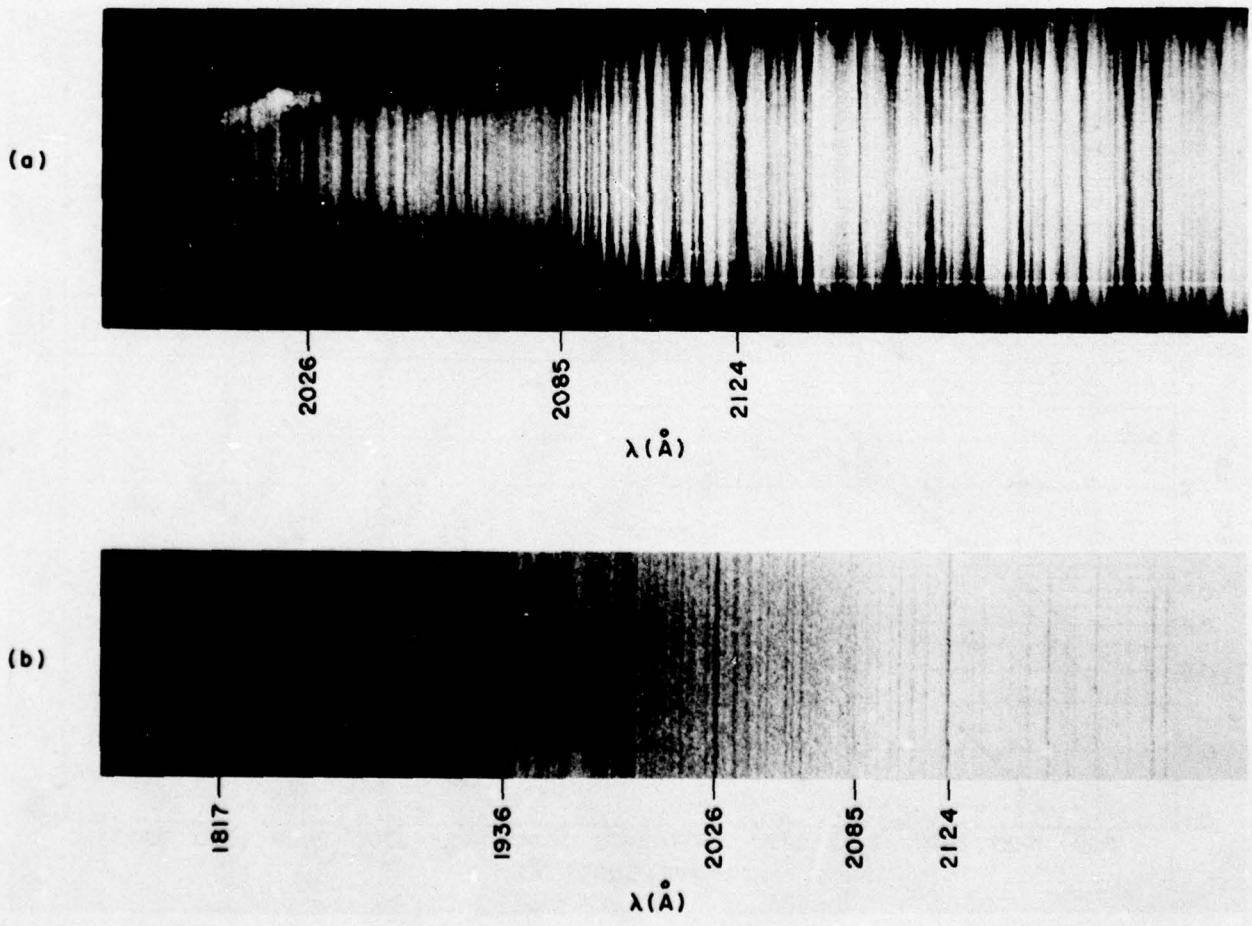


Fig. 16-4. Solar spectrograms showing abrupt changes in intensity at 2085 and 1936 Å; (a) by Rense, University of Colorado, (b) by Jursa, AF Cambridge Research Laboratories.

Table 16-6. Solar emission lines in the region 1817 to 1207 Å, observed in August, 1957. (After W. Behring, H. McAllister, and W. Rense, *Astrophys. J.* v. 127, p. 676, 1958, and A. Aboud, W. Behring and W. Rense, *Astrophys. J.* v. 130, p. 381, 1959.)

Observed Wavelength (Å)	Identification		Flux (erg cm^{-2} sec^{-1})	Excitation Potential (eV)
1816.94	Si II	1816.94, 17.42	1.65	14.94
1808.01	Si II	1808.01	1.05	14.94
1772.88	Fe II	1772.16		
1672.56	Fe II	1670.76	0.21	15.60
1659.2	C I	1656.26	0.28	7.46
		1658.11	0.20	7.45
1642.27	He II	1640.33, .47, .49	0.27	72.64
1561.4 ?	C I	1560.31	0.04	7.91
		1561.40	0.08	7.91
1552.11	C IV	1550.77	0.31	91.11
1549.44	C IV	1548.20	0.55	91.12
1534.53	Si II	1533.44	0.06	16.20
1527.71	Si II	1526.70	0.03	16.20
1402.95	Si IV	1402.73	0.17	66.50
1394.01	Si IV	1393.73	0.24	66.56
1335.98	C II	1335.68	0.33	20.45
1334.74	C II	1334.52	0.31	20.45
1309.08	Si II	1309.28	0.04	17.57
1306.08	O I	1306.02	0.04	9.48
1304.89	O I	1304.86	0.04	9.48
1302.18	O I	1302.17	0.04	9.48
1264.81	Si II	1265.04	0.02	17.91
1215.67	H Ly-α	1215.67	3.43	10.15
1206.57	Si III	1206.52	0.23	34.61

Table 16-7. Flux at a distance of 1 astronomical unit produced by the strongest solar emission lines. (From C. R. Detwiler, D. L. Garrett, J. D. Purcell, and R. Tousey, *Annales de Geophysique*, Tome 17-Fascicule 3, p. 263, 1961.)

Observed Wavelength (Å)	Ident.	Flux (erg cm^{-2} sec^{-1})	Observed Wavelength (Å)	Ident.	Flux (erg cm^{-2} sec^{-1})
1892.03	Si III	0.10	1265.04	Si II	0.020
1817.42*	Si II	0.45	1260.66*	Si II	0.010
1808.01	Si II	0.15	1242.78*	N V	0.003
1670.81	Al II	0.08	1238.80	N V	0.004
1657.00*	C I	0.16	1215.67	H Ly-α	5.1**
1640.47	He II	0.07	1206.52	Si III	0.030
1561.40*	C I	0.09	1175.70*	C III	0.010
1550.77	C IV	0.06	1139.89*	C I	0.003
1548.19	C IV	0.11	1085.70*	N II	0.006
1533.44	Si II	0.041	1037.61*	O VI	0.025
1526.70	Si II	0.038	1031.91	O VI	0.020
1402.73	Si IV	0.031	1025.72	H Ly-β	0.060
1393.73	Si IV	0.030	991.58*	N III	0.010
1335.68	C II	0.050	989.79*	N III	0.006
1334.51	C II	0.050	977.03	C III	0.050
1306.02	O I	0.025	949.74	H Ly-δ	0.010
1304.86	O I	0.020	937.80	H Ly-ϵ	0.005
1302.17	O I	0.013	835.*	O II, III	0.010

* Blend of lines or unresolved multiplet.
** Value applies to intensity within 1Å wide central portion of line.

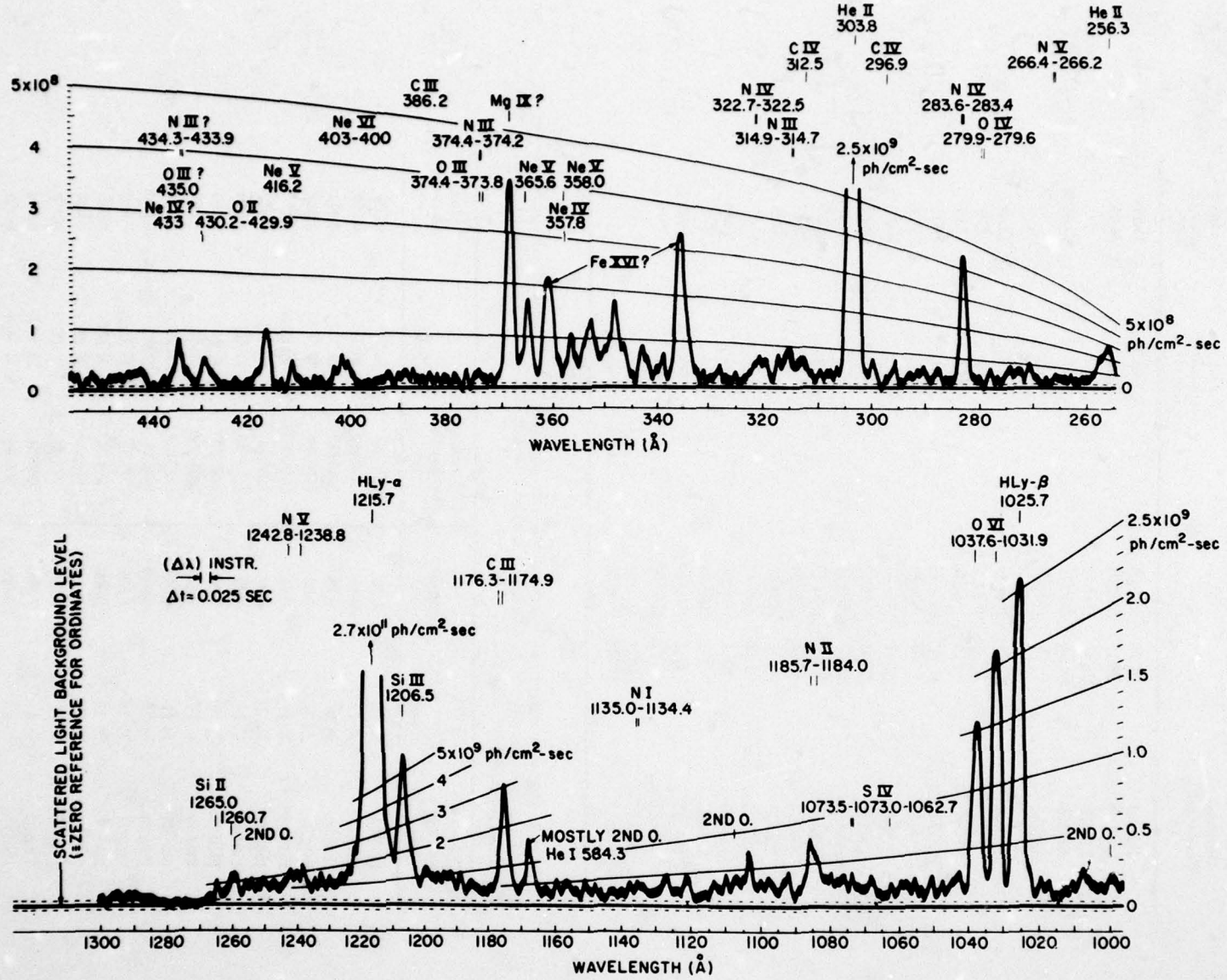


Fig. 16-5. Solar spctrum at 225 km altitude, averaged from 3 scans with a grazing incidence monochromator and a photomultiplier-type detector on 23 August 1961, White Sands, N. M., 1004 h MST. Origin and wavelength of most emission lines and other prominent features are identified; many second-order lines are identified (2nd O). Flux in photon cm^{-2} sec^{-1} can be read by referring to the variable ordinate scale. (Figure by L. A. Hall, L. K. Damon, and H. Hinteregger, AFCRL.)

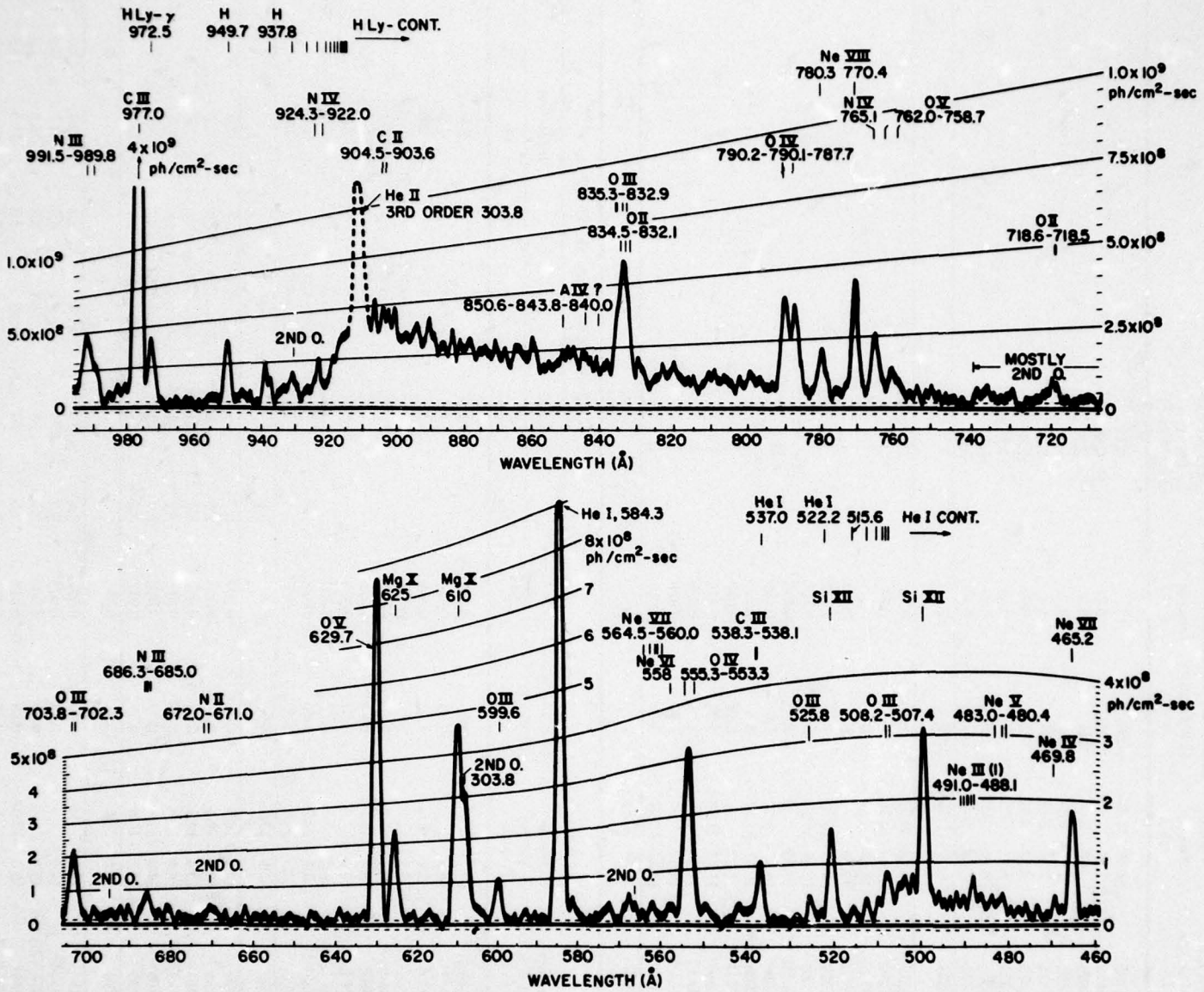


Fig. 16-5. Solar spctrum at 225 km altitude, averaged from 3 scans with a grazing incidence monochromator and a photomultiplier-type detector on 23 August 1961, White Sands, N. M., 1004 h MST. Origin and wavelength of most emission lines and other prominent features are identified; many second-order lines are identified (2nd O). Flux in photon cm^{-2} sec^{-1} can be read by referring to the variable ordinate scale. (Figure by L. A. Hall, L. K. Damon, and H. Hinteregger, AFCRL.)

Table 16-8. Solar extreme ultraviolet flux for essentially quiet solar conditions (July 1963); values of H. E. Hinteregger and L. A. Hall, AFCRL.

Wavelength Region or line (Å)	Photon Energy (eV)	Flux (10^9ph cm^{-2} s^{-1})	Flux (erg cm^{-2} s^{-1})	Total Absorption Cross Section for O_2 (10^{-18} cm^2)
1775 - 1725	6.98 - 7.19	1060	12	0.17
1725 - 1675	7.19 - 7.40	700	8.2	0.86
1675 - 1625	7.40 - 7.63	420	5.0	2.2
1625 - 1575	7.63 - 7.87	260	3.2	5.2
1575 - 1525	7.87 - 8.13	133	1.7	8.0
1525 - 1475	8.13 - 8.41	73	0.96	11.3
1475 - 1425	8.41 - 8.70	37	0.50	14.3
1425 - 1375	8.70 - 9.02	18.3	0.26	14.3
1375 - 1325	9.02 - 9.36	17.7	0.26	5.8
Σ 1775 - 1325	6.98 - 9.36	2700	32	
1325 - 1275	9.36 - 9.72	11.8	0.18	low and highly variable
1275 - 1200	9.72 - 10.16	26	0.41	
1215.7 H Ly-α	10.20	270	4.4	
1206.5 Si III	10.28	4.3	0.071	
1220 - 1200*	10.16 - 10.33	7.4	0.121	
1200 - 1180	10.33 - 10.51	5.5	0.092	
1175.7 C III	10.55	2.5	0.042	
1180 - 1130*	10.51 - 10.97	5.8	0.100	
1130 - 1090	10.97 - 11.37	4.4	0.079	
1085.7 N II	11.42	0.48	0.009	
1090 - 1040*	11.37 - 11.92	4.2	0.078	
1037.6 O VI	11.95	1.33	0.025	
1031.9 O VI	12.01	1.89	0.036	
1040 - 1027*	11.92 - 12.07	0.69	0.013	
Σ 1325 - 1027	9.36 - 12.07	350	5.7	

Wavelength Region or line (Å)	Photon Energy (eV)	Flux (10^9ph cm^{-2} s^{-1})	Flux (erg cm^{-2} s^{-1})	Effective Cross Sections (10^{-18} cm^2) Total O	Total O_2	Total N_2	Ionization O	Ionization O_2	Ionization N_2
1025.7 H Ly-β	12.1	2.3	0.045		1.6	0		0.9	
991.5 N III	12.5	0.33	0.007		1.9	0.3 - 2.5		0.76	
1027 - 990*	12.1 - 12.5	2.4	0.049		1.9	0.06 - 0.4		0.76	
977.0 C III	12.7	4.0	0.081		2.0 - 6.0	0.23 - 1.8		0.8 - 2.4	
972.5 H Ly-γ	12.7	0.55	0.011		40	150 - 350		18.0	
990 - 950*	12.5 - 13.1	0.97	0.021		5.5 - 11.0	0.5 - 2.8		2.8 - 5.5	
949.7 H Ly-δ	13.1	0.25	0.005		5.9	2.2 - 6.3		3.0	
937.8 H Ly-ε	13.2	0.17	0.004		5.2	2.7 - 8.0		2.9	
950 - 920*	13.1 - 13.5	1.07	0.022		7.0	0.8 - 6.0		4.2	
920 - 911	13.5 - 13.6	1.25	0.028		7.4	1.1 - 6.5		4.8	
Σ 1027 - 991	12.1 - 13.6	13.4	0.27	0			0		0
911 - 890	13.6 - 13.9	4.0	0.089	2.7	9.3	1.2 - 7.5	2.7	7.9	
890 - 860	13.9 - 14.4	4.2	0.096	2.9	8.9	1.4 - 8.5	2.9	6.2	
860 - 840	14.4 - 14.8	2.0	0.047	3.1	11.7	2.9 - 7.0	3.1	5.3	
835.2 O III	14.8	0.54	0.013	3.2	11.5	4.2 - 21	3.2	4.6	
840 - 810*	14.8 - 15.3	2.0	0.048	3.2	26	2.1 - 4.6	3.2	9.1	
810 - 796	15.3 - 15.6	0.7	0.017	3.3	40	6.0 - 7.5	3.3	14	
Σ 911 - 796	13.6 - 15.6	13.4	0.31						0
790.1 O IV	15.7	0.36	0.008	3.3	33	28	3.3	13.4	14.0
787.7 O IV	15.7	0.32	0.008	3.3	28	9.7	3.3	11.2	4.9
780.3 Ne VIII	15.9	0.15	0.004	3.3	33	13.8	3.3	16.8	7.6
796 - 780*	15.6 - 15.9	0.75	0.019	3.3	28	26	3.3	13.9	14.3
770.4 Ne VIII	16.1	0.41	0.011	3.4	20	13.8	3.4	10.2	8.3
765.1 N IV	16.2	0.21	0.006	3.4	25	71	3.4	13.9	49
780 - 760*	15.9 - 16.3	0.73	0.019	3.4	22	24	3.4	11.2	14.5
760 - 740	16.3 - 16.8	0.48	0.013	3.4	22	25	3.4	13.0	17.7

(Continued)

Table 16-8. Solar extreme ultraviolet flux for essentially quiet solar conditions (July 1963); values of H. E. Hinteregger and L. A. Hall, AFCRL. (Continued)

Wavelength Region or line (Å)	Photon Energy (eV)	Flux (10^9ph cm^{-2} s^{-1})	Flux (erg cm^{-2} s^{-1})	Effective Cross Sections (10^{-18} cm^2) Total O	Total O_2	Total N_2	Ionization O	Ionization O_2	Ionization N_2
740 - 732	16.8 - 16.9	0.18	0.005	3.5	41	25	3.5	29	17.4
703.8 O III	17.6	0.25	0.007	8.1	33	26	8.1	23	23
732 - 700*	16.9 - 17.7	0.53	0.015	7.7	35	22	7.7	25	20
700 - 665	17.7 - 18.6	0.68	0.020	8.3	27	27	8.3	22	24
665 - 630	18.6 - 19.7	0.54	0.017	11.5	33	26	11.5	31	25
Σ 796 - 630	15.6 - 19.7	5.6	0.15						
629.7 O V	19.7								
625 Mg X	19.8	1.77	0.056	12.0	35	23	12.0	33	23
630 - 600*	19.7 - 20.7	1.2	0.039	12.5	39	22	12.5	37	22
584.3 He I	21.2	1.56	0.053	13.0	29	23	13.0	28	21
600 - 580*	20.7 - 21.4	0.40	0.013	12.9	27	23	12.9	25	21
580 - 540	21.4 - 23.0	1.41	0.050	13.0	30	26	13.0	26	22
540 - 510	23.0 - 24.3	0.48	0.018	13.0	29	26	13.0	26	23
510 - 500	24.3 - 24.8	1.04	0.041	13.0	28	25	13.0	25	22
500 - 480	24.8 - 25.8	1.02	0.042	12.9	27	25	12.9	24	21
480 - 460	25.8 - 27.0	0.70	0.030	12.1	26	24	12.1	23	21
Σ 630 - 460	19.7 - 27.0	9.6	0.34						
460 - 435	27.0 - 28.5	0.49	0.022	10.5	25	22	10.5	23	19.8
435 - 400	28.5 - 31.0	0.99	0.047	12.5	24	17.0	12.5	24	17.0
400 - 370	31.0 - 33.5	0.56	0.029	11.1	23	13.1	11.1	23	13.1
Σ 460 - 370	27.0 - 33.5	2.0	0.098						
368.1 Mg IX	33.6	0.58	0.031	10.3	22	11.3	10.3	22	11.3
370 - 355*	33.5 - 34.9	0.93	0.050	10.0	22	10.6	10.0	22	10.6
355 - 340	34.9 - 36.5	0.77	0.044	9.3	22	9.1	9.3	22	9.1
340 - 325	36.5 - 38.1	0.75	0.045	8.7	21	7.7	8.7	21	7.7
325 - 310	38.1 - 40.0	0.74	0.047	8.1	20	6.4	8.1	20	6.4
303.8 He II Ly-α	40.8	3.8	0.25	9.8	19.5	5.0	9.8	19.5	5.0
310 - 280*	40.0 - 44.3	1.65	0.113	9.2	18.7	4.9	9.2	18.7	4.9
Σ 370 - 280	33.5 - 44.3	9.2	0.58						
280 - 260	44.3 - 47.7	0.84	0.062	8.0	16.0	4.2	8.0	16.0	4.2
257 Si X 256.3 He II	48.2	0.30	0.023	7.2	14.4	3.8	7.2	14.4	3.8
260 - 240*	47.7 - 51.7	0.81	0.064	6.7	13.4	3.6	6.7	13.4	3.6
240 - 220	51.7 - 56.4	0.94	0.081	5.6	11.2	3.1	5.6	11.2	3.1
220 - 205	56.4 - 60.5	0.63	0.059	4.7	9.4	2.8	4.7	9.4	2.8
Σ 280 - 205	44.3 - 60.5	3.5	0.29						
205 - 190	60.5 - 65.3	1.62	0.163	4.0	8.0	2.4	4.0	8.0	2.4
190 - 180	65.3 - 68.9	2.33	0.250	3.4	6.8	2.2	3.4	6.8	2.2
180 - 165	68.9 - 75.1	3.22	0.371	2.9	5.7	1.9	2.9	5.7	1.9
Σ 205 - 165	60.5 - 75.1	7.2	0.78						
165 - 138	75 - 90	0.7	0.092	2.1	4.2	1.4	2.1	4.2	1.4
138 - 103	90 - 120	0.6	0.099	1.1	2.2	0.9	1.1	2.2	0.9
103 - 83	120 - 150	0.7	0.149	0.7	1.4	0.55	0.7	1.4	0.55
83 - 62	150 - 200	0.5	0.137	0.4	0.8	0.37	0.4	0.8	0.37
62 - 41	200 - 300	0.35	0.135	0.22	0.44	0.18	0.22	0.44	0.18
41 - 31	300 - 400	0.15	0.083	0.1	0.2	0.07	0.1	0.2	0.07
31 - 22.8	400 - 540	5×10^{-3}	0.004	0.045	0.09	1.0	0.045	0.09	1.0
22.8 - 15	540 - 830	3×10^{-3}	0.003	0.35	0.7	0.36	0.35	0.7	0.36
15 - 10	830 - 1240	5×10^{-4}	0.001	0.135	0.27	0.15	0.135	0.27	0.15
10 - 5	1240 - 2480	1.5×10^{-4}	0.001	0.037	0.075	0.045	0.037	0.075	0.045
5 - 3	2480 - 4140	2×10^{-6}	$< 10^{-5}$	0.006	0.012	0.0065	0.006	0.012	0.0065
3 - 1	4140 - 12400	10^{-8}	$< 10^{-7}$	0.001	0.002	0.0015	0.001	0.002	0.0015
Σ 165 - 1	75 - 12400	3.0	0.70						

* Exclusive of lines listed.

CHAPTER 16

16.3 SOLAR RADIO EMISSION

This section describes the sun's radiation in the wavelength range of about 10^{-3} to 15 m. Many of the fundamental concepts and definitions used are explained in Chapters 15 and 22; other concepts are defined as introduced.

Solar emissions are separated into two classes: emission from the quiet sun, and emission from the disturbed sun. The term *quiet sun* refers to the absence of sunspots on the solar disk over a period of several months. Emission from the quiet sun is called minimum radiation, or the basic component of solar radiation. Radio emission from the disturbed sun is divided into two types: a slowly varying component with maximum energy at 10 to 21 cm, and a rapidly varying component with a maximum in the meter-wavelength range.

Different regions of the sun are observed at different wavelengths. At millimeter wavelengths, the radiation is from the photosphere. In the centimeter range, radiation partly of chromospheric origin is observed. Decimeter and meter wavelengths are radiated from various heights in the corona; at meter wavelengths the observed radiation comes from heights ranging from 100,000 to 200,000 km above the photosphere. For receiving equipment on the earth, the low-frequency limit for observation is the frequency at which radio waves are reflected by the ionosphere (around 10 Mcps). The high-frequency limit is set by absorption of radiation by atmospheric oxygen and water vapor.

16.3.1 Quiet Sun Temperature and Flux

If the sun radiated only as a thermal source, the emitted energy density would vary with frequency and temperature, according to Planck's radiation law (see Appendix B). In the radio region, the Rayleigh-Jeans approximation for blackbody radiation is valid; the *brightness,* radiance per unit bandwidth, see Eq. (B-5), would be

$$B_f = 2\,kTf^2\,c^{-2} = 2\,kT\lambda^{-2}. \qquad (16\text{-}3)$$

In Eq. (16-2), if

f, the frequency, is in cycles per second;
λ, the wavelength, is in meters;
T, the temperature, is in degrees Kelvin;
c, the velocity of light, is in meters per second; and
k, Boltzmann's constant, is in joules per degree Kelvin;

then B_f is in W m^{-2} cps^{-1} sr^{-1}. Values of temperatures, T_b, calculated from Eq. (16-3) are referred to as *equivalent blackbody temperature* or as *brightness temperature,* defined as the temperature of a blackbody that would produce the observed radiance at the specified frequency.

The radiant power received in a given frequency band per unit effective area of the detecting element is called the *power flux density* (irradiance per bandwidth), see Eq. (B-5), and is strictly defined as the integral of $B_f d\Omega_s$ between the limits f and f + Δf, where Ω_s is the solid angle subtended by the source. In solar radio astronomy the relationship used is

$$F_s = B_f \Omega_s = 2\,kT_d\Omega_s\lambda^{-2}, \qquad (16\text{-}4)$$

where T_d, the *apparent* or *disk temperature,* is that temperature which a uniform source of the same angular size as the solar optical disk must have in order to produce F_s, the power-flux density received from the sun. Values of power-flux density are usually given in W m^{-2} cps^{-1} but may be reported in *Janskys* (one Jansky is one W m^{-2} cps^{-1}). Because the measurable quantity is angular diameter, and instrument readings are in degrees of arc, an approximation commonly used is

$$F_s = 2\,kT_d\Delta\omega/3280\,\lambda^2, \qquad (16\text{-}5)$$

where Δω is $\pi\alpha^2/4$, and α is the angular diameter in degrees. This approximation is valid for sources which subtend very small angles.

It is only at millimeter wavelengths that solar radio emission approximates a 6000°K blackbody. At wavelengths longer than 1 cm, the equivalent blackbody temperature ranges between 10^4 and 10^6 °K for the quiet sun, and from 10^4 to 10^{10} °K for the disturbed sun, depending on the condition of the sun and the time in relation to the 11-yr sunspot cycle. Furthermore, if the quiet sun temperature observed during a sunspot-minimum period, such as 1954, is compared to that observed during a different phase of the sunspot cycle (e.g., decreasing from maximum as in 1958 to 1960), there may be a factor-of-two variation at some frequencies. Figure 16-8 shows the distributions of power-flux density for the sun and for blackbodies at various temperatures, see Eq. (B-8). In plotting the solar radiation curve, for simplicity it was assumed that the disk observed at radio frequencies is the same diameter as the optical disk and that the temperature distribution across the disk is uniform. Note that the peaks on the curves in Fig. 16-8 show the wavelength, $\lambda_{f\,max}$, at

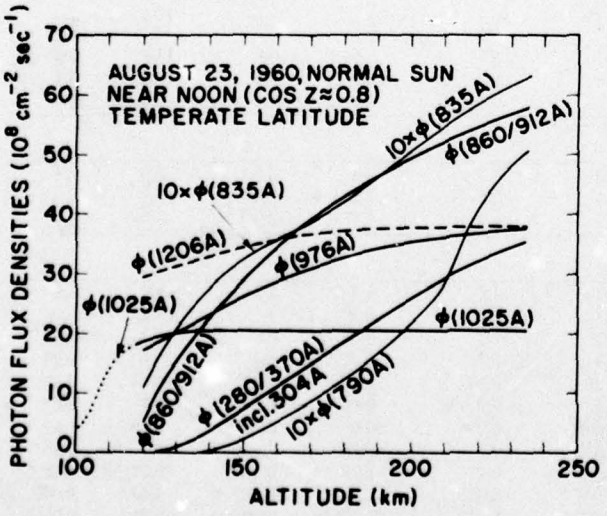


Fig. 16-6. Attenuation of solar ultraviolet radiation by the earth's atmosphere based on a single experiment (23 August 1960). Emission line or wavelength band is given beside each curve; note that fluxes at 835 Å and 790 Å are 10 times that for other curves. (Figure by H. Hinteregger.)

which the energy is maximum, not the wavelength λ_{max} shown in Fig. 16-1.

The millimeter range of wavelengths is generated in the photosphere. Average emission corresponds to an equivalent blackbody temperature of about 6000°K, but the value for a particular frequency varies between 4500 and 9500°K. The centimeter range of wavelengths is generated in the chromosphere and lower corona. Emission depends on characteristics of both the photosphere-chromosphere interface and the chromosphere-corona interface as well as on the characteristics of the chromosphere; emissions correspond to a brightness temperature between 10^4 and 5×10^5 °K. The meter wavelengths are generated in the solar corona; emission corresponds to an equivalent blackbody temperature of 10^6 °K.

The observed solar brightness temperature not only depends upon the wavelength, it also varies with the position on the solar disk of the region observed. There is a variation from center to limb which is different in the polar regions than in the equatorial region. Measurements also show an increase in temperature near the limb (limb brightening) at centimeter and low-decimeter wavelengths, and a decrease in temperature (limb darkening)

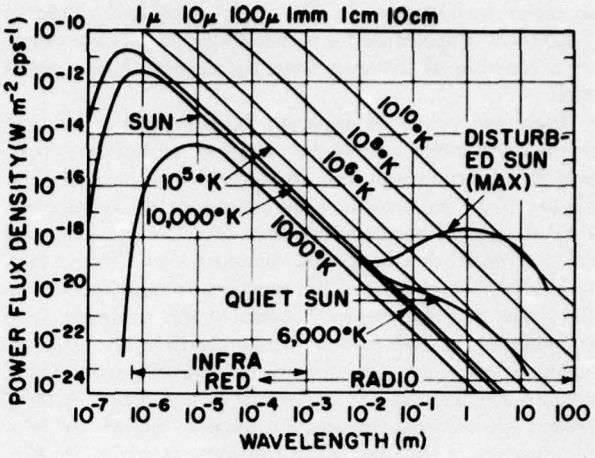


Fig. 16-8. Solar spectrum and spectra of blackbody radiation at various temperatures. The solar power-flux density (power per unit area per unit bandwidth) is plotted against wavelength, hence the maxima of these curves do not occur at the same wavelength as the curves in Fig. 16-1.

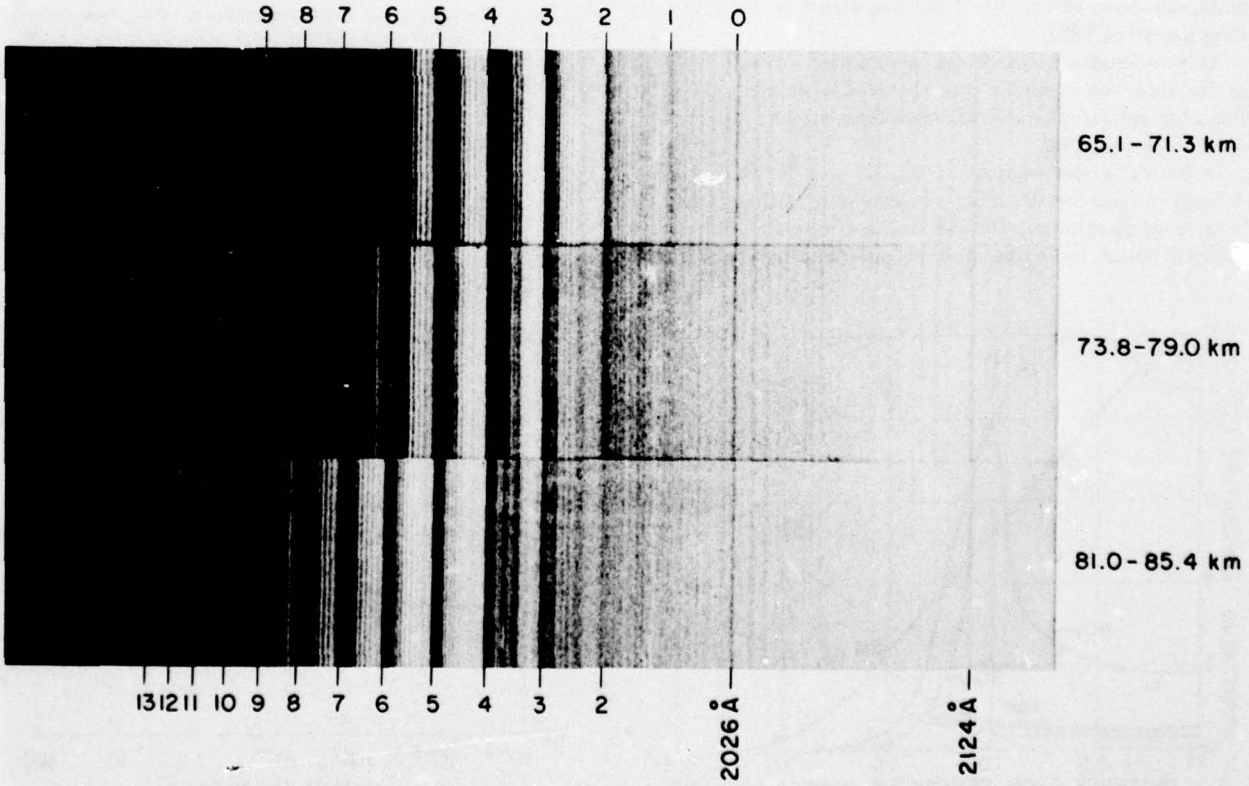


Fig. 16-7. Solar spectrum in the region 1750 to 2125Å obtained by rocket-borne instrument through long atmospheric pathlengths at sunset. Absorption by atmospheric molecular oxygen, the Schumann-Runge bands, is very pronounced.

at meter wavelengths. In Fig. 16-9, calculated values of brightness temperature for selected wavelengths are shown as a function of distance from the center of the optical disk.

Predicted values of apparent temperatures of the sun in the radio range are based on temperatures of the corona and the chromosphere that are derived from optical data. Figure 16-10 indicates how the apparent (disk) temperature at selected frequencies varies for different values of coronal and chromospheric temperatures. The actual measured temperature of the quiet sun should fall within the limits of these curves. Because of this variation with chromospheric and coronal temperatures even when no sunspots are present, the date of observations from which a quiet sun temperature is derived is significant. A theoretical spectrum of the sun's equivalent blackbody temperature as a function of wavelength is given in Fig. 16-11. This spectrum is derived by assuming that the temperature of the corona is 10^6 °K, the chromosphere is 40,000°K, and the photosphere is 6000°K.

Meter wavelengths are characterized by much burst activity; thus, quiet sun temperatures at these wavelengths are determined by making observations over a period of weeks or months. The low temperature to which the sun periodically returns, but never goes below during this period, is taken to be the quiet sun value; it is of the order of 10^6 °K. At 225 Mcps, a 20% decrease from the quiet sun value of October 1959 was found in the April-June period of 1962.

At wavelengths below 1 cm, a variation of 5 to 10% in the quiet sun emission was observed over a period of time; the indication is that the variations may be observed down to about 8 mm.

In the decimeter region (at 10, 21, and 50 cm), it is difficult to measure the quiet sun emission at times other than sunspot minima. During sunspot maxima and the adjacent years, the value must be estimated by statistical

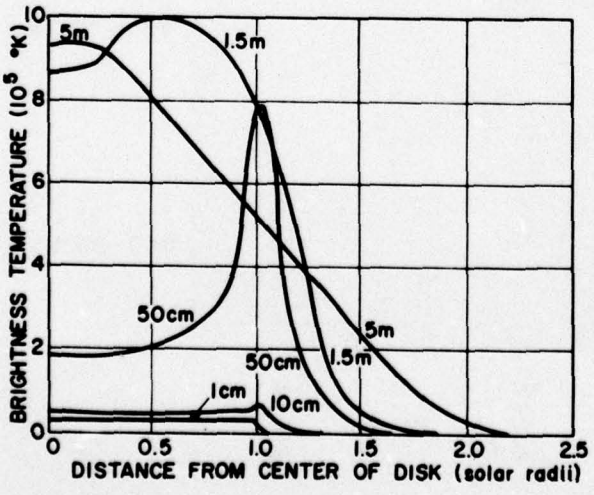


Fig. 16-9. Calculated distribution of brightness temperatures across the solar disk. The solar radius is that of the optical disk. (After Smerd [Pawsey and Smerd, 1953].)

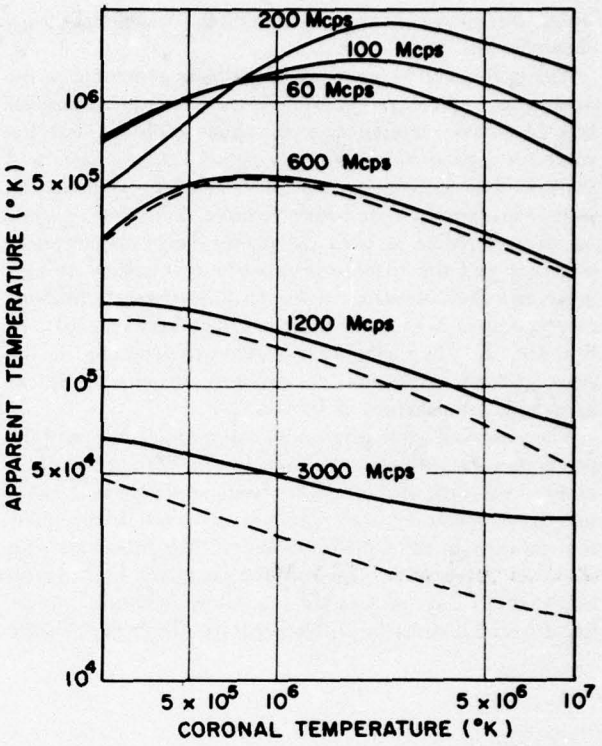


Fig. 16-10. The variation of computed apparent (disk) temperature with coronal temperature at selected frequencies, logarithmic scales. The assumed chromospheric temperatures are 3×10^4 °K (solid lines) and 10^4 °K (dashed lines.) (After Smerd [Pawsey and Smerd, 1953].)

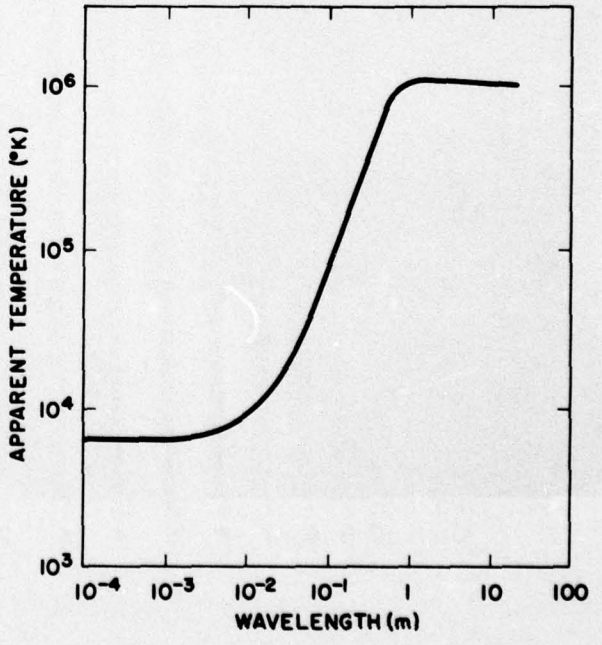


Fig. 16-11. Theoretical curve of apparent temperature of the quiet sun as a function of wavelength, assuming 40,000°K chromospheric and 10^6 °K coronal temperature. Logarithmic scales.

methods. Many observations must be made over a period of months. Then the solar temperature at a specific frequency is plotted against a projected sunspot area (the area of a spot on the solar sphere projected onto a flat disk placed perpendicular to the line of sight), and the most representative line is fitted to the points. A temperature corresponding to zero sunspot area is determined by extrapolation; this is considered to be the quiet sun temperature. One justification for this method is that flux measured in the 3- to 60-cm range varies with time in the same manner as does sunspot number, see Fig. 16-12.

Temperature and power-flux density of the quiet sun at 21 cm obtained by this method during period of sunspot maximum are twice as large as those obtained at sunspot minimum; for details, see Christiansen and Warburton [1955]. Limb brightening on the equator and darkening at the poles are evident during both periods. For measurements at 10.7 cm, a smaller change (10 to 7 ratio) is reported. Covington [1961] indicates that the low point of the monthly plot of the flux density at 2800 Mcps (see Fig. 16-16) may be considered a first approximation to the emission from the quiet sun.

Apparent temperature and power-flux densities of the quiet sun during the IGY period of sunspot maximum are given in Table 16-9. Figure 16-13 shows the quiet sun power-flux densities and apparent temperatures vs wavelength for the IGY period. The observed data agree well with the curves in Fig. 16-8 and 16-11, particularly at frequencies where the slope of the curves changes. From points in either one of these curves, the other curve may be constructed by solution of Eq. (16-5).

Figure 16-14 gives measurements of the power-flux density in the millimeter range, and calculated curves for the quiet and the disturbed sun from 1 mm to 10 cm. In Fig. 16-15, the flux densities measured at 1300 Mcps (23.1 cm) during September-October 1959 are compared with the measurements made at 2800 Mcps during the same period. Indications are that in the 3-cm range, the quiet sun values are rather constant over the sunspot cycle. They vary slightly in the 10-cm range (ratio of 10 to 7), and show considerable change (2 to 1) in the 21-cm range.

16.3.2 Calculation of Solar Temperature and Flux from Antenna Temperature

The power, P_s, received at the antenna due to solar radiation is conveniently expressed in terms of the effective *antenna temperature*, T_A, that is corrected for any RF losses. T_A is defined by

$$P_s = kT_A\Delta f. \tag{16-6}$$

T_A is readily measured with suitably calibrated instruments.

The equation for calculating the solar power-flux density from a given antenna temperature measured at a given installation [Ko, 1961] is

$$F_s = 2\,kT_AL/A_e, \tag{16-7}$$

where A_e is the *effective* area of the antenna in square meters, and L is a dimensionless correction factor related to the antenna response shape and to the diameter and temperature distribution across the source. The value of L is unity only if the antenna half-power beamwidth is very large compared to the source. L exceeds unity when the ratio of the antenna half-power beamwidth to the solar angular diameter drops below about 5; thus, it is desirable to use a parabola small enough so the half-power beamwidth is more than five times the solar angular diameter. (For solar flux measurements, it is a disadvantage to use an antenna so large that it has a beamwidth of less than 3° at a given frequency.) If a small antenna reflector is used, A_e can be measured on an antenna range. If a large dish is used, A_e is computed by comparison with the signal received from a stellar source; for details, see Castelli [1962].

Once the solar flux is known, the apparent temperature and the brightness of the solar disk may be calculated

Table 16-9. Quiet sun at sunspot maximum.

Frequency (Mcps)	Minimum Emission Height* (km)	Apparent Temperature for ½° Source (°K)	Power Flux Density (10^{-22} W m^{-2} cps^{-1})	
25	500×10^3	2×10^6	0.3	Outer Corona
50	300×10^3	2×10^6	2	
100	100×10^3	2×10^6	4	Inner Corona
125	100×10^3	2×10^6	6	
200	90×10^3	1.5×10^6	13	
300	80×10^3	1.1×10^6	20	
425	70×10^3	8×10^5	30	
550	60×10^3	7×10^5	40	
1000	20×10^3	3.5×10^5	70	Chromosphere
2000	10×10^3	1.7×10^5	140	
4000	7×10^3	7×10^4	230	
10000	5×10^3	1.5×10^4	310	

* Above 1 solar radius (6.96×10^5 km from center).

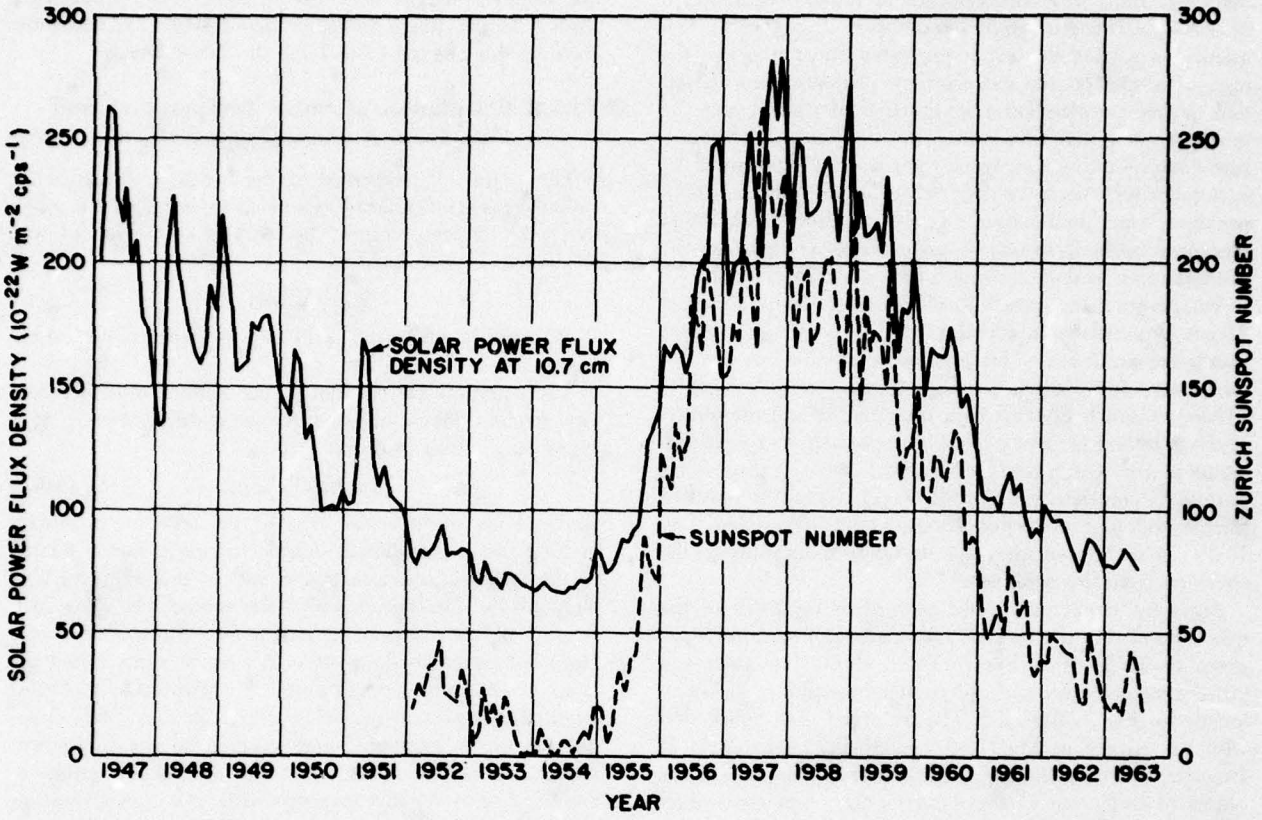


Fig. 16-12. The slowly varying component of solar radio emission at 10.7 cm from the disturbed sun (NRC, Ottawa) compared with Zurich sunspot numbers.

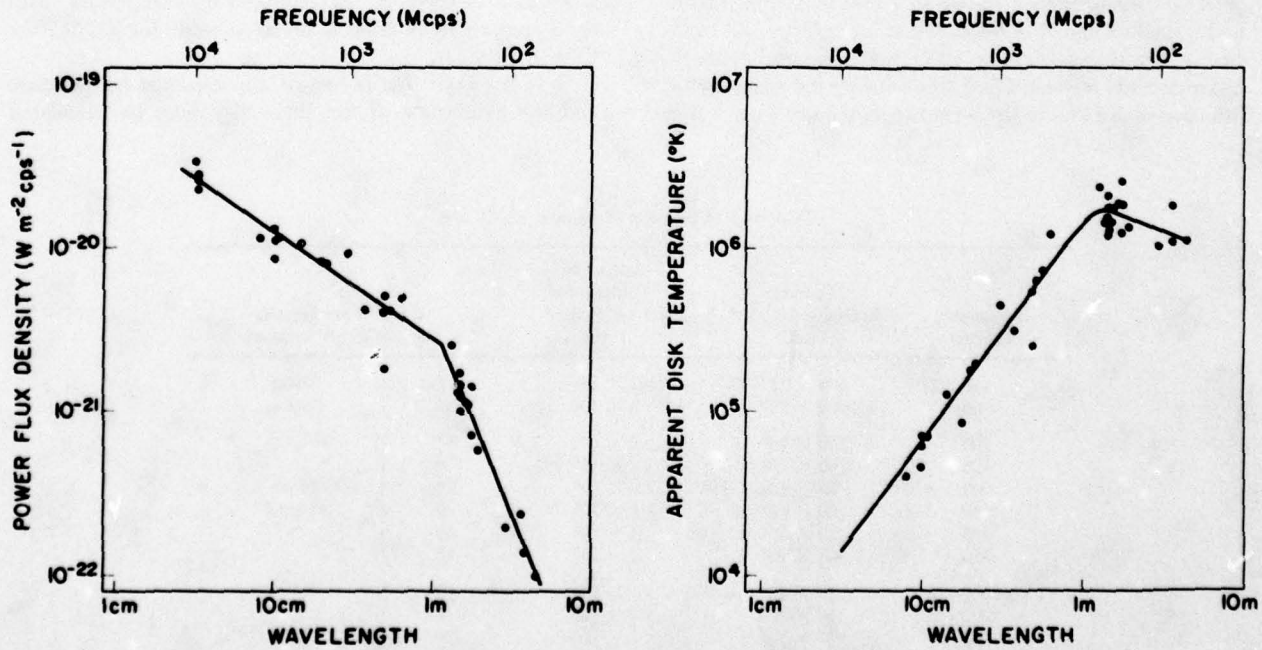


Fig. 16-13. Quiet-sun spectrum of power-flux density and of apparent temperature of disk for the IGY period July 1957 through December 1958, by S. F. Smerd (private communication to A. Maxwell). Logarithmic scales.

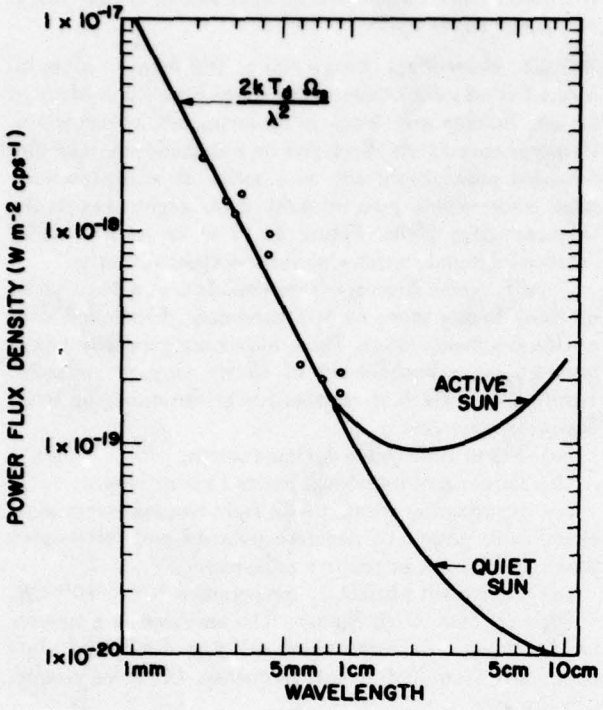


Fig. 16-14. Calculated solar power-flux density vs wavelength from 1 mm to 10 cm and some observed values (indicated by circles).

from Eq. (16-4) or (16-5) and (16-3). Apparent temperature can also be determined directly from the relationship between the solid angle of the source, Ω_s, the antenna solid angle, Ω_A, and the antenna temperature;

$$T_d = \frac{T_A L \Omega_A}{\eta \Omega_s} , \qquad (16\text{-}8)$$

where η is the antenna radiation efficiency. The antenna solid angle is

$$\Omega_A = \eta \lambda^2 / A_e . \qquad (16\text{-}9)$$

If a source subtends a very small total angle, then its solid angle can be represented by

$$\Omega_s = \pi \alpha^2 / 4 , \qquad (16\text{-}10)$$

where α is the angular diameter in radians. For the sun, with a mean angular diameter 0.00931 rad (32′), Ω_s is 6.8×10^{-5} sr.

16.3.3 Flux of the Slowly Varying Component

Emission in the wavelength region from about 1 to 100 cm is characterized by a slowly varying component with periods of days, weeks, or months; the intensity is closely correlated with sunspot number (see Fig. 16-12). At wavelengths less than 10 cm, the radiation is partly circularly polarized.

Eclipse observations or interferometric measurements provide the best data, but these often are not available.

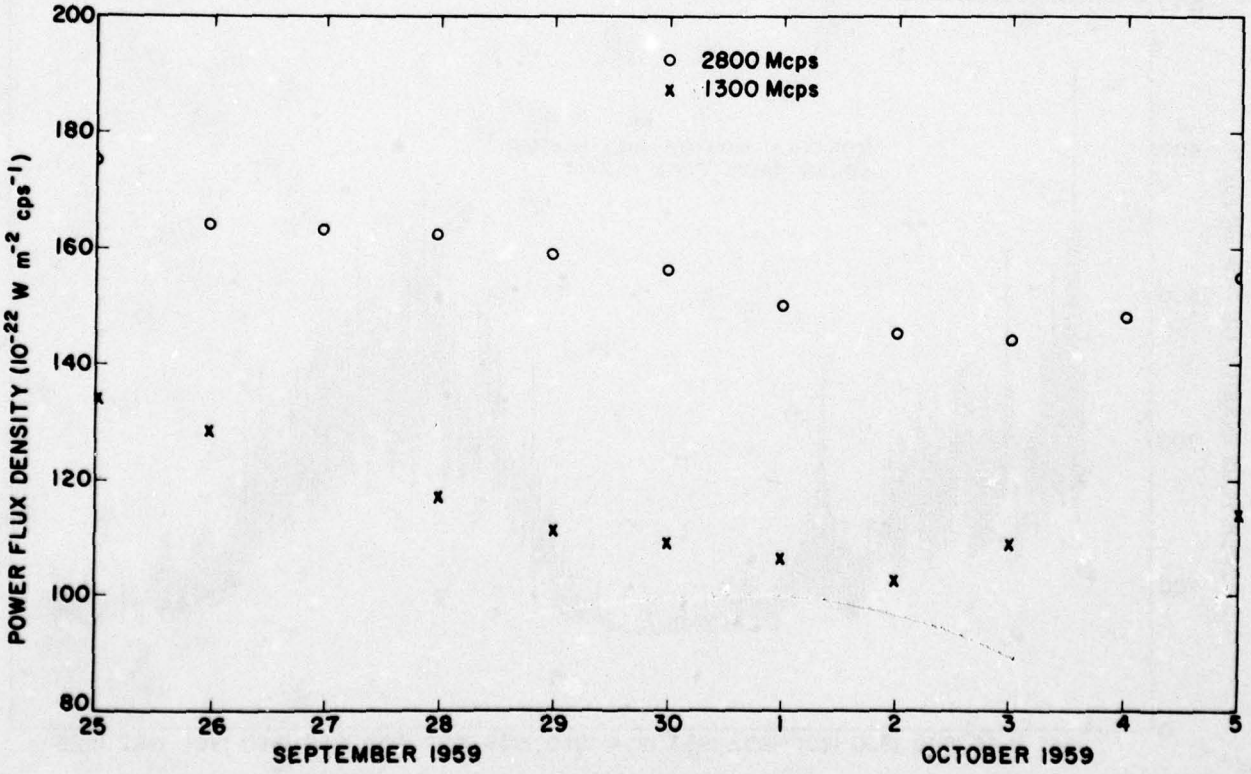


Fig. 16-15. Comparison of solar power-flux densities at 2800 Mcps (NRC, Ottawa) with flux at 1300 Mcps (AFCRL).

Information on the slowly varying component usually must be derived from daily flux measurements. Observations of the 10.7-cm solar radiation, made daily since 1947, are given in Table 16-13, at end of chapter. Low values of power-flux density coincide with sunspot minimum, high values with peaks of sunspot activity. Figure 16-16 shows the amplitude of the persistent 27-day variation of the slowly varying component; a pair of numbers giving the highest and lowest values of daily power-flux densities for each month is represented by a line. The lower envelope of the lines traces out the lowest total value of the solar flux and is a first approximation to the emission from the quiet sun. The upper envelope traces out the variations of the monthly maxima. Average solar emission is between these extremes. This graph can be extended by means of daily flux measurements that are published monthly by the National Bureau of Standards.

16.3.4 Description of the Rapidly Varying Component

During periods of sunspot activity, there may be large increases (bursts) in radio emission lasting anywhere from a few seconds to several hours. Characteristics of the bursts vary with wavelength. Bursts in the meter-wave range (12 m to about 50 cm) are classified by spectral type. No spectral classification exists for the decimeter- or centimeter-wave region. Bursts have not been detected at millimeter wavelengths.

16.3.4.1 *Meter-Wave Range (25 to 580 Mcps).* Most information on solar bursts in the range from 12 m to about 50 cm is obtained from swept-frequency observations. Dynamic spectra are displayed on a cathode-ray tube and recorded photographically as a series of intensity-modulated traces which give intensity as a brightening in the frequency-time plane. Figure 16-17 is an illustration of idealized dynamic spectra of various types of bursts.

Type I, Noise Storms—This emission is a long series of short bursts more or less randomly distributed over a wide frequency range. These bursts are generally superimposed on a background of slowly varying radiation (continuum) which is enhanced over the quiet sun level. Characteristics are:

(a) 100 to 1000 peaks during a storm;

(b) duration of individual bursts 1 sec or longer;

(c) polarization circular with right-handed waves associated with a spot of negative polarity and left-handed waves with a spot of positive polarity;

(d) equivalent blackbody temperature 10^9 to 10^{10} °K.

Type II, Slow Drift Bursts—The emission is a narrow band of intense radiation which drifts gradually and often irregularly from high to low frequency. Observed characteristics are:

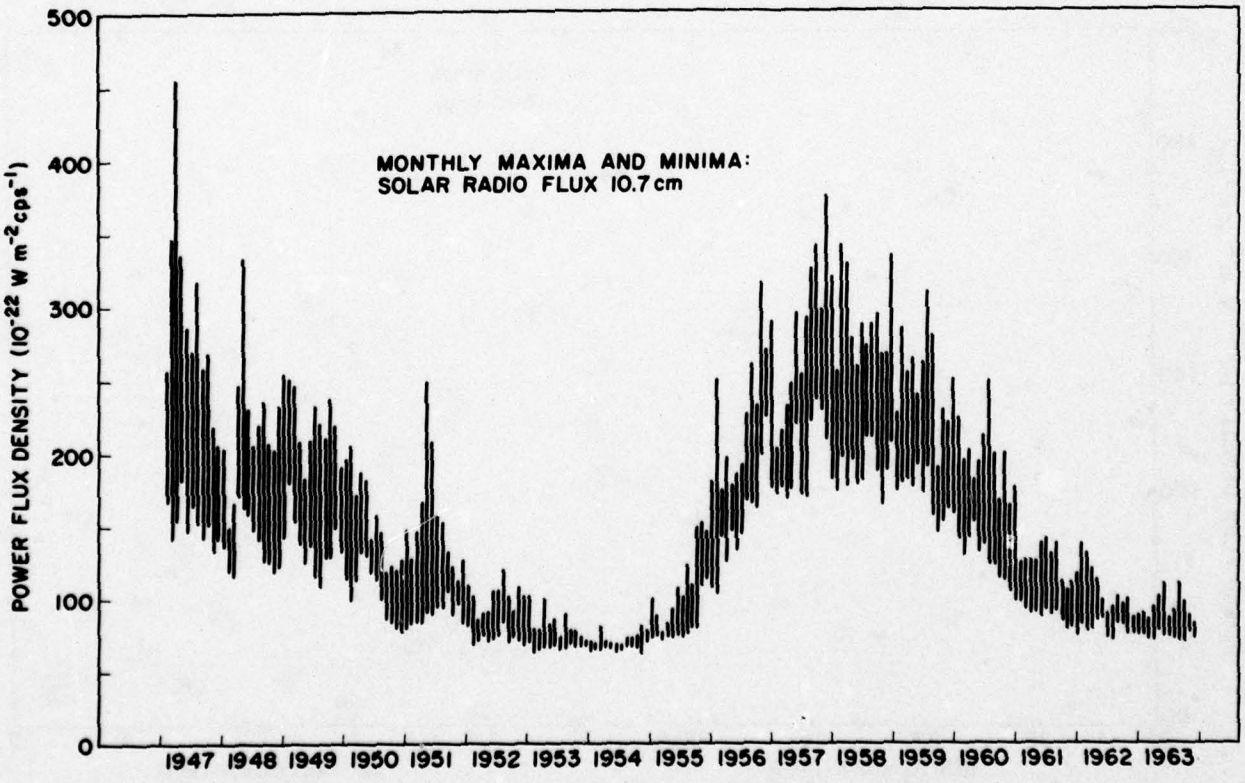


Fig. 16-16. Monthly maxima and minima of 10.7-cm solar power-flux density. (Courtesy of A. E. Covington and the National Research Council of Canada).

(a) drift rate of 0.2 Mcps from high to low frequency (may be as high as 1 Mcps as there seems to be some frequency dependence);

(b) duration about 10 to 20 min;

(c) polarization random for 95% of the events;

(d) second-harmonic content in 50% of the bursts, higher order harmonics absent;

(e) equivalent blackbody temperature 10^{11} °K.

Type II bursts are generally associated with optical flares.

Type III, Fast Drift Bursts—The emission has the following characteristics:

(a) drift rate of the order of 30 Mcps from high to low frequency;

(b) duration of approximately 10 sec;

(c) random, elliptical, or circular polarization;

(d) second-harmonic response in a small percentage of bursts;

(e) equivalent blackbody temperature of 10^{11} °K.

Type III bursts are also associated with flares.

Type IV, Continuum—This is a featureless (free of details in time and frequency) type of burst in which the signal level increases without fluctuation. The following characteristics have been noted:

(a) bandwidth is broad, of the order 100 Mcps;

(b) intensity variation is smooth;

(c) circular polarization;

(d) duration a few minutes to hours;

(e) equivalent blackbody temperature 10^{10} to 10^{12} °K.

(Various kinds of continuum emission are called Type IV in the literature; see Fokker [1963].)

Type V, Short Continuum—This is a broad-band Type IV emission of short duration (order of 1 min) that is preceded by a Type III meter-wave burst and accompanied by centimeter-wave bursts. Polarization may be elliptical.

Certain variations in the above classification are:

(a) *Inverted U Bursts*—At times, Type III bursts drift in the initial stage from high to low frequency, and then from low to high frequency; in the dynamic spectra, the record is in the form of an inverted U.

(b) *Reverse Drift Bursts*—Sometimes, at frequencies lower than 50 Mcps. a short, sharp frequency drift occurs from low to high frequency; this is very often repeated within 1 to 2 sec and may occur isolated or as a structural feature of Type III.

16.3.4.2 *Decimeter-Wave Range (500 to 950 Mcps).* The variety of bursts in the meter-wave range are not observed in the 60- to 31-cm range, see Kundu et al [1961]. The features are:

(a) *Continuum*—This is a broad-band emission analogous to the Type IV meter-wave bursts but with some structure in time and frequency. A succession of very short duration bursts over a wide frequency range may be emitted simultaneously or the bursts may drift from high to low frequency.

(b) *Fast Drift Bursts*—These correspond to Type III in the meter-wave range, but the drift rate is faster. The great majority do not extend below 400 Mcps; they occur typically between 400 and 800 Mcps. There are, however, occasions on which these are accompanied by Type IV events at 2000 to 4000 Mcps. Groups of these bursts may occur in isolation or in close time-proximity to meter-wave bursts. Observed characteristics are: frequency-drift rate greater than 100 Mcps; and drift may be from high to low frequency or vice versa.

16.3.4.3 *Centimeter-Wave Range (3000 to 30,000 Mcps).* Solar emission in the 10- to 1-cm range does not show as rapid fluctuations as emission in the meter-wave range. There are no brief emissions like Type I, II, or III bursts. Certain solar flares produce a gradual rise-and-fall type of burst in this range; it is broad-band and featureless.

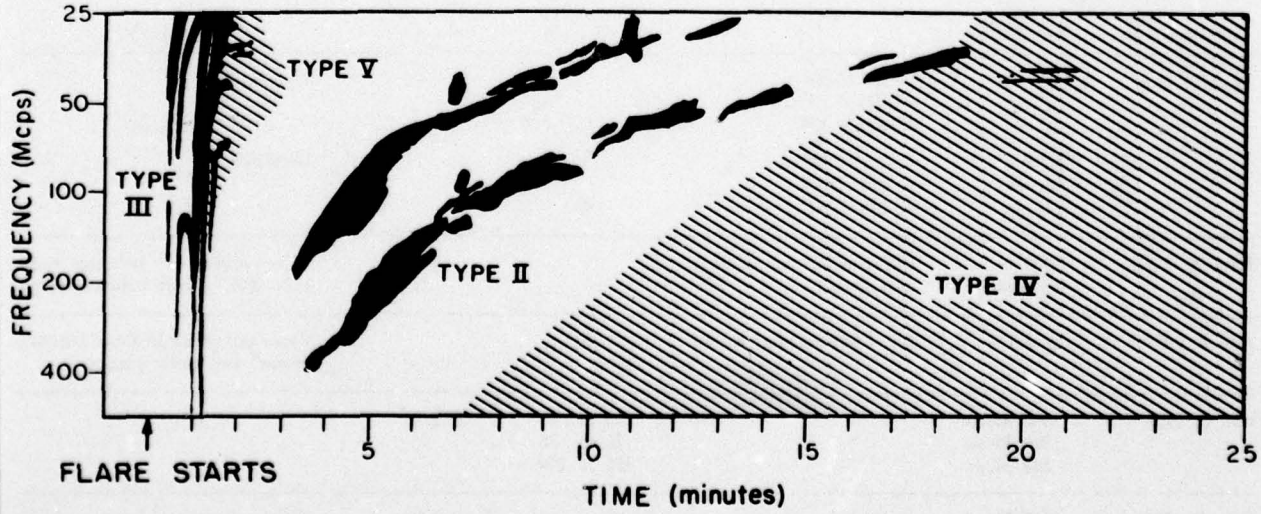


Fig. 16-17. Idealized illustration of the record of a complete solar radio outburst. (From J. P. Wild [1963].)

Large bursts correspond to a temperature of 10^6 °K, and the frequency may extend to meter wavelengths. Less intense bursts are limited to the centimeter range. The dynamic spectra resemble Type IV meter-wave bursts; the smoothness, polarity, broad-band spectrum, and duration support the assumption that centimeter-wave bursts are probably the same nature as Type IV bursts.

16.3.5 The Disturbed Sun as a Radio Source

The slowly varying component of solar radio emission is associated with magnetically complex sunspots. The current hypothesis is that the slowly varying component is emitted by regions in the corona where the density is much higher than normal. (Because of its low density, the normal corona would not emit radiation at wavelengths 1 to 100 cm.) The radiation is thermal; the upper limit of the brightness temperature is close to that of the normal corona. The emitting regions invariably overlie chromospheric plage regions and extend radially outward. Their lifetime, about three months, is longer than that of the associated groups of spots. When observed at wavelengths from 3 to 21 cm, these regions are similar in shape and size to the corresponding plages.

Table 16-10 is a summary of observations of enhanced radio emission made during solar eclipses. Table 16-11 lists the main features of the results of a combined study by radio and optical observers of a single active region on the sun. This region had its central meridian passage on 3-4 December 1957 (a time of high sunspot activity) at a solar latitude of 18°S. The results agree with the hypothesis that the slowly varying component of solar radiation arises from condensation regions in the corona.

The brightness temperature distribution of emitting regions is determined by observations made with aerial arrays of high resolving power. Daily spectroheliograms are taken at 21 cm (C.S.I.R.O., Radiophysics Laboratory, Sydney, Australia) and at 9.1 cm (Stanford University). The Stanford spectroheliograms are published from time to time [NBS]. Brightness contours on such maps may be compared with those of the chromospheric plage areas on

Table 16-11. Radio observations of randomly polarized slowly varying component of solar radiation originating from a selected active region located radially above a plage centroid.

Wavelength (cm)	Angular Diameter (minute of arc) at CMP	Angular Diameter (minute of arc) at Limb	Height Above Photosphere (km)	Height Above Limb (km)	Brightness Temp (10^6 °K)
7.5 (4.5′ fan beam)	5.5	4.5	20,000 ±10,000		0.6
21 (3′ pencil beam)	6.0*	4.0*	20,000 ±10,000		1.5
88 (4.8′ fan beam)	≈ 6 to 8		130,000 ±40,000	200,000	1.5
176 (3.8′ fan beam)	6 to 8		200,000?	300,000?	1 to 2

CMP is central meridian passage.
* Shape similar to plage.

Table 16-10. Summary of data on enhanced radio emission obtained from solar eclipse observations.

Date of Eclipse	Frequency or Wavelength	Brightness Temperature (°K)	Height Above Photosphere (10^3 km)	Angular Diameter (min of arc)	Remarks
Apr. 19, 1958	5.1 cm	3.6×10^6			Unpolarized
	3.3 cm	1.65×10^6			
	2.0 cm	$< 200 \times 10^3$			
	5.1 cm	775×10^3			Polarized
	3.3 cm	350×10^3			
	2.0 cm	$< 120 \times 10^3$			
June 20, 1955	3000 to 4000 Mcps	Order of 10^6 not uniform over region		4	Close agreement between radio spot and optical calicum plage.
Apr. 8, 1959	21 cm	1.5×10^6 for large region	70		Close agreement in shape between optical and radio plages.
Oct. 2, 1959	3000 Mcps		13 to 26	1	
	1300 Mcps		26 to 35		
	224 Mcps		105 to 140		
Feb. 15, 1962	9700 Mcps	1.5×10^5	10 to 15	0.75	Close agreement between radio spot area and emission areas.
	1270 Mcps	9×10^5	20 to 25	1	

the daily solar maps published by the Fraunhofer Institute, Freiburg, West Germany. Daily maps of the distribution of the observed intensities of centers of activity at 169 Mcps (1.8 m) as a function of their distance from the center of the solar disk made at Nançay, France, are published periodically [NBS, and C.S.I.R.O.]. The centers of activity at 169 Mcps persist for a much shorter duration than do the centers of higher frequencies.

The rapidly varying component is usually associated with an optical flare. A flare event appears to have two distinct phases: in the first phase a group of Type III meter-wave bursts is followed by a short continuum burst (Type V); the second phase begins with the onset of a Type II burst and, especially with the largest flares, this is followed by Type IV continuum [Wild, 1963].

All but Type I of the meter-wave bursts are believed to originate in a localized disturbance that travels outward through the solar atmosphere, exciting the local plasma frequency and creating synchrotron radiation. (The plasma frequency at the base of the corona is the order of 300 Mcps, and decreases with height.) By assuming that the level at which the burst-frequency originates is near the height of the appropriate plasma frequency, the velocity of the disturbance may be deduced from the drift rate of the burst and knowledge of the variation of electron density in the corona. Figure 16-18 shows coronal electron densities as a function of radial distance from the center of the sun. The two experimental points are derived from analyses of Type III bursts. Because bursts occur over active regions where the coronal electron density is higher than normal, calculations of the velocity of the disturbance are based on the Baumbach-Allen model with the electron density increased by a factor of about 10.

The velocity of the disturbance calculated from the drift rate of Type III bursts lies in the range 2 to 15×10^4 km sec^{-1} (up to half the velocity of light). The velocity of the disturbance calculated for a Type II burst is in the range 1000 to 1500 km sec^{-1}. This is several times the speed of sound in the corona, which leads to the hypothesis that the disturbance responsible for the slow drift burst is a shock front. The sudden commencement of geomagnetic storms 1 to 3 days after the occurrence of Type II bursts supports the idea that solar corpuscular streams are ejected from the sun at these velocities.

In the meter-wave continuum, all frequencies are believed to come from about the same source position. The signal may originate in synchrotron radiation from the accelerated electrons in the disturbance. Usually, the higher the importance of the associated flare, the longer

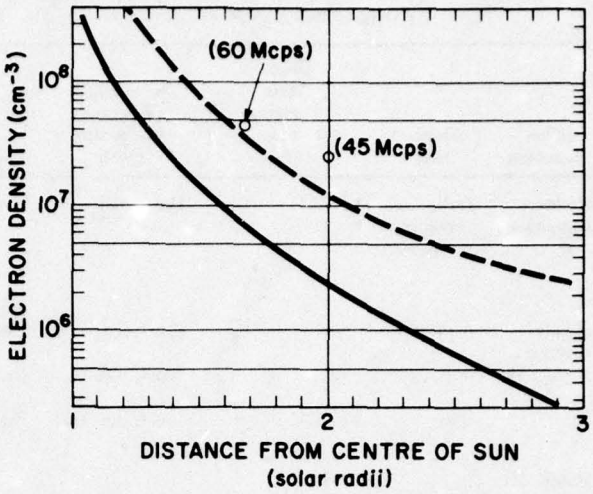


Fig. 16-18. Electron densities in the solar corona as a function of radial distance from the center of the sun. The Baumbach-Allen model is the solid curve; the dashed curve is that of Newkirk for the corona above an average active center (1956-1958). Experimental points are for disturbed regions in which Type III meter-wave bursts originate.

the duration of the continuum radiation; Type IV bursts of duration less than 15 min are associated with flares of importance 1 or less, and bursts longer than 4 h with flares of importance 3. Type IV bursts are also associated with the emission of high, as well as low, energy corpuscular radiation (fast protons, solar cosmic rays).

All centimeter-wave bursts are associated with solar flares, although only 75% of solar flares of importance 2 or greater are accompanied by centimeter-wave bursts (for details, see Kundu and Haddock [1961]). The high equivalent temperatures suggest that the emissions are of nonthermal origin, probably synchrotron radiation from electrons with medium energies, and probably closely akin to Type IV and V meter-wave bursts.

Type I meter-wave bursts are associated with active centers; however, sunspot groups of area less than 4×10^{-4} of the solar disk are seldom accompanied with recognizable noise storms. Observations at 169 Mcps show considerable variations in the height and diameter of the emitting region, see Boischot [1958].

Table 16-12 summarizes the characteristics of bursts and also the slowly varying and basic components.

Table 16-12. Resume of solar radio emission. (After Wild [1963] and R. Coutrez, "Radioemission d'Origine Solaire," *Rend. Scuola Intern. Fis. "Enrico Fermi,"* v. 12, p. 117, 1960.)

Phenomenon	Duration	Brightness Temperature (°K)	Wavelength Region ( ) means rarely	Polarization	Characteristics of the Source: Diameter (min of arc)	Characteristics of the Source: Remarks	Associated Phenomena
Basic component	Indiscernible variation	10^{6}*	Unlimited	Random	32*	Thermal; Limb darkening at mm and m, brightening at cm, dm. Equatorial and polar differences.	
Slowly varying component	months	$< 2 \times 10^{6}$	(cm), dm, (m)	Random	1 to 10	Thermal; Large scale condensation (faculae)	Spots, plages, coronal streamers
	days	$< 5 \times 10^{5}$	(cm), dm, (m)	Partly circ.	1	Thermal +; Medium scale condensations	
	min	$< 5 \times 10^{5}$	(cm), dm, (m)	Partly circ.	0.5	Thermal +: Small scale condensations	
Meter-wave bursts:							
Type I, Noise storms	sec (peaks) h (storm)	10^{9} to 10^{10}	m, narrow-band peaks	Circular	1 or 2	Nonthermal; Disturbance located above magnetically complex active centers	Large area groups of spots
Type II, Slow drift	min	10^{11}*	m, Dm. Sharp cutoff at low frequencies	Usually random		Nonthermal; Disturbance travelling at 1000 to 1500 km sec^{-1}, probably shock front in plasma	Second phase of optical flare
Type III, Fast drift	sec	10^{11}*	dm, m, Dm	Elliptical, or circular	10*	Nonthermal; Disturbance travelling at $\approx$ c/2, possibly emitted electrons with plasma pinch effect.	First phase of optical flare
Type IV, Continuum	min to h	10^{10} to 10^{12} (sometimes**)	dm, m	Circular	10^{10} to 10^{12}*	Nonthermal; Synchrotron, probably emitted by fast electrons. Source of meter wavelengths may show outward movement then return to stabilized position.	Follows Type II bursts, especially in large flares. Emission of fast proton streams and solar cosmic rays.
Type V, Short continuum	min	10^{10}**	Dm	Elliptical?		Nonthermal; Synchrotron, probably from $\approx$ 1 Mev electrons, possibly partly trapped in magnetic field. Source rising (like Type IV), then stabilized.	Follows Type III bursts, accompanied by cm-wave bursts. Second part of minor flares.
Inverted U	1/2 min		m, Dm			Nonthermal; Synchrotron (Type III, source rising, then moving back 50,000 km sec^{-1}).	Surges in the chromosphere.

* Increases with wavelength.
** Decreases with wavelength.
\+ Also may include nonthermal radiation associated with the local magnetic field.

Table 16-13. Daily Values of Solar Power Flux Densities (10^{-22} W m^{-2} cps^{-1}) at 2800 Mcps (10.7 cm) Recorded at National Research Council, Ottawa, Canada.

DAY	Jan	Feb	Mar	Apr	May	June	July	Aug	Sept	Oct	Nov	Dec
						1947						
1		—	—	252.0	258.4	—	—	216.7	—	203.1	189.0	177.8
2		—	—	260.6	264.8	252.7	194.5	231.3	259.0	—	—	145.6
3		—	—	301.4	272.1	219.1	196.2	—	234.1	248.3	154.7	148.6
4		—	—	295.8	—	214.8	203.6	244.6	231.1	270.2	146.1	140.8
5		—	309.2	346.5	262.2	214.8	197.5	241.6	226.8	—	147.3	172.2
6		—	308.8	—	219.3	210.5	—	252.8	231.1	237.1	134.0	175.2
7		—	324.3	456.1	235.6	237.6	209.6	295.8	—	242.2	132.7	173.1
8		—	348.8	423.0	226.1	—	198.8	289.8	229.4	235.4	—	161.5
9		—	—	355.8	220.1	—	195.0	307.4	219.0	225.9	—	171.3
10		—	328.6	334.1	221.4	239.3	204.4	—	226.8	212.2	134.9	167.9
11		—	305.8	298.0	—	182.6	210.9	314.7	184.7	201.8	—	173.1
12		—	307.5	233.9	235.2	146.5	204.4	319.4	180.8	195.0	158.1	164.0
13		—	362.1	—	255.4	170.1	—	294.1	198.0	—	164.1	179.5
14		258.1	268.8	167.7	190.9	171.0	216.4	296.2	—	159.7	169.7	—
15		—	224.6	—	181.9	—	225.9	271.7	167.5	151.1	189.5	174.4
16		—	—	—	230.4	177.9	259.4	228.3	158.9	161.0	—	202.3
17		232.3	180.7	156.6	234.3	208.4	271.0	—	157.6	167.5	177.0	206.6
18		—	157.9	158.3	—	250.9	251.7	203.0	159.3	151.1	186.9	198.9
19		181.6	141.6	153.6	247.6	278.0	254.3	192.2	155.9	—	197.2	191.1
20		166.1	141.6	—	282.4	270.3	—	175.4	146.8	192.0	199.4	179.1
21		—	150.2	157.4	328.0	287.0	244.4	160.8	—	191.5	211.0	—
22		—	159.7	165.2	293.6	—	256.4	155.7	155.4	213.9	214.0	154.2
23		—	—	186.7	327.6	282.3	237.5	151.4	182.9	231.5	218.7	160.2
24		166.5	164.8	226.6	—	258.2	236.6	—	217.3	237.9	205.8	152.0
25		195.3	161.0	237.4	—	261.7	201.8	153.1	217.3	237.9	195.1	—
26		173.4	182.0	296.3	299.6	234.6	202.3	175.4	207.4	—	190.3	171.8
27		—	194.5	—	293.6	220.0	—	186.2	200.1	227.2	184.3	176.5
28		236.2	199.2	281.2	337.5	244.5	164.0	195.6	—	214.3	192.9	—
29			226.7	293.7	326.7	—	170.0	209.4	204.0	199.7	170.1	184.2
30			226.7	291.5	289.3	205.8	176.5	243.8	227.2	199.3	—	197.1
31			257.7		253.6		212.2	—		192.4		185.1
MEAN		201.2	234.7	263.7	261.1	226.6	215.2	231.0	199.1	207.7	177.6	173.5
						1948						
1	—	126.1	132.2	170.7	199.1	201.1	204.0	206.4	148.6	124.9	137.9	121.5
2	204.6	129.6	133.4	182.8	—	190.8	196.7	195.2	140.4	126.2	136.6	124.5
3	176.3	133.4	119.7	197.8	178.9	198.5	191.1	206.4	137.8	125.8	145.6	143.0
4	—	130.9	118.0	199.1	202.1	199.8	175.2	220.1	—	131.8	154.2	137.0
5	170.3	133.4	115.0	191.8	229.1	205.4	165.7	206.0	132.2	132.6	155.1	—
6	173.7	121.4	124.0	195.7	266.5	—	152.4	185.8	136.1	130.5	155.1	153.3
7	176.3	127.8	—	186.2	296.2	183.9	150.3	184.0	127.1	138.7	—	168.3
8	169.0	120.5	134.3	186.7	318.5	201.9	147.3	181.5	132.7	162.7	187.8	177.4
9	150.5	128.7	138.2	183.2	—	194.2	161.9	150.9	132.7	144.7	171.4	182.1
10	144.5	142.5	151.5	194.0	335.7	186.9	165.3	145.8	135.7	—	166.7	192.0
11	137.6	139.0	155.8	—	319.4	172.3	—	155.2	146.0	—	172.7	189.8
12	141.0	131.7	163.1	206.0	305.8	169.7	176.5	166.4	163.6	195.4	175.7	—
13	142.8	127.8	153.2	226.2	291.0	—	174.3	140.6	176.5	207.4	186.0	203.2
14	144.0	—	151.5	248.5	282.4	163.3	178.2	153.1	185.5	200.6	—	193.7
15	140.2	—	145.5	217.6	245.9	158.1	185.9	154.0	189.8	192.0	180.0	206.6
16	144.5	140.7	134.3	210.7	—	161.5	185.1	160.8	200.1	184.2	191.6	210.0
17	138.9	133.0	133.4	—	219.3	183.5	186.8	166.0	199.7	179.9	189.0	218.2
18	140.6	139.5	125.7	212.0	192.6	196.8	—	175.9	223.3	166.2	196.8	216.5
19	148.3	150.6	124.0	231.8	183.6	196.3	173.9	196.9	235.8	168.7	204.1	231.9
20	154.8	149.3	132.2	215.9	172.8	—	189.8	201.2	222.1	169.6	201.1	233.2
21	146.6	142.0	130.4	225.8	187.9	196.8	182.5	181.9	—	178.2	—	224.2
22	159.5	143.8	124.4	228.3	162.5	198.1	191.1	—	—	161.9	183.9	231.5
23	152.2	142.9	113.2	221.0	—	220.8	184.6	185.3	—	162.3	152.9	218.2
24	148.3	125.7	114.1	232.2	174.1	231.2	—	154.0	—	159.3	144.3	222.9
25	—	131.3	120.6	229.6	174.6	220.4	199.3	155.2	—	164.9	147.3	—
26	147.9	126.6	—	217.6	172.4	216.5	184.2	164.3	—	157.6	134.5	—
27	147.5	123.1	—	226.2	188.3	—	197.1	162.6	165.3	143.8	133.6	205.3
28	134.6	—	—	206.9	195.2	217.8	207.0	—	164.5	141.7	—	198.9
29	—	119.3	—	191.4	193.9	209.2	205.3	158.7	132.7	154.1	126.3	178.7
30	154.4		154.1	183.1	—	209.2	206.1	146.2	127.1	145.1	118.6	186.4
31	—		166.5		196.9		199.7	147.5		133.5		163.6
MEAN	153.4	133.1	134.9	207.9	226.3	195.5	182.8	172.7	163.3	158.1	163.4	190.1

(Continued)

Table 16-13. Daily Values of Solar Power Flux Densities (10^{-22} W m^{-2} cps^{-1}) at 2800 Mcps (10.7 cm) Recorded at National Research Council, Ottawa, Canada. (Continued)

DAY	Jan	Feb	Mar	Apr	May	June	July	Aug	Sept	Oct	Nov	Dec
						1949						
1	—	191.5	198.8	156.1	—	165.8	182.9	228.7	162.7	146.8	147.8	181.2
2	—	206.5	201.4	138.9	164.7	156.8	169.2	194.8	177.4	162.7	149.9	173.5
3	141.9	216.0	207.4	196.1	180.1	159.8	159.3	187.5	177.8	163.6	165.0	173.9
4	143.6	228.0	210.0	187.9	173.3	150.8	149.0	168.6	—	191.1	167.1	—
5	153.9	228.9	209.1	196.1	183.2	149.9	132.2	165.6	168.8	216.9	172.3	169.6
6	150.9	243.0	200.9	208.1	169.0	153.4	133.1	139.8	168.8	238.8	—	177.8
7	143.6	231.9	196.2	197.8	163.4	146.1	133.1	129.5	164.5	222.9	204.9	171.3
8	153.5	206.9	215.5	172.0	—	149.5	129.2	117.4	168.3	230.2	219.6	180.4
9	—	216.4	237.5	179.8	165.5	146.5	120.6	108.0	173.5	237.9	212.2	166.6
10	164.2	202.2	249.5	—	152.6	137.0	—	114.4	169.2	225.1	182.6	170.1
11	164.7	220.7	228.9	181.1	136.7	144.3	115.0	109.7	—	225.5	186.0	176.9
12	168.5	—	216.4	184.5	136.7	149.1	116.7	126.0	186.0	—	168.8	—
13	164.7	—	—	186.2	126.0	150.4	123.6	138.1	184.2	214.3	—	191.1
14	169.0	234.4	213.8	175.9	139.7	143.5	131.8	—	203.6	198.0	176.6	162.8
15	208.1	238.7	219.0	—	—	141.3	143.8	160.0	195.0	187.7	195.9	161.0
16	—	250.8	210.0	174.6	148.3	152.9	149.4	164.7	211.3	188.5	200.2	152.4
17	254.5	245.2	219.0	—	149.6	144.3	142.5	182.3	195.4	171.8	217.0	155.4
18	209.4	237.9	223.7	—	156.1	137.5	143.4	187.9	195.8	152.0	201.9	—
19	234.3	237.9	231.4	179.3	153.5	—	148.1	205.1	189.0	146.4	186.0	144.3
20	230.0	219.4	—	196.5	154.8	142.2	165.3	215.8	179.1	140.4	—	132.2
21	205.5	204.4	223.7	186.2	149.2	149.1	163.6	214.6	174.8	144.3	154.7	134.4
22	227.9	197.5	198.3	195.7	—	151.6	146.4	221.0	184.7	147.3	150.8	146.4
23	211.9	191.9	182.4	176.8	144.0	153.4	162.3	208.1	170.0	—	153.8	143.8
24	189.6	179.4	185.5	—	—	160.2	—	215.4	164.9	162.7	168.4	—
25	182.7	231.4	178.6	174.6	154.8	161.5	180.3	219.7	—	132.6	170.1	—
26	176.3	191.9	171.3	194.8	145.3	—	190.7	206.0	148.1	127.5	170.1	—
27	169.0	—	—	189.2	149.6	193.3	203.6	193.5	144.3	141.7	157.7	155.9
28	160.8	205.2	153.2	187.9	147.9	208.8	215.2	—	130.5	144.7	171.0	160.6
29	151.3		159.2	182.8	—	202.4	229.8	186.2	128.8	146.0	—	161.0
30	—		171.7	157.4	160.8	209.7	221.6	185.3	127.9	—	183.5	156.3
31	175.4		171.7		165.1		234.5	181.9		149.8		—
MEAN	181.0	218.3	203.0	182.3	154.8	157.5	159.9	175.0	172.0	177.0	178.2	162.5
						1950						
1	149.6	127.0	117.1	135.5	156.1	121.1	—	124.3	96.6	—	93.6	109.0
2	—	125.3	115.8	—	161.2	127.2	—	135.9	91.8	96.5	97.1	—
3	152.6	121.8	125.3	156.6	157.4	—	111.6	146.2	86.7	93.1	100.5	—
4	147.5	111.9	125.3	159.1	157.4	128.0	118.0	134.6	92.7	91.0	—	109.9
5	150.9	111.5	—	165.2	175.4	—	—	—	94.0	93.1	—	107.3
6	143.2	99.1	136.0	166.0	—	123.7	—	—	91.0	91.4	120.7	115.9
7	133.3	102.1	157.1	—	176.7	121.6	135.6	—	92.7	—	113.0	119.8
8	128.6	102.9	153.2	181.1	182.3	128.0	—	119.1	88.4	—	113.0	125.8
9	119.5	105.5	162.2	—	178.9	135.3	—	114.0	88.0	—	113.4	—
10	114.0	113.2	173.0	—	166.4	—	130.9	112.3	—	107.7	113.4	—
11	—	—	161.4	164.3	159.1	—	125.3	108.4	95.3	113.3	—	127.9
12	129.4	—	—	171.2	153.9	142.6	121.5	—	97.0	106.9	—	118.1
13	127.3	151.5	158.4	160.9	—	134.5	118.5	—	106.9	109.0	102.2	116.8
14	—	161.4	159.2	180.6	—	139.2	124.5	117.4	112.0	—	106.9	103.0
15	—	188.0	157.1	—	136.3	141.3	—	118.7	112.0	—	110.8	96.1
16	130.3	—	148.5	—	128.6	134.9	—	113.1	—	122.8	108.2	—
17	125.1	185.9	145.5	162.2	146.6	—	126.6	128.6	—	121.0	98.8	83.2
18	—	194.5	134.7	161.3	152.2	—	149.4	132.0	117.6	112.4	—	82.8
19	138.5	—	—	153.1	169.4	124.6	150.7	—	109.9	106.9	—	79.4
20	169.8	206.9	117.1	131.2	—	123.3	152.8	—	109.0	94.8	86.3	81.1
21	170.7	184.6	122.7	134.6	—	123.7	158.4	131.6	108.2	—	86.7	79.4
22	—	176.8	112.5	—	158.7	127.6	—	126.5	101.3	—	88.0	76.4
23	182.7	162.7	—	—	165.1	126.3	—	130.3	—	84.9	79.9	78.9
24	196.9	149.8	116.7	170.3	—	—	—	128.2	—	83.6	82.0	80.2
25	182.3	136.9	113.2	175.0	171.1	—	141.7	127.7	95.3	88.4	—	—
26	162.5	—	—	187.9	161.7	137.5	140.8	—	94.8	88.4	—	—
27	164.7	127.8	116.7	187.5	—	130.6	138.2	—	94.0	84.9	91.9	98.3
28	163.8	120.5	125.3	177.2	—	122.9	132.6	105.4	93.5	—	102.7	99.6
29	—		133.4	—	135.0	117.3	—	101.5	90.5	—	104.8	98.7
30	148.8		142.5	—	130.7	120.7	—	99.4	—	100.4	101.8	—
31	134.6		137.7		130.7		136.9	102.4		94.0		—
MEAN	148.6	142.1	137.2	164.0	157.0	128.7	134.1	120.8	98.3	99.3	100.7	99.4

(Continued)

Table 16-13. Daily Values of Solar Power Flux Densities (10^{-22} W m^{-2} cps^{-1}) at 2800 Mcps (10.7 cm) Recorded at National Research Council, Ottawa, Canada. (Continued)

DAY	Jan	Feb	Mar	Apr	May	June	July	Aug	Sept	Oct	Nov	Dec
						1951						
1	—	124.4	103.4	—	108.2	98.0	94.5	106.6	104.5	94.4	106.1	—
2	95.3	129.0	96.8	89.6	106.9	—	—	101.1	—	90.6	103.6	96.4
3	86.5	—	—	88.7	98.0	—	99.5	102.8	—	100.0	—	93.4
4	100.0	—	—	82.9	95.1	—	101.7	—	107.6	102.9	106.1	93.5
5	111.6	98.7	87.5	85.8	—	132.1	103.7	—	113.9	97.5	112.9	90.9
6	—	97.0	91.3	92.3	—	154.5	108.0	—	113.8	—	112.9	83.4
7	—	85.7	85.5	—	90.1	186.8	—	130.5	124.3	98.1	—	87.6
8	112.5	87.3	84.6	—	101.9	199.5	—	142.7	—	—	111.2	—
9	110.4	85.2	87.1	97.7	113.6	198.6	138.8	139.5	—	100.3	112.0	84.2
10	107.1	99.2	—	104.8	138.0	191.1	147.7	153.8	124.0	—	—	86.2
11	89.9	—	—	108.1	154.8	197.7	157.7	—	126.5	109.1	110.8	85.0
12	86.9	87.9	86.3	129.2	—	199.5	153.9	—	129.1	119.7	102.0	89.2
13	—	84.1	86.8	140.2	208.8	205.0	148.9	122.6	121.1	—	97.8	90.4
14	—	92.5	86.3	141.8	231.5	209.1	—	118.3	121.5	—	99.5	95.5
15	80.2	89.6	85.8	167.8	239.6	202.3	—	116.2	—	118.5	99.5	—
16	83.9	89.6	88.8	150.2	242.4	—	139.2	111.9	—	121.5	98.6	—
17	83.1	—	—	153.9	243.3	—	—	103.5	110.5	120.6	100.7	106.0
18	86.8	—	—	162.9	245.9	198.7	122.3	—	114.3	120.2	97.3	103.4
19	86.1	100.1	107.8	157.0	248.9	188.9	116.4	—	121.4	123.5	96.4	113.5
20	—	98.5	111.1	154.5	240.1	180.5	106.3	101.5	126.1	111.6	97.3	114.7
21	—	103.9	130.5	—	249.8	165.4	—	97.6	133.3	103.2	96.1	125.0
22	101.9	106.9	119.2	—	236.3	155.7	—	98.1	—	93.2	98.6	—
23	111.9	107.2	—	145.7	204.1	—	93.3	99.3	—	89.0	100.3	127.0
24	104.2	—	148.1	144.8	184.9	—	96.3	96.9	120.6	90.6	—	119.0
25	130.1	—	—	141.9	171.4	118.7	—	98.2	109.2	91.0	99.8	—
26	137.2	122.1	—	—	156.1	101.3	97.1	—	111.7	100.3	100.7	112.7
27	—	115.3	124.6	139.0	—	93.4	95.8	91.8	111.3	102.3	102.7	105.1
28	—	116.5	117.9	—	119.5	92.1	—	95.6	104.9	112.4	105.7	106.8
29	149.4		107.3	—	111.9	89.5	—	95.7	—	109.9	103.2	104.7
30	146.8		106.5	112.8	106.5	—	99.2	97.7	—	107.4	109.2	—
31	140.0		—		102.3		106.7	101.1		110.4		103.1
MEAN	106.4	101.0	102.0	126.9	168.5	161.7	116.4	109.7	117.5	105.3	103.1	100.7
						1952						
1	—	82.9	—	86.2	84.1	—	97.1	87.6	—	76.3	75.5	75.8
2	93.6	—	—	85.1	79.5	76.1	92.8	83.8	—	76.3	—	—
3	87.8	—	71.2	82.5	—	75.7	93.3	87.2	103.0	79.6	71.3	75.0
4	86.5	82.0	70.7	88.8	—	74.0	87.8	87.2	97.8	87.3	70.9	72.4
5	—	88.8	74.9	—	85.4	72.3	84.0	84.7	91.6	82.6	75.5	73.7
6	—	86.7	75.4	—	88.3	71.8	78.6	85.6	85.2	85.1	72.2	—
7	88.1	88.4	74.5	83.3	90.0	72.7	77.8	91.8	82.3	85.1	72.5	—
8	94.9	87.5	—	85.8	88.8	71.9	83.2	91.8	80.6	83.4	—	82.5
9	102.5	—	—	88.8	85.0	73.1	87.8	91.0	78.1	81.3	74.2	86.3
10	108.3	—	81.7	80.4	79.6	74.9	92.8	—	74.8	79.6	72.5	89.2
11	110.3	89.7	80.0	—	70.7	72.7	100.0	84.7	75.2	—	74.2	94.3
12	—	87.8	82.5	88.0	70.7	74.0	104.7	85.1	78.1	82.2	75.8	90.9
13	—	94.5	86.2	—	73.2	75.3	106.0	86.7	73.9	79.3	76.7	—
14	110.4	95.8	84.2	—	74.9	76.6	105.1	87.2	71.3	76.7	77.1	—
15	106.7	—	—	78.3	74.5	80.3	103.4	90.6	71.8	75.9	—	101.0
16	95.7	101.0	—	74.9	76.2	81.2	102.1	—	77.7	77.1	—	99.8
17	97.8	—	80.0	75.4	76.2	84.1	100.5	86.3	77.3	74.1	87.7	102.3
18	89.4	103.1	78.4	78.0	77.0	85.7	92.9	88.0	76.4	74.1	91.9	100.5
19	—	95.9	76.2	—	77.9	86.6	89.9	85.6	82.3	78.3	109.5	—
20	—	88.8	76.2	—	78.3	87.4	85.7	86.0	79.3	78.8	95.6	—
21	92.7	86.2	76.7	89.3	74.0	90.9	80.2	90.1	82.3	85.1	98.7	—
22	87.3	79.1	—	90.1	80.4	91.3	80.7	90.1	85.5	90.2	91.0	81.6
23	106.6	—	—	85.5	81.7	99.7	75.6	96.9	83.9	91.0	91.9	83.7
24	88.9	80.3	73.3	87.2	78.8	96.7	75.6	100.6	83.5	91.5	91.4	81.3
25	86.8	79.1	75.5	83.4	—	98.0	76.0	102.4	84.8	—	94.4	—
26	—	72.0	74.6	—	84.2	98.4	76.0	113.3	82.2	88.5	84.8	76.2
27	—	71.2	80.4	—	86.7	106.4	79.1	112.0	—	86.4	75.8	—
28	85.2	70.7	85.5	83.4	91.8	103.5	81.5	120.5	—	87.6	76.3	—
29	84.7	69.0	—	84.3	88.3	106.8	78.5	119.2	78.9	86.0	—	69.1
30	83.9		—	82.5	83.8	101.9	86.9	—	75.1	84.7	—	69.0
31	81.5		84.2		83.0		97.5	—		81.3		80.7
MEAN	94.1	85.5	78.2	83.9	80.8	84.8	88.8	93.2	81.3	82.3	82.4	84.3

(Continued)

Table 16-13. Daily Values of Solar Power Flux Densities (10^{-22} W m^{-2} cps^{-1}) at 2800 Mcps (10.7 cm). Recorded at National Research Council, Ottawa, Canada. (Continued)

DAY	Jan	Feb	Mar	Apr	May	June	July	Aug	Sept	Oct	Nov	Dec
						1953						
1	—	—	—	85.5	83.7	72.3	66.8	—	69.2	71.3	—	67.4
2	73.1	76.4	72.4	85.9	—	—	67.1	64.9	68.4	69.2	73.0	70.0
3	—	77.7	71.1	89.7	—	75.2	69.3	67.4	68.4	—	70.9	69.5
4	—	79.5	—	86.2	80.8	76.9	—	70.0	68.4	65.8	71.7	69.5
5	79.2	78.6	73.2	—	76.6	72.3	68.0	71.1	—	68.3	70.5	—
6	92.3	77.8	72.4	79.1	76.3	—	68.4	70.7	72.2	73.4	72.2	70.8
7	87.7	—	—	78.7	70.7	73.1	68.8	71.7	73.5	72.4	—	71.6
8	96.9	—	—	86.8	72.1	72.3	69.7	—	74.2	70.4	70.9	71.2
9	95.7	75.7	68.2	80.0	—	71.5	73.5	—	73.4	70.0	70.5	70.4
10	—	77.0	69.8	—	—	70.1	72.6	80.8	78.1	—	69.2	68.7
11	—	77.0	67.7	—	66.5	72.3	74.3	89.3	76.4	70.8	69.2	68.7
12	99.9	74.0	64.8	—	67.3	67.6	74.3	87.3	—	71.7	68.3	—
13	98.3	74.1	68.6	70.3	67.8	—	73.5	88.9	76.4	71.2	69.2	—
14	101.6	—	—	66.9	67.8	74.0	73.5	88.5	79.3	78.0	67.9	67.4
15	85.7	—	—	68.2	66.9	73.2	75.2	88.9	79.7	76.7	69.6	68.2
16	89.0	73.2	64.8	66.0	—	86.7	73.0	84.3	79.3	74.7	69.2	69.4
17	—	69.3	68.7	66.4	71.6	75.7	72.7	82.1	77.6	71.8	70.0	67.3
18	—	66.4	66.5	—	—	74.0	73.1	75.8	77.6	70.5	70.9	69.0
19	77.7	66.1	—	—	72.8	74.0	70.6	76.2	73.9	71.3	70.9	—
20	74.7	65.7	70.4	66.4	72.8	—	65.5	75.4	71.3	70.5	70.5	—
21	73.8	—	—	70.6	73.7	73.2	69.7	75.8	74.7	70.5	—	69.5
22	73.1	—	—	75.4	73.3	72.4	71.0	—	74.2	72.2	74.7	71.6
23	72.6	67.3	65.3	77.0	—	72.7	69.3	69.5	72.5	72.6	70.9	68.6
24	—	62.7	—	86.7	73.7	71.8	68.0	70.4	75.1	—	71.7	70.7
25	70.9	69.0	74.6	—	75.0	71.8	—	66.5	74.7	69.2	68.7	—
26	72.1	68.6	68.7	89.3	69.9	71.5	65.5	66.6	—	71.2	72.5	71.6
27	72.1	68.1	67.4	95.9	70.3	—	65.9	68.2	—	72.1	71.2	—
28	72.6	—	—	100.6	72.4	70.2	66.4	67.4	71.8	69.6	70.0	69.5
29	71.3		—	93.5	72.8	70.6	65.9	—	71.3	71.2	—	70.7
30	73.8		78.4	94.7	—	68.9	65.9	—	75.6	72.9	69.9	69.0
31	—		79.1		71.6		67.5	68.2		—		—
MEAN	82.0	72.2	70.1	80.9	72.5	73.0	69.8	75.4	74.1	71.5	70.5	69.6
						1954						
1	—	69.8	70.3	69.2	—	64.9	68.1	69.5	68.0	73.7	69.6	75.6
2	68.6	68.6	69.4	63.5	68.6	66.4	64.4	69.5	68.0	—	70.0	74.7
3	—	67.0	69.7	—	67.8	67.1	67.0	68.5	71.3	66.1	62.0	72.4
4	67.1	70.1	69.4	—	69.2	67.1	67.9	67.8	—	73.2	67.1	—
5	67.4	68.8	69.2	67.4	69.0	68.5	68.0	68.7	69.1	75.6	68.7	73.8
6	64.2	—	—	67.5	67.6	66.8	68.4	70.8	69.3	75.9	—	70.3
7	67.5	—	—	69.2	68.6	67.6	—	70.6	66.5	74.6	—	71.6
8	67.0	67.8	69.9	71.5	—	67.5	67.5	70.2	68.3	75.1	73.5	70.9
9	—	—	69.9	69.7	—	69.3	67.5	71.2	70.7	74.2	76.9	72.4
10	—	68.8	70.1	70.3	68.9	69.1	—	72.9	69.4	—	79.7	70.0
11	71.2	68.6	69.9	68.2	68.6	68.1	—	70.7	—	—	82.8	—
12	69.4	—	69.9	71.0	68.0	66.5	68.1	70.9	70.3	72.3	78.4	72.6
13	66.2	—	—	71.2	68.0	66.5	68.6	69.5	67.0	74.2	—	71.8
14	67.5	—	—	69.2	68.0	68.5	68.4	—	69.8	75.1	—	73.7
15	69.6	69.4	83.3	70.7	66.6	68.0	68.2	70.4	69.1	73.5	75.4	79.0
16	—	67.7	80.0	—	—	68.7	66.8	70.0	69.0	—	73.4	80.0
17	66.0	—	79.1	69.7	68.4	67.4	68.1	68.2	70.3	74.9	72.5	76.8
18	67.9	68.1	77.1	69.2	67.8	68.1	66.6	68.7	—	74.2	72.2	—
19	69.4	66.7	77.7	68.8	—	67.3	67.2	67.2	—	72.9	71.3	77.3
20	66.7	—	71.2	67.4	66.3	64.5	67.4	68.5	71.8	74.0	—	75.9
21	70.1	—	72.4	70.3	67.6	65.2	65.7	—	69.6	71.0	68.3	74.4
22	67.5	66.7	70.7	69.1	68.0	66.0	—	70.0	69.6	71.2	67.7	74.1
23	—	69.0	68.7	67.0	66.2	67.6	67.9	72.1	71.3	—	70.7	75.3
24	—	67.7	69.8	67.7	68.0	67.7	—	72.1	70.5	70.9	71.4	75.8
25	66.3	69.4	69.4	68.3	68.6	67.7	67.0	71.7	—	72.3	69.8	—
26	68.0	70.1	64.5	68.2	68.2	66.9	68.8	71.6	70.0	72.3	67.9	73.7
27	66.9	—	—	67.7	69.1	63.0	69.5	69.5	71.3	69.7	—	71.8
28	68.3	69.9	68.7	66.5	66.1	69.6	68.2	—	71.3	71.2	—	—
29	67.0		—	67.0	—	69.1	68.9	68.0	72.8	69.2	68.3	72.4
30	—		—	67.4	67.6	68.2	69.3	68.7	74.3	—	71.9	75.3
31	—		67.4		68.6		—	67.8		69.9		78.1
MEAN	67.7	68.6	71.6	68.6	68.0	67.3	67.7	69.8	69.9	72.7	71.7	74.2

(Continued)

Table 16-13. Daily Values of Solar Power Flux Densities (10^{-22} W m^{-2} cps^{-1}) at 2800 Mcps (10.7 cm). Recorded at National Research Council, Ottawa, Canada. (Continued)

DAY	Jan	Feb	Mar	Apr	May	June	July	Aug	Sept	Oct	Nov	Dec
						1955						
1	—	80.7	—	77.1	81.1	79.7	87.9	83.0	100.9	97.4	152.5	136.0
2	73.9	82.4	76.7	77.9	79.8	79.7	88.6	80.9	103.9	100.7	134.9	137.7
3	73.5	85.4	77.4	77.2	83.0	79.5	92.0	84.3	107.3	112.9	121.1	134.4
4	78.9	86.3	74.4	77.1	82.6	79.2	90.9	85.2	—	118.0	116.4	145.4
5	85.4	81.7	78.1	81.1	82.8	78.8	94.8	89.9	110.3	—	109.1	146.7
6	95.9	83.5	76.9	82.8	83.2	76.0	101.5	—	108.6	—	107.8	147.7
7	100.1	85.3	74.1	79.0	—	75.1	102.6	103.2	106.9	124.5	116.0	143.1
8	—	87.3	73.9	—	—	79.4	102.1	110.8	110.3	112.4	120.7	140.1
9	97.6	88.5	74.1	78.9	77.9	84.4	101.3	124.3	110.3	115.0	124.8	138.2
10	93.2	82.0	77.9	76.4	77.7	85.7	101.0	117.0	106.0	119.8	130.5	134.4
11	95.0	79.2	72.5	78.2	75.0	92.3	96.7	112.9	98.3	113.7	134.0	146.4
12	95.5	—	73.2	75.8	75.0	—	97.0	109.7	97.0	—	139.6	140.9
13	91.9	84.5	—	75.4	73.5	97.1	93.5	—	97.0	99.1	131.3	133.1
14	90.8	80.5	74.1	74.1	72.0	102.4	90.3	101.1	93.5	95.7	126.9	136.0
15	—	79.8	74.0	79.6	—	102.0	88.6	95.5	88.8	86.2	131.3	137.0
16	85.0	76.1	74.2	—	74.0	108.2	85.4	90.8	84.5	85.8	133.9	139.4
17	83.3	73.4	71.4	75.2	79.9	107.2	83.4	86.9	85.4	78.9	130.6	135.7
18	80.6	76.2	73.9	75.6	77.7	103.9	81.3	78.7	84.1	84.5	128.0	132.8
19	80.6	77.0	—	74.3	77.9	105.2	82.1	78.7	84.5	87.1	131.0	131.8
20	75.5	82.0	74.4	75.7	86.0	107.0	81.9	78.3	83.7	87.5	131.6	130.5
21	73.0	78.9	73.0	75.4	93.7	101.6	78.1	76.6	81.1	94.0	123.7	118.5
22	73.7	76.0	—	75.6	92.3	90.8	77.2	78.7	80.2	96.1	122.1	122.3
23	73.9	82.7	71.6	75.8	91.4	93.2	75.9	76.6	80.7	104.3	123.0	117.1
24	78.6	83.7	71.6	75.6	90.4	82.9	73.3	75.7	—	112.9	123.6	114.9
25	78.7	81.2	74.1	73.2	91.1	77.9	73.8	75.7	86.7	133.5	127.5	115.0
26	78.1	80.5	—	75.3	91.3	—	74.0	79.6	86.7	138.6	135.0	113.6
27	73.2	—	—	80.9	92.9	78.8	—	—	91.4	138.2	136.0	122.5
28	76.9	78.5	—	79.0	87.2	76.9	75.9	85.2	92.7	140.0	135.0	122.5
29	78.8		75.1	80.1	87.4	80.3	79.1	85.6	96.6	143.8	131.6	124.1
30	—		74.8	79.5	79.2	82.0	81.1	91.2	97.8	140.0	143.9	135.1
31	81.6		75.9		80.7		—	100.7		149.4		128.8
MEAN	83.1	81.3	74.5	77.2	82.7	88.8	87.3	90.6	94.8	111.1	128.5	132.3
						1956						
1	—	114	153	—	151	155	—	174	181	191	241	225
2	128	116	159	135	158	148	—	176	179	202	225	240
3	125	116	153	129	157	148	157	175	—	222	225	250
4	123	116	146	136	157	149	152	184	182	219	251	251
5	116	106	144	134	162	149	158	184	181	216	274	261
6	120	103	148	145	164	147	156	185	213	208	301	255
7	124	107	149	—	165	146	166	196	209	214	302	251
8	122	109	—	164	166	141	174	197	203	212	319	245
9	116	116	154	175	169	138	172	204	217	212	305	257
10	112	121	158	188	179	134	169	194	217	209	284	270
11	116	133	156	185	177	137	179	181	237	215	283	272
12	124	154	—	186	178	137	192	181	247	207	293	264
13	135	163	163	193	175	147	183	179	261	201	278	249
14	136	185	175	198	167	147	—	176	247	186	269	250
15	156	219	172	—	161	160	161	171	234	168	251	254
16	161	240	166	194	156	158	154	167	238	163	257	249
17	170	248	167	191	161	159	146	174	218	162	255	254
18	177	251	169	191	170	171	146	—	210	162	228	230
19	174	248	171	179	168	179	144	188	197	185	223	236
20	173	244	163	175	176	187	144	204	195	183	216	230
21	174	236	163	188	162	187	156	228	189	186	205	242
22	181	220	163	187	156	182	165	212	179	191	230	254
23	177	204	169	163	147	170	181	223	173	184	203	258
24	174	178	164	166	147	173	172	219	175	191	199	252
25	153	—	157	152	153	158	170	—	176	194	213	—
26	137	154	154	156	159	138	159	220	173	199	214	259
27	124	142	161	137	157	134	160	213	167	213	205	272
28	121	143	163	—	165	139	155	207	166	219	217	226
29	109	157	168	125	177	148	158	214	172	229	218	234
30	107		154	136	167	—	162	199	174	232	238	244
31	110		155		155		168	190		234		—
MEAN	139	166	160	166	163	154	163	194	200	200	247	249

(Continued)

Table 16-13. Daily Values of Solar Power Flux Densities (10^{-22} W m^{-2} cps^{-1}) at 2800 Mcps (10.7 cm), Recorded at National Research Council, Ottawa, Canada. (Continued)

DAY	Jan	Feb	Mar	Apr	May	June	July	Aug	Sept	Oct	Nov	Dec
						1957						
1	—	197	186	219	175	218	256	203	275	268	300	295
2	275	182	182	203	176	229	242	200	268	252	289	270
3	274	185	179	183	182	230	254	198	273	265	266	283
4	283	181	177	193	190	218	249	194	247	237	236	278
5	286	183	180	192	202	222	238	187	237	245	240	273
6	291	193	180	169	198	226	224	187	223	250	239	271
7	264	186	195	171	204	221	211	185	222	253	243	234
8	248	200	198	195	207	223	201	181	227	261	235	242
9	233	190	197	209	228	233	198	175	233	275	230	229
10	216	184	199	193	227	220	188	169	245	275	232	210
11	215	190	216	186	234	224	170	173	268	278	246	211
12	217	193	209	180	228	226	176	177	277	284	257	209
13	206	175	214	186	242	245	188	172	268	281	250	222
14	197	180	200	183	248	247	187	182	259	289	248	228
15	191	188	198	202	235	255	188	183	255	277	242	236
16	184	176	201	209	239	264	203	197	264	289	242	252
17	194	181	200	212	212	268	217	216	271	272	228	278
18	203	188	197	204	214	288	227	216	275	294	247	291
19	215	173	193	207	201	292	220	214	301	291	251	293
20	233	172	195	209	—	295	230	199	302	303	261	333
21	223	184	198	204	230	295	244	194	327	282	274	348
22	226	186	202	217	212	293	236	185	328	274	294	365
23	233	204	203	214	207	297	250	197	294	295	280	377
24	252	185	196	215	210	277	255	199	285	280	285	370
25	232	184	198	224	196	253	246	210	261	259	271	—
26	241	180	193	233	184	260	231	219	270	266	259	356
27	237	183	215	214	198	259	232	222	259	296	258	342
28	207	180	198	199	181	261	212	238	259	323	255	317
29	197		209	188	183	260	201	238	256	342	247	282
30	188		195	177	199	265	193	263	262	344	278	276
31	176		201		211		191	294		318		280
MEAN	228	185	197	200	208	252	218	202	266	281	256	282
						1958						
1	257	195	195	331	266	219	215	274	261	231	234	268
2	263	217	209	326	276	220	215	254	281	221	241	259
3	262	222	223	302	—	227	224	237	270	219	224	241
4	261	233	232	295	280	246	232	216	256	215	220	241
5	246	249	233	290	269	256	238	221	233	199	222	253
6	254	252	251	289	263	260	232	239	216	189	204	249
7	255	257	256	283	249	238	237	235	216	189	206	253
8	255	250	251	272	236	233	232	236	211	187	191	260
9	259	234	255	250	239	252	218	225	235	192	180	254
10	274	231	242	244	209	234	208	222	245	198	169	269
11	273	228	235	216	211	235	203	225	250	210	166	256
12	290	226	232	196	209	227	188	222	270	219	166	257
13	310	222	238	179	203	220	191	236	285	225	163	260
14	321	210	227	177	194	208	182	235	290	228	166	258
15	309	202	217	188	196	197	181	231	271	230	166	235
16	297	187	214	197	194	191	192	215	263	253	169	217
17	285	183	208	207	194	182	188	211	259	286	173	204
18	260	177	210	213	197	177	190	218	246	286	174	202
19	238	173	220	221	197	189	205	219	243	296	183	187
20	251	172	232	226	197	193	200	220	231	278	187	199
21	239	175	224	229	199	194	209	231	221	277	194	198
22	227	176	266	237	199	213	214	239	249	270	200	211
23	210	194	268	235	206	217	213	243	226	240	213	215
24	211	206	274	244	211	221	228	253	225	227	229	224
25	206	207	258	241	207	226	240	263	222	191	243	—
26	220	205	284	245	210	233	260	264	218	194	264	238
27	200	197	302	247	201	237	261	252	219	191	268	227
28	189	—	295	258	202	232	290	244	225	209	259	223
29	194		332	255	219	220	285	252	227	220	263	219
30	181		344	265	213	217	287	249	228	228	264	224
31	187		338		209		288	259		222		226
MEAN	248	210	250	246	219	220	224	237	243	226	207	234

(Continued)

Table 16-13. Daily Values of Solar Power Flux Densities (10^{-22} W m^{-2} cps^{-1}) at 2800 Mcps (10.7 cm) Recorded at National Research Council, Ottawa, Canada. (Continued)

DAY	Jan	Feb	Mar	Apr	May	June	July	Aug	Sept	Oct	Nov	Dec
						1959						
1	235	205	187	256	204	193	188	214	282	150	159	222
2	250	205	181	236	194	198	174	228	269	145	168	217
3	266	204	181	216	195	198	171	240	257	144	165	202
4	270	201	178	215	184	190	177	236	239	148	154	199
5	282	191	179	196	186	197	176	229	220	155	151	204
6	—	195	190	196	202	210	188	227	200	174	157	202
7	306	182	188	217	208	198	192	212	192	169	161	191
8	278	182	191	215	244	213	185	204	199	155	173	193
9	268	174	198	215	249	223	185	204	209	153	183	173
10	282	190	204	220	259	228	201	202	201	149	194	174
11	260	199	201	232	264	226	194	200	203	147	193	171
12	251	199	194	224	266	220	234	196	195	154	192	169
13	235	201	207	209	264	212	243	194	189	155	191	162
14	224	199	215	198	244	208	264	189	196	153	187	165
15	207	213	235	189	228	225	245	190	184	160	182	171
16	213	214	246	188	222	220	261	201	168	167	175	164
17	220	220	259	190	224	225	240	224	170	169	161	167
18	237	218	274	181	213	228	231	229	167	171	155	169
19	265	218	281	196	199	237	222	215	175	173	157	180
20	294	228	285	203	201	226	208	224	185	175	154	178
21	315	224	287	203	201	228	189	230	182	175	154	185
22	337	219	262	199	201	219	178	243	188	187	173	171
23	328	212	258	213	198	220	178	262	182	183	187	166
24	334	220	247	213	199	232	181	245	183	181	205	163
25	321	227	248	211	203	233	182	253	175	186	226	—
26	314	219	247	218	205	238	182	257	164	190	221	161
27	322	211	246	212	208	240	200	279	163	—	218	167
28	304	201	248	216	195	224	205	302	162	—	227	172
29	262		245	211	176	219	207	308	159	—	225	171
30	224		258	220	177	196	204	312	156	—	230	179
31	214		254		179		208	305		161		167
MEAN	271	206	228	210	213	217	203	234	194	164	183	179
						1960						
1	—	225	137	201	152	166	208	140	137	115	124	136
2	175	213	137	184	160	167	207	134	152	112	129	145
3	182	215	138	179	158	167	210	125	149	120	130	152
4	193	209	139	188	156	172	212	122	142	132	131	163
5	213	209	140	182	152	170	209	126	142	132	144	159
6	215	192	135	169	156	175	200	127	149	132	148	161
7	224	187	139	165	162	185	187	134	162	144	157	152
8	219	183	141	147	168	185	176	145	170	143	168	154
9	201	183	143	148	170	181	176	152	173	151	175	150
10	194	178	132	156	170	178	166	170	175	159	200	151
11	200	175	132	159	180	171	153	187	175	152	188	144
12	184	166	129	168	179	167	142	214	177	159	168	140
13	178	167	135	179	170	162	135	234	181	162	180	136
14	176	167	134	183	162	166	139	238	181	166	192	132
15	183	160	137	190	162	166	146	240	178	165	183	138
16	183	158	142	183	155	157	144	241	177	165	174	134
17	179	153	140	178	151	153	153	247	185	167	164	125
18	176	151	133	176	153	139	159	250	190	154	153	118
19	164	—	137	170	153	140	156	234	199	153	150	115
20	157	142	143	175	160	133	152	219	195	149	147	118
21	162	156	145	163	164	131	153	201	189	144	139	116
22	172	149	150	160	164	130	148	189	184	141	127	106
23	188	143	154	166	163	136	151	171	175	134	116	103
24	210	140	158	165	164	132	159	162	162	129	113	106
25	230	147	157	147	163	140	148	158	155	130	111	111
26	242	147	—	143	158	155	149	162	148	132	117	116
27	248	147	—	140	166	164	150	150	142	132	119	125
28	252	140	175	142	171	184	149	140	132	122	117	136
29	237	140	181	153	170	190	154	129	124	131	119	145
30	230		193	16[illegible]	170	194	146	129	121	128	131	159
31	223		182		159		145	132		127		163
MEAN	200	169	146	167	163	162	164	174	164	141	147	136

(Continued)

Table 16-13. Daily Values of Solar Power Flux Densities (10^{-22} W m^{-2} cps^{-1}) at 2800 Mcps (10.7 cm), Recorded at National Research Council, Ottawa, Canada. (Continued)

DAY	Jan	Feb	Mar	Apr	May	June	July	Aug	Sept	Oct	Nov	Dec
						1961						
1	164	123	103	113	125	86	104	90	110	98	86	105
2	176	122	103	105	119	88	99	87	110	97	83	108
3	175	118	104	101	111	92	104	91	117	97	81	111
4	165	118	96	103	104	89	103	88	118	102	82	105
5	160	118	94	107	103	86	106	90	114	108	87	101
6	143	121	93	106	97	88	102	92	112	101	87	101
7	132	114	95	98	97	89	105	99	115	99	93	94
8	125	111	94	104	94	91	107	105	117	98	99	96
9	122	108	90	96	96	100	112	113	126	107	98	92
10	115	104	91	93	92	102	124	122	130	106	101	87
11	110	101	98	92	98	110	138	130	127	107	99	82
12	103	98	92	89	101	108	137	128	130	111	94	78
13	96	97	93	88	97	114	141	128	130	111	91	82
14	96	97	91	93	93	123	136	127	137	105	86	81
15	97	98	98	98	91	129	136	123	135	106	84	81
16	100	96	99	103	88	132	132	119	133	100	86	81
17	102	96	98	105	88	137	137	119	124	97	83	79
18	103	96	101	107	95	136	131	116	115	95	79	81
19	102	96	102	105	100	131	126	113	108	95	77	82
20	102	99	105	103	105	131	123	109	101	93	80	88
21	104	100	105	104	110	132	118	104	96	92	83	90
22	102	102	106	103	109	134	119	103	92	89	84	99
23	100	103	110	105	110	135	118	98	90	85	87	101
24	103	104	116	111	108	117	118	97	97	85	87	104
25	103	106	118	111	106	111	117	93	97	83	92	—
26	108	101	121	126	88	108	115	95	98	83	93	102
27	109	103	125	120	95	99	111	95	96	84	95	103
28	125	103	126	114	91	95	105	100	96	86	98	98
29	132		126	121	91	102	103	103	102	85	98	98
30	129		125	122	88	103	92	106	100	87	104	94
31	123		117		88		91	108		86		93
MEAN	120	105	104	105	99	110	116	106	112	96	89	93
						1962						
1	—	110	121	88	—	98	—	71	84	86	80	77
2	—	103	112	83	—	92	—	73	93	86	80	81
3	79	101	100	80	—	87	—	72	98	83	80	83
4	81	104	89	78	91	85	90	73	99	82	82	82
5	78	92	86	76	87	85	88	70	98	86	82	82
6	77	86	81	78	86	87	86	72	100	84	83	83
7	77	82	80	77	83	92	88	71	100	85	84	86
8	74	82	77	77	84	90	83	72	97	87	85	84
9	74	83	79	78	87	91	80	73	94	86	86	83
10	75	81	76	81	—	90	81	76	91	93	—	84
11	76	82	78	88	98	89	83	74	90	93	87	78
12	77	81	82	93	98	88	82	76	93	93	88	76
13	74	84	81	102	96	89	86	79	92	95	93	77
14	82	83	82	110	94	89	86	83	95	95	99	76
15	86	33	84	111	—	93	85	92	93	94	95	76
16	84	86	86	119	82	95	84	90	91	91	99	76
17	87	87	94	114	93	98	84	89	78	91	94	78
18	94	91	98	110	91	97	82	85	86	89	88	83
19	99	108	116	109	97	98	80	83	84	87	89	84
20	107	107	118	109	103	96	80	84	84	88	86	86
21	112	114	127	112	106	90	79	82	83	87	81	85
22	111	121	128	113	—	90	80	80	81	85	79	82
23	116	136	130	108	—	86	78	79	82	84	77	79
24	114	134	126	105	110	87	78	79	82	89	80	79
25	115	129	128	101	112	90	74	77	84	87	77	—
26	115	129	118	100	110	92	76	75	84	87	77	—
27	115	136	117	100	108	93	74	73	84	86	75	—
28	115	122	109	96	105	91	74	72	83	82	74	74
29	109		103	93	104	—	73	72	86	80	75	—
30	101		99	91	105	—	72	72	90	82	77	—
31	102		92		—		73	75		81		—
MEAN	89.6	101.32	99.9	96.0	97.1	91.0	80.7	77.2	89.3	87.2	83.9	80.6

(*Continued*)

Table 16-13. Daily Values of Solar Power Flux Densities (10^{-22} W m^{-2} cps^{-1}) at 2800 Mcps (10.7 cm). Recorded at National Research Council, Ottawa, Canada. (Continued)

DAY	Jan	Feb	Mar	Apr	May	June	July	Aug	Sept	Oct	Nov	Dec
						1963						
1	—	87	74	73	82	84	75					
2	—	86	75	74	82	81	77					
3	77	85	78	74	81	81	80					
4	79	88	80	70	82	79	—					
5	77	87	82	72	84	78	78					
6	77	85	85	78	87	77	77					
7	77	83	84	80	88	84	76					
8	76	82	83	81	86	90	76					
9	78	79	82	82	88	93	77					
10	80	79	80	82	87	99	73					
11	81	76	78	88	84	103	—					
12	78	74	77	93	87	109	74					
13	79	74	74	89	89	107	75					
14	86	75	80	87	95	100	77					
15	85	76	80	88	98	96	76					
16	82	77	79	88	100	89	76					
17	82	79	79	87	100	86	75					
18	80	81	80	88	98	82	—					
19	78	79	77	84	99	79	76					
20	78	77	77	78	91	75	77					
21	76	74	76	74	88	73	—					
22	75	76	76	72	89	72	73					
23	74	75	75	71	93	72	73					
24	73	76	75	73	89	72	72					
25	74	78	75	72	83	74	—					
26	73	77	73	72	76	74	73					
27	81	75	74	75	80	72	74					
28	80	74	73	78	79	74	73					
29	79		75	78	80	73	77					
30	78		74	80	83	76	84					
31	82		73		89		85					
MEAN	78.4	79.1	77.5	79.4	87.6	83.5	76.8					

16.4 REFERENCES

Aboud, A., W. Behring, and W. Rense, 1959, "Emission-Line Intensities in the Solar Ultraviolet," *Astrophys. J.*, v. 130, p. 381.

Aldrich, L. B., and W. H. Hoover, 1954, The Solar Constant Since 1939, "Annals Astrophysical Observatory," v. 7, Chapter 2, Smithsonian Institution, Washington, D.C.

Boischot, A., 1958, "Etude du Rayonnement Radioélectrique sur 169 MHz, a l'aide d'un Grand Interferometre a Réseau," *Annales D'Astrophysique*, v. 21, p. 273.

Castelli, J. P., 1962, "Solar Flux Measurements, April 1962, and Antenna Considerations," *Air Force Cambridge Research Laboratories Research Note*, AFCRL-62-1111.

Christiansen, W. N., and J. A. Warburton, 1955, "The Distribution of Radio Brightness over the Solar Disk at a Wavelength of 21 cm," *Australian J. Phys.*, v. 8, p. 474.

Chubb, T. A., H. Friedman, R. Kreplin, R. L. Blake, and A. E. Unzicker, 1961, "X-ray and Ultraviolet Measurements during the Eclipse of October 12, 1958; X-ray Solar Disk Photograph," *Mem. Soc. Roy. Sci. Liége*, 5e Ser., Tome IV, Institut D'Astrophysique, Cointe-Sclessin, Belgique.

Covington, A. E., 1961, "Solar Emission at Ten Centimeter Wavelength, 1947-1960," *J. Royal Astron. Soc. Canada*, v. 55, p. 172.

C.S.I.R.O. *Quarterly Bulletin on Solar Activity*, Radio Physics Laboratory, Sydney, Australia.

Fokker, A. D., 1963, Summary of Discussion on Type IV Radio Emission, "The Solar Corona," ed. J. W. Evans, Academic Press, New York.

Friedman, H., 1961, X-Ray and Ultraviolet Radiation Measurements from Rockets, "Space Astrophysics," ed. W. Liller, McGraw-Hill Book Co., Inc., New York.

Hall, L., K. Damon, and H. Hinteregger, 1962, "Solar Extreme Ultraviolet Photon Flux Measurements in the Upper Atmosphere of August 1961," *Space Research III*, Proceedings of Third International Space Science Symposium, W. Priester, ed., North Holland Publishing Co., Amsterdam.

Hinteregger, H. E., and L. A. Hall, 1965, "Solar Extreme Ultraviolet Radiation and Neutral Particle Distribution in July 1963 Thermosphere," *Space Research V*, Proceedings of the Fifth International Space Science Symposium, North Holland Publishing Co., Amsterdam.

IGY, 1958, Radiation Instruments and Measurements, "Annals of International Geophysical Year, Vol. III," Pergamon Press, New York.

Johnson, F. S., 1954, "The Solar Constant," *J. Meteorol.*, v. 11, no. 6, p. 431.

Ko, H. C., 1961, "On the Determination of the Disk Temperature and the Flux Density of a Radio Source Using High Gain Antennas," *IRE Transactions on Antennas and Propagation*, v. AP-9, no. 5.

Kundu, M. R., and F. T. Haddock, 1961, "Centimeter-Wave Solar Bursts and Associated Effects," *IRE Transactions on Antennas and Propagation*, v. AP-9, no. 1.

Kundu, M. R., J. A. Roberts, C. L. Spencer, and G. P. Kuiper, 1961, "A Comparison of the Dynamic Spectra of Solar Radio Bursts in the Decimeter and Meter Wavelength Ranges," *Astrophys. J.*, v. 133, p. 255.

McAllister, H. C., 1960, *A Preliminary Photometric Atlas of the Solar Ultraviolet Spectrum from 1800 to 2965 Å*, University of Colorado Printing Services.

NBS, "Solar Geophysical Data," *Monthly Bulletin of the Central Radio Propagation Laboratory*, CRPL series F, National Bureau of Standards.

Pawsey, J. L., and S. F. Smerd, 1953, Solar Radio Emission, "The Sun," G. P. Kuiper, ed., University of Chicago Press.

Sterne, T. E., and N. Dieter, 1958, "The Constancy of the Solar Constant," *Smithsonian Contribution to Astrophysics*, v. 3, no. 3, p. 9.

Violett, T., and W. Rense, 1959, "Solar Emission Lines in the Extreme Ultraviolet," *Astrophys. J.*, v. 130, p. 954.

Wild, J. P., 1963, "Fast Phenomena in the Solar Corona," "The Solar Corona," J. W. Evans, ed., Academic Press, New York.

Chapter 17

CORPUSCULAR RADIATION

C. Dubs
R. Filz
L. Katz
D. Smart
A. Weinberg
K. Yates

This chapter outlines current knowledge of corpuscular radiation in the vicinity of earth; this includes the charged particles trapped in the geomagnetic field, cosmic radiation, and high-energy solar particles associated with solar flares. The trapped radiation cannot yet be specified as a function of position, direction, energy, and time with desirable accuracy. Primary cosmic rays of energies about 1 to 10^9 GeV, their interactions with the geomagnetic field and the atmosphere, and the secondary radiations resulting from these interactions are fairly well known. The sources, acceleration mechanisms, diffusion through space, and solar modulation processes are not well understood. The prediction of the occurrence of high-energy solar particle emission and of the characteristics of corpuscular radiation emitted during solar flare events is still an unsolved problem.

17.1 BASIC RELATIONS

17.1.1 Nomenclature and Definitions

Corpuscular radiation is usually characterized by the energy of the particle in electron volts. (The international symbol for 10^9 eV, now adopted by the U.S. Bureau of Standards, is GeV, rather than BeV.) The total energy is the sum of the kinetic energy, E_k, plus rest-mass energy,

$$E_T = E_k + m_o c^2 = mc^2, \qquad (17\text{-}1)$$

where m_o is the rest mass, m the relativistic mass, and c the speed of light in vacuo. For the proton, $m_o c^2$ is 938 MeV; for the electron, $m_o c^2$ is 0.511 MeV. It is customary in the literature to give values of the energy per nucleon for heavier particles.

The total energy is related to the particle momentum, p, by

$$E_T = (p^2 c^2 + m_o^2 c^4)^{1/2}. \qquad (17\text{-}2)$$

In the absence of electric fields and of time-varying magnetic fields, E_T and p are constants of the particle's motion. In cosmic ray physics the momentum is often given in units of eV/c.

Observations of the intensity of corpuscular radiation are reported in various units depending upon the detection method. The *unidirectional differential intensity*, J(E), is the flux (number per unit time) of particles of a given energy per unit energy interval in a unit solid angle about the direction of observation, incident on a unit area perpendicular to the direction of observation; the units are usually particles cm^{-2} sec^{-1} sr^{-1} MeV^{-1}. *Unidirectional integral intensity*, J (>E), is the intensity of particles with energy greater than a threshold energy, E,

$$J(>E) = \int_E^\infty J(E)\,dE. \qquad (17\text{-}3)$$

Omnidirectional intensities are J(E), or J (>E), integrated over 4π solid angle.

The *differential energy spectrum* is J(E) plotted against E. The *integral energy spectrum* is J (>E) plotted against E. J(E) and J (>E) sometimes can be expressed as a power law;

$$J(E) \approx J_o E^{-\gamma}, \qquad (17\text{-}4)$$

$$J(>E) \approx J_o(\gamma - 1)^{-1} E^{-\gamma+1}, \qquad (17\text{-}5)$$

where $\gamma > 1$.

Observations of counts per unit time or of ionization rates are often difficult to interpret and convert to J(E) or J (>E). When considerations of the effects of corpuscular radiation on personnel are of primary concern, intensities or counting rates must be converted to dose or dose rates. The rad is the unit of absorbed dose; one rad is 100 erg absorbed per gram of absorbing material. Conversion of observed particle fluxes to absorbed dose rate, however, is not straightforward and is sometimes impossible for lack of necessary details; the conversion depends in a complex way on the energies and kinds of particles and on geometrical configurations of the absorbers and direction of the incident beam, as well as on the different absorbing properties of materials.

The *magnetic rigidity*, P, of a particle is a measure of its resistance to a magnetic force that deflects the particle from a straight-line trajectory. The rigidity is defined as

$$P = pc/q, \tag{17-6}$$

where q is the charge of the particle. If pc is in electron volts, then q is the number of electronic charge units and P is in volts. The geomagnetic field acts as a magnetic analyzer, removing charged particles of low rigidity from the flux incident at the top of the atmosphere; particles of progressively lower rigidity are detected as the distance north or south of the geomagnetic equator increases. The *cutoff* or *threshold rigidity* of cosmic rays is the minimum rigidity that permits entry of a charged particle arriving from a given direction into the earth's atmosphere at a given latitude and longitude; particles of lower rigidity are not observed because of this geomagnetic cutoff.

At a given location on the surface of the earth, only those cosmic ray particles that arrive from certain specific directions with respect to the station can be detected. These allowed directions form the *asymptotic cone of acceptance*; for asymptotic cones of acceptance of various cosmic ray stations see McCracken [1962.]

17.1.2 Trapped Particle Motion in a Magnetic Field

Figure 17-1 illustrates the motion of a charged particle trapped in a magnetic dipole field. The particle is confined to the surface of a tube of magnetic lines of force, moving in a quasi-helical path with a rotational period τ_1, and oscillating back and forth between mirror points with a period τ_2. The *pitch angle*, α, is the angle between the momentum vector, p, and the magnetic vector, B; at the mirror point, α is 90°. The particle also rotates slowly around the earth with an azimuthal drift period τ_3. In the geomagnetic field the orders of magnitude of the periods are: τ_1 for electrons, 10^{-6} sec; τ_1 for protons, 10^{-3} sec; τ_2 for electrons and protons, 1 sec; τ_3 for electrons and protons, 10^3 sec.

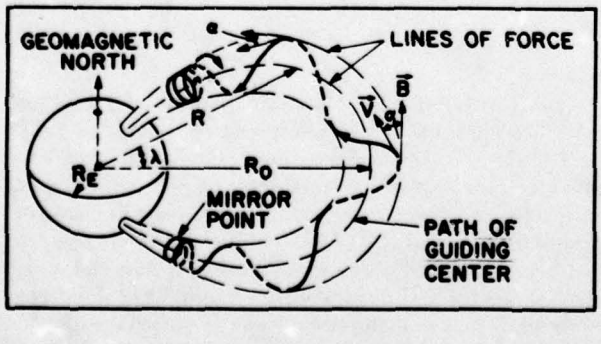


Fig. 17-1. Diagram of the simplified motion of a charged particle trapped in a magnetic dipole field; azimuthal drift is ignored. V is the particle velocity, B the magnetic induction vector of the dipole field, and α is the pitch angle. (After Singer and Lenchek [1962].)

The period τ_1 is the reciprocal of the gyrofrequency (cyclotron frequency). τ_1 is $2\pi\, m/qB$ or $2\pi\, E_T/c^2qB$; in mixed CGS (Gaussian) units, τ_1 is $2\pi\, E_T/cqB$. In the absence of an electric field, the magnitude of the momentum, $|p| = p$, is constant. The radius of gyration, r_g, is $(p \sin \alpha)/qB$ [in Gaussian units, $(pc \sin \alpha)/qB$]. Because geomagnetic lines of force converge toward the poles, the particle penetrates regions of increasing magnetic flux density as it leaves the equatorial region. It is repelled by a force that depends upon r_g and gradient B, so that the component of momentum parallel to the magnetic line of force, p cos α, decreases and becomes zero ($\alpha = 90°$) at the mirror point. The particle then spirals back to regions of lower magnetic flux density.

If the spacial and temporal variation of the magnetic field is not too rapid ($r_g |\text{ grad B}| << B$ and $\tau_1\, dB/dt << B$), the path can be considered a circular motion about a center that moves along the line of magnetic force perpendicular to the circle and located at its center; this center is the *guiding center*. The rotating charge generates a *magnetic moment* parallel to B and of magnitude $r_g^2B\,(q^2c^2/2E_T)$, or $p^2c^2 \sin^2 \alpha/2E_TB$. The repelling force is the product of this magnetic moment and dB/ds, where ds is the element of length along the guiding center path. Under the conditions of slow variation for which the guiding center approximation is valid, the magnetic moment is constant; it is called the *first adiabatic invariant*. For a constant magnetic moment (constant magnetic flux through the area $\pi\, r_g^2$),

$$B_m = B/\sin^2 \alpha, \tag{17-7}$$

where B is the magnetic field at a position where the pitch angle is α, and B_m is the field at the mirror point. B_m depends only on the initial conditions of the particle direction and the magnetic field; it is independent of particle charge, mass, and energy.

The *longitudinal invariant*, or *second adiabatic invariant*, is

$$J_a = \int_{s1}^{s2} p \cos \alpha \, ds, \tag{17-8}$$

where ds is the element of path length of the guiding center from one mirror point, s1, to its conjugate, s2. From Eq. (17-7) and (17-8)

$$I = J_a/p = \int_{s1}^{s2} [1 - (B/B_m)]^{1/2}\, ds. \tag{17-9}$$

I is the invariant used in establishing the magnetic shell parameter L (Sec. 17.2.1). I is assumed to be conserved if there is no perturbation in the guiding magnetic line of force in a time comparable to τ_2.

The *bounce period*, τ_2, is the time of travel from one mirror point to the other and back;

$$\tau_2 = 2 \int_{s2}^{s1} \frac{E_T\, ds}{c^2 p \cos \alpha}. \tag{17-10}$$

In principle, the complete motion in a dipole field may be calculated to any desired degree of accuracy (for proofs and derivations, see Northrup [1963]). For example, the drift (east for negative charges and west for positive) can be calculated from the combined inertial force and the force due to the gradient of the magnetic field. In practice, however, the deviation of the main geomagnetic field from a true dipole is such that it is expedient to make an approximate calculation of useful parameters from an experimentally fitted harmonic expansion of the earth's field (Sec. 11.2.2).

17.2 TRAPPED RADIATION

Trapped energetic charged particles were detected in 1958 by measurements from Geiger tubes on Explorer I and III. The primary difficulty with the interpretation of the earliest observations and of most data obtained with counters is the lack of exact knowledge of the nature of the radiation counted. Results obtained with nuclear emulsions, where an electron cannot be confused with a proton are relied on to help interpret such data. This difficulty can be overcome under steady-state conditions by making numerous measurements with different devices. When time or spacial variations occur, it is not clear whether the variation is in intensity, composition, energy spectra, or a combination of these. Only since late in 1962 have counters been flown that are sufficiently sophisticated to supply observational data capable of unique interpretation of the particle specie and energy.

17.2.1 Spatial Parameters of Trapped Particles

In order to determine and describe the trapping regions, a two-parameter convention, which identifies the various regions wherein particles are contained, has evolved. These parameters are based on the guiding center approximation. The rapid (τ_1) motion perpendicular to the field lines is ignored. The slower (τ_3) azimuthal motion around the earth may be treated as a perturbation of the guiding center motion. If the drift is ignored, the guiding center moves along one magnetic line of force. Figure 17-1 shows this guiding center path, the lines of magnetic force, and the reflection (mirroring) from one hemisphere to the other.

For any given azimuthal angle, two parameters suffice to describe the motion. Two such parameters (by no means the only possible ones) are B_m, the scalar magnetic field at the point where the particle is reflected, and R_o, the maximum excursion of the guiding center trajectory (i.e., the magnetic field line) from the center of the geomagnetic field. Because B_m is an adiabatic invariant of the particle motion, it is a useful parameter with an obvious physical meaning. However, R_o is not an invariant. Due to the azimuthal asymmetry of the geomagnetic field, R_o for a given particle can vary as much as 10% as the particle drifts around the earth. The variation depends not only on the initial value of R_o and the azimuthal angle, but also on B_m.

A second adiabatic invariant, the longitudinal invariant I (Eq. 17-9), is available; but I does not have a clear physical or geometrical meaning. In a pure dipole field with moment M, R_o is determined by B_m and I; $R_o^3 B_m/M = F(I^3 B_m/M)$. In the geomagnetic field this relation does not hold. McIlwain [1961] replaced R_o by L and defined this new parameter by the relation

$$L^3 B_m/M = F(I^3 B_m/M), \qquad (17\text{-}11)$$

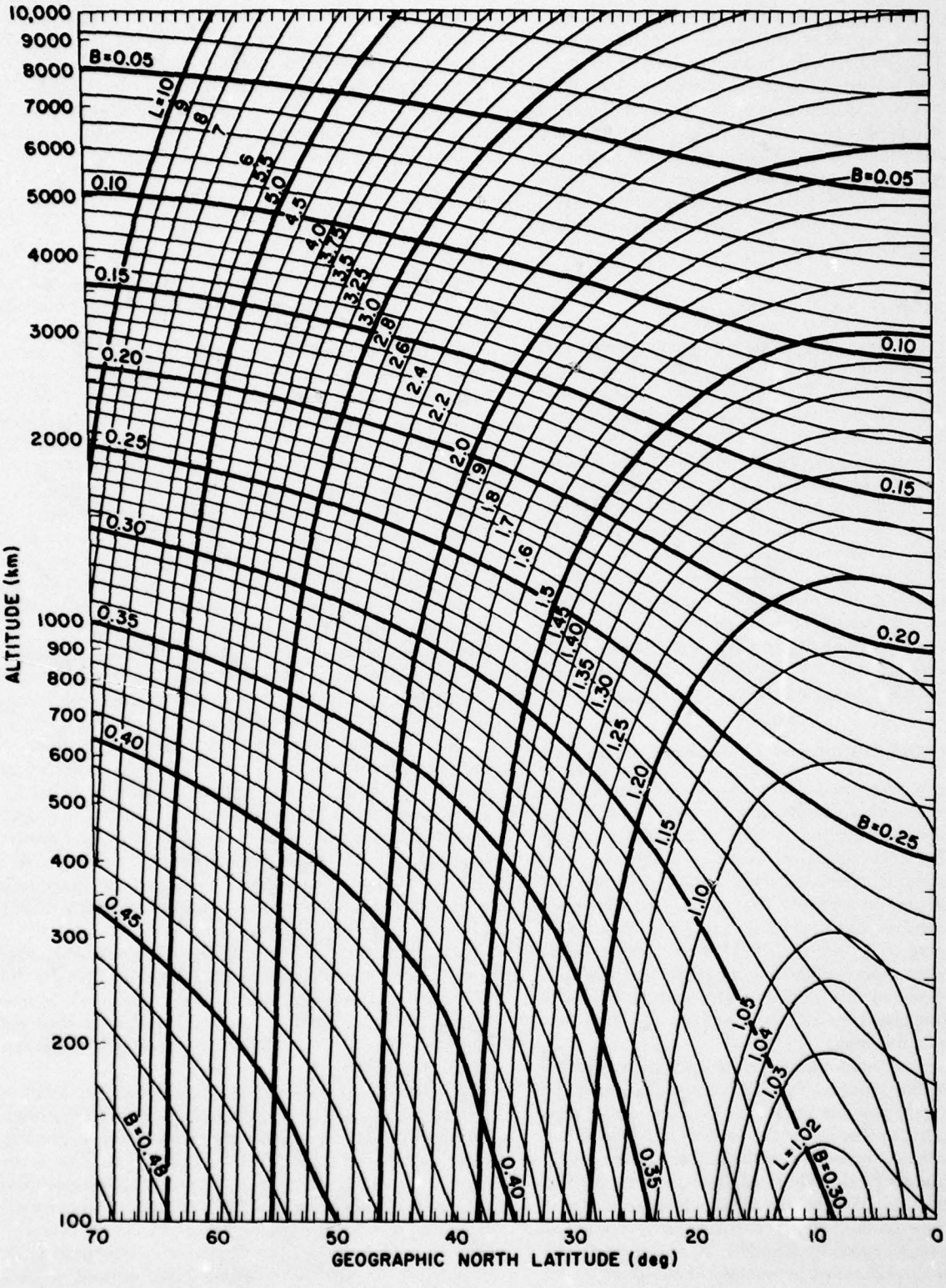
where $M = 0.311653$ gauss-R_E^3 (R_E is the earth's radius). Table 17-1 gives sets of values for the function $F(I^3 B_m/M)$.

For particles traveling along a given field line, the L value depends only slightly on where the particles mirror. Because the geomagnetic field is nearly a dipole, $L \approx R_o$; thus, L has an approximate geometrical meaning. L can be calculated for any part of the geomagnetic field of interest; therefore, L and B_m are used extensively to describe the trapping regions.

It is implicit in the definition of L that the value of L at any given point in space is an adiabatic invariant of the motion of those particles which mirror at the given point [Stone, 1963]. All particles passing through the point do not in general have that particular value of L, but they do have L values within a few percent of it. The locus of all points with a given L value is called an L-shell. All particles with a particular L must mirror on the corresponding L-shell, but their motion may otherwise deviate from the shell by distances equal to a few percent of L. From a practical standpoint, the accuracy of measurements has not progressed to a point where these deviations from an L-shell are significant, but ignoring them has led to confusion as to the significance of L. As more precise data become available, these details will assume greater importance. Figure 17-2 shows contours of constant L and B at zero geographic longitude. (Values of the magnitude of B at various altitudes and locations are given in Fig. 11-9 and 11-15 through 11-22.)

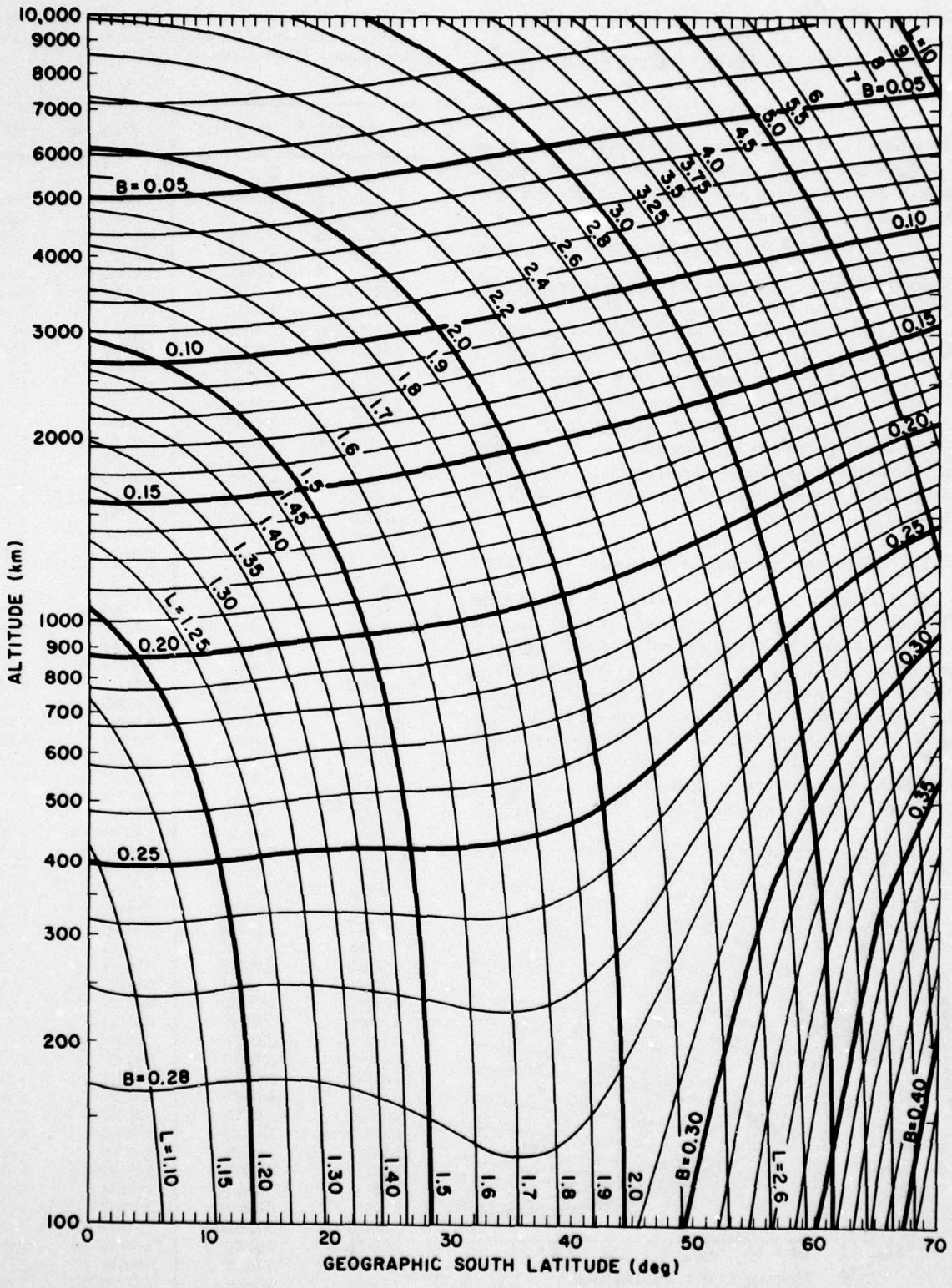
The pitch angle at the geomagnetic equator is used sometimes as a more convenient parameter than B_m for interpreting results. In practice, the value of L is also calculated at the equator. The equatorial value does not correspond exactly to L at the mirror point, but is accurate to a few percent.

A coordinate system useful in obtaining an intuitive feeling for experimental results, as well as in the interpretation of data, effectively transforms the real geomagnetic field into a pure dipole representation. This is accomplished by substituting for B and L in the equations for a pure dipole field, the B and L of the real geomagnetic field. The coordinates are the distance from the center of the dipole, R, and the *equivalent geomagnetic latitude*, λ. This dipole is not the centered dipole defined in Sec. 11.2.2.1, and λ is not the geomagnetic latitude used in Sec. 17.3; values are similar but not identical. The R, λ coordinates are obtained for any point in real space by calculating values of B and L for the main geomagnetic



(a)

Fig. 17-2. Lines of constant L (earth radii) and B (gauss) are zero geographic longitude as a function of geographic latitude and altitude. (From Aerospace Corp. Rept. No. TDR 169 (3510-41) TR-4, Contract AF04(695)-169.)



(b)

Fig. 17-2. Lines of constant L (earth radii) and B (gauss) are zero geographic longitude as a function of geographic latitude and altitude. (From Aerospace Corp. Rept. No. TDR 169 (3510-41) TR-4, Contract AF04(695)-169.)

field, and substituting these values in the following equations:

$$R^6 + (3M^2/LB^2)\,R - 4M^2/B^2 = 0, \quad (17\text{-}12)$$

and

$$\cos^2 \lambda = R/L, \quad (17\text{-}13)$$

where R and L are in earth radii and M is 0.311653 gauss-R_E^3. Equation (17-12) must be solved numerically, but when R and λ are specified, L is obtained directly from Eq. (17-13), and B from

$$B = M\,(4 - 3\cos^2 \lambda)^{1/2}/R^3. \quad (17\text{-}14)$$

Figure 17-3 shows the relation between parameters B_m and L and the coordinates R and λ.

In the R, λ coordinate system the spherical earth takes on an irregular shape. Essentially, these coordinates distort the geographic coordinates in such a way that the geomagnetic field appears as a pure dipole; the surface $R = 1$ in this coordinate system, referred to as the invariant earth, has no relationship to the earth's geoid. The true surface, the invariant surface, and a 1000-km polar orbit for 0° longitude in the R, λ system are included in Fig. 17-9 for comparison.

17.2.2 Injection and Loss of Particles

The mechanism by which low-energy protons and the electrons of all energies are injected into the trapping region is not completely understood at present. The *neutron albedo hypothesis* explains the presence of some of the high-energy protons in the radiation belt. High-energy neutrons are created in the upper atmosphere by the interaction of cosmic rays. Because of the 12-min mean lifetime of the free neutron, a small number of neutrons will decay into a proton, an electron, and an antineutrino within the geomagnetic field, thus directly injecting pro-

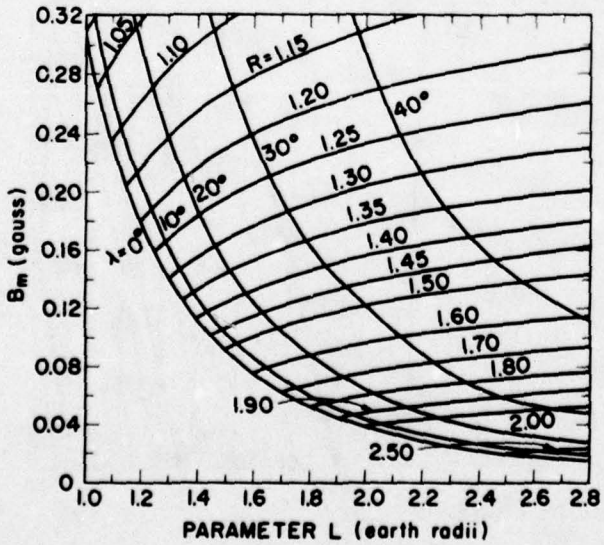


Fig. 17-3. Transformation of polar coordinates R (earth radii) and λ (degree) to parameters B_m and L, according to Eq. (17-8) and (17-9). (From McIlwain [1961].)

Table 17-1. Values for Eq. (7-11); plus and minus numbers indicate power of ten by which the entry and succeeding entries should be multiplied. (From McIlwain [1961].)

$I^3\,B_m/M$	$L^3\,B_m/M$	$I^3\,B_m/M$	$L^3\,B_m/M$
2.37529 −15	1.00002 0	7.78642	5.87648
1.72697 −12	1.00016	9.12680	6.28994
3.70298 −11	1.00045	1.07055 +1	6.74720
2.37086 −9	1.00180	1.25680	7.25432
2.70390 −8	1.00406	1.47699	7.81840
1.52215 −7	1.00722	1.73787	8.44781
5.82114	1.01131	2.04766	9.15245
1.74352 −6	1.01632	2.41655	9.94413
4.41257	1.02228	2.85705	1.08369 +1
9.87364	1.02919	3.38471	1.18478
2.01130 −5	1.03707	4.01899	1.29973
3.80506	1.04596	4.78427	1.43104
6.78113	1.05585	5.71146	1.58179
1.15049 −4	1.06680	6.83985	1.75576
1.87314	1.07881	8.21991	1.95767
2.94482	1.09194	9.91695	2.19347
4.49250	1.10620	1.20162 +2	2.47069
6.67702	1.12165	1.46301	2.79896
9.69961	1.13832	1.79085	3.19079
1.38095 −3	1.15626	2.20532	3.66255
1.93121	1.17553	2.45179	3.93495
2.65795	1.19618	2.73402	4.23601
3.60595	1.21827	3.05069	4.56967
4.82943	1.24187	3.41513	4.94049
6.39281	1.26706	3.82642	5.35387
8.37277	1.29392	4.30241	5.81615
1.08602 −2	1.32252	4.84311	6.33486
1.39624	1.35298	5.47285	6.91896
1.78056	1.38538	6.19343	7.57921
2.25380	1.41985	7.03884	8.32855
2.83332	1.45650	8.01427	9.18267
3.53938	1.49547	9.16824	1.01607 +2
4.39567	1.53691	1.05125 +3	1.12862
5.42973	1.58097	1.21182	1.25883
6.67358	1.62782	1.40095	1.41032
8.16455	1.67767	1.62942	1.58767
9.94598	1.73070	1.90201	1.79669
1.20681 −1	1.78716	2.23574	2.04483
1.45893	1.84729	2.64005	2.34175
1.75772	1.91135	3.14300	2.70014
2.11103	1.97966	3.76361	3.13689
2.52798	2.05255	4.55081	3.67477
3.01912	2.13036	5.54426	4.34504
3.59672	2.21352	6.83524	5.19133
4.27504	2.30245	8.51087	6.27578
5.07058	2.39766	1.07567 +4	7.68892
6.00263	2.49967	1.37789	9.56603
7.09352	2.60911	1.79974	1.21153 +3
8.36934	2.72664	2.39555	1.56683
9.86054	2.85300	3.27489	2.07743
1.16025 0	2.98905	4.60402	2.83877
1.36367	3.13571	6.73169	4.02645
1.60116	3.29403	1.02942 +5	5.98740
1.87843	3.46520	1.67841	9.47159
2.20216	3.65056	2.96984	1.63048 +4
2.58020	3.85161	5.95512	3.17247
3.02183	4.07005	1.44453 +6	7.49153
3.53799	4.30783	5.00559	2.51887 +5
4.14164	4.56716	1.47748 +7	7.32706
4.84816	4.85057	4.09266	2.00752 +6
5.67587	5.16095	1.91226 +8	9.28013
6.64657	5.50164	6.50554	3.12969 +7
		5.20779 +9	2.50188 +8

tons and electrons into the trapping region. This source is small and requires long lifetimes (about 100 yr) to produce present intensities of trapped protons. Such long lifetimes are thought to exist for protons which mirror significantly above the sensible atmosphere and do not have excessively high energy [Singer and Lencheck, 1962].

There are several other possible sources of trapped particles (e.g., scattered cosmic rays, or local acceleration and diffusion across magnetic field lines of solar corpuscular radiation), but the present lack of sufficiently accurate calculations precludes checking these hypotheses for their consistency with observations.

There are two important mechanisms by which trapped particles escape: loss due to interaction of trapped particles with the atmosphere, and loss due to failure of the magnetic trapping mechanism. (Magnetic deceleration is assumed to be unimportant.) Atmospheric interaction losses generally occur in the region in which a particle mirrors. Collision with atmospheric particles decreases the trapped particle's energy by ionization loss. Catastrophic loss is a collision in which the trapped particle scatters directly into the atmosphere or loses most of its energy. Small-angle scattering lowers the mirror point of any particle that is at or very near its mirror point.

Loss in the outer regions of the trapping zone appears to be caused by failure of the trapping mechanism due to nonadiabatic effects. This failure can result from the deviation of the geomagnetic field from a pure dipole, or from geomagnetic disturbances due to solar effects (Sec. 11.4.2). The breakdown of the trapping mechanism is presumed to limit the energy of a proton that can be trapped for long periods at high altitudes. Figure 17-4 shows the relation between maximum proton energy and the magnetic shell parameter as obtained from experimental data and as calculated by considering breakdown of the trapping mechanism.

17.2.3 Measurements of Naturally Occurring Trapped Radiation

For convenience of discussion, the naturally occurring trapped electrons and protons are separated into three regions:

(a) The lower region, where particles spend an appreciable time within the upper atmosphere, is the lower edge of the inner Van Allen belt.

(b) The middle region, where particles rarely interact with the atmosphere and large temporal variations in the magnetic field do not occur, contains the heart of the inner Van Allen belt.

(c) The outer region, where the effect of magnetic storms is significant and particles which come from the sun during solar flares may be trapped (at least temporarily), is the outer Van Allen belt.

Complete measurements of the natural radiation were not obtained prior to the detonation of a high altitude thermonuclear device (9 July 1962) that changed the electron flux considerably. Because of the long lifetime of particles in the middle region, it will be impossible for some years to observe only the naturally occurring electrons trapped in this region. No source of high energy protons is expected from a thermonuclear detonation, so it is usually assumed that proton fluxes measured in the middle region are entirely of natural origin. There was, however, some effect on the trapped protons in the lower region, as evidenced by a number of measurements; for example, see Filz et al [1964].

17.2.4 Protons

Measurements of the energy spectrum of protons were obtained from nuclear emulsions recovered from rockets and satellites. The most reliable emulsion results available prior to July 1962 are those of Naugle and Kniffen [1961] in which it was possible to obtain the energy spectra of protons at different points of a rocket trajectory by rotating a cylindrical stack of emulsions past a thin window. Figure 17-5 shows the trajectory in R, λ coordinates relative to flux density contours of the inner Van Allen belt. Figure 17-6 gives the differential energy spectra of protons in the energy range 15 to 300 MeV at five different locations in the lower region; L values are between 1.79 and 1.47 R_E. Table 17-2 lists proton intensities determined from emulsions and counter measurements at the same locations.

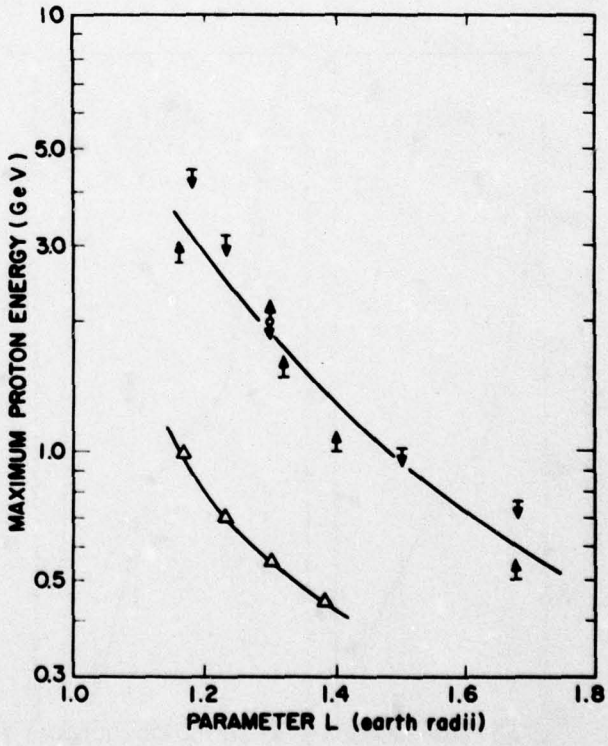


Fig. 17-4. Maximum proton energy as a function of the magnetic shell parameter, calculated from breakdown of the trapping mechanism (upper curve) and from Explorer XI observations (lower curve). (From G. Garmire, *J. Geophys. Res.*, v. 68, no. 9, p. 2627, 1963.)

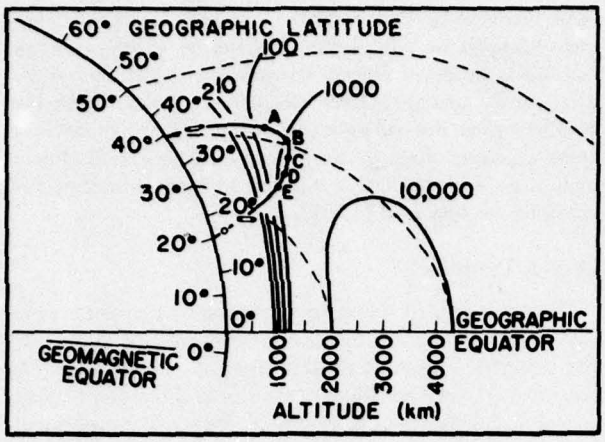


Fig. 17-5. Trajectory of emulsion package, flown on 19 September 1960, in relation to the geomagnetic field lines (dashed curves) and contours of the inner Van Allen belt (solid curves). Numbers (protons cm^{-2} sec^{-1}) on contours are protons with energy $\geqq$ 31 MeV. (After J. E. Naugle and D. A. Kniffen, NASA, GSFC-X-611-63-35.)

Table 17-2. Intensities of protons with energies $\geqq$ 31 MeV from observations with emulsions (Fig. 17-5 and 17-6) and counters (satellite data, McIlwain, private communication).

			Intensity		
			(protons cm^{-2} sec^{-1} sr^{-1})	(protons cm^{-2} sec^{-1})	
Location	L (R_E)	B (gauss)	Emulsion	Emulsion	Counter
A	1.79	0.231	90	440	220
B	1.72	0.198	180	1160	1000
C	1.64	0.196	220	1360	1600
D	1.54	0.209	230	1230	1290
E	1.47	0.223	250	1000	390

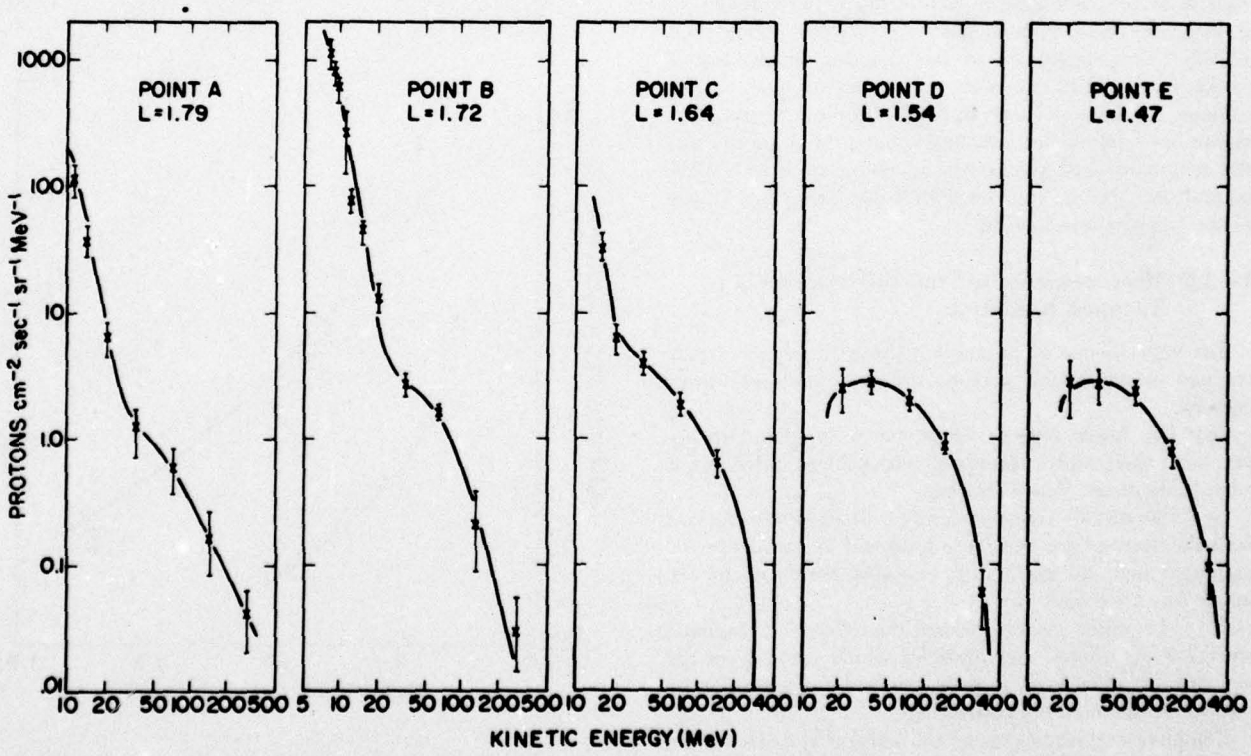


Fig. 17-6. Differential energy spectra of protons from emulsion package flown on 19 September 1960; L values are in earth radii. Locations of points A through E are shown in Fig. 17-5. (NERV data from J. E. Naugle and D. A. Kniffen, NASA, GSFC-X-611-63-35.)

There is an indication of a drop out at the low energy end for the two lowest L values. Lencheck [1962] interprets this on the basis of the neutron albedo theory of trapped proton origin. Assuming that the high-energy portion of the spectrum results from the decay of neutrons produced from galactic cosmic rays and that the ultimate source of the low-energy portion is solar cosmic rays, the preferred incidence of the solar cosmic rays to high latitude would limit the protons produced by neutron decay from this source to the higher L-shells. For high altitudes (low B), the lifetimes of these low-energy protons will be long; thus, large transients will not be expected following solar flares. For low altitudes, where lifetimes are short, transients should occur following solar flares. This may be the cause of some of the variations reported by Pizzella et al [1962].

Figure 17-7 shows recent observations of the directional intensity of low-energy protons; the flux of locally mirroring protons is plotted as a function of the magnetic induction for various magnetic shells. The intensity and the spacial distribution of these low-energy protons are not that predicted by the polar-cap neutron albedo hypothesis. Figure 17-8 gives directional proton intensities at the geomagnetic equator as a function of L for various energy ranges. It shows a secondary peak that is a higher energy proton phenomena. Detailed comparison of counting rates from Relay I [Fillius and McIlwain, 1964] shows that the softest spectrum occurs at $L = 1.9$ and that the spectra become harder toward higher L values.

Figure 17-9 shows contours of constant intensity of trapped protons in the energy range 40 to 110 MeV. There are protons of this energy present outside of the region

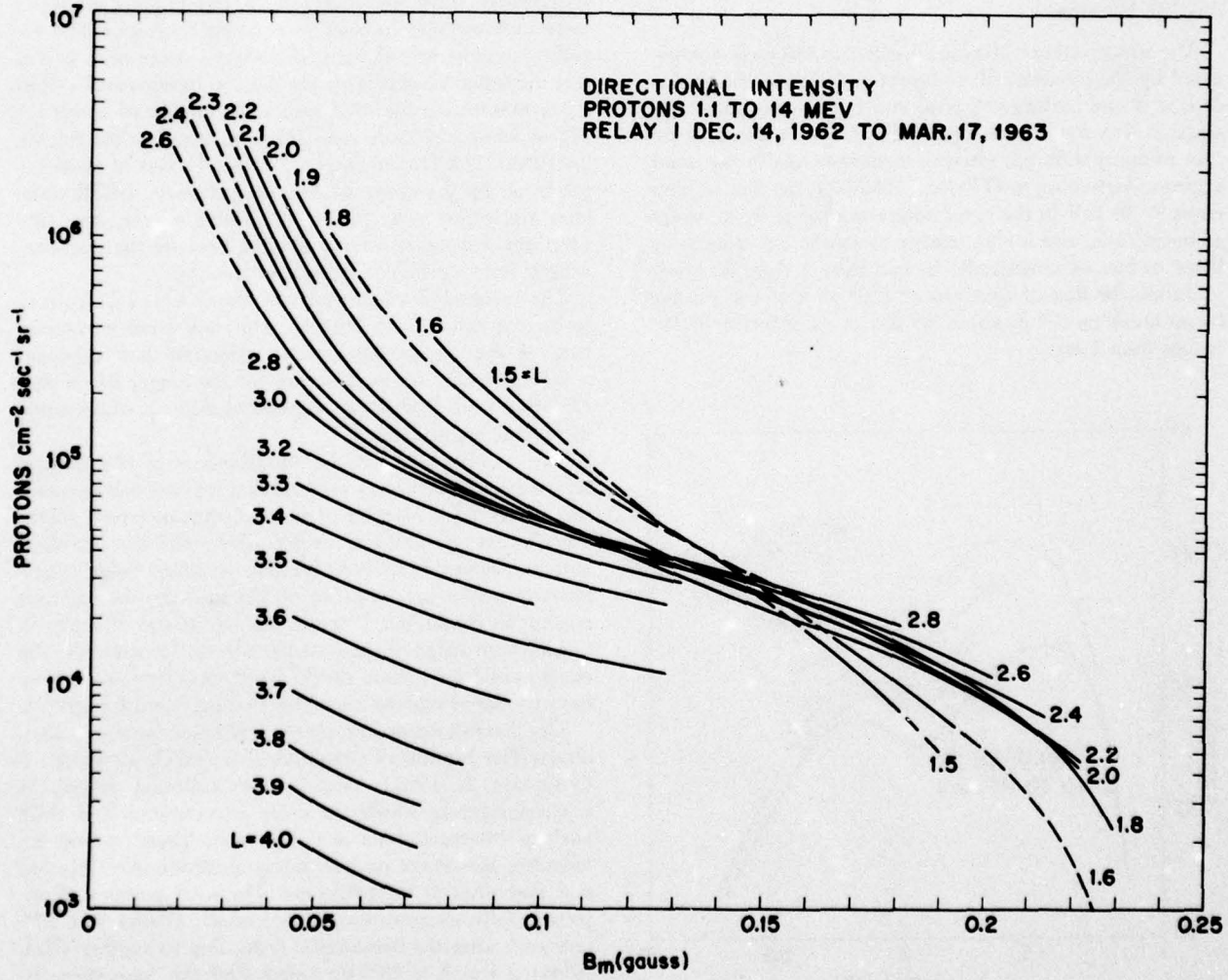


Fig. 17-7. Intensities of locally mirroring protons in various magnetic shells; dashed lines are extrapolated or interpolated. The magnetic equator is the minimum value of B_m for the particular L value except for $L = 2.1$ and 1.9 earth radii; these are not extrapolated to their minimum B_m. (From Fillius and McIlwain [1964].)

shown, but the intensity is below the detector threshold. From nuclear emulsions flown in low polar orbiting satellites, it has been determined that, over the South Atlantic magnetic anomaly, measurable fluxes of trapped protons exist as low as about 300 km above the earth's surface. The time history, between 30 August 1961 and April 1963, of protons was followed on emulsions carried on recoverable satellite capsules. Figure 17-10 shows the relative flux of 55 MeV protons observed over this time span; there is no detectable variation from August 1961 through June 1962. Preliminary data on higher energy protons, however, indicate a possible slow increase over this period. Such an increase is predicted because during this period the atmospheric density in this altitude region decreases as the 11-yr sunspot cycle approaches minimum (Sec. 3.6.2). A definite peak in the proton flux follows the 9 July 1962 and the October nuclear detonations.

17.2.5 Electrons

The measurement of natural electron fluxes is complicated by the presence of high-proton fluxes in the region of $L < 2$ and by large spectral and time variations of the electron flux for $L > 2$. Figure 17-11 shows a consolidation of many different electron measurements in the outer regions. According to O'Brien [1962-63], the flux of electrons ≥ 40 keV in the outer zone can change by an order of magnitude, and higher energy electrons can change by three orders of magnitude, in less than a day. At lower altitudes, the flux of electrons of $E \geq 40$ keV can change by as much as 10^6 in about 30 sec, or by a factor of 10^3 in less than 1 sec.

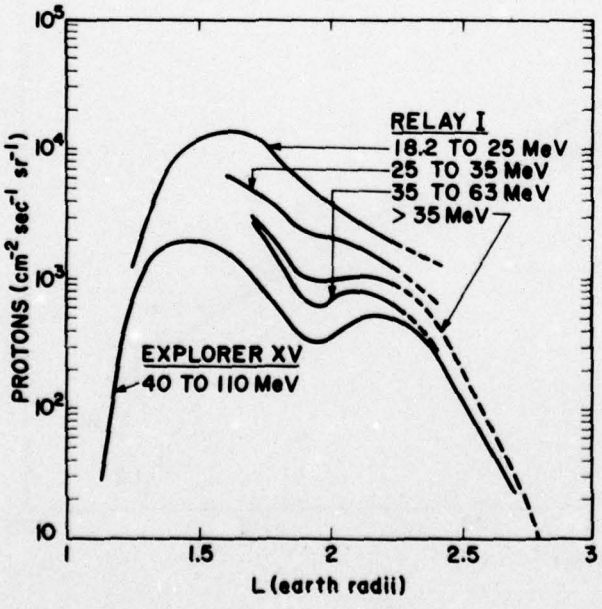


Fig. 17-8. Directional intensities of protons mirroring at the magnetic equator; observations from Relay I compared to Explorer XV. (After Fillius and McIlwain [1964].)

Figure 17-12 shows the large differences in integral energy spectra of electrons for various regions of space; characteristic spectral shapes for the inner and outer belts are also evident. Figure 17-13 shows the variation in the differential energy spectra of lower energy electrons for various L-values. Figures 17-14 and 17-15 are contour maps of measurements in November 1962. Figures 17-12 through 17-15 must be used with care, because they are from measurements of the combination of natural and artificially produced electrons.

17.2.6 Man-Made Trapped Radiation

In the Argus nuclear tests (1959), electrons were deliberately injected into the magnetosphere by detonating a kiloton nuclear device at a few hundred km altitude over the South Atlantic. (Reexamination of data in the light of current knowledge provides evidence that, during the August 1958 weapons test in the Pacific, electrons were unknowingly injected into trapped orbits.) The resulting narrow belt of trapped electrons decayed so that it was indistinguishable from the natural background within a few months. In the 1962 tests a detonation of about 1.4 MT at 400-km altitude over Johnson Island in the Pacific on 9 July 1962 (called Starfish) created a belt of electrons produced by the decay of fission fragments. USSR tests, later the same year, produced similar effects, but they were not detectable after 6 months because the electrons were injected at higher latitude at $L \approx 1.8$.

The residual Starfish shell (at about $L = 1.2$) proved to have a rather long lifetime, although from extrapolation of the Argus data, many scientists had expected a short lifetime. An explanation for the longer life is that electrons were injected in equatorial regions where some have pitch angles near 90°.

The number and spacial distributions of the natural trapped electrons are so variable that it is difficult to establish firmly what fraction of the electrons observed subsequently are of artificial origin. The difficulty increases with increasing L number because transient solar events have an increasing influence on the total natural electron content in the higher L shells. An additional difficulty is lack of knowledge of the possible effects; for example, the magnetohydrodynamic shock from the detonation may have produced rearrangement of existing natural particles.

The Starfish event was, and is still being, studied extensively. The Journal of Geophysical Research, v. 68, no. 3 (February 1, 1963), contains the collected papers of a symposium in which the early observations and their various interpretations are discussed. There is still no complete agreement on how many electrons were injected and just what is their lifetime. The total number of injected electrons according to one model (Hess) was 10^{26} one week after the detonation; according to another (Van Allen) it was 8×10^{24} six hours after the detonation. In the Hess model it is assumed that many of the electrons observed at high L values were injected artificially, whereas in the Van Allen model these electrons are assumed to be of natural origin. The Hess model, constructed from sparse early data from various satellites and extrapolated

to regions for which no data were available, probably gives values in excess of the true picture; how much in excess is debatable.

The early decay of electrons injected by the Starfish explosion was monitored on Injun I utilizing a Geiger tube shielded by about 4 g cm^{-3}. Figure 17-16 shows the data compared with calculated values in the region $1.175 \leq L \leq 1.195$.

There is evidence of some disturbance in the proton distributions in the Van Allen belt at low altitudes. Figure 17-10 shows the sharp increase in 55 MeV protons detected over the South Atlantic; however, the subsequent decay is uncertain.

Observations of electrons injected by the USSR tests in 1962 were made by instruments designed for measurement of fission electrons and more detailed data are available. The early spectra resemble fission spectra, and the pitch angle distributions demonstrate that injection was not at the equator. Figure 17-17 shows the increase in electrons of energy greater than 1 MeV; for further details, see Katz et al [1964].

17.3 COSMIC RADIATION

Primary cosmic radiation is a small flux of high-energy particles of extraterrestrial origin. Galactic cosmic radiation is of galactic or extragalactic origin and is believed to exist throughout all space unoccupied by dense matter. The flux of galactic cosmic radiation is essentially isotropic; for a discussion of anisotropy, see Dorman [1963]. The flux that reaches the vicinity of the earth, however, is modulated by plasma emitted from the sun, and is sometimes enhanced by high-energy solar particles, the solar cosmic rays (Sec. 17.4).

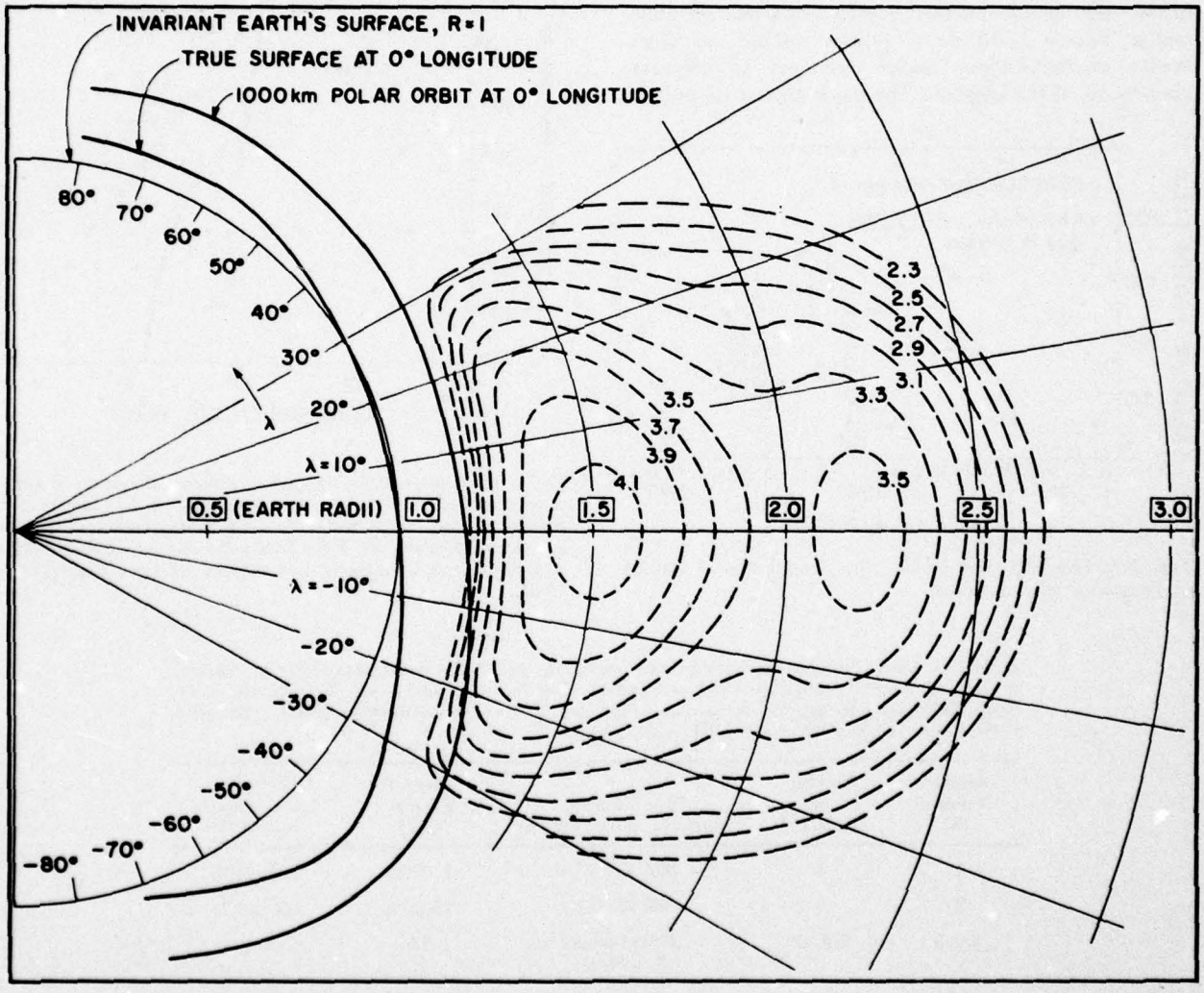


Fig. 17-9. Contours of constant intensity of 40 to 110 MeV protons in the inner Van Allen belt, as determined from scintillation detectors on Explorer XV, plotted in coordinates, R and λ; numbers on contours are units of $\log_{10}(1.4J_o)$, where J_o is omnidirectional intensity (number cm^{-2} sec_{ms}^{-1}). The invariant earth's surface and the actual surface are shown compared to a 1000-km polar orbit. (After McIlwain [1963].)

CHAPTER 17

In the magnetosphere and outside the terrestrial atmosphere, primary particles in general follow curved paths; in the atmosphere, the primary rays can be considered to follow practically rectilinear paths. *Secondary cosmic radiations* are produced by interaction of the primary particles with matter. Most of the primaries interact with the earth's atmosphere to produce the secondaries; few primaries reach sea level. The atmosphere thus contains a mixture of primary and secondary radiation in proportions depending mainly on altitude.

17.3.1 Composition and Energy

About 83% of the galactic primaries are protons, 12% are α particles, and approximately 1% are nuclei of other elements. About 3% are electrons and about 1% are gamma rays; it is not known what fraction, if any, of the electrons are positive in charge. Less than 0.1% of the nuclei with atomic number greater than one are antimatter. Figure 17-18 shows relative cosmic ray abundances of the various nuclei compared to universal abundances of the elements. The much greater proportion of Li, Be, and B in cosmic rays than in average galactic matter is thought to be due to their production by fragmentation of heavier cosmic-ray particles colliding with the interstellar gas. Table 17-3 gives estimates of integral-energy power laws for the spectra of nuclear components of the primary cosmic radiation.

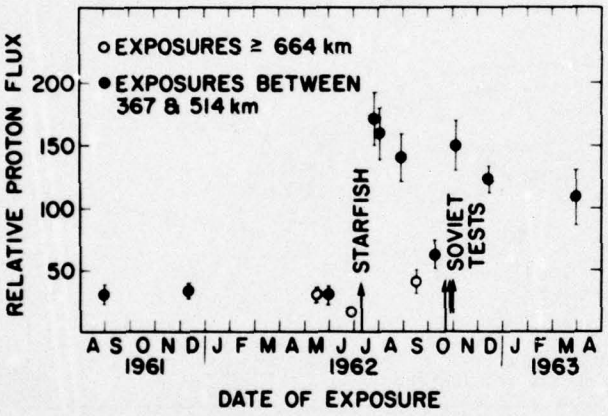


Fig. 17-10. Flux of 55 MeV protons normalized to 400 km altitude as determined from emulsions.

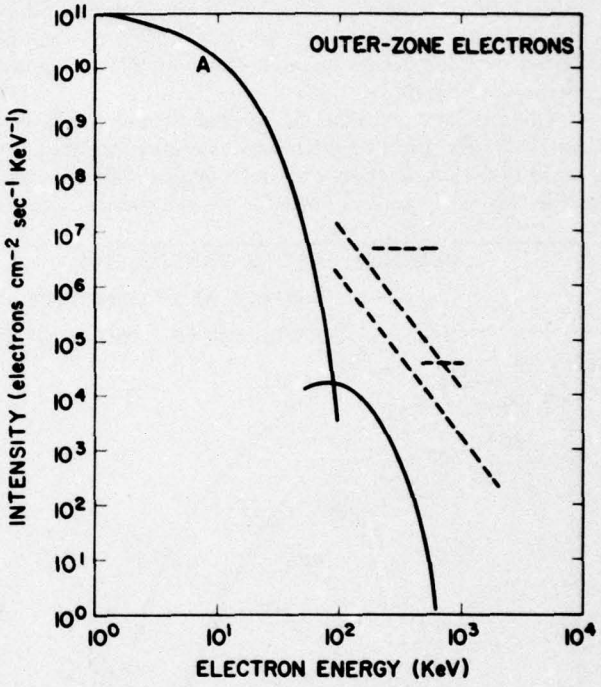


Fig. 17-11. Representative samples of differential spectra of outer zone electrons. Curve A is derived from Injun I data acquired at 1000 km altitude on 25 September 1961. Dotted lines are measurements from Explorer VI. Solid lines and curves are measurements at various times by different investigators. (After O'Brien [1962-1963].)

Table 17-3. Integral energy spectra of primary cosmic ray nuclei; E_n is the total energy per nucleon in GeV. (After S. F. Singer in *Progress in Elementary Particle and Cosmic Ray Physics*, v. IV, North Holland Publishing Co., Amsterdam, 1958, and H. E. Aizu, M. Koshiba, and E. Lohrmann, *J. Phys. Soc. Japan*, v. 17, Supp. A-III, p. 34, 1962.)

Atomic Number (Z)	Number of Nucleons*	Best Estimate (nuclei m^{-2} sec^{-1} sr^{-1})	Range of Validity (GeV)	Extreme Limits of Exponent of E_n
1	1	$4000\ E_n^{-1.15}$	2 to 20	1.05 to 1.25
2	4	$460\ E_n^{-1.6}$	1.5 to 8	1.3 to 1.7
3, 4, 5	7, 9, 11	$\approx$ 37% of value for Z = 6 to 9	1.6	—
6, 7 8, 9	12, 14 16, 19	$24\ E_n^{-1.6}$	3 to 8	1.45 to 1.75
$\geq$ 10	$\geq$ 20	$16\ E_n^{-2.0}$	3 to 8	1.85 to 2.25

* For the most abundant natural isotope.

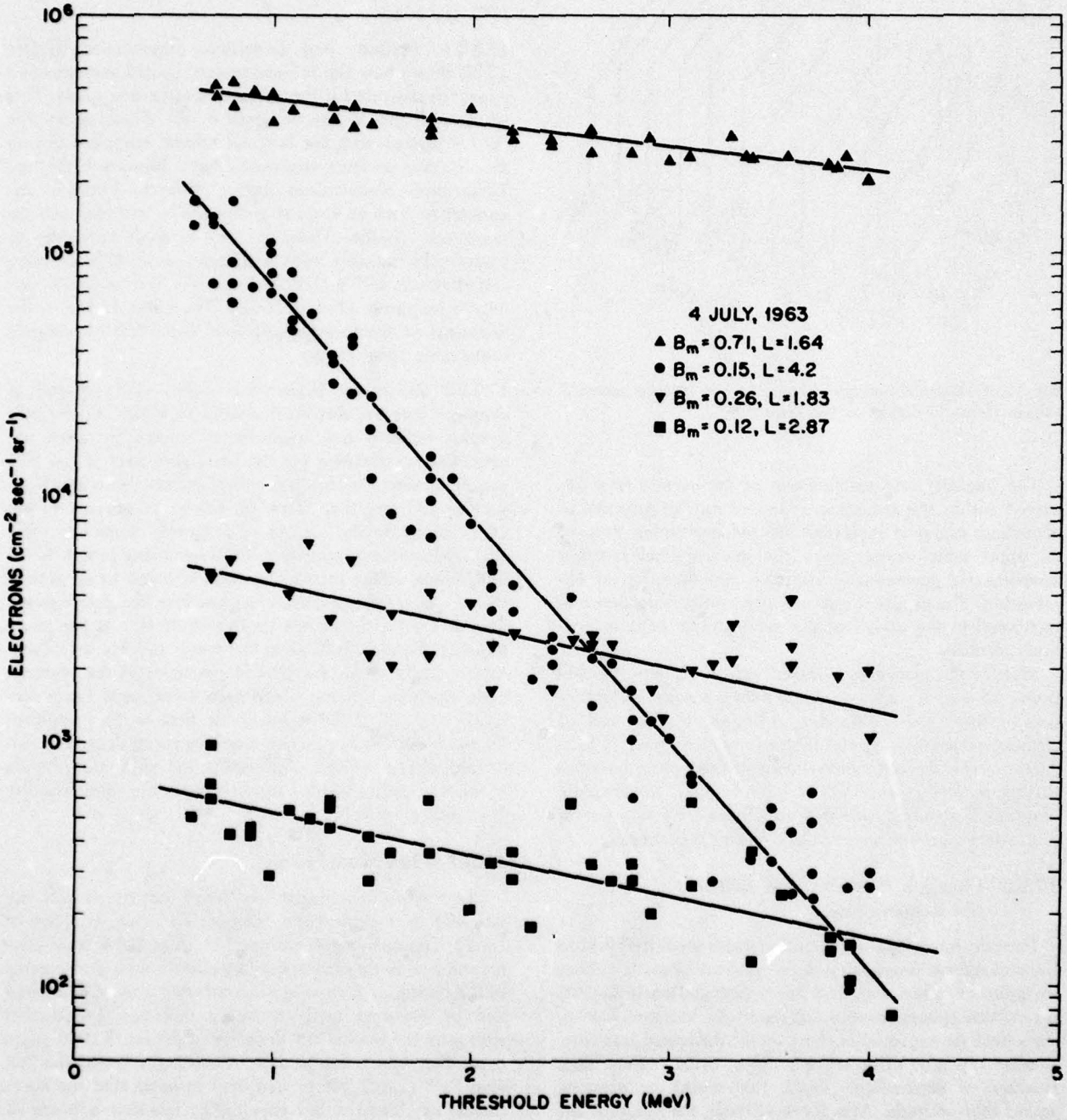


Fig. 17-12. Integral energy spectra for electrons on 4 July 1963. (After Paolini et al [In Press].)

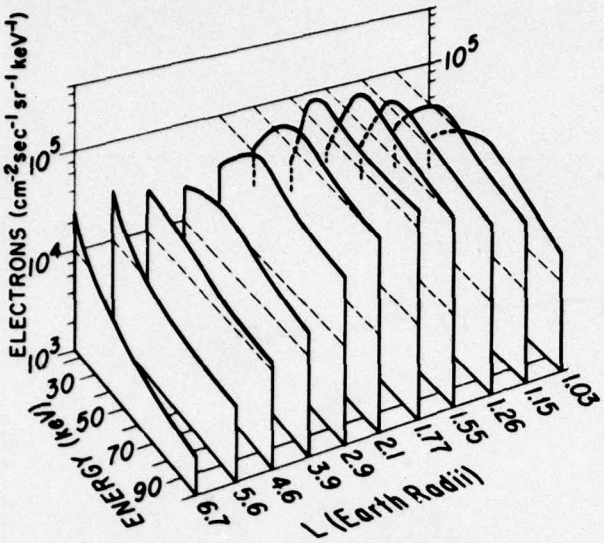


Fig. 17-13. Differential energy spectra on 4 July 1963 for various L values. (From Paolini et al [In Press].)

The intensity and composition of the cosmic rays observed within the atmosphere depend on the quantity of absorbing material traversed before observation and, to an appreciable extent, upon the geographical location (particularly geomagnetic latitude) and direction of observation. The geographical and directional dependence is attributed to the action of the geomagnetic field on primary particles.

Most of the primaries interact with air at altitudes between 15 and 35 km, producing high-energy secondary cosmic rays. This secondary radiation is composed of elementary particles and at least some nuclei heavier than protons. The high-energy secondaries interact to produce further secondary rays, etc. Figure 17-19 is a schematic diagram illustrating this process. Table 17-4 is a list of elementary particles and some of their properties.

17.3.2 Charged Particle Flux Within the Atmosphere

Particle intensity, or ionization rate, measured within the atmosphere depends upon the amount of matter above the point of observation and on its distribution in height; hence, atmospheric conditions, especially barometric pressure, have an appreciable effect on the measured intensity. Cosmic ray intensities are, therefore, usually given as a function of *atmospheric depth* (air mass) or pressure rather than altitude. At a given altitude, the value of the pressure in mb is close to 2% less than that of the depth in g cm^{-2}. Figure 17-20 shows atmospheric depth as a function of altitude; Ely [1962] also gives graphs and tables for computing air masses at various zenith angles. Figures 17-21 and 17-22 show ionization rates in the atmosphere at various atmospheric depths; observed rates vary considerably, particularly in relation to the solar cycle. In theory, the intensity of any specified secondary component can be derived from the spectrum and the yield function for the specified component. At present, the yield functions are not known with the desired accuracy; results of current studies will be found in the literature in 1965 and 1966.

17.3.2.1 *Latitude and Longitude Dependence.* Figure 17-23 shows how the ionization rate should increase and approach the rate for the primary flux in free space. This increase is due to the decrease in the shielding by the earth's shadow and, for low and middle latitudes, also to the decrease in the geomagnetic field. Figures 17-24 and 17-25 show observations during different years of the ionization rates at various geomagnetic latitudes and atmospheric depths. There is also a small variation of cosmic ray intensity with longitude; at 40.8°N geomagnetic latitude, 90° to 112°W longitude, it is −0.24% per degree longitude [Neher, 1952]. The effect is due to the departure of the geomagnetic field from that of a dipole at the geographic center.

17.3.2.2 *Minimum Momentum.* Table 17-8 (at end of chapter) lists the vertical threshold rigidities, P_t, by geographic latitude and longitude, calculated by using approximate corrections for the nondipole part of the geomagnetic field and for penumbral effects. Recent investigations indicate that these rigidities are correct within 10%, except in the regions of magnetic anomalies (Sec. 11.2) where deviations up to 24% are being found. If the momentum of the primary nucleus is equal to or greater than P_t Ze/c, the particle can penetrate the geomagnetic field at vertical incidence (zenith angle 0°) at the given location. Figure 17-26 gives the cutoff rigidity as a function of zenith angle for positive particles in the geomagnetic equatorial plane; corrections were made for eccentricity and tilt of the geomagnetic field as they apply to longitude 80°W. In practice a unique cutoff does not exist in midlatitude regions where there are alternating bands of allowed and forbidden rigidities near the cutoff rigidity (penumbral effect).

17.3.3 Flux Modulations

There is no experimental evidence that the cosmic ray intensity has undergone long-period changes [Neher, 1958]. The radioactive isotope C^{14} (5×10^3 yr half-life) is produced in the atmosphere by cosmic rays. Agreements in the dating of archeological artifacts by the C^{14} method and by classical methods imply that any long-period change in the cosmic ray intensity in the last 30,000 years is smaller than a few percent. Counting rates of the isotope Be^{10} (2.5×10^6 yr half-life) indicate that the mean cosmic ray intensity has changed by less than a factor of 10 in the past 10^6 years.

The variation of cosmic ray flux with the 11-yr solar cycle (Fig. 15-9) is indicated by the variations from year to year shown in Fig. 17-21, 17-22, and 17-24. An increase in solar activity corresponds to a decrease in galactic cosmic ray intensity; the low-energy particles tend to be removed from the flux in the vicinity of earth. This modu-

lation is thought to be caused by interactions with magnetic fields contained in plasmas ejected by the sun in increased amounts during active periods. Changes in cosmic ray intensity, however, lag changes in sunspot number by 9 to 12 months. As the sunspot number increases from minimum, primary particles of increasing energy are affected; particles with rigidity higher than about 10 GV, however, seem to be unaffected. From minimum to maximum, the energy density of the primary galactic cosmic rays in the vicinity of the earth decreases by about 40%.

There are also 27-day and diurnal variations in the cosmic ray flux; for detailed discussions of these and the variation with geomagnetic disturbances, see Dorman [1963]. The 27-day variations are related to processes in the solar atmosphere and their effect on the conditions of the interplanetary medium at great distances from the earth. The 24-h variations are about 0.25%; they imply a small anistropy in the particles incident upon the earth. There is also evidence of an enhanced diurnal variation associated with geomagnetic disturbances. Figure 17-27 is an example of changes in daily maximum counting rate during a disturbed period; as the days progressed, the maximum occurred earlier each day.

Starting at or a few hours after the onset of a geomagnetic storm (Sec. 11.4), the cosmic ray intensity may decrease rather sharply for about a day to a minimum that is sometimes as much as 10% below the original value. The intensity then increases rather slowly, generally taking several days to recover. This phenomenon, called a *Forbush decrease*, is associated with interactions between primary particles and the magnetic fields of solar corpuscular streams and interplanetary plasma. Some large geomagnetic storms, however, are followed by no significant change in cosmic ray intensity. A few increases that are not associated with solar flares have been observed during magnetic storms [Yoshida and Wada, 1959]. During geomagnetic storms when the field decreases, a decrease in cutoff rigidity would be expected with a corresponding increase in cosmic ray intensity; Obayashi [1959] gives predicted changes in cutoff rigidity during magnetic storms of various intensities.

Although the neutron flux is a part of secondary radiation only (primary radiation includes no neutrons), neutron monitors that measure the local neutron production by the nucleonic component of cosmic rays are advantageous for the study of primary flux variations. They are sensitive to the low-energy component of the primary radiation, which shows much greater variation with time than the high-energy component. The only atmospheric condition that affects neutron intensity is the pressure; the intensity decreases 10% for each pressure increase of 1 cm Hg [Lockwood and Yingst, 1956].

Because the primary radiation is affected by the geomagnetic field, the neutron flux also depends on location. Figure 17-28 shows the results of two years' measurement of the latitudinal and pressure (altitude) variation of slow neutron flux; the experiments were carried out on

Table 17-4. Some elementary particles and their properties. (After G. A. Snow and M. M. Shapiro, *Revs. Modern Phys.*, v. 33, p. 231, 1961.)

Class	Name	Symbol and Charge	Spin ($h/2\pi$)	Mass		Approx. Mean Life (sec)
				(m_e)*	(MeV)	
Photon	photon	γ^0	1	0	0	stable
Leptons	neutrino	ν^0	½	0	0	stable
	electron positron	e^- e^+	½	1	0.511	stable
	muon (mu meson)	$\mu^{+,-}$	½	207	106	10^{-6}
Mesons	pi meson (pion)	π^0	0	264	135	10^{-16}
		$\pi^{+,-}$	0	273	140	10^{-8}
	**K meson	$K^{+,-}$	0	967	494	10^{-8}
		K_1^0	0	974	498	10^{-10}
		K_2^0	0	974	498	10^{-7}
Baryons						
Nucleons	proton	p^+	½	1836	938	stable
	neutron	n^0	½	1839	940	10^3
Hyperons	**	Λ, Σ, Ξ	½	2180 to 2580	1115 to 1318	10^{-10}

* m_e, the rest mass of the electron, is 9.109×10^{-31} kg.
** K mesons and hyperons are the "strange particles."

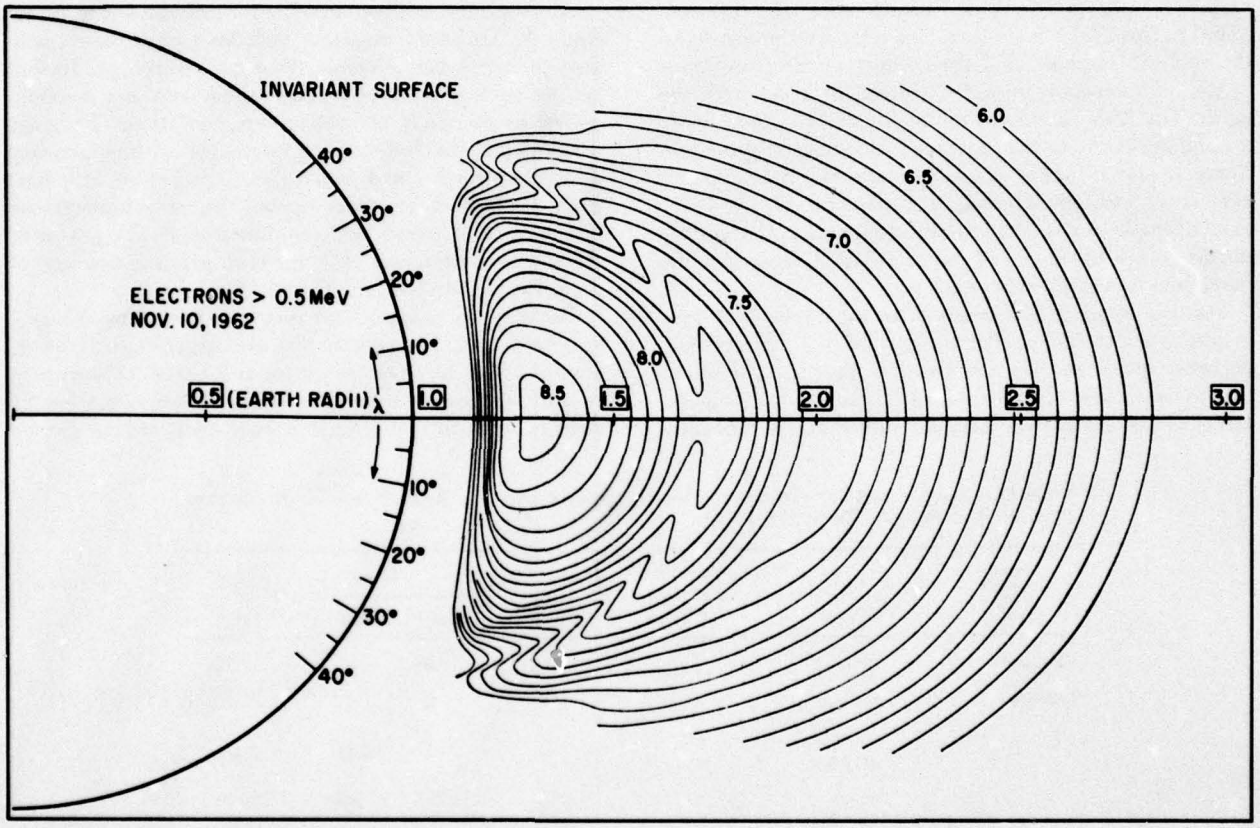


Fig. 17-14. Contours of constant intensity of electrons with energy greater than 0.5 MeV in R, λ coordinates. Numbers on contours are units of $\log_{10}(J_o/1.5)$, where J_o is omnidirectional intensity (number cm^{-2} sec^{-1}). (From McIlwain [1963].)

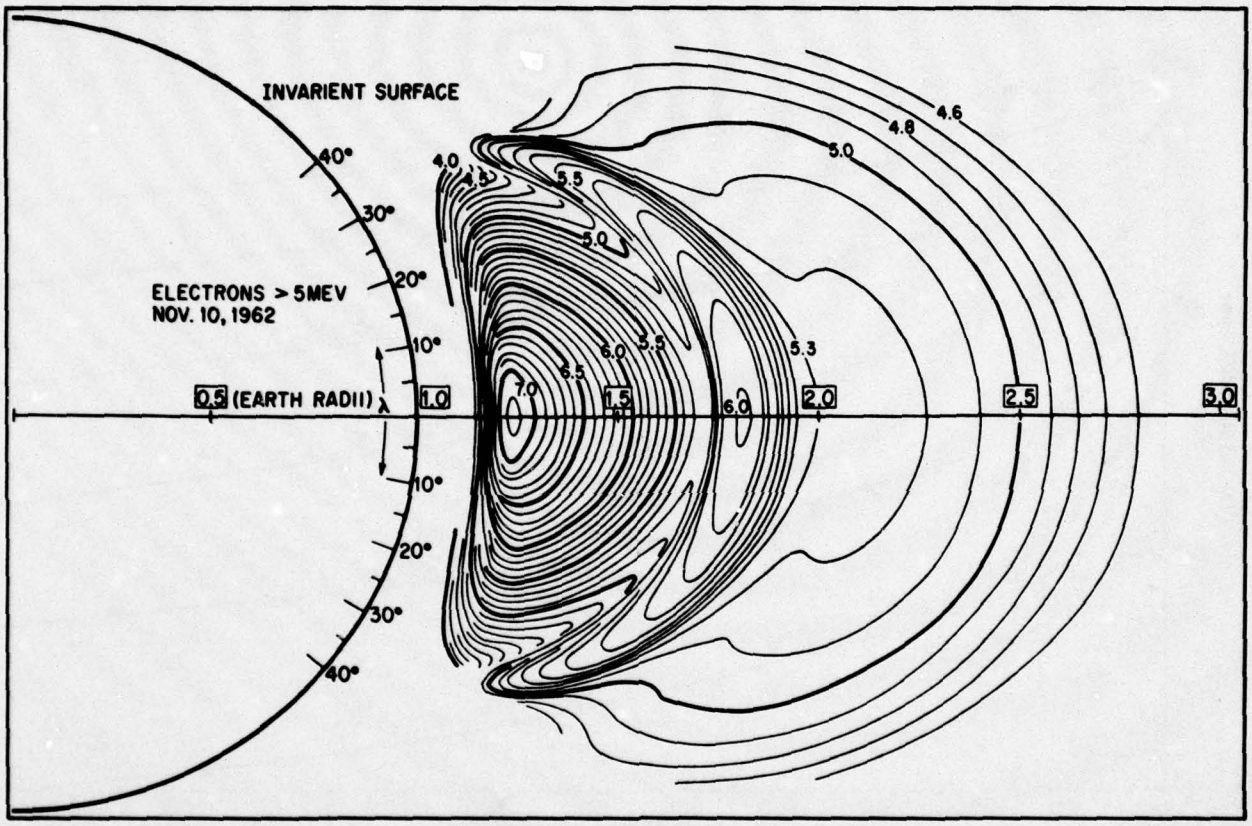


Fig. 17-15. Contours of constant intensity of electrons with energy greater than 5 MeV in R, λ coordinates. Numbers on contours are units of $\log_{10}(J_o/1.5)$, where J_o is omnidirectional intensity (number cm^{-2} sec^{-1}). (From McIlwain [1963].)

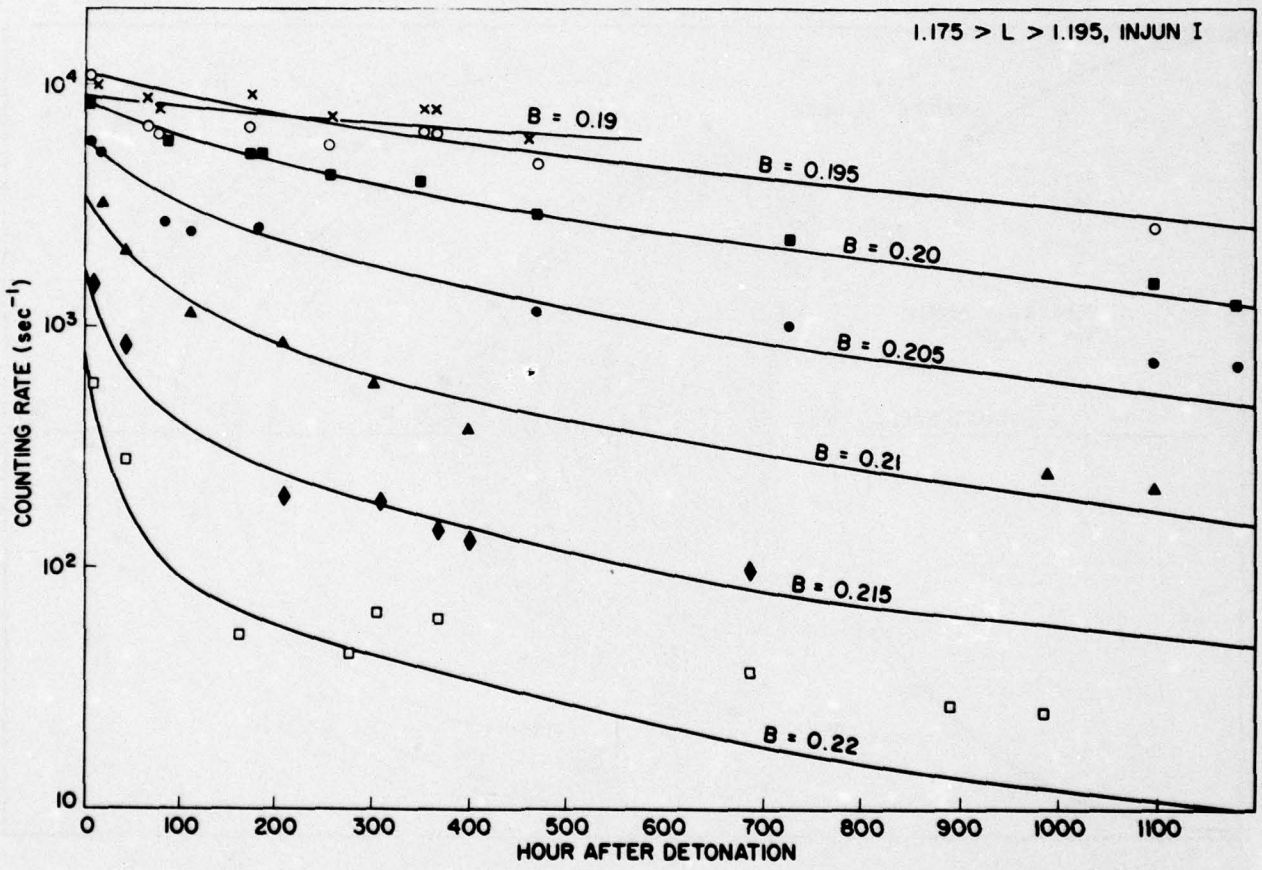


Fig. 17-16. Theoretical and experimental values of counting rates after Starfish event. Experimental points are from Van Allen. The solid lines are calculated for the magnetic shell L = 1.185 earth radii. (From A. D. Anderson, G. E. Crane, W. E. Francis, L. L. Newkirk and M. Walt, Final Report (DASA 1480) on Contract DA 49-146-XZ-204, June 1964.)

balloons in the Northern Hemisphere from August 1952 to September 1954. Data for a complete solar cycle, beginning in 1956, are being obtained by a worldwide network of neutron monitors. McCracken [1962] lists the geographic coordinates and asymptotic directions of approach for various rigidities for 13 of these stations.

17.4 HIGH ENERGY PARTICLES FROM SOLAR FLARES

Observations of solar corpuscular radiation are directly related to the history of available detectors. Early instruments could detect only the rare, very high energy events that are associated with a few of the largest flares visible on the face of the sun (Fig. 15-13). This high-energy corpuscular radiation was called *solar cosmic rays*; although their composition and energy spectra are not the same as galactic cosmic rays, this name is now firmly established in the literature. In solar physics, they are more often called proton showers (Sec. 15.5). As particles of lower energy were detected with higher sensitivity instruments, it appeared that almost all large flares emit some energetic particles. Only under special circumstances, however, are they of sufficient energy and intensity to reach the earth's surface in measurable quantities. In addition, the initial direction of the emitted radiation or effects due to magnetic fields associated with the sun can channel the charged particles in such directions that the particles from even a large flare are not detected in the vicinity of the earth. Figure 17-29 shows the number and dates of occurrences of solar cosmic rays that were detected at sea level in relation to solar cycle no. 19.

A detailed description of instantaneous particle fluxes and energy spectra for all solar flare events is not yet meaningful in terms of a future event; variations from one flare to the next are too erratic. This section gives a general description of the high energy particles produced by large flares during the period for which reliable measurements are available; for detailed descriptions of individual events, see Dorman [1963] and McDonald [1963].

17.4.1 Composition, Rigidity, and Flux of Solar Cosmic Rays

The high energy corpuscular radiation emitted by a solar flare consists primarily of protons and alpha particles, with about 1% or less nuclei of charge greater than two for the same value of the rigidity. During many flares, there are as many alpha particles of the same rigidities as there are protons. The actual percentage of heavy nuclei varies from one flare to the next. There is probably no low energy limit to solar cosmic radiation. The highest energy detected to date is the order of one GeV for protons. The maximum energy to which a proton can be accelerated on the sun depends on the maximum magnetic field, the area that this field encompasses, and the acceleration mechanisms. Calculations predict a maximum energy of about 10^5 GeV for a proton that could be contained by the magnetic field of a large sunspot (several thousand gauss and ten million square miles area). Since protons of this energy have not been observed, it may be that acceleration mechanisms are not present to provide such energy. If these protons were present in only small numbers, however, they would be difficult to detect. It is possible that in future events protons of energy considerably above one GeV could be detected.

Integral rigidity spectra of high energy protons from solar flares are best represented [Freier and Webber, 1963] by an exponential form,

$$J(>P) = J_o \exp(-P/P_o); \qquad (17\text{-}15)$$

$J(>P)$ is the integral intensity and P the magnetic rigidity. Table 17-5 gives values of J_o and P_o for six flares at a particular time of measurement; P_o varies from 65×10^6 to 375×10^6 V and J_o from 60 to 30,000 protons cm^{-2} sec^{-1} sr^{-1}. Figure 17-30 shows the integral rigidity spectra at the specified time for these events. Figure 17-31 shows the variation of P_o and J_o with time during the November 1960 events. The possibility of an event as much as ten times more intense than any which has been observed cannot be ruled out; hence, these data

Table 17-5. Values of constants for integral exponential rigidity spectra of solar protons, Eq. (17-15). (After Freier and Webber [1963].)

Year	Optical Flare Maximum (UT)	Time of Measurement (UT)	J_o (no. cm^{-2} sec^{-1} sr^{-1})	P_o (10^6 V)
1959	2118 May 10	0500 May 12	30×10^3	65
		0520-0915 May 12	30×10^3	65
1959	2145 July 16	1200 July 17	3×10^3	125
1960	0110 Sept. 3	1408 Sept. 3	60	180
		0930-1700 Sept. 3	60	180
1960	0221 Nov. 15	0500 Nov. 15	250	375
1961	1600 July 12	0910 July 13	2.1×10^3	60
1961	1950 July 16	1720 July 18	10^3	150

Table 17-6. Some major solar cosmic ray observations during 1956-1961. (After McDonald [1963].)

Solar Flare Data							Cosmic Ray Data							
					Maximum Radio Emission		Onset or Rise Time (h)		Decay Time (h)		Peak Flux (no. cm^{-2} sec^{-1})		Integrated Intensity (no. cm^{-2})	
Date		Importance	Heliographic Position (deg)	Optical Maximum (UT)	(•)	(UT)	> 30 MeV	> 100 MeV	> 30 MeV	> 100 MeV	> 30 MeV	> 100 MeV	> 30 MeV	> 100 MeV
1956	Feb 23	3+	N22 W74	0340	20,000	0341	6-8	3-4	30	16	6,200	5,000	6.5×10^8	3.2×10^8
1957	Jan 20	3+	S25 W30	1120							2,000-3,000	100-200	3×10^8	10^7
	Mar 23	3+	S14 E78	1005	10,000	1004			(40)	(20)	1,200-1,500	≈ 50	2×10^8	5×10^6
	Jul 7	3+	N25 W08	0115	2,000	0112			32	16-20	1,500-2,000	≈ 80	3×10^8	7×10^6
1958	Aug 16	3+	S14 W50	0440	6,200	0442	10		18		200		2×10^7	
	Aug 22	3	N18 W10	1448			10-12	3-4	20	8-12	500	20	5×10^7	1×10^6
	Aug 26	3	N20 W54	0027	6,700	0025	≈ 9		(12)		1,100		5.3×10^7	
	May 10	3+	N23 E47	2118	10,000		18-22	12-18	22	10-14	6,000-8,000	1,000	7×10^8	7.5×10^7
1959	Jul 10	3+	N22 E70	0222	15,000	0224	30-40	18-20	40	20	4,000	1,200	8.8×10^8	1.0×10^8
	Jul 14	3+	N16 E07	0349	6,300	0352	16-20	12-18	18	9-12	10,000-12,000	1,200	1.1×10^9	6.3×10^7
	Jul 16	3+	N08 W26	2145	6,500	2200	12-14	4-5	30	18	16,000-18,000	1,500	8.1×10^8	1.3×10^8
	Apr 1	3	N12 W10	0859			2-3	< 1	12	4-6	50	6	2.7×10^6	1.5×10^5
	Apr 5	2+	N10 W61	02[illegible]	≈ 8,000	0203			12		40		2×10^6	
	Apr 28	3	S05 E34	0130			8-10	3-4	18 24	8	300	20	2.5×10^7	7×10^5
	May 4	3+	N14 W90	1020			2-3	< 1	8	4	200	40	7×10^6	7×10^5
1960	Sep 3	3	N18 E88	0110	12,000	0108	12-16	7-9	32	26	240	60	4×10^7	7×10^6
	Nov 12	3+	N27 W02	1329	10,000	1329	12-16	8-10	18-24	14-18	12,000	2,500	1.4×10^9	3.5×10^8
	Nov 15	3+	N30 W32	0221	14,000	0227	10-16	3-5	16-20	8-12	6,000	2,400	5.2×10^8	1.2×10^8
	Nov 20	3	N28 W113	2020			3-4	≈ 1	10-16	4-6	1,000	4,000	6×10^7	6×10^6
	Jul 11	3	S06 E32	1700	2,500		8-10	4	22-26	18	20	3	2×10^6	3×10^5
	Jul 12	3+	S07 E22	1030	7,500		8-12	6	16-20	12	120	15	1.0×10^8	1.6×10^6
1961	Jul 18	3+	S06 W60	1010	5,000		6-10	2-3	24	12	2,500	600	2.1×10^8	4.8×10^7
	Jul 20	3+	S07 W90	(1600)	2,500		4-6	1.5	6-8	3	300	70	9×10^6	1.2×10^6
	Sep 28	3	N14 E30	2223									2.2×10^5	9.7×10^4

• Units of 10^{-22} W m^{-2} cps^{-1} at 3 to 10 kMcps.

should not be considered upper limits. There are plausible arguments, however, that events as large as those produced in the November 1960 flare might not occur again for twenty or more years.

17.4.2 Variations in Time and Direction of Solar Cosmic Rays

Table 17-6 lists data for some of the important flares during 1956 through 1961. The *onset time* is the interval from the occurrence of the optical flare maximum to detection of the first particles at the earth. The *rise time* is the interval from the first detection at earth to the time at which the intensity is maximum. Both onset and rise time vary from event to event and are strongly energy dependent; the higher energy particles arrive first and reach peak intensity in a shorter time. Because the decay of intensity is exponential most of the time for most energies, a decay time, τ, is defined:

$$I(>E) = I_{max}(>E) \exp(-t/\tau),$$

where $I(>E)$ is the intensity of particles with energy greater than E at time t after the peak intensity, $I_{max}(>E)$. Decay time also varies from event to event and is energy dependent; it ranges from 3 to 4 h for high-energy particles to several days for low-energy particles. Maximum integral omnidirectional intensities observed were less than 2×10^9 protons cm^{-2} [redacted] for $E \geq 30$ MeV and less than 4×10^8 protons cm^{-2} [redacted] for $E \geq 100$ MeV. The maximum unidirectional intensity observed was less than about 10^4 protons $cm^{-2}\ sec^{-1}\ sr^{-1}$ for $E > 20$ MeV and less than 5×10^2 protons $cm^{-2}\ sec^{-1}\ sr^{-1}$ for $E > 100$ MeV.

A number of events exhibit directional characteristics during their early phases. Figure 17-32 shows contours of constant solar cosmic ray flux for the early phase of the 4 May 1960 event. Table 17-7 gives rise times, position of flares, and observed anisotropy of events for which these data are available.

Present knowledge of the magnetic conditions in sun-to-earth space during solar flares is not sufficient to provide a quantitative description or even to determine which of the proposed models [Dorman, 1963; McCracken, 1962] best represents actual mechanisms. If at the time of a large solar flare there are magnetic field lines directly connecting the flare with the earth and if high-energy particles are emitted, then these particles will travel rapidly in a spiral path along the field lines to the earth. (For example, a proton with 1-GeV kinetic energy has a gyroradius of 5×10^6 km in a field of 10^{-5} gauss.) The observed intensity will rise rapidly to its maximum value and be directional in character. Because of the radial nature of the solar magnetic fields and the rotation of the sun, this direct connection to the earth happens most frequently when the flare occurs on the western face of the sun; thus, the rapid rise times occur most often for flares on the western face. If the magnetic field lines from a flare do not connect with the point of observation, particles must cross the field lines to be observed. This requires a longer time, and the flux observed will tend to be diminished and isotropic in nature. In many flares the maximum intensity occurs about 1 day following the optical flare; this time of maximum is probably related to the travel time for the solar plasma cloud from the sun to the earth.

The position of the flare on the face of the sun is just one of the factors that determines the character and intensity of radiation received by the earth and its environs. The magnetic field configuration in space is altered by the plasma emitted by a solar flare. The plasma evidently forms inhomogeneities in the field which complicates the prediction of the motion of high energy particles emitted by the flare itself and also by flares occurring in the immediate period following a large disturbance. Solar flares from which the emission of large amounts of high-energy particles were observed tend to occur during increasing and decreasing phase of the 11-yr sunspot cycle (Fig. 17-29) and not at periods of maximum or minimum.

In order to predict the effects to be expected from an optical flare, a considerable amount of information must be available concerning the magnetic field configuration in the region between the earth and the sun at the time of the flare, as well as a more reliable method of predicting what the intensity of the particle emission will be. The former could be obtained through the use of a number of interplanetary space stations in orbit between the earth and the sun, but the latter requires further study of the nature of solar flares to discover some characteristic of solar disturbance which will be a reliable indicator of the ejection of solar cosmic rays (Sec. 15.5).

Table 17-7. Rise times, position of the parent flare on the solar disk, and observed anisotropy; after McCracken [1962].

Date of Event	Rise Time	Flare Position	Anisotropy
*May 4, 1960	7 min	90°W	very marked
*February 23, 1956	0.5 h	80°W	marked
*November 15, 1960	0.7 h	45°W	very marked
*November 19, 1949	0.7 h	70°W	very marked
March 7, 1942	0.8 h	90°W	marked
February 28, 1942	1.5 h	4°W	poorly defined
July 25, 1946	2.0 h	15°E	not noticeable
*November 12, 1960	2.3 h	10°W	poorly defined
*July 17, 1959	4.2 h	30°W	none
September 3, 1960	5.8 h	90°E	none

* Event for which many observations are available and on which the greatest reliance can be placed.

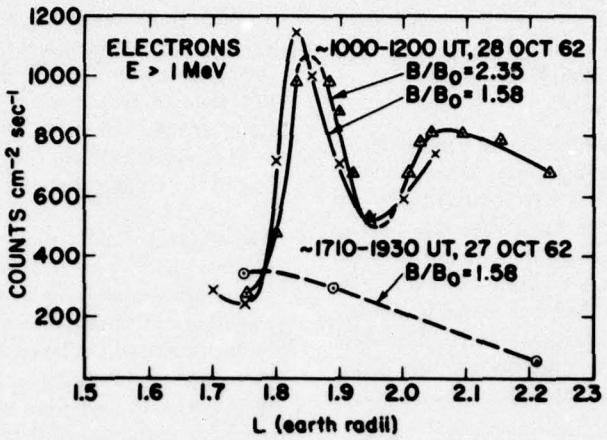


Fig. 17-17. Change in omnidirectional flux of electrons of energy > 1 MeV observed before and after USSR nuclear tests in October 1962; B_0 is the magnitude of the magnetic field at the equatorial crossing point of the particles.

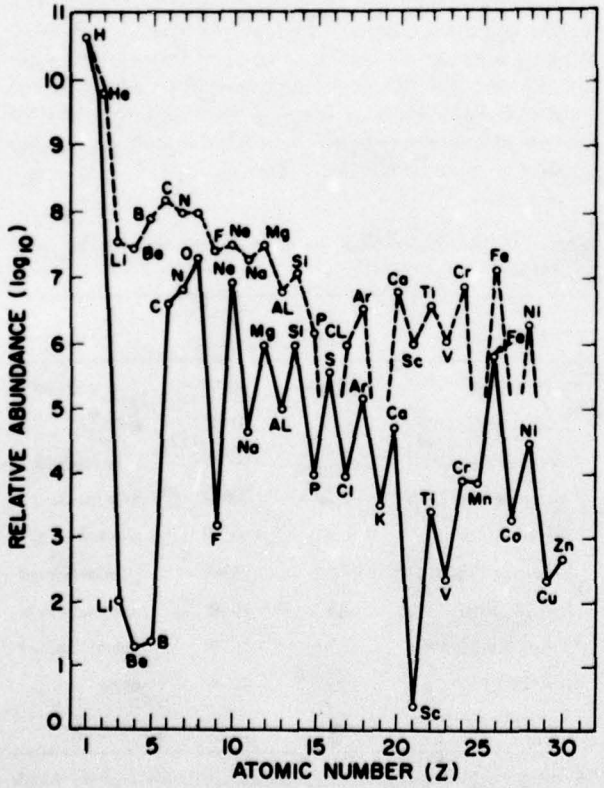


Fig. 17-18. Relative abundance of nuclei in the primary galactic cosmic radiation (dashed line) normalized to the cosmic abundance of hydrogen, and relative cosmic abundance of the elements (solid line). (After C. J. Waddington, *"Progress in Nuclear Physics,"* J. G. Wilson, ed., v. 8, Pergamon Press, N. Y., 1960.)

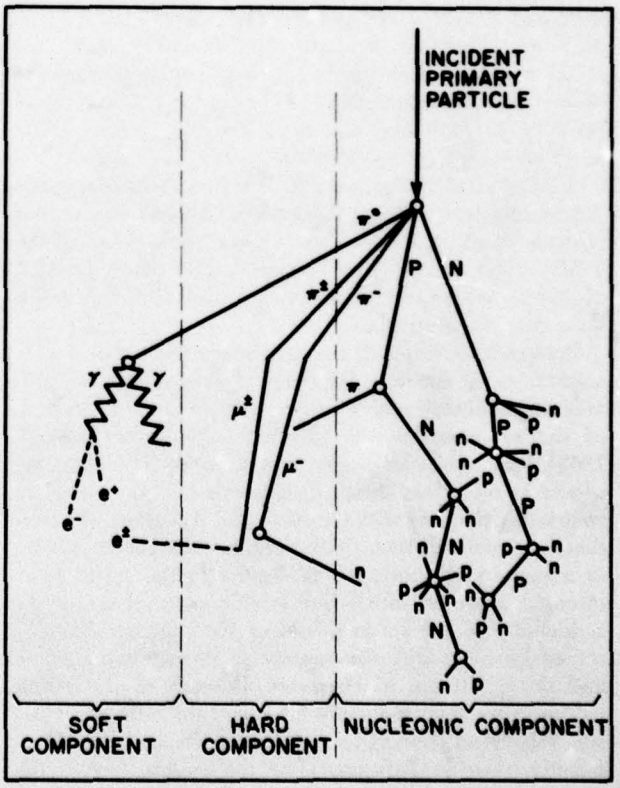
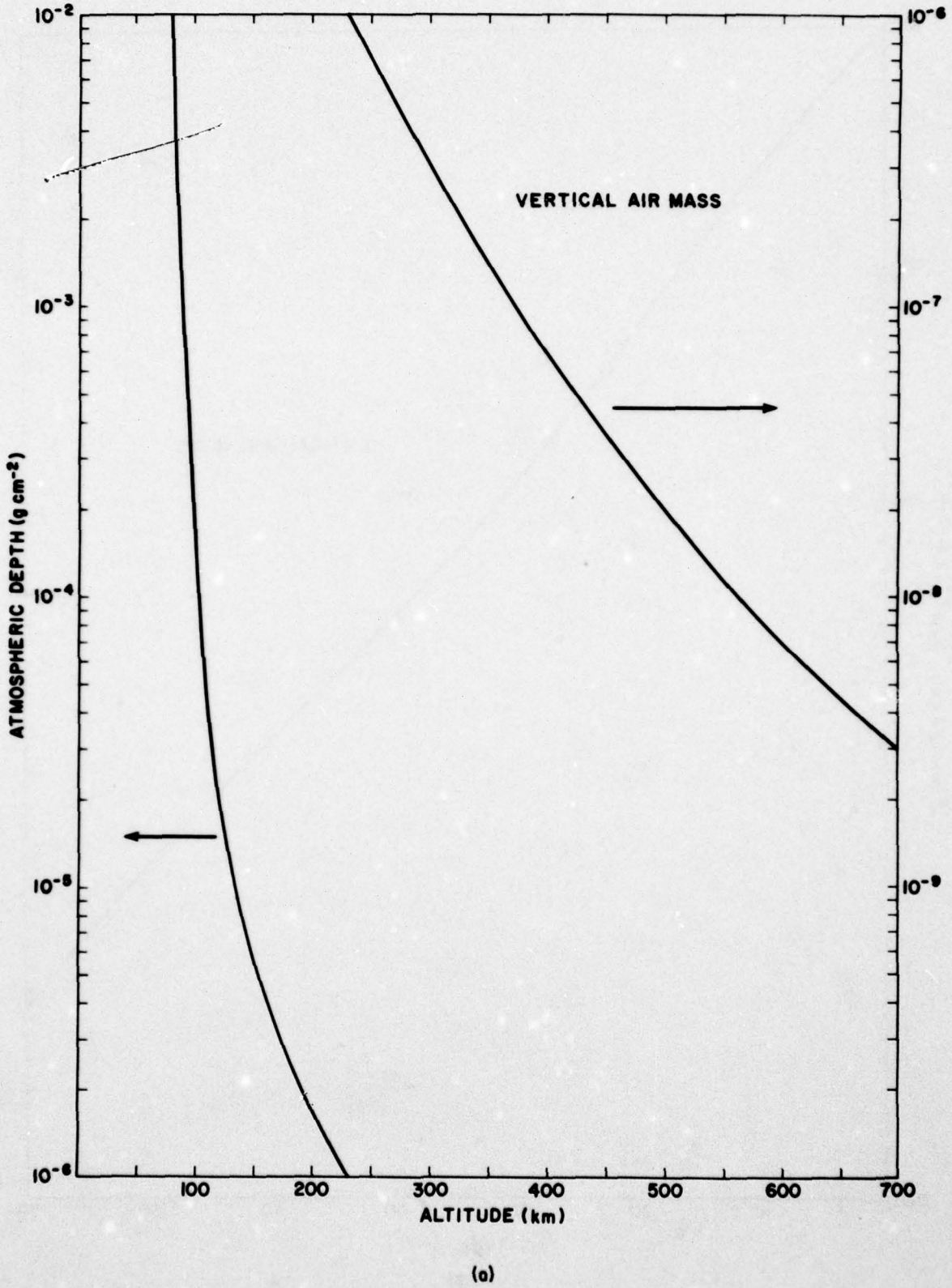


Fig. 17-19. Schematic diagram of a cosmic ray shower. N and P are high energy, n and p disintegration-product, neutrons and protons; for other symbols see Table 17-4.



(a)

Fig. 17-20. The mass of air per unit area in a vertical column extending upward from a height H km above sea level. (From Ely [1962].)

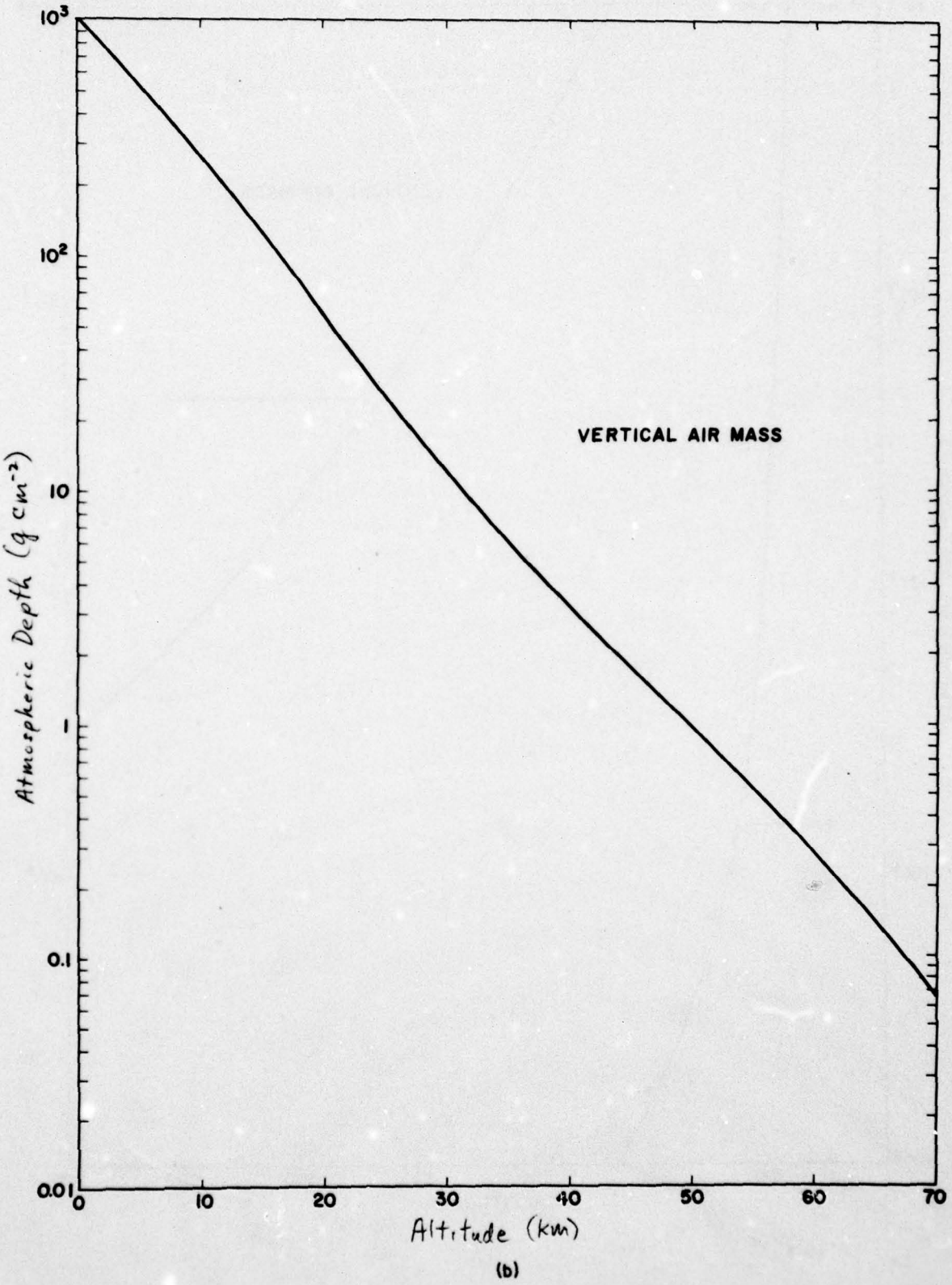


Fig. 17-20. The mass of air per unit area in a vertical column extending upward from a height H km above sea level. (From Ely [1962].)

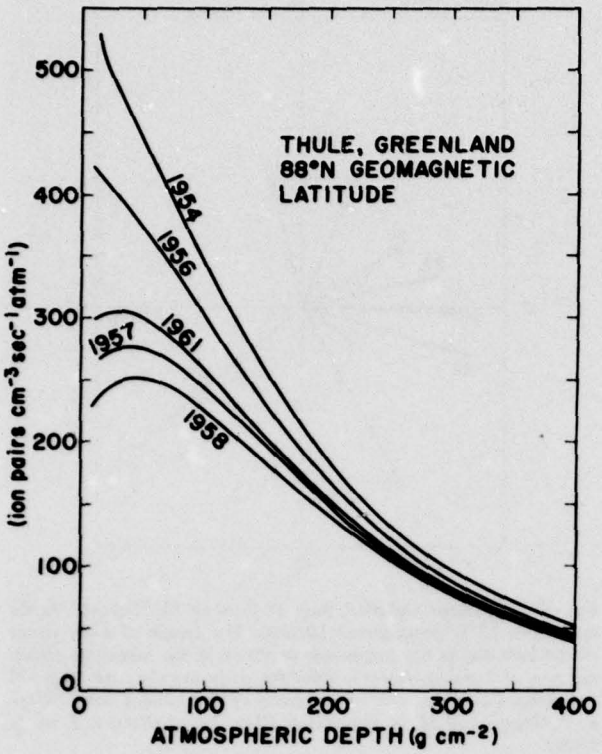


Fig. 17-21. Yearly average of cosmic ray ionization rate per atmosphere of air as a function of atmospheric depth. (From Neher and Anderson [1962].)

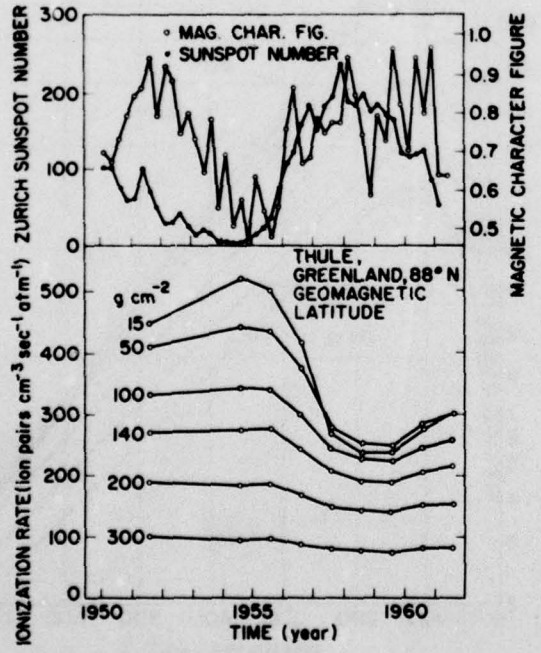


Fig. 17-22. Cosmic ray ionization rate per atmosphere of air as a function of time for selected atmospheric depths. Quarterly Zurich sunspot number and quarterly planetary magnetic character figures are shown for comparison. (From Neher and Anderson [1962].)

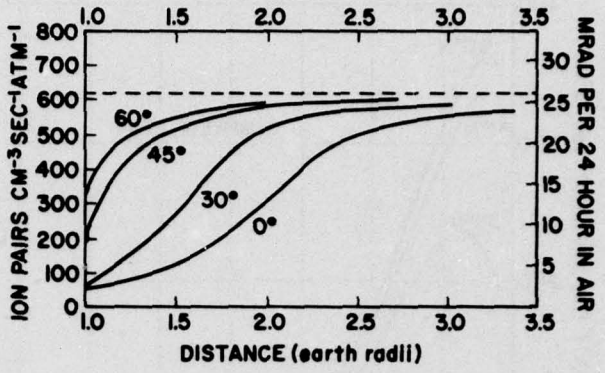


Fig. 17-23. A schematic plot of typical cosmic ray ionization rate per atmosphere of air at several geomagnetic latitudes during a medium sunspot period vs distance from the earth; it is assumed there are no primaries of rigidity below approximately 1 GeV. (After J. A. Van Allen "Physics and Medicine of the Upper Atmosphere," C. S. White and O. O. Benson, Jr., eds., University of Mexico Press, Albuquerque, 1952.)

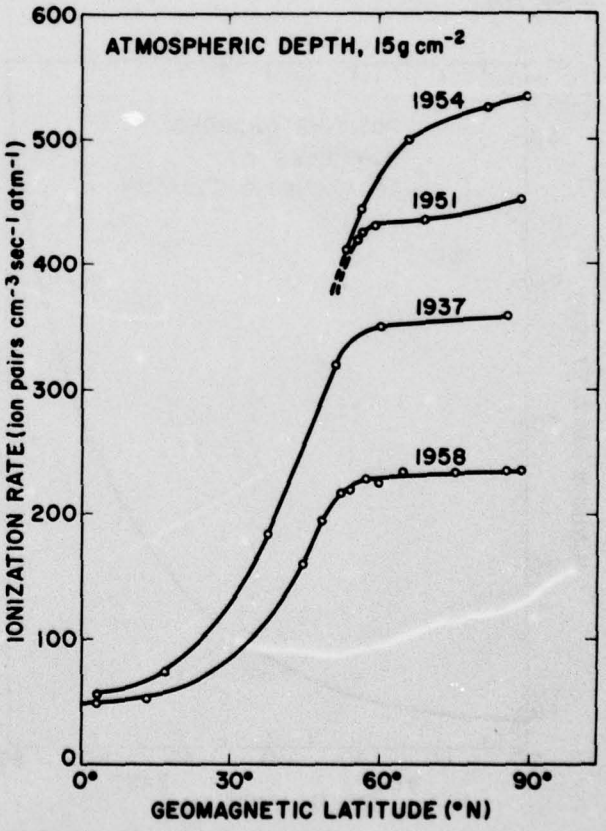


Fig. 17-24. Cosmic ray ionization rates per atmosphere of air near the top of the atmosphere as a function of latitude for various years. (From Neher and Anderson [1962].)

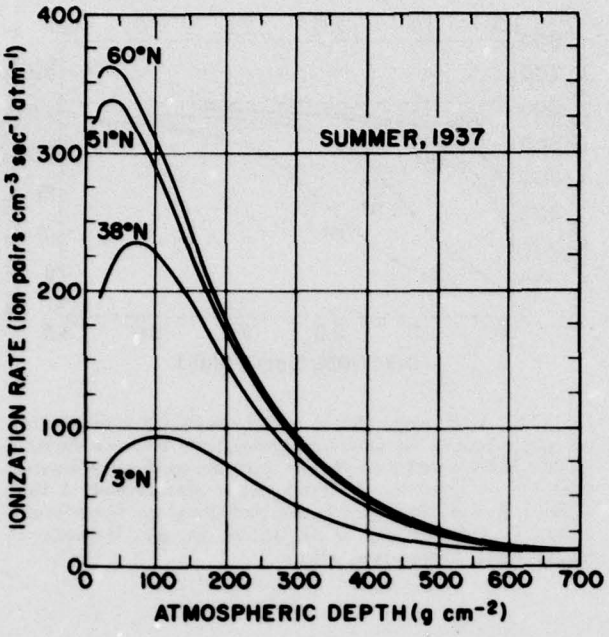


Fig. 17-25. Ionization rate per atmosphere of air as a function of atmospheric depth at several geomagnetic north latitudes. (After I. S. Bowen, R. A. Millikan and N. V. Neher, *Phys. Rev.*, v. 53, p. 855, 1938.)

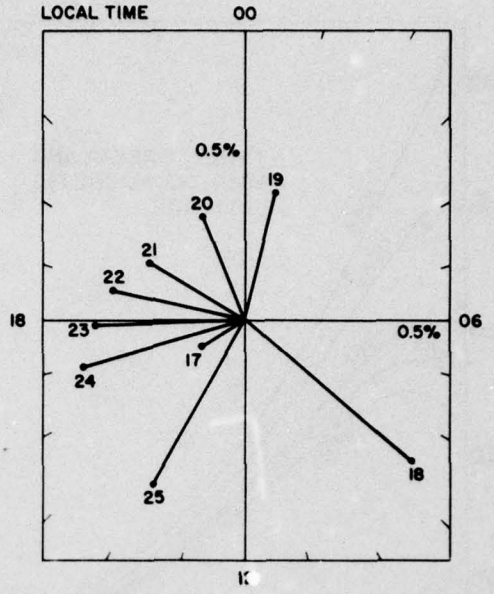


Fig. 17-27. Diurnal variation, July 17 through 25, 1961 at Swarthmore, Pa., 52°N geomagnetic latitude. The length of each vector on the 24-h dial is the percentage deviation of the maximum counting rate of a meson detector from the daily average; the angle of the vector shows the hour of maximum on the labeled date. (From S. P. Duggal and M. A. Pomerantz, *Phys. Rev. Letters*, v. 8, no. 5, 1962.)

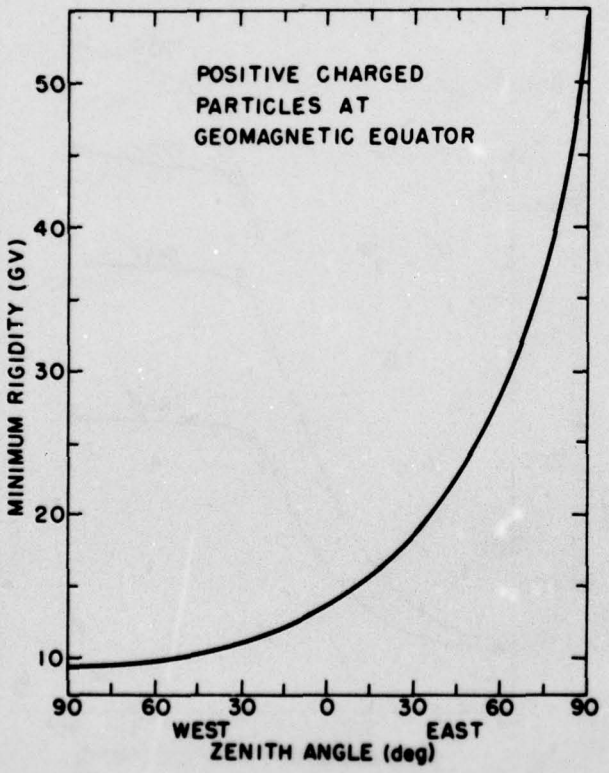


Fig. 17-26. Cutoff rigidity in the east-west plane of the geomagnetic equator at 80°W longitude for positive primary cosmic rays as a function of zenith angle. (After Neher [1952].)

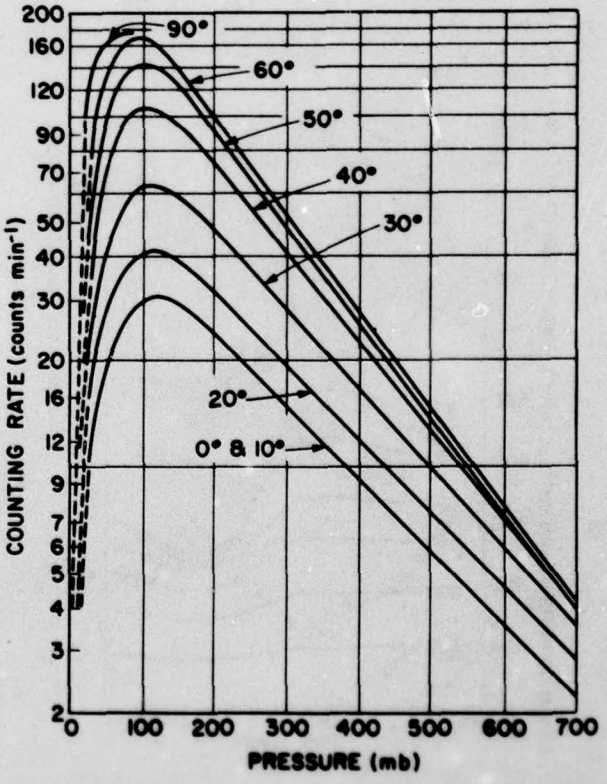


Fig. 17-28. Relative neutron intensity vs atmospheric pressure for various northern geomagnetic latitudes, August 1952 to September 1954. (From R. K. Soberman, *Phys. Rev.*, v. 102, p. 1409, 1956.)

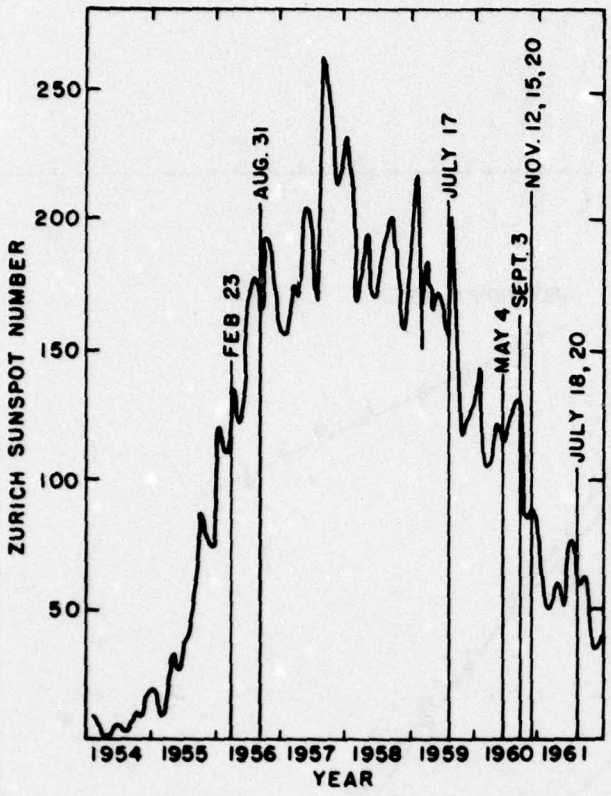


Fig. 17-29. Solar cosmic ray events detected at sea level during the current sunspot cycle.

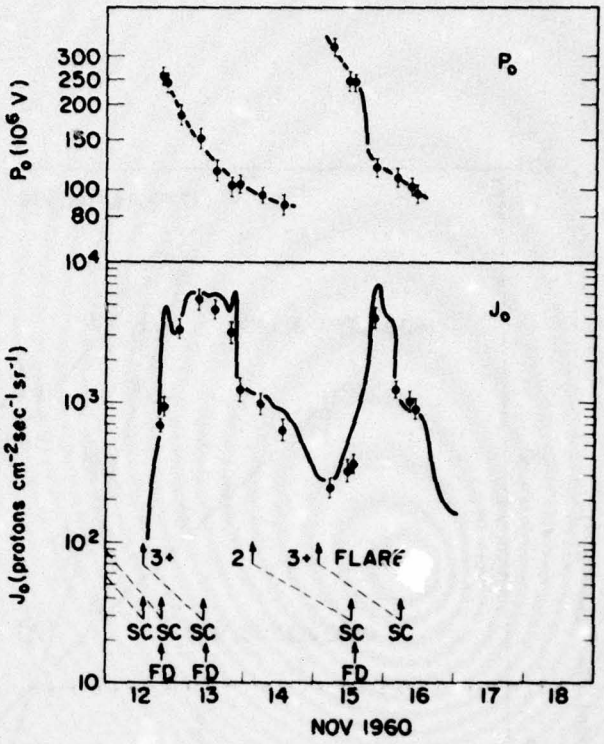


Fig. 17-31. The time variation of P_o and J_o, Eq. (17-15). The measured values of P_o are connected with a continuous curve. The measured values of J_o are plotted, but the continuous curve is from calculations using riometer absorption from Longyearbyen station. Times of major optical flares, sudden commencements (SC), and Forbush decreases (FD), are indicated by arrows. (From Freier and Webber [1963].)

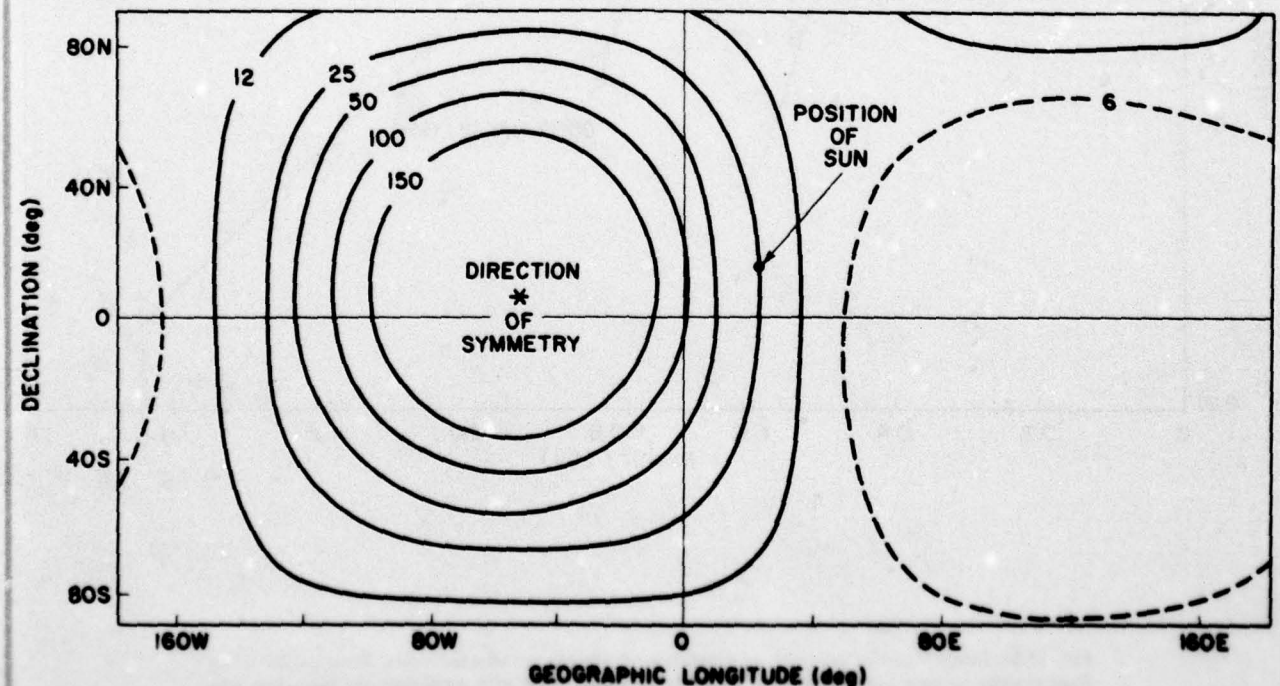


Fig. 17-32. Contours of equal cosmic ray flux during the interval 1045-1100 UT on 4 May 1960, calculated by K. G. McCracken [McDonald, 1963]; the unit of intensity is arbitrary.

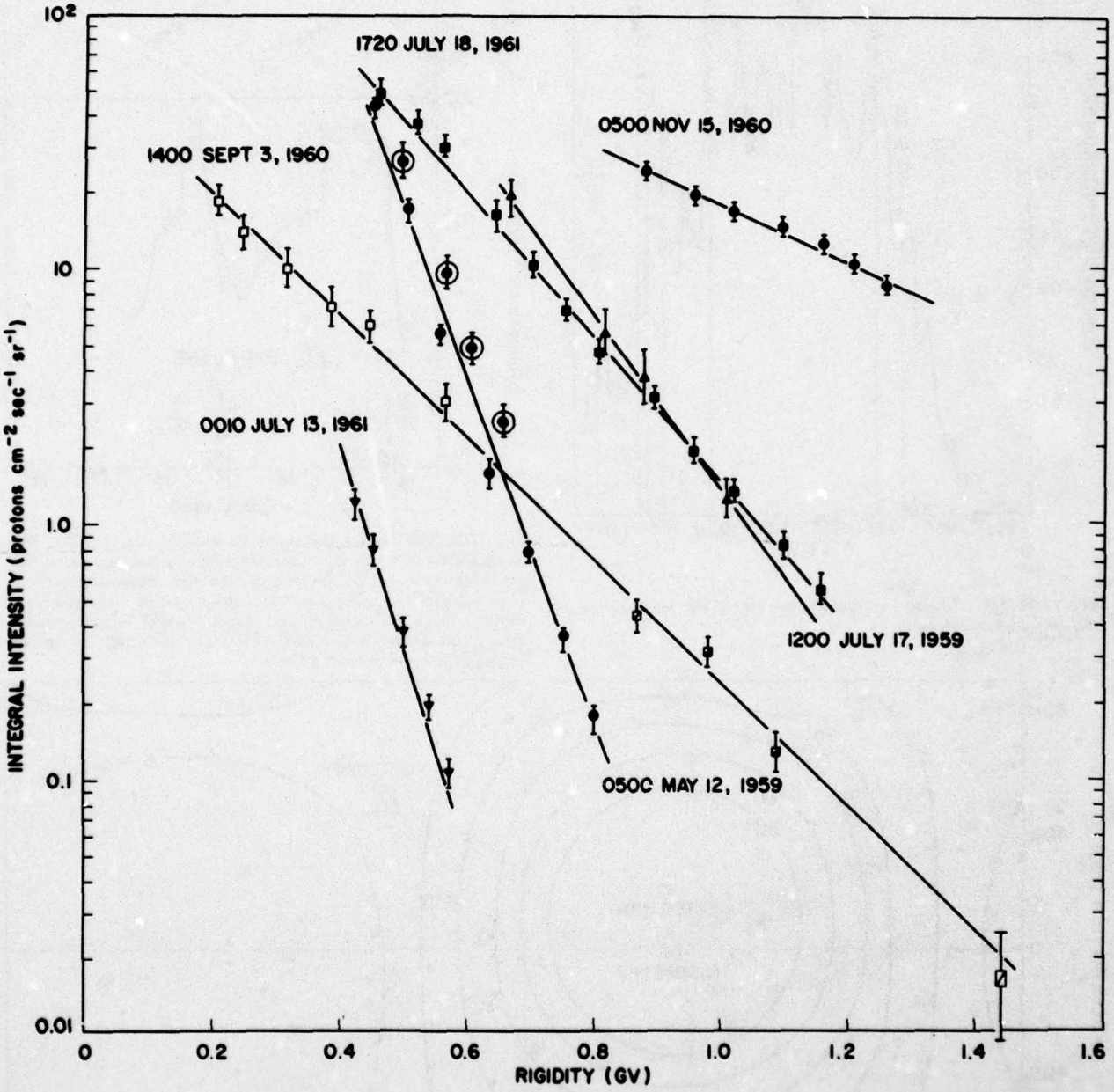


Fig. 17-30. Integral proton intensity as a function of rigidity at selected times. Data points taken from counter ascents are shown as solid symbols; those taken with emulsions, as open symbols. The time of observation is shown for each spectrum; the time of flares is given in Table 17-5. (From Freier and Webber [1963].)

Table 17-8. Cutoff rigidities (GV) for vertical incidence at various geographic latitudes and longitudes. (After J. J. Quenby and G. J. Wenk, 1962, *Phil. Mag.*, v. 7, no. 81, p. 1457.)

Lat.	Longitude (°E) 0	10	20	30	40	50	60	70	80	90	100	110
70°N	0.274	0.341	0.376	0.408	0.453	0.475	0.505	0.52	0.54	0.55	0.55	0.55
65	0.505	0.65	0.70	0.74	0.79	0.82	0.82	0.91	0.96	1.00	1.02	1.04
60	1.12	1.23	1.28	1.29	1.42	1.49	1.54	1.61	1.70	1.75	1.82	1.86
55	1.92	2.08	2.21	2.29	2.41	2.56	2.58	2.64	2.67	2.71	2.79	2.84
50	3.06	3.38	3.60	3.73	3.81	3.77	3.77	3.77	3.84	3.87	3.98	4.11
45	4.73	5.05	5.2	5.4	5.4	5.6	5.7	5.7	5.8	5.9	5.9	6.1
40	6.7	6.9	7.2	7.4	7.6	7.7	7.8	7.9	8.2	8.7	9.4	9.6
35	8.8	9.2	9.6	9.7	10.0	10.3	10.4	11.0	12.0	12.7	13.0	13.1
30	11.2	11.4	11.6	12.2	12.6	13.0	13.5	14.1	14.3	14.5	14.5	14.6
25	13.4	13.7	13.8	14.1	14.4	14.8	15.2	15.4	15.6	15.7	15.9	15.8
20	14.4	14.6	14.9	15.2	15.5	15.9	16.1	16.3	16.5	16.8	16.8	16.7
15	14.9	15.2	15.5	15.8	16.1	16.5	16.7	17.0	17.2	17.4	17.4	17.1
10	15.1	15.4	15.6	15.9	16.4	16.7	17.0	17.2	17.6	17.7	17.7	17.5
5°N	14.9	15.2	15.5	15.7	16.1	16.5	16.7	17.1	17.5	17.6	17.7	17.5
0	14.4	14.6	14.9	15.2	15.7	16.1	16.3	16.6	16.8	17.1	17.2	17.2
5°S	13.7	13.8	14.0	14.3	14.8	15.2	15.5	15.7	15.9	16.0	16.2	16.4
10	12.5	12.4	12.4	12.9	13.4	14.0	14.4	14.7	14.9	15.0	15.0	15.1
15	11.4	10.9	11.1	11.5	12.1	12.5	12.8	13.1	13.5	13.5	13.5	13.4
20	10.5	10.0	10.2	10.4	10.7	10.7	10.5	10.3	10.8	11.3	10.9	10.6
25	9.7	9.4	9.4	9.3	8.6	8.3	7.8	7.6	7.2	7.0	7.1	7.0
30	8.9	8.1	7.9	7.5	6.8	6.4	5.9	5.4	5.01	4.78	4.62	4.62
35	7.5	6.9	6.2	5.6	5.06	4.58	4.36	4.02	3.58	3.44	3.25	3.18
40	6.3	5.3	4.59	4.03	3.77	3.51	3.18	2.79	2.48	2.18	2.03	1.93
45	4.75	4.03	3.58	3.20	2.76	2.42	2.10	1.75	1.50	1.31	1.18	1.11
50	3.76	3.16	2.65	2.22	1.81	1.54	1.34	1.11	0.90	0.77	0.63	0.59
55	2.73	2.20	1.79	1.49	1.21	0.99	0.82	0.68	0.512	0.376	0.294	0.269
60	1.90	1.57	1.24	0.99	0.77	0.63	0.512	0.376	0.281	0.185	0.136	0.103
65	1.27	1.05	0.82	0.63	0.494	0.376	0.281	0.194	0.130	0.076	0.0443	0.0302
70°S	0.82	0.68	0.512	0.408	0.294	0.224	0.136	0.067	0.055	0.0279	0.0136	0.0056

Lat.	Longitude (°E) 120	130	140	150	160	170	180	190	200	210	220	230
70°N	0.56	0.57	0.57	0.55	0.512	0.475	0.421	0.358	0.288	0.211	0.161	0.097
65	1.07	1.07	1.07	1.04	0.97	0.91	0.82	0.76	0.63	0.475	0.347	0.246
60	1.87	1.88	1.90	1.82	1.76	1.69	1.55	1.39	1.20	0.95	0.75	0.56
55	2.90	2.96	3.00	3.02	3.00	2.91	2.70	2.38	2.00	1.68	1.35	1.09
50	4.15	4.23	4.26	4.37	4.37	4.26	4.09	3.67	3.22	2.73	2.23	1.84
45	6.1	6.4	6.4	6.4	6.2	5.8	5.7	5.1	4.60	4.13	3.56	2.95
40	9.6	9.3	9.0	9.0	8.5	8.2	7.7	7.1	6.2	5.6	4.99	4.42
35	13.1	13.0	12.6	11.9	11.2	10.4	9.9	9.3	8.3	7.6	6.7	5.9
30	14.5	14.3	13.9	13.5	13.1	12.7	12.3	11.5	10.4	9.7	8.9	8.2
25	15.5	15.3	14.9	14.5	14.1	13.8	13.4	13.1	12.7	12.1	11.1	10.4
20	16.4	16.2	16.0	15.3	14.8	14.5	14.2	13.9	13.7	13.5	13.2	12.8
15	16.9	16.7	16.4	16.0	15.6	15.1	14.8	14.6	14.4	14.3	14.2	14.0
10	17.1	16.9	16.5	16.3	16.0	15.7	15.4	15.2	15.0	14.8	14.7	14.6
5°N	17.2	17.1	16.7	16.3	16.2	16.0	15.7	15.6	15.4	15.3	15.2	15.0
0	17.0	16.8	16.5	16.2	16.2	16.0	15.9	15.7	15.6	15.5	15.4	15.2
5°S	16.3	16.2	16.1	16.0	15.9	15.8	15.7	15.6	15.5	15.4	15.3	15.1
10	15.1	15.2	15.2	15.2	15.2	15.4	15.3	15.2	15.2	15.0	14.8	14.8
15	13.3	13.6	13.8	14.0	14.1	14.2	14.3	14.4	14.4	14.4	14.4	14.4
20	10.5	10.6	11.1	11.4	12.1	12.5	12.6	13.0	13.3	13.6	13.8	14.0
25	7.0	7.5	7.8	8.1	8.6	9.3	10.2	11.2	12.1	12.5	12.9	13.3
30	4.70	4.91	5.2	5.7	6.2	6.9	7.7	8.5	9.5	10.6	11.7	12.3
35	3.25	3.38	3.64	4.02	4.36	4.87	5.55	6.2	7.2	8.1	9.0	10.0
40	1.98	2.05	2.28	2.63	3.01	3.58	4.03	4.56	5.2	5.8	6.7	7.6
45	1.16	1.18	1.25	1.51	1.79	2.27	2.76	3.20	3.64	4.16	4.67	5.5
50	0.55	0.57	0.63	0.80	1.02	1.22	1.45	1.86	2.29	2.89	3.39	4.03
55	0.257	0.246	0.246	0.333	0.475	0.63	0.82	1.08	1.39	1.78	2.27	2.87
60	0.096	0.086	0.086	0.129	0.194	0.294	0.458	0.61	0.82	1.11	1.42	1.81
65	0.0236	0.0180	0.0198	0.0350	0.073	0.136	0.224	0.347	0.494	0.66	0.85	1.08
70°S	0.00329	0.00178	0.00245	0.0089	0.0256	0.055	0.109	0.185	0.269	0.376	0.512	0.68

(Continued)

Table 17-8. Cutoff rigidities (GV) for vertical incidence at various geographic latitudes and longitudes. (After J. J. Quenby and G. J. Wenk, 1962, *Phil. Mag.*, v. 7, no. 81, p. 1457.) (Continued)

Lat.	Longitude (°E)											
	240	250	260	270	280	290	300	310	320	330	340	350
70°N	0.056	0.0297	0.0152	0.0093	0.0082	0.0106	0.0177	0.0337	0.061	0.096	0.151	0.216
65	0.156	0.100	0.062	0.0430	0.0405	0.0450	0.065	0.100	0.157	0.233	0.347	0.475
60	0.381	0.255	0.174	0.138	0.125	0.136	0.181	0.246	0.365	0.53	0.72	0.94
55	0.80	0.58	0.434	0.330	0.304	0.314	0.388	0.53	0.73	0.99	1.34	1.66
50	1.44	1.13	0.85	0.71	0.63	0.62	0.73	0.96	1.28	1.61	2.24	2.68
45	2.42	1.98	1.57	1.29	1.18	1.11	1.24	1.55	2.00	2.52	3.36	4.12
40	3.83	3.20	2.52	2.21	1.97	1.88	2.06	2.43	3.01	3.86	4.94	5.8
35	5.25	4.60	4.02	3.48	3.15	3.05	3.22	3.66	4.39	5.4	6.6	7.8
30	7.3	6.4	5.6	4.94	4.45	4.31	4.48	4.97	5.8	7.2	8.8	10.3
25	9.6	8.7	7.7	6.8	6.3	6.0	6.4	6.9	8.0	9.1	10.7	12.8
20	12.0	11.1	9.8	8.9	8.3	8.0	8.5	9.0	10.1	11.1	12.8	14.0
15	13.6	13.0	12.5	11.2	10.7	10.3	11.0	11.6	12.5	13.3	14.2	14.7
10	14.5	14.1	13.3	12.4	11.8	11.7	12.4	13.1	13.6	14.2	14.6	14.8
5°N	14.9	14.6	14.1	13.3	12.6	12.5	13.2	13.7	14.1	14.3	14.5	14.7
0	15.1	15.0	14.6	14.1	13.5	13.4	13.6	13.9	14.1	14.1	14.2	14.2
5°S	15.1	15.0	14.7	14.4	13.9	13.7	13.7	13.8	13.8	13.8	13.6	13.5
10	14.8	14.7	14.6	14.4	14.0	13.6	13.6	13.6	13.4	13.3	13.1	12.7
15	14.4	14.3	14.3	14.2	13.9	13.4	13.2	13.2	12.9	12.6	12.4	11.8
20	14.0	14.0	14.0	14.0	13.6	13.0	12.8	12.7	12.2	11.8	11.4	10.8
25	13.5	13.6	13.7	13.6	13.2	12.5	12.3	12.2	11.6	11.0	10.6	10.0
30	12.6	12.8	13.1	13.1	12.6	12.1	11.8	11.6	11.1	10.4	9.9	9.5
35	10.8	11.5	12.2	12.3	12.1	11.8	11.4	11.2	10.7	9.9	9.0	8.1
40	8.3	9.0	9.7	10.2	10.4	10.9	10.2	10.0	9.3	8.8	8.0	7.0
45	6.1	7.0	7.6	8.4	8.9	9.3	9.4	9.2	8.5	7.5	6.6	5.8
50	4.50	5.1	5.6	6.2	6.8	7.2	7.3	7.1	6.7	5.9	5.1	4.36
55	3.42	3.88	4.35	4.84	5.3	5.6	5.7	5.6	5.3	4.68	4.05	3.38
60	2.19	2.64	3.05	3.55	3.89	4.03	4.15	4.07	3.85	3.38	2.81	2.37
65	1.38	1.65	1.97	2.30	2.52	2.62	2.72	2.72	2.56	2.29	1.90	1.57
70°S	0.85	1.05	1.27	1.46	1.57	1.65	1.69	1.69	1.61	1.46	1.24	1.05

17.5 REFERENCES

Dorman, L. I., 1963, "Progress in Elementary Particle and Cosmic Ray Physics VII," J. G. Wilson and S. A. Worthuysen, eds., North Holland Publishing Co., Amsterdam.

Ely, J. T. A., 1962, "Atmospheric Depth and Effective Solid Angle for Radiation Penetrating the Atmosphere," *Geophys. Res. Papers No.* 74, AFCRL.

Fillius, R. W., and C. E. McIlwain, 1964, "Anomalous Energy Spectrum of Protons in the Earth's Radiation Belt," *Phys. Rev. Letters*, v. 12, no. 22, p. 609.

Filz, R. C., H. Yagoda, and E. Holeman, 1964, "Observations of Trapped Protons in Emulsions Recovered from Satellite Orbits," *Space Research IV*, Proceedings of the Fourth International Space Science Symposium, Warsaw, Poland, P. Muller, ed., North Holland Publishing Co., Amsterdam.

Freier, P. S., and W. R. Webber, 1963, "Exponential Rigidity Spectra for Solar Flare Cosmic Rays," *J. Geophys. Res.*, v. 68, no. 6, p. 1605.

Katz, L., D. Smart, F. R. Paolini, R. Giacconi, R. J. Talbot, Jr., 1964, *Space Research IV*, Proceedings of the Fourth International Space Science Symposium, Warsaw, Poland, P. Muller, ed., North Holland Publishing Co., Amsterdam.

Lencheck, A. M., 1962, "On the Anomalous Component of Low-Energy Geomagnetically Trapped Protons," *J. Geophys. Res.*, v. 67, no. 6, p. 2145.

Lockwood, J. A., and H. E. Yingst, 1956, "Correlation of Meteorological Parameters with Cosmic-Ray Neutron Intensities," *Phys. Rev.*, v. 104, p. 1718.

McCracken, K. G., 1962, "Cosmic Ray Flare Effect," *J. Geophys. Res.*, v. 67, no. 2, p. 431.

McDonald, F. B., ed., 1963, *Solar Proton Manual*, NASA Tech. Rept., NASA TR R-169.

McIlwain, C. E., 1963, "Radiation Belts, Natural and Artificial," *Science*, v. 142, p. 355.

McIlwain, C. E., 1961, "Coordinate for Mapping the Distribution of Magnetically Trapped Particles," *J. Geophys. Res.*, v. 66, no. 11, p. 3681.

Nangle, J. E., and D. A. Kniffen, 1961, "Flux and Energy Spectra of the Protons in the Inner Van Allen Belt," *Phys. Rev. Letters*, v. 7, p. 3.

Neher, H. V., and H. R. Anderson, 1962, "Cosmic Rays at Balloon Altitudes and the Solar Cycle," *J. Geophys. Res.*, v. 67, no. 4, p. 1309.

Neher, H. V., 1952, "Progress in Cosmic Ray Physics, I," J. G. Wilson, ed., North Holland Publishing Co., Amsterdam.

Neher, H. V., 1958, "The Primary Cosmic Radiation," *Annual Reviews of Nuclear Science*, v. 8, p. 217, Annual Reviews Inc., Palo Alto.

Northrup, T. G., 1963, "Adiabatic Motion of Charged Particles," John Wiley and Sons, New York.

Obayashi, T., 1959, *Rept. Ionosphere and Space Res., Japan*, v. 13, p. 201.

O'Brien, B. J., 1962-1963, "Reviews of Studies of Trapped Radiation with Satellite-Borne Apparatus," *Space Science Reviews*, C. G. Jager/Utrecht, ed., v. 1, p. 415.

Paolini, F. R., R. Giacconi, J. R. Waters, L. Katz, and D. Smart, in press, *Space Research V*, Proceedings of the Fifth International Space Science Symposium, Florence, Italy, D. King-Hele, ed., North Holland Publishing Co., Amsterdam.

Pizzella, G., C. E. McIlwain, and J. A. Van Allen, 1962, "Time Variations of Intensity in the Earth's Inner Radiation Zone," *J. Geophys. Res.*, v. 67, no. 4, p. 1235.

Singer, S. F., and A. M. Lencheck, 1962, Geomagnetically Trapped Radiation, "Progress in Elementary Particle and Cosmic Ray Physics VI," J. G. Wilson and S. A. Worthuysen, eds., North Holland Publishing Co., Amsterdam.

Stone, E. C., 1963, "Physical Significance and Application of L, B_0, and R_0 to Geomagnetically Trapped Particles," *J. Geophys. Res.*, v. 68, p. 4157.

Yoshida, S., and M. Wada, 1959, "Storm-Time Increase of Cosmic-Ray Intensity," *Nature*, v. 183, p. 381.

Chapter 18

INTERPLANETARY SPACE AND THE SOLAR ATMOSPHERE

Marvin L. White

Very little is known about interplanetary conditions. Theoretical models are available, however, from which reasonable speculations can be made. Because the sun is the primary source of the interplanetary gas, particular emphasis is placed on the sun's atmosphere (the photosphere, chromosphere, and the corona as a hydrodynamic whole).

The CGS electromagnetic system of units is used in the equations in this chapter with the few exceptions for which practical units are explicitly stated. Symbols used frequently are as follows:

- B is the magnetic field vector (magnetic flux density);
- g_s is acceleration of solar gravity;
- g_o is acceleration of solar gravity at the limb (2.74×10^4 cm sec^{-2});
- G is the gravitational constant;
- k is the Boltzmann constant;
- L is height above the solar limb in solar radii;
- m is particle mass;
- m_p is mass of the proton;
- M is mass of the sun;
- N is the number of particles cm^{-3};
- N_e is the number of electrons cm^{-3};
- r is radial distance from the sun (unless otherwise specified);
- r_s is the solar radius (7×10^{10} cm from center to limb);
- R is radial distance in solar radii (r/r_s);
- T is temperature (°K);
- η is the kinematic viscosity;
- θ is solar colatitude;
- κ is the coefficient of thermal conductivity;
- μ is the viscosity;
- ν is the collision frequency;
- ρ is the mass density (gram cm^{-3});
- σ is the electrical conductivity;
- ϕ is the solar azimuth angle; and
- ω is angular velocity.

Other symbols used are defined in the text.

18.1 OBSERVATIONAL DATA FOR INTERPLANETARY SPACE

18.1.1 Electron Densities

During solar eclipses, the diffuse corona can be seen extending beyond the limb; some coronal structures have been observed out to 20 solar radii. Figure 18-1 shows electron densities derived from observations during an eclipse (February 1952) of the light scattered by the visible and the extended solar corona.

Studies of the zodiacal light were used to provide information on the nature of the coronal gas near the earth's orbit. (Zodiacal light is assumed to be the scattering of sunlight by extraterrestrial particles in the vicinity of the earth's orbit.) Measurements of the brightness of zodiacal light and of coronal brightness at the same

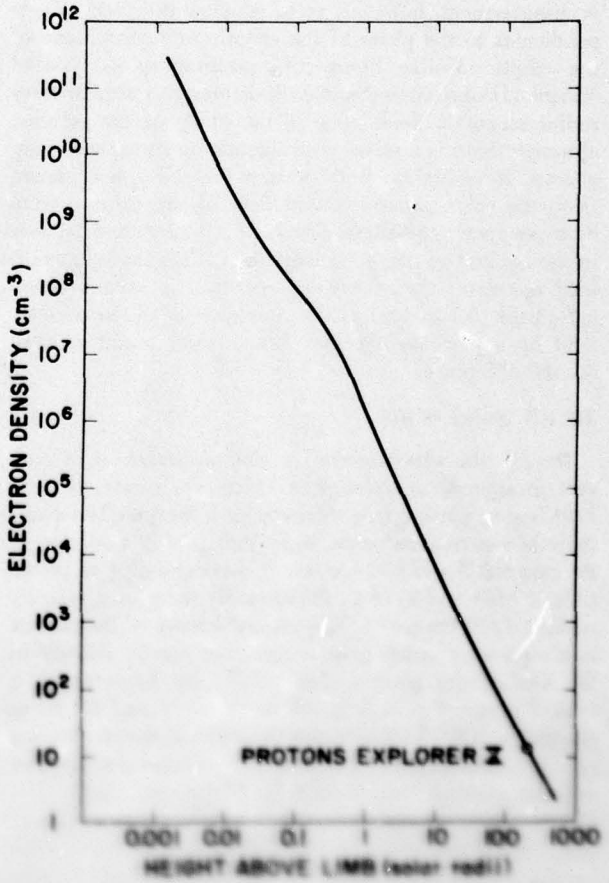


Fig. 18-1. Electron density as a function of distance above the solar limb in the equatorial plane at about the time of sunspot minimum. (After A. B. Severny, *Astrophys. J.*, v. 123, p. 44, 1956.)

wavelength during an eclipse plotted against distance from the sun fall on a smooth curve. This suggested a common origin, namely the scattering of solar radiation by the particles of a highly extended corona. Because it had been assumed that scattering by interplanetary dust particles would not introduce a polarized component, high electron densities (order of 500 cm^{-3}) were postulated to account for the observed polarization. Polarization effects of the interplanetary dust, however, are important. Calculations taking this into account indicated a quiescent electron density of less than 120 electrons cm^{-3} at the earth's orbit; during disturbed conditions, a value of 300 electrons cm^{-3} was estimated. It does not now seem possible for the electron density to be so high; therefore, the contribution of the extended corona to the zodiacal light appears to be negligible.

18.1.2 Interplanetary Magnetic Fields

Observations from Pioneer V, Explorer X, and Mariner II flights are in general agreement as to the existence of a stable interplanetary magnetic field of 2.5 to 3 γ ($10^5 \gamma$ is one gauss) that increases from 10 γ up to 40 γ during disturbed periods. There is also general agreement that the direction is perpendicular to the sun-earth line. There is disagreement, however, as to whether this field is perpendicular to the plane of the ecliptic or in the plane of the ecliptic. Unlike Pioneer V, preliminary analysis of Mariner II magnetometer data indicates an interplanetary radial magnetic field lying in the plane of the ecliptic, although there is a substantial fluctuating transverse component. It is highly unlikely that the 2.5-γ field arises from the solar general dipole field of one gauss; from hydromagnetic considerations such a field should be zero in the equatorial plane (Sec. 18.3.2). This interplanetary field is greater than the space-averaged interstellar magnetic field (0.1 to 1 γ) but compression of the interstellar field by a permanent solar plasma wind might account for the difference.

18.1.3 Solar Wind

During the observational period approaching a sunspot minimum, interplanetary space was rarely, if ever, field free or plasma free. According to Mariner II results, there is a permanent solar wind with proton velocities in the range 563 and 690 km sec^{-1}, corresponding to potentials of 1664 and 2476 V. Occasionally the proton velocity reaches 1250 km sec^{-1}. The energy density of the plasma is always very much greater than the energy density in the field. From plasma observations by Explorer X, a typical proton flux is 4×10^8 cm^{-2} sec^{-1} and the mean energy is 500 eV, hence the velocity is about 300 km sec^{-1}. Combining flux and energy measurements, typical number densities are from 6 to 20 protons cm^{-3}. The escape velocity varies according to the *exospheric level;* this is the height at which evaporative escape occurs. This level is not spherically symmetrical and varies with time, but a value of about 360 km sec^{-1} for the escape velocity is an acceptable estimate. A credible first approximation is that the solar evaporative escape velocity would be maintained throughout the sun-earth distance, so the 300 km sec^{-1} derived from Explorer X data for the solar wind seems reasonable.

18.2 MODELS OF THE CORONAL ATMOSPHERE

No one model for the solar corona is generally acceptable. Initial assumptions are more or less arbitrary and may be unrealistic. There is agreement that the maximum coronal temperature is about 2×10^6 °K (some estimates are as low as 0.8×10^6 °K), but no complete theory is available to explain the necessary transport of energy. For discussions of these problems, see papers by Allen, Chapman and Parker [Evans, 1963].

18.2.1 Inverse Square and Semi-Empirical Models

From Fig. 18-1 it is evident that a straight line, inverse square relationship approximates the electron density distribution, provided distance is measured from the solar limb and not from the solar center. Table 18-1 lists the electron densities used in plotting Fig. 18-1, and densities calculated from the relation

$$N_e = (8 \times 10^5)\, L^{-2}. \qquad (18\text{-}1)$$

By assuming that a balance between the force of gravity and the outward pressure of the compressed gas (hydrostatic equilibrium) prevails in the photosphere and above, and that the pressure is NkT (ideal gas), coronal electron temperatures can be calculated from the density data.

Table 18-1. Electron density distributions for two models; column A is Pottasch's compilation, Fig. 18-1, and column B the inverse square model, Eq. (18-1).

Distance Above Limb		Electron Density (no. cm^{-3})	
(cm)	(solar radii)	A	B
3×10^8	4.31×10^{-3}	3.5×10^{10}	4.3×10^{10}
5×10^8	7.18×10^{-3}	1.16×10^{10}	1.56×10^{10}
1×10^9	1.44×10^{-2}	2.5×10^9	3.85×10^9
2×10^9	2.87×10^{-2}	7.2×10^8	9.8×10^8
3×10^9	4.31×10^{-2}	3.65×10^8	4.3×10^8
5×10^9	7.18×10^{-2}	1.64×10^8	1.56×10^8
1×10^{10}	1.44×10^{-1}	7.0×10^7	3.85×10^7
2×10^{10}	2.87×10^{-1}	2.5×10^7	9.8×10^6
3×10^{10}	4.31×10^{-1}	1.27×10^7	4.3×10^6
5×10^{10}	7.18×10^{-1}	3.8×10^6	1.56×10^6
1×10^{11}	1.44	7.4×10^5	3.85×10^5
2×10^{11}	2.87	1.4×10^5	9.8×10^4
3×10^{11}	4.31	5.55×10^4	4.3×10^4
5×10^{11}	7.18	1.7×10^4	1.56×10^4
1×10^{12}	14.4	3.92×10^3	3.86×10^3

When hydrostatic equilibrium prevails,

$$k\,\frac{dT}{dh} + \frac{kT}{N_e}\,\frac{dN_e}{dh} = -\,(0.608\,m_p)\,g_s, \tag{18-2}$$

where h is height above the solar limb and g_s is $g_o(L+1)^{-2}$. The 0.608 factor $g_o(L+1)^2$ includes a completely ionized helium content in a ratio with protons of 1 to 10; for a pure proton-electron gas the factor would be 0.500. Table 18-2 is a compilation of electron temperatures derived from Eq. (18-2) for the two models of electron density given in Table 18-1. Figure 18-2 shows the temperature profiles.

Without adjusting any constants, the temperature profile obtained by using Eq. (18-1) gives the temperature maximum as 1.65×10^6 °K at 0.7 solar radii above the limb, and a temperature of 3500°K near the solar limb (2.5×10^{-4} solar radii); at the earth's orbital distance (≈ 215 solar radii), the temperature is about 20,000°K. The temperature law corresponding to this profile is

$$T = 1.40 \times 10^7\,L^2\left[\frac{1+2L}{L\,(L+1)} + 2\ln\left(\frac{L}{L+1}\right)\right], \tag{18-3}$$

where the solar corona is considered to be electrons, protons, and totally ionized helium. (For a gas of electrons and protons only, the maximum coronal temperature would be 1.35×10^6 °K.) For L greater than 2 or 3 solar radii, the temperature profile of Eq. (18-3) is proportional to L^{-1}. $T \propto L^{-1}$ and the density $N \propto L^{-2}$ are consistent with a coronal model in polytropic expansion. As $L \to \infty$, T and $N \to 0$ and the corresponding pressure, which is proportional to NkT, vanishes. The total integrated solar mass becomes infinite for $N_e \propto L^{-2}$; however, the integration is cut off at a finite distance as is customary in problems involving the gravitational inverse square law.

In the fundamental equation of motion for a steady state, the mass times acceleration term, Eq. (18-9) on the left, is zero if the outward velocity from the sun is a constant (independent of R). The radial wind component of high velocity evaporation from the sun, v(R), should be about constant over 215 solar radii. In this case, pressure and gravitational forces are in balance. From the equation of continuity of particle flux, $N(R)v(R)R^2$ is constant; thus, the number density N(R) should be inversely proportional to R^2. These are the conditions used to obtain the temperature profile for the extended corona ($L = R - 1 \approx R$), so that the curve labeled $N_e \propto L^{-2}$ in Fig. 18-2 is also valid for a constant solar wind. These two regimes (hydrostatic equilibrium and high velocity solar wind) can in fact hold simultaneously; they seem mutually compatible (Sec. 18.2.6).

In integral form, Eq. (18-2) becomes

$$kTN_e - (kTN_e)_D = -\,(0.608\,m_p)\,g_o\,r_s \int_{L_D}^{L} N_e\,(L+1)^{-2}\,dL \tag{18-4}$$

where subscript D indicates values to be taken at a selected datum level. This form is easily adapted to Simpson's rule for integration. The semi-empirical curve in Fig. 18-2 gives the results of such integration when Pottasch's density distribution is used. The temperature profile has a maximum at 1.5×10^6 °K at L = 0.23, and a second peak at 1.4×10^6 °K just above L = 0.7. The temperature at the earth's orbital distance is 20,000°K and the temperature at the solar limb (2.5×10^{-4} solar radii) is about 3000°K. Integration of Eq. (18-2) by an iteration method gives 1.43×10^6 °K as the maximum temperature, but leads to inaccuracies from the datum level (10^9 cm above limb) out to 10^{11} cm and to uncertainties in the height (somewhere between L = 0.1 and 2.0) corresponding to the maximum temperature.

Table 18-2. Two models of temperature distributions. Values for the inverse square model calculated from Eq. (18-3) using Eq. (18-1); values for the semi-empirical model calculated from Eq. (18-4) using data of Table 18-1, column A.

Distance Above Limb		Electron Temperature (°K)	
(cm)	(solar radii)	Inverse Square	Semi-empirical
3×10^8	4.31×10^{-3}	5.4×10^4	5.6×10^4
5×10^8	7.18×10^{-3}	9.4×10^4	1.01×10^5
1×10^9	1.44×10^{-2}	1.8×10^5	2.47×10^5
2×10^9	2.87×10^{-2}	3.3×10^5	5.03×10^5
3×10^9	4.31×10^{-2}	4.6×10^5	7.36×10^5
5×10^9	7.18×10^{-2}	6.8×10^5	1.11×10^6
1×10^{10}	1.44×10^{-1}	1.1×10^6	1.37×10^6
2×10^{10}	2.87×10^{-1}	1.4×10^6	1.50×10^6
3×10^{10}	4.31×10^{-1}	1.5×10^6	1.35×10^6
5×10^{10}	7.18×10^{-1}	1.6×10^6	1.39×10^6
1×10^{11}	1.44	1.45×10^6	1.26×10^6
2×10^{11}	2.87	1.08×10^6	9.36×10^5
3×10^{11}	4.31	8.0×10^5	7.18×10^5
5×10^{11}	7.18	5.4×10^5	5.02×10^5
1×10^{12}	14.4	2.8×10^5	2.76×10^5

18.2.2 Chapman's Model

Chapman [1957] developed a model for the extended corona from a self-consistent theory which relies on observation only at the datum level $T = 10^6$ °K at R = 1.06 solar radii. Hydrostatic equilibrium and a perfect gas are assumed. The outward transfer of energy is assumed to be only by thermal conduction of protons and electrons with the total outward conduction of heat assumed to be a constant. Conservation of energy is satisfied. From this condition for conductive equilibrium, the temperature is proportional to $R^{-2/7}$, in sharp contrast to the semi-empirical temperature profiles. The semi-empirical results

should be more reliable; they involve one less assumption. Because the temperature decreased with distance far too slowly in the original model (219,000°K at the earth's orbital distance), Chapman introduced eddy conductivity as a means of thermal conduction. The coefficients of eddy conductivity are arbitrarily adjusted to achieve agreement with semi-empirical temperature profiles. The corona, however, has a Reynolds number of about one (Sec. 18.4.2) so that eddy conductivity should be unimportant up to $R = 1.7$; beyond this there is a temperature inversion so that eddys may develop.

Neither the electron density nor pressure are well behaved in Chapman's model. After reaching a minimum at 175 solar radii for a datum temperature of 10^6 °K, the electron density increases with distance. The pressure is finite at infinity, having a value well in excess of the value for interstellar pressure, although a finite pressure at infinity contradicts the assumption of hydrostatic equilibrium.

18.2.3 Chamberlain's Models

Chamberlain [1961] proposes a steady state model using two of the same basic equations as Parker (Sec. 18.2.5) in a hydrodynamic approach; however, the first law of thermodynamics with heat conduction is substituted for the polytropic gas law. The equations are solved numerically, beginning from an arbitrary but mathematically convenient distance (577 solar radii) and proceeding inward toward the sun; integrations are carried out for several assumed initial values of electron density and expansion velocity. The solutions give a reasonable value for the maximum coronal temperature only if the conditions at 577 solar radii are taken as 5.7 km sec^{-1} and 20 electrons cm^{-3}. The calculated electron densities, however, are not then in agreement with the values obtained from eclipse observations (Fig. 18-1). This discrepancy is rectified by a reduction in the thermal conductivity (by a factor of from 5 to 8) which is attributed to inhibiting effects of an interplanetary magnetic field. The velocity values appear too low compared with Explorer X flux data. Temperatures in the vicinity of the earth agree with Fig. 18-2.

Chamberlain [1960] also considered the problem of coronal evaporation using kinetic theory for the escape of planetary and stellar atmospheres. His addition to Jean's theory for evaporative escape, Eq. (18-7), includes particles falling in along hyperbolic orbits from infinity. The correction is unimportant in so far as computations of electron densities are concerned. According to this model,

$$N(r) = N_o \exp\,[-(\lambda_o - \lambda_r)], \qquad (18\text{-}5)$$

and

$$\lambda_r = GmM/kTr; \qquad (18\text{-}6)$$

where λ_o is the value of λ at r_o, T_o, N_o. The equivalent temperature, at large distances, varies as $r^{-1/2}$. Chamberlain states that hydrodynamic escape differs in no essential way from evaporation.

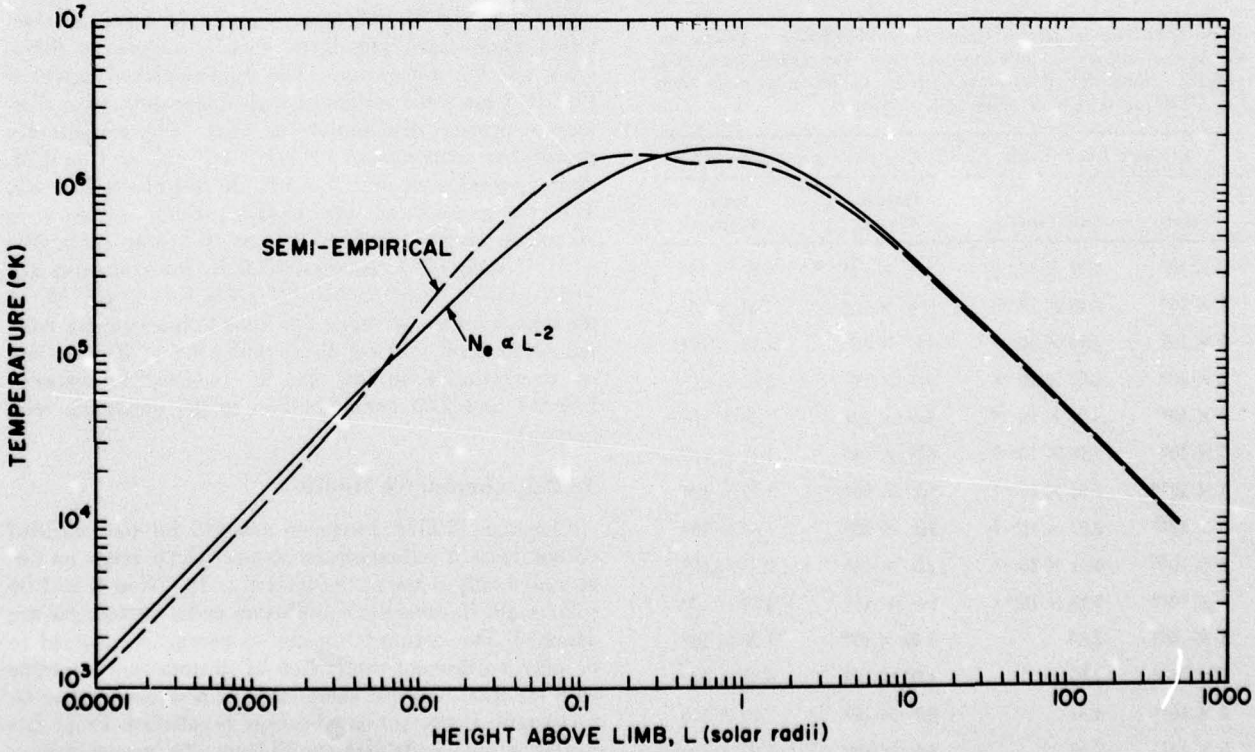


Fig. 18-2. Two models of electron temperature distribution. The semi-empirical curve was derived by using in Eq. (18-4) the electron density distribution shown in Fig. 18-1; the $N_e \propto L^{-2}$ curve by using in Eq. (18-3) the electron densities given by Eq. (18-1).

18.2.4 Sen's Electric Field Models

Sen (private communication) revives the concept that, because of the greater electron mobility, an electric field is set up which modifies or counteracts effects of the gravitational field. He uses *Jean's formula* for the escape of gases from an isothermal planetary atmosphere,

$$F_x = N_s (2\pi m/kT_s)^{-1/2} (1 + \lambda_x) \exp(-\lambda_s). \quad (18\text{-}7)$$

F_x is the flux loss (no. cm^{-2} sec^{-1}) at the exospheric level, N_s is number density at the surface, T_s is surface temperature; λ_x is the value of λ at the exospheric level, and λ_s is the value of λ at the surface. Sen assumes equality of flux for protons and electrons at the exospheric level to avoid the build-up of an inordinately high solar charge. The result is that an electron field potential of 488 V is developed which virtually annuls the solar gravitational attraction for the proton. Table 18-3 lists the results for one set of assumed initial conditions. The quantities are those predicted by the theory to occur at the earth's orbital distance from the sun; they are tabulated for various threshold values of detector sensitivity. Sen finds good agreement between his calculated densities and observed densities. Agreement can always be improved by introducing a suitable cutoff of the Maxwellian tail or adjusting the exospheric height.

It is difficult to see why the potential difference does not introduce a radial current that leaves the sun with a net charge, violating the assumption of flux equality between protons and electrons. A somewhat oversimplified premise is that below the exosphere the field is zero and that above the exosphere the conductivity is zero, so in either case no current develops. For the actual sun, a more realistic approach might be to associate the electric fields with meridional current systems which return to the sun and prevent any charge build-up. In this case, however, the electric field would add to the gravitational potential well at some solar latitudes.

Table 18-3. Protons in the extended solar atmosphere at the earth's orbital distance calculated by Sen for the conditions $T_o = 1.64 \times 10^6$ °K, $N_o = 9 \times 10^5$ protons cm^{-3} at the exospheric level of 2.5 solar radii.

Detector Threshold		Number Density	Integral Flux	Mean Energy Per Proton
$v \geqq$ (10^7 cm sec^{-1})	$E \geqq$ (eV)	(cm^{-3})	(cm^{-2} sec^{-1})	(eV)
0	0	30.5	5.66×10^8	283
1	52	26.3	5.35×10^8	297
2	209	12.1	3.19×10^8	408
3	470	2.56	8.81×10^7	644
4	835	0.244	1.05×10^7	997
5	1300	0.012	5.73×10^5	1460

18.2.5 Parker's Models

Parker [1960] developed a time-independent hydrodynamic theory, based on conservation of mass and momentum, for an expanding, spherically symmetrical corona. He postulates that the corona is heated isothermally from a reference level, r_o, out to an arbitrary, adjustable radius and then expands adiabatically beyond this distance. Parker defines a radially directed kinetic energy parameter, ψ, as a function of three dimensionless parameters ψ_o, α, λ, and an independent variable, ξ. ψ is the ratio of kinetic energy at distance ξ to thermal energy; $\psi(\xi) = m[v(\xi)]^2/2kT_o$. The radial distance, r, is given in terms of a reference level r_o; $\xi = r/r_o$. ψ_o is the kinetic energy parameter at the reference level, $\xi = 1$; $\psi_o = mv_o^2/2kT_o$. The relation $T(\xi) = T_o[N(\xi)/N_o]^{\alpha-1}$ defines α; T_o and N_o are the temperature and number density at $\xi = 1$. λ is the gravitational potential parameter (Eq. 18-6) at $\xi = 1$.

For the isothermal region ($\alpha = 1$), he derives the relation

$$\psi - \ln \psi = \psi_o - \ln \psi_o + 4 \ln \xi - \lambda + \lambda/\xi, \quad (18\text{-}8)$$

and defines a critical point ($\psi = 1$, $\xi = \lambda/4$) for which there is a critical value of the velocity (v_c) at the reference level; his critical value $(\psi_o)_c$ is $mv_c^2/2kT_o$. Parker concludes that the only solutions of Eq. (18-8) appropriate to the solar corona are those which go from a low critical velocity at r_o, pass through the critical point, and become supersonic ($\sim$ 500 km sec^{-1}) at infinity. This solution is physically significant for the free expansion of gas into a vaccum. For various reasons, he discards the other solutions.

Parker's model requires coronal heating out to many solar radii. In comparison, Sen obtains the same high solar winds by postulating an electric field that removes the protons from the gravitational potential well.

18.2.6 Alternate Interpretations of Parker's Equations

It appears that all the solutions rather than just one critical solution may be possible. For a hydrodynamic model, it is not necessary to assume zero pressure at infinity; if there is a solar wind, the pressure should not vanish at infinity. The problem of a finite density at infinity might be avoided by adding to the mass of the central body all the enclosed atmospheric mass within $r \geqq r_s$ (the Milne effect). The mass of the solar atmosphere is not a constant, but a function of r. With inclusion of this effect, the solutions for velocities below v_c need not be discarded.

Figure 18-3 shows one set of solutions for Eq. (18-8) divided into phase space by the two solutions that pass through the critical point. Particles in region I, the high velocity domain, travel faster than the escape velocity, slow down at intermediate distances, and then increase and level off at the original escape velocity when they reach the vicinity of earth; particle evaporation from the exosphere ($\xi = 1$) constitutes the high velocity domain.

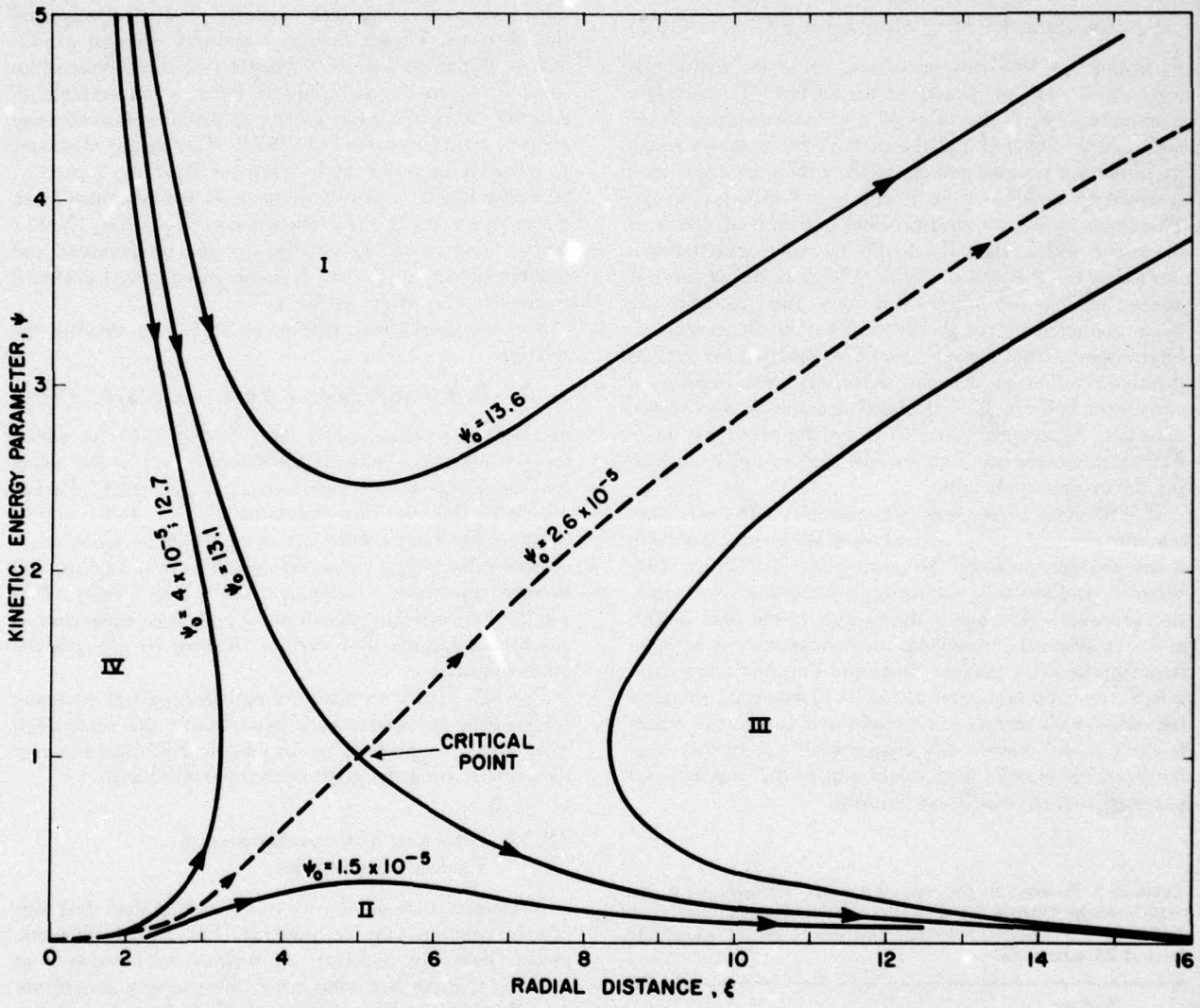


Fig. 18-3. Radial kinetic energy parameter, ψ, of an interplanetary hydrogen atom in an isothermal region ($\alpha = 1$) and strong potential field ($\lambda = 20$); $\psi(\xi) = m\,[v(\xi)]^2/2kT_o$, and $\xi = r/r_o$. The critical solutions ($\psi_o = 13.1$ and $\psi_o = 2.6 \times 10^{-5}$) divide the space into four domains: I is the high velocity domain, II is the quasi-hydrostatic domain, III is the Keplerian domain, and IV the diffusive-evaporative equilibrium domain. The dashed curve is Parker's model for this case. (After Parker [1960].)

Domain II corresponds to the low velocity regime or quasi-steady state solution; Chamberlain's models are included explicitly in the general solutions for Eq. (18-8). These low velocity particles cannot escape the solar gravitational field and so must be in nearly hydrostatic equilibrium. They may be thought of as an ambient background. (The total density should consist roughly of an ambient or near ambient background and a flow density.) Their density variation is exponential in the vicinity of the sun and inverse square at large distances, which is close to that given by Milne [1923].

The equivalence of particle dynamics and hydrodynamics is particularly evident in domain III, the Keplerian regime. At large solar distances, particle interactions are small so that in the equation of motion,

$$Nmv\frac{dv}{dr} = -\frac{d}{dr}(2NkT) - \frac{GNmM}{r^2}, \tag{18-9}$$

the middle (interaction) term is small and may be neglected. For the radially symmetric case (the one dimensional problem), $v = \frac{dr}{dt}$. Equation (18-9) then reduces to the equation of motion for the two body problem in one dimension,

$$\frac{dv}{dt} = -\frac{GM}{r^2}. \tag{18-10}$$

For this case, the square of the period is proportional to the cube of the amplitude (Kepler's third law). Particles in the Keplerian regime behave more or less independently, remaining in their own particular orbits about the sun. Particles characterized by high radial velocities (upper branch of the curve) are either entering or leaving the solar environ in strongly hyperbolic orbits; those leaving should contribute to the solar wind. Particles in the lower branch of the curve, where the radial velocity component is always small, are in nearly circular orbits; particles travel both toward and away from the sun. For particles moving in nearly circular orbits, the Keplerian angular velocity is $6.275 \times 10^{-4}\ R^{-3/2}$ rad sec^{-1}. The Keplerian angular velocities and the angular velocities for an atmosphere in quasi-hydrostatic equilibrium are equal at about $R = 100$.

The inner domain, IV, is interpreted as the region of the solar corona that is in diffusive-evaporative equilibrium. The upper branch of the curve represents material evaporating back into the inner corona while material represented by the lower part is slowly diffusing outward.

Figure 18-3 shows the isothermal case ($\alpha = 1$) and strong potential field ($\lambda = 20$). This case is particularly clear cut; the domains are distinctive and curves from the various families do not overlap. The reason for this may be that the same Maxwellian distribution occurs throughout, characterized by the temperature at the coronal base. But even for those models where T is not constant and the regimes are no longer distinct, these interpretations give some insight into the dynamical state of the medium and permit classification of the interplanetary medium into statistical species on a dynamical basis.

The possible effects of electric fields are also incorporated within the framework of Parker's equations. λ may be considered as the net result of the gravitational and an electric potential. Mathematically, this is equivalent to varying the characteristic length r_o.

Figure 18-4 shows Parker's solutions for a non-isothermal case $\left(\alpha = \frac{3}{2}\right)$ and a weak field ($\lambda = 3$). This model is compatible with the semi-empirical model ($N \propto L^{-2}$ and $T \propto L^{-1}$) if the wind velocity is either constant or small. The temperatures and scale heights of the electronic and ionic components differ and the exospheric levels will also differ. Diffusion below the exospheres will set up potential differences. The effect of the magnetic field may be to inhibit the flow, but at the same time it may raise the height of the exospheric level and hence facilitate evaporation.

18.2.7 Scale Heights for the Solar Atmosphere

If an atmosphere is in hydrostatic or nearly hydrostatic equilibrium, the number density drops by a factor of 1/e when the height, h, increases by the scale height, H;

$$N_h = N_o \exp(-h/H). \tag{18-11}$$

The scale height is a characteristic length defined by the relation,

$$H = kT/\bar{m}g_s, \tag{18-12}$$

where $\bar{m}$ is the mean mass of the atmospheric particles. Table 18-4 lists the scale heights and mean free paths for layers of various heights above and below the solar limb. The heights were determined primarily from solar eclipse measurements during the second and third contacts; because of the rapidity with which these various layers are covered and uncovered, it is difficult to determine h exactly. The temperatures used in calculating H are those of the semi-empirical hydrostatic model (Fig. 18-2). The formula used for calculating the mean free path is $6.2 \times 10^5\ T^{1/2}\ \nu^{-1}$; values of ν are listed in Table 18-10.

18.3 SOLAR AND INTERPLANETARY MAGNETIC FIELDS

During sunspot minimum the corona shows the typical three-streamer pattern shown in Fig. 15-8. (During the minimum in 1954, however, only two coronal plumes, symmetrical about the equatorial plane, were observed.) The plumes are absent at sunspot maximum, when the corona is more extensive and characteristically almost spherically symmetrical. The existence of the plumes is evidence of a general poloidal solar magnetic field.

Coronographic studies indicate that the streamers have a degree of permanency; the coronal pattern lifetime is up to 0.5 yr. The degree of coronal activity depends upon the degree of activity in the photosphere and chromosphere at the base of the ray. The corona rotates as a nearly solid body and has a characteristic equatorial bulge with a net negative space charge which may vary over the sunspot cycle.

According to the model discussed in this section, the solar magnetic energy oscillates between a toroidal and a poloidal field. The energy for the oscillation comes from the variation of eddy transport with latitude. A general solar-wide circulation (Sec. 18.4.4), together with the magnetic coupling between the hemispheres, can account for the solar magnetic and sunspot cycles as well as prominence morphology. Magnetic clouds in the circulation system produce magnetic linkage of the solar atmospheric layers to form prominences and flares.

18.3.1 Solar Magnetic Cycle and Sunspots

The solar magnetic cycle has a period approximately twice that of the sunspot cycle. (Figure 15-9 shows the periodicity of the sunspot cycle.) This conclusion is based in part on currently incomplete observations of the variations in the photospheric magnetic field. It appears that the magnetic poles reverse with approximately an 11-yr period, presumably making a complete cycle in about 23 yr; the reversal occurs about the time of the sunspot maximum.

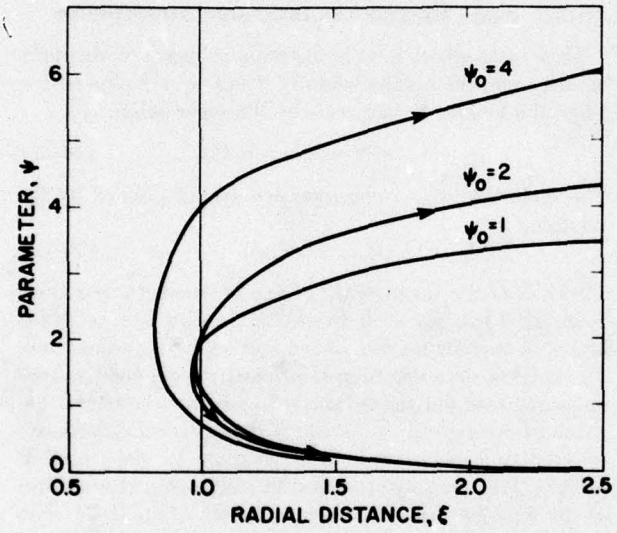


Fig. 18-4. Parker's solutions for the kinetic energy parameter ψ vs ξ for a non-isothermal case ($\alpha = 3/2$) and weak potential field ($\lambda = 3$). (After Parker [1960].)

A feasible explanation is that there is a magnetic band (a ring of lines of force) in each hemisphere underlying the active regions. Such lines of force must be just beneath the photosphere because a 23-yr periodic change in a body as large as the sun must be a surface phenomenon. Also, if the magnetic field of a sunspot arose deeper in the solar interior, the rapidly increasing temperature and electrical conductivity would result in a frozen-in condition and the lifetime of a sunspot would be many years. If the fields are reversed in the two hemispheres (Sec. 18.5), the force of attraction between the two magnetic bands causes the migration of the active regions toward the solar equator, thus accounting in part for the changes in distribution of sunspots with solar cycle (butterfly diagram).

Figure 18-5 is a typical butterfly diagram, showing how the spot distribution migrates toward the equator during a sunspot cycle. The butterfly diagram is typical of a velocity vs time plot for a nonlinear oscillator, and the latitudinal migration of the sunspots may be considered as corresponding to changes in angular velocity. According to this viewpoint, the sunspot cycle is a nonlinear oscillation that arises from the weak interaction of the two hemispheric systems. At times, two magnetic poles of the same polarity occur in opposite hemispheres, which indicates that the oscillations in the two hemispheres are only weakly coupled.

The butterfly diagram indicates that the magnetic bands remain at the minimum latitude for a major portion of the sunspot cycle; this is the time required for the two hemispheric bands to join together and diffuse into space. Sunspots, normally produced when magnetic lines of force emerge perpendicular to the surface, are not present at the absolute minimum because the field is weakened and parallel to the surface. At this time the polar magnetic plumes are strongest. Approaching maximum, the polar

Table 18-4. Scale heights and mean free paths for the solar atmosphere.

Radial Distance (solar radii)	Height (cm)	Temperature (°K)	Mean Mass (10^{-24}g)	Gravity (cm sec^{-2})	Scale Height (cm)	Mean Free Path (cm)
3	1.4×10^{11}	1.1×10^{6}	1.02	3.04×10^{3}	4.9×10^{10}	1.5×10^{11}
1.5	3.5×10^{10}	1.39×10^{6}	1.02	1.22×10^{4}	1.5×10^{10}	1.3×10^{10}
1.06	4.0×10^{9}	1.0×10^{6}	1.02	2.44×10^{4}	5.5×10^{10}	1.9×10^{8}
1.01	7.0×10^{8}	1.5×10^{5}	1.02	2.68×10^{4}	7.6×10^{8}	1.7×10^{5}
1.0014	1.0×10^{8}	5.3×10^{3}	1.67	2.74×10^{4}	1.6×10^{7}	2.3
1.0000	0	4.5×10^{3}	1.67	2.74×10^{4}	1.4×10^{7}	6.6×10^{-2}
0.9997	-2.10×10^{7}	5.0×10^{3}	1.67	2.74×10^{4}	1.5×10^{7}	2.1×10^{-3}
0.9995	-3.35×10^{7}	7.5×10^{3}	1.67	2.74×10^{4}	2.2×10^{7}	1.1×10^{-4}

plumes subside and the toroidal fields build up as manifested by increased sunspot activity. After maximum, the solar-plumes return, presumably with reversed magnetic polarity, the energy having transferred from a toroidal to a poloidal field. The energy for this cycle comes from differential rotation and from the resulting amplification of the toroidal field (Sec. 18.4).

Figure 18-6 illustrates a possible *model for the magnetic fields of a sunspot.* In the umbra of sunspots, the repression of convection cells (Sec. 15.4.2) is no doubt due to the presence of large vertical magnetic fields. Magnetic pressure in the spot implies a gas pressure and therefore a temperature lower than the surroundings (assuming quasi-static equilibrium). This mechanism would account in part for the temperature of the spot being approximately 2000°K cooler than the undisturbed photosphere. In the penumbra, the magnetic field is not nearly as vertical as in the umbra. The departure of the magnetic lines of force from the vertical gives a horizontal component of the magnetic field along which the granules can be aligned, thus giving the penumbra its characteristic appearance of spokes radiating from the umbra on the surface of the photosphere. The penumbra is warmer than the umbra because there is less suppression of the convection cells in the penumbra. According to this model, M regions could result from an underlying magnetic field that is too weak or at too great an angle from the vertical to cause a sunspot.

18.3.2 Interplanetary Magnetic Field and Distortion of Solar Dipole Field

Assuming a radial source of completely ionized hydrogen gas and a centered dipole field for the undisturbed state, the poloidal field components of an adiabatically expanding corona in the radial, B_r, and colatitudinal, B_θ, directions are

$$B_r = 2\, M_d \cos\theta\, F\,(1, 4, -\Lambda/r)/r^3,$$
$$B_\theta = M_d \sin\theta\, F\,(2, 4, -\Lambda/r)/r^3. \tag{18-13}$$

The equation for the lines of force is

$$\frac{\sin^2\theta}{r}\, F\left(1, r, -\frac{\Lambda}{r}\right) = \text{constant}. \tag{18-14}$$

In these equations, M_d is the dipole moment, r is distance from the dipole center, and F is the confluent hypergeometric function (F may be interpreted as a magnetohydrodynamic distortion factor to the pure dipole field). The length parameter Λ is $4\pi\ \Phi\ \sigma_o/a$, where Φ is the number of particles emitted in a unit solid angle per second from the sun and σ_o and a are proportionality constants defined by Eqs. (18-15) and (18-16);

$$\sigma = \sigma_o T^{3/2}, \tag{18-15}$$

and

$$N = aT^{3/2}. \tag{18-16}$$

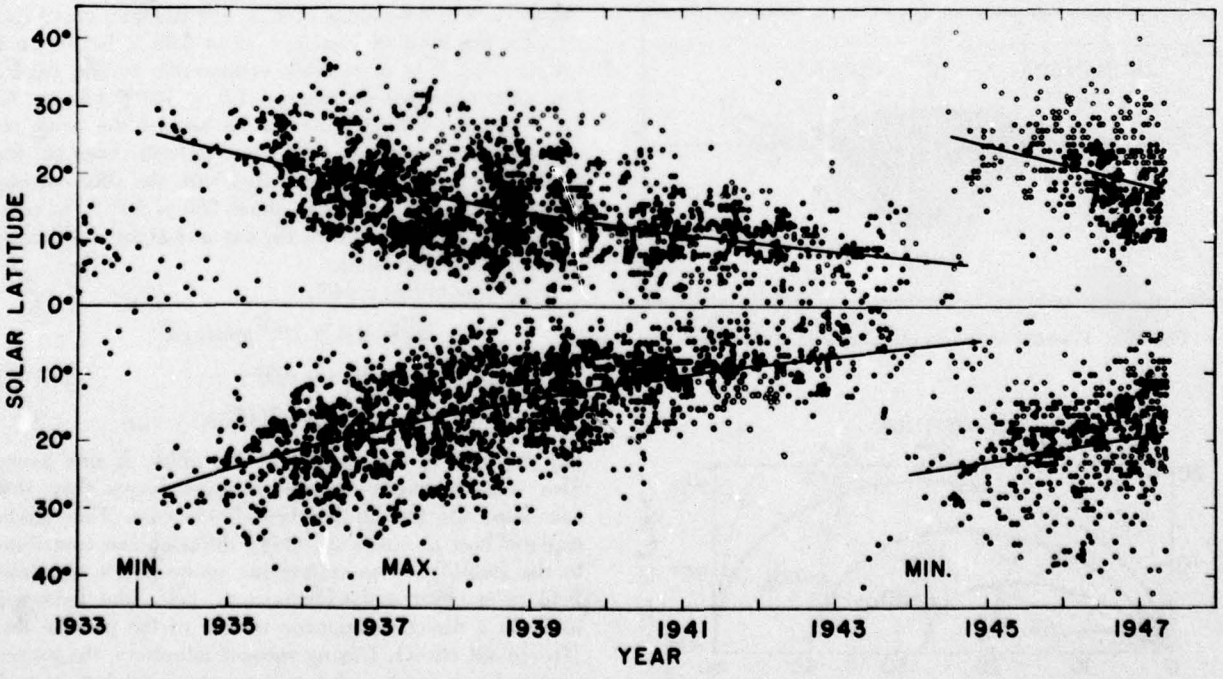


Fig. 18-5. Typical butterfly diagram of variation in distribution of sunspots with time; during a sunspot cycle the distribution migrates toward the solar equator (Mount Wilson and Palomar Observatories).

As $\Phi \rightarrow 0$, $\Lambda \rightarrow 0$, and by definition $F \rightarrow 1$, Eqs. (18-13) and (18-14) become the usual formulas for an undisturbed dipole field. The limit of (B_r/B_θ) as $\Lambda \rightarrow \infty$ is infinite for $\theta \neq 90°$, so that the solar magnetic field is purely radial for infinite particle emission. Thus when particle flux is emitted, the poloidal magnetic field is weakened. (If particle flux is injected into the parent body, as during star formation, the poloidal field is strengthened.) Figure 18-7 illustrates the distortion of a line of force as particle emission (Λ) increases.

On the basis of the proton flux measured by Mariner II, the total emission is 5×10^{36} particle sec^{-1} during sunspot minimum, thus minimum conditions represent $\Lambda \rightarrow \infty$. As a result, during minimum the solar magnetic field should be predominantly radial; B_θ is almost negligible. At $\theta = 90°$, however, B_r vanishes because of the cosine factor, so the component of the magnetic field perpendicular to the equatorial plane observed at sunspot minimum probably derives from the interstellar magnetic field. This model accounts for the apparent presence of a dipole field only near the solar magnetic poles, both in the photosphere and the corona. Apparently below 55° latitude, B_r has fallen below the observational level. A possible explanation, according to this model, for the mutual exclusion of plasma and magnetic field found by Explorer X, is that particle emission causes a field weakening so that the medium behaves diamagnetically. (For particle injection, the dipole field is strengthened and the interplanetary medium behaves ferromagnetically.)

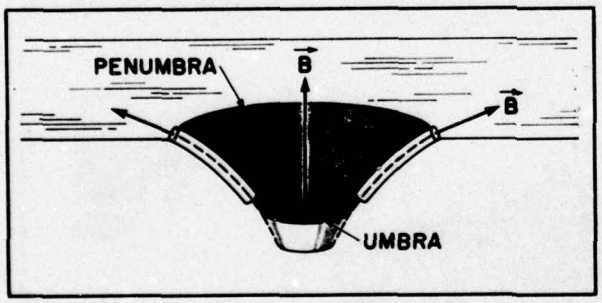


Fig. 18-6. Tentative model for magnetic field of a sunspot.

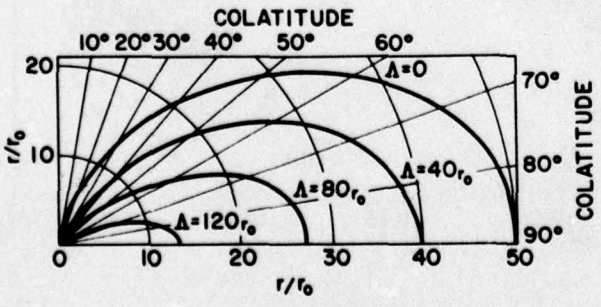


Fig. 18-7. Distortion of magnetic dipole field contour as a function of particle emission (parameter Λ) calculated from Eq. (18-14) using 1/50 r_0 as the constant; r_0 is any arbitrary base length.

The distortion in the poloidal lines of force may be accompanied by a toroidal (azimuthal) current system. If the emitting flux is weak, the current system will be unimportant. If the particle flux is too strong, the magnetic lines of force will be swept out radially ($B_\theta \approx 0$) and no dynamo current system will be set up. At an intermediate value for emitted particle flux ($\Lambda = 9.2\ r_s$), the azimuthal current system will be optimized. The total maximized current, i, enclosed within the radius r is

$$i(\Lambda, r) = \frac{6 M_d}{\pi \Lambda^2}\left[\frac{\Lambda}{r_s} - \exp\left(-\frac{\Lambda}{r_s}\right) - \frac{\Lambda}{r} + \exp\left(-\frac{\Lambda}{r}\right) + 2E\left(0, \frac{\Lambda}{r}\right) - 2E\left(0, \frac{\Lambda}{r_s}\right)\right] \qquad (18\text{-}17)$$

where $E(0, x)$ is the function $\int_0^x \frac{1 - e^{-x}}{x} dx$; for tabulations of this function, see Staff of the Computation Laboratory of Harvard University XXI Tables of Generalized Exponential-Integral Function, Harvard University Press, 1949. The current density is

$$j = \frac{\Lambda}{4\pi} \frac{M_d \sin\theta}{r^5} F\left(2, 4, -\frac{\Lambda}{r}\right). \qquad (18\text{-}18)$$

If the asymptotic value of B_r is one gauss in the solar photosphere, and a corresponding total solar flux is 5×16^{36} particle sec^{-1} for a coronal temperature of 10^6 °K and coronal densities of 2×10^6 particles cm^{-3}, for $r = 2\ r_s$ the limit of j as $\Lambda \rightarrow \infty$ is $2.85 \times 10^{-12} \sin\theta$ (A cm^{-2}). This is roughly comparable to the earth's ionospheric current densities of 1.6×10^{-11} (A cm^{-2}). For sunspot minimum, the flux is beyond the value required to maximize the total space current. Even so, the total azimuthal current associated with the solar corona and the corona extended is about 200×10^9 A as compared with 200×10^3 A for the day and night ionospheric dynamo current systems.

According to this model,

$$M_d = 8.8 \times 10^{43} \text{ gauss cm}^3,$$
$$B_r = B_o \cos\theta / R^2, \qquad (18\text{-}19)$$
$$B_\theta = B_o \sin\theta / R\,(\Lambda / r_s);$$

B_o, the field at the surface of the poles, is one gauss. This solar magnetic moment is much larger than that calculated for the undisturbed dipole case. This model explains how an outward particle diffusion can contribute to the stability of an underlying photospheric magnetic field or a chromospheric magnetic field; the field will move in a direction opposite to that of the particle flux (frozen-out effect). During sunspot minimum, the prominent polar magnetic plumes are not radial but curved. This model indicates a negligible evaporative wind from the polar exosphere. The polar exosphere is close to the solar surface because of rotational flattening and electric force fields.

18.3.3 Effects of Rotation on Magnetic Lines of Force

Figure 18-8 shows how the magnetic lines of force are distorted by rotation in the presence of a steady radial solar wind of about 300 km sec^{-1}; for a slower speed the lines would have more curvature. Although the lines of force appear to end in space (their return path cannot be shown in such a projection), as many lines of force must return to the sun as leave, so that $\nabla \cdot B = 0$ is always satisfied. The statement that $B_\theta = 0$ often occurs in the literature; however, although it is small compared with B_r during sunspot minimum, B_θ must be finite to allow for completion of the lines of force.

Solar flares occurring on the west limb of the sun more often produce fluxes of high energy protons at the earth than the flares occurring on the east limb (Sec. 17.4.2). This effect indicates that the protons emitted are guided by magnetic lines of force that are bent as shown in Fig. 18-8. The frame of reference (rotating or nonrotating with sun) is not very important because the 25- to 31-day solar rotational period is so much longer than the proton transit time to the earth.

The rotation-induced bending of the lines of force is often explained by the "garden hose" effect. A sprinkler shoots out water at a constant velocity and rotates with a constant angular velocity so that the water follows an Archimedes spiral; $r = \beta(\phi - \phi_0)$, where β is a constant and ϕ is azimuthal angle. According to this concept

$$B_\phi = B_r \sin\theta \frac{\omega (r - b)}{u}, \qquad (18\text{-}20)$$

where u is the constant radial velocity of the protons and ω is the angular velocity at radius $r = b$. The approximation of constant velocity is reasonable (Sec. 18.1.3).

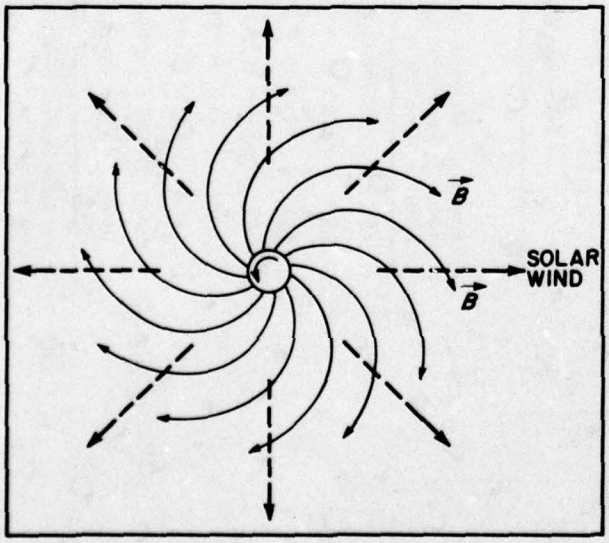


Fig. 18-8. The solar magnetic lines of force, *B*, projected on the equatorial plane as seen from the north (solar rotation counter clockwise) during quiet solar conditions; a steady solar wind of about 300 km sec^{-1} is assumed.

Another way of looking at this problem is to consider the "cam" effect where the lines of force are thought of as so many curved wires. As the wires rotate, the intersection of the radius vector from the sun to the earth and a given line of force will approach the earth at a constant velocity if the curves are Archimedes spirals.

The presence of B_ϕ alters the field-free values for the transport coefficients and must affect any transient or perturbing force fields which develop in space. Even at 90° colatitude, where B_r and hence B_ϕ are zero, there is a finite component perpendicular to the equatorial plane; $B_\theta \neq 0$, however small it may be. Thus, space is not field free, even if there is no interstellar field present. As a consequence, the conduction of heat outward is affected even in the equatorial plane. Outside the equatorial plane, the effect of B_ϕ will be felt far into interplanetary space; its strength falls off as $1/R$ compared to $1/R^2$ for B_r, or $1/R^3$ for an undisturbed dipole.

18.4 SOLAR METEOROLOGY AND ENERGY TRANSPORT

Observations show that the angular velocity for the photosphere and chromosphere are about equal. The Reynold's number for the corona is approximately one, indicating that the corona is highly viscous and should rotate as a solid body. According to present theory, the coronal magnetic lines of force are fluid controlled so that at large distances the magnetic lines of force will be bent azimuthly. This field, small as it is, may control the path of high speed ionized particles emitted by the sun and greatly reduce thermal conduction of solar energy in the radial direction. The solid-body coronal rotation and the corresponding large centrifugal force at the equator accounts for the overall flattening of the coronal profile and results in a higher exosphere at the equator and therefore increased evaporation from the equatorial regions. This will, in turn, draw coronal material into the equatorial region to account for the streamlined appearance of the equatorial corona (rays). The base of the rays seems to be under magnetic control, as are many solar atmospheric phenomena. Magnetic energy may be pealing off the photosphere and the corona throughout the solar magnetic cycle.

18.4.1 Solar Rotation

Observations of the east to west motions of long-lived sunspots show a daily angular velocity that varies with solar colatitude;

$$\omega_s = 14.38 - 2.77 \cos^2\theta, \qquad (18\text{-}21)$$

where ω_s is in degree per day. The equatorial solar rational period according to Eq. (18-21) is 25.[illegible] days. (The corresponding period seen from the earth is ~~27.275~~ 26.89 days because of earth's orbital motion.) The equatorial angular velocity calculated from Doppler shifts of absorption lines in the reversing layer is 14.23 degree per day; values obtained from some lines show ω_s increasing with height. The period of solar rotation may be correlated with the sunspot cycle.

Table 18-5. Reynolds numbers, R_η, for the solar atmosphere.

Distance (solar radii)	Electron Density (cm^{-3})	Mass Density ($g\ cm^{-3}$)	Viscosity Coefficient ($g\ cm^{-1}\ sec^{-1}$)	Kinematic Viscosity ($cm^2\ sec^{-1}$)	Velocities and Reynolds Numbers							
					Acoustic		Observational		Rotational		Continuity	
					($cm\ sec^{-1}$)	R_η*	($cm\ sec^{-1}$)	R_η*	($cm\ sec^{-1}$)	R_η*	($cm\ sec^{-1}$)	R_η*
3.0	3.3×10^5	5.52×10^{-19}	0.138	2.5×10^{17}	1.74×10^7	3.40	3.8×10^7	7.43	6.30×10^5	0.123	8.87×10^6	1.73
1.5	6.4×10^6	1.07×10^{-17}	0.258	2.4×10^{16}	1.96×10^7	12.6	1.85×10^6	1.18	3.15×10^5	0.201	1.85×10^6	1.18
1.06	2.2×10^8	3.65×10^{-16}	0.124	3.4×10^{14}	1.66×10^7	2.71×10^2	—	—	2.23×10^5	3.63	1.08×10^5	1.76
1.01	5.5×10^9	9.20×10^{-15}	1.39×10^{-3}	1.5×10^{11}	6.43×10^6	3.22×10^4	—	—	—	—	4.75×10^3	23.8
1.0014	5.0×10^{10}	3.34×10^{-11}	4.0×10^{-4}	1.20×10^7	8.52×10^5	1.14×10^6	—	—	—	—	—	—
1.0000	1.3×10^{12}	1.33×10^{-8}	3.6×10^{-4}	2.67×10^4	7.84×10^5	4.00×10^8	8.1×10^4	4.1×10^7	—	—	—	—
0.9997	5.0×10^{12}	1.52×10^{-7}	3.8×10^{-4}	2.51×10^3	8.27×10^5	4.93×10^9	—	—	—	—	—	—
0.9995	2.0×10^{14}	4.35×10^{-7}	4.9×10^{-4}	1.13×10^3	1.00×10^6	1.95×10^{10}	4.2×10^4	8.2×10^8	—	—	—	—

* See Table 18-4 for characteristic lengths (scale heights) used in these calculations.

Table 18-6. Magnetic Reynolds numbers, R_B, for the solar atmosphere.

Distance (solar radii)	Electrical Conductivity ($sec\ cm^{-2}$)	Magnetic Reynolds Numbers*			
		For Acoustic Velocities	For Observed Velocities	For Rotational Velocities	For Continuity Velocities
3.0	2.32×10^{-5}	2.49×10^{14}	5.43×10^{14}	9.01×10^{12}	1.27×10^{14}
1.5	3.28×10^{-5}	1.25×10^{14}	1.18×10^{13}	2.00×10^{12}	1.18×10^{13}
1.06	2.0×10^{-5}	2.32×10^{13}	—	3.12×10^{11}	1.51×10^{11}
1.01	1.16×10^{-6}	7.14×10^{10}	—	—	5.27×10^7
1.0014	7.72×10^{-10}	1.33×10^5	—	—	—
1.0000	6.02×10^{-10}	7.96×10^4	8.34×10^3	—	—
0.9997	7.08×10^{-10}	1.12×10^5	—	—	—
0.9995	1.25×10^{-9}	3.47×10^5	1.45×10^4	—	—

* See Table 18-5 for velocities, and Table 18-4 for characteristic lengths (scale heights) used in these calculations.

18.4.2 Reynolds and Prandtl Numbers

Physically, the Reynolds number, R_η, represents the ratio of the internal reaction to the viscous force (the inertial term divided by the viscous term of the equation of motion for a fluid). It is defined as Ud/η, where U is the characteristic speed, d is the characteristic length of flow, and η is the kinematic viscosity. The *kinematic viscosity* is μ/ρ, where μ is the coefficient of viscosity and ρ the density of the gas. Although the critical Reynolds number for a given system is ordinarily unknown, $R_\eta \leq 1$ certainly indicates that a highly viscous fluid is involved and that in rotation the fluid would behave almost as a solid body.

Table 18-5 gives the Reynolds numbers for the solar atmosphere computed for acoustic, rotational, and other velocities. In these computations, the scale heights given in Table 18-4 are taken as the characteristic lengths;

$$R_\eta = UH/\eta. \tag{18-22}$$

The acoustic velocities are computed for a monatomic neutral hydrogenic gas (ratio of specific heats 5/3). The rotational velocities are obtained from the angular velocities given in Table 18-11. The observed velocity at 3 solar radii is the escape velocity; at 1.5 solar radii it is that obtained from Doppler shifted reflections in an experiment performed by Lincoln Laboratory. The observed photospheric velocities are the velocities of the gravitational waves (ripples) on the sun measured at AFCRL Sacramento Peak Observatory. The continuity velocities are extrapolated by assuming conservation of particle flux and using data from probes in the vicinity of the earth.

It appears that although the corona is diffuse, it rotates almost as a solid body because the computed Reynolds number is of the order of one. Most of the rotational drop or slippage should occur in the solar photosphere where the Reynolds number is high; observations, on the contrary, show no such slippage. This discrepancy affords indirect evidence for the transport of momentum by solar-wide circulations.

A *magnetic Reynolds number* is defined as

$$R_B = 4\pi\sigma Ud, \tag{18-23}$$

where σ is the electrical conductivity in abmho per centimeter (sec cm^{-2}); $1/4\pi\sigma$ is the coefficient of diffusion for magnetic lines of force. R_B is a measure of the relative importance of magnetically "frozen" conditions to magnetic diffusion. (A magnetic bottle is difficult to devise because the characteristic length is relatively small, and R_B becomes sizable only if the time required for particle containment is of the order of a microsecond.) Using for the chromosphere an electrical conductivity of 2×10^{-8} sec cm^{-2}, a temperature of 10^4 °K, and $R_B = 1$, frozen-in and diffusion conditions are comparable for a magnetic cloud with a 250-km characteristic length of flow and a characteristic speed of 50 km yr^{-1}. Thus, if the subphotospheric magnetic field is at 250-km depth, the field can diffuse out in 5 yr.

Table 18-6 gives the magnetic Reynolds number computed for the same velocities as the Reynolds numbers given in Table 18-5. The values of σ are computed from Eq. (18-15) using $\sigma_o = 2 \times 10^{-14}$ at 1.01 solar radii and above, and $\sigma_o = 2 \times 10^{-15}$ at 1.0014 solar radii and below. Temperatures and scale heights used are those listed in Table 18-4. Comparison of the Reynolds number and the magnetic Reynolds number indicates that magnetic viscosity is important in the photosphere whereas kinematic viscosity is dominant in the corona.

The *Prandtl number* is the ratio of the kinematic viscosity to the coefficient of thermal conductivity, κ;

$$P = \eta/\kappa = \mu/\rho\kappa. \tag{18-24}$$

In effect, it denotes the coefficient for momentum diffusion divided by the coefficient for the diffusion of heat, and is inversely proportional to the density of the solar atmosphere. For the ionized regions of the solar atmosphere,

$$P = (2.33 \times 10^{-10})/\rho; \tag{18-25}$$

for the neutral regions,

$$P = (3.23 \times 10^{-9})/\rho. \tag{18-26}$$

Table 18-7 gives Prandtl numbers for the solar atmosphere. The presence of a magnetic field causes an increase in the Prandtl number, hence it will help to sustain any temperature differentials.

18.4.3 Transport Coefficients from Gas Kinetics

For the photosphere and lower chromosphere where the gas is predominantly neutral hydrogen, the coefficient of viscosity is

$$\mu = (2.67 \times 10^{-21})\ T^{1/2}/\alpha^2\ [\text{g cm}^{-1}\ \text{sec}^{-1}], \tag{18-27}$$

where α is the self-collision transport cross section for neutral hydrogen [Orrall and Zirker, 1961]. The coefficient of thermal conductivity is

$$\kappa = 3.1 \times 10^8 \mu\ [\text{g cm sec}^{-3}\ \text{degree}^{-1}]. \tag{18-28}$$

Table 18-8 lists values of α^2, μ, and κ for the neutral hydrogen solar atmosphere.

The coefficient of viscosity for a completely ionized hydrogenic gas [Chapman, 1954] with all types of collision included is

$$\mu_i = \frac{1.6 \times 10^{25}}{f(N)}\ (kT)^{5/2}\ [\text{g cm}^{-1}\ \text{sec}^{-1}], \tag{18-29}$$

where $f(N) = \ln(1+y^2) - y^2/(1+y^2) \approx 2 \ln y - 1$, and $y = (1.7 \times 10^{19})\ kTN^{-1/3}$. The particle density appears only in the correction factor f(N), thus μ_i is almost independent of the particular model chosen for particle density. For the density values listed in Table 18-9, f(N) varies from about 20 to 40.

The coefficient of thermal conductivity for a gas of completely ionized hydrogen with all types of collisions included is,

$$\kappa_i = \frac{7 \times 10^{34}}{f(N)}\ (kT)^{5/2}\ [\text{g cm sec}^{-3}\ \text{degree}^{-1}]. \tag{18-30}$$

Again, the particle density appears only in the correction factor. Table 18-9 lists values of μ_i and κ_i for an ionized gas of protons and electrons for several temperatures.

The transport properties for a completely ionized gas are highly sensitive to the presence of a magnetic field. The medium becomes anisotropic with respect to the conduction of heat or electricity. The conductivity parallel to the magnetic field is unaffected by the field and is the same as for the field-free case. The transverse conductivity (subscript t) is for a direction perpendicular to both the magnetic field and the force. (The force may be electrical or it may depend on a temperature gradient.)

Table 18-7. Prandtl numbers for solar atmosphere, calculated from Eq. (18-25) and (18-26).

Distance (solar radii)	Density (g cm^{-3})	Prandtl Number
3.0	5.52×10^{-19}	4.22×10^{8}
1.5	1.07×10^{-17}	2.18×10^{7}
1.06	3.65×10^{-16}	6.38×10^{5}
1.01	9.2×10^{-15}	2.54×10^{4}
1.0014	3.34×10^{-11}	96.6
1.0000	1.33×10^{-8}	0.243
0.9997	1.52×10^{-7}	2.12×10^{-2}
0.9995	4.35×10^{-7}	7.45×10^{-3}

Table 18-8. Coefficient of viscosity for a solar atmosphere of neutral hydrogen gas.

Distance (solar radii)	Collision Cross Section (10^{-16} cm^2)	Viscosity Coefficient (g cm^{-1} sec^{-1})	Thermal Conductivity Coefficient (g cm sec^{-1} deg^{-1})
0.0014	4.90	4.0×10^{-4}	12.4×10^{4}
1.0000	5.04	3.55×10^{-4}	11.0×10^{4}
0.9997	4.95	3.8×10^{-4}	11.8×10^{4}
0.9995	4.65	4.9×10^{-4}	15.2×10^{4}

Table 18-9. Coefficients of viscosity (μ_i) and of thermal conductivity (κ_i) for a solar atmosphere of electrons and protons.

		Coefficients	
Distance (solar radii)	Temperature (°K)	Viscosity (g cm^{-1} sec^{-1})	Thermal Conductivity (g cm sec^{-1} deg^{-1})
3	1.1×10^{6}	0.14	6×10^{8}
1.5	1.4×10^{6}	0.26	1×10^{9}
1.06	1×10^{6}	0.12	5×10^{8}
1.01	1.5×10^{6}	0.0014	6×10^{6}

The perpendicular conductivity (subscript $\perp$) is for a direction perpendicular to the magnetic field in the plane containing both the force and the magnetic field.

The anisotropic electrical conductivities in the presence of a magnetic field are

$$\sigma_\perp = \frac{\nu^2}{\nu^2 + \omega^2}\,\sigma, \qquad (18\text{-}31)$$

and

$$\sigma_t = \frac{\omega\,\nu}{\nu^2 + \omega^2}\,\sigma, \qquad (18\text{-}32)$$

where ν is the collision frequency and ω (the gyrofrequency) is eB/m. In a field of one gauss, for electrons, $\omega^2 = 3.1 \times 10^{14}$ sec^{-2} and for protons, $\omega^2 = 9.2 \times 10^{7}$ sec^{-2}. Table 18-10 gives values of the magnetic correction factors $\nu^2/(\nu^2 + \omega^2)$ and $\omega\nu/(\nu^2 + \omega^2)$ for electrons; these are also the magnetic correction factors for the anisotropic thermal conductivities.

Rough approximations, for a solar atmosphere composed of equal numbers of protons and electrons, are:

$$\nu = 15\,\mathrm{N}\,\mathrm{T}^{-3/2}\ [\mathrm{sec}^{-1}], \qquad (18\text{-}33)$$

where N is particles per cubic centimeter; and

$$\sigma = 2 \times 10^{-14}\,\mathrm{T}^{3/2}\ [\mathrm{sec\ cm}^{-2}]. \qquad (18\text{-}34)$$

For the photosphere, where collisions with neutrals are important, ν is increased and σ decreased by a factor of ten. Table 18-10 lists values of ν and σ calculated from these approximations. In the photosphere at a temperature of 5,000°K, σ is the order of 10^{-9} (sec cm^{-2}), which is about that of salt water. In the deep interior where $\mathrm{T} = 10^{7}$ °K, σ is 6×10^{-4} (sec cm^{-2}), which is about that of copper.

18.4.4 Solar-Wide Atmospheric Motions

A technique called dishpan experiments simulates a rotating atmosphere by rotating a shallow pan containing a fluid; the fluid is cooled at the center (axis of rotation) and heated at the periphery. Convection alone produces patterns which are axially symmetric. The introduction of rotation causes cloverleaf patterns centered on the axis of rotation to develop. Such patterns are called *Rossby waves*. As the rotational velocity is increased, the departure from axially symmetric flow is accentuated and the number of cloverleaves in the pattern increases. A systematic asymmetry in the Rossby wave pattern offers a method for transferring angular momentum from regions of lower angular velocity (high solar latitudes) to regions of higher angular velocity (equatorial latitudes) thus accounting for the solar equatorial acceleration.

The criterion for the presence of a Rossby wave pattern is a Rossby number, which may be defined as the ratio of the convective velocity to the absolute rotational velocity. The Rossby number for the earth's troposphere is about 0.1. By using the ratio of the latitudinal difference in angular velocity to an average angular velocity ($\Delta\omega_s/\omega_s$), a mean Rossby number for the photosphere of about 0.034 is obtained. This implies a general photospheric circulation of the Rossby type and a photospheric jet, with the isobars and the jet winds following a wavelike pattern on the solar surface.

A temperature differential between pole and equator is necessary to establish Rossby wave patterns. The temperature differential is produced by the inhibiting effect of rotation on convection. (The polar magnetic field of one gauss is too small to exert any inhibiting effect.) This inhibiting effect is greatest at the poles, which are thus cooler than the equator. Winds from the east (the easterlys of the earth's atmospheric circulation) will develop, and the general circulation will be poleward at chromospheric heights. This circulation is manifested in the poleward movement of coronal flocculi that carry magnetic fields, which are formed in the active zones, poleward. A comparison of the ionized calcium lines that originate at the equator with those that originate at the poles shows a temperature difference of $98° \pm 18°$ or of $86° \pm 16°$ (depending on the values used for the continuous absorption coefficient); the poles at chromospheric heights are hotter than the equator. However, observations of the limb (using thermocouples sensitive to temperature differences of 20°K), show no temperature difference between the limb at the equator and at the poles.

If a Rossby number proportion to the differential rotation is defined as

$$R_\omega = \left| \frac{1}{\omega} \frac{d\omega}{d\theta} \right| , \qquad (18\text{-}35)$$

substitution into Eq. (18-21) gives

$$R_\omega = \left| \frac{5°54 \sin\theta \cos\theta}{14°38 - 2°77 \cos^2\theta} \right| . \qquad (18\text{-}36)$$

Table 18-11 gives Rossby numbers calculated from this relation for angular velocities calculated from Eq. (18-21). At 40° colatitude this flow pattern is axially symmetric; at higher or lower angles the flow patterns become more like Rossby waves with six lobes. At the poles and the equator, the zonal pattern should become so multilobed with small amplitude lobes that axially symmetric patterns are reestablished. R_ω is constant at a given photospheric latitude at any given time for an idealized steady state condition. Because of changing conditions indicated by the sunspot cycle, however, the Rossby patterns are possibly more time dependent than latitude dependent.

In a steady state Rossby regime, the flow is primarily zonal. The pure *Hadley regime* sets in when the convective velocity approaches the magnitude of the rotational velocity (Rossby numbers greater than about 0.3). Meridional flow is possible only in the Hadley regime. The Rossby and Hadley regimes are mutually exclusive according to observations of dishpan experiments, which indicate that a high viscosity (low Reynolds number) is favorable to a Hadley regime.

Table 18-11. Angular velocities of the photosphere from Eq. (18-21) and Rossby number calculated from Eq. (18-36).

Solar Latitude (deg)	Angular Velocity (deg day^{-1})	Rossby Number R_ω
0	14.38	0
10	14.30	0.067
20	14.06	0.127
30	13.69	0.175
40	13.23	0.206
45	12.99	0.209
50	12.76	0.214
55	12.52	0.208
60	12.30	0.194
70	11.93	0.149
80	11.69	0.081
90	11.61	0

Table 18-10. Electrical conductivities and magnetic correction factors calculated by Eq. (18-31), (18-32), (18-33), and (18-34).

Distance (solar radii)	Temperature (°K)	Electron Density (cm^{-3})	Collision Frequency ν (sec^{-1})	Magnetic Correction Factors* $\frac{\nu^2}{\nu^2+\omega^2}$	$\frac{\omega\nu}{\nu^2+\omega^2}$	Electrical Conductivity σ (sec cm^{-2})
3.0	1.1×10^6	3.3×10^5	4×10^{-3}	6×10^{-20}	2×10^{-10}	2×10^{-5}
1.5	1.4×10^6	6.4×10^6	6×10^{-2}	1×10^{-17}	3×10^{-9}	3×10^{-5}
1.06	1.0×10^6	2.2×10^8	3	3×10^{-14}	2×10^{-7}	2×10^{-5}
1.01	1.5×10^5	5.5×10^9	1×10^3	7×10^{-9}	8×10^{-5}	1×10^{-6}
1.0014	5.3×10^3	5.0×10^{10}	2×10^7	0.5	0.5	8×10^{-10}
1.0000	4.5×10^3	1.3×10^{12}	6×10^8	1	3×10^{-2}	6×10^{-10}
0.9997	5.0×10^3	5.0×10^{12}	2×10^9	1	8×10^{-3}	7×10^{-10}
0.9995	7.3×10^3	2.0×10^{14}	5×10^{10}	1	4×10^{-4}	1×10^{-9}

* For electrons and assuming a field of one gauss so that $\omega = 1.76 \times 10^7$ sec^{-1}.

A *thermal Rossby number* may be defined as

$$R_T = \frac{g_s \epsilon z}{2\omega(\omega r_s)} \frac{\Delta T}{r_s \Delta \theta}, \qquad (18\text{-}37)$$

where ϵ is the volume expansion coefficient, z is the depth of the layer, 2ω is a Coriolis parameter, ωr_s is the rotational velocity, and $\Delta T/r_s\Delta\theta$ is the latitudinal temperature gradient in the surface perpendicular to z. The expression $g_s \epsilon z \Delta T/2\omega(r_s\Delta\theta)$ is simply the thermal wind through the vertical layer of depth z due to a horizontal temperature difference. For hydrostatic equilibrium, z is the scale height, Eq. (18-12), and R_T is then proportional to T.

Figure 18-9 is a schematic representation of this interpretation of the photospheric, chromospheric, and coronal circulations. According to this model, a Rossby regime (primarily zonal circulation) in the photosphere goes to a Hadley regime (meridional circulation) in the chromosphere. This accounts for the poleward motion and subsequent rotational elongation observed in chromospheric flocculi, which is characteristic of the spiral streamline patterns of the symmetric Hadley regime. Dishpan experiments to simulate photospheric-chromospheric circulation patterns indicate the possibility of a meridional flow restricted to rather narrow regions in the viscous boundary layers near the bottom, at the outer wall, and near the top surface in the pan. In the interior of the fluid, the motion is often almost completely zonal.

The low viscosities and high Reynolds numbers computed for the photosphere and lower chromosphere indicate considerable slippage (in contrast to the corona where low Reynolds numbers indicate that the corona should rotate as a solid body). These same conditions may also be considered as indication of zonal circulation and equatorial acceleration in the photosphere. Because of the observed equatorial acceleration, the Rossby patterns in the photosphere cannot be simple sine or cosine but must be distorted so that more angular momentum is transferred to the equator than to the poles.

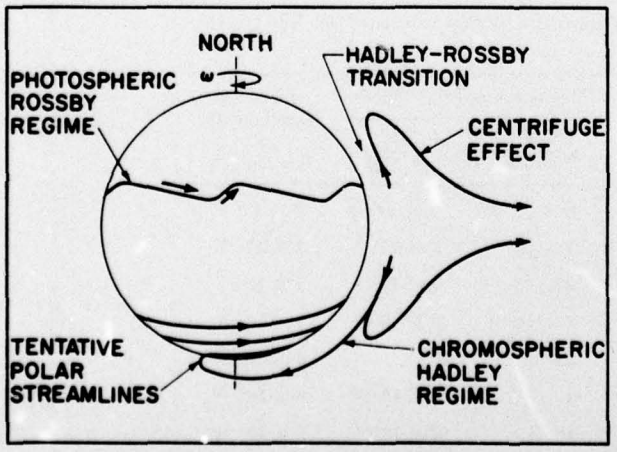


Fig. 18-9. Model of suggested circulations with primarily zonal circulation (Rossby regime) in the photosphere that goes to meridional circulation (Hadley regime) in the chromosphere.

18.4.5 Energy Transport Processes

A temperature profile proportional to L^{-1} (Sec. 18.2.1) implies a spherically symmetric model of outward heat transport in a medium of constant thermal conductivity. Assumptions of spherical symmetry, however, are not justified at sunspot minimum. It is doubtful if gas kinetic transport is important for the extended corona. The Reynolds number of the corona is low, so that transport by eddies does not seem possible. It is likely that magnetic forces and magnetic focusing action must be considered. Hydromagnetic heating is believed to be important for the inner corona and may also prove important for the extended corona. The energy source for coronal heating is customarily assumed to be the photosphere, but there is probably a source much higher that is supplied by an electric field.

Magnetic effects on energy transport depend on the relative importance of thermal conduction and on the degree of ionization. In a completely ionized gas, the thermal and electrical conductivities are reduced greatly by an imposed magnetic field, except in the direction parallel to the field. (For example, a radial magnetic field would not affect a radially directed solar wind.) A magnetic field as small as one gauss can reduce conductivities of the ionized gas by many orders of magnitude (Table 18-10) depending on the orientation of the field; the medium then becomes an almost perfect insulator in some directions. For some orientations of the magnetic field, electric field buildup caused by Hall currents could cancel out the effect of a magnetic field.

While radiative transfer of energy is the important mechanism at the visible surface of the sun, in the subphotosphere (down to 1/3 radii), transport by convection predominates, whether by eddies or by large scale circulation. The tops of the subphotospheric convection cells (the granules) are shown in Fig. 15-2. They can be simulated when a very thin layer of liquid in a dishpan experiment is heated uniformly. A semi-regular cellular regime is observed on the surface during the first phase. Later, a permanent regime of regular hexagons forms (Bénard cells) develop because of instabilities arising from an adverse temperature gradient. (The photosphere is cooler than the layer beneath so there is an adverse temperature gradient.) Rotation of the dishpan causes the cells to contract and inhibits the onset of the cells. The same effect is observed when a magnetic field is imposed perpendicular to the surface but for apparently different reasons; it is possible that the rotational and magnetic effects may oppose one another. On the sun there should be fewer cells at the poles than at the equator; if so, a temperature differential between poles and equator will develop. (It would be most instructive if photospheric photographs could be obtained for the polar regions of the sun.) This temperature differential can produce a general circulation with Rossby wave patterns and equatorial acceleration.

18.5 TENTATIVE MORPHOLOGY OF THE SOLAR CYCLE

Sunspot pairs often occur simultaneously in each hemisphere; the magnetic polarity of the lead spot in one hemisphere is always the reverse of that of the lead spot in the other hemisphere. A poloidal-like magnetic field (B_p) in the subphotosphere (Sec. 18.3.1) that is distorted by equatorial acceleration into a toroidal field (B_t), accounts for the reversed polarity of lead spots as well as equatorial migration of sunspots. Figure 18-10 illustrates the reversed polarity of sunspot pairs and the Rossby wave pattern (Sec. 18.4.4). According to this model, as the underlying magnetic band is drawn to the equatorial zone through magnetic coupling (attractive) with its counterpart in the opposite hemisphere, the Rossby wave pattern becomes more washed out. Magnetic loops or vortices develop within the lobes of the Rossby wave pattern. One or more of these loops may rise to the surface through magnetic buoyancy and form a sunspot pair or group. In the equatorial region the magnetic loop can break off and the toriodal magnetic field can either diffuse out into space, or it can drift poleward as a magnetic cloud in a general poleward atmospheric circulation. This can account for the reversal of the poloidal magnetic field at about the maximum of the sunspot cycle.

Figure 18-11(a) illustrates the magnetic loops (chromospheric flocculi) that have broken off and are drifting poleward. These high latitude magnetic clouds with their continual outward magnetic diffusion not only force out the existing poloidal field (the polar plumes) but, because they contain a field of about 50 gauss, are able to overcompensate and form a poloidal field.

Figure 18-11 illustrates why the new poloidal field will have a reversed polarity. The detailed interaction of the polar plumes with the oncoming magnetic cloud is complicated by the poleward chromospheric drift. This drift assists in the formation of new polar magnetic clouds from the old polar plumes. The result is the ejection of the old poloidal field in the form of elongated magnetic clouds and the submersion of the old oncoming clouds with reversed magnetic polarity into the subphotosphere. This photospheric field of reverse polarity is then amplified both by equatorial acceleration and by equatorial migration, thus regenerating the solar magnetic cycle. The ejection of the magnetic clouds at the poles may be, in part, the source of M-regions.

The equatorial drift of the magnetic band becomes more and more pronounced as the underlying toroidal field continues to be amplified. By the time the magnetic band reaches 15° latitude, the magnetic clouds from the previous cycle drifting poleward in the atmospheric circulation pass over this photospheric band, creating a favorable condition for the release of electric and magnetic energy. Figure 18-11 indicates how the magnetic clouds may affect the magnetic field of a sunspot (b) or induce a loop prominence (c). The brightest flares would form when the magnetic cloud passes over an active spot group, which agrees with observations. Loop prominences would occur where there is less extensive magnetic coupling between chromosphere and photosphere. The prominence zone should thus always be poleward of the sunspot zones. Such a latitude difference (15°) is actually observed.

The energy for the flare and prominence action is probably electrical in nature. The rotating sun acting as a giant centrifuge creates a large negative space charge in the equatorial region, with the electrons having higher mobility than the protons. This is just the space charge required (Sec. 18.2.4) to help the coronal protons escape the gravitational potential well to form the solar wind. A pole-to-equator potential difference of 10^8 V is estimated. Active prominences and flares are then explained by the magnetic linking of the solar atmospheric layers and by the discharge of electrical energy.

The proposed photospheric circulation required by the model (from pole to equator in the subphotosphere) is in accord with the general circulation (convection) derived from the theory of stellar interiors. Magnetic variable stars (the sun is a magnetic variable) satisfy the criterion of rapid axial rotation and an outer convection zone, conditions favorable to the onset of Rossby waves. In addition, the flare stars (Sec. 21.7.1.2) have peculiar spectra indicative of the large scale flocculi that are identified with the magnetic clouds in this model of solar flare production.

The proposed model suggests a mechanism for M-regions and favors the continuous emission of solar magnetic clouds; such clouds could be responsible for the permanent magnetometer variations at the earth's surface.

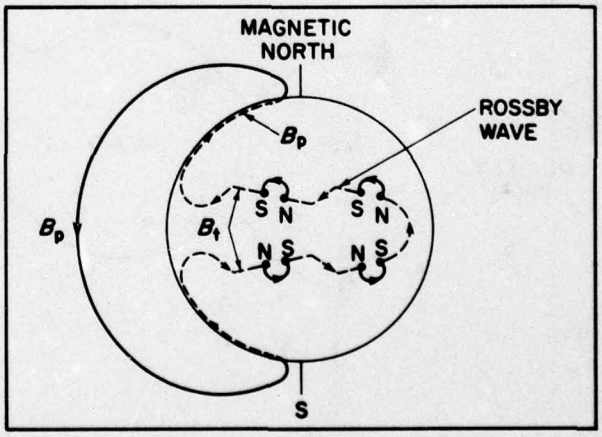


Fig. 18-10. Sunspot pairs in northern and southern hemispheres with underlying band of magnetic lines of force (B_t) in a Rossby wave pattern. Solid lines are exterior poloidal magnetic field, B_p; dashed lines are the interior, poloidal (B_p) and toroidal (B_t) fields.

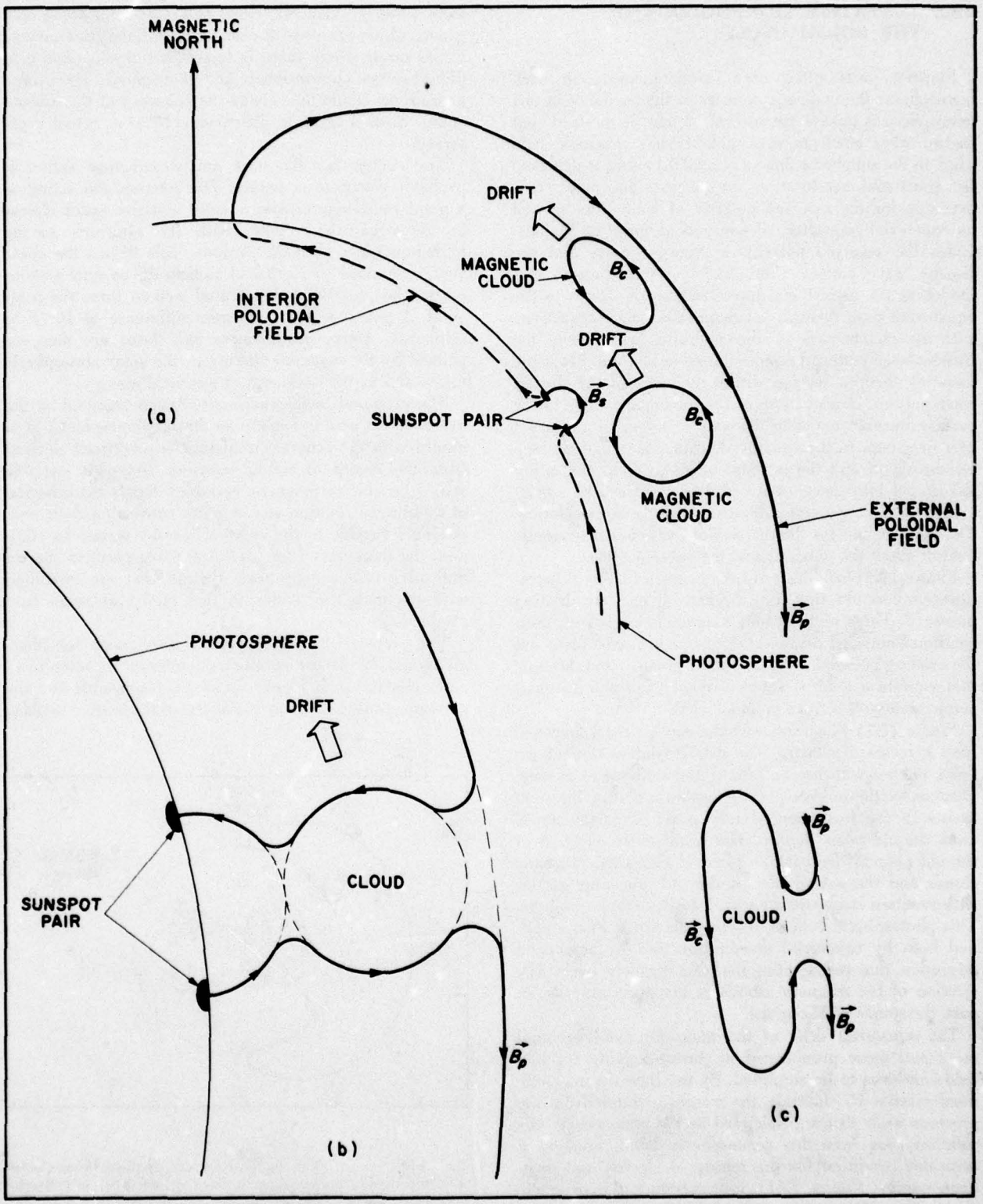


Fig. 18-11. Sketch illustrating: (a) poleward drift of magnetic clouds (chromospheric flocculi) that have broken off from the toroidal magnetic field and formed an independent circuit, B_c; (b) effect of a magnetic cloud that passes close over a sunspot pair on the magnetic fields; and (c) effect of a magnetic cloud high in the chromosphere on the external poloidal field, B_p.

18.6 REFERENCES

Chamberlain, J. W., 1961, "Interplanetary Gas III: A Hydrodynamic Model of the Corona," *Astrophys. J.*, v. 133, p. 675.

Chamberlain, J. W., 1960, "Interplanetary Gas II: Expansion of a Model Solar Corona," *Astrophys. J.*, v. 131, p. 47.

Chapman, S., 1957, "Notes on the Solar Corona and the Terrestrial Ionosphere," *Smithsonian Contributions to Astrophysics*, v. 2, no. 1.

Chapman, S., 1954, "Viscosity and Thermal Conductivity of a Completely Ionized Gas," *Astrophys. J.*, v. 120, p. 151.

Evans, J. W., 1963, "The Solar Corona," Academic Press, New York.

Parker, E. N., 1960, "Hydrodynamic Theory of Solar Corpuscular Radiation and Stellar Winds," *Astrophys. J.*, v. 132, p. 821.

Milne, E. A., 1923, "Escape of Molecules from an Atmosphere, with Special Reference to the Boundary of a Gaseous Star," *Trans. Cambridge Phys. Soc.*, v. 22, p. 483.

Orral, F. Q., and J. B. Zirker, 1961, "Coefficient of Thermal Conductivity in the Sun's Atmosphere," *Astrophys. J.*, v. 134, p. 63.

Chapter 19

THE LUNAR ENVIRONMENT

Sections 19.1-19.6 John W. Salisbury
Sections 19.7-19.9 Donald H. Eckhardt
Mahlon S. Hunt

More is known concerning the moon than any of the planets. It is apparent that the major portion of our space effort will be directed first toward exploration of the moon, with exploration of planets following; thus the lunar environment is treated in some detail, although much of the information is necessarily speculative.

19.1 ATMOSPHERE

The lunar atmosphere is known to be extremely tenuous; just how tenuous is debatable. Surface shadows on the moon are very black and sharply delineated, and there are neither clouds nor sunset effects. As calculated from polarimetric observations, the surface density of the lunar atmosphere is less than 10^{-9} terrestrial atmospheres. Estimates from occultations of radio stars by the moon are that the atmosphere must be less than 10^{-13} terrestrial atmospheres [Costain et al, 1955]. Öpik and Singer [1960] postulated that the lunar atmosphere might have a pressure of essentially zero because of the repulsion of ionized gas molecules by the positively charged lunar surface. It is generally conceded, however, that the minimum density of the lunar atmosphere must be at least the density of the interplanetary medium. In the absence of experimental verification of a lower pressure, the pressure of the lunar atmosphere is assumed to be 10^{-13} terrestrial atmospheres at the lunar surface. This pressure corresponds to a terrestrial altitude of greater than 300 km. Terrestrial meteors begin to vaporize at a maximum altitude of about 150 km, so the lunar atmosphere cannot shield the lunar surface from the impact of meteorites. It also will not attenuate appreciably cosmic and solar radiations.

The composition of the lunar amtosphere is an unsolved problem. Some radiogenic Kr, Xe, A, Rn, and He should be continually released from the interior, while trace amounts of Xe, He, Ne, and A will be produced by cosmic-ray bombardment of the surface [Edwards and Borst, 1958]. In addition, occluded gases will be liberated upon the impact and vaporization of meteorites, and some water vapor will be released, either from the interior or during the slow vaporization of possible relict solid phases present in perpetually shadowed zones [Watson et al, 1961]. The rapid escape of all these gases from the moon is assured by the low lunar escape velocity (about 2.4 km sec^{-1}) and by the repulsion of the ionized gases from the positively charged moon. The composition of this transient lunar atmosphere will depend largely upon the production rate of the various gases. No doubt the composition is complex and may even be changing. The major constituents are probably water, carbon dioxide, and hydrogen. The electron density of the lunar ionosphere is probably between 200 and 350 cm^{-3} [Weil and Barasch, 1963].

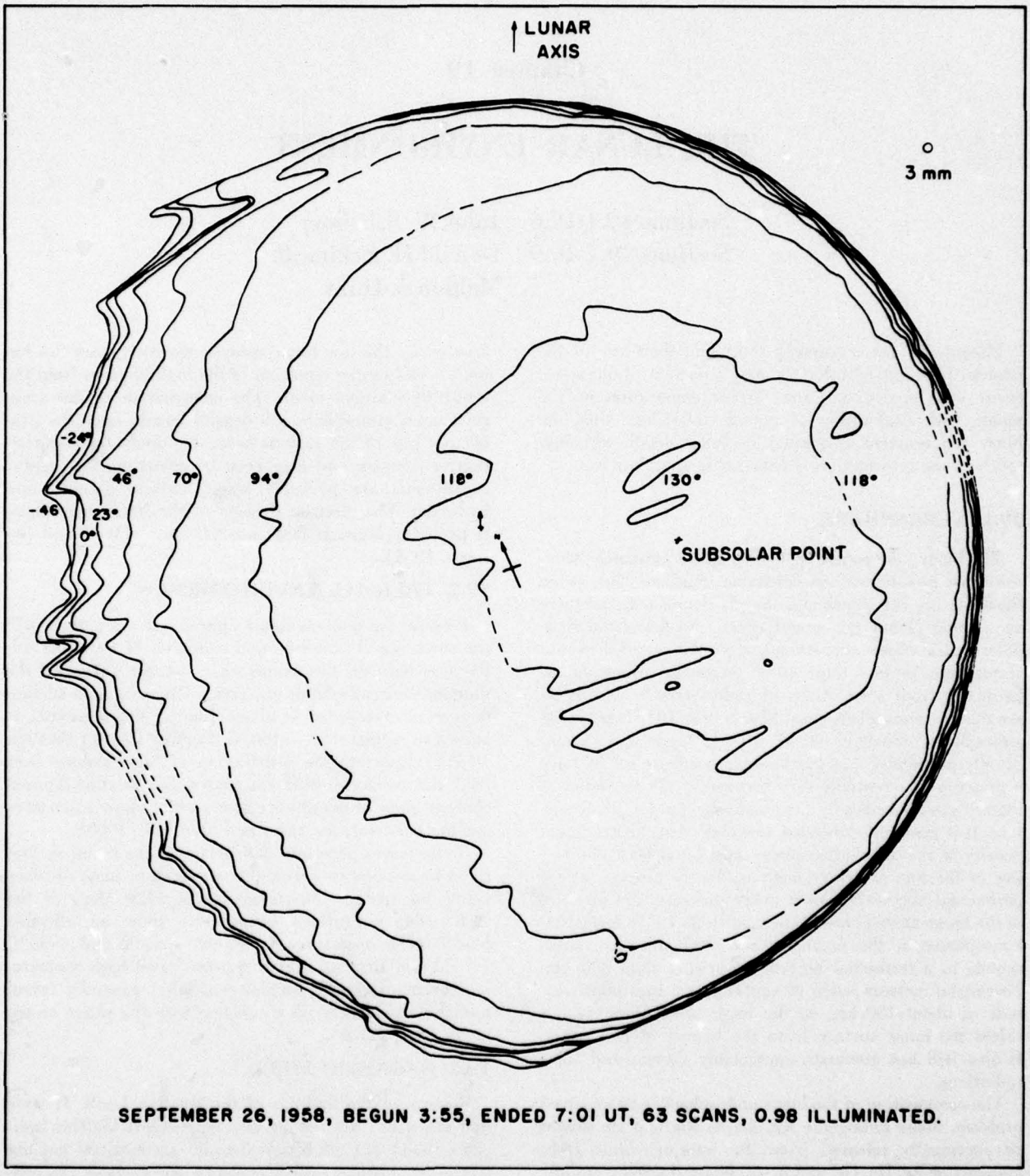
19.2 THERMAL ENVIRONMENT

Because the tenuous lunar atmosphere does not shield the surface and prevent rapid radiation of heat, the differences between the temperatures on the dark and the illuminated hemispheres are great. The maximum surface temperature recorded is about 130°C; the minimum is known to be less than —168°C. Figures 19-1(a) through 19-1(d) illustrate the distribution of temperatures over the lunar surface at different phases. For detailed thermal contour maps of the rayed craters, which show anomalous cooling behavior, see Saari and Shorthill [1963].

Radio waves penetrate the surface of the moon so that radio measurements reveal the temperature some distance below the surface. Measurements at 1420 Mcps of the steady-state subsurface temperature show an effective blackbody temperature of between —23°C and —53°C [Medd and Broten, 1961]. Shorter wavelength measurements (at presumably shallower depths) generally reveal higher temperatures which change with the phase of the moon (Sec. 22.3.1).

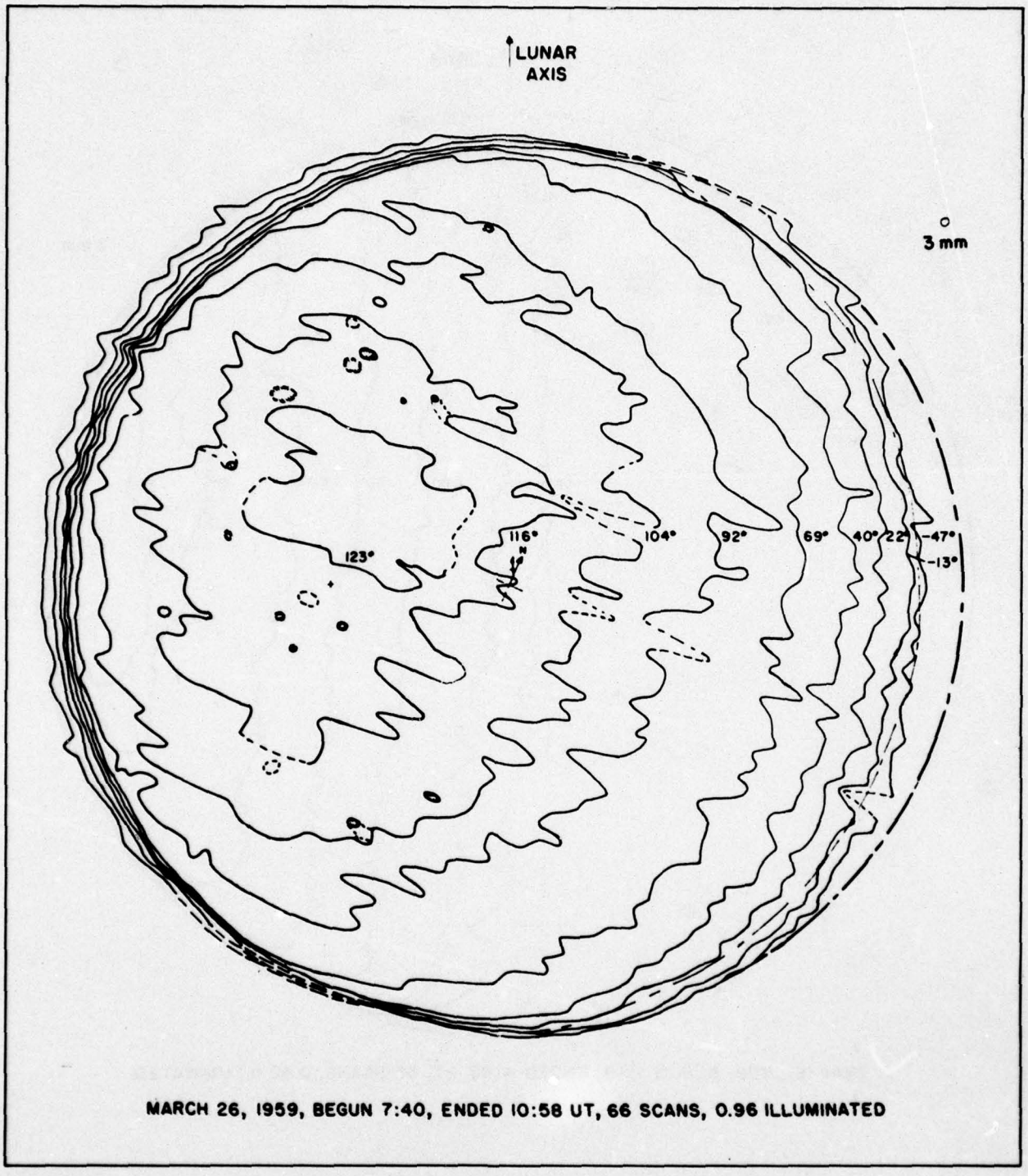
19.3 MAGNETIC FIELD

Reports of the findings of the Russian Lunik II state that this probe did not detect a magnetic field. This indicates a field strength of less than 30 gamma (one gamma equals 10^{-5} gauss); other evidence corroborates this conclusion [Kopal, 1959]. Studies of lunar luminescence reveal that the luminescence around Aristarchus ceases at the instant the sun drops below the lunar horizon. This indicates that the corpuscular radiation which causes the luminescence is not deflected by a magnetic field, hence any lunar magnetic field must be only a small fraction of the terrestrial field.



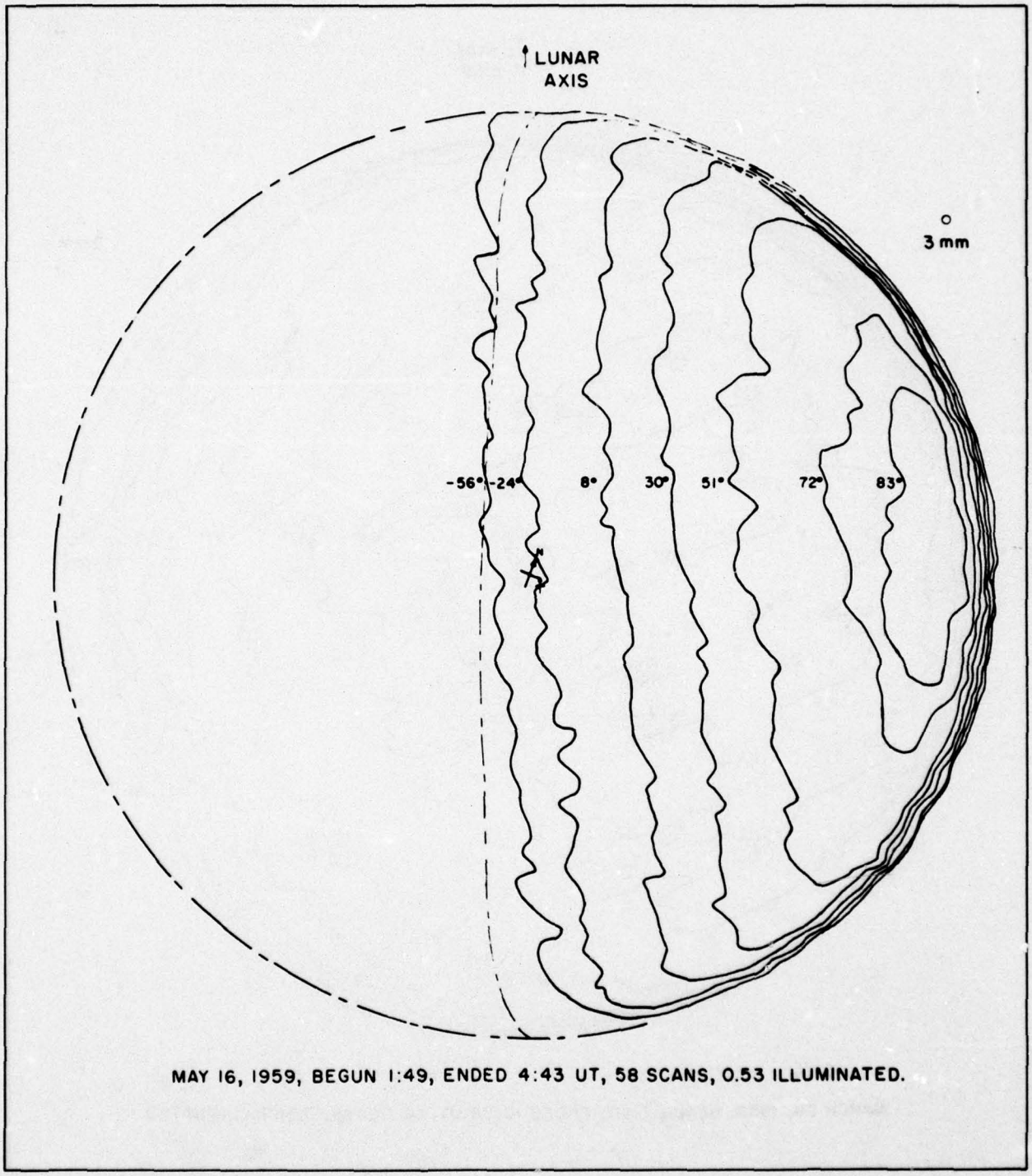
(a)

Fig. 19-1 Distribution of lunar temperatures in °C at various phases. The small circle in the upper right-hand corner indicates the maximum error in positioning the isothermal contours. The subsolar point is marked with a small cross. (From A. R. Goeffrion, M. Korner, and W. M. Sinton, Lowell Observatory Bul. No. 106, 1960.)



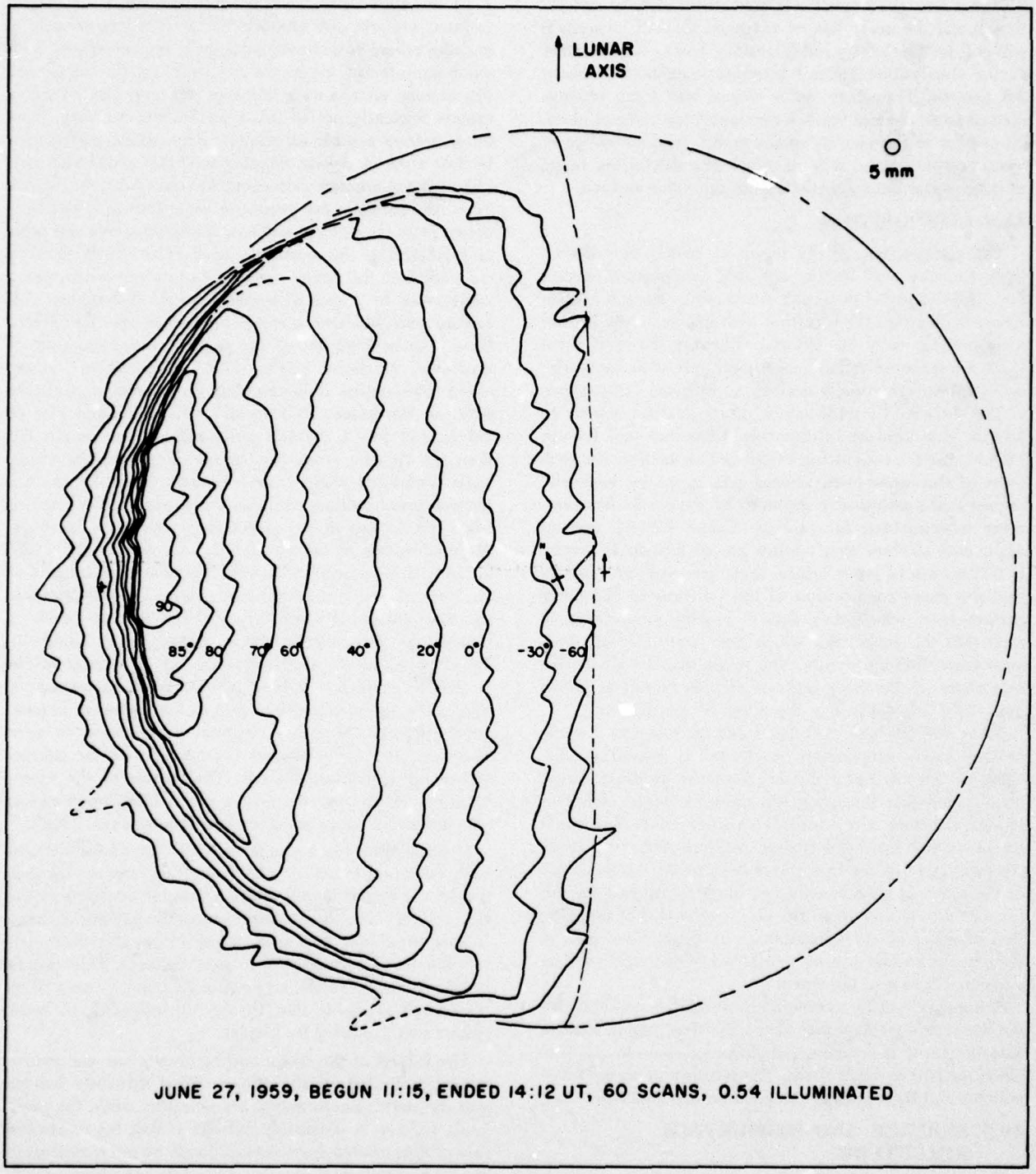
(b)

Fig. 19-1 Distribution of lunar temperatures in °C at various phases. The small circle in the upper right-hand corner indicates the maximum error in positioning the isothermal contours. The subsolar point is marked with a small cross. (From A. R. Goeffrion, M. Korner, and W. M. Sinton, Lowell Observatory Bul. No. 106, 1960.)



(c)

Fig. 19-1 Distribution of lunar temperatures in °C at various phases. The small circle in the upper right-hand corner indicates the maximum error in positioning the isothermal contours. The subsolar point is marked with a small cross. (From A. R. Goeffrion, M. Korner, and W. M. Sinton, Lowell Observatory Bul. No. 106, 1960.)



(d)

Fig. 19-1 Distribution of lunar temperatures in °C at various phases. The small circle in the upper right-hand corner indicates the maximum error in positioning the isothermal contours. The subsolar point is marked with a small cross. (From A. R. Goeffrion, M. Korner, and W. M. Sinton, Lowell Observatory Bul. No. 106, 1960.)

If it is true (as seems likely from theoretical considerations) that the moon has no magnetic field of its own, it will still be affected by interplanetary fields. The intensity of the steady-state general interplanetary field is about 2.5 gamma. Transitory fields frozen into solar plasmas ejected from the sun reach a maximum intensity of about 40 gamma in the vicinity of the moon. In the absence of more complete data, it is assumed that this is the range of intensity of the magnetic field at the lunar surface.

19.4 COMPOSITION

The composition of the moon is largely speculative. Both Kozyrev and Dubois obtained luminescent spectra from the vicinity of the crater Aristarchus [Kopal, 1959]; Kozyrev identifies his spectrum with quartz, while Dubois identifies his with the mineral willemite. Even if these spectra were more reliable, they deal only with local minerals, and information is needed on the gross composition of the surface. To some investigators, tektites appear to provide this kind of information. Chapman and Larson [1963] present convincing evidence that tektites are portions of the lunar crust blasted into space by meteorite impact and subsequently captured by the earth; however, other investigators, for example Cohen [1960], present arguments to show that tektites are of terrestrial origin. If tektites are of lunar origin, their composition must reflect the gross composition of the portions of the lunar surface from which they derive. Tektite composition is such that the rock from which they were formed must have been silicic in nature. The maria may be silicic differentiates of the more basic highlands materials [Lowman, 1963], but this is in the realm of speculation.

Many authors have postulated that the moon as a whole has the same composition as chronditic meteorites. Because of the low lunar density, however, it must always be assumed that the moon has gained a larger share of lighter elements. Urey [1952] suggested that this could be accounted for by a higher concentration of silicate phase relative to the iron phase because of accumulation of the moon at a sufficiently low temperature that its silicates could not volatilize. He also suggested that the addition of water of crystallization in oxidized chrondites to the extent of about 1% by weight would give them a density equal to that of the moon.

It appears best to assume a chronditic composition for the moon as a whole minus about 5% iron, and to assume that the crust has undergone differentiation to produce silicic as well as basic rocks. The location of these differentiates and their precise composition are unknown.

19.5 SURFACE AND SUBSURFACE STRUCTURE

Lunar surface and subsurface structures are an important factor in the design of rocket and roving vehicles or of lunar bases. Unfortunately, the nature of both is dependent upon the origins of the major surface features, which are debatable. The complexity of the lunar environment does not admit of easy generalizations, hence the current diversity of opinion is reviewed before arriving at the lunar model adopted here.

At this time there are two main theories of the origin of lunar craters; one supports an internal igneous origin, and the other, an external meteoroid impact origin. Volcanic craters on earth are typically small, cup-shaped depressions on top of a volcano; the majority of lunar craters is clearly not of this type. On the contrary, most lunar craters are broad, shallow depressions surrounded by low rims of debris. Similar features, called *calderas*, although not common, do occur in some volcanic regions on earth. Calderas are produced when molten material is blown from beneath the surface, emptying a lava reservoir and fracturing the overlying rock. The overlying rock collapses into the empty chamber to produce a depression surrounded by a ring of expelled debris. Subsequent volcanism may produce new volcanic cones on the caldera floor. Figure 19-2 shows the sequence of formation of a caldera. As shown in Fig. 19-3, the appearance of the crater Ptolemaeus indicates that such features probably exist on the moon. Ptolemaeus lacks a marked rim of debris and has a definite polygonal outline and a flat floor. It appears from this morphology that the crater walls foundered along crustal fracture zones to produce the polygonal outline, while an outpouring of lava or ash filled the bottom of the crater to produce the flat floor. Most adherents of the volcanic school of thought would agree to this sequence of events. This does not mean that all lunar craters are volcanic in origin. On the contrary, the morphology of a more typical lunar crater, such as Copernicus, is consistent with an impact origin [Baldwin, 1949]. The feature most suggestive of an impact origin is the near-circular outline, which is characteristic of hypervelocity impact craters even at low angles of impact. Although often slightly polygonal in response to rock structure, they never assume the extreme outline characteristic of a collapse feature. The nature of the ejecta blanket and rays surrounding a crater like Copernicus is also indicative of an impact origin [Shoemaker, 1962].

It is possible for a single crater to be the product of both caldera formation and meteoroid impact. In such a case, the impact would create a zone of weakness in the lunar crust which would later localize the igneous activity. In fact, there may be a complete spectrum of crater types ranging from pure impact to pure igneous. One cannot firmly defend a single origin for all lunar craters. It is considered probable that by far the majority of lunar craters was produced by impact.

The origins of the maria and highlands are less controversial than that of the craters. Most scientists believe that the dark smooth maria are volcanic, while the highlands are not. A dissenting opinion is that the maria are seas of dust eroded from the highlands by micrometeoroid impact and radiation damage. This dust hypothesis [Gold, 1959] has received such wide circulation by popular news media that mention of the evidence against it appears necessary.

The chief difficulty with the dust hypothesis is the inadequacy of the postulated means by which the dust could have been transported from the highlands to the maria basins. Electrostatic charging of dust grains by solar

radiation has been considered a means of levitating the dust grains by mutual repulsion and thus permitting them to migrate downhill. This charging is not sufficient to accomplish the mass levitation of particles, although a small particle put in motion by micrometeorite impact will tend to have its duration of flight extended by an electrostatic cushion [Singer and Walker, 1962]. Laboratory experiments in a simulated lunar environment [Salisbury et al, 1964] show that as soon as a dust particle touches the surface, it will stick fast. An examination of the physical features of the moon also bears upon the validity of the dust hypothesis. Obviously local depressions in the highlands as well as the ocean basins would accumulate dust if downhill transport takes place on a large scale, but this does not occur. The presence of a dark flat floor in a crater such as Ptolemaeus would indicate a dust filling with only the walls of the crater acting as a "drainage area." If this were possible, then all craters of similar size and age should have similar flat floors, which they do not. Thus, one can discount the theory of maria composed of dust and the concept of dust hundreds of feet deep. Local concentrations of dust up to 3 or 4 ft deep, however, should commonly occur (Sec. 19.5.1).

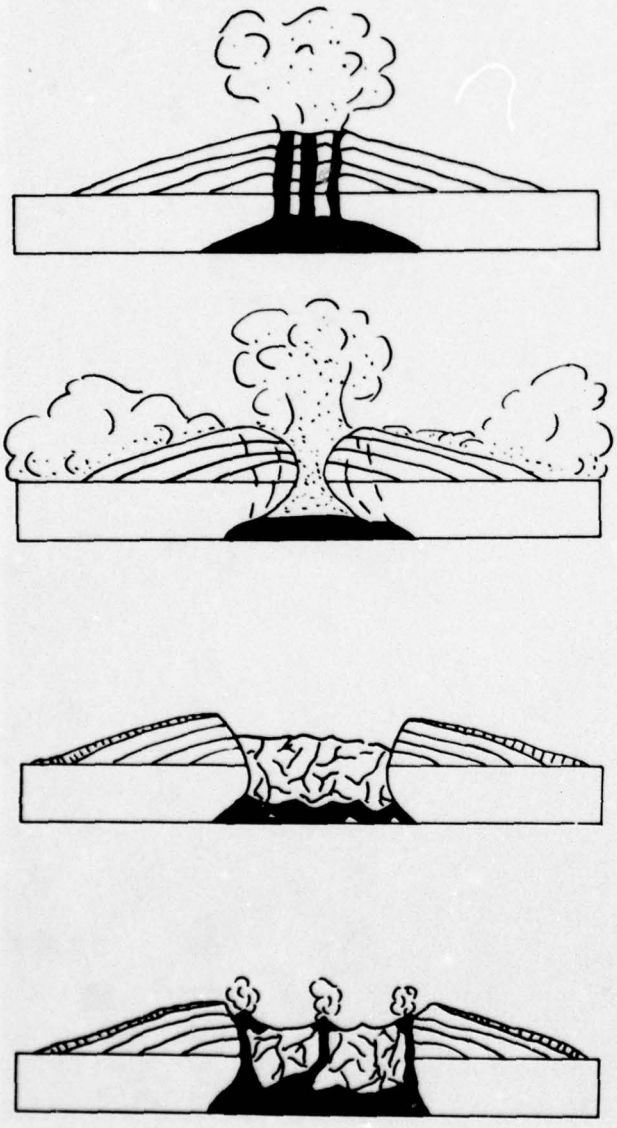


Fig. 19-2. Steps in the formation of a caldera. (After J. Green, Proceedings of Lunar Planetary Exploration Colloquium, v. 1, no. 4, p. 3, 1959.)

The maria are thought to be volcanic in nature, but many researchers believe that the volcanism was in the form of lava flows while others believe that it was in the form of ash flows. An ash flow is no more than a lava flow literally blown to bits by gas pressure, but there is a difference in form and character of the resulting deposits. A lava flow may be vesicular or bubble-filled near its top but generally forms a hard, dense rock. An ash flow is usually composed of loose material near its top but is sintered into a hard mass below a depth of a few feet; it is generally of rather low density and may even be highly porous.

It is reasonable to suspect that the maria may be covered with ash flows rather than lava flows, although the evidence is not completely convincing. First, the maria do not appear to have any of the flow fronts or steep terminations that are typical of lava flows. Second, where pre-existing craters are covered, they are reflected in the topography of the flow surface, indicating a significant volume decrease after deposition. With a constant percentage volume decrease, the thicker portions of the flow suffer a greater change in elevation than the thinner portions, because the thicker the layer, the greater the total change. Such a marked volume change does not take place in lavas, indicating the presence of ash flows over the ghost craters. This is not to say that there are no lava flows, nor that a single ash flow covered a particular mare. It is more likely that the maria were covered by a series of ash flows, possibly mixed with lava flows, significantly separated in time. The surface of the maria has subsequently been lightly cratered by impacts to produce local rubble layers, which may be several thousand feet thick in the vicinity of a major crater such as Copernicus, but which must thin rapidly to discontinuous patches in intercrater areas. Figure 19-4 shows an envisioned cross section of a typical mare.

In contrast to the maria, the highlands have evidently had a much simpler history. As shown in Fig. 19-5, the lunar crust appears to have been subjected to a long history of bombardment by meteorites and comets, leading to the formation of a complex rubble layer composed of overlapping, discontinuous lenses of debris. The thickness of this rubble layer is highly variable, most of it being concentrated in and near crater rims. Considering the volume of rubble produced by highland craters, an average depth of at least 90 ft is a reasonable value for rubble in intercrater areas. Depths of 275 ft associated with the rims of one-mile diameter craters should be common, and many thousands of feet of rubble should be present around major impacts.

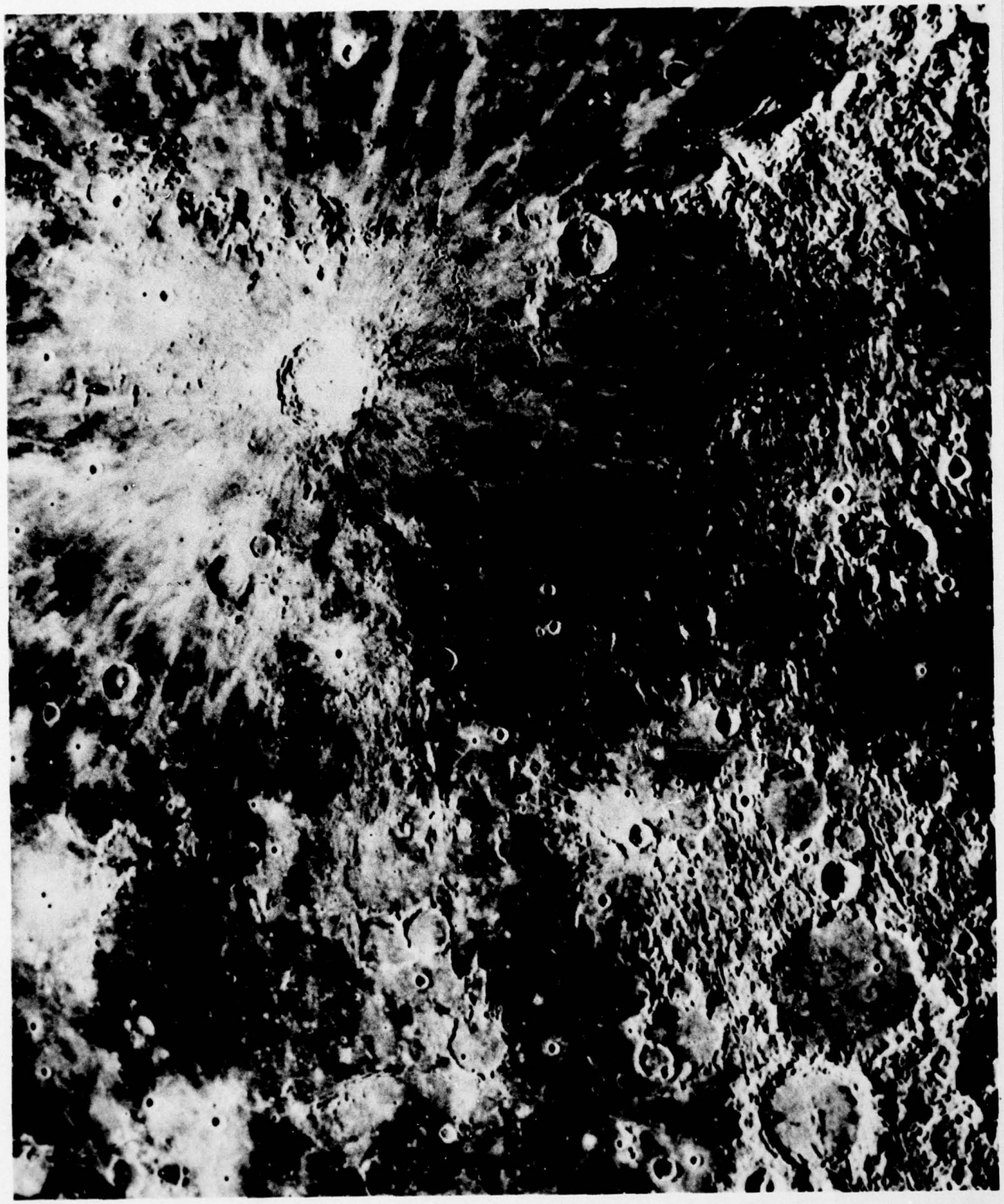


Fig. 19-3. Mt. Wilson Observatory photograph showing the craters Copernicus (upper left) and Ptolemaeus (lower right). The crater diameters are 56 and 90 miles respectively.

19.5.1 Lunar Surface Roughness

When it is accepted that the surface of the highlands is entirely covered with rubble ejected from meteorite craters and the surface of the maria is partially so, it is usually assumed that the surface must be very rough. Unless studied carefully, however, lunar surface roughness becomes a subject upon which it is easy to make erroneous judgments. One of the first mistakes generally made is not to specify the scale at which roughness is being described. Yard-scale roughness differs from mile-scale roughness and is significant for different reasons.

Mile-scale topography can be observed directly, leaving little room for argument but much room for misconceptions. The most common misconceptions are that the highly cratered highlands are rugged terrain on a mile scale, and that lunar craters are steep-sided features. Figures 19-7 and 19-8 show this is not true for the large craters. For example, in Fig. 19-6, the craters Aristillus and Autolycus appear to be deep and cup-shaped. Actually, as Fig. 19-7 shows, they are shallow, bowl-shaped features with relatively flat slopes. Figure 19-8 shows that Piton, which seems to be a needle-sharp peak in Fig. 19-6, is a low ridge. The source of the illusion of steepness is shadow exaggeration; photographs taken at a very low sun angle near lunar sunset have long shadows which make gentle features appear rugged.

The small crater Archimedes C does, however, have a steep slope on its western side. The average inner slope angle of small craters (diameter less than 15 to 20 miles) is more than 30°. Small craters comprise the vast majority of all craters, and such steep slopes are common; however, the percentage of total surface area covered by these steep slopes is very small. The generalization, therefore, is usually made that the moon is relatively smooth on a mile scale.

Surface roughness on a yard scale is of greatest interest to designers of space suits and exploration vehicles. The assumed presence of large amounts of coarse rubble on the lunar surface, particularly in the highlands, has generally led to the conclusion that the surface should be extremely rough. However, the rubble layers have been laid down during the course of a long time. The large craters which produce the greatest amount of rubble are the result of rare events. The typical rubble layer has been exposed to the lunar environment for millions of years. Over this span of time, the impacts of countless micrometeorites have acted as a potent erosion mechanism. The fine debris produced by these impacts has tended to collect in local depressions, armoring them against further erosion, while high points are gradually worn down. Figure 19-9 illustrates this condition. The collection of dust in local depressions, which makes possible the reduction of surface roughness, is a function of two processes. One

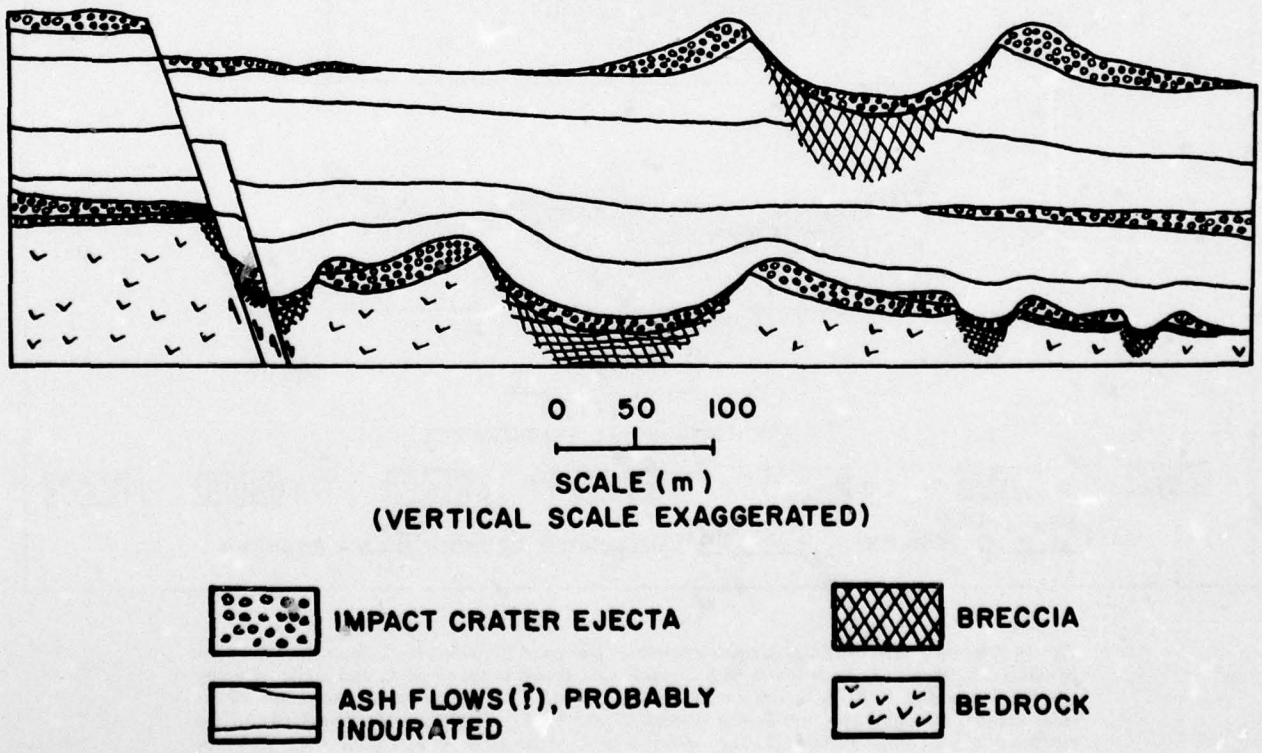


Fig. 19-4. Cross section of a typical mare.

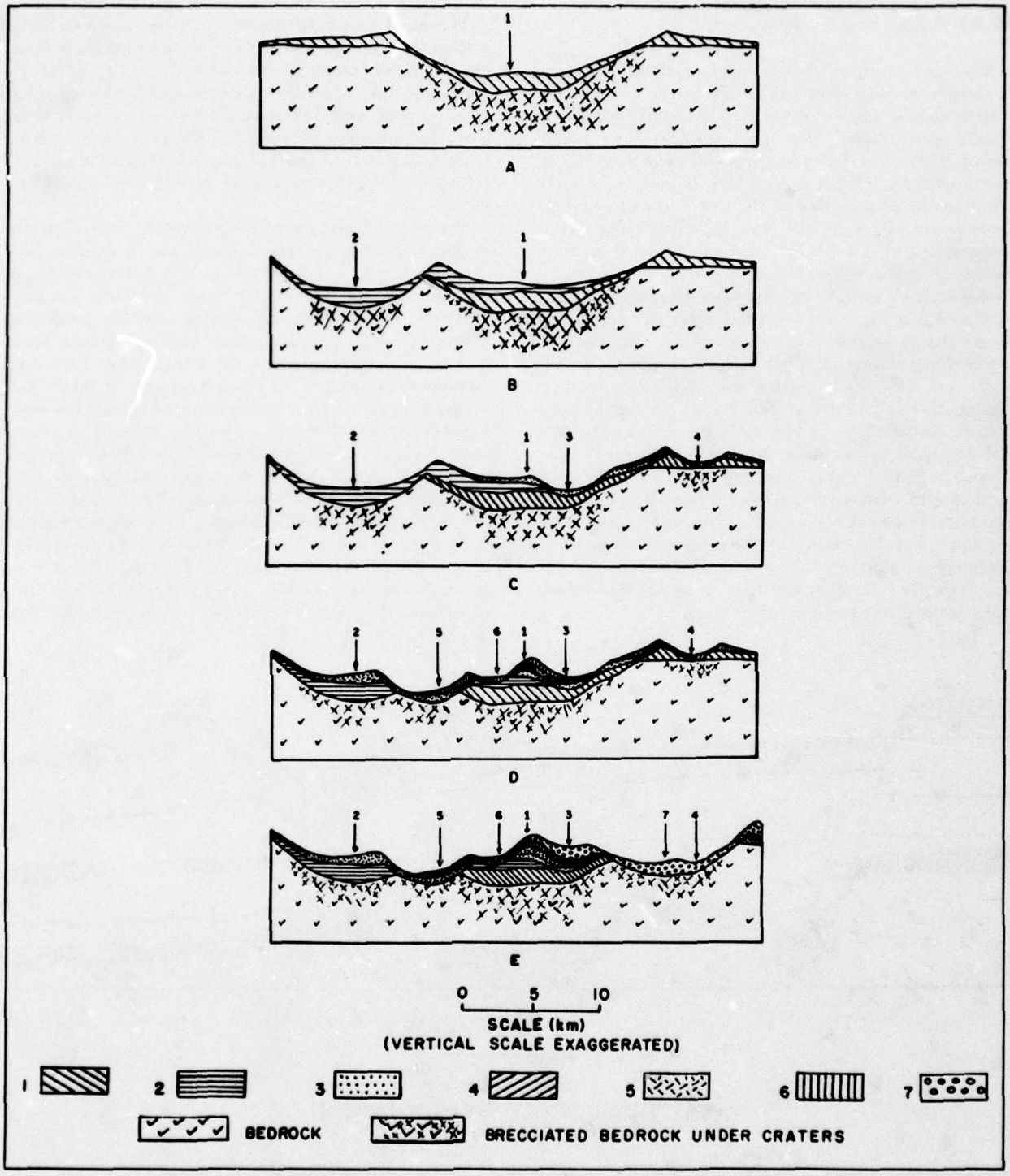


Fig. 19-5. Cross section of typical highlands terrain. Creation of simplified lunar subsurface structure by meteoritic impact. A single crater with its associated debris is shown in A, and a second crater is created beside it in B. In C, two smaller craters (3 and 4) have penetrated the debris of the older craters, and in D two overlapping craters (5 and 6) have added to the complexity of the structure. A final large crater (7) has destroyed most of crater 4 in E. Actual lunar structure will be even more complex. Negative accretion would change the thicknesses of the layers, but not the essential structure. (Key: 1-7, Debris symbols for each of the seven consecutive meteorite craters.)

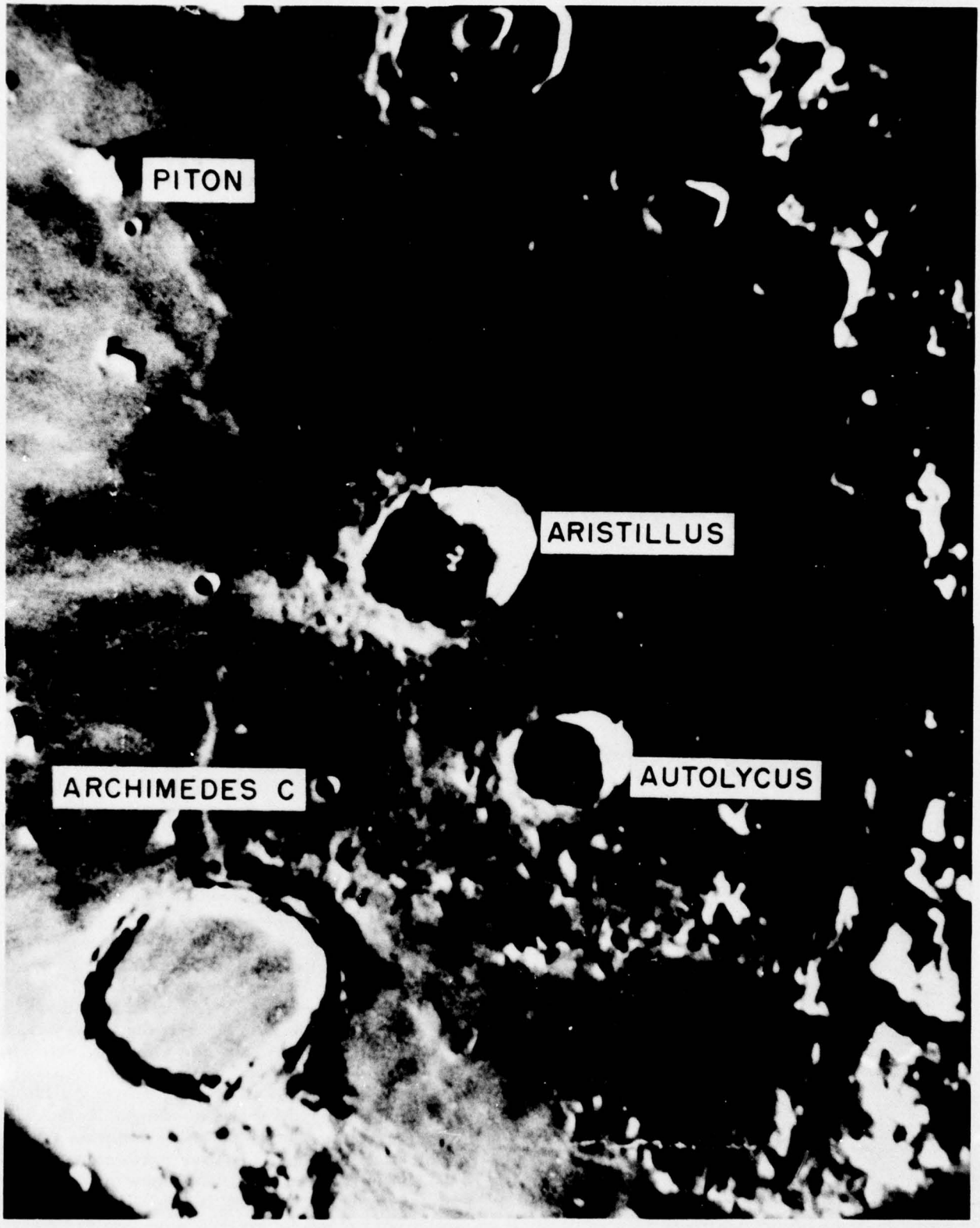


Fig. 19-6. Eastern position of Mare Imbrium (Pic-du-Midi Observatory photograph).

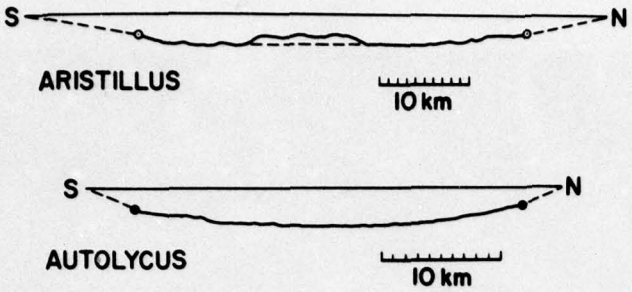


Fig. 19-7. Cross sections of the craters Aristillus and Autolycus. (From Z. Kopal, GRD Research Notes No. 67, 1961.)

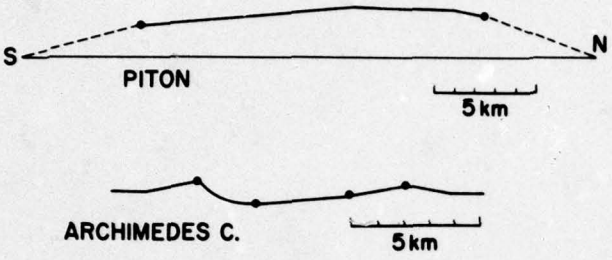


Fig. 19-8. Cross sections of the small crater Archimedes C and the mountain Piton. (From Z. Kopal, GRD Research Notes No. 67, 1961.)

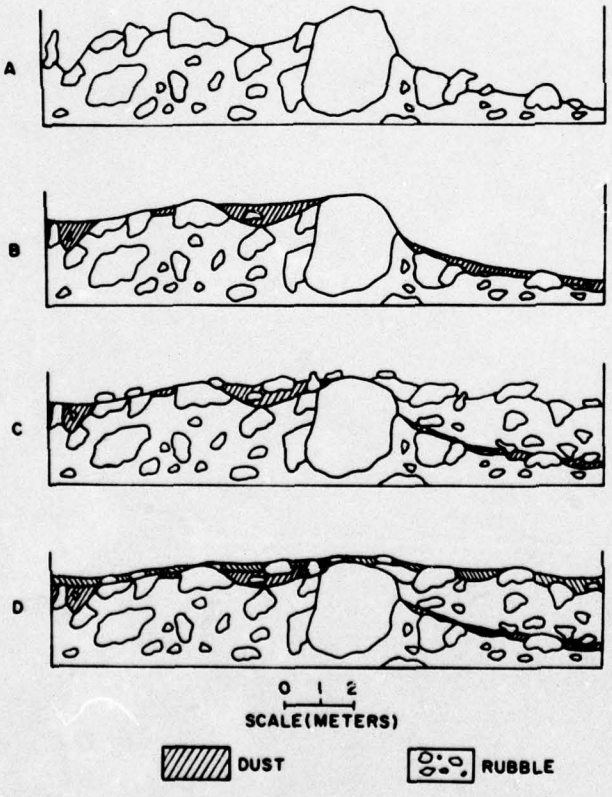


Fig. 19-9. Erosion of rubble layers to reduce relief.

process is the entrapment of debris from an impact within a depression by its walls, thus making the depth of dust increase faster in a depression than it would on flat ground. The other process, which is partly speculative, assumes that the electrostatic repulsion between a charged particle and a surface of like charge will extend the time of flight of a particle, and because the effect of gravity always tends to make such a particle migrate downhill, there is preferential filling of local depressions.

Evidence for the resulting smoothness of the lunar surface is obtained from the way in which radar waves are reflected by the moon. Because the reflections of a radar pulse come almost entirely from the center of the disk and not from its edges, the surface must be smooth at a scale equivalent to the wavelength of radar waves; if the surface were rough, it would act as a diffuse reflector and approximately as much energy would be reflected from the edges of the disk as from the center. Diffuse reflection does occur at the wavelengths of visible light; the full moon is equally bright visually over the whole disk. Thus, there is a change from smoothness to roughness between the scale of the shorter radar wavelengths of about an in. and optical wavelengths of less than a micron [Murray and Wildey, 1963].

As in the case of the mile-scale measurements, the yard-scale measurements do not indicate complete smoothness. They are usually taken to mean an average surface gradient of 1 in 10. In places where a recent rubble layer was laid down, such as around the crater Copernicus, the surface is a great deal rougher than this. Recent craters as large as Copernicus are rare, but recent craters a few hundred feet in diameter should be relatively common, even on the lightly cratered maria. (In this context "common" would be within a radius of 2 or 3 miles of the typical landing site.) The maximum diameter of a block ejected from such a crater is about 15 ft. Thus, the rubble layer surrounding the crater should have significant relief on a yard scale. Yet, as in the case of the mile-scale steep slopes, the percentage of the total lunar surface area covered by rough rubble layers is small, so that the moon is generally referred to as smooth on a yard scale. (Ranger photographs, which were made after this chapter had been written, show that the surfaces of the maria photographed are even smoother than predicted here.)

Because the smoothness of most of the highlands' surface results from the collection of fine debris in depressions on ancient rubble layers, the character of this material is of interest. Recent experiments show that rock fragments, like metals, stick together at ultrahigh vacuum [Salisbury et al, 1964]. The dust layer may, however, have a rather high porosity, and the points of contact and sticking between grains may be few, making it a highly crushable material of low bearing strength. On the other hand, seismic shocks from impacting meteorites and the occasional mixing in of a layer of slightly coarser debris of sand or even gravel size should compact the typical dust layer and give it a significant bearing strength, probably on the order of that for wet snow. Even deep dust pockets should not, in any event, exceed a yard or two in depth.

Engineering implications of the lunar model described [Salisbury and Glaser, 1964] differ according to the particular application. It is significant for designers of rockets and roving vehicles that the bearing strength of the surface will vary markedly from one area to another depending upon the degree and kind of volcanism which has occurred there. Lava flows will probably have produced lava caverns. These features occur when a hard crust forms over the lava, and then the molten material flows out from underneath it. Lava caverns constitute a definite collapse hazard as would highly vesicular flow tops.

The rubble layers offer no collapse hazard, but the deep pockets of dust between boulders require design compensations. Because of high vacuum adhesion, however, these design compensations should be no more extreme than those for a vehicle which will traverse wet snow on earth.

Dust adhesion may be an advantage when bearing strength is considered, but it is a disadvantage in other ways. When micrometeorite impacts or rocket vehicle exhausts eject small particles from the surface, any that strike the surface of a vehicle will tend to stick to that surface. Portholes, mirror surfaces, and camera lenses may become obscured, and the efficiency of solar cells or heat radiation panels may be destroyed. Design of these features must take this phenomenon into account.

The roughness of the lunar surface is extremely variable from place to place, but most of the surface is smooth at all but near-microscopic scales. If a vehicle must be designed to land or rove anywhere on the surface, the design constraints are severe; if rough areas may be avoided, design problems are greatly reduced.

19.6 LUNAR RESOURCES

Utilization of indigenous lunar materials to reduce the cost of interplanetary exploration is desirable. Many suggestions have been made, but on close examination of the cost factors, most of these are not feasible. In its simplest form, the cost analysis depends upon the difference between the cost of transporting material to the moon ($5000/pound) and the cost of each man hour necessary to produce the material on the moon ($75,000/man-hour).

Of all possible lunar resources, the surficial rubble seems to be the most economically usable. It can be used as a shielding material for nuclear reactors or base modules; no processing is necessary if a rubble layer with the proper distribution of block size is nearby.

There is good reason to believe that water will be available on the moon, either as ice or in the form of hydrated minerals. After electrolysis to hydrogen and oxygen, it could be used to refuel rocket vehicles. A refueling station on the moon would be particularly desirable for interplanetary exploration where refueling would allow the use of Apollo-type vehicles for extended space missions. The thousands of pounds of water needed to refuel a series of Mars and Venus missions, together with the quantity needed to maintain the lunar base, make it possible to amortize the cost of water extraction and processing equipment; with a semiautomatic operation requiring less than one-fifteenth of a man-hour per pound of water extracted, it will be economical [Salisbury et al, 1963].

Other lunar resources may be discovered as knowledge of the moon is improved but none are apparent at this time.

19.7 LUNAR MOTION

During the yearly revolution of the center of mass (barycenter) of the earth-moon system about the sun, as the moon revolves monthly about the earth, it rotates and wobbles about its own center of mass. The theory of the orbital motion of the moon about the earth is primarily a problem of three bodies: moon, earth, and sun; the effects of the planets and of the ellipsoidal figures of the earth and moon are relatively minor, though not negligible. Neglecting effects of the sun and other perturbative masses, the theoretical orbit of the moon around the earth is a Kepler ellipse with the earth at one focus; however, departures from this two-body approximation (called inequalities) are large enough to have been observed by ancient astronomers.

Detailed information is available from many sources. Brown [1896] is a comprehensive treatise on the methods of lunar theory, including the method of Hill which is the basis of current lunar ephemerides. The theory of Hill, which Brown extended, is treated with some detail by Brouwer and Clemence [1961]. Danby [1962] contains excellent accounts of the fundamentals of lunar motion or libration; it is recommended as an introduction. Kopal [1962] discusses lunar theory, librations, and dynamics of the earth-moon system. Jeffreys [1959] includes information on the figure of the moon, empirical and hydrostatic, and the secular acceleration of its mean motion.

The *American Ephemeris and Nautical Almanac*, an annual publication (U.S. Government Printing Office), contains several tables concerning the moon. For 0 h and 12 h for each day, the apparent longitude and latitude of the moon are tabulated to 0.01 sec of arc, and the parallax is tabulated to 0.001 sec of arc. Another table gives the hourly apparent right ascension and the hourly apparent declination. A list of the optical and physical librations of the moon in latitude, longitude and position angle as well as tables for making topocentric corrections also are included. The *Improved Lunar Ephemeris* 1952-1959 [1954] includes a detailed discussion of the construction of the lunar ephemeris from Brown's theory. Details for the construction of ephemerides for other lunar quantities are given in the *Explanatory Supplement to the Ephemeris* [1961].

19.7.1 Rotation and Librations

The rotation of the moon is fairly accurately described by three empirical rules known as Cassini's laws:

1. The moon rotates uniformly about its axis with a period of rotation equal to the mean sidereal period (27.3 day) of its orbit around the earth;

2. The inclination of the lunar equator to the ecliptic, I, is a small constant angle, approximately 1.5°; and

3. The ascending node (point of intersection) of the lunar orbit on the ecliptic coincides with the descending node of the lunar equator on the ecliptic.

The inclination of the lunar orbit to the plane of the ecliptic, i, is about 5°; thus, the inclination of the lunar equator to the orbit, I + i, is about 6.5°. The orientation of the orbital plane, however, is not constant; the perpendicular describes a cone of revolution in 18.6 yr. As a result, the points of intersection of the orbital motion with the ecliptic regress (move westward) with an 18.6-yr period. The node of the lunar equator regresses with the same period. The mean longitude of lunar perigee advances, however, completing one revolution in 8.9 yr.

Because of its inclination to the ecliptic, an observer on earth views the polar axis from different directions. During one revolution around the earth, the north and south lunar poles are alternately tipped earthward; this is the *optical libration in latitude*. The magnitude is about 6.5°. Whereas lunar rotation about the polar axis is uniform, the orbital angular velocity is maximum at perigee and minimum at apogee. Accordingly, the angular orbital displacement is at times larger or smaller than the angle of lunar rotation so to an observer on earth, the moon appears to oscillate about its polar axis. This effect is the *optical libration in longitude*; the maximum magnitude is almost 8°. There is also a *topocentric optical libration* which allows about 1° more of the lunar surface to be seen from the north and south poles of the earth and at moonrise and sunset.

A dynamical investigation of the libration reveals residual librations which are real oscillations of the moon about its center of gravity; these are *physical librations*. Physical librations are difficult to detect; the amplitude of the largest component is only 0.4% of the optical libration, about 2 min of arc on the moon and less than 1 sec of arc as seen from the earth. The net lunar librational effect is to allow 59% of the surface of the moon to be visible from somewhere on the earth at some time or another.

19.7.2 Librations and the Lunar Mechanical Figure

Studies of the librations provide information concerning the lunar mechanical figure. The principal moments of inertia are: C, the moment about the lunar axis of rotation; A, the moment about the lunar axis in the mean direction of earth; and B, the moment about the lunar axis orthogonal to the axes of A and C.

Librations are stable only if the mechanical figure of the moon is a triaxial ellipsoid, for which $C > B > A$. The nonsphericity of the moon allows the earth to apply torques which constrain the moon to follow Cassini's laws; it also accounts for other torques caused by the earth which result in physical librations. The apparent position of the earth from the moon changes with time according to the center equation and the inequalities of the lunar orbit; the resulting torques cause the forced physical librations. Even if the apparent position of the earth remained constant, there would be a resonant frequency at which the moon could oscillate under the restoring force of the earth. This free physical libration, however, would be dampened by tidal friction on the moon. It is frequently assumed to be negligible; nevertheless, inequalities of the lunar orbit with periods close to the resonant period have an enhanced effect on the forced librations.

The differential equations relating the moon's orientation, rotations, and angular accelerations to the torques in the earth's gravity field could be integrated to derive amplitudes and periods of the librations, if A, B, and C were known. In practice the independent quantities are usually taken as the inclination, I, and the *mechanical ellipticity*, $f = (C - B)/(C - A)$. I and f are best derived iteratively by finding the values for which the theoretical librations most nearly match the observed librations. A singularity at $f = 0.66$ is troublesome; recent studies suggest that of the two solutions falling on opposite sides of the singularity, the lower value of f should be used. I can be measured from the optical librations and is known to a much higher precision than f. The measurement of f depends on the detection of the small physical librations. Table 19-1 lists values of libration constants based on a comprehensive reduction of heliometer observations.

In terms of the spherical coordinates, r (radial distance), ψ (selenographic co-latitude), and λ (selenographic longitude), the surface of a uniform-density lunar ellipsoid may be represented by

$$r = a\,(1 + S_2), \tag{19-1}$$

where a is the radius of a sphere of the same volume. The second degree harmonic, S_2, is

$$-\frac{1}{3}\,[\text{redacted}]\,P_2^0\,(\cos\psi) + \frac{1}{6}\,[\text{redacted}]\,P_2^2\,(\cos\psi)\cos 2\lambda,$$

$$\text{where } P_2^0\,(\cos\psi) = \frac{1}{2}\,(3\cos^2\psi - 1), \text{ and}$$

$$P_2^2\,(\cos\psi) = 3\sin^2\psi.$$

19.8 LUNAR GRAVITY FIELD

The contribution of the ellipsoid to the gravitational potential above the moon is

$$-\frac{GM}{r}\left[1 + \frac{3}{5}\,\frac{a^2}{r^2}\,S_2\right],$$

where G is the gravitational constant and M is the lunar

Table 19-1. Libration constants and selenographic coordinates of crater Mösting-A. (After K. Koziel, *Space Research IV*, Proceedings of the Fourth International Space Science Symposium, Warsaw, Poland, P. Muller, ed., North Holland Publishing Co., Amsterdam, 1964.)

Mechanical ellipticity of the moon:	$f = 0.663 \pm 0.011$
Mean inclination of the moon's axis of rotation to the perpendicular of the ecliptic:	$I = 1° 32' 1\overset{''}{.}0 \pm 7\overset{''}{.}1$
Selenographic longitude:	$\lambda = 5° 9' 50\overset{''}{.}0 \pm 4\overset{''}{.}5$
Selenographic co-latitude:	$\psi = 93° 10' 47\overset{''}{.}0 \pm 4\overset{''}{.}4$
Height above mean lunar level:	$\Delta h = +0\overset{''}{.}40 \pm 0\overset{''}{.}19$

mass. The contribution of forces caused by orbital motion and of tidal forces caused by the earth to the potential is approximately

$$-\frac{GM}{r}\ \frac{r^3}{a^3}\ Y_2,$$

where the second degree harmonic is

$$Y_2 = \mu \frac{a^3}{r^3}\left[-\frac{5}{6}\,P_2^0\,(\cos\psi) + \frac{1}{4}\,P_2^2\,(\cos\psi)\,\cos 2\lambda\right].$$

The ratio of the mass of the earth to the mass of the moon, $1/\mu$, is taken as 81, and the mean separation as 220 a. The total potential is

$$U = -\frac{GM}{r}\left[1 + \frac{3}{5}\ \frac{a^2}{r^2}\,S_2 + \frac{r^3}{a^3}\ Y_2\right]. \tag{19-2}$$

On the surface of the lunar ellipsoid, the first-order approximation of the potential is

$$-\frac{GM}{a^2}\left[1 - \frac{2}{5}\ S_2 + Y_2\right]. \tag{19-3}$$

If the moon were in hydrostatic equilibrium, this would be an equipotential surface; S_2 would equal $\frac{5}{2}\ Y_2$. The moon, however, is not in hydrostatic equilibrium; its ellipsoid deviates from a sphere much more than an equipotential ellipsoid. According to hydrostatic theory for a homogeneous moon, f is 0.25; this is considerably less than the empirical ratio, $f \approx 2/3$.

The gravitational acceleration above the surface of the moon is

$$-\frac{\partial U}{\partial r} = -\frac{GM}{r^2}\left[1 + \frac{9}{5}\ \frac{a^2}{r^2}S_2 - 2\,\frac{r^3}{a^3}\ Y_2\right]. \tag{19-4}$$

On the surface of the lunar ellipsoid, the first order approximation of the acceleration is

$$g = \frac{GM}{a^2}\left[1 - \frac{1}{5}\ S_2 - 2\,Y_2\right], \tag{19-5}$$

or

$$g \approx g_0\,[1 + 80 \times 10^{-6}\,P_2^0\,(\cos\psi) + 9 \times 10^{-6}\,P_2^2\,(\cos\psi)\,\cos 2\lambda], \tag{19-6}$$

where $g_0 = \frac{GM}{a^2}$ (about one-sixth the gravity acceleration on the earth's surface, or ≈ 1.6 m sec^{-2}). On the lunar ellipsoid, g varies with latitude and longitude. Departures from g_0 may be as much as 1 part in 8000.

The actual surface of the moon may be represented by

$$r = a\left(1 + S_2 + \sum_{n=3}^{\infty} S_n\right), \tag{19-7}$$

where S_n is an n-th order spherical surface harmonic. The radial deviations, a $\sum_{n=3}^{\infty} S_n$, from the ellipsoid may be considered as *topography*. In this sense, topography on the moon differs from topography on the earth. On earth, elevations are measured from the geoid, an equipotential surface that departs from the terrestrial ellipsoid by 100 m at most. On the moon, the elevations must be measured from the lunar ellipsoid which, because of the apparent absence of first-order hydrostatic equilibrium, may depart from the *selenoid* (equipotential surface) by hundreds of meters.

Corrections for the acceleration of gravity due to this topography are difficult because data on the harmonic terms are lacking. The corrections may be partially investigated by examining the effects of lunar mountains. The mountains are represented by high-order harmonic terms, and their elevations above the surrounding lower topography can be estimated. Elevations of the surrounding topography above or below the ellipsoid are represented, however, by lower-order harmonic terms that are unknown.

The effects of the mountains on the value of g may be considered by assuming an absence of second and higher order isostatic compensation; this seems a reasonable assumption in view of the apparent absence of first-order isostatic compensation. For a plateau, with the same density as the rest of the moon, at an elevation h, above the surrounding plains, the change in g from surrounding lower topography is about $\frac{gh}{2a}$. For a height of 500 m, the change in g amounts to about 1 part in 7000; this is almost the maximum change due to latitude and longitude. Because lunar mountains may have elevations of 6 km, the predominant influence on the moon's surface gravity appears to be the local topography; selenographic location is probably secondary.

19.9 SUGGESTED VALUES OF LUNAR CONSTANTS

Consistent sets of best values for astronomical constants of the solar system have not been established. For the present, suggested values for use in computations are as follows:

Mass 7.35×10^{25} g

Mean density 3.34 g cm^{-3}

Mass ratio, earth to moon 81.29 ± 0.11
(From D. Brouwer, Symposium 21, I.A.U., Paris, May 27-31, 1963)

Mean radius 1738 ± 1 km

Semidiameter (mean distance) observed, 932.70 ± 0.04 sec of arc (computed, 932.60 sec of arc)
(From H. Spencer Jones, *Monthly Notices Royal Astron. Soc.*, v. 85, p. 11, 1924.)

Moon's distance from earth 384,400.2 ± 1.2 km
(From D. Brouwer et al, Symposium 21, I.A.U., Paris, 1963)

Mean dynamical parallax 3422.610 ± 0.13 sec of arc
(From I. Fischer, *Astron. J.*, v. 67, p. 373, 1962.)

Synodic month 29.530589 mean solar day

Sidereal month (rotation period) 27.321661 mean solar day

19.10 REFERENCES

Baldwin, N. B., 1949, "The Face of the Moon," Univ. Chicago Press, Chicago, Ill.

Brouwer, D., and G. M. Clemence, 1961, "Methods of Celestial Mechanics," Academic Press, New York.

Brown, E. W., 1896, "An Introductory Treatise on the Lunar Theory," Cambridge Univ. Press. (Reprinted, 1960, Dover Publications, Inc., New York.)

Chapman, D. R., and H. K. Larson, 1963, "On the Lunar Origin of Tektites," *J. Geophys. Res.*, v. 68, no. 14, p. 4305.

Cohen, A. J., 1960, "Trace Element Relationships and Terrestrial Origin of Tektites," *Nature*, v. 188, p. 653.

Costain, C. H., B. Ellsmore, and G. R. Whitfield, 1955, "Radio Observations of a Lunar Occultation of the Crab Nebula," *Monthly Notices Royal Astron. Soc.*, v. 116, p. 380.

Danby, J. M. A., 1962, "Fundamentals of Celestial Mechanics," The Macmillan Co., New York.

Edwards, W. F., and L. B. Borst, 1958, "Possible Sources of a Lunar Atmosphere," *Science*, v. 127, p. 325.

"Explanatory Supplement to the Ephemeris," 1961, H. M. Stationery Office, London.

Gold, Q., 1959, "Dust on the Moon," *Vistas in Astronautics*, v. 2, p. 261.

"Improved Lunar Ephemeris 1952-1959," 1954, U. S. Government Printing Office, Washington, D. C.

Jeffreys, H., 1959, "The Earth," 4th ed., Cambridge Univ. Press, London.

Kopal, Z., 1962, "Physics and Astronomy of the Moon," Academic Press, New York.

Kopal, Z., 1959, "Does the Moon Possess a Magnetic Field?" *Space J.*, v. 2, no. 1, p. 3.

Lowman, P. D., 1963, "The Relation of Tektites to Lunar Igneous Activity," *Icarus*, v. 2, p. 35.

Medd, W. J., and N. W. Broten, 1961, "Lunar Temperature Measurements at 3200 Mcps," *Planetary and Space Science*, v. 5, p. 307.

Murray, B. C., and R. L. Wildey, 1963, "Stellar and Planetary Observations at 10 Microns," *The Astrophys. J.*, v. 137, p. 692.

Öpik, E. J., and S. F. Singer, 1960, "Escape of Gases from the Moon," *J. Geophys. Res.*, v. 65, p. 3065.

Saari, J. M., and R. W. Shorthill, 1963, "Isotherms of Crater Regions on the Illuminated and Eclipsed Moon," *Icarus*, v. 2, p. 115.

Salisbury, J. W., and P. E. Glaser, eds., 1964, "The Lunar Surface," Academic Press, New York.

Salisbury, J. W., P. E. Glaser, B. A. Stein, and B. Vonnegut, 1964, "Adhesive Behavior of Silicate Powders in Ultrahigh Vacuum," *J. Geophys. Res.*, v. 69, no. 2, p. 235.

Salisbury, J. W., P. E. Glaser, and A. E. Wechsler, 1963, "The Implications of Water as a Lunar Resource," *Proceedings of the Lunar and Planetary Exploration Colloquim*, v. 3, no. 3, p. 39.

Shoemaker, E. M., 1962, Interpretation of Lunar Craters, "Physics and Astronomy of the Moon," Z. Kopal, ed., Academic Press, New York.

Singer, S. F., and E. H. Walker, 1962, "Electrostatic Dust Transport on the Lunar Surface," *Icarus*, v. 1, no. 2, p. 112.

Urey, H. C., 1952, "The Planets," Yale Univ. Press.

Watson, K., B. Murray, and H. Brown, 1961, "On the Possible Presence of Ice on the Moon," *J. Geophys. Res.*, v. 66, p. 1598.

Weil, H., and M. L. Barasch, 1963, "A Theoretical Lunar Ionosphere," *Icarus*, v. 1, no. 4, p. 346.

Chapter 20

PLANETARY ENVIRONMENTS

Roger A. Van Tassel
John W. Salisbury

Our knowledge of planetary environments is largely speculative. Models which satisfy all the observations are not available. Except for Mars and Venus, only brief descriptions and tabular data are given; for detailed descriptions and evaluations of the data available in 1960, see Kuiper and Middlehurst [1961].

Magnitudes given in the tabular data are defined in Sec. 21.2.5, with exception of $V(1,0)$ and V_o. $V(1,0)$ is the apparent visual magnitude of the planet reduced to a standard reference distance; $V(1,0) = V - 5 \log rd - \Delta m(\alpha)$, where r is the planet's distance from the Sun, d its distance from the Earth, and $\Delta m(\alpha)$ the correction for the variation in magnitude with phase angle of the planet. V_o is the mean opposition magnitude; $V_o = V(1,0) + 5 \log a(a-1)$, where a is the planet's semimajor axis. Color differences (value for planet minus solar value) are based on the following solar values:

V	V(1,0)	U−B	B−V	V−R	R−I
−26.81	−28.81	0.14	0.63	0.45	0.29

Note that these values are not identical with those given in Sec. 21.2.1. Unless a source of the tabular data is designated, the values quoted are from the Smithsonian Physical Tables.

20.1 MERCURY

20.1.1 General

Mercury, with a diameter of 4840 km, is the smallest principal planet in the solar system; its diameter is only 1.4 times that of the moon. Mercury is so near the sun that it has been constrained by powerful sunraised tides to rotate and revolve in the same period, keeping the same face toward the sun. Because of the large eccentricity, the libration in longitude leaves only 30% of the planetary surface in permanent darkness.

The low escape velocity of Mercury (4.3 km sec^{-1}) suggests that it should have very little atmosphere, and observations of polarization of reflected sunlight indicate that only a tenuous atmosphere is present. Measurements of the surface temperature of Mercury indicate a maximum of 688°K on the sunward side of the planet. No radiation has been detected from the dark side where the temperature must be extremely low.

20.1.2 Tabular Data for Mercury

Mean radius: 2420 km (American Ephemeris)
0.380 Earth radii
3.34 sec of arc at 1 AU
Mass: 3.30×10^{26} g (American Ephemeris)
Sun/Mercury, 6×10^6
Mercury/Earth, 0.055
Mean density: 5.46 g cm^{-3}
Surface gravity: Mercury/Earth, 0.38
Escape velocity at equator: 4.3 km sec^{-1}
Rotation period: 88.0 Earth days
Sidereal period: 87.97 days
0.241 tropical year
Mean distance from Sun: 0.387 AU
57.9×10^6 km
Inclination of orbit to the ecliptic: 7°
Eccentricity of orbit: 0.2056
Magnitudes [Harris, 1961]: B − V, 0.93
V − R, 0.85
R − I, 0.52
V(1,0), −0.36

Color difference, Mercury minus Sun [Harris, 1961]:

B,	0.30	R,	−0.40
V,	0.00	I,	−0.63

20.2 VENUS

20.2.1 Atmosphere

The composition of the atmosphere as a whole is rather speculative; the only portion of the atmosphere accessible to spectroscopic investigation is above the cloud layer. The volume composition of the entire atmosphere is generally assumed to be approximately 90% CO_2, 9% N_2, and 1% Ar and other gases.

Spectroscopic studies have positively identified only CO_2; estimates of the concentration are between 100 and 1000 m-atm above the cloud layer, and between 2000 to 7000 m-atm in the atmosphere as a whole. Water vapor was tentatively identified [Sagan, 1961a] in the upper atmosphere, but the results were marginal. An unsuccessful spectroscopic search [Spinrad, 1962] resulted in an upper limit of 10^{-5} for the mixing ratio of water vapor above the level of high atmospheric temperature and pressure. Emission bands of N_2^+ and of neutral and

ionized oxygen in the spectrum of the night side of Venus were reported [Warner, 1960]; there are sufficient discrepancies, however, to make identification inconclusive. It is assumed, by analogy with the terrestrial atmosphere, that some nitrogen and at least traces of argon (resulting from radioactive decay of potassium) are present.

20.2.1.1 *Clouds.* The nature of the layer of cloud which obscures the lower atmosphere and surface of Venus is a perplexing problem. The clouds are a pale lemon yellow color with a visual albedo between 0.64 and 0.71 [Kuiper, 1957]. The most common substance that has such a high reflectivity and is condensable at the temperature of the top of the cloud layer is water, either as droplets or ice crystals. The high temperature indicated by radio measurements not far below the top of the cloud layer implies, however, that extensive water clouds could not exist. The polarization curve of water droplets closely fits that obtained from observations of Venus [Lyot, 1929]; but the polarization curve produced by scattering from nearly spherical quartz particles 5 to 10μ in diameter also fits, indicating the ambiguity of polarization measurements. Other molecules suggested to explain the yellow coloration of the clouds are polymerized carbon suboxide, ammonium nitrite, and nitrogen textroxide. Because all these substances have low reflectivities, it is unikely that the clouds are composed primarily of any of these, but small amounts of polymerized carbon suboxide may contribute to the coloration of the clouds. Öpik [1961] suggested that the clouds are composed of dust particles. The apparent high temperature of the surface and of the lower atmosphere, and the indications of a low dielectric constant, agree with this concept. Both water clouds and dust clouds might exist at appropriate levels in the atmosphere; the solution of this problem must await further data.

20.2.1.2 *Pressure and Temperature.* So little is known concerning the variation of temperature and pressure with depth in the Cytherean atmosphere that there is no one atmospheric model which is generally accepted. Confirmation of a high surface temperature has at least eliminated the low temperature models. Figure 20-1 shows the model of Menzel and De Vaucouleurs; Öpik [1961] and Sagan [1962] give different models. The major disagreement is on atmospheric pressure. Estimates of the pressure at the surface range from 1.2×10^6 to 50×10^6 dyne cm^{-2}.

20.2.1.3 *Circulation.* Figure 20-2 shows the circulation pattern of the Cytherean atmosphere, as deduced from the pattern of dark shadings seen in visible and ultraviolet light. Such a circulation pattern is highly speculative, but it is the only model available.

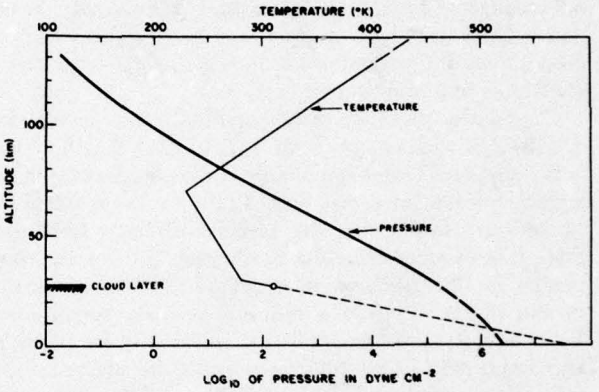


Fig. 20-1. Model atmosphere for Venus; assumed values are surface temperature 580°K, pressure at the top of the cloud layer 1.6×10^5 dyne cm^{-2}, and mean solar mass 42.5. (From De Vaucouleurs and Menzel [1960].)

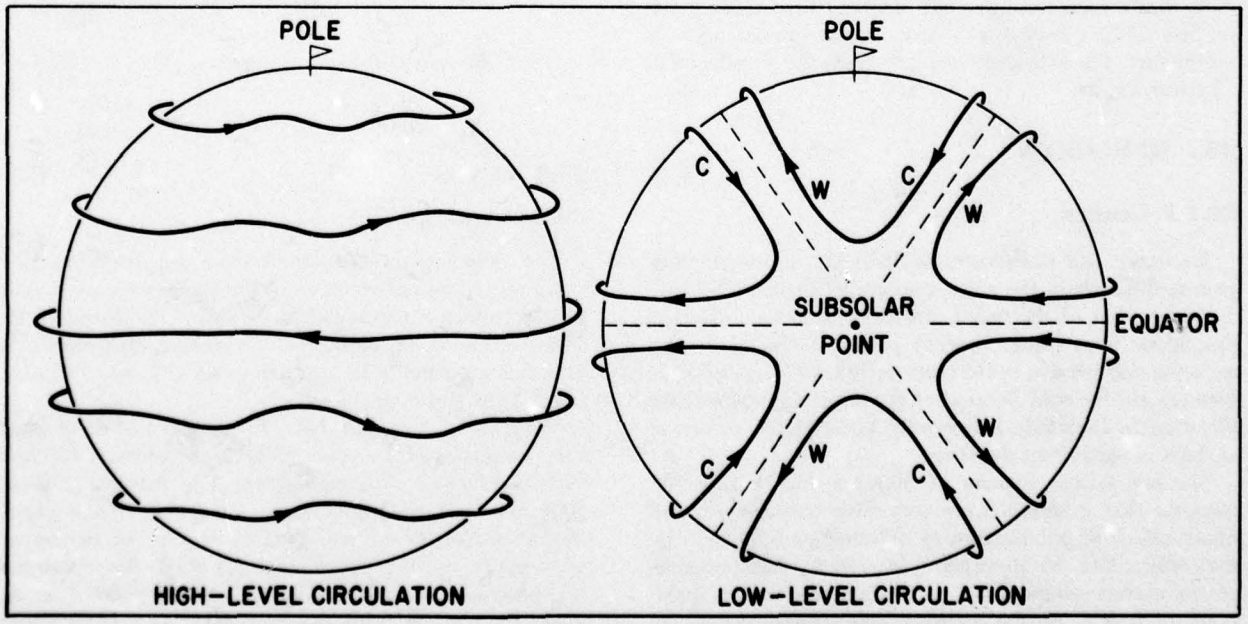


Fig. 20-2. Low level cellular circulation and high level zonal circulation of the Cytherean atmosphere; W indicates warm currents, C, cold currents. (From Y. Mintz, "Planetary and Space Science," v. 5, p. 141, 1961 Pergamon Press, by permission.)

20.2.2 Thermal Environment

Centimeter-wavelength radiation is thought to penetrate the Cytherean atmosphere and represents the thermal emission from the surface. Measurements at these wavelengths indicate an average surface temperature of approximately 580°K that does not change from a light to dark side of Venus. Such a high surface temperature could be the result of a greenhouse effect, wind friction at the surface, or a combination of both. It has been suggested that the source of the centimeter emission might be a fluctuation of electrical charges on particles in the amtosphere or plasma radiation from an ionosphere rather than thermal emission from the surface. However, the electrical characteristics of the Cytherean atmosphere [Muhleman, 1963] and preliminary results from Mariner II appear to rule out the ionospheric model. Preliminary results of the microwave measurements performed by Mariner II [1963] indicate a limb darkening, which is consistent with the source of the high temperatures being deep in the atmosphere or at the surface of the planet.

Measurements made at 8.6 mm wavelengths indicate temperatures in the neighborhood of 400°K with strong phase effects. It may be that these shorter wavelengths originate from a portion of the atmosphere that has its temperature affected by solar illumination. It is also possible that the millimeter radiation is emitted by the surface, but appears to have a lower temperature because of molecular absorption and scattering by particles in the atmosphere. The phase effect could then be due to a condensable or sublimable cloud layer which is transparent at centimeter wavelengths, but slightly opaque in the millimeter region.

Infrared measurements give a much lower apparent temperature, about 233°K. Limb darkening demonstrates that the infrared radiation comes from a region of the atmosphere in which the temperature decreases with height above the surface. Infrared spectra show no evidence of absorption at wavelengths where CO_2 bands occur, indicating that the layer emitting the infrared lies above most of the CO_2 in the atmosphere. From the fact that the temperature is nearly the same for the sunlit and dark hemispheres, it is inferred that the layer emitting the infrared does not absorb solar radiation but receives its heat from within the atmosphere or from the latent heat of condensation of a vapor. On this basis, it seems reasonable to assume that the top of a highly reflective cloud layer is the major source of the infrared radiation.

Figure 20-3 shows measurements of the distribution of the brightness temperature of Venus in the 8- to 14-μ region; there is a general symmetry about the plane of the orbit, and a transient temperature anomaly in the southern hemisphere. The anomaly illustrates the variability in thermal profile that must be present in the atmosphere, but the model shown in Fig. 20-1 may be considered representative.

20.2.3 Magnetic Field

According to theory, the temperature of the interior of Venus exceeds the Curie point of iron, hence Venus should have a magnetic field; one calculation of the predicted intensity gives a field strength at the poles 5000 times that of Earth. It appears likely, however, that the magnetic field of Venus is either very weak or nonexistent. Mariner II instruments did not detect trapped charged particles associated with the planet Venus. The closest approach was 41,000-km radial distance from the center of the planet on the sunward side, so the magnetosphere of Venus, if any, does not extend to that distance. A plausible inference is that the upper limit for the dipole magnetic moment of Venus is 0.18 times that of Earth. If this is true, then the effectiveness of Venus in screening the Earth from solar corpuscular radiation cannot be attributed to Venus' magnetic field and is unexplained.

20.2.4 Surface Features

Photographs of Venus taken in ultraviolet and blue light show bright and dark markings, nearly perpendicular to the terminator. Visual observations reveal occasional vague dark markings and bright patches. Although the visual observations of dark markings were doubted as optical illusions, it now appears that these markings are real. It is generally conceded that all markings are atmospheric effects. The surface features of Venus are, therefore, completely unknown; but there is much speculation concerning the gross characteristics of the surface.

One hypothesis, that the entire surface is covered with water, was eliminated by the measurements of a surface temperature of 600°K. Hoyle assumed a great excess of hydrocarbons over water on primitive Venus, with subsequent oxidation of the hydrocarbons to carbon dioxide until all the water was depleted, and suggested that the surface is covered with the remainder of the hydrocarbons. Again, the high surface temperature of Venus makes this theory very doubtful. A recently revived hypothesis is that the surface of Venus is an arid desert. Sagan envisions the surface to be hot, arid, calm, and overcast. If the dust storm model of Öpik is correct, and wind friction does supply most of the heating at the surface, then it will hardly be calm. Calculations [Mintz, 1962] suggest wind velocities up to 450 mile h^{-1}, but these are based on many assumptions and subject to understandable error.

Whether or not high velocity winds are present, as seems likely, the dielectric constant of the surface obtained from radar measurements suggest that the surface of Venus is similar to rocky terrestrial terrain [Pettengill et al, 1962] and relatively smooth, being twice as smooth as that of Mercury, but rougher than that of Mars [Carpenter and Goldstein, 1963].

20.2.5 Satellites

No satellite has so far been identified for Venus. It appears that no large satellite could possibly go unnoticed, but one or more small satellites no larger than 5 to 12 km in diameter could be present.

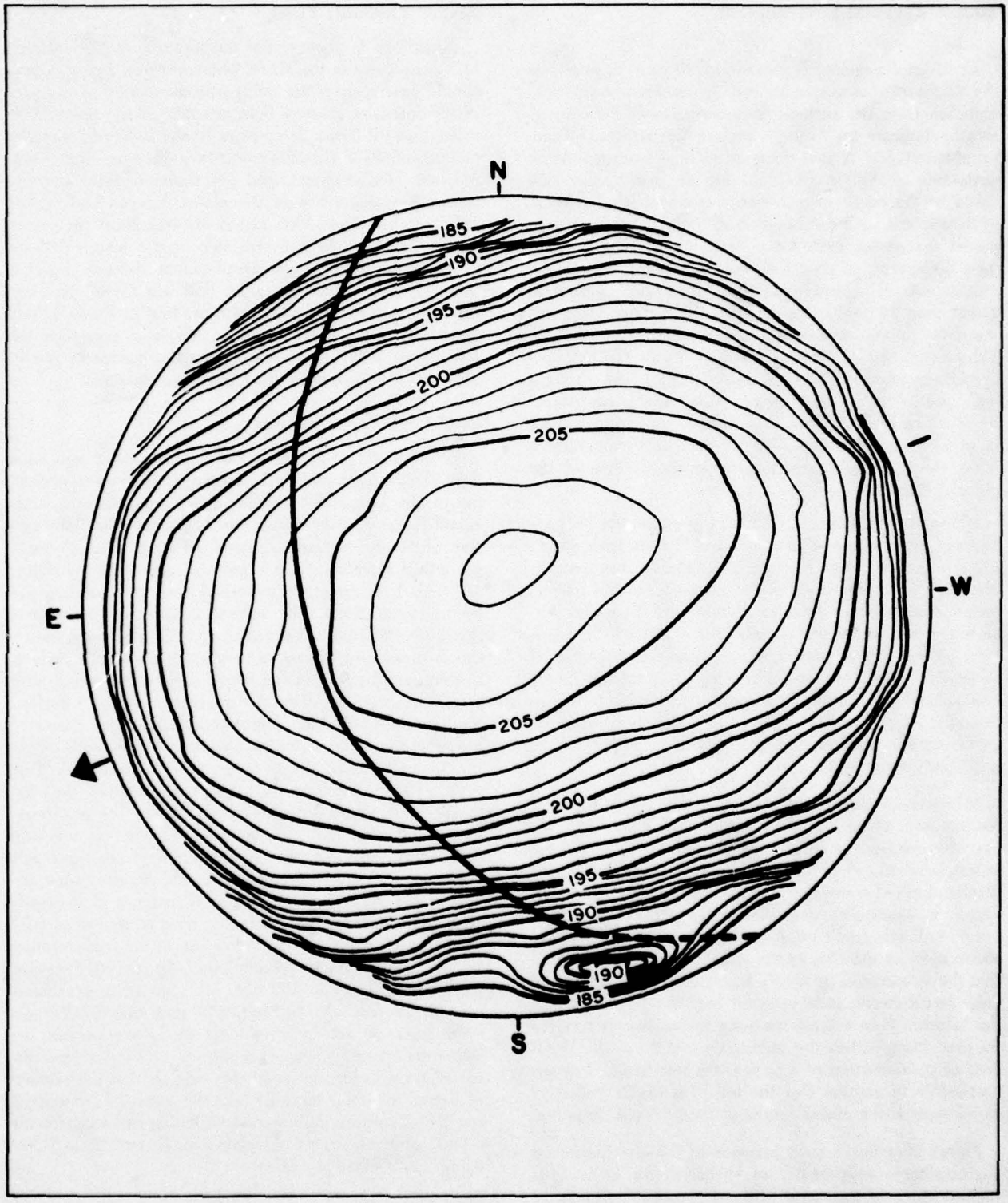


Fig. 20-3. Brightness temperature contour map of Venus in 8- to 14-μ region for 15 December 1962, 1334 to 1422 UT. The heavy black line shows the terminator; the arrow indicates the projected direction to the sun. Brightness temperatures shown are systematically too low (between 7 and 28°K) because of uncertain telescope transmission losses. (From B. C. Murray, R. L. Wildey, and J. A. Westphal, *Science*, v. 140, no. 3665, p. 391, 1963.)

20.2.6 Tabular Data for Venus

Radius [De Vaucouleurs and Menzel, 1960]:
Of solid globe, 6089 ± 6 km
At top of cloud level, 6100 ± 4 km
8.41 sec of arc at 1 AU
0.955 Earth radii
Mass (American Ephemeris): 4.86×10^{27} g
Sun/Venus, 408,000
Venus/Earth,
0.813 ± 0.01
Density [Shaw and Bobrovnikoff*]: 5.5 g cm^{-3}
Gravity [Shaw and Bobrovnikoff*]:
0.86 Earth gravity
874.3 cm sec^{-2}
Escape velocity at equator: 11.9 km sec^{-1}
Orbit [Shaw and Bobrovnikoff*]:
Mean distance to Sun, 108.1×10^6 km
Maximum distance to Sun, 109.4×10^6 km
Minimum distance to Sun, 106.5×10^6 km
Eccentricity of orbit, 0.007
Inclination of orbit to plane of ecliptic, 3° 24′
Minimum distance to Earth (inferior conjunction), 42×10^6 km
Maximum distance to Earth (superior conjunction), 257×10^6 km
Sidereal period, 225 day
Rotation period: 240 Earth days retrograde
[Goldstein and Carpenter, 1963]
Oblateness: None observed
Obliquity of equator to the plane of the orbit [Richardson, 1955]: Between 14° and 34° (speculative)
Magnitudes [Harris, 1961]: U — B, 0.50
B — V, 0.82
V (1, 0), −4.29
Color difference, Venus minus Sun [Harris, 1961]:
U, 0.55
B, 0.19
V, 0.00

*Unpublished data

20.3 MARS *

Figure 20-4 shows variation of brightness of Mars with rotational period. The variation of V (1, 0) and B — V shows a change in the blue and ultraviolet region considerably less than in the visual or red. The Martian atmosphere is nearly opaque to ultraviolet and blue light, where the disk of the planet shows little contrast with rotational phase. The atmosphere is more transparent at longer wavelengths and the contrast of the surface shows the rotational variation more clearly.

20.3.1 Atmospheric Composition

Only two molecules have been positively identified in the atmosphere of Mars, CO_2 and H_2O. The amount of CO_2 estimated from the 1.6-μ absorption band was twice that present in the terrestrial atmosphere. However, a detailed analysis [Grandjean and Goody, 1955], which takes into account the pressure broadening of the spectral lines and the overlapping of the CO_2 bands in the Martian and terrestrial atmospheres, gives the fraction of CO_2 by volume in the Martian atmosphere as $f = (160 \pm 50)/P^2$, where P is the total surface pressure in mb. If the surface pressure is 85 mb, as polarimetric and photometric evidence indicates, then there is about 2.2% CO_2 by volume (3100 atm-cm) or about 14 times more CO_2 on Mars than on Earth. However, if the surface pressure is 25 mb as indicated by recent spectroscopic measurements, then there is about 26% CO_2 by volume (36,000 atm-cm) or about 160 times more CO_2 on Mars than on Earth.

Preliminary examination of measurements of weak water vapor lines in the near-infrared spectrum indicates that the Martian H_2O abundance is probably near 5 to 10 μ of precipitable water vapor (5×10^{-4} to 1×10^{-3} g cm^{-2}) over the poles [Spinrad et al, 1963]. This value is in good agreement with theoretical estimates based on the seasonal transfer of water from one polar cap to the other. Derivation of the water vapor pressure above the sublimating edge of the polar cap can be made if the temperature of the cap boundary is known. By using theoretical estimates of this temperature, water vapor abundances in excess of 10^{-3} g cm^{-2} are estimated. If the difference between theoretical and observed surface temprature is interpreted to be the result of the carbon dioxide-water vapor greenhouse effect, and if atmospheric circulation is neglected, values of water vapor between 1×10^{-3} and 2×10^{-2} g cm^{-2} are derived [Sagan, 1961b].

It has been customary to assume, by terrestrial analogy, that the remaining 98% of the atmosphere is largely composed of N_2 with only trace amounts of radiogenic argon. Unfortunately, neither has spectral features in either the visible or infrared and so must be investigated in the ultraviolet region that is absorbed by the earth's atmosphere. An unambiguous determination of these constituents of the atmosphere of Mars is yet to be performed.

A completely nonterrestrial atmosphere on Mars composed by nitrogen peroxide (NO_2 and N_2O_4) was postulated; for example, the striking decline in spectral intensity from 5700 to 4500 Å relative to that of the moon, closely resembles curves for absorption of NO_2 and N_2O_4. Subsequent evidence [Sinton, 1961], however, gives the upper limit of NO_2 and N_2O_4 at 2.2 mm-atm; this value is used here. Table 20-1 summarizes the possible composition of the Martian atmosphere; spectroscopic upper limits were determined for O_2, O_3, N_2O, CH_4, C_2H_4, C_2H_6, NH_3, and CO, see Kuiper [1952] and Sinton [1959].

20.3.2 Atmospheric Structure

The surface pressure of Mars, derived polarimetrically by Dollfus [1957], is between 80 and 90 mb, assuming that the Martian atmosphere has the same scattering coefficient as the terrestrial atmosphere, and that Rayleigh scattering dominates. This value is in good agreement with the value derived photometrically. However, a recent

* Note. The results of Mariner IV measurements near Mars contradict the theoretical estimates of composition and surface pressure of the Martian atmosphere given in this chapter. For preliminary results of Mariner IV observations, see Science, Volume 149, pp 1226-1248, 10 September 1965.

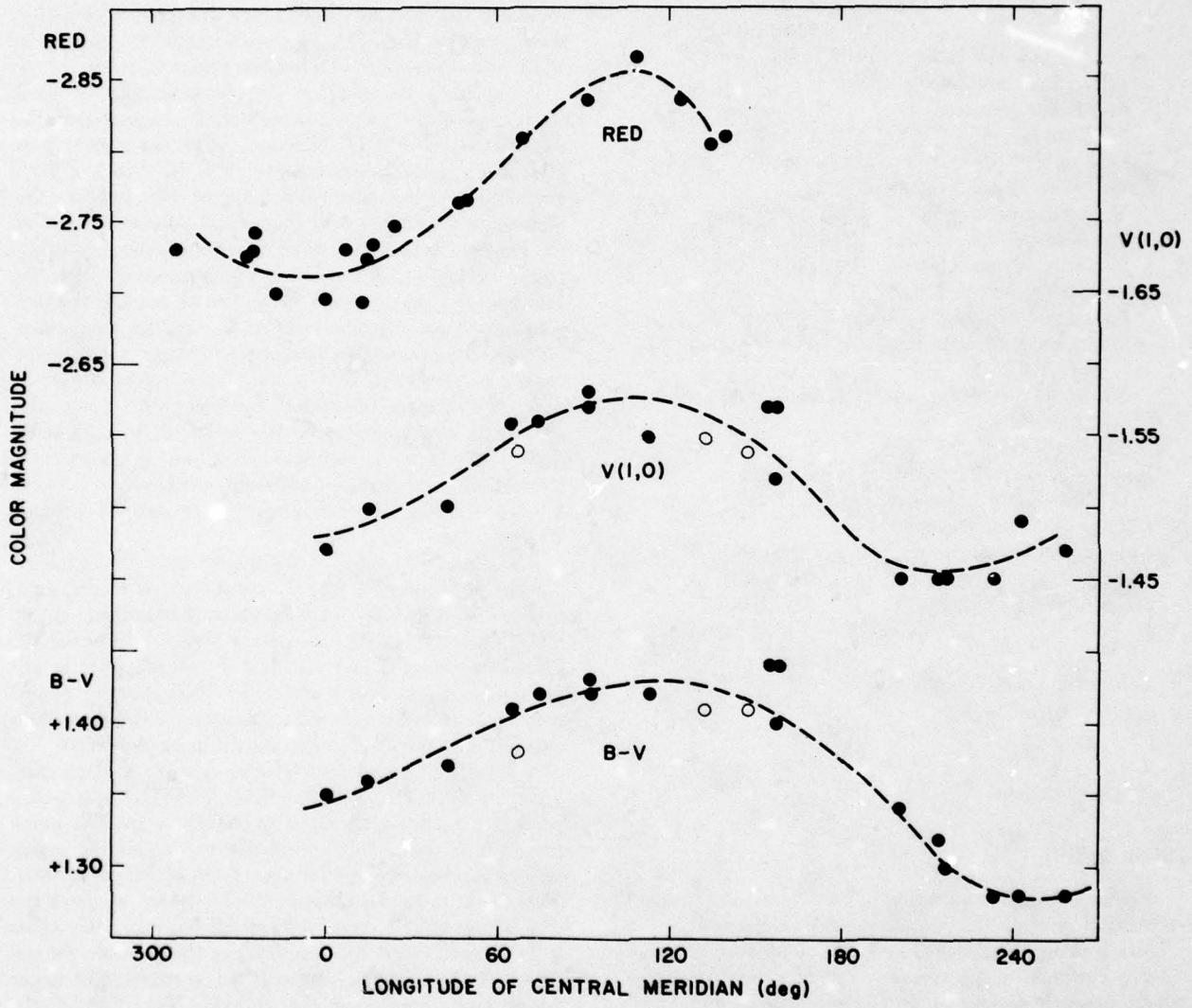


Fig. 20-4. Variation in color magnitude of Mars with rotational phase angle; the red curve shows the difference in red magnitude between Mars and the star β Geminorum. (From Harris [1961] by permission.)

spectrographic determination of surface pressure [Kaplan, Munch and Spinrad, 1964] indicates a surface pressure of 25 ± 15 mb. If correct, this would have a profound effect on re-entry vehicle design, and, as has already been pointed out, on the composition of the atmosphere.

Very little is known concerning the structure of the Martian atmosphere. The variation in pressure is determined by methods that assume a surface air temperature and convective equilibrium such that an adiabatic lapse rate for the temperature gradient applies immediately above the surface. By a radiative equilibrium argument, the temperature of the tropopause is derived; the adiabatic lapse rate breaks off and, at greater altitudes, an isothermal stratosphere prevails and extends to the region where photodissociation occurs and the thermosphere begins. Figure 20-5 shows two estimates of the temperature profile. The difference in these profiles lies primarily in the fact that Goody assumed a surface temperature of 270°K and Ohring used a more realistic value of 230°K. In terrestrial desert regions, the air temperature a few meters above the ground near noon can be very much less than the ground temperature itself. By analogy, the maximum near-surface atmospheric temperature on Mars might be 50°K less than the maximum ground temperature.

Figure 20-6 is an extension of the Goody model of the lower atmosphere through the mesosphere and thermosphere. Because of the lack of ozone in the Martian atmosphere, a temperature maximum (mesopeak) does not occur. A temperature minimum of 76°K occurs at 128 km and indicates the level of the mesopause. Below this, at 114 km, vibrational relaxation begins; between 114 km and 128 km CO_2 becomes photodissociated, leading to strong cooling and convection at the mesopause, and a conductive heat flux from the thermosphere neutralizes the radiative cooling, causing the thermosphere to stabilize its temperature to 1100°K at 1500 km. Chamberlain completes his model with a few highly tentative estimates of ionospheric levels. Assuming the presence of O_2 in the mesopause, he predicts an E_1 region through photoionization of O_2 at that level, an E_2 region at 200 km (in the thermosphere), and an F_1 region about 320 km. If an F_2 region occurs, it would appear at 700 km. Yanow [1961] suggests the existence of a fairly dense, multilayered, high-altitude ionosphere about Mars between 200 and 650 km. His electron density versus altitude results are sensitive to the surface temperatures selected, and by using a somewhat lower temperature than 273°K, his altitudes and densities may be lowered into good agreement with Chamberlain's estimates.

Table 20-1. Estimated composition of the Martian atmosphere.

Gas	Concentration (atm-cm)	Volume (%)
N_2	165,000	93
Ar	7,000	4 to 5
CO_2	3,100	1 to 2
H_2O	5 to 10 μ*	
O_2	< 250	
O_3	< 0.05	
N_2O	< 200	
CH_4	< 10	
C_2H_4	< 2	
C_2H_6	< 1	
NH_3	< 2	
NO_2 and N_2O_4	< 0.22	
CO	< 10	

* Microns of precipitable water vapor

20.3.3 Atmospheric Circulation

The circulation on Mars is different from that on Earth; changes in circulation take place on Mars which cannot take place on Earth because of the water vapor in our atmosphere and the liquid in our oceans. Figure 20-7 is a schematic map of a suggested atmospheric circulation of Mars during winter, prepared by combining the surface temperature distribution and some 18 wind directions obtained from the drift of clouds. Figure 20-8 shows a postulated generally stable symmetric regime in early fall and late spring. Figure 20-9 illustrates the proposed change to a wave regime in winter. In summer, Mintz postulates a reversal in the temperature gradient which sets up a reversed symmetric circulation. In the symmetric regime the atmosphere is heated near the equator and ascends, moves toward the poles, descends and returns

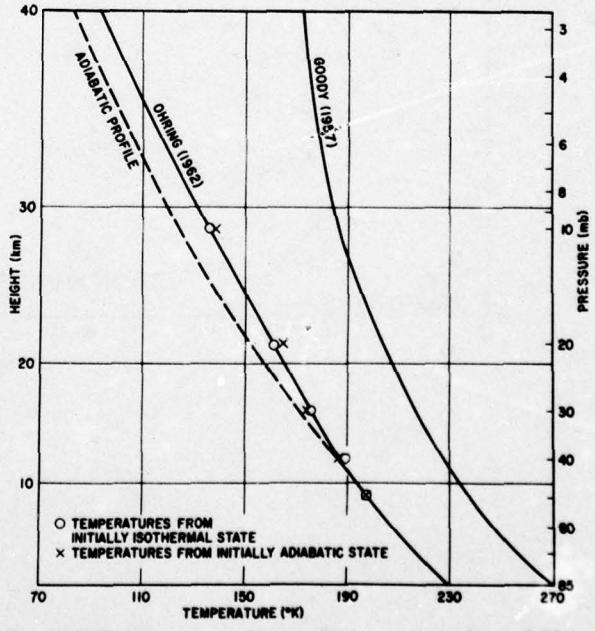


Fig. 20-5. Temperature profiles in the lower atmosphere of Mars, assuming an atmosphere of 98% N_2 and 2% CO_2. (From G. Ohring, *Icarus*, v. 1, p. 328, 1963.)

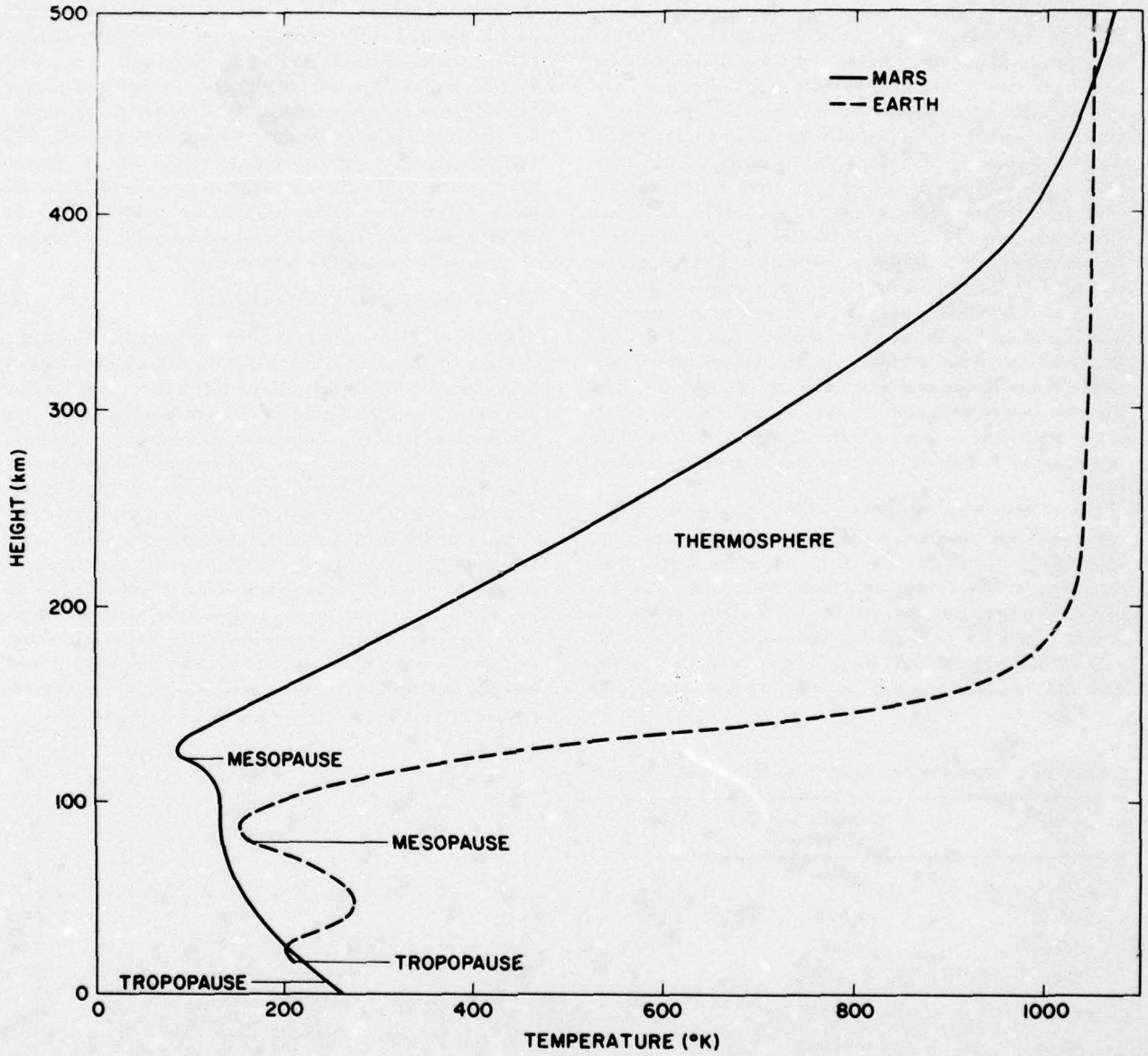


Fig. 20-6. Mars model atmosphere. (From J. W. Chamberlain, *Astrophys. J.*, v. 136, p. 582, 1962, by permission.)

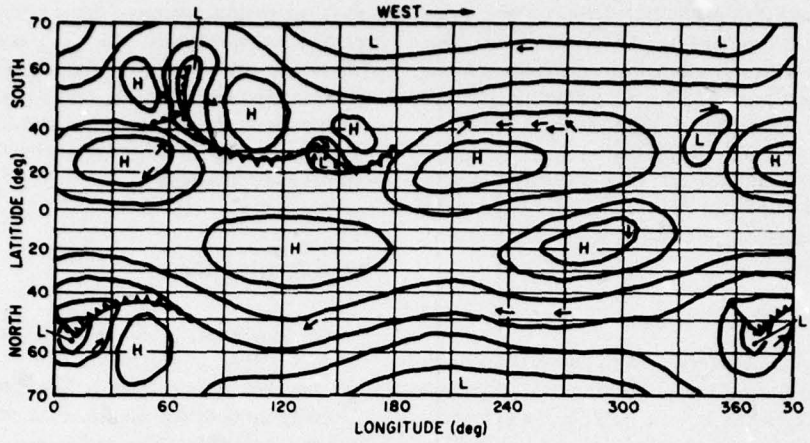


Fig. 20-7. Schematic streamline map of atmospheric circulation of Mars; winter in the northern hemisphere. Arrows represent observed cloud-drift directions; L and H denote low and high pressures, respectively. (From S. L. Hess, *J. Meteorol.*, v. 7, no. 1, p. 1, 1950, by permission.)

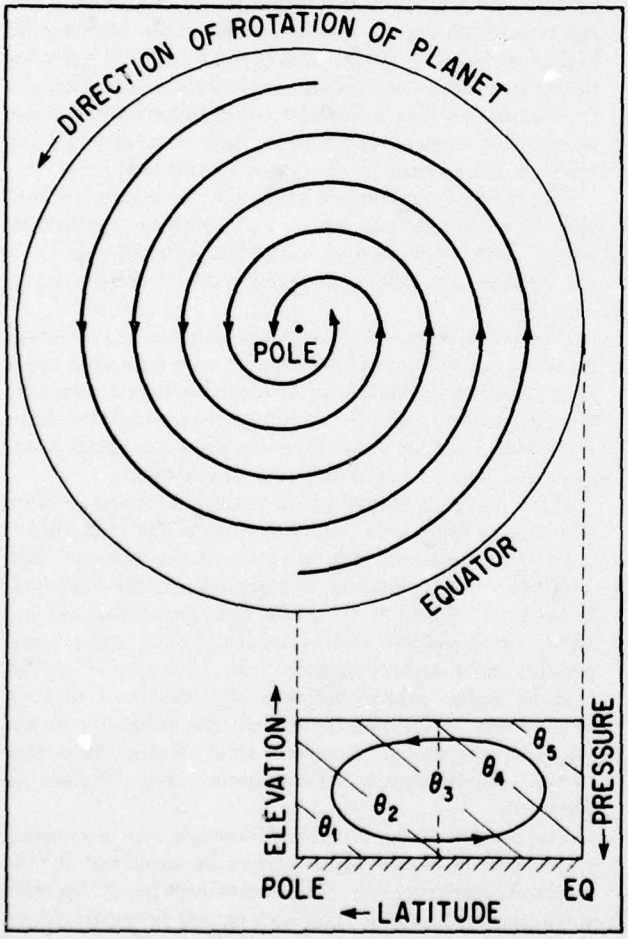


Fig. 20-8. Symmetric regime of general circulation of Mars in early fall and late spring. Upper diagram shows streamlines of the flow at the upper levels; lower diagram is a cross section showing the meridional projectional of the circulation and isotherms of potential temperature θ. (From Y. Mintz in Appendix B [Kellog and Sagan, 1961].)

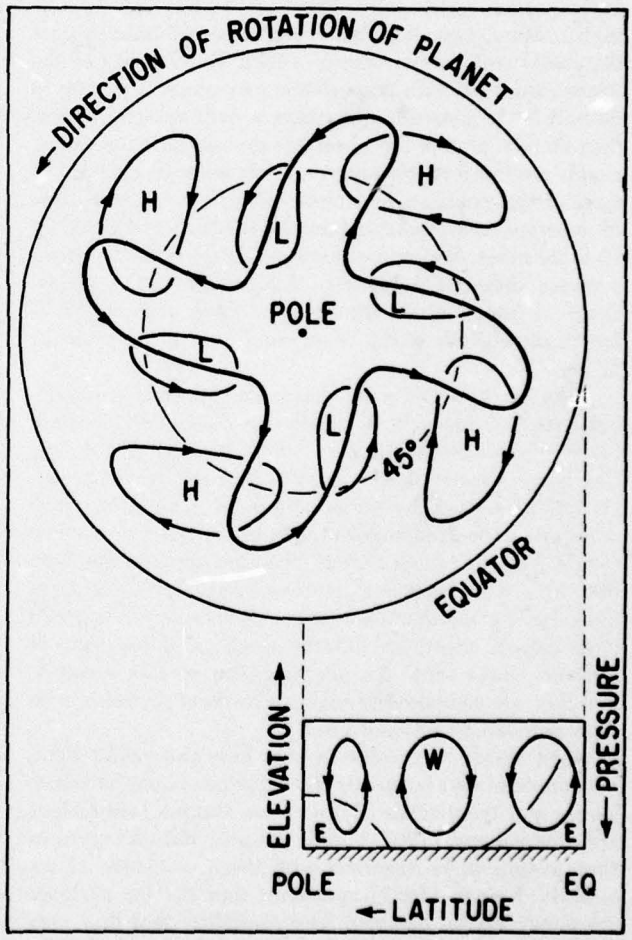


Fig. 20-9. Wave regime of general circulation of Mars in winter. Upper sketch shows streamlines of the flow at the middle and upper levels (heavy line) and near the ground (thin line); L is low and H is high pressure. Lower sketch is a cross section showing the zonally-averaged meridional circulation and the zonally-averaged zonal wind; W is westerly and E is easterly wind. (From Y. Mintz in Appendix B [Kellog and Sagan, 1961].)

to the equator. Because the globe is rotating, there is an atmospheric velocity component in the direction of rotation which increases with altitude within the troposphere. In the wave regime, large amplitude horizontal waves exist in the upper troposphere accompanied by large horizontal eddies near the surface. The tongues of warm fluid move toward the equator at other latitudes to produce a net poleward transport of heat. These large-scale disturbances are the familiar migrating highs and lows of the daily weather map.

20.3.4 Yellow and White Clouds

The yellow clouds appear visually to be yellowish or yellowish white. They are best photographed in yellow light and are almost invisible in blue light. Some are quite small, some almost transparent, while others are major formations covering large areas and obliterating all surface detail. The large formations are rare; examples were recorded in 1924, 1944, and 1956. The smaller, more frequent formations usually disappear within one or two nights, but occasionally move hundreds of miles across the planet and last for several weeks. The velocity of the winds associated with these clouds may reach values up to 60 mile h^{-1}; generally, they have a drift velocity of less than 20 mile h^{-1}. A few observers thought that the yellow clouds are low-level phenomena a few miles in height, but most of the examples best observed and most susceptible of accurate measurements have been found at heights of 18 to 20 miles. Sinton and Strong [1960] indicate a temperature differential between the ground and a yellow cloud of about 40°C. Assuming a lapse rate of 3.5°C km^{-1}, the altitude of the cloud would be on the order of 11 km.

Although there is some disagreement, it is generally believed that the yellow clouds are composed of windblown dust particles. Slipher [1962] believes that yellow clouds are sometimes composed of dust and water, a conclusion supported by observations of temporary dark areas often observed adjacent to many of the dense yellow clouds. The very small amount of water vapor in the Martian atmosphere makes a hydrous origin for these areas unlikely. The polarization curve of an opaque yellow cloud most closely resembles tobacco smoke and not that of ordinary earth dust. An interpretation of this result is that they are composed of highly absorbent particles, with diameters falling between 2 to 5 μ.

White clouds are visible in both blue and yellow light, but cannot always be clearly distinguished from the yellow clouds and the patches of blue haze. Dollfus (see Kuiper and Middlehurst [1961]) finds the polarization curves of these clouds to be identical with those of clouds of ice crystals. Kuiper [1952] concludes that the ice particles are about 1 μ in diameter. The possibility that they may be CO_2 crystals cannot definitely be ruled out, because the temperature of the Martian upper atmosphere is not known; it might be less than 140°K, at which the CO_2 would begin to condense. The white clouds are frequently observed as thick, white shrouds over the winter pole lasting for several months. In the midlatitudes, they last for days or weeks, change shape irregularly, and at times extend conspicuously over the terminator. Thin, white mists are often detected polarimetrically both as extensions of the thick clouds and as mists of brief duration occurring with sudden temperature drops. Thus, mists formed during the night appear on the sunrise limb, but are quickly dissipated.

20.3.5 Blue Haze

The blue haze, or clouds, is a diffuse and variable phenomenon that obscures surface features at wavelengths shorter than about 4500 Å. The blue haze, while usually covering most of the planet, does clear on occasion, allowing the surface features to be seen in blue light; this phenomenon is called the *blue clearing*. It should be emphasized that the haze is not itself blue; because it extinguishes the blue wavelengths, it probably would appear reddish. Mars is much less bright in the blue than in the red wavelength region. Our knowledge of the blue haze is highly speculative at the present time; several explanations exist, but no completely satisfactory explanation has been advanced. The information that follows summarizes an excellent treatment of the blue haze in a report by the Space Science Board [Kellogg and Sagan, 1961].

The standard explanation of the blue haze is that it consists of a high-altitude layer in the Martian atmosphere which causes extinction of solar blue light reflected from the surface, but which is transparent at longer wavelengths.

When the effects of observational selection are removed, there is a correlation of blue clearing with favorable opposition. Cases are also known of blue clearings at unfavorable oppositions, of blue clearings several months from opposition, and of local blue clearings on small topographical scales down to the limit of resolution.

It is a common observation that the blue image of Mars increases in brightness from the center of the limb toward the disk. An optically thin absorbing layer will give limb darkening instead of limb brightening, so the blue haze is not produced solely by a thin homogeneous absorbing layer. Condensation and crystallization of water (and possibly even carbon dioxide) can be expected on the twilight limbs; this would certainly contribute to limb brightening. If the blue haze were due primarily to absorption, regions of increased local density (the blue clouds) should appear darker, rather than brighter as observed.

The opacity of the blue haze increases with decreasing wavelength at a rate which cannot be explained by the Rayleigh scattering law. The increased size of the disk when observed in blue light also cannot be explained by Rayleigh scattering alone. Spectra of the blue haze give some evidence that absorption features exist at 4015, 4250, 4495, and 4695 Å. The absorption must occur either in the blue haze itself or in the overlying atmosphere. The presence of these features suggests that there is an absorption component to the blue haze extinction.

Polarization measurements were interpreted as indicating that the blue haze is composed of ice particles with diameter of the order of 0.3 μ. The extinction in the blue is explained by strong forward scattering of blue light by such particles, so that little light is reflected and the haze is dark in the blue. At longer wavelengths the haze is transparent. However, a completely forward scattering layer cannot account for the blue haze, because light scattered forward to the planetary surface will be reflected back by the surface and then forward scattered by the layer out of the atmosphere; a purely forward-scattering layer above a reflecting surface is transparent. If it is assumed that the blue haze is composed of small particles which, although predominantly forward-scattering in the blue, do have a small back-scattering lobe, then most of the incident solar light is transmitted to the surface but a small fraction is scattered back to space. The critical point here is that blue light is reflected from the surface with a very low albedo, about 0.05. Therefore, if more than 5% of the incident solar radiation in the blue region is initially back-scattered, the light reflected back from the Martian surface in the blue region will be swamped by even this small percentage of back-scattered solar radiation in the blue, and the surface features will be obscured. Another viewpoint is that if the layer is assumed to consist of both Rayleigh and Mie scattering particles, the extinction in the blue can be explained by Mie theory for particles larger than the wavelength of light.

The suggestion was made that the blue haze might be caused by solar protons striking the upper Martian atmosphere and producing such ions as CO_2^+, CO^+, and N_2^+, all of which absorb in the blue and violet, and that the correlation of blue clearing with favorable oppositions might conceivably be explained by the deflection of solar protons by the earth's magnetic field. Objections to this hypothesis are that high energies, high fluxes, and impossibly low interplanetary magnetic field strengths are required.

Two remaining explanations are that the clearing is either a gravitational settling of suspended particles or a phase change of a condensable or sublimable substance. For suspended particles to settle out at the rate usually observed, the minimum particle size would be about 10 μ. If the blue haze is due to forward scattering particles, then this size is too large. However, if it is due to a combination of absorption and scattering, particles of 10 μ are not excluded; they would scatter equally well at all visible wavelengths and would have to be responsible for the absorption in the blue. Actually, clearing has occurred in periods of a few hours, and for such rapid settling, the sizes would have to be increased beyond 10 μ. For a substance which changes its absorptive properties with phase, similar difficulties ensue. The substance would have to be ordinarily quite close to the temperature at which phase change occurs, so that small temperature variations could have large consequences. For a blue clearing to occur over the entire Martian disk, the absorbing substance must be sitting poised near the phase change temperature at all points on Mars. Then the temperature change must occur uniformly at all latitudes, multiplying the improbabilities.

20.3.6 Magnetic Field

The similarity in the densities of the terrestrial planets lead to the general belief that the interior of all terrestrial planets is similar to that of Earth; for a detailed discussion of the internal constitution, see MacDonald [1962]. Theoretically, Mars is supposed to possess a small iron core. If this is the case, the planet may also possess a small magnetic field. It is assumed to be present but small. There is no observational evidence for or against a magnetic field.

20.3.7 Surface Temperatures and Features

From radiometric measurement of the maximum surface temperature of Mars at a favorable opposition, the maximum temperature for a desert area near the equator appears to be close to 25°C; for a dark area it is about 8°C hotter. These temperatures are surface temperatures and are certainly higher than the air temperature near the ground. The minimum surface temperature is uncertain, but for a bright area on the equator at perihelion it is probably near −70°C. Averaged over the entire disk, the mean measured temperature is about −13°C, which is very close to the predicted greysphere temperature of −20°C.

Figure 20-10 illustrates the lag of the Martian daily temperature maximum behind the curve of incoming solar radiation. The lag appears to be between 1 and 1.5 h (a shorter lag of about 0.5 h has been suggested). Figures 20-11, 20-12, and 20-13 show the variation in temperature over the Martian surface at different seasons of the year; the isotherms appear to generally conform to the outline of the dark areas.

The white polar caps are generally the most conspicuous feature of the planet, either visually or photographically. The caps grow and shrink annually in the manner expected from the inclination of the axis and consequent seasonal changes in temperature. They can extend as far as 55° latitude (northern cap) and 42° latitude (southern cap) at maximum extension. Usually most of the polar cap evaporates during the summer. Because of the eccentricity of the orbit, however, the northern cap does not vary in size as much as the southern and rarely vanishes completely.

The infrared spectrum and the polarization of the polar caps are similar to that of H_2O frost at low temperature. The thickness of the polar caps is subject to some speculation. Because of their swift disappearance with the approach of summer, and because of the low water-vapor content of the Martian atmosphere, the caps must be very thin. Estimates of their thickness range from a maximum thickness of about 1 mm to a few millimeters.

The retreat of the south polar cap is marked by the appearance, first, of an irregular outline and, second, of a detached area of frost. The persistent area (called Mountains of Mitchell) is generally assumed to have a

higher elevation than the surrounding terrain. It is more likely, however, that a protective southerly slope, rather than simply higher elevation, permits the frost to linger at this spot. This interpretation is supported by photometric measurements which indicate that the Martian surface can be only slightly rolling, and by the low density gradient and lapse rate of the Martian atmosphere. Associated with the retreat of the polar cap is a dark irregular band, or rim, surrounding the cap. Kuiper points out that it cannot be liquid water because of the low surface temperatures near the poles, and suggests that the color is not unlike that of black lichens found in northern countries.

The dark markings of Mars are largely confined to the southern hemisphere, although a few isolated dark areas occur in the northern hemisphere. There is some disagreement concerning their color. They appear to be various shades of green in the telescope, but this is at least partially a result of the contrast between the dark areas and adjacent bright orange areas. Some apparent coloration may also be an effect of atmospheric scattering. The dark markings are probably very close to grey in color. Seasonal changes of the dark markings occur. In the Martian spring, a wave of darkening spreads toward the equator from the poles. The wave of darkening moves at an average speed of about 2 mile h^{-1} and is thought to be an effect of moisture carried by the atmosphere. During the summer, the markings remain dark, then fade again in the winter.

Weak absorption bands found in the infrared spectra of the dark markings indicate the presence of organic molecules. This observation is often used to support the hypothesis of life on Mars; however, the existence of organic molecules does not necessarily assure the presence of life on the planet. Öpik pointed out that, unless the dark markings possess some form of rejuvenation, the surface dust storms should long ago have obscured them. Kuiper suggested that the dark areas may be smooth lava fields, and postulates that they are swept free by winds. McLaughlin proposed that the markings are downwind areas of deposition of ash from Martian volcanoes. The seasonal changes of the dark markings, their spectral indications of the presence of organic molecules, and the apparent rejuvenation of these markings all indicate that the vegetation theory is probably the correct explanation of their origin.

One type of dark marking, the canals, has been the subject of a great deal of speculation. The limited resolution of terrestrial telescopes does not permit the eye to distinguish between an illusion created by the chance arrangement of discontinuous markings and continuous curves. The canals are undoubtedly real in the sense that markings exist, but it is not possible to draw any conclusions about their nature.

The bright areas of Mars are a reddish orange color, which does not change with the seasons. The polarization measurements indicate that these areas are covered with a fine powder composed of discrete opaque particles, similar in polarization properties to powdered limonite. On the other hand, a brownish fine-grained felsite closely matches the Mars reflectivity spectra. Insufficient information is available to draw any firm conclusion concerning the composition of the Martian surface materials.

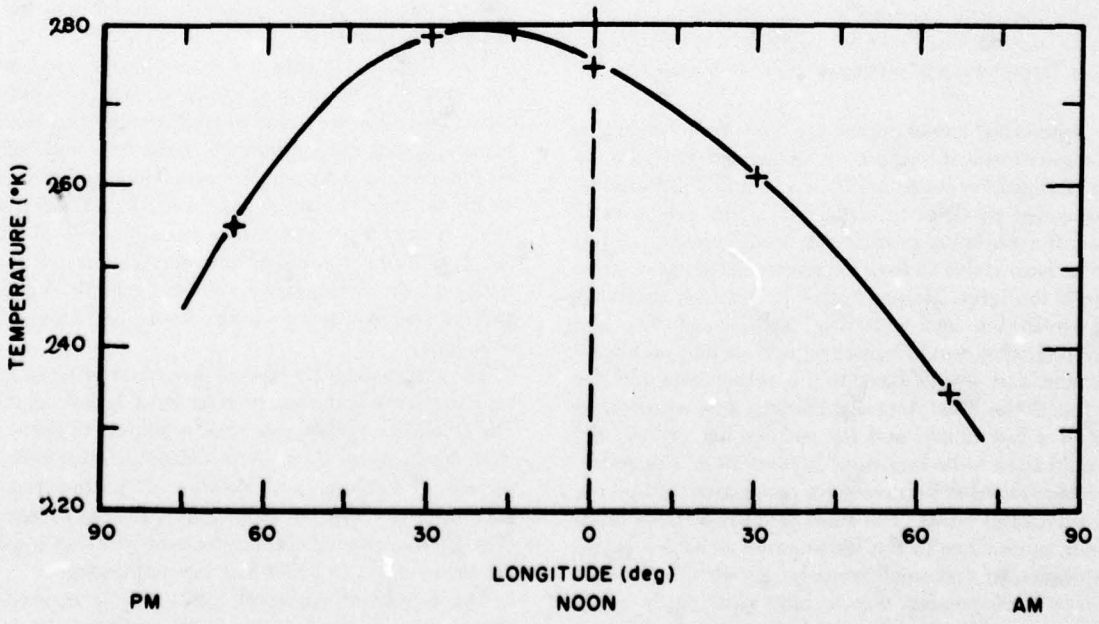


Fig. 20-10. Average diurnal temperature variation near the Martian equator. The number of individual observations average for each point is indicated. (From F. Gifford, Jr., [1956] by permission.)

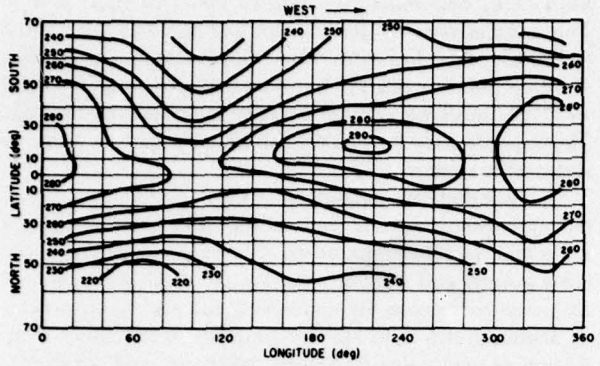


Fig. 20-11. Average Martian isotherms in °K; summer in the southern hemisphere. (From F. Gifford, Jr., [1956] by permission.)

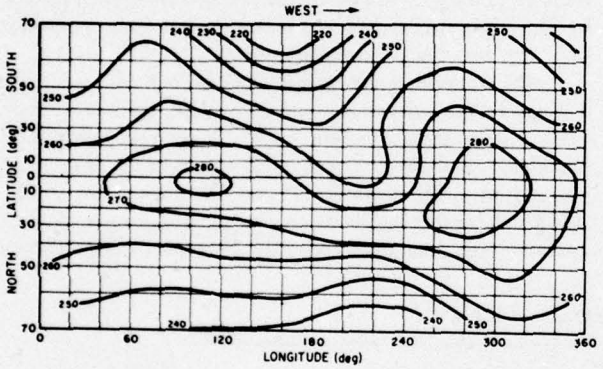


Fig. 20-12. Average Martian isotherms in °K; fall in the southern hemisphere. (From F. Gifford, Jr., [1956] by permission.)

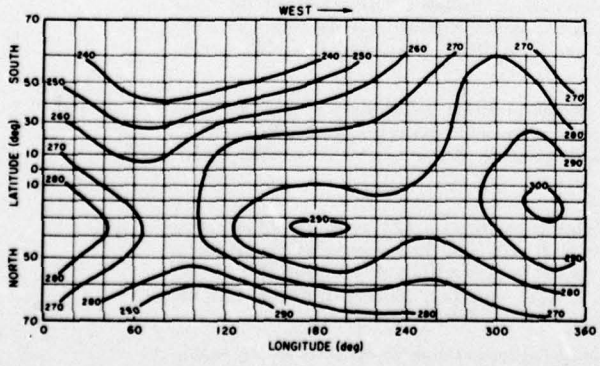


Fig. 20-13. Average Martian isotherms in °K; winter in the southern hemisphere. (From F. Gifford, Jr., [1956] by permission.)

20.3.8 Satellites

Very little is known about the two small satellites of Mars, Phobos and Deimos, because of their small size. The sizes are only roughly estimated from their brightness and by assuming reasonable values for their albedo. Their B — V color is 0.6 magnitude. Phobos completes a sidereal revolution in less than one-third the period of the planet's rotation. No other identified satellite in the solar system revolves in a shorter interval than the rotation period of its primary. Table 20-3 presents the known facts concerning these satellites.

20.3.9 Tabular Data for Mars

Radius (American Ephemeris): 3332 km
0.523 Earth radii
4.68 sec of arc at 1 AU

Mass (American Ephemeris): 0.6406×10^{27} g
Sun/Mars, 3,093,500
Mars/Earth, 0.107

Density: 4.12 g cm^{-3}

Gravity: Mars/Earth, 0.39

Escape velocity at equator: 5.1 km sec^{-1}

Rotation period (American Ephemeris): $24^h\ 37^m\ 22.^s65$
1.03 Earth days

Sidereal period [Kirby, 1960]: 1.88082 yr
686.980 day

Mean distance from Sun: 227.9×10^6 km (American Ephemeris)
1.52369 AU

Perihelion distance: 1.38143 AU
206.7×10^6 km

Aphelion distance: 1.665954 AU
249.2×10^6 km

Inclination of orbit to ecliptic: 1.8499° (American Ephemeris)

Eccentricity of orbit: 0.0934 (American Ephemeris)

Mean orbital velocity [Kirby, 1960]: 24.13 km sec^{-1}

Magnitudes [Harris, 1961]:

U — B,	0.58	V(1, 0),	−1.52
B — V,	1.36	V_o,	−2.01
V — R,	1.12	R — I,	0.38

Color difference, Mars minus Sun [Harris, 1961]:

U,	−1.17	R,	−0.67
B,	+0.71	I,	−0.76
V,	0.00		

20.4 JUPITER

Jupiter is the largest planet in the solar system and is more massive than all the other planets combined. It is brighter than other planets except Venus and occasionally Mars (when at perihelic opposition) and revolves in a period of nearly 12 yr at more than 5 times the Earth's distance from the Sun. Jupiter exhibits a variety of changing detail and color in its cloudy atmosphere.

Vsekhsvyatskii [1962] proposed that the dark equatorial belt of Jupiter can be interpreted as the shadow of a tenuous ring of meteoritic or cometary matter. This dust ring is not visible, but the movements of the equatorial

belt with changing solar position are appropriate to the shadow interpretation. Zotkin [1962], however, points out that the drawings of the equatorial belt are too imprecise to warrant such a conclusion.

The banded structure is thought to be associated with Jupiter's very short rotation period. The bands or belts change rapidly and, on occasion, a whole belt may disappear completely. The equator is usually occupied by a bright zone called the equatorial zone. On either side of this are the north and south tropical belts (usually the most prominent), then the north and south temperate belts, and finally the north and south polar caps. Irregular cloud markings and bright and dark spots break the continuity of the bands. Some are short lived and change from day to day, while others persist for a very long time.

Especially remarkable is the *great red spot* which has been visible for at least a century. This elliptical, sometimes brick-red, spot (it has been as long as 50,000 km) drifts about like a solid floating in the near-liquid lower atmosphere. It was suggested that because Jupiter rotates so rapidly, a shallow topographical feature of the "solid planet" will be attenuated very slowly with height and manifest itself at the level of a heavy cloud at the top of the atmosphere; this hypothesis, however, is not generally accepted.

The composition of the atmosphere of Jupiter is partially revealed by spectroscopic data. The spectrum of reflected sunlight contains absorption bands of methane and ammonia, and indicates that these gases rotate slower than the visible cloud layer [Spinrad et al, 1962]. Zabriskie [1962] determined the amount of H_2 to be 5 km-atm. The radiometrically determined temperatures are about −130°C; this indicates that the methane is gaseous (boiling point −162°C) but the ammonia (melting point −78°C) must be present largely as clouds of crystals. The crystals may be colored by contact with sodium or some other element.

Star occultations indicate that the molecular weight of the atmosphere is 4.3, contributed mainly by hydrogen molecules and brought up to this value presumably by some helium and smaller abundances of the methane and ammonia molecules. By combining the optical properties of Jupiter's disk with spectroscopically determined abundances of molecular hydrogen, methane, and ammonia, the estimated composition [Öpik, 1962] of the observable atmosphere is: He, 97.2%; H_2, 2.3%; Ne, 0.39%; CH_4, 0.063%; Ar, 0.042%; and NH_3, 0.0029%. This yields a mean molecular weight of 4.02.

The strong wavelength dependence of the anomalous polarization at the poles of Jupiter (up to 8%) found by Gehrels [1962] is in good agreement with that predicted by Rayleigh scattering; scattering by gaseous molecules fully explains the polarization effects.

Radio emission from Jupiter has been measured from 5 Mcps to the microwave region and found to be much more intense than it would be if it were just a result of blackbody emission. Table 20-2 summarizes the radio observations. The hypothesis that the decametric radiation from Jupiter is caused by Jupiter occulting a discrete radio source has been recently disproved. The theory

Table 20-2. Radio observations of Jupiter.

Frequency (Mcps)	Equivalent Blackbody Temperature (°K)	Remarks
5, 10, 15, 18, 19.7, 27.6 and 85.5	——	Signal increased monotomically with decrease in frequency. (T. D. Carr et al, *Astron. J.*, v. 67, p. 572, 1962.)
178	8.6×10^4	(J. F. R. Gower, *Nature*, v. 199, p. 1273, 1963.)
610	16,000	Showed partial linear polarization. (D. Barber and G. L. Moule, *Nature*, v. 198, p. 947, 1963.)
960, 1390	—— ——	Magnetic poles are at System III longitudes of 200° and 20° and magnetic axis is inclined 9° to the rotational axis. (D. Morris and G. L. Berge, *Astrophys. J.*, v. 136, p. 276, 1962.)
1440	2190 to 3630	Indicate a degree of linear polarization of 25% to 45%. This is in good agreement with other observations. (A. C. Miller and B. L. Gary, *Astron. J.*, v. 67, p. 727, 1962.)
Wavelength		
9.4 cm	658	Found 21% linear polarization, 12° inclination of magnetic axis to rotational axis, and the positions of the magnetic poles with respect to System III were 190° and 10°. (W. K. Rose, J. M. Bologna, and R. M. Sloanaker, *Astron. J.*, v. 68, p. 78, 1963.)
8.35 mm	144	Corresponds to the temperature at the level of the visible cloud cover. (D. D. Thornton and W. J. Welch, *Icarus*, v. 2, p. 228, 1963.)

[Landovitz and Marshall, 1962] that the radiation is caused by electrons making spin-flip transitions in the Jovian magnetic field, when that field is perturbed by impinging solar particles, is adopted here.

The decametric radiation is most likely caused by synchrotron radiation from a shell of relativistic electrons in a dipole field. The partially polarized decametric radiation observed to come from Jupiter could be obtained from such electron shells, provided that a large number of electrons have relatively flat helices. Magnetic fields of the order of 0.1 to 1 gauss in the emitting region and about sixty times as much at the poles are required. The intensity of the polar magnetic field has been estimated at 7 gauss [Barrow, 1960] on the basis of observations of radio noise.

The interior of Jupiter is not known. The oblateness of the planet, however, implies that, with its swift rotation, the planet would bulge at the equator even more than it does if its mass were not highly concentrated toward its center. The low temperature and low average density (1.3) of the whole planet also require very light material in the outer parts.

20.4.1 Satellites

Table 20-3 summarizes the known characteristics of Jupiter's 12 known satellites.

20.4.2 Tabular Data for Jupiter

Equatorial radius
(American Ephemeris): 71,370 km
11.20 Earth radii
98.47 sec of arc at 1 AU
Mass (American Ephemeris): 1892.3×10^{27} g
Sun/Jupiter, 1047.35
Jupiter/Earth, 316.7
Polar radius: 66,230 km
10.39 Earth radii
91.91 sec of arc at 1 AU
Mean density: 1.33 g cm^{-3}
Surface gravity: Jupiter/Earth, 2.65
Escape velocity: 61.0 km sec^{-1}
Rotation period: 0.41 days
Mean distance to Sun: 5.203 AU
777.8×10^6 km
Sidereal period: 4332.58 mean days
11.862 tropical yr
Inclination of orbit to the ecliptic: 1.306°
Inclination of equator to orbit: 3.12°
Eccentricity of orbit: 0.0484
Magnitudes [Harris, 1961]:

U — B,	0.48	R — I,	−0.03
B — V,	0.83	V(1, 0),	−9.25
V — R,	0.50	V_o,	−2.55

Color difference, Jupiter minus Sun:

U,	0.54	R,	−0.05
B,	0.20	I,	+0.27
V,	0.00		

20.5 SATURN

Saturn ranks second to Jupiter in size, mass, and number of known satellites. It has the least mean density and the greatest oblateness of any principal planet. The short period of rotation combined with the large size and low density of Saturn causes its conspicuous oblateness. That the equatorial bulge is not even more pronounced indicates that the material of Saturn, as in the case of Jupiter, is strongly concentrated toward its center. Again it is assumed that hydrogen and helium are the main constituents.

Saturn resembles Jupiter in many respects. The atmospheric markings are arranged in bands, which are more regular but less distinct. A broad yellowish band overlies the equator, and greenish caps surround the poles. The absorption bands of ammonia in the spectrum are much weaker while those of methane are stronger than in Jupiter's spectrum. It is generally thought this is due to the lower temperature (−150°C) at the cloud levels of Saturn, which freezes out more of the ammonia gas so that the sunlight penetrates farther down through the methane of the planet's atmosphere.

The atmospheric composition estimated from spectroscopic observations is: CH_4, 35,000 atm-cm; $NH_3 < 250$ atm-cm; $O_3 < 0.1$ atm-cm; and $SO_2 < 0.01$ atm-cm. The equivalent blackbody temperature in the infrared is less than 105°K; at 3.45 cm it is 106°K and at 10 cm, 196°K.

Saturn is encircled by three concentric rings in the plane of its equator. They are generally called the outer ring, the middle (bright) ring, and the inner (crepe) ring. The diameter of the entire ring system is 273,000 km, or 2.3 times the equatorial diameter of the planet. The bright ring is 25,600 km in width and is separated from the outer ring by the 5000-km gap known as Cassini's division. The rings are extremely thin, their thickness not exceeding 15 km. The rings consist of a multitude of separate particles revolving in nearly circular orbits in the direction of planetary rotation. Infrared spectra suggest that these particles are composed of ice.

20.5.1 Satellites

Saturn has nine known satellites, the known characteristics of which are summarized in Table 20-3. Only Phoebe, the most distant satellite, revolves from east to west as does Jupiter's outer satellite. Two of Saturn's satellites are known to rotate and revolve in the same periods as indicated by their variations in brightness in the periods of their revolutions. Titan, the largest of Saturn's satellites, is remarkable for being the only satellite in the solar system known to have an atmosphere. Kuiper has recognized methane absorption bands in its spectrum, and also points out that Titan's unusual orange color is probably the result of a chemical reaction between the atmosphere and surface material. Kuiper also concludes, from their very high reflecting power (0.8) and low densities, that the inner satellites of Saturn are probably composed primarily of ice.

20.5.2 Tabular Data for Saturn

Equatorial radius
(American Ephemeris): 60,400 km
9.48 Earth radii
83.33 sec of arc at 1 AU
Mass (American Ephemeris): 566.0×10^{27} g
Sun/Saturn, 3501.6
Saturn/Earth, 94.7
Polar radius: 54,050 km
8.48 Earth radii
74.57 sec of arc at 1 AU
Mean density: 0.71 g cm^{-3}
Surface gravity: Saturn/Earth, 1.17
Escape velocity: 36.7 km sec^{-1}
Rotation period: 0.43 days
Mean distance from Sun: 1426.1×10^6 km
9.54 AU
Sidereal period: 10759.20 mean days
29.458 tropical years
Inclination of orbit to the ecliptic: 2.49°
Eccentricity of orbit: 0.0557
Magnitudes [Harris, 1961]:

U − B,	0.58	V(1,0),	−8.88
B − V,	1.04	V_o,	+0.67

Color difference, Saturn minus Sun [Harris, 1961]:

U, 0.85	B, 0.41	V, 0.00

20.6 URANUS

Uranus is unusual in that its equator is inclined nearly at right angles to the plane of the ecliptic. With the telescope it appears as a small disk on which markings are not clearly discernible. The spectrum shows dark bands of methane, as well as a broad absorption band in the near infrared that has been attributed to molecular hydrogen. From spectroscopic measurements, Kuiper [1952] estimated the following composition: CH_4, 150,000 atm-cm; $O_3 < 0.1$ atm-cm; and $SO_2 < 0.01$ atm-cm. Decametric radiation has not been detected.

20.6.1 Satellites

Uranus has five known satellites, and all revolve from west to east. Table 20-3 summarizes their known characteristics.

20.6.2 Tabular Data for Uranus

Mean radius
(American Ephemeris): 24,850 km
3.90 Earth radii
34.28 sec of arc at 1 AU
Mass (American Ephemeris): 86.66×10^{27} g
Sun/Uranus, 22.869
Uranus/Earth, 14.58
Mean density: 1.56 g cm^{-3}
Gravity: Uranus/Earth, 1.05
Escape velocity: 22.4 km sec^{-1}
Rotation period: 0.45 days
Mean distance from Sun: 2869.1×10^6 km
19.191 AU
Sidereal period: 30685.91 mean days
84.015 tropical yr
Inclination of orbit to the ecliptic: 0.773°
Inclination of equator to orbit: 98°
Eccentricity of orbit: 0.0472
Magnitudes [Harris, 1961]:

U − B,	0.28	R − I,	−0.80
B − V,	0.56	V(1,0),	−7.19
V − R,	−0.15	V_o,	+5.52

Color difference, Uranus minus Sun [Harris, 1961]:

U,	+0.07	R,	0.60
B,	−0.07	I,	+1.69
V,	0.00		

20.7 NEPTUNE

Through the telescope Neptune appears as a small greenish disk upon which a few faint markings have been seen. Spectroscopic investigations indicate that Neptune, like Uranus, has methane in its atmosphere. Kuiper estimated the amount as 250,000 atm-cm.

20.7.1 Satellites

Neptune has two known satellites; their characteristics are given in Table 20-3.

20.7.2 Tabular Data for Neptune

Mean radius
(American Ephemeris): 26,500 km
4.16 Earth radii
36.56 sec of arc at 1 AU
Mass (American Ephemeris): 10.2×10^{27} g
Sun/Neptune, 19,314
Neptune/Earth, 17.0
Mean density: 2.47 g cm^{-3}
Surface gravity: Neptune/Earth, 1.23
Escape velocity: 25.6 km sec^{-1}
Rotation period: 0.66 days
Mean distance from Sun: 4495.6×10^6 km
30.071 AU
Sidereal period: 60187.60 mean days
164.788 tropical yr
Inclination of orbit to the ecliptic: 1.744°
Inclination of equator to orbit: 29°
Eccentricity of orbit: 0.0086
Magnitudes [Harris, 1961]:

U − B,	0.21	V − R,	−0.33
B − V,	0.41	R − I,	−0.80

Color difference, Neptune minus Sun [Harris, 1961]:

U,	−0.15	R,	+0.78
B,	−0.15	I,	+1.87
V,	0.00		

20.8 PLUTO

20.8.1 General

Pluto, the latest discovered (1930) planet, is remarkable in a number of ways. Its eccentricity is the highest (0.247) of any in the solar system, causing it to be closer to the Sun at perihelion than Neptune. Because it is so small, the diameter cannot be measured directly and can only be inferred by measuring the total light reflected from the planet and assuming reasonable values for its albedo. The values that follow should be recognized as only "educated guesses."

20.8.2 Tabular Data for Pluto

Mean radius: Pluto/Earth, 0.45
3600 miles
Mass: Pluto/Earth, < 0.1 (?)
Mean density in terms of water: < 5.5 (?)
Surface gravity: Pluto/Earth, < 0.5 (?)
Escape velocity: < 5.3 km sec^{-1}
Rotation period: (?)
Mean distance to Sun: 39.457 AU
5898.9×10^6 km
Sidereal period: 90469.27 mean days
247.697 tropical yr
Inclination of orbit to the ecliptic: 17.143°
Inclination of equator to orbit: (?)
Eccentricity: 0.2485

Table 20-3. Tabular data for satellites.

Satellite	Diameter (km)	Distance from Planet (10^3 km)	Sidereal Period of Revolution (days)	Magnitude V(1,0)	Magnitude V_o	Eccentricity of Orbit	Mass (earth mass)
Mars							
Phobos	8*	9.4	0.318910	12.1	11.6	0.21	
Deimos	5*	23.5	1.262441	13.3	12.8	0.003	
Jupiter							
V	240?	182	0.4982	+6.3	13.0	0.0006 ± 0.0004	0.0121
I Io	3200	422	1.769	−1.90	4.80	0.0075 ± 0.0008	0.0079
II Europa	2900	671	3.551	−1.53	5.17	0.0796 ± 0.0013	0.0260
III Ganymede	5000	1070	7.155	−2.16	4.54	0.4218 ± 0.0005	0.0162
IV Callisto	4500	1880	16.69	−1.20	5.50		
VI	160?	11,400	250.6	+7.0	13.7		
VII	56?	11,700	260.1	+9.3	16		
X	24?	11,740	260	+11.9	18.6		
XII	22?	20,800	617	+12.1	18.8		
XI	30?	22,400	692	+11.4	18.1		
VIII	56?	23,400	735	+12.1	18.8		
IX	27?	23,500	758	+11.6	18.3		
Saturn							
I Mimas	480?	184	0.9424	+2.6	12.1		
II Enceladus	560	237	1.370	+2.22	11.77	0.004	
III Tethys	800	292	1.888	+0.72	10.27		
IV Dione	800	374	2.737	+0.89	10.44	0.002	
V Rhea	1600	523	4.518	+0.21	9.76	0.001	
VI Titan	4550	1220	15.95	−1.16	8.39	0.0287	
VII Hyperion	480?	1470	21.28	+4.61	14.16		
VIII Iapetus	1280	3530	79.33	+1.48	11.03		
IX Phoebe	320?	12,870	550.4	—	—		
Uranus							
V Miranda	?	130	1.413	3.8	16.5	$<< 0.01$	
I Ariel	960?	190	2.520	1.7	14.4	0.0028 ± 0.0005	
II Umbriel	640?	265	4.144	2.6	15.3	0.0035 ± 0.0004	
III Titania	1600?	435	8.706	1.30	14.01	0.0024 ± 0.0002	
IV Oberon	1400?	583	13.46	1.49	14.20	0.0007 ± 0.0002	
Neptune							
I Triton	3760	352	5.877	−1.16	13.55	0	
II Nereid	300	5,500	359.4	+4.0	18.7	0.75	0.0227 ± 0.0040

* After G. H. Herbig and C. E. Worley, *Astronomical Society of the Pacific, Leaflet No. 325*, 1956.

20.9 REFERENCES

Barrow, C. H., 1960, "Magnetic Field of Jupiter," *Nature*, v. 188, p. 924.

Carpenter, R. L., and R. M. Goldstein, 1963, "Radar Observations of Mercury," *Science*, v. 142, no. 3590, p. 381.

De Vaucouleurs, G., and D. H. Menzel, 1960, "The Occultation of Regulus by Venus," *Scientific Rept. No. 1, Contract AF19(604)-7461*, and *Nature*, v. 188, no. 4744, p. 28.

Dollfus, A., 1957, "Étude Des Planètes Par La Polarisation De Leur Lumière," *Ann. d'Astrophys.*, Supp. No. 4.

Gehrels, T., 1962, "The Polarization of the Sunlit Sky and Poles of Jupiter," *Astron. J.*, v. 67, p. 272.

Gifford, F., Jr., 1956, "The Surface Temperature Climate of Mars," *Astrophys. J.*, v. 123, no. 1, p. 154.

Goldstein, R. M., and R. C. Carpenter, 1963, "Rotation of Venus: Period Estimated from Radar Measurements," *Science*, v. 139, no. 3558, p. 910.

Grandjean, J., and R. M. Goody, 1955, "The Concentration of Carbon Dioxide in the Atmosphere of Mars," *Astrophys. J.*, v. 121, p. 548.

Harris, D. L., 1961, Photometry and Colorimetry of Planets and Satellites, "Planets and Satellites," G. P. Kuiper and B. M. Middlehurst, eds., University of Chicago Press.

Kaplan, L. D., G. Munch, and H. Spinard, 1964, "An Analysis of the Spectrum of Mars," *Astrophys. J.*, v. 139, p. 1.

Kellogg, W. M., and C. Sagan, eds., 1961, "The Atmospheres of Mars and Venus," *A Report by the ad hoc Panel on Planetary Atmospheres of the Space Science Board, Pub. No. 944*, National Academy of Sciences, Washington, D.C.

Kirby, D. S., 1960, "Summary of Orbital and Physical Data for the Planet Mars," *Rand Memorandum, RM-2567*.

Kuiper, G. P., and B. M. Middlehurst, eds., 1961, "Planets and Satellites, Vol. III of The Solar System," University of Chicago Press.

Kuiper, G. P., 1957, Atmosphere and Cloud Layers of Venus, "The Threshold of Space," M. Zelikoff, ed., Pergamon Press, New York.

Kuiper, G. P., ed., 1952, "The Atmosphere and the Earth and Planets," University of Chicago Press.

Landovitz, L., and L. Marshall, 1962, "Stimulated Electron Spin-flip Transition as the Source of 18 Megacycle Radiation on Jupiter," *Nature*, v. 195, p. 1186.

Lyot, B., 1929, *Ann. Obs. Meudon, Univ. Paris*, v. 8.

MacDonald, G. J. F., 1962, "On the Internal Constitution of the Inner Planets," *J. Geophys. Res.*, v. 67, p. 2945.

"Mariner II, 1963, Preliminary Reports on Measurements of Venus," *Science*, v. 139, no. 3558, p. 905.

Mintz, Y., 1962, "The Energy Budget and Atmospheric Circulation on a Synchronously Rotating Planet," *Icarus*, v. 1, no. 2, p. 172.

Muhleman, D. O., 1963, "The Electrical Characteristics of the Atmosphere and Surface of Venus from Radar Observations," *Icarus*, v. 1, no. 5-6, p. 401.

Öpik, E. J., 1962, "Jupiter: Chemical Composition, Structure and Origin of a Giant Planet," *Icarus*, v. 1, p. 200.

Öpik, E. J., 1961, "The Aeolosphere and Atmosphere of Venus," *J. Geophys. Res.*, v. 66, p. 2807.

Pettengill, G. H., et al, 1962, "A Radar Investigation of Venus," *The Astrophys. J.*, v. 67, p. 181.

Richardson, R. S., 1955, "Observations of Venus Made at Mount Wilson in the Winter of 1954-1955," *Publ. Astron. Soc. Pacific*, v. 67, p. 304.

Sagan, C., 1962, "Structure of the Lower Atmosphere of Venus," *Astron. J.*, v. 67, p. 281.

Sagan, C., 1961a, "The Planet Venus," *Science*, v. 133, p. 849.

Sagan, C., 1961b, "The Abundance of Water Vapor on Mars," *Astrophys. J.*, v. 66, p. 521.

Sinton, W. M., 1959, "Further Evidence of Vegetation on Mars," *Science*, v. 130, p. 1234.

Sinton, W. M., and J. Strong, 1960, "Radiometric Observations of Mars," *Astrophys. J.*, v. 131, p. 459.

Sinton, W. M., 1961, "An Upper Limit to the Concentration of NO_2 and N_2O_4 in the Martian Atmosphere," *Publ. Astron. Soc. Pacific*, v. 73, p. 125.

Slipher, E. C., 1962, "The Photographic Story of Mars," Sky Publishing Company and Northland Press.

Spinrad, H., G. Munch, and L. D. Kaplan, 1963, "The Detection of Water Vapor on Mars," *Astrophys. J.*, v. 137, p. 1319.

Spinrad, H., G. Munch, and L. M. Trafton, 1962, "Recent Spectroscopic Investigations of Jupiter and Saturn," *Astron. J.*, v. 67, p. 587.

Spinrad, H., 1962, "A Search for Water Vapor and Trace Constituents in the Venus Atmosphere," *Icarus*, v. 1, no. 3, p. 266.

Vsekhsvyatskii, S. K., 1962, "Possible Existence of a Ring of Comets and Meteorites Around Jupiter," *Soviet Astronomy-A. J.*, v. 6, p. 226.

Warner, B., 1960, "The Emission Spectrum of the Night Side of Venus," *Monthly Notices Royal Astron. Soc.*, v. 121, p. 279.

Yanow, G., 1961, "A Study of the Martian Upper Atmosphere and Ionosphere," *J. Astronautical Sci.*, v. 8, p. 103.

Zabriskie, F. R., 1962, "Hydrogen Content of Jupiter's Atmosphere," *Astron. J.*, v. 67, p. 168.

Zotkin, I. T., 1962, "On the Ring Encircling Jupiter," *Soviet Astronomy-A. J.*, v. 6, p. 236.

Chapter 21

ASTROPHYSICS AND OPTICAL ASTRONOMY

Shea L. Valley*

In the largest sense, our space environment is the Milky Way galaxy, which is one of the larger galaxies within the universe of galaxies. This chapter provides an outline of our current knowledge of this environment.

21.1 GENERAL SURVEY

The *Milky Way galaxy* (our Galaxy) is a rotating lenticular disk, between 25,000 and 30,000 parsecs in diameter, of stars, gas clouds, and cosmic dust. Surrounding the disk is the *galactic halo*, a sparse distribution of clusters of stars and occasional single stars in a spheroidal volume about the galactic center. Matter in the disk rotates around the galactic center somewhat as the planets around the sun; the farther from the center, the longer the period of revolution and the slower the tangential velocity. Objects in the halo do not share this motion. The sun is located about 10 kiloparsec from the galactic center, slightly north of the galactic plane. The period of revolution of the sun and its neighboring stars, which travel in almost circular orbits around the galactic center, is about 2×10^8 yr (one galactic year).

Figure 21-1 shows a spiral galaxy that is thought to resemble our Galaxy as seen in space from the direction of the galactic pole. Figure 21-2 shows another similar galaxy seen nearly edge-on. The direction of rotation of spiral galaxies is not conclusively established, but evidence is in favor of the direction that would wind up the spiral arms; that is, trailing arms.

Spectroscopic studies indicate that other galaxies are receding from us at radial velocities, v_r, directly proportional to their distance, r, from the solar system. (To visualize this expansion, imagine inflating a balloon covered with dots that represent galaxies; an observer on any dot would observe every other dot receding as the balloon expands, and the more distant the other dot, the greater its speed of recession.)

The proportionality constant, H, in the relation

$$v_r = Hr$$

is *Hubble's constant*. (Note that in Astronomy, the convention is that radial velocities are positive if receding from, and negative if approaching, the observer.) The true value of H is uncertain because of difficulties in determining distances to remote galaxies. A current estimate is 100 km sec^{-1} $megaparsec^{-1}$, or 3×10^{-18} sec^{-1}; however, values up to two or three times this have been used.

Extrapolating backward in time, the Hubble age of the universe is $1/H$; currently the value most frequently used is 13×10^9 yr. This is the basis of the Big Bang theory of the origin of the universe; it assumes a violent explosion of highly compressed matter, which subsequently dispersed and is still in a state of progressive expansion and decreasing space density. The Steady State theory assumes continuous creation of matter rather than a cataclysmic origin; the rate of creation is assumed equal to the observed rate of dispersal, so that the space density would remain constant with time.

21.2 DEFINITIONS, UNITS, AND BASIC RELATIONS

21.2.1 Time, Distance, and Motion; Solar Values as Units

Methods of measuring time are now so precise that irregularities in the period of the earth's rotation cause difficulties in using this rotation as a standard of time. The International Committee of Weights and Measures authorized an atomic definition of the second (at 1725 Paris time, 8 October 1964) based temporarily (in expectation of a more exact definition in the future) on an invariant transition of cesium 133, to which the value 9,192,631,770 hertz is assigned.

The fundamental unit of civil (or universal) time is the *mean solar second*, s_u, defined as 1/86,400 of the mean solar day. A *mean solar day*, $(86{,}400 + 0.0016T)\ s_e$, is the interval between two successive transits of the mean sun (a fictitious sun moving uniformly along the celestial equator) through the meridian. Because the earth's orbital velocity is not constant and the equatorial plane is inclined to the orbital plane, the observed sun crosses the local meridian before or after the mean sun on all but four days a year; the variation, calculated for each day, is called the equation of time. The hour angle

*This chapter is based mainly upon a condensation of extensive material provided by Gordon W. Wares.

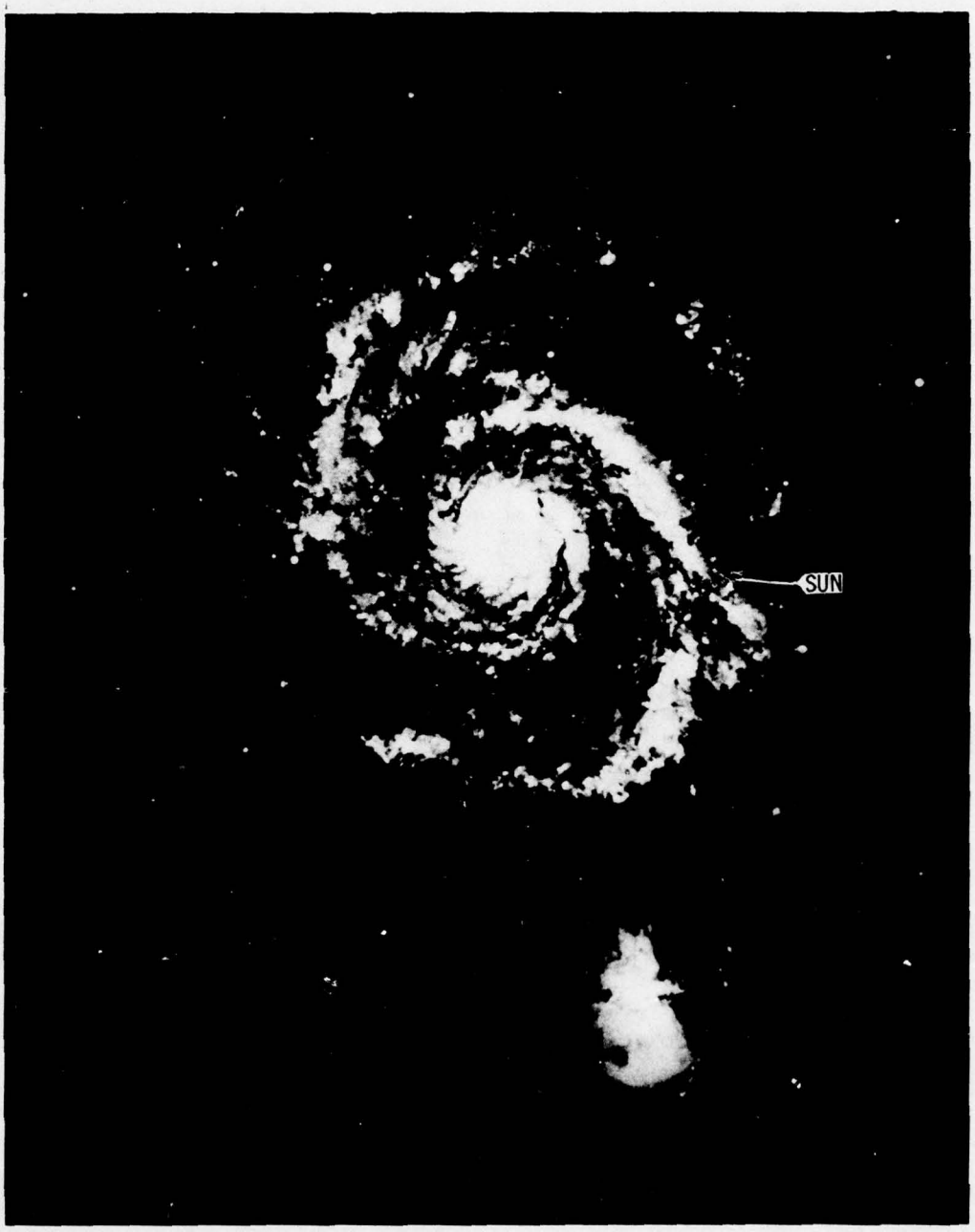


Fig. 21-1. Spiral galaxy NGC5194 (M51), the Whirlpool Nebula, resembles our Milky Way galaxy, but the spiral arms of the Milky Way are more tightly wound. The marker indicates roughly where the solar system would be. The irregular object at the bottom is NGC5195, a companion galaxy. (Mt. Palomar Observatory photograph.)

(Sec. 21.2.2.2) of the mean sun plus 12 h is mean solar time; this is called *local civil time*. Because *universal time* (UT) is defined as local civil time at the meridian of geographic longitude zero (Greenwich, England), it is also called Greenwich time.

In 1960, *ephemeris time* was adopted for the prediction of positions of astronomical bodies in the American Ephemeris and Nautical Almanac (published yearly by the U.S. Government Printing Office). The *ephemeris second*, s_e, is defined as 1/86,400 of the ephemeris day and equal to 1/31,556,925.9747 of the tropical year 1900.0; $s_u/s_e = 1 + 1.90 \times 10^{-8}$ T, where T is Julian centuries of 36,525 days from 1900 Jan 0.5 universal time. The *sidereal day* (86,164.0905 s_u) is the interval between two successive transits of the mean vernal equinox (Sec. 21.2.2) across the meridian; sidereal hours, minutes, and seconds correspond to the sidereal day ($1^d = 24^h = 1440^m = 86{,}400^s$). The sidereal second is slightly less than the ephemeris second. *Sidereal time* is the hour angle of the vernal equinox. If the true vernal equinox is used for the measurements, it is the apparent sidereal time; if the mean equinox is used, it is mean sidereal time.

Figure 21-3 is a schematic representation of three methods of defining the year. The mean solar year, called the *tropical year*, is the interval between two successive transits of the sun through the vernal equinox; it is 365.2422 mean solar days, or in ephemeris seconds, $3.15569259747 \times 10^7 - 0.530$ T. The 26,000-yr precession of the equinoxes causes the tropical year to be about a third of an hour shorter than the sidereal year. The *sidereal year* is the interval between two successive transits of the sun with respect to a "fixed" star; in ephemeris seconds this period is $3.155814998 \times 10^7 + 0.010$ T. The *anomalistic year* is the period of the earth's passage from perihelion to perihelion; in ephemeris days it is $365.25964134 + 0.00000304$ T, or nearly 2½ h longer than the tropical year (perihelion advances in the direction of the earth's orbital motion).

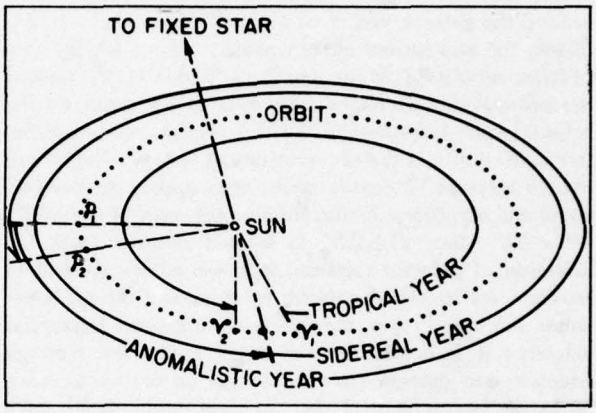


Fig. 21-3. Sketch illustrating different methods of determining periods of the earth's revolution about the sun. Differences are highly exaggerated, and for simplicity the positions of the perihelion, (p_1 and p_2) and the vernal equinox (Υ_1 and Υ_2) are not in their true locations.

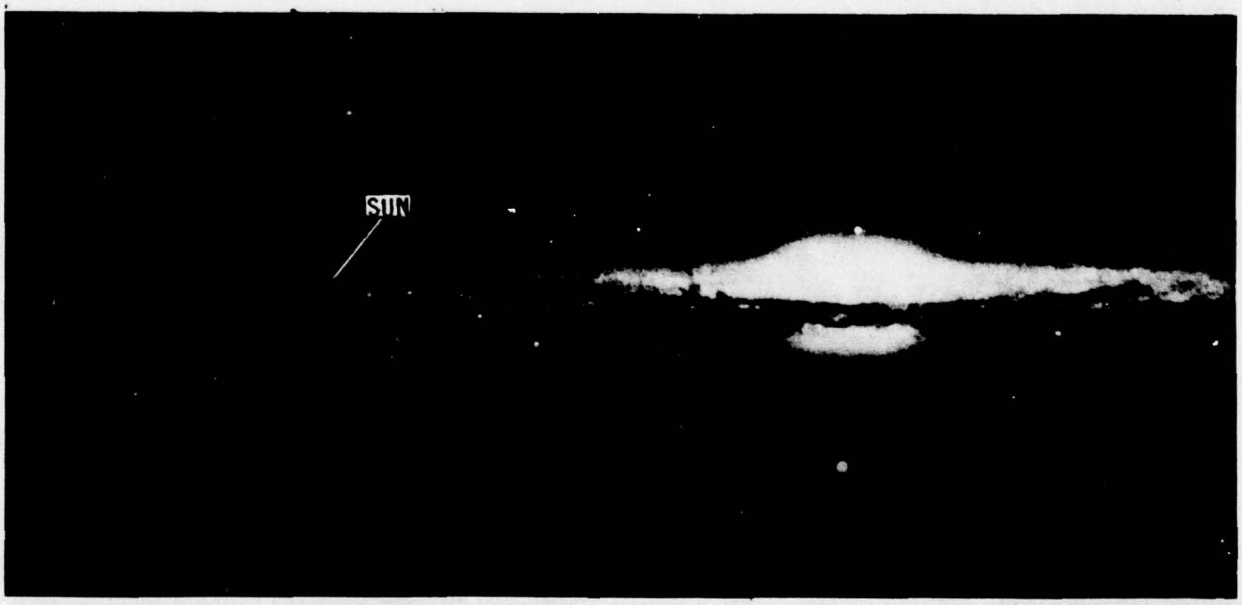


Fig. 21-2. Spiral galaxy NGC4565, observed edge-on, shows the thin disk of gas and dust in the galactic plane that is characteristic of the arms. The nuclear bulge is the dust-free ellipsoidal clump of stars around the center; the halo is not visible. Our Galaxy has a larger nuclear bulge and would appear less flattened. The marker indicates roughly the relative position of the solar system in our Galaxy. (Mt. Wilson Observatory photograph.)

The *parsec* is the distance to a star whose trigonometric parallax (Sec. 21.8.1) is 1 sec of arc; it is 3.26 light yr, 2.06×10^5 AU, 3.09×10^{13} km. The *light year* (l.y.) is the distance traveled in 1 yr at the speed of light in vacuum; it is 9.460×10^{12} km, 6.32×10^4 AU. The *astronomical unit* (AU) is the mean value of the greatest and least distance of the earth's orbit from the sun; the currently accepted value is 1.496×10^8 km.

The arm of the Milky Way galaxy in which the solar system is located (the Orion Arm) has a rotational speed around the galactic center of about 260 km sec^{-1}. In addition, the sun moves among nearby stars with its own *peculiar motion* of 20 km sec^{-1} (4.22 AU yr^{-1}) toward the constellation Hercules. The *apex* is the point on the celestial sphere determined by this velocity vector. Peculiar motion affects the observations of radial velocity and proper motions of nearby stars; they appear to have an equal and opposite velocity. Because the apex at $l^{II} = 57°$, $b^{II} = 22°$ (Sec. 21.2.2.5) is located not far from the direction of galactic rotation, it is sometimes difficult to separate the effects of galactic rotation and the sun's peculiar motion. *Proper motion* is an apparent tangential velocity; it is defined as the angular distance through which a star appears (to an observer on earth) to move in the sky in one tropical year. At right angles to the sun's peculiar motion, the average stellar proper motions are maximum and directed away from the apex. The effect of differential galactic rotation causes proper motions to be directed toward or opposite to the direction of rotation.

Because the sun is an average star in radius, mass, density, and luminosity, solar quantities serve as convenient units for corresponding quantities of other stars. The solar units are:

Radius, $R_\odot$	$(6.9598 \pm 0.0007) \times 10^{10}$ cm
Mass, $m_\odot$	$(1.989 \pm 0.002) \times 10^{33}$ g
Luminosity, $L_\odot$	$(3.90 \pm 0.04) \times 10^{33}$ erg sec^{-1} 6.41×10^7 W m^{-2}
Luminosity per unit mass	1.96 erg g^{-1} sec^{-1}
Mean density, $\bar{\rho}_\odot$	1.409 g cm^{-3}
Surface gravity, $g_\odot$	$(2.7398 \pm 0.0004) \times 10^4$ cm sec^{-2}
Escape velocity at sun's surface	617.7 km sec^{-1}

Magnitudes:	apparent	absolute
	$U = -26.06$	$M_U = +5.51$
	$B = -26.16$	$M_B = +5.41$
	$V = -26.78$	$M_V = +4.79$
	$m_{bol} = -26.85$	$M_{bol} = +4.72$
Color:		$B - V = +0.62$
		$U - B = +0.10$

These values are from Allen [1963], a standard source for astrophysical values.

21.2.2 Celestial Coordinate Systems

Figure 21-4 represents the celestial sphere of infinite radius drawn for an observer on earth at latitude ϕ. His zenith, vertically overhead, is defined by the negative of the gravity direction (plumb line); his horizon is the great circle normal to this vertical. The zenith and the visible celestial pole define the *local meridian;* this is a portion of the great circle passing through the zenith and the celestial poles that intersects the horizon at the north and south points. *The celestial equator* is the projection of the earth's equator on the celestial sphere; it intersects the horizon at the east and west points. (In astronomy, eastward always means counterclockwise as seen looking down from the north; westward, or *retrograde* motion, is clockwise.) The *hour circle* of a star is half of a great circle on the celestial sphere that passes through the star and the celestial poles.

Figure 21-5 shows the earth's orbit around the sun in relation to the celestial sphere. The *ecliptic* is the intersection of the earth's orbital plane with the celestial sphere; it is the apparent path of the sun. The *vernal equinox* ♈, also called the first point of Aries, is the point of intersection of the ecliptic and the celestial equator where the sun appears to cross the equator moving from south to north (ascending node). Because the celestial pole precesses about the pole of the ecliptic (period about 26,000 yr), there is a slow westward movement of ♈ along the ecliptic of about 50 sec of arc yr^{-1}. The accompanying nutation, which has a principle period of 18.6 yr, can be considered as a small irregular motion superimposed on the precession that moves ♈ ahead and behind its mean position. A fictious mean vernal equinox, that moves uniformly along the celestial equator at a rate that precession alone would produce, is defined so that the sidereal days are of equal length.

21.2.2.1 *Horizon System (Azimuth and Altitude).* North and south points of the local horizon are defined as azimuth $A = 0°$ and $A = 180°$; east and west points are at $A = 90°$ and $A = 270°$. Altitude, h, is the angular distance of a star from the point where the vertical circle that is defined by the arc from zenith to the star intersects the horizon, see Fig. 21-4.

21.2.2.2 *Equatorial Systems.* Both equatorial coordinate systems define declination, δ, as the angular distance (in degrees) of a star from the point of intersection of its hour circle with the celestial equator; it is positive toward the north.

In the hour angle (t) *and declination* (δ) *system,* hour angle is the coordinate parallel to the celestial equator; it is the angular distance from the meridian to the hour circle measured in units of time (1^h is 15°; $1''$ is 0.067^s) and is positive toward the west.

The right ascension (α) *and declination* (δ) *system* is used for cataloging and mapping the positions of celestial objects. Zero for the right ascension coordinate is the vernal equinox; α is measured eastward along the celestial equator from the vernal equinox to the hour circle of the celestial object. Values of α are reported in units of time. Because of the precession, there is a slow increase in values of α (slow westward movement of ♈) and small changes in δ (northward in some parts of the celestial

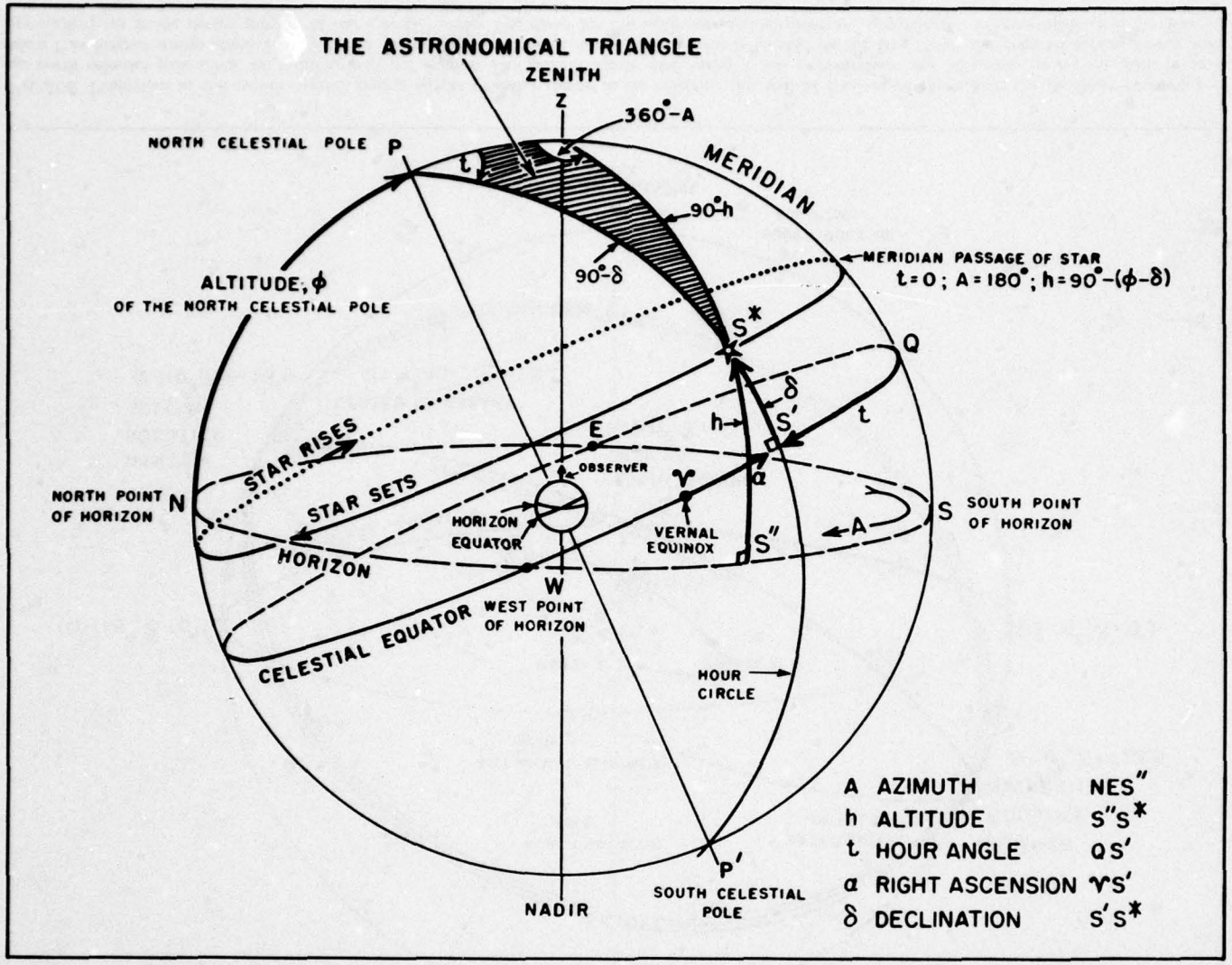


Fig. 21-4. Horizon and Equatorial Coordinates. The north celestial pole is above the observer's horizon at altitude ϕ (the latitude of the observer). The arc PZS is the observer's meridian. For a star located at S*, the arc ZS* defines a vertical circle that intersects the horizon at S". Azimuth of the star is measured along the horizon from N through E to S". The altitude is measured along the vertical circle from S" to S*. PS*P' is the hour circle of the star; it intersects the celestial equator at S'. Hour angle is measured from Q (the intersection of the meridian and the celestial equator) along the equator to S'; the direction shown is positive. Right ascension is measured eastward along the celestial equator from Υ to S'. Declination is measured along the hour circle from S' to S*; the direction shown is positive. The spherical triangle PZS* is the astronomical triangle used for conversion of coordinates. (Figure by Gordon W. Wares.)

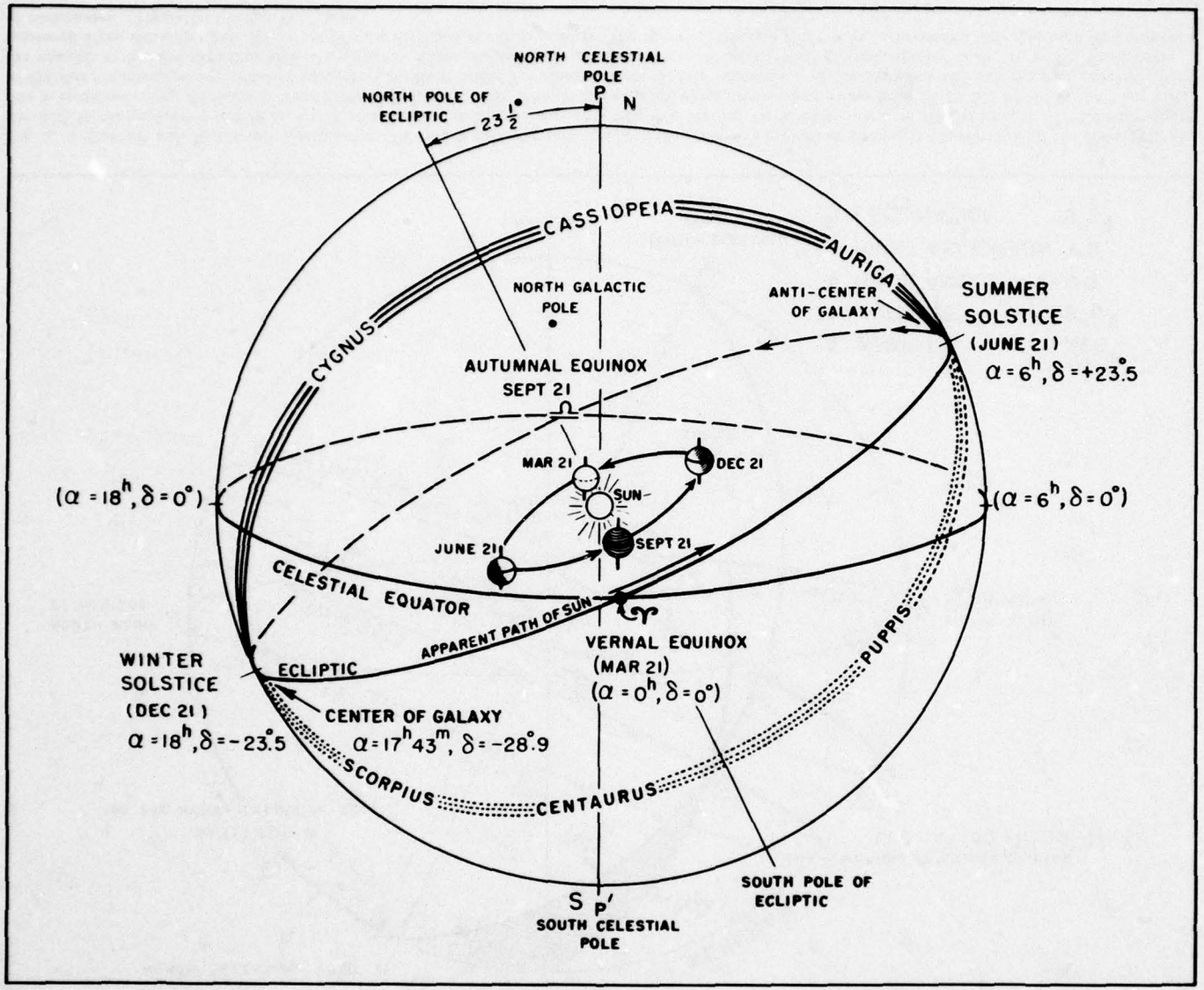


Fig. 21-5. Projection of the earth's oribtal motion on the celestial sphere is the ecliptic; this will be unchanged throughout the 26,000-yr precession of the north celestial pole about the north pole of the ecliptic. The galactic circle (for which a few constellations are indicated) is for the 20th century, when P is located within about 1° of α Ursae Minoris (Polaris). The north galactic pole is located on the far side of the celestial sphere (away from the reader), as is the dotted portion of the galactic circle. The dates for the equinoxes and solstices are approximate. (Figure by Gordon W. Wares.)

sphere, southward in others). Nutation causes small additional changes (9 sec of arc maximum).

21.2.2.3 *Conversion Between Horizon and Equatorial Systems.* Conversion involves the solution of the Astronomical Triangle. Knowing the latitude, ϕ, and given A and h (or δ and either t or α), the unknowns can be found by spherical trigonometry. The coordinates α and t differ only in their origin and direction of measurement along the celestial equator; to convert, the sidereal time, θ, is determined, and the relation $\theta = \alpha + t$ is used. Note that while α is always positive, t is negative east of the meridian.

21.2.2.4 *Ecliptic System.* This system is useful only within the solar system; the coordinates can be visualized by referring to Fig. 21-5. Celestial longitude is measured eastward along the ecliptic from the vernal equinox. Positive celestial latitude is measured northward from the ecliptic toward the north pole of the ecliptic.

21.2.2.5 *Galactic Systems.* The *galactic equator*, also called the *galactic circle*, is a great circle on the celestial sphere inclined 62° to the celestial equator. Figure 21-6 shows the new galactic coordinates in relation to the constellations. *Galactic latitude*, b, is measured from the galactic circle, positive toward the north galactic pole. A *new galactic system* (1958 Revision) with the origin of *new galactic longitude*, $l^{II} = 0°$, toward the galactic center and with a slightly shifted galactic plane, was adopted by the International Astronomical Union. The new *north galactic pole* is $\alpha = 12^h49^m$, $\delta = 27\overset{\circ}{.}4$. The position of the vernal equinox for the precise instant of time, 1950.0, was adopted as reference for the next few decades. The north galactic pole in the old system was at $\alpha = 12^h40^m$, $\delta = +28°$. *Old galactic longitude*, l^I, was measured from 0^h to 24^h eastward and northward along the galactic equator from its intersection with the celestial equator in Aquila near right ascension 12^h40^m. The old galactic center was near $l^I = 327°$. New conversion tables for the 1950.0 equinox are published in the *Annals of the Lund Observatory*, Nos. 15, 16, and 17, 1961. Both precise and approximate interpolation tables are provided for conversion between the equatorial and new galactic systems and between new and old galactic systems. An approximate conversion is $l^{II} \approx l^I + 32\overset{\circ}{.}31$.

21.2.3 Names and Categories of Stars

Originally the visible stars were identified by proper names, and many of these are still used for the brightest stars; e.g., Altair, Betelgeuse, Rigel, Sirius, Vega, etc. Identification by proper names was superseded by a system based on the constellations. In each constellation, the brightest star is designated by α preceding the constellation's name, the second brightest by β, and so on (through a sequence of Greek and English lower case letters and arabic numerals); examples are α Orionis (Betelgeuse), β Orionis (Rigel), and 61 Cygni A. The letter A, B, or C, etc., following the name designates the primary, secondary, or tertiary, etc., component of multiple stars.

A few faint stars that have special properties, such as Barnard's star with the largest discovered proper motion and van Maanen's star with mean density of almost a ton per cubic centimeter, are also identified by name. The majority of faint stars, however, are designated by their number in a particular catalogue, preceded by the abbreviation for the catalogue's name (or by the compiler's name); HD designates the star listed in the Henry Draper catalogue, BD the Bonner Durchmusterung, and CD the Cordoba Durchmusterung.

21.2.3.1 *Supergiants, Giants, Dwarfs, and White Dwarfs.* Stars are grouped in four major categories according to their luminosity, size, and density. Table 21-1 gives the properties of some stars of these groups in the Milky Way galaxy. *Dwarfs* are stars on the main sequence of the H-R diagram (Sec. 21.2.10). Most of the observable stars are main sequence. The sun is an average dwarf star located at about the middle of the main sequence. *White dwarfs* are stars with low intrinsic luminosity, high surface temperature, and enormous density; numerically they exceed all but main sequence stars. *Giants* are stars with high intrinsic luminosity, large size, and low density. Giants and main sequence are not clearly separable for spectral types B0 and A0, see Fig. 21-8. *Supergiants* are extremely luminous stars of very low density (up to 10 times larger and 100 times more luminous than giants); they are rare, but their high intrinsic luminosity allows them to be seen from greater distances than other stars. The range in luminosity of known stars is a factor of 10^{10}. Radii vary from about 0.3 ~~earth~~ solar radii (a small white dwarf) to about 10^3 ~~earth~~ solar radii (a supergiant). The mean density of a white dwarf may be 10^{13} times the density of a red supergiant.

21.2.3.2 *Binary and Multiple Stars.* A binary (double) star, also called a physical pair, is a pair of stars revolving about a mutual center of gravity. A multiple star consists of three or more stars bound gravitationally in orbital motion; systems of five or more components are not uncommon. Binaries are classified according to the method of observation. *Visual binaries* are detected visually, photographically and by interferometric methods. Proper motion (tangential velocity) that varies sinusoidally reveals the revolution of an invisible companion about a star. *Eclipsing binaries* are pairs whose orbital motions lie in a plane nearly parallel to the line of sight from the earth so that periodically one companion obscures the other and a regular periodic variation in brightness is observed. *Spectroscopic binaries* are detected by a periodic variation in the Doppler displacement of their spectral lines. Members of binary (or multiple) systems generally are not of the same spectral type. Double-lined spectra are observed when both stars have about the same luminosity; usually a single-lined spectrum from the brighter companion, the *primary*, is detected. The periods of binaries range from a few hours to many years for typical visual binaries, and to undetermined centuries in

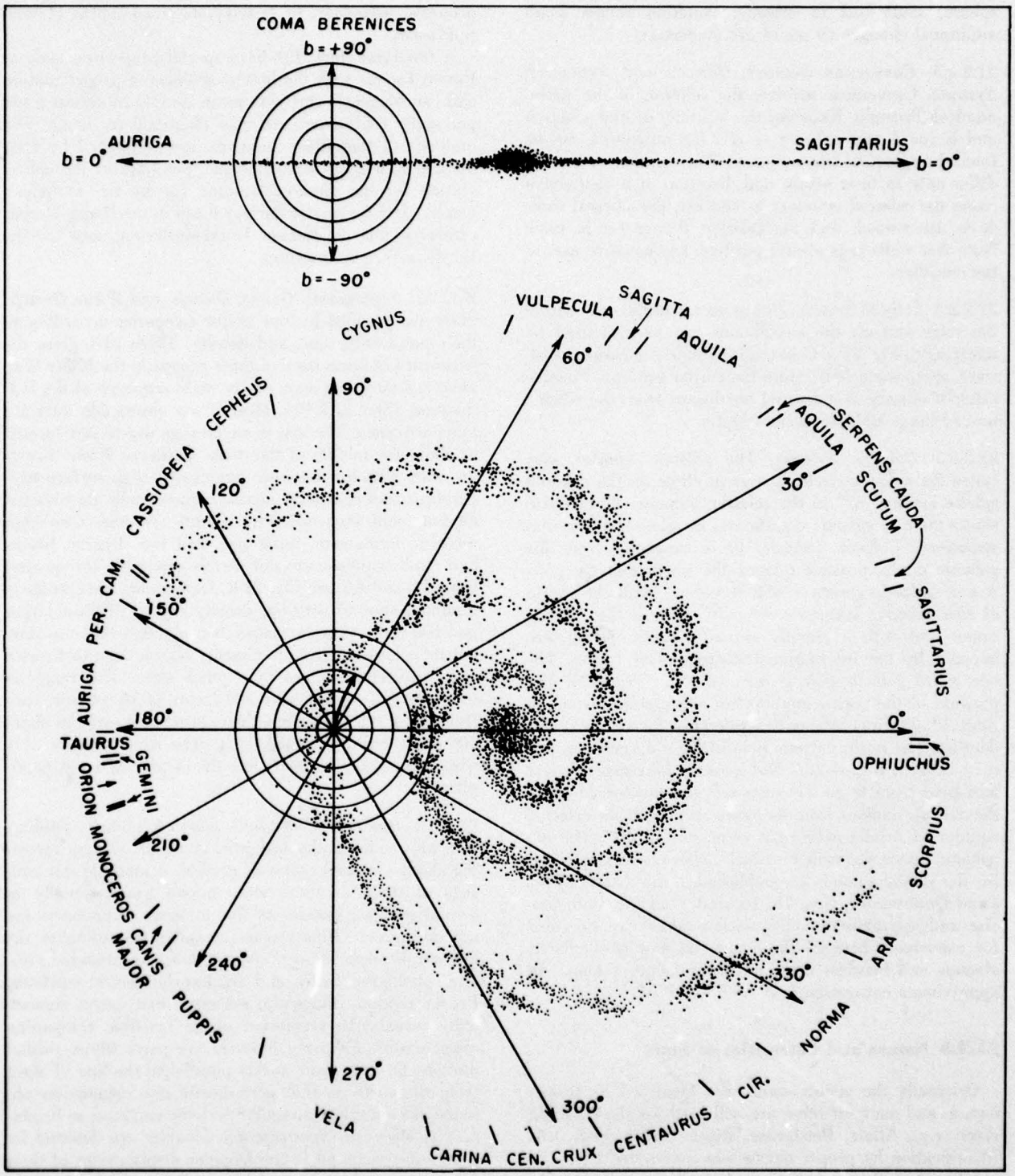


Fig. 21-6. Section and plan views of the Milky Way galaxy, showing the new galactic longitude and latitude. Concentric rings indicate 1-kiloparsec intervals from the sun. The location of the sun near the inner edge of the Orion arm is accurate and the constellations along the new galactic circle for the year *1950.0 are shown at the correct* longitudes, but the spiral arms are indicated only roughly. The curved arrow shows the clockwise direction of galactic rotation in this view, which is looking down from north. In the section view, positive galactic latitude is on the northern side of the galactic plane; $b = 0°$ is the galactic plane. (Figure by Gordon W. Wares.)

the case of stars with common proper motions that are presumed to be gravitationally connected. A system called a binary for historical reasons often may include a third star that was detected later, or one component of a long-period visual binary may have turned out to be a rapidly revolving close spectroscopic binary.

21.2.4 Stellar Magnitudes

The ancient system of classifying the stars designated the brightest stars as first magnitude and the faintest visible to the naked eye as sixth magnitude. In the modern system, *apparent magnitude*, m, is a measure of the irradiance on a detector at the earth's orbit. It is a function of stellar distance and attenuation by the interstellar medium and also depends upon the method of observation, particularly the color sensitivity of the detector. The scale of apparent magnitudes ranges from −26.7 for the sun to +24 for the faintest star photographed with the 200-in. telescope. A zero magnitude star is one that would produce an illuminance of 2.65×10^{-6} lumen ft^{-2} if measured under conditions of no attenuation by the earth's atmosphere. A difference of five magnitudes is defined as an apparent brightness ratio (or a luminosity ratio) of exactly 100 to 1; a difference of one magnitude is equivalent to a ratio of $100^{1/5}$ to 1. The apparent brightness ratio, E_2/E_1, of any two stars of apparent magnitudes m_2 and m_1 is

$$E_2/E_1 = 10^{2\ (m_1 - m_2)/5} = 10^{0.4\Delta m},$$

and

$$m\Delta = m_1 - m_2 = 2.5 \log\ (E_2/E_1). \qquad (21\text{-}1)$$

A difference of one magnitude is thus equivalent to 4 dB.

Absolute magnitude, M, is defined as the apparent magnitude a star would have if it were located at a standard distance of 10 parsecs and if there were no absorption or scattering along the path. The relation between absolute and apparent magnitude is

$$\begin{aligned} M &= m + 5 - 5\ (\log r) - A \\ &= m + 5 + 5\ (\log p) - A, \end{aligned} \qquad (21\text{-}2)$$

where r is the distance (in parsecs) of the star from the solar system, p is the parallax of the star (in sec of arc), and A is the total interstellar scattering and absorption (in magnitudes) over the path length. The quantity

Table 21-1. Properties of some supergiant, giant, main sequence, and white dwarf stars in the Milky Way galaxy (by Gordon W. Wares).

Star	Visual Magnitude (m_v)	Visual Magnitude (M_v)	Visual Luminosity ($L_\odot$)	Spectral Class.	Temperature (°K)	Mass ($m_\odot$)	Radius ($R_\odot$)	Mean Density ($\rho_\odot$)
Supergiants								
α Carinae (Canopus)	−0.9	−7.4	80,000	F0 I-II	8,000	210	158	0.000,005
β Orionis (Rigel)	0.15	−6.4	18,000	B8 Ia	12,500	42	54	0.000,26
α Orionis (Betelgeuse)	0.7	−5.8	25,100	M2 Iab	3,100	15	1,100	0.000,000,011
α Cygni (Deneb)	1.26	−4.8	10,000	A2 Ia	10,000	42	34	0.001
α Scorpii (Antares)	0.98	−2.6	1,320	M1 Ib	3,100	30	480	0.000,000,3
Giants								
β Pegasi	2.6	−1.4	437	M5 III	2,900	9.0	170	0.000,002
α Aurigae (Capella)	0.09	−0.6	209	G5 III	5,500	4.2	15	0.001,2
α Bootis (Arcturus)	−0.06	−0.3	158	K2 IIIb	4,100	3.0	30	0.000,3
α Tauri (Aldebaran)	1.1	−0.1	132	K5 III	3,300	4.0	60	0.000,02
Main Sequence								
β Centauri	0.7	−3.3	2,510	B0 V	21,000	25	8.3	0.044
γ Scorpii	4.3	−0.8	250	B3	17,000	5.2	3.2	0.16
α Lyrae (Vega)	0.04	0.5	76	A0 V	11,200	3.0	2.5	0.19
β Aurigae	2.8	0.6	69	A0	11,200	2.2	2.4	0.13
α Canis Majoris A (Sirius)	−1.43	1.5	27	A1 V	11,200	2.4	1.6	0.58
α Aquilae (Altair)	0.8	2.3	14	A7 IV, V	8,600	1.7	1.7	0.34
α Canis Minoris Procyon)	0.5	3.0	7.6	F5 IV, V	6,500	1.1	1.9	0.16
α Centuri A	0.3	4.7	1.6	G2 V	6,000	1.1	1.0	1.1
Sun	−26.73	4.84	1.0	G2 V	5,784	1.0	1.0	1.0
70 Ophiuchi A	4.3	5.7	0.6	K0 V	5,100	0.9	1.0	0.9
61 Cygni A	5.0	8.4	0.05	K5 V	3,800	0.45	0.7	1.3
Kruger 60 A	9.2	11.2	0.004	M4 V	3,300	0.26	0.34	9.0
(Barnard's Star)	9.7	13.4	0.0005	M4 V	3,100	0.18	0.16	45
(von Biesbroeck's Star)	—	19.0	0.000,01	M7 V	3,100	0.1	0.01	100,000
White Dwarfs								
o_2 Eridani B	9.50	11.0	0.0028	A	11,000	0.44	0.022	52,000
(van Maanen's Star)	12.36	14.2	0.00016	G	7,500	0.14	0.013	260,000

m — M is the *distance modulus*. The difficulty in observing stars of a given absolute magnitude increases with the distance modulus. If the absolute magnitude of a star can be determined by spectroscopic or other methods, and if the attenuation can be estimated or neglected, then r or p may be computed from Eq. (21-2).

The method of observation is indicated by subscripts. Visual magnitudes are m_v or V (Sec. 21.2.5). A change of 0.1 m_v corresponds to about a 10% change in brightness. Photovisual magnitudes, m_{pv}, are visual magnitudes simulated photographically by using a suitable yellow filter to obtain an effective wavelength of about 5400 Å. Photographic magnitudes, m_{pg}, have an effective wavelength in the blue region at about 4300 Å. Bolometric magnitude, M_{bol}, indicates that the total power radiated at all wavelengths is used to determine the magnitude. Because of atmospheric attenuation, there is no direct method for measuring inside the earth's atmosphere the total luminosity of a star. Therefore, *bolometric corrections* ($\Delta M_{bol} = M_{bol} - M_{pv}$) to absolute photovisual magnitudes are estimated in various ways, preferably from model stellar atmospheres. For a recommended scale of bolometric corrections, which is based on model atmospheres for stars of spectral type F0 or earlier and on stellar energy distributions for stars of later spectral type, see Walker [1964].

21.2.5 Color Index and Photometric Color Systems

The *color index* (C.I.) is m_{pg} minus m_v, or m_{pg} minus m_{pv}. By definition, C.I. is zero for stars of spectral type A0; it is negative for hotter (bluer) and positive for cooler (redder) stars. With the use of photoelectric techniques for precise stellar photometry, several new color systems were introduced.

A widely accepted color system is the U, B, V color. V is essentially m_v or m_{pv}; it is the magnitude observed with a broad band pass filter (about 4900 to 6500 Å) with a maximum near 5500 Å. B is the apparent magnitude observed through a blue filter with the maximum near 4200 Å; the short wavelength cutoff is greater than 3800 Å. U is the apparent magnitude in the ultraviolet region; the broad band filter is centered near 3500 Å. Both B and U are adjusted to give B — V = 0 and U — B = 0 for stars of spectral type A0 luminosity class V (Sec. 21.4.1). The B — V color approximates C.I.

A combination of the U, B, V system with the R, I system is sometimes used for a five-color photometry system (Chapter 20). The R, I system consists of photoelectric observations with relatively broad band filters at 6800 Å (R) and at 8250 Å (I). Many of the standard stars for R — I color are common to the list of standards for U — B and B — V color. For details of these and other photometric systems, see the review by H. L. Johnson [Strand, 1963].

21.2.6 Spectroscopic Terminology

The spectrum arising from excited states of the neutral atom is called the first spectrum of the element; that produced by transitions in an ionized atom with n electrons removed is the $(n+1)^{th}$ spectrum of the element. The state of ionization is identified by a Roman numeral following the chemical symbol; HI is neutral hydrogen, HII ionized hydrogen (proton). An *atomic specie* is a given element in a given ionization state, e.g., there are 21 atomic species of the element of atomic number 20 (CaI, CaII, . . . CaXXI). Each specie has its individual series of excited states.

Composite spectra have lines that originate in more than one star; for example, the spectra of close binaries or unresolved physical and optical binaries. *Combination spectra* have features normally arising only under widely different conditions of excitation.

The lines of the *Balmer series* (transitions between the first excited state and higher atomic energy levels) in HI are identified as the Hα or red line (6563 Å), Hβ or green line (4861 Å), and Hγ or blue line (4340 Å). The series converges to a limit at 3646 Å at which the *Balmer continuum* begins. In absorption, the Balmer continuum greatly reduces the intensity of spectra; however, the decline sets in at wavelengths longer than the series limit. There is a discontinuity between the intensities of the continuum at long and at short wavelengths when these are extrapolated at 3646 Å; this is the *Balmer jump*. Ground level transitions of HI are the *Lyman series lines* (Lα at 1216 Å, Lβ at 1026 Å, limit at 912 Å); they cannot be observed on the earth's surface because of atmospheric absorption.

In astronomical spectroscopy, all elements heavier than hydrogen are customarily referred to collectively as metals. *Weak lined* spectra show a relative deficiency of lines due to elements heavier than hydrogen; the stars are called metal-poor. *Strong lined* spectra show many lines of the heavier elements; the stars are called *metal rich*. Certain absorption lines in stellar spectra are customarily identified by the corresponding Fraunhofer line in the solar spectrum; e.g., the lines of CaII at 3968 and 3934 Å are called the *H and K lines*.

The intensity of an absorption line is defined by its *equivalent* width, W_λ; this is the width (Å) of a completely black line of rectangular profile that would subtract from the continuum the same amount of energy as does the real line.

21.2.7 Curve of Growth

A plot of log W_λ vs log Nf is called the curve of growth; N is the number of the atomic specie per square centimeter (cross section along line of sight) absorbing energy at wavelength λ, and f is the oscillator strength (f-value) for the transition that produces the line. When N is small, the curve of growth is linear, $W_\lambda \propto Nf$, with slope unity for faint lines. As saturation effects set in, the curve tends to flatten out for some distance depending on the damping constant Γ. As the broad wings of the line dominate the absorption (very large N), the curve again rises linearly; $W_\lambda \propto (Nf\Gamma)^{1/2}$ in this region.

For a star with many lines, an empirical curve of growth can be constructed by using multiplets of lines

from the same atomic specie so that while N is unknown, it is identical for all members of each multiplet in each spectrum. By suitable shifting of each multiplet parallel to the log Nf axis, an empirical curve of growth is constructed. If the f value for the particular specie is known, then N can be determined from this empirical curve of growth. The natural damping constant is sometimes dominated by the effect of turbulent motions in the stellar atmosphere, in which case turbulent velocities can be estimated from the extent and behavior of the flat portion of the curve of growth.

21.2.8 Spectral Type and Temperature

Table 21-2 lists spectral types of the classification system used in the Henry Draper Catalogue and its Harvard Extensions. The principal sequence, types O, B, A, F, G, K, and M, includes most of the known stars. Subdivisions within types are indicated by suffix 0 through 9. Subdivisions of type O were at one time a through e. Suffix e now indicates that HI emission lines are present. (Roman numeral suffixes are defined in Sec. 21.4.1.1.) At one time, prefixes a, b, or c were used to indicate stars whose spectra have broad, intermediate, or narrow absorption lines. Prefix c is still used; it indicates an early-type supergiant (very narrow absorption lines). Prefixes g, d, and wd indicated giant, dwarf, and white dwarf. Stars of spectral types R and N are sometimes called carbon stars. Wolf-Rayet stars are often designated by WC (carbon sequence) and WN (nitrogen sequence) with numeral suffixes, rather than by spectral type. Stars of type O and B are often grouped and referred to as *OB stars;* they are also called *young* or *early type* stars.

The sequence O through M is one of decreasing ionization and essentially decreasing temperature; not all stars of the same spectral type, however, have the same temperature (Sec. 21.4.1). Temperature is the dominant influence on the degree of ionization in a stellar atmosphere, but a decrease in density also produces increased ionization. Opposing effects control the relationship between the temperature and the stellar spectrum. The probability of an atomic specie being excited to a given energy level increases with temperature; however, increasing the temperature also increases the probability of ionization

Table 21-2. Classification of stars according to their spectra.

Spectral Type	Approximate* Temperature (°K)	Features
O	50,000	Lines of HeII, SiIV, NIII, etc.; weak HI.
B0	25,000	HeII absent; HeI strong (max. at B2); SiIII and OII present; HI stronger.
B5	15,600	HeI strong; HI stronger; SiII and MgII present.
A0	11,000	HI max.; HeI absent; MgII and SiII strong; FeII, TiII, weak; CaII weak.
A5	8700	HI strong; MgII, SiII, FeII, TiII near maximum; CaII stronger; FeI and other neutral metals weak.
F0	7600	HI weaker; CaII strong; FeII, CrII, etc., about equal to FeI, CrI, etc.
F5	6600	CaII very strong; lines of FeI and other neutral species predominate over FeII, etc.
G0	6000	Like the sun (G2); CaII max.; large number of FeI and other neutral species lines; CH bands present.
G5	5500	CaII and neutral metal lines very strong; CH bands stronger; CN strong, especially in giant stars.
K0	5100	HI relatively weak; neutral atomic lines all very strong; molecular bands stronger.
M0	3600	Neutral lines very strong; bands of TiO present.
M5	3000	Resembles M0, but 4226 Å line of CaI very strong; TiO bands stronger.
R and N	3060	Bands of CN, CH, and C_2 strong; TiO absent; line spectrum like K or M stars.
S	3000	Bands of ZrO, YO, and LaO, not present in other types, are strong; neutral species lines strong, including Zr and Tc.

* These are traditional values; for B5 and above they are too low, and for A0 and below, they are somewhat too high.

so that ultimately a particular specie will disappear. For example, the strength of HI Balmer lines begins to increase rapidly at about 5000°K, reaches a maximum about 11,000°K, then declines as an increasing number of hydrogen atoms become protons. All other elements have successive ionization states, and each successive specie has its own maximum at increasingly higher temperature. Figure 21-7 illustrates this for species whose absorption lines are used in determining spectral types.

21.2.9 Saha Theory of Ionization

The electron pressure at the surface of a star, P_e, is a function of surface gravity, g_s, and of temperature, T.

$$P_e = n_s m_e g_s, \tag{21-3}$$

where n_s is the number of electrons per unit surface area and m_e is the mass of the electron. Also

$$P_e = N_e kT, \tag{21-4}$$

where N_e is the number of the electrons per unit volume and k is Boltzmann's constant. (For tabulations of the relation of electron pressure to gas pressure as a function of temperature for two different stellar chemical compositions, see Greenstein [1960].) Figure 21-7 shows that hydrogen is usually the principal source of electrons in the hotter stars. Calcium, iron, etc. supply the electrons in stars below spectral type F0, despite the relatively low abundance of metals.

The relationship between the electron pressure, temperature, and excitation and ionization of a given element derived by Saha is

$$\frac{N_{r+1}}{N_r} P_e = \frac{(2\pi m_e)^{3/2} (kT)^{5/2}}{h^3} \frac{2 U_{r+1}(T)}{U_r(T)} e^{-I/kT}. \tag{21-5}$$

I is the ionization potential from state r to r + 1, N_r is the number of a given atomic specie per unit volume in the state r, N_{r+1} is the number per unit volume of the succeeding specie of the same element in the next higher state of ionization, the functions U(T) are the corresponding partition functions, and h is Planck's constant. Standard references for ionization potentials and partition functions are Moore [1949 et seq], Allen [1963], and Aller [1963].

21.2.10 Luminosity, Temperature, and H-R Diagrams

For many purposes it is useful to consider a star as a blackbody radiator (see Appendix B); the temperature of a star is then determined by fitting the available portions of its spectrum to a blackbody curve. Estimations of the temperature from Wien's displacement law (Eq. B-8) are not reliable because the deviation of stellar emission from true blackbody radiation introduces too large an error.

The *luminosity* (radiant power) of a star, L, is defined as the total power emitted at all wavelengths; in units of magnitude, L is M_{bol}. A subscript indicates power in a specific spectral region; e.g., L_v is the visible luminosity. For a star of radius R, an *effective temperature*, T_e, is defined by the relation (Eq. B-7),

$$L = 4\pi R^2 W = 4\pi R^2 \sigma T_e^4. \tag{21-6}$$

From the slope of the main sequence curve on H-R diagrams, the relation between the luminosity and the temperature of main sequence stars appears to be

$$L \propto T^{5.5}. \tag{21-7}$$

H-R (Hertzsprung-Russell) diagrams are plots of absolute magnitudes or luminosities of stars (ordinate) vs spectral type or a related parameter such as temperature or color (abscissa). Figure 21-8 is an H-R diagram that shows the locations of various classes of stars.

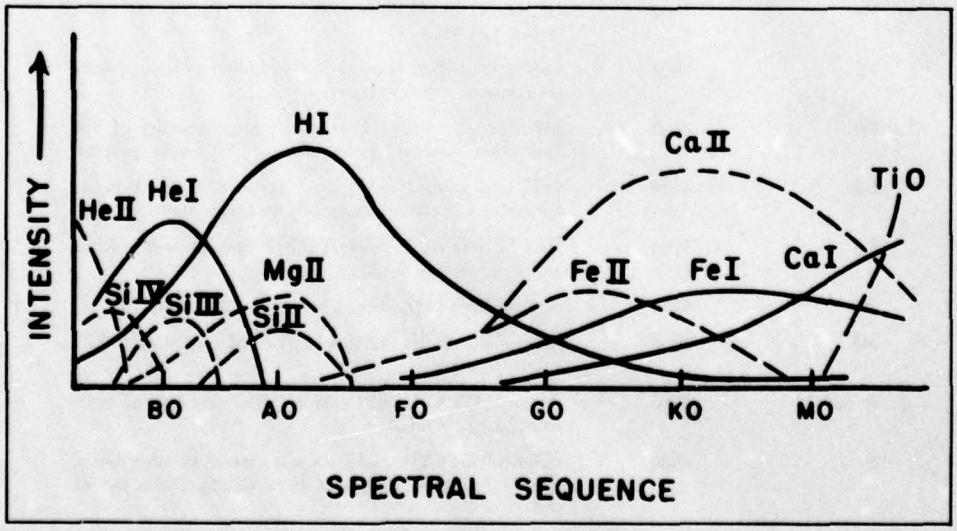


Fig. 21-7. Relative intensities of some absorption lines in stellar spectra vs spectral type; see also Table 21-2. (After O. Struve, B. Lynds, and H. Pillans, "Elementary Astronomy," Oxford University Press, 1959.)

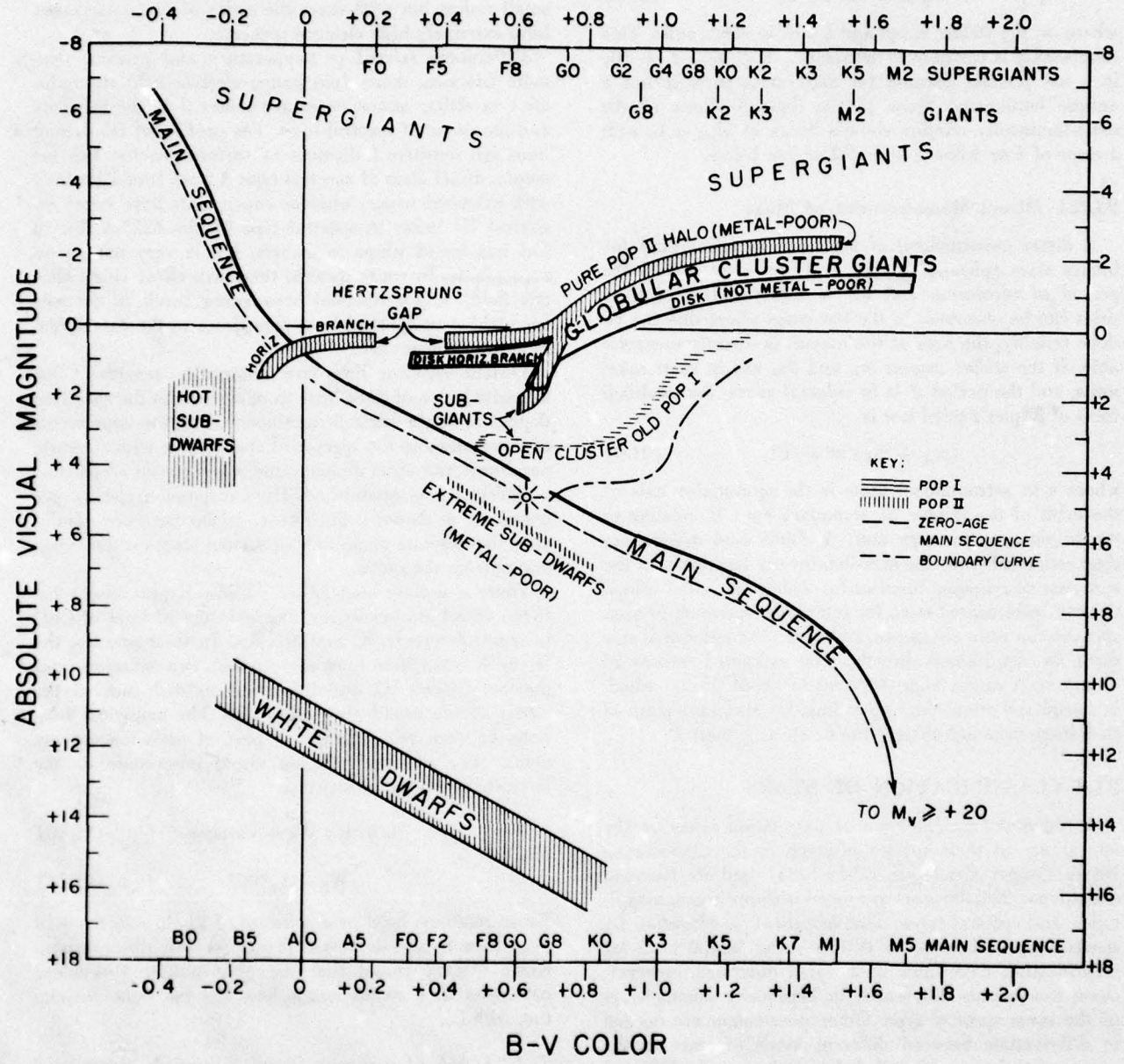


Fig. 21-8. H-R diagram with spectral type equivalents of B — V color magnitude for the main sequence, giants, and supergiants indicated. The halo globular clusters are represented by M92. The disk globular clusters are represented by NGC6356, which is a typical disk cluster that is not metal-poor, but not as metal-rich as most open clusters. An unusually old open cluster, M67, represents old Population I of about the same age as the globular clusters. No correction was made for line blanketing of the extreme subdwarfs. To the right of and below the boundary curve, no stars that are generating energy by thermonuclear reactions in their core have been observed. (Figure by Gordon W. Wares.)

CHAPTER 21

21.3 STELLAR MASSES AND LUMINOSITIES

An empirical *mass-luminosity law* for main sequence stars is

$$\log L = 3.3 \log m, \qquad (21\text{-}8)$$

where m, the stellar mass, and L are in solar units. This relationship is useful over the range $-8 < M_{bol} < +10$; it is not precise, because for each mass there is not a unique luminosity. Some of the determinations of the mass-luminosity relation show a break at $M_{bol} = 6$, with a slope of 3 or 4 above and of 2 or less below.

21.3.1 Direct Measurement of Mass

A direct measurement of mass can be made only for binary stars (physical pairs), and then only if both the period of revolution and the semi-major axis of their orbit can be observed. In the few cases where this can be done reliably, the sum of the masses is directly measureable. If the stellar masses m_A and m_B are in solar mass units, and the period P is in sidereal years, the modified form of Kepler's third law is

$$(m_A + m_B) = a^3/P^2, \qquad (21\text{-}9)$$

where a in astronomical units is the semi-major axis of the orbit of the fainter or secondary star, B, relative to the brighter or primary star, A. Individual masses are then estimated from the mass-luminosity law. Only in the rare case of eclipsing binaries for which the radial velocities can be measured from the individual spectrum of each star can the ratio of masses, and hence the individual star mass, be determined directly. The estimated masses of binary stars range from $0.035\, m_\odot$ to about $65\, m_\odot$, which is considered about the upper limit for stability; stars of such large mass are observed to be ejecting matter.

21.4 CLASSIFICATION OF STARS

A systematic classification of stars based solely on the appearance of their spectra is given in the nine-volume Henry Draper Catalogue (1919-1924) and its Harvard extensions; 225,300 stars are listed with positions, magnitudes, and spectral types. This empirical classification by spectral type (Harvard or Draper class) is still used for identification (see Table 21-2). H-R diagrams, however, show tremendous differences in luminosity among stars of the same spectral type. Other parameters are needed to differentiate between different kinds of stars of the same spectral type. (Detailed descriptions and additional systems of classification are given in Strand [1963].)

21.4.1 Luminosity Criteria

Supergiants are highly luminous primarily because of their enormous surface area (Eq. 21-6). Their temperatures are somewhat lower than main sequence stars of the same spectral type, but their slightly lower temperature is offset by increased ionization resulting from lower electron pressure. Because surface gravity is proportional to the mass, which is somewhat larger for giants, and inversely proportional to the square of the radius, which is much larger for giants, the electron pressure in giants and supergiants is considerably less than that in normal dwarfs (Eq. 21-3). The white dwarf stars, with extremely small radius but with mass the order of one solar mass, have extremely high electron pressure.

Differences related to temperature and pressure (kinetic energies, mean free paths, electric field strengths, etc.) in stellar atmospheres are reflected in the intensity and the shape of spectral lines. The profiles of HI Balmer lines are sensitive indicators of surface gravity. For example, dwarf stars of spectral type A have broad HI lines with extended wings, whereas supergiants have relatively narrow HI lines; in spectral type M, the 4227-Å line of CaI has broad wings in dwarfs, but is very narrow in supergiants. In white dwarfs, the Stark effect (high electric field) and collisional broadening result in extreme broadening of spectral lines sometimes to the extent that lines are unobservable.

Certain spectral lines are luminosity sensitive. The intensity ratios of these lines to other lines in the spectrum depend upon the intrinsic luminosity. From measurements of these ratios in the spectra of stars whose trigonometric parallaxes and absolute magnitudes are known accurately, a calibration is established. High dispersion spectra are necessary to measure the ratios; when these are obtainable, the absolute magnitude of distant stars can be determined from the ratios.

There is a close correlation (Wilson-Bappu effect) between visual luminosity and the structure of lines of CaII in spectral type G, K, and M stars. In these spectra, the H and K absorption lines each contain two emission components (called H2 and K2), one on each side of the center of the broad absorption line. The empirical relations between separation of a pair of emission components, W_0, and the absolute visual magnitude or the intrinsic visual luminosity, are

$$M_v = \log W_0 + \text{Constant} \qquad (21\text{-}10)$$

and

$$W_0 \propto L_v^{1/6}. \qquad (21\text{-}11)$$

These relations hold over a range of about -6 to $+10$ M_v. There is no established theory for this phenomenon. Kraft [1959] found that the photospheric turbulence parameter of a stellar atmosphere has the same correlation with L_v.

21.4.1.1 *MK (Luminosity Class) System.* A widely used two-dimensional spectral classification which applies to Population I stars (Sec. 21.6.3) is the MK or Yerkes system. An essential feature is the use of an array of standard stars of specified spectral type and luminosity class presented in a photographic atlas [Morgan et al, 1943; Johnson and Morgan, 1953]. Each observer reobserves with his own equipment to provide his own working standards. The method is adapted to low dispersion (140 Å mm^{-1}) to permit its use with faint stars. With the exception of luminosity O, which was introduced to designate the very brightest supergiants ($M_v \approx -9$),

luminosities are indicated by Roman numerals following the spectral type designation. The designations are: I for supergiants; II for bright giants; III for normal giants; IV for subgiants; V for main sequence; and VI for subdwarfs. Subdivisions are represented by suffixes a, ab, and b. Tables 21-3 and 4 give absolute visual magnitudes and provisional values of the effective temperature for these luminosity classes; magnitudes given for the hotter stars are approximate. Because recent observations of stellar energy made outside the atmosphere create much uncertainty in the temperature scale for the hotter stars of the main sequence, additional data are required to establish a definitive scale. Table 21-5 lists the principal groups of stars that do not fit the MK system of classification and some of their characteristics.

21.4.1.2 *Two-Color Diagram (U—B vs B—V).* The two-color diagram supplements the H-R diagram in the interpretation of the U,B,V photometry of a group of stars. Figure 21-9 gives curves (unreddened) for luminosity classes I, III, and V together with the curve for a blackbody and the reddening slope. Curves for all luminosity classes lie below the blackbody curve because of line absorption in the atmosphere of stars.. Table 21-6 lists B—V and U—B color for various spectral types and luminosity classes.

Table 21-3. Absolute visual magnitudes of luminosity classes. (From P. C. Keenan, "Basic Astronomical Data," K. Aa. Strand, ed., University of Chicago Press, 1963, by permission.)

Spectral Type	Main Sequence V	Subgiants IV	Giants III	Giants II	Supergiants* Ib
O9	− 4.8	−5.4	−6.0	—	—
B0	− 4.1	−4.6	−5.0	−5.6	−6.2
B1	− 3.5	−3.9	−4.4	−5.1	−6.0
B2	− 2.5	−3.0	−3.6	−4.4	−5.9
B3	− 1.7	−2.3	−2.9	−3.9	−5.8
B5	− 1.1	−1.6	−2.2	−3.7	−5.7
B7	− 0.6	−1.0	−1.6	−3.6	−5.6
B8	− 0.2	−0.6	−1.2	−3.4	−5.5
B9	+ 0.2	−0.3	−0.8	−3.1	−5.4
A0	+ 0.6	0.0	−0.6	−2.8	−4.9
A1	+ 1.2	+0.3	−0.4	−2.6	−4.8
A2	+ 1.4	+0.6	−0.2	−2.4	−4.7
A3	+ 1.7	+0.9	0.0	−2.3	−4.6
A5	+ 2.1	+1.2	+0.3	−2.1	−4.5
A7	+ 2.4	+1.5	+0.5	−2.0	−4.5
F0	+ 2.6	+1.7	+0.6	−2.0	−4.5
F2	+ 3.0	+1.9	+0.6	−2.0	−4.5
F5	+ 3.4	+2.1	+0.7	−2.0	−4.5
F6	+ 3.7	+2.2	+0.7	−2.0	−4.5
F8	+ 4.0	+2.4	+0.6	−2.0	−4.5
G0	+ 4.4	+2.8	+0.6	−2.0	−4.5
G2	+ 4.7	+3.0	+0.4	−2.1	−4.5
G5	+ 5.2	+3.2	+0.3	−2.1	−4.5
G8	+ 5.6	+3.2	+0.3	−2.1	−4.5
K0	+ 5.9	+3.2	+0.2	−2.1	−4.5
K2	+ 6.3	—	−0.1	−2.2	−4.5
K3	+ 6.9	—	−0.2	−2.3	−4.5
K5	+ 8.0	—	−0.3	−2.3	−4.5
M0	+ 9.2	—	−0.4	−2.4	−4.5
M1	+ 9.7	—	−0.5	−2.4	−4.5
M2	+10.1	—	−0.5	−2.4	−4.5
M3	+10.6	—	−0.5	−2.4	−4.5
M4	+11.3	—	−0.5	−2.4	−4.5
M5	+12.3	—	—	—	—
M6	+13.4	—	—	—	—

* For class Ia, M_V is estimated as ≈ -7.0

Table 21-4. Provisional scale of effective temperatures for MK luminosity classes. (From P. C. Keenan, "Basic Astronomical Data," K. Aa. Strand, ed., University of Chicago Press, 1963, by permission.)

Spectral Type	Temperature (°K)
B0	27,000
B1	23,000
B2	20,000
B3	18,000
B5	16,000
B6.5	14,000
B8	12,500
B9	11,200
A0	10,400
A1	9700
A2	9100
A3	8500
A5	8200
A7	7600
F0	7200

	V	IV	III	II	Ib
F2	6900	6830	6800	6700	6600
F5	6700	6600	6500	6350	6200
F6	6500	6370	6250	6020	5800
F8	6200	6050	5900	5720	5450
G0	6000	5720	5500	5350	5050
G2	5740	5420	5100	4950	4750
G5	5520	5150	4800	4650	4500
G8	5320	4950	4600	4450	4300
K0	5120	4750	4400	4350	4100
K1	4920	4550	4150	4000	3850
K2	4760	——	3970	3860	3750
K3	4600	——	3820	3720	3600
K5	4350	——	3700	3600	3500
K6	4000	——	——	——	——
M0	3750	——	3500	3400	3300
M1	3600	——	3300	3150	3050
M2	3350	——	3100	2050	——
M3	3100	——	2900	——	——
M4	——	——	2700	——	——

Table 21-5. Principal stellar groups that do not fit the MK system. (After P. C. Keenan and W. W. Morgan, "Astrophysics, A Topical Symposium," J. A. Hynek, ed., McGraw-Hill, New York, 1951.)

Group	Typical Stars	Features and Possible Causes
Population II stars	δ Lepus 31 Aquila	Weakening of CN bands relative to normal G and K type; great strengthening of CH bands in type R stars. Relative abundance of C and H probably involved.
Stars of type B or A with emission lines	105 Taurus κ Draco	HI emission lines. Extended gaseous envelope around star.
Stars of type A-F with wide, shallow lines	η Ursa Maj. α Aquila	Shallow, broad profiles in all absorption lines. Rapid axial rotation.
Stars of type A-F with metallic lines	τ Ursa Maj. 63 Taurus	CaII K line abnormally weak relative to metallic lines.
Peculiar stars of type A; Eu stars, Mn stars, etc.	α Andromeda	Abnormal and variable line intensity of MnII, SiII, EuII, GrII, SrII, (one or more). Intensification of some lines by stellar magnetic field; unusual distribution of species over stellar surface.
Wolf-Rayet stars: WC5-WC8; WN5-WN8	HD 192103 HD 192163	Broad emission lines of carbon or nitrogen. Relative abundance of carbon and nitrogen.
Carbon stars, type R and N	U Hydra UX Draco	Strong absorption bands of C_2 and CN; many TiO bands. Abundance of carbon.
S-type stars	HR 1105 R Andromeda	Absorption bands of ZrO, YO, LaO, usually TiO present. Abundance of zirconium.

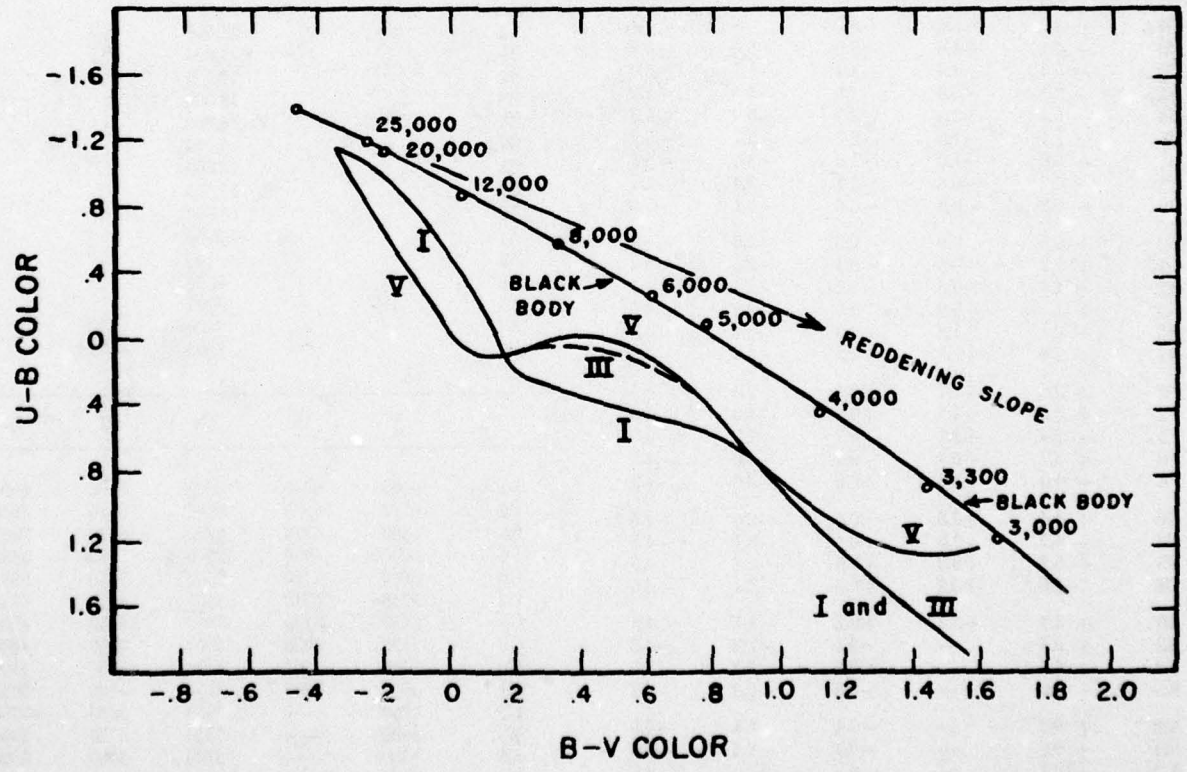


Fig. 21-9. The two-color relation, U — B vs B — V. Temperature points for the blackbody curve are in °K. Below this curve are the standard relations (zero reddening) for stars of luminosity classes I (supergiant), III (giants), and V (main sequence). The effect of interstellar reddening upon any characteristic point is to displace that point downward and to the right, parallel to the small reddening slope, which is only approximately linear. (Figure by Gordon W. Wares, after H. C. Arp, *Astrophys. J.*, v. 133, p. 874, 1961.)

21.4.2 Quantitative Methods of Spectral Classification

The assignment of a star to a particular spectral type and luminosity class usually involves some compromise between conflicting criteria. Two systems that depend upon measurement of continuously variable parameters are Barbier and Chalonge's, and Strömgren's. Both methods, however, are limited to stars with spectra from which the Balmer jump can be measured.

Table 21-6. Best available values of intrinsic colors of various spectral types and luminosity classes. (From H. L. Johnson, "Basic Astronomical Data," K. Aa. Strand, ed., University of Chicago Press, 1963, by permission.)

Spectral Type	B–V Color (magnitude)				
	V	III	II	Ib	Ia
O5	−0.32	−0.32	−0.32	−0.32	−0.32
O6	− .32	− .32	− .32	− .32	− .32
O7	− .32	− .32	− .32	− .31	− .31
O8	− .31	− .31	− .31	− .29	− .29
O9	− .31	− .31	− .31	− .28	− .28
O9.5	− .30	− .30	− .30	− .27	− .27
B0	− .30	− .30	− .29	− .24	− .24
B0.5	− .28	− .28	− .26	− .22	− .22
B1	− .26	− .26	− .24	− .19	− .19
B2	− .24	− .24	− .22	− .17	− .17
B3	− .20	− .20	− .18	− .13	− .13
B5	− .16	− .16	− .14	− .09	− .09
B6	− .14	− .14	− .12	− .07	− .07
B7	− .12	− .12	− .10	− .05	− .05
B8	− .09	− .09	− .07	− .02	− .02
B9	− .06	− .06	− .04	.00	.00
B9.5	− .03	− .03	− .01	+ .01	+ .01
A0	.00	.00	+0.01	+ .01	+ .01
A1	+ .03	+ .03	—	+ .01	+ .01
A2	+ .06	+ .06	—	.00	.00
A3	+ .09	—	—	.00	.00
A5	+ .15	+0.15	—	+ .07	+ .07
A7	+ .20	—	—	+ .13	+ .13
F0	+ .30	—	—	+ .24	+ .24
F2	+ .38	—	—	+ .34	+ .34
F5	+0.45	—	—	+0.45	+0.45
	U–B Color (magnitude)				
O5	−1.15	−1.15	−1.15	−1.15	−1.15
O6	−1.14	−1.14	−1.14	−1.14	−1.14
O7	−1.14	−1.14	−1.14	−1.14	−1.14
O8	−1.13	−1.13	−1.13	−1.13	−1.13
O9	−1.12	−1.12	−1.12	−1.12	−1.12
O9.5	−1.10	−1.11	−1.12	−1.09	−1.10
B0	−1.08	−1.09	−1.10	−1.05	−1.07
B0.5	−1.01	−1.03	−1.05	−1.01	−1.04
B1	−0.93	−0.96	−1.00	−0.96	−1.00
B2	−0.86	−0.89	−0.95	−0.91	−0.96
B3	−0.71	−0.74	−0.83	−0.82	−0.87
B5	−0.56	—	−0.69	−0.72	−0.78
B6	−0.49	—	−0.62	−0.67	−0.73
B7	−0.42	—	—	−0.62	−0.68
B8	−0.30	—	—	−0.53	−0.60
B9	−0.19	—	—	−0.48	−0.56
B9.5	−0.10	—	—	—	—
A0	0.00	—	—	—	—

21.4.2.1 *Barbier-Chalonge Classification.* Microdensitometer tracings of spectrograms that show HI lines in the region centered about 3647 Å may be analyzed to obtain the parameters D and λ_1. Figure 21-10 gives an idealized tracing and schematic diagram which define D and λ_1. The parameter D represents a drop in the continuum intensity. Parameter λ_1 is the wavelength at which the logarithm of the continuum intensity has decreased by D/2. One advantage of this system is that the parameters D and λ_1 are independent of interstellar reddening;

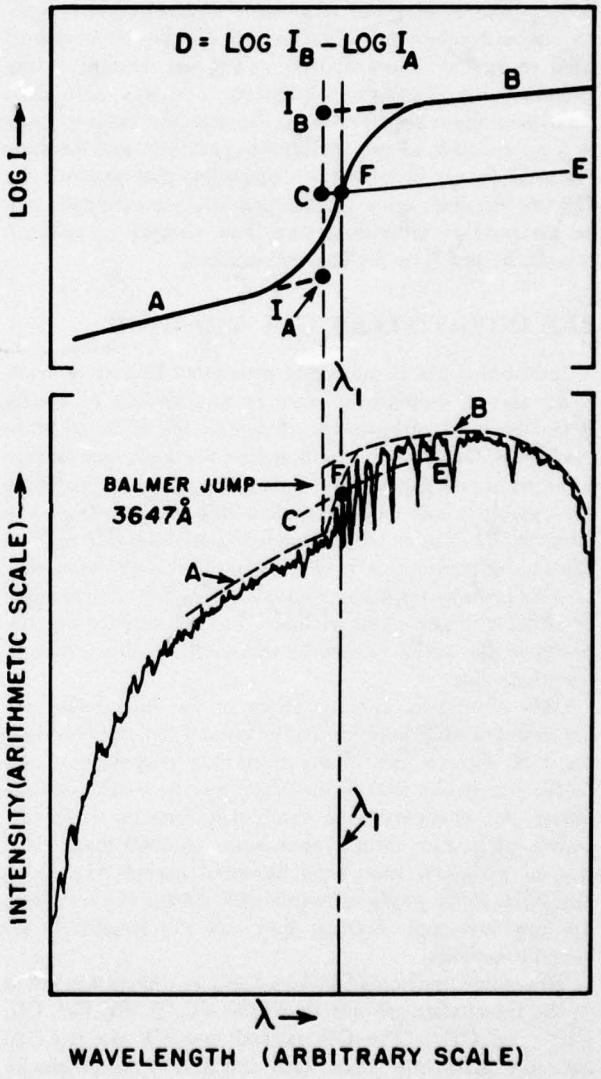


Fig. 21-10. Microdensitometer tracing showing the envelopes and the Balmer jump, and a schematic diagram illustrating the determination of parameters D and λ_1. (The shape of the envelope curve is distorted in the diagram for simplicity.) I_A and I_B are located by extrapolation of the straight portions of the envelope curve to 3700 Å. The value of D is log (I_B/I_A). The point C is located at D/2. A line through C is drawn parallel to the straight portion B and intersects the envelope curve at F, which determines λ_1.

another is that D and λ_1 can be obtained from spectrograms with less dispersion (about 250 Å mm^{-1}) than those required for MK classification. The method has high accuracy for spectral type B, A, and F stars. A third parameter, ϕ, the gradient of the continuum curve in the region 3800 to 4600 Å, may be added to obtain a 3-dimensional classification. ϕ is related to color magnitude B and is affected by interstellar reddening.

21.4.2.2. *Strömgren's Narrow-Band Photometry*. The parameters are the Balmer jump (index c) and the strength of the 4861 Å Hβ absorption line (index l). The total energy in narrow wavelength regions (isolated by interference filters) is measured directly by photoelectric techniques and compared to calibrated standards. A plot of total energy absorbed by Hβ versus the amount of the Balmer jump (lc diagram) clearly separates supergiant stars from main sequence stars. Because the Balmer jump is a good index of the surface temperature, and because the total energy absorbed by transitions that produce the Hβ line depends upon surface gravity, accurate ages can be assigned to individual stars and clusters of spectral type B, A, and F by Strömgren's method.

21.5 INTERSTELLAR GAS AND DUST

Interstellar gas is primarily hydrogen. Radiation from a B1 star of luminosity class II is sufficient to totally ionize atomic hydrogen gas of density less than 10 atom cm^{-3}. An O-type star could ionize the hydrogen within a radius of several hundred light years. Regions in which the hydrogen is ionized are called *HII regions*; the more common *HI regions* are atomic hydrogen gas. HII regions can be detected optically by emission lines (electron capture by protons results in excited states of H atoms, some of which radiate in the visible), but HI regions are detected in the radio region by emission or absorption of the 21-cm line.

Only cosmically rare elements in the interstellar gas are detected by absorption in the optical region. The resonance absorption lines of the more abundant elements are in the ultraviolet that is absorbed by the earth's atmosphere. All elements with resonance lines at favorable wavelengths and cosmic abundance greater than 10^{-7} that of hydrogen have been observed except AII, CoII, and NiII. If the predicted equivalent widths of these lines are approximately correct, they are not detectable by current methods.

The atoms, molecules, and radicals positively identified in the interstellar gas are H, Na, K, Ca, Ti, Fe, CH, CN, CH^+ and OH^-. The OH radical and HI are detected by radio astronomy (Sec. 22.5 and 22.6), the others by absorption lines in optical spectra.

21.5.1 Interstellar Absorption Lines

Table 21-7 lists the wavelengths and sources of the optical interstellar absorption lines. Interstellar lines arise from the ground state, the only populated state under the prevailing conditions of low density ($\approx 10^{-24}$ g cm^{-3}), low temperatures ($\approx 100°K$), and the low energy-density of stellar radiation. The lines are invariably sharp, with narrow natural breadth and very narrow Doppler breadth. The strongest interstellar absorption lines are the H and K lines of CaII in spectra of OB-type stars; their stellar lines are not strong enough to mask the interstellar lines, while these stars are luminous enough to be observed at such great distances that the intervening gas is sufficient to be detected. At the threshold of detection, the number of the absorbing atomic specie per unit cross section of the optical path is the order of 10^{11} or 10^{12}. Interstellar absorption lines are particularly noticeable in spectra of OB-type binary stars. The wavelength of the stellar lines in spectra of binary stars varies continuously, whereas the wavelength of lines resulting from absorption by matter between the stars and the solar system is constant. As a result, the interstellar lines were called *stationary lines*.

Empirical curves of growth for interstellar absorption lines are constructed by using the doublets of CaII and of NaI. Sufficient range in strength of the lines is obtained by using spectra of stars with large differences in line-of-sight distance. Interstellar lines are not strong enough to show wing effects, and generally the empirical curve falls in the region where $W_\lambda \propto Nf$. Because the relative f-value of the K line in CaII is twice that of the H line, the two points must be separated by log 2 on the log Nf coordinate. Shifting all such pairs of points parallel to the log Nf coordinate produces a smooth curve of growth from which N can be found. If the distance to the star is known, the average number of interstellar CaII ions per unit volume between earth and the star's photosphere is obtained.

Table 21-7. Wavelengths (Å) and sources of optical interstellar absorption lines.

Atomic	Molecular	Diffuse
3302.4 NaI	3143.2 CH	4430.6*
3303.0 NaI	3878.8 CH	
5890.0 NaI, D_2	3886.4 CH	4760
5895.9 NaI, D_1	3890.2 CH	
	4300.3 CH	4890
7664.9 KI	3874.0 CN	5780.6
7699.0 KI	3874.6 CN	
	3875.8 CN	5797.1
4226.7 CaI		6180
3933.7 CaII, K	3579 CH^+	6203.0
3968.5 CaII, H	3745.3 CH^+	
	3957.7 CH^+	6270.0
	4232.6 CH^+	
3073.0 TiII		6283.9
3229.2 TiII		
3242.0 TiII		6614
3383.8 TiII		
3720.0 FeI		
3859.9 FeI		

* Tentatively identified as H_2 by G. H. Herbig, *Astrophys. J.*, v. 137, p. 200, 1963.

21.5.2 Interstellar Gas Clouds

High dispersion spectra of distant OB stars show sharp interstellar lines with two or three (occasionally four or more) Doppler displacements. These multiple lines result from the different radial velocities of separate clouds of interstellar gas in the optical path. The clouds are called CaII or NaI clouds according to the relative prominence of the H and K lines or of the D lines in the spectrum. Statistical studies indicate that a typical 1000-parsec line of sight in the galactic plane passes through a half dozen clouds of diameter 10 to 100 parsec. The densities of these clouds (derived indirectly from optical data) are 1 to 10 atoms of hydrogen per cubic centimeter. The clouds occupy from 14% to 7% of the space volume and move with radial velocity dispersion of 7 km sec^{-1} (root mean square). The aggregate of these gas clouds partakes of approximately the same rotation about the galactic center as do their neighboring stars, but there are differences between the motions of individual gas clouds and stellar motions.

In the direction perpendicular to the galactic plane, the number of clouds in the range from 500 to 1000 parsec is larger than that predicted from analyses of the distribution function of velocity components in the galactic plane. Components of velocity perpendicular to the galactic plane, the *z-velocities*, are unexpectedly high, as much as 50 km sec^{-1} toward or away from the plane. To account for the existence of such clouds with estimated lifetimes of about 4×10^7 yr, a restraining force is necessary; otherwise clouds at large distances from the galactic plane would have expanded and lost their identity. Münch and Zirin [1961] suggest that a galactic corona exerts pressure that prevents dissipation of a high velocity cloud. High velocity clouds show CaII much stronger than NaI, whereas the reverse is true for low velocity clouds; ionization due to a high electron temperature of the proposed galactic corona could also account for this anomaly.

21.5.3 Interstellar Reddening and Color Excess

Radiation from distant stars is scattered, as well as absorbed, by interstellar matter. This scattering, called *selective absorption*, causes greater attenuation of the violet and blue wavelengths, hence distant stars appear redder than their true color. When this interstellar reddening occurs, the observed color magnitudes have a color excess, E, which is a measure of the attenuation. E is defined by the equations

$$E_{B-V} = (m_B - m_V)_{obs} - (M_B - M_V)_{std},$$
$$E_{U-B} = (m_U - m_B)_{obs} - (M_U - M_B)_{std}. \quad (21\text{-}12)$$

The color excess is a function of the galactic latitude, b. A recent analysis gives the relationship

$$E_{B-V} = 0.058 \csc b. \quad (21\text{-}13)$$

An empirical value for the slope of the line that indicates the displacement on the two-color diagram is 0.72; this is the value used for the reddening slope shown in Fig. 21-9. The relationship is not actually linear. For O type stars, the relation

$$E_{U-B} = 0.72\ E_{B-V} + 0.05\ (E_{B-V})^2 \quad (21\text{-}14)$$

is used to predict the displacement on the two-color diagram. The coefficient of the second order term, however, is not accurately known.

21.5.3.1 *Interstellar Dust and Polarization.* If scattering by the interstellar gas were the cause of selective absorption, the attenuation would be proportional to λ^{-4} (Rayleigh scattering law). Observations show selective absorption in the visible region more nearly proportional to λ^{-1}. This type of scattering is caused by particles with diameters the order of 0.1 to 1 μ, hence reddening must be caused by interstellar dust. Studies of the optical polarization of light from stars located close together on the celestial sphere (not necessarily in physical proximity) tend to be parallel. Polarization from stars close to the Milky Way tends to be parallel to the galactic plane. Polarization increases with increasing color excess, although color excess is not necessarily accompanied by any polarization. The presence of interstellar dust seems necessary but not sufficient. The dust grains must be elongated or birefringent and be oriented in a preferred direction. Alignment by bombardment of gas flowing in a direction perpendicular to the galactic plane was proposed, but this effect appears to be too small to produce the observed polarization. It is more probable that the orientation is maintained by magnetic fields. Estimates of galactic magnetic fields are the order of 10^{-6} to 10^{-4} gauss; all investigations indicate that the field is not uniform.

21.5.3.2 *Statistically Corrected Distance of a Star.* A useful empirical relation between color excess and total attenuation in the visible region (A_V) is

$$A_V = 3.0\ E_{B-V}; \quad (21\text{-}15)$$

the coefficient is determined statistically. From this relation, A_V can be calculated directly from measurements of B and V color magnitudes. Substituting into Eq. (21-2) gives

$$M_V = m_V + 5 - 5 \log r - 3\ E_{B-V}. \quad (21\text{-}16)$$

By using the value of M_V for the particular luminosity class and spectral type of the star (Table 21-3), the *statistically corrected distance*, r, can be obtained for stars in obscured regions.

21.5.4 Relation of Dust Clouds to Gas Clouds

Observations of the interstellar absorption lines of the sodium D doublet combined with color excess measurements indicate that a gas cloud is also a dust cloud. In directions where there is strong reddening, each D line has several components. Each component corresponds to a discrete, and relatively opaque, gas cloud with a radius of about 5 to 10 parsec containing about 5×10^{-8} sodium atoms per cubic centimeter. The value of N per

cloud is approximately 5×10^{12} cm^{-2}. Absorption by atomic species and molecules can contribute only a small fraction of the total observed attenuation. Scattering by dust appears to be responsible for most of this attenuation. In directions where the color excess is small, the gas clouds are less dense.

The *zone of avoidance*, where almost no extragalactic nebulae are observed, delineates the dust clouds of the Milky Way. (It is assumed that the extragalactic distribution is normal, but dust in our Galaxy obscures the distant galaxies.) A comparison of this zone of avoidance with two-dimensional contour diagrams of the density of atomic hydrogen gas, as determined from the 21-cm line, shows sufficient agreement to support the hypothesis that gas and dust clouds occupy the same volume of space.

21.6 STELLAR EVOLUTION

21.6.1 Nuclear Reactions, Stellar Interiors, and H-R Diagrams

Although there are several theories of evolution which differ in important details, the features described in this section are those most generally accepted. (The basic reference is Schwarzschild [1958].)

Condensations of interstellar material contract gravitationally (called the Helmholtz contraction). The temperature at the center of this low density protostar gradually rises, and when the temperature reaches a few million degrees Kelvin a proton-proton reaction begins to generate thermonuclear energy. Protons (p) combine to produce, through intermediate products (a deuterium nucleus, d, and a helium nucleus of atomic mass three, He^3), an α particle (helium nucleus of atomic mass four). This three-step process is the *proton cycle:*

$$p(p, \beta^+)d;\ d(p, \gamma)He^3;\ He^3(He^3, 2p)\alpha.$$

At this phase in a star of about one solar mass or less, the radius and temperature become stable. In much more massive stars, contraction may continue until the temperature reaches about 10^8 °K, and α particles can be formed by both the proton and the carbon cycles. The *carbon cycle* is a six-step process in which an α particle is formed through intermediate nuclei in reactions initiated by C^{12}, and C^{12} is recovered as an end product;

$$C^{12}(p, \gamma)N^{13};\ N^{13} \rightarrow C^{13} + \beta^+ + \nu;\ C^{13}(p, \gamma)N^{14};$$

$$N^{14}(p, \gamma)O^{15};\ O^{15} \rightarrow N^{15} + \beta^+ + \nu;\ N^{15}(p, \alpha)C^{12}.$$

The production of α particles by either cycle is called *hydrogen burning.*

During contraction, the star moves leftward on the H-R diagram onto the main sequence; this is the arbitrary zero point in the age scale, and the star is *zero-age main sequence.* Estimates of the contraction period are from 10^9 to 10^5 yr, depending on the mass; the greater the mass, the more rapid the gravitational contraction. The length of time a star remains in the main sequence also depends upon the mass. For one solar mass it is about 10^{10} yr. It is longer for smaller masses and shorter for larger masses. The luminosity of main sequence stars is maintained nearly constant by burning the hydrogen in the core. The available hydrogen is probably 12% or 15% of the total hydrogen content.

When the available hydrogen is exhausted, the outer layers of the star expand, but the inert core of pure helium contracts. The central temperature then rises, and hydrogen in the shell outside the core begins to burn. The inert core grows in size and its temperature increases. The temperature of the core finally may become so high that C^{12} can be produced from α particles by the two-step process,

$$\alpha(\alpha, \gamma)\ Be^8;\ Be^8(\alpha, \gamma)C^{12}.$$

This process, *helium burning*, is a precursor of subsequent nuclear reactions in which the other elements can be formed. (A satisfactory theory of nucleogenesis is given by Burbidge et al [1957].) During this stage the instabilities observed in the intrinsically variable stars may set in.

At the onset of expansion of the outer layers, the star moves off the main sequence; this is called the *turn-off point.* The surface of a massive bright star cools as it expands, but its luminosity remains roughly constant. Such stars move more or less directly to the right on the H-R diagram and become red giants. For less massive stars, the surface temperature remains nearly constant, or may increase at first; such stars move upward and then to the right on the H-R diagram. The aging process proceeds most rapidly in the most massive stars. Subsequently the giant star moves leftward on the H-R diagram, crosses the main sequence (becoming unstable in the Hertzsprung gap or crossing it quickly), and ends up as a white dwarf. Neither the path nor the processes involved in going from the stage of red giant or of variable star to white dwarf are established.

The pressure and temperature of the stellar gas and its opacity to outward flow of radiation from the central nuclear reactions affect the equilibrium and luminosity of the star. In an ordinary star like the sun, the mean density is 10 g cm^{-3}, but the central density is 10^2 g cm^{-3}. All atoms in the interior are stripped of their electrons, and these nuclei occupy such small volumes that the gas is considered to be an ideal gas. A form of the ideal gas law useful for stellar interiors is

$$P = \rho kT/\mu m_p, \qquad (21\text{-}17)$$

where ρ is the mass density, m_p the mass of the proton, and μ the mean molecular weight factor (the mean number of proton masses per free particle). The electrons somewhat outnumber the ions because helium and traces of heavier elements are present. Because of their high density and because they are subject to the Fermi exclusion principle, the electrons may be degenerate and possess far more than their share of the internal energy. This occurs in the white dwarf stars that are, except for the negligible mass in their atmosphere, totally degenerate. At certain stages in the evolution of red giant stars, degeneracy can occur in their centers if their mass is in the narrow range just greater than one solar mass.

21.6.2 Loss of Mass During Evolution

According to the Chandrasekhar theory of completely degenerate gas, white dwarf stars can have total mass no greater than 1.2 to 1.5 $m_\odot$ (the factor depends upon the assumed composition). Stars much above the sun on the main sequence must lose mass at some stage of their later evolution. The loss from thermonuclear processes is not sufficient to reduce masses very much greater than the sun by the necessary amount, nor is the steady mass ejection observed in some red supergiants. Various processes have been suggested, but it is not certain that they provide the necessary mass loss; examples are the nova and supernova processes, and less drastic processes such as flares and tidal loss of material in close binary star systems.

Surrounding the star T Tauri there is a small gas nebulosity of about 10^{-4} $m_\odot$, which extends 750 AU from the star. If the observed radial velocity (170 km sec^{-1}) represents outflow from the star, it is losing mass at the rate of one solar mass in 2×10^5 yr, and is replacing the nebulosity every 20 yr. Such ejection during contraction could provide a reduction factor of one-half or one-third before the star reaches the main sequence stage.

It is possible that matter ejected from Population II stars may produce an outward motion of the Population I spiral system. According to theory, the spiral arms in the Milky Way galaxy should be more tightly wound, because our Galaxy is some 20 or 30 revolutions (galactic years) old.

21.6.3 Populations I and II

The classification of stars into Population I and Population II distinguishes between stars with different distributions on the H-R diagram, different spacial distributions and motions, and characteristically different spectra (metal rich or metal poor). Although this classification is known to be an oversimplification, it is a useful concept.

The spectra of all stars show the presence of some elements heavier than hydrogen. The heavier elements are much more abundant in stars classified as Population I, often by a factor of 100 or more. An hypothesis that explains this difference is that primordial hydrogen was first converted into helium and heavier elements in stellar interiors, this material was ejected into space during the evolution of the stars, and later this ejected matter formed into new stars. On this basis, the youngest stars are condensed from material that has passed through one or more earlier generations of stars during which the metals were formed. If so, pure Populations I and II represent the extremes of a population of mixed ages. (It also appears necessary to distinguish between chemical composition due to time of formation and that which may result from possible local spacial irregularities in the material from which the star condensed.)

Population II stars are those with a deficiency of heavy elements; they have weak-lined spectra. These stars are considered to be the old, first generation stars. Population II stars are found in globular clusters (Sec. 21.6.4.3), elliptical galaxies, and the nuclear bulge of spiral galaxies. Stars near the galactic center possibly may be not Population II but very old Population I. Yellow giants are typical Population II stars. The most luminous Population II stars are red giants; there are no main sequence stars of spectral type O, B, or A in Population II (see Fig. 21-8). Population II stars in a late stage of evolution apparently undergo instability in the Hertzsprung gap region of the H-R diagram in which no star seems to be stable.

Population I stars have metal-rich spectra. They are found in the arms of spiral galaxies and in irregular galaxies. Hot, luminous stars at the upper end of the main sequence (spectral types O, B, and A) are characteristic of pure Population I stars.

21.6.4 Clusters and Associations

Clusters are groups of stars held together by gravitational attraction and assumed to have a common origin. Although clusters differ in age, all members of a given cluster are assumed to be generally of the same age and chemical composition. This assumption of uniform age is believed to be a good approximation insofar as the formation of stars within a cluster occupied a short time relative to the age of the cluster. Some star clusters have well-known names, but most are designated by catalogue number. Abbreviations for these catalogues are: M for Messier's Catalogue, 1781; NGC for New General Catalogue, 1888; and IC for the Index Catalogue that is an extension of the NGC, 1895 and 1908. *Globular clusters* are roughly spherical groups containing on the average a hundred thousand stars, with a concentration of stars near the center; M3 in Canes Venatici is a typical globular cluster. *Galactic (open) clusters* are less compact groups of dozens or hundreds of stars with no localized concentration; the Pleiades are a galactic cluster of Population I stars. *Stellar associations* are loose groupings of stars that are thought to have a common origin, but are expanding and dissipating; they cover too large an area and are too sparse to be classified as open clusters.

21.6.4.1 *O and T Associations.* O-associations are groups of spectral type O and B stars; most of these associations have a space density less than 0.1 $m_\odot$ so that the gravitational field of the galaxy, not mutual gravitation of the group members, should govern their motions. Because of their large size and the characteristically high luminosity of their members, they are useful in delineating the spiral arms of the Milky Way. O-associations outline the Perseus (outer) arm, our own Orion arm, and the Sagittarius (inner) arm. Extrapolating the outward velocities of member stars backward to their region of apparent origin gives estimates of the expansion ages of different O-associations that range from 4×10^5 to about 7×10^6 yr. This agrees with the prediction of short lives for stars as massive and luminous as the OB stars, which according to theory could not continue radiating at such high rates for more than a few times 10^7 yr. The T-associations are groups of T Tauri stars; it is not established that these

associations are expanding, but they are connected with expanding nebulosity. In some cases, as in the Orion nebula region, a T-association occupies essentially the same volume of space as an O-association.

21.6.4.2 *Galactic (Open) Clusters.* Galactic star clusters are loose aggregates of stars held together gravitationally against moderate outside forces. They range from 1.5 to 15 or 20 parsec in width, and the density of stars ranges from 1 to about 80 parsec^{-3}. The mean absolute magnitude is about -3.5; the presence of blue and red supergiants in the young clusters accounts for the high luminosities. These clusters are strongly concentrated toward low galactic latitude; only a few, such as the Coma cluster in Coma Berenices, are seen in the direction of high galactic latitude. The open clusters at our distance from the galactic center move in galactic orbits as do the sun and nearby Population I stars; they are historically called low velocity objects in contrast to the apparent high velocity of globular clusters. Estimated ages of galactic clusters range from a few million years for h and χ Persei, to around 10^9 yr for M67. Recent developments show there is no completely clear-cut distinction between extremely old galactic clusters, such as M67, and the globular clusters.

21.6.4.3 *Globular Clusters.* Globular clusters are almost spherical groupings of Population II stars. Gravitational attraction is stronger than in the open clusters, and the globular clusters may retain their configuration indefinitely. The absolute magnitude of a globular cluster ranges from -5 to -10. If only stars brighter than absolute magnitude $+3.8$ (as faint as usually can be observed in a globular cluster) are counted, the average bright-star density is about 0.5 parsec^{-3}. The density at the center is 100 times this value. Globular clusters are distributed roughly in a sphere around the galactic center; in the direction of the disk opposite to the center, the sky is nearly devoid of globular clusters. Most globular clusters contain RR Lyrae variables. The distance of such clusters is known (to within the uncertainty in the absolute magnitude of the RR Lyrae stars); the nearest is 2.5 kiloparsec away. The globular clusters in our Galaxy do not share the orbital revolution of the spiral arms around the galactic center and so are called high velocity objects. The galactic rotation velocity in the solar neighborhood is determined from statistical studies of radial velocities of the globular clusters. The old clusters seem to have highly elongated orbits about the galactic center at various inclinations to the disk. Many distant and apparently faint globular clusters are thought to be located in intergalactic space. One estimate is that as high as one third of the known globular clusters are intergalactic.

The globular clusters are relatively free of dust and gas. This condition is explained by two hypotheses. One is that the globular clusters are very old first-generation objects (pure Population II). This is consistent with the observation of metal-deficient spectra. Spectra of globular clusters near the galactic center, however, show less metal deficiency, and the disk clusters are not metal poor; this is one of many observations that make gradations between the extremes of Populations necessary. The other hypthesis is that each globular cluster has, in its lifetime, passed several times through the plane of the galaxy; the probability of a collision between a star of the cluster and one in the disk is negligible, but the interpenetration would sweep the globular cluster free of dust and gas. Evidence of some dust within globular clusters can be reconciled within the framework of these hypotheses as probably resulting from material ejected from stars within the globular cluster during the time since a previous passage through the galactic plane.

21.6.5 H-R Diagrams of Clusters

The stars of any one cluster are at approximately the same distance from the earth. Therefore, the distance uncertainties can be avoided to a considerable extent in plotting diagrams of apparent magnitude vs color. By assuming that all galactic clusters have main sequence stars that are portions of a common main sequence, each set of points for a given cluster can be shifted in the magnitude direction until the main sequences for all clusters join smoothly together. This determines the absolute magnitudes relative to the Hyades, and the absolute magnitudes for the Hyades stars are accurately known. (A second approximation must be made after cluster ages are determined in order to fit all clusters to the zero-age main sequence.)

Figure 21-11 shows the absolute magnitude vs color diagrams obtained by this method for galactic clusters and the globular cluster M3. The old galactic cluster M67 is comparable in age to M3. For the globular clusters, color vs magnitude diagrams show relatively little variation from one cluster to another; all have the horizontal branch and most have RR Lyrae variables in the Hertzsprung gap.

In the simple theory for the analysis of the color-magnitude diagrams of star clusters, it is assumed that along the main sequence there is initially a continuous mass distribution of stars that have just finished their Helmholtz contraction; these are *zero-age main sequence.* The various theories of stellar evolution agree that a newly evolving star stays close to the main sequence until a critical fraction of its hydrogen is exhausted. Different theories give different values for this fraction, so estimates of the time spent on the main sequence vary. After some time, however, the star moves off the main sequence; this is the *turn-off point.* From the Schonberg-Chandrasekhar theory of stellar evolution, the age, τ (in years), of a cluster whose luminosity at the turn-off point is L_T, is given by the equation

$$\tau = (1.10 \times 10^{10}) \frac{m}{L_T} . \qquad (21\text{-}18)$$

The mass, m, is determined from Eq. (21-8). Recent stellar evolution models, however, emphasize the importance of initial chemical composition.

21.7 INTRINSICALLY VARIABLE STARS

This section is a brief description; several kinds of variable stars, for example spectrum and magnetic variables, are not mentioned. For more detailed information and basic references, see the chapters by Kukarkin and Parenago, Kraft, and Gaposchkin in Strand [1963].

As any variable star is positively identified, it is designated by letters preceding the genative form of the constellation in which it occurs. The first to be found is R, the second S, and so on through Z, followed by RR to RZ, SS to SZ and so on to ZZ; if further designations are required, they continue with AA to AZ, BB to BZ, etc. Stars whose brightnesses and radial velocities change in such a manner that the observed variations cannot be attributed solely to eclipses are the *intrinsically variable* stars. There are many different kinds, but in general these stars are: *irregular* or *semi-regular variables* with fluctuations in brightness at intervals that are not strictly periodic but tend to cluster around a preferred value typical of the star; *pulsating stars* with periodic oscillations in brightness; or *exploding stars* (supernovae, novae, and nova-like variables) with sudden increases in brightness and ejection of material that recur at approximately the same interval for any one star. At present, there is no single system of classification and nomenclature that is accepted as standard; as new properties are discovered and less obvious differences identified, re-evaluation is necessary and some confusion is inevitable. Groups of variable stars with similar properties, however, are often named for a particular star which serves as a prototype.

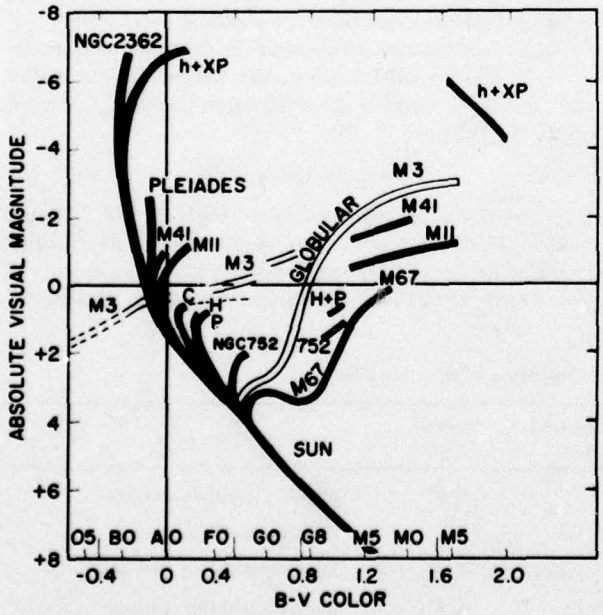


Fig. 21-11. Composite color-magnitude diagram of open clusters (solid curves) compared to the globular cluster M3 including its horizontal branch. C, H, and P designate the Coma, Hyades, and Praesepe clusters. (Figure by Gordon W. Wares.)

21.7.1 Dwarf Irregular Variable Stars

These stars are too faint to be observed at great distances. The T Tauri, UV Ceti, and U Geminorum stars are currently important in studies of stellar evolution. All have explosive brightening, broad emission lines, and an ultraviolet continuum. The T Tauri are single stars associated with dust clouds. UV Ceti flare stars are well separated binaries free of dust association. The U Geminorum stars are close binaries free of dust association.

21.7.1.1 *T Tauri Stars.* These are extreme Population I stars. The mean value of their apparent magnitude is about +3. A star is classified as T Tauri on the basis of its spectrum. Spectra have HI and CaII emission lines, and the fluorescent FeI emission lines (unique in T Tauri stars) at 4063 and 4132 Å. In addition, SII and OI emission lines are usually present; FeII and TiII are generally the next strongest emissions. HeI lines are often strong in the later spectral types. The absorption spectrum is often veiled due to a variable ultraviolet continuum; when it is visible, strong LiI absorption at 6078 Å indicates a T Tauri star. Absorption lines are broad, presumably as a result of axial rotation; values, ranging from 20 to 65 km sec^{-1}, are much higher than for normal stars. A high lithium-to-metals ratio in T Tauri stars is deduced from the strong resonance line at 6708 Å. The lithium abundance is roughly that of the earth and similar to certain meteorites in the solar system; it is 100 times the abundance in the sun and about 10 times that of the dust clouds surrounding the T Tauri stars.

T Tauri stars are found exclusively in regions obscured by dust and only in or near galactic nebulosity; usually the obscuration is heavy and extensive. The frequency of occurrence tends toward regions where young O- and B-type stars have formed, such as the Orion nebula. On the H-R diagram, T Tauri stars lie above and to the right of the main sequence; the K and M spectral types are over-luminous by two or three magnitudes. These characteristics are all consistent with the hypothesis that T Tauri types are stars still in the process of contracting from the diffuse material around them, having not yet reached the main sequence. While this hypothesis is accepted by many astronomers, there is also a strong feeling that T Tauri stars may be at a somewhat later stage of evolution, subsequent to the stage of the nebulous stars present in the same dust clouds.

21.7.1.2 *Flare or UV Ceti Stars.* Extremely rapid variations are characteristic of these stars; brightness may increase 10 fold in a few seconds and return to the original value in 3 to 6 min. They are intrinsically faint (M_v is +8.5 to +19), so the only ones observed are within about 20 parsec of the sun; UV Ceti itself is 2.6 parsec. These stars are main-sequence red dwarfs (spectral type M) with strong, broad emission lines of HI, HeI, and

HeII and a strong ultraviolet continuum. They are usually visual or well-separated spectroscopic binaries, and are not associated with nebulosity. The 6-magnitude increase at the rate of a magnitude every four seconds observed in UV Ceti on 25 September 1952 is about 500 times the rate of increase in Nova Aquila 1918, the brightest nova observed since 1604. It is generally believed that the source of these flares is in the stellar surface or atmosphere. Typically, the brightness of a flare star increases by about 1.5 m_v (a 4-to-1 ratio). An effective temperature of about 10,000°K is estimated from spectra observed during the outbursts; the normal temperature of these red dwarfs is 3000°K. These temperatures correspond to a brightness ratio in the *visible* region of almost 400 to 1; this, combined with the observed brightness ratio of 4 to 1 implies that a typical flare involves about 1% of the stellar hemisphere's surface. A class 3 solar flare involves the same proportion of the sun's surface (see Table 15-1). It is generally assumed that stellar and solar flares are similar phenomena. The flares in UV Ceti stars appear exaggerated by contrast with the very low total luminosity of these cool dwarfs.

21.7.1.3 *U Geminorum (SS Cygni) Stars.* Repeated outbursts that resemble novae but are usually less violent are characteristic of these Population II stars, which are also called dwarf novae. The brightness increases about 2 to 4 magnitudes at intervals from 10 to 150 days; each star has its own characteristic mean interval. Typically, the rise takes about one day. The peak is not sharp and after a few days the brightness declines at a slower rate than the increase. The minimum has rapid variations (the order of 5 min) but these are weak and seldom observed. The emission lines are broad, 15 to 20 Å, and there is a strong UV continuum. Observations of SS Cygni, AE Aquarii, and RU Pegasi show that a star of this kind is a binary pair. The components, consisting of a red late-type dwarf or subgiant and a blue subdwarf of high density, each surrounded by gaseous envelopes, are very close together and have masses comparable to the sun. The period of revolution about their center of gravity is very short. If the extended atmospheres rotated with the stars, broad emission and absorption lines would result. The redder component is difficult to classify; absorption lines are usually veiled by the strong UV continuum and are probably also rotationally broadened. Spectroscopic parallaxes cannot be determined with any accuracy and trigonometric parallaxes are discordant, so that absolute magnitudes are uncertain. For SS Cygni, M_v lies between +4 and +9. U Geminorum stars are possibly a type intermediate between novae and normal stars.

21.7.2 Pulsating Stars

Pulsating stars are usually giants or supergiants; exceptions are the dwarf Cepheids and the δ Scuti variables. Characteristics of the principal groups of pulsating variables are given in Table 21-8. Figure 21-12 is an H-R diagram showing the locations of pulsating stars compared to the T Tauri stars and the very old stars that are members of globular clusters.

Pulsating stars regularly expand and contract; the source of the initial instability is not established. According to the simplest model of a pulsating gaseous sphere, the highest temperature, and hence maximum brightness, should occur at the time of greatest compression; that is, at minimum radius and zero radial velocity. *Light curves*, which are plots of magnitude vs phase of the period, and curves of the radial velocity vs phase do not as a rule support this simple model. Figure 21-13 shows the case of maximum brightening occurring at the maximum speed. In the β Canis Majoris variables, however, maximum brightness does correspond to minimum radius. In many pulsating stars multiple periodicity and corresponding beat-frequency phenomena are observed; possibly all pulsating stars have more than one mode of oscillation.

Neglecting perturbations such as damping and variations in density distribution, the period of the radial oscillation, P_o, depends upon the mean density, $\bar{\rho}$, according to the relation,

$$Q = P_o (\bar{\rho}/\rho_\odot)^{1/2}; \qquad (21\text{-}19)$$

Q is the *pulsation constant*. Q is different for different models of pulsating stars. Because the density distribution in different stars varies considerably, the mean density is useful only when comparing stars of the same density dis-

Table 21-8. Typical characteristics of some types of pulsating stars.

Type and Population		Period	Q_{obs}*	Approx. M_v	Amplitude (Δm)	Spectral Type	Cycle
Dwarf Cepheid	I	3^h	0.045	+2	1	A, F	Regular, multiple periods
δ Scuti	I	3^h	(0.041)	+2	0.1	F	Regular, multiple periods
β Canis Majoris	I	4^h	0.027	−3	0.1	B	Regular, multiple periods
RR Lyrae	II	0.5^d	0.075	0	1	A, F	Regular, multiple periods
Classical Cepheid	I	7^d	0.0365	−3	1	F, G	Regular
W Virginis	II	15^d	0.160	−2	1	F, G	Regular, but slow changes in periods
RV Tauri	II	75^d	0.25	−2	2	G, K	Some irregularity

* See Sec. 21.7.2.3; the value in parentheses is theoretical, see Eq. (21-19).

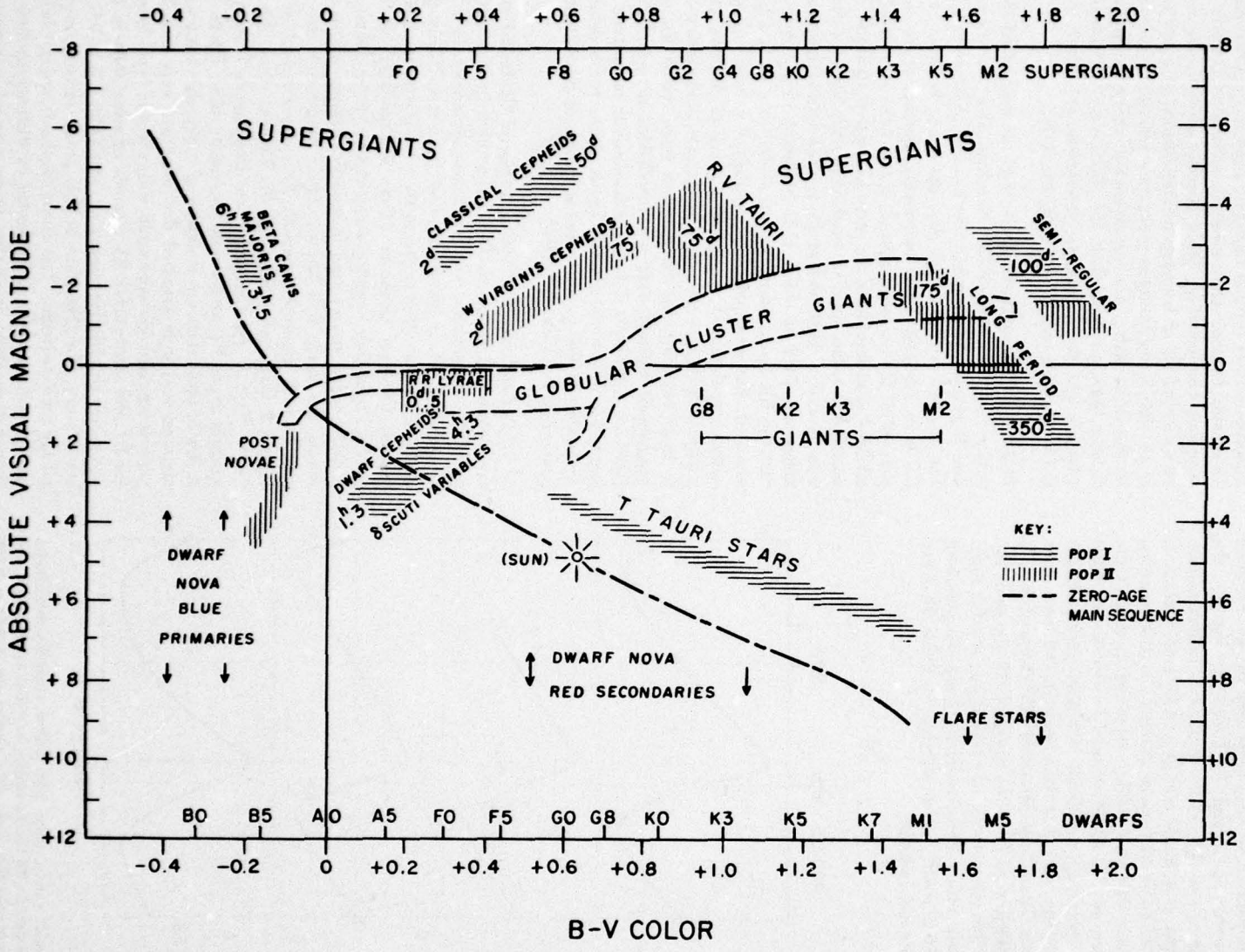


Fig. 21-12. H-R diagram of some groups of variable stars. Flare stars are on the main sequence but they are so faint (M_V is +8 to about +20) that they are mainly off-scale in this figure. The range of periods of the pulsating stars are given in hours (h) or days (d). The zero-age main sequence line and the location of the globular cluster are indicated for comparison. The location of supergiants is also indicated; it appears from recent measurements that all supergiants are slightly variable. (Figure by Gordon W. Wares.)

tribution. Factors that affect the pulsation constant are the variations of density with radius, the ratio of the specific heats, and, for very luminous stars, the radiation pressure.

It is customary to compute "observed" values, Q_{obs}, from determinations of M_v (adjusted by an assumed bolometric correction), and T_e. From M_v and T_e, the radius is calculated (Eq. 21-6). From this radius and an assumed mass, $\bar{\rho}$ is found and Q_{obs} calculated. Values of Q_{obs} given in Table 21-8 were obtained in this manner. However, there are no reliable values for masses of the variable stars, and T_e usually cannot be established from a spectrum (spectra are difficult to obtain, especially for a rapidly varying star), but must be estimated from color measurements. There is no empirical calibration of B — V color as a function of T_e in the range of RR Lyrae or the giant and supergiant stars; all calibrations are for main sequence stars which differ radically from the pulsating variables. As a result, values of Q_{obs} in Table 21-8 are indicative but not reliable.

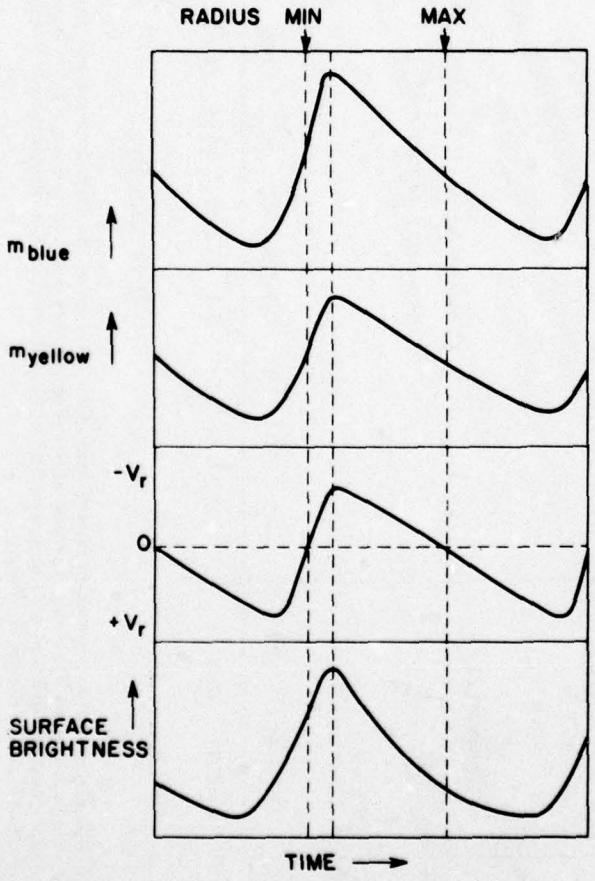


Fig. 21-13. Light curves (blue and yellow apparent magnitudes vs phase) compared with the variations in radial velocity (v_r) and in surface brightness with phase, for δ Cephei, the prototype of the classical Cepheids; note that negative radial velocity is toward the observer. (After L. Binnendijk, "Properties of Double Stars, A Survey of Parallaxes and Orbits," University of Pennsylvania Press, 1960.)

The concept that upward compression waves meet gases descending from the previous expansion is supported by the spectra from RR Lyrae. Observations during the steep rise of the light curves reveal a set of narrow HI Balmer absorption lines formed relatively high in the atmosphere (indicated by their sharpness) in gases that are still descending (indicated by their Doppler shift to the red), and a broad set of broadened lines formed at a low level in gas that is beginning to move outward again (indicated by the violet shift). The appearance of sharp, undisplaced Balmer lines corresponds to the shock-wave excitation of colliding gas flows. Similar phenomena are observed in the W Virginis and β Canis Majoris stars.

21.7.2.1 *RR Lyrae Stars.* These stars are also called *short period Cepheids* and *cluster variables.* They are Population II giants and are abundant in most globular clusters. The average period is 0.5 day, the range is from about 1.5 h to 1.5 day. Their luminosity appears to be independent of the pulsation period. It was once accepted that all RR Lyrae stars have the same absolute magnitude; the traditional value, used in establishing the distance scale, was $M = 0.0$. This had to be revised and current estimates are $+0.2$ or $+0.5$. It is becoming clear, however, that the RR Lyrae stars are not as uniform as had been assumed. For example, they encompass a range of ages within Population II, and hence a range of chemical composition; there may also be differences in composition due to local variations in the material from which the star condensed. Present data are insufficient to establish if there are significant differences in absolute magnitude between the disk and halo RR Lyrae stars; for a detailed discussion of this problem and a review of characteristic properties, see Preston [1964].

21.7.2.2 *Cepheids. W Virginis (Type II Cepheids)* stars are Population II giants. They occur both in and outside globular clusters, but are much less abundant than RR Lyrae stars. Their luminosity increases, from about that of the RR Lyrae stars to about $M_v = -3$, with increasing period. *Classical Cepheids (Type I Cepheids)* are obscured Population I supergiants located at great distances; recently a few were found in galactic clusters whose distances are fairly well known. Their luminosity also increases with increasing period. They are brighter by at least 1.5 magnitudes than the W Virginis stars. The *β Canis Majoris (β Cepheids)* are Population I stars of spectral types B1 to B3 and luminosity class III to IV. A few of these stars are members of relatively young associations, and it is assumed that none are very old. The periods are strongly correlated with spectral type, longest for B1 and shortest for B3. Periods of some stars in this group are steadily increasing at rates from 1.2 to 3.0 sec per century. Possibly stars in this group recently moved off the main sequence. The *dwarf Cepheids* are not bright enough ($M_v \approx +2$) to be useful as distance probes, although they show increasing luminosity with increasing period. P_o ranges from 0.05 day for spectral type A to 0.2 day for spectral type F. A double period is observed in many of these stars; in all cases the ratio of the second

period to P_o is 0.8 (within a few percent). δ Scuti was originally classified as a dwarf Cepheid, but is now considered the prototype of a very small group of stars located on the H-R diagram just to the right of the brighter dwarf Cepheids. These *δ Scuti variables* are distinguished by the large variety in the phase relationships between the light curves and radial velocities.

21.7.3 Novae and Supernovae

Novae and supernovae stars suddenly explode, throwing off shells which expand rapidly. There is a sudden enormous increase in luminosity lasting a few hours or days, followed by a decline lasting a few weeks, months, or even years, to their former magnitude. In a large galaxy such as ours, fifty ordinary novae may occur in a year, but on the average we observe only a few. Supernovae are more spectacular, but rare.

Novae are typically distant Population II stars that suddenly show an increase in brightness of 10 to 12 magnitudes over a period of several days. Shortly before and during maximum brightness, the spectra are similar to spectral type A and F supergiants. Immediately after maximum, bright bands appear and the absorption lines are displaced toward the violet. Gradually the spectrum becomes more complex; emission and absorption lines corresponding to high excitation and ionization appear. The emission bandwidths correspond to expansion velocities of 100 to 1000 km sec^{-1}. When the star eventually returns to pre-nova brightness, it is an underluminous blue star; its spectrum resembles the pre-nova spectrum, which often lack absorption and emission lines.

Supernovae are characterized by a sudden increase in brightness of 20 or more magnitudes. At maximum, the brightness may be comparable to that of an entire galaxy. Their decline is steeper than that for ordinary nova. They are rarely observed in the Milky Way galaxy. We have definite records of three, all of which were observed visually: the supernova of 1054, which was recorded by the Chinese in the position now occupied by the Crab Nebula, Tycho's "nova" of 1572, and Kepler's "nova" of 1604. Supernovae are observed in many other galaxies; estimates of the probable frequency vary from once in 100 yr to once in several hundred years. Supernovae are classified as Type I or Type II. Type I is a homogeneous group, but Type II is best described as including all supernovae that are not Type I.

Type I supernovae are the brightest; the average M_{pg} is −19. The light curves show a drop of about 2 or 3 magnitudes in 20 to 30 days, and about 4 magnitudes in roughly 100 days. After this, the decay is approximately exponential; the half-life during exponential decay is roughly 40 to 100 days. The gaseous envelope may be about 0.1 solar masses and is ejected at 1000 to 2000 km sec^{-1}. Type I supernovae are probably Population II stars.

Type II supernovae are not as bright at maximum as Type I; the average M_{pg} is between −17 and −18. The initial decline is less steep and the final decline is steeper than in Type I. They are found predominantly in the arms of spiral galaxies, and are thought to be Population I stars.

Spectroscopic data on either type are scarce. The few spectra obtained show broad features most of which cannot be identified. The mass ejected in Type I supernovae is estimated as between 1% and 10% of the original mass. In Type II supernovae, estimates range from 10% to as high as 90% of the original mass.

21.8 DETERMINATION OF STELLAR DISTANCES

The determination of distances to remote objects is still a fundamental problem. The distance to nearby stars can be calculated directly by trigonometric parallax. If the probable error is taken as 0.005 sec of arc for a star whose measured parallax is 0.01 sec of arc, there is a 50% probability that the star lies between 67 and 200 parsec. Thus, for measuring distances of remote stars, indirect methods must be used. These indirect methods depend on statistical calculations or determinations of absolute magnitude. Equation (21-2) or (21-16) is then used to calculate the distance.

21.8.1 Parallax and Proper Motion

Trigonometric parallax is defined as the angle, p, subtended at the star by the mean radius of the earth's orbit; actually, p is calculated from measurements of the star's angular displacement on the celestial sphere from positions on opposite sides of the earth's orbit. By definition, a star with parallax of one second of arc is at a distance of one parsec, so

$$1/p = r, \qquad (21\text{-}20)$$

where p is in seconds of arc and r is the distance to the star in parsecs. (Distances in parsecs do not depend on the numerical value adopted for the astronomical unit, as do distances in units of light years.)

The distance to a star can be found by using as the base line the distance the sun travels in 1 yr due to its peculiar motion, if the direction of the star's own motion is known. Generally it is not possible to determine whether an observed small proper motion results from small tangential velocity at relatively close distance, or from a large tangential velocity at a great distance, because the direction of the velocity vector usually is not known.

Some galactic clusters are *moving clusters;* all members of the group move with equal velocities parallel to one another in space. For example, the stars of the Hyades are receding from the sun toward an apparent convergent point on the celestial sphere about 26° from their present location. Because the direction through space of this motion is known and because the individual stars have large proper motions, the distances to stars in the Hyades are determined independently and with high accuracy from observations of the radial velocities and proper motions. These values do not depend on an H-R diagram or assignment of an absolute magnitude according to luminosity class. Moving clusters, however, are generally so far away

that satisfactory observations of the proper motions are not obtainable. For a sufficiently large group, it is assumed that the peculiar motions of individual stars are random and that, on the average, the radial components are as large as the tangential. A statistical determination of a representative mean distance is made by assigning large tangential velocities to stars with small proper motions but large radial velocities. This mean distance for the group of stars is the *statistical parallax*.

21.8.2 Spectroscopic Methods

If the apparent luminosity of a Population I star is such that a spectrum can be obtained, the absolute magnitude may be estimated from its classification in the MK system (Table 21-3). If a high dispersion spectrum can be obtained, the absolute magnitude can be determined from the intensity ratios of luminosity sensitive lines (Sec. 21.4.1). Distances calculated by using in Eq. (21-2) or (21-16) values of absolute magnitude determined in this manner are called *spectroscopic parallaxes*. A method which applies to spectral type G, K, and M stars uses absolute magnitudes derived from the internal structure of the H and K absorption lines of CaII (Sec. 21.4.1). The amount of the Doppler red-shift is also used as an indication of the distance of galaxies for which spectra can be obtained.

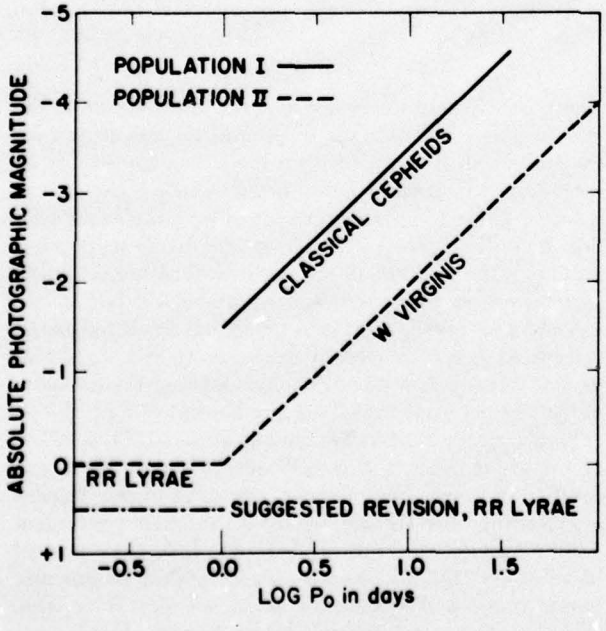


Fig. 21-14. Period-luminosity relation. Absolute photographic magnitude midway between maximum and minimum vs logarithm of the period in days. The traditional value of $M_{pg} = 0.0$ for the RR Lyrae stars is shown; suggested revisions are +0.2 and +0.5. (After O. Struve and V. Zebergs, "Astronomy of the 20th Century," The Macmillan Company, New York, 1962.)

21.8.3 The Period-Luminosity Relation

Observations of some types of pulsating stars established an empirical relation between the period of pulsation and the intrinsic luminosity of certain types of these stars. Figure 21-14 shows a simplified version of the traditional period-luminosity relation. The method of determining distances of very remote objects depends upon absolute magnitudes derived from such relations. In essence, the period and apparent magnitudes of the variable star are observed, and M is found from a period-luminosity relation. If the interstellar absorption is known or can be estimated, the distance is calculated by Eq. (21-2) or (21-16); otherwise the distance modulus is used as an indicative distance.

The crucial problem is in establishing a calibration for the absolute magnitude scale; relative values are reliable, but an error of ± 1.5 in assigning the zero point halves or doubles the distances calculated. No star of the classical Cepheid or the W Virginis type is close enough to measure the distance by trigonometric parallax and thus determine the absolute magnitude directly. None has yet been found in a moving cluster for which the distance is fairly well established. In the past, the only method available was basing the absolute magnitude scale on distances determined by statistical parallaxes. Studies of the few classical Cepheids recently found in galactic clusters for which spectroscopic parallaxes are known are beginning to provide more reliable data.

21.8.4 The Distance Scale

By 1950 it became obvious that the zero point for the classical Cepheids or for the RR Lyrae variables was wrong. Subsequent adjustment of the zero point for the classical Cepheids (magnitudes increased by −1.5) resulted in two separate relations (Fig. 21-14) and doubled the distances previously accepted for objects outside our Galaxy. Even this revision is inadequate. The confused status of the distance scale is recognized and redeterminations are in progress. A tentative correction to Hubble's 1936 distance moduli (m − M) for galaxies in the local group is +2.3 magnitudes (absolute magnitudes were underestimated); for galaxies beyond the local group an additional +1.8 magnitudes (total +4.1) may be necessary.

21.9 GALAXIES

The following brief discussion is intended only to introduce the nomenclature and symbols used in literature; for a comprehensive review of classification and morphology, see de Vaucouleurs [1959]. *Nebula* is the traditional name for a cloudy or misty celestial object. The original nebulae are now recognized as diffuse or planetary galactic nebulae, unresolved globular clusters, and other galaxies. Galaxies are still called *extragalactic nebulae*, and the spiral galaxies are called *spiral nebulae*.

Galaxies are identified according to the number assigned in catalogues of nebulae compiled in the 19th century; M for Messier's, NGC for the New General Cata-

logue. This results in multiple designations: M31, the Andromeda nebula, is also NGC224; M32 is NGC221, etc. The small-scale distribution of galaxies is not random; there is a marked tendency toward occurrence in systems of two or more. Some appear to be isolated in space, but more often they seem to be part of a physical group. The Milky Way galaxy belongs to the *local group*, which consists of at least 17 galaxies within a diameter of 10^6 parsec (about 3×10^6 l.y.). Among the local group are: the two Magellanic Clouds (companions to our galaxy); the Andromeda nebula, with four companions; and the dwarf elliptical galaxies, Sculptor and Fornay, which have the population type and appearance of a low-concentration globular cluster but are of galactic dimensions.

Hubble's classification, with some variations, is the most generally used method of classifying according to form [Sandage, 1961]. I designates an irregular galaxy such as the Small or the Large Magellanic Cloud, S is a normal spiral, SB is a barred spiral (arms curving from diametrically opposite ends of a bar extending from the nucleus), and E is an elliptical galaxy. The spirals are subdivided into types Sc, Sb, and Sa (or SBc, etc.); each type has successively greater amounts of Population II stars and more tightly wound arms. Hubble includes, between the spirals and ellipticals, a type SO; these contain very little dust and have no arms, but do have a definite central nucleus. Shapley's system omits SO and subdivides the spirals into types Sd through Sa, and the elliptical galaxies into types E7 through E0, according to decreasing eccentricity (zero for type E0). It was once thought that the various types might form an evolutionary sequence beginning with the irregular galaxies and proceeding through the spirals and the ellipticals. A more recent suggestion is that the various galactic types may reflect differences in initial conditions of formation rather than a purely evolutionary sequence.

In the Yerkes Y and Y′ systems of classification, stellar population and composite spectra are taken into account as well as form. There is a direct correlation between the apparent concentration of luminosity toward the center of a galaxy and the spectral class of the integrated radiation from the mixture of stars and other objects in the galaxy. Morgan [1958 and 1959] gives a detailed Y system classification of all 1250 galaxies brighter than magnitude +13.1 in the Shapley-Ames Catalogue and north of declination −25°. The I, S, B, and E of the Hubble classification are retained, and additional symbols are introduced. The Y′ system is a highly simplified version of the Y system, see Morgan [1962]. Examples of the variety of classification are: the Andromeda nebula is classified in the Y′ system as 6S, whereas in the Y system it is gkS5, and in Hubble's system it is Sb; NGC5194, the Whirlpool nebula, is 4S or fgSl or Sc; NGC4565 is 6S or gkS7 or Sc.

21.10 REFERENCES

Allen, C. W., 1963, Astrophysical Quantities, 2nd ed., University of London, The Athlone Press, London.

Aller, L. H., 1963, "Astrophysics; The Atmospheres of the Sun and Stars," 2nd ed., The Ronald Press Company, New York.

Burbidge, E. M., G. R. Burbidge, W. A. Fowler, and F. Hoyle, 1957, "Synthesis of the Elements in Stars," *Revs. Mod. Phys.*, v. 29, no. 4, p. 547.

de Vaucouleurs, G., 1959, General Physical Properties of External Galaxies, "Handbuch der Physik," v. 53, S. Flügge, ed., Springer-Verlag.

Greenstein, J. L., ed., 1960, "Stellar Atmospheres," University of Chicago Press, Chicago.

Johnson, H. L., and W. W. Morgan, 1953, "Fundamental Stellar Photometry for Standards of Spectral Type on the Revised System of the Yerkes Spectral Atlas," *Astrophys. J.*, v. 117, no. 3, p. 313.

Kraft, R. P., 1959, "On the Variation of the K2 Emission Width as a Function of Absolute Visual Magnitude in the Spectra of Late-Type Stars," *Ann. Astrophys.*, v. 22, p. 164.

Moore, C. E., 1949 et seq., "Atomic Energy Levels," *National Bureau of Standards Circular No. 467*, and "Ultraviolet Multiplet Tables," *National Bureau of Standards Circular No. 488;* U.S. Government Printing Office, Washington, D.C.

Morgan, W. W., 1962, "Some Characteristics of Galaxies," *Astrophys. J.*, v. 135, no. 1.

Morgan, W. W., 1958 and 1959, "A Preliminary Classification of the Forms of Galaxies According to Their Stellar Population, Part I," *Publ. Astron. Soc. Pacific*, v. 70, pp. 364-391, Part II, *Publ. Astron. Soc. Pacific*, v. 71, pp. 394-411.

Morgan, W. W., P. C. Keenan, and E. Kellman, 1943, "An Atlas of Stellar Spectra," University of Chicago Press, Chicago.

Münch, G., and H. Zirin, 1961, "Interstellar Matter at Large Distances from the Galactic Plane," *Astrophys. J.*, v. 133, no. 1, p. 11.

Preston, G. W., 1964, RR Lyrae Stars, "Annual Review of Astronomy and Astrophysics, Vol. 2," L. Goldberg, ed., Annual Reviews, Inc., Palo Alto.

Sandage, A., 1961, "The Hubble Atlas of Galaxies," Publication No. 618, Carnegie Institution of Washington.

Schwarzschild, M., 1958, "Structure and Evolution of Stars," Princeton University Press, Princeton, N. J.

Strand, K. A., ed., 1963, "Basic Astronomical Data," University of Chicago Press, Chicago.

Walker, R. G., 1964, "Celestial Background Radiation: 1. A Revised Scale of Bolometric Corrections," *Air Force Surveys in Geophysics No. 155 (1)*, AFCRL.

Chapter 22

RADIO ASTRONOMY

N. H. Dieter
J. P. Castelli
D. W. Ushakoff

Radio astronomy is the branch of astronomy concerned with the passive reception of radiation in radio wavelengths from extraterrestrial sources. The science is new and subject to the uncertainties of youth in instrumentation, observation, and theory; it is a growing field with new developments occurring so rapidly that no summary of progress can long escape obsolescence. Two aspects of this subject are the study of the sources of radiation and the study of the effects produced by the terrestrial atmosphere on the radiation received. For solar radio astronomy, see Sec. 16.3.

Many types of radio telescopes are in use at present; they include steerable and fixed paraboloids, cross arrays, and multi-element interferometers. The trend in design responds to three main astronomical requirements: increased collecting area for the study of faint sources, increased angular resolution for accurate position finding and fine mapping, and increased precision in antenna pointing. For lists of the paraboloid radio telescopes, their properties and locations, see Bracewell [1961].

22.1 FUNDAMENTAL CONCEPTS AND DEFINITIONS

All observations in radio astronomy consist of the measurement of an antenna temperature and the conversion of that temperature to a measure of power received from the source.

The term equivalent, or apparent, blackbody temperature, used to describe a radio source, means that the radiation received is of the same magnitude as that which would be received from an ideal radiator (blackbody, see Appendix B) at this temperature, subtending the same solid angle as the source producing the observed radiation. The temperature of the source may be of thermal or unknown origin; only if the source radiates as a true blackbody will its physical temperature equal the apparent blackbody temperature.

In any electrical conductor or resistor, there are small voltage fluctuations due to internal random motion. The ordinary random (thermal) motion of electrons and ions is the equivalent of random varying electric currents; for moving charges radiate electromagnetic waves at all frequencies. The average value of these thermal fluctuations is zero; the spectral density, $GV(f)$, is given by

$$GV(f)\,\Delta f = 4\,RkT\,\Delta f, \qquad (22\text{-}1)$$

where Δf is bandwidth, R is resistance, k is Boltzmann's constant, and T is temperature in °K. *Johnson noise* is the noise generated in a resistor so matched to a circuit that there is no flow of current. The power of the Johnson noise from this matched resistor at temperature T is

$$P = kT\,\Delta f. \qquad (22\text{-}2)$$

The relation between Johnson noise and thermal noise is as follows. A resistor is connected to an antenna where the radiation impedance is the same as the resistor; the connection is made through a transmission line that is also matched to the resistor and antenna. Then, if the antenna is surrounded by a blackbody at the same temperature as the resistor, the thermal radiation from the blackbody will be transmitted to, and completely absorbed by, the resistor. Johnson noise in the resistor will be transferred to, and completely absorbed by, the blackbody. Since the temperatures of the resistor and the blackbody are equal, the power from each is the same.

The measure of the power of the beam of radiation intercepted by the antenna is the *antenna temperature*, T_A; the antenna is receiving power, P_A, equivalent to that from a resistor at the temperature T_A. The defining equation is

$$P_A = kT_A\,\Delta f. \qquad (22\text{-}3)$$

Johnson-noise power per unit frequency is frequency independent, and blackbody radiation power per unit frequency is proportional to f^2 (Rayleigh-Jeans approximation, see Appendix B), but thermodynamic balance of the two sources is achieved because the antenna becomes more directive at higher frequencies. As the frequency increases, the antenna accepts radiation from a decreasing solid angle. The average absorption cross section, $\bar{A}$, of an antenna such as a parabola is

$$\bar{A} = \lambda^2/4\pi = c^2/4\pi f^2. \qquad (22\text{-}4)$$

When the product of the brightness per unit bandwidth [radiant emittance per unit frequency, see Eq. (B-5)]

and the antenna cross section is integrated over the receiver bandwidth and antenna solid angle, the f^2 terms cancel. Hence, an antenna surrounded by or immersed in a blackbody reservoir at a constant temperature will have a constant power output independent of frequency.

The *power flux density* (power per unit bandwidth per unit area) is a function of source brightness per unit bandwidth, $B(\phi, \theta)$, the antenna pattern, and the solid angle subtended by the source. A unit of power flux density, S, frequently used is the Jansky, which is one W m^{-2} $(cps)^{-1}$. The Rayleigh-Jeans approximation for *brightness (radiance) per unit bandwidth*, B_f, as a function of brightness (blackbody) temperature, T_s, is valid in the radio region, so that

$$B_f = 2kT_s f^2/c^2 = 2kT_s/\lambda^2. \quad (22\text{-}5)$$

Thus, the power flux density for a source that subtends a small solid angle, Ω_s, is

$$S = 2kT_s\Omega_s/\lambda^2. \quad (22\text{-}6)$$

The *apparent power flux density* is

$$S_A = 2kT_A/A_{em} = 2kT_A\Omega_A/\eta_r\lambda^2, \quad (22\text{-}7)$$

whereas the true power flux density is

$$S = 2kT_A\,(L)/A_{em}, \quad (22\text{-}8)$$

where L is an antenna correction factor $\left(\dfrac{\Omega_s}{\iint_{source} f(\phi, \theta)\, d\Omega}\right)$ which must be used when θ_H, the antenna half-power beamwidth, is less than five times the angular diameter of the source. For θ_H greater than five times, the apparent flux is essentially the true flux.

The brightness, or average disk temperature, is

$$T_s = T_A\Omega_A/\eta_r\Omega_s. \quad (22\text{-}9)$$

The antenna temperature is fundamentally

$$T_A = \frac{1}{4\pi}\iint T(\phi, \theta)\, D(\phi, \theta)\, d\Omega, \quad (22\text{-}10)$$

where $T(\phi, \theta)$ is the sky brightness distribution, $D(\phi, \theta)$ is the antenna directivity function, and $d\Omega$ is $\sin\theta\, d\theta\, d\phi$. The antenna temperature of a source can be found by a differential method, using drift technique. If $T_s(\phi, \theta)$ is the brightness temperature distribution of the source, and $f(\phi, \theta)$ is the normalized antenna pattern,

$$T_A = \frac{\eta_r\eta_\Omega}{\Omega_M}\iint_{source} T_s(\phi, \theta)\, f(\phi, \theta)\, d\Omega. \quad (22\text{-}11)$$

The antenna radiation efficiency is

$$\eta_r = R_r/(R_r + R_L); \quad (22\text{-}12)$$

R_r is the radiation resistance, and R_L the ohmic loss.

The antenna beam solid angle efficiency, η_Ω, represents the degree of concentration of radiated power in the region of the main lobe;

$$\eta_\Omega = \xi_A A_{phy}\Omega_M/\eta_r\lambda^2 = \Omega_M/\Omega_A. \quad (22\text{-}13)$$

The stray factor is $1 - \eta_\Omega$.

Ω_M is the antenna main lobe solid angle, that is, to the first minimum. For Gaussian response

$$\Omega_M = \theta_H^2\,(1.1133)/3280 \text{ [steradian]}, \quad (22\text{-}14)$$

and for Bessel function response,

$$\Omega_M = \theta_H^2\,(1.008)/3280 \text{ [steradian]}. \quad (22\text{-}15)$$

θ_H, the antenna half-power beamwidth, is the width of main lobe at half-power point; in these equations it is in angular degrees. Ordinarily, θ_H is determined experimentally by drifts, but a simple approximation is

$$\theta_H = 70°/D_\lambda. \quad (22\text{-}16)$$

Ω_A, the antenna solid angle, is the solid angle through which all power radiated by the antenna would flow if the radiation intensity equalled its maximum value over the solid angle of the antenna;

$$\Omega_A = \eta_r\lambda^2/A_{em} = \iint_{4\pi} f(\phi, \theta)\, d\Omega. \quad (22\text{-}17)$$

The antenna aperture efficiency is

$$\xi_A = A_{em}/A_{phy}. \quad (22\text{-}18)$$

A_{phy} is the physical area, and A_{em}, the antenna maximum effective area, is

$$A_{em} = \eta_r\lambda^2/\Omega_A = G_m\lambda^2/4\pi, \quad (22\text{-}19)$$

where G_m is the maximum gain. The directivity is

$$D_m = G_m/\eta_r = 4\pi/\Omega_A. \quad (22\text{-}20)$$

An equatorial antenna mount is constructed so that one axis is perpendicular to, and one parallel to, the earth's axis. The *drift technique* utilizes a stationary antenna, and the source passes through the antenna beam as the earth rotates.

22.2 EFFECTS OF THE EARTH'S ATMOSPHERE

22.2.1 Refraction

The deviation of electromagnetic waves in the lower atmosphere is influenced by the pressure of dry air, water vapor, and temperature (see Chapter 9). There is greater refraction at radio wavelengths than in the microwave region because the index of refraction of the ionosphere varies inversely with the square of the frequency. In general the refraction decreases as altitude increases. Because of local irregularities, however, refraction at a given elevation may be slightly greater in some cases than at a lower angle; there are variations from day to day and during the course of one day.

22.2.2 Scintillation

At some frequencies, the intensity of signals received from discrete sources is not steady but exhibits fluctuations or scintillations. Fluctuations in the microwave region are of long period and seem to originate in the troposphere. At frequencies from 60 to 400 Mcps, ionospheric scintillations are always present at elevations less than three degrees. In general, the number and amplitude of the scintillations vary inversely with some power of the frequency; scintillations at higher frequencies are much less noticeable than at lower frequencies.

The magnitude and the number of ionospheric scintillations seem to depend on magnetic activity. On occasion, during periods of intense magnetic disturbance, an inversion occurs; the higher frequency records show more scintillations than the lower frequency records [Kidd et al, 1962]. It appears that inversion is strongly localized and temporary. The ordinary scintillations are well correlated at different frequencies, but the scintillations present in the inversion show a phase difference in the signals at different frequencies. Ordinary scintillations probably result from single scattering by an area of different electron density and refractive index than the surrounding media; inversion is probably the result of multiple scattering by irregularities in the atmosphere.

22.2.3 Absorption

Energy from radio sources is absorbed and scattered by molecular oxygen and water vapor in the atmosphere, particularly at short cm and mm wavelengths. At 8.7 mm, absorption is about equally due to water vapor and oxygen. At longer wavelengths, the major part of the absorption is by oxygen, whereas at shorter wavelengths absorption is primarily by water vapor.

Figure 22-1 shows attenuation as a function of frequency. The amount of attenuation depends upon the elevation and the zenith angle at which the readings are taken, the temperature, and the amount of water vapor present. Attenuation is increased by decreasing the elevation or by increasing the zenith angle at which the readings are taken. Attenuation is also increased by an increase in temperature and water vapor content of the atmosphere.

22.3 RADIO EMISSION FROM THE MOON AND PLANETS

The planets for which observations at radio frequency are available at present are Mercury, Venus, Earth, Mars, Jupiter, and Saturn; for references to the original papers prior to 1961, see Kuiper and Middlehurst [1961]. Radiation of thermal origin is detectable out to wavelengths of tens of centimeters. In addition to thermal radiation, there is a nonthermal component of radiation from Earth and Jupiter. Studies of the thermal component permit investigation of thermodynamic properties of the planetary ionospheres, atmospheres, and surfaces. Studies of the nonthermal component permit investigation of the origin, time variations, and precipitation of fast trapped particles from magnetic radiation belts.

22.3.1 The Moon

The lunar thermal emission at 1.25 cm is maximum at about 3½ days after full moon. The lag between the phases of radio emissions and the visible lunar phase is greater at mm wavelengths; little or no delay is found at longer wavelengths. Because the phase of the subsurface temperature variation will lag the phase of the surface temperature variation and the visible lunar phase, it was deduced from these observations that the lunar surface is partially transparent to radio waves. During lunation, large temperature changes in emissions at 4 to 15 mm are found; no significant change has been observed at 20 cm.

Attempts to observe variations of lunar temperature during lunar eclipses revealed no significant changes in temperature at wavelengths above about 7 mm. Observations at 4.3 mm (eclipse of August 25, 1961) showed a change from 232°K during the eclipse to 238°K one hour after the eclipse.

There are two components in the lunar radiation. The constant component is the time average of the radio emission; a variable component is superimposed on this constant component. There is no strong dependence on wavelength in the constant component. Observations, some of which are given in Table 22-1, indicate that the time average of the radio-brightness temperature at the center of the moon's disk is about 210°K.

22.3.2 The Planets

The observable characteristics of planetary radio radiation are the intensity, the polarization, and the direction of arrival of the waves. Because of the low resolving power of radio telescopes, emission from different regions of the planetary disk cannot be resolved. In the centimeter and decimeter wavelength range, the contribution of reflected solar radiation is a negligible addition to the planetary radiation.

Steady radiation, of presumably thermal origin, is observed from Venus at 3.15 and 9.4 cm, from Mars and Jupiter at 3.15 cm, and from Saturn at 3.75 cm. The high intensity of radio emission from Venus suggests that the surface of the planet is at a very high temperature; however, it is possible that the radiation may be a combina-

Table 22-1. Radio brightness temperature of moon at center of disk, T_c, or averaged disk, T_d.

Wavelength (cm)	Temperature (°K)
0.43	$T_c = 232$ to 238
0.86	$T_c = 145$ to 225
3.15	$T_c = 195 - 12\ (\pm 5) \cos [\omega t - 44\ (\pm 15)]$*
9.7	$T_d = 223 \pm 11$
25	$T_d = 230 \pm 16$
75	$T_d = 185$ (constant to 10%)

* ωt is degrees from new moon.

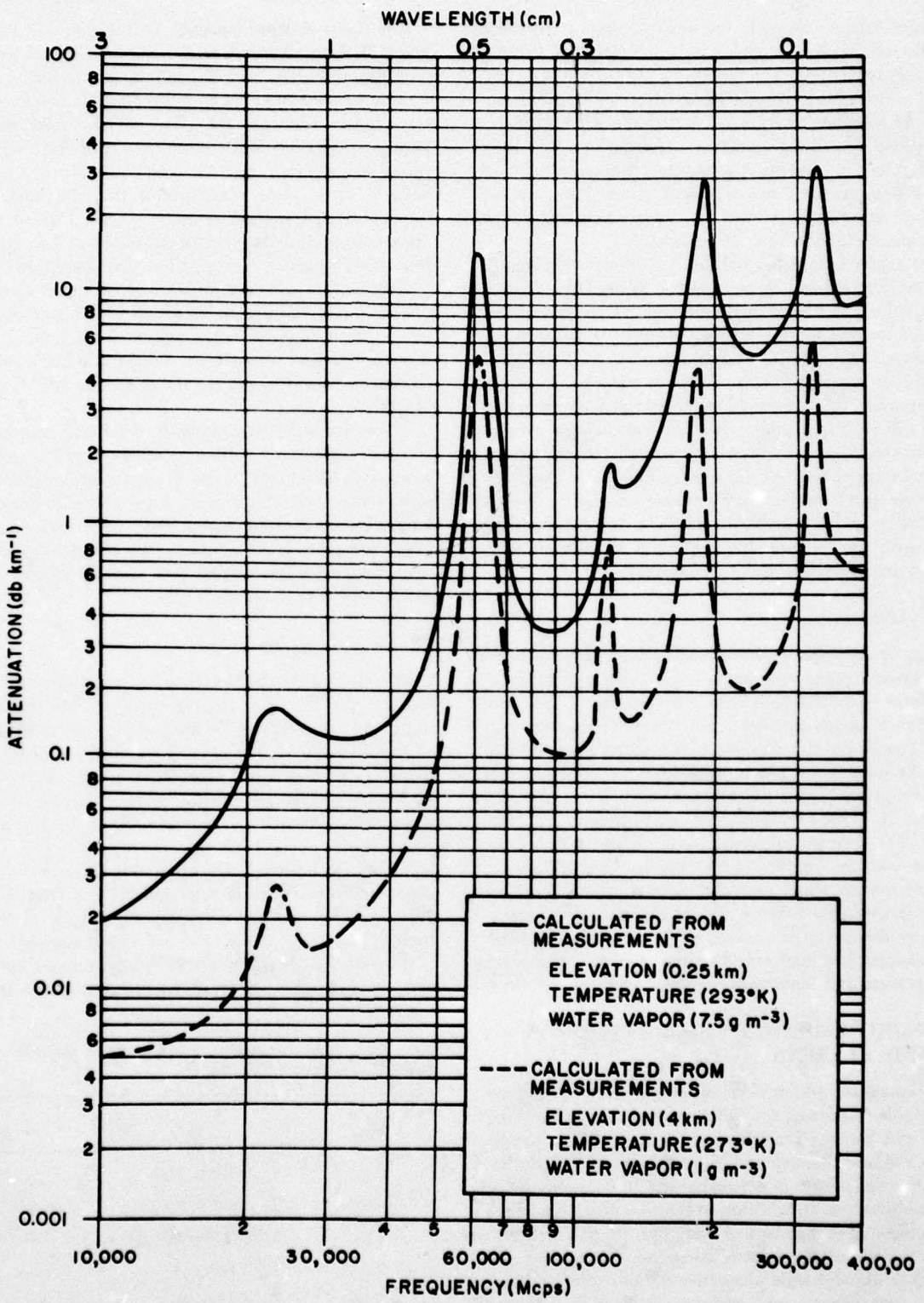


Fig. 22-1. Attenuation, calculated from measurements, by combined water vapor and oxygen. (After C. W. Tolbert, A. W. Straiton, J. H. Douglas, *Electrical Engineering Lab. Rept. No. 104*, University of Texas, 1958.)

tion of thermal and nonthermal components. Jupiter's spectrum is definitely not that of a blackbody radiator; the radiation received from this planet probably is a combination of thermal and nonthermal components. The radiation from Mars and Saturn seems to be of thermal origin. Because of the distances, small diameters, or low temperatures, the thermal radiation from the remaining planets is expected to be of very low intensity. There have been no attempts yet to measure their radio emission.

22.3.2.1 *Mercury.* Observers at the University of Michigan, using the 85-ft radio telescope, detected radio emission from Mercury for the first time; at 3-cm wavelength they found a temperature of 400°K ±40% [Miller, 1961].

22.3.2.2 *Venus.* The average equivalent blackbody disk temperature, determined from the radio emission, is 550°K near inferior conjunction and 600°K about a month before and after conjunction. Some observers, however, do not find this variation with phase [Drake, 1962]. Venus emits radiation at cm wavelengths with a blackbody spectrum corresponding to about 580°K. At 8 mm, temperatures are observed to be in the 300° to 400°K region. Because the atmosphere of Venus is relatively transparent to cm wavelength radiation, and the carbon dioxide and water vapor cause little absorption, radiation at these wavelengths may originate at or near the planetary surface. At mm wavelengths, the carbon dioxide and water vapor in the atmosphere cause more absorption; therefore, the radiation may originate at higher levels in the atmosphere.

22.3.2.3 *Mars.* Only two observations of radio emissions are presently available. In September 1956, observations at 3.15 cm gave an apparent blackbody disk temperature of 218 ±50°K. From observations at 3.14 cm in November 1958, the apparent blackbody temperature was 211 ±20°K. It is theorized that the radio radiation may come from below the surface of Mars as it does with the moon. Perhaps a variation in temperature with wavelength is caused by varying depths below the surface of Mars where the radiations may arise.

22.3.2.4 *Jupiter.* Radio emission from Jupiter has been observed at many wavelengths. The apparent blackbody temperature increases with wavelength from about 150°K at 3 cm to 50,000°K at 68 cm. There are also indications of long-time changes in radio emission. Some, but not all, observations indicate changes in emission as a function of rotation. At 31 cm, the radiation is about 30% linearly polarized with the electric vector approximately parallel to Jupiter's equator. Also, the diameter of the source seems to be larger than the diameter of Jupiter; the source of polarization is consistent with an equatorial ring about three times the diameter of Jupiter.

In general, there seem to be three different types of radio emission from Jupiter. At very short cm wavelengths, emission is predominantly thermal radiation from the atmosphere. At decimeter wavelengths, the predominant source is nonthermal and may be radiation from relativistic charged particles trapped in Jupiter's magnetic field; the discovery of the polarized ring about Jupiter at 31 cm lends support to this theory. At very long wavelengths (near 15 m), emissions are short intense bursts resembling interference; the cause is unknown.

22.3.2.5 *Saturn.* Emission from Saturn observed at 3.75 cm gave an antenna temperature of only 0.04°K; the observations indicated that the rings do not emit 3.75-cm radiation as efficiently as the body of the planet. More recent observations at 3.4 cm yielded an apparent blackbody disk temperature of 106 ±21°K, neglecting any possible radiation from the rings.

22.4 SOURCES OF RADIO EMISSIONS

22.4.1 Maps of Background Radiation

Many surveys have been made at various frequencies of the background radio emission from the sky, and maps have been compiled. Figures 23-2 through 23-6 show five of these maps, ranging in frequency from 38 to 960 Mcps. The maps are Mercator projection with coordinates right ascension and declination (Sec. 21.2.2.2). Observations made with a particular radio telescope may not agree exactly with the maps because of differences in antenna

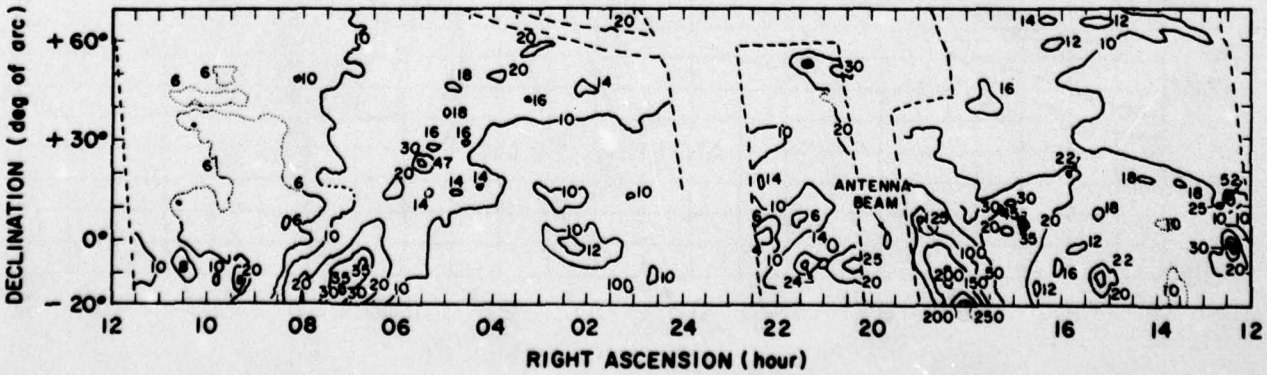


Fig. 22-2. Background radiation at 38 Mcps. (From J. H. Blythe, *Monthly Notices of the Royal Astron. Soc.*, v. 117, no. 6, p. 652, 1957, by permission.)

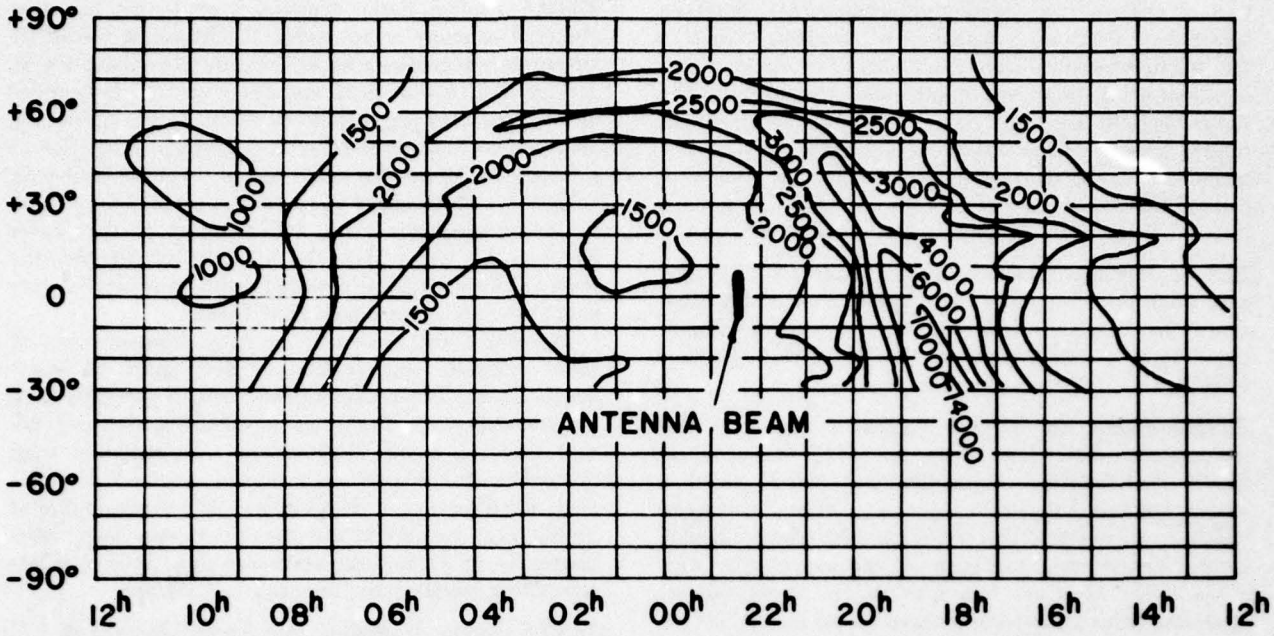


Fig. 22-3. Background radiation at 81 Mcps; contour units are °K. (From J. D. Kraus and H. C. Ko, *Scientific Rept. No. 1*, Radio Observatory, Department of Electrical Engineering, Ohio State University, 1957.)

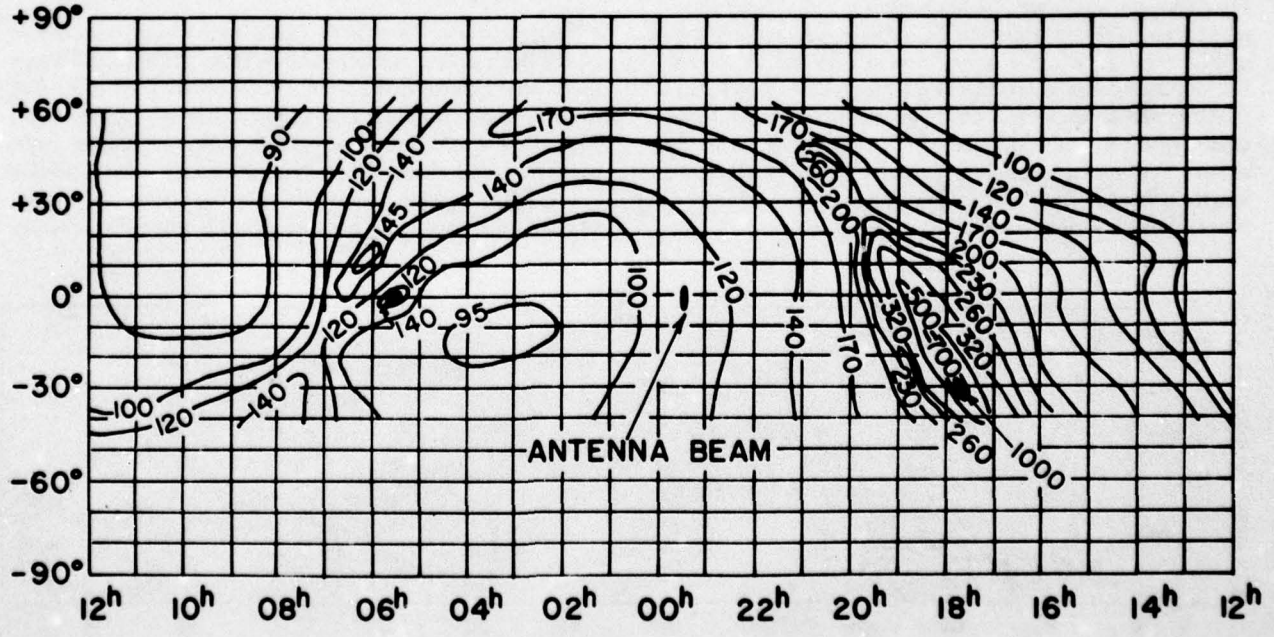


Fig. 22-4. Background radiation at 250 Mcps, as observed by Kraus and Ko, Ohio State University; contour units are °K.

size and shape, receiver sensitivity, and values of absolute calibration. These maps show that most of the radio emission background is due to radiation from the galactic plane. It increases toward the galactic center with the coldest regions near the galactic poles.

22.4.2 Discrete Sources

In addition to background radio radiation from the entire sky, certain areas emit additional radiation; these are called discrete radio sources. Several thousand discrete sources, covering a wide range in intensity, have been discovered. Discrete sources with an angular extent of a degree or more are called extended sources. Sources of smaller angular extent are localized sources; sufficiently small ones are point sources.

The flux density of discrete sources is strongly dependent upon frequency. Sources for which the flux density decreases with increasing frequency are called nonthermal; those for which the flux density increases with increasing frequency are called thermal. Most discrete radio sources are nonthermal.

The five brightest discrete sources are Cassiopeia A, Cygnus A, Taurus A, Virgo A, and Centaurus A; they are all of nonthermal origin. Their positions, in right ascension and declination for 1960, and angular diameters are given in Table 22-2. Table 22-3 lists the flux densities of the sources at various frequencies. Because the data in this field are expanding rapidly, the current literature should be consulted. As a guide, references from which this material was taken are listed in Sec. 22.7.2. Figures 22-7 through 22-11 show the flux density vs frequency; note that the ordinate is $23 + \log S$, where S is the flux density in units of $W\ m^{-2}\ (cps)^{-1}$.

22.5 HYDROGEN 21-CM LINE

In addition to the radiation that covers a broad band of frequencies, radiation of one spectral line is observed

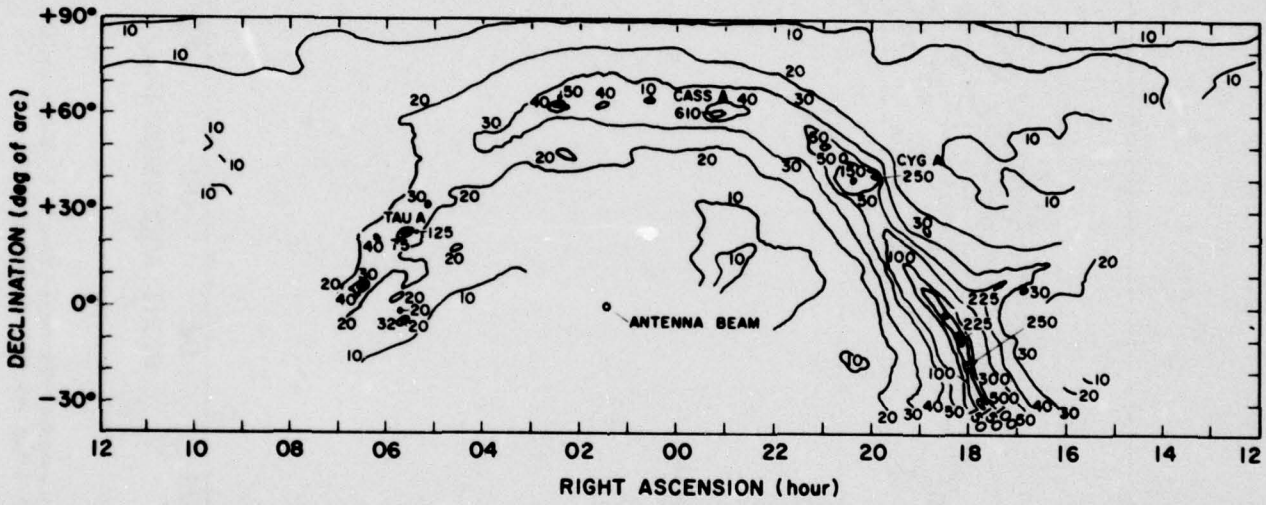


Fig. 22-5. Background radiation at 400 Mcps. (After C. L. Seeger, F. L. H. M. Stumpers, and N. van Hurck, *Philips Tech. Review*, v. 21, no. 11, 1959-1960.)

Table 22-2. Positions and angular diameters of the five brightest discrete sources.

Source	Right Ascension h	m	s	Declination (deg)	(min)	Position (deg E of N)	Angular Diameter (min)	Comments
Cassiopeia A	23	21	38.9	58	35.4	0 90	3.5 3.8	Circularly symmetrical
Cygnus A	19	58	05.3	40	36.6		0.7 each	2 sources, intensity ratio 1.2/1, separation 1.58 min for major axis at 109°
Taurus A	05	32	07.6	21	59.6	0 90	3.3 3.7	Radiation concentrated in inner mass of Crab Nebula
Virgo A	12	28	48.4	12	36.8	core halo	0.6 6.5	Core surrounded by halo which contributes 48% of the flux
Centaurus A	13	23	05.1	−42	49.3	0 90	3.8 2.0	2 sources, approx. equal intensities, separation of 7.1 min at 46°; extended sources 3° by 8°

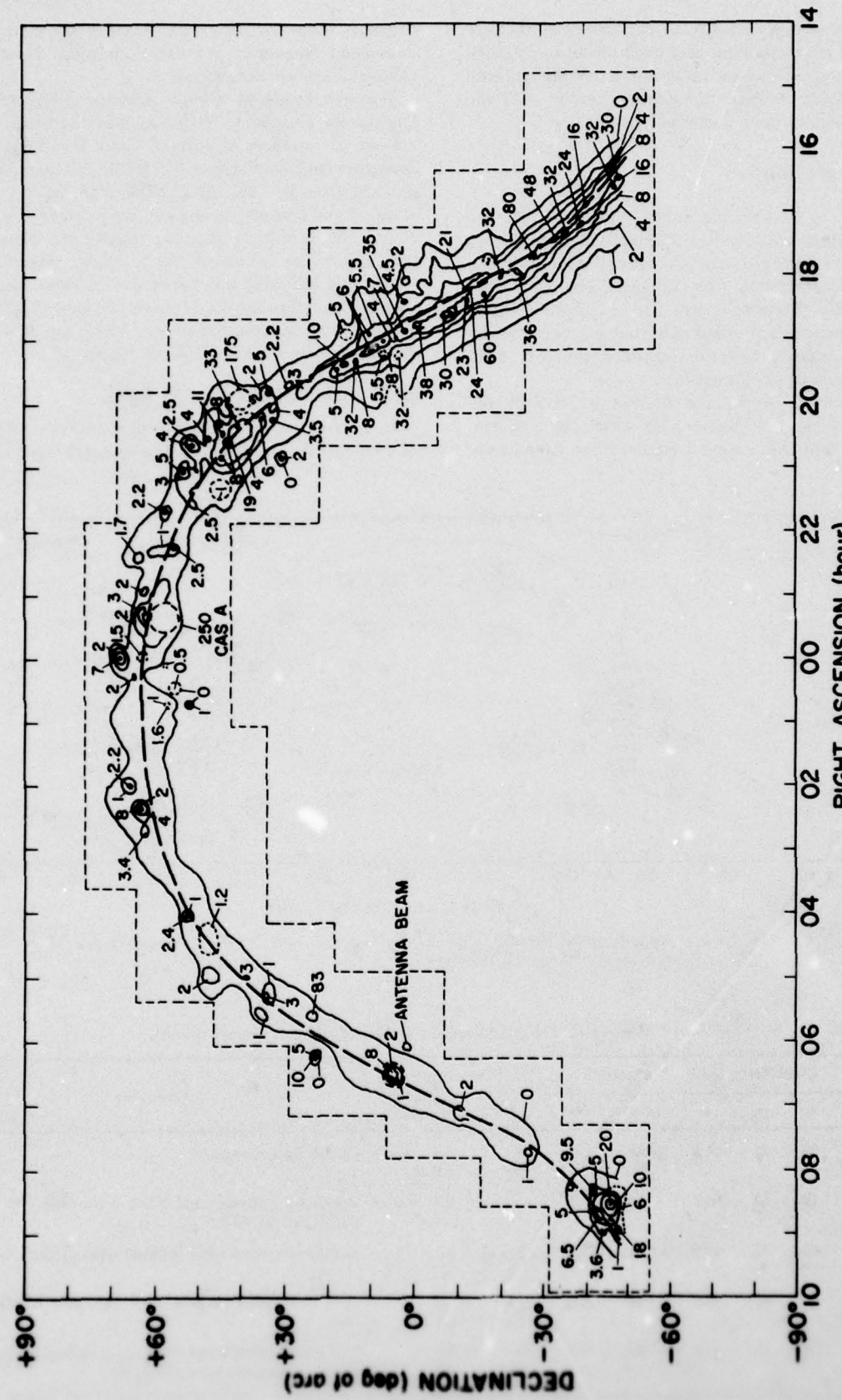


Fig. 22-6. Background radiation at 960 Mcps. (From R. W. Wilson, and J. A. Bolton, *Publ. Astron. Soc. Pacific*, v. 72, no. 428, p. 331, 1960, by permission.)

in the microwave region. This is the 21-cm wavelength line of interstellar neutral atomic hydrogen, which results from transitions between the hyperfine levels of the ground state. The rest frequency is 1420.4056 Mcps. Because the energy difference between the levels is so small (5.6×10^{-6} eV), the line can be observed in emission even at the low temperature of interstellar space, which precludes emission at optical wavelength energies. The maximum brightness temperature determined from 21-cm observations is 125°K. The extreme weakness of the radiation, however, requires special techniques with exceptionally sensitive and stable receivers to detect this line. Attempts to observe the corresponding line of deuterium at 9.6 cm so far have not been successful.

The 21-cm line is an extremely useful tool for the study of the large scale structure of our galaxy. Hydrogen line radiation is strongly concentrated toward the galactic plane, reflecting the concentration of interstellar hydrogen gas. Galactic rotation broadens the line, in some cases as much as 800 kcps, which corresponds to a radial velocity broadening of about 170 km sec^{-1}. This rotational broadening makes it possible to study the distribution and motion of neutral hydrogen at large distances from the sun. The interstellar hydrogen is concentrated in fairly discrete regions in the spiral arms (Sec. 21.5). With the advent of more sensitive receivers and larger antennas, it is now possible to extend the observations of emission to other galaxies and to study both the structure and motions within galaxies that are relatively nearby and the overall motion and amount of neutral hydrogen present in the more distant galaxies.

In addition to studies based on the emission from hydrogen atoms, several cases of absorption have been discovered. The interstellar hydrogen in the path between some of the continuum radio sources and the earth produces an absorption line in the spectrum of the source similar to those caused by interstellar calcium and sodium in the optical range.

The current literature must be consulted to obtain valid information on this rapidly developing research. Groups at Leiden, Holland, Sydney, Australia, and Harvard College Observatory are especially active in this field. In addition to such journals as the Astronomical Journal, the Astrophysical Journal, and the Australian Journal of Physics, some of the other sources of information are: the Bulletin of the Astronomical Institutes of the Netherlands; Publications of the National Radio Astronomy Observatory; Observations of the California Institute of Technology Radio Observatory; and Scientific Reports, Radio Observatory, Department of Electrical Engineering, Ohio State University.

22.6 OH LINE AT 18 CM

The first detection of a microwave line other than the hydrogen line was achieved by Weinreb et al [1963] with the observation of the lines at 1665 and 1667 Mcps of the hydroxyl (OH) radical. The measurement was made in the absorption spectrum of Cas A at velocities near those measured in the hydrogen line spectrum. This opens a new area of research in the study of the interstellar gas.

Table 22-3. Flux density vs frequency.

Frequency (Mcps)	Flux Density ($W\ m^{-2}\ cps^{-1} \times 10^{-26}$)
Cassiopeia A	
81.5	23,200
81.5	22,000
82	23,200
100	17,000
158	9300
159	13,000
178	11,000
440	6310
750	4119
915	3150
960	3120
1200	2820
1390	3100
1400	2500
2930	1240
3000	1360
3200	1500
3200	1340
8000	620
Cygnus A	
60	22,000
81.5	13,500
81.5	14,200
82	14,000
100	12,500
101	13,000
158	5700
159	8600
178	8100
440	4800
750	2990
915	2500
960	2150
1200	1860
1390	1900
1400	1550
1400	1900
2930	630
3000	665
3200	700
3200	710
8000	232
Taurus A	
60	1850
81.5	1850
81.5	1250
82	1850
100	1900
100	1850
101	1900
159	1500
160	1850
178	1420
440	1240
960	1030
1200	955
1390	1120
1400	910
1400	1120
2930	670
3000	699
3200	800
3200	680
8000	464
Virgo A	
18.3	11,000
60	2500
81.5	1700
81.5	1050
82	1700
100	1250
101	1200
159	1100
178	970
440	574
750	356
960	300
1200	242
1390	254
1400	210
1400	210
2930	100
3000	105
3200	140
8000	44
Centaurus A	
19.7	28,000*
60	3200
85.5	8700*
100	1850
100	1600
101	1600
440	1110
440	6750*
960	1800
1200	381
1200	1240*
1400	310
2930	160*
3200	200
8000	40

* Value corrected for source size.

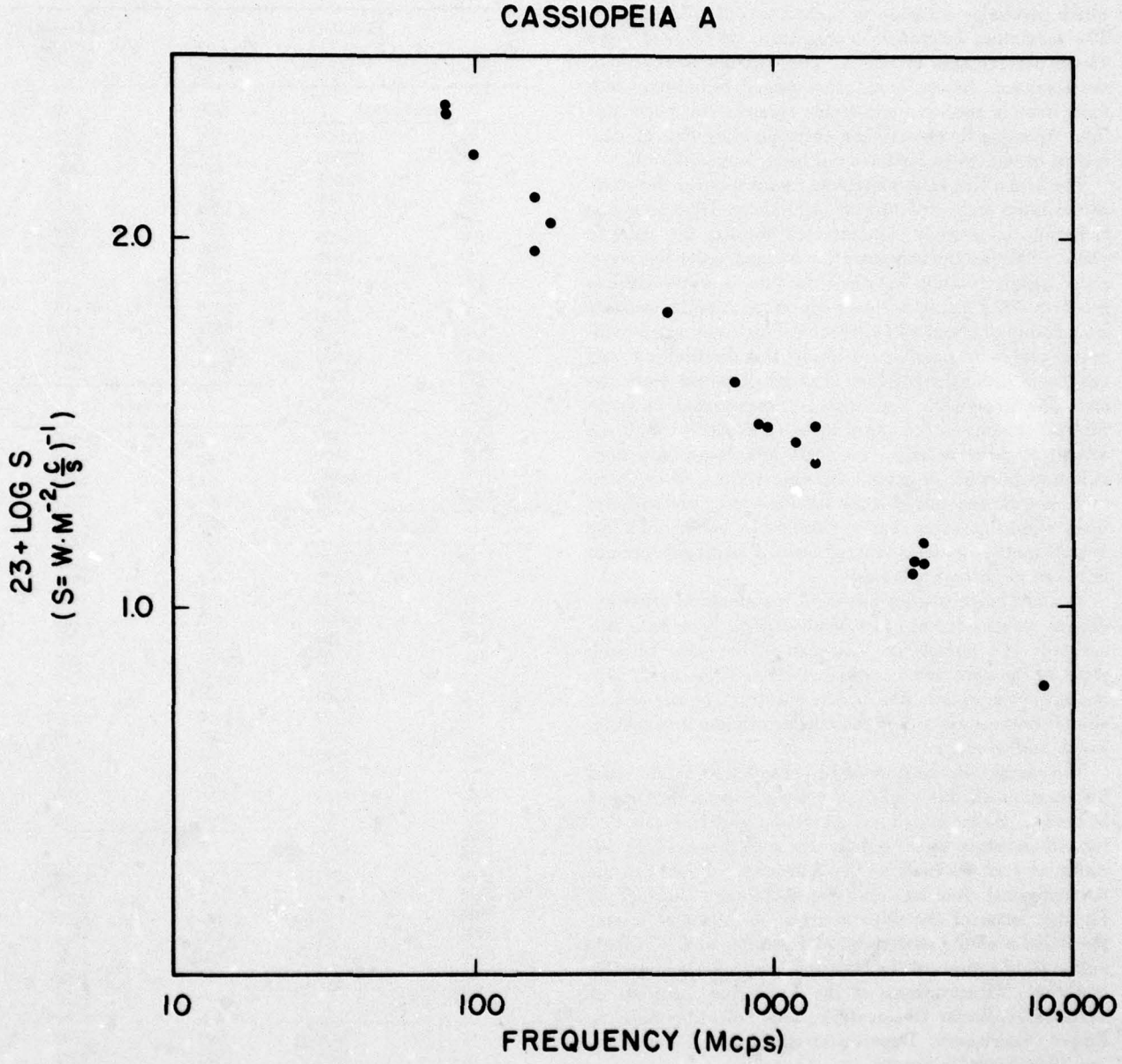


Fig. 22-7. Spectrum of the radio source Cassiopeia A; the flux density, S, is in W m^{-2} cps^{-1}.

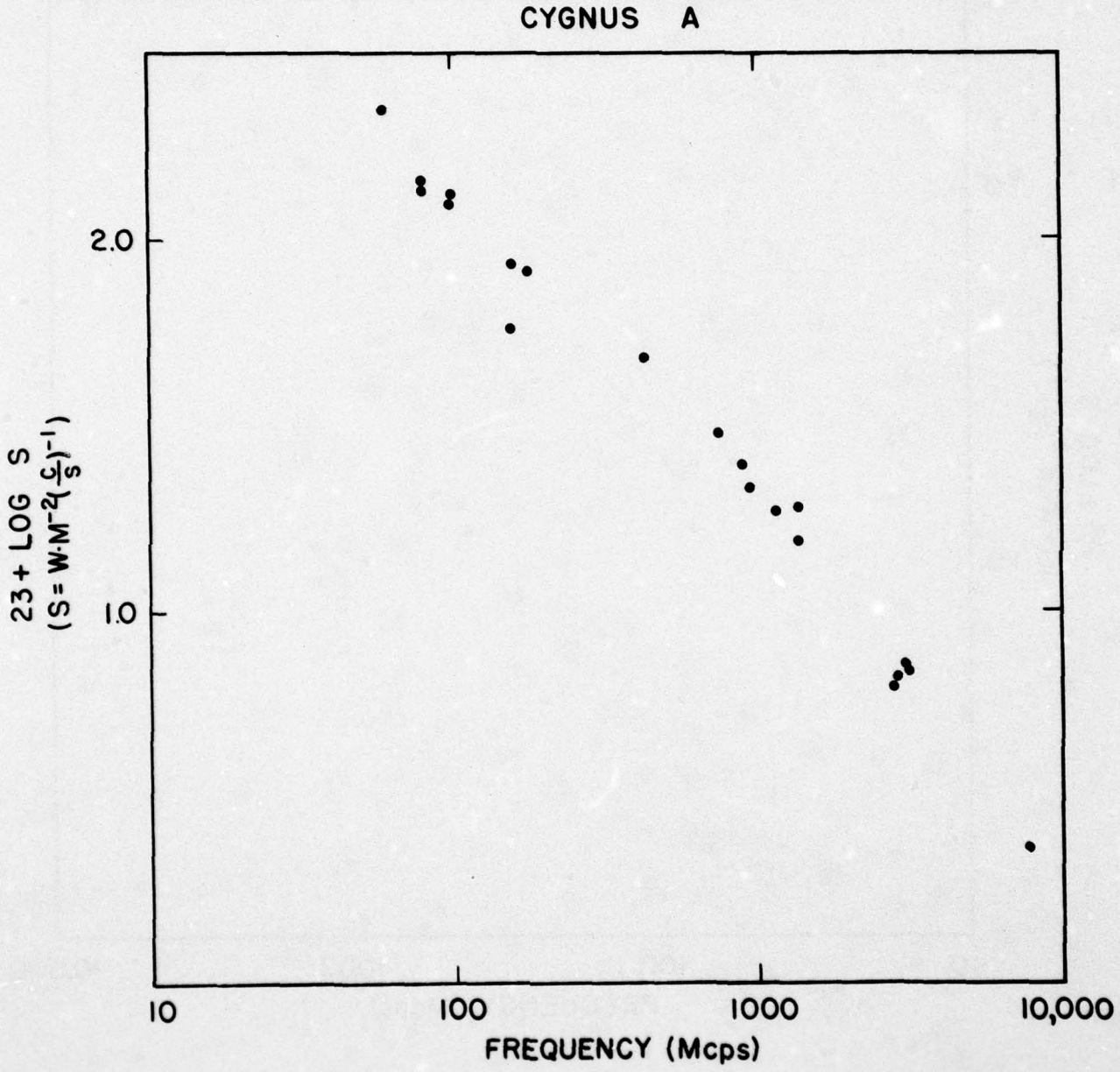


Fig. 22.8. Spectrum of the radio source Cygnus A; the flux density, S, is in W m^{-2} cps^{-1}.

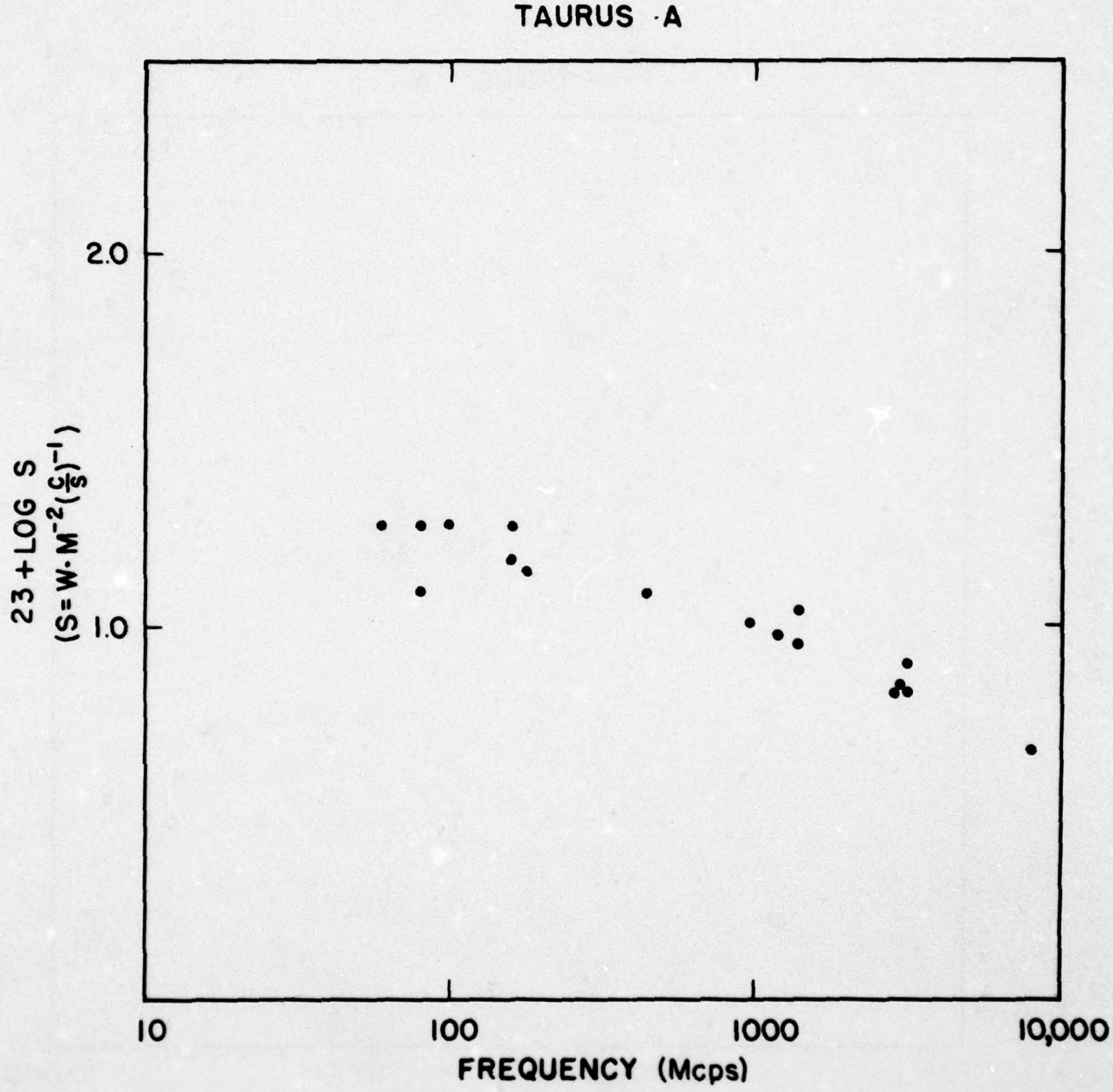


Fig. 22-9. Spectrum of the radio source Taurus A; the flux density, S, is in W m⁻² cps⁻¹.

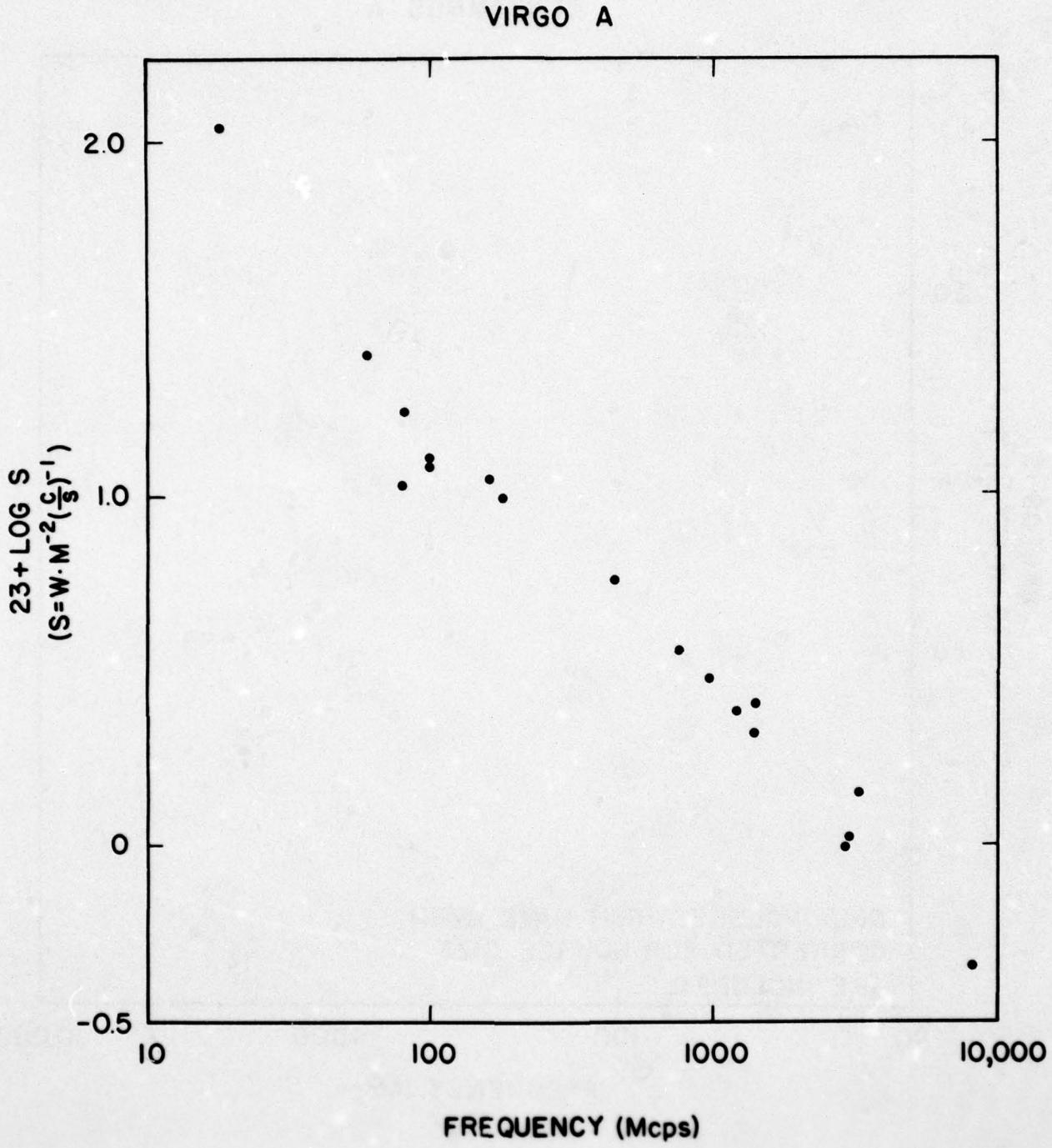


Fig. 22.15. Spectrum of the radio source Virgo A; the flux density, S, is in W m^{-2} cps^{-1}.

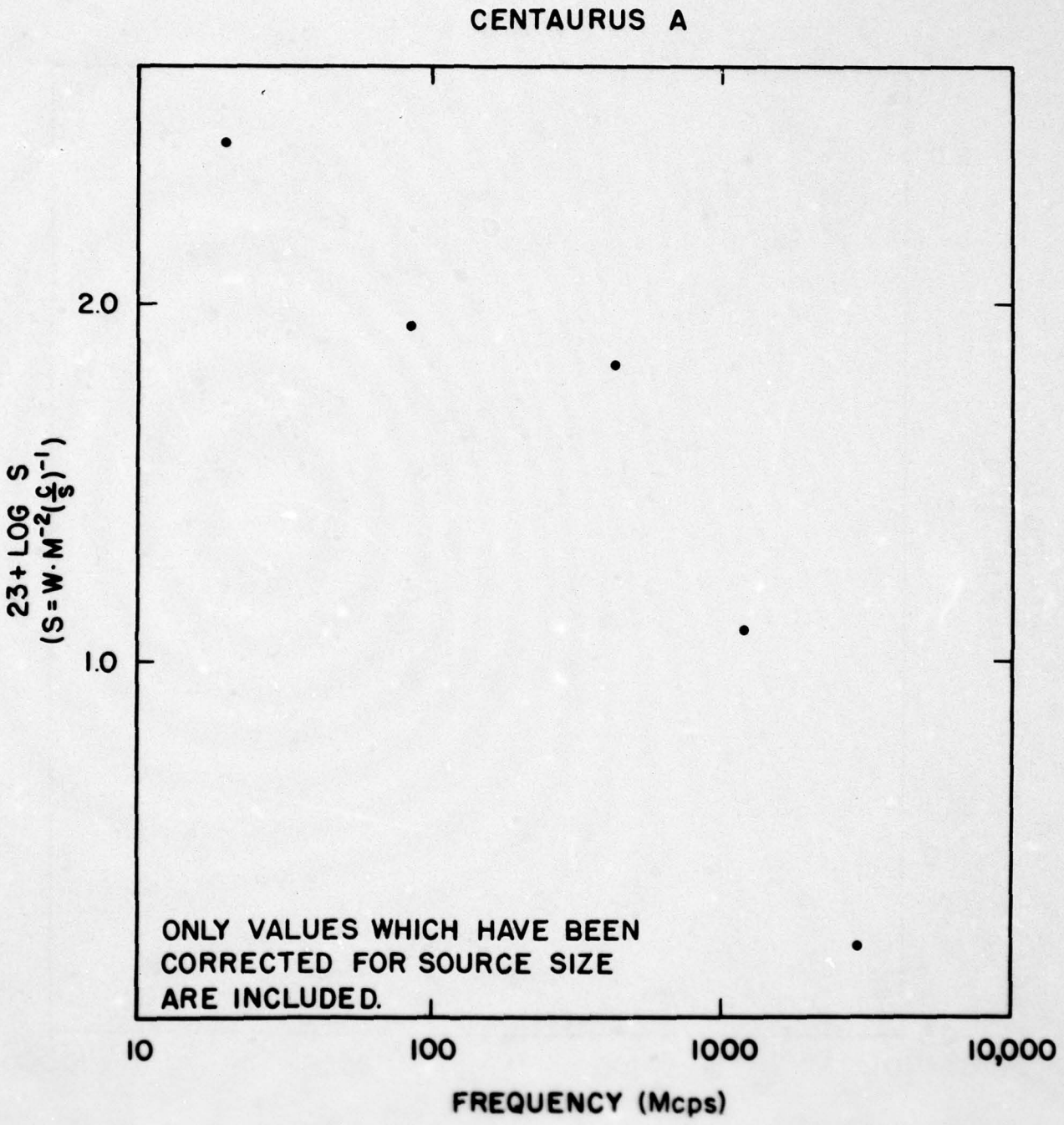


Fig. 22.11. Spectrum of the radio source Centaurus A; the flux density, S, is in W m^{-2} cps^{-1}.

22.7 REFERENCES

22.7.1 Cited References

Bracewell, R. N., 1961, "Radio Telescopes Today and Tomorrow," *IRE Student Quart.*, v. 7, no. 4.

Drake, F. D., 1962, "10 Centimeter Observations of Venus in 1961," *Publ. Natl. Radio Astron. Obs.*, v. 1, no. 11, p. 165.

Kidd, W., H. Silverman, H. Whitney, and J. Aarons, 1962, "Scintillations of Radio Stars and Satellites During Intense Magnetic Disturbances," *Nature*, v. 193, p. 1246.

Kuiper, G. P., and B. M. Middlehurst, eds., 1961, "The Solar System, Vol. III: Planets and Satellites," University of Chicago Press, Chicago.

Miller, F. D., 1961, "The Observatories of the University of Michigan," *Astron. J.*, v. 66, p. 458.

Weinreb, A. H. Barrett, M. L. Meeks, and J. C. Henry, 1963, *Nature*, v. 200, p. 829.

22.7.2 Uncited References on Radio Sources

Broten, N. W., and W. J. Medd, 1960, "Absolute Flux Measurements of Cassiopeia A, Taurus A, and Cygnus A at 3200 Mcs," *Astrophys. J.*, v. 132, p. 279.

Edge, D. O., J. R. Shakeshaft, W. B. McAdam, J. E. Baldwin, and S. Archer, 1959, "A Survey of Radio Sources at a Frequency of 159 Mcs," *Mem. Royal Astron. Soc.*, v. 68, p. 37.

Elsmore, B., M. Ryle, and P. R. R. Leslie, 1959, "The Positions, Flux Densities, and Angular Diameters of 64 Radio Sources Observed at a Frequency of 178 Mcs," *Mem. Royal Astron. Soc.*, v. 68, p. 60.

Heeschen, D. S., 1961, "Radio Observations of Galaxies," *Publ. Natl. Radio Astron. Obs.*, v. 1, no. 9, p. 132.

Heeschen, D. S., 1961, "Observations of Radio Sources at Four Frequencies," *Astrophys. J.*, v. 133, no. 1, p. 322.

Maltby, P., and A. T. Moffet, 1962, "Brightness Distribution in Discrete Radio Sources: The Structure of the Sources," *Astrophys. J. Suppl.*, no. 67.

Shain, C. A., 1958, "The Radio Emission from Centaurus A and Fornax A," *Australian J. Phys.*, v. 11, no. 4, p. 517.

Sheridan, K. V., 1958, "An Investigation of the Strong Radio Sources in Centaurus, Fornax, and Puppis," *Australian J. of Phys.*, v. 11, no. 3, p. 400.

Sloanaker, R. M., and J. H. Nichols, 1960, "Positions, Intensities, and Size of Bright Celestial Sources at a Wavelength of 10.2 cm," *Astron. J.*, v. 65, p. 109.

Westerhout, Gart, 1958, "A Survey of the Continuous Radiation from the Galactic System at a Frequency of 1390 Mcs," *Bull. Astron. Institutes Netherlands*, v. 14, no. 488, p. 215.

APPENDIX A

UNITS, CONSTANTS, AND CONVERSION FACTORS

Table A-1. Some units defined by the International Committee of Weights and Measures. (After *NBS Technical News Bulletin*, October 1963, and *Physics Today*, v. 15, no. 6, June 1962.)

Meter (m)	1,650,763.73 wavelengths in vacuo of the unperturbed transition $2p_{10}$—$5d_5$ in Kr^{86}
Kilogram (kg)	mass of the international kilogram at Sèvres, France
Second (s)	* 1/31,556,925,9747 of the tropical year at 12^h ET, 0 January 1900
Ampere (A)	that constant current intensity which, when maintained in two parallel rectilinear conductors of infinite length and negligible circular cross section placed at mutual distance 1 m apart in vacuo, will produce between these conductors a force per unit length of 2 N m^{-1}.
Degree Kelvin (°K)	defined in the thermodynamic scale by assigning 273.16°K to the triple point of water (freezing point, 273.15°K = 0°C)
Unified atomic mass unit (u)	1/12 the mass of an atom of the C^{12} nuclide
Mole (mol)	amount of substance containing the same number of molecules as there are atoms in 12 g of pure C^{12}.
Normal atmospheric pressure (atm)	101,325 N m^{-2} (kg m^{-1} s^{-2})
Standard acceleration of free fall (g_n)	9.80665 m s^{-2}

* The International Committee of Weights and Measures authorized an atomic definition of the second (at 1725 Paris time, 8 October 1964), based temporarily on an invariant transition of atomic cesium in anticipation of a more exact definition in the future.

Table A-2. Multiples and submultiples of units.

Factor	Symbol	Prefix
10^{12}	T	tera
10^9	G	giga
10^6	M	mega
10^3	k	kilo
10^2	h	hecto
10	da	deka
10^{-1}	d	deci
10^{-2}	c	centi
10^{-3}	m	milli
10^{-6}	μ	micro
10^{-9}	n	nano
10^{-12}	p	pico
10^{-15}	f	femto
10^{-18}	a	atto

APPENDIX A

Table A-3. Values for physical constants recommended by the U. S. National Academy of Sciences and U. S. National Bureau of Standards. (From *NBS Technical News Bulletin*, October 1963.)

Constant		Value	Est. Δ Error Limit	Système International (MKSA)		Centimeter-gram-second (CGS)	
Speed of light in vacuum	(c)	2.997925	3	$\times 10^{8}$	$m\ s^{-1}$	$\times 10^{10}$	$cm\ s^{-1}$
Elementary charge	(e)	1.60210 4.80298	7 20	10^{-19}	C	• 10^{-20} † 10^{-10}	$cm^{1/2}\ g^{1/2}$ $cm^{3/2}\ g^{1/2}\ s^{-1}$
Electron rest mass	(m_e)	9.1091	4	10^{-31}	kg	10^{-28}	g
Charge-to-mass ratio for electron	(e/m_e)	1.758796 5.27274	19 6	10^{11}	$C\ kg^{-1}$	• 10^{7} † 10^{17}	$cm^{3/2}\ g^{-1/2}$ $cm^{1/2}\ g^{-1/2}\ s^{-1}$
Proton rest mass	(m_p)	1.67252	8	10^{-27}	kg	10^{-24}	g
Neutron rest mass	(m_n)	1.67482	8	10^{-27}	kg	10^{-24}	g
Planck constant	(h)	6.6256	5	10^{-34}	J s	10^{-27}	erg s
Avogadro constant	(N_A)	6.02252	28	10^{23}	mol^{-1}	10^{23}	mol^{-1}
Gas constant	(R)	8.3143	12	1	$J\ °K^{-1}\ mol^{-1}$	10^{7}	$erg\ °K^{-1}\ mol^{-1}$
Normal volume of perfect gas	(V_0)	2.24136	30	10^{-2}	$m^3\ mol^{-1}$	10^{4}	$cm^3\ mol^{-1}$
Boltzmann constant	(k)	1.38054	18	10^{-23}	$J\ °K^{-1}$	10^{-16}	$erg\ °K^{-1}$
Second radiation constant	(c_2)	1.43879	19	10^{-2}	m °K	1	cm °K
Wien displacement constant	(b)	2.8978	4	10^{-3}	m °K	10^{-1}	cm °K
Stefan-Boltzmann constant	(σ)	5.6697	29	10^{-8}	$W\ m^{-2}\ °K^{-4}$	10^{-5}	$erg\ cm^{-2}\ s^{-1}\ °K^{-4}$
Gravitational constant	(G)	6.670	15	10^{-11}	$N^2\ m^2\ kg^{-2}$	10^{-8}	$dyn\ cm^2\ g^{-2}$

• Electromagnetic system.
† Electrostatic system.
Δ Estimated error is applied to last digits of the value; it is based on 3 standard deviations.

Table A-4. Energy conversion factors. (After *NBS Technical News Bulletin*, October 1963.)

Unit	Factor	Multiply by for result in MKSA		CGS	
Electron-volt	1.60210	10^{-19}	$J\ (eV)^{-1}$	10^{-12}	$erg\ (eV)^{-1}$
Energy associated with:					
Electron rest mass, m_e	5.11006	10^{5}	$eV\ m_e^{-1}$	10^{5}	$eV\ m_e^{-1}$
Proton rest mass, m_p	9.38256	10^{8}	$eV\ m_p^{-1}$	10^{8}	$eV\ m_p^{-1}$
Neutron rest mass, m_n	9.39550	10^{8}	$eV\ m_n^{-1}$	10^{8}	$eV\ m_n^{-1}$
Unified atomic mass unit, u	9.31478	10^{8}	$eV\ u^{-1}$	10^{8}	$eV\ u^{-1}$
Quantum-charge ratio (h/e)	4.13556	10^{-15}	eV sec	10^{-15}	eV sec
Wavelength (ch/e)	1.23981	10^{-6}	eV m	10^{-4}	eV cm
Cycle (e/h)	2.41804	10^{14}	$(eV)^{-1}\ sec^{-1}$	10^{14}	$(eV)^{-1}\ sec^{-1}$
Wave number (e/ch)	8.06573	10^{5}	$(eV)^{-1}\ m^{-1}$	10^{3}	$(eV)^{-1}\ cm^{-1}$
$°K\left(\frac{e}{k}\right)$	1.16049	10^{4}	$°K\ (eV)^{-1}$	10^{4}	$°K\ (eV)^{-1}$

Table A-5. Conversions for electromagnetic formulas. Expressions in mixed units (e.g., Gaussian) must be converted to purely electrostatic (subscript s) or purely electromagnetic (subscript m) before substitution.

	CGS		MKSA
Charge:	Q_s	$\longleftrightarrow$	Q
	$^{\bullet}Q^2_s$	$\longrightarrow$	$Q^2/4\pi\epsilon_o$
	Q_m	$\longleftrightarrow$	Q
	$^{\bullet}Q^2_m$	$\longrightarrow$	$Q^2\mu_o/4\pi$
	$^{\bullet}Q^2_m c^2$	$\longrightarrow$	$Q^2/4\pi\epsilon_o$
Permittivity, vacuum	$(1)/4\pi$	$\longleftarrow$	ϵ_o
Permeability, vacuum	$4\pi(1)$	$\longleftarrow$	μ_o
Field Vectors:	E_s	$\longleftrightarrow$	E
	D_s	$\longleftrightarrow$	$4\pi D$
	B_m	$\longleftrightarrow$	B
	H_m	$\longleftrightarrow$	$4\pi H$
Electric Polarization,	P_s	$\longleftrightarrow$	P
Magnetic Flux,	Φ_m	$\longleftrightarrow$	Φ
Magnetic Pole,	m_m	$\longleftrightarrow$	$m/4\pi$
Magnetic Polarization,	J_m	$\longleftrightarrow$	$J/4\pi$
Magnetization,	M_m	$\longleftrightarrow$	M

* In vacuum, and when permittivity in esu is assumed equal to one or permeability in emu is assumed equal to one.

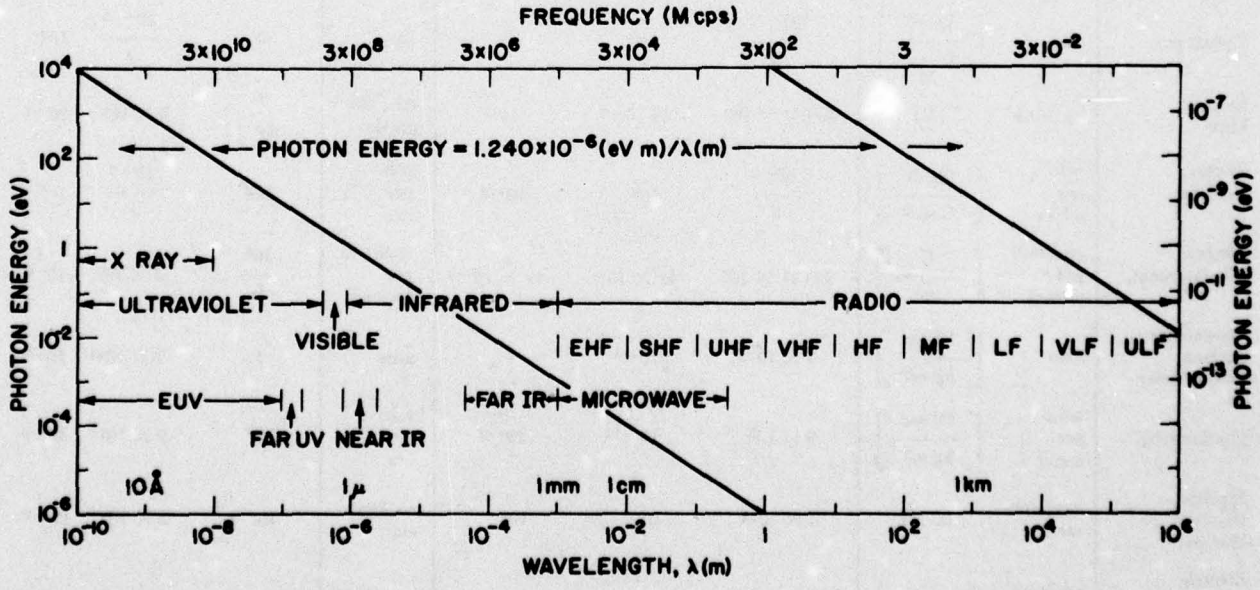


Fig. A-1. Electromagnetic spectrum from 1 Å to 10^3 km.

APPENDIX A

Table A-6. Electric and magnetic units and conversion factors. (After F. B. Silsbee, "Systems of Electrical Units," *National Bureau of Standards Monograph 56*, U. S. Government Printing Office, August 1963; *Physics Today*, v. 15, no. 6, June 1962; and W. R. Varner, "Fourteen Systems of Units," 3rd ed. rev., Vantage Press, New York, 1961.)

	Système International (MKSA Rationalized)					Practical			
			Multiply By For Result In				Multiply By For Result In		
Quantity	Units		ESU	EMU	Practical	Units	MKSA	ESU	EMU
Force	newton	$\left[\frac{kg\ m}{sec^2}\right]$	10^5	10^5	10^5	dyne	10^{-5}	1	1
Energy	joule	$\left[\frac{kg\ m^2}{sec^2}\right]$	10^7	10^7	1	joule	1	10^7	10^7
Power	watt	$\left[\frac{kg\ m^2}{sec^3}\right]$	10^7	10^7	1	watt	1	10^7	10^7
Charge	coulomb	[C]	3×10^9	10^{-1}	1	coulomb	1	3×10^9	10^{-1}
Current	ampere	$\left[\frac{C}{sec}\right]$	3×10^9	10^{-1}	1	ampere	1	3×10^9	10^{-1}
Current Density	ampere per meter^2	$\left[\frac{C}{m^2\ sec}\right]$	3×10^5	10^{-5}	10^{-4}	ampere per cm^2	10^4	3×10^9	10^{-1}
Potential; Electromotive Force	volt	$\left[\frac{kg\ m^2}{C\ sec^2}\right]$	$\frac{10^{-2}}{3}$	10^8	1	volt	1	$\frac{10^{-2}}{3}$	10^8
Capacity	farad	$\left[\frac{C^2\ sec^2}{kg\ m^2}\right]$	9×10^{11}	10^{-9}	1	farad	1	9×10^{11}	10^{-9}
Resistance	ohm	$\left[\frac{kg\ m^2}{C^2\ sec}\right]$	$\frac{10^{-11}}{9}$	10^9	1	ohm	1	$\frac{10^{-11}}{9}$	10^9
Electric Flux	coulomb	[C]	$4\pi(3) \times 10^9$	$4\pi\ 10^{-1}$	4π	coulomb per 4π	$\frac{1}{4\pi}$	3×10^9	10^{-1}
Electric Gradient, *E*	volt per meter	$\left[\frac{kg\ m}{C\ sec^2}\right]$	$\frac{10^{-4}}{3}$	10^6	10^{-2}	volt per cm	10^2	$\frac{10^{-2}}{3}$	10^8
Electric Displacement, *D*	coulomb per meter^2	$\left[\frac{C}{m^2}\right]$	$4\pi(3) \times 10^5$	$4\pi \times 10^{-5}$	$4\pi \times 10^{-4}$	coulomb per 4π cm^2	$\frac{10^4}{4\pi}$	3×10^9	10^{-1}
Conductance; Surface Conductivity	mho	$\left[\frac{C^2\ sec}{kg\ m^2}\right]$	9×10^{11}	10^{-9}	1	mho	1	9×10^{11}	10^{-9}
Conductivity	mho per meter	$\left[\frac{C^2\ sec}{kg\ m^3}\right]$	9×10^9	10^{-11}	10^{-2}	mho per cm	10^2	9×10^{11}	10^{-9}
Electric Dipole Moment	coulomb-meter	[C m]	3×10^{11}	10	10^2	coulomb-cm	10^{-2}	3×10^9	10^{-1}
Electric Polarization (dipole moment per volume)	coulomb per meter^2	$\left[\frac{C}{m^2}\right]$	3×10^5	10^{-5}	10^{-4}	coulomb per cm^2	10^4	3×10^9	10^{-1}

(Continued)

Table A-6. Electric and magnetic units and conversion factors. (After F. B. Silsbee, "Systems of Electrical Units," *National Bureau of Standards Monograph 56*, U. S. Government Printing Office, August 1963; *Physics Today*, v. 15, no. 6, June 1962; and W. R. Varner, "Fourteen Systems of Units," 3rd ed. rev., Vantage Press, New York, 1961.) (Continued)

Centimeter-Gram-Second (CGS)								
ESU (Electrostatic)					EMU (Electromagnetic)			
	Multiply By For Result In					Multiply By For Result In		
Units*	MKSA	EMU	Practical		Units*	MKSA	ESU	Practical
dyne $\left[\frac{\text{g cm}}{\text{sec}^2}\right]$	10^{-5}	1	1		dyne $\left[\frac{\text{g cm}}{\text{sec}^2}\right]$	10^{-5}	1	1
erg $\left[\frac{\text{g cm}^2}{\text{sec}^2}\right]$	10^{-7}	1	10^{-7}		erg $\left[\frac{\text{g cm}^2}{\text{sec}^2}\right]$	10^{-7}	1	10^{-7}
erg per second $\left[\frac{\text{g cm}^2}{\text{sec}^3}\right]$	10^{-7}	1	10^{-7}		erg per second $\left[\frac{\text{g cm}^2}{\text{sec}^3}\right]$	10^{-7}	1	10^{-7}
statcoulomb or franklin $\left[\frac{\text{g}^{1/2}\,\text{cm}^{3/2}}{\text{sec}}\right]$ [Fr]	$\frac{10^{-9}}{3}$	$\frac{10^{-10}}{3}$	$\frac{10^{-9}}{3}$		abcoulomb $[\text{g}^{1/2}\,\text{cm}^{1/2}]$	10	3×10^{10}	10
statampere $\left[\frac{\text{g}^{1/2}\,\text{cm}^{3/2}}{\text{sec}^2}\right]$	$\frac{10^{-9}}{3}$	$\frac{10^{-10}}{3}$	$\frac{10^{-9}}{3}$		abampere or biot $\left[\frac{\text{g}^{1/2}\,\text{cm}^{1/2}}{\text{sec}}\right]$ [Bi]	10	3×10^{10}	10
statampere per cm^2 $\left[\frac{\text{g}^{1/2}}{\text{cm}^{1/2}\,\text{sec}^2}\right]$	$\frac{10^{-5}}{3}$	$\frac{10^{-10}}{3}$	$\frac{10^{-9}}{3}$		abampere per cm^2 $\left[\frac{\text{g}^{1/2}}{\text{cm}^{3/2}\,\text{sec}}\right]$	10^5	3×10^{10}	10
statvolt $\left[\frac{\text{g}^{1/2}\,\text{cm}^{1/2}}{\text{sec}}\right]$	3×10^2	3×10^{10}	3×10^2		abvolt $\left[\frac{\text{g}^{1/2}\,\text{cm}^{3/2}}{\text{sec}^2}\right]$	10^{-8}	$\frac{10^{-10}}{3}$	10^{-8}
statfarad [cm]	$\frac{10^{-11}}{9}$	$\frac{10^{-20}}{9}$	$\frac{10^{-11}}{9}$		abfarad $\left[\frac{\text{sec}^2}{\text{cm}}\right]$	10^9	9×10^{20}	10^9
statohm $\left[\frac{\text{sec}}{\text{cm}}\right]$	9×10^{11}	9×10^{20}	9×10^{11}		abohm $\left[\frac{\text{cm}}{\text{sec}}\right]$	10^{-9}	$\frac{10^{-20}}{9}$	10^{-9}
statcoulomb per 4π $\left[\frac{\text{g}^{1/2}\,\text{cm}^{3/2}}{\text{sec}}\right]$	$\frac{10^{-9}}{4\pi(3)}$	$\frac{10^{-10}}{3}$	$\frac{10^{-9}}{3}$		abcoulomb per 4π $[\text{g}^{1/2}\,\text{cm}^{1/2}]$	$\frac{10}{4\pi}$	3×10^{10}	10
statvolt per cm $\left[\frac{\text{g}^{1/2}}{\text{cm}^{1/2}\,\text{sec}}\right]$	3×10^4	3×10^{10}	3×10^2		abvolt per cm $\left[\frac{\text{g}^{1/2}\,\text{cm}^{1/2}}{\text{sec}^2}\right]$	10^{-6}	$\frac{10^{-10}}{3}$	10^{-8}
statcoulomb per 4π cm^2 $\left[\frac{\text{g}^{1/2}}{\text{cm}^{1/2}\,\text{sec}}\right]$	$\frac{10^{-5}}{4\pi(3)}$	$\frac{10^{-10}}{3}$	$\frac{10^{-9}}{3}$		abcoulomb per 4π cm^2 $\left[\frac{\text{g}^{1/2}}{\text{cm}^{3/2}}\right]$	$\frac{10^5}{4\pi}$	3×10^{10}	10
statmho $\left[\frac{\text{cm}}{\text{sec}}\right]$	$\frac{10^{-11}}{9}$	$\frac{10^{-20}}{9}$	$\frac{10^{-11}}{9}$		abmho $\left[\frac{\text{sec}}{\text{cm}}\right]$	10^9	9×10^{20}	10^9
statmho per cm $\left[\frac{1}{\text{sec}}\right]$	$\frac{10^{-9}}{9}$	$\frac{10^{-20}}{9}$	$\frac{10^{-11}}{9}$		abmho per cm $\left[\frac{\text{sec}}{\text{cm}^2}\right]$	10^{11}	9×10^{20}	10^9
statcoulomb-cm $\left[\frac{\text{g}^{1/2}\,\text{cm}^{5/2}}{\text{sec}}\right]$	$\frac{10^{-11}}{3}$	$\frac{10^{-10}}{3}$	$\frac{10^{-9}}{3}$		abcoulomb-cm $[\text{g}^{1/2}\,\text{cm}^{3/2}]$	10^{-1}	3×10^{10}	10
statcoulomb per cm^2 $\left[\frac{\text{g}^{1/2}}{\text{cm}^{1/2}\,\text{sec}}\right]$	$\frac{10^{-5}}{3}$	$\frac{10^{-10}}{3}$	$\frac{10^{-9}}{3}$		abcoulomb per cm^2 $\left[\frac{\text{g}^{1/2}}{\text{cm}^{3/2}}\right]$	10^5	3×10^{10}	10

(Continued)

APPENDIX A

Table A-6. Electric and magnetic units and conversion factors. (After F. B. Silsbee, "Systems of Electrical Units," *National Bureau of Standards Monograph 56*, U. S. Government Printing Office, August 1963; *Physics Today*, v. 15, no. 6, June 1962; and W. R. Varner, "Fourteen Systems of Units," 3rd ed. rev., Vantage Press, New York, 1961.) (Continued)

	Système International (MKSA Rationalized)				Practical			
		Multiply By For Result In				Multiply By For Result In		
Quantity	Units	ESU	EMU	Practical	Units	MKSA	ESU	EMU
Permittivity (Capacivity)	farad per meter $\left[\frac{C^2\,sec^2}{kg\,m^3}\right]$	$4\pi(9)\times10^9$	$4\pi\times10^{-11}$	$4\pi\times10^{-2}$	farad per 4π cm	$\frac{10^2}{4\pi}$	9×10^{11}	10^{-9}
Magnetic Flux	weber $\left[\frac{kg\,m^2}{C\,sec}\right]$	$\frac{10^{-2}}{3}$	10^8	10^8	maxwell	10^{-8}	$\frac{10^{-10}}{3}$	1
Magnetic Induction, B	tesla $\left[\frac{kg}{C\,sec}\right]$	$\frac{10^{-6}}{3}$	10^4	10^4	gauss	10^{-4}	$\frac{10^{-10}}{3}$	1
Magnetic Field Strength, H	ampere-turn per meter $\left[\frac{C}{m\,sec}\right]$	$4\pi\,(3)\times10^7$	$4\pi\times10^{-3}$	$4\pi\times10^{-3}$	oersted	$\frac{10^3}{4\pi}$	3×10^{10}	1
Magnetmotive Force	ampere-turn $\left[\frac{C}{sec}\right]$	$4\pi\,(3)\times10^9$	$\frac{4\pi}{10}$	$\frac{4\pi}{10}$	gilbert	$\frac{10}{4\pi}$	3×10^{10}	1
Inductance	henry $\left[\frac{kg\,m^2}{C^2}\right]$	$\frac{10^{-11}}{9}$	10^9	1	henry	1	$\frac{10^{-11}}{9}$	10^9
Magnetic Pole Strength	weber $\left[\frac{kg\,m^2}{C\,sec}\right]$	$\frac{10^{-2}}{4\pi(3)}$	$\frac{10^8}{4\pi}$	10^8	gauss-cm^2	10^{-8}	$\frac{10^{-10}}{4\pi(3)}$	$\frac{1}{4\pi}$
Magnetic Moment	ampere-meter^2 $\left[\frac{m^2\,C}{sec}\right]$	3×10^{13}	10^3	10^4	ampere-cm^2	10^{-4}	3×10^9	10^{-1}
Magnetic Dipole Moment	weber-meter $\left[\frac{kg\,m^3}{C\,sec}\right]$	$\frac{1}{4\pi(3)}$	$\frac{10^{10}}{4\pi}$	10^{10}	gauss-cm^3	10^{-10}	$\frac{10^{-10}}{4\pi(3)}$	$\frac{1}{4\pi}$
Magnetization (magnetic moment per volume)	ampere turn per m $\left[\frac{C}{m\,sec}\right]$	3×10^7	10^{-3}	10^{-2}	ampere per cm	10^2	3×10^9	10^{-1}
Magnetic Polarization (dipole moment per volume)	tesla $\left[\frac{kg}{C\,sec}\right]$	$\frac{10^{-6}}{4\pi(3)}$	$\frac{10^4}{4\pi}$	10^4	gauss	10^{-4}	$\frac{10^{-10}}{4\pi(3)}$	$\frac{1}{4\pi}$
Reluctance	ampere turn/weber $\left[\frac{C^2}{kg\,m^2}\right]$	$4\pi(9)\times10^{11}$	$4\pi\times10^{-9}$	$4\pi\times10^{-9}$	gilbert per maxwell	$\frac{10^9}{4\pi}$	9×10^{20}	1
Permeability	henry per meter $\left[\frac{kg\,m}{C^2}\right]$	$\frac{10^{-13}}{4\pi(9)}$	$\frac{10^7}{4\pi}$	$\frac{10^7}{4\pi}$	gauss per oersted	$4\pi\times10^{-7}$	$\frac{10^{-20}}{9}$	1
Poynting Vector	watt per meter^2 $\left[\frac{kg}{sec^3}\right]$	$4\pi\times10^3$	$4\pi\times10^3$	$4\pi\times10^{-4}$	watt per cm^2	$\frac{10^4}{4\pi}$	10^7	10^7
Electric Constant	Permittivity of vacuum $\epsilon_0 = 10^{-9}/4\pi(9)$ [farad/m]				$\epsilon_0 = 10^{-11}/9$ [farad/cm]			
Magnetic Constant	Permeability of vacuum $\mu_0 = 4\pi\times10^{-7}$ [henry/m]				$\mu_0 = 1$			

NOTE For greater precision, replace: 3 by 2.9979; 1/3 by 0.33356; 9 by 8.9876 and 1/9 by 0.11127.

Table A-6. Electric and magnetic units and conversion factors. (After F. B. Silsbee, "Systems of Electrical Units," *National Bureau of Standards Monograph 56*, U. S. Government Printing Office, August 1963; *Physics Today*, v. 15, no. 6, June 1962; and W. R. Varner, "Fourteen Systems of Units," 3rd ed. rev., Vantage Press, New York, 1961.) (Continued)

Centimeter-Gram-Second (CGS)

ESU (Electrostatic)					EMU (Electromagnetic)				
		Multiply By For Result In					Multiply By For Result In		
Units*		MKSA	EMU	Practical	Units*		MKSA	ESU	Practical
statfarad per 4π cm	[1]	$\frac{10^{-9}}{4\pi(9)}$	$\frac{10^{-20}}{9}$	$\frac{10^{-11}}{9}$	abfarad per 4π cm	$\left[\frac{\text{sec}^2}{\text{cm}^2}\right]$	$\frac{10^{11}}{4\pi}$	9×10^{20}	10^9
statweber	$[g^{1/2}\,cm^{1/2}]$	3×10^2	3×10^{10}	3×10^{10}	maxwell	$\left[\frac{g^{1/2}\,cm^{3/2}}{\text{sec}}\right]$	10^{-8}	$\frac{10^{-10}}{3}$	1
statweber per cm^2	$\left[\frac{g^{1/2}}{cm^{3/2}}\right]$	3×10^6	3×10^{10}	3×10^{10}	gauss	$\left[\frac{g^{1/2}}{cm^{1/2}\,\text{sec}}\right]$	10^{-4}	$\frac{10^{-10}}{3}$	1
statampere turn per 4π cm	$\left[\frac{g^{1/2}\,cm^{1/2}}{\text{sec}^2}\right]$	$\frac{10^{-7}}{4\pi(3)}$	$\frac{10^{-10}}{3}$	$\frac{10^{-10}}{3}$	oersted	$\left[\frac{g^{1/2}}{cm^{1/2}\,\text{sec}}\right]$	$\frac{10^3}{4\pi}$	3×10^{10}	1
statampere turn per 4π	$\left[\frac{g^{1/2}\,cm^{3/2}}{\text{sec}^2}\right]$	$\frac{10^{-9}}{4\pi(3)}$	$\frac{10^{-10}}{3}$	$\frac{10^{-10}}{3}$	gilbert	$\left[\frac{g^{1/2}\,cm^{1/2}}{\text{sec}}\right]$	$\frac{10}{4\pi}$	3×10^{10}	1
stathenry	$\left[\frac{\text{sec}^2}{\text{cm}}\right]$	9×10^{11}	9×10^{20}	9×10^{11}	abhenry	[cm]	10^{-9}	$\frac{10^{-20}}{9}$	10^{-9}
	$[g^{1/2}\,cm^{1/2}]$	$4\pi(3) \times 10^2$	3×10^{10}	$4\pi(3) \times 10^{10}$	pole	$\left[\frac{g^{1/2}\,cm^{3/2}}{\text{sec}}\right]$	$4\pi \times 10^{-8}$	$\frac{10^{-10}}{3}$	4π
statampere-cm^2	$\left[\frac{g^{1/2}\,cm^{7/2}}{\text{sec}^2}\right]$	$\frac{10^{-13}}{3}$	$\frac{10^{-10}}{3}$	$\frac{10^{-9}}{3}$	abampere-cm^2	$\left[\frac{g^{1/2}\,cm^{5/2}}{\text{sec}}\right]$	10^{-3}	3×10^{10}	10
	$[g^{1/2}\,cm^{3/2}]$	$4\pi(3)$	3×10^{10}	$4\pi(3) \times 10^{10}$	pole-cm	$\left[\frac{g^{1/2}\,cm^{5/2}}{\text{sec}}\right]$	$4\pi \times 10^{-10}$	$\frac{10^{-10}}{3}$	4π
statampere per cm	$\left[\frac{g^{1/2}\,cm^{1/2}}{\text{sec}^2}\right]$	$\frac{10^{-7}}{3}$	$\frac{10^{-10}}{3}$	$\frac{10^{-9}}{3}$	abampere per cm	$\left[\frac{g^{1/2}}{cm^{1/2}\,\text{sec}}\right]$	10^3	3×10^{10}	10
	$\left[\frac{g^{1/2}}{cm^{3/2}}\right]$	$4\pi(3) \times 10^6$	3×10^{10}	$4\pi(3) \times 10^{10}$	pole per cm^2	$\left[\frac{g^{1/2}}{cm^{1/2}\,\text{sec}}\right]$	$4\pi \times 10^{-4}$	$\frac{10^{-10}}{3}$	4π
	$\left[\frac{\text{cm}}{\text{sec}^2}\right]$	$\frac{10^{-11}}{4\pi(9)}$	$\frac{10^{-20}}{9}$	$\frac{10^{-20}}{9}$	gilbert per maxwell	$\left[\frac{1}{\text{cm}}\right]$	$\frac{10^9}{4\pi}$	9×10^{20}	1
	$\left[\frac{\text{sec}^2}{cm^2}\right]$	$4\pi(9) \times 10^{13}$	9×10^{20}	9×10^{20}	gauss per oersted	[1]	$4\pi \times 10^{-7}$	$\frac{10^{-20}}{9}$	1
erg per cm^2-sec	$\left[\frac{g}{\text{sec}^3}\right]$	$\frac{10^{-3}}{4\pi}$	1	10^{-7}	erg per cm^2-sec	$\left[\frac{g}{\text{sec}^3}\right]$	$\frac{10^{-3}}{4\pi}$	1	10^{-7}
Permittivity of vacuum $\epsilon_0 = 1$					$\epsilon_0 = 10^{-20}/9$ $[\text{sec}^2\,\text{cm}^{-2}]$				
Permeability of vacuum $\mu_0 = 10^{-20}/9$ $[\text{sec}^2\,\text{cm}^{-2}]$					$\mu_0 = 1$				

* The 4π factor is an abbreviation necessary to conserve space. For example, the electric flux in esu, "statcoulomb per 4π," should read "the total flux present when the source is $1/4\pi$ statcoulomb of charge."

APPENDIX B

BLACKBODY RADIATION

There is no single standard nomenclature for radiometric concepts. Terminology and symbols in different chapters of this handbook vary because those common in the literature for the particular topic are used. In each case, however, the concept is initially identified by the name given in Section B.1. Because different systems of units are also used, dimensions in Sec. B.2 and B.3 are given in mass (m), length (l), time (t), and unit solid angle (Ω_o). Formulae are for unpolarized blackbody radiation. For additional definitions and functions, and for a discussion of this nomenclature, see Pivovonsky and Nagel [1961], Planck [1912], and Bell [1959].

B.1 NOMENCLATURE, SYMBOLS, DEFINITIONS, AND UNITS

The Système International (MKSA) units are used here, with the exceptions of *wavelength interval*, which is in microns, and *wavenumber*, which is in reciprocal centimeters.

Surface area, A, [m^2].

Angle between normal to surface and direction of energy propagation, θ, [rad].

Solid angle, $d\Omega = 2\pi \sin\theta \, d\theta$;
$\Omega = 2\pi (1 - \cos\theta)$, [sr].

Unit solid angle, Ω_o is 1 steradian.

Radiant energy, U, [J].

Radiant energy density, $u = \frac{1}{c}\int_o^{4\pi} N d\Omega$, [$J\,m^{-3}$].

Radiant power, $P = dU/dt$
$= 2\pi \iint N dA \cos\theta \sin\theta d\theta$, [W].

Radiance, $N = \frac{\partial^2 P}{\partial A \, \partial\Omega \cos\theta}$, [$W\,m^{-2}\,sr^{-1}$].

Radiant emittance is radiant power per unit area emitted from a surface, $W = \int N d\Omega$, [$W\,m^{-2}$].

Irradiance (equivalent to the Poynting vector) is the radiant power per unit area incident on a surface element normal to the direction of energy propagation, $H = \frac{dP}{dA \cos\theta}$, [$W\,m^{-2}$].

Radiant intensity is the radiant power per solid angle from a point source, $J = \frac{dP}{d\Omega}$, [$W\,sr^{-1}$].

Frequency, ν, [cps].

Bandwidth, $\Delta\nu$ or $d\nu$, [cps].

Wavelength, λ, [m].

Wavelength interval (wavelength band), $\Delta\lambda$ or $d\lambda$, [μ].

Wavenumber, σ, [cm^{-1}].

Subscript λ indicates monochromatic radiation or radiation per wavelength interval, and the quantity is then called *spectral*, for example:
u_λ is spectral energy density, [$J\,m^{-3}\,\mu^{-1}$],
W_λ is spectral radiant emittance, [$W\,m^{-2}\,\mu^{-1}$].

Subscript ν indicates radiation per bandwith, for example:
u_ν is radiant energy density per bandwidth, [$J\,m^{-3}\,cps^{-1}$] or [J sec m^{-3}],
H_ν is irradiance per bandwith, [$W\,m^{-2}\,cps^{-1}$] or [$J\,m^{-2}$].

Subscript σ indicates radiation per unit wavenumber, for example: N_σ is radiance per reciprocal centimeter [$W\,m^{-2}\,sr^{-1}\,(cm^{-1})^{-1}$] or [W cm $m^{-2}\,sr^{-1}$].

B.2 PLANCK'S RADIATION FUNCTIONS

Planck's law for the energy per unit volume of unpolarized blackbody radiation of frequency ν is

$$u_\nu = \frac{8\pi h\nu^3}{c^3\,[\exp(h\nu/kT) - 1]}, \qquad \text{(B-1)}$$

where T is the temperature of the blackbody in °K, h is Planck's constant, k is Boltzmann's constant, and c the speed of propagation. (For plane polarized radiation, divide formulae by 2; e.g., for u_ν the numerator would be 4π h ν^3.) From equation (B-1) and the relationships

$$u_\lambda = u_\nu c/\lambda^2, \qquad \text{(B-2)}$$

and

$$u = \int_0^\infty u_\lambda \, d\lambda = \int_0^\infty u_\nu \, d\nu, \qquad \text{(B-3)}$$

many different functions are obtained.

The formulae that follow are used for various applications in this handbook. The *second radiation constant*, c_2, is used in wavelength equations; the "first radiation constant" is not used because there is no commonly ac-

cepted definition (Planck uses hc^2/Ω_o; other forms found in the literature are $8\pi hc$, πhc^2, $2\pi hc^2$, and $2hc^2/\Omega_o$, with correspondingly different numerical values quoted).

$$
\begin{aligned}
u_\lambda &= 8\pi hc\lambda^{-5}\,[\exp(c_2/\lambda T) - 1]^{-1} \quad [m\,l^{-2}\,t^{-2}],\\
N_\nu &= 2h\nu^3 c^{-2}\,\Omega_o^{-1}[\exp(h\nu/kT) - 1]^{-1} \quad [m\,t^{-2}\,\Omega_o^{-1}],\\
N_\lambda &= 2hc^2\,\Omega_o^{-1}\,\lambda^{-5}\,[\exp(c_2/\lambda T) - 1]^{-1} \quad [m\,l^{-1}\,t^{-3}\,\Omega_o^{-1}],\\
N_\sigma &= 2hc^2\,\sigma^3\,\Omega_o^{-1}[\exp(c_2\,\sigma/T) - 1]^{-1} \quad [m\,l\,t^{-3}\,\Omega_o^{-1}],\\
W_\nu \text{ (or } H_\nu) &= 2h\nu^3 c^{-2}\,[\exp(h\nu/kT) - 1]^{-1} \quad [m\,t^{-2}],\\
W_\lambda \text{ (or } H_\lambda) &= 2hc^2\,\lambda^{-5}\,[\exp(c_2/\lambda T) - 1]^{-1} \quad [m\,l^{-1}\,t^{-3}].
\end{aligned}
\tag{B-4}
$$

Figures B-1 through B-4 show N_λ, N_σ, and N_ν for blackbodies at various temperatures as a function of λ, σ and ν. Figures B-5 through B-7 are plots of the number of photons of a given wavelength, wavenumber, or frequency emitted per unit area per unit solid angle by a blackbody at various temperatures. In plotting these curves, the values $c_2 = 1.4380$ cm °K, $2hc^2/\Omega_o = 1.1909 \times 10^{-12}$ W cm^2 sr^{-1}, and for Wien's displacement constant 0.28962 cm °K, were used; the values recommended by the National Bureau of Standards were published after calculations were completed.

B.3 LIMITING CASES OF PLANCK'S LAW

Two approximations of Eq. (B-1) are the Rayleigh-Jeans and the Wien radiation formulae.

The *Rayleigh-Jeans approximation* is applicable to low-frequency, long-wavelength radiation (radio region) where $h\nu << kT$. A few of the forms are:

$$
\begin{aligned}
u_\nu &= 8\pi\nu^2 kTc^{-3}\\
u_\lambda &= 8\pi kT\lambda^{-4}\\
N_\nu &= 2\nu^2 kTc^{-2}\,\Omega_o^{-1}\\
N_\lambda &= 2ckT\Omega_o^{-1}\,\lambda^{-4}\\
N_\sigma &= 2c\sigma^2 kT\Omega_o^{-1}\\
W_\nu \text{ (or } H_\nu) &= 2\nu^2 kTc^{-2}\\
W_\lambda \text{ (or } H_\lambda) &= 2ckT\lambda^{-4}
\end{aligned}
\tag{B-5}
$$

The *Wien radiation function* is useful for high-frequency, short-wavelength radiation where $h\nu >> kT$. Formulae are:

$$
\begin{aligned}
N_\nu &= 2h\nu^3 c^{-2}\,\Omega_o^{-1}\exp(-h\nu/kT),\\
N_\lambda &= 2hc^2\,\Omega_o^{-1}\,\lambda^{-5}\exp(-c_2/\lambda T),\\
N_\sigma &= 2hc^2\,\sigma^3\,\Omega_o^{-1}\exp(-c_2\,\sigma/T),\\
W_\nu \text{ (or } H_\nu) &= 2h\nu^3 c^{-2}\exp(-h\nu/kT),\\
W_\lambda \text{ (or } H_\lambda) &= 2hc^2\,\lambda^{-5}\exp(-c_2/\lambda T).
\end{aligned}
\tag{B-6}
$$

B.4 STEFAN-BOLTZMANN AND WIEN DISPLACEMENT LAWS

The Stefan-Boltzmann law states that the total energy density of blackbody radiation depends only on the temperature of the body; $u = aT^4$. (The constant of proportionality, a, is $8\pi^5 k^4/15\,c^3 h^3$.) Thus the radiant emittance of a blackbody is

$$W = \frac{c}{4\pi}\,a\,T^4 = \sigma T^4; \tag{B-7}$$

σ is the Stefan-Boltzmann constant.

Wien's displacement law is usually given in the form

$$\lambda_{max}\,T = c_2/r_\lambda = 2.8978 \times 10^{-3}\ [m\ °K), \tag{B-8}$$

where λ_{max} is the wavelength at which the spectral radiant emittance is maximum ($dW_\lambda/d\lambda = 0$), r_λ is the positive root of the equation $x = 5\,[1 - \exp(-x)] = 4.9651$ and 2.8978×10^{-3} is Wien's displacement constant. Two forms which are less common but for some purposes more useful are:

frequency at which the energy is maximum ($dH_\nu/d\nu = 0$),

$$\nu_{max} = r_\nu kT/h = 5.8820 \times 10^{10}\,T\ [cps]; \tag{B-9}$$

wavelength at which the energy is maximum ($dH_\nu/d\lambda = 0$),

$$\lambda_{\nu\,max}\,T = \frac{c\,T}{\nu_{max}} = c_2/r_\nu = 5.0968 \times 10^{-3}\ [m\ °K], \tag{B-10}$$

where r_ν is the positive root of the equation $x = 3 \times [1 - \exp(-x)] = 2.8214$. Note that for a given temperature, the maximum of the energy distribution spectrum is not the same as the maximum of the conventional spectral distribution (spectral radiant emittance vs wavelength).

B.5 REFERENCES

Bell, Ely E., 1959, "Radiometric Quantities, Symbols and Units," *Proc. IRE*, v. 47, no. 9, p. 1432.

Pivovonsky, M., and M. R. Nagel, 1961, "Tables of Blackbody Radiation Functions," The Macmillan Co., New York.

Planck, Max, 1912, "Theory of Heat Radiation," authorized translation, reprinted by Dover Publications, Inc., New York, 1959.

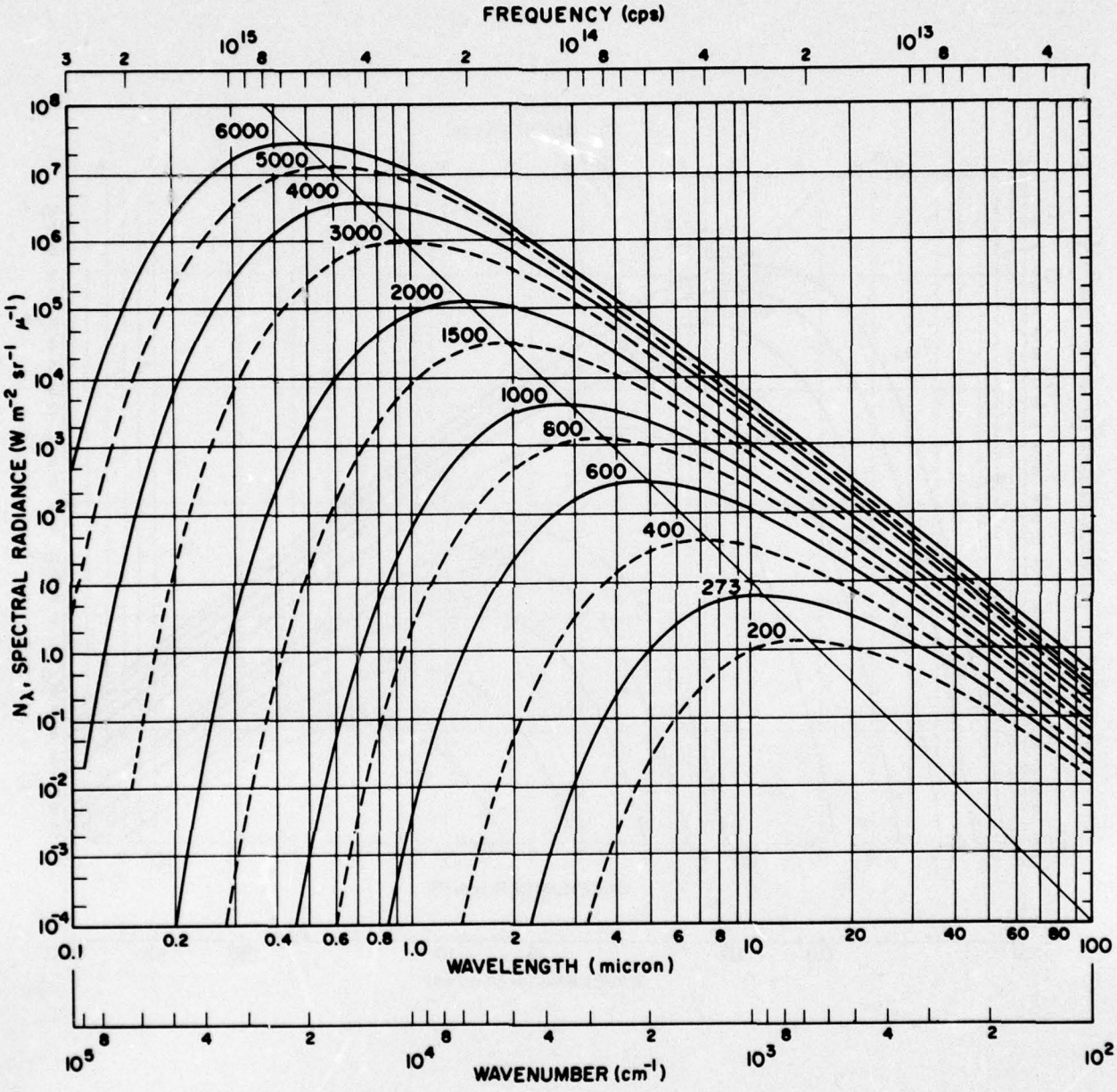


Fig. B-1. Spectral radiance of a blackbody, N_λ, at the temperature in °K shown on each curve; beyond 100 μ the curves continue to be linear (plotted on logarithmic scales). The diagonal line, intersecting the curves at their maxima, shows Wien's displacement law. (Subdivisions of the ordinate scale are at 2 and 5.) Figure by P. R. Gast.

APPENDIX B

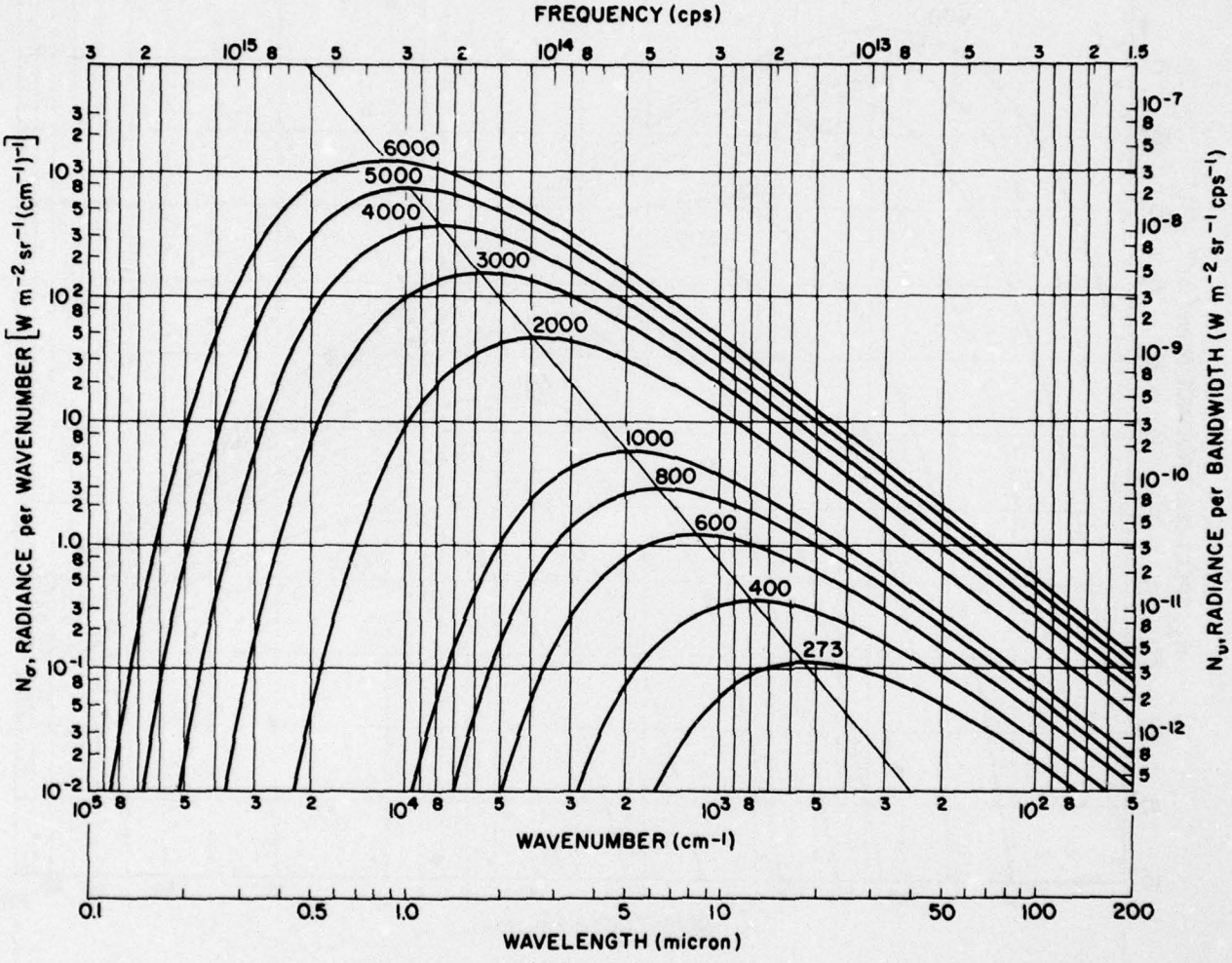


Fig. B-2. Radiance per reciprocal centimeter, N_σ, and radiance per unit frequency, N_ν, for a blackbody at various temperatures; at frequencies less than 3×10^{12} cps, wavenumber <100 cm^{-1}, the curves continue to be linear (plotted on logarithmic scales). The diagonal line, intersecting the curves at their maxima, shows Wien's displacement law. Figure by P. R. Gast.

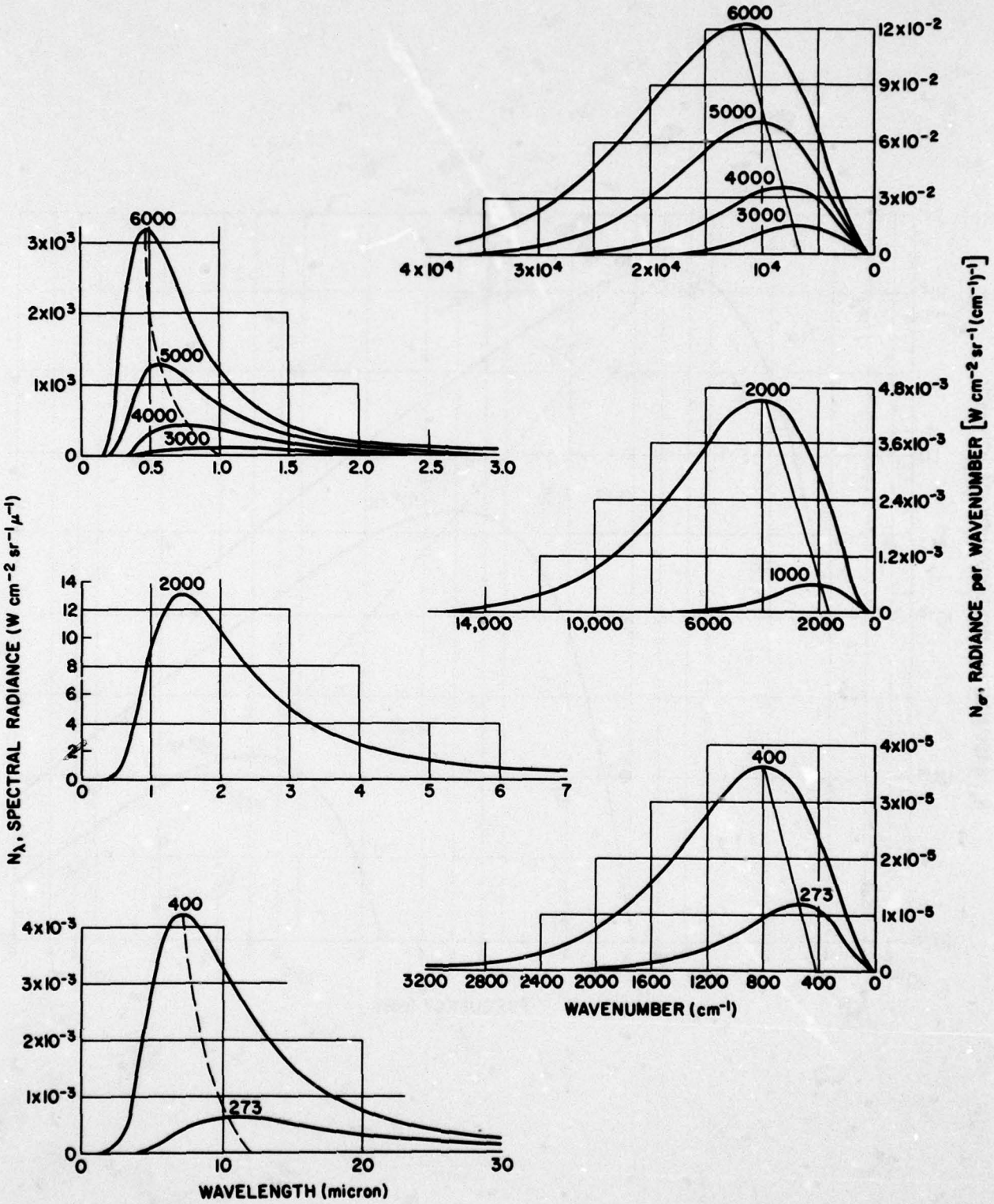


Fig. B-3. Spectral radiance N_λ and radiance per reciprocal centimeter N_σ of blackbodies at various temperatures (°K) plotted on arithmetic scales; note values given are per square centimeter of surface and must be multiplied by 10^4 to obtain values in W m^{-2} sr^{-1} μ^{-1} or W m^{-2} sr^{-1} (cm^{-1})$^{-1}$. The dashed and diagonal lines show Wien's displacement law. Figure by P. R. Gast.

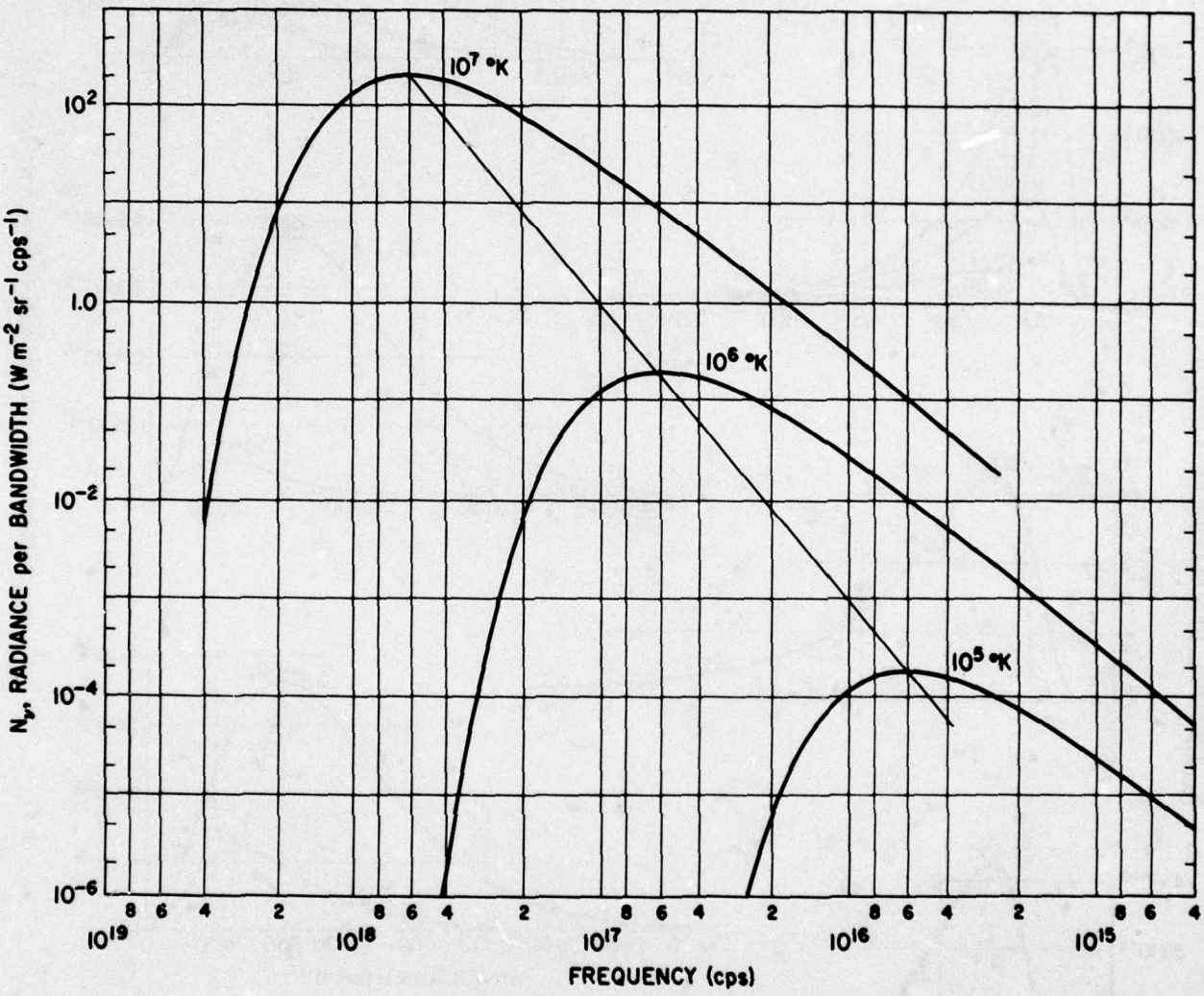


Fig. B-4. Radiance per unit frequency, N_ν, for blackbodies at high temperatures vs frequency (wavelength region 0.75Å to 0.75μ). The diagonal line shows Wien's displacement law. Subdivisions of ordinate scale are at 2 and 5. Figure by P. R. Gast.

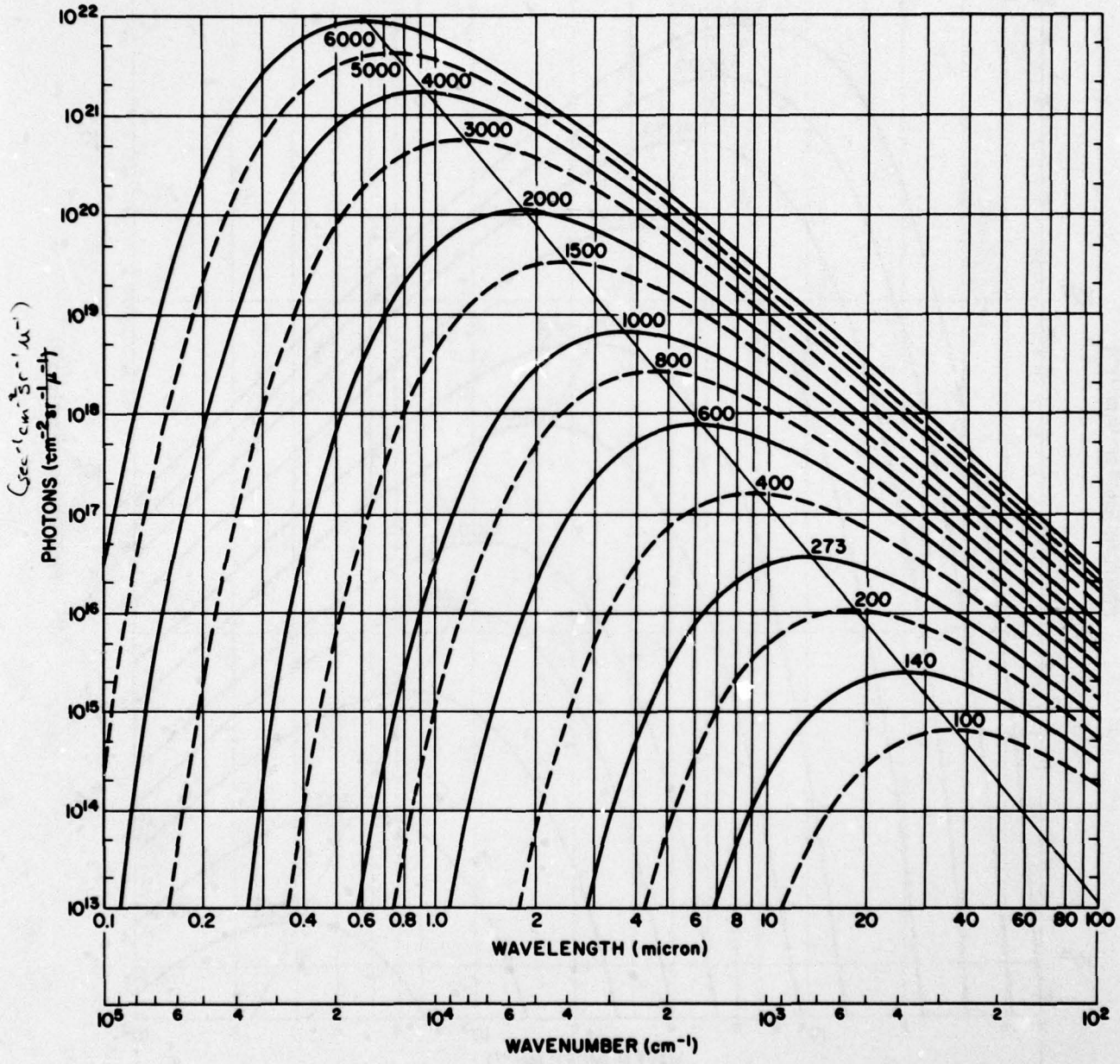


Fig. B-5. Number of photons emitted per square centimeter per steradian per micron by a blackbody at various temperatures (°K); subdivisions of the ordinate scale are at 2 and 5. The diagonal line, intersecting the curves at their maxima, shows Wien's displacement law. Figure by P. R. Gast.

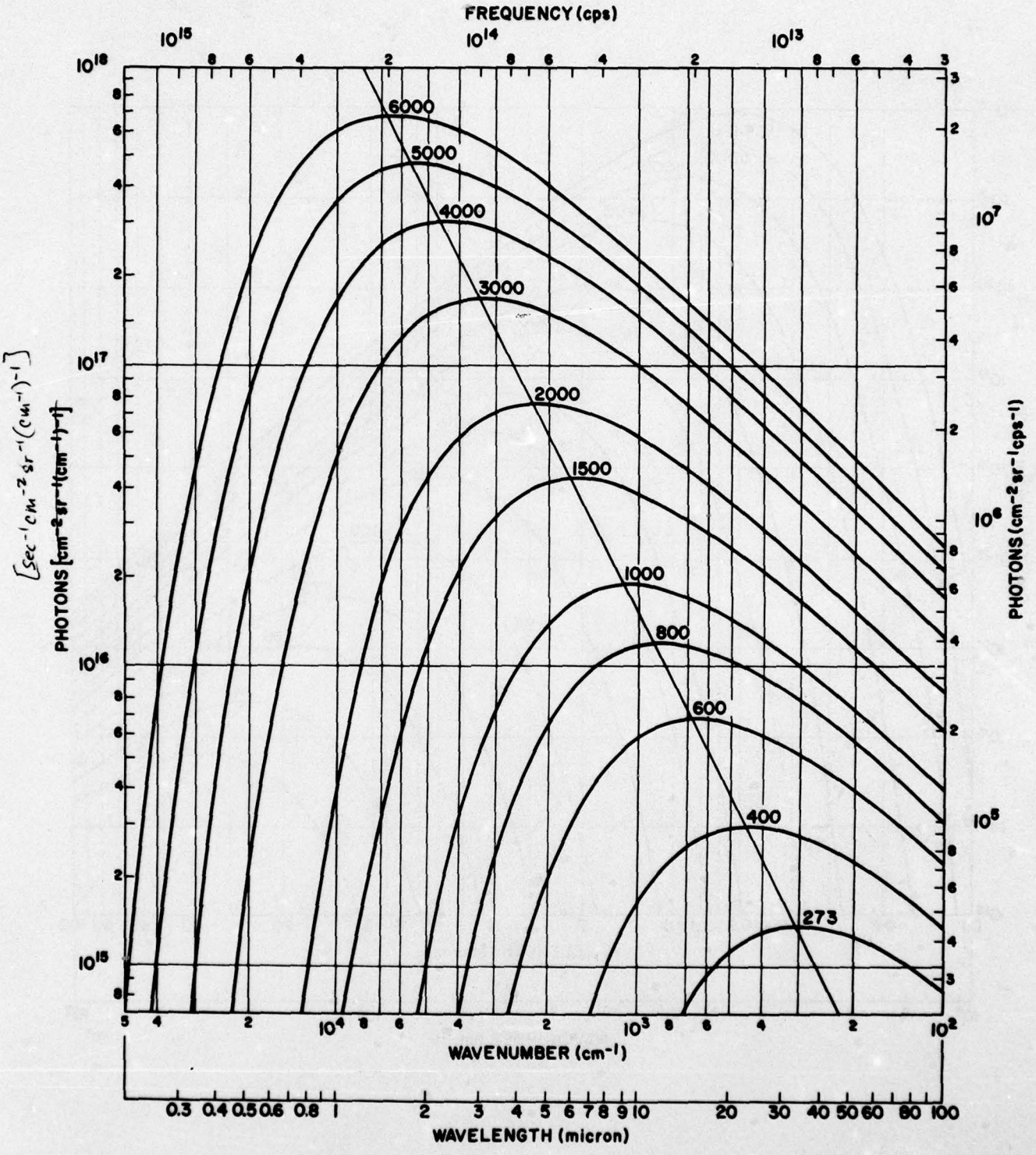
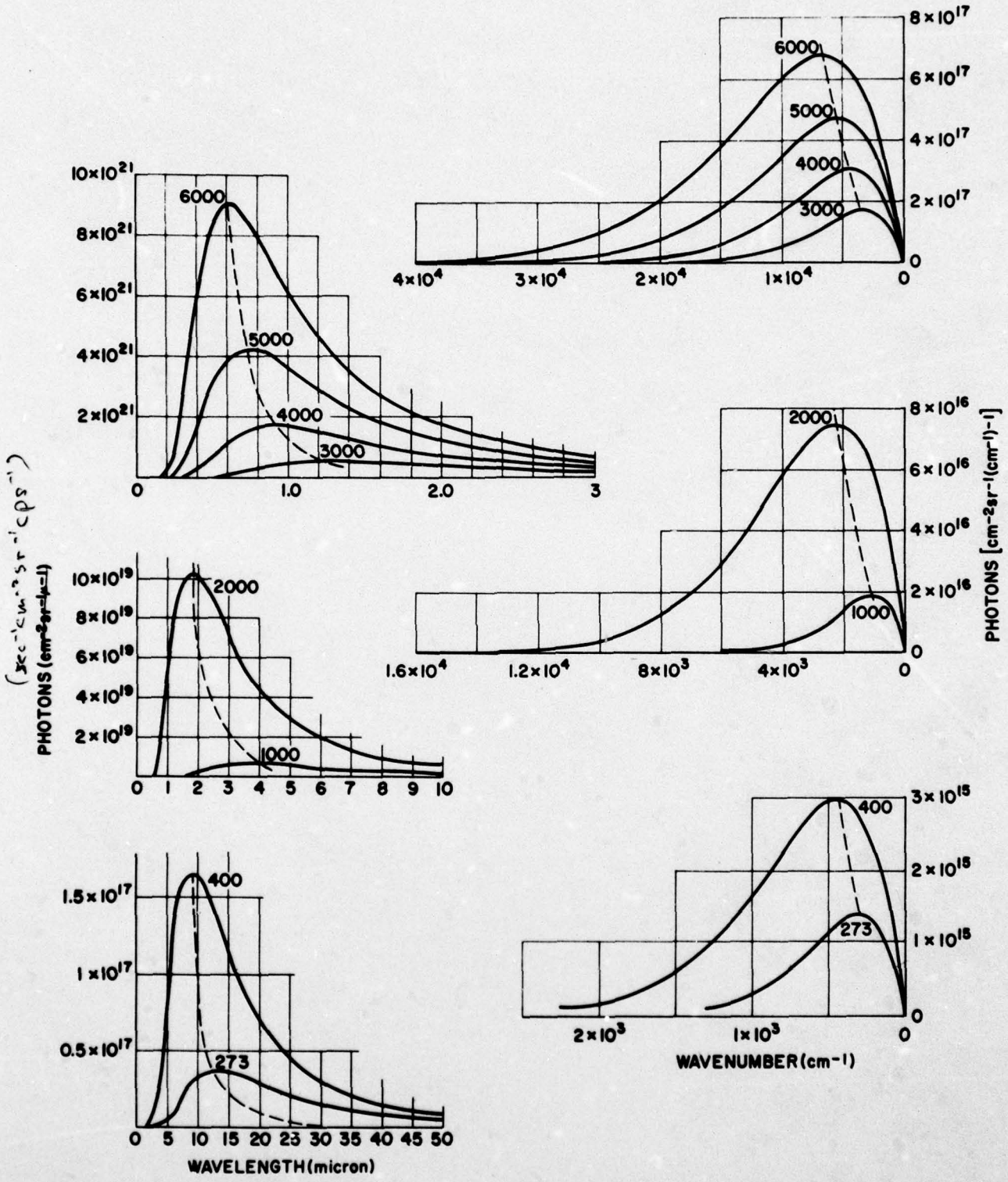


Fig. B-6. Number of photons per square centimeter per steradian per reciprocal centimeter (left ordinate scale) and number of photons per square centimeter per steradian per unit frequency (right ordinate scale) emitted by a blackbody at various temperatures (°K). The diagonal line, intersecting the curves at their maxima, shows Wien's displacement law. Figure by P. R. Gast.



Number of per second

Fig. B-7. Photons emitted by blackbodies at various temperatures (°K) plotted on arithmetic scales. Figure by P. R. Gast.

INDEX

(Also see Table of Contents)

A

Absorption, events, auroral zone, 12-1, 12-2
  polar cap, 12-1, 12-2
  sudden commencement, 12-2
infrared radiation, carbon dioxide, 10-2, 10-4, 10-6
  ozone, 10-2, 10-4
  water vapor, 10-2 to 10-7
interstellar, 21-18
microwave radiation, ice, 9-3, 9-4, 9-9
  snow, 9-3, 9-4, 9-9
  water, 9-3, 9-4, 9-9
optical radiation, 7-6 to 7-9, 9-1
processes in upper atmosphere, 6-7 to 6-9
  ozone, 7-9 to 7-11
radio wavelengths, anisotropic medium, 12-21 to 12-24
  electron collisions, 12-25, 12-26
  ion collisions, 12-25, 12-27, 12-28
  isotropic medium, 12-17 to 12-21
  nondeviative, 12-15 to 12-28
  oxygen, 22-3
  water vapor, 9-1, 9-2, 9-8, 22-4
selective, 21-19
solar spectrum, 15-1, 15-3, 15-4
ultraviolet and x rays, average coefficients, 6-15, 6-16
  cross sections, 6-14, 6-15, 16-16, 16-17
  minor atmospheric constituents, 6-14
  nitric oxide, 6-13
  nitrogen, 6-9, 6-13, 6-14
  oxygen, 6-12 to 6-14
Activity, auroral, 13-6
geomagnetic indices, 11-30 to 11-43
  character figure, 11-37
  daily ranges, 11-30
  equivalent planetary amplitudes, 11-32
  intervals, 11-32, 11-37, 11-39
geomagnetic storms, 11-28, 11-30
solar, active centers, 15-10
  flares, 15-11, 15-12, 17-19 to 17-30
  magnetic, 18-8, 18-9, 18-17, 18-18
  photosphere, 15-8, 18-16
  relative sunspot number, 15-7
  sunspots, 15-7, 15-8, 15-10, 18-8
Adiabatic invariants, trapped particles, 17-2
Adiabatic lapse rates, atmosphere, 3-11
Admittance, thermal, 3-20, 3-22
Aerosols, characteristics, 5-24, 5-25
composition, 5-23 to 5-25
concentrations, 5-23
definition, 5-22
distribution, 5-23, 5-24
impact effect on aircraft, 5-25, 5-26
interaction with radioactive material, 5-25
mass, 5-23, 5-24
Mie scattering, 7-8
nomenclature, 5-22
scattering, attenuation coefficient, 7-1, 7-2
size range, 5-22, 5-23
Airglow, intensity, 13-1, 13-3
spectrum, 13-1, 13-2, 13-10 to 13-14
variations, 13-1 to 13-4, 13-14 to 13-18
Air, equation of state, 2-1
dielectric properties, 9-3
mean molecular weight, 6-1
Airy-Heiskanen isostatic systems, 1-15
Aitken particles, 5-22 to 5-25
Albedo, planetary, Earth, 3-1
Alfvén speed, 9-23
Anomaly, gravity, 1-10, 1-17
geomagnetic field, 11-7
  regional, 11-7
  surface, 11-7
mean, gravity
  (*see* orbital perturbations)
Antenna temperature, radio astronomy, 16-21, 22-1
Appleton-Hartree formula, 9-14, 9-16
Arago point, 7-7
Astronomical unit, 21-4
Astronomy, optical, 21-1
radio, 22-1
Asymptotic cone of acceptance, 17-2
Arctic model atmosphere, summer, 2-17
  winter, 2-18
Atmosphere, absorption
  (*see* absorption)
attenuation models, 7-1, 7-2
  (*see also* attenuation)
composition, 6-1, 6-2
density
  (*see* density, air)
electric field
  (*see* electricity, atmospheric)
electrons
  (*see* ionosphere)
humidity
  (*see* water vapor, atmospheric)
ions, 6-2, 6-18 to 6-23
  (*see also* ionosphere)
models, 2-2 to 2-22
  Arctic summer, 2-17
  Arctic winter, 2-18
  ARDC, 1956 and 1959, 2-2
  extreme, 2-6, 2-8
  midlatitude summer, 2-13
  midlatitude winter, 2-14
  subarctic summer, 2-14
  subarctic winter, 2-15 to 2-17

subtropical summer, 2-11, 2-12
subtropical winter, 2-12, 2-13
supplemental, 2-2, 2-6, 2-11 to 2-18
tropical, 2-11
U.S. Standard, 1962, 2-2 to 2-5, 2-19 to 2-22
moisture properties, 2-10
(*see also* water vapor, atmospheric)
optical polarization, 7-7, 7-8
pressure
(*see* pressure, air)
Rayleigh, 7-2
scattering, Mie, 7-8
Rayleigh, 7-1, 7-7, 7-8
structure, 2-1
temperature
(*see* temperature, air)
turbid, 7-1, 7-2
upper, absorption processes, 6-7 to 6-9
absorption cross sections, 6-14 to 6-16, 16-16, 16-17
constituents, 6-1 to 6-7, 6-9 to 6-14
detachment processes, 6-18 to 6-20
photoionization cross section, 6-7, 6-8
recombination processes, 6-15 to 6-17
total absorption cross section, 6-8
viscosity coefficients, 2-19 to 2-22
Atmosphere, Mars, 20-5 to 20-10
Moon, 19-1
Sun
(*see* solar atmosphere)
Venus, 20-1, 20-2
Atmospheric depth, 17-14
Atmospheric reduced equivalent thickness, 16-7
Attenuation, infrared radiation, 10-2 to 10-7
interstellar, 21-19
meteoroid, atmosphere, 14-2, 14-3
microwave radiation, ice, 9-3 to 9-5
rainfall, 9-14, 9-15, 9-18
Rayleigh approximations, 9-4
snow, 9-3, 9-14, 9-15
water, 9-3, 9-4, 9-9, 9-14, 9-15
model, clear standard atmosphere, 7-1, 7-2
coefficients, 7-1, 7-2
optical thickness parameters, 7-1, 7-2
transmission calculations, 7-2
optical radiation, 7-6
radio waves, 9-3 to 9-14, 22-3
solar radiation, 6-7 to 6-16, 16-7 to 16-10
Aurorae, altitudes, 13-6
brightness index, 13-5
classical, 13-4
color class, 13-6
conditions, 13-5
formation, 13-4
forms, 13-4, 13-5, 13-20
isoaurorae, 13-6, 13-27
isochasms, 13-6
low latitude, 13-4
occurrences, 13-6
polar glow, 13-4
radio, 13-4
spectra, 13-6, 13-9, 13-21 to 13-28
structure, 13-5
variations, 13-6
visual, 13-4
Auroral zone, 13-6
Azimuth, astronomical, 1-3, 21-4
geodetic, 1-3

B

Babinet point, 7-7
Backing wind, 4-2
Backscattering, cross section, 9-4, 9-5, 9-12
microwave radiation, 9-9, 9-13, 9-14, 9-16
Mie region, 9-5
Rayleigh region, 9-3, 9-5, 9-12
Barbier-Chalonge classification, stars, 21-17, 21-18
Blackbody, definition, 10-1
Balmer series hydrogen lines, 21-10
Planck's radiation functions, B-1 to B-9
Rayleigh-Jeans approximation, B-2
Wien's approximation, B-2
Stefan-Boltzmann law, B-2
Wien displacement law, B-2
Bolide meteor, 14-1
Bolometric corrections, stars, 21-9
Bolometric measurements, atmospheric temperature, 2-19
Bouguer reduction, 1-14
Bounce period, 17-2
Brewster point, 7-7
Bright band, 9-13
Brightness index, aurorae, 13-5
Bursts, solar radio emissions, 16-24, 16-25

C

Carbon cycle, stars, 21-20
Carbon dioxide, infrared absorption, 10-2, 10-4, 10-6
Cassini's laws, 19-14
Ceiling, clouds, 5-11
Celestial coordinate systems, 21-4 to 21-7
Centrifugal force, gravity potential, 1-6
Chamberlain's model, coronal atmosphere, 18-4
Chapman's model, coronal atmosphere, 18-3, 18-4
Chromosphere, thickness, 15-3
spectrum, 15-3
spicules, 15-5
steady state features, 15-3 to 15-6
temperature, 15-3
Clock hourly rates, precipitation, 5-1 to 5-3
Clouds, ceiling, 5-11, 5-13
cirrus, horizontal extent, 5-15, 5-18
vertical extent, 5-14
cumulonimbus, 5-18, 5-19
infrared radiation properties, 10-15, 10-17, 10-18
interstellar dust and gas, 21-18 to 21-20
frequency of occurrence, 5-12 to 5-17
Mars, 20-10

noctilucent, 5-21 to 5-23
reflectance, 7-5
scattering properties, 9-13
water content, 5-9, 5-15, 5-18 to 5-20
Clusters, galactic and globular, 21-21, 21-22
Color excess, interstellar attenuation, 21-19
Color systems, stars, 21-10
Conductivity, Earth's atmosphere
(see electricity, atmospheric)
thermal, ionized gas, 18-13, 18-14
soil, 3-20
Corona, solar, density, 15-6
emission lines, 15-5
halo, 15-5
heating, 15-6
interactions with prominences, 15-9
model atmospheres, 18-2 to 18-7
temperatures, 15-5, 15-6, 18-2 to 18-6
true, 15-5
variation with sunspot cycle, 18-7
visible features, 15-3
white light, 15-5, 15-6
Corpuscular radiation
(see cosmic rays and trapped radiation)
Cosmic dust, meteoroids, 14-1
Cosmic radiation
(see cosmic rays)
Cosmic rays, atmospheric depth, 17-14, 17-23 to 17-25
composition, 17-12
energy spectra, 17-12
flux, 17-11, 17-14 to 17-21, 17-27
Forbush decrease, 17-15
geographic variation, 17-14, 17-15, 17-25, 17-26
geomagnetic cutoff, 17-2
(see also cosmic rays, threshold)
magnetic storm effects, 17-15
neutrons, 17-15, 17-26
nuclear component, 17-12
primary, 17-11
rigidity, definition, 17-2
secondary, 17-12
solar, 15-11 to 15-13, 17-19 to 17-22
(see also solar cosmic rays)
threshold, momentum, 17-14
rigidity, 17-14, 17-29, 17-30

D

D region, 12-1
Datums, geodetic systems, 1-3
Dawn chorus, ionospherics, 9-24
Day glow,
(see airglow)
Deflection of the vertical, components, 1-3
formulas, 1-3, 1-8, 1-9
Density, air, correlations with wind, 3-27
distribution, below 30 km, 3-23, 3-25 to 3-27, 3-44 to 3-46
30 to 90 km, 3-27 to 3-29
90 to 300 km, 3-34, 3-37
interlevel correlations, 3-26, 3-44 to 3-46
isopycnic level, 3-23
measurements, 3-35, 3-37
model atmospheres, 2-11 to 2-22
Arctic summer, 2-17
Arctic winter, 2-18
midlatitude summer, 2-13
midlatitude winter, 2-14
subarctic summer, 2-14
subarctic winter, 2-15 to 2-17
subtropical summer, 2-11
subtropical winter, 2-12
tropical, 2-11
U.S. Standard 1962, 2-19 to 2-22
profiles, 3-23, 3-25, 3-26, 3-28, 3-44 to 3-46
variability above 200 km, 3-38 to 3-43
variations, diurnal and interdiurnal, 3-25, 3-26, 3-28, 3-29
latitudinal and seasonal, 3-23, 3-25, 3-26, 3-28, 3-29
Density, electron
(see electron density)
ice, 9-3, 9-9
ion,
(see ions, density variations)
meteoroids, 14-1
planets
(see Mars, Venus, etc.)
snow, 9-3, 9-9
Sun
(see solar atmosphere)
Density scale height, 6-1
Dewpoint
(see frostpoint)
Disk temperature, 16-18, 22-2
Dissociation, nitric oxide, 6-13
nitrogen, 6-1, 6-9 to 6-11
oxygen, 6-1, 6-12, 6-13
Disturbing potential, gravity, 1-21
Dust, cosmic, 14-1
interstellar, 21-18, 21-19
particles, zodiacal, 15-5
D region, 12-1
Dwarf and white dwarf stars, 21-7, 21-9

E

E region, 12-1
Earth/air interface, energy balance, 3-2
temperature, 3-19 to 3-21
Earth, reference surfaces, 1-1, 1-2
ellipsoid, 1-4, 1-5
geoid, 1-1, 1-8, 1-10
spheroid, 1-6
Ecliptic, 21-4, 21-7

Electricity, atmospheric, 8-1 to 8-22
current density, 8-2
equilibrium conditions, 8-4 to 8-8
fields, 8-1, 8-2
maintenance of Earth's charge, 8-6
space charge density, 8-2
thunderstorms, 8-6 to 8-11
variations in exchange layer, 8-5, 8-9, 8-12 to 8-19
variations in free atmosphere, 8-5, 8-20, 8-21
worldwide current system, 8-6
Electromagnetic wave propagation, attenuation
(*see* attenuation)
backscattering, troposphere, 9-2 to 9-14
ionosphere, non-deviative absorption, 12-15 to 12-25
ionospheric interactions, 9-14, 9-16, 9-17
refractive modulus, troposphere, 9-1, 9-2, 9-7, 9-8, 9-10
Electron density, auroral zone, 12-4, 12-12
interplanetary space, 18-1, 18-2
ionosphere, 12-2
above F region, 12-4, 12-6, 12-13
rocket data, 12-2 to 12-8
satellite data, 12-2 to 12-4, 12-9 to 12-13
vertical incidence sounder data, 12-2
meteor trails, 9-17
solar corona, 16-26, 18-2, 18-3, 18-12
Elementary particles, 17-14, 17-15
Ellipsoids, Earth, 1-2, 1-4, 1-5
Energy cycles, Earth/atmosphere system, 3-1 to 3-3
Epheremis time, 21-2
Exosphere, 2-2

F

F region, 12-1
Faculae, 15-10
Faraday effect, 12-6, 12-15
Fastest mile, wind, 4-33
Fireball meteor, 14-1
Flare, solar, 15-11, 15-12
(*see also* solar cosmic rays)
stars, 21-23
Forbush decrease, 17-14, 17-15, 17-26
Fraunhofer lines, 15-1, 15-4
Frostpoint, 3-33 to 3-35, 3-37
F-value, 21-10

G

Galactic coordinate system, 21-7
corona, 21-19
halo, 21-1
Galaxies, classification, 21-29
local group, 21-29
nomenclature, 21-28, 21-29
spiral, 21-1, 21-2, 21-8
Galaxy, our
(*see* Milky Way)
Gas, interstellar, 21-18 to 21-20, 22-9
kinetics, 18-13, 18-14
(*see also* atmosphere)
Geocentric coordinate system, 1-20, 1-21
Geodesy, geometrical, 1-1 to 1-6
gravimetrical, 1-6 to 1-17
measurements, 1-17, 1-18
satellite, 1-19 to 1-26
Geodetic coordinates, 1-2
Geoid, definition, 1-1
undulation, 1-9
Geomagnetic coordinate systems, 11-2, 17-3 to 17-6
equivalent latitude, 17-3
hour, 11-2
latitude, 11-2
Geomagnetic field, 11-1
dip equator, 11-2
dip poles, 11-2
direct solar flare effect, 11-28, 11-29, 17-21
distant, 11-44, 11-45
disturbances, 11-28
daily variations, 11-30
D-field, 11-30, 11-31
irregular field, 11-30
L and S variations, 11-28
magnetic activity indices, 11-30 to 11-43
random variation, 11-30, 11-31
rapid variation, 11-39, 11-44
diurnal variation, 11-28, 11-29
effects, cosmic rays, 17-2
trapped particles, 17-2, 17-3
elements, 11-1, 11-2
declination, 11-2
inclination, 11-2
total field, 11-1, 11-2
vertical intensity, 11-1, 11-2
L parameter, 17-3, 17-4
main field, definition, 11-1
magnetic charts, 11-6 to 11-16
origin, 11-7
regional anomalies, 11-7
spherical harmonic analysis and extrapolation, 11-17 to 11-27
surface anomalies, 11-7
Taylor series analysis and extrapolation, 11-18, 11-19
measurements, 11-1, 11-2, 11-7
poles, 11-2
prime geomagnetic meridian, 11-2
storm, 11-28, 11-30, 15-13
units, 11-1
Geopotential, 1-6
Giant and supergiant stars, 21-7, 21-9
Gradient, air temperature, horizontal, 3-6
vertical, 3-11, 3-12, 3-14
refractive modulus, optical, 9-1, 9-2, 9-4 to 9-6
radio, 9-1, 9-2, 9-6
wind, 4-3

Gravitation, acceleration, 1-7
potential, Earth, 1-6
Moon, 19-14
Gravity, Earth, anomaly, 1-8
anomalies, 1-10, 1-17
definition, 1-6
deflection of vertical, 1-2, 1-9
disturbance, 1-7, 1-17
disturbing potential, 1-7
field at high altitudes, 1-15, 1-17
geoid undulation, 1-9
geopotential, 1-6
gravitation vs gravity, 1-6
isostatic equilibrium, 1-14, 1-15
international gravity formula, 1-7
measurements, 1-13, 1-16
normal gravity, 1-6, 1-7, 1-15, 1-17
observed gravity anomaly, 1-8
potential, 1-7
reduction of measurements, 1-14, 1-15
variation of normal gravity, 1-7
Moon, 19-15
Gray body, 10-1
Great red spot, Jupiter, 20-14
Ground level events, solar flares, 15-11, 17-19
Guiding center, trapped particles, 17-2
Gusts, wind, 4-20, 4-28
Gyrofrequency, 9-17, 9-23, 12-21
Gyroradius, 17-2

H

H-R diagrams, 21-12, 21-13, 21-20, 21-22, 21-23
Hadley regime, 18-15
Hail, extent, horizontal, 5-5, 5-6
vertical, 5-6
formation, 5-5
size, 5-6
Haze, visible, 5-22
Heat capacity, soil, 3-20
Heating degree day, 3-23
Heat of ablation, meteoroid, 14-2
Helium, atmospheric, 6-1, 6-2
Helmert's projection, 1-3
Hiss, ionospherics, 9-24
Hour circle, 21-4
Hourly surface wind speed, 4-34 to 4-37
H-regions, I and II, 21-18
Hubble's constant, 20-1
Humidity
(*see* water vapor, atmospheric)
Hydrodynamic theory, solar corona, 18-5
Hydrogen, Earth's atmosphere, 6-1, 6-2
interstellar 21-cm line, 22-7, 22-9
Hydromagnetic waves, 9-19, 9-20, 9-23
Hydrostatic equations, 2-1, 18-3

I

Ice, attenuation properties, 9-14, 1-15
dielectric properties, 9-3
particles, thunderstorms, 5-5
scattering properties, 9-5
Index of refraction, radio wavelengths, 9-14, 9-16, 9-17, 9-22, 9-23, 12-17
(*see also* refractive modulus)
Infrared radiation, absorption, carbon dioxide, 10-2, 10-4, 10-6
ozone, 10-2, 10-4
water vapor, 10-2 to 10-7
celestial backgrounds, 10-20
Milky Way, 10-25
Moon, 10-28
planets, 10-28
stars, 10-25 to 10-27
Sun, 10-28
zodiacal light, 10-28
detectors, 10-1, 10-2
emission, atmosphere, 10-6 to 10-20
sources, 10-1
spectra, atmospheric molecules, 10-2, 10-3
Sun, 10-2, 10-3, 10-9 to 10-12
transmittance, carbon dioxide, 10-4, 10-33 to 10-35
water vapor, 10-2, 10-4, 10-29 to 10-32
window materials, 10-2
windows, 10-4, 10-6, 10-8
Insolation, 3-1
Interplanetary space, electron densities, 18-1, 18-2
temperatures, 18-2
magnetic field, 18-2, 18-9 to 18-11
models, 18-2 to 18-7
proton, number density, 18-2
showers, 15-12
solar wind, 18-2, 18-9
International gravity formula, 1-7
Interstellar space, dust, 21-19, 21-20
gas clouds, 21-19, 21-20
magnetic field, 21-19
polarization, 21-19
reddening, 21-19
selective absorption, 21-19
spectral lines, 21-18, 22-7, 22-9
zone of avoidance, 21-20
Inverse square model, solar corona, 18-2
Inversion, temperature, 2-1
Inversion layer, 3-14
Ionization, atmospheric radioactivity, 8-5, 8-8
cosmic rays, 8-5, 8-8, 17-25, 17-26
meteoroids, 14-3, 14-4
meteor trails, 9-17, 9-19
photoionization, 6-7 to 6-15
cross sections, 6-14, 6-15, 16-16, 16-17
efficiency, 6-7
Saha theory, 21-12
Ionosondes and Ionograms, 9-17, 9-19, 12-2

Ionosphere, D, E, and F regions, 12-1
disturbances, 12-1, 12-2
auroral zone absorption, 12-2
F region, 12-1, 12-2
polar cap absorption, 12-1, 12-2
sudden ionospheric disturbance, 12-1, 15-13
electron densities, 12-2 to 12-13
temperature, 12-6, 12-13, 12-14
total content, 12-6, 12-15
ion density and temperature, 12-3, 12-4, 12-6 to 12-10, 12-14
sporadic E, classifications, 12-36
occurrence, 12-36, 12-37, 12-40 to 12-52
winds, characteristic velocity, 12-35, 12-36, 12-38
correlation ellipses, 12-35 to 12-37, 12-41
drift directions, variations, 12-28 to 12-34
drift velocities, 12-34, 12-35
Ionospheric phenomena, absorption
auroral zone, 12-1, 12-2
polar cap, 12-1, 12-2
sudden commencement, 12-2
Faraday effect, 12-6, 12-14, 12-15
ionospherics, 9-20 to 9-22, 9-24
polarization, radio wavelengths, 12-14, 12-15
propagation, radio wavelengths, 9-14, 9-16, 9-17
(*see also* index of refraction)
scintillations, radio wavelengths, 22-3
sudden ionospheric disturbance (SID), 12-1, 15-13
whistlers, 9-19 to 9-24
Ionospherics, definition and types, 9-20, 9-21
occurrence statistics, 9-24
theory, 9-22
Ions, atmospheric composition, 6-2
atmospheric electricity, 8-1 to 8-6, 8-8
attachment coefficients, 8-3, 8-4
continuity equations, 8-3
density variations, 8-4 to 8-8, 8-20
diffusion coefficients, 8-3 to 8-5
mobility, 8-2, 8-3
pollution particle content, 8-5, 8-21
production rates, 8-5, 8-19
volume recombination coefficient, 8-3, 8-4
dissociation, 6-1, 6-9 to 6-13
ionosphere, collisions, 6-19, 12-25
densities, 12-2 to 12-13
temperature, 12-6, 12-13, 12-14
negative ions, 6-18 to 6-20
production processes, 6-7 to 6-16, 6-18
(*see also* ionization)
reaction with neutrals, 6-20, 6-22
recombination, 6-15 to 6-17, 8-3, 8-4
Iron meteoroid, 14-1, 14-2
Irradiance, celestial backgrounds
(*see* infrared radiation, celestial backgrounds)
solar, 16-1 to 16-11
Isoaurorae, 13-6
Isochasms, 13-6
Isopycnic level, 3-23
Isotachs, 4-21, 4-44
Isostatic equilibrium, 1-15

J

Jean's formula, planetary atmosphere, 18-5
Jet streams, 4-21, 4-44, 4-45
low level types, 4-4 to 4-6
Johnson noise, 22-1
Jupiter, astronomical data, 20-13 to 20-15
great red spot, 20-14
radio observations, 20-14, 22-5

K

Kepler's equation, 1-21
Kinematic viscosity, 18-13
Kinetics, solar atmosphere, 18-13 to 18-15

L

Lagrangian planetary equations, 1-22
Lapse rates, 2-1, 3-11
dry adiabatic, 3-11
saturation adiabatic, 3-11
temperature, 3-15 to 3-18
Latitude, astronomical, 1-2
geodetic, 1-3
geomagnetic, 11-2, 17-3
Libration, lunar, 19-13 to 19-15
angular rate, 12-15
Lightning, 8-6 to 8-22
discharges, 8-6
dart leader, 8-6
return stroke, 8-6
stepped leaders, 8-6
distribution within cloud, 8-10, 8-21
effect on aircraft, 8-8
fields, electric, 8-7, 8-20, 8-21
magnetic, 8-11
frequency characteristics, 8-11
flash frequency, 8-9
strike characteristics, 8-8 to 8-10
stroke path, 8-8 to 8-10
total charge, 8-10, 8-11
Light year, 21-4
Line absorbing layer, 15-1 to 15-4
Local civil time, 21-3
Local meridian, 21-4
Longitude, astronomical, 1-2
geodetic, 1-3
geomagnetic, 11-2
Luminosity, classes, 21-14
meteoroids, 14-1 to 14-3
stars, 21-12, 21-14, 21-28
Lyman series hydrogen lines, 21-10

M

Macroclimatology, 3-17, 3-19
Magnetic field, Earth
(*see* geomagnetic field)
galactic, 21-19
interplanetary space, 18-2, 18-9, 18-10
Mars, 20-11
Moon, 19-1, 19-2
Sun, 18-7 to 18-11, 18-17 to 18-18
sunspots, 15-10, 18-8 to 18-10, 18-17, 18-18
Venus, 20-3
Magnetic rigidity, 17-2
Magnetic storms, 11-28, 11-30, 15-13
effects, atmospheric density, 3-40, 3-41
atmospheric temperature, 3-43
cosmic ray intensity, 17-15
sudden commencements, 11-28, 15-12
Magneto-ionic formulas, ionospheric interactions, 9-16, 9-17, 9-21
Magnetosphere, 11-1
Magnitudes, meteor, 9-17, 14-1, 14-2
planetary, 20-1
stellar, 21-9, 21-10
Mars, astronomical data, 20-13
atmospheric composition, 20-5
atmospheric structure, 20-7, 20-8
magnetic fields, 20-11
surface temperature and features, 20-11 to 20-13
satellites, 20-13
Mean free path, Earth's atmosphere, 2-19 to 2-22
solar atmosphere, 18-8
Mean solar time, 21-1
Meridian ellipse, 1-2
Mercury, astronomical data, 20-1
Mesopause, 2-2
Mesosphere, 2-1
Meteor, bolide, 14-1
fireball, 14-1
heights of occurrence, 14-4
light curve, 14-4
magnitude, 9-17, 14-1, 14-2
corrections, 14-2, 14-3
radiant, 14-1
showers, 14-1, 14-7, 14-8
sporadic, 14-1
trail characteristics, 9-17, 9-19
Meteorite, 14-1
Meteoroid, composition, 14-1, 14-2
density, 14-1
depth of penetration, 14-8
drag coefficient, 14-2
flux, 14-5 to 14-7
interaction with atmosphere, 14-2, 14-3
ionization, 14-3, 14-4
mass, 14-2, 14-5 to 14-7
speed, 14-4, 14-5
Microclimatology, 3-17, 3-19
Micrometeorites, 14-1
Microwave, attenuation
(*see* attenuation, microwave radiation)
radiation
(*see* radiation, microwave)
Mie scattering, optical wavelengths, 7-8
radio wavelengths, 9-4, 9-5
Milky Way, description, 21-1
dust clouds, 21-20
hydrogen gas, 22-7
infrared background emission, 10-25
radio background emission, 22-5 to 22-8
rotation, 21-1, 21-4
Mixing ratio, water vapor, 3-31, 3-33 to 3-35, 3-37, 3-38
MK system, stellar classification, 21-14 to 21-16
Model atmospheres
(*see* atmosphere, models)
Moisture properties, model atmosphere, 2-10
(*see also* water vapor, atmospheric)
Molecular scale temperature, 2-1
Molecular weight, atmosphere, 3-38, 6-1
Molecular thermal conductivity, soil, 3-20
Moon, astrodynamic constants, 19-15
atmosphere, 19-1
composition, 19-6
escape velocity, 19-1
gravity, 19-14, 19-15
librations, 12-15, 19-13, 19-14
magnetic field, 19-1, 19-2
mechanical figure, 19-14
natural resources, 19-13
radio emission, 22-3
reflection, 12-6, 12-14, 12-15
rotation, 19-13, 19-14
surface and subsurface structure, 19-6 to 19-10
surface roughness, 19-9 to 19-13
thermal environment, 19-1 to 19-5
M region, 15-13, 15-14, 18-17

N

Nebula, extragalactic, 21-28
spiral, 21-28
Neptune, astronomical data, 20-16
Nightglow
(*see* airglow)
Nitric oxide, 6-13
Nitrogen, atomic, 6-13
molecular, 6-12
Noctilucent clouds, 5-21 to 5-23
Novae and supernovae, 21-27

O

Optical air mass, definition, 16-7
depletion of solar irradiance, 16-7, 16-8
variation with zenith angle, 16-7
Optics, atmospheric attenuation models, 7-1 to 7-4
atmospheric scattering, 7-6 to 7-9
flux from Earth's atmosphere, 7-6
reflectance, clouds, 7-5
ground surfaces, 7-3 to 7-5
skylight, 7-9 to 7-13
Orbital perturbations, artificial satellites, 1-21, 3-39
Oxygen, atomic, 6-13, 6-14
molecular, 6-12, 6-13
Ozone, absorption coefficients, 7-1 to 7-3, 7-9 to 7-11
atmospheric attenuation model, 7-1
effects, 6-2
formation in atmosphere, 6-3
infrared absorption, 10-2, 10-4
total distribution, 6-3 to 6-5
vertical distribution, 6-3, 6-6, 6-8, 6-9

P

Parker's equations, solar corona, 18-5 to 18-8
Parsec, 21-4
Penumbra, sunspots, 15-10, 18-10
Photoionization, 6-7 to 6-14
cross sections, 6-7, 6-8, 16-16, 16-17
Photons, absorption in upper atmosphere, 6-7 to 6-14, 16-16, 16-17
Photosphere, circulation, 18-14 to 18-16
features, 15-1, 15-2, 15-8
rotation, 18-11, 18-15
Pitch angle, trapped particle motion, 17-2
Pizzetti's projection, geodesy, 1-3, 1-4
Plages, solar activity, 15-10
Planck's radiation functions, B-1 to B-9
Planets, environments (*see* Mars, Venus, etc.)
radio emission, 22-3, 22-5
Plasma oscillation frequency, 9-16, 9-21, 12-17
Pluto, astronomical data, 20-17
Polar cap event, 12-2, 15-11
Polarization, atmospheric, Arago point, 7-7
Babinet point, 7-7
Brewster point, 7-7
Faraday rotation, 12-15
ground reflectance, 7-4
interstellar dust, 21-18, 21-19
Population I and II stars, 21-21
Power flux density, radio astronomy, 22-2
solar radio emission, 16-18 to 16-23
flux at 10.7 cm, 3-39, 3-40, 16-22, 16-24
Prandtl numbers, 18-13, 18-14
Pratt-Hayford hypothesis, isostatic systems, 1-15
Precipitation, atmospheric, 5-1 to 5-11
distributions, 5-11
hail, 5-5, 5-6
size distribution, 5-6
model atmospheres, 5-7 to 5-9
rainfall, clock hourly rates, 5-1 to 5-3
extreme rates, 5-4, 5-5
instantaneous rates, 5-2 to 5-4
separation from snowfall, 5-4
surface rates, 5-1 to 5-5
size distribution, rain and snow, 5-9, 5-10
snow, density, 9-3, 9-9
falling speed, 5-9
rates of snowfall, 5-7, 5-9
separation from rainfall, 5-4
thunderstorms, 5-10, 5-11
water content of clouds, 5-9
Precipitable centimeters of water, 3-27
Pressure, air, 3-29 to 3-31, 3-34, 3-38
effect of solar activity, 15-14
effect on cosmic rays, 17-14
effect on refractive modulus, 9-1, 9-2
extremes at sea level, 3-30, 3-31
mean heights, pressure surfaces, 3-32
model atmospheres, 2-11 to 2-22
Arctic summer, 2-17
Arctic winter, 2-18
midlatitude summer, 2-13
midlatitude winter, 2-14
subarctic summer, 2-14
subarctic winter, 2-15 to 2-17
subtropical summer, 2-11
subtropical winter, 2-12
tropical, 2-11
U.S. Standard, 1962, 2-19 to 2-22
variations, daily and seasonal, 3-30 to 3-33
diurnal and semidiurnal, 3-31, 3-33
Pressure scale height, 3-1
Pressure, planetary atmospheres (*see* Mars, Venus, etc.)
Prime geomagnetic meridian, 11-2
Prominences, solar, 15-7 to 15-9
Proton cycle, 21-20
showers, 15-12
Protons, cosmic rays, 17-12
solar cosmic rays, 17-19
solar wind, 18-2, 18-5, 18-10
time of flight, Sun to Earth, 15-12
Van Allen belt, 17-7 to 17-10
Pulsating stars, 21-24 to 21-27

Q

Quiet sun, features, 15-1 to 15-6 (*see also* solar atmosphere)
irradiance, 16-1 to 16-11
power flux density, radio emission, 16-18 to 16-23
temperature, 16-1, 16-18 to 16-23
ultraviolet and x-ray emission, 16-10 to 16-18

R

Radar reflections from precipitation, 9-9, 9-13, 9-14, 9-16, 9-18
Radiation, airglow
(*see* airglow)
aurorae
(*see* aurorae)
background, radio astronomy, 22-5 to 22-8, 22-10 to 22-14
infrared, celestial, 10-20 to 10-29
skylight, 7-9, 7-12
belts
(*see* trapped radiation)
blackbody, 10-1, B-1, B-9
corpuscular
(*see* cosmic rays and trapped radiation)
cosmic
(*see* cosmic rays)
flux from atmosphere, 3-1, 7-6
gray body, 10-1
hydrogen 21-cm line, 22-7, 22-9
infrared
(*see* infrared radiation)
long wave, terrestrial, 3-2
microwave, 9-3 to 9-18
net, terrestrial, 3-2
optical, 7-1, 7-6 to 7-9, 16-1 to 16-10
radio, solar, 16-18 to 16-26
stellar
(*see* radio astronomy)
solar irradiance, 16-1 to 16-11
effects on atmosphere, 3-1, 3-39 to 3-43, 15-13
ultraviolet and x rays, solar, 16-10 to 16-18
Van Allen
(*see* trapped radiation)
Radio astronomy, antenna temperature, 16-21, 22-1, 22-2
atmospheric effects, absorption, 22-3, 22-4
refraction, 22-2
scintillations, 22-3
average disk temperature, 22-2
background emission maps, 22-5, 22-7, 22-9
definitions, 22-1, 22-2
discrete sources, 22-7, 22-10, 22-14
spectra, 22-10, 22-14
drift technique, 22-2
hydrogen 21-cm line, 22-7, 22-9
hydroxyl 18-cm line, 22-9
Johnson noise, 22-1
Moon, 22-3
planets, 22-3, 22-5
power flux densities, 22-2, 22-9 to 22-14
Sun
(*see* solar emissions, radio wavelengths)
Radio aurorae, 13-4
Radio reflections, ionosphere, 9-17
lunar, 12-6
meteor trails, 9-17 to 9-19
troposphere, 9-9, 9-13, 9-14
Radioactivity, emanation from Earth's surface, 8-3
interactions with aerosols, 5-25
natural atmospheric, 8-5, 8-19
Radiometric units, blackbody radiation, B-1
Rain, attenuation of microwaves, 9-4, 9-14, 9-15, 9-18
clouds, 5-9
dielectric properties, 9-3
particle size distribution, 5-9
Rainfall, clock hourly rates, 5-1 to 5-3
distributions, 5-11
extreme rates, 5-4, 5-5
five-year expectancy, 5-4, 5-5
instantaneous rates, 5-2 to 5-4
separation from snowfall, 5-4
surface rates, 5-1 to 5-5
thunderstorms, 5-10, 5-11
worldwide expectancy, 5-4, 5-5
Rayleigh atmosphere, 7-2
Rayleigh-Jeans approximation, blackbody, B-2
Rayleigh scattering
(*see* scattering, Rayleigh)
Recombination
(*see* ions, recombination)
Reference surfaces, Earth, 1-1
ellipsoid, 1-2
geoid, 1-1
Moon, ellipsoid, 9-14
selenoid, 9-15
Reflectance, cloud, 7-5
ground and water, 7-3 to 7-5
polarization, 7-4
spectral, 7-3
Refractive modulus, clouds, 9-2, 9-7, 9-8, 9-10, 9-11
microwaves, 9-1, 9-2, 9-4 to 9-7
optical wavelengths 9-1, 9-3
standard profiles, 9-1, 9-2, 9-6
Relative humidity
(*see* water vapor, atmospheric)
Return period, wind speed, 4-38
Return stroke, lightning, 8-6
Reynolds numbers, 18-13, 18-15
Rigidity, cosmic rays, 17-2, 17-29, 17-30
Rossby waves, 18-14 to 18-16

S

Saha theory, 21-12
Satellite geodesy, 1-20
Satellites of the planets, 20-18
Saturn, astronomical data, 20-15, 20-16
Scattering, atmospheric, infrared, 10-6, 10-7
optical, 7-6 to 7-9
microwave, 9-9, 9-13, 9-14
meteor trails, 9-19
Mie, 7-1, 7-2, 7-8
Rayleigh, 7-1 to 7-3, 7-7, 7-8, 9-3 to 9-5, 9-12
Scintillation, atmospheric, 22-3
Selective absorption, 21-19

Semi-empirical model, solar corona, 18-2
Sen's models, solar corona, 18-5
Sferics, 8-11
Shelter temperature, meteorology, 3-4
Sidereal time, 21-3
Skylight, 7-9, 7-12, 7-13
Snow, attenuation of microwaves, 9-13 to 9-15
density, 9-3
dielectric properties, 9-3
falling speed, 5-7, 5-9
particle size distribution, 5-10
separation from rainfall, 5-2
Soil, heat capacity, 3-20
moisture, 3-2, 3-20 to 3-22
reflectance, 7-3, 7-4
temperature variations, 3-20 to 3-22
thermal admittance, 3-20, 3-21
conductivity, 3-20
diffusivity, 3-20
Solar atmosphere, circulations, 18-14 to 18-16
conductivity, electric, 18-12, 18-14, 18-15
thermal, 18-13, 18-14
electric current effects, 18-10
energy transport, coefficients, 18-13 to 18-15
processes, 18-16
magnetic effects
(*see* solar magnetic field)
meteorology, 18-11 to 18-18
Hadley regime, 18-15
Reynolds and Prandtl numbers, 18-13 to 18-15
Rossby numbers, 18-14, 18-16
Rossby waves, 18-14, 18-15
models, corona, 18-2 to 18-7
electron densities, 18-1, 18-2, 18-12
electron temperatures, 18-1, 18-2
rotation, photosphere, 18-11
velocities, 18-13 to 18-15
scale heights, 18-7, 18-8
viscosity coefficients, 18-13, 18-14
Solar constant, 3-1, 15-6, 16-1
Solar cosmic rays, composition, 17-19
energies, 17-19
flux, 17-19
observations, 17-20, 17-27
proton showers, 15-12
relation to optical flare, 17-19
rigidity spectra, 17-19, 17-21, 17-30
rise time, 17-21
variations, 7-21, 17-26
Solar cycles, magnetic, 18-8
(*see also* solar magnetic field)
sunspot, 15-7, 15-8, 15-10
Solar emissions, infrared, 10-3
irradiance at Earth's orbit, 16-1 to 16-6
particles
(*see* solar cosmic rays and solar wind)
radio wavelengths, bursts, 16-24, 16-25
power flux densities, 16-18, 16-19 to 16-23
rapidly varying component, 16-24, 16-27, 16-28
regions of generation, 16-19
slowly varying component, 16-23, 16-24
spectral distribution, 15-4, 16-2
ultraviolet and x rays, lines, 16-13, 16-16, 16-17
spectrum, 16-10, 16-19
Solar flares, characteristics, 5-11
effects, 15-12 to 15-14
(*see also* solar cosmic rays)
importance class, 15-11
physical processes, 15-11, 18-17
prediction, 15-12, 17-21
Solar magnetic field, cycle, 18-8, 18-17
dipole, distortion, 18-9 to 18-11
variation with sunspot cycle, 18-8, 18-9
magnetic cloud, 18-17, 18-18
morphology, tentative model, 18-17, 18-18
poloidal field, 18-7, 18-9, 18-17, 18-18
sunspots, 18-8 to 18-10, 18-17, 18-18
field strength, 15-10
toroidal field, magnetic bands, 18-7 to 18-9, 18-17
Solar units for astronomy, 21-4
Solar wind, data, 18-2
effect on solar magnetic field, 18-9 to 18-11
models, 18-2 to 18-7
Sound speed in air, 2-19 to 2-22, 3-14
speed vs temperature, 3-16
speed, solar atmosphere, 18-12
Space, interplanetary
(*see* interplanetary space)
interstellar
(*see* interstellar space)
Spectral reflectance, terrestrial surfaces, 7-3
Spectroscopic terminology, astronomy, 21-10
Spherical harmonic extrapolation
(*see* geomagnetic field)
Spheropotential, Earth, 1-7
Spicules, solar, 15-5
Sporadic E, 12-36, 12-37, 12-42 to 12-51
Standard Atmosphere 1962, U.S., 2-2 to 2-5
Standard Meteorological Sounding System, 4-20
Stars, associations, 21-2, 21-21
binary and multiple, 21-7, 21-9
Cepheids, 21-26, 21-27
classification systems, luminosity class, 21-14, 21-15
quantitive methods, 21-17, 21-18
spectral type, 21-11, 21-12
clusters, galactic and globular, 21-21, 21-22
H-R diagram, 21-23,
color, diagram, 21-15 to 21-17
index (C.I.), 21-10
U, B, V and R, I systems, 21-10
coordinates, conversion, 21-5
systems, 21-4 to 21-7
distance, determinations, 21-27, 21-28
modulus, 21-9, 21-28
scale, 21-28
statistically corrected, 21-19
dwarfs and white dwarfs, 21-7, 21-9
electrons, surface pressure, 21-12

evolution, gravitational contraction, 21-20
interior nuclear reactions, 21-20
mass loss, 21-21
relation to H-R diagrams, 21-20, 21-22, 21-23
giants and supergiants, 21-7, 21-9
gravity, surface, 21-12
H-R diagrams, 21-12, 21-13, 21-20, 21-22, 21-23
intrinsic variables, 21-23 to 21-27
luminosity, definition, 21-12
mass-luminosity relation, 21-14
period-luminosity relation, 21-28
magnitudes, 21-9, 21-10
luminosity classes and spectral types, 21-15
main sequence, 21-7, 21-13, 21-25
mass, 21-14
motions, proper and peculiar, 21-4, 21-27, 21-28
names and catalogue numbers, 21-7, 21-9
novae and supernovae, 21-27
parallaxes, 21-27, 21-28
Populations I and II, 21-21
pulsating, characteristics, 21-24, 21-26
pulsation constant, 21-24
RR Lyrae, 21-26, 21-28
temperatures for luminosity classes and spectral types, 21-15
spectroscopic studies, Balmer jump, 21-17, 21-18
curve of growth, 21-10, 21-11
excitation, ionization vs temperature, 21-11, 21-12
terminology, 21-10
units, solar values, 21-4
Station temperature, meteorology, 3-2, 3-4
Stefan-Boltzmann law, blackbody, B-2
Stone meteoroid, 14-1, 14-2
Stratopause, 2-1
Stratosphere, 2-1
Sudden ionosphere disturbance, 12-1, 15-13
Sun, active centers, 15-10
(*see also* sunspots)
chromosphere, 15-3 to 15-5
corona, 15-5, 15-6
(*see also* solar atmosphere)
cycles
(*see* solar cycles)
density, mean, 21-4
distance from earth, 21-4
disturbed, 15-7, 16-26
energy, 15-6, 15-7
escape velocity, 18-2, 21-4
faculae, 15-10
filaments, 15-7
flares
(*see* solar flares)
flocculi, 18-17, 18-18
gravity, 18-8, 21-4
line-absorbing layer, 15-1 to 15-3
magnetic field
(*see* solar magnetic field)
mass, 15-1, 21-4
photosphere, 15-1 to 15-4, 15-8
plages, 15-10
prominence, 15-7 to 15-9
quiet, 15-1 to 15-6, 16-18
radius, 21-4
rotation, 15-1, 18-11
spicules, 15-5
sunspots
(*see* sunspots)
temperatures, 16-1, 16-18, 16-20
Sunspots, cycle, 15-7, 18-8, 18-9
features, 15-10, 15-11
latitudinal distribution vs time, 15-10, 18-8
magnetic field
(*see* solar magnetic field)
number, 15-7
Superadiabatic layer, 3-14
Supergeostropic wind, 4-4
Surface air temperature, 3-2, 3-4

T

Temperatures, air, 3-1 to 3-23, 3-34 to 3-36, 3-38, 3-41, 3-43
below 30 km, 3-12, 3-14
vertical profiles, 3-15, 3-17
30 to 90 km, 3-11 to 3-14
90 to 300 km, 3-34 to 3-36, 3-38, 3-41, 3-43
extremes, 3-8 to 3-13
gradient, 2-1
horizontal, 3-6
vertical, 3-11, 3-12, 3-14, 3-18
ground/air interface, 3-19 to 3-21
heating degree day, 3-23
inversion, 2-1, 3-14
lapse rate, 2-1, 3-11, 3-15 to 3-18
model atmospheres, 2-11 to 2-22
Arctic summer, 2-17
Arctic winter, 2-18
midlatitude summer, 2-13
midlatitude winter, 2-14
subarctic summer, 2-14
subarctic winter, 2-15 to 2-17
subtropical summer, 2-11
subtropical winter, 2-12
tropical, 2-11
U.S. Standard, 1962, 2-19 to 2-22
molecular-scale temperature, 2-1
variation with altitude, 3-35, 3-36
probability distributions, 3-7
surface air, 3-2, 3-4 to 3-11
station temperature, 3-2, 3-4 to 3-11
variability above 200 km, 3-41, 3-43
variations, diurnal, 3-16, 3-17
seasonal, 3-12 to 3-14
Temperature, interplanetary, 18-2
Mars, 20-11
Moon, 19-1 to 19-5
runway, 3-7
soil, 3-19 to 3-22

solar, 16-1, 16-18
stellar
(*see* stars, spectroscopic studies)
Venus, 20-3
Terrain correction, gravity, 1-14
Thermosphere, 2-2
Threshold rigidity, cosmic ray cutoff, 17-2, 17-26, 17-29
Thunderstorms, electrostatic field, 8-7, 8-10, 8-11, 8-20 to 8-22
lightning effects and patterns, 8-8 to 8-10
precipitation, 5-10
radiation, frequency characteristics, 8-11
Time, units and definitions, 21-1, 21-3
Trapped radiation, electrons, 17-10, 17-12 to 17-14, 17-16 to 17-18, 17-22
guiding center, 17-3
L-values, 17-3 to 17-6
measurements, 17-3, 17-7 to 17-10
mirror point, 17-2
motion in magnetic field, 17-2 to 17-6
pitch angle, 17-2
protons, 17-7 to 17-12
spacial distribution, 17-11, 17-16, 17-17
variations with time, 17-10
Triangulation, geodesy, 1-2
electronic distance measurements, 1-17
rocket flash, 1-18
Tropic model atmosphere, 2-11
Tropopause, 2-1
Troposphere, 2-1
Turbid atmosphere, 7-1
Turbulence, Great Plains Field Program, 4-2
Turn-off point, stellar evolution, 21-22
Twilight glow
(*see* airglow)

U

Ultraviolet radiation, effect on atmosphere, 6-7 to 6-16
solar emission, 16-10 to 16-19
Umbra, sunspots, 15-10
Universal time, definition, 21-2
Uranus, astronomical data, 20-16

V

Van Allen belts
(*see* trapped radiation)
Veering, wind, 4-2, 4-3
Venus, astronomical data, 20-5
atmosphere, 20-1, 20-2
magnetic field, 20-3
satellites, 20-3
surface features, 20-3
thermal environment, 20-3, 20-4
Vernal equinox, 21-4, 21-6

W

Water
(*see* precipitation)
Water vapor, atmospheric, 3-31 to 3-34
frostpoint, 3-33
infrared absorption, 10-2, 10-4, 10-6
maximum content, 3-31
mixing ratio, 3-31
models, mid-latitude, 3-34, 3-35, 3-37
polar, 3-34
tropical, 3-34, 3-38
precipitable water, 3-31, 3-32
Whistlers, description, 9-20, 9-21
observations, 9-23
theory, 9-22
Wien, displacement law, B-2
radiation functions, B-2
Wind, above 100,000 feet, 4-45, 4-52, 4-53
below 100,000 ft., 4-38, 4-44, 4-46 to 4-51
design data, 4-29 to 4-53
gradient, 4-3
gusts, 4-20, 4-28
ionospheric
(*see* ionosphere, winds)
isotachs, 4-44
jet streams, 4-4, 4-5, 4-22, 4-44, 4-45
mean wind, 4-1 to 4-6
profiles, ballistic, 4-28 to 4-32
synthetic, 4-21 to 4-27
roughness parameter, 4-1, 4-2
shear, 4-17
horizontal, 4-17
vertical, 4-17 to 4-21
shifts, below 10,000 ft., 4-2 to 4-4
backing, 4-2
veering, 4-2, 4-3
solar
(*see* solar wind)
speeds, distribution, 4-38, 4-39
extreme surface, 4-33, 4-38 to 4-43
fastest mile, 4-33
hourly surface, 4-33 to 4-37
return period, 4-38
strongest gust, 4-33
supergeostrophic, 4-4
variations, below 300 ft., 4-1, 4-2
structure, large scale, 4-6
variability, up to 30 km, 4-6 to 4-8, 4-46 to 4-51
above 30 km, 4-6, 4-8 to 4-15
diurnal, 4-4 to 4-6, 4-17, 4-18
seasonal, 4-15 to 4-17, 4-52, 4-53
Wind chill, 3-23

X

X rays, atmospheric absorption, 6-7
solar emission, 16-10 to 16-19

Z

Zero-age main sequence, stars, 21-20, 21-22
Zodiacal light, 15-5, 18-1, 18-2
Zone of avoidance, 21-20
Zurich sunspot number, 15-7